Proceedings of SAIP2012
The 57th Annual Conference of the South African Institute of Physics

University of Pretoria
9 - 13 July 2012

Edited by Johan Janse van Rensburg

UNIVERSITEIT VAN PRETORIA
UNIVERSITY OF PRETORIA
YUNIBESITHI YA PRETORIA
Denkleiers • Leading Minds • Dikgopolo tša Dihlalefi

South African Institute of PHYSICS
THE VOICE OF PHYSICS IN SOUTH AFRICA

Department of Physics **www.up.ac.za/physics**

PUBLISHER: Department of Physics, University of Pretoria

The Proceedings of SAIP2012, the 57th annual conference of the South African Institute of Physics (SAIP) will only be available electronically on compact disk (CD) and on the SAIP website www.saip.org.za.

ISBN: 978-1-77592-070-0

SAIP2012

Proceedings of SAIP2012,
the 57th annual conference of the
South African Institute of Physics

Hosted by the University of Pretoria

9 – 13 July 2012
University of Pretoria
Pretoria
South Africa

Edited by
Johan Janse van Rensburg

SA Institute of Physics 2012 ISBN: 978-1-77592-070-0

Table of Contents

Message from the Conference Chair

The Physics Department of the University of Pretoria volunteered to host the 57th Annual SAIP conference in 2012 to coincide with its one hundredth year celebration. Prof PG Gundry, who was appointed in 1908 as professor of "Mathematics and Physics", became the head of the "Department of Physics" in 1912. It was this "unbundling" of physics into its own department that prompted the department to host this conference.

This conference was particularly memorable as it was held one week after the 4 July 2012 announcement by the ATLAS and CMS experimental groups at CERN's Large Hadron Collider that they had each observed a new particle in the mass region around 126 GeV. This particle is consistent with the Higgs boson predicted by the Standard Model. A number of South African physicists were actively part of this huge experimental undertaking and it was an honour to be able to arrange a special session on this discovery.

This was also the first time that a full session was dedicated to the growing field of biophysics. The development of biophysics as a specialist field is making steady progress. It is clear that there is exciting science to be done at this interface between traditional disciplines.

It is also fitting to thank the SAIP office, and in particular Mr Brian Masara, Ms Lynette White and Mr Roelf Botha, for their support given to the LOC.

Chris Theron

SAIP2012 Conference Chair

Message from the SAIP2013 Review Committee

The SAIP2012 review committee received 183 paper contributions towards the proceedings, and subjected these to a peer-review process. For each contribution, the review committee selected at least two independent reviewers that could provide impartial expert opinions. Two or more independent reviews for 156 papers were received from reviewers who had no conflicts of interest for the paper (declarations were made by all reviewers to indicate possible conflicts of interests that may have been overlooked by the review committee). Unfortunately, for 27 papers the full review process could not be completed, since two independent review reports could not be secured for these. The main challenges were to find appropriate reviewers, as well as obtaining timeous responses from the identified reviewers. It is with great regret that these 27 papers could not be included, since authors have put in a great deal of time and effort into these manuscripts.

A total of 146 subject specialists, of which 142 hold at least a PhD in Physics, assisted with the review process. Most of the reviewers were sourced within South Africa, while a few from other countries also offered their help. The review panel at the University of Pretoria consisted of 9 members, (all holding a PhD in Physics). This panel considered cases where reviewers' reports were in conflict or an additional review was required to satisfy the requirement for a full peer-review. The final selection of papers was made by the the review panel, based on the outcome of the peer-review process. A total of 105 contributions were finally accepted (57%), with each paper reporting on original research which has not been published previously.

The style used for the proceedings is the British Institute of Physics Conference Series, the same style used for the previous SAIP conference proceedings.

The review committee would like to express its gratefulness to all the reviewers, who diligently and timeously provided feedback to the manuscript assigned to them. The time and effort put into the writing of detailed feedback and suggestions is well appreciated.

Johan Janse van Rensburg

On behalf of the SAIP2012 Review Committee

Conference Chairs and Committees

SAIP2013 Conference Chair

Chris Theron, Department of Physics, University of Pretoria

SAIP2013 Programme Chair

Johan Janse van Rensburg, Department of Physics, University of Pretoria

SAIP Division Chairs

Division A: Japie Engelbrecht (Nelson Mandela Metropolitan University)
Division B: Simon Mullins (iThemba LABS)
Division C: Erich Rohwer (University of Stellenbosch)
Division D1: Patrick Woudt (University of Cape Town)
Division D2: Andrew Collier (University of Kwa-Zulu Natal)
Division E: Sam Ramaila (University of Johannesburg)
Division F: Freddie Vorster (Nelson Mandela Metropolitan University)
Division G: Frederik Scholtz (National Institute for Theoretical Physics)

Finance Chair

Walter Meyer, Department of Physics, University of Pretoria

Proceedings Editorial Team

Editor: Johan Janse van Rensburg (University of Pretoria)
Advisor: Ilsa Bason (UNISA)
Advisor and online administration: Roelf Botha (HartRAO and SAIP)
Online administration and PDF Compilation: Juan Grey (SAIP)

Review Panel and Sub-editors

Julien Dangbegnon (University of Pretoria)
Mmantsae Diale (University of Pretoria)
Tjaart Krüger (University of Pretoria)
Augusto Machatine (University of Pretoria)
Johan Malherbe (University of Pretoria)
Ncholu Manyala (University of Pretoria)
Walter Meyer (University of Pretoria)
Jackie Nel (University of Pretoria)
Chris Theron (University of Pretoria)
Claudia Zander (University of Pretoria)

List of Reviewers

Dr.	ALBERS, Claudia	University of Johannesburg
Prof.	ALLIE, Saalih	University of Cape Town
Prof.	AMOLO, George	University of Dar-es-Salam (Tanzania)
Dr.	ASANTE, Joseph	Tshwane University of Technology
Prof.	AURET, Danie	University of Pretoria
Dr.	BELLO, Abdulhakeem	University of Pretoria
Dr.	BIETENHOLZ, Michael	Hartebeeshoek Radio Astronomy Observatory (HartRAO)
Ms.	BOTES, Danniell	South African Nuclear Energy Corporation (Necsa)
Dr.	BOTHA, Andre	University of South Africa
Dr.	BOTHA, J R	Nelson Mandela Metropolitan University
Dr.	BOTHA, Lourens	Council for Scientific and Industrial Research
Dr.	BOTTCHER, Markus	North-West University
Dr.	BRAUN, Artur	Swiss Federal Laboratories for Materials Science and Technology (Germany)
Prof.	BRAUN, Moritz	University of South Africa
Prof.	BRITTON, David	University of Cape Town
Prof.	BURGER, Renier	North-West University
Dr.	BUTHELEZI, Zinhle	iThemba Labs
Dr.	CHANGUNDENGA, Jesman	University of Johannesburg
Prof.	CHAWANDA, Albert	Midlands State University (Zimbabwe)
Prof.	CHETTY, Nithaya	University of Pretoria
Dr.	CHURMS, Cecil	De Beers Technology South Africa
Dr.	CILLIERS, Pierre	South African National Space Agency (SANSA)
Prof.	CLEYMANS, Jean	University of Cape Town
Prof.	COMRIE, Craig	University of Cape Town
Prof.	CONNELL, Simon	University of Johannesburg
Prof.	CRESS, Catherine	University of the Western Cape
Dr.	CROSBY, Charles	Council for Scientific and Industrial Research
Dr.	DANGBEGNON, Kouadio Julien	University of Pretoria
Mr.	DE BEER, Frikkie	South African Nuclear Energy Corporation (Necsa)
Dr.	DEANE, Roger	University of Cape Town
Prof.	DEJENE, Francis	University of the Free-State
Prof.	DERRY, Trevor	University of the Witwatersrand
Dr.	DHLAMINI, Mokhotjwa	University of South Africa
Dr.	DIALE, Mmantsae	University of Pretoria
Dr.	DODOO-ARHIN, David	University of Pretoria
Prof.	DUVENHAGE, Rocco	University of Pretoria
Prof.	ENGELBRECHT, Japie	Nelson Mandela Metropolitan University
Dr.	FALTENBACHER, Andreas	University of the Witwatersrand
Prof.	FERREIRA, Stefan	North-West University
Dr.	FERRER, Phil	University of the Witwatersrand
Mr.	FISH, Derek	University of Zululand
Dr.	FRANKLYN, Chris	South African Nuclear Energy Corporation (Necsa)
Dr.	FRESCURA, Fabio	University of the Witwatersrand
Prof.	GIBBON, Tim	Nelson Mandela Metropolitan University
Prof.	GILBANK, David	South African Astronomical Observatory (SAAO)
Dr.	GOEDHART, Sharmila	South African Square Kilometer Array (SA SKA)
Dr.	HAMILTON, Andrew	University of Cape Town

Dr.	HARRIS, Richard	Mintek
Dr.	HATWAAMBO, Sylvester	University of Zambia
Prof.	HEISS, Dieter	University of Stellenbosch
Prof.	HEYDENRYCH, Mike	University of Pretoria
Dr.	HILONGA, Askwar	Nelson Mandela African Institution of Science and
Dr.	HLATSWAYO, Thulani	University of Pretoria
Dr.	IREETA, Winston Tumps	Nelson Mandela Metropolitan University
Prof.	JONES, Glyn	University of South Africa
Prof.	JOUBERT, Daniel	University of the Witwatersrand
Prof.	KARATAGLIDIS, Steven	University of Johannesburg
Dr.	KARSTEN, Aletta	Council for Scientific and Industrial Research
Prof.	KEARTLAND, Jonathan	University of the Witwatersrand
Dr.	KHAMLICH, Saleh	iThemba Labs
Prof.	KONRAD, Thomas	University of Kwa-Zulu Natal
Prof.	KROON, Ted	University of the Free-State
Dr.	KRÜGER, Tjaart	University of Pretoria
Dr.	LAWRIE, Elena	iThemba Labs
Dr.	LEEUW, Lerothodi	University of Johannesburg
Prof.	LINDSAY, Robert	University of the Western Cape
Prof.	LING, F C C	University of Hong Kong
Prof.	LOMBARDI, Enrico	University of South Africa
Dr.	LONZECHE, Lodya	SASOL
Dr.	MACHATINE, Augusto	University of Pretoria
Prof.	MADJOE, Reggie	North-West University
Dr.	MAFUSIRE, Cosmas	Council for Scientific and Industrial Research
Dr.	MAGNUS, Lindsay	South African Square Kilometer Array (SA SKA)
Dr.	MAKAKA, Golden	University of Fort Hare
Prof.	MALHERBE, Johan	University of Pretoria
Dr.	MALUTA, Eric	University of Venda
Dr.	MANYALA, Ncholu	University of Pretoria
Prof.	MANYALA, Reccab	University of Zambia
Dr.	MATHE, Bhekumusa	University of the Witwatersrand
Dr.	MATTHEWS, Alan	University of Kwa-Zulu Natal
Prof.	MEINTJIES, Pieter	University of the Free-State
Dr.	MEYER, Walter	University of Pretoria
Dr.	MOJI, Cable	University of Pretoria
Dr.	MOLEPO, Mahlaga	University of Pretoria
Dr.	MOOLLA, S	University of Kwa-Zulu Natal
Dr.	MOTHUDI, Bakang Moses	University of South Africa
Dr.	MTUNZI, Patience	Council for Scientific and Industrial Research
Dr.	MUJAJI, Marjorie	University of the Witwatersrand
Dr.	MUNYATI, Onesmus	University of Zambia
Dr.	MUNYEME, Geoffrey	Dyesol Australia
Prof.	MURONGA, Azwinndini	University of Johannesburg
Prof.	MWEENE, Habatwa	University of Zambia
Dr.	NAICKER, Vishnu	North-West University
Prof.	NAIDOO, Deena	University of the Witwatersrand
Dr.	NAIDOO, Mervin	University of the Witwatersrand
Dr.	NAIR, Padmanabhan	University of Johannesburg
Dr.	NEL, Jacqueline	University of Pretoria
Prof.	NETSHISAULU, Tom	University of Limpopo

Dr.	NEVELING, Retief	iThemba Labs
Prof.	NEWMAN, Richard	University of Stellenbosch
Dr.	NGOM, Balla Diop	iThemba Labs
Dr.	NKOSI, Steven	Council for Scientific and Industrial Research
Dr.	NOLTING, Volkmar	Vaal University of Technology
Prof.	NTWAEABORWA, Odireleng	University of the Free-State
Dr.	NYAMHERE, Cloud	University of Pretoria
Dr.	OOZEER, Nadeem	South African Square Kilometer Array (SA SKA)
Dr.	PAPKA, Paul	University of Stellenbosch
Mr.	PARE, Phillip	South African Nuclear Energy Corporation (Necsa)
Dr.	PRINSLOO, Aletta	University of Johannesburg
Dr.	PRINSLOO, Linda	University of Pretoria
Prof.	RAKITANSKI, Sergei	University of Pretoria
Dr.	RAMAILA, Sam	University of Johannesburg
Prof.	RAMPHO, Joel	University of South Africa
Dr.	RIBEIRO, Valerio	University of Cape Town
Dr.	RORO, Kittessa	Council for Scientific and Industrial Research - National Laser Centre
Prof.	ROUX, Stef	Council for Scientific and Industrial Research
Dr.	SCHMIDT, Matthias	University of Pretoria
Prof.	SCHOLTZ, Frederik	University of Stellenbosch
Prof.	SHARPEY-SHAFER, John	iThemba Labs
Dr.	SHEPPARD, Charles	University of Johannesburg
Dr.	SMIT, Kobie	Council for Scientific and Industrial Research
Dr.	SNYMAN, Izak	University of the Witwatersrand
Prof.	SPANIER, Felix	North-West University
Dr.	SPARROW, Raymond	Council for Scientific and Industrial Research
Prof.	STRYDOM, Andre	University of Johannesburg
Prof.	SWART, Hendrik	University of the Free-State
Prof.	TERBLANS, Koos	University of the Free-State
Prof.	THERON, Chris	University of Pretoria
Dr.	TRIAMBAK, Smarajit	University of the Western Cape
Dr.	UKPONG, Aniekan	University of Pretoria
Dr.	URGESSA, Zelalem	Nelson Mandela Metropolitan University
Dr.	UYS, Hermann	Council for Scientific and Industrial Research
Dr.	VÄISÄNEN, Petri	South African Astronomical Observatory (SAAO)
Prof.	VAN DYK, Ernest	Nelson Mandela Metropolitan University
Dr.	VAN SOELEN, Brian	University of the Free-State
Prof.	VENTER, Andre	Nelson Mandela Metropolitan University
Dr.	VENTER, Christo	North-West University
Dr.	VERMAAK, Jan	South African Nuclear Energy Corporation (Necsa)
Dr.	VORSTER, Frederik	Nelson Mandela Metropolitan University
Dr.	WARMBIER, Robert	University of the Witwatersrand
Dr.	WHEATON, Spencer	University of Cape Town
Prof.	WINKLER, Hartmut	University of Johannesburg
Prof.	WOOD, John	Georgia Institute of Technology
Prof.	WOUDT, Patrick	University of Cape Town
Dr.	WU, Lorinda	Council for Scientific and Industrial Research - National Laser Centre
Dr.	ZANDER, Claudia	University of Pretoria

Division A – Division for Condensed Matter Physics and Materials

Electrical properties of $Mn_{0.5}Co_{0.5}Fe_2O_4$ nanoparticle synthesized via high-energy milling technique

Hafiz M I Abdallah, Thomas Moyo

School of Chemistry and Physics, Westville Campus, University of KwaZulu-Natal, Private Bag X54001, Durban 4000, South Africa

hafizspin@gmail.com

Abstract. The $Mn_{0.5}Co_{0.5}Fe_2O_4$ sample was produced from high-purity metal oxides by high-energy ball milling method. Single-phase cubic spinel structure and nanoparticle structure of the synthesized sample were confirmed by X-ray diffraction (XRD) and high-resolution transmission electron microscopy (HRTEM). The results show that the produced powder of the as-prepared sample has average grain size of about 8 nm. Bulk samples in the form of pellets were also produced from the as-prepared sample for resistivity measurements. The temperature dependence of the electrical resistivity for samples sintered from 873 to 1373 K under argon atmosphere were studied using the four-probe method from room temperature to about 390 K. Two possible mechanisms for resistivity involving T^{-1} and $T^{-1/2}$ dependences were investigated which we associate with semiconducting and inter-grain conductivity respectively. The $T^{-1/2}$ dependence is found to fit the data better and predicts higher activation energies. The resistivity was observed to be sensitive to the surface of the pellet being probed and the annealing temperature.

1. Introduction

The Spinel ferrites are widely used in several applications due to the combination of electrical and magnetic properties [1]. These properties depend on the chemical composition, cation distribution, grain size and preparation method. The substitution by different magnetic or non-magnetic cations at different sites in ferrite systems can provide different types of electrical and magnetic properties. The ferrites are a group of oxides which have spinel structure. The large oxygen ions are packed close together in the face centred cubic arrangement. The smaller metal ions occupy the space between the oxygen ions. This leads to the formation of two kinds of oxygen polyhedra, namely tetrahedron (A site) and octahedron (B site) [2]. Ferrite materials have high resistance because the metal ions are isolated by oxygen ions from each other. In general, spinel ferrites behave like semiconductors with high resistivity. The electrical resistivity appears to obey an exponential dependence of the electrical resistivity with temperature. This also depends on the composition of the compound and the cation distribution. The resistivity is expected to be due to the presence of divalent Fe^{2+} and trivalent M^{3+} metal ions. The extra electron from Fe^{2+} or the positive hole from M^{+3} can move through the crystal lattice. The existence of Fe^{2+} results in n-type behaviour and p-type behaviour from M^{3+}. The movement of a charge carrier is described based on a hopping mechanism where the charge carrier jumps from one ionic site to another site as the temperature increases [3]. The hopping depends on the activation energy associated with energy barriers experienced by the electrons during the hopping

process. The electrical conductivity can also be described based on a granular tunnelling mechanism in which the charge carriers tunnel between neighbouring ferrite grains that are separated by grain boundaries [4]. In this report, we investigated the variation of resistivity as a function of T^{-1} and $T^{-1/2}$ respectively for $Mn_{0.5}Co_{0.5}Fe_2O_4$ spinel ferrite.

2. Experimental details

The $Mn_{0.5}Co_{0.5}Fe_2O_4$ compound was synthesized by the high-energy ball milling technique from $MnFe_2O_4$ and $CoFe_2O_4$ single-phase spinel ferrites. The experimental procedure employed here has been discussed elsewhere [5]. Single-phase formation and structure analysis of the samples was based on XRD data obtained at room temperature. The XRD spectra of the samples were obtained using CoK radiation with wavelength λ = 1.7903 Å on a Phillips diffractometer type PW1710. The average particle diameters of the powders were also obtained by high-resolution electron microscopy (HRTEM) measurement on a type Jeol_JEM-2100 instrument in order to confirm estimates of average particle size from XRD measurement. The D C resistivity measurements were carried out in air by the four-point probe method from about 300 to 400 K in a Proportional-Integral-Derivative (PID) controlled micro-oven. The electrical measurements were performed on both faces of the same pelletized sample annealed from 873 to 1373 K under argon atmosphere. The pellet was annealed for 6 h at each annealing temperature after being initially compacted in an evacuated 13 mm diameter ICL die at a pressure of 1.5×10^8 N m^{-2} for about 2 min. The pellet was positioned so as to ensure equal exposure to argon gas for the two faces in the furnace. In the present four-probe set-up the spacing between the probes was fixed to 0.2 cm. The pelletized sample studied had a thickness of about 0.06 cm. Hence, the relevant equation used to calculate resistivity was based on the formula

$$\rho = t(\pi/\ln 2)(V/I) \quad (1)$$

V is the measured voltage across the two inner probes and I is the current through the sample [6].

3. Results and discussion

Figure 1 shows the XRD diffraction patterns of the as-prepared sample and for annealed sample at 673 K for $Mn_{0.5}Co_{0.5}Fe_2O_4$. Typical HRTEM microstructure of the as-prepared sample is shown in figure 2. The grains appear to be nearly cubic in shape. The average crystalline size of 8 nm was estimated from XRD data by using Debye-Scherrer formula [5] which confirmed the HRTEM measurement. The bulk densities of the sample annealed at different temperatures were calculated using physical dimensions of the pellets [5]. Figure 3 shows the effect of the annealing temperature on the bulk density of the pellet.

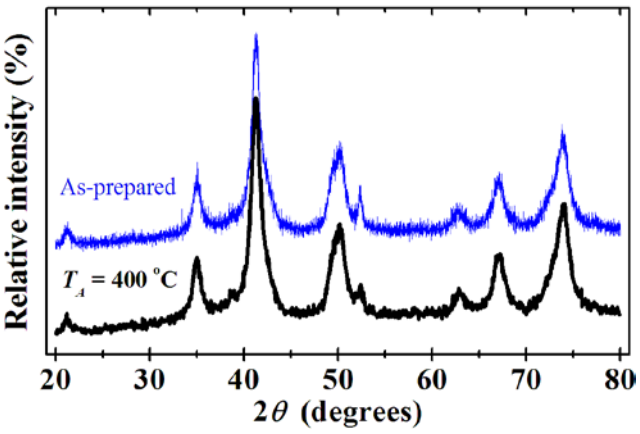

Figure 1. XRD of the as-prepared sample and sample annealed at 673 K of $Mn_{0.5}Co_{0.5}Fe_2O_4$ sample.

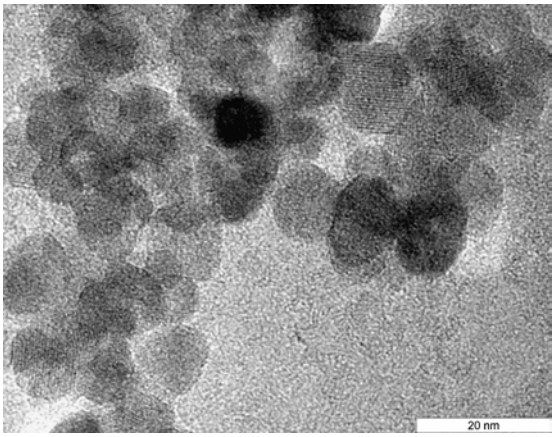

Figure 2. HRTEM image for the as-prepared $Mn_{0.5}Co_{0.5}Fe_2O_4$ compound.

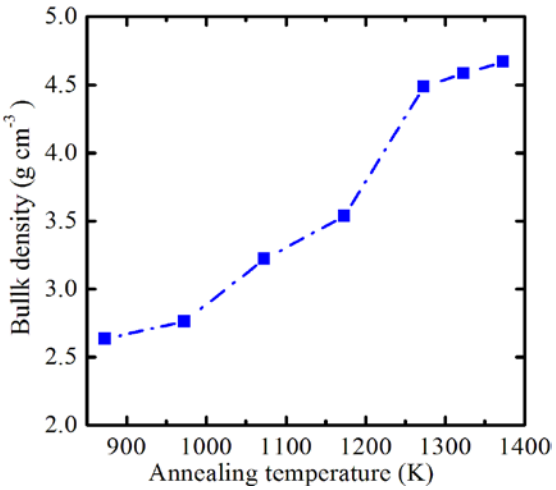

Figure 3. Variation of bulk density as a function of annealing temperature for $Mn_{0.5}Co_{0.5}Fe_2O_4$.

In this study, we have performed systematic measurements of the resistivity on a single pellet following each annealing procedure where we take into account the surface that is being probed. The two surfaces of a pellet slightly differ in appearance. One surface is on the shiny side (face 1) and the other is on the dull side (face 2). Two distinct sets of plots at higher (face 2) and lower (face 1) values of resistivities can be identified. Different characteristics of the two surfaces suggest slight non-uniformity in the compaction of the pellets. This suggests a concentration gradient across the thickness of the pellet.

Ferrites have been reported to exhibit semiconductor behaviour based on a hopping mechanism that obeys the Arrhenius equation [7] where the resistivity at a finite temperature varies as

$$\rho(T) = \rho(0)\exp(E_{a1}/k_BT). \quad (2)$$

E_{a1} is the activation energy which is the minimum energy needed for an electron to jump from one ion to a neighbouring ion and $\rho(0)$ is a constant. The activation energy depends on the magnetic state of a material. In the ordered state in a ferromagnet, the activation energy is lower compared to the value for a paramagnet due to the effect of magnetic spin-disorder. In the paramagnetic state, the sintering temperature decreases the concentration of the current carriers and this changes the conduction mechanism [7]. One way in which the ferrite electrical resistivity can be explained is through the Verwey-de Boer mechanism [8]. In this mechanism, the electrons are exchanged between the ions of different valence states amongst the same element in a compound. Increasing the measuring temperature may also lead to a random distribution of the ions over equivalent crystallographic lattice sites tetrahedral (A-site) or octahedral (B-site). The B site sublattices are known to be responsible for electrical resistivity in ferrites [9]. Therefore, partial reduction of Fe^{3+} to Fe^{2+}, Mn^{3+} to Mn^{2+} or Co^{3+} to Co^{2+} can be expected to occur in $Mn_{0.5}Co_{0.5}Fe_2O_4$. The variation of the resistivity with composition in ferrites can therefore be explained as an electron exchange transfer between the same elements [10]. The resistivity also depends on the sintering conditions and the number of ions which form during the preparation of such samples [8]. The electrical resistivity can also be explained on the basis of the tunnelling effect of electrons between charge carriers. In this process, the conductivity in granular materials occurs because of the transport of the electrical charge by tunnelling between grains. The charge carriers are generated from the transfer of electrons from neutral to neighbouring charged grains. The possible polaronic conduction process can therefore be written as: $Fe^2 \rightarrow Fe^{3+} + e^-$, $Mn^2 \rightarrow Mn^{3+} + e^-$, and $Co^2 \rightarrow Co^{3+} + e^-$. The variation of the tunnelling resistivity with temperature in granular metals strongly depends on the electrostatic charge energy which is needed to generate the positive and negative charged grains. In this system, the charge carriers can be thermally activated at high temperature. Sheng et al [11] have suggested that the temperature dependence of resistivity due to the tunnelling between neighbouring grains follows the equation

$$\rho(T) = \rho(0)\exp[2(E_{a2}/k_BT)^{1/2}] \quad (3)$$

where E_{a2} is the tunnelling activation energy between grains. The temperature variation of resistivity of our sample has therefore be tested against equations (2) and (3). Figures 4 and 5 show the variations of electrical resistivity as a function of T^{-1} and $T^{-1/2}$ respectively for a pellet of a $Mn_{0.5}Co_{0.5}Fe_2O_4$ sample which was annealed at 873, 973, 1073, 1173, 1273 and 1373 K under Ar atmosphere.

Annealing the samples under air atmosphere and its effect to the resistivity is not reported in this study. The variation of resistivity according to equation (2) is similar to that of semiconductor materials. This is associated with the hopping movements of electrons or holes between divalent and trivalent metal cations. In the present case for $Mn_{0.5}Co_{0.5}Fe_2O_4$ sample, the hopping is suspected to be between Fe^{2+} and Fe^{3+} (or Mn^{2+} and Mn^{3+} or Co^{2+} and Co^{3+}) ions through intervening oxygen anions. The obtained values of $E_A > 0.2$ eV suggest that conduction mechanism due to polaron-hopping [12]. The conduction mechanism in Mn-Co ferrite by using polaron hopping also indicated by discontinuity (break) in resistivity versus T at higher region [13]. Similar results have been reported for $Ni_xMg_{0.5-x}Cu_{0.1}Zn_{0.4}Fe_2O_4$ ferrites [13].

The resistivity measurements appear to distinguish the characteristics of the two surfaces. Higher resistivities were obtained when the dull surface (face 2) was probed. Therefore, any systematic measurements on different pellets must take into account the surfaces of the pellets being probed.

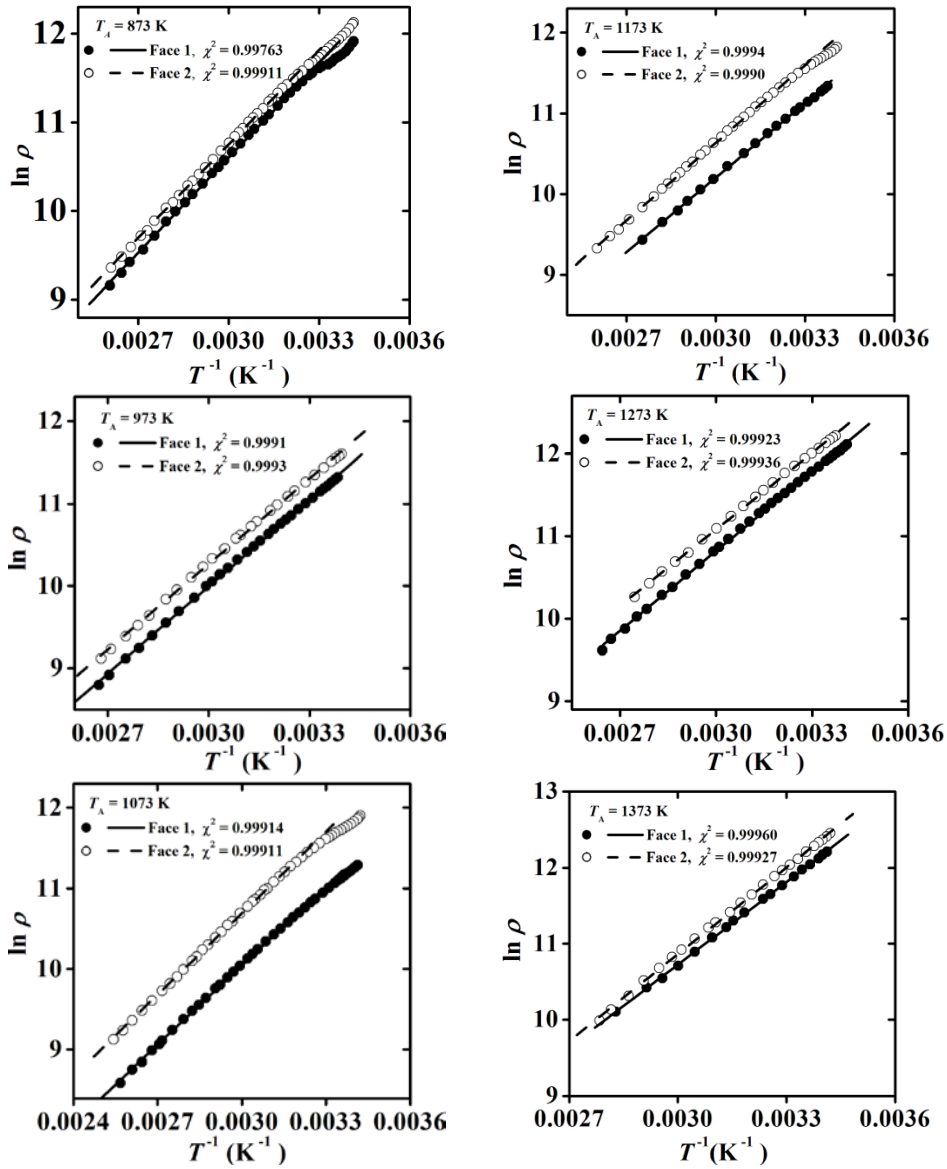

Figure 4 $\ln \rho$ versus T^{-1} for $Mn_{0.5}Co_{0.5}Fe_2O_4$ pellet samples annealed at 873, 973, 1073, 1173, 1273 and 1373 K. The *open-points* and *close-points* represent the resistivity data and *solid-line* and *dot-line* are the result of fittings to equation (2).

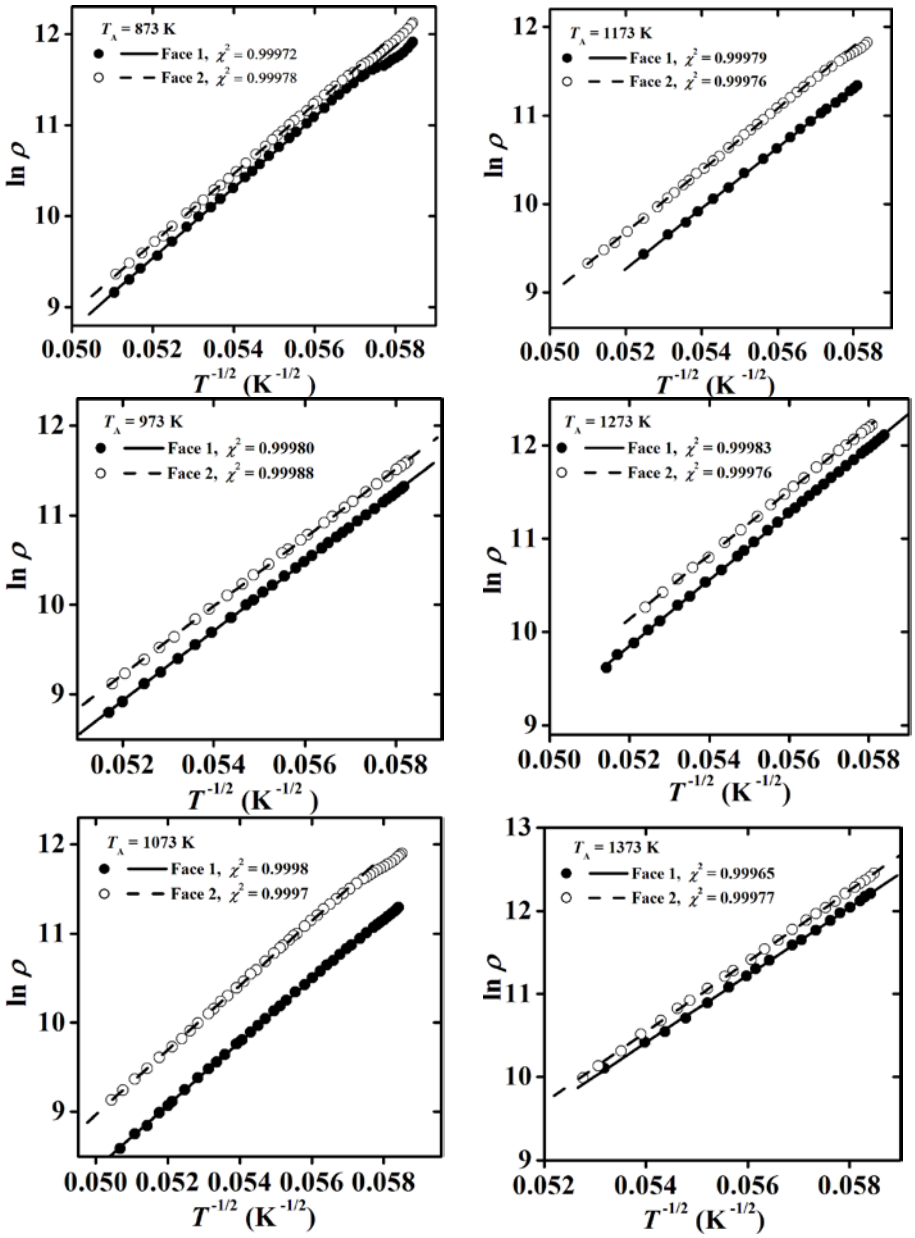

Figure 5. $\ln \rho$ versus $T^{-1/2}$ for $Mn_{0.5}Co_{0.5}Fe_2O_4$ pellet samples annealed at 873, 973, 1073, 1173, 1273 and 1373 K. The *open-points* and *close-points* represent the resistivity data and *solid-line* and *dot-line* are the result of fittings to equation (3).

Good linear fits are obtained to fits data in figures 4 and 5. Plots of $\ln \rho$ versus $T^{-1/2}$ have slightly better correlation coefficients to the plots $\ln \rho$ versus T^{-1} (average of 0.99914) than for movements between charged and neutral grains (average of 0.99977).

The values of E_{a1} and E_{a2} deduced from the slopes in figures 4 and 5 are plotted as a function of annealing temperature in figures 6. Similar trends are observed which indicate similar intrinsic behaviour in the measurements on either faces of the pellets. Minimum values of activation energies are obtained for annealing temperatures around 1173 – 1273 K. We suspect that for this range of annealing temperature, T_A, values the sample may be transforming from single-domain to multi-domain structure. The activation energies based on equation (2) are consistent with some previous

measurements [1, 14]. The resistivity based on tunnelling between grains gives much larger activation energies and better fits to the experimental data than that based on semiconductor behaviour. We suspect that higher activation energies would be required in order to promote conduction by hole or electron.

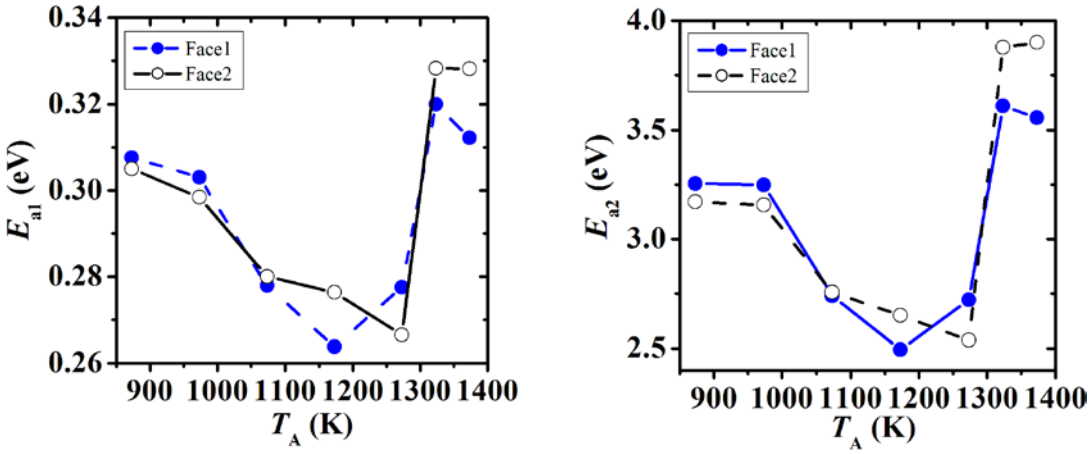

Figures 6. Variations of activation energy with annealing temperature for $Mn_{0.5}Co_{0.5}Fe_2O_4$ deduced from the best fits of equations (2) and (3).

4. Conclusions

We have made $Mn_{0.5}Co_{0.5}Fe_2O_4$ nanoparticle compounds using high-energy ball milling from $MnFe_2O_4$ and $CoFe_2O_4$ ferrites as starting materials. The temperature dependence of resistivity of $Mn_{0.5}Co_{0.5}Fe_2O_4$ nanosized compacts seems more favourable to the tunnelling effect of charge carriers between grains. Analysis of the resistivity based on tunnelling between grains gives much larger activation energies and better fits to the data. The resistivity and activation energy of a sample have been found to depend on the annealing temperature and the surface of the pellet being probed. The top or bottom surface of the pellet while in the die could make a difference. Our results show minimum activation energies at around 1173 K.

References

[1] Ashiq M, Saleem S, Malana M and Ur-Rehman A 2009 *J. Alloys Compd.* **486** 640
[2] Cullity B D and Graham C D 2009 *Introduction to Magnetic Materials*, 2nd edition, John Wiley & Sons, Hoboken, New Jersey p. 175-180
[3] Viswanathan B and Murthy V R K 1990 *Ferrite Materials* (Narosa Publishing House, New Delhi, India) p. 2-23, 25-37
[4] Roshen W A 2007 *J. Magn. Magn. Mater.* **312** 245
[5] Abdallah H M I, Moyo T and Msomi J Z 2010 *J. Phys.: Conf. Ser.* **217** 012141
[6] Bautista K 2003 *Four-Point Probe Operation* (Texas and Dallas University, 1st edition, USA)
[7] Thakur A, Mathur P and Singh M 2007 *J. Phys. Chem. Solids* **68** 378
[8] Devan R S, Kanamadi C M, Lokare S A and Chougule B K 2006 *Smart Mater. Struct.* **15** 1877
[9] El Hiti M A and Abo El Ata A M 1999 *J. Magn. Magn. Mater.* **195** 667
[10] El-Sayed M A 2003 *J. Magn. Magn. Mater.* **82** 583
[11] Sheng P, Abeles B and Arie Y 1973 *Phys. Rev. Lett.* **31** No. 1 44
[12] Bammannavar B K, Naik L R, Pujar R B and Chougule B K 2008 *Progress In Electromagnetics Research Letters* **4** 121
[13] Bachhav S G, Patil A A and Patil D R 2013 *Advances in Ceramic Science and Engineering* **2** 89
[14] Gul I H and Maqsood A 2008 *J. Alloys Compd.* **465** 227

Synthesis and characterization of europium activated lanthanum oxysulphide by sol-combustion method.

Ali AG, Dejene BF[a*] and Swart[b] HC.
[a]Department of Physics, University of the Free State (Qwaqwa Campus), Private Bag X13, Phuthaditjhaba, 9866, South Africa.
[b]Department of Physics, University of the Free State, P.O. Box 339, Bloemfontein, 9300, South Africa.
* Corresponding author: Tel: +27 58 718 6259; Fax: +27 58 718 5444; E-mail: aliag@qwa.ufs.ac.za

Abstract
Sol-combustion synthesis was used to obtain nanocrystalline La_2O_2S red-emitting phosphors. X-ray diffraction (XRD) was employed to determine that the powders in the as-synthesized samples were crystalline. Upon increasing La/S molar ratios, the crystallinity in the nanosized particles increased, which resulted in a higher photoluminescence emission intensity of these phosphors. Fourier-transform infrared spectrometry analysis showed that there is a negligible difference in the absorbed impurities with various molar ratios. Hence, it was concluded that the La/S molr ratio plays an important role in the luminescence intensity of these phosphors.

I. Introduction

Lanthanide (La) oxysulfides with high thermal and chemical stability are known as wide-bang gap (4.6-4.8 eV) materials suitable for doping ion activation [1]. Compared with the lanthanide oxides, oxysulfide is a more efficient phosphor with a broader excitation band. Therefore, the lanthanide oxysulfides become a very important family of inorganic materials that have high potential for applications in various fields, such as color television picture tubes [2], radiographic imaging [3], field emission displays [4, 5] and long-lasting phosphorescence [6-8]. Among them, Eu^{3+} activated lanthanide oxysulfide has been extensively investigated due to its very efficiency to be used as a red phosphor applied in television picture tubes.

In this paper we investigate the effect of varying fuel to host ratio in the luminescence intensity of europium activated lanthanum oxysulphide.

2. Experimental.

La $(NO_3)_3.6H_2O$, NH_2CSNH_2, $Eu(NO_3)_3.6H_2O$, ethanol, distilled water were mixed in required stoichiometric ratios and dissolved by stirring using magnetic stirrer for 5 -10 minutes. Mixture heated in an air tube furnace to ignition temperature of 400^0c. White foamy product obtained after combustion reaction. Several samples with different La/S molar ratios were then prepared via similar route. The formation mechanism for La_2O_2S and La (OH)- CO_3 was proposed.

The Photoluminescence spectrum was investigated by Cary Eclipse fluorescent spectrophotometer equipped with a 150 W xenon lamp as an excitation source with the slit of
1. 0 nm and scan speed of 240 nm min. To determine the average particle diameter and the phase of the samples, X-ray powder diffraction spectra were measured with a D8 Bruker Advanced AXS GmbH X-ray diffractometer using Cu *Ka* radiation at a wavelength of 0.154056 nm, the size and morphology of the as-prepared particles were carried out by using Scanning electron microscope, SHIMADZU SSX-550 SPERSCAN.

3. Results and Discussion.

3.1. Crystal structure.

Figure 1 shows that the XRD pattern of the La_2O_2S powders synthesized by the Sol-Combustion process at 400 °C. Majority of the peaks can be indexed as the pure hexagonal La_2O_2S phase
with cell constants *a*) 0.4047 nm, *c*) 0.6944 nm, which are close to the reported data (JCPDS Cards File: 27-0263)

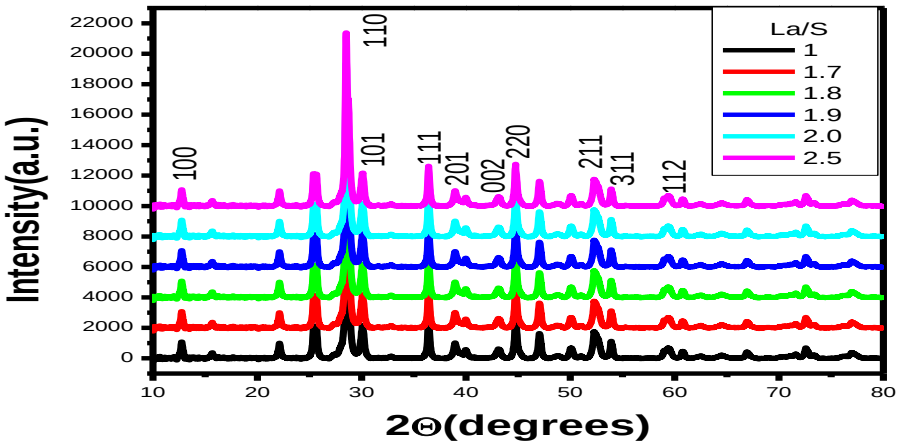

Figure1. X- ray diffraction of La_2O_2S with different La/S ratio

The average crystalline size of the La_2O_2S particles calculated using most intense reflection at 2θ= 28.596° are tabulated in table 1. Estimated according to the Scherrer's equation, the average crystalline size of the powders is determined to be 180 nm, which is basically in consistent with the crystalline size estimated by SEM images.

La/S	2θ°	$\beta 1/_2$	Grain size(nm)
1.0	28.586	0.37861	178
1.7	28.627	0.42738	175
1.8	28.608	0.4519	189
1.9	29.988	2.4113	175
2.0	3.0272	2.2562	182
2.5	33.657	2.0459	184

Table 1

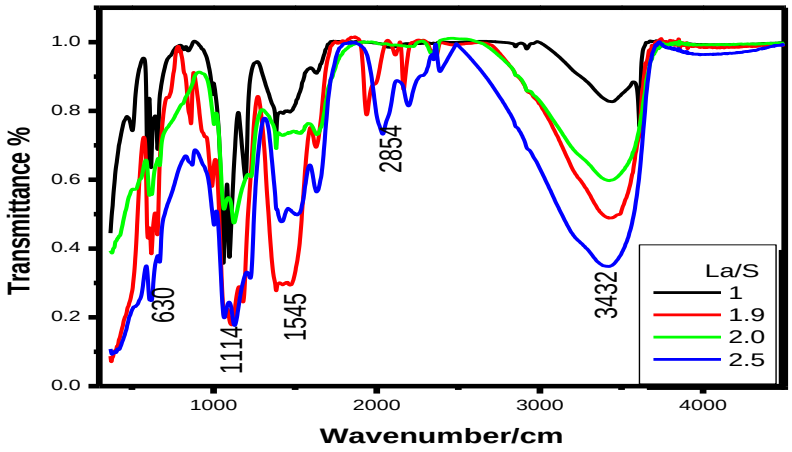

Figure 2 Fourier-transform infrared of the as-prepared La_2O_2S: Eu^{3+} powders.

To identify the presence of La_2O_2S, we employed FTIR studies in the wave number range 400 cm^{-1} to 4500 cm-1. From fig. 2 above its revealed that the strong broad absorption band at 3500 cm-1 is due to water [12]. The weaker absorption bands at 1114, 1545 and 2854 cm-1 are due to host La_2O_2S, since the dopant have no effect. The presence of the vibrational peaks at around 630 cm-1 corresponds to La-O stretching modes [13], because by increasing La/S molar ratios the bonds also increase.

3.2 Morphology

Figure 3 shows SEM images of La_2O_2S: Eu^{3+} nanocrystalline powders. It is obvious that all the powders yield nanoparticles and they tend to aggregate together. The images showed that the morphology consisted of a foamy, porous agglomeration and a continuous three-dimensional network. The agglomerates ranged in size between 5 and 20 mm, while the primary particles ranged in size between 175 to 184 nm. The average sizes of the nanoparticles are about 180 nm.

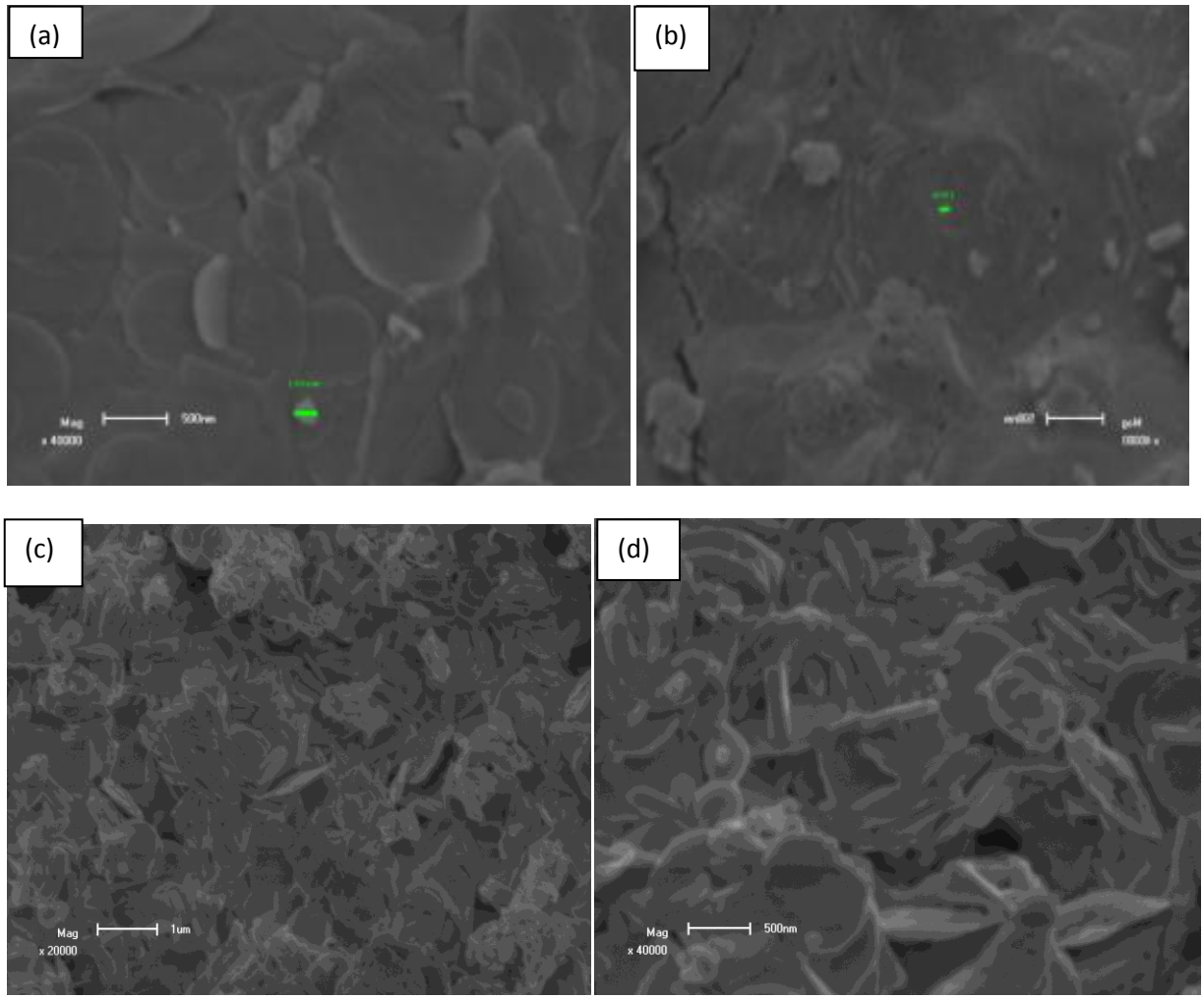

Fig.3(a)-----(b)----(c)-----(d)----(e)----- SEM micrographs of the as-prepared La_2O_2S: Eu^{3+} powders at 40000 field of view.

3.3 Photoluminescence

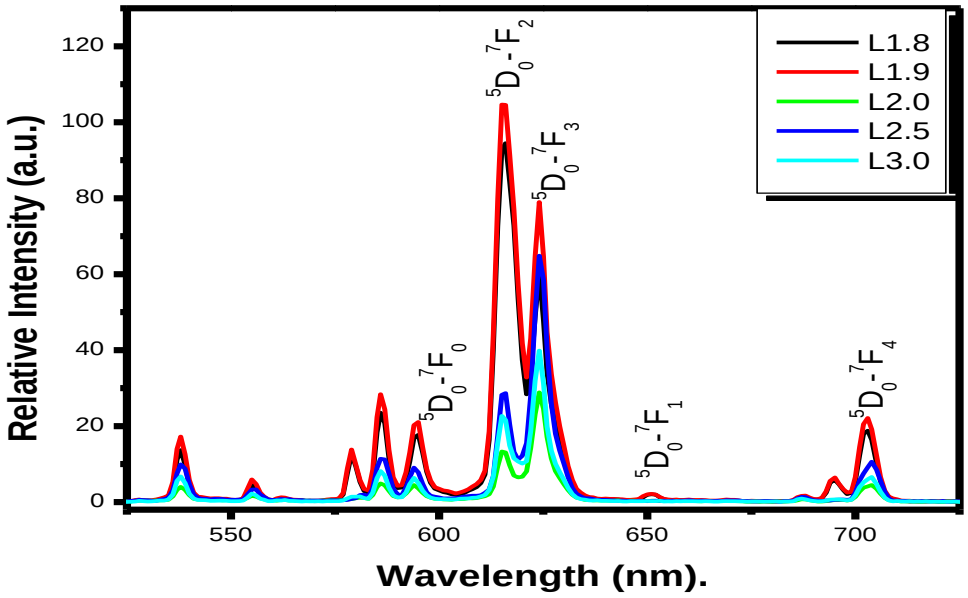

Fig.4 PL emission spectra of La_2O_2S with different La/S molar ratios.

Fig.4. shows the emission spectra of Eu^{3+} which are assigned to $^5D_0 \rightarrow {}^7F_{0,\,1,2,3,4}$ transitions of Eu^{3+}. There is no obvious difference in all the emissions of samples doped with Eu^{3+} except the peak position shifted at La/S molar ratios of 2.5 at 615nm wavelength. The peak intensity quenches at a wavelength of 624nm.

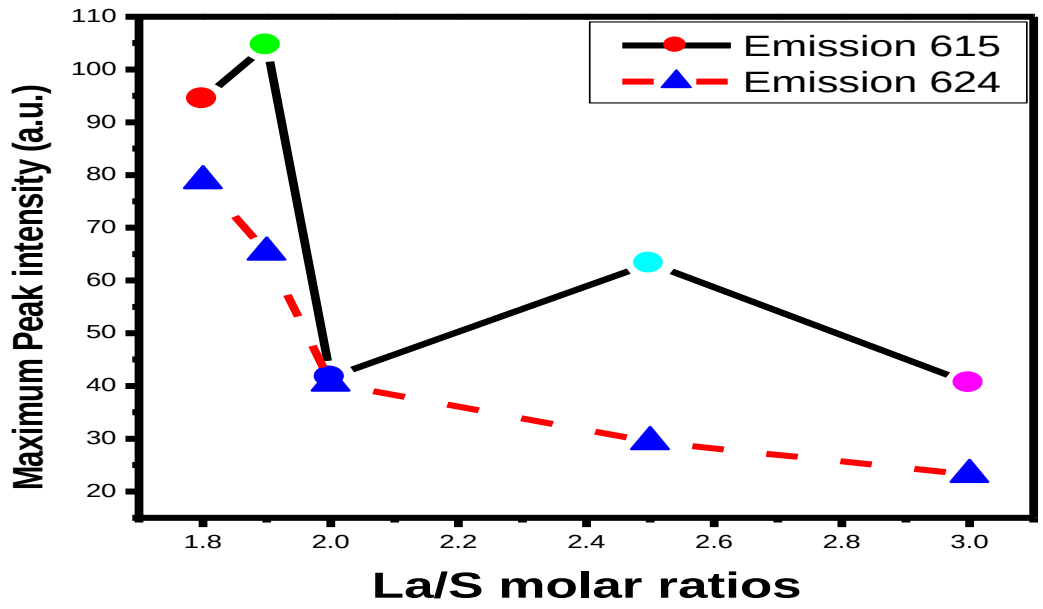

Fig.5 Graph of La/S molar ratio versus maximum peak intensity.

The graph of maximum PL intensity of the as-prepared powders as a function of La/S molar ratios is shown in Fig.5. The emission peak intensity decreased when the La/S molar ratio increased, and a maximum value was found when La/S= 1.9, thereafter the emission intensity quenches gradually. Persistent luminescence curves of the phosphor powders were shown in the fig. 6. It can be seen from the curve that the powders showed differences in initial intensity and medium persistence when the powders were efficiently activated by UV lamp. The results indicate that the initial luminescence intensity and the decay time of phosphors are enhanced with a decrease in the La/S molar ratios..

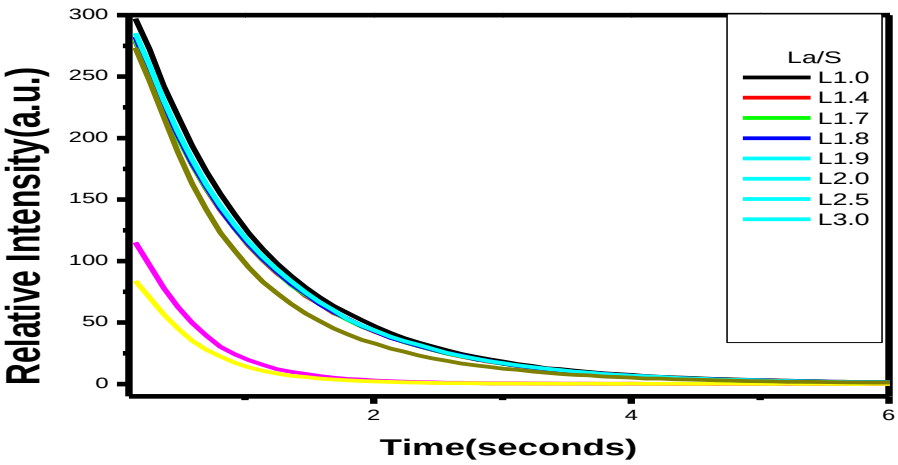

Fig.6 Afterglow characteristics of La_2O_2S with different La/S molar ratios.

The decay behavior can be analyzed by curve fitting, relying on the following triple exponential equation:
$I= A_1 \exp(-t/\tau_1) + A_2 \exp(-t/\tau_2) + A_3 \exp(-t/\tau_3)$. ---------- (1)
Where I is phosphorescence intensity, A_1, A_2, and A_3 are constants, t is time, τ_1, τ_2, and τ_3 are decay constants, deciding the decay rate for rapid, medium and slow exponentially decay components, respectively. The fitting results of parameters t_1, t_2 and t_3 are listed in Table 2 below.

La/S	1.0	1.4	1.7	1.8	1.9	2.0	2.5	3.0
Components				Decay	Const.(s)			
Fast(τ_1)	0.97	0.95	0.91	0.88	0.82	0.76	0.68	0.54
Medium(τ_2)	1.08	0.99	0.97	0.87	0.75	0.63	0.58	0.46
Slow(τ_3)	3.43	3.23	3.17	3.06	2.96	2.75	2.14	1.98

Table 2 Results for the fitted decay curves of the phosphor powders with different La/S molar ratios.

Three components namely slow, medium and fast are responsible for the persistent luminescence from the synthesized phosphor. A trend can be observed (fig.7) that the decay constants of the phosphors decrease gradually with the increasing La/S molar ratios.

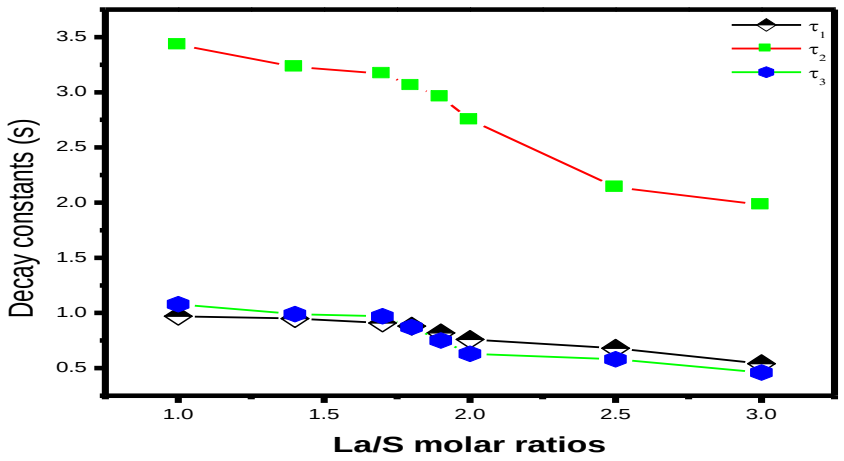

Fig.7 Graph of decay constants verse La/S molar ratios.

4. Conclusions

The XRD pattern of as-synthesized powder revealed that the La_2O_2S phase crystallized directly from the combustion reaction with fuel to oxidizer ratios at ignition temperatures of 400^0C. Powders synthesized with a lower La/S ratio, were contaminated by residual carbonaceous material. De-hydration of the reactants was crucial for the successful synthesis of the oxysulfide phase. SEM images of as-synthesized powders showed that the morphology consisted of a foamy, porous agglomeration and a continuous three-dimensional network.

Acknowledgement

The authors would like to acknowledge National Research Foundation (NRF) of South Africa and University of the Free State (UFS) for financial support.

References

[1] P.Majewski , M.Rozumek, H.Schluckwerder, F. Aldinger, Int. J. Inorganic Mater. 3 (2001) 1343.
[2] Garcia-Murillo, C. Luyer, C. Garapon, C. Dujardin, E. Bernstein, C. Pedrini, J. Mugnier, Opt. Mater. 19 (2002) 161.
[3] W. Jungowska, J. Thermal Anal. Calorimetry 60 (2000) 193.
[4] T, Feldmann, Justel, C. Ronda, P. Schmidt, Adv. Funct. Mater. 13 (7) (2003) 511.
[5] Y. Nakanishi, in: Proc. of the III Int. meeting on Information Display, IMID, Daegu, Korea, 2003, p. 203.
[6] V.L. Levshin, M.A. Konstantinova, E.A. Trapeznikova, On the application of rare-earth elements in the chemistry of phosphors, in: Rare-earth Elements, USSR AN Publishing, Moscow, 1959, p. 314.
[7] T. Hisamune, Technical trend of phosphors for plasma display panels, in: Proceedings of the 9th International Display Workshops, 2002, p. 685.
[8]. T. Justel, H. Nikol and C. Ronda. Angew. Chem. Int. 37 (1998), 3085.
[9]. S. Shionoya and W.M. Yen, Editors, Phosphor Handbook, CRC Press, Boca Raton, FL (1998).
[10]. C.F. Bacalski, M.A. Cherry, G.A. Hirata, J. Mckittrick, J. Mourant, J. Soc. Inf. Display (Suppl-1) (2000) 93.
[11]. G.C. Kim, H.L. Park and T.W. Kim. Mater. Res. Bull. 36 (2001), p.1603.
[12]. M. Kottaisamy, D. Jeyakumar, R. Jagannathan and M.M. Rao. *Mater. Res. Bull.* **31** (1996), p. 1013.
[13]. L.E. Shea, J. Mckittrick, O.A. Lopez, E. Sluzky and M.L. Phillips. *J. Soc. Inf. Display* **5** (1997), p. 117.
[14]. J. McKittrick, L.E. Shea, C.F. Bacalski and E.J. Bosze. *Displays* **19** (1999), p. 169.
[15]. K.C. Patil and S. Ekambaram. *J. Alloys Compounds* **248** (1997), p. 7.

Stable charge states and half-metallic ferromagnetic ordering in Fe-doped diamond

E M Benecha[1] **and E B Lombardi**
Department of Physics, University of South Africa, P.O Box 392, UNISA 003, Pretoria, South Africa

E-mail: ebenecha@gmail.com

Abstract. Half-metallic ferromagnetic semiconductors are of considerable interest for the injection and transport of spin polarised currents necessary for spintronic device development. We report *ab initio* pseudopotential DFT calculations on the magnetic ordering properties of Fe-doped diamond and show that half-metallic ferromagnetic ordering can be achieved in diamond – which is a well known material for its extreme properties – by incorporating Fe^{+1} at the substitutional lattice site. We show that substitutional Fe^{+1} possesses a magnetic moment of 1.0 μ_B per atom, and a large ferromagnetic stabilization energy of 33 meV, with the Fermi level crossing bands for only the spin-up orientation. We predict substitutional Fe^{+1} to be the most stable form of Fe in *p*-type boron doped diamond; co-doping with boron is likely to further increase the spin charge concentration.

1. Introduction

Half-metallic ferromagnetic semiconductors (HMFS) by definition have only one spin component (either spin-up or spin-down) available for conduction, with the Fermi level crossing bands for only one spin orientation, and a band gap for the other spin orientation [1]. Such asymmetric electronic density of states for different spin channels at the Fermi level, in principle, means that electrical current in half-metallic materials can be completely spin polarised, and therefore HMFS materials are of considerable interest in spintronic device applications (such as memory devices and computer processors [2]) for injection and transport of highly spin polarised currents.

Half-metallic band structures have theoretically been predicted for certain ferromagnetic materials, mainly in Heusler alloys [3-5], among others [1], and were first experimentally confirmed in manganese perovskite [1]. In view of the potential application of HMFS materials in achieving spin-based electronic devices, substantial research efforts have been made towards understanding and improving the mechanisms of spin injection, transport and detection in this class of materials, but low Curie temperatures (T_C) and lack of other fundamental material properties [6] has remained a major challenge towards practical implementation in room temperature device applications. Therefore there is a need to explore new half-metallic ferromagnetic materials which may successfully be used for room temperature spintronic applications.

The prediction that the T_C of a Diluted Magnetic Semiconductor (DMS) scales with the host semiconductor's lattice constant a_0 as $1/a_0^3$ [7,8] makes diamond an excellent candidate for high T_C spintronic applications since it has the smallest lattice constant compared to all other known

[1]Author to whom correspondence should be addressed.

semiconductors. In addition, diamond is a promising material for many electrical and electronic applications due to its high electrical breakdown field and excellent thermal and electrical conductivities, compared to other semiconductors [9,10], which makes diamond an attractive material for the development of spin-based electronic devices in the emerging field of spintronics.

In this study, we report the energetic and magnetic ordering properties of Fe-doped diamond using *ab initio* pseudopotential DFT calculations, and show that diamond is likely to become a half-metallic ferromagnetic semiconductor which may be considered for high T_C spintronic device applications.

2. Computational details

The formation energy, stable structures and magnetic ordering properties of Fe in diamond, were modelled at various lattice sites and charge states, using *ab initio* pseudopotential Density Functional Theory, as implemented in the CASTEP code [11]. Formation energy and band structure calculations were carried out using a 64-atom diamond supercell constructed from $2 \times 2 \times 2$ conventional fcc diamond unit cells with an optimized lattice constant of 3.569 Å, in close agreement with the experimental value of 3.567 Å [12]. Full geometry optimization was performed without any symmetry or spin restrictions, with the Fe atom in various charge states (+2, +1, 0, -1, -2) placed at the divacancy, substitutional, tetrahedral interstitial or hexagonal interstitial lattice sites in a diamond supercell. For each lattice site and charge state, various initial positions of the Fe atom were considered, while the initial spin was systematically varied (from 0 μ_B to 6 μ_B) in order to determine the most stable geometries and spin states.

The Perdew-Burke-Ernzerhof generalized gradient approximation (GGA) [13] was used to treat the exchange-correlation effects of electron-electron interactions, together with Ultrasoft Vanderbilt pseudopotentials [14] incorporating non-linear core corrections [15,16] for the Fe atom.

A $4 \times 4 \times 4$ Monkhorst-Pack grid sampling [17] for integration over the Brillouin zone (32 *k*-points in the irreducible wedge of the Brillouin zone) was employed for spin and geometry optimization, with a planewave cut-off energy of 310 eV. Increasing the number of *k*-points or plane wave cut-off energy resulted in negligible changes in the total energy and structural relaxation effects (less than 10^{-4}eV and 10^{-3} Å, respectively).

In order to determine the energetically most favourable site of Fe in the diamond lattice as a function of charge state, the formation energy, E_f of Fe in the diamond supercell was calculated for each lattice site and charge state from

$$E_f^q = E_T - \sum_i n_i \mu_i + q\left(\varepsilon_V + \varepsilon_F\right),$$

where E_f^q is the total energy of the diamond supercell in a charge state q, while μ_i is the chemical potential of each atomic species, with n_i atoms per atomic species; ε_F is the Fermi energy measured relative to the energy of valence band maximum ε_V.

To predict the ground state magnetic ordering and other possible magnetic states in Fe-doped diamond, magnetic interactions were modelled using a 128 atom diamond supercell containing two Fe atoms (corresponding to an impurity concentration of 1.56 %) separated by an effective distance of two diamond lattice constants (7.138Å). For each charge state, different spin configurations corresponding to ferromagnetic, antiferromagnetic and nonmagnetic spin alignments of the Fe atoms were allowed so as to establish the most stable magnetic ordering and magnetic stabilization energies. Calculations of the energy differences between the different spin configurations and magnetic ordering were done using the final geometries obtained from the 64 atom supercellcalculations, using a well converged $4 \times 4 \times 2$ Monkhorst-Pack mesh of *k* points. Full geometry optimization using the enlarged 128 atom supercell in selected cases resulted in no changes in geometries or induced magnetic moments, with negligible changes in the magnetic stabilization energies (less than 0.01 meV). This approach has previously been used to successfully predict magnetic ordering in other semiconductors and oxides [18-22].

3. Results and discussion

3.1. Formation energy and stable charge states

The calculated formation energies of Fe for the most stable charge states in *p*-type (B-doped), and *n*-type (N- or P-doped) diamond at the divacancy and substitutional sites are summarized in table 1. At the interstitial sites (not shown), we find the formation energy of Fe to be considerably higher (by at least ~5 eV) compared to the substitutional or divacancy sites in any charge state [23], which makes it unlikely for interstitial Fe to be observed in diamond at equilibrium conditions. Importantly, we find the formation energy of Fe in diamond at any lattice site to be significantly dependent on the charge state (and hence the type of diamond doping), with the positive or negative charge states being significantly lower in energy in *p*-type and *n*-type diamond, respectively, compared to the neutral charge state.

We predict substitutional single positive Fe_S^{+1} and doubly positive iron Fe_S^{+2} to be the most favourable charge states in *p*-type diamond for Fermi energies close to the top of the valence band, while the substitutional neutral iron Fe_S^{0} is the most stable charge state in intrinsic diamond. In contrast, we find doubly negative iron at a divacancy Fe_{2V}^{-2} to be the most stable charge state in *n*-type diamond for Fermi energies ranging from the middle of the diamond band gap to the conduction band minimum (Table 1). This suggests that the most stable form of Fe in diamond is strongly dependent on the type of diamond doping (intrinsic, *p*-type or *n*-type), and therefore on the position of the Fermi level as influenced by other impurities (such as boron, nitrogen or phosphorus) in diamond.

Table 1: Formation energies and optimized point symmetries of Fe in different charge states (+2, +1, 0, −1, −2), together with carbon nearest neighbour (C_{NN}) distortions at divacancy and substitutional lattice sites in diamond. Numbers in brackets indicate the multiplicity of each Fe-C_{NN} distortion. C_1 indicates a relaxation with no unique symmetry. Formation energies are given in *p*- and *n*-type diamond, with Fermi levels pinned to acceptor or donor levels of boron (Ev + 0.37 eV, *p*-type), as well as nitrogen (E_c − 1.6 eV, *n*-type) or phosphorus (E_c − 0.6 eV, *n*-type), respectively. Lowest formation energies at each lattice site in each type of doped diamond are indicated in bold.

	Formation energy, E_f(eV)			Symmetry	Fe-C_{NN} distortion (Å)	Fermi energy (eV)
	B-doped	N-doped	P-doped			
(a) Divacancy Fe						
Fe^{+2}	6.42	13.46	15.46	D_{3d}	0.10(6)	-
Fe^{+1}	**6.04**	9.56	10.56	C_2	0.24(2), 0.09(2), -0.05(2)	0.00 - 0.87
Fe^{0}	6.54	6.54	6.54	C_1	0.20(2), 0.07, 0.06, -0.050(2)	0.87 - 2.46
Fe^{-1}	8.90	5.38	4.38	D_{3d}	0.05(6)	-
Fe^{-2}	10.72	**3.68**	**1.68**	D_{3d}	0.04(6)	2.46 - 5.49
(b) Substitutional Fe						
Fe^{+2}	**5.62**	12.66	14.66	T_d	0.22(4)	0.00 - 0.37
Fe^{+1}	**5.62**	9.14	10.14	T_d	0.21(4)	0.37 - 0.98
Fe^{0}	6.23	**6.23**	6.23	T_d	0.19(4)	0.98 - 4.64
Fe^{-1}	10.50	6.98	**5.98**	C_{3v}	0.20(3), 0.94	4.64 - 4.89
Fe^{-2}	15.25	8.21	6.21	T_d	0.21(4)	4.89 - 5.49

3.2. Magnetic interaction

We find substitutional Fe_S^{+1} and Fe_S^{+2} iron, which are the energetically most stable charge states in *p*-type diamond, order ferromagnetically with significant magnetic moments of 1.0 μ_B and 1.8 μ_B per atom, and ferromagnetic stabilization energies (ΔE) of 33.3 meV and 7.5 meV, respectively. On the other hand, we find the spin interactions in divacancy iron Fe_{2V}^{-2}, which is the most stable charge state in *n*-type diamond, to be antiferromagnetic, with the ferromagnetic spin state being higher in energy by 1.7 meV compared to the antiferromagnetic spin state. In intrinsic diamond, however, we find the most stable charge state, substitutional iron Fe_S^0, to be non-magnetic.

Since the achievable Curie temperature in a DMS is proportional to its ferromagnetic stabilization energy, $\Delta E = E_{FM} - E_{AF}$ [24], our results therefore indicate that substitutional iron in the single positive charge state Fe_S^{+1} may order ferromagnetically in *p*-type diamond at significantly larger Curie temperatures compared to other transition metals in diamond which have been considered so far [25,26].

To assess the spin character of the impurity bands at the Fermi level in Fe-doped diamond, Figure 1 shows the calculated spin-up and spin-down band structures of ferromagnetic Fe^{+1} doped-diamond at the substitutional site, while Figure 2 illustrates the corresponding spin polarised partial density of states, showing the contribution from Fe and the sum of carbon orbitals to the impurity bands, respectively. It is evident that incorporation of Fe^{+1} into diamond induces strongly spin-polarised impurity bands into the diamond band-gap, while maintaining the semiconducting property of diamond. These impurity bands are seen to originate from *s,p-d* hybridization between carbon 2*s*, 2*p* and Fe 3*d* orbitals. In addition, we find that the Fe 4*p* orbitals also make a significant contribution to the unoccupied spin-up and spin-down bands in the middle of the band gap, though they are absent from the partly occupied spin-down bands lower in the band gap.

Interestingly, the Fermi level in substitutional Fe_S^{+1}-doped diamond crosses bands in only one spin channel, the spin-down bands. Consequently, electrons at the Fermi level will be exclusively spin-down polarized, with the spin-up band acting as an insulator for the spin-up electrons, indicating that substitutional Fe^{+1}-doped diamond is a half-metallic ferromagnetic semiconductor. This is particularly significant for efficient spin injection of spin polarized current in spintronic device applications, since charge carriers travelling at the Fermi surface will undergo 100% spin polarisation.

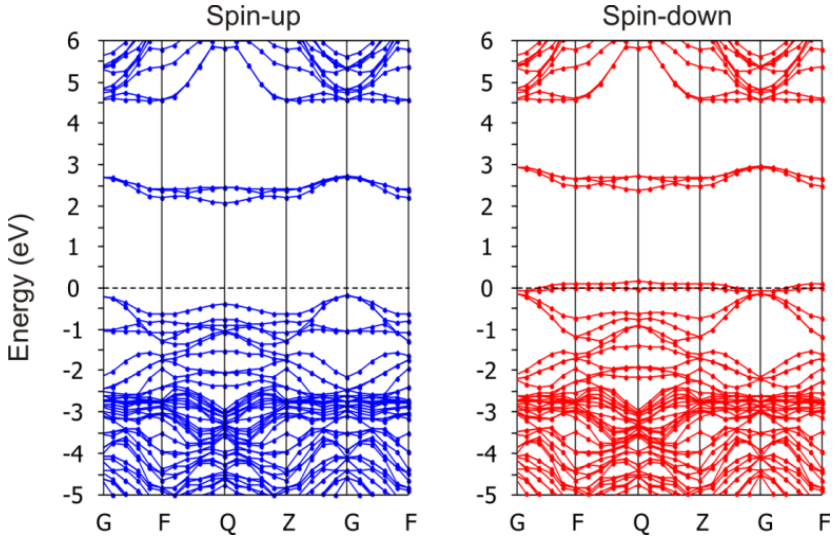

Figure 1: Spin-up and spin-down band structures of Fe^{+1} doped diamond illustrating half-metallicity of states at the Fermi level. Energies are relative to the respective Fermi levels, shown with horizontal dashed lines. Dots correspond to data points; lines guide the eye.

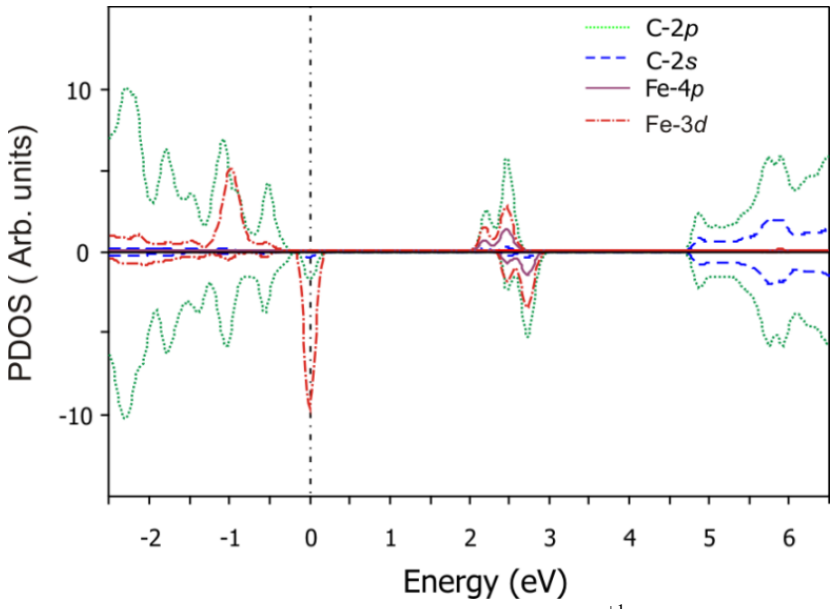

Figure 2: Partial density of states (PDOS) of substitutional Fe^{+1} in diamond. All energies are relative to the Fermi energy shown with the vertical dashed line.

4. Conclusion

The energetic stability and magnetic ordering properties of Fe-doped diamond have been investigated using *ab initio* pseudopotential DFT calculations at various charge states and lattice sites. We find the formation energy of Fe in diamond at any lattice site to be significantly dependent on the charge state and hence the type of diamond doping (intrinsic, *n*-type or *p*-type), with the positive or negative charge states having lower formation energies in *p*-type and *n*-type diamond, respectively, compared to the neutral charge state. Similarly, the magnetic properties of Fe-doped diamond are also strongly dependent on the charge state and the type of diamond doping, and therefore on the position of the Fermi level in the diamond band gap as influenced by other impurities (such as boron, nitrogen or phosphorus) in diamond samples.

We predict substitutional Fe_S^{+1} and Fe_S^{+2} to be the most favourable charge states in *p*-type diamond for Fermi energies close to the top of the valence band, while divacancy Fe_{2V}^{-2} is the most stable charge state in *n*-type diamond for Fermi energies ranging from the middle of the diamond band gap to the conduction band minimum. Importantly, we find that substitutional Fe_S^{+1} orders ferromagnetically in diamond with a magnetic moment of 1.0 μ_B and a large ferromagnetic stabilization energy of 33.3 meV. The impurity bands at the Fermi level exhibit a half-metallic character, with the Fermi level crossing bands in only the spin-down bands, indicating that substitutional Fe^{+1}-doped diamond is a half-metallic ferromagnetic semiconductor which islikely to order ferromagnetically with higher Curie temperatures, than has previously been achieved in other semiconductors [24]. In addition, we have subsequently shown [27] that the interaction remains strongly ferromagnetic at all the Fe-Fe separations considered (up to two lattice constants), while some clustering of Fe atoms may occur after high temperature annealing.

5. References

[1] Katsnelson M I, Irkhin V Y, Chioncel L, Lichtenstein A I and R.A. de Groot 2008 *Rev. Mod. Phys*. **80** 315
[2] Awschalom D D and Kikwaka J 1999, *Phys. Today* 33
[3] Picozzi S, Continenza A and Freeman A J 2002 *Phys. Rev.* B **66** 094421
[4] Galanakis I 2005 *Phys. Rev.* B **71** 012413
[5] Wurmehl S, Fecher G H, Kandpal H C, Ksenofontov V, Felser C and Lin H-J 2006 *Appl. Phys.*

Lett. **88** 032503
[6] Wolf S A, Awschalom D D, Buhrman R A, Daughton J M, von Molnar S, Roukes M L, Chatcehlkanova A Y and Treger D M 2001 *Science* **294** 1488
[7] Dietl T, Ohno H, Matsukura F, Cibert J and Ferrand D 2000 *Science* **287** 1019
[8] Dietl T, Ohno H and Matsukura F 2001 *Phys. Rev.* B **63** 195205
[9] Wort J H and Balmer R S 2008 *Mater. Today* **11** 22
[10] Kalish R, 2007 *J. Phys. D: Appl. Phys* **40** 6467
[11] Clark S J, Segall M D, Pickard C J, Hasnip P J, Probert M J, Refson K and Payne M C 2005 *Zeitschrift fuer Kristallographie* **220** 567
[12] Donnay J D H and Ondik H M 1973 *Crystal Data: Determinative Tables Vol. 2, 3rd ed.* (US Department of Commerce - National Bureau of Standards - JCPDS)
[13] Perdew J P, Burke K and Ernzerhof M 1996 *Phys. Rev. Lett.* **77** 3865
[14] Vanderbilt D 1990 *Phys. Rev.* B **41** 7892
[15] Fabris S, de Girancoli S, Baroni S, Vicario G and Balducci G 2005 *Phys. Rev.* B **72** 237102
[16] Fabris S, de Gironcoli S, Baroni S, Vicario G and Balducci G 2005 *Phys. Rev.* B **71** 041102(R)
[17] Monkhorst H J and Pack J D 1976 *Phys. Rev.* B **13** 5188
[18] Kronik L, Jain M and Chelikowsky J R 2002 *Phys. Rev.* B **66** 041203
[19] Pardo V, Blaha P, Iglesias M, Schwarz K, Baldomir D and Arias J E 2004 *Phys. Rev.* B **70** 144422
[20] Osuch K, Lombardi E B and Adamowicz L 2005 *Phys. Rev.* B **71** 165213
[21] Osuch K, Lombardi E B and Gebicki W 2006 *Phys. Rev.* B **73** 075202
[22] Los A and Los V 2010 *J. Phys.: Condens. Matter* **22** 245801
[23] Benecha E M and Lombardi E B *in Proceedings of SAIP 2011, the 56th Annual Conference of the South African Institute of Physics*, p 20 ISBN: 978-1-86888-688-3
[24] Sato K, Schweika W, Dederichs P H and Yoshida H K 2000 *Phys. Rev.* B 70 201202(R)
[25] Benecha E M and Lombardi E B 2011 *Phys. Rev.* B **84** 2352001
[26] Lombardi E B 2008 *Diamond Rel. Mater.* **17** 1345
[27] Benecha E M and Lombardi E B 2013 *J. Appl. Phys.* **114** 223703

Defects in the traditional analogy between the dipolar structure of a circular current and a simple electric dipole's

M Chirwa

Physics Department, Faculty of Science, Engineering and Technology, Walter Sisulu University, P/Bag X1, Nelson Mandela Drive, Mthatha 5117, South Africa.

E-mail: mmchirwa@wsu.ac.za

Abstract. It is shown that when a circular current is resolved into merged distributions of distinct Cartesian *x* and *y* component line current elements, each distribution is a complete magnetic dipole that selectively creates *like* Cartesian components of the magnetic torque and *azimuthal* magnetic vector potential, plus only the magnetic field's *other* Cartesian components. All these are expressible in terms of a distribution's *own* magnetic dipolar moment, which is traditionally attributed to the *whole* circular current. In contrast a simple electric dipole aligned on the *z*-axis, creates its *x* and *y* electric torque components, its full cylindrically symmetric electric field and the electric scalar potential, all of which are expressible in terms of the sole electric dipolar moment. Each magnetic or electric Cartesian torque component is expressible as a cross product of a distribution's dipolar moment and one Cartesian field component parallel to an exclusive Cartesian plane perpendicularly bisecting the mutually parallel intra-dipolar displacements, while the distribution's corresponding potential vanishes in that plane. Under such special conditions, tradition compares one *surviving* Cartesian component of the magnetic torque or of the magnetic vector potential to respectively the electric dipole's combined *x* and *y* torque components or the whole scalar potential. Seemingly from this and the equality of the magnetic dipolar moments of the two component distributions of the cylindrically symmetric circular current, tradition *incorrectly* defines either of these magnetic dipolar moments as that of the *entire* circular current.

1. Introduction

As a follow up on the earlier paper [1], we show that the traditional analogy of the magnetic dipolar structure of a circular current to that of a simple electric dipole consisting of separated electric scalar charges of identical size but opposite signs has many short comings. This is done by evaluating the dipolar moments, the torques in external fields, the dipolar magnetic vector and electric scalar potentials and their related magnetic and electric fields. To begin with an electric current element is a vector resolvable into perpendicular components, unlike an elemental electric scalar charge which can never be similarly resolved. With respect to their dipolar alignment vectors, magnetic dipolar moments are normal whereas electric dipolar moments are collinear. A magnetic torque is a triple vector product with Cartesian components due to equally perpendicular electric current components. An electric torque is a duo vector product with Cartesian components due to the same electric scalar charge.

Here an elemental current is depicted as an elemental magnetic vector charge since this is more consistent with its nature when contrasted with the elemental electric scalar charge as sources of respective magnetic vector and electric scalar potentials and related fields.

2. Moments of and torques on Cartesian magnetic and electric dipoles

On a circle of radius ρ lying in the *xy*-plane and centred at the origin O in figure 1(a), an azimuthal line elemental magnetic *vector* charge at point P_j in the j^{th} quadrant is

$$d\mathbf{Q}_j = \mathbf{I}_j \mu_0 d\ell_j \equiv \hat{\boldsymbol{\varphi}}_j I\mu_0 \rho\, d\phi_j = \left(-\hat{\mathbf{x}}\sin\phi_j + \hat{\mathbf{y}}\cos\phi_j\right) I\mu_0 \rho\, d\phi_j, \quad j = 1, 2, 3, 4 \tag{1}$$

where $\hat{\boldsymbol{\varphi}}_j I\mu_0$ is the line magnetic *vector* charge density and $\phi_j = \phi + \frac{\pi}{2}(j-1)$, as the position vector $\boldsymbol{\rho}_j$ is at an angle $0 \le \phi \le \frac{\pi}{2}$ to the *x*-axis. Hence the Cartesian magnetic vector charge components are

$$d\mathbf{Q}_{j_x} = \pm\hat{\mathbf{x}} dQ_a = \pm\hat{\mathbf{x}} I\mu_0 \rho \sin\phi\, d\phi \tag{2a}$$

$$d\mathbf{Q}_{j_y} = \pm\hat{\mathbf{y}} dQ_b = \pm\hat{\mathbf{y}} I\mu_0 \rho \cos\phi\, d\phi \tag{2b}$$

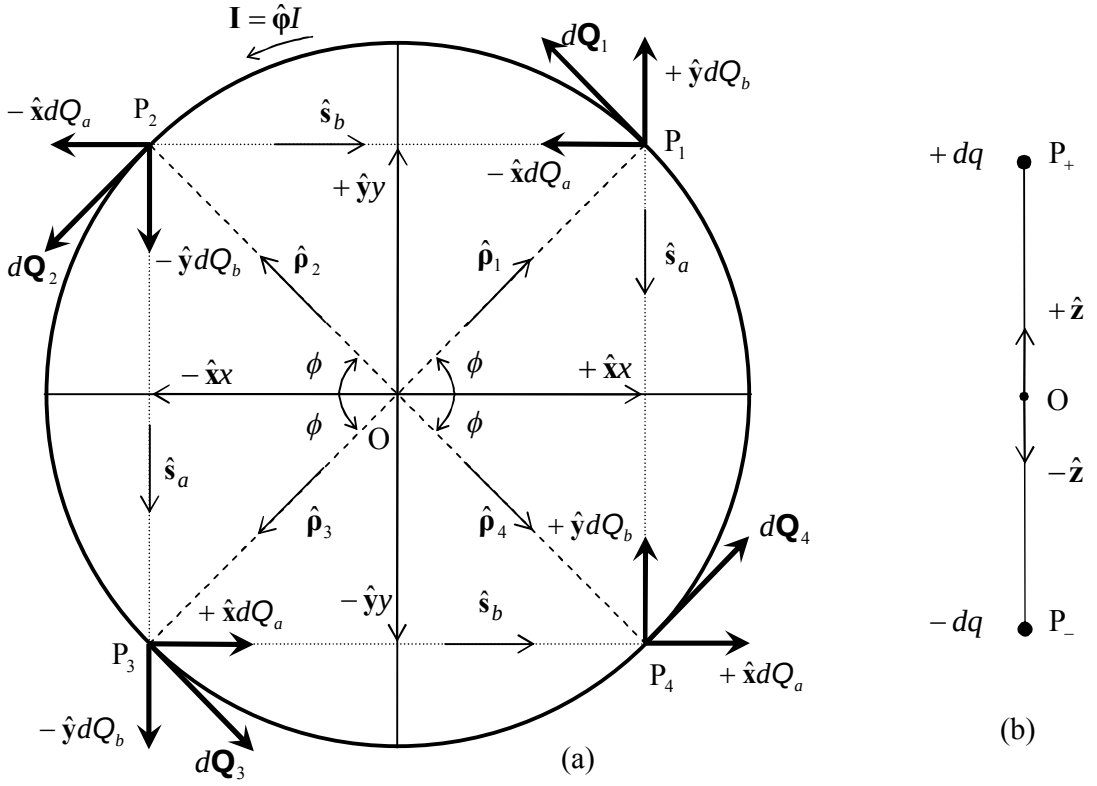

Figure 1. Pairing separated elemental entities (same magnitude, opposite sign) into dipoles: (a) Cartesian magnetic *vector* charges on a circle and (b) electric *scalar* charges on a *z*-axis.

Pairing the Cartesian components at P_2 with the matching but oppositely directed components at P_1 and P_3 constitutes the *a* and *b* Cartesian elemental magnetic dipoles.

While in figure 1(b) at the points P_+ and P_-, of axial position vectors $\mathbf{z}_+ = +\hat{\mathbf{z}}z$ and $\mathbf{z}_- = -\hat{\mathbf{z}}z$ on the *z*-axis, the line elemental electric *scalar* charges (forming an elemental electric dipole) are

$$+dq = +\lambda\, dz \qquad \text{and} \qquad -dq = -\lambda\, dz \tag{2c}$$

Here λ is the magnitude of the electric scalar line charge density.

The two magnetic elemental dipoles and the one electric elemental dipole have *di*polar moments of

$$d\boldsymbol{m}_a = d\boldsymbol{m}_{a_+} + d\boldsymbol{m}_{a_-} = \hat{\boldsymbol{\rho}}_3 \rho \times \hat{\mathbf{x}} dQ_a + \hat{\boldsymbol{\rho}}_2 \rho \times (-\hat{\mathbf{x}} dQ_a) \equiv \mathbf{s}_a \times \hat{\mathbf{x}} dQ_a = \hat{\mathbf{z}} dm_a \tag{3a}$$

$$d\boldsymbol{m}_b = d\boldsymbol{m}_{b_+} + d\boldsymbol{m}_{b_-} = \hat{\boldsymbol{\rho}}_1 \rho \times \hat{\mathbf{y}} dQ_b + \hat{\boldsymbol{\rho}}_2 \rho \times (-\hat{\mathbf{y}} dQ_b) \equiv \mathbf{s}_b \times \hat{\mathbf{y}} dQ_b = \hat{\mathbf{z}} d m_b \tag{3b}$$

$$d\mathbf{p} = d\mathbf{p}_+ + d\mathbf{p}_- = \hat{\mathbf{z}} z dq + (-\hat{\mathbf{z}} z)(-dq) = \mathbf{s}_\mathrm{e} dq \equiv \hat{\mathbf{z}} dp \tag{3c}$$

where their intra dipolar displacements or dipolar orientation vectors in Cartesian directions are

$$\mathbf{s}_a = -\hat{\mathbf{y}} s_a = -\hat{\mathbf{y}} 2\rho \sin\phi \qquad \mathbf{s}_b = \hat{\mathbf{x}} s_b = \hat{\mathbf{x}} 2\rho \cos\phi \qquad \mathbf{s}_\mathrm{e} = \hat{\mathbf{z}} s_\mathrm{e} = \hat{\mathbf{z}} 2z \tag{4}$$

The (sub) subscripts + and – in (3a) to (3c), and in subsequent discussions below, signify entities due to opposing individual elemental vector or scalar charges, that is, *mono*polar contributions.

Integrating (3a) and (3b) from $\phi = 0$ to $\phi = \pi$ and (3c) from $z = 0$ to $z = z$ yield the moments:

$$\boldsymbol{m}_a = \hat{\mathbf{z}} \mu_0 I \pi \rho^2 \equiv \hat{\mathbf{z}} m_a \qquad \boldsymbol{m}_b = \hat{\mathbf{z}} \mu_0 I \pi \rho^2 \equiv \hat{\mathbf{z}} m_b \qquad \mathbf{p} = \hat{\mathbf{z}} \lambda z^2 \equiv \hat{\mathbf{z}} p \tag{5}$$

Thus the overall magnetic dipolar moment $\boldsymbol{m} = \boldsymbol{m}_a + \boldsymbol{m}_b = \hat{\mathbf{z}} 2\mu_0 I \pi \rho^2$ is twice the traditional value for a circular current [2–8], which would be $\hat{\mathbf{z}} \mu_0 I \pi \rho^2$ in the *Kennelly* convention. Note the similarity in the three distinct moments in (5), each involves an apparent area vector, existent or nonexistent.

In external magnetic $\mathbf{H}$ and electric $\mathbf{E}$ fields the Cartesian elemental magnetic and electric dipoles are characterized by paired magnetic forces $\pm d\mathbf{F}_{\mathrm{m}_a}$, $\pm d\mathbf{F}_{\mathrm{m}_b}$ and electric forces $\pm d\mathbf{F}_\mathrm{e}$. As coupled moments of the forces acting on the elemental dipoles, the magnetic and electric torques are:

$$d\boldsymbol{\tau}_a = d\boldsymbol{\tau}_{a_+} + d\boldsymbol{\tau}_{a_-} \equiv \mathbf{s}_a \times d\mathbf{F}_{\mathrm{m}_a} = -\hat{\mathbf{y}} s_a \times \left(\hat{\mathbf{x}} dQ_a \times \mathbf{H}\right) = -\hat{\mathbf{y}} s_a \times \left(\hat{\mathbf{z}} dQ_a H_y - \hat{\mathbf{y}} dQ_a H_z\right) \tag{6a}$$

$$d\boldsymbol{\tau}_b = d\boldsymbol{\tau}_{b_+} + d\boldsymbol{\tau}_{b_-} \equiv \mathbf{s}_b \times d\mathbf{F}_{\mathrm{m}_b} = +\hat{\mathbf{x}} s_b \times \left(\hat{\mathbf{y}} dQ_b \times \mathbf{H}\right) = +\hat{\mathbf{x}} s_b \times \left(\hat{\mathbf{x}} dQ_b H_z - \hat{\mathbf{z}} dQ_b H_x\right) \tag{6b}$$

$$d\boldsymbol{\tau}_\mathrm{e} = d\boldsymbol{\tau}_{\mathrm{e}_+} + d\boldsymbol{\tau}_{\mathrm{e}_-} = \mathbf{s}_\mathrm{e} \times d\mathbf{F}_\mathrm{e} = \hat{\mathbf{z}} s_\mathrm{e} \times \left(dq\mathbf{E}\right) = \hat{\mathbf{z}} s_\mathrm{e} \times \left(\hat{\mathbf{z}} dq E_z + \hat{\mathbf{y}} dq E_y + \hat{\mathbf{x}} dq E_x\right) \tag{6c}$$

Note the triple vector products in (6a) and (6b), and the duo vector product in (6c). The Cartesian components of the torques become

$$\begin{aligned}
d\boldsymbol{\tau}_{\mathrm{m}_x} &= d\boldsymbol{\tau}_a = \hat{\mathbf{z}} s_a dQ_a \times \hat{\mathbf{y}} H_y \equiv \left\{\mathbf{s}_a \times \hat{\mathbf{x}} dQ_a\right\} \times \hat{\mathbf{y}} H_y = d\boldsymbol{m}_a \times \hat{\mathbf{y}} H_y \neq d\boldsymbol{m}_a \times \mathbf{H} \\
d\boldsymbol{\tau}_{\mathrm{m}_y} &= d\boldsymbol{\tau}_b = \hat{\mathbf{z}} s_b dQ_b \times \hat{\mathbf{x}} H_x \equiv \left\{\mathbf{s}_b \times \hat{\mathbf{y}} dQ_b\right\} \times \hat{\mathbf{x}} H_x = d\boldsymbol{m}_b \times \hat{\mathbf{x}} H_x \neq d\boldsymbol{m}_b \times \mathbf{H} \\
d\boldsymbol{\tau}_{\mathrm{e}_x} &= \hat{\mathbf{z}} s_\mathrm{e} dq \times \hat{\mathbf{y}} E_y \equiv \left\{\mathbf{s}_\mathrm{e} dq\right\} \times \hat{\mathbf{y}} E_y = d\mathbf{p} \times \hat{\mathbf{y}} E_y \neq d\mathbf{p} \times \mathbf{E} \\
d\boldsymbol{\tau}_{\mathrm{e}_y} &= \hat{\mathbf{z}} s_\mathrm{e} dq \times \hat{\mathbf{x}} E_x \equiv \left\{\mathbf{s}_\mathrm{e} dq\right\} \times \hat{\mathbf{x}} E_x = d\mathbf{p} \times \hat{\mathbf{x}} E_x \neq d\mathbf{p} \times \mathbf{E}
\end{aligned} \tag{7}$$

Note the matched inequalities. Using (5), the overall magnetic and electric torques become

$$\boldsymbol{\tau}_\mathrm{m} = \boldsymbol{\tau}_a + \boldsymbol{\tau}_b = \boldsymbol{m}_a \times \hat{\mathbf{y}} H_y + \boldsymbol{m}_b \times \hat{\mathbf{x}} H_x \equiv \hat{\mathbf{z}} m_a \times \left(\hat{\boldsymbol{\rho}} H_\rho + \hat{\mathbf{z}} H_z\right) \equiv \boldsymbol{m}_a \times \mathbf{H} \neq \boldsymbol{m} \times \mathbf{H} \tag{8}$$

$$\boldsymbol{\tau}_\mathrm{e} = \boldsymbol{\tau}_{\mathrm{e}_x} + \boldsymbol{\tau}_{\mathrm{e}_y} = \mathbf{p} \times \hat{\mathbf{y}} E_y + \mathbf{p} \times \hat{\mathbf{x}} E_x \equiv \hat{\mathbf{z}} p \times \left(\hat{\boldsymbol{\rho}} E_\rho + \hat{\mathbf{z}} E_z\right) \equiv \mathbf{p} \times \mathbf{E} \neq 2\mathbf{p} \times \mathbf{E} \tag{9}$$

Thus the traditional choice [2–8] of $\boldsymbol{m}_a$ or $\boldsymbol{m}_b$ as the total magnetic dipolar moment is unjustified. The inequalities in (8) and (9) nullify the traditional analogy between magnetic and electric torques.

3. Dipolar magnetic vector and electric scalar potentials and associated fields

When the magnetic vector and electric scalar charge distributions in figure 1 are the sources of magnetic vector and electric scalar potentials, as well as the associated magnetic and electric fields at a field point P, the charges and their positions are signified by primed symbols. Thus, in figure 2 the field point P in a $z\rho$-plane is at position $\mathbf{r} = \hat{\mathbf{r}} r$ from the origin O and its displacements from the source elemental Cartesian magnetic vector charges at points P'_j, $j = 1, 2, 3$ on the circle are

$$\mathbf{R}_j = \hat{\mathbf{R}}_j R_j = \hat{\mathbf{R}}_j f_j^{\frac{1}{2}} r = \hat{\mathbf{R}}_j \left(1 + \eta_j\right)^{\frac{1}{2}} r = \mathbf{r} - \boldsymbol{\rho}'_j \equiv \hat{\mathbf{r}} r - \hat{\boldsymbol{\rho}}'_j \rho' = \hat{\mathbf{z}} z + \hat{\boldsymbol{\rho}} \rho - \hat{\boldsymbol{\rho}}'_j \rho', \quad j = 1, 2, 3 \tag{10}$$

where $\rho = r \sin\theta$ and the geometrical factor f_j (or η_j) is a function of r, θ, ϕ, ρ', ϕ'. Similarly in figure 3, displacements of the field point P from the electric scalar charges $+\mathrm{d}q'$ and $-\mathrm{d}q'$ at P'_+ and P'_- on the z-axis are

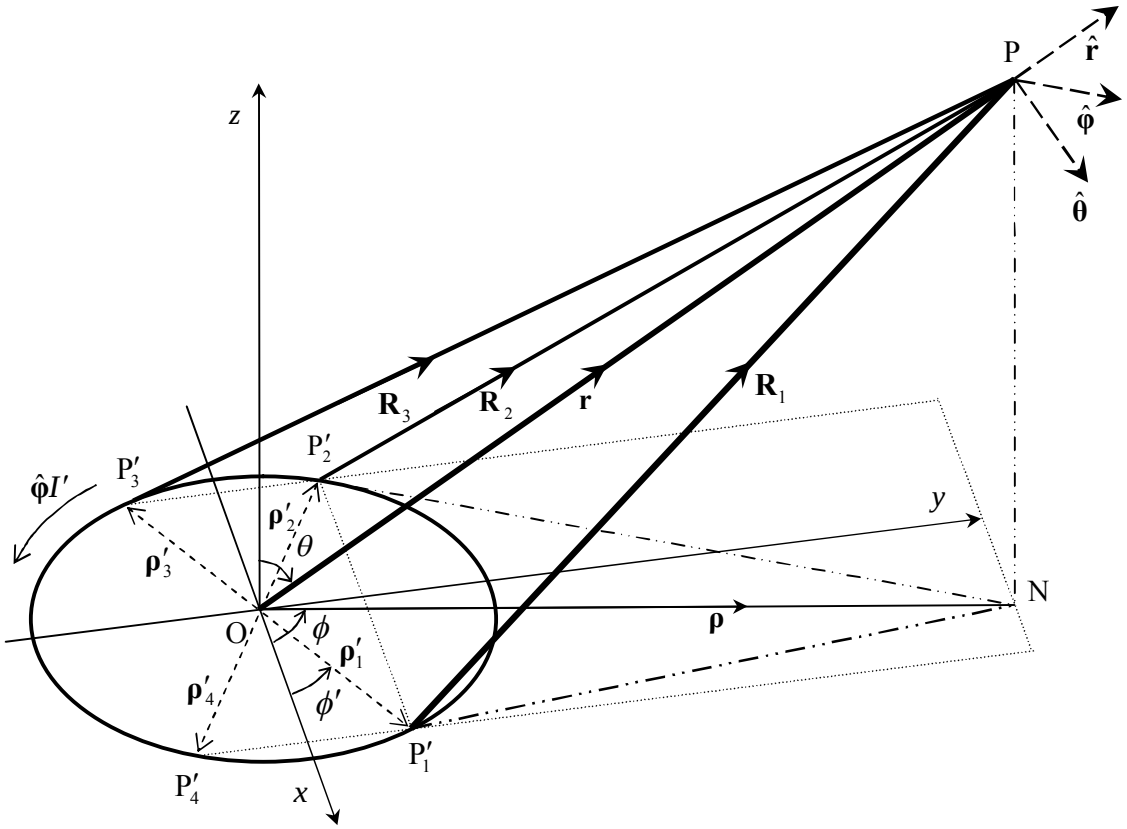

Figure 2: A field point P in a zρ-plane and magnetic source points P'_1, P'_2, P'_3, P'_4 on an *xy*-circle.

$$\mathbf{R}_\pm = \hat{\mathbf{R}}_\pm R_\pm = \hat{\mathbf{R}}_\pm f_\pm^{\frac{1}{2}} r = \hat{\mathbf{R}}_\pm (1+\eta_\pm)^{\frac{1}{2}} r = \mathbf{r} - \mathbf{z}'_\pm = \hat{\mathbf{r}}\left(r \mp \tfrac{1}{2} s'_\mathrm{e} \cos\theta\right) \pm \hat{\boldsymbol{\theta}} \tfrac{1}{2} s'_\mathrm{e} \sin\theta \tag{11}$$

where $s'_\mathrm{e} = 2z'$, with the geometrical factor $f_\pm$ (or $\eta_\pm$) being a function of r, θ, z' only.

Below, each ensuing first order approximation for $\rho' << r$ or $z' << r$ is after binomial expansion of $f_j^{-\frac{n}{2}}$ or $f_\pm^{-\frac{n}{2}}$, where $n=1$ for potentials and $n=3$ for fields, and application of equations (3a) to (3c). Then the two Cartesian elemental magnetic dipoles on the circle in figure 2 and the electric dipole on the z-axis in figure 3 will generate at P the magnetic vector and electric scalar potentials

$$d\mathbf{A}_a = d\mathbf{A}_{a_+} + d\mathbf{A}_{a_-} = \left(f_3^{-\frac{1}{2}} - f_2^{-\frac{1}{2}}\right)\frac{\hat{\mathbf{x}} dQ'_a}{4\pi\mu_0 r} \approx -\hat{\mathbf{x}} \sin\phi \sin\theta \frac{s'_a dQ'_a}{4\pi\mu_0 r^2} \equiv -\hat{\mathbf{x}} \sin\phi \sin\theta \frac{dm'_a}{4\pi\mu_0 r^2} \tag{12a}$$

$$d\mathbf{A}_b = d\mathbf{A}_{b_+} + d\mathbf{A}_{b_-} = \left(f_1^{-\frac{1}{2}} - f_2^{-\frac{1}{2}}\right)\frac{\hat{\mathbf{y}} dQ'_b}{4\pi\mu_0 r} \approx +\hat{\mathbf{y}} \cos\phi \sin\theta \frac{s'_b dQ'_b}{4\pi\mu_0 r^2} \equiv +\hat{\mathbf{y}} \cos\phi \sin\theta \frac{dm'_b}{4\pi\mu_0 r^2} \tag{12b}$$

$$dV = dV_+ + dV_- = \left(f_+^{-\frac{1}{2}} - f_-^{-\frac{1}{2}}\right)\frac{dq}{4\pi\varepsilon_0 r} \approx \cos\theta \frac{s'_\mathrm{e} dq}{4\pi\varepsilon_0 r^2} \equiv \cos\theta \frac{dp'}{4\pi\varepsilon_0 r^2} \tag{12c}$$

Integrating and changing from Cartesian to spherical unit vectors shows that each of $\mathbf{A}_a$ and $\mathbf{A}_b$ varies with ϕ, but V does not:

$$\mathbf{A}_a = \left[-\left(\hat{\mathbf{r}} \sin\theta + \hat{\boldsymbol{\theta}} \cos\theta\right) \sin\phi \cos\phi + \hat{\boldsymbol{\varphi}} \sin^2\phi\right] \frac{m'_a \sin\theta}{4\pi\mu_0 r^2} \tag{13a}$$

$$\mathbf{A}_b = \left[+\left(\hat{\mathbf{r}}\sin\theta + \hat{\boldsymbol{\theta}}\cos\theta\right)\sin\phi\cos\phi + \hat{\boldsymbol{\varphi}}\cos^2\phi\right]\frac{m_b'\sin\theta}{4\pi\mu_0 r^2} \tag{13b}$$

$$V = \frac{p'\cos\theta}{4\pi\varepsilon_0 r^2} \tag{13c}$$

Due to the equations in (5), the total magnetic vector potential become

$$\mathbf{A} = \mathbf{A}_a + \mathbf{A}_b \equiv \left(-\hat{\mathbf{x}}\sin\phi + \hat{\mathbf{y}}\cos\phi\right)\frac{m_a'}{4\pi\mu_0 r^2} = \hat{\boldsymbol{\varphi}}\sin\theta\frac{m_a'}{4\pi\mu_0 r^2} \equiv \hat{\boldsymbol{\varphi}}\sin\theta\frac{m_b'}{4\pi\mu_0 r^2} \tag{14}$$

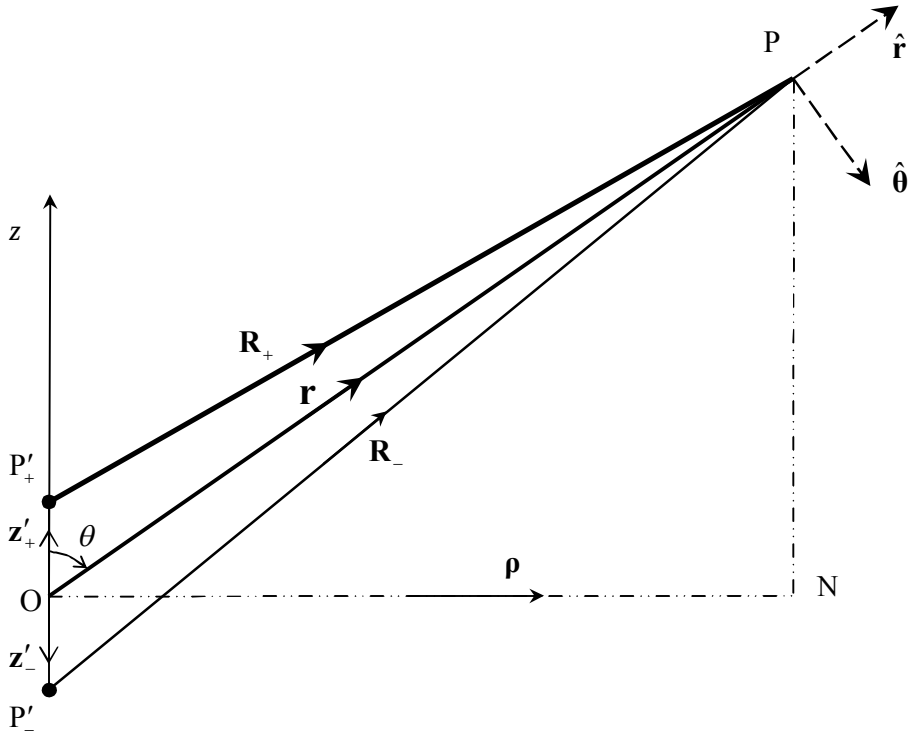

Figure 3: A field point P in a $z\rho$-plane or $r\theta$-plane and electric source points P'_+, P'_- on a z axis.

Similarly, the fields at point P due to the two distinct Cartesian elemental magnetic dipoles in figure 2 and the electric dipole in figure 3 are

$$\begin{aligned} d\mathbf{H}_a = d\mathbf{H}_{a_+} + d\mathbf{H}_{a_-} &= \frac{\hat{\mathbf{x}}dQ_a'}{4\pi\mu_0 r^3}\times\left(\mathbf{R}_3 f_3^{-\frac{3}{2}} - \mathbf{R}_2 f_2^{-\frac{3}{2}}\right) \\ &\approx \left[\hat{\mathbf{y}}3\sin\phi\cos\theta\sin\theta + \hat{\mathbf{z}}\left(1-3\sin^2\phi\sin^2\theta\right)\right]\frac{s_a'dQ_a'}{4\pi\mu_0 r^3} \end{aligned} \tag{15a}$$

$$\begin{aligned} d\mathbf{H}_b = d\mathbf{H}_{b_+} + d\mathbf{H}_{b_-} &= \frac{\hat{\mathbf{y}}dQ_b'}{4\pi\mu_0 r^3}\times\left(\mathbf{R}_1 f_1^{-\frac{3}{2}} - \mathbf{R}_2 f_2^{-\frac{3}{2}}\right) \\ &\approx \left[\hat{\mathbf{x}}3\cos\phi\cos\theta\sin\theta + \hat{\mathbf{z}}\left(1-3\cos^2\phi\sin^2\theta\right)\right]\frac{s_b'dQ_b'}{4\pi\mu_0 r^3} \end{aligned} \tag{15b}$$

$$d\mathbf{E} = d\mathbf{E}_+ + d\mathbf{E}_- = \frac{dq'}{4\pi\varepsilon_0 r^3}\left(\mathbf{R}_{e_+} f_+^{-\frac{3}{2}} - \mathbf{R}_{e_-} f_-^{-\frac{3}{2}}\right) \approx \left(\hat{\mathbf{r}}2\cos\theta + \hat{\boldsymbol{\theta}}\sin\theta\right)\frac{s_e'dq'}{4\pi\varepsilon_0 r^3} \tag{15c}$$

Integrating (15a) to (15c), and transforming unit vectors from Cartesian to spherical systems shows that both $\mathbf{H}_a$ and $\mathbf{H}_b$ vary with ϕ, but $\mathbf{E}$ does not:

$$\mathbf{H}_a = \left[\hat{\mathbf{r}}\cos\theta + \hat{\boldsymbol{\theta}}\left(3\sin^2\phi - 1\right)\sin\theta + \hat{\boldsymbol{\varphi}}3\cos\phi\sin\phi\cos\theta\sin\theta\right]\frac{m'_a}{4\pi\mu_0 r^3} \tag{16a}$$

$$\mathbf{H}_b = \left[\hat{\mathbf{r}}\cos\theta + \hat{\boldsymbol{\theta}}\left(3\cos^2\phi - 1\right)\sin\theta - \hat{\boldsymbol{\varphi}}3\cos\phi\sin\phi\cos\theta\sin\theta\right]\frac{m'_b}{4\pi\mu_0 r^3} \tag{16b}$$

$$\mathbf{E} = (\hat{\mathbf{r}}2\cos\theta + \hat{\boldsymbol{\theta}}\sin\theta)\frac{p'}{4\pi\varepsilon_0 r^3} \tag{16c}$$

Then as $m'_a = m'_b$ (equations 5), the overall magnetic field acquires cylindrical symmetry when expressed exclusively in terms of either m'_a or m'_b:

$$\mathbf{H} = \mathbf{H}_a + \mathbf{H}_b = \frac{m'_a}{4\pi\mu_0 r^3}\left(2\hat{\mathbf{r}}\cos\theta + \hat{\boldsymbol{\theta}}\sin\theta\right) \equiv \frac{m'_b}{4\pi\mu_0 r^3}\left(2\hat{\mathbf{r}}\cos\theta + \hat{\boldsymbol{\theta}}\sin\theta\right) \tag{17}$$

Clearly the similarity between (15c) and (17) cannot justify the tradition [2–8] of taking $\boldsymbol{m}'_a$ or $\boldsymbol{m}'_b$ as the circular current's *only* magnetic moment. Again the traditional analogy fails.

4. Conclusions

It has been shown that traditional analogies between the structures and torques of electric and magnetic dipoles are deceptively erroneous. A circular current is resolvable into merged distributions of distinct Cartesian *x* and *y* component line current elements, each distribution being a complete magnetic dipole that selectively creates *like* Cartesian components of the magnetic torque and *azimuthal* magnetic vector potential, plus only the magnetic field's *other* Cartesian components. All these are expressible in terms of a distribution's *own* magnetic dipolar moment, which is traditionally attributed to the *whole* circular current. In contrast a simple electric dipole aligned on the *z*-axis, creates its *x* and *y* electric torque components, its full cylindrically symmetric electric field and the electric scalar potential, all of which are expressible in terms of the sole electric dipolar moment.

References

[1] Chirwa M 2011. "Magnetic vector charges in the mystery of a circular current's pair of distinct Cartesian elemental magnetic vector charges" *Proceedings of SAIP2011*, the 56th Annual Conference of the South African Institute of Physics, edited by I. Basson and A.E. Botha (Pretoria: University of South Africa) pp 56–61. Available online at http:\\www.saip.org.za

[2] Jackson J D 1975 *Classical Electrodynamics* 2nd ed. (New York: John Wiley & Sons) pp168–86

[3] Lorrain P, Corson D P and Lorrain F 1987 *Electromagnetic Fields and Waves* 3rd ed. (New York: W H Freeman & Co) pp 331–41

[4] Purcell E M 1985. *Electricity and Magnetism* 2nd ed. (London: McGraw-Hill) pp 124–6 and 405–19

[5] Boyer T H 1988. The force on a magnetic dipole *Am. J. Phys.* **56**(8) 688–92

[6] Vaidman L 1990 "Torque and force on a magnetic dipole" *Am. J. Phys.* **58**(10) 978–83

[7] Griffiths D J 1999 *Introduction to Electrodynamics* 3rd ed. (London: Prentice–Hall) pp 242–58

[8] Deissler R J 2008. "Dipole in a magnetic field, work, and quantum spin" *Phys. Rev. E* **77** 036609–18

Green density effects on the structural and magnetic properties of $(Cd, Zn)_{0.5}Ni_{0.5}Fe_2O_4$ ferrites produced by combustion technique

T Moyo[1], P R Silva[2], H Saitovitch[2], J Z Msomi[1]

[1]*School of Chemistry and Physics, Westville Campus, University of KwaZulu-Natal, Private Bag X54001, Durban 4000, South Africa*

[2]*Centro Brasileiro de Pesquisas Fisicas, Rua Dr Xavier Sigaud, 150; 22.290-180 Rio de Janeiro, Brazil*

E-mail: moyo@ukzn.ac.za

Abstract. We present results of structural and magnetic measurements derived from x-ray diffraction, magnetization and Mössbauer spectroscopy for $(Cd, Zn)_{0.5}Ni_{0.5}Fe_2O_4$ ferrites prepared by combustion technique. The changes in properties are investigated as a function of pressure or green density used to compact the pellets before sintering. Information on lattice parameters, grain sizes, porosity, coercive fields, saturation magnetization, Curie points and hyperfine field distributions are correlated with the pressure effect, bulk densities of the samples and differences in ionic sizes of Cd and Zn atoms. Evidence of trapped porosity and optimum sample preparation conditions are also deduced from the data.

1. Introduction

Ni-Zn ferrites are amongst some of the well-studied and used ferrimagnetic materials. They are characterized by soft magnetic properties and high resistivity [1]. The desired phase is easy to form and materials produced have the advantage of high stability and low cost [2]. This accounts for the wide use of Ni-Zn ferrites in magnetic and electrical applications [3, 4]. The research interest in these materials is aimed at improving the quality, reliability and consistency in the material properties. A good understanding of the evolution of properties imposed by the methodology and sample preparation conditions is therefore critical. The techniques used to arrive at the final product are known to influence the properties [5]. However, it is expected that better techniques for sample preparation in different places under similar conditions should produce samples with greater consistency because of the use of common raw materials of similar or identical purity. The conventional technique used to produce ferrites is the ceramic technique, which involves at least two stages of grinding of the starting oxides. Here the final level of homogeneity depends on the type and duration of grinding process and the initial particle size of the oxides. Hence the same level of homogeneity every time and in different places is harder to achieve when samples are produced by mechanical methods. There is also greater chance of contamination and sample loss during milling

operations [2, 6, 7]. Prolonged heating of the samples at high temperature also gives rise to further mass loss.

In materials produced by wet chemical methods a higher degree of homogeneity of the starting solution can be achieved. The samples produced by these techniques should demonstrate a higher degree of consistency. Unfortunately, this appears not to be the case when two sets of data are compared in two recent reports [2, 7]. It is therefore important to develop firm criteria that can be used to compare properties of samples from different sources. The effect of green density on the thermomechanical properties of ceramics after sintering has been reported [8]. Die pressing before sintering can lead to higher toughness and preferred particle orientation [9]. We have employed the combustion technique [2, 6, 7] to produce samples of high quality from a well-homogenized mixture of starting nitrates and urea. The main interest was to investigate the extent to which material properties evolve from samples prepared from the same homogenized and ignited mixture under different conditions of applied pressure (related to the green density) in the production of sample pellets. The effect of totally replacing Zn^{2+} ions by the larger Cd^{2+} in the $Zn_{0.5}Ni_{0.5}Fe_2O_4$ compound was also investigated.

2. Experimental details

The nominal compositions of $(Cd, Zn)_{0.5}Ni_{0.5}Fe_2O_4$ ferrites were prepared from a mixture of stoichiometric amounts of $Cd(NO_3)_2{\cdot}4H_2O$ or $Zn(NO_3)_2{\cdot}6H_2O$, $Ni(NO_3)_2{\cdot}6H_2O$, $Fe(NO_3)_3{\cdot}9H_2O$) and NH_2CONH_2 (synth.). The quantity of urea used was such that it matched the number of N atoms in the nitrate mixture [2]. The mixture was then dissolved in some distilled water and well homogenized in a vitreous porcelain basin placed on a cold plate of a heater inside a fume cupboard. The mixture was then gradually heated until self-ignition of the mixture was finally completed at about 600 °C in a period of about an hour. This process of heating ensured a very high degree of homogeneity of the mixture and minimized the likelihood of spillage if the mixture had been placed on a preheated plate at 600 °C. The final product was homogenized by using an agate mortar and pestle. The powder was then pressed into pellets of almost the same mass at different pressure for about two minutes to produce pellets of different compaction or states of green density. The samples were finally sintered in air in a preheated tube furnace at 1210 °C for about 6 hours. A typical sintered pellet was roughly about 0.4 grams with diameter of about 7 mm and 2 mm thickness. The diameters increased while the thickness of the sintered pellets decreased with increase in green density. Bulk density measurements of the sintered pellets were performed on small mass fragments using Archimedes principle. This involved direct measurement of the buoyant force on solid fragments in a suitable oil medium using a Mettler AT261 Delta Range electronic balance with precision of 0.00001 grams [10]. Density measurements based on the geometry of the pellets were found to be unreliable. The structure of the samples produced was determined by x-ray diffraction (XRD) using a DRX-HGZ/Herzog model 1D 3000 unit with CuKα(1) radiation ($\lambda = 1.5418$ Å). The angle 2θ was varied by 0.2° intervals. The magnetic measurements were performed at room temperature using a ^{57}Fe Mössbauer spectrometer and vibrating sample magnetometer (VSM). The accuracy of the VSM measurements was counter checked by a Quantum Design MPMS XL squid magnetometer.

3. Results and discussion

Typical XRD spectra for $(Cd, Zn)_{0.5}Ni_{0.5}Fe_2O_4$ compounds are presented in Figure 1. Virtually all the significant peaks are indexed. Hence all the samples produced had single-phase formation. The spectra are consistent with the spectrum published by Costa *et al*. [2] on similar compounds produced by the combustion technique. In Table 1 we present results of bulk density, lattice parameter, grain size and porosity as a function of applied pressure (or green density). Slight but definite changes with pressure are observed. Zn- and Cd-based samples have comparable values of the lattice parameters, with those of Cd-based samples being slightly larger. We attribute this largely due to differences in ionic sizes because

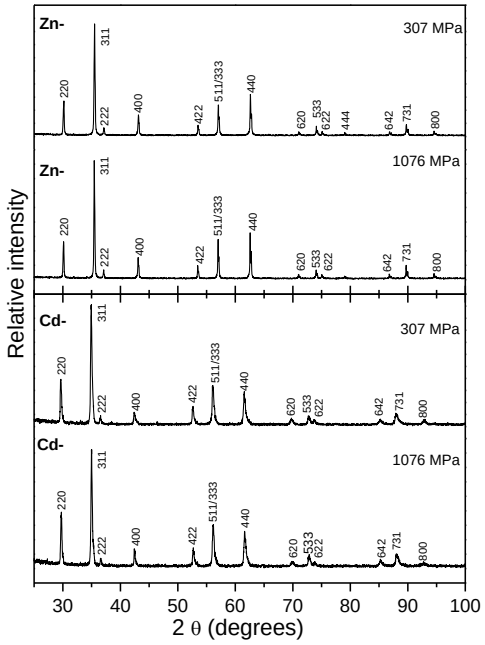

Figure 1. Typical XRD spectra of sintered (Cd, $Zn)_{0.5}Ni_{0.5}Fe_2O_4$ oxides. Pre-sintered pellets were formed at pressures of 307 and 1076 MPa.

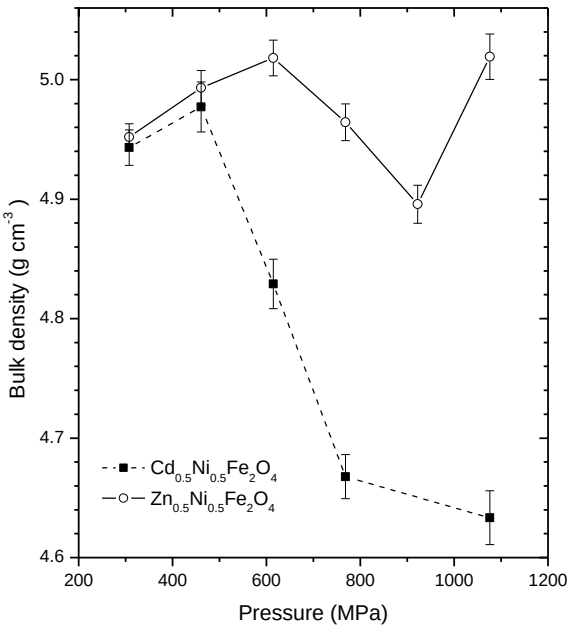

Figure 2. Bulk densities of sintered (Cd, $Zn)_{0.5}Ni_{0.5}Fe_2O_4$ oxides plotted as a function pressure (or green density) of pre-sintered pellets.

Table 1. Bulk density ρ, lattice parameter a, grain size D and porosity P_o as a function of applied pressure (or green density) (P) for (Cd, $Zn)_{0.5}Ni_{0.5}Fe_2O_4$.

	P (MPa) ±10	ρ (g/cm^3) ±0.02	a (Å) ±0.001	D (nm) ±0.7	P_o (%) ±0.05
Zn	307	4.95	8.385	45.6	7.57
	461	4.50	8.384	49.1	6.83
	615	5.02	8.384	49.5	6.37
	769	4.96	8.391	51.2	7.15
	922	4.90	8.393	51.7	8.37
	1076	5.02	8.382	48.8	6.40
Cd	307	4.94	8.516	32.1	12.04
	461	4.98	8.504	39.4	11.79
	615	4.83	8.482	28.2	15.09
	769	4.67	8.508	30.9	17.17
	1076	4.63	8.505	35.7	17.87

$$\frac{(a)_{\mathrm{Zn}}}{(a)_{\mathrm{Cd}}} \approx \frac{r_{\mathrm{ionic,Zn}}}{r_{\mathrm{ionic,Cd}}}. \quad (1)$$

The ionic sizes for Zn and Cd are 0.74 Å and 0.97 Å respectively [11]. The crystalline grain size D for each sample has been estimated using the Scherrer formula [2, 12, 13]

$$D = \frac{\lambda}{\beta \cos\theta}, \quad (2)$$

where λ is the wavelength of the CuKα radiation and β is the full width at half maximum of the (311) intensity peak. The grain sizes are larger for Zn-based compounds reflecting the well-known tendency of Zn to enhance the desired phase formation. In addition there is a systematic increase of the grain size to a maximum value around 770 MPa in Zn-based compounds. Grain sizes are lower in Cd-based samples. We attribute this to the larger ionic size of Cd. This would tend to weaken inter-ionic interactions resulting in smaller crystallites. An important parameter that measures the average coordination of atoms in the entire sample is the bulk density. This parameter has information of the average compaction of the atoms and includes also the effect of the empty spaces (a measure of porosity). The results of bulk density measurements as a function of pelletizing pressure are presented in Figure 2. Costa *et al*. [2] prepared a similar set of compounds by combustion technique but at a pre-sintering pressure of 392 MPa. They found a bulk density of 5.00 g cm^{-3} for the Zn-based sample sintered at 1200 °C. This is consistent with the present results. However, there is an apparent anomaly in the variation of the bulk density with pressure P. A slight increase in bulk density is observed initially which reduces with further increase in the green density. We believe that these results can be explained on the basis of a significant amount of trapped porosity. The pelletizing pressure can interfere with escape routes of excess gases from a pellet during sintering process. The porosity of the samples can be calculated from the knowledge of bulk density and x-ray density deduced from the size of the unit cell. The porosities are also given in Table 1. Cd-based samples with smaller particle sizes have higher porosity $(P_o)_{\mathrm{Cd}} \approx 2(P_o)_{\mathrm{Zn}}$.

The $(Cd, Zn)_{0.5}Ni_{0.5}Fe_2O_4$ samples were observed to have a ferromagnetic effect at room temperature in response to a small bar magnet. Isothermal magnetization $\sigma(H)$ measurements were performed at room temperature in the field range: $-6\,\mathrm{kOe} \le H \le 6\,\mathrm{kOe}$. The samples appear to have significant superparamagnetic character. Typical low field isothermal magnetization curves are given in Figure 3 for $Cd_{0.5}Ni_{0.5}Fe_2O_4$ sample. The hysteresis curve for the Ni calibration sample is also given in Figure 3 to illustrate the limit of the accuracy of our measurements. The results show very little hysteresis loss at room temperature. In Table 2 we show the data of coercive fields and saturation magnetization. There is no significant change in saturation magnetization as function of pressure. However, there appears to be a slight correlation between coercive and bulk density. Lower coercive field seems to be associated with higher bulk density in Zn-based samples.

Mössbauer spectroscopy measurements were performed at room temperature. Typical spectra are given in Figure 4, which show ordered magnetic phase at room temperature. The spectra are characterized by broad peaks, which indicate a range of hyperfine fields. The appropriate analysis is therefore to deduce hyperfine field distributions from the spectra. Figure 5 shows such distributions. The plots clearly show systematic change of the hyperfine field distributions as a function of pelletizing pressure (green density). We can identify four principle gaussian peaks that make up the hyperfine distributions as illustrated in Figure 6 for the hyperfine distribution at 1076 MPa.

The Curie points of the samples were determined using the zero velocity Mössbauer technique, which is associated with the relative change of the transmission of gamma ray through an absorber in ordered and disordered states. No significant change of Curie points with green density was observed. The average Curie point was determined to be 554±4 K.

Table 2. Coercive field (H_C) and saturation magnetization (σ) as a function of applied pressure (or green density) (P) for $(Cd, Zn)_{0.5}Ni_{0.5}Fe_2O_4$.

	P (MPa) ±10	H_C (Oe) ±0.5	σ (emu/g) ±0.2
Zn	307	3.7	74.2
	461	1.9	72.8
	615	2.2	73.5
	769	0.6	75.1
	922	4.5	74.1
	1076	2.7	75.3
Cd	307	3.4	56.1
	461	3.2	56.0
	615	3.4	56.9
	769	3.8	58.0
	1076	4.9	57.9

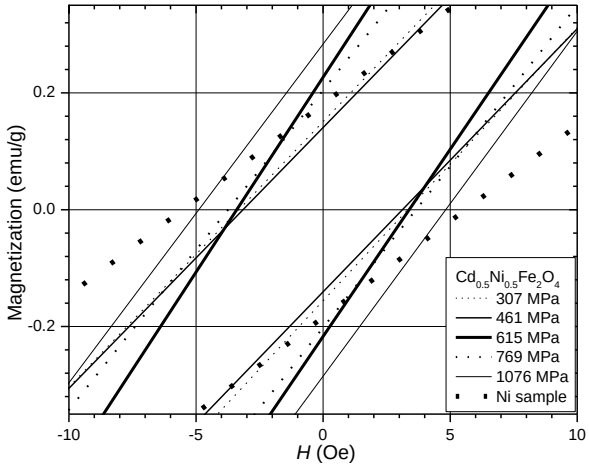

Figure 3. Isothermal magnetization curves in low magnetic fields. A saturating field is initially applied to the samples.

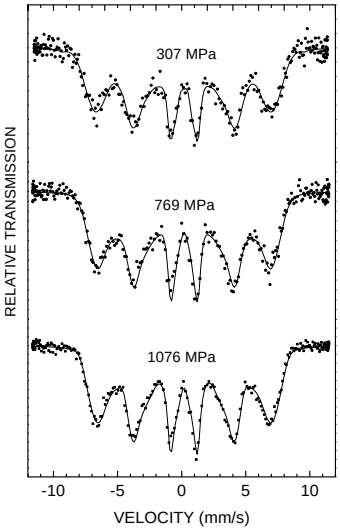

Figure 4. Typical Mössbauer spectra for $Cd_{0.5}Ni_{0.5}Fe_2O_4$ samples.

4. Conclusions

Our results show a significant influence of the green density on the final bulk density of $(Cd, Zn)_{0.5}Ni_{0.5}Fe_2O_4$ ferrites investigated. The bulk density measurements are important because they can provide information of the quality of the materials and how their properties are influenced by the

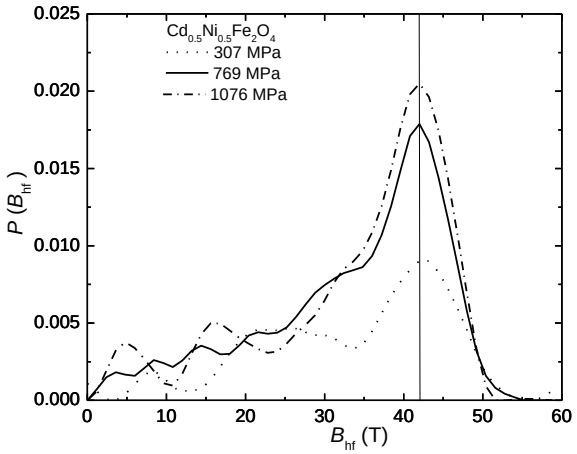

Figure 5. Hyperfine field distributions for $Cd_{0.5}Ni_{0.5}Fe_2O_4$ samples.

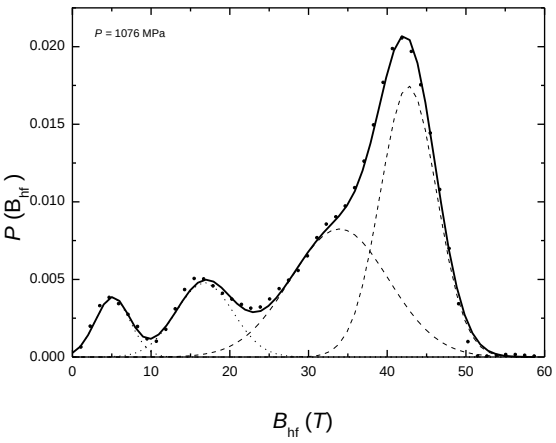

Figure 6. Gaussian fits to the hyperfine field distribution for $Cd_{0.5}Ni_{0.5}Fe_2O_4$.

sample preparation conditions such as the pre-sintering green density. Our results show that a maximum bulk can be obtained for a pressure of about 600 MPa. Samples produced from different states of green density can easily be distinguished from the hyperfine field distributions. Other parameters like lattice constants, grain sizes, porosity, coercive fields and saturation magnetization are less significantly affected by the pelletizing pressure.

Acknowledgements
One of us TM wishes to acknowledge the travel and financial support of the Third World Academy of Science (TWAS) and the generous hospitality of CBPF/MCT of Brazil during the research visit at CBPF.

References

[1] Anil Kumar P S, Shrotri J J, Kulkami S D, Deshpande C E, Date S K 1996 Mat. Lett. **27** 293
[2] Costa A C M, Tortella E, Morelli M R and Kiminami R H G A 2003 J. Magn. Magn. Mat. **256** 174
[3] Bhise B V, Dongare M B, Patil S A, Sawant S R, J. Mater. Sci. Letter **10** 1991 922
[4] Abraham T, Am. Ceram. Soc. Bull. **73** 1994 62
[5] Verma A, Goel T C, Mendiratta R G, Alam M I, Sci. Eng. **B60** 1999 156
[6] Mangaranja R V, Ananthakumar S, Manohar P and Gnanam F. D 2000 *Ferrites: Proceedings of the Eighth International Conference on Ferrites* (ICF 8), Kyoto and Tokyo Japan, The Japan Society of Powder and Powder Metallurgy 313
[7] Mangaranja R, Ananthakumar S, Manohar P and Gnanam F D 2003 Materials Letters **57** 1151
[8] Schoenberg S E, Green D J, Messing G L, 2006 J. Am. Ceram. Soc. **89** 2448
[9] Chou Y, Green D J, 1992 J. Am. Ceram. Soc. **75** 3346
[10] Moyo T, Silva P R J and Saitovitch H, Notas Tecnicas, Centro Brasileiro de Pesquisas Fisicas, ISSN 0101-9201, CBPF-NT-005/03 June 2003
[11] Weast R C, Astle M J, Beyer W H, *Handbook of Chemistry and Physics,* 65th Edition (1984-1985), CRC Press, Florida, F165
[12] Chinnasamy C N, Narayanasamy A, Ponpandian N, Joseyphaus R J, Jeyadevan B, Tohji K and Chattopadhyay K 2002 J. Magn. Magn. Mat. **238** 281
[13] Vaidyanathan S, Sendhilnathan S, Arulmurugan R 2007 J. Magn. Magn. Mat. **313** 293

On the calculation of solvation free energy from Kirkwood-Buff integrals: A large scale molecular dynamics study

Wynand Dednam and André E. Botha

Department of Physics, University of South Africa, P.O. Box 392, Pretoria, South Africa

E-mail. bothaae@unisa.ac.za

Abstract. Solvation of (bio)molecules in water is severely affected by the presence of co-solvent within the hydration shell of the solute structure. Furthermore, since solute molecules can range from small molecules, such as methane, to large protein structures, it is imperative to understand the detailed structure-function relationship on the microscopic level. Although such an understanding can be obtained through molecular dynamic simulations, excessively large system sizes and simulation times are required in order to obtain meaningful results. In this context, Kirkwood-Buff (KB) theory, which connects the microscopic pair-wise molecular distributions to global thermodynamic properties, together with the recently developed technique called finite size scaling, may provide a method to reduce computational times. In this paper, we present a molecular dynamics test simulation to calculate and compare the KB integrals, for the solvation of methane in methanol in water, calculated via two different methods: via the radial distribution functions and via the fluctuation method. In the results reported here we demonstrate that the latter method can produce equivalent results by using a relatively small system size. In future work we thus intend using the fluctuation method and finite size scaling to study the conformational transitions of large (bio)macromolecules.

1. Introduction

The solvation thermodynamics of solutes in water are extremely sensitive to the presence and concentration of co-solvents such as alcohols, osmolytes and salts [1-4]. Their presence in the hydration shell of the solute in aqueous solution usually determines how well the solute is solvated by the solution [1]. In other words, the free energy of solvation depends on the relative proportions of co-solvent and water in the mixture, and the more negative the free energy of solvation, the greater the extent to which the solute is solvated by the mixture. Understanding the effects of co-solvents on the solvation of solutes in aqueous solutions and on the magnitude of the solvation free energy sheds light on, for instance, why proteins tend to unfold or "denature" in the presence of alcohols and urea [3], and the salting "in" and "out" effects on hydrophobic solutes due to favourable interactions between the solute and large monovalent ions of low charge density, on the one hand, and unfavourable interactions between the solute and small ions of high charge density, on the other [2, 4]. This paper presents the results of molecular dynamics (MD) simulations of an important initial test, namely the solvation of methane (hydrophobic solute) in a methanol (co-solvent) and water (solvent) mix. Our results demonstrate that by applying the method of finite size scaling [5-7] to relatively small systems (which are computationally less expensive to simulate), results equivalent to much larger systems can be obtained.

2. Theory

2.1. Kirkwood-Buff Theory of Solutions

Macroscopic thermodynamic properties of solute – water – co-solvent systems can be directly obtained from microscopic molecular distributions. More specifically, the Kirkwood-Buff theory of solutions [8-9] connects fluctuations in the grand canonical ensemble to macroscopic thermodynamic properties through the so-called Kirkwood-Buff integrals (KBIs) between components *i* and *j* of the solution :

$$G_{ij} = \mathrm{V}\left[\frac{\left\langle \mathrm{N_i N_j}\right\rangle - \left\langle \mathrm{N_i}\right\rangle\left\langle \mathrm{N_j}\right\rangle}{\left\langle \mathrm{N_i}\right\rangle\left\langle \mathrm{N_j}\right\rangle} - \frac{\delta_{\mathrm{ij}}}{\left\langle \mathrm{N_j}\right\rangle}\right] \tag{1}$$

$$= 4\pi\int_0^\infty \left\{g_{ij}^{\mu VT}(\mathrm{r}) - 1\right\}\mathrm{r}^2\mathrm{dr} \tag{2}$$

where quantities in $\left\langle \cdot \right\rangle$ represent averages in the grand canonical ensemble, V is the volume of the simulation domain, N_i is the number of particles in the simulation domain and $g_{ij}^{\mu VT}(\mathrm{r})$ is the radial distribution function (RDF) in the grand canonical (VT) ensemble. G_{ij}, the Kirkwood-Buff integral between component *i* and *j*, is a local quantity that measures the deviation of the intermolecular distribution from that of a random one, i.e., an ideal gas. Hence, it is also a measure of the affinity of these two components for each other in the solution environment. The macroscopic quantity of interest for this work is the free energy of solvation of the solute in the methanol – water mixture. This quantity can be expressed in terms of the G_{ij} and solution component number densities $_i$ as [8]

$$\left(\frac{\partial \Delta \mathrm{G_c}}{\partial \rho_\mathrm{c}}\right)_{\mathrm{p,T}} = \frac{-\mathrm{RT}\rho_\mathrm{c}(G_{\mathrm{cc}} - G_{\mathrm{cw}})}{1 + \rho_\mathrm{c}(G_{\mathrm{cc}} - G_{\mathrm{cw}})} \tag{3}$$

for a binary system of water and co-solvent, and as [8]

$$\left(\frac{\partial \Delta \mathrm{G_s}}{\partial \mathrm{x_c}}\right)_{\mathrm{p,T}} = \lim_{\rho_\mathrm{s}\to 0}\frac{\mathrm{RT}(\rho_\mathrm{w} + \rho_\mathrm{c})^2}{\eta}(G_{\mathrm{sw}} - G_{\mathrm{sc}}) \tag{4}$$

for a ternary system in the limit of infinite dilution of the solute. Here $\Delta \mathrm{G_s}$ is the free energy of solvation of the solute, x_c is co-solvent mole fraction, R is the universal gas constant, T the temperature, and $\eta = \rho_\mathrm{w} + \rho_\mathrm{c} + \rho_\mathrm{w}\rho_\mathrm{c}(G_{\mathrm{ww}} + G_{\mathrm{cc}} - 2G_{\mathrm{cw}})$. This paper outlines two independent methods for computing eq. (3) that permits a comparison of the results obtained and a means by which to assess their robustness. The first involves generating the $g_{ij}^{\mu VT}(\mathrm{r})$ at every concentration by simulation. This, in turn, enables numerical evaluation of the second expression in eq. (1) and hence the G_{ij} needed for eq. (3). The second method, Finite Size Scaling, is described in the section that follows.

2.2. Finite Size Scaling

The KBI between component *i* and *j* for a given methanol concentration can also be calculated by an innovative particle counting and extrapolation scheme referred to as finite size scaling [5-7]. This involves computing KBIs for a system of theoretically infinite size which ensures that an accurate value for the G_{ij} at the concentration in question is obtained. The first step involves repeating a count of the number of particles of type *i* and *j* that fall within a cubical sub-volume, randomly positioned within the simulation domain but not touching its boundaries, and then taking the average of these quantities by dividing by the number of times counted. This process is repeated using cubical sub-volumes of increasing side length *L* on the order of the correlation length (between 0.2 and 4.0 nm, roughly the range over which the radial distribution function for this system size exhibits large fluctuations before settling down to its asymptotic value of 1). The results of this process and eq. (1) can then be used to calculate the G_{ij} for every cube size. This is possible because the numbers of molecules counted in this way approximate the average quantities in Eq. (1) in the grand canonical ensemble for a reasonably large system size, which could be for as few as 20000 molecules [10].
For the concentration in question, plotting the G_{ij} versus the inverse of the cube side lengths permits an estimation of the KBI for a cubical sub-volume of infinite size. In practice this is achieved by carrying out an interpolation of the data over the range in which the G_{ij} scale linearly with $1/L$ and extrapolating to the ordinate ($1/L = 0$) where *L* is infinite. The KBIs thus determined can then be used to evaluate Eq. (2) for every concentration, and the results compared with those obtained by the method outlined in the previous section.

3. Methodology

Five mixtures of methanol and water were prepared with the concentrations of methanol given by x_c = 0, 0.24, 0.5, 0.75 and 1 mole fraction. The solvent – co-solvent system always contained a total of 20000 molecules. An additional 250 methane molecules were added as solute.

In order to simulate the mixtures, the GROMACS molecular dynamics simulation package was used [11]. The methanol and water molecules were modeled using the GROMOS43a1 and SPC water force fields, respectively. All-atom simulations were carried out in the NpT ensemble with pressure maintained by the Berendsen Barostat at a pressure of 1 atm and a coupling time of 0.5 ps [12]. The integration time step used was 1 fs for all concentrations. All the simulations were allowed to equilibrate for 15 ns, after which the trajectory was extended by a further 15ns. Only the last 15ns of the trajectories were used to calculate the Kirkwood Buff integrals. The electrostatic interactions in the all-atom simulations were handled by means of the particle mesh Ewald.

Calculations of the KBIs, based on the particle fluctuation method (Eq. 1), were implemented in the Python programming language. Several Python scripts were developed to extract the coordinates of each atom from the system trajectories and then to count the number of each atomic species within small sub-volumes (cubes of side length *L*) of the simulation box (of side length L_t). In order to speed up these calculations these python scripts were parallelized to make use of 8 CPUs simultaneously, by using the multiprocessing module. This produced a fourfold increase in speed, which allowed the calculations to be run overnight, rather than for two to three days.

4. Simulation results

Initially, to test the water and methanol force fields a detailed comparison of the computed KBIs was made with the experimentally determined KBIs from Refs. [13-14]. Figure 1 shows the KBIs, as

calculated from the RDFs (solid lines) for a 50% methanol water mixture. The experimental values are given by the horizontal dashed and dotted lines for EXP 1 (Ref. [13]) and EXP 2 (Ref. [14]) respectively. In this simulation there were 10000 methanol and 10000 water molecules.

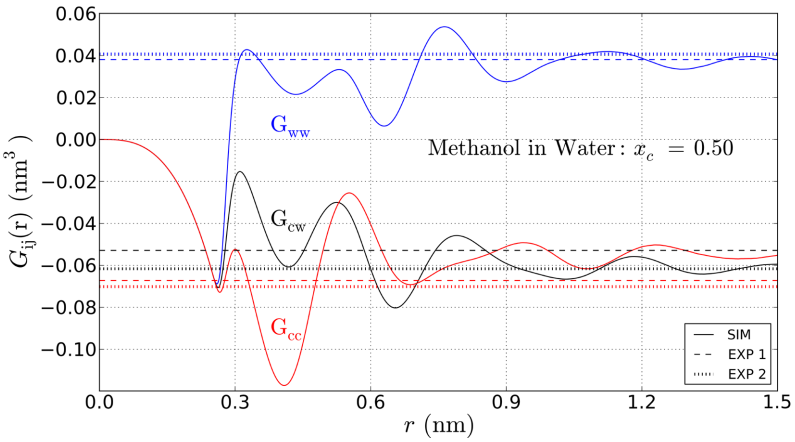

Figure 1: The Kirkwood Buff Integrals (KBIs) calculated via the radial distribution functions (solid curves) compared to the experimental values in references [13] (EXP 1) and [14] (EXP 2).

Figure 1 shows that the KBIs reach a reasonably well-defined plateau beyond r=1.5 nm, which is a good indication that the chosen system size for this work (20000 molecules in total) is sufficiently large. We arrived at this size by starting with a smaller system size and then doubling the system size until convergence in the KBIs was observed and no longer improved appreciably upon an increase in system size, up to 80000 molecules. Thus our system is sufficiently large to approximate the thermodynamic limit. In spite of this, however, we could not obtain agreement (within the experimental uncertainties) for concentrations of methanol below about 15% and we attribute this discrepancy to the well-known inaccuracies in the force fields employed here [15-17]. For the present work, in which our main aim is to compare the KBIs obtained from the same force field via two different methods, such inaccuracies in the force fields should not matter, and in view of the difficulties associated with re-parameterization of the force fields [17], we have chosen to ignore this problem in the present work.

In Fig. 2 we illustrate how the fluctuation method was used to obtain the KBIs via Eq. (1). In Fig. 2 the side length L of the sample volume (in this case a cube) was varied from about half the total simulation box size, down to one twentieth of the simulation box size. As expected from theory [7], the KBI value (in this case for water-water) scales linearly over a certain range of sample system volumes. The KBI for a system of infinite size is therefore well approximated for each concentration by extrapolating to best line fit to infinite L, i.e. to the intercept corresponding to $1/L$=0.

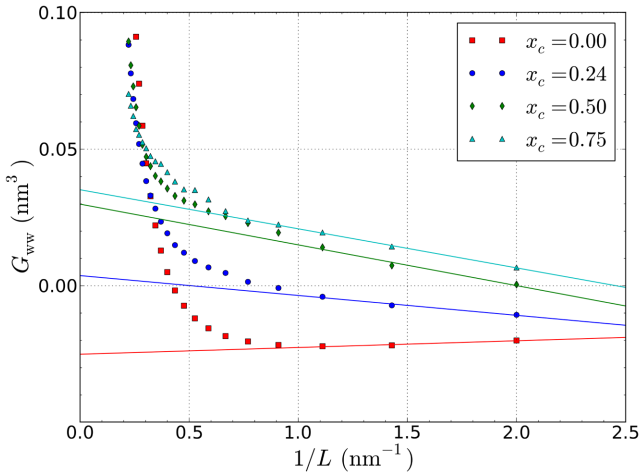

Figure 2: Illustration of the method of finite size scaling for four different concentrations of co-solvent for the methane (250 molecules), methanol (co-solvent) and water system.

Figures 3 (a) to (e) show comparisons of the KBIs obtained via the fluctuation method (Eq. 1) and the radial distribution functions (Eq. 2) for five different concentrations of the methane, methanol and water system. In Fig 3 (a), which is for pure water, the agreement between the two methods is satisfactory. Even though the system contains only 250 Methane molecules the RDF method still produces a KBI which shows a reasonably well-defined plateau, which indicated that in the calculation of the KBI, via the RDF method, the 15ns trajectory was sufficiently long for the purposes of a comparison between the two different calculation methods. In Fig. 3 (b) the two methods do not agree very well and the reason for this is not clear at present. One possibility could be that the inaccuracies in the methanol force field at lower concentrations produce unphysical clustering. The resolution of such clustering effects via the fluctuation method may require the use of much longer system trajectories (longer than the 15ns used here).

5. Discussion and conclusion

We have developed a test case in order to compare two methods for calculating KBIs from simulations of the hydration of Methane (hydrophobic solute) in a water – co-solvent mixture. Unlike the traditional method, which makes use of the RDF, the main advantage of the newer fluctuation method is that it can make use of relatively small systems to obtain results that are comparable to those which would require substantially longer simulation times. This advantage is due to the finite size scaling method, which allows the results from finite size systems to be extrapolated to systems which approach the thermodynamic limit.

The fluctuation method we employed made use of cubic sub-volumes to determine the particle fluctuations. This geometry becomes problematic when the linear dimensions of the sub-volume are on the order of the sizes of the molecules themselves [7]. These so-called nook and corner effects can be avoided by using spherical sub-volumes instead [5-7]. Although we have not done so in the present work, we thus expect that the agreement between the two methods discussed here could be improved by using spherical sub-volumes instead of cubes.

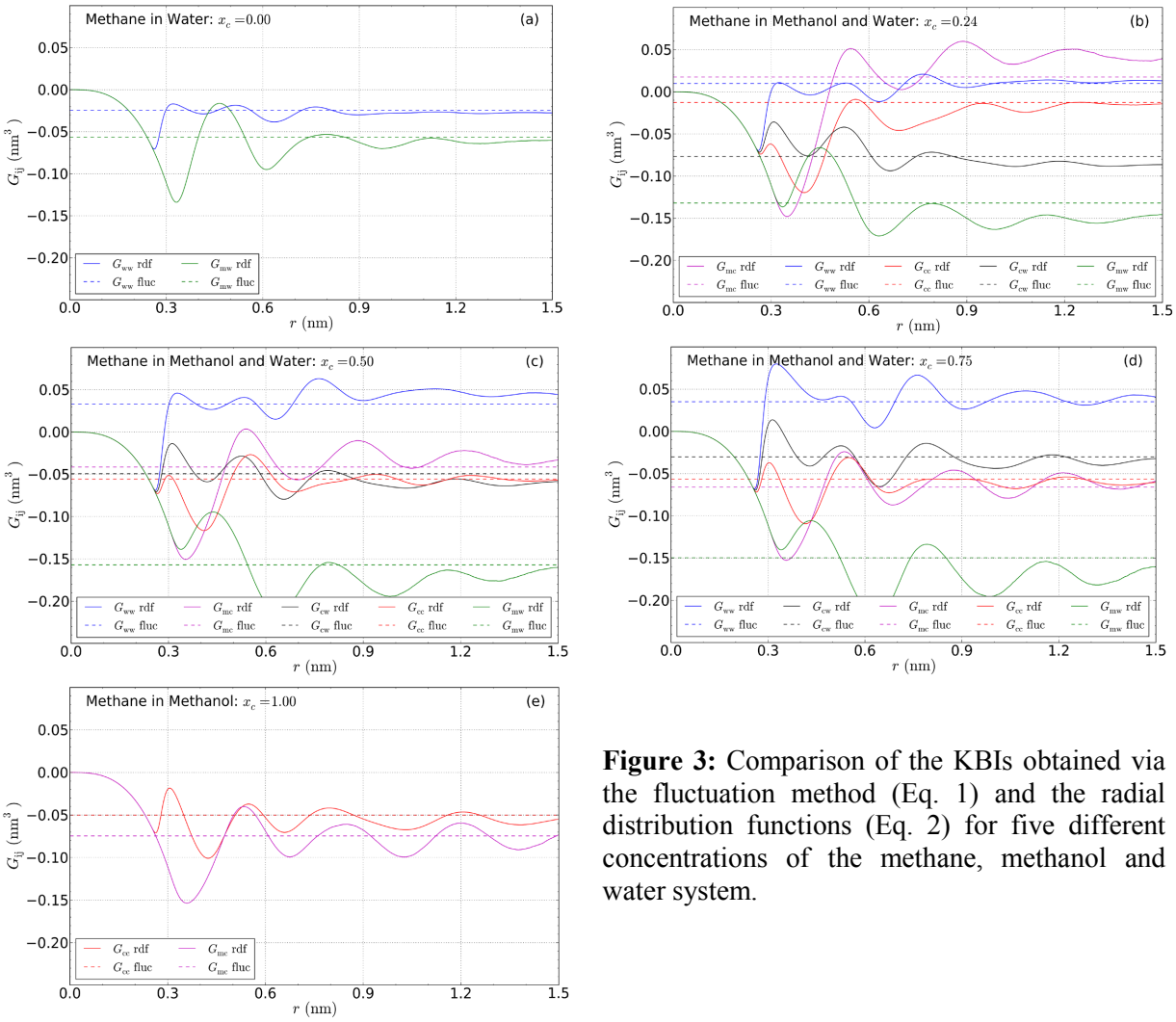

Figure 3: Comparison of the KBIs obtained via the fluctuation method (Eq. 1) and the radial distribution functions (Eq. 2) for five different concentrations of the methane, methanol and water system.

Problems with force field have prevented us from making a meaningful comparison of the solvation free energies with the experimental results. The difficulties associated with obtaining force field parameters that are applicable over a wide range of concentrations and to a variety of different systems are non-trivial [15-17] and since chemical potentials (and hence solvation free energies) are very sensitive to force field parameters, further refinement of the force fields would be required to facilitate a quantitative comparison of these quantities obtained from MD simulations and experimental results. However, the present work clearly demonstrates that finite size scaling *can* be used in the above context to reduce simulation times.

Acknowledgements

Both authors would like to thank Dr Debashish Mukherji for his assistance with this work. This work is based upon research supported by the National Research Foundation (NRF) of South Africa. Any opinion, findings and conclusions or recommendations expressed in this material are those of the authors and therefore the NRF do not accept any liability in regard thereto.

References

[1] Roccatano D, Colombo G, Fioroni M, and Mark A E 2002 Proceedings of the National Acadamy of Sciences **99** 12179
[2] Sadeghi R and Jahani F 2012 J. Phys. Chem. B **116** 5234
[3] Bennion B J and Daggett V 2003 Proceedings of the National Acadamy of Sciences **100** 5142
[4] Van der Vegt N F A and Van Gunsteren W F 2004 J. Phys. Chem. B **108** 1056
[5] Schnell, S. K. *et al*. 2011 J. Phys. Chem. B **115** 10911
[6] Liu X *et al*. 2011 J. Phys. Chem. B **115** 12921
[7] Schnell, S. K. *et al*. 2012 Molecular Physics **110** 1069
[8] Ben-Naim, A. Molecular Theory of Solutions; Oxford University Press: New York, 2006.
[9] Kirkwood, J G and Buff F P J 1951 Chem. Phys. **19** 774
[10] Mukherji D *et al*. 2012 J. Chem. Theory Comput., **8** 375
[11] Lindahl E, Hess B, and Van der Spoel D 2001 J. Mol. Mod. **7** 306
[12] Berendsen H J C *et al*. 1984 J. Chem. Phys. **81** 3684
[13] Perera A, Sokolić F, Almásy L, and Koga Y 2006 J. Chem. Phys. **124** 124515
[14] Matteoli E and Lepori L 1984 J. Chem. Phys. **80** 2856
[15] Weerasinghe S and Smith P E 2003 J. Chem. Phys. **118** 5901
[16] Weerasinghe S and Smith P E 2005 J. Phys. Chem. B **109** 15080
[17] Hawlica E and Rybicki M *Molecular Dynamic Simulation of the Ion Solvation in Methanol-Water Mixtures*, in Molecular Dynamics - Theoretical Developments and Applications in Nanotechnology and Energy, ed. Lichang Wang (InTech, 2012)

Thermal stability studies of platinum Schottky contacts on n- Si (111) and the defects introduced during fabrication and annealing processes.

M. Diale*, FD Auret, HT Danga, and SMM Coelho.

***molemi@up.ac.za**

Department of Physics, University of Pretoria, Private bag X28, Hatfield, 0028, South Africa.

Abstract. The electron beam deposition process was used to fabricate Pt Schottky contacts onto n-Si (111). Subsequently these contacts were annealed at temperatures varying from 50°C to 600°C for ten minutes at each temperature. The forward *I-V* characteristics show that the diodes were stable at lower voltages and suffer series resistance effects at voltages higher than 0.5 V. The reverse *I-V* curves shows increasing leakage current with increasing annealing temperature. At lower annealing temperatures, the reverse leakage current is constant at about 10^{-9} A. The ideality factor increased from 1.02 to 2.61 while the barrier height decreased from 0.80 to 0.70 eV as the annealing temperature increased. DLTS revealed that electron beam deposition introduced defects which were identified as the E-centre (VP centre), the A-centre (VO centre), the interstitial carbon (C_i) and the interstitial carbon-substitutional carbon (C_iC_s) pair. Isochronal annealing at 10 minutes intervals revealed that the E-centre vanishes between 125 and 175°C annealing while the concentration of the A-centre increased in this range. The A-centre annealed out above 350°C and after 400°C, all the electron beam induced defects were all removed.

1. Introduction

Metal silicides have been used as electrical conductors in silicon integrated circuits (SIC) since the beginning of the 20th century due to electrical properties such as low resistivities, easy fabrication and general stability in most processing techniques [1]. The resistivities of transition metal silicides are comparable with those of metals and metal-alloys, making this group of silicides good electrical conductors. Applications of metal-silicides have focused on Schottky barrier and ohmic contacts, gate and interconnection metal and as epitaxial conductor in heterostructures. Silicides with high melting points are attractive to use in high temperature device fabrication and operating environments [2]. In the fabrication of silicides, metals are deposited according to their melting points in different metallization systems. In particular, the electron-beam deposition (EBD) is used to deposit metals with high melting points, with an added advantage of uniform deposition rates. The EBD process, like many other metallization processes, introduces defects at and close to the metal-semiconductor interface, which has adverse effects on the device performance [3]. The defects responsible for the alteration of the barrier height of the metal contacts are those formed when energetic particles reach the semiconductor surface, creating damage in the lattice. In Si-based devices, defects created by proton and electron radiation increase the switching speed of the devices [4]. For high open circuit voltage Si photovoltaic devices, defect degradation in electrical properties of the device has been reported [5]. Defects introduced during EBD of metals on Si grown by Czochralski and float zone methods have previously been reported, where the E-centre (VP) and the A-centre (VO) appeared as dominant [6]. A defect similar to a divicancy was also observed [7]. The difference between the observed defects in reference [6] and [7] may be attributed to different EBD

systems used, different vacuum conditions as well as the use of Si with different concentrations of impurities such as C and O In this work, Pt Schottky contacts on n-Si (111) were fabricated and electrical properties of the contacts were investigated. We also report on the electronic properties of defects introduced during metal deposition and the effects of annealing on the defects.

2. Experimental Procedure

We have used epitaxially grown, 12 μm thick, Si doped with P to a level of 3.5×10^{15} cm^{-3} grown on a n^{++}Si substrate for our investigation. Before metallization, samples were first degreased in trichloroethylene (TCE), isopropanol (ISO) and methanol for 5 minutes each followed by dipping into HF for 60 seconds. Immediately thereafter, the samples were loaded into the EBD vacuum system that was pumped down overnight to a pressure below 10^{-6} mbar. Pt Schottky contacts 0.6 mm in diameter and of various thicknesses were deposited in an EBD vacuum system through a mechanical mask. Typically, eight Schottky Pt contacts were fabricated onto piece of 3 mm x 5mm Si. A Varian 10 KW electron gun (model 989-1118) vacuum evaporation system was used for metallization of Pt. The vacuum before evaporation was 10^{-6} mbar and this would increase to 10^{-5} mbar during deposition. After contact formation, current-voltage (*I-V*) and capacitance-voltage(*C-V*) measurements were performed to assess the quality of the diodes and to determine the free carrier density of Si. It was found that the free carrier density of the EPI Si was 3.5×10^{15} cm^{-3}. *I-V* and *C-V* measurements were repeated after every annealing cycle in Ar gas, for ten minutes from 50°C to 600°C in steps of 50°C. The diodes were irradiated with electrons from a Sr-90 source with a dose of up to 1×10^{15} cm^{-2}. Conventional DLTS was used to study defects introduced during the metallization and irradiation processes. High resolution Laplace DLTS was used to separate the conventional DLTS signals of defects with closely spaced energy levels. The signatures of the defects for electron traps, E_γ and their apparent cross-section σ_a were determined from Arrhenius plots of $\ln(T^2/e)$ versus $1000/T$, where e is the electron emission rate and T is the measurement temperature.

3. Results and Discussion

I-V characteristics of the diodes presented here are deduced from the thermionic emission current-transport model [1]. Figure 1 shows the semilog forward and reverse bias I-V characteristics of the samples in the annealing temperature range 100°C to 600°C. The forward I-V characteristics of the diodes annealed at temperatures up to 100°C show that the diodes were stable at lower voltages and suffer the series resistance effects at voltages higher than 0.5V. Series resistance increases sharply as the annealing temperature increases. Diodes annealed at temperatures higher than 250 °C suffer series resistance at voltages lower than 0.3 V. Figure 2 shows the graph of SBH and reverse leakage current at -1V as a function of annealing temperature. The reverse leakage current increased with increasing annealing temperature, from 9.4×10^{-4} μA to 7.0×10^{-2} μA. Throughout the annealing process the reverse leakage current at -1V remains in the same order of magnitude of μA. At about 300°C, the Schottky barrier height drops significantly while the reverse leakage current at -1V reaches its highest value.

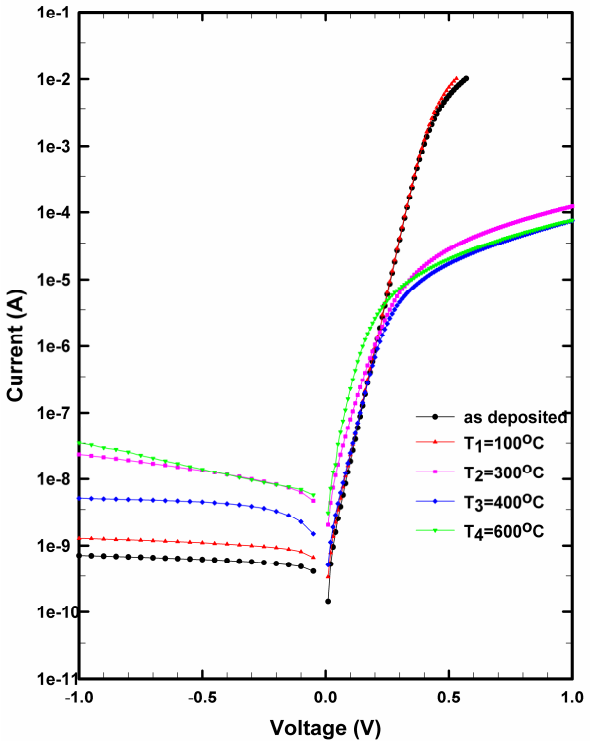

Figure 1: The I-V characteristics of SBD of Pt/n-Si(111) after isochronal thermal treatment at different annealing temperatures

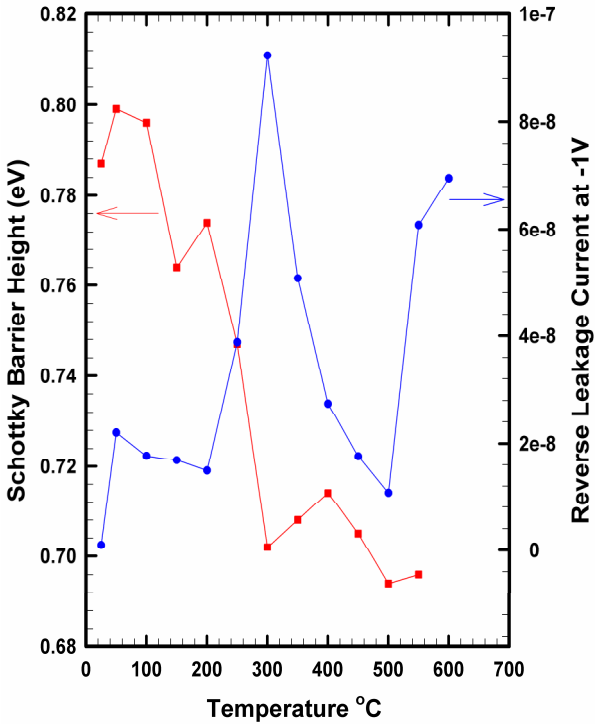

Figure 2: SBH and reverse leakage current at -1V factor as a function of temperature

Figure 3 shows the plots of Pt/n-Si Schottky barrier reverse biased C^{-2}-V characteristics at 1.0 MHz for different annealing temperatures. The plots of C^{-2} as a function of reverse bias voltage are near linear, indicating the formation of Schottky diode and constant non-compensated ionized donor concentration [8]. The SBH of the C^{-2}-V plots were found to be 0.88 eV before annealing while the I-V barrier height was 0.80 eV. Due to different nature of measurements techniques, SBH obtained by I-V and C-V are not the same [1]. Figure 4 shows the SBH and the ideality factor as a function of annealing temperature. The Schottky barrier height (SBH) deduced from the thermionic emission current model, decreased from 0.80eV to 0.70 eV, while the corresponding ideality factor increased from 1.02 to 2.61 as the annealing temperature increased. At temperatures between 240°C and 260 °C there appears a clear transition for the diodes where the ideality factor, SBH and the reverse leakage current at -1V changes.

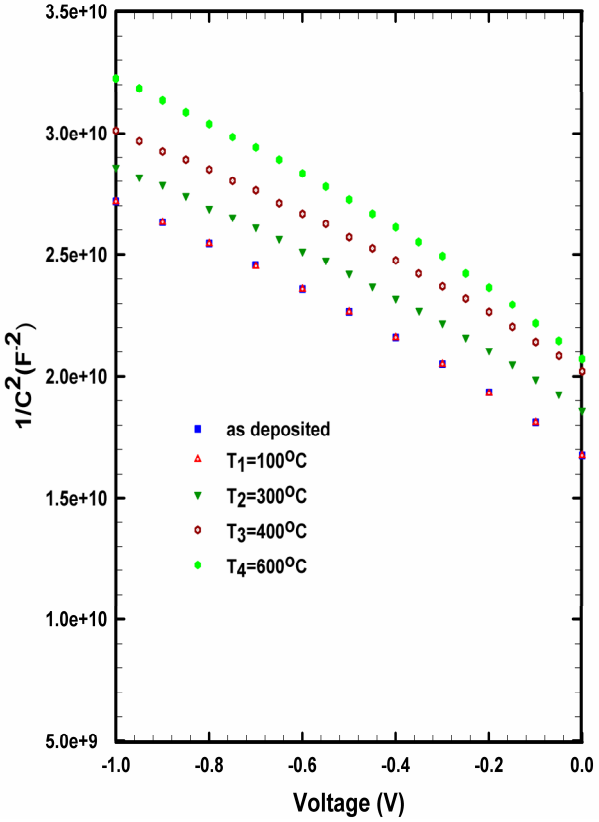

Figure 3: The C-V characteristics of SBD of Pt/n-Si(111) after isochronal thermal treatment at different annealing temperatures

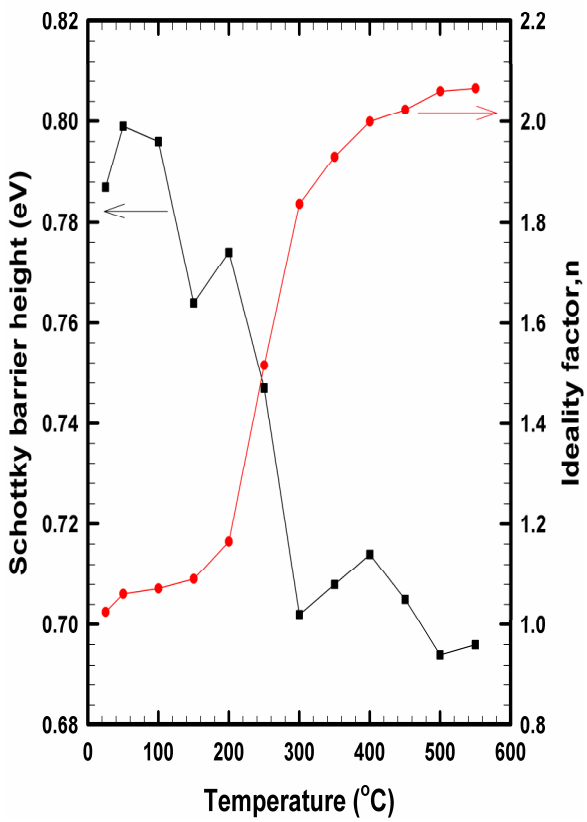

Figure 4: SBH and ideality factor as a function of temperature

We suggest that there is significant reaction between Si and Pt to form a Pt-Si intermix (25°C to 200°C), Pt_2Si (210°C to 280°C) and PtSi (280°C and 350°C). The changes in both SBH and ideality factor coincides with these three regions of Pt-silicidation: between 25°C to 200°C, 200°C to 300°C and 300°C and 550°C, as shown in Fig 4. It has been reported that Pt-Si starts forming at room temperature because of Pt atoms attaching themselves to Si atoms via the Si dangling bonds [10]. In addition, Larrieu et al has reported on the Pt-Pt_2Si-PtSi reaction chain completed within 2 minutes in the temperature range 300°C, 400°C and 500°C [11]. Furthermore, platinum silicides compounds are reported to grow sequentially as the temperature increases. Pt_2Si phase grows between the 210°C and 280°C due to the diffusion of Pt atoms into bulk Si, a process that continues until all the Pt is depleted from the surface [10]. PtSi forms between 300°C and 350°C, starting from the interface between Pt_2Si and Si, by in-diffusion of Si atoms into Pt_2Si lattice. This process is very rapid and comes to completion in about 2 minutes at 350°C [12]. In this work, the diode characteristics show that there Pt on Si formed a rectifying metal contact where the diodes characteristics followed a known pattern where SBH decreases with increasing temperature and the ideality factor increases with increasing temperature. The SBH, ideality factor and reverse leakage current at temperatures between 240°C and 260°C shows that there is a transition of the metal contacts, where Pt_2Si formed. The ideality factor is lowest at temperature range 50°C to 200°C and increases sharply from 200°C to 300°C, and then stabilizes after 300°C, further evidence due to different phase of silicide. The reserve leakage current

is lowest at lower annealing temperatures, but increases immediately with increasing temperature. We have found that Pt_2Si is a more stable compound for metal contacts for devices operating at lower temperatures while PtSi is suitable for devices operating at higher temperatures. In the case of solar cells which are exposed to radiation where temperatures fluctuate, a further study of PtSi as contact will be investigated.

Since we will be comparing the defects introduced during electron beam deposition (EBD) with those introduced by high energy (MeV) electrons, we first discuss the latter defects in n-type Si. High energy electron irradiation of Si introduces single vacancies and self interstitials that are mobile at room temperature [13]. These defects are created when the atoms are displaced by elastic scattering of the high-energy electrons. If a mobile interstitial moves next to a substitutional carbon (C_s) in the Si lattice, it may replace C_s to create C_i, which is also mobile at room temperature [14]. The DLTS spectrum that we record after room temperature irradiation will therefore contain the products that form when vacancies, interstitials and C_i form when reacting with each other (V_2, C_iC_s,) and with impurities in the lattice (VP, VO, C_iP_s) [15].

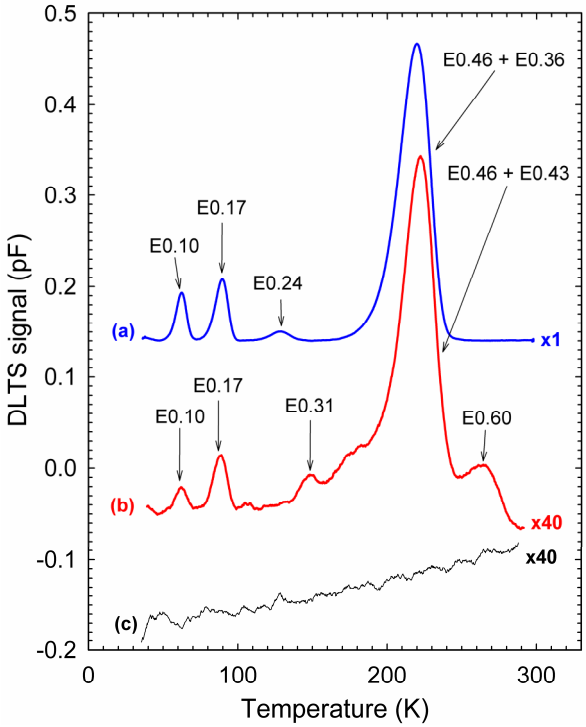

Figure 5: DLTS spectra of EPI n-Si: (a) Irradiated with MeV electrons; (b) Pt Schottky diode deposited by EBD, (c) control spectrum of resistively deposited Schottky diode.

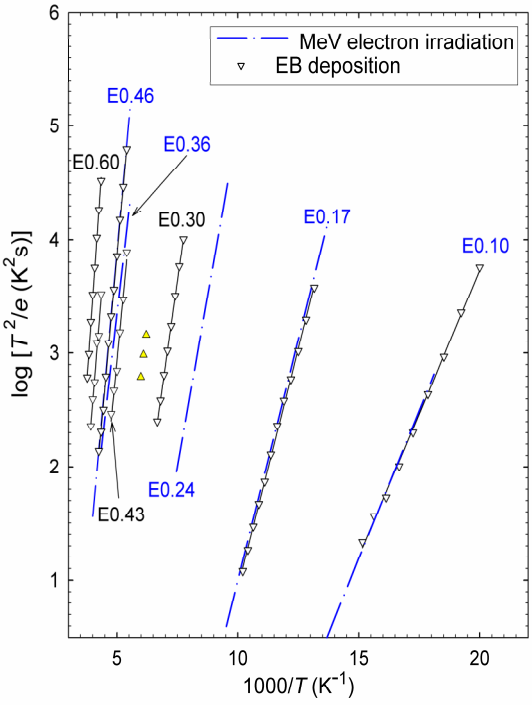

Figure 6: Arrhenius plots for defects introduced by: MeV electron irradiated n-Si (blue dot-dash line); and electron beam deposition (down triangles).

Curve (a) in Fig. 5 is the DLTS spectrum of MeV electron irradiated EPI n-Si recorded directly after irradiation with a fluence of 10^{15} e^- cm^{-2}. It contains at least four DLTS peaks. From the Arrhenius plots where the signatures of these defects were determined (Fig. 6), these peaks are identified as E0.10 (C_i), E0.17 (superposition of A-center (VO) and C_iC_s), E0.24 ($V_2^{=/-}$) and the superposition of E0.46 + E0.36 [13]. Here the E0.46 and E0.36 contributions to the peak at 220 K were determined by high resolution Laplace DLTS measurements. E0.46 is the VP or E-centre, while E0.36 has a similar signature as one of the metastable components of the C_iP_s centre [17]. The concentration ratio of VP to E0.36 is about 5:2. The VP + E0.36 peak also contains a small contribution due to the $V^{-/0}$ but this is too small to be distinguished from the two main peaks (VP and E0.36).

The DLTS spectrum recorded from Pt Schottky contacts that were fabricated by EBD, without any intentional shielding, is shown in curve (b) of Fig. 5. The similarities between some of the defects introduced by EBD and by MeV electron irradiation are evident. Both processes introduce E0.10 (C_i), E0.17 (VO + C_iC_s) and E0.46 (VP) [13 – 17]. This correspondence is confirmed by the Arrhenius plots in Fig. 6. From the Laplace DLTS spectra it was found that EBD does not introduce the E0.36 defect, but instead a defect peak E0.43 of which the DLTS peak also overlaps with that of the E0.46 (VP) peak. From the spectra in Fig. 5 it is also evident that EBD introduces at least two other defects not seen after MeV electron irradiation: E0.30 (similar, but not the same, signature as VOH [19]) and a defect E0.60. This latter defect consists of two closely spaced levels (see the Arrhenius plots in Fig. 6). This defect was also not observed in all EBD samples. It is also noteworthy that no divacancies ($V_2^{=/-}$) in measurable concentrations could be detected in samples prepared by EBD. Previously, a defect with very similar properties to $V_2^{=/-}$ was reported to be introduced after EBD of metal contacts on CZ Si [5].

4. Conclusions

Pt Schottky barrier diodes were fabricated onto n-Si(100) using electron beam deposition. The behaviour of the Schottky barrier diodes (SBD) was investigated under various annealing conditions. The variation of SBH and ideality factor with annealing temperature can be attributed to interfacial reactions of Pt and n-Si(100) and the subsequent formation of platinum silicides. The electrical properties of the Pt Schottky barrier diodes revealed the as deposited ideality factor of 1.02 and SBH of 0.80 eV. Pt_2Si was formed at temperatures between 210°C and 280°C with ideality factor increasing to 1.16 and SBH decreasing to 0.77 eV. At 300°C, PtSi has formed increasing the ideality factor to 1.83 while the SBH decreased to 0.70 eV. DLTS revealed that electron beam deposition introduced defects which were identified as the E-centre (VP centre), the A-centre (VO centre), the interstitial carbon (C_i) and the interstitial carbon-substitutional carbon (C_iC_s) pair.

Acknowledgements

This work has been made possible by the financial assistance of the South African National Research Foundation and the University of Pretoria.

References

[1] Rhoderick EH and Williams RH, Metal-Semiconductor Contacts, Clarendon Press, Oxford University Press, Oxford, (1988) 19.

[2] Murarka SP, Intermetallics **3** (1995) 173.

[3] Christensen C, Petersen JW and Nylandsted Larsen A, Appl. Phys. Lett. **61** (1992) 1426.

[4] Sawko DC and Bartko J, Appl. Phys. Lett. **30** (1983) 1756.

[5] Blakers AW and Green MA, IEEE Electron Device Letters **EDL-5** (1984) 246.

[6] Dobaczewski L, Kaczor P, Hawkins ID and Peaker AR, J. Appl. Phys. **76** (1994) 194.

[7] Dobaczewski L, Peaker AR, and Bode Nielsen, J. Appl. Phys. **96** (2002) 1821.

[8] Sze SM, Physics of Semiconductor Devices, John Wiley & Son, (1981) 254.

[9]Tsang JC, Yokota Y, Matz R and Rubloff G, Appl. Phys. Lett. **44** (1984) 430.

[10] Wittmer M, Phys Rev B 43 (1991) 4385.

[11] Larrier G, Dubos E., Wallart X, Baie X and Katcki J, J. Appl. Phys. **94** (2003) 7801.

[12] Zhou SM, Hundhausen M and Ley L, Thin Solid Films **358** (2000) 73.

[13] Watkins GD, Materials Science in Semiconductor Processing 3, (2000) 227.

[14] Jellison (Jr) GE, J. Appl. Phys. 53, 5715 (1982).

[15] Watkins GD, In: *Properties of crystalline silicon*, ed R. Hull (London: INSPEC, 1999 [Chapter 11.1].

[16]] Gurer E, Benson BW and Watkins GD, Mater. Sci. Forum **83 – 87**, (1992) 339.

Characterization and XPS information of commercially $Y_2O_2S:Eu^{3+}$ powder phosphor

JJ Dolo, FB Dejene and HC Swart*

Physics Department, University of the Free State, P.O. Box 339, Bloemfontein, 9300, South Africa

Corresponding author: swarthc@ufs.ac.za

Abstract. Trivalent-europium doped yttrium oxysulphide phosphor (band gap ~ 4.2 – 4.8 eV) is an important phosphor system extensively applied in colour televisions, high resolution displays, memory devices, after glow phosphors, etc.. We report on the characterization of a red long-lasting phosphorescent material, $Y_2O_2S:Eu^{3+}$. The morphology and optical properties of the powder phosphor were characterized, the morphologies thereof shows that the particles differ in terms of sizes and shapes. Energy Dispersive X-ray analysis (EDX) confirms all the elements on the surface. X-ray diffraction (XRD) investigation showed a pure hexagonal phase of Y_2O_2S. All peaks have been perfectly indexed as the pure hexagonal phase. From the Photoluminescence (PL) spectrum, the main emission peaks are ascribed to the Eu^{3+} ion transition from ^5D_J (J=0, 1, 2) to ^7F_J (J=0, 1, 2, 3, 4). After irradiation with a wavelength of 320 nm, the phosphor emitted red long-lasting phosphorescence. X-ray photo electron spectroscopy (XPS) peaks for the $Y_2O_2S:Eu^{3+}$ have been observed for Y 3d at 156 and 158 eV, Y 3p at 298.5 and 310.5 eV, S 2p at 164.5 eV and S 2s at 228 eV, respectively.

1. Introduction

Phosphor is defined as a material that emits photons with high luminescence efficiency. The cathodoluminescent phosphors convert electron energy into visible light and are used in display devices as screen material. Trivalent rare-earth ions have usually been selected to be used as activators in line-emitting phosphors because the spectral emission lines of trivalent rare-earth ions in the host lattice are rather narrow [1,2]. Yttrium oxysulfide doped with europium ($Y_2O_2S:Eu^{3+}$) red phosphor is a high efficiency cathodoluminescent material that is used extensively in the phosphor screens. $Y_2O_2S:Eu^{3+}$ has sharper emission lines leading to better colorimetric definition and higher luminescence efficiency than the other red phosphors [3,4]. But compared with the other color persistent phosphors [5], the progress on the research of red persistent phosphors is very limited. Therefore, the development of red long-lasting phosphors with high luminescence and good chemical stability is urgently needed. Yttrium oxysulfide has been known as an excellent phosphor host material for a long time. While doped with Eu^{3+}, Mg^{2+}, and Ti^{4+} a red long- lasting afterglow phosphor that has the afterglow time of above 3h was synthesized [6]. However, the progress on the systemic research of Y_2O_2S: Eu^{3+}, Mg^{2+}, Ti^{4+} was very slow and their luminescent mechanism was not well understood. In this study the Y_2O_2S: Eu^{3+} crystal structure, surface morphology, photoluminescence and surface state were characterized.

2. Characterization

Commercially available Y_2O_2S: Eu^{3+} phosphor powders, obtained from Phosphor Technology were characterized using different techniques. Scanning Electron Microscopy (SEM) images were taken with a Gemini LEO 1525 Model to determine the particle morphology. The crystalline structure of the phosphor powders were investigated using a Burker D8 (Burker Co, German) X-ray diffractometer with Cu Kα = 1.5406 Å. The 100 μm, 25 W, 15 kV energy X-ray beam of a PHI 5400 XPS Versaprobe was used to analyze the S 2p, O 1s, O 2s, Y 3d and Y 3p binding energy peaks (pass energy 11.8 eV, analyser resolution ≤ 0.5 eV). The possible chemical states maybe identified with the Multipak version of 8.2c computer software [7] using Gaussian-Lorentz fits.

3. Results and Discussion

Figure 1 shows the XRD pattern of the Y_2O_2S: Eu^{3+} phosphor powder. The position and relative intensity of the XRD lines are in good agreement with the data of JPCDS file No.24-1424 [8], which shows the pure Y_2O_2S hexagonal structure.

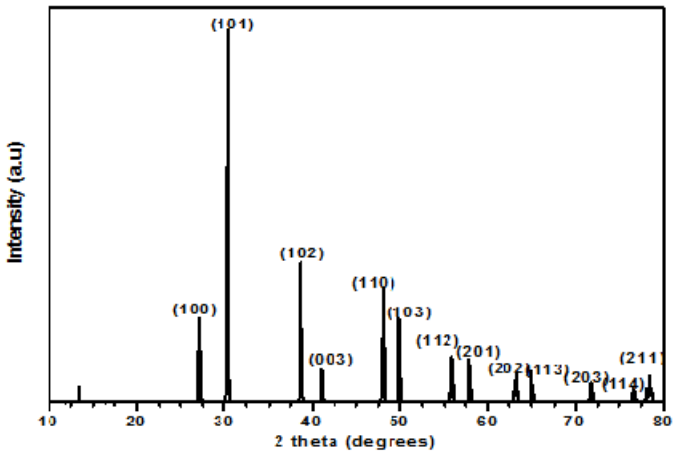

Figure 1. XRD pattern for the Y_2O_2S:Eu^{3+} phosphor powder.

Figure 2 (a) and (b) shows the SEM image of the Y_2O_2S:Eu^{3+} phosphor powder at different magnifications. The particles are polyhedron in shape and agglomerated, showing relatively good close packing which is one requirement for the cathode ray display (CRT) or X-ray intensifying screens and the particles differ in sizes and shapes. Figure 2 (c) shows the EDS data which confirms the presence of all the elements in the matrix, i.e (Y, O and S) together with the adventitious C. Eu^{3+} ions were not detected probably due to their relatively low concentration in the Y_2O_2S:Eu^{3+} matrix.

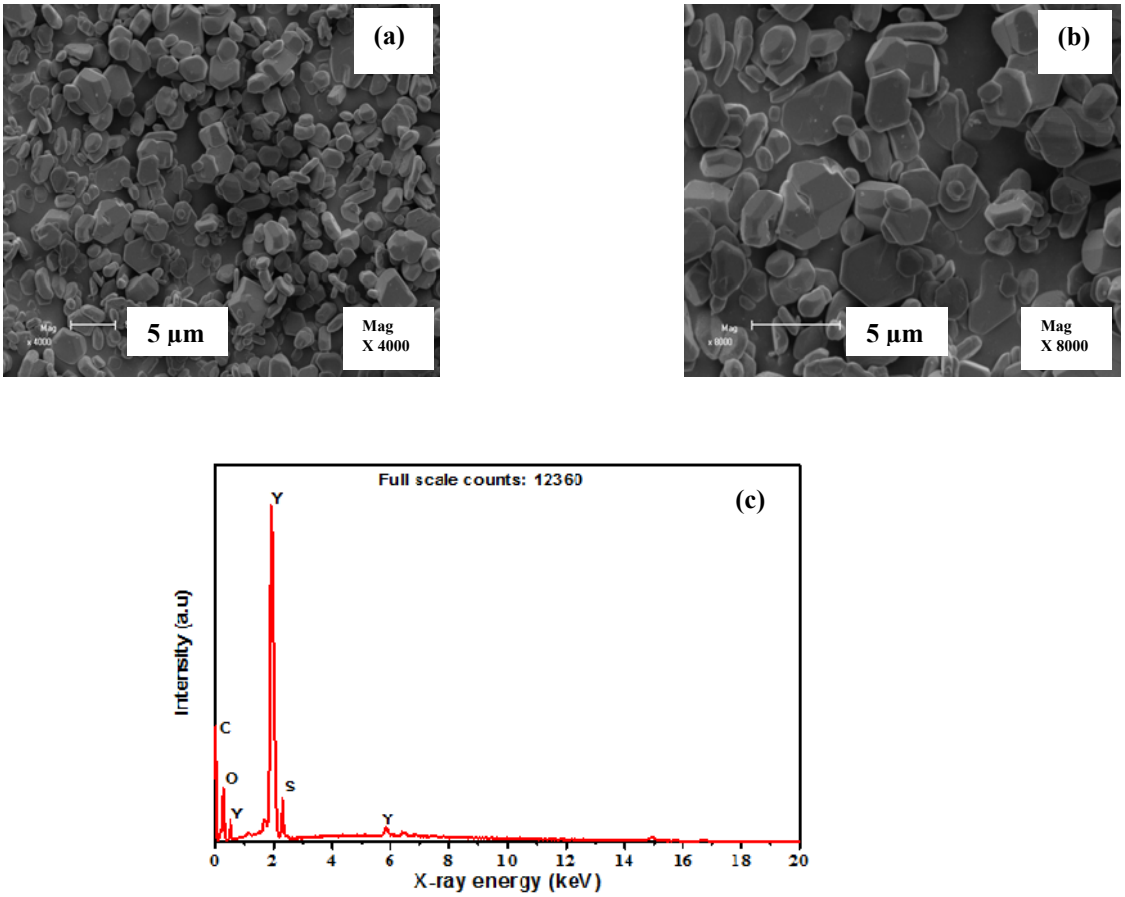

Figure 2. (a) and (b) SEM image at different magnifications and (c) EDS spectrum of the $Y_2O_2S:Eu^{3+}$ phosphor powder.

Figure 3, shows the PL spectra of $Y_2O_2S:Eu^{3+}$ phosphor powder with excitation energy (λ_{ex}= 320 nm). The main emission peaks are due to the Eu^{3+} transition $^5D_j \rightarrow {}^7F_j$. The stronger red emission peaks lines at 618 and 627 nm are due to the transition $^5D_0 \rightarrow {}^7F_2$. The shorter wavelength line at 595 nm corresponds to the transitions $^5D_0 \rightarrow {}^7F_1$. The PLE (Photoluminescence excitation) spectra consist of extremely broad bands that extend well into the near-UV region. Therefore, $Y_2O_2S:Eu^{3+}$ can be used as a red emitting phosphor in a three-band white LED excited by near-UV LEDs.

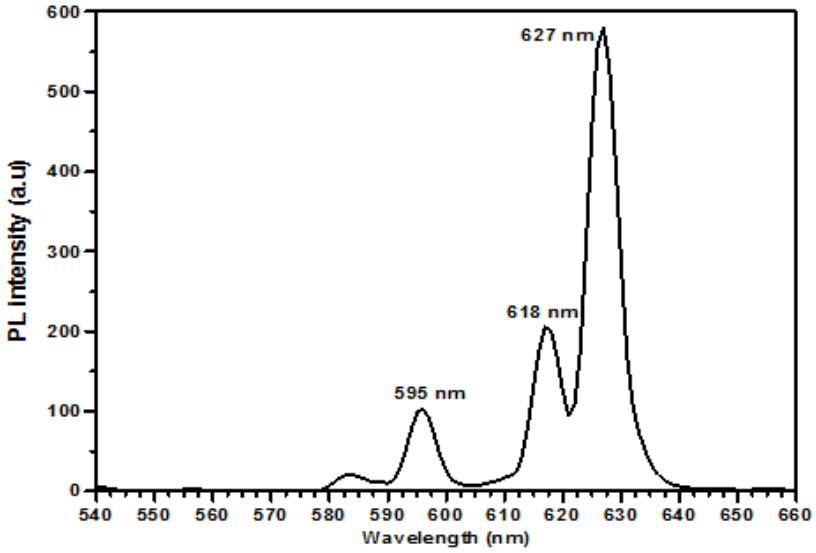

Figure 3. PL spectra for $Y_2O_2S:Eu^{3+}$ phosphor powder.

Figure 4, shows the XPS surface measurement of the $Y_2O_2S:Eu^{3+}$ phosphor after sputtered clean (sputtering done with Ar^+, 2 kV, 2 µA, 1x1 mm raster). The XPS spectra of the $Y_2O_2S:Eu^{3+}$ shown in figure 4, reveals the presence of yttrium and sulphur in the expected stoichemistry Y:S). The spectra showed no extraordinary features.

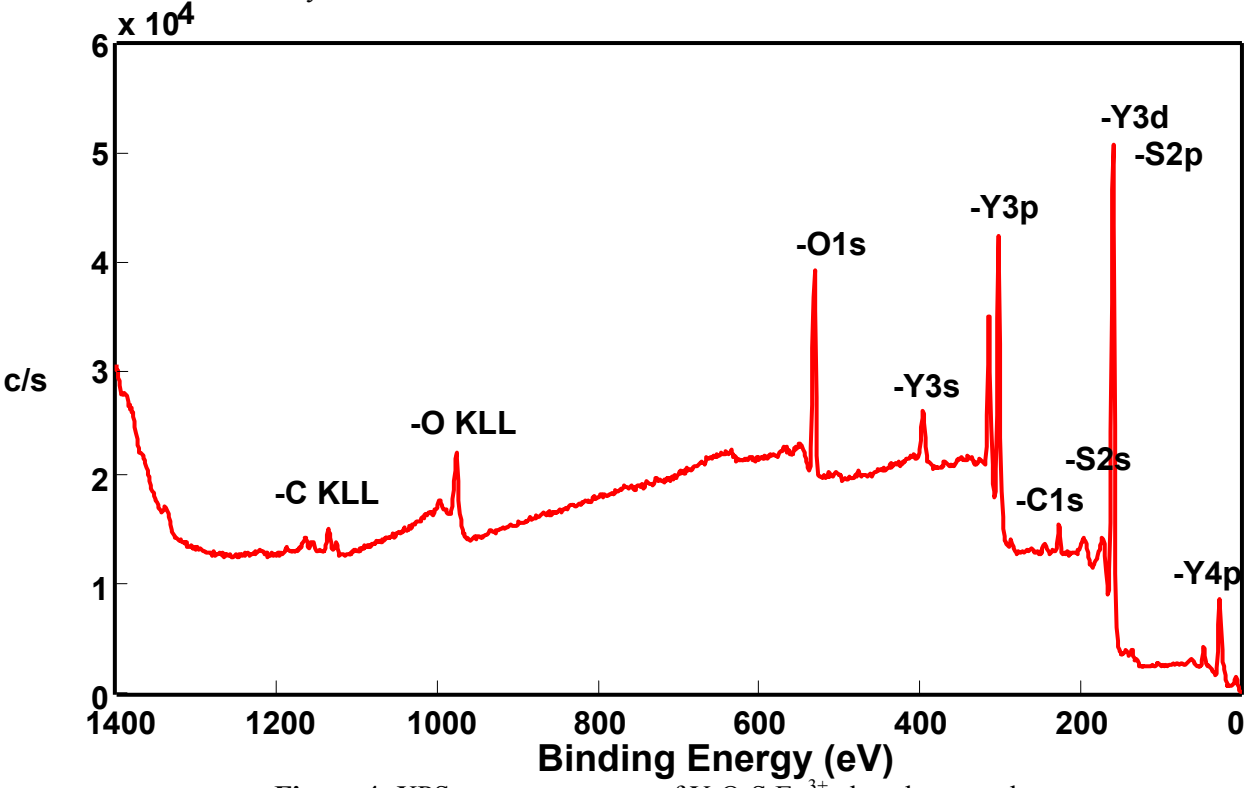

Figure 4: XPS survey spectrum of $Y_2O_2S:Eu^{3+}$ phosphor powder

Figure 5 (a), shows the XPS measured spectra of O 2s, Y 4p as well as the S 3s and Eu 5d peaks. The Y 4p lines are located at about 23.7 eV ($Y4p_{3/2}$) and 24.8 eV ($Y4p_{1/2}$), O 2s around 23 eV, S 3s at 18 eV, Eu 5p at 19 eV [9]. The Eu 3d peaks are shown in figure 5 (b). It is clear that both Eu^{2+} and Eu^{3+} are present in the Y_2O_2S. The Eu^{3+} species are, however, much more then the Eu^{2+}.

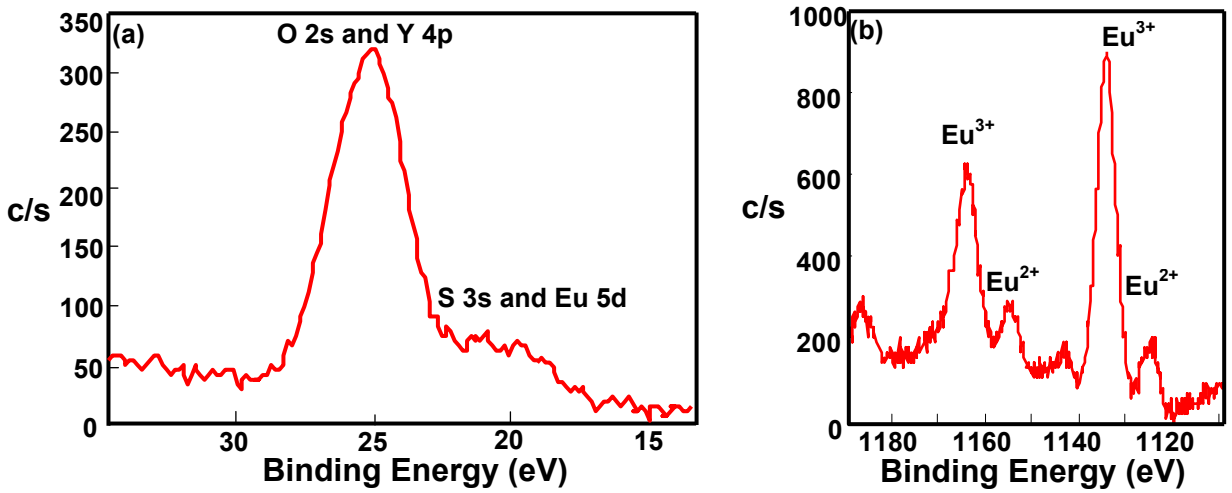

Figure 5. (a) XPS measured spectra of the O2s and Y4p of $Y_2O_2S:Eu^{3+}$ phosphor powder and (b) the spectra of Eu 3d.

Figure 6, shows the XPS measured spectrum of Y 3d from $Y_2O_2S:Eu^{3+}$. It has been reported that the $Y3d_{5/2\text{-}3/2}$ doublet position is at 157.2 eV and 159.7 eV [10]. Figure 6 (b) shows the XPS spectrum of O 1s with two different oxygen states. O1s peaks were located at 531.3 eV and 532.0 eV. The lower energy O1s peak is very consistent with normal Y-O bonding energy in Y_2O_2S [10].

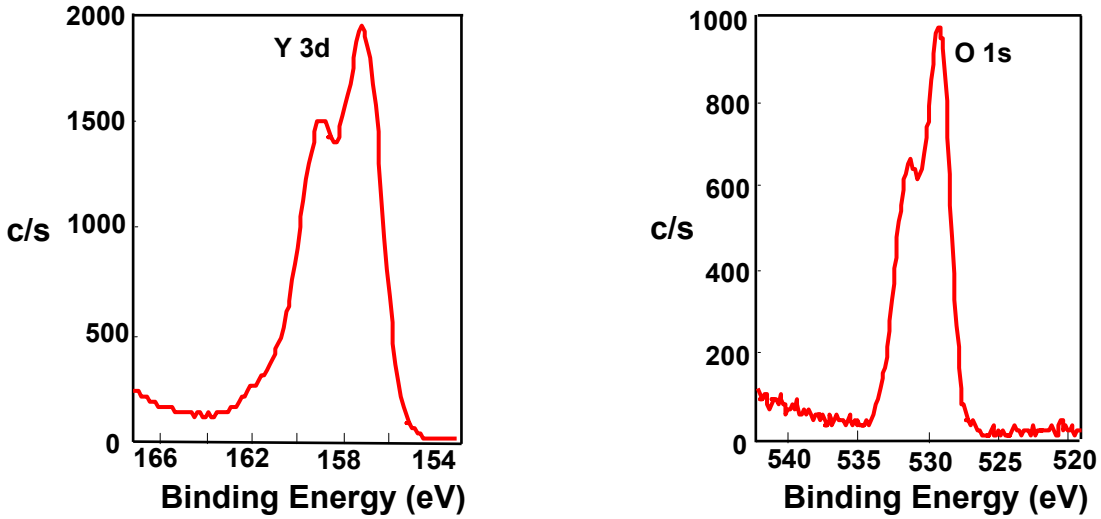

Figure 6. XPS measured spectra of the (a) Y 3d and (b) O 1s of $Y_2O_2S:Eu^{3+}$ phosphor powder.

Figure 7 (a) and (b), show the XPS of S 2s and S 2p of $Y_2O_2S:Eu^{3+}$ respectively. The low signal-to-noise ratio in some of the XPS spectra in the region of both S 2s and S 2p peaks made systematic quantification of the different sulphur species present in the samples difficult. However, two sulphur species can be identified in the S 2p peak, at the binding energies of 167.8 eV and 164.9 eV. In the light of the S 2p peak analyses, only minor amounts of surface sulphate were present in the reacted

samples. More work is, however, needed to deconvoluted all the peaks, especially those peaks in which overlapping of the different species occurred, to determine the correct binding energy positions.

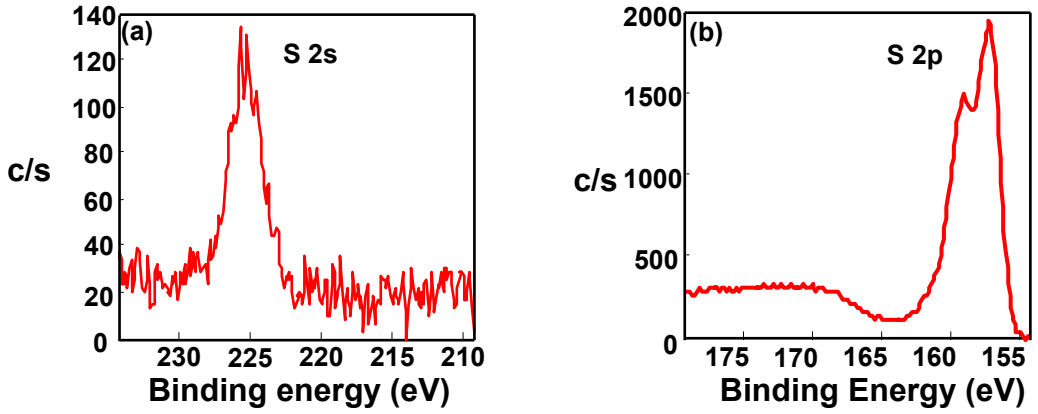

Figure 7: XPS measured spectra of the (a) S 2s and (b) S 2p of $Y_2O_2S:Eu^{3+}$ phosphor powder.

4. Conclusion

EDS analysis confirms the presence of all elements on the surface of $Y_2O_2S:Eu^{3+}$. The hexagonal phase of $Y_2O_2S:Eu^{3+}$ was successfully determined by XRD. The elemental state of the surface was also determined with XPS. The SEM images with different magnifications revealed spherical particles with different shapes and sizes. CL degradation for both powders and thin films of $Y_2O_2S:Eu^{3+}$ will be done to confirm some species on the surface.

Acknowledgement

The authors send gratitude to the National Research Foundation (NRF) for funding the project and the University of Free State (Physics department, Center for microscopy and Geology department) for the research techniques used in this study.

Reference

[1] Yost D M, Russel T R and Garner C S, The Rare Earth Elements and their Compounds, Wiley, New York, 1950.
[2] Taylor K N R, M I Darby M.I, Physics of Rare Earth Solids, Chapman & Hall, London, 1965.
[3] Royce M R 1968 U.S. Patent 3, **245** 418
[4] Yocom P N 1968 U.S. Patent 3, **247** 418
[5] Wang X X, Zhang Z T, Tang Z L, Lin Y H 2003 *Mater. Chem. Phys*. **80** 1.
[6] Murazaki Y, Arak K and Ichinomiya K 1999 *J. Rare Earth Jpn.* **35** 41.
[7] Moulder F, Stickle W.F., Sobol P.E., Bombe K.D. 1995 Handbook of X-ray Photoelectron Spectroscopy, ULVAC-PHI, Inc., 370 Enzo, Chigasaki, Japan **143**.
[8] Zhou X, Xing M, Jiang T, Fu Y, PengY, Wang H and Luo H 2014 J. Alloys Compd. **585** 376
[9] Thirumalai J, Chandramohana R, Auluck S, Mahalingam T and Srikumar S R 2009 J. of Colloid Interf. Sci. **336** 889.
[10] de Rouffignac P, Park J-S and. Gordon R G 2005 *Chem. Mater*. **17** 4808.

The effect of nano sized Alq_3 on the external quantum and power conversion efficiencies of OLEDs

M M Duvenhage[1], O M Ntwaeaborwa[1], E Wrzesniewski[2], J Xue[2] and H C Swart[1,3]

[1]Physics Department, University of the Free State, P.O. Box 339, Bloemfontein, 9300, South Africa
[2]Department of Materials Science and Engineering, University of Florida, USA

[3]Email: swarthc@ufs.ac.za

Abstract Alq_3 is widely used in organic light emitting diodes (OLEDs) as emission and electron transport layer. Commercial Alq_3 is normally used in the fabrication of OLEDs. In this study nano sized Alq_3 was synthesized using a co-precipitation method and it was purified using temperature gradient sublimation. The Alq_3 was then used to fabricate a simple two layer OLED with a device structure: ITO/NPB/Alq_3/Cs_2CO_3:Al. The electroluminescence (EL) spectrum of the device consisted of a broadband with a maximum at ~520 nm and was similar to the photoluminescence (PL) spectrum observed from the synthesized Alq_3 powder. The luminance (L)–current density (J)–voltage (V) characteristics of the device showed a turn on voltage of ~ 2V, which was lower than the current density of the device fabricated using the commercial Alq_3. The external quantum efficiency (η_{EQE}) and the luminous power conversion efficiency (η_P) of the device were 1% and 2 lm/W, respectively.

1. Introduction

Since its first report in 1987 by Tang and Van Slyke [1], tris-(8-hydroxy-quinoline) aluminium (Alq_3) has been used in organic light emitting devices (OLEDs) both as a green light emitting material and an electron transporting layer (ETL). An OLED device consists of an electroluminescent (EL) medium of thin organic layers (<0.2 μm) sandwiched between two electrodes. Some organic layers transport holes and others electrons. When a potential difference is applied between the anode and the cathode the holes and electrons will migrate towards the oppositely charged electrode. Holes and electrons will then be transferred to the emitting material forming tightly bound excitons which emit photons upon relaxation. These photons are then capable of escaping from the device architecture through the transparent anode and out of the glass substrate.

In this study we have synthesized nano-sized Alq_3 for use in fabricating OLEDs by thermal evaporation process. Thermal evaporation utilizes high vacuum and direct heating of materials to deposit nanoscale layers of material onto a desired substrate and is an ideal technique for the deposition of organic small molecules due to the fine control and relatively gentle method of deposition. A description of this method and the tools necessary are presented.

In this study Alq_3 was used as both the ETL and emitting layer (EML) of the OLED, while commercial N,N'-di(naphthalen-1-yl)-N,N'-diphenyl-benzidine (NBP) was used as the hole transporting layer (HTL). Indium tin oxide (ITO) coated onto a glass substrate was used as the anode, while the Al:Cs_2CO_3 top electrode was used as the cathode. The devices fabricated using the synthesized Alq_3 are compared with those fabricated using the commercially available Alq_3. Furthermore, the current-voltage-luminance characteristics were also measured and the external quantum and power efficiencies of the two devices are compared.

2. Experimental

2.1 Synthesis and purification of Alq_3

Alq_3 phosphor powder was synthesized using the co-precipitation method. 0.625g of 8-hydroxyquinoline (8-Hq) was added to a mixture of 6.5 ml H_2O and 6.5 ml of glacial acetic acid. The mixture was stirred for 15 minutes. 0.5 g of $Al(NO_3)_3$ was added to 20 ml of H_2O and this mixture was also stirred for 15 minutes. The $Al(NO_3)_3$ solution was added drop wise to the 8-Hq solution with vigorous stirring. The resulting brown solution was stirred for 15 minutes. 5 ml of NH_4OH was added drop wise to the solution while stirring vigorously. A yellow green precipitate was formed. The precipitate was filtered and washed 8 times with distilled water. The precipitate was dried in an oven overnight at 80°C. After drying, the precipitate was ground to get a fine powder. The powder was dissolved in 10 ml acetone and left to recrystallize in air at room temperature.

During purification of Alq_3, three quartz tubes (segments) were used. These tubes were placed in an outer quartz tube. 0.394 g of raw material was loaded in the first segment. The outer quartz tube was sealed with quartz wool to prevent any solids from entering the vacuum pumps. The tube was connected to a roughing pump and turbo molecular pump and was evacuated to a pressure of 2×10^{-6} Torr. The second segment was heated to 150 °C in 90 minutes. The first segment was heated to 50 °C above this temperature and segment three was heated to 50 °C below this temperature, yielding a temperature gradient of 100 °C over the segments. The setup was left for 24 hours. After that the heaters were switched off and the system was allowed to air cool back to room temperature. Impurities were left in the first segment and had a dark brown color, while the purified Alq_3 crystals were collected in the second segment (bright yellow color). Almost no material was present in the third segment. Segment two was harvested for purified material and 0.140 grams (35.53%) of the material was yielded. The impurities yielded almost 15% and 50% of the raw material was lost during the purification.

2.2 Fabrication of OLEDs

Glass substrates precoated with an indium tin oxide (ITO) anode (sheet resistance ~ 20 Ω/sq) were degreased in detergent and de-ionized water, and cleaned with ultrasonic baths of acetone and isopropanol consecutively for 15 minutes each. The substrates were then exposed to an ultraviolet-ozone ambient for 15 minutes immediately before loading into a high vacuum thermal evaporation system (base pressure ~ 3×10^{-7} Torr). All the organic and metal layers were deposited successively without breaking the vacuum. The device structure consisted of ITO/NPB/Alq_3/Cs_2CO_3:Al layers and they are shown in figure 1. The NPB and Alq_3 layers were 50 nm thick each, the Cs_2CO_3 layer was 1nm and the Al layer was 80 nm thick.

Figure 2 shows the energy level diagram of the fabricated OLED device [2]. A barrier for electron injection is commonly present at the metal-organic contact when the work function of the metal is larger than the lowest unoccupied molecular orbital (LUMO) of the organic materials, the use of a low work function metal is highly desirable to facilitate the injection of electrons. By adding sub-monolayer amounts of LiF or Cs_2CO_3 between the cathode and ETL, the work function of the metal can be decreased dramatically [3]. Electrons are injected from the cathode (Al:Cs_2CO_3) into the Alq_3 layer, which acts as the ETL. The hole-injecting contact requires a metal of high work function to match the highest occupied molecular orbital (HOMO) of the organic hole transporting layer. This contact must also be transparent to permit light to exit the device in an effective manner. Most OLEDs rely on the transparent and conductive indium tin oxide (ITO) as the anodic material to facilitate the hole-injection. The work function of ITO ranges from 4.5 to 5.0 eV [4] and is strongly dependent on the methods of surface treatment. Treatment of ITO glass substrates using UV-ozone substantially increases its work function and also enhances the hole-injection from the ITO anode into the HTL. Holes are simultaneously injected from the anode (ITO) into the NPB layer, which acts as a hole transporting layer. The Alq_3 layer acts as the emissive layer and electron-hole recombination takes

place just next to the interface between Alq_3 and NPB on the Alq_3 side. During recombination photons with the wavelength of 520 nm are released.

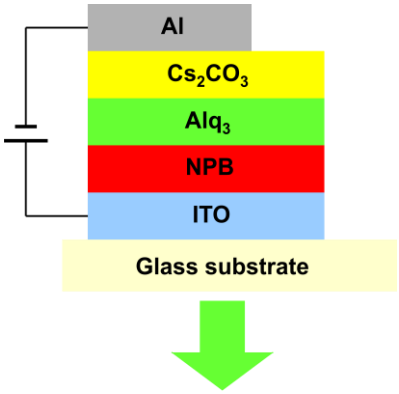

Figure 1: Schematic illustration of the device structure.

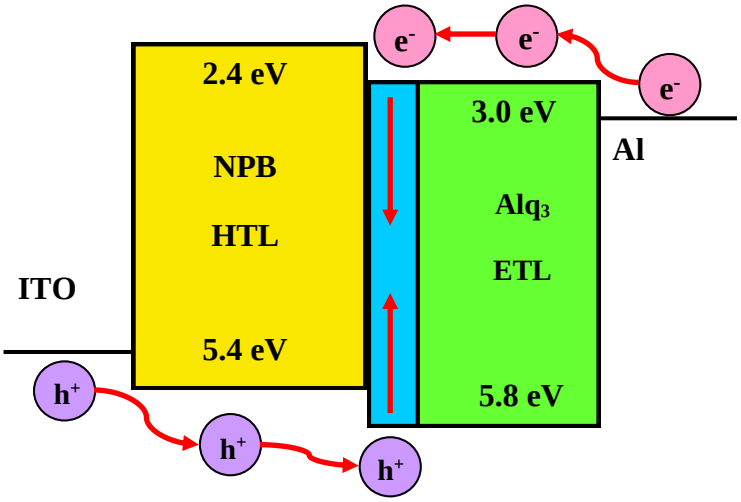

Figure 2: Energy level diagram of the fabricated OLED.

2.3 Characterization

The average particle size of the samples was estimated from the XRD data recorded using a Bruker D8 Advance Diffractometer equipped with a Cu Kα source. Luminance (*L*)–current density (*J*)–voltage (*V*) measurements were conducted in ambient conditions using an Agilent 4155C semiconductor parameter analyzer and a Newport 818-UV photodetector. The luminance of the OLEDs was calibrated using a Konica Minolta LS-100 luminance meter assuming a Lambertian emission pattern. Electroluminescence (EL) spectra were recorded using an Ocean Optics Jaz spectrometer.

3. Results

The crystallanity of the Alq_3 powders was determined by XRD and the spectrum is shown in figure 3. The peaks are in agreement with the data reported by Mao et al [5], confirming that the chemical compund we synthesized was indeed Alq_3. The standard data available on various XRD databases for Alq_3 does not match with the sample, because the standard data that was reported by Taylor et. al. [6] in 1973 was for tris(quinolin-8-olato)titanium(III) (Tiq_3) and not for Alq_3. There is therefore a mismatch between the standard data referenced in JCPDS 26-1550 with the Alq_3 sample prepared in this study. Peaks marked with an arsterik (*) are not yet identified at present. The average particle size determined by using Schrerrer's equation was found to be 40 ± 4 nm.

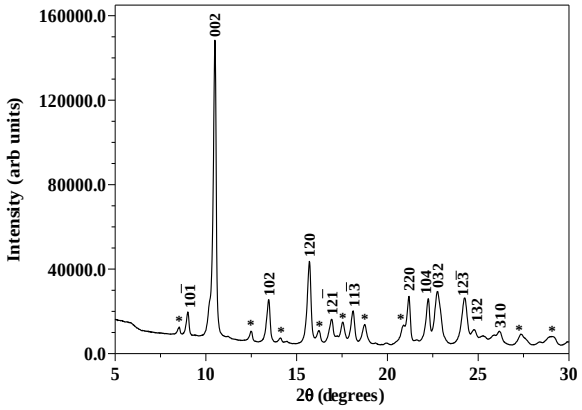

Figure 3: XRD spectra of Alq_3 after recrystallized in acetone.

A potential difference of 4 V was applied to the OLED at a constant current of 400 µA and the electroluminescence (EL) of the device was measured. The device's EL was compared to a device fabricated with commercial Alq_3. The normalized EL curves are shown in figure 4. Both devices show emission at 520 nm. This emission is consistent with the photoluminescence (PL) data reported previously [7] for nano sized Alq_3 powder.

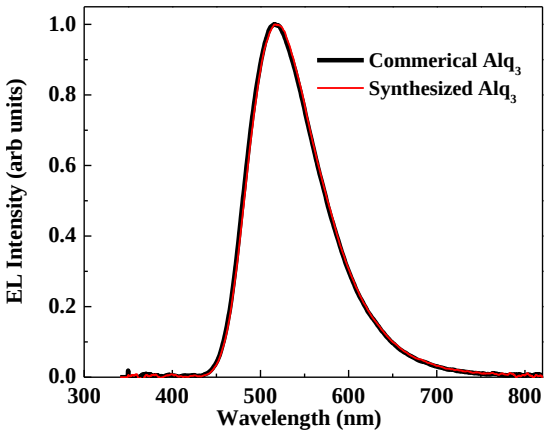

Figure 4: The EL spectra of commercial and synthesized Alq_3, both are showing a broad emission peak with a maximum at 520 nm.

Figure 5 compares the *L-J-V* characteristics of OLED devices fabricated using the synthesized and commercial Alq_3. Both devices were found to have a turn on voltage of ~ 2 V. The current density of the device fabricated using the commercial Alq_3 was higher than that of the one fabricated with the synthesized Alq3. The luminance of the commercial Alq_3 device was 1.5× more intense than that of the synthesized Alq_3 device. The luminance of both devices dropped to 0 cd/m^2 at 10 V, pointing to a complete breakdown of the device. The external quantum efficiency (η_{EQE}) and power conversion efficiency (η_P) were calculated based on the methods recommend by Forrest et al [8] and the plots of η_{EQE} and η_P versus luminance are shown in figure 6. Both devices show a maximum η_{EQE} of just above 1%. This is consistent with other η_{EQE} values reported for devices fabricated with commercial Alq_3 [9]. The η_P value at 100 cd/m^2, which is an important luminance level for display devices, was about 2.5 lm/W for the commercial Alq_3 device and it dropped to 2 lm/W for the synthesized Alq_3 device. This is an indication that the synthesized Alq_3 layer degrades faster, especially under high voltages. This might be due to some impurities like hydroxyquinoline and Al-O compounds which were probably still present in the Alq_3 even after purification.

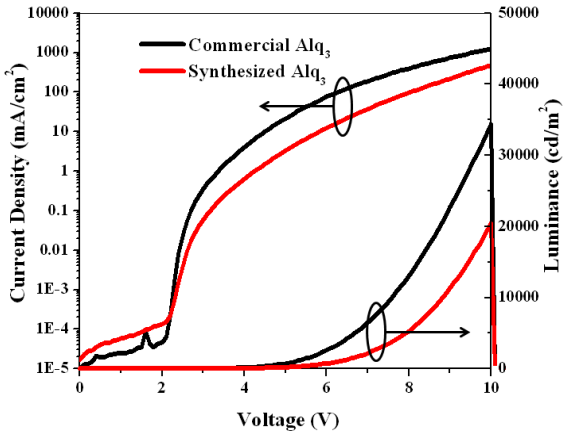

Figure 5: *L-J-V* characteristics of the OLEDs.

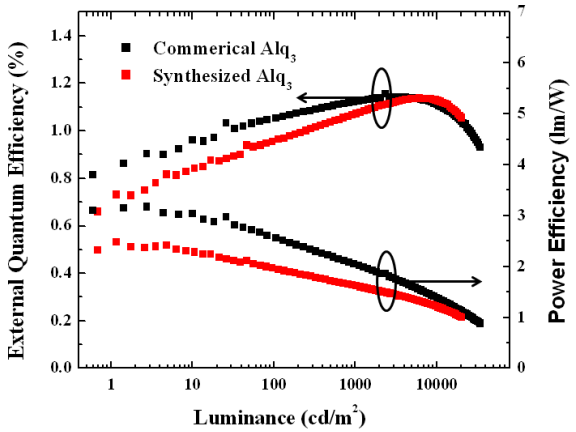

Figure 6: η_{EQE} and η_P as a function of luminance for the two devices.

4. Conclusion

Alq_3 powder was successfully synthesized using the co-precipitation method. The XRD measurements confirmed that Alq_3 with an average particle size of 40 ± 4 nm was synthesized successfully. Both devices' normalized EL spectra showed emission at 520 nm and this corresponds with reported PL results. Both devices have a turn on voltage of 2 V. The synthesized Alq_3 device has lower current density, luminance and η_P values compared to the commercial Alq_3 device. The nano sized Alq_3 particles can lead to quantum confinement effects that influences the EL device properties [10]. These lower values are an indication that the synthesized Alq_3 layer degrades faster, especially under higher voltages. The reason for the degradation could be due to residual impurities that could not be removed by purification. Also no buffer layer was inserted and it is known that devices without a buffer layer tend to degrade rapidly [11]. The η_{EQE} and η_P can be increased by using Alq_3 just as ETL and using a host like 4,4'-bis(9H-carbazol-9-yl)biphenyl (CBP) doped with a green dopant like tris(2-phenylpyridine)iridium (Ir(ppy)3).

Acknowledgements

The authors wish to thank the National Research Foundation (NRF), the Cluster program of the University of the Free State and the Photonic Initiative of South Africa (PISA) for their financial support.

5. References

[1] Tang C W and Vanslyke S A 1987 *Appl. Phys. Lett.* **51** 913
[2] Lin T C, Hsiao C H and Lee J H 2005 *Proc. of SPIE* **5937** Q1
[3] Shabeen S E, Jabbour G E, Morrell M M, Kawabe Y, Kippelen B and Peyghambarian N 1998 *J. Appl. Phys.* **84** 2324
[4] Hung L S and Chen C H 2002 *Mater. Sci. Eng.* **R 39** 143
[5] Mao C J, Wang D C, Pan H C and Zhu J 2011 *J. Ultrason. Sonochem.* **18** 473
[6] Taylor F and Wilkins J 1973 *Chem. Soc. Dalton Trans.* **1** 87
[7] Duvenhage M M, Ntwaeaborwa O M and Swart H C 2012 *Physica B-Condensed Matter* **407** 1521
[8] Forrest S R, Bradley D D C and Thompson M E 2003 *Adv. Mater.* **15** 10
[9] Lee Y H, Kim W J, Kim T Y Jung J, Lee J Y, Park H D, Kim T W and Hong J W 2007 *Curr. Appl. Phys.***7** 409
[10] Nukeaw J, 2003 *J. Min. Met. Mat.* **13** 17
[11] Li W, Jones R A, Allen S.C, Heikenfeld J C and Steckl A J 2006 *J. Display Technol.* **2** 143

Magnetic Phase Diagram of $Cr_{1-x}Ir_x$ alloys

PR Fernando, CJ Sheppard, ARE Prinsloo[1] and AM Strydom

Department of Physics, University of Johannesburg, PO Box 524, Auckland Park, 2006

Author e-mail address: alettap@uj.ac.za

Abstract. Cr alloyed with group-8 nonmagnetic transition metals Ir, Os, Ru, Re and Pt show large anomalies of magnetic origin at the phase transition temperatures. Doping with these metals increase the electron to atom ratio of Cr and their magnetic phase diagrams contain the commensurate (C) spin density wave (SDW) phase, as well as the paramagnetic (P) phase, the transverse (T) incommensurate (I) SDW and longitudinal (L) ISDW phases. A triple point exists where the ISDW, CSDW and P phases coexist, while the CSDW phase is observed for impurity concentrations (x) above the triple point concentration (x_L). The magnetic phase diagrams of both CrRe and CrRu show interesting features for $x >> x_L$, including possible superconducting properties and quantum critical behaviour. In this contribution we extend these investigations to the phase diagram of $Cr_{1-x}Ir_x$, previously not determined for $y > 0.04$. A polycrystalline $Cr_{1-x}Ir_x$ sample series, with $0.02 < x < 0.14$, was prepared and characterized using scanning electron microscopy, electron microprobe analysis and X-ray diffraction. These reveal that the alloys with $x \leq 0.12$ are homogenous in composition and single-phase. Electrical resistivity (ρ) measurements as function of temperature (T) for $2K < T < 1000K$ was used to obtain the magnetic transition temperatures of the samples and determine the magnetic phase diagram of the $Cr_{1-x}Ir_x$ alloy system for $x > 0.04$.

1. Introduction

In Cr and its alloys the electron and hole Fermi surfaces nest on cooling through the Néel temperature (T_N) resulting in the formation of the spin-density-wave (SDW) when the antiferromagnetic (AFM) phase is entered. This nesting decreases the energy of the system through electron-hole pair condensation and results in the appearance of SDW energy gaps at the Fermi surface in certain directions of k-space on cooling through T_N. The first parameter of importance in influencing the formation of the SDW is the effect of electron concentration on the area of the electron and hole Fermi surface sheets that nests [1]. The nesting area, and concomitantly the stability of the SDW state, depends on the electron concentration per atom (e/a) which can easily be tuned by alloying Cr (e/a = 6) with elements having different e/a ratios. Diluents that increase the electron concentration in Cr alloys, such as Mn (e/a = 7) as well as group-8 nonmagnetic transition metals, increase the area of the electron sheet, resulting in a better nesting of the Fermi surface sheets and the formation of a commensurate (C) SDW phase at certain diluent concentrations.

Of special interest is Cr alloys with group-8 nonmagnetic transition metals Ru, Os, Rh, Ir and Pt. These alloys show large anomalies of magnetic origin at the phase transition temperatures [1]. These impurities increase the electron to atom (e/a) ratio of Cr and therefore the phase diagrams of the Cr alloys with group-8 nonmagnetic transition metals contain the commensurate (C) SDW phase, as well as the paramagnetic (P) phase, the transverse (T) incommensurate (I) SDW and longitudinal (L) ISDW

phases. A triple point exists on the magnetic phase diagrams of these alloys were the ISDW, CSDW and P phases coexist [1]. For impurity concentrations (x) below the triple point concentration (x_L) the dilute Cr alloys with group-8 impurities LISDW, TISDW and P phases are observed, while for $x > x_L$ we also observe a CSDW phase. The spin-flip phase transition (at temperature T_{SF} defined as the transition temperature between LISDW and TISDW magnetic phases), the Néel transition at temperature (T_N) of Cr and the ISDW-CSDW magnetic phase transition at temperature T_{IC} of certain Cr alloys with group-8 nonmagnetic transition metals are first order transitions and hysteresis effects can be observed in certain of the physical properties [1,2].

Much of the previous work on the $Cr_{100-x}Ir_x$ system focussed on alloys close to x_L [1,9] and little attention was given to high diluent concentrations. Since the magnetic phase diagrams of many Cr alloys with group-8 metals show very interesting properties [1], it is surprizing that the Cr-Ir magnetic phase diagram has not been fully explored and is still unknown for concentrations above 4 at.% Ir [10]. Fascinating features of the magnetic phase diagrams of both the Cr-Re and Cr-Ru systems include possible superconducting properties, as well as quantum critical behaviour [1,3,4] for $x >> x_L$. These properties are strongly aligned with current interests as is reflected in recent literature [5,6,7,8]. Extending these investigations to the Cr-Ir system will prove most interesting and in this paper the first step in doing this is taken by determining the magnetic phase diagram of the Cr-Ir system at higher diluent come, which will give much scope for future research.

2. Experimental

The polycrystalline binary $Cr_{1-x}Ir_x$ alloys, with $0.02 \leq x \leq 0.14$ were prepared by arc melting in a purified argon atmosphere from Cr and Ir of mass fractional purities 99.999% and 99.99%, respectively. The constituent metals were melted fifteenth times in total, turning it upside down between melts with two crushes after every five melts in order to improve the homogeneity. Samples were prepared as cast and for comparison certain samples were annealed at 1000°C for 7 days. The complex nature of the chemical phase diagram of Cr-Ir indicate possible difficulties in preparing single phase Cr-Ir alloys, as was outlined by Waterstrat *et al.* [11]. For this reason it was essential to characterize the samples structurally. Powder X-ray diffraction (XRD) analyses, using Cu-K_α were used to confirm whether the samples were single or multi-phase. The approximate chemical compositions of the individual alloys were obtained using a scanning electron microprobe (SEM) and energy-dispersive X-ray spectrometry (EDS). The actual elemental composition and homogeneity were determined using electron microprobe analyses. Electrical resistivity (ρ) were measured in the range $2 \leq T \leq 380$ K, using standard Physical Properties Measurement System (PPMS) incorporating appropriate measuring options. Resistivity measurements for the temperature range 273 K – 1000 K were performed in an inert environment using the standard dc-four probe method with Keithley instrumentation. In order to eliminate the thermal EMF the sample current was reversed for each set of readings [12].

3. Results and discussion

Figure 1 (a) and (b) shows the XRD patterns for the as-cast $Cr_{0.90}Ir_{0.10}$ and $Cr_{0.86}Ir_{0.14}$ samples, respectively, together with the XRD pattern for pure Cr. The XRD pattern for $Cr_{0.90}Ir_{0.10}$ was compared to the Joint Council of Powder Diffraction Database for pure Cr and only the primary reflections [110], [200], [211] and [220] were obtained. These reflections were shifted to lower angles with substitution of Ir in the lattice, corresponding to an increase in the lattice parameter. This is expected as the Ir atoms are larger than Cr atoms. The lattice parameter increased from 0.28839 nm (pure Cr) to 0.3092 nm for the $Cr_{0.90}Ir_{0.10}$ alloy. On analyzing the XRD pattern for the $Cr_{0.86}Ir_{0.14}$ alloy in a similar manner, additional reflections were identified that can be associated with that of Cr_3Ir (A15-phase), which was previously described by Waterstrat *et al.* [11]. Figure 2 gives the lattice parameters for $Cr_{1-x}Ir_x$ alloys with $0 \leq x \leq 0.12$. Linear behaviour is observed in this concentration range.

The backscattered-electron micrographs of the as-cast $Cr_{0.90}Ir_{0.10}$ and $Cr_{0.86}Ir_{0.14}$ alloys are shown in figure 3 (a) and (b), respectively. The images for these samples are very similar indicating uniform surface morphology with no distinguishable features that can be associated with other Cr-Ir phases.

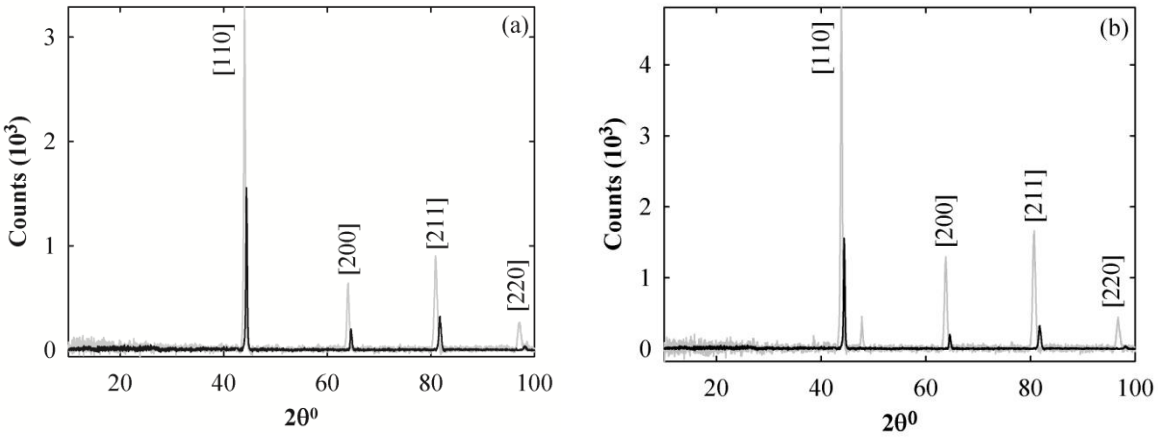

Figure 1. The XRD pattern for the (a) $Cr_{0.90}Ir_{0.10}$ and (b) $Cr_{0.86}Ir_{0.14}$ alloys are shown in grey, together with the pattern expected for pure Cr shown in black. The (*hkl*) Miller indices of the various reflections obtained from the JCPDD expected for the profile of bcc Cr are indicated.

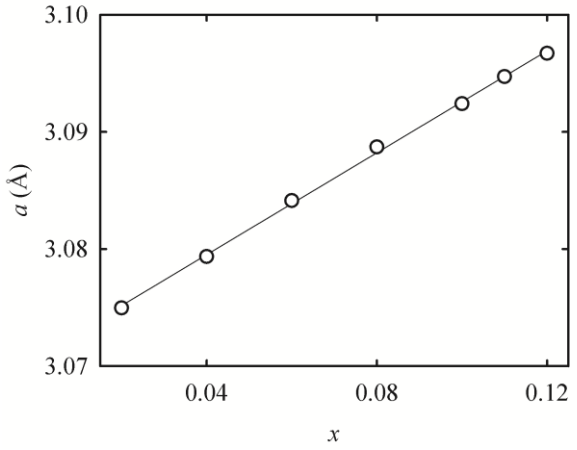

Figure 2. The lattice constants (*a*) as function of *x* for various $Cr_{1-x}Ir_x$ alloys.

Microprobe analysis for the $Cr_{0.90}Ir_{0.10}$ sample indicate homogeneous composition with a Cr concentration of (90.0 ± 0.6) at.% and Ir of (10.1 ± 0.6) at.%. For the $Cr_{0.86}Ir_{0.14}$ sample microprobe analysis also indicates homogeneous composition with a Cr concentration of (85.4 ± 0.7) at.% and Ir of (14.6 ± 0.7) at.%. The light and the dark regions observed in the images shown in figure 3 (a) and (b) differ only slightly in concentration. In an attempt to improve the quality of the samples it was annealed, but this resulted in the deterioration of sample quality. Figure 4 (a) and (b) shows the XRD and backscattered-electron image of the $Cr_{0.90}Ir_{0.10}$ sample after annealing. The XRD pattern of the annealed $Cr_{0.90}Ir_{0.10}$ sample show several additional peaks, not associated with the bcc phase expected in Cr alloys.

Comparing the backscattered-images of figures 3 (a) and 4 (b) for the $Cr_{0.90}Ir_{0.10}$ sample, a significance difference is observed between the as-cast and annealed samples. The annealed sample is of inhomogeneous morphology showing needle-like structures on a smooth background, comparable to results found by Waterstat *et al.* [11]. According to EDS analysis, in this case the needle like structures in the annealed $Cr_{0.90}Ir_{0.10}$ sample has Cr and Ir concentrations of (81.2 ± 0.1) at.% and (18.8 ± 0.2) at.%, respectively. However, the background has Cr and Ir concentrations of (94.4± 0.7) at.% and (5.6 ± 0.7) at.%, respectively. After annealing the backscattered-image of the $Cr_{0.86}Ir_{0.14}$ sample shows no needle-like structures, only large sections of a light regions with (81.5 ± 0.6) at.%

Cr and (18.5 ± 0.6) at.% Ir, together with smaller dark regions with (93.0 ± 0.5) at.% Cr and (7 ± 1) at.% Ir. Interestingly in these two samples the background/dark regions, as well as the needle-like/light regions have similar concentrations, independent of the initial diluent concentrations.

The $\rho(T)$ curves for $Cr_{1-x}Ir_x$ alloys, with $0.02 \leq x \leq 0.14$ are shown in figure 5 (a) and (b). Well defined anomalies in the form of clear minima followed by prominent domes are seen in all the $\rho(T)$ curves for alloys with $x < 0.14$. This behaviour is associated with the formation of the SDW on entering the antiferromagnetic phase on cooling through the Néel temperature [1]. The sudden increase in resistivity on cooling through T_N finds its origin in the condensation of electron and hole Fermi surfaces during the nesting process on SDW formation. This leads to a reduction in the charge carriers available for conduction resulting in an increase in resistivity just below T_N [1]. T_N is often defined for Cr and its dilute alloys as the temperature of the minimum in $d\rho/dT$ accompanying the magnetic phase transition [1]. This definition was implemented for the present study of the $Cr_{1-x}Ir_x$ system. The single-phase bcc alloys reveal one clear transition at T_N. However, the multi-phase alloy with $x = 0.14$ shows two anomalies in $\rho(T)$, as can be seen in figure 5 (b). These are associated with the two different phases that would be in agreement with the observations in the XRD and backscattered images of this sample. The experimental error in the absolute value of ρ amounts to 5% and originates mainly from errors in determining the sample dimensions, while the instrumentation used permitted a resistivity resolution of 0.5%.

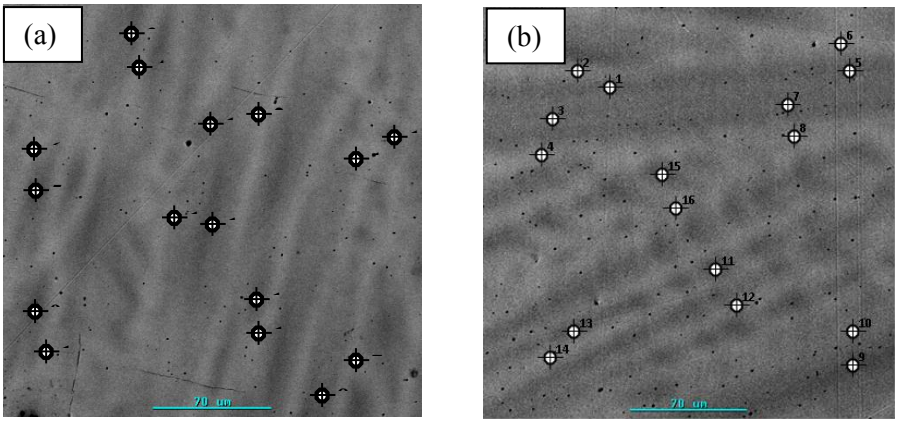

Figure 3. The backscattered-electron images for the as cast (a) $Cr_{0.90}Ir_{0.10}$ and (b) $Cr_{0.86}Ir_{0.14}$ alloys. Positions where the concentrations in light and dark phases were determined using EDS are indicated.

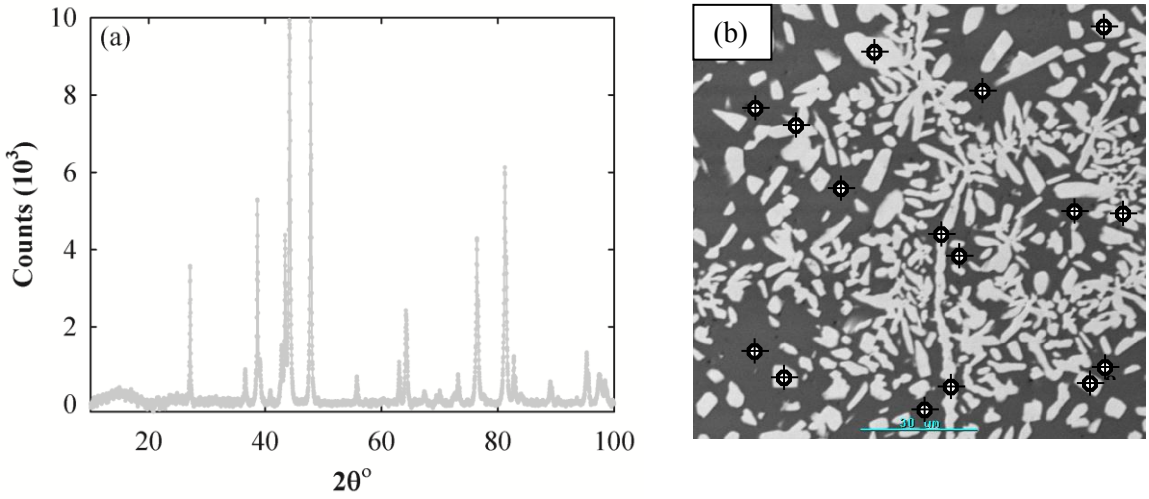

Figure 4. The (a) XRD pattern and (b) backscattered-electron image for the annealed $Cr_{0.90}Ir_{0.10}$ alloy.

The positions where the concentrations in the light and dark phases were determined using EDS are indicated in (b).

Figure 6 shows the magnetic phase diagram constructed from the T_N-values obtained from the current $\rho(T)$ measurements together with those obtained in previous studies [9,10,13-16], as a function of Ir concentration. The error in the current T_N values falls within the size of the data points. The solid lines are guides to the eye through the data points. It is evident that the current results correspond well with those previously obtained on this alloy system. The present study extends results to much higher Ir diluent concentrations than previously determined [9]. The magnetic phase diagram obtained for Cr-Ir alloy system resembles the typical behaviour of Cr alloys with group-8 metals, similar to that observed for Cr-Ru and Cr-Re.

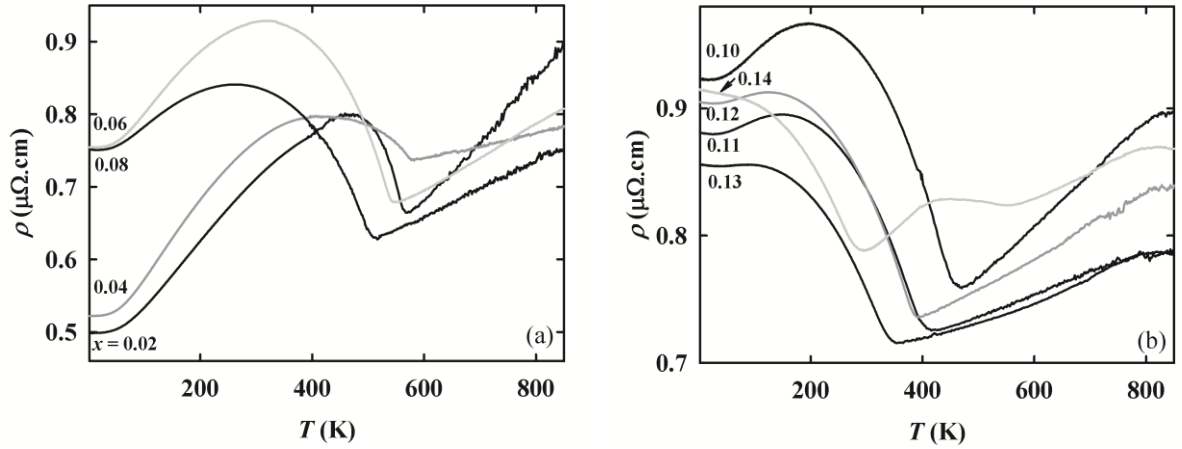

Figure 5 (a) and (b). The temperature dependence of the electrical resistivity, ρ, of $Cr_{1-x}Ir_x$ alloy system. The values of x associated with the various curves are indicated on the graphs.

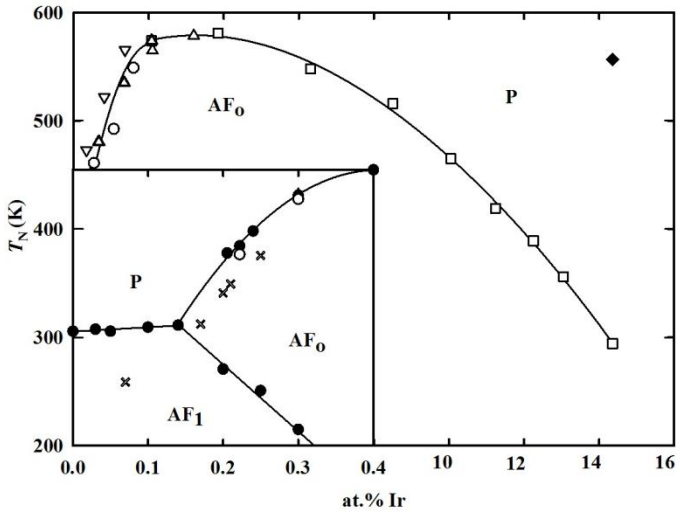

Figure 6. The magnetic phase diagram for the $Cr_{1-x}Ir_x$ alloy system as function of the Ir concentration, showing T_N values obtained through electrical resistivity in present study (□). The second transition temperature observed for the $Cr_{0.86}Ir_{0.14}$ sample are indicated by ◆. Data points from previous studies indicated on the figure: Fukamichi *et al.* [9] (△), Yakhmi *et al*. [14] (○), De Young *et al.* [15] (▽), Butylenko *et al.* [17] (●) and Martynova *et al.* [10] (✖). The error in the T_N values obtained from the current study falls within the size of the data points. The solid lines are guides to the eye.

4. Conclusion.

The magnetic phase diagram for the $Cr_{1-x}Ir_x$ alloys system was for the first time determined to concentrations as high as 12 at.% Ir. The present results compare well with that previously obtained [10,13-17] on this alloy system for $x < 0.04$ and the general behaviour is similar to that observed for other Cr alloys with group-8 non-transition metals such as Cr-Ru and Cr-Re [1]. These results will be extended to include the T_N-values obtained from additional physical properties measurements, firstly for $T < 400$ K and then in the second stage for $T > 400$ K.

This project has addressed the fundamental questions regarding the behaviour of the Cr-Ir magnetic phase diagram at high diluent concentrations necessary to evolve the research on this alloy system to a higher level. This will include investigations into quantum critical behaviour and possible superconductivity in the Cr-Ir alloy system, in line with current interests as is reflected in recent literature [5,6,7,8].

Acknowledgements

This work was supported by the NRF of South Africa under grant numbers 78832 and 61388.

References

[1] Fawcett E, Alberts HL, Galkin VY, Noakes DR and Yakhmi JV 1994 *Rev. Mod. Phys.* **66** 25
[2] Fawcett E 1988 *Rev. Mod. Phys.* **60** 209
[3] Jacobs BS, Prinsloo ARE, Sheppard CJ and Strydom AM 2011 *Proceedings of SAIP* 105
[4] Reddy L, Alberts HL, Strydom AM, Prinsloo ARE and Venter AM 2008 *J. Appl. Phys.* **103** 07C903-1
[5] Yeh A, Soh Y-A, J Brooke J, Aeppli G, Rosenbaum TF and Hayden SM 2002 *Nature* **419** 459
[6] Lee M, Husmann A, Rosenbaum TF and Aeppli G 2004 *Phys. Rev. Lett.* **92** 187201
[7] Jaramillo R, Feng Y, Wang J and Rosenbaum TF 2010 *Proc. Nat. Acad. of Sci. USA (PNAS)* **107** 13631
[8] Sheppard CJ, Prinsloo ARE, Alberts HL and Strydom AM 2011 *J. Appl. Phys.* **109**(7) 07E104
[9] Martynova J, Alberts HL and Smit P 1998 *J. Magn. Magn. Mat.* **197** 345
[10] K Fukamichi and Siato H 1975 *J. Less Common Met.* **40** 357
[11] Waterstat RM and Manuszewski RC 1973 *J. Less Common Met.* **32** 79
[12] Gopalakrishnan IK,Yakhmi JV and Iyer RM 1984 *J. Magn. Magn. Mat.* **46** 207
[13] Arajs S, Rao KV, Åström HU and De-Young F.Tice 1973 *Physica Scripta*.vol.8 109-112
[14] Yakhmi JV, Gopalakrishnan IK and Iyer RM 1983 *J. Less Common Met*. **91** 327-331
[15] De Young F.Tice, Arajs S and Anderson EE 1971 *Amer. Inst. Phys. Conf. Proc. Magn and Magn. Mat*. **5** 517.
[16] Butylenko AK and Nevadcha VV 1980 *Dokl. Akad. Nauk Ukr.SSR* **5**A 67

Synthesis and characterization of green $SrAl_2O_4:Tb^{3+}$ phosphor using solution combustion method

K E Foka[1], F B Dejene[1] and H C Swart[2]

[1]Department of Physics, University of the Free State (QwaQwa campus, Private Bag X13, Phuthaditjhaba, 9866, South Africa) (e-mail address: fokake@qwa.ufs.ac.za)
[2]Department of Physics, University of the Free State, P.O Box 339, Bloemfontein 9300, South Africa
Corresponding author e-mail: dejenebf@qwa.ufs.ac.za or swarthc@ufs.ac.za

Abstract. $SrAl_2O_4:Tb^{3+}$ phosphors doped with different concentration of Tb^{3+} varied from 0.25 - 2% were synthesized by the solution combustion method. The crystalline structure, morphology and luminescent properties of the phosphors were studied by X-ray diffraction (XRD), scanning electron microscopy (SEM) and photoluminescence (PL) spectroscopy respectively. The XRD analysis reveals a polycrystalline monoclinic structure and the calculated average particle sizes ranged between 80 and 90 nm. SEM images show non uniform and irregular shape particles. The Tb^{3+} doped $SrAl_2O_4$ phosphor showed green emission when illuminated with an excitation wavelength of 229 nm. The emission spectra show a weak blue emission in the region of 415—459 nm and strong green emission in the 489—622 nm range. The 4f—4f emission from $^5D_4$ to ^7F_J (J= 6, 5, 4, 3) states of Tb^{3+} were found at 489, 543, 585 and 622 nm, respectively. Other emission peaks from the $^5D_3$ to ^7F_J (J=5, 4, and 3) transitions (blue) were found at 415, 436 and 459 nm. The decay curves of $SrAl_2O_4:Tb^{3+}$ phosphor showed rapid decay followed by a long afterglow. The intensity of the phosphorescent decreased with an increase in the concentration of the Tb ions of 1% in the host lattice.

1. Introduction

Long lasting phosphor materials are energy storing materials and can potentially light up for long times in darkness. The materials can absorb visible light, store the energy and gradually release the energy as visible light [1]. $SrAl_2O_4$ is one of the typical matrices for long duration luminescent materials, which are doped with Eu, Ce, Tb, etc. and is an efficient host lattice with a wide band gap which can generate a broad band emission [2]. As compared with other synthesis methods, the combustion method is very simple, saving energy and it takes only a few minutes without requiring subsequent intermediary calcination stages [3, 4]. Tb^{3+} is one of the most widely used rare-earth ions activator for green luminescent materials and has been used widely in tri-color energy saving fluorescent lamps and its emission mainly originate from the $^5D_4$ to ^7F_J (J=0-6) transitions [5, 6]. The $SrAl_2O_4$ host belongs to the tridymite-like structure. The structure is formed by a three dimensional corner-sharing AlO_4 tetrahedron frame-work. The divalent Sr^{2+}cation balance the charge and occupies an interstitial site within the tetrahedral frame-work [7, 8].

In the present work we have prepared and investigated $SrAl_2O_4$ phosphor material doped Tb^{3+} ion as an activator. The different concentrations of Tb^{3+} were used and its effect on structure, photoluminescence and luminescence lifetimes was investigated.

2. Experimental

2.1. Sample Preparation

The nitrates of Sr, Al, Tb and urea were taken as starting materials, and were dissolved in enough deionized water and kept stirring for 30 minutes until the solution becomes clear. The mixed solution was placed into a muffle furnace maintained at 500 ^{o}C. In about five minutes the solution boiled and underwent dehydration followed by decomposition with escaping large amounts of gases (oxides of nitrogen and ammonia) then spontaneous combustion with enormous swelling produced foamy and voluminous powder. As soon as the reaction was over, the product was cooled at room temperature. The foamy powder was crushed into powder using a pestle mortar and the obtained white powder was characterized. This was repeated for different concentrations of Tb 0.25, 0.4, 0.5, 1, 1.5 and 2%.

2.2. Characterization

The crystalline structure and particle size of the phosphor were investigated using the D8 advanced AXS GmbH X-ray diffractometer (XRD), the morphology and chemical composition analyses have been carried out using a Shimadzu's SSX-550 scanning electron microscope (SEM) equipped with an electron dispersive X-ray spectrometer (EDS). PL measurements were made on a Carry Eclipse photoluminescence spectrophotometer system, equipped with a 150 W xenon lamp as the excitation source.

3. Results and Discussion

3.1. X-ray diffraction

Figure 1 shows the XRD patterns of the $SrAl_2O_4$:Tb^{3+} phosphor doped with different concentration of Tb^{3+}. It was found that the main peaks formed correspond to the $SrAl_2O_4$ monoclinic phase according to the JCPDS, card number (74-0794). Although the main peaks of the crystal structures were observed there were some unknown peaks (marked with stars and dots) and maybe attributed to impurity phases such as $SrAl_{11}O_{19}$ and $Sr_7Al_2O_{25}$, or some of the unreacted precursors during the combustion method. The particle sizes of each peak of the phosphor were calculated using the Scherrer's equation and are shown in table 1.

Table 1. Particle sizes for $SrAl_2O_4$:xTb^{3+}(x=0.4, 0.5, 1 and 2%) phosphor

hkl	020	211	220	211	031	400	
$SrAl_2O_4$:xTb^{3+}			Particle sizes				Average
X=2%	88nm	84nm	98nm	94nm	60nm	72nm	82nm
X=1%	94nm	90nm	104nm	108nm	56nm	62nm	86nm
X=0.5%	88nm	88nm	98nm	102nm	56nm	52nm	80nm
X=0.4%	92nm	90nm	98nm	100nm	56nm	52nm	82nm

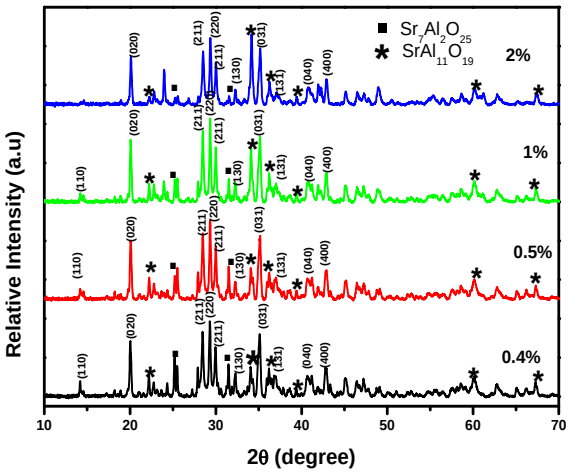

Figure 1. XRD patterns of $SrAl_2O_4:Tb^{3+}$ with different concentration of terbium

3.2. Scanning Electron Microscopy and Energy Dispersive Spectroscpy

Figure 2 shows SEM images of (a) $SrAl_2O_4:0.5Tb^{3+}$ and (b) 1% phosphor prepared by the combustion method. The samples show the pores and voids on the surface that formed by the escaping gases during the combustion method. The morphology of the powders reflects the inherent nature of the combustion process. The images show non uniform and irregular shapes of the particles and there was no big difference as the concentration of Tb increased from 0.5% up to 2%. Among the images the 0.5 % was presented. All the elements were included in $SrAl_2O_4:Tb^{3+}$phosphor were detected in EDS spectra, except for dopant Tb^{3+}, this is because its concentration was too far small to be detected. The presence of $SrAl_2O_4:Tb^{3+}$ is confirmed with the Ca, Al, and O peaks. Carbon peak in EDS spectra is for carbon tape. The EDS spectra are similar for all samples and therefore the representative spectrum is provided.

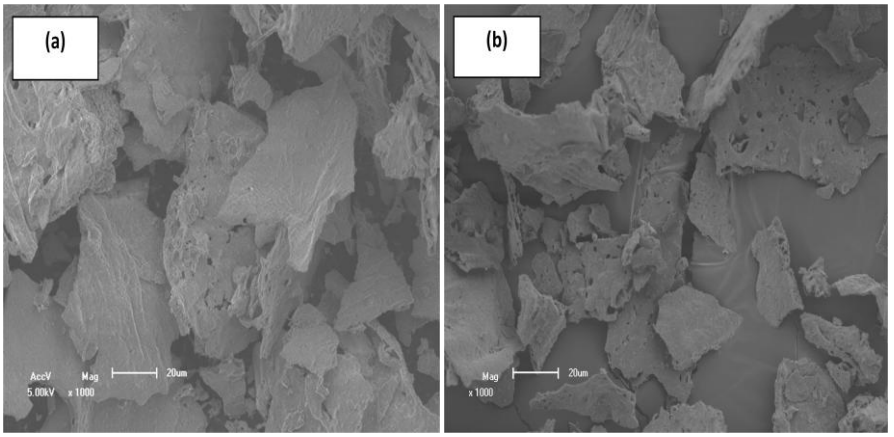

Figure 2. SEM image of $SrAl_2O_4:0.5\%Tb^{3+}$ (a) and $SrAl_2O_4:0.5\%Tb^{3+}$ (b) at 1000x magnification

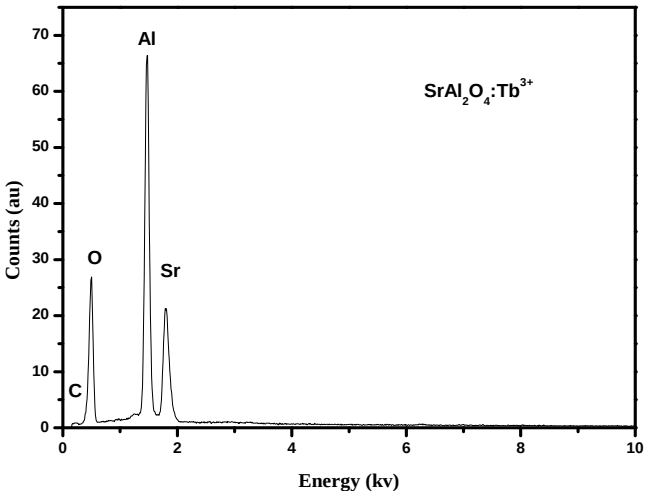

Figure 3. EDS spectrum of $SrAl_2O_4$:0.5%Tb^{3+}

3.3 Photoluminescence

Figure 4 shows the excitation spectra for the $SrAl_2O_4$ doped with different moles concentration of Tb^{3+}. A broad band centred at 229 nm was observed when the 543 nm emission of Tb^{3+} was monitored. The strong 229 nm peak is related to the f–d excitation of the Tb^{3+}. Figure 5 shows the emission spectra of the $SrAl_2O_4$:Tb^{3+} phosphor. The Tb^{3+} doped $SrAl_2O_4$ phosphor shows a green emission when illuminated by 229 nm. The emission spectra show the weak blue emission in the region of 415—459 nm and strong green emission in the 489—622 nm range. The 4f—4f emission from $^5D_4$ to ^7F_J (J= 6, 5, 4, 3) states of Tb^{3+} are found at 489, 543, 585 and 622 nm, respectively. Other emission peaks from the $^5D_3$ to ^7F_J (J=5, 4, and 3) transitions were also found at 415, 436, and 459 nm [8,9].

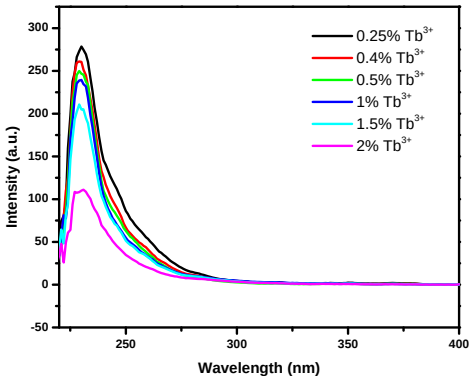

Figure 4. Excitation spectra of $SrAl_2O_4$:Tb^{3+} with different concentration of Tb^{3+} λ_{em}=543 nm

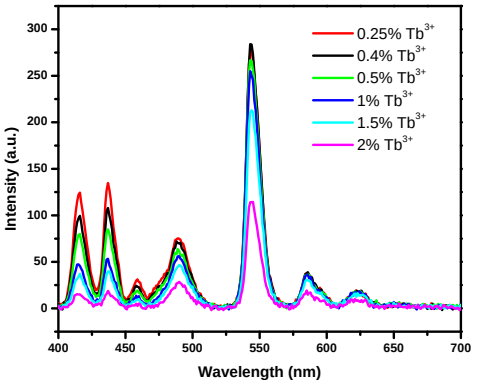

Figure 5. Emission spectra of $SrAl_2O_4$:Tb^{3+} with different concentration of Tb^{3+} λ_{ex}=229 nm

It was found that when the mole concentration of the terbium was increased up to 1% in the host lattice, there was a significant decrease in intensity of all the Tb transition due to the concentration quenching as shown in figure 6. The average distance between luminescent centers is related to the luminescent intensity. The distance between active ions decreases with the increase of doping concentration. When this distance is short enough, the interaction between active ions cause concentration quenching [10].

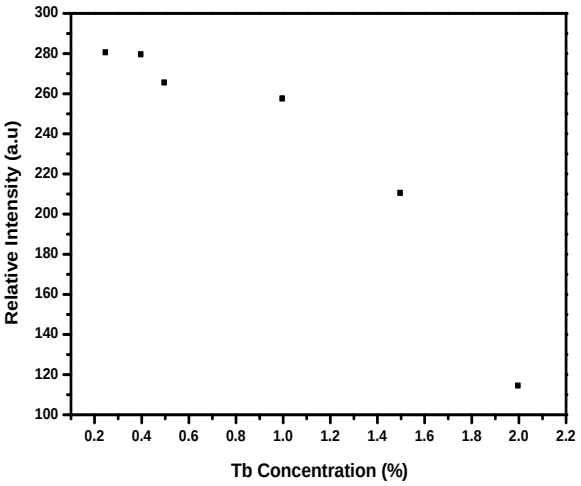

Figure 6. Graph of concentration dependence of the emission maximum intensity of Tb^{3+} doped $SrAl_2O_4$

3.3. Decay curves and afterglow characteristics

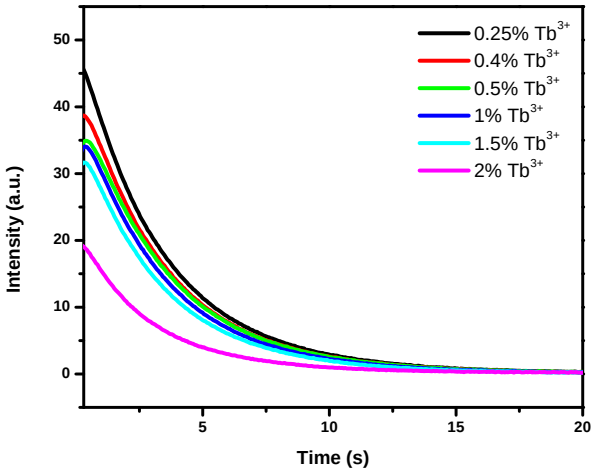

Figure 7. Decay curves of $SrAl_2O_4:Tb^{3+}$ with different concentration of Tb

Figure 7 shows decay curves of $SrAl_2O_4:Tb^{3+}$ phosphor with different moles concentration of Tb^{3+}**.** The phosphor showed the rapid decay and long afterglow. The initial intensity of the phosphorescent decreases as the concentration of terbium ions increased in the host lattice. The exponential decay times as shown in table 2 are described as (1) initial rapid decay, and (2) slow decay components. The decay constants have higher values for sample with concentration of 0.25 mol% and lower value for the sample with 2 mol%.

Table 2. Decay parameters of the $SrAl_2O_4:Tb^{3+}$ phosphor with different Tb^{3+} concentrations

Tb^{3+} %	0.25%	0.4%	0.5%	1%	1.5%	2%
Components		**Decay constants**				
τ_1 (ms)	0.25	0.21	0.20	0.17	0.11	0.01
τ_2 (ms)	3.52	3.42	3.40	3.32	3.39	3.18

4. Conclusion

$SrAl_2O_4:Tb^{3+}$ phosphor has been successfully prepared by the combustion method. The XRD results showed that the phosphor has a monoclinic crystal structure. Characteristic green luminescence from Tb^{3+} was observed. The $SrAl_2O_4:Tb^{3+}$ exhibited a predominant green emission at 543 nm, which was assigned to the $^5D_4$ to $^7F_5$ transition of Tb^{3+}. The $SrAl_2O_4:Tb^{3+}$ (0.25 mol%) phosphor showed the maximum emission intensity. The non uniform and irregular shapes of the particles was shown by scanning electron microscopy. All the elements of $SrAl_2O_4:Tb^{3+}$ were confirmed by EDS. The decay curves of the phosphors were observed and its intensity was decreased as concentration of Tb^{3+} increased to 1%.

References

[1] Song H, Chen D, Tang W and Peng Y 2008 *Displays*. **29** 41-44
[2] Zuoling F, Shihong Z and Siyuan Z 2005 *J. Phys. Chem.* B **109** 14396-14400
[3] Huajie S and Donghua C 2007 *Luminescence*. **22** 554-558
[4] Barros B S, Melo P S, Kiminami R H G A, Costa A C F M, de Sá G F and Alves Jr S 2006 *J. Mater Sci*. **41** 4744-4748
[5] Verma R K, Kumar K and Rai S B 2010 *Solid State Sciences*, **12** 1146-1151
[6] Zhang Y, Li L, Zhang X, Wang D and Zhang S 2008 *J. Rare Earths*. **26** 656
[7] Ryu H and Bartwal K S 2009 *Physica.* B **404** 1714-1718
[8] Shin-Hei C, Nam-Hoon K, Young-Hoon Y and Sung-Churl C 2006 *J. Ceramic Processing Research.* **7** 62-65
[9] Lu C H, Godbole S V and Natarajan V 2005 *Materials Chemistry and Physics*. **94** 73-77
[10] Zhu H, Yang D, Yang H, Zhu L, Li D, Jin D and Yao K 2008 *J. Nanopart Res*. **10** 307-312

Spin-density-wave behaviour in the $(Cr_{84}Re_{16})_{100-y}V_y$ system

BS Jacobs, ARE Prinsloo, CJ Sheppard and AM Strydom

Department of Physics, University of Johannesburg, PO Box 524, Auckland Park, 2006

E-mail address: alettap@uj.ac.za

Abstract. In this study, the possibility of tuning the $Cr_{84}Re_{16}$ alloy system to a quantum critical point through V addition is investigated, by considering the spin-density-wave behaviour in the $(Cr_{84}Re_{16})_{100-y}V_y$ alloy system with $0 \leq y \leq 14$. The evolution of Seebeck coefficient (S) as a function of temperature (T) on increasing the V content is described in terms of a simple model. This relates the temperature behaviour of S to the energy dependence of the decrease in the scattering rate of electrons by phonons and an increase in the resistivity on decreasing temperature. The temperature – composition magnetic phase diagram obtained from the $S(T)$ and previously reported $\rho(T)$ measurements depicts a critical point, occurring at $T = 0$ K for a critical V concentration $y_c = 10.5$. Specific heat measurements were used to determine the Sommerfeld coefficient (γ) as a function of V concentration (y) for this series and a minimum is observed in the $\gamma(y)$ close y_c. This is indicative of the existence of a possible quantum critical point at this concentration.

1. Introduction

The antiferromagnetic (AFM) properties exhibited by Cr and its alloys can be attributed to a linearly polarized spin-density-wave (SDW) [1]. The Fermi surface of Cr is composed of electron and hole octahedra, the nesting of which is responsible for establishing a SDW [2]. The behaviour around critical points of Cr alloys can be probed by fine tuning the parameters that influence SDW formation. The extent of nesting and the stability of the SDW depends on the electron concentration per atom (e/a). This parameter can easily be tuned by alloying Cr ($e/a = 6$) with other elements. In pure Cr, the electron sheet is slightly smaller than the hole sheet, resulting in a SDW that is incommensurate (I) with the lattice [2]. Alloying Cr with Re, an electron donor having $e/a = 7$, brings the size of the electron and hole Fermi sheets more in line with each other. The SDW eventually becomes commensurate (C) with the lattice. As the Re concentration is increased, the Néel temperature (T_N) first increases up to approximately 7 at.% Re and then decreases [2]. This behaviour is presently not well understood, but corresponds to that observed in CrRu [2].

Doping Cr with V ($e/a = 5$) results in suppression of spin fluctuations [3,4], lowering of resistivity [5] and destruction of the first-order transition from the paramagnetic to the antiferromagnetic phase [6]. Yeh *et al.* [7] also demonstrated that Cr can be driven to a quantum critical point (QCP) by doping with V in the $Cr_{1-x}V_x$ alloy system. Characteristics typically associated with QCP can be observed in the low temperature behaviour of electrical resistivity (ρ), magnetic susceptibility (χ), Hall coefficient (R_H) and Sommerfeld coefficient of specific heat (γ) [7,8]. Recently, Reddy *et al*. reported the existence of a CSDW QCP at $z_c = 10.4$ in the $(Cr_{86}Ru_{14})_{100-z}V_z$ alloy system [9,10]. It is therefore appropriate to extend these studies to the Cr-Re system, as it has a temperature – composition ($T - c$) magnetic phase diagram similar to that of Cr-Ru [2]. For this purpose, in the present study, thermal transport and specific heat measurements were utilized to investigate the existence of a possible QCP in the $(Cr_{84}Re_{16})_{100-y}V_y$ alloy system.

2. Experimental

Polycrystalline $(Cr_{84}Re_{16})_{100-y}V_y$ alloys with $0 \leq y \leq 14$ were prepared from Cr, Re and V of mass fractional purities 99.99%, 99.99% and 99.8%, respectively, by repeated arc melting in purified argon atmosphere. The samples were individually sealed in quartz ampoules filled with pure argon gas at low pressure. These ampoules were annealed at 1343 K for seven days and quenched in iced water. Powder X-ray diffraction (XRD) analyses confirmed the expected body centered cubic (bcc) crystal structure [11]. Electron microprobe analyses of the samples showed the actual elemental composition and good homogeneity of the alloys [11]. Samples of desired dimensions for the various measurements were prepared from the alloy ingots using spark erosion techniques. The Seebeck coefficient (S) was measured in the temperature range 2 K $\leq T \leq$ 390 K while the specific heat (C_p) was measured in the temperature range 2 K $\leq T \leq$ 80 K using the Quantum Design Physical Properties Measurement System (PPMS) incorporating appropriate measuring options.

3. Results and discussion

The temperature dependence of electrical resistivity, ρ, for $(Cr_{84}Re_{16})_{100-y}V_y$ alloys with y = 0, 5.7, 8.5 and 10.4 at.% V have been reported previously [11]. Well defined anomalies in the vicinity of T_N were observed for alloys with y = 0, 5.7 and 8.5. In general, the size of the anomaly as well as T_N decreases with increase in V concentration, becoming almost imperceptible in the y = 10.4 alloy. The anomalies, which appeared as sudden increase in resistivity on cooling through T_N, were attributed to the condensation of electron and hole Fermi surfaces during the nesting process on SDW formation. This leads to a reduction in the charge carriers available for conduction, resulting in an increase in resistivity just below T_N [2].

The Seebeck coefficient is sensitive to the changes in the electronic structure and scattering mechanisms that are consequential to the AFM phase [2]. This results in a much stronger anomaly seen in the $S(T)$ curve on SDW formation compared to those observed in $\rho(T)$ [2]. Previous research on Cr alloys indicated that $S(T)$ measurements are particularly useful in locating T_N in alloys showing weak SDW anomalies near T_N [2].

Figure 1 (a) shows the temperature dependence of Seebeck coefficient, S, for $(Cr_{84}Re_{16})_{100-y}V_y$ alloys with y = 0, 4, 5.7, 8.5 and 10.4. T_N for the various samples were taken at the temperature corresponding to the minimum observed in the $dS(T)/dT$ curves, an example of which is shown in figure 1 (b) for the y = 8.5 sample. T_N obtained in this manner compares well with that obtained from the $\rho(T)$ curves for the y = 5.7, 8.5 and 10.4 alloys [11]. For the y = 0 alloy the Néel transition could not be observed in $S(T)$, as measurements using the PPMS apparatus could only be done up to 400 K. From resistivity measurements, T_N was found to be at 423 K for this alloy. Anomalies in the form of a dome, normally associated with T_N, are observed in the $S(T)$ curves for samples with y = 4, 5.7, 8.5 and 10.4. On increasing y, the magnitude of this dome is suppressed and its position shifts to lower temperatures, corresponding to a decrease in T_N. In addition to the observed T_N-dome, low temperature valleys are seen for the y = 0, 4 and 5.7 samples. The valley is initially weak and broad for y = 0, becoming more pronounced and shifting to lower temperatures on increasing y. With further increase in V concentration this valley disappears and no such anomaly is observed for the alloys with y > 5.7. A small low temperature dome is also seen in the y = 0 sample which is not well understood at present, but is in correspondence to that observed in a previous study [12].

In order to understand the $S(T)$ behaviour of the $(Cr_{84}Re_{16})_{100-y}V_y$ alloy series, it must be considered that for a magnetic material the absolute thermoelectric power can be approximated as [13]:

$$S = S_{pd} + S_{mag} + S_{diff}, \quad (1)$$

where S_{pd} is the phonon drag term, S_{mag} is the magnon drag term and S_{diff} is due to the diffusion of the electrons. The first two terms dominate at low temperatures and the latter at elevated temperatures, to such an extent that at high temperatures, $S \approx S_{diff}$. The thermopower due to carrier diffusion is given by [2,14]:

$$S = \frac{\pi^2 k_B^2 T}{3e}\left[\frac{\partial \ln \sigma}{\partial E}\right] \quad (2a)$$

$$S \approx \frac{\pi^2 k_B^2 T}{3e}\left[\frac{\partial \ln \Sigma}{\partial E} + \frac{\partial \ln \langle l \rangle}{\partial E}\right], \quad (2b)$$

where σ is the electrical conductivity, Σ is the area of the Fermi surface that has not been destroyed when entering the AFM SDW state, $\langle l \rangle = \langle \tau v \rangle$ the average mean free path of charge carriers over Σ, $\langle \tau \rangle$ is the relaxation time of the electron and $\langle v \rangle$ the velocity at the Fermi surface. Σ is in many cases sensitive to the energy E, but for T just below T_N, where a dome is observed in $\rho(T)$, the second term in equation (2b) can dominate when the electron scattering may be largely determined by $\langle l \rangle$.

In agreement to the previously investigated Cr alloys [2], $S(T)$ for the $(Cr_{84}Re_{16})_{100-y}V_y$ alloy system show behaviour in the form of a relatively large peak associated with the Néel temperature just below T_N, similar to that observed in $\rho(T)$. Trego *et al.* [14] discussed this behaviour in terms of a model in which the dominant effect is the decrease in the scattering rate of electrons by phonons when the AFM phase is entered on decreasing temperature. The Fermi surface area decreases as a result of the electron and hole surfaces that are partially annihilated and this practically results in the observed increase in ρ just below T_N on cooling. As indicated by equation (2b), S is determined by the energy dependence of both Σ and $\langle l \rangle$. The second term of equation (2b) dominates [14] giving a net positive contribution to S at temperatures below T_N.

The effects of Re and V as diluents in Cr in the present alloy series, should be considered. The low temperature minima in $S(T)$ and the way in which the minima in $S(T)$ deepen with increased V content can possibly be attributed to a phonon drag component to S. This effect was shown to be of importance when alloying Cr with elements that have an atomic mass greater than that of Cr, such as Mo and W [2,14]. In addition to a peak, associated with the Néel transition observed in $S(T)$ for the Cr-Mo and Cr-W alloys, a low-temperature valley was also noticed. This valley becomes increasingly shallower on increasing the Mo or W concentration and is finally suppressed at higher concentrations [2,14]. This behaviour is attributed to a decrease in the mean free path length $\langle l \rangle$ due to the scattering by the heavier impurity. Re has an atomic mass approximately four times that of Cr and comparable to that of W and this implies that Re as an impurity in Cr will also bring about phonon drag that might contribute to the low temperature valleys observed in the $S(T)$ curves for the $(Cr_{84}R_{16})_{100-y}V_y$ alloys, with y = 0, 4 and y = 5.7.

The $S(T)$ curves of binary Cr-V [2,14] show a clear dome just below T_N, but no additional minimum is seen at low temperatures in $S(T)$ of these alloys. V has an atomic mass comparable to Cr and appears to have nearly no influence on phonon drag effect as a dopant in Cr. In the current $(Cr_{84}Re_{16})_{100-y}V_y$ alloy series, it is expected that the effect of doping with V will increasingly dominate the $S(T)$ behaviour with increasing y. An increase in V concentration also effectively reduces the Re content of the $(Cr_{84}Re_{16})_{100-y}V_y$ alloys. These combined effects are expected to decrease possible phonon drag contributions to $S(T)$ with increasing V content, resulting in the disappearance of the low temperature valley for samples with $y \geq 8.5$ and only a positive dome is observed just below T_N for these alloys.

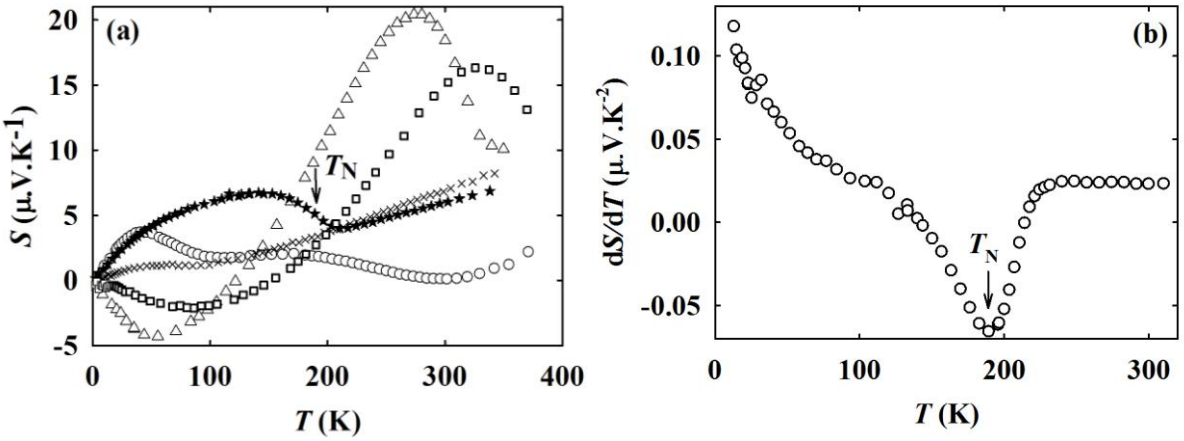

Figure 1: (a) The temperature dependence of Seebeck coefficient, S, for $(Cr_{84}Re_{16})_{100-y}V_y$ alloys with y = 0 (○), 4 (□), 5.7 (△), 8.5 (★) and 10.4 (×). (b) The temperature dependence of d$S(T)$/dT for the $(Cr_{84}Re_{16})_{91.5}V_{8.5}$ alloy. T_N, corresponding to the minimum in the d$S(T)$/dT curve, is marked by an arrow in figures (a) and (b) for y = 8.5.

Figure 2 shows the magnetic phase diagram for the $(Cr_{84}Re_{16})_{100-y}V_y$ alloy system. The critical concentration, y_c, for which T_N continuously tends to a zero value was obtained from a fit to the experimental data (solid line in figure), using a power law of the form $T_N = a(y_c - y)^b$, where a and b are fitting parameters. The numerical values for these fitting parameters are a = (140 ± 20) K, b = 0.49 ± 0.07 and y_c = 10.5 ± 0.0001.

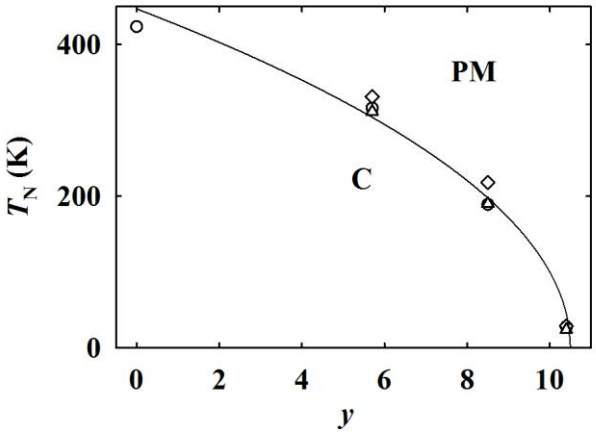

Figure 2: Magnetic phase diagram for the $(Cr_{84}Re_{16})_{100-y}V_y$ alloy system with T_N values obtained from the minima in temperature derivative of electrical resistivity (○), magnetic susceptibility (◇) and Seebeck coefficient (△) measurements. The error bars are within the size of the data points. The solid line shows a power law fit through the data.

A representative example of a specific heat (C_p) versus T curve is shown in figure 3 for the $(Cr_{84}Re_{16})_{94.3}V_{5.7}$ alloy. The Sommerfeld electronic specific heat coefficient, γ, is obtained for the $(Cr_{84}Re_{16})_{100-y}V_y$ alloy system from these measurements at low temperatures considering the equation: $C_p = \gamma T + \beta T^3$. Here, the first term represents the electronic specific heat component and the lattice contribution is represented by the second term. γ is determined from least-square fits to the low temperature specific heat measurements, giving linear behaviour for C_p/T versus T^2 in the temperature range 2 K ≤ T ≤ 10 K, as shown by the inset of figure 3.

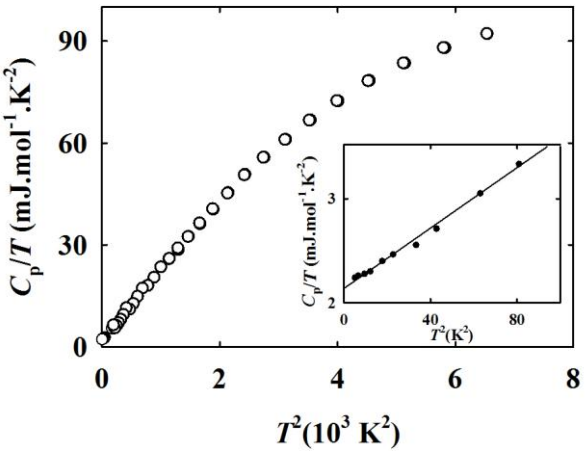

Figure 3: The dependence of C_p/T on T^2 for the $(Cr_{84}Re_{16})_{94.3}V_{5.7}$ alloy. The inset shows a linear fit through the low temperature experimental data for this alloy.

Figure 4 shows the curve of Sommerfeld electronic specific heat coefficient γ, obtained as described above, as a function of V concentration for the $(Cr_{84}Re_{16})_{100-y}V_y$ alloy system. Takeuchi *et al.* [8] reported on the behaviour of γ in the quantum critical $Cr_{1-x}V_x$ alloy system. They observed an increase in $\gamma(x)$ in the AFM phase up to the QCP where a discontinuity in $\gamma(x)$ is observed. This is followed by a gradual decrease as x is increased in the paramagnetic phase. Sheppard *et al.* [15] also observed similar behaviour below the critical concentration $z_c \approx 0.04$ in the $(Cr_{0.98}Si_{0.02})_{1-z}Mo_z$ system. In the quantum critical $(Cr_{86}Ru_{14})_{100-x}V_x$ system, Reddy *et al*. [10] observed rather unexpected behaviour in $\gamma(x)$. They reported a sharp decrease in $\gamma(x)$ in the AFM CSDW phase up to $x \approx 0.08$ followed by a jump-like increase and then a further sharp decrease of $\gamma(x)$ that continues through the critical concentration into the paramagnetic phase [10]. The behaviour of γ is thus a key indicator of quantum critical behaviour. In the $(Cr_{84}Re_{16})_{100-y}V_y$ alloy system, γ decreases on increasing y, but a minimum is observed in the $\gamma(y)$ curve at 10.4 at.% V, close to the critical concentration of $y_c = 10.5$. We are in the process of extending the research work to include more samples so as to confirm the exact concentration associated with the minimum in the *γ(y)* curve.

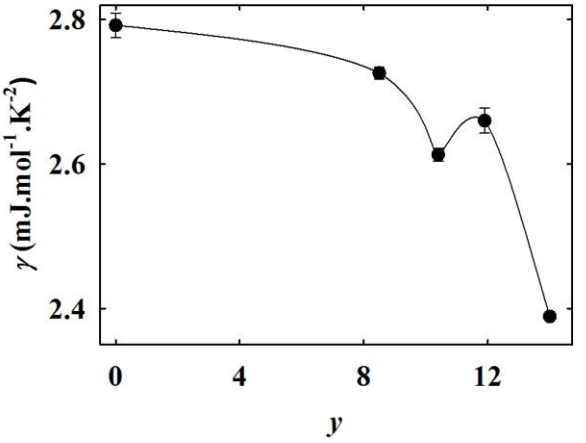

Figure 4: Sommerfeld electronic specific heat coefficient, γ, as a function of V concentration. The solid line is a guide to the eye.

4. Conclusion

Electrical resistivity and thermopower measurements on the $(Cr_{84}Re_{16})_{100-y}V_y$ alloy system indicate that V doping of $Cr_{84}Re_{16}$ reduces T_N and suppresses it down to 0 K at a critical concentration of 10.5 at.% V. Specific heat measurements were used to determine the Sommerfeld coefficient (γ) as a function of V concentration (y) for this series. A minimum is observed in the $\gamma(y)$ curve close to y_c. This is indicative of the existence of a possible quantum critical point at this concentration. However, more samples need to be prepared, especially in the region of the critical concentration. Hall coefficient and magnetic susceptibility measurements which are vital to locate and classify the QCP need to be performed to validate whether this critical point is a quantum critical point.

Acknowledgments

Financial support from the South African NRF (Grant numbers 61388 and 78832) is acknowledged.

References

[1] Galkin V Y 1991 *Sov. Phys. Solid State* **33** 10
[2] Fawcett E, Alberts H L, Galkin V Y, Noakes D R and Yakhmi J V 1994 *Rev. Mod. Phys.* **66** 25
[3] Dubiel S M, Cieslak J and Wagner F E 1996 *Phys. Rev.B* **55** 1
[4] Fawcett E 1992 *J.Phys.: Condens Matter* **4** 923
[5] Moller H B, Trego A L and Mackintosh A R 1965 *Solid State Commun*. **3** 137
[6] Fawcett E, Roberts R B, Day R and White G K 1986 *Europhys. Lett.* **1** 473
[7] Yeh A, Soh Y A, J Brooke J, Aeppli G, Rosenbaum T F and Hayden S M 2002 *Nature* **419** 459
[8] Takeuchi J, Sasakura H and Masuda Y 1980 *J. Phys. Soc. Japan* **49** 508
[9] Reddy L, Alberts H L, Prinsloo A R E and Venter A M 2006 *J. Alloys Comp.* **426** 83
[10] Reddy L, Alberts H L, Strydom A M, Prinsloo A R E and Venter A M 2008 *J. Appl. Phys.* **103** 07C903-1
[11] Jacobs B S, Prinsloo A R E, Sheppard C J and Strydom A M 2011 *SAIP Conference Proceedings* 105
[12] Thiruvikraman P K, 1999 PhD thesis, Mangalore University
[13] Arajs S, Anderson E E and Rao K V 1971 *J. Less-Common Metals* **26** 157
[14] Trego A L and Mackintosh A R 1968 *Phys. Rev.* **166** 495
[15] Sheppard C J, Prinsloo A R E, Alberts H L and Strydom A M 2011 *J. Appl. Phys.* **109** 07E104

Optical Properties of SiN:H thin films obtained by hydrogen dilution

S Jacobs[1], T F G Muller[1*], G F Malgas[2], and C J Arendse[1]

[1]Department of Physics, University of the Western Cape, Modderdam Road, Private Bag X17, Bellville, 7535, South Africa

[2]CSIR National Centre for Nano-Structured Materials, P. O. Box 395, Pretoria, 0001, South Africa

E-mail: tmuller@uwc.ac.za

Abstract. Silicon Nittride **(**SiN) thin films were deposited on Corning 7059 glass and crystalline silicon <100> substrates. UV-VIS spectra were obtained in reflection and transmission modes on the silicon and glass substrate respectively, and the optical modelling was performed using a Bruggerman Effective Medium Approximation (EMA). Optical fits for the spectra were obtained using TFCompanion® and Scout® software. The mean square error function values for single layer homogenous materials on substrates indicate inaccurate fits and subsequent extracted optical properties of the material. Hence a virtual multi-layered approximation for a single film was adopted to describe a material that possesses dissimilar optical properties in its bulk compared to interface regions. In the EMA matrix Cauchy /OJL materials were mixed with particles required to describe SiN, and the results obtained for the different fits are contrasted in terms of their optical constants**.** .

Introduction

Amorphous silicon nitride (a-SiN) is a material with a high dielectric function, large tuneable band gap, and a low refractive index [1]. These properties allow SiN to be used in many industries, depending on the required structural and optical characteristics. Different deposition methods produce varying structural characteristics of the material, and in each specific system the required optical and structural properties of the thin film can be tuned and controlled through the conditions during the deposition. In Industry, the preferred method of manufacturing SiN is through the use of Plasma Enhanced Chemical Vapour Deposition (PECVD). Thin films produced by PECVD are of poor quality, and for use in industry may not be ideal. Recently an alternative method known as Hot Wire Chemical Vapour Deposition (HWCVD) has started gaining popularity [2].

Thin films deposited by PECVD as compared to those deposited by HWCVD are less dense due to the high hydrogen incorporation in the thin films [2]. Recently much focus has been placed on the manufacturing of SiN as an antireflective coating on top of microcrystalline silicon (mc-Si) solar cells. HWCVD offers high growth rates with stable, dense films exhibiting excellent optical and structural properties, in comparison to PECVD.

In this study SiN was deposited by diluting silane and ammonia with hydrogen in a HWCVD chamber. The total hydrogen content in the film influences the distribution of the Si-Si bonds [2], and in HWCVD-deposited films the atoms are tightly packed, which yields high-quality material, a consequence of the improved structural properties of thin films produced by HWCVD. For application as photovoltaic material the hydrogenated silicon nitride (SiN:H) thin films need to be optically

* To whom any correspondence should be addressed.

characterised in order to determine the effects of light scattering, reflection and transmission off and through the surface and bulk of the thin film. The optical constants of the material, i.e. the refractive index (n) and extinction coefficient (k), which are related to the dielectric function (ε), can be computed over a range of wavelengths and subsequently the Tauc band gap [3] values (E_g) can be determined from the absorption coefficient (α). At present many mathematical models to describe the dielectric functions exist in literature and are used in experimental works to obtain the calculated optical constants. Since n and k cannot be calculated directly they are instead determined through an indirect measurement, which can be done in two ways [4]. The first method involves calculating and fitting the measured reflection and transmission ultraviolet-visible (UV-vis) spectra from the complex dielectric function of the material. The filmstack parameters are inferred from the best fit of the measured data to the data simulated/generated by using a suitable optical model of the filmstack. Another commonly used method for determining n and k of an amorphous semiconductor is through an inversion process as described by Swanepoel's [5] envelope method.

In this work both methods are utilised and compared. Firstly, the model proposed by O' Leary *et al* in 1997 [6] (OJL) is used in simulations and the results compared to those of the Cauchy [7] model for refractive index dispersion, and the Swanepoel method [5].

Experimental

The SiN thin films used in this study were produced by the thermal catalytic decomposition of silane, ammonia and hydrogen gas in a HWCVD chamber. The pressure within the chamber was set to 100 μbar for the duration of the deposition, with the tantalum (Ta) wire temperature at 1490 ^{0}C. The substrate heater temperature was kept at 240 ^{0}C while the source gas flow rates were kept at 20 sccm hydrogen, 5 sccm silane, and 7 sccm ammonia. The resulting thin films were deposited on both crystalline silicon <100> as well as Corning 7059 glass substrates; each used for the different characterisation techniques and reflection/transmission UV-vis geometry. The glass substrates were used for optical transmission measurements, as well as X-ray diffraction (XRD), while optical reflection measurements were performed on the silicon substrates. XRD was performed using a Panalytical X'Pert Pro system in reflection geometry utilising Copper $K\alpha_1$ radiation of wavelength 1.54 Å with a scan step-size of $2\theta = 0.03°$. UV-vis transmission measurements were performed on a Carey 1E UV-visible spectrophotometer over the range 400 to 850 nm while the reflection measurements were performed on a Semiconsoft MProbe Thin Film measurement system over a wavelength range of 300 to 800 nm. Surface roughness was measured with a Veeco Atomic Force Microscope (AFM) probe.

Results and Discussion

3.1 X-ray Diffraction and surface morphology

A diffraction pattern was obtained for the thin film deposited on the Corning 7059 glass substrate, and is shown in figure 1. The absence of crystalline peaks, and the presence of a broad amorphous 'halo' around 27°, signifies that the thin films are amorphous in nature, possessing no long range order.

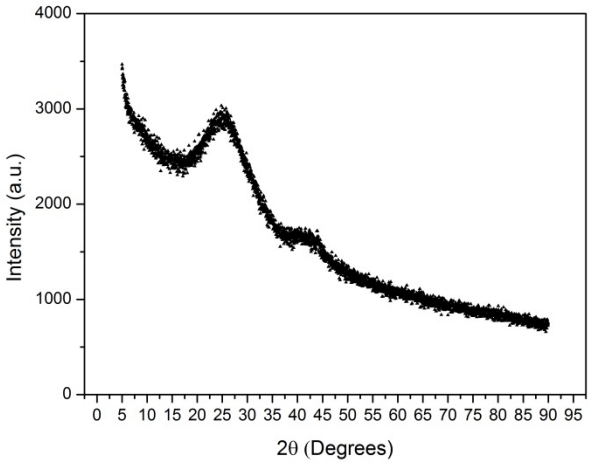

Figure 1: XRD pattern of SiN:H film on glass**.**

The root-mean-square surface roughness was measured using AFM and was determined to be 2 nm; this is in agreement to what was reported by Verlaan *et.al* [8] who reported values between 0.4 nm and 4.8 nm which can be attributed to the N/Si bonding ratios obtained by varying the deposition parameters [8].

3.2 Optical Modelling

The dielectric function of a material describes the behaviour of the material in response to an electromagnetic (EM) stimulus with certain photon energy. The dependencies of n and k on allow for the interpretation of the EM interaction with the material, which is normally generalised to the Cauchy dispersion model of the form $n(\lambda) = N_0 + \frac{N_2}{\lambda^2} + \frac{N_4}{\lambda^4}$. In the expression N_0, N_2, and N_4 are fitting parameters for a generalised dispersion relation, which holds up well in the visible region [9]. In TFCompanion® software [10] the parameters are determined by fitting a parameterised material with a known dispersion relation to the Cauchy equation. The calculation is carried out through a Marquardt-Levenberg iterative process. The calculated spectra are then fitted onto the measured spectra and a mean square error (MSE) is calculated. On the other hand the software program Scout® [11] implements the OJL-modified density of states (DOS) theoretical framework in its calculations. The DOS of a system describes the number of available sites per unit of energy at each sequential energy level that may be occupied by electrons. The OJL modelling approach in describing the dielectric functions of such materials is founded on the principals of the DOS for amorphous semiconductor materials. The OJL approach assumes that the valence and conduction DOS follows a parabolic function with the tail regions decaying exponentially into the forbidden region (band gap) [6]. It also allows for transitions between the band and the tail regions in the DOS function [6] and the extent of the tailing into the band gap region. Initial guesses for each parameter were selected and the simulation was allowed to run its course. A downhill simplex method was employed in the optical fitting regime with an automatic fitting process; this ensures that the deviation between the spectrum and the fit is kept to a minimum.

The growth of the thin film on the substrate is dependent on the substrate position relative to the hot filament; the variation in position causes inhomogeneity in the film growth. The heterogeneous nature of the thin films does not only relate to the thickness profiles of the deposited film on the substrate, but also to the material properties. Heterogeneity in the structure leads to heterogeneity in the optical spectrum and optical properties as well, and the use of a simple, single material model (Cauchy or

OJL) to describe the thin film system is ineffective. Thus more complex models consisting of composite materials are needed. In this work the Bruggerman Effective Medium Approximation [12] (BEMA) is used to describe the heterogeneous thin film material. The BEMA consists of a host matrix with an embedded particle having a separate dielectric function from the host. The effective dielectric function on a macroscopic level can be used to describe the overall optical characteristics of the material. The BEMA function can be expressed mathematically as $\sum_i f_i \frac{\varepsilon_i - \varepsilon_{eff}}{\varepsilon_i + 2\varepsilon_{eff}} = 0$ where $_i$ represents the dielectric function of the ith component in the composite system and f_i is its respective volume fraction. The EMA can describe the layer containing varying volume fractions of the composite materials, this leads to varying optical properties throughout the thin film. A host matrix was selected, either a Cauchy amorphous semiconductor (TFCompanion®), or an OJL amorphous semiconductor (Scout®). Particles of material that could be present in the material, such as silicon crystallites, and particles of air to represent voids, could have an influence on the optical properties of the material. The dielectric functions of these materials in the Bruggeman form were incorporated in the virtual material, as well as a mixture of non-stoichiometric and stoichiometric silicon nitride.

However, the use of a single EMA is also not sufficiently mathematically complex enough to describe the complex SiN material obtained by the dilution of hydrogen in silane and ammonia, as shown in figure 2. The OJL model is able to approximate some of the interference fringes, whereas the Cauchy cannot. This necessitated the construction of a multi-layered EMA model [13] to represent one film. The optical models consisted of three layers as well as a fourth oxide surface layer, where each virtual layer represents a section of the thin film. The third layer constitutes of an intermediate layer between the substrate and the bulk of the film, where initial film growth took place. The bulk or middle layer is usually found to be the thickest layer and contributes most to the overall optical properties of the film. The first layer represents the final growth phase of the thin film, the settling of the final radicals after power has been cut to the hot filament, or the shutter controlling deposition has been inserted between the film surface and hot filament. Post deposition oxidation occurs as soon as the thin film is exposed to atmosphere. This occurs due to the structural characteristics of the thin film at the surface, and necessitates the insertion of a thin oxidation layer on the surface of the film to accurately model the real film structure, and thus realistically approximate the optical properties of the thin film. Cauchy and OJL optical models incorporating EMA particles were thus built according to the inhomogeneous virtual layer set up as described above. Figure 2 displays the resulting fits for each model type on the reflection and transmission spectrum respectively.

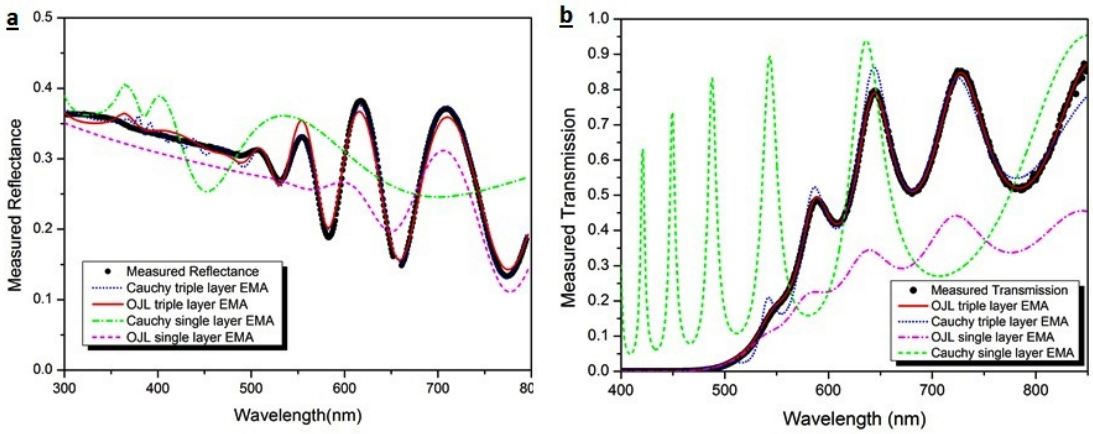

Figure 2: Measured and calculated spectra for (a) reflection and (b) transmission modes.

Excellent fits were achieved with the modelling for the OJL + EMA virtual multi-layered structure especially. The Cauchy dispersion formula is an empirical mathematical formula, and does not take

into account the effects of defect states and band tailing. Its results are not consistent with the two other methods. The OJL model on the other hand describes how the dielectric function of the material is affected by the defect states, band tailing and the interaction path of the light as it travels through the material. It is hence a genuine description of a semiconductor. For this reason we favour the results obtained by OJL modelling over the application of a Cauchy type. For the virtually layered structure we now obtain the overall absorption coefficient of the thin film from Beer's Law [14] as a weighted average of the absorption coefficient by thickness, namely $\sum_{i=1}^{n} \frac{\alpha_i X_i}{X_T}$, where α_i represents the absorption coefficient of the i^{th} layer, and X_T the total thickness of the thin film [13].The absorption coefficient obtained from the 3-layer OJL + EMA reflection spectrum closely follows the absorption coefficient obtained from the 3-layer OJL + EMA transmittance spectrum over the energy range, whereas the absorption coefficient obtained from the Swanepoel [5] method starts to diverge at higher energies.

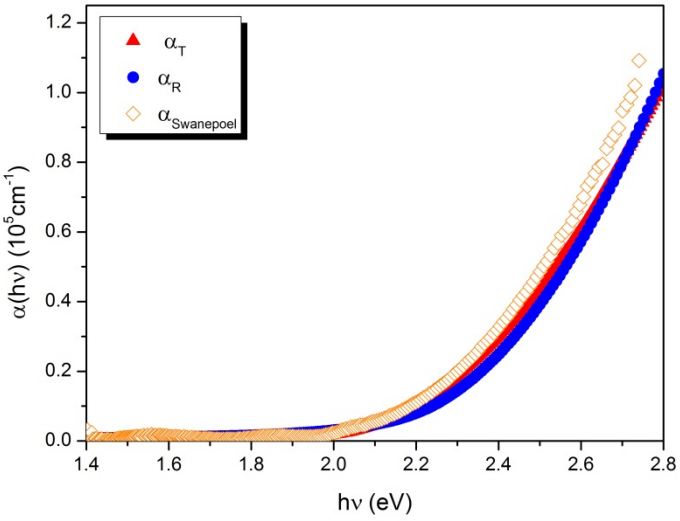

Figure 3: Plots of absorption coefficient obtained from the 3-layer OJL + EMA modelling.

For comparison we have extracted the optical constants and energy values for the material by different modelling approaches in Table 1 below. Similar values for n_o of the OJL model have been observed by Holt [15].

Table 1. Calculated optical constants and energies for 3 layer filmstack.

Spectra	Modelling Type	n_0	E_g (eV)	E (eV) at α_{10^4}	X_T (nm)	Deviation/ MSE
Reflectance	**Cauchy**	**2.78**	**2.64**	**3.07**	**489**	**8.00×10^{-2}**
	OJL	***2.53***	***2.06***	***2.25***	**642**	**6.64×10^{-4}**
Transmission	**OJL**	***2.52***	***2.00***	***2.19***	**800**	**2.25×10^{-5}**
	Swanepoel	**2.51**	**2.08**	**2.19**	**805**	**1 % error**
	Cauchy	**1.03**	**1.99**	**3.20**	**1504**	**9.10×10^{-2}**

Table 1 displays the superior nature of the 3-layer OJL optical model for both the reflection and transmission results compared to the Cauchy model. The difference in thickness evident from the modelling of reflection and transmittance spectra, utilising the same 3-layer OJL model, is due to the positioning of the two substrates relative to the parallel filaments in the reaction chamber. Substrates positioned directly underneath the filament normally grow thicker films on top. The close matching of the optical functions displayed in the table above indicates that the structural properties of the thin films grown on the two substrates are the same.

Conclusion

The a-SiN:H thin films obtained by the dilution of ammonia and silane in hydrogen was found to be too complex to characterise conventionally by single layer optical models, and more thought must be given to construct a virtual analogy of the physical system under consideration. Data were extracted from the virtual multi-layered assumption for the different approaches and the values of the optical constants compared. From the results it is evident that the values obtained from the OJL modelling are fairly consistent whether the reflection or transmission spectrum is considered, and can account for effects of crystallinity in materials that show up in reflection spectra

References

[1] F. Giorgis, C. F. Pirri, E. Tresso, 1997, *Thin Solid Films* **307**, 298.
[2] B. Stannowski, J.K. Rath, R.E.I. Schropp, 2003, *J. Appl. Phys.* **93**, 2618.
[3] J. Tauc, 1968, *Materials Research Bulletin* **3**, 37.
[4] A. Solieman, A.A. Abu-Sehly, 2011, *Materials Chemistry and Physics* **129**, 1000.
[5] R. Swanepoel, 1983, *J. Phys. E.: Sci. Instrum.* **16**, 1214.
[6] S. K. O'Leary, S.R. Johnson, P.K. Lim, 1997, *J. Appl. Phys.* **82**, 3334.
[7] Jai Singh (ed), *Optical Properties of Condensed Matter and Applications*, John Wiley & Sons Ltd, Chichester, England, 2006.
[8] V. Verlaan, '*Silicon Nitride at high growth rates using hot wire chemical vapor deposition'*, PhD Thesis, Utrecht University, Netherlands, 2008.
[9] F. A. Jenkins, H. E. White, '*Fundamentals of Optics, 3rd Edition'*, McGraw-Hill Book Company, 1957.
[10] TFCompanion Thin Film Analysis Software (2008) manual, www.semiconsoft.com, retrieved 13 October 2011.
[11] Scout spectrum interpretation by simulation software (2008) by W.Theiss, www.mtheiss.com, retrieved 6 August 2010.
[12] D.A.G. Bruggeman, 1935, *Ann. Phys.* (*Leipzig*) **24**, 636.
[13] T.F.G. Muller, C.J. Arendse, S. Halindintwali, D. Knoesen, R.E.I. Schropp, 2011, *Thin Solid Films* **519**, 4462.
[14] K. J. Laildler, J. H. Meiser, '*Physical Chemistry, 2nd Edition'*, Houghton Mifflin Company, Boston, 1995.
[15] J. K. Holt, *'Hot-wire Chemical Vapor Deposition of Silicon and Silicon Nitride for Photovoltaics:Experiments, simulations, and applications'* ,PhD Thesis, California Institute of Technology, California, U.S.A., 2003.

Defects identification in $FeTiO_3$ using positron annihilation technique

T P Jili[1,2], E Sideras-Haddad[2], D Wamwangi[2], F Tuomisto[3] and L Kilanski[3]

[1] Department of Physics, University of Zululand, P/B X1001, Kwa-Dlangezwa, 3886, South Africa

[2] Department of Physics, University of the Witwatersrand, Johannesburg, PO Wits 2025, South Africa

[3]Department of Applied Physics, Aalto University, P.O. Box 11100, Otakaari 1 M, FI-02150, Espoo, Finland

E-mail : tjili@pan.uzulu.ac.za

Abstract. Positron lifetime measurements are conducted in metal oxide material with hexagonal structure, in the temperature range from 30 K to 500 K. The analysis of the positron lifetime spectra is best fitted to two lifetime components. The positron lifetime in a defect-free region ranges from 177 ps to 186 ps in the temperature range. The second lifetime components of localized positron range from 350 ps to 462 ps in the temperature range. The second positron lifetime components are attributed to positron trapping at vacancy complexes. A close analysis of second lifetime components coupled with the fact that annihilation ratios are greater than threshold value of 1.4 suggests a formation of vacancy clusters in the temperature range from about 250 K to 500 K.

1. Introduction

Iron titanium oxide ($FeTiO_3$) has drawn much attention because of titanium which finds its application in the manufacturing of aircrafts parts and in many other applications. Therefore it is extremely crucial that reliability be maintained in order to minimize or control defect density in the material.

Positron annihilation technique (PAT) in the past decade has become a reliable tool in which positrons are used as probes for various forms of open volume defects. This technique has been employed extensively for defect investigations in semiconductors and metals experiments but little research has been conducted in metal oxide perovskite structures.

Positrons in a sample can have several states associated with different kinds of defects each of which gives a characteristic lifetime. The positron lifetime is given by a reciprocal of the annihilation rate given by

$$\lambda=\pi r\_o\^2\ c\int d\ r\ |\psi\_(+)\ (r)|\^2\ \ n\_(r)\ \ \gamma[n\_-\ (r)] \tag{1}$$

where r_o is the classical radius of the electron, $\psi_+(r)$ is the positron wavefunction, $n(r)$ the electron density and $\gamma[n(r)]$ the enhancement factor [1]

The objective of the present work is to determine the vacancy complexes as a function of temperature using annihilation rates at various temperature points.

2. Experiment

$FeTiO_3$ samples of thickness 2 mm and a diameter of 6 mm were prepared from $FeTiO_3$ powder using a standard pelletizing technique. A $^{22}NaCl$ source of activity of 20 μCi sealed by two electron-welded aluminium foils of thickness 7 μm, was placed between two equal FeTiO3 samples in a standard sandwich arrangement. The sample chamber was kept at 10^{-4} Torr pressure.

The lifetime measurement was carried out using standard coincidence setup by employing two fast scintillator detectors (XP2020) for the start (1275 keV) and stop (511 keV) signals. The time resolution of the positron lifetime coincidence-setup used for the measurements was of the order of 280 ps at FWHM. The measurements were performed between 30 K and 500 K. The sample temperature was monitored through thermocouples and was stabilized to ± 1 K. About 10^6 counts for each spectrum were collected.

Source correction was carried out because 10 – 15 % annihilations take place in the source material and in the encasing foil. Aluminium foil has a positron lifetime component of 210 ps and the intensity was calculated using Bertolucci-Zappa formula given by [2]

$$I_{foil}(\%) = k = 0.324 Z^{0.93} \times \Omega^{\alpha} \qquad (2)$$

where Ω is the surface density of the foil in mg cm^{-3} and $\alpha = 3.45 \times Z^{0.4}$.

3. Results and discussion

Positron annihilation ratios, λ_d / λ_b, shown in figure 1, at various temperature points are certainly above a threshold of 1.5. This is an indicates a reliable positron lifetime values

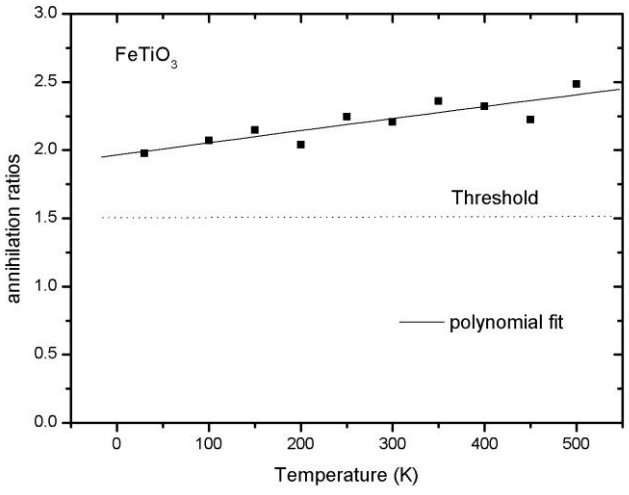

Figure 1. Annihilation ratios indicating a clear separation of two positron lifetime components.

The annihilations in the bulk, i.e. the defect-free region, and in vacancies are shown in figure 2. The average positron lifetime, τ_{av}, which represents a statistically accurate parameter is shown in figure 3. The short lifetime of 185 ps is typically attributed to the free annihilation of positrons. The observed first positron lifetime component agrees very well with a theoretically calculated free positron lifetime of 188.05 ps in the bulk. The second positron lifetime component arises from

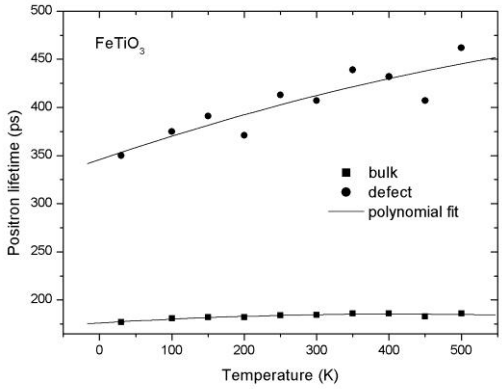

Figure 2. First and second positron lifetime components

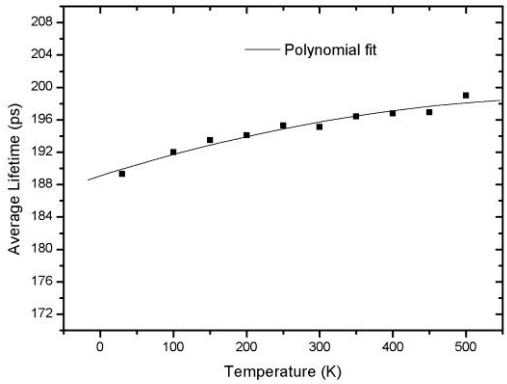

Figure 3. Average positron lifetime as a function of temperature

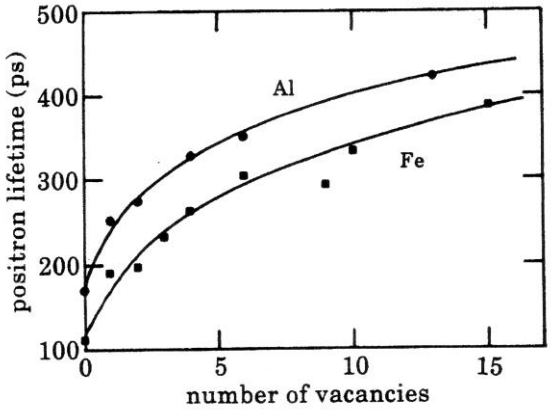

Figure 4. Number of vacancies as a function of positron lifetime in Fe [5]

annihilation of positrons at defect sites. In this case it is believed to be coming from annihilation of positrons at vacancy complexes possibly formed as clusters. Average positron lifetime of 196.18 ps compares very well with a theoretically value of 197.17 ps in which a deviation is within 0.5 %.

Fe free-atom vacancy has annihilation rate of 4.8260 /ns which was calculated using Local Density Approximation (LDA) in which the enhancement is calculated from Boronski – Nieminen [3]. Ti free-atom vacancy calculated by Mizuno [4] has an annihilation rate of 4.975 /ns which is higher than that for Fe. This is an indication of uneven distribution of positron wavefunctions at various metal vacancies. The observed average positron lifetime value of 196.18 ps in figure 3 suggest a divacancy type of defect at Fe-ion sites. This is confirmed by a theoretically calculated [5] value as shown in figure 4.

4. Conclusion

Positron annihilation technique clearly reveals the temperature dependent of vacancy complexes. The variation of free-atom annihilation rates gives a contribution of individual metal ion in terms of the distribution of positron wavefunctions in the vicinity of individual metal ions.

Acknowledgement
The authors wish to thank iThemba LABS (Gauteng) for the facilities, the University of Zululand and NRF (National Research Foundation) for their financial support. We would also like to thank Positron Laboratory staff at Aalto University in Finland for sharing with us their knowledge and positron lifetime equipment.

References

[1] Alato M, Barbiellini B, Hakala M, Kauppinen H, Korhonen T, Puska MJ, Saarinen K, Hautorjavi P and Nieminen RM 1996 *Phys. Rev.* B **54**, 2397
[2] Bertolaccini M and Zappa L 1967 *Nuovo Cimento* B **52,** 487
[3] Boronski E and Nieminen RM 1986 *Phys. Rev.* B **34**, 3820
[4] Mizuno M, Araki H and Shirai Y 2002 *Materials Transactions* **43**(7), 1451-1455
[5] Puska MJ and Nieminen RM 1983 *J. Phys. F* **13**, 333

The Lattice Dynamics of Mercuric Chloride

Jonathan M. Keartland and Eric Newby

School of Physics and Materials Physics Research Institute, WITS 2050, South Africa

E-mail: jonathan.keartland@wits.ac.za

Abstract.

Measurements of the nuclear spin-lattice relaxation time (T_1) of the ^{35}Cl nuclei in a high purity sample of the molecular solid mercuric chloride ($HgCl_2$) have been made over the temperature range 9 K - 485 K using pure nuclear quadrupole resonance (NQR). Spin-lattice relaxation in this material appears to be dominated by lattice vibrations and/or molecular librations over the entire temperature range investigated. Analysis of the data using available spin-lattice relaxation models has allowed us to estimate the Debye temperature, and to follow changes in the lattice dynamics as a function of temperature. At temperatures above 340 K deviations from the expected quadratic relationship between the spin-lattice relaxation rate and temperature have been noted. Further analysis shows this is a thermally activated process related to the $HgCl_2$ molecules changing their position in a double-well potential. A previously unobserved doublet in the NQR spectrum of the ^{35}Cl nuclei was seen at temperatures above 340 K. The perturbation underlying the changed line-shape appears to be related to hindered re-orientations of the $HgCl_2$ molecules in the crystal lattice. The correlation time of the perturbation was calculated for a range of temperatures. The temperature dependence of the correlation time may be understood by noting the fact that the structure of the unit cell of the lattice is temperature dependent. We conclude that there is a correlation between the high temperature T_1 results and the doublet observed in the NQR spectrum.

1. Introduction

Mercuric chloride ($HgCl_2$) crystallizes in a distorted rhombohedral structure. It is a molecular solid with essentially straight Cl-Hg-Cl molecules that form herring bone layers in the mirror plane of the *Pnma* space group at ambient pressures [1]. This results in two distinct non-cubic sites for the Cl atoms in the crystal, giving rise to a unique electric field gradient (EFG) at each site [2]. In this paper the two sites will be labelled A and B, where A is the site with the larger EFG. As the temperature of the crystal increases the orthorhombic distortion constants of the crystal lattice decrease [1]. Both the ^{35}Cl and the ^{37}Cl nuclei have a spin of $I = \frac{3}{2}$. The presence of an EFG, and the fact that the nuclei have a quadrupole moment, allow for the use of pure nuclear quadrupole resonance (NQR) to probe the properties of solid $HgCl_2$. The two inequivalent sites in $HgCl_2$ result in two distinct NQR frequencies at a particular temperature. At room temperature the ^{35}Cl resonance frequencies for two sites are 22.2489 MHz (Site A) and 22.0655 MHz (Site B). The difference in frequencies decreases as the temperature increases, and the frequencies approach one another as the temperature moves toward the melting temperature (549 K) [3].

A number of NQR investigations of $HgCl_2$ have been reported. The resonance frequency of the Cl nuclei was first reported by Dehmelt *et al* [2], while the asymmetry parameter η

was investigated by Dinesh and Narasimhan [4] and Negita *et al* [5]. More recently, Keartland and Newby [3] have presented a comprehensive study of the temperature dependence of the quadrupole resonance frequency in $HgCl_2$ over the temperature range 4 K - 500 K. The variation of the spin-lattice relaxation time (T_1) with temperature of the ^{35}Cl nuclei in $HgCl_2$ was reported by Dinesh and Smith (DS) [6] over the temperature range 77 K - 398 K. DS also measured the temperature dependence of the inverse line-width parameter T_2^* of the NQR spectrum. The temperature dependence of T_1 of the ^{35}Cl nuclei in a related material (the molecular solid $NaClO_3$) has been measured by Zamar *et al* [7] over a wide range of temperature.

In this paper we describe measurements of T_1 and the NQR spectrum of the ^{35}Cl nuclei in $HgCl_2$, made using pulsed NQR methods over a wide temperature range (9 K - 485 K). We show that lattice vibrations dominate the measured spin-lattice relaxation rate up to 340 K, and that a thermally-activated process becomes important at higher temperatures. The NQR spectrum splits into a doublet for $T \geq 340$ K. Hindered re-orientation of the $HgCl_2$ molecules is identified as a likely mechanism to describe both the T_1 results, and the changes in the NQR spectrum.

2. Experimental Considerations

A commercially obtained high purity powder sample of $HgCl_2$ was sealed in a quartz ampoule under vacuum. No further purification of the sample was undertaken. NQR measurements were made using a standard coherent pulsed radio frequency spectrometer operating in the range 17 - 23 MHz. Averaging, quadrature detection and phase-cycling were used to obtain quadrupolar spin-echoes with an excellent signal-to-noise ratio. Relaxation times were obtained using an inversion-recovery-echo pulse sequence applied at the resonance frequency of the nuclear spin system. Measurements of T_1 were made at both lattice sites for the ^{35}Cl nuclei. Quadrupolar spin-echoes were recorded at each temperature, and the NQR spectra obtained from Fast Fourier Transforms (FFTs) of the spin-echo signals. Temperature control was achieved to an accuracy of better than 0.1 K using two separate arrangements. For measurements between 300 K and 500 K the sample was placed inside a copper can fitted with a heater and copper-constantan thermocouple. The entire can was placed inside a thermally insulated sleeve. Temperature control is via an Oxford ITC503 temperature controller. For temperatures below 300 K an Oxford continuous flow cryostat was used in conjunction with the temperature controller and the built-in cryostat thermocouple. Liquid nitrogen and liquid helium were used as cryogens. The temperature for each measurement was obtained from a previous careful calibration of the NQR frequency [3].

3. Results and Analysis

3.1. Spin-Lattice Relaxation Time

The spin-lattice relaxation times of the ^{35}Cl nuclei in $HgCl_2$ over the entire temperature range (9 K - 485 K), are plotted in Fig. 1. The spin-lattice relaxation times at site A and site B differ slightly at the same temperature. In the discussion that follows we identify three temperature ranges: below 100 K (low temperature), between 100 K and 340 K (intermediate temperature), and above 340 K (high temperature). Where it is appropriate we compare our results to those of DS [6].

Spin-lattice relaxation in the temperature range 9 K - 280 K should be dominated by the vibrational or librational modes of $HgCl_2$. Two models were fitted to the data in this temperature range, and the fits to the models for Site A are shown in Fig. 2. A two-phonon Raman model [8] provides an excellent fit to the data, and the Debye temperature extracted from the fit is 47 ± 5 K. A value for the Debye temperature of $HgCl_2$ could not be sourced from the literature for comparison. The model for molecular librations [9] (assuming a single mode) provides a less satisfactory fit, and gives a characteristic temperature of 31.6 ± 0.4 K (corresponding to a wave number of 22 cm^{-1}). This does not correspond to any lattice modes observed previously

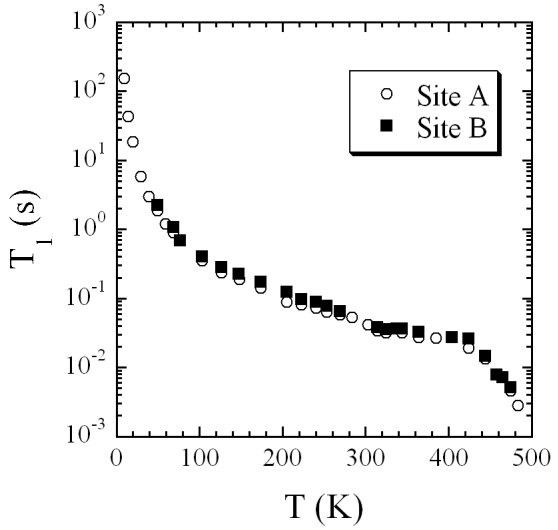

Figure 1. A plot T_1 vs T for the entire temperature range studied (9 K - 485 K). Three regions are identified for analysis: 9 K - 280 K, 100 K - 340 K and above 340 K.

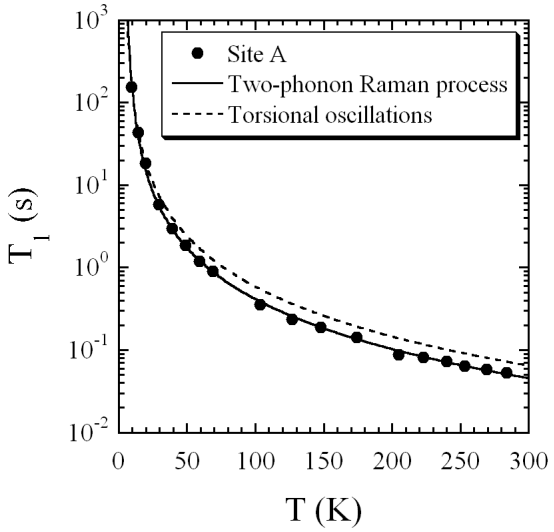

Figure 2. A plot of T_1 vs T for the temperature range 9 K - 280 K. The fits of a two-phonon Raman model [8]and a model for torsional oscillations [9] are shown.

Table 1. Comparison of the values of n obtained in this paper with those obtained by DS [6]

Site	n (this work)	n (DS [6])
A	2.04 ± 0.06	1.79 ± 0.16
B	2.11 ± 0.08	1.89 ± 0.15

using Raman spectroscopy, although there is a mode at 18 cm^{-1} [10]. It is possible that a number of modes contribute, in which case it is the lowest wave number modes that dominate. It is reasonable to ascribe spin-lattice relaxation in this temperature region to acoustic phonons, and to offer the value for the Debye temperature extracted as realistic estimate of the Debye temperature of $HgCl_2$.

The relaxation rate in the intermediate temperature range 100 K - 340 K was analysed using the well-known relation for the vibrational relaxation rate [11]

$$\left(\frac{1}{T_1}\right)_{vib} = AT^n. \tag{1}$$

It is expected that $n \simeq 2$ in this temperature range. A plot of $-\ln T_1$ vs T for both lattice sites in the intermediate temperature range is shown in Fig. 3, and the extracted results for n are given in Table 1. The T_1 data obtained by DS [6] for the same temperature range were analysed using (1), and the results for n are also given in Table 1. The values of n for site B agree within experimental error, while those for site A show a small discrepancy. The rate parameter A was determined for each site by fitting (1) to the data for 100 K - 340 K for each site using $n = 2$, and the results for A obtained were used in analysis of the high temperature data that follows.

The relaxation rate attributed to the vibrational modes was subtracted from the total relaxation rate for temperatures above 340 K, and the resulting data were fitted to an Arrhenius

Table 2. Values of the activation energy E_A obtained using the Arrhenius model (2) for the spin-lattice relaxation data above 340 K.

Site	E_A (kJ mol^{-1})
A	97 ± 14
B	83 ± 10

model of the form [7]

$$\left(\frac{1}{T_1}\right)_{total} - \left(\frac{1}{T_1}\right)_{vib} = B \exp\left[-\frac{E_A}{k_B T}\right]. \quad (2)$$

The results are shown in Fig. 4. The resulting activation energies E_A are tabulated in Table 2, where E_A is the height of the potential barrier. Zamar *et al* [7] obtained an activation energy of 26.4 ± 1 kJ.mol^{-1} for $NaClO_3$, and proposed that orientational disorder accounts for the deviation from relaxation governed by vibrations. We propose that the increase in the spin-lattice relaxation rate at high temperatures is due to re-orientations of the $HgCl_2$ molecules in a double-well potential. Evidence for this is provided by the changes observed in the NQR spectrum (as discussed below).

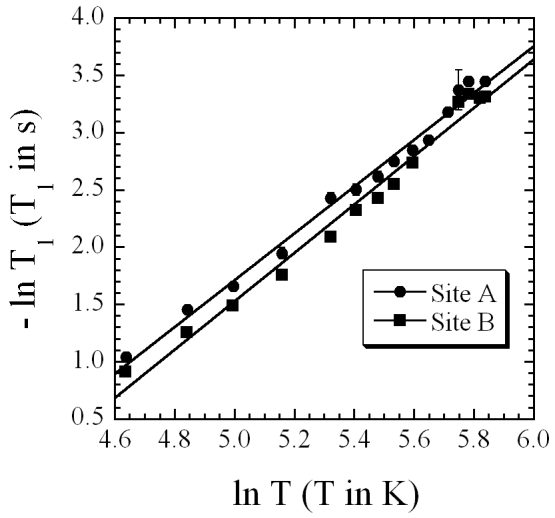

Figure 3. A plot of $-\ln T_1$ vs T for the intermediate temperature range (100 K - 340 K). An expression for the vibrational relaxation rate (1) was fitted to the data, and a value of n for each site was extracted, and the results are presented in Table 1.

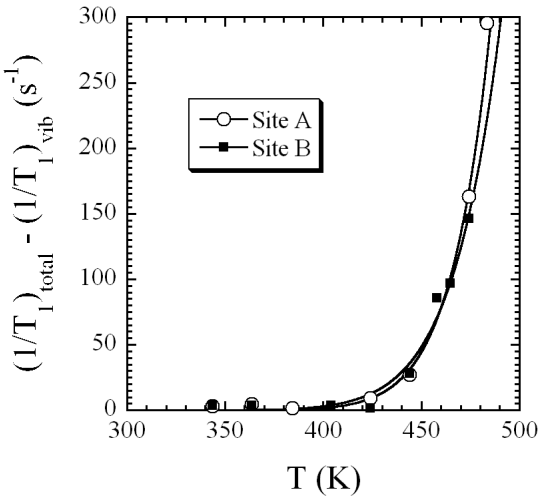

Figure 4. A plot of the total relaxation rate less the vibrational relaxation rate as a function of temperature for the T_1 data in the temperature range $T > 340$ K. An Arrhenius model (2) is fitted to the data, and the results are presented in Table 2.

3.2. NQR Spectrum

The NQR spectra obtained from FFTs of the quadrupolar spin echoes are shown in Fig. 5. Seliger [12] has pointed out that the NQR spectrum will split into a doublet when conditions such as those considered by Zamar *et al* [7] are applicable. Zamar *et al* do not report a doublet in the ^{35}Cl spectra at high temperatures in $NaClO_3$, while the spectra in Fig. 5 show clear evidence of an emerging doublet at 350 K, and the frequency difference between the doublet

peaks increase the temperature increases. The doublet arises from a perturbation, in the form of a two-site exchange, to the unperturbed quadrupolar Hamiltonian. The correlation time τ_c of the perturbation causing the change in the observed resonance line may be calculated by manipulating the expressions derived by Seliger [12]. The temperature range was divided into two regions; temperatures below which the doublet is observed (118 K - 332 K), and temperatures above which the doublet is observed (350 K - 425 K). Full details of the calculation will be presented elsewhere. The calculated values of the correlation time of the perturbation for 118 K - 425 K are shown in Fig. 6.

A number of physical phenomena could lead to changes to the NQR resonance line-shape. They include vibration and re-orientation of the $HgCl_2$ molecules, interconversions between molecular conformers, and diffusion of molecules through the crystal lattice [13]. Re-orientation of the $HgCl_2$ molecules is considered to be the most likely underlying mechanism. The molecule re-orientates in a periodic potential arising from inter-molecular forces [13], which restrict the re-orientation. Three types of transitions may be identified; the molecule could make transitions between states in the same potential well, the molecule could tunnel through the potential barrier, or the molecule could be excited to a level above the barrier, rotate classically as a rigid system and drop into another potential well [13]. We suggest that the doublet in the NQR spectrum results from a two-site exchange which eliminates the first type of transition mentioned above. The second type of transition is only significant at low temperatures [13], and may also be eliminated. The third type of transition (two-site exchange) is the most likely mechanism, and we propose that the essentially straight Cl-Hg-Cl molecule rotates through π radians. It can be seen from Fig. 6 that the correlation time of the rotation of the $HgCl_2$ molecule which causes the perturbation decreases as the temperature increases from $T = 118$ K until it reaches a minimum at $T \simeq 300$ K. This occurs because the energy of the molecules in the crystal lattice increases, allowing them to rise above the potential barrier and execute a rotation. It follows that the molecules spend less time in each state and so the correlation time decreases. We suggest that the increase in τ_c above 300 K is related to the change in the orthorhombic distortion constants of the $HgCl_2$ crystal lattice. This results in an increase in the height of the potential barrier between states, making it less likely that a molecule would execute a rotation. The T_2^* measurements of DS [6] also show a turning point at $T \approx 300$ K although their turning point is, as expected, a maximum instead of a minimum (T_2^* is a measure of width in the time domain, and the linewidth is measured in the frequency domain). This behavior of T_2^* was not discussed in any detail by DS. We note that the linewidth in our sample has a minimum at approximately 300 K, in agreement with both the results of DS, and the calculated correlation time.

Fig. 5 shows that the frequency difference between the two peaks in the doublet increases with temperature, in agreement with the decrease in the orthorhombic distortion constants of the crystal. This changes the structure of the potential well, and the resonance frequency of each well changes. The thermally activated increase in the relaxation rate at elevated temperatures, and changes the spectrum line-shape may be traced to the same underlying physical mechanism.

4. Conclusion

A comprehensive study was made of the temperature dependence of the spin-lattice relaxation time of the ^{35}Cl nuclei in $HgCl_2$. It was found that the data could be divided into three temperature ranges and models were successfully fitted to the data in each of the temperature ranges as can be seen in Figs. 2, 3 and 4. The T_1 values in the temperature range 100 K - 340 K were found to agree with the values previously obtained by DS [6]. Hindered re-orientations of the Cl-Hg-Cl molecules are identified as a likely physical model for the appearance of a doublet in the NQR spectrum. The broadening of the split is ascribed to the decrease of the orthorhombic distortion constants of the $HgCl_2$ lattice at high temperatures. The correlation times of the

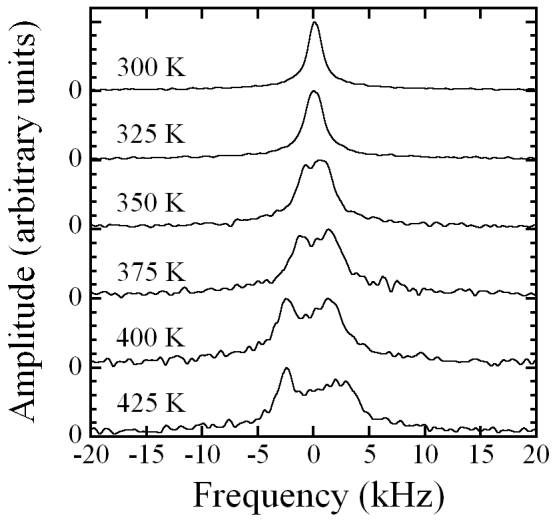

Figure 5. The NQR spectra of ^{35}Cl in $HgCl_2$ for a number of temperatures showing the emergence of a doublet as the temperature increases above 340 K. The linewidth is a minimum at $T \simeq 300$ K.

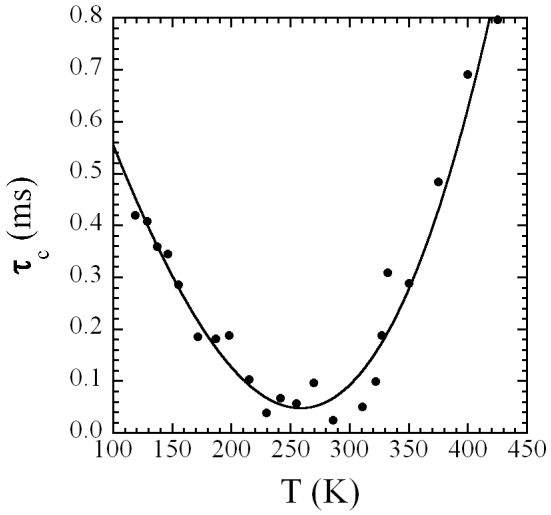

Figure 6. A plot of the extracted correlation time (τ_c) as a function of temperature using a modification of the model suggested by Seliger [12]. The solid line is a guide for the eye.

re-orientations were calculated in the temperature range 118 K - 425 K by assuming that the re-orientations could be modelled as a symmetric two site exchange and making use of the model developed by Seliger [12]. The model considered provides a satisfying description of changes in both the relaxation rate and the resonance line-shape with temperature.

Acknowledgments

The authors gratefully acknowledge the financial support of the National Research Foundation, and the School of Physics and the Materials Physics Research Institute of the University of the Witwatersrand. Technical support from the staff of the Physics Workshop has been invaluable.

References

[1] Hostettler M and Schwarzenbach D 2005 *C. R. Chimie* **8** 147–156
[2] Dehmelt H G, Robinson H G and Gordy W 1954 *Phys. Rev.* **93** 480–482
[3] Keartland J M and Newby E 2011 Temperature variation of the electric field gradient in mercuric chloride *Proceedings of SAIP2011, the 56th Annual Conference of the South African Institute of Physics* ed Basson I and Botha A (University of South Africa, Pretoria) pp 134–139 ISBN 978-1-86888-688-3
[4] Dinesh and Narasimhan P T 1966 *J. Chem. Phys.* **45** 2170–2174
[5] Negita H, Tanaka T and Okuda T 1966 *Inorg. Chem.* **5** 2126–2127
[6] Dinesh and Smith J A S 1974 *Advances in Nuclear Quadrupole Resonance* **1** 31
[7] Zamar R C, Gonzalez C E and Pusiol D J 1998 *Phys. Rev. B* **58** 2476–2481
[8] Abragam A 1968 *The Principles of Nuclear Magnetism* 1st ed (Oxford University Press)
[9] Bayer H 1951 *Z. Phys.* **130** 227–238
[10] Adams D M and Appleby R 1977 *J. Chem. Soc., Dalton Trans.* **16** 1530–1535
[11] Woessner D E and Gutowsky H S 1963 *J. Chem. Phys.* **39** 440–456
[12] Seliger J 1993 *J. Mag. Res., Ser. A* **103** 175–182
[13] Rushworth F A and Tunstall D P 1973 *Nuclear Magnetic Resonance* 1st ed (Gordon and Breach Science Publishers)

Microstructural properties of thermal induced microcrystalline silicon carbide thin films deposited by HWCVD

J Khoele, S Halindintwali, B A Julies and S Mkhwanazi

Physics department, University of the Western Cape, Private Bag X17, Bellville 7535, South Africa

E-mail: 3075072@uwc.ac.za

Abstract. Amorphous Silicon carbide samples were prepared by Hot –Wire Chemical Vapor Deposition (HWCVD) at low temperature of the substrate. A gradual thermal annealing under vacuum induced a network rearrangement as shown by a change in the samples microstructure. The breaking of Si-H_n and C-H_n bonds, followed by hydrogen effusion, led all the available carbon atoms, originating mainly from C-H_n groups to bond to the Si atoms originating mainly from the SiH_n groups, and crystallize into SiC phase. The structural details are presented as studied by Fourier transform infrared spectroscopy (FTIR), transmission electron microscopy (TEM) and non contact atomic force microscopy (AFM).

1. Introduction

Crystalline silicon carbide (SiC) has a number of unique properties, like a wide band gap and high carrier mobility, which make the material an excellent candidate for various optoelectronic devices [1]. The wide optical band gap and the good electrical properties of SiC make the material particularly suitable for application as a window layer in silicon (Si) based solar cells. Because of the aptitude of the HWCVD to avail a high density of H radicals, crucial for microcrystalline growth, this deposition technique has been used by many groups to produce microcrystalline SiC films at low temperature of the substrate below 400 °C using monomethyl-silane (MMS) [1-4]. In this study we employed a $SiH_4/CH_4/H_2$ mixture to grow amorphous and nanocrystalline SiC by HWCVD at a low substrate temperature of 260°C. Thermal annealing of the films led to a fully crystalline SiC phase. We monitor these changes using FTIR and AFM analytical techniques.

2. Experimental details

The samples used in this study were deposited onto Corning glass and c-Si (100) substrates kept at 260 ºC; a tungsten filament temperature of 2000 ºC and a process pressure of 7.5 Pa were used in a commercial HWCVD system described elsewhere [5]. All samples were processed for a period of 40 minutes in order to achieve a thickness of less than 1μm. The thickness of the deposited layer was measured by a Veeco Dektak profilometer using the procedure described in [6]. Table 1 summarizes the deposition conditions. In order to study the re-organization and thermal crystallization, the samples were annealed at 700°C, 900°C and 1100°C for 60 minutes under vacuum conditions. FTIR absorption measurements were performed using a PerkinElmer Spectrum 100 spectrometer in the range between

400 and 4000 cm^{-1}. The surface morphology of the films were investigated using a non-contact atomic force microscope (AFM) using a nanoscope instrument from Veeco Metrology Group. The TEM investigation was carried out by a TECNAI F20 (S)TEM instrument equipped with EDX (Energy Dispersive X-ray Spectroscopy) and EELS (Electron Energy Loss Spectroscopy).

Table 1. Deposition conditions of the samples used in this study.

Sample	$F(SiH_4)$ (sccm)	$F(CH_4)$ (sccm)	$F(H_2)$ (sccm)	Thickness (nm)
S_1	1.5	6	25.3	450
S_2	1.5	6	5	580

3. Results

3.1. Structural properties

Figure 1 shows the FTIR spectra of the samples as deposited on c-Si substrate and of those annealed under vacuum at different temperatures. The spectra of the as-deposited samples (top graphs figure 1(a) and figure1 (b)) show the characteristic features corresponding to $(SiH_2)_n$ rocking / wagging at 630 cm^{-1} [7] in both samples S_1 and S_2; this peak is more pronounced in S_2 that has been deposited with a much smaller partial flow rate of hydrogen in the gas mixture. Additional features of SiH_n are observed in the sample S_2 at ~830 cm^{-1} and 930 cm^{-1} that have been assigned to SiH_2 and SiH_3 bending modes respectively [7]. Both spectra show also a sharp absorption peak due to SiC stretching bonds at 670 cm^{-1} and a broad band that extends from 960 cm^{-1} to 1100 cm^{-1} due to CH_n wagging/bending modes for the lower wavenumbers below 1050 cm^{-1} and to the asymmetric Si-O-Si stretching vibration or Si-O-C stretching modes for the higher wavenumbers above 1050 cm^{-1} [8-10]. Again additional absorption bands observed in the S_2 spectrum provides more insight into the SiC bonding: Well defined absorption bands were observed at 765 cm^{-1} and 800 cm^{-1}, they are assigned to $SiCH_3$ stretching /wagging mode [11] and ordered Si-C crystalline phase [2] respectively. Moreover the absorption band from 960 cm^{-1} to 1100 cm^{-1} show much better distinguishable CH_n and oxidation corresponding components. The three subsequent graphs in fig. 1(a) and fig. 2(b) display the spectra of the samples annealed at 700°C, 900°C and 1100°C. The main observation drawn from the spectra of the annealed samples at 700°C is a complete disappearance of the SiH_n related vibration bands in S_1 and a sharp decrease in their intensity in S_2.The main feature observed on the spectra of the annealed samples at 900°C is a re-crystallization into SiC phase as shown by the emergence of the SiC signal at 800 cm^{-1} wavenumber but the CH_n component just above 960°C is still visible. The bottom graphs in figure 1(a) and figure 1(b) of the samples annealed at 1100°C display the only remaining vibration band centred around 800°C with a superimposed shoulder above 840 cm^{-1} wavenumber concomitant with the disappearance of the CH_n vibration component above 960 cm^{-1}.

Figure 2 gives the AFM images of the as-deposited films and of those annealed. The images of both as- deposited films show as smooth surface with clear dispersed crystals; these are mainly Si polycrystals (as it has been revealed by the EDX investigation in STEM mode). The AFM images of the samples annealed at 700°C show distorted elongated grains; at this temperature the cracking of the SiH_n and the effusion of the released hydrogen are complete. The images of the samples annealed at 900°C reveal an increased density of the crystallites with conical shape while at 1100°C temperature of anneal, the AFM images of both studied samples show a microstructure characterized by a coalescence of the small grains in large clusters. Table 2 gives a summary of the average roughness and grains/clusters diameter calculated from AFM data.

Figure 3(a) displays a typical cross-section TEM image of the films as taken from the as-deposited S_2 sample; a crystalline columnar growth mainly perpendicular to the c-Si substrate is observed. This feature is similar to that obtained in microcrystalline Si (μc-Si:H) films with high crystalline volume

fraction [12]. The crystalline columns are built from smaller crystalline grains of a few tens of nanometers in size; in low crystalline material the column structure is less developed and individual small features are normally observed [13]. The EDX spectrum profile collected over a line scan in STEM mode of the same sample (see figure 3(b)) shows a much more dominant peak of Si compared to that of C; this result indicates that the observed SiC phase is embedded in a μc-Si:H matrix.

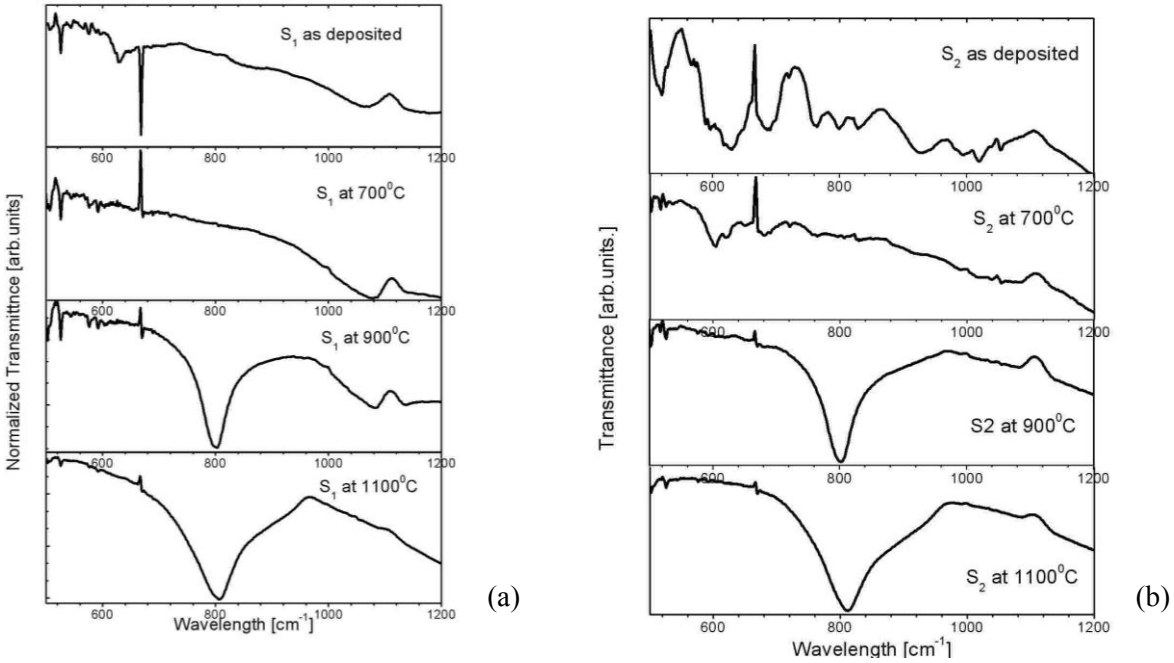

Figure 1. FTIR spectra of as- deposited and annealed samples (a) sample S_1 (b) sample S_2

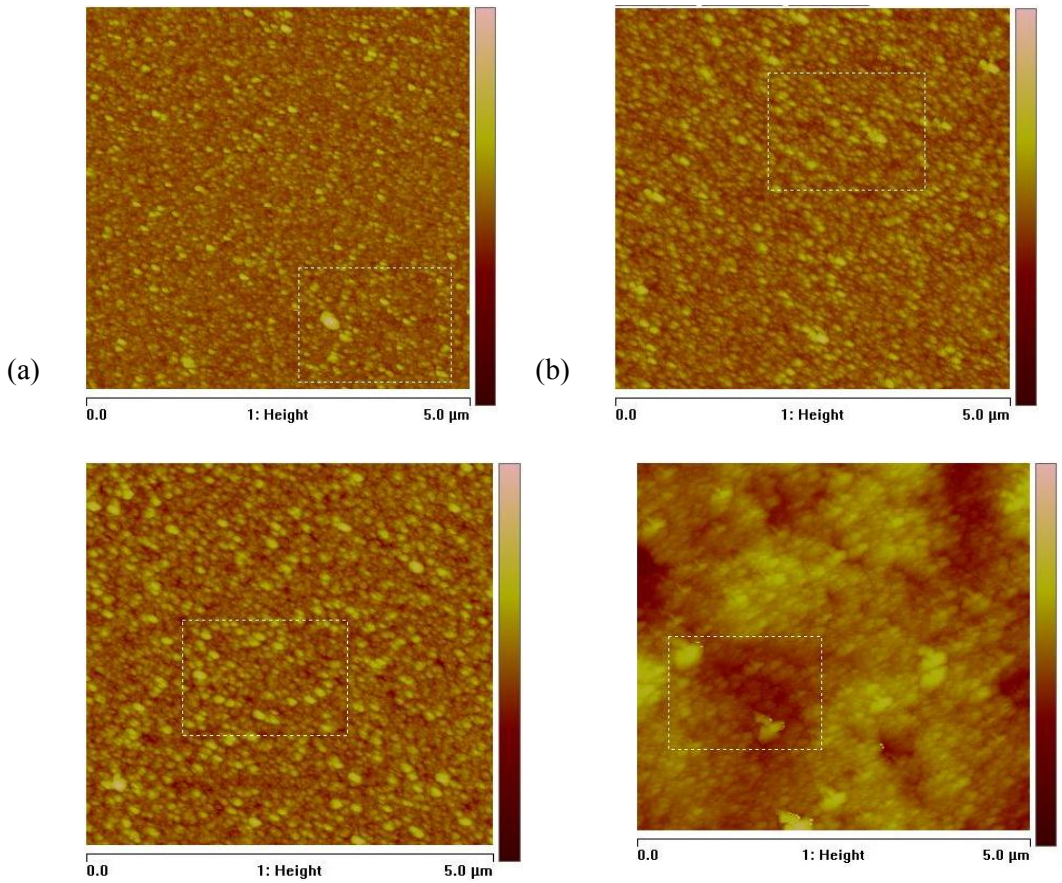

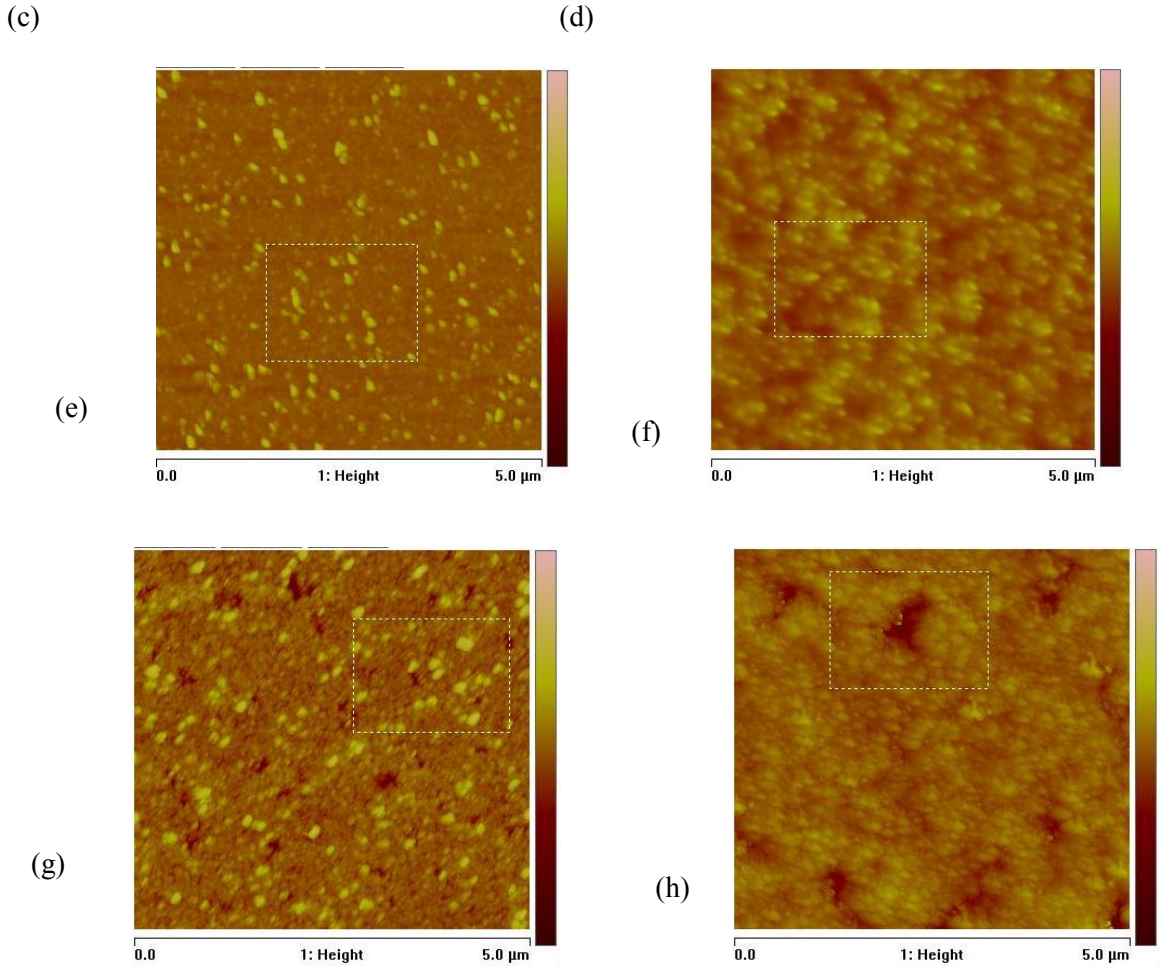

Figure 2. AFM images of the samples as-deposited and annealed: (a) S_1 as deposited, (b)-(d) S_1 annealed at 700°C, 900°C and 1100°C respectively; (e) S_2 as deposited, (f)-(h) S_2 annealed at 700°C, 900°C and 1100°C respectively.

Table 2. Average roughness and crystals/clusters diameter.

Sample		As-depo	700°C	900°C	1100°C
S1	Roughness (nm)	4.83	5.27	6.19	21.10
	Diameter (µm)	0.15	0.14	0.22	0.34
S2	Roughness (nm)	3.27	4.18	5.64	13.30
	Diameter (µm)	0.14	0.13	0.16	0.30

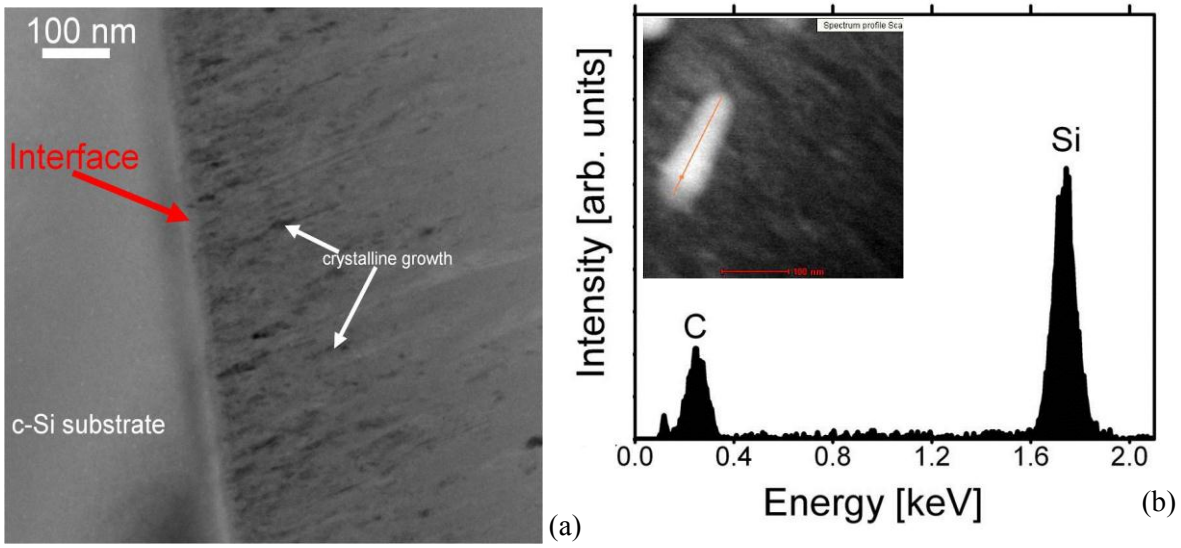

Figure 3. (a) TEM cross-section image of a specimen prepared from sample S_2 as-deposited.(b) EDX spectrum taken at one of the points of the line scan indicated on the STEM micrograph in the insert.

3.2. Discussion

The microstructure of thermally induced μc-SiC:H was extensively investigated by FTIR, AFM and TEM. The films are grown either as amorphous (S_1) or nanocrystalline SiC:H (S_2). The annealing treatment of the samples causes first the cracking of the Si_H_n molecules whose absorption bands in FTIR are observed to decrease in intensity and vanish at 700°C annealing temperature. At this stage, following the effusion of hydrogen from the samples, a rearrangement of the network is observed on the AFM image that shows rather distorted crystal grains. On the sample annealed at 900°C, a quasi-symmetrical absorption band due to crystalline SiC phase coexists with a signature of the remaining C-H_n bonds around 1000 cm^{-1}. A much more interesting fact though is observed at the annealing temperature of 1100°C where a shoulder is appearing on the 800 cm^{-1} SiC vibration peak around 850 cm^{-1} wavenumber while the 1000 cm^{-1} CH_n vibration band is simultaneously disappearing. The resultant band is only well fitted by 2 Gaussian peaks centred at 770 cm^{-1} and 856 cm^{-1} as well as a Lorentzian centred at 800 cm^{-1}. While the first Gaussian at 770 cm^{-1} and the Lorentzian at 800 cm^{-1} along with another SiH related Gaussian peak at 830cm^{-1} – 850cm^{-1} have been widely reported in as-deposited SiC materials [2, 14-15], to our knowledge this broad Gausian peak observed at high wavenumber in annealed samples has not been reported previously. Given the nature of its wide width, it signifies a broad distribution of SiC bond lengths and bond angles in the network. We propose thus that it should be included in the estimation of the SiC crystalline volume fraction (f_{SiC}) in the films; f_{SiC} should be given by

$$f_{SiC} = \frac{A_{800}}{A_{770} + A_{800} + A_{856}} \quad (1)$$

where A_{770}, A_{800} and A_{856} are the areas under the deconvoluted peaks centred at 770 cm^{-1}, 800 cm^{-1} and 856 cm^{-1} respectively. Applied to the annealed films at 1100°C, the method returns f_{SiC} values equal to 43.8 % and 48.3 % for S_1 and S_2 samples respectively.

4. Conclusion

a-SiC:H and nc-SiC:H have been prepared by the HWCVD process using a $SiH_4/CH_4/H_2$ mixture at low temperature of the substrate. The samples have been subjected to a vacuum annealing up to 1100°C. The structural properties of the films are studied by FTIR, AFM and TEM. It is shown that the SiH_n related peaks are the first to disappear at the annealing temperature of 700°C while those associated to CH_n crack completely only above 900°C. The resulting material at the last annealing temperature of 1100 °C shows a unique vibration signature corresponding to crystalline SiC, as detected by FTIR at 800 cm^{-1} wavenumber. This peak can be deconvoluted into two broad disorder-related Gaussian components at 770 cm^{-1} and 856 cm^{-1}, and a narrow Lorentzian peak that signifies the presence of SiC ordered phase.

Acknowledgements

The authors wish to thank the National Research Foundation (NRF) for funding the main author's research project, the Chemistry department at UWC and iThemba LABS for FTIR and AFM measurements respectively.

References

[1] Finger F, Astakhov O, Bronger T, Carius R, Chen T, Dasgupta A, Gordijn A, Houben L, Huang Y, Klein S, Luysberg M, Wang H and Xiao L 2009 *Thin Solid Films* **517** 3507
[2] Chen T, Köhler F, Heidt A, Huang Y, Finger F and Carius R 2011 *Thin Solid Films* **519** 4511
[3] Miyajima S, Haga K, Yamada A and Konagai M 2006 *Jpn. J. Appl. Phys.* **45** 432
[4] Kunii T, Honda T, Yoshida N and Nonomura S 2006 *J. Non-Cryst. Solids* **352** 1196
[5] Halindintwali S, Knoesen D, Swanepoel R, Julies B A, Arendse C, Muller T, Theron C C, Gordijn A, Bronsveld P C P, Rath J K and Schropp R E I 2007 *Thin Solid Films* **515** 8040
[6] Halindintwali S, Knoesen D, Swanepoel R, Julies B A, Arendse C, Muller T, Theron C C, Gordijn A, Bronsveld P C P, Rath J K and Schropp R E I 2009 *South Afric. J. Sci.* **105** 290
[7] Lau W S 1999 *Infrared Characterization of Microelectronics* World Scientific (Singapore)
[8] Zhang S, Pereira L, Hu Z, Ranieiro L, Fortonato E, Ferrira I and Martins R 2006 *J. Non Cryst. Solids* **352** 1410
[9] Waman V S, Kamble M M, Pramod M R, Gore S P, Funde A M, Hawaldar R R, Amalnerkar D P, Sathe V G, Gosavi S W and Jadkar S R 2011 *J. Non Cryst. Solids* **357** 3616
[10] Swain B P 2006 *Materials letters* **60** 2767
[11] Swain P B and Dusane O R 2006 *Materials Chemistry and Physics* **99** 240
[12] Finger F 2010 *Thin-Film Silicon Solar Cells* EPFL Press (Switzeland) 97-143
[13] Houben L, Luysberg M, Hapke P, Carius R, Finger F and Wagner H 1998 Philos. Mag. A **77** 1447
[14] Chen T, Yang D R, Carius R and Finger F 2010 *Jpn. J. Appl. Phys*. **49/4**
[15] Kerdiles S and Rizk R 2002 Philos. Mag. A Phys. Condens. Matter Struct. Defects Mech. Prop. **82/3** 601

Structural and luminescent properties of ZnO flower-like nanostructures synthesized using the chemical bath deposition method

LF Koao[1], FB Dejene[1*] and HC Swart[2]

[1]Department of Physics, University of the Free State (Qwaqwa Campus), Private Bag X13, Phuthaditjhaba, 9866, South Africa
[2]Department of Physics, University of the Free State, P.O. Box 339, Bloemfontein, 9300, South Africa.

*Corresponding author: Tel: +27 58 718 5307; Fax: +27 58 718 5444; E-mail: dejenebf@ufs.ac.za

Abstract. Crystalline zinc oxide (ZnO) flower-like nanostructures were synthesized by the chemical bath deposition (CBD) method. The temperature of the bath was maintained at 80˚C. The effect of different mol% of zinc acetate and different synthesis time on the structure, morphology and optical properties of nanostructures were obtained. The X-ray diffraction (XRD) pattern for the ZnO flower-like nanostructures showed crystalline peaks corresponding to a hexagonal wurtzite ZnO structures. There was no effect on the structure as the mol% of zinc acetate and different synthesis time were varied, respectively. The estimated average grain sizes were found to be 45 nm. It was found that the estimated grain sizes increases with an increase in zinc mol% and synthesis time, respectively. Scanning electron microscopy (SEM) observations showed the presence of flower-like aggregates. In the case where a higher mol% of zinc acetate and reaction time was used in the preparation process, respectively, the nanoflower-like structures were larger in size. The shape however did not change. Transmission electron microscopy (TEM) micrographs of the ZnO powder revealed the formation of ZnO flower-like nanostructures. Energy dispersive X-ray (EDS) analysis showed all expected elements. The ZnO powder revealed good optical properties with high absorptions properties in the UV region. The band gap energies increased slightly with an increase in the molar concentration of the zinc acetate and again in synthesizing time. The estimated band energy gaps are 3.24, 3.26 and 3.27 eV for sample synthesized for 10 minutes, 5 minutes and 1 minute, respectively which were lower than that of bulk ZnO (3.37eV). The luminescence intensity was found to decrease with an increase in the zinc acetate mol% and synthesis time, respectively. There was no effect on luminescence band. The photoluminescence measurements reveal a strong emission peak at around 606 nm.

1. Introduction

Zinc oxide (ZnO) has been intensively studied in the past decade and it is a wide, direct band gap (3.37 eV) semiconductor, which crystallizes in both the cubic and hexagonal form. It is commercially used as a phosphor for cathode ray tubes in flat panel displays [1] and is widely used in photovoltaic devices [2]. ZnO has attracted much attention because of different properties in nano forms in comparison with those of the bulk materials. Size dependence on optical properties of nanocrystalline semiconductors makes them an interesting candidate for phosphor applications [3]. Many methods have been described in the literature for the production of ZnO nanostructures such as laser ablation [4], sol–gel method [5], chemical vapor deposition [6], and combustion method [7]. Some of these synthetic processes require long reaction time, high synthesis and annealing temperatures. To avoid some of these challenges the chemical bath deposition (CBD) method was used, is a simple, cheap and

convenient process to prepare semiconducting materials. The more recent interest in all things 'nano' has provided a boost for CBD, since it is a low temperature, solution (almost always aqueous) technique, crystal size is often very small and it gives better homogeneity. The aim of this paper was to investigate the effect of different preparation parameters (e.g. Synthesis time and mol% of zinc acetate) on the particle size of the ZnO.

2. Experimental

The ZnO powders were prepared by varying the molar concentrations of zinc acetate and holding the amount of thiourea and ammonia constant in the precursor. Ammonia was used as a complexing agent. The different molar concentrations of zinc acetate were dissolved in 60 mL of deionized water. 0.18 M thiourea was dissolved in 500 mL of deionized water and 123.5 mL of ammonia were dissolved in 500 mL of deionized water. Then a magnetic stirrer was used to stir each of the mixtures for overnight at room temperature to ensure homogenous distribution of the solution reagents. An equal volume ratio (1:1:1) was considered for each solution in the following order: 60 mL quantity of zinc acetate was first added to the beaker which was placed in the water bath, followed by addition of 60 mL of thiourea solution and the mixture was stirred for 30 s, following that, 60 mL of ammonia solution was then added slowly in the mixture, while continuously stirring for 5 min. Water bath was maintained to be at a constant desired temperature of 80 ºC. The precipitates were then left overnight and filtered thereafter. After the precipitates were filtered and washed with 50 mL of ethanol. The obtained particles were dried at ambient conditions for several days. After that the powders were ready to be characterized. The particle size and morphology and the structural and luminescent properties of the as-synthesized phosphors were examined by means of scanning electron microscopy (SEM), X-ray diffraction (XRD), Uv-vis spectroscopy and Photoluminescence (PL).

3. Results and Discussion

3.1 Structural analysis and Composition analysis

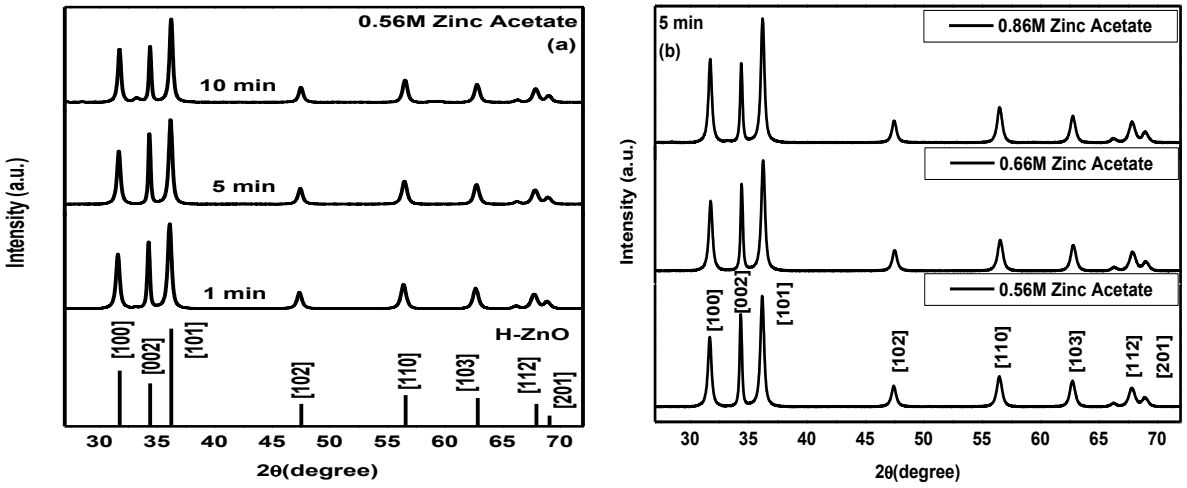

Figure 1. X-ray powder diffraction patterns for ZnO structures prepared at (a) different synthesizing times but constant molar concentrations and (b) different molar concentrations of lead acetate at constant synthesizing time.

Figure 1 (a) shows the XRD patterns of the ZnO nanostructures synthesised at constant mol**%** of zinc acetate of 0.56M but for different synthesizing times. The average estimated values of the cell constants of a and c are 3.257 and 5.215 Å, which matched perfectly with standard data available in

JCPDS card no. (36-1451, a = 3.24982 and c= 5.20661 Å). The XRD results (broad peaks) indicate that the ZnO nanostructures were composed of single hexagonal wurtzite nanocrystallites. No structural dependence on the synthesis time and precursor concentration were observed, figure 1 (a) and (b). The average size of the as-prepared crystals can be estimated from the Full Width Half Maximum (FWHM) of the diffraction peaks using the Debye formula [8]. The average grain sizes was estimated using the XRD spectra are found to be 48, 45 and 42 nm for particles synthesized for 10 minutes, 5 minutes and 1 minute, respectively. In Figure 2 the estimated average grain sizes are plotted for the samples prepared at different molar concentrations of zinc acetate synthesized for 10 minutes and 5 minutes, respectively, it is clear that the estimated average grain size increases with an increase in the zinc acetate concentration.

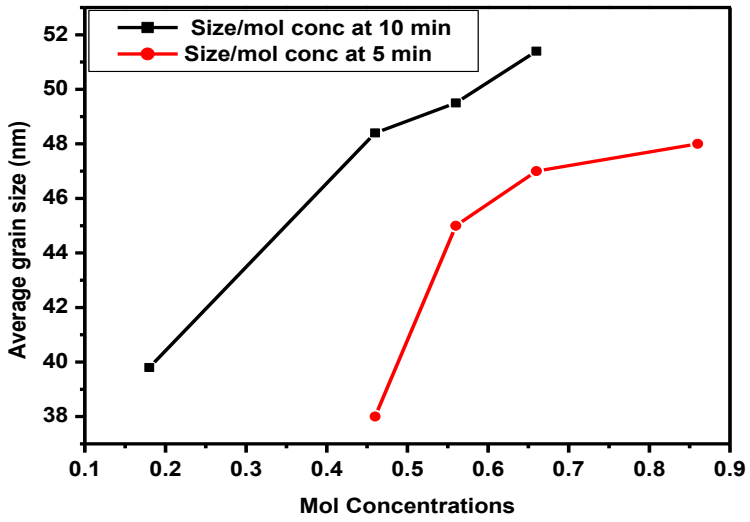

Figure 2. The dependence of average grain sizes of the ZnO on the zinc acetate concentration for different synthesis time.

3.2 Surface morphological analysis

Figure 3 (a) and (b) show SEM images of the as prepared ZnO nanostructures prepared at different molar concentrations of zinc acetate but synthesized at constant time. The surface aspects of all the SEM images are composed of flower-like structures. It is clear that the flower-like structures are clustered with some surrounded by spherical nanoparticles. By comparing the SEM micrographs it is clearly seen that by increasing the molar concentration of zinc acetate there is an increase in the grain sizes.

The TEM micrograph of ZnO synthesized for 5 minutes using 0.56M zinc acetate is shown in figure 4(a). The presences of ZnO flower-like nanostructures are clearly visible in the TEM images. The nanostructures are aggregated. The elemental composition of the ZnO samples were analysed using EDS. From Figure 4 (b) the elemental analysis of the ZnO flower-like nanostructures suggests the existence of Zn and O (from the cores and the outside shell) and C (from the C double sided tape).

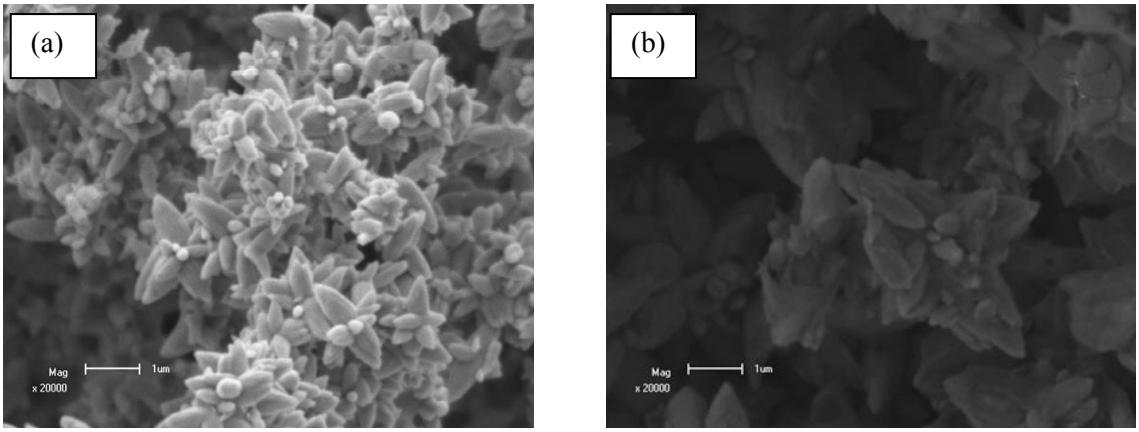

Figure 3. SEM images of ZnO nanostructures for (a) 0.56M and (b) 0.86M zinc acetate concentration synthesized at constant time.

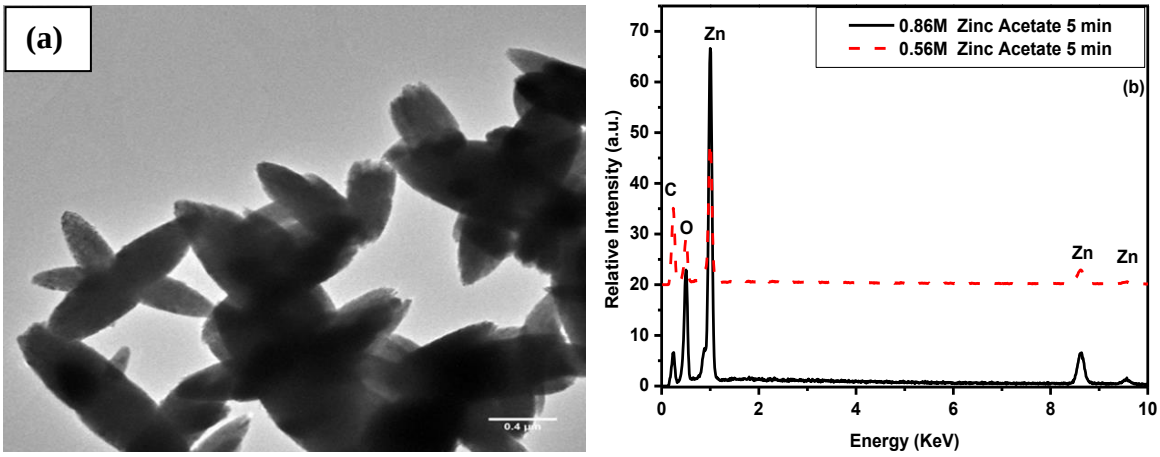

Figure 4. (a) and (b) representative TEM and EDS spectra of the ZnO nanoflower-like structures prepared at different molar concentration of zinc acetate for a constant time of 5 min.

3.3 Optical properties

The absorption spectra exhibit a shoulder peaks at around 333 nm for sample synthesized for 1 minute and 348 nm for samples synthesized for 5 and 10 minutes, respectively, which are attributed to the exitonic absorption corresponding to 3.5 eV [9], figure 5. By increasing the synthesizing time the absorption peak shoulders shift slightly to higher wavelengths. This shift from 333 to 348 nm may be due to the particles sizes that were decreasing as the synthesizing time decreases [10]. The absorption edges were not affected by the synthesizing time. This may be due to the morphology which was homogeneous. The ZnO is a direct bandgap material. The energy band gaps of these materials were estimated using the Tauc relation [11],

$$\alpha=(\boldsymbol{h\nu}-E_g)^n \qquad (1)$$

where α is the absorption coefficient, $\boldsymbol{h\nu}$ is the photon energy, E_g is the band gap n=2 for direct transitions. The energy band gaps were measured with the help of absorption spectra plotting graphs of $(\alpha\boldsymbol{h\nu})^2$ versus $\boldsymbol{h\nu}$, and the corresponding band gaps obtained from extrapolating the straight portion of the graph on the $\boldsymbol{h\nu}$ axis at α= 0. All the calculated band gap energies were below the theoretical band gap value of 3.37 eV.

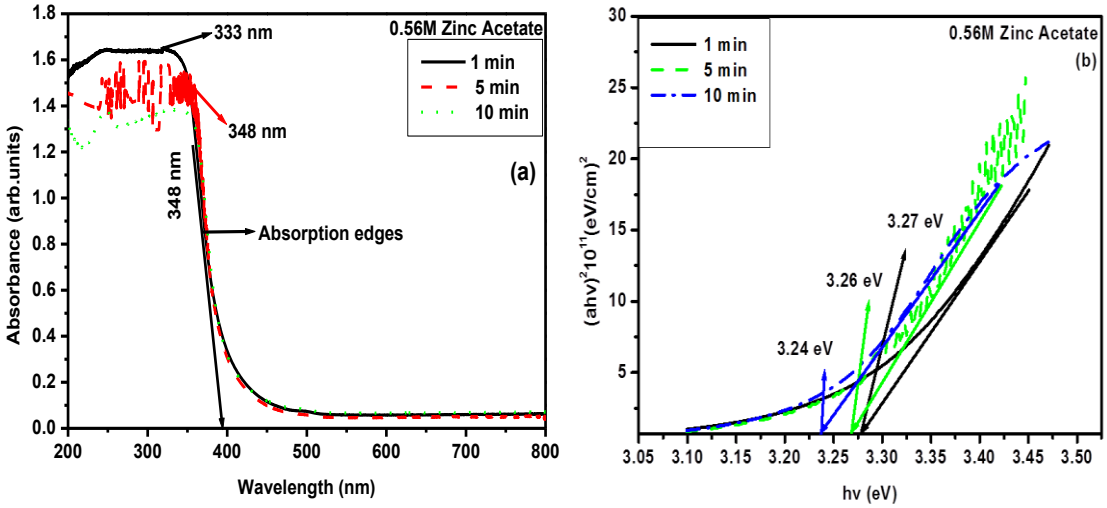

Figure 5. The absorbance spectra (a) and the band gap energy (b) of ZnO structures prepared at different synthesizing times and at constant zinc acetate concentration.

This may be due to the particle sizes which are bigger than the exciton bohr radius of ZnO [12]. From figure 5 (b) it is clear that the band gap energy of ZnO structures decreases slightly (band gap energy do not change a lot) with an increase in synthesizing time. Even as the molar concentration of zinc acetate increased the band gap energy slightly increased which is not shown here. This decrease in band gap energy is in accordance with the particle size that is increasing as the synthesizing time increased as confirmed by SEM and XRD results.

3.4 Photoluminescence

The photoluminescence (PL) measurement of the ZnO nanoflower-like structure was carried out at room temperature with 325 nm excitation. Figure 6(a) shows strong and broad emission spectrums, which are mainly located in the orange region with its maximum luminescence intensity at around 606 nm. It has been suggested that the orange band emission correspond to the oxygen interstitials, showing excess of oxygen in the ZnO nanoflower-like [13]. Comparing the three patterns, the maximum luminescence intensity is reached at the ZnO synthesized for 5 minutes, by increasing the synthesizing time further the luminescence intensity decreases. Even as the molar concentration of zinc acetate increases the luminescence intensity decreases as shown in figure 6(b). This decrease in luminescence intensity may be due to the increase in particle size as confirmed by the XRD. There was no shift in the luminescence band of ZnO flower-like nanostructures for samples prepared at different synthesizing times and constant molar concentration of zinc acetate; this may be due to the uniform particle sizes as observed with the SEM.

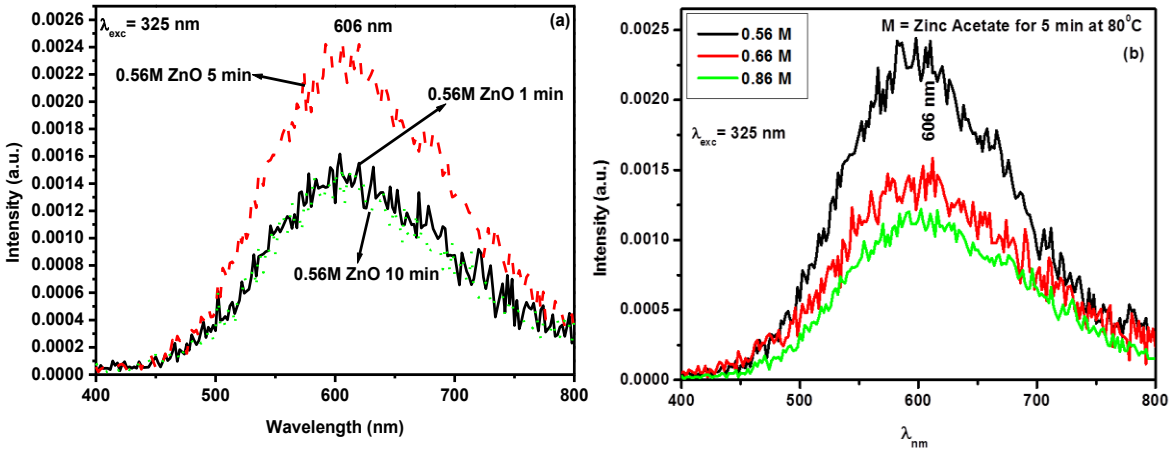

Figure 6. The PL spectra of ZnO nanostructures, prepared at (a) different synthesizing times but synthesized at constant molar concentration of zinc acetate and (b) fits to the 5 min sample luminescence spectra of ZnO nanoflower-like prepared by the CBD method.

4. Conclusion

The ZnO nanostructures have been successfully synthesized by the chemical bath deposition technique at 80°C. XRD showed that the structure of the material obtained is hexagonal wurtzite ZnO. UV spectroscopy showed that the band gap energy of the ZnO nanoflower-like decreased with an increase in the synthesizing time. PL showed that the emission intensity of the nanostructures depends on the synthesizing time and the molar concentration of the zinc acetate.

Acknowledgement

The author would like to acknowledge the National Research Foundation and Department of science and technology and the University of the Free State for financial support.

Reference

[1] Prevenslik T V 2000 *J. Lumin.* **1210** 87-89
[2] Ghosh P K, Mitra M K and Chattopadhyay K K, 2005 *Nanotech.* **16** 107–112
[3] Ntwaeabora O M, Kroon R E, Kumar V, Ahn J-P, Park J-K and Swart H C 2009 *J. of Phys and Chem of solids* **70** 1438-1442
[4] Scarisoreanu N, Metai D G, Dinescu G, Epurescu G, Ghica C, Nistor L C, Dinescu M, 2005 *Appl. Surf. Sci.* **247** 518–525
[5] Ristiac M, Musiac S, Ivanda M, Popoviac S, 2005 *J. Alloys Compd*. **397** L1–L4
[6] Wu J J, Liu S C, 2002 *Adv. Mater*. **14** 215–218
[7] Lamas D G, Lascalea G E, Walsoc N E 1998 *J. Eur. Ceram. Soc.* **18** 1217–1221
[8] Cullity B D1978, 1956*Elements of X-ray Diffraction (2nd Ed)*, (Addison Wesley) 285-284
[9] Valle G G, Hammer P, Pulcinelli S H and Santilli C V 2004 *J. of the European Ceramic Society* **24** 1009-1013
[10] Wang Y and Herron N, 1991 *J. Phys. Chem.* **95** 525-532
[11] Sharma T P, Patidar D, Saxen N S and Sharma K 2006 *Indian J Pure and Appl. Phys*. **44** 125-128
[12] Gu Y, Igor L, Igor L K, Yin M, O'Brien S and Neumark G F, 2004 *App. Phys. Lett.* 85 3833-3835
[13] Ong H C, and Du G T, 2004 *J. Cryst. Growth* **265** 471

The characterization of MnO nanostructures synthesized using the chemical bath deposition method

LF Koao[1], F B Dejene[1*] and HC Swart[2]

[1]Department of Physics, University of the Free State (Qwaqwa Campus), Private Bag X13, Phuthaditjhaba, 9866, South Africa
[2]Department of Physics, University of the Free State, P.O. Box 339, Bloemfontein, 9300, South Africa.

*Corresponding author: Tel: +27 58 718 5307; Fax: +27 58 718 5444; E-mail: dejenebf@ufs.ac.za

Abstract. Manganese oxide (MnO) nanoparticles were synthesized by the chemical bath deposition method. The pH of the solution was varied during the deposition process to determine the effect thereof. The temperature of the bath was maintained at 80^0C. The final yields were characterized for structural, morphology and luminescence properties. The X-ray diffraction spectrum of the MnO nanoparticles was monoclinic. The particle size was found to be dependent on the pH. Scanning electron microscopy micrographs depict irregular nanoparticles at low pH and flakes-like nanoparticles structures at a higher pH. Fourier transformed infrared spectroscopy analyses confirmed these MnO compositions. Photoluminescence spectra indicated that the nanoparticles product had emission peaks at 364, 381, 415 and 452 nm. The sample which was obtained at a pH of 9.01 has the broadest luminescent peak.

1. Introduction

It is well known that the synthesis of semiconductors nanostructures has attracted much attention in materials science for several years. Nanostructures can be used in microelectronic, electronic, optical and magnetic devices [1-2]. Manganese oxide (MnO) is also of interest due to its wide band gap (7.8 eV). It is semiconductor that can be used as optical window in optoelectronic devices and luminescent materials [3]. MnO nanostructure can easily be incorporated into polymer, glassy matrices where they can be applicable in fiber optics telecommunication [4] and the structures can also be incorporated in semiconductor nanoparticles (e.g. ZnO and ZnS) where they can be applied in light emitting diodes, laser diodes and ultraviolet photodetectors [4]. The optical property of the materials is related to its size and morphology, which encourage us to synthesize nanostructured MnO. The chemical bath deposition (CBD) is a simple, cheap and convenient process to prepare semiconducting materials. The more recent interest in all things 'nano' has also provided a boost for CBD, since it is a low temperature, solution (almost always aqueous) technique, crystal size is often very small. The aim of this paper is to investigate the effect of pH on the material properties of MnO.

2. Experimental

The MnO nanostructures were synthesized using the CBD process by varying the pH of the solution. The chemicals used for the preparation of the nano-powders were of analytical grade, which includes manganese acetate (Mn $(CH_3COO)_2.4H_2O$), Thiourea ($(NH_2)_2CS$) and Ammonia (25% NH_3). During the preparation of the nano-powders, the ammonia solution was used as a complexing agent. The temperature of the bath was kept constant at 80^oC. The precipitates were filtered and washed with ethanol and later dried at ambient conditions for several days. The particle size and morphology and the structural and luminescent properties of the as-synthesized phosphors were examined by means of

scanning electron microscopy (SEM), X-ray diffraction (XRD), Fourier transformed infrared spectroscopy (FTIR), X-ray photoelectron spectrometry (XPS) and Photoluminescence (PL).

3. Results and Discussion

3.1 Structural analysis and Composition analysis

The X-ray diffraction patterns of the MnO samples prepared at fixed manganese acetate to thiourea mole ratio of 1:1 but at different pH are shown in figure 1. All diffraction peaks at low pH of 7.73 could be indexed to the monoclinic MnO structure (JCPDS Number 39-1218). No characteristic peaks of any other impurities such as $Mn(OH)_2$ or precursors used are observed, indicating the formation of a pure phase of MnO. Further increase in pH to 9.01 does not affect the structure of the MnO phase. The broadness of the diffraction peaks indicates the presence of nanocrystallites in the MnO structures.

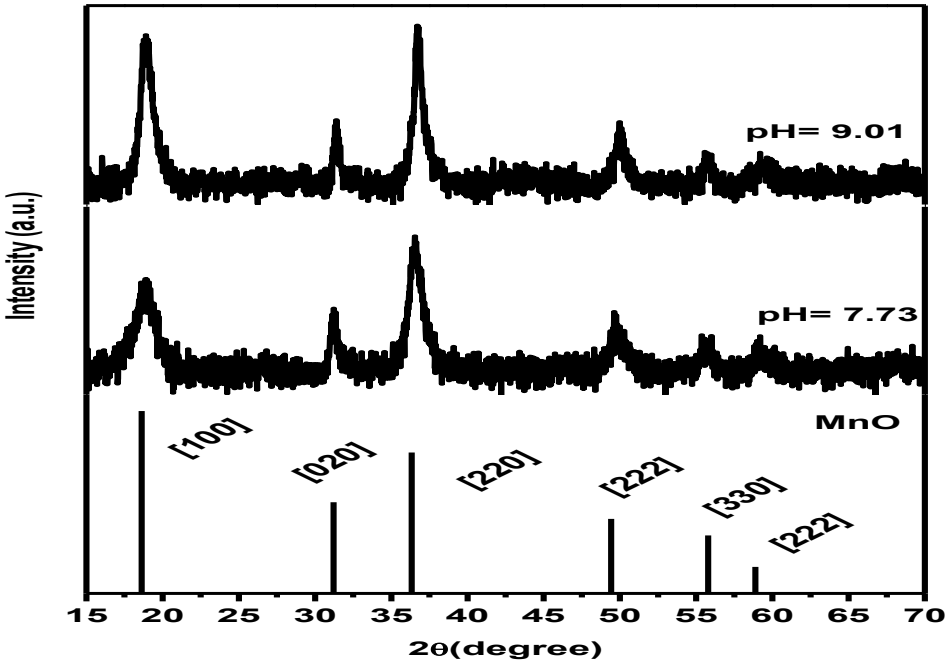

Figure 1. X-ray powder diffraction patterns for MnO prepared at different pH values.

The average size of the as-prepared nanocrystals can be calculated from the Full Width Half Maximum (FWHM) of the diffraction peaks using the Debye-Scherrer formula [5]. All major diffraction peaks for all samples are chosen to estimate the average size of the nanocrystals by the least square method. The estimated particle sizes were 28 and 44 nm for pH of 7.7 and 9.01, respectively. It is clear that the average particle size increased as the pH increased. The sizes of the products were found to be affected by the precursor concentration and synthesis time.

3.2 Surface morphological analysis

SEM micrographs of MnO prepared at low (7.74) and high (9.01) pH shown in figure 2, depict that the powders consisted out of agglomerated fluffy (flake-like) particles which contained nanocrystalites according to the XRD spectra. In comparing the SEM micrographs it is clear that at the high pH value the nanostructures are less agglomerated. The flakes-like appearance is more pronounced at the high pH value.

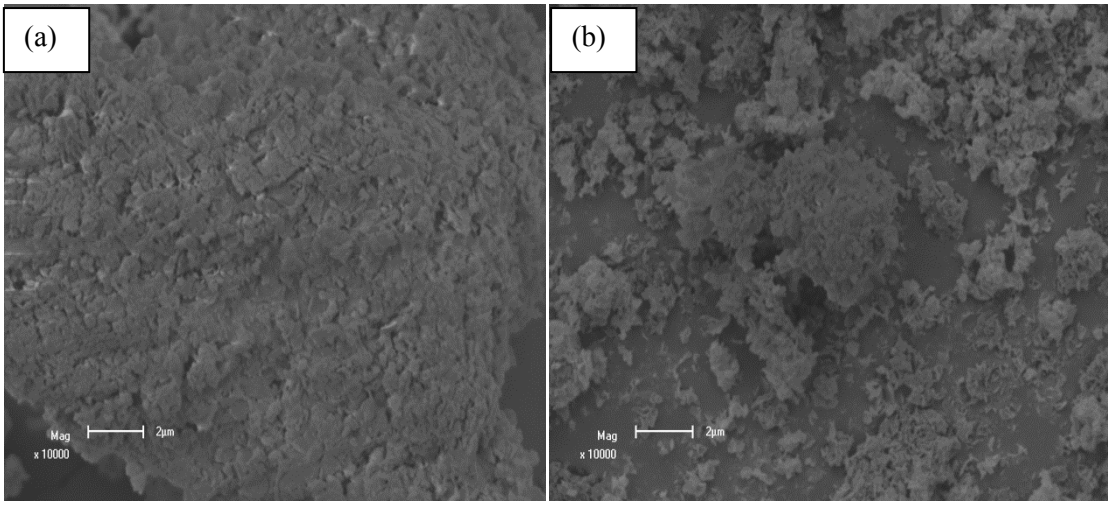

Figure 2. SEM images of MnO nanostructures as synthesized at pH values of (a) 7.74 and (b) 9.01.

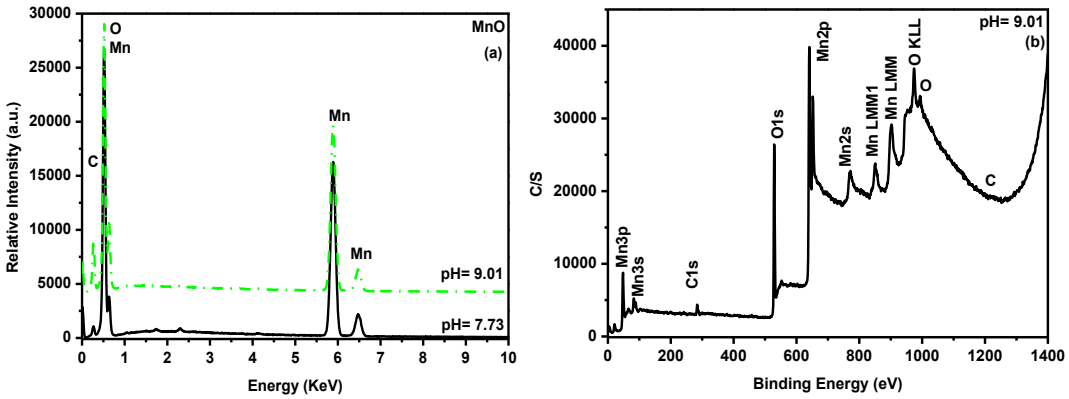

Figure 3. Representative (a) EDX and (b) XPS spectra of the MnO nanocrystals prepared at different pH values.

The elemental analysis and purity of the MnO samples were analysed using EDS and XPS. The EDS spectra in Figure 3(a) show the presence of Mn and O for all the samples. The pH does not have significant effect on the EDS spectra. The existence of C (carbon) is originating from the double sided carbon tape. The stub (sample holder) was covered with double sided carbon tape so that the powder samples can easily be adhered to avoid the sample from falling. XPS results in figure 3(b) shows the survey spectrum of the MnO nanoflakes-like structures prepared at a pH solution of 9.01. Mn, O and C were present. The peaks located at 47, 77, 642, 768, 849 and 902 eV are assigned to the binding energies of Mn_{3p}, Mn_{3s}, Mn_{2p}, Mn_{2s}, Mn_{LMM1} and Mn_{LMM}, respectively; and those at 530 and 973 eV are ascribed to the binding energies of O_{1s} and O_{KLL}. All of the observed binding energy values for Mn and O are consistent with the data reported in the literature [6]. The existence of C impurity in the XPS results is believed to have originated from the surface contamination in the atmosphere and the C tape. Both EDS and XPS measurements indicate that MnO nanostructures obtained were pure.

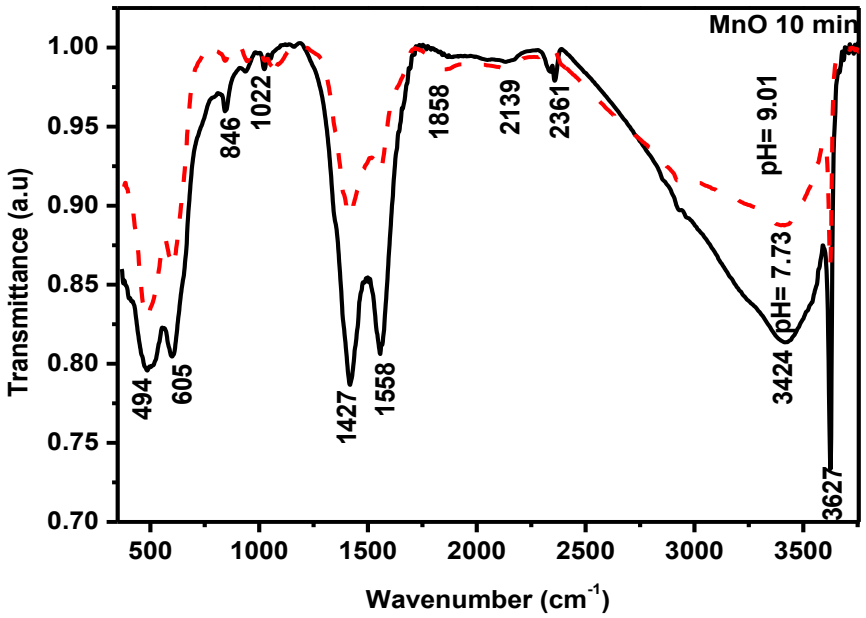

Figure 4. Representative FTIR spectra of the MnO nanocrystals prepared at different pH values.

Figure 4 represents the FTIR spectra recorded for the MnO nanostructures in the range of 350 cm^{-1} to 4500 cm^{-1}. IR spectral analyses allowed us to investigate the bonding type and further elucidate the identity of the products. MnO has been reported to display a single peak at around 626 with a broad peak between 400-600cm^{-1} [7]. The broad absorption peaks at 3424 and 1427 cm^{-1} are attributed to the stretching and bending vibration of hydroxyl, respectively [8]. The narrow band at around 3627 cm^{-1} is assigned to the symmetric –OH. The peaks at around 494 and 605 cm^{-1} are due to the Mn-O lattice vibrations [9]. The peaks at around 1858 and 2139 cm^{-1} are due to the C-C and C-CH_3 stretching modes. The peaks at around 1036 and 1558 cm^{-1} are assigned to the symmetrical C-N or N-CH_3. From the FTIR analysis it can observed that by increasing the pH of the solution reduces the amount of material absorbed for all the peaks appearing in the spectrum.

3.3 Photoluminescence

Figure 5(a) shows the PL spectra of the samples when excited at a 330 nm wavelength. At low pH (7.73), the emission spectrums depict a strong broad peak at around 376 nm. At high pH the PL spectra shows two peaks at around 376 and 420 nm. These emissions are associated with the transitions occurring within localized states in nanocrystalline structures [8]. The increase in broadness of the luminescence peak with an increase in the pH may be attributed to the increase in particle size, secondly it may be due to non-aggregated nanoflakes-like as confirmed by SEM and lastly may be due to the improvement of the crystallinity as the pH increased. The highest luminescence intensity is obtained at pH of 8.74. As shown in Figure 5(b), the Gaussian-multi curve fits of the broad peak with peaks at around 376 and 420 nm (red fit) and other peaks such as 373 (magenta fit) and 420 nm (blue fit) fits very well with the experimental curve of the MnO nanoflakes at pH solution of 9.01. These emissions may be ascribed to a high level transition in MnO semiconductors crystallites.

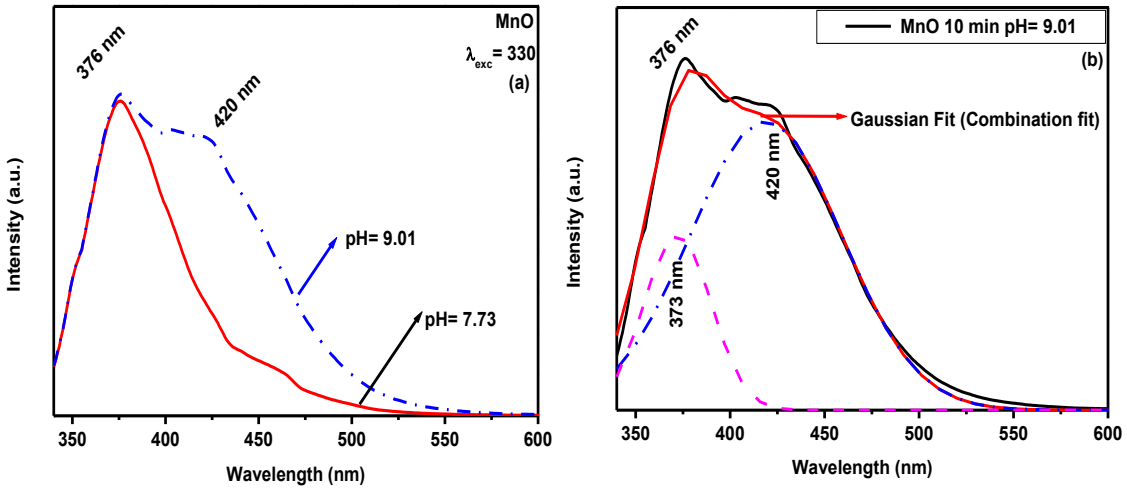

Figure 5. The PL spectra of MnO nanostructures prepared at (a) different pH and (b) a Gaussian fit of the 9.01 PL spectrum of the MnO nanoflakes-like prepared by the CBD method.

4. Conclusion

The MnO nanostructures have been successfully synthesized by the chemical bath deposition technique at 80°C. XRD showed that the structure of material is a monoclinic phase. EDS, XPS and FTIR confirmed the presence of the MnO nanostructures. PL showed that the emission spectra of the nanostructures depend on the pH. It was observed that the luminescence band become broad as the pH increased.

Acknowledgement

The author would like to acknowledge the National Research Foundation and Department of Science and Technology and the University of the Free State for financial support. We are also grateful to people currently of Centre for Microscopy at UFS for EDS, SEM, XPS, PL and X-ray diffraction measurements.

Reference

[1] Hu J, Odom T W and Lieber C M 1999 *Acc. Chem. Res.* **32** 435-455
[2] Dekker C, 1999 *Phys. Today* **52** 22-28
[3] Bredow T and Gerson R 2000 *Phys. Rev. B*. **61** 5194-5201
[4]Ntwaeabora O M, Kroon R E, Kumar V, Ahn J-P, Park J-K and Swart H C 2009 *J. of Phys and Chem of Solids* **70** 1438-1442.
[5] Cullity B D1978, *1956 Elements of X-ray Diffraction (2nd Ed), (Addison Wesley)* 285-284.
[6] Wagner C D, Riggs W M, Davis L E, Moulder J F and Muilenberg G E, 1979 *Handbook of X-ray photoemission spectroscopy, Perkin Elmer Corp. Publishers*,(Eden Prairie MN), 74-75.
[7] Shen X M and Clearfield J 1986 *J. Solid State Chem*. **64** 270-282
[8] Xiang X, Cheng X F, He S B, Yuan X D, Zheng W G, Li Z J, Liu C M, Zhou W L and Zu X T 2011 *Chin. Phys. B.* **20** 127801-2 to 127801-4
[9] Liping K, Menming Z, Zong-Huai L and Kenta O 2007 *Spectrochimica Acta Part A* **67** 864–869

Clebsch-Gordan coefficients for scattering tensors in Bi_2Se_3

A. G. J. Machatine[1], H. W. Kunert[1], P. Niyongabo[1], M. Govender[1, 2], and B. W. Mwakikunga[2]

[1]Department of Physics, University of Pretoria, Pretoria 0002, South Africa
[2]DST/CSIR National Centre for Nano-Structured Materials, P. O. Box 395, Pretoria 0001, South Africa

E-mail: Augusto.Machatine@up.ac.za

Abstract. The analysis of Raman and Brillouin scattering spectra requires the knowledge of scattering tensors. Based on Birman's method, we compute the Clebsch-Gordan coefficients for first-order Raman and Brillouin scattering for Bi_2Se_3 with D_{3d}^5 space group symmetry. The linear combination of Clebsch-Gordan coefficients gives the matrix elements of scattering tensors. Our calculations are useful for interpretation of spectra in Raman and Brillouin scattering measurements.

1. Introduction

The topological insulator Bi_2Se_3 crystallizes into the trigonal space group D_{3d}^5 with five atoms per unit cell. It has a layered structure and an energy gap of 0.3 eV. Topological insulators are new quantum states of matter which are insulating in the bulk, but possess "non-trivial" edge conducting surface states with time-reversal symmetry protected against backscattering [1, 2]. Raman studies were conducted on Bi_2Se_3 nanopallets and showed broadening of peaks [2]. This result and the electron-phonon interactions in the Raman analysis are not well understood. Ab initio calculations of thin films have been performed, and quantum confinement effects were discussed in an attempt to understand the results [3]. It is thus imperative to understand the phonon scattering processes.

Raman and Brillouin spectroscopy are techniques used to understand the nature of the phonons in a sample. In these scattering processes, photons excite the crystal under investigation, causing the quasi-particles such as phonons, polarons, magnons and polaritons to be either created or annihilated, and thereafter reemit photons with a frequency shift. It is well known that the states of particles and quasi-particles in the crystal are classified according to the irreducible representation (irreps) of the space group of a crystal [4].

The Raman scattering involving one-phonon processes are related to the zone centre optical phonons. One-phonon Brillouin scattering arises from the interaction of light with acoustic phonons close the zone centre. Birman et al. [5] and Berenson [6] have shown that the first-order Raman scattering are precisely linear combinations of certain Clebsch-Gordan coefficients (CGC's). They also showed that near the highest symmetry point $\Gamma(\boldsymbol{k}=0)$, the Brillouin tensor is proportional to the strain tensor [7]. In order to calculate the CGC's, we need the generators of matrix representations of the groups. These generators are contained in the Cracknell, Davies, Miller, Love (CDML) tables, along with the

Kronecker product (KP) of symmetrized, anti-symmetrized squares and cubes for the 230 space group irreps [8]. In this paper, we focus on the calculation of the CGC's and construction of first-order Raman and Brillouin scattering tensors.

2. Scattering tensors and Clebsch-Gordan coefficients

In this section we present a summary of CGC's theory that will be used for determination of Raman and Brillouin scattering tensors. The complete theory of CGC's for a crystal space group has been outlined by several authors [7]. Particularly, Kunert et al. [4], Birman [5] and Berenson [6] have calculated the CGC's and scattering tensors for C_{6v}, T_d and O_h point groups, respectively. In this work, we extend our calculation to D_{3d} space symmetry group.

If the incident light has unit polarization vector ε_1 with component $\varepsilon_{1\alpha}$ and the unit polarization vector for the scattered light ε_2 with component $\varepsilon_{2\beta}$ $(\alpha,\beta = x,y,z)$, the intensity of the scattered light is then given as

$$I = C\left|\varepsilon_{2\alpha} P_{\alpha\beta} \varepsilon_{1\beta}\right|^2, \tag{1}$$

where $P_{\alpha\beta}$ is the scattering tensor and C a constant. The scattering tensor operator involved in different processes are expanded in terms of Taylor series with respect to different coordinates. In the next subsection we give the expansion for the Raman scattering tensor and the Brillouin scattering tensor operators.

2.1 Raman scattering tensors

For the Raman scattering process, the operator $P_{\alpha\beta}$ is expanded in terms of the normal coordinate Q_σ^j to give

$$P_{\alpha\beta} = P^{(0)}{}_{\alpha\beta} + \sum P^{(1)}_{\alpha\beta}(R^0; j\sigma) Q^j_\sigma + \sum_{jj'\sigma\sigma'} P^{(2)}_{\alpha\beta}(R^0; j\sigma; j'\sigma') Q^j_\sigma Q^{j'}_{\sigma'} + \ldots. \tag{2}$$

The coefficients of these series correspond to the Raman scattering tensors for various orders. The linear term is the first-order (one-phonon) Raman scattering tensor and the bilinear term is the second-order Raman scattering tensor. Birman et al. showed that coefficients of the expansion are related to the CGC's. The first-order tensor is written as $P^{(1)ii'}_{\alpha\beta} = C(j) U_{\alpha\beta,j\sigma}$ where $C(j)$ is a constant, R^0 the equilibrium ion coordinate in the unit cell, j (Γ_j) is the allowed Raman irrep with degeneracy σ, $i,i' = x,y,z$ and $U_{\alpha\beta,j\sigma}$ is the unitary matrix element (CGC's) [6].

The Raman active modes are contained in the symmetrized squares of the vector representation $(V-\mathrm{rep})$. For D_{3d} space symmetry group, the vector representation is given by

$$V = \Gamma_{2-}(z) \oplus \Gamma_{3-}(x,y), \tag{3}$$

and the symmetrized square is given by

$$[V \otimes V]_2 = [(\Gamma_{2-} \oplus \Gamma_{2-}) \otimes (\Gamma_{3-} \oplus \Gamma_{3-})] = 2\Gamma_{1+} \oplus 2\Gamma_{3+}. \tag{4}$$

The ordinary product $\Gamma_{2-}(z) \otimes \Gamma_{3-}(x,y) = \Gamma_{3+}(zx, zy)$ is not contained in the symmetrized square and therefore does not appear in the Raman scattering tensor. Similar features were observed in ZnO with symmetry C_{6v} [4] when the $V-\mathrm{rep}$ is a direct sum of irreps. The calculated CGC's are tabulated in Table 1.

Table 1. Clebsch-Gordan coefficients for Raman Scattering tensors for D_{3d}^5.

$[\Gamma_{2-} \otimes \Gamma_{2-}]_{(2)} \oplus [\Gamma_{3-} \otimes \Gamma_{3-}]_{(2)} =$	Γ_{1+}	$\oplus$	Γ_{3+}
xx	0	0	0
xy	$1/\sqrt{2}$	0	1
yx	$1/\sqrt{2}$	1	0
yy	0	0	0
zz	1	0	0

The first-order Raman scattering tensors are matrices constructed from Table 1 in the matrix form $\begin{pmatrix} xx & xy & xz \\ yx & yy & yz \\ zx & zy & zz \end{pmatrix}$, and are listed in Table 2.

Table 2. First-order Raman scattering tensors for D_{3d}^5.

$$P_{\alpha\beta}^{(1)}(\Gamma_{1+}) = \begin{pmatrix} 0 & \frac{1}{\sqrt{2}} & 0 \\ \frac{1}{\sqrt{2}} & 0 & 0 \\ 0 & 0 & 0 \end{pmatrix}; \quad P_{\alpha\beta}^{(1)}(\Gamma_{3+}) = \begin{pmatrix} 0 & 1 & 0 \\ 0 & 0 & 0 \\ 0 & 0 & 0 \end{pmatrix}; \quad P_{\alpha\beta}^{(1)}(\Gamma_{3+}) \begin{pmatrix} 0 & 0 & 0 \\ 1 & 0 & 0 \\ 0 & 0 & 0 \end{pmatrix}.$$

In the next subsection, we construct the first-order Brillouin scattering.

2.2 Brillouin scattering

For Brillouin scattering, the operators are expanded in terms of acoustic phonon polarization $\frac{\partial Q_\sigma^j}{\partial \chi_i} = q_i Q_\sigma^j$ with the polarization σ_j and phonon q_i resulting in

$$P_{\alpha\beta} = P^{(0)}{}_{\alpha\beta} + \sum_{i,j} P_{\alpha\beta}^{(1)ij}(R^0; j\sigma) q_i Q_\sigma^j + \frac{1}{2}\sum_{ijj'i'} P_{\alpha\beta}^{(2)iji'j'}(R^0; j\sigma; j'\sigma') q_{1i} q_{2i'} Q_\sigma^j Q_{\sigma'}^{j'} + \ldots, \quad (3)$$

where $P_{\alpha\beta}^{(1)ij}$ is the first order Brillouin scattering tensor. The Raman tensor $P_{\alpha\beta}^{(1)i\sigma} = \sum U^*_{\alpha\beta,i\nu}{}^{[V\otimes V]_2} U^{V\otimes V}_{\sigma i,i\nu} P^{(1)}_{\alpha\beta}$ is the first-order Brillouin tensor, and is a linear combination of the first-order Raman scattering tensor $P_{\alpha\beta}^{(1)}$. The matrix $U^{[V\otimes V]_{(2)}}$ and $U^{[V\otimes V]}$ are the unitary matrices for the symmetrised square and ordinary KP, respectively [9].

Using the obtained first-order Raman scattering tensors, we construct the first-order Brillouin scattering tensor as linear combinations of CGC's from Table 1. As an example, an acoustic phonon incident in the *x*-direction is scattered in in the *y*-direction resulting in a Brillouin tensor $P_{\alpha\beta}^{(1)xy}$. The Brillouin tensors $P_{\alpha\beta}^{(1)xx} = P_{\alpha\beta}^{(1)yy} = 0$ and so

$$P_{\alpha\beta}^{(1)xy} = \frac{A_1}{\sqrt{2}} \begin{pmatrix} 0 & \frac{1}{\sqrt{2}} & 0 \\ \frac{1}{\sqrt{2}} & 0 & 0 \\ 0 & 0 & 0 \end{pmatrix} + B_1 \begin{pmatrix} 0 & 1 & 0 \\ 0 & 0 & 0 \\ 0 & 0 & 0 \end{pmatrix}. \quad (4)$$

The non-zero Brillouin scattering tensors are listed in Table 3 where $A_{1,2,3}$ and $B_{1,2}$ are arbitrary constants subject to measurements.

Table 3. First-order Brillouin Scattering Tensors for D_{3d}^5.

$$P_{\alpha\beta}^{(1)xy} = \frac{A_1}{\sqrt{2}}\begin{pmatrix} 0 & \frac{1}{\sqrt{2}}+\frac{B_1}{A_1}\sqrt{2} & 0 \\ \frac{1}{\sqrt{2}} & 0 & 0 \\ 0 & 0 & 0 \end{pmatrix};\ P_{\alpha\beta}^{(1)yx} = \frac{A_2}{\sqrt{2}}\begin{pmatrix} 0 & \frac{1}{\sqrt{2}} & 0 \\ \frac{1}{\sqrt{2}}+\frac{B_2}{A_2}\sqrt{2} & 0 & 0 \\ 0 & 0 & 0 \end{pmatrix};$$

$$P_{\alpha\beta}^{(1)zz} = A_3\begin{pmatrix} 0 & \frac{1}{\sqrt{2}} & 0 \\ \frac{1}{\sqrt{2}} & 0 & 0 \\ 0 & 0 & 0 \end{pmatrix}.$$

5. Discussion

In summary, we have calculated the CGC's from which the matrix elements of the first-order Raman and Brillouin scattering are constructed. In the symmetrised square of the V-rep the product representation $\Gamma_{2-}(z)\otimes\Gamma_{3-}(x,y)=\Gamma_{3+}(zx,zy)$ is excluded. Gachter [10] attributed this interaction in D_{3d} symmetry to resonance Raman which is different from first-order Raman. The results given here are applicable to the class of materials belonging to space group D_{3d}. Koster et al. [11] and Loudon [12] have tabulated CGC's and scattering tensors for 32 point groups using different bases, and so it is pertinent to compare and extend the use of scattering tensors. We used CDML bases which contain irreps for the 230 space groups and their subgroups for high symmetry points and lines in the respective Brillouin zones. Our calculations of CGC's based on Birman's method, are useful for the construction of higher order Raman and Brillouin scattering tensors for morphic effects. Scattering tensors are used in polarization and experimental intensity studies due to phonon scattering. Also invariants needed in phase transition studies as well as effective Hamiltonians [13] can be easily derived from our results.

6. Conclusion

We have calculated the Clebsch-Gordan coefficients for the first-order Raman and first-order Brillouin scattering tensors. We show that the first-order Brillouin scattering tensors are obtained from the first-order Raman scattering tensors in D_{3d}^5. Our results will be used in the interpretation of polarized of Raman scattering and Brillouin spectroscopy. From these experimental assignments, the intensity of phonons and elastic constants of materials can be determined.

References

1. H. Zhang, C. Liu, X. Qi. X. X. Dai, Z. Fang, and S. Zhang, Nature **5** (2009) 438
2. J. Zhang, Z. Peng, A. Soni, Y.Zhao, Y. Hiong, B. Peng and J. Wang, Nano Lett. **11** (2011) 2407
3. W. Cheng, Phys. Rev. B 83 (2011) 094301-1
4. M. Cardona, in Light Scattering in Solids edited by M. Cardona, G. Gunthevodt, (Springer-Verlag) ISBN 038711913 (1983).
5. H.W. Kunert et al. Phys. Status Solidi **B** (2010) 1.
6. J.L. Birman and R. Berenson, Phys. Rev. **B 9** (1974) 4512
7. R. Berenson, J. Phys. Chem. Solids **42** (1981) 391.
8. A.P. Cracknell, B.L. Davies, S.C. Miller, W.F. Love, Kronecker Product Tables, (Ifl/Plenum, New York, 1979) Vol. 1-4.
9. J.L. Birman, Theory of Crystal Space Groups and Lattice Dynamics (Springer-Verlag, Berlin) (1984).
10. B. Gachter, J. Mol. Spect. **63** (1976) 1
11. G.F. Koster, Phys. Rev. **109** (1958) 227
12. R. Loudon, Adv. Phys. **13** (1964) 13
13. J.L. Birman and T. Lee, **14** (1976) 318

Segregation measurements of In and S on a Cu(In,S) ternary alloy using Auger Electron Spectroscopy coupled with a linear programmed heater

MJ Madito, HC Swart and JJ Terblans[1]

Department of Physics, University of the Free State, P. O. Box 339, Bloemfontein, ZA-9300, South Africa

E-mail: terblansjj@ufs.ac.za

Abstract. In this study a dilute Cu(In,S) ternary alloy was prepared by a diffusion doping process. From a prepared Cu(In,S) ternary alloy, the segregation behaviour of In and S was measured using the Auger Electron Spectroscopy (AES) coupled with a linear programmed heater. From the measured segregation profiles it was found that the In segregated first and was followed by S. The S completely replaced the In from the surface indicating that S has as larger segregation energy than In. From the segregation profiles the segregation parameters, namely the pre-exponential factors (D_0), the activation energies (Q), the interaction energies (Ω) and the segregation energies (ΔG) were extracted with the modified Darken model for In ($D_0 = (2.2 \pm 0.5) \times 10^{-5}$ m^2/s, $Q = 184.3 \pm 1.0$ kJ/mol, $= -62.8 \pm 1.4$ kJ/mol, $\Omega_{Cu-In} = 3.0 \pm 0.4$ kJ/mol), S ($D_0 = (8.8 \pm 0.5) \times 10^{-3}$ m^2/s, $Q = 213.0 \pm 3.0$ kJ/mol, $= -120.0 \pm 3.5$ kJ/mol, $\Omega_{Cu-S} = 23.0 \pm 2.0$ kJ/mol) and the atomic interaction ($\Omega_{In-S} = -4.0 \pm 0.5$ kJ/mol) for In and S.

1. Introduction

It is a general observation that certain elements (impurities) in a dilute homogeneous alloy, accumulate at the grain boundaries and free surfaces of a material as a result of a segregation process [1]. The grain boundaries are responsible for the strength and hardness of a material [2]. The free surface of a material is a very active region for processes such as catalytically reactions, epitaxial growth of thin films, corrosion, thermionic emission, etc. Therefore, the segregation of impurities to the grain boundaries of a material influences the metal-metal bonding at the grain boundaries and as a result the strength and hardness of a material can be influenced. The segregation at the free surface can influence processes mentioned above that take place at the free surface of the material. Consequently, segregation of impurities at the grain boundaries and free surfaces of a material play a vital role in engineering of materials.

There are a considerable number of segregation studies that involve impurities such as Bi, Sb, Sn, S, Ag, etc. in Cu [3–7]. Despite the considerable number of publication concerning segregation of impurities from a Cu crystal, no study was found for In segregating from a Cu crystal. Therefore, this study is most likely the first to report on the segregation of In from a Cu crystal. Note that S is a regular impurity in a Cu crystal (with bulk concentration in the order of few parts per million (ppm)) and is anticipated to segregate with In to give a Cu(In,S) ternary alloy.

[1] To whom any correspondence should be addressed.

This study focuses mainly on the segregation of In from a Cu crystal. The segregation of S from a Cu crystal will also receive attention. Nevertheless, the segregation of S from a Cu crystal was experimentally observed by Viljoen et al. [4] and in this observation only the pre-exponential factor (D_0) and the activation energy (Q) were reported. The segregation of In and S will be measured from a prepared Cu(In,S) alloy with Auger electron spectroscopy (AES) coupled with a linear programmed heater. From the measured segregation profiles a set of segregation parameters, namely the pre-exponential factor (D_0), activation energy (Q), segregation energy (ΔG) and interaction energy (Ω) will be extracted for both In and S segregation from a Cu crystal using the modified Darken model. The initial parameters for the Darken calculations were extracted from the fits obtained from the Fick's and Guttmann model.

2. Theory

In segregation studies the primary mechanism of surface enrichment is the diffusion from the bulk. Hence it is possible to determine the bulk diffusion parameters (D_0 and Q) of the segregating impurities. Theoretically, one of the known model in this regard is the modified semi-infinite model of Fick [4,8]. In this model the surface enrichment factor ( ) at temperature, T, is given by $= (X^{\phi}(T) - X^{B}) / X^{B}$ where $X^{\phi}(T)$ is the surface concentration at temperature, T, and X^{B} is the bulk concentration of the segregating impurity. The temperature dependence of the enrichment factor is given by

$$^{2}(T) = \gamma \int_{T_0}^{T_F} e^{-Q/RT}\, dT \tag{1}$$

where $\gamma = 4D_0 /$ ^{2}, D_0 is the pre-exponential factor, is the constant heating rate, d is the thickness of the segregated layer, T_0 is the initial crystal temperature, T_F is the final crystal temperature, Q is the activation energy and R is the gas constant.

The modified semi-infinite model of Fick is adopted for describing the kinetic region of the segregation profiles and for extracting the D_0 and Q values from a single segregation run. During the segregation process, the concentration of the segregating impurities change between the bulk layers, B, and the surface layer, ø. The impurity concentrations in the surface layer of the crystal increases until the total energy of the crystal is minimised (the equilibrium is reached). The model that is known to describe the equilibrium region of the segregation profiles in multicomponent alloys is the Guttmann model given by [9]

$$X_1^{\phi} = \frac{X_1^{B} e^{(\Delta G_1/RT)}}{1 - X_1^{B} + X_1^{B} e^{(\Delta G_1/RT)} - X_2^{B} + X_2^{B} e^{(\Delta G_2/RT)}} \tag{2}$$

$$X_2^{\phi} = \frac{X_2^{B} e^{(\Delta G_2/RT)}}{1 - X_2^{B} + X_2^{B} e^{(\Delta G_2/RT)} - X_1^{B} + X_1^{B} e^{(\Delta G_1/RT)}} \tag{3}$$

where $\Delta G_1 = \Delta G_1^{0} + 2\Omega_{13}\left(X_1^{B} - X_1^{\phi}\right) + \Omega'\left(X_2^{\phi} - X_2^{B}\right)$, $\Delta G_2 = \Delta G_2^{0} + 2\Omega_{23}\left(X_2^{B} - X_2^{\phi}\right) + \Omega'\left(X_1^{\phi} - X_1^{B}\right)$, $\Omega' = \Omega_{12} - \Omega_{13} - \Omega_{23}$, ΔG_i is the segregation energy for a segregating impurity i and Ω_{ij} is the interaction energy between the atoms of the impurity i and the crystal j.

Therefore, the Guttmann model yields the segregation ΔG and the interaction Ω energies. The modified semi-infinite model of Fick and the Guttmann model describe the kinetic and the equilibrium regions of the segregation profiles respectively and independently. Nonetheless, the modified Darken model describes both the kinetic and the equilibrium regions [9].

In the modified Darken model the crystal is divided into $N + 1$ layers of thickness d, parallel to the surface. According to this model, the driving force behind the segregation is the minimization of the total energy of the crystal (the change in the chemical potential) and is given by

$$\Delta\mu_i^{(j+1,j)} = \left(\mu_i^{(j+1)} - \mu_i^{(j)}\right) - \left(\mu_m^{(j+1)} - \mu_m^{(j)}\right) \tag{4}$$

where $_i^{(j+1)}$ is the chemical potential of impurity i in layer $j + 1$ and $_m^{(j+1)}$ is the chemical potential of the bulk atom m in layer $j + 1$.

In the modified Darken model the concentration change of impurity i between the $(j + 1)$-th layer and the j-th layer of the crystal as function of time is given by

$$\frac{\partial X_i^{(j)}}{\partial t} = \left[\frac{M_i^{(j+1\to j)} X_i^{(j+1)}}{d^2} \Delta\mu_i^{(j+1\to j)} - \frac{M_i^{(j\to j-1)} X_i^{j}}{d^2} \Delta\mu_i^{(j\to j-1)} \right] \tag{5}$$

where $M_i = D_i/RT$ is the mobility of the segregating impurity i in the bulk for a dilute alloy, D is the diffusion coefficient $D=D_o\exp(-Q/(RT)$ and d is the thickness of the segregated layer.

Using the modified Darken model (equation 5), the entire segregation profile can be calculated and a set of segregation parameters can be extracted.

3. Experimental details

Cu crystals (0.70 mm thick and 10 mm diameter) with a S bulk concentration of 0.0008 at% (8 ppm) were obtained from a high purity (99.99 %) polycrystalline Cu. The Cu crystals were doped with a low concentration of In of 0.059 at%. A detailed Cu(0.059 at% In) alloy preparation procedure will be published. One side of the doped crystal was chosen as the front side and was mechanically polished to 0.05 m using a diamond suspension solution. The crystal was further mounted on a heater inside the ultra high vacuum (UHV) chamber ($P = 1.0 \times 10^{-9}$ Torr). The crystal temperature was measured directly from the back of the crystal with a chromel–alumel thermocouple (Type K) and the measured temperature was calibrated in terms of the true surface temperature of the crystal. AES was used to monitor the concentration build up on polished surface of the crystal during linear heating. A 5.0 keV primary electron beam with a current of 0.7 A was used for the AES measurements and the modulation energy was 2.0 eV. The scan rate was 5.0 eV/s and the time constant was 0.1 s. The ion gun used for sputter cleaning was operated at a beam energy of 2.0 keV, an argon pressure of 1.5×10^{-5} Torr and the beam was rastered over a 2 mm × 2 mm area. The crystal was tilted with the normal of the crystal surface at a 30° angle with respect to the direction of the incident electron beam.

Before the segregation run the crystal was pre-heated at 1073 K for 24 hours and cooled to 373 K at a cooling rate of −0.05 K/s to restore the initial condition of the crystal (uniform bulk concentration). The crystal was pre-heated at T_0 = 373 K for 1 hour and sputter cleaned for exactly 30 s. Immediately after sputtering Auger peak to peak heights (APPHs) were recorded as a function of time for Cu (922 eV), S (153 eV) and In (405 eV) as the crystal temperature, T, was increased linearly with time at a constant heating rate, , of 0.05 K/s from 373 K to 1073 K. In this regard the time, t, scale is converted to temperature, T, using the relation given by

$$T = T_0 + \alpha t \tag{6}$$

The APPH data was quantified using the method discussed in the appendix of Ref. [10] and the sensitivity factors were determined from the pure elemental standards under the same conditions. In the quantification, the backscattering factor from Shimizu as discussed by Seah [11], the inelastic mean free path (IMFP) calculated with the TPP-2M formula [12] were used. The Auger spectra of the crystal were obtained and showed only the segregation of In and S.

4. Results and Discussion

Figure 1 shows the surface enrichment of In and S from a dilute Cu(In,S) ternary alloy which was obtained by using a linear heating method at a heating rate of 0.05 K/s. In figure 1 four different regions are shown: Region A, the crystal temperatures are low and the bulk diffusion coefficients (D) of In and S are low, hence In and S do not enrich the surface layer of the crystal. Region B, (the In kinetic region) In segregated to the surface and reached a maximum surface concentration of 25 %. Region C, (the S kinetic region) the segregation rate of S increased, thus increasing the surface concentration of S. As S segregated to the surface, it replaced the In from the surface layer. Region D, (the equilibrium region) S reached a maximum surface concentration of 30 % and the In maximum surface concentration reached almost 0 % after being replaced by S.

The maximum surface concentrations of In and S are determined by the segregation and interaction energies. According to the Guttmann model, a large difference between the segregation energies for

segregating impurities leads to a behaviour whereby an impurity with greater segregation energy (more negative) replaces the one with lesser segregation energy (less negative). Therefore, The In replacement by S could be as a result of the segregation energy for S that could be greater (more negative) than that for In. Swart et. al. [13] have demonstrated that a repulsive interaction between two segregating impurities (In and S in this study) lead to a higher equilibrium concentration of impurity 2 (S in this study) and a lower equilibrium concentration of impurity 1 (In in this study). Therefore, the interaction between the In and S atoms could be repulsive.

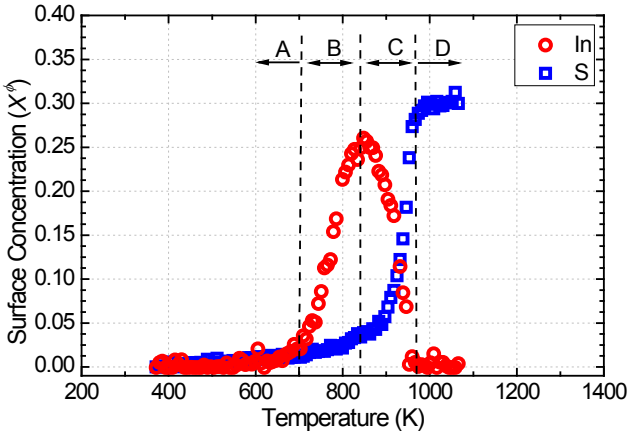

Figure 1. The surface enrichment of In and S from a Cu(In,S) ternary alloy obtained at a heating rate of 0.05 K/s.

The surface concentration scale in figure 1 was converted to the enrichment factor ( ) (discussed in the theory section above) as shown in figure 2. The modified semi-infinite model of Fick (equation 1) was fitted through the In kinetic region (region B in figure 1) and the S kinetic region (region C in figure 1) of the segregation profiles and from the best fits (shown in figure 2) the D_0 and the Q values were extracted (see the insert text of figure 2).

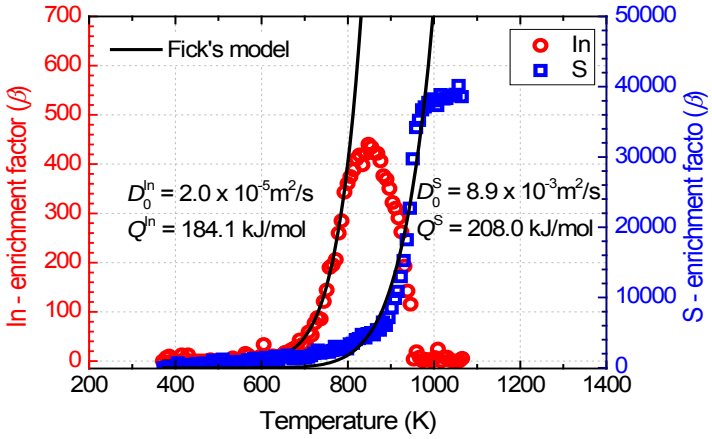

Figure 2. The enrichment factor ( ) for In and S segregation from a Cu(In,S) alloy obtained at a heating rate of 0.05 K/s.

The Guttmann model (equation 2 and 3) was fitted through the equilibrium region (region D in figure 1) of the In and S segregation profiles and from the best fits (shown in figure 3) the ΔG and the Ω values were extracted (see the insert text of figure 3).

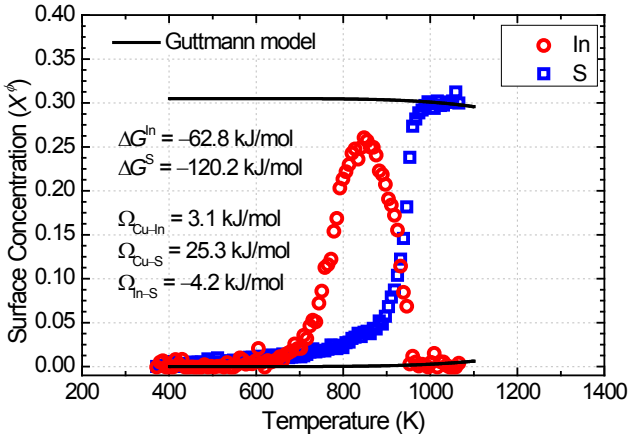

Figure 3. The surface enrichment of In and S from a dilute Cu(In,S) ternary alloy fitted with Guttmann model (solid lines).

Furthermore, using the values of the parameters D_0, Q, ΔG and Ω extracted from the best fits of the Fick's and Guttmann model as the initial parameters in the Darken calculations (equation 5), the profiles that best simulate the measured segregation profiles were calculated (see figure 4). The parameters of the Darken calculations shown in figure 4 are listed in table 1.

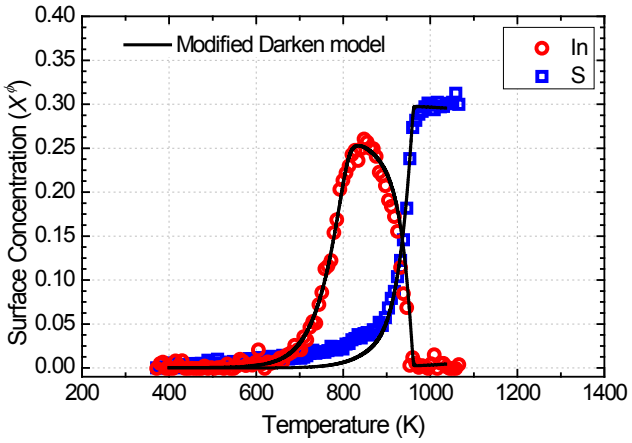

Figure 4. The surface enrichment of In and S from a Cu(In,S) alloy. The solid lines are calculated with the Darken model.

Table 1. In and S segregation parameters extracted from the modified Darken model (figure 4). The interaction energy for In and S (Ω_{In-S}) is −4.0 ± 0.5 kJ/mol. X in Ω_{X-Cu} denotes either In or S.

Segregated Impurities	Segregation parameters			
	D_0 (m^2/s)	Q (kJ/mol)	ΔG (kJ/mol)	Ω_{X-Cu} (kJ/mol)
In	$(2.2 \pm 0.5) \times 10^{-5}$	184.3 ± 1.0	−62.8 ± 1.4	3.0 ± 0.4
S	$(8.8 \pm 0.5) \times 10^{-3}$	213.0 ± 3.0	−120.0 ± 3.5	23.0 ± 2.0

In table 2 it is clear that the activation energy (Q) and the pre-exponential factor (D_0) for In bulk diffusion are smaller than for S. Therefore, In diffuses faster in the bulk than S. The activation energy

for In (Q = 184.3 kJ/mol) is lower than that for S (Q = 213.0 kJ/mol) hence In segregates first (before S) at low crystal temperatures. In addition, a higher bulk concentration of In (0.059 at%), which is much higher than that of S (0.0008 at%), increases the segregation rate of In at low crystal temperatures. The attractive interaction between the In and Cu atoms (Ω_{Cu-In} = 3.0 kJ/mol) set a preference for unlike first-neighbour bonds formation between the In and Cu atoms and that suggest that an In atom prefers to be surrounded by Cu atoms in the Cu(In) system. Similarly, the attractive interaction between the S and Cu atoms (Ω_{Cu-S} = 23.0 kJ/mol) set a preference for unlike first-neighbour bonds formation between the S and Cu atoms. The repulsive interaction between the In and S atoms (Ω_{In-S} = −4.0 kJ/mol) shows less or no tendency of In–S atomic bonds formation. There is a large difference in the segregation energies for In (= −62.8 kJ/mol) and S (= −120.0 kJ/mol) and that elaborates the displacement of In in the surface layer by S (the segregation of S is more energetically favourable than that of In).

5. Conclusion

The segregation behaviour of In in a Cu crystal was observed. S (regular impurity in a Cu crystal) was also observed to segregate with In. From the measured segregation profiles, the segregation parameters were successfully obtained for In and S segregation in a Cu crystal using the linear heating method. The segregation data for In segregation in Cu crystal was not found in literature; hence the results of this study are not compared to literature findings. However, the pre-exponential factor ($D_0 = 8.8 \times 10^{-3}$ m^2/s) and the activation energy (Q = 213.0 kJ/mol) obtained in this study for S segregation in a Cu crystal are in good agreement with those reported by Viljoen et al. [4] ($D_0 = 1.8 \times 10^{-3}$ m^2/s and Q = 212.0 kJ/mol obtained using the linear heating method). In this study, processes such as grain boundary diffusion, segregation at grain boundaries, the segregation dependence of different grain surface orientations, segregation from bulk and grain boundaries could not be separated from each other. Therefore, the segregation parameters obtained in this study take all active processes into account and yields average results.

Acknowledgments

The authors would like to thank the National Research Foundation (NRF) and the Cluster programme of the University of the Free State for their financial assistance.

References

[1] 1990 *Surface Segregation Phenomena*, ed PA Dowben and A Miller (Florida: CRC Press, Inc.)
[2] 2006 *The Science and Engineering of Materials*, ed DR Askeland, PP Phulé (Canada: Thomson)
[3] Viljoen EC and du Plessis J 1994 *Surface and Interface Analysis* **22** 598
[4] Viljoen EC and du Plessis J 1995 *Surface and Interface Analysis* **23** 110
[5] Terblans JJ and van Wyk GN 2004 *Surface and Interface Analysis* **36** 935
[6] Wang JY, du Plessis J, Terblans JJ and vanWyk GN 1999 *Surface Science* **423** 12
[7] Terblans JJ, Swart HC 2009 *e-Journal of Surface Science and Nanotechnology* **7** 480
[8] Viljoen EC, du Plessis J 1999 *Surface and Interface Analysis* **431** 128
[9] J du Plessis 1990 *Solid State Phenomena* - Part B, Volume 11, Diffusion and Defect Data (Brookfield USA: Sci-Tech Publications)
[10] du Plessis J, Viljoen PE and Van Wyk GN 1991 *Surface and Interface Analysis* **244** 277
[11] 1990 *Practical Surface Analysis by Auger and X-ray Photoelectron Spectroscopy* 1st edition, ed D Briggs and MP Seah (Chichester: John Wiley & Sons Ltd.) p 146 pp 201-212
[12] Tanuma S, Powell CJ and Penn DR 2004 *Surface and Interface Analysis* **36** 1
[13] Swart HC, Roos WD and Terblans JJ 2004 *Surface and Interface Analysis* **36** 285

Synthesis and Magnetic properties of $Mg_{0.2}Cr_{1.8-x}Fe_xO_3$ oxides

K. Mbela[1] , T. Moyo[1], J. Z. Msomi[1]

[1]School of Chemistry and Physics, University of KwaZulu-Natal, Durban 4000, South Africa

Mbelak@ukzn.ac.za

Abstract. We report the magnetic properties of $Mg_{0.2}Cr_{1.8-x}Fe_xO_3$ (x = 0.3, 0.5, 0.7 and 0.9) compounds. The oxides were produced by hydrothermal process and sintered at 600 ºC for 12 hours. The X-ray diffraction (XRD) data indicate single phase corundum structure in all the samples. The Mössbauer spectra recorded at about 300 K show transition from paramagnetic to ordered magnetic spin state at x = 0.5. The magnetization data reveals superparamagnetic nature of the oxides presented. The shift in hysteresis loops observed along the magnetic field axis is associated with exchange bias effect.

1. Introduction

The design, synthesis, and characterization of nanophase materials of the type α-Fe_2O_3 have been the subject of intense research in recent years [1-4]. These studies are motivated by the novel properties of these materials at nanoscale as well as by their potential applications in heterogenous catalysts, biomedicine and biotechnology. Various methods have been reported for the synthesis of iron oxide nanoparticles, such as sol-gel reactions and chemical solutions [9-11]. These methods have the advantage that no surfacant need to be removed from the nanoparticles before application into precision industry and biomedical field. In this work we report the exchange bias effect observed in $Mg_{0.2}Cr_{1.8-x}Fe_xO_3$ produced by hydrothermal technique.

2. Experimental details

The compounds $Mg_{0.2}Cr_{1.8-x}Fe_xO_3$ (x = 0.3, 0.5, 0.7, 0.9) were produced from a mixture of required stochiometric proportions of magnesium chloride, chromium (III) chloride and iron (III) chloride hexahydrate solutions. Excess aqueous ammonia was slowly added to the chloride mixture until full precipitation. The precipitate was boiled under reflux for 3 hours. The products were then filtered, washed with deionised water for several times until no chloride ions were detected by addition of silver nitrate standard solution. The clean products were finally washed with ethanol and then dried under an infrared lamp. The resulting homogeneous powders were heated in air at 600 ºC for 12 hours. The XRD patterns of the samples were obtained by using CoK_α radiation (λ = 1.7903 Å) on a Phillips diffractometer (type: PW1710). The Mössbauer spectra were recorded at about 300 K using a conventional constant acceleration spectrometer with a ^{57}Co source sealed in Rh matrix. Magnetization measurements were obtained by using a Quantum Design vibrating sample magnetometer between 10 K and 400 K

3. Results and discussion

In Fig. 1 we show the XRD spectra of $Mg_{0.2}Cr_{1.8-x}Fe_xO_3$ (x = 0.3, 0.5, 0.7, 0.9) oxides. The patterns confirm the formation of the basic corundum structure in all samples. The XRD spectra are similar to that of Sn doped α-Fe_2O_3 [3]. No other impurity phases were observed. The refinement of XRD spectra was performed by a Rietveld analysis (FullProf Suite for Windows) using a model involving a combination of both interstitial and substitutional Mg^{2+} ions in octahedral coordination. The lattice parameters deduced from XRD data are shown in Table 1. There was no significant change in lattice constants with increasing Fe concentration. The average particle sizes calculated by using the Debye Scherrer formula [6] are also shown in Table 1. The particle sizes appear to be sensitive to Cr concentration. The smallest grains (about 33 nm) were formed in a sample with the smallest Cr concentration (x = 0.9).

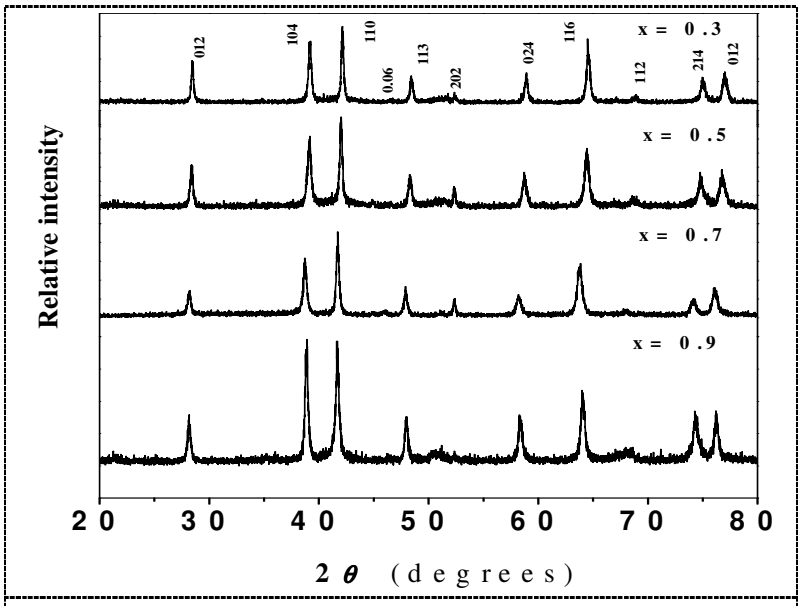

Figure 1. XRD spectra for $Mg_{0.2}Cr_{1.8-x}Fe_xO_3$ oxides.

The variation of Mössbauer spectra as a function of x is shown in Fig. 2. The spectra for compounds with low Fe concentration ($x \leq 0.5$) were best fitted to two doublets. Doublets are associated with Fe ions in paramagnetic spin state. For x = 0.7 and 0.9 magnetic splitting is observed. The spectra could be fitted with two sextets and one doublet. There was no significant change in isomer shifts and quadrupole splitting with increasing x. A slight increase in hyperfine fields from 433 kOe to 455 kOe and 439 kOe to 480 kOe with increasing x has been observed for the two fitting sextets. This can be explained by an increasing Fe concentration in the structure.

The zero field (ZFC) and FC (50 Oe) magnetization curves are shown in Fig. 3. During field cooling (FC), the oxides were cooled from 400 K to 10 K in the presence of an external magnetic field of 50 Oe. For ZFC measurements, the applied field of 50 Oe was kept constant during cooling to 10 K and the magnetization was recorded during warming up to 400 K in the presence of the same external field. The magnetization in the FC curve decreases continuously with increasing temperature. In ZFC the state of magnetization increases with increasing temperature. This behaviour is characteristic of spin glass like behaviour [7]. The width of the peak in ZFC curve is associated with particle size distribution. Each particle with a particular size has a certain blocking temperature [11]. A narrower peak observed in ZFC curve for x = 0.9 indicates narrow distribution of particle sizes. The

linear fits for the temperature dependence of the inverse magnetization shows that the samples exhibit Curie-Weiss type behaviour above about 286 K and 290 K for x = 0.7 and x = 0.9 respectively. The corresponding extrapolated paramagnetic Curie temperatures θ_P are -354 K and -722 K. In Fig. 4 we show typical results for x = 0.9. The large negative values of θ_P indicate that the antiferromagnetic (AFM) interactions in $Mg_{0.2}Cr_{1.8-x}Fe_xO_3$ are strong.

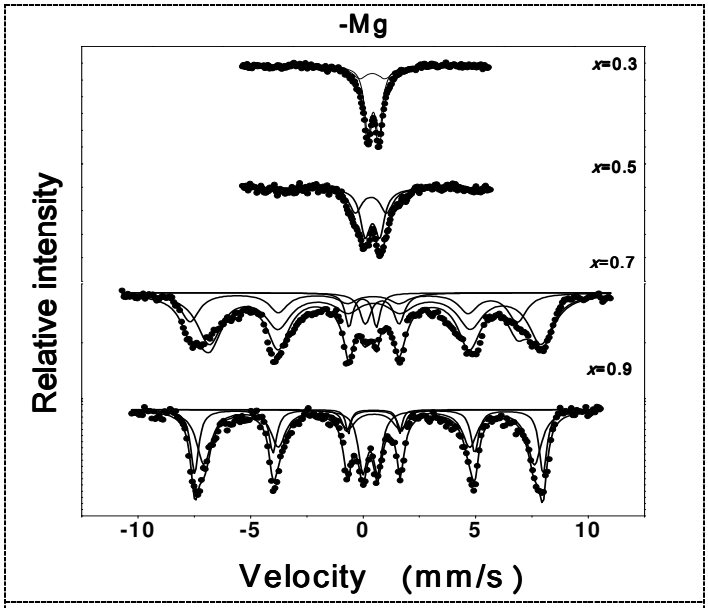

Figure 2. Mössbauer spectra for $Mg_{0.2}Cr_{1.8-}Fe_xO_3$ oxides.

The variation of hysteresis curves of $Mg_{0.2}Cr_{1.8-x}Fe_xO_3$ as a function of x recorded at 400 K and 10 K is shown in Fig. 5. The amplified view of hysteresis loops at low fields is also shown in the insets. An anomalous variation of magnetization with low magnetic field is observed. This behavior might have application in magnetic switching devices. The small values of coercive fields observed in hysteresis curves measured at room temperature indicate superparamagnetic nature of the compounds. An increase in coercivity was observed from 400 K to 10 K. The measurements of hysteresis loops at 10 K were performed after FC and ZFC measurements. The loops are not symmetrical about the origin but are slightly shifted to the left side. The shift of the hysteresis curves along the field axis is associated with exchange bias effects [8]. The direct exchange interaction between ferromagnetic and anti-ferromagnetic spins in a common interface results in an unidirectional magnetic anisotropy seen as exchange bias. The theory on exchange bias effect is discussed in reference [2]. In the present case for $Mg_{0.2}Cr_{1.8-x}Fe_xO_3$ compounds we suspect the exchange bias to be due to exchange interaction between antiferromagnetic and ferromagnetic spins in Cr and Fe, respectively. The exchange bias phenomenon has applications in magneto-electronic switching devices, random access magnetic storage units, magnetic sensors and spintronics devices [1]. The exchange bias field is defined as $H_{EB} = (H_{C1} - H_{C2})/2$, where H_{C1} and H_{C2} are coercive fields at the left and right side of the shifted magnetization curve [1]. The values of exchange bias deduced from hysteresis loops measured at 10 K are shown in Table 2.

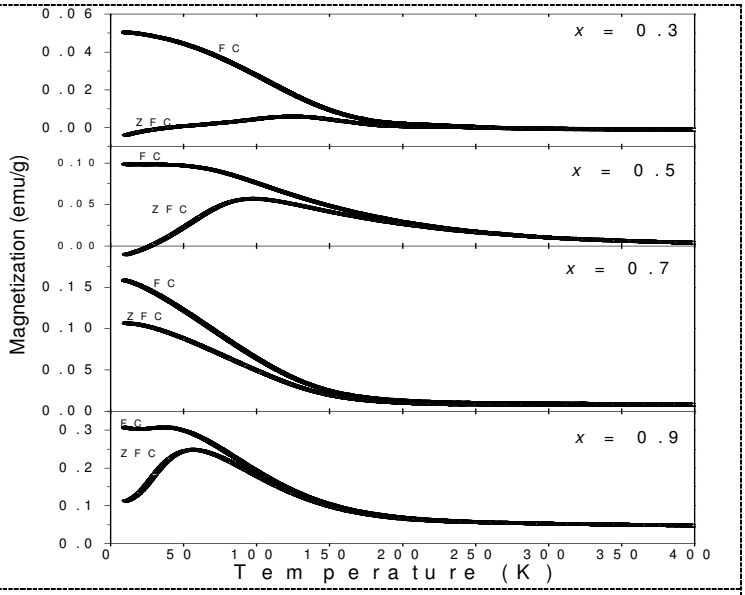

Figure 3. ZFC and FC (50 Oe) curves for $Mg_{0.2}Cr_{1.8-x}Fe_xO_3$ oxides

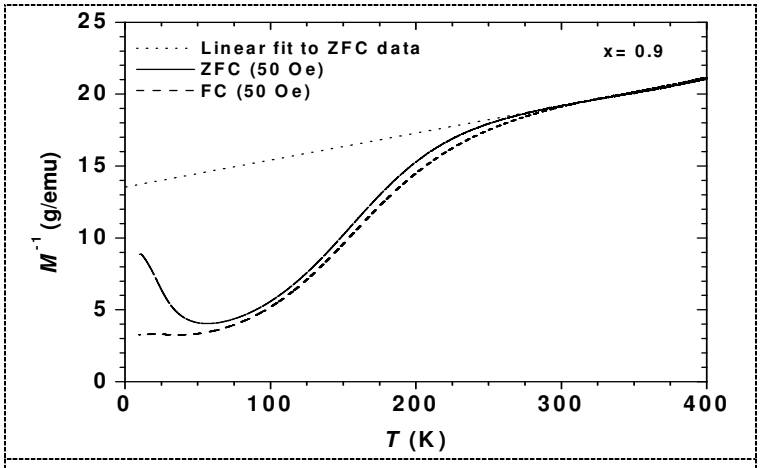

Figure 4. Linear fit for the temperature dependence of the inverse magnetization.

Table 1. Grain size (D), lattice parameters for $Mg_{0.2}Cr_{1.8-x}Fe_xO_3$ oxides

x	a = b (Å)	c (Å)	D (nm)
0.3	4.986	13.621	55.6
0.5	4.986	13.643	42.5
0.7	5.001	13.622	65.9
0.9	4.962	13.586	32.8

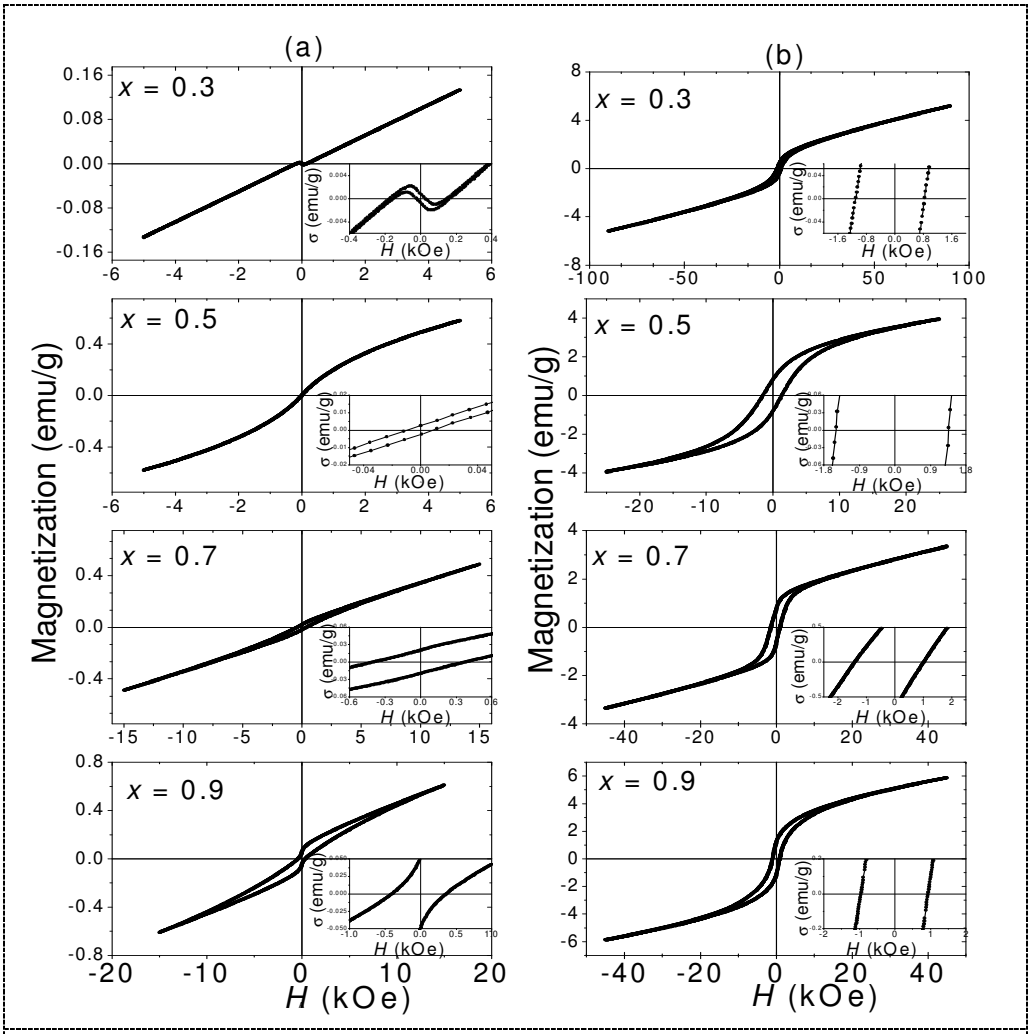

Figure 5. Magnetization curves of $Mg_{0.2}Cr_{1.8-x}Fe_xO_3$ measured at (a) 400 K and (b) 10 K .

Table 2. Values of exchange bias fields for $Mg_{0.2}Cr_{1.8-x}Fe_xO_3$ oxides.

x	0.3	0.5	0.7	0.9
H_{EB} (Oe) ±1	135	64	192	10

4.Conclusion

We have successfully made $Mg_{0.2}Cr_{1.8-x}Fe_2O_3$ compounds by hydrothermal process. An anomolous variation of magnetization in low fields has been observed. The oxides exhibit exchange bias effects which appear to be sensitive to grain sizes. Samples with larger grains show more enhanced exchange bias effect. Our results from 400 K to 10 K also show evidence of strong antiferromagnetic interactions in the compounds.

References

[1] Demirci E and Özturk M 2011 J. Supercond. Nov. Magn (accepted for publication).
[2] Kiwi M 2001 *J. Magn. Magn. Mat* 234 584
[3] Berry F.J., Greaves C, Mortimer J, McManus J.,G and Oates G 1997 *J. Solid. State. Chem*. 130 272
[4] Berry F J, Greaves C, Helgason O, MacManus J G, Padlmer H M and Williams R T 2000 *J. Solid. State. Chem* 151 157.
[5] Ayub I, Berry F J, Johnson C, Johnson D A, Moore E A, Ren X and Widatallah H M 2000 *Solid State Commun* 123 141.
[6] Young R A 1993 The Rietveld Method, Oxford University Press, New York.
[7] Leslie. D.L, Ricke R D 1996 *Chem. Mater* 8 1770.
[8] Meiklejohn W H and Bean C P 1956 *Phys. Rev*. 102 1413.
[9] Liu X, Huang K, Zhou S, Zhao P, Meridor U, Frydman A and Gedanken A 2006 *J.Mag. Mag. Mat.* 305 504
[10] Msomi J and Moyo T 2009 *J. Magn. Magn. Mat* 321 1246.
[11] Cannas C, Concas G, Gatteeschi D, Falqui A, Musinu A, Piccaluga G, Sangregorio C and Spano G 2001 *J. Phys. Chem* 3 832.

Non-destructive investigation of a polycrystalline carbonado diamond

TB Moipolai[1], AM Venter[2], TP Ntsoane[2], MAG Andreoli[3]andSH Connell[1]

[1] Department of Physics, University of Johannesburg, Johannesburg, South Africa
[2]Research and Development Division, Necsa Limited, South Africa
[3] Nuclear Liability Management Department, Necsa Limited, South Africa

Corresponding author: Andrew.Venter@necsa.co.za

Abstract. This study reports a non-destructive investigation of a polycrystalline carbonado diamond in its raw as-discovered form. The carbonado has a porous structure and is mostly composed of carbon, oxygen and nitrogen. The carbon is crystallised as cubic diamond, but no specific crystalline oxide or nitride phases were observed. Residual stress values, determined using the $\sin^2\psi$ technique at depths of 240 μm, indicated stress values ranging from -35 ± 85MPa to 135 ± 50 MPa, i.e. within the experimental accuracy and constraints imposed by the surface roughness, the averaged surface stresses are close to zero.

1. Introduction

Diamond, the hardest of the naturally occurring materials, is an allotrope of carbon in which the carbon atoms are arranged in specific lattice symmetries, the cubic one with tetravalent covalent bonds being the one most common in nature. Carbon occurs as a native element in several polymorphs, of which the most familiar are graphite (very soft, hexagonal, black, as anisotropic sheets) and diamond (extremely hard, cubic, various colours, generally translucent). In addition there are the polycrystalline fine-grained aggregates discussed here (carbonado and related forms), and other rare polymorphs [1].

Our research interest is in the characterization of the residual stresses locked in polycrystalline diamonds from different origins to add information towards unravelling their still very controversial origin [2]. With respect to residual stress investigations the only reported study was performed on surface modified (cut and polished) carbonado samples using Raman spectroscopy [3, 4]. Since surface modifications cause stress redistribution we have subsequently adopted a non-destructive approach by investigating the sample in its natural as-discovered form.

Residual stresses in solids result, amongst others, from the conditions prevailing during their formation, i.e. temperature and pressure, as well as the effects of inclusions that contribute differences in coefficients of thermal expansion (CTE).

The typical, primary requirements for natural diamond formation are combinations of high pressures (HP) and high temperatures (HT). Possible mechanisms of formation are [5]:

- Igneous crystallisation from C-rich kimberlite melts in the mantle [HT-HP].
- Solid state conversion from graphite as a result of subduction of oceanic/continental crust to mantle depth [HP-HT].
- Shock-metamorphism in meteorite impact processes [Ultra HT-PT].

- Presolar.

The sample of our investigation, carbonado, generally are a few mm to cm size pebbles from soils/sediments, contain inclusions of foreign phases and may have been formed from any of the above mechanisms. Commonly known as "Black Diamond", carbonado is a natural polycrystalline diamond found in alluvial deposits in the Central African Republic and Brazil [6]. It is a porous aggregate of micron-sized diamond crystals and black or dark grey in colour. It does not seem to occur with normal diamonds in kimberlite pipes, suggesting a very different mode of origin. It is postulated that the hexagonal form of diamond, called lonsdaleite, would result purely from the latter two mechanisms mentioned above [7].

We report results from exploratory non-destructive investigations on a polycrystalline carbonado originating from Brazil. Investigations included scanning electron microscopy for elemental identification and imaging, as well as X-ray diffraction (XRD) for chemical phase identification and residual stress determination of the sub-surface region to a depth in the order of 240 μm.

2. Experimental

Since the sample is of significant scientific value, no surface preparation, apart from surface cleaning with compressed air, has been performed to remove loose deposits. Characterisation investigations have been performed with: Laboratory X-rays for chemical phase identification and residual stress analysis; Supplemented by scanning electron microscopy (SEM) in secondary electron (SE) and backscattered electron (BSE) imaging and energy dispersive X-ray spectroscopy (EDS) for elemental identification to aid in the diffraction characterization. All the investigations have been done at the Necsa facilities within the Research and Development Division.

2.1. Sample

A photograph of the carbonado is shown in figure 1. It has a distinctive irregular pebble (stone) shape and of approximate size 13.5 x 10 x 3.5 mm^3, characteristically black in colour with clear crevices and porosity visible with the naked eye.

Figure 1: Photograph of the carbonado. Investigation were performed at the four positions indicated which were selected to be representative of as-flat-as-possible positions on the sample surface. The irregular topography of the sample is clearly evident. Note the bubble-like void appearance covering the entire surface.

2.2 Investigations

XRD investigations were done with a Bruker D8 Discover instrument equipped with a 1/4 Eulerian cradle goniometer stage, highly collimated Cu radiation, incident beam size 0.8 mm in diameter, and an area detector system. In conjunction with the laser video alignment system of the instrument, picking of measurement positions and aligning to the instrument rotation axis were possible to within 20 μm accuracy. The beam penetration depth into carbon by Cu radiation was calculated to be 240 μm. Chemical phase identification was done against the International Centre for Diffraction Database (ICDD) search / match function and residual stress investigations were performed with the $sin^2\psi$ side-inclination technique for ψ angles 0 ° to 70°. The residual stress technique is based on the accurate

determination of the (311) Bragg reflection of diamond, typically observed at 2θ = 92.093°, at various sample tilt angles with respect to the fixed incident and diffracted beam paths. Data analysis was done using the software package Leptos version 6 supplied by Bruker AXS. Stress-free d-spacings were taken as the psi = 0º measurement. Since an essential requirement for residual stress analysis by XRD is that the surface needs to be flat to at least 20% of the penetration depth of the X-rays, four positions were selected on the sample surface that offered as-flat-as-possible surfaces for the investigations.

The SEM investigations were done with a Quanta FEI 200 SEM/EDS instrument equipped with a silicon drift detector. The instrument parameters employed were 30kV voltage, 0.67 nA current, working distance WD = 15.00 mm and magnification 500X.

For the XRD investigations the sample was mounted in a sample holder to ensure repeatable sample setup. For the SEM analyses the sample was taped to the sample stage with carbon tape to limit charging. All SEM investigations were done at low vacuum of 0.45 Torr.

2.3 Residual stress analysis

Residual stress is the stress that remains in a solid sample with no external forces applied. Positive values indicate tensile (expansion) stress whilst negative values indicate a compressive (contraction) state. The deformation per unit length is the strain [8].

The X-ray diffraction method measures macroscopic strains from the interplanar spacings through the application of the $sin^2\psi$ side-inclination technique shown in figure 2. With this technique the lattice plane spacing of a specific *(hkl)* reflection is accurately measured as function of sample tilt angles ψ (inclination angles). The residual stress for a bi-axial (in-plane) condition (assumed with XRD due to the limited penetration depth) is deduced through the equation

$$\varepsilon_{\emptyset} = \frac{d_{\psi} - d_0}{d_0} = \frac{1+\nu}{E}(\sigma_{\emptyset} sin^2\psi) - \frac{\nu}{E}(\sigma_{11} + \sigma_{22})$$

where E and ν are the Young's modulus and Poisson's ratio of the material under study, d_{ψ} is the lattice spacing at each ψ, and d_0 is the value of d at $\psi = 0^o$, σ_{11} and σ_{22} are the in-plane principal stresses and σ_{33} the normal stress component. S_1, S_2 and S_3 represent these principal stress components in the sample coordinate system. This strain equation describes a linear dependence for data plots of ε versus $sin^2\psi$ with the in-plane stress σ_{ϕ} determined from a least squares fit of the curve gradient. For the principal stress to be resolved, measurements need to be performed for at least 3 (azimuthal) phi rotations.

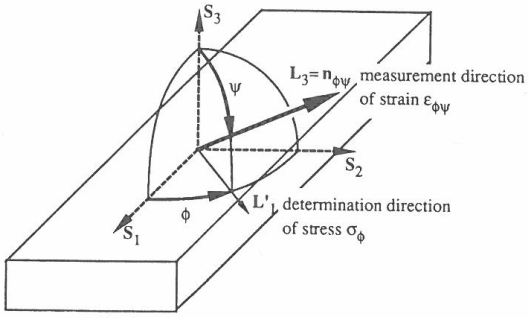

Figure 2: XRD residual stress measurement geometry [9].

3. Results

Figure 3 shows SEM secondary electron (SE) images taken at each of the measurement positions. The porosity of the sample with distinctive crevices is clearly evident. The carbonado surface is quite complex: a spot analysis has identified the dark areas in the SE image as carbon and the paler regions indicative of heavier elements. The pore sizes are estimated to be 40 – 100 μm with no visible partially closed cavities within which foreign material could be entrapped.

Figure 4 shows the elemental and chemical phase analyses results taken at the four measurement positions and summarized in table 1.

Figure 5(a) displays the *strain* versus $sin^2\psi$ results that were measured at the four positions. It is clear that the residual stress analyses are adversely affected at large sample ψ-tilt angles by the severe surface roughness of the sample, leading to deviation from a linear trend. This is ascribed to the surface roughness leading to partial screening of the incident and diffracted beam paths causing

anomalous absorption of the beam, with the resulting peak determination of the altered peak leading to artifacts and shifts in the perceived beam centre. Since the $sin^2\psi$ is based on a linear dependence, data analyses were subsequently limited to $sin^2\psi$ values smaller than 0.7 for which a linear dependence does exist as shown in figure 5(a). To demonstrate the feasibility of the $sin^2\psi$ technique overall, figure 5(b) shows results measured on our equipment from a polycrystalline diamond (PCD) compact that has a flat smooth surface, that is ideally suited for stress analyses up to $sin^2\psi$ values of 0.9. The latter result is indicative of a stress of -836 ± 78 MPa.

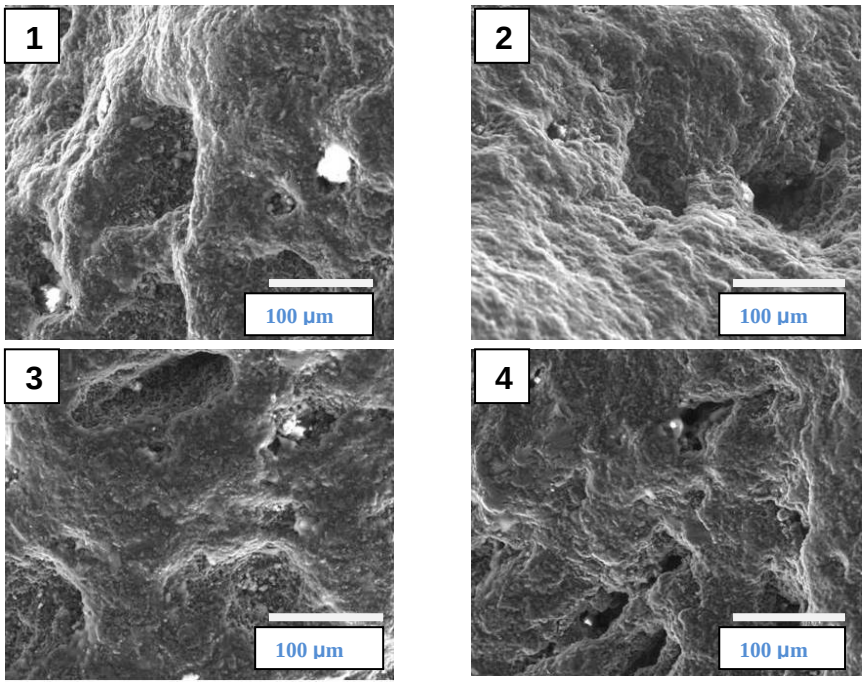

Figure 3: Secondary electron images for the carbonado sample at the four positions of interest.

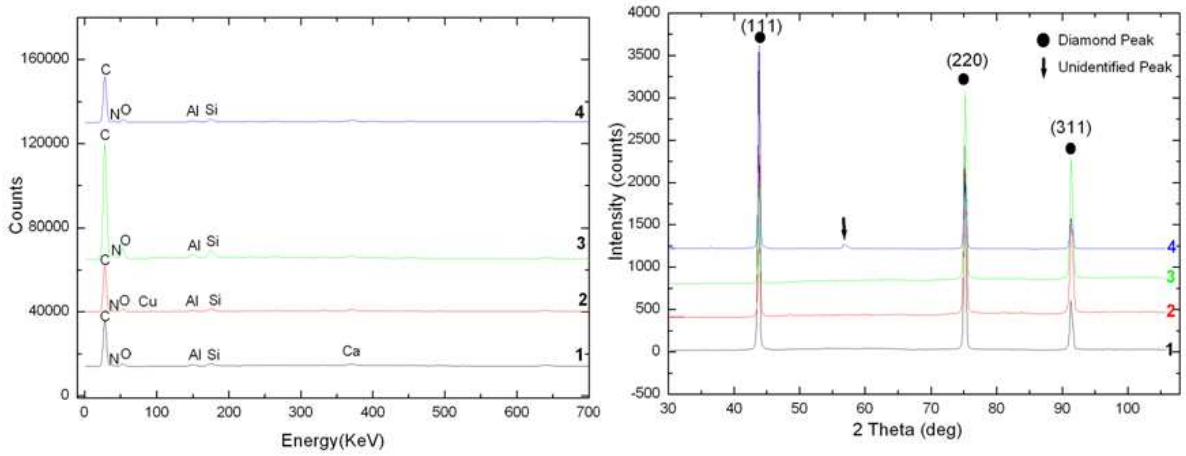

(a) **(b)**

Figure 4: Analyses results obtained at the four positions of interest on the carbonado sample: (a) Elemental composition determined with the EDS function of the SEM unit; (b) Chemical phase identification using XRD.

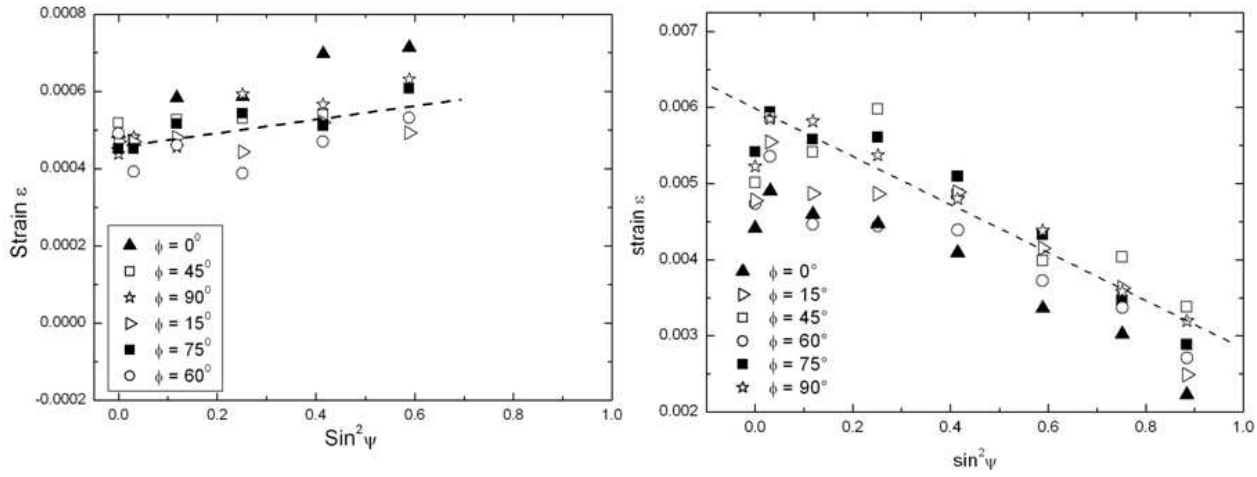

(a) **(b)**

Figure 5: *Strain* versus $sin^2\psi$ curves (a) Carbonado sample; (b) PCD compact sample as control. The large variation of curves (a) at 0.9 is anomalous and ascribed to the sample roughness. Only values up to 0.7 were subsequently used for the determination of the gradients and thus the stress values. The dotted lines in both curves give the linear trends of the data analysis.

The experimental results obtained from the various analyses at the four positions are summarized in table1. The stress analysis excluded the data points at $sin^2\psi > 0.7$ since these values were inconsistent with a linear trend. As a control, a flat surface PCD was also measured and the trend shown as reference. The EDS results indicated the major elements carbon, nitrogen and oxygen. The XRD patterns primarily show diamond in its cubic structure.

Table 1: Summary of experimental results

Measurement position	Elemental content (EDS)		Chemical phase content (XRD)	Residual stress σ_φ [MPa]
	Major	Minor		
1	C (56%) O (21%) N (12%)	Si (1.5%) Al (1.1%) Mg (0.9%)	Diamond: Cubic	55 ± 42
2	C (67%) O (16%) N (14%)	Si (1.2%) Al (0.7%) Cu (0.7%)	Diamond: Cubic	-5 ± 42
3	C (67%) O (16%) N (14%)	Si (1.3%) Al (0.8%)	Diamond:Cubic	-34 ± 85
4	C (68%) O (16%) N (13%)	Si (1.6%) Al (1.2%)	Diamond:Cubic	135 ± 50
PCD	-	-	Diamond:Cubic	-836 ± 78

Notwithstanding the literature reports of entrapments and speculation on the possible presence of the hexagonal phase of diamond, lonsdaleite, and amorphous carbon, our results do not indicate the presence of any of these. Presence of amorphous phases would manifest as a broad increase in the background of diffraction patterns at angles below 40º 2θ. The carbon versus oxygen ratios observed in this investigation does not correlate with that of normal atmospheric conditions. This in

conjunction with the sample being under a partial vacuum during the SEM analyses indicates that these gases may be present in an entrapped form (N is trapped in as a lattice impurity and O as a termination species). It is known from the literature, that minerals from the environment where the carbonado samples have been discovered, and gases such as N_2 and O_2, can be entrapped in the pores [6].

Conclusion

Notwithstanding the irregular sample shape and severe surface roughness of the carbonado, an estimate of the surface residual stress was possible by careful selection of the site of measurement and objective data analysis. Within the measurement accuracy of the X-ray technique, constrained by the sample surface roughness contributions, the stress values are generally low. The SEM results indicated the presence of large O and N contents, which could not be identified as specific chemical phases with the XRD analyses. No presence of the hexagonal lonsdaleite, or amorphous carbon was observed.

Acknowledgements

Access and personnel assistance with the XRD and SEM instruments of Necsa Limited, with special thanks to Mr.R van der Merwe and Ms. J Kabini, who assisted with the SEM analyses, as well as financial support from the NRF Internship and SANHARP student support programs are acknowledged. Prof F Viljoen, University of Johannesburg Geology Department is specifically thanked for providing the carbonado.

References

[1] *Diamond Deposits*, Eds. EI Erlichand WD Hausel, Society for Mining, Metallurgy and Exploration, Inc. USA (2002) ISBN 0-87335-213-0

[2] Y.A Litvin 2009 *Russian Geology and geophysics***50**1188-1200

[3] H. Kagi and S. Fukura . Infrared and raman spectroscopic observations of central African carbonado and implications for its origin. European Journal of mineralogy **20** (2008), 387-393

[4] S. Fukura , T. Nakagawa, and H. Kagi. High spatial photoluminesce and raman spectroscopic measurements of a natural polycrystalline diamond, carbonado. Diamond and Related Materials, **14** (2005), 1950-1954.

[5] G Kletetschka, PT Taylor, PJ Wasilewski, H.G.M. Hill 2000 *Earth and Planetary Science* Letters **181** 279-290

[6] J. Garai, S.E. Haggerty, S. Rekhi and M. Chance 2006 *The Astrophysical Journal* **653** L153-L156

[7] S De, PJ Hearnay, EP Vincenzi, J Wang 2001 *Earth and Planetary Science Letters***185** 315-330

[8] *Fundamentals of solid mechanics*, Ed. ML Gambhir, PHI Learning Private Limited, New Delhi (2009) ISBN 978-81-203-3870-8

[9] *Handbook of measurement of residual stress*, Ed. J Lu, The Fairmont Press Inc. USA (1996) ISBN 0 88173-229-X, Chapter 5 pp71 – 131.

Synthesis and characterization of a narrowband $Ca_5(PO_4)_3(OH):Gd^{3+}, Pr^{3+}$ phosphor for medical applications

P.P. Mokoena, I.M.Nagpure, H.C. Swart and O.M Ntwaeaborwa

[1] Department of Physics, University of the Free State, Bloemfontein, ZA9300, South Africa

[3]Corresponding author e-mail: ntwaeab@ufs.ac.za

Abstract: In this study, we investigate photoluminescent properties of calcium phosphate ($Ca_5(PO_4)_3(OH)$) co-doped with gadolinium (Gd^{3+}) and praseodymium (Pr^{3+}) synthesized using a wet chemistry method. The dried and calcined $Ca_5(PO_4)_3(OH):Gd^{3+},Pr^{3+}$ powder phosphors were characterized using X-ray Diffraction (XRD) and photoluminescence (PL) spectroscopy. The XRD patterns showed a single hexagonal ($Ca_5(PO_4)_3(OH)$) phase. The diffraction peaks became sharper and narrower when the calcination temperature was increased from 700 - 900 °C indicating an increase in the degree of crystallininty. PL excitation measurements showed that the phosphor can be efficiently excited at 221 nm and 274 nm. The PL emission spectrum consisted of two narrow band emission peaks with the major emission at 316 nm and the minor emission at 630 nm, which correspond to radiative transitions of Gd^{3+}. In addition a narrow emission peak at 603 nm corresponding to radiative transition of Pr^{3+} was observed from $Ca_5(PO_4)_3(OH):Pr^{3+}$. The $Ca_5(PO_4)_3(OH):Gd^{3+}$, Pr^{3+} phosphor is evaluated for a possible application as a light source in phototherapy lamps.

1. Introduction

Hydroxylapatite is one of the three occurring mineral forms of apatite (a calcium-phosphate mineral). These minerals are flourapatite ($Ca_5(PO_4)_3F$), chlorapatite ($Ca_5(PO_4)_3Cl$ and hydroxylapatite ($Ca_5(PO_4)_3OH$) [1]. Hydroxylapatite has been found to be an attractive new functional material. It has good optical properties for medical applications in artificial bones, tooth enamel and skin treatment such as psoriasis, vitiligo, atopic dermatitis and others [2]. It is also a good host for rare-earth elements to prepare phosphors that can be used, among other things, in phototherapy lamps. In this study, we investigate the optical properties of hydroxylapatite phosphor co-doped with gadolinium (Gd^{3+}) and praseodymium (Pr^{3+}). Gd^{3+} ion is a well-known quantum cutting or photon cascade emission ion [3]. Gd^{3+} ion has $4f^7$ electronic configuration and the energy gap between the ground state ($^8S_{7/2}$) and the excited state ($^6P_{7/2}$) is 32 000cm^{-1}[4]. The spectral properties of Gd^{3+} have been theoretically and experimentally studied under vacuum ultraviolet (VUV) excitation. In addition, up-conversion emission of Gd^{3+} has also been reported which shows Gd^{3+} emission peaks in the range of ~280- 320 nm. These spectral characteristics suggest that Gd^{3+} can have a wide range of UV applications. Pr^{3+} is a promising candidate for luminescence lamps due to the fact that it exhibits the photon cascade emission. Its electronic structure gives rise to luminescence in the ultra-violet (UV), visible and infrared (IR) wavelength ranges. $Ca_5(PO_4)_3(OH):Gd^{3+}$, Pr^{3+} has been reported to be a good candidate of efficient ultra-violet B (UVB) phosphor excited by VUV–light. The Pr^{3+} and Gd^{3+} ions were selected because Pr^{3+} was found that it transfer energy to Gd^{3+} to enhance the efficiency of the UV emission of the Gd^{3+} [5].The 4f-5d transition of Pr^{3+} directly absorb VUV light and transferred it non-radiatively to Gd^{3+}[6]. In this study, we have applied standard JCPDS file to determine the crystal structure of $Ca_5(PO_4)_3(OH):Gd^{3+}$, Pr^{3+} and also studied the PL properties of $Ca_5(PO_4)_3(OH):Gd^{3+}$, Pr^{3+} under UV light excitation using different concentrations. The intense is required for medical applications.

2. Experimental

2.1 Synthesis

$Ca_5(PO_4)_3(OH):Gd^{3+},Pr^{3+}$ phosphor was synthesized by the reaction of diammonium hydrogen phosphate ($(NH_4)_2HPO_4$), sodium hydroxide (NaOH) and calcium nitrate tetrahydrate (Ca $(NO_3)_3{\cdot}4H_2O$) in distilled water. In a typical preparation, 100 ml of 0.4M ($(NH_4)_2HPO_4$) solution with pH= 6.5, 100 ml of 0.1M (NaOH) solution with pH = 13.5, and 100ml of 0.6M (Ca $(NO_3)_3{\cdot}4H_2O$) with addition of 1M Pr $(NO_3)_3{\cdot}6H_2O$ and 11M Gd $(NO_3)_3{\cdot}5H_2O$ at pH = 7.3 were prepared and all the solutions were stirred vigorously at room temperature. Throughout the mixing process the pH of the system was maintained at a pH = 6.5, and after adding 0.1M NaOH the pH of the solution was maintained at 10.8. The obtained white precipitate was stirred for 12 hours at room temperature. The precipitate was first washed with distilled water and then ethanol to increase the dispersion characteristics, and finally it was dried at 80 °C for 24 hours. The dried powder was ground by using a mortar and pestle and was calcined at 900 °C for 2 hours. Different products were collected due to different concentration of Gd^{3+} and Pr^{3+} used during synthesis.

2.2 Characterization

The crystalline structure was analyzed using an X-ray Diffraction (XRD), Bruker AXS D8 Advance diffractometer using Cukα radiation (λ = 1.5406 Å). An accelerating voltage was set at 40 kV and current at 40 mA. The crystallite size (D) was calculated from XRD peaks using Scherrer equation:

$$D = 0.89\lambda / \beta \cos\theta \qquad (1)$$

where λ is the wavelength of the used Cu Kα radiation, β is the full width at the maximum of the $Ca_5(PO_4)_3(OH):Gd^{3+},Pr^{3+}$ line and θ is the diffraction angle. Photoluminescence (PL) measurements were carried out at room temperature using a Varian Cary Eclipse fluorescence spectrophotometer coupled with a monochromatized xenon lamp with an output power of (60-75W).

3. Results and discussion

Figure 1 shows the XRD patterns of $Ca_5(PO_4)_3(OH):Gd^{3+},Pr^{3+}$ powder and the peaks of the diffractogram confirms that the products had a high degree of crystallinity. Diffraction peaks of ($Ca_5(PO_4)_3(OH)$, $Ca_5(PO_4)_3(OH):Pr^{3+}$, $Ca_5(PO_4)_3(OH):Gd^{3+}$ and $Ca_5(PO_4)_3(OH):Gd^{3+},Pr^{3+}$ all correspond to the single hexagonal phase of $Ca_5(PO_4)_3(OH)$ referenced in the JCPDS file No. 73-0293. There are impurities detected around 2θ=28 and 31 on $Ca_5(PO_4)_3(OH):Gd^{3+}$ and $Ca_5(PO_4)_3(OH):Gd^{3+},Pr^{3+}$ powders. These peaks correspond to Gd^{3+} diffraction patterns [7] and they are also confirmed by JCPDS file No. 02-0864. The XRD patterns shows that the sample was well annealed at 900 ^{0}C. The average particle size was calculated from the full width at half maxima of the diffraction peaks by Scherer equation (1) and the crystallite size of the powder was ~ 70-90 nm for the samples calcined at 900 °C.

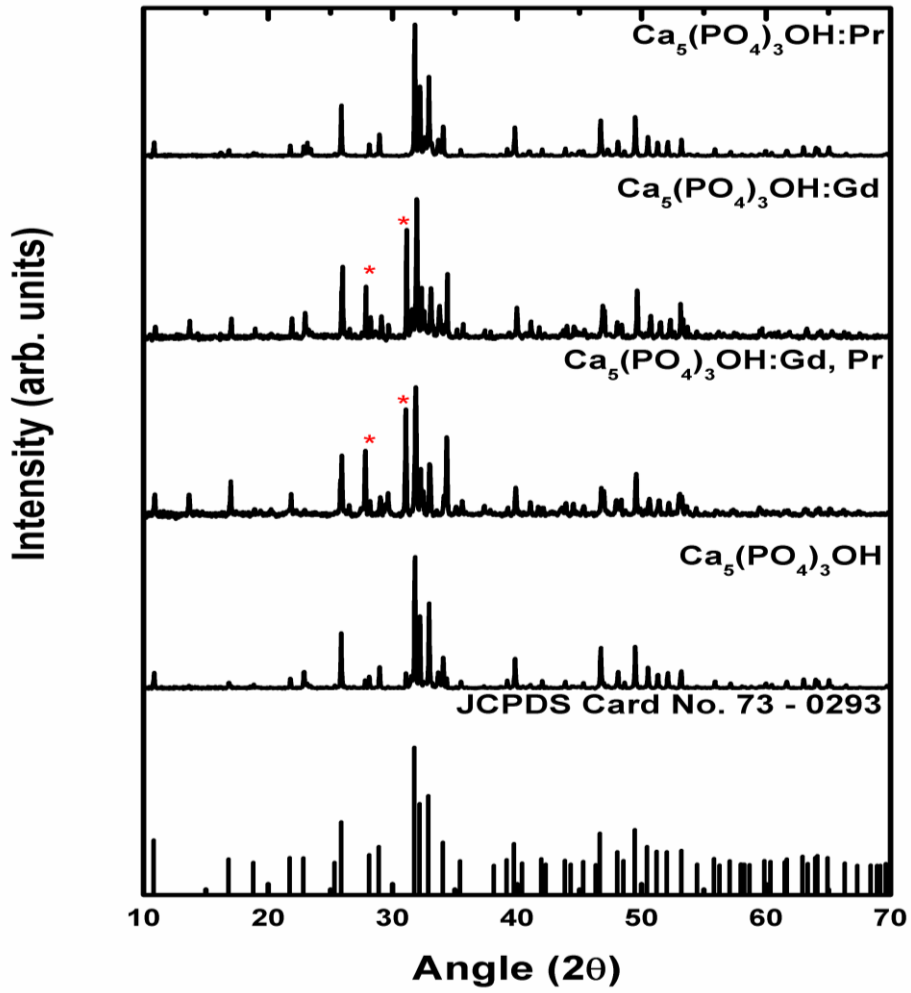

Figure 1: XRD patterns of $Ca_5(PO_4)_3(OH):Gd^{3+}, Pr^{3+}$ powder and JCPDS match (card no. 73-0293)

Figure 2 shows the PL emission and excitation spectra of $Ca_5(PO_4)_3(OH):Gd^{3+}$ calcined at 900 ^oC. The excitation spectrums were recorded when monitoring emissions at 610 nm. The excitation peaks at 221 and 274 nm are due to the $^8S_{7/2}\rightarrow{}^6G_j$ and $^8S_{7/2}\rightarrow{}^6I_j$ transitions of Gd^{3+} [8]. The PL emission of Gd^{3+} consists of two narrow band peaks with a major emission at 610 nm and minor emission at 316 nm corresponding to the $^6P_{7/2}\rightarrow{}^8S_{7/2}$ and $^8G_{7/2}\rightarrow{}^8P_{5/2}$ transitions of Gd^{3+} respectively [9]. From the UV-visible spectroscopic characteristics and luminescence properties of $Ca_5(PO_4)_3(OH):Gd^{3+}$ it was found that the quantum cutting by energy transfer from Gd^{3+} improve the red emission of Gd^{3+} ion under UV excitation but only part of the excitation energy in the excited ^6P_j states can be transferred to its red emission and nonradiative energy transfer efficiency from ^6P_j to ^6G_j. The fact that Gd^{3+} excited by $^8S_{7/2}\rightarrow{}^6G_j$ transition emits a red photon due to $^6G_{7/2}\rightarrow{}^6P_{5/2}$ transition and an UV photon due to $^6P_{7/2}\rightarrow{}^8S_{7/2}$ transition confirms the occurrence of quantum cutting of Gd^{3+} in the sample [8]. We have also varied Gd^{3+} concentrations to determine the best concentration that gives optimum PL emission intensity. Gd^{3+} emission shows concentration quenching for concentrations above 10 mol % with an emission wavelength (λ_{emi} = 610 nm) this is shown in the inset of figure 2.

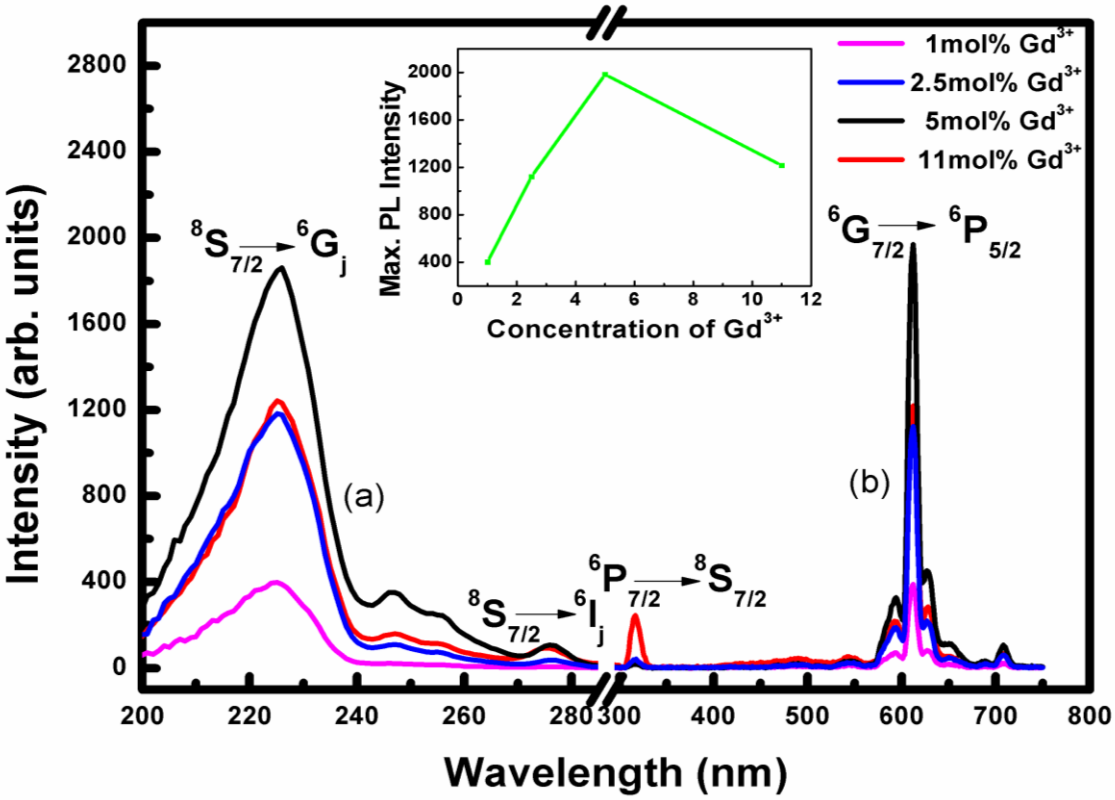

Fig 2. PL (a) excitation and (b) emission spectra of $Ca_5(PO_4)_3OH:Gd^{3+}$

Figure 3 shows the PL emission and excitation spectra of $Ca_5(PO_4)_3OH:Pr^{3+}$ calcined at 900 ^{0}C. The excitation at 447 nm (λ_{emi} = 603 nm) and 483 nm (λ_{emi} = 603 nm) are assigned to $^3H_4 \rightarrow {}^3P_2$ and $^3H_4 \rightarrow {}^3P_0$ transitions of Pr^{3+} respectively. The PL emission consists of a narrow peak at 603 nm corresponding to $^3P_0 \rightarrow {}^3H_4$ transition of Pr^{3+}. From the UV-visible spectroscopic characteristics and luminescence properties of Pr^{3+}, it was found that Pr^{3+} can exhibit different excitation bands in the UV-visible region (300~ 500 nm) [10]. We also varied the concentrations of Pr^{3+} to determine the optimum concentration for improved PL emission intensity. The inset in the figure shows that as we increase the concentration of Pr^{3+}, the PL intensity decreases and this can be attributed to concentration quenching effects.

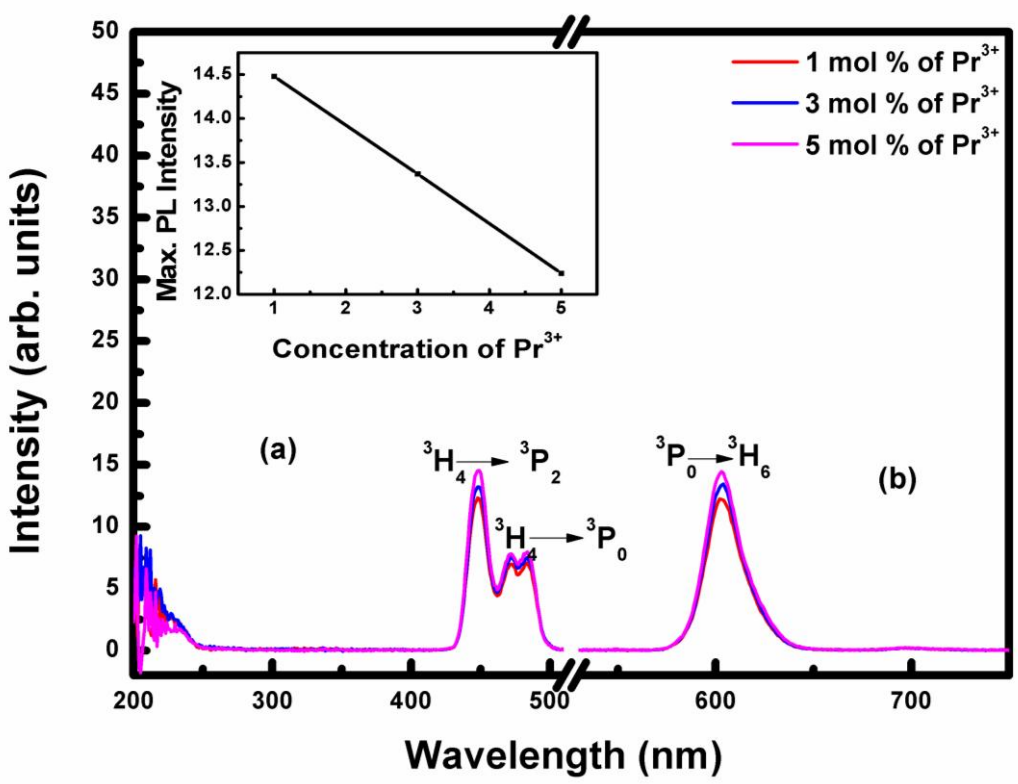

Fig 3. PL (a) excitation and (b) emission spectra of $Ca_5(PO_4)_3OH:Pr^{3+}$.

Figure 4 shows the emission and excitation spectra of $Ca_5(PO_4)_3OH:Gd, Pr^{3+}$ calcined at 900 ^{0}C. The excitation peaks at 221 nm and 274 nm (λ_{emi}=316 nm) are assigned to $^8S_{7/2}\rightarrow{}^6G_j$ and $^8S_{7/2}\rightarrow{}^6I_j$ transitions of Gd^{3+} respectively. The PL emission of $Ca_5(PO_4)_3OH:Gd^{3+},Pr^{3+}$ consists of two narrow band peaks with a major emission at 316 nm and minor emission at 630 nm corresponding to $^6P_{7/2}\rightarrow{}^8S_{7/2}$ and $^6G_{7/2}\rightarrow{}^6P_{5/2}$ transitions of Gd^{3+}. In this study Pr^{3+} acts as a sensitizer, the electrons are excited from ground state to the excited state of Pr^{3+} and eventually the excitation energy is transferred to Gd^{3+} resulting in enhanced PL emission of the peak at 316 nm. Energy is probably transferred from the ^6G_j or ^6I_j state of Pr^{3+} to the ^{6}Pj state of Gd^{3+}. As shown in the inset, the maximum PL intensity and probably the efficient energy transfer were obtained when concentrations of Gd^{3+} and Pr^{3+} are 10 and 2 mol% respectively.

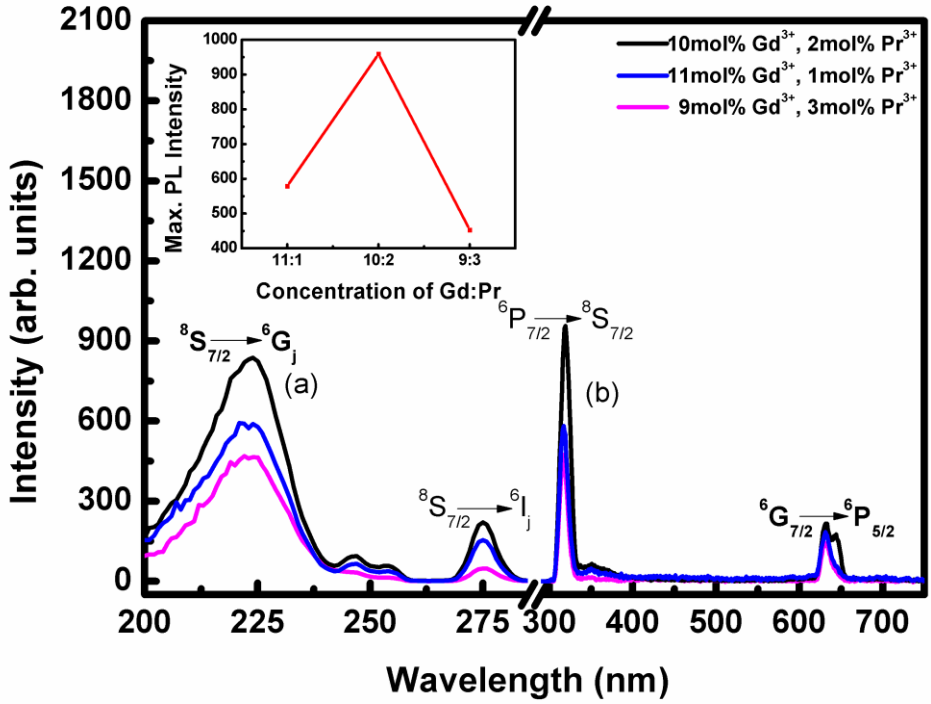

Fig 4. PL (a) excitation and (b) emission spectra of $Ca_5(PO_4)_3OH:Gd^{3+}$, Pr^{3+} .

4. Conclusion

In summary, $Ca_5(PO_4)_3(OH):Gd^{3+},Pr^3$ phosphor was successfully synthesized via wet chemical method. Gd^{3+} exhibited a narrowband red emission at 610 nm in the $Ca_5(PO_4)_3(OH):Gd^{3+}$system and it exhibited a dual emission in the UV (316 nm) and in the visible region (610 nm) in the $Ca_5(PO_4)_3(OH):Gd^{3+},Pr^{3+}$ phosphor. The UV emission was more intense than the red emission. In addition, the UV emission was enhanced by energy transfer from Pr^{3+}.

5. Acknowledgement

The authors would like to thank the University of The Free Sate and South African National Research Foundation (NRF) for financial support.

6. References

[1] http://skywalker.cochise.edu/wellerr/students/apatite/project.htm[2012/04/12]
[2] Nakashima K, Takami M, Ohta M, Yasue T, Yamauchi J, *2005 Journal of Luminescence*, **111**, 113-120
[3] Han B, Liang H, Su Q, Huang Y, Gao Z, Tao Y, *2010, Applied Physics B*, **100** 865-869
[4] Cao C, Qin W, Zhang J, Wanh Y, Zhu P, Wei G,Wang G, Kim R, Wang L, *2008, Optical Letters*, **33,** 857-859
[5] Legendziewics J, Guzik M, Cybinska J, Stefan A, Lupei V, *2008, Journal of Alloys and Compounds*, **451**, 158-164
[6] Shinji O, Rika U, Keisuke K, Hajime Y, *2009, Journal of Applied Physics*, **106**, 013522 1-5
[7] Yin Y, Hong G, *2006, Journal of Nanoparticle Research*, **8**, 755-760
[8] Zhong J, Liang H, Su Q, Zhou J, Huang Y, *2010, Applied Physics B*, **98**, 139-147
[9] Wegh R.T, Donker H, Meijerink A, *1997, Physical Review B*, **56**, 13 841- 13 848
[10] Bing Y, Xiaowen C, Xiuzhen X, *2009, Springer Science*, **19**, 221-228

Temperature dependence of current-voltage characteristics of *p*-silicon Schottky diodes for radiation-hard detectors.

S J Moloi[1]
Department of Physics, P. O. Box 392, University of South Africa, Pretoria 0003, South Africa.

E-mail address: moloisj@unisa.ac.za

Abstract: Current-voltage measurements were carried out on Schottky diodes in the temperature range of 280 – 330 K. The diodes were fabricated on undoped and on gold-doped *p*-type silicon. The temperature dependence of the saturation current, Schottky barrier height and the ideality factor were investigated. The results obtained are in good agreement with those presented in the literature and are interpreted in terms of defect levels that are induced by gold in the energy gap of silicon material. These levels are responsible for the conversion of silicon from a lifetime material to a relaxation material. The diodes fabricated from relaxation material are characterized by the Ohmic behavior and low conductivity due to the recombination of charge carriers by the levels. Properties of these relaxation diodes are not affected by the incident radiation. Thus, the diodes can be used to devise the radiation-hard detectors.

1. Introduction

Silicon diodes are used widely to fabricate radiation detectors [1]. However, the detectors do not operate efficiently due to the defect levels that are induced by the incident radiation in the energy gap of silicon [2]. In trying to improve the efficiency, much work has been carried out on silicon doped with gold [3]. This metal creates "midgap defect" (~ 0.56 eV) which is a defect level that is found very close to the centre of the energy gap [4]. The defect level is responsible for the relaxation behavior of the material [4]. The diodes fabricated from the relaxation material show the Ohmic behavior with high resistivity [4]. In silicon material, the midgap defect suppresses the effects of the incident radiation and makes properties of the diodes fabricated from the material to be independent of the incident radiation, hence to be the radiation-hard [3-4].

The results presented in the reviewed literature are based only on gold-doped *n*-type silicon [5]. At this stage the results obtained from these studies have not been fully analyzed nor understood. There is also not much literature available on gold-doping in *p*-type silicon that could be used to compare the results obtained on *n*-type silicon. It is thus essential that the effects of gold in *p*-type silicon are investigated. This paper attempts to address this weakness.

In this work Schottky diodes were fabricated on undoped and on gold-doped *p*-silicon. The diodes were characterized by current-voltage (*I-V*) technique at the temperature ranging from 280 to 330 K. The measured current is found to be increasing with temperature. This increase in the current has been found to be more pronounced on the undoped diodes than on the gold-doped diodes. This shows that the temperature does not have strong effects on the gold-doped diodes. This effect of the metal on the properties of the diodes is discussed in the paper.

[1] Corresponding author. Tel.: +27 124298018; Fax +27 124293643.

2. Experimental procedure

Current-voltage (*I-V*) measurements were carried out on the undoped and on the gold-doped *p*-silicon diodes placed in the dark. The data were acquired using a Keithley 6487 picoammeter with a voltage source. The measurements were carried out at the temperature ranging from 280 to 330 K. The data were taken from -10 V to 10 V with a voltage step of 0.01 V. A detailed description of the material preparation, device preparation and characterization has been given [6] elsewhere and will not be repeated here.

3. Results and discussion

3.1. Undoped p-silicon diodes

A variation of the reverse *I-V* characteristic with temperature for the undoped *p*-silicon diodes is shown in figure 1. It can be seen from the figure that the current increases with temperature at voltages lower than the break down voltage. The current increases by a factor of 5.0 from that of 280 K to the one of 330 K. These results show that as the temperature increases more carriers with sufficient energy are collected to the opposite electrodes to contribute to the measured current.

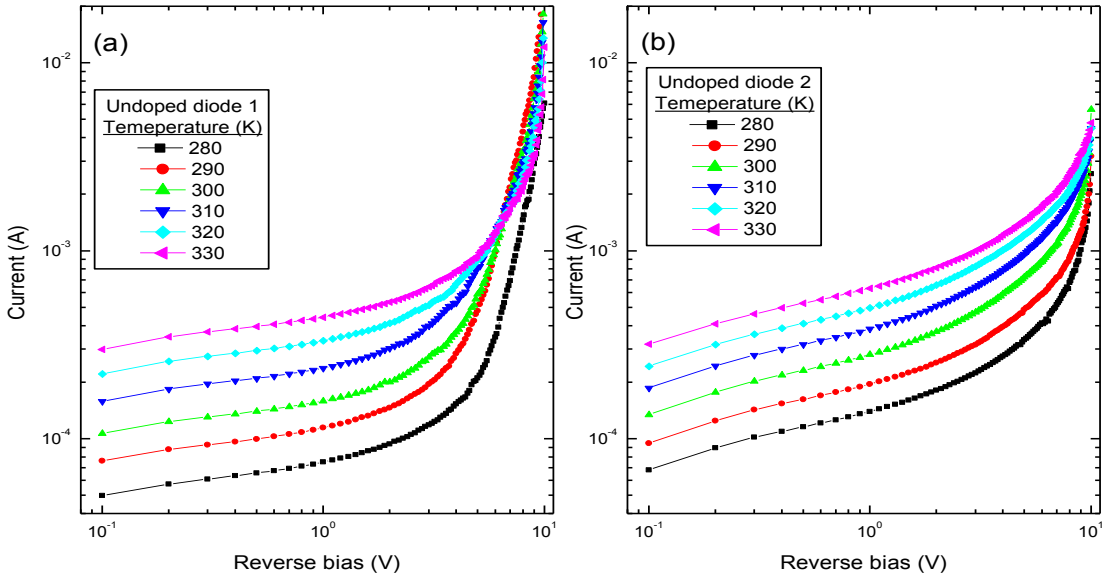

Figure 1. *A variation of the reverse I-V characteristic with temperature for the undoped p-silicon diodes.*

The reverse current (*I*) varies with temperature [7] as

$$\exp\left(\frac{E_a}{k_B T}\right) \tag{1}$$

where E_a is the activation energy of the material and $k_B T$ is the thermal energy. Equation (1) shows that a plot of ln (*I*) against T^{-1} is a linear relation from which the slope can be used to determine E_a. Figure 2 shows the plots of ln (*I*) against T^{-1} for the undoped *p*-silicon diodes. The activation energy for diodes 1 is found to be 0.29 eV and 0.24 eV for diode 2. The difference in the quantities is due to the inhomogeneous deposition of gold during the formation of Schottky contact [6].

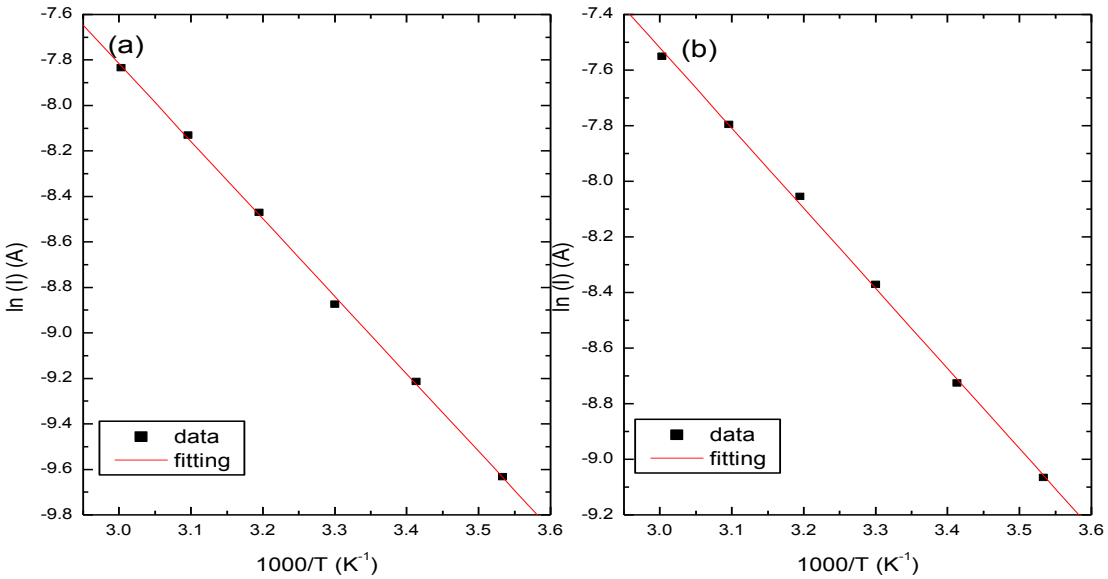

Figure 2. *The plots of ln (I) versus T $^{-1}$ at a constant reverse bias of 0.5 V for the undoped p-silicon diodes.*

Figure 3 shows the forward *I-V* characteristic of the undoped *p*-silicon diodes as a function of temperature. It can be noticed that the forward current increases with temperature for the same voltage. This increase of the current with temperature is not pronounced as that observed in figure 1, for the reverse current. This is because the reverse current is due to the generated carriers while the forward current is due to the diffusion mechanism [4]. The trends are found to be parallel to each other, especially at low voltages to indicate that they are not affected by temperature.

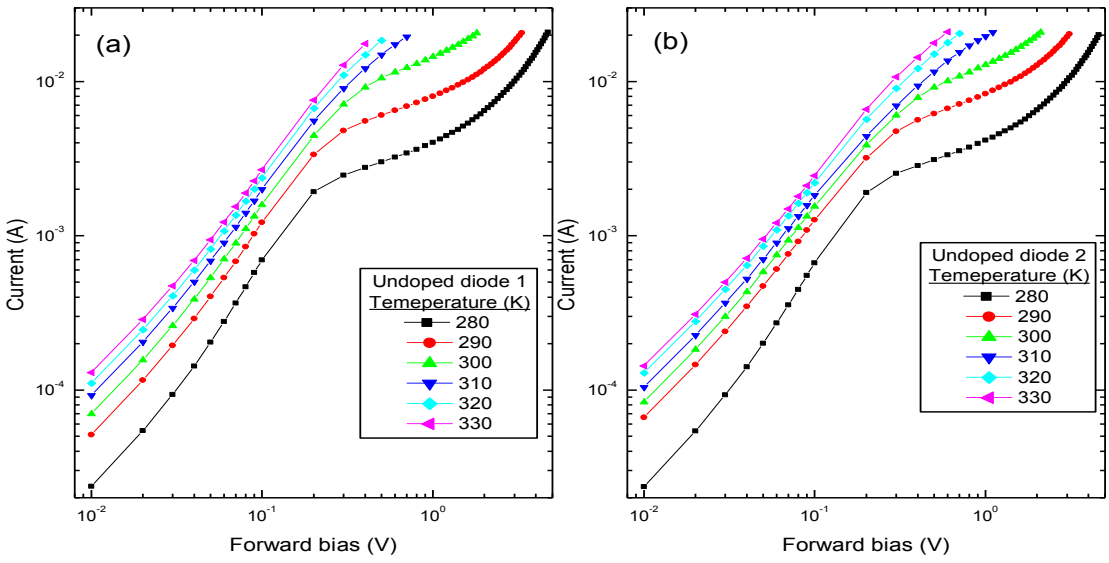

Figure 3. *A variation of the forward I-V characteristic with temperature for the undoped p-silicon diodes.*

Using the forward bias profile, the measurements were used to investigate the variation of the saturation current (I_s), the ideality factor (η) and the Schottky barrier height Φ with temperature. The procedure to determine these parameters have been documented in the literature [5-6]. The temperature measurements were taken on the four diodes fabricated on the same undoped *p*-silicon and the variation of the parameters with temperature was investigated. The average values of the parameters for all diodes were taken and are presented in table 1 for the undoped *p*-silicon diode.

Table 1: A variation of the parameters obtained from the undoped *p*-silicon diodes with temperature.

Temperature (K)	**280**	**290**	**300**	**310**	**320**	**330**
I_s (μA)	32.1	65.8	86.7	115	145	175
η	1.36	1.29	1.24	1.18	1.13	1.04
Φ (V)	0.63	0.63	0.62	0.63	0.62	0.62

The saturation current is a function of temperature [8] and the results obtained show that it increases with temperature. This shows that the amount of carriers withdrawn to the opposite electrodes to contribute to the measured current increases with temperature.

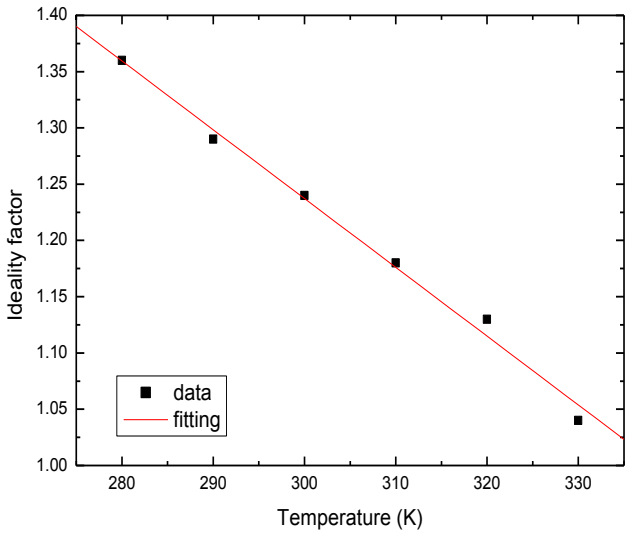

Figure 4. *Temperature dependence of the ideality factor for the undoped p-silicon diode.*

The variation of the ideality factor with temperature is not due to the slope obtained from the plot of ln (*I*) versus V. Since the trends are all parallel to each other the slopes are almost constant. Re-arranging the diode equation that relates the current with voltage [6], it can be noticed that the ideality factor decreases with an increase in temperature at the constant slope. This temperature dependence of the ideality factor for the undoped diode can be seen in figure 4. The linear relation is observed with the slope evaluated as -0.006 K^{-1}.

The results obtained in this work show that the Schottky barrier height is independent of the temperature. This independence disagrees with the results presented in the literature [9] based on the result that were obtained on the diodes fabricated on *p*-Si. The results in that case were interpreted in terms of the metal-semiconductor interface charges. The obtained results, however, agree with those presented in Ref. [10] where tungsten was used for the Schottky contacts on *p*-Si. This independence

could be due to the fact that the rate at which the temperature increases is the same as the rate at which the saturation current increases in the logarithmic scale. These rates cancel each other and make the Schottky barrier to be independent of the temperature. These results, thus, also show that the measured current is due to the space charge region not the interface charges since the Schottky barrier height is independent of the temperature.

3.2. Gold-doped p-silicon diodes

The plots of the reverse *I-V* characteristic of gold-doped *p*-silicon diodes were also generated. The plots are not shown here due to the limited size of the paper. Unlike in the case of undoped *p*-silicon diodes, the trends for gold-doped diodes were found to be close to each other to show that effects of temperature have been reduced. The trends were also found to be linear with voltage (Ohmic). This Ohmic behavior of the diodes was discussed in terms of the defect levels that were induced by gold in the energy gap of silicon material [6]. These levels recombine charge carriers and this leads to a reduction of the measured current. As a result, the resistivity of the material increases to show the relaxation behavior [9].

The plots of ln(*I*) against T^{-1} for gold-doped *p*-silicon diodes were also generated. The linear relations were found and the activation energy for diode 1 was found to be 0.16 eV and 0.18 eV for diode 2. Both activation energies are lower than those obtained from the undoped diodes. It is usual to get the activation of the control sample to be higher than the one of the defect induced samples [7; 10-11]. In the case of Ref.[7], the activation energy of the unirradiated n^+p diode was found to be 0.54 eV and 0.50 eV of the irradiated diode while in the case of Ref.[10] the activation energy of the unirradiated silicon *p-i-n* diodes was found to be 0.87 eV and 0.54 eV for the irradiated diodes. In Ref. [11] the activation energy of the control sample (silicon-germium detector) was found to be 0.43 eV and 0.27 eV for the irradiated detector. A decrease of the activation energy shows that the rate at which the carriers are generated by temperature is reduced by the defect levels induced in the material. These levels recombine the thermal generated carriers as a result, the effects of temperature on the characteristics of the diode are reduced.

The plots of the forward current of gold-doped *p*-silicon diodes were generated (not shown) and found to be Ohmic and independent of the temperature. The independence was found to be more pronounced at high voltages. At the voltages lower than 1 x 10^{-1} V the trends were parallel and very close to each other to show that the effects of temperature were reduced due to the induced defect levels.

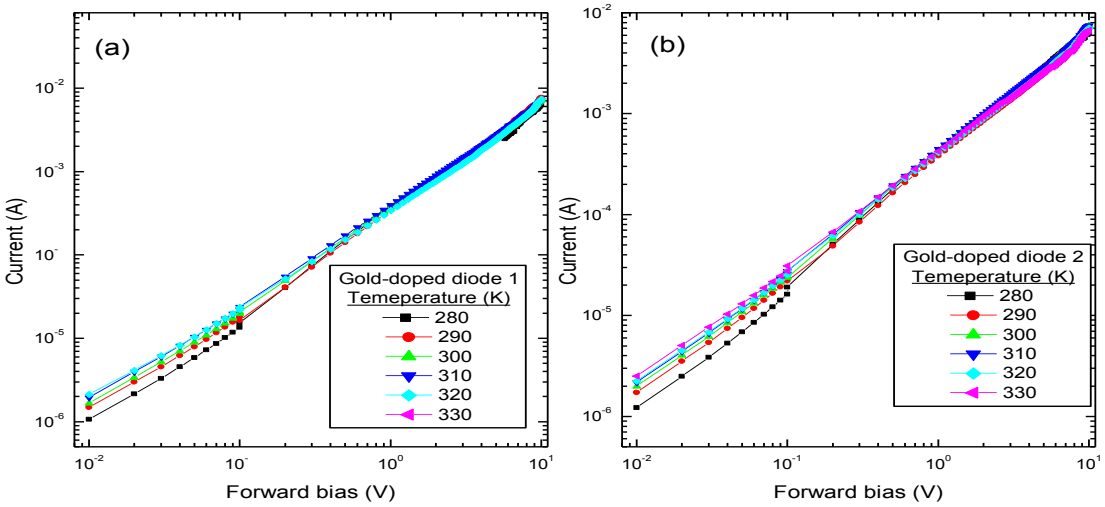

Figure 5: *A variation of the forward I-V characteristic with temperature for the gold-doped p-silicon diodes.*

The forward *I-V* characteristic of gold-doped *p*-silicon diodes shown in figure 5 was also used to determine a variation of the saturation cdurrent, the ideality factor and the Schottky barrier height with temperature. The results are shown in table 2. Similar to the undoped *p*-silicon diodes the saturation current was found to be increasing with temperature. The saturation current has been increased by the factor of 1.4, which is lower than the one obtained from the undoped *p*-silcon diodes (5.0), from that of 280 K to the one of 330 K. The Schottky barrier height, on the other hand, is found to be still independent of the temperature.

Table 2: A variation of the parameters obtained from the gold-doped *p*-silicon diodes with temperature.

Temperature (K)	**280**	**290**	**300**	**310**	**320**	**330**
I_s (μA)	10.2	11.1	11.9	12.6	13.1	13.9
η	1.90	1.87	1.84	1.80	1.76	1.73
Φ (V)	0.68	0.7	0.69	0.68	0.68	0.69

The linear relation of the ideality factor as a function of temperature was observed with the slope of $-0.003\ K^{-1}$. The magnitude of the slope is lower than the one obtained from undoped *p*-silicon diodes ($-0.006\ K^{-1}$) to show that the rate in which the carriers are thermally generated have reduced after doping with gold.

4. Conclusion

At temperatures ranging from 280 K to 330 K the effects of temperature on the *I-V* characteristics of the gold-doped *p*-silicon diodes is found to be reduced. The reduction of these effects can be justified by the reduction in magnitude of E_a after gold doping. This is due to the defects levels that are induced by gold in the energy gap of silicon. The levels recombine the charge carriers that are generated by temperature. These results are similar to those presented for the irradiated diodes under illumination [12]. Similarly, the effects of light were found to be reduced after irradiation. Thus, the gold-doping of is similar to the heavy radiation-damage. They both create defect levels that are responsible for the Ohmic behavior and increase in the resistivity (relaxation behavior) of the material. This relaxation material has been found to be radiation-hard (radiation-resistant) [3].

Acknowledgements

I kindly acknowledge the National Research Foundation (NRF) for financial assistance.

Reference

[1] Wysocki J J *et al*. 1966 *Appl. Phys. Lett.* **9** 44.
[2] Lugakov P F *et al.* 1982 *Phys. Stat. Sol.* **74** 445.
[3] Dixon R L and Ekstrand K E 1986 *Radiation Protection Dosimetry* **17** 527.
[4] Jones B K and McPherson M 1999 *Semicond. Sci. Technol.* **14** 667.
[5] Msimanga M and McPherson M 2006 *Material Sci. Engineering B* **127** 47.
[6] Moloi S J and McPherson M 2009 *Physica B* **404** 3922.
[7] Pattabi M *et al.* 2007 *Solar Energy* **81** 111.
[8] Sze S M 1981 *Physics of Semiconductor Devices*, 2nd ed. (Wiley: New York).
[9] Karatas S *et al*. 2007 *Physica B* **392** 43.
[10] Aboelfotoh M O 1991 *Solid-State Electronics* **34** 51.
[11] McPherson M 2002 *Nucl. Instr. Meth. A* **488** 100.
[12] Moloi S J and McPherson M 2011 *Nucl. Instr. Meth. A* **632** 59.

On the temperature dependence of the electron capture cross-section of the E3 deep level observed in single crystal ZnO

Wilbert Mtangi[1], Matthias Schmidt[1], P. Johan Janse van Rensburg[1], Walter E. Meyer[1], Danie F. Auret[1], Jacqueline M. Nel[1], Mmantsae Diale[1], Albert Chawanda[2]

1 Department of Physics, University of Pretoria, Private bag X20, 0028 Hatfield, South Africa
2 Midlands State University, Private Bag, 9055 Senga Gweru, Zimbabwe

E-mail: wilbert.mtangi@up.ac.za

Abstract. We report on the temperature dependence of the capture cross-section of the E3 deep level defect observed in single crystal ZnO samples. Temperature dependent deep level transient spectroscopy reveals an increase in the DLTS peak height with an increase in the rate window frequency for the E3 level which is a proof that the E3 deep level has a temperature activated capture cross-section. However the observed capture rate is not constant during the filling pulse but depends on the occupancy of the defect itself. This phenomenon is in contradiction with what is expected of an ideal deep level.

1. Introduction

ZnO is a wide and direct bandgap semiconductor with experimental bandgap energy of about 3.4 eV. Deep level transient spectroscopy (DLTS) measurements performed on differently grown ZnO crystals reveal the presence of the E3 deep level defect with an activation enthalpy of between 0.29 eV and 0.31 eV and an apparent capture cross-section of 5×10^{-16} cm^2 to 10^{-14} cm^2 [1, 2, 3, 4, 5, 6]. However its ionisation energy as well as its energy barrier for electron capture is not known yet, whereas in established semiconductors such as GaAs and Si, capture barrier energies for most defect levels are well known. The capture barrier is usually obtained using emission rate DLTS scans and varying the filling pulse width as suggested by Henry and Lang [7]. A second method which uses DLTS rate window scans with short filling pulses (less than 10 μs) has been employed by Zhao *et al.* [8], Criado *et al.* [9], Telia *et al.* [10] and Cavalcoli *et al.* [11]. In this paper, we report on the electronic properties of the E3 deep level in a bulk single crystal ZnO sample obtained from Cermet Inc.

2. Sample preparation

In preparation of the DLTS measurements, crystal cleaning was performed as in reference [12]. Ohmic contacts with a composition of Al/Au were deposited on the O-polar face using the resistive evaporation technique at a pressure of approximately 10^{-6} Torr. Finally, Iridium Schottky contacts with a diameter of 0.5 mm and thickness of 100 nm were electron beam deposited onto the Zn-polar face under vacuum at a pressure of approximately 10^{-7} Torr.

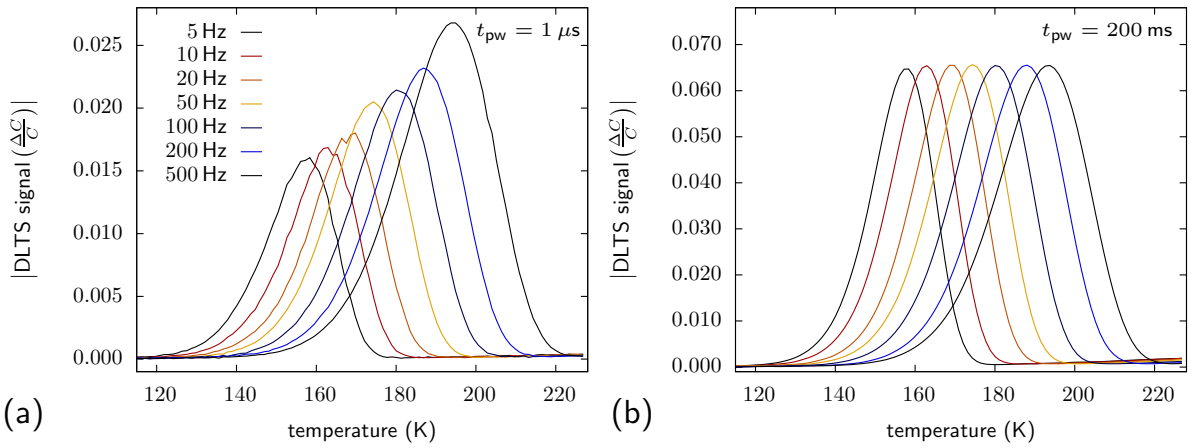

Figure 1. The E3 peak in deep level transient spectroscopy temperature scans conducted at different rate window frequencies using 1 μs filling pulses (a) and 200 ms filling pulses (b) that flattened the bands. During the recording of the capacitance transients the sample was reverse biased at 2 V.

Current voltage measurements at room temperature confirmed that the sample was suitable for DLTS measurements and a net doping density of $N_{\mathsf{net}} = 4.6 \times 10^{16}\,\mathrm{cm}^{-3}$ was obtained from CV measurements using the van Opdorp analysis [13].

3. Results and discussion

Emission DLTS rate window scans were performed in the dark in a closed cycle helium cryostat and revealed the presence of the E3 deep level, as shown in Figure 1. Arrhenius analysis[1] of the temperature dependence of the thermal emission rate of the E3 level yielded an activation enthalpy of 0.30 eV and an apparent capture cross-section of $10^{-14}\,\mathrm{cm}^2$. It was observed that the spectra differ depending on the filling pulse width (t_{pw}). For $t_{\mathsf{pw}} = 1\mu$s filling (Figure 1(a)), the DLTS peak height increases with an increase in rate window frequency, whereas for long enough filling pulse widths (Figure 1(b)), the peak height was constant for all rate window frequencies. The variation of the DLTS peak height with chosen rate window frequency for the E3 deep level has previously been observed but to the best of our knowledge, no explanation was given. In the following we are going to shed some light on this observed effect. The DLTS experiment allows one to prepare an initial probability to find a defect state occupied by an electron, q_{in}. This is achieved by the application of a filling pulse and monitoring the capacitance transient afterwards. The DLTS signal peak height, $\Delta C/C$ is related to the trap concentration N_{t} and the difference in the occupancy probabilities by,

$$\frac{\Delta C}{C} = -\frac{N_{\mathsf{t}}}{2N_{\mathsf{net}}}\left(q_{\mathsf{fin}} - q_{\mathsf{in}}\right) \tag{1}$$

where q_{fin} is the final occupation probability. The differential equation for the time evolution of the occupancy probability $q(t)$ of a defect state is [14]

$$\frac{\mathrm{d}q(t)}{\mathrm{d}t} = c_{\mathsf{n}}\left[1 - q(t)\right] - e_{\mathsf{n}}^{\mathsf{th}} q(t). \tag{2}$$

[1] ZnO effective mass: 0.27 m_{e}

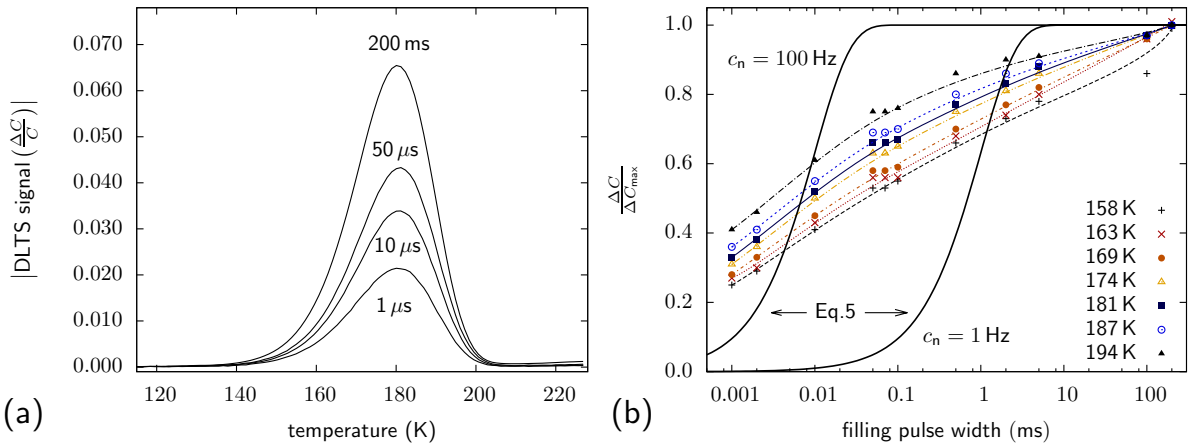

Figure 2. a) Dependence of the E3 DLTS peak height on filling pulse width t_{pw} at a rate window frequency of 100 Hz. b) Symbols represent the variation of the measured, normalised DLTS peak height with filling pulse width and sample temperature. The black solid lines are the graphical representation of equation 5 assuming a constant capture cross-section during the filling process.

c_{n} denotes the thermal capture rate for electrons and its temperature-dependence is given by

$$c_{\mathsf{n}}(T) = \sigma_{\mathsf{n}}(T)\,\langle v_{\mathsf{th}}\rangle\,(T) n(T) = \sigma_{\mathsf{n}}^{\infty} \exp\left(-\frac{E_{\mathsf{b}}}{k_{\mathsf{B}} T}\right) \langle v_{\mathsf{th}}\rangle\,(T) n(T) \tag{3}$$

where E_{b} is the barrier for electron capture, $\langle v_{\mathsf{th}}\rangle\,(T)$ is the thermal velocity of electrons and n is the free electron concentration available for capture. Since at a particular temperature, c_{n} is considered to be a constant and assuming that during the filling process, $e_{\mathsf{n}}^{\mathsf{th}} \ll c_{\mathsf{n}}$, the solution of equation 2 is given by

$$q(t) = 1 - \exp\left(-c_{\mathsf{n}} t\right). \tag{4}$$

Thus, equation 1 can be written as,

$$\frac{\Delta C}{C} = \frac{N_{\mathsf{t}}}{2N_{\mathsf{net}}}\left(1 - \exp\left[-c_{\mathsf{n}} t_{\mathsf{pw}}\right]\right) \tag{5}$$

since for the maximum DLTS peak height, $q_{\mathsf{fin}} \approx 0$.

In the light of this, we studied the filling process of E3 by varying the filling pulse width at fixed rate window frequency. The results are presented in Figure 2(a). As expected, the DLTS peak height increases with increasing filling pulse width as well as increasing temperature, Figure 2(b). However this increase is not in accordance with equation 5 and therefore the Henry and Lang approach [7] cannot be applied. In particular, the slope of the measured, normalised DLTS peak height versus filling pulse width plot is less steep compared to the one predicted by equation 5. A suggestion of this is as follows.

Since every solution of equation 2 must be exponential if c_{n} and $e_{\mathsf{n}}^{\mathsf{th}}$ are constant, only a change of c_{n} during the filling process can explain our observations. According to equation 3, this change can be attributed to either a decrease in σ_{n} (at the same temperature) or a decrease in n in the vicinity of the defect while it is being filled. The first possibility might originate from defect-defect interaction which cannot be excluded at doping levels of $N_{\mathsf{net}} = 4.6 \times 10^{16}\,\mathrm{cm}^{-3}$. The latter, which to our opinion might be more probable, is due to the charging up of grain

boundaries. This results in a double Schottky barrier and therefore a depletion region which lowers the local electron density [15]. Further investigations and analysis are required and will be performed.

4. Conclusions

In conclusion, the electron capture of the E3 deep level in ZnO was studied in detail by DLTS. The capture process cannot be described by a single exponential filling of the defect state, as would be the case for a simple capture barrier of an isolated point defect. Due to this difficulty, the capture barrier could not be obtained from emission DLTS rate window scans with varying pulse widths without employing a more involved analysis. Furthermore there is a high uncertainty associated with the high temperature limit of the capture cross-section obtained from standard Arrhenius analysis which is frequently reported.

Acknowledgments

The authors wish to thank the University of Pretoria for the financial support. Matthias Schmidt was funded by the Postdoctoral Fellowship Program of the University of Pretoria. This work is based upon research supported by the National Research Foundation (NRF). Any opinion, findings and conclusions or recommendations expressed in this material are those of the author(s) and therefore the NRF does not accept any liability in regard thereto.

References

[1] F.D. Auret, S.A. Goodman, M.J. Legodi, W.E. Meyer, and D.C. Look. *Electrical characterization of vapor-phase-grown single-crystal ZnO*. Appl. Phys. Lett., **80** 1340–1342, (2002).

[2] A.Y. Polyakov, N.B. Smirnov, A.V. Govorkov, E.A. Kozhukhova, S.J. Pearton, D.P. Norton, A. Osinsky, and A. Dabrian, *Electrical Properties of Undoped Bulk ZnO Substrates*. J. Electron. Mater., **35** 663-669, (2006)

[3] F.D. Auret, W.E. Meyer, P.J. Janse van Rensburg, M. Hayes, J.M. Nel, H. von Wenckstern, H. Schmidt, G. Biehne,H. Hochmuth, M. Lorenz, M. Grundmann, *Electronic properties of defects in pulsed-laser deposition grown ZnO with levels at 300 and* 370 meV *below the conduction band*. Physica B, **401-402** 378-381 (2007)

[4] H. von Wenckstern, K. Brachwitz, M. Schmidt, C.P. Dietrich, M. Ellguth, M. Stlzel, M. Lorenz and M. Grundmann, *The E3 Defect in MgZnO*. J. Electron. Mater., **39** 584-588, (2010)

[5] W. Mtangi, F.D. Auret, P.J. Janse van Rensburg, S.M.M. Coelho, M.J. Legodi, J.M. Nel, and W.E. Meyer, *A comparative study of the electrical properties of Pd/ZnO Schottky contacts fabricated using electron beam deposition and resistive/thermal evaporation techniques*. J. Appl. Phys., **110** 094504, (2011)

[6] Matthias Schmidt, *Space Charge Spectroscopy Applied to Defect Studies in Zinc Oxide Thin Films*, PhD thesis, Universität Leipzig, Germany (2012).

[7] C.H. Henry and D.V. Lang, *Nonradiative capture and recombination by multiphonon emission in GaAs and GaP*. Phys. Rev. B **15** 989-1016 (1977).

[8] J.H. Zhao, T.E. Schlesinger, and A.G. Milnes, *Determination of carrier capture cross sections of traps by deep level transient spectroscopy of semiconductors*. J. Appl. Phys. **62** 2865–2870 (1987).

[9] J. Criado, A. Gomez, E. Muñoz, and E. Calleja, *Novel method to determine capture crosssection activation energies by deeplevel transient spectroscopy techniques*. Appl. Phys. Lett. **52** 660-661 (1988).

[10] A. Telia, B. Lepley, and C. Michel, *Experimental analysis of temperature dependence of deeplevel capture crosssection properties at the Au oxidized InP interface*. J. Appl. Phys. **69** 7159-7165 (1991).

[11] D. Cavalcoli, A. Cavallini, E. Gombia, *Anomalous temperature dependence of deep-level-transient-spectroscopy peak amplitude*. Phys. Rev. B **56** 14890-14892 (1997).

[12] W. Mtangi, F.D. Auret, C. Nyamhere, P.J. Janse van Rensburg, M. Diale, and A. Chawanda, *Analysis of temperature dependent I-V measurements on Pd/ZnO Schottky barrier diodes and the determination of the Richardson constant*. Physica B **404** 1092-1096 (2009).

[13] C. van Opdorp. *Evaluation of doping proles from capacitance measurements*. Solid State Electron., **11** 397 (1968).

[14] P. Blood and J.W. Orton. *The Electrical Characterization of Semiconductors: Majority Carriers and Electron States*, volume 1. Academic Press, US, 1992.

[15] F. Greuter and G. Blatter, *Electrical properties of grain boundaries in polycrystalline compound semiconductors*. Semicond. Sci. Technol. **5** 111-137 (1990).

Modification of the near surface optical and electrical properties of bulk GaSb (100) resulting from a sulphur-based chemical treatment

DM Murape, N Eassa, K Talla, JH Neethling, JR Botha and A Venter

Department of Physics, Nelson Mandela Metropolitan University, PO Box 77000, Port Elizabeth, 6031, South Africa

E-mail: Davison.Murape@nmmu.ac.za (corresponding author)

Abstract. An alternative sulphur blended solution ($[(NH_4)_2S/(NH_4)_2SO_4]$ + S) is reported for stabilizing the very reactive surface of bulk Te doped *n*-GaSb (100). Scanning electron microscopy shows a significant improvement in morphology due to an etching effect while the photoluminescence is enhanced three-fold. The surface state density, calculated from the forward *I-V* characteristics of a Au/*n*-GaSb Schottky, is ~10^{14} cm^{-3} and concentrated around the middle of the band gap. Notably, a three-fold reduction in the surface state density is observed following treatment. Treatment also seems to unpin the Fermi level as is evidenced by an increase in the barrier height. Importantly, the reverse leakage current also reduces.

1. Introduction

GaSb is a versatile III-V semiconductor material and heterojunctions of GaSb show great promise as near infra-red (IR) lasers, light emitting diodes (LEDs), pollutant gas detectors, thermo-photovoltaic devices and photo-detectors in the wavelength regions 2-5 and 8-14μm [1, 2]. Additionally, its matching lattice parameter renders it an excellent substrate for the epitaxial growth of ternary and quaternary III-V compound semiconductors and strained layer superlattices such as (AlGaIn)(AsSb). By varying the composition of ternary semiconductors, the lattice constant and band gap can be tailored for specific applications. Undesirably however, the GaSb surface is highly reactive, resulting in the spontaneous formation of a native oxide (Ga-O and Sb-O) layer. This, together with an interfacial Sb layer contributes substantially to the presence of surface and interface states that may act as either traps or nonradiative recombination centres that will impede the development of GaSb based photonic devices.

Passivation of the GaSb surface has been demonstrated as an important step in the development of GaSb based devices. Dutta *et al.* [3], studied ruthenium passivation of the GaSb surface while Hearn *et al*. [4], studied the passivation of GaSb by ZnS. In addition to this, Dutta *et al.* [5] and Liu *et al.* [6, 7] also studied the effect of sulphur passivation on predominantly the electrical properties of this material. The purpose of this study was to investigate the effect of an alternative sulphur blended $[(NH_4)_2S0_4/(NH_4)_2S]$ solution (from hereon called ($[(NH_4)_2S/(NH_4)_2SO_4]$ + S)) on the surface, optical and electrical properties of bulk *n*-GaSb. Current-voltage (*I-V*) characteristics of Au/*n*-GaSb Schottky barrier diodes (SBDs) were used to study the effect of sulphurization on the surface state density (N_{ss}).

2. Experimental

Bulk Te-doped *n*-GaSb (supplied by Semiconductor Waver, Inc., $n \sim 2 \times 10^{17}\ cm^{-3}$) was sulphurized in an aqueous solution of $[(NH_4)_2S/(NH_4)_2SO$ + S] in an attempt to reduce the surface state density. The material was degreased by successively (×3) boiling it in trichloroethylene, acetone and methanol, followed by a quick rinse in de-ionized (DI) water (ρ = 18.2 MΩ.cm). The samples were then blown dry with nitrogen. Two samples were subsequently investigated:

i) *Sample A:* no further treatment after degreasing (referred to as reference or as-received).
ii) *Sample B:* etched in 18.5 % HCl, rinsed in DI water, then immersed in ($[(NH_4)_2S/(NH_4)_2SO_4]$ + S) at 60°C for 30 min. The solution was prepared by dissolving 0.2 g of sulphur in 15 ml of a 10% aqueous $(NH_4)_2S$ solution. According to the supplier, each litre of $(NH_4)_2S$ contained 4.7g of $(NH_4)_2SO_4$, resulting in a pH of 8.2.

Following treatment, the samples were again rinsed in DI water, blown dry and promptly loaded into a Jeol JSM-700 1F Field Emission Scanning Electron Microscope (FESEM) for surface

morphology assessment. In order to investigate possible etching by the sulphur treatment, half of a sample was masked using wax followed by sulphur treatment. The surfaces were subsequently de-waxed, rinsed (DI H_2O) and dried where-after the surface was profiled using a Dektak 150 Surface Profiler.

For photoluminescence (PL) measurements, samples were loaded in a closed-cycle liquid helium cryostat. Spectra were recorded at 11 K using the 514.5 nm line of an Ar^+ laser (set at 7 mW) as the excitation source. The PL signal was detected by a liquid nitrogen cooled Ge photo-detector. For (*I-V*) measurements, Au Schottky barrier diodes were fabricated on both the reference and the ($[(NH_4)_2S/(NH_4)_2SO_4]$ + S) treated *n*-GaSb samples. After degreasing but prior to sulphur treatment, ohmic contacts were fabricated on one side of the sample by resistively depositing a 100 nm AuGe (88:12) layer followed by a 50 nm Ni layer, capped with a 50 nm Au layer. The contact resistance was minimized by annealing samples in Ar at 300°C for five minutes. The samples were again degreased, sulphurized and then blown dry with pure N_2 prior to loading into a vacuum system with a base pressure of $2 \times 10^{-5}\ torr$. Circular Au Schottky contacts ($\phi = 0.50\ mm$), 100 nm thick, were subsequently resistively evaporated through a metal shadow mask. Room temperature *I-V* measurements were performed to assess the electrical response of the SBDs.

3. Results and Discussion

Figure 1 A and B depicts typical SEM micrographs of the as-received and sulphurized GaSb surfaces. The surface of the reference (*sample A*) is rather irregular and contains a multitude of, what appears to be, supplier related polishing scratches. Samples treated with ($[(NH_4)_2S/(NH_4)_2SO_4]$ + S) (*sample B*), however, appear smooth suggesting either uniform etching or covering of the surface features by a sulphur treatment related deposit.

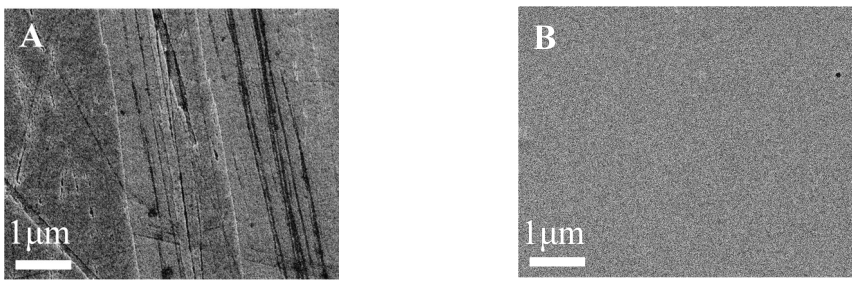

Figure 1, SEM micrographs of (A) the reference and (B) the ($[(NH_4)_2S/(NH_4)_2SO_4]$ + S) treated samples.

Figure 2 depicts Dektak step measurements of the GaSb surface after exposing it to ($[(NH_4)_2S/(NH_4)_2SO_4]$ + S) for predetermined time intervals. A non-linear time dependent etching effect is clearly evident. Treatment for a period of 30 minutes resulted in an etch step of approximately 6μm across the sulphur exposed surface. It is instructive to note that the etch rate is temperature dependent as it deviated considerably (±20%) for repeat experiments due to fluctuations in the bath temperature.

Figure 3 shows PL spectra obtained from *samples A* and *B*. Both spectra exhibit a broad range of transitions as is expected for bulk material. Two main peaks at 0.755 eV and 0.754 eV respectively are clearly visible. Two "shoulders", one towards the higher energy (0.777 eV) and the other towards the lower energy (0.733 eV) side are clearly distinguishable. Undoped GaSb is intrinsically *p*-type due to gallium vacancies (V_{Ga}) and gallium antisite defects (Ga_{Sb}), acting as acceptors. These acceptors are reported to induce a luminescence band, called the A band, centred around 777 meV [8].

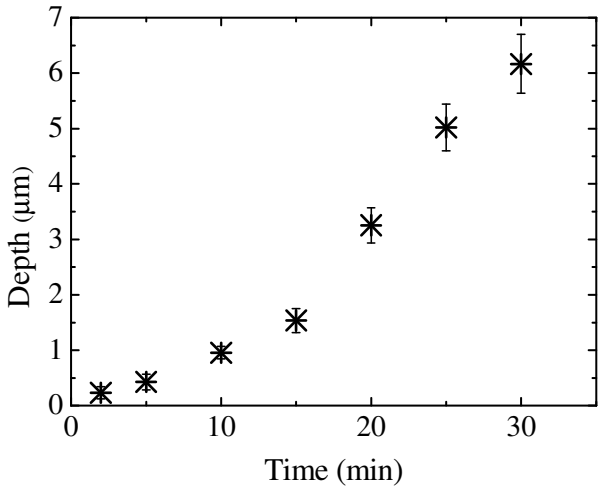

Figure 2, The etch rate of bulk n-GaSb treated with the aqueous ($[(NH_4)_2S/(NH_4)_2SO_4]$ + S) solution for predetermined times.

There are clear differences in the PL intensity and line width for these samples. The intensity of spectrum *B* is approximately 3 times of that of spectrum *A* suggesting that sulphur treatment improves the quantum efficiency in the near surface region of the material.

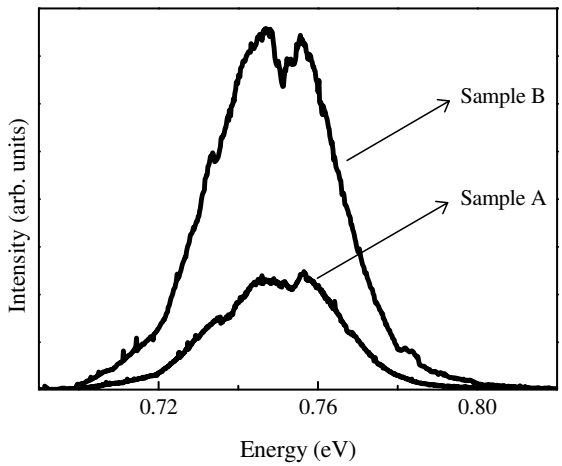

Figure 3, PL spectra obtained from the reference and the sulphur treated GaSb surfaces.

Diode characteristics extracted from *I-V* curves measured at room temperature revealed an ideality factor of 3.1 and a barrier height of 0.43 eV for *sample A*. Additionally, the reverse leakage current for *sample A* was significantly higher than for *sample B*. A rectification ratio of 5, determined at at ±0.2 V was obtained for *sample A*. For samples treated with *($[(NH_4)_2S/(NH_4)_2SO_4]$ + S)* the ideality factor reduced from 2.73 to 1.17 while the barrier height increased from 0.44 eV to 0.54 eV [9]. The rectification ratio increased 10 fold suggesting that surface states responsible for tunnelling and surface recombination currents, had been reduced. The reverse leakage currents for both *samples A* and *B* do not saturate, possibly suggesting that surface states responsible for recombination have only been partially "passivated" by sulphurization. It is instructive to note also that the "high" free carrier concentration of these samples will result in a narrow depletion favouring quantum mechanical tunnelling. Apart from being detrimental to general device operation, large reverse leakage currents also pose a challenge for the analysis of electrically active defects in materials by Deep Level Transient Spectroscopy (DLTS).

In Schottky structures the logarithm of the current is linearly proportional to the applied bias only if the series resistance (R_s) is negligible. Surface states will contribute to the series resistance of the device and will cause the logarithm of the current to deviate from linearity (bend downward) for increasing forward biases. When surface states are present, the capture and release of charge

from them will dominate the current through the device consequently affecting the effective barrier height [10]. This bias dependence of ideality factor (and barrier height) therefore enables the quantification of the surface state density (N_{ss}) and its distribution within the band-gap of the semiconductor.

According to Card and Rhodherick [11] the interface state density (N_{ss}) for a Schottky diode in equilibrium with the semiconductor is given by:

$$n(V) = 1 + \frac{\delta}{\varepsilon_i}\left[\frac{\varepsilon_s}{W} + qN_{ss}\right],$$

where *n(V)* is the voltage dependent ideality factor, W is the space charge width, ε_s and ε_i, are the permittivity of the semiconductor and the interfacial layer respectively. δ is the thickness of the interfacial layer [12, 13, 14] which has been estimated from XPS depth profiles. Figure 4 depicts the energy distribution of the interface states with respect to the bottom of the conduction band ($E_c - E_{ss}$).

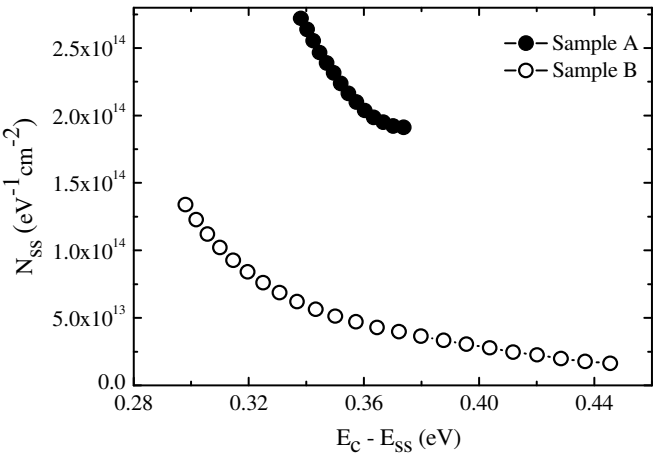

Figure 4, Density of the interface states (N_{ss}) as a function of position in the band gap ($E_c - E_{ss}$) for the diodes fabricated on sample A and *sample B respectively.*

An exponential increase in the surface state density is apparent for both samples ranging from mid-gap towards the bottom of the conduction band, similar to observations reported by Hudait et al. and Karatas et al. [12, 13] respectively. Clearly the surface state density is higher in s*ample A* compared to *sample B,* suggesting that sulphurization reconstructs/"passivates" the GaSb surface, consequently reducing the surface state density. This reduction may account for the lowering in the ideality factor and reverse leakage via trap assisted tunnelling.

4. Conclusions

The sulphur blended [$(NH_4)_2S/(NH_4)_2SO_4$] solution etches the bulk *n*-GaSb surface resulting in improved morphological, optical and electrical properties. Treatment enhances the observed photoluminescence, an indication of partial passivation of nonradiative recombination centres. Passivation also improves the electrical properties of Au/*n*-GaSb Schottky structures as evidenced by a lower reverse leakage current, a larger barrier height and lower ideality factor for *sample B* compared to *sample A*. Quantification of the interface state density shows that it is significantly reduced by sulphur treatment.

Acknowledgements
This work is based upon research supported by the SA Research Chairs Initiative of the Department of Science and Technology and National Research Foundation, as well as by the NMMU. The authors also thank Mr D O'Connor and JB Wessels for technical assistance.

References

[1] P.S. Dutta, H.L. Bhat, V. Kumar, *J. App. Phys,* vol. 81, p. 5821, 1997.

[2] J.A. Robinson, S.E. Mahoney, *J. Appl. Phys,* vol. 96, p. 2684, 2004.

[3] P. S. Dutta, K. S. R. Koteswara Rao, H. L. Bhat, V. Kumar, *J. Appl. Phys,* vol. 77, p. 4825, 1995.

[4] G. Hearn, K. Bernerjee, S. Mallick, S. Ghosh, *Journ. Undergrad. Res,* vol. 1, p. 76, 2007.

[5] P.S Dutta, K.S. Sangunni, H.L. Bhat, V. Kumar, *Appl. Phys. Lett.,* vol. 65, p. 1695, 1994.

[6] Z.Y. Liu, T.F Kuech, *Appl. Phys. Lett,* vol. 83, p. 2587, 2003.

[7] Z. Y. liu, D.A. Saulys, T. F. Kuech, *Appl. Phys. Lett,* vol. 85, p. 4391, 2004.

[8] P. Hidalgo, B. Mendez, P. S. Dutta, J. Piqueras, E. Dieguez, *Phys. Rev. B,* vol. 57, p. 6479, 1997.

[9] D.M. Murape, N. Eassa, J.H. Neethling, R. Betz, E. Coetse, H.C. Swart, J.R. Botha, A. Venter, *Applied Surface Science,* vol. 258, p. 6753, 2012.

[10] V. Mikhelashvili, G. Eisenstein, R. Uzdin, *Solid-State Electronics,* vol. 45, p. 143, 2001.

[11] H.C. Card, E.H. Rhoderick, *J. Phys. D,* vol. 4, p. 1589, 1971.

[12] A. Taratoglu, S Altindal, *Microelectronic Engineering,* vol. 85, p. 233, 2008.

[13] M.K. Hudait, S.B. Krupanidhi, *Materials Science and Engineering,* vol. B87, p. 141, 2001.

[14] S. Karatas, S. Altindal, A. Turut, M. Cakar., *Physica B,* vol. 392, p. 43, 2007.

Signature of Electron-Phonon Correlation in the Band Structure of $Sr_4Ru_3O_{10}$

P. Ngabonziza, E. Carleschi and B.P. Doyle

Department of Physics, University of Johannesburg, P.O. Box 524 Auckland Park 2006, Johannesburg, South Africa

E-mail: ecarleschi@uj.ac.za

Abstract. We report the first angle resolved photoemission spectroscopy measurements on the three-layered strontium ruthenate $Sr_4Ru_3O_{10}$. These data reveal the presence of kinks in the near-Fermi-level band dispersion, with energies ranging from 30 meV to 69 meV. The kink energies have a good correspondence with the energy of the phononic modes previously reported by Raman spectroscopy measurements and lattice dynamic calculations. We interpret this as the fingerprint of strong electron-phonon coupling present in this system.

1. Introduction

In correlated electron systems, electronic excitations are characterized by an energy E and a momentum $\hbar k$ which are related through the dispersion relation $E(k)$. The interactions of electrons with other excitations, such as phonons or spin excitations, may produce anomalies in the dispersion relation that lead to sudden changes, referred to as *kinks*, in the slope of the energy-momentum dispersion close to the Fermi-level. The kink energies are often related to the relevant energy scales present in the investigated system, such as the coupling of electrons with other excitations. In particular, when relevant phonon modes are present in the system, investigation of kink energies can give rich information about the electron-phonon coupling present in the compound.

In numerous works on strongly correlated electron systems, a detailed analysis of the quasiparticle band dispersion has been performed and the existence of kinks has been revealed at energies within 100 meV from the Fermi level [1, 2]. For high-T_c cuprate superconductors in particular, kinks have been intensively investigated in order to clarify and understand the coupling mechanism that leads to superconductivity in these compounds [3]. In some cases, multiple coexisting energy scales were reported in the kink behaviour of these compounds [4]. For example, in Bi-based high-T_c cuprate superconductors, the kink in the normal state was reported to be at an energy of approximately 40 meV, while this energy increases to approximately 70 meV in the superconducting state [5]. Nonetheless, a general agreement on the origin of the behaviour of kinks in band dispersions of the high-T_c cuprates has not yet been reached and the interpretation of kinks has been controversial in these systems. In some cases the presence of kinks was attributed to an electron-phonon coupling [6, 7], while in others their presence was linked to spin-fluctuation-based ordering mechanisms [8, 9]. More recently, a novel, purely electronic mechanism leading to kinks has been reported, which does not require any coupling to phonons or other excitations but only a three-peak structure in the spectral function $\mathcal{A}(k, \omega)$

[10]. This proposed mechanism applies to correlated systems such as transition metal oxides, and can account for kinks at energies as high as a few hundred meV from the Fermi level, beyond any phononic energy scale.

Kinks have also been reported in the band dispersion of other correlated systems such as colossal magnetoresistance compounds [11], f-electron systems [12] and in single (Sr_2RuO_4) [13, 14] and double ($Sr_3Ru_2O_7$) [15] layered strontium ruthenates. In particular, the kinks resolved in band dispersions of Sr_2RuO_4 and $Sr_3Ru_2O_7$ have the same energy scale as the kinks in the high-T_c superconductors.

The three-layered strontium ruthenate $Sr_4Ru_3O_{10}$ has been reported to order ferromagnetically below $T_c \sim 105$ K, while it shows anisotropic magnetic behaviour below $T_M \simeq 65$ K: its magnetic susceptibility further increases below T_M for magnetic fields applied along the c-axis, while it decreases when the magnetic fields are applied along the ab-plane with evidence of a metamagnetic transition [16, 17]. Such behaviour was suggested to originate from the rearrangement of electrons in Ru $4d$ orbitals due to the increased dimensionality and lattice distortions in this compound [18]. Iliev *et al.* [19] performed Raman spectroscopy measurements on $Sr_4Ru_3O_{10}$. They observed Raman lines of A_g and B_{1g} symmetry, assigned to particular atomic vibrations. In particular, the B_{1g} phonon mode was associated to the internal vibrations of the RuO_6 octahedra, while the A_g phonon mode was related to the in-plane rotations of the middle RuO_6 octahedra and to the out-of-plane vibrations of O, Ru and Sr atoms. The Raman lines of B_{1g} symmetry were found to show a hardening with the ferromagnetic ordering at 105 K. Furthermore, Gupta *et al.* [20] performed magnetic field-dependent Raman measurements, where they observed significant changes in the B_{1g} phonon frequency while decreasing the temperature near T_c and around the second transition temperature T_M. This behaviour was interpreted as a evidence of the presence of spin-phonon coupling in this compound.

In this work we report the first observation of kinks in the electronic band dispersion of $Sr_4Ru_3O_{10}$ by means of high-resolution angle resolved photoemission spectroscopy (ARPES). We resolved five different kink features, whose energies were found to be very close to the energies of the previously reported vibrational states detected by Raman spectroscopy measurements and predicted by lattice dynamics calculations (LDC) [19]. This is interpreted as evidence for strong electron-phonon coupling in this system.

2. Experimental

$Sr_4Ru_3O_{10}$ single crystals were grown using the flux-feeding floating zone technique with Ru self-flux. The growth conditions are reported elsewhere [21]. The quality of the crystals was checked using X-ray diffraction, resistivity and energy dispersive microscopy, and the samples were found to be pure single crystals of $Sr_4Ru_3O_{10}$. The ARPES measurements were performed at the beamline CASSIOPÉE of the synchrotron facility SOLEIL in Paris (France) using a Scienta R4000 electron energy analyser, which allowed us to measure simultaneously many energy distribution curves (EDC) in an angular range of 30°. The samples were cleaved *in situ* at a pressure of approximately 2×10^{-10} mbar and kept at a constant temperature of 5 K throughout the experiment. The spectra presented here were measured with a photon energy of 60 eV. The overall energy and angular resolutions were 21 meV (as confirmed by the broadening of the Fermi level) and 0.15°, respectively.

3. Results and Discussion

In figures 1a-e we show raw ARPES intensity cuts for selected positions in the first Brillouin zone (BZ) in a direction parallel to the Γ-X high symmetry line. Focusing on the spectral features indicated by red arrows, one observes that they disperse upward in energy with decreasing momentum. The photoemission intensity distribution of these bands varies, some of them are

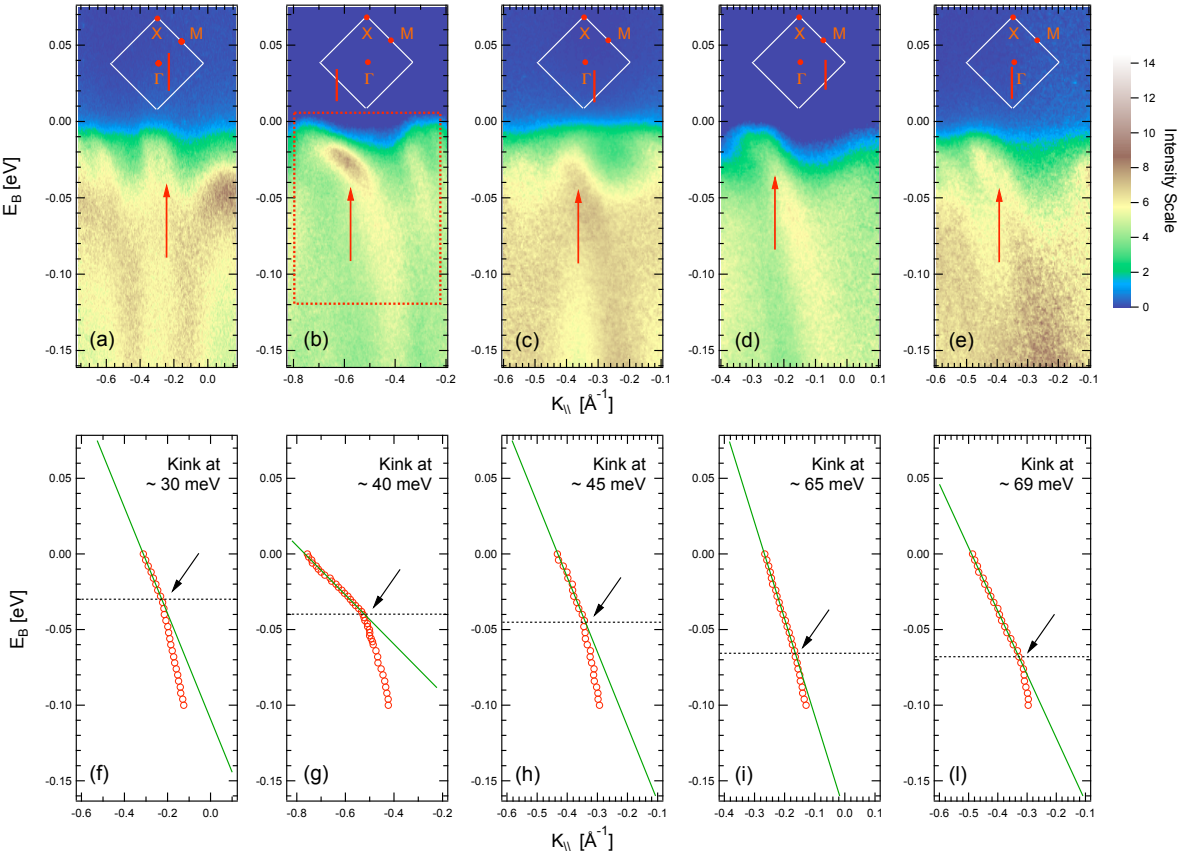

Figure 1. Panels (a)-(e): ARPES intensity cuts measured at different positions in the first BZ. The red arrow in each cut indicates the band of interest. The rotated square at the top of each cut is a schematic drawing of the first BZ of $Sr_4Ru_3O_{10}$. The position of the high symmetry points X, M, and Γ in the first BZ is also indicated. The red vertical line on the BZ shows the position and the direction in which the corresponding cut was acquired. Panels (f)-(l): Experimental dispersion (red circles) extracted from the fitting of the MDC's extrapolated from the corresponding cuts in the upper panels for the band of interest. Black arrows point to where kinks are observed. The green straight lines represent the linear fit to the low energy data.

more enhanced and better resolved (see for example figure 1b) as they approach the Fermi-level than others (see for example figure 1a).

The dispersion of these spectral features can be found from the raw data by fitting the momentum distribution curves (MDC's) extracted from each two-dimensional image. As an example of this procedure, we report in figure 2a the series of MDC's extracted from the red box highlighted in figure 1b, where each MDC has been generated by integrating the intensity of the ARPES cut over a binding energy range of 10 meV in 2 meV steps. As one can see from 2a, the line shape is rendered complicated by the presence of several features in the momentum region of interest. Each MDC has been fitted with a linear combination of Lorentzian line shapes, an example of which is shown in 2b. The binding energy of the MDC maxima for the particular band of interest have been followed down to a binding energy of −0.1 eV, and it is plotted as a function of momentum in figures 1f-l for direct comparison with the raw data. This is a commonly used technique to obtain the experimental dispersion from ARPES intensity maps [22]. We observe a change in the slope in the dispersion of these bands, the so-called

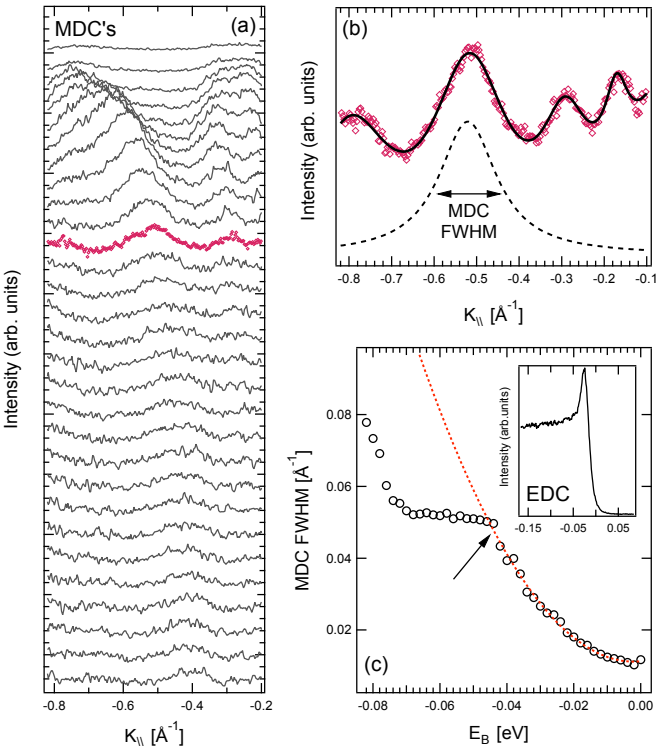

Figure 2. (a) Series of MDC spectra extracted from the red box in figure 1b by integrating over a binding energy range of 10 meV in 2 meV steps. The MDC spectrum in purple symbols is reported separately in (b) together with the overall fitting (solid black line) performed with Lorentzian line shapes. The Lorentzian peak for the band of interest is also reported (dashed black line). (c) MDC FWHM for the band of interest in figure 1b plotted versus the binding energy of the peak. The dashed red curve represents a quadratic fit to the low-energy data. The arrow marks the position of the kink. The inset shows a typical energy distribution curve (EDC) for the same peak showing the high resolution of these measurements.

kink. In order to obtain the energy of these five kinks, the low energy parts of the experimental dispersions close to the Fermi-level were fitted with a straight line passing through the Fermi momentum k_F (see green straight lines in figure 1), and the kink energy is taken as where the MDCs peak maxima starts to deviate significantly from the near-Fermi-level linear dispersion (indicated by black arrows). After a careful analysis of each of these experimental dispersions, we extracted the values of the kink energies of approximately 30, 40, 45, 65 and 69 meV. This energy range is comparable with what was previously reported for the low energy kinks in the high-T_c superconductors. Moreover, our results are consistent with the 40 meV kink reported for Sr_2RuO_4 and $Sr_3Ru_2O_7$ [13].

The presence of kinks is also confirmed by the analysis of the MDC full width at half maximum (FWHM) versus the binding energy of the peaks. Figure 2c represents, as a typical example, the plot for the band of interest in figure 1b. The FWHM of the MDC is directly proportional to the imaginary part of the self energy [22], which represents the scattering rate of the quasiparticles in the system. As one can see, the scattering rate shows a discontinuity at an energy of 43 meV,

ARPES kinks (meV)	30 ± 3	40 ± 2	45 ± 2	65 ± 1	69 ± 4
Raman spectroscopy (meV)	29.15 (A_g)	38.08 (B_{1g})	47.1 (B_{1g})	-	72.95 (A_g)
Theory-LDC (meV)	28.66 (A_g)	40.5 (B_{1g})	43.92 (B_{1g})	63.52 (A_g)	68.48 (A_g)

Table 1. Comparative table of experimental ARPES kink energies from this study with the phonon mode obtained in the previous Raman spectroscopy study together with lattice dynamic calculations from ref. [19].

which is in very good agreement with the 40 meV kink observed for this particular feature. The low energy part of the curve can be fitted with a quadratic low energy behaviour (FWHM $\propto E^2$, solid red curve), which is thought to be a signature of the presence of quasiparticles in a Fermi liquid type in the system [22].

In order to understand the origin of the kinks in low energy band structure of $Sr_4Ru_3O_{10}$, we compare in table 1 the kink energies obtained in this ARPES study to the phonon modes observed in the previous Raman spectroscopy study and lattice dynamic calculations from ref. [19]. The symmetry of the Raman modes, either B_{1g} or A_g, is also indicated in the table. The comparison shows that the kink energies resolved in our ARPES data are approximately equal to the energy of the phononic modes, revealing a compatibility between their energy scales. In particular, the 380 cm^{-1} B_{1g} phonon mode, which was found in ref. [19] to demonstrate evidence of a structural contribution to magnetic order in $Sr_4Ru_3O_{10}$, corresponds to the ARPES kink of 45 meV. We interpret these observations as being due to a strong coupling between electrons and phonons in this compound.

4. Conclusions

In conclusion, we have reported angle resolved photoemission spectroscopy measurements on the three-layered strontium ruthenate $Sr_4Ru_3O_{10}$, revealing the presence of kinks in the near-Fermi-level band dispersion. The kink energies have a good correspondence with the energy of the phononic modes previously reported by Raman spectroscopy measurements and lattice dynamic calculations, and can be interpreted as the fingerprint of strong electron-phonon coupling present in $Sr_4Ru_3O_{10}$.

Acknowledgements

We are grateful to R. Fittipaldi, A. Vecchione and V. Granata for proving the single crystals for the measurements, M. Cuoco, V.B. Zabolotnyy and S. Borisenko for useful discussion, and A. Taleb-Ibrahimi and F. Bertran for technical support during the experiment. We acknowledge financial support from the South African National Research Foundation (NRF) through travel grant no. 74033.

References

[1] Hengsberger M et al. 1999 *Phys. Rev. Lett.* **83** 592
[2] Valla T et al. 1999 *Phys. Rev. Lett.* **83** 2085
[3] Rotenberg E et al. 2000 *Phys. Rev. Lett.* **84** 2925
[4] Meevasana W et al. 2007 *Phys. Rev.* B **75** 174506
[5] Cuk T et al. 2004 *Phys. Rev. Lett.* **93** 117003
[6] Lanzara A et al. 2001 *Nature* **412** 510
[7] Shen Z X et al. 2002 *Phil. Mag.* B **82** 1349
[8] He H et al. 2001 *Phys. Rev. Lett.* **86** 1610
[9] Mannella N et al. 2004 *Nature* **427** 692
[10] Byczuk B et al. 2007 *Nature* **3** 168
[11] Sun Z et al. 2006 *Phys. Rev. Lett.* **97** 056401
[12] Durakiewicz T et al. 2004 *Europhys. Lett.* **65** 816
[13] Aiura Y et al. 2004 *Phys. Rev. Lett.* **93** 117005
[14] Iwasawa H et al. 2005 *Phys. Rev. B* **72** 104514
[15] Iwasawa H et al. 2006 *Physica* C **445** 73
[16] Mao Z Q et al. 2005 *Phys. Rev. Lett.* **96** 077205
[17] Fobes D et al. 2007 *Phys. Rev.* B **75** 094429
[18] Malvestuto M et al. 2011 *Phys. Rev.* B **83** 165121
[19] Iliev M N et al. 2005 *Physica* B **358** 138
[20] Gupta R et al. 2006 *Phys. Rev. Lett.* **96** 067004
[21] Fittipaldi R et al. 2007 *Cryst. Growth and Design* **7** 2495
[22] Kordyuk A A et al. 2006 *Phys. Rev. Lett.* **97** 017002

Magnetic 4f-systems and their applications in spintronics

V Nolting

Vaal University of Technology, Private Bag X021, Vanderbijlpark 1900, South Africa

volkmarn@vut.ac.za

Abstract. Magnetic semiconductors are materials that exhibit magnetic behaviour as well as typical semiconductor properties that are useful in the processing of information in conventional electronic devices. However, whereas traditional devices only control the charge carriers, magnetic semiconductors also give access to the electron spin and thus the storage of information. It is shown that a thin layer of Fe grown on top of (GaMn)As induces ferromagnetic ordering of the Mn magnetic ions several layers across the interface. Furthermore, the magnetization persists at temperatures close to room temperature which makes hybrid ferromagnetic metal/semiconductor structures promising applications in spintronics. Spintronics or spin electronics is a new area of research where the results of conventional magnetism and semiconductor physics are correlated. Hybrid structures of the above type have the potential to optimize information storage and processing in the design of enhanced electronic devices.

1.Introduction

In conventional electronic devices the processing of information is done in semiconductors based on the charge of the electron. On the other hand, information storage is done in metal based magnetic devices using the electron spin. Much energy and time could be saved if storage and processing of information could be brought together on a single chip. To achieve this spin dependent electron transport phenomena would be desirable that are typically observed in ferromagnetic metals due to a spin dependent energy splitting between the ↑ and ↓ density of states, or alternatively in magnetic 4f-systems where magnetism and the electric current are carried by two different electron groups. The magnetic moment stems from the only partially filled 4f-shell of the rare earth atom while the outer 6s-electrons become the quasi free conduction electrons that can move through the entire system.
Prototypes of these materials are the EuX, X=O, S, Se, Te or the metallic Gd; the europium chalcogenides have the additional advantage that they are semiconductors with all the above mentioned useful properties.

Magnetic semiconductors are theoretically described by the sf-model [1] that is introduced in the following section. In Section 3 it is then shown that the sf-model describes magnetism in magnetic semiconductors reasonably well. However, their disadvantages are their low critical temperatures. In Section 4 hybrid metal/semiconductor structures are shown to overcome these difficulties with promising applications to electronic devices and components.

2.The sf-Model

The sf-model describes the mutual effects between the two different electron groups in magnetic semiconductors and is defined by the Hamiltonian

$$H = H_s + H_f + H_{sf}$$
$$H_s = \sum_{ij\sigma} T_{ij}\, c^+_{i\sigma}\, c_{j\sigma} + \frac{1}{2}\, U \sum_{i\sigma} n_{i\sigma}\, n_{i-\sigma} \quad (1)$$

Here $c^+_{i\sigma}$ denotes the creation operator for a σ-electron at lattice site R_i, $c_{i\sigma}$ is the corresponding annihilation operator and

$$n_{i\sigma} = c^+_{i\sigma}\, c_{i\sigma}$$

H_s describes the system of itinerant conduction electrons that are treated as s-electrons and has the well known form of the Hubbard model. Note that the Coulomb interaction is only considered in its simplified intraatomic version. U is the corresponding Coulomb matrix element: T_{ij} are the hopping integrals. The subsystem of localized magnetic moments is described in a realistic manner by the Heisenberg model

$$H_f = -\sum_{ij} J_{ij}\, S_i \cdot S_j \quad (2)$$

The spins at R_i and R_j interact via the exchange integrals J_{ij}. The two subsystems are coupled by an sf-exchange, i.e. a local interaction between the 4f-spin S_i and the conduction electron spin σ_i

$$H_{sf} = -g \sum_i \sigma_i \cdot S_i = -\frac{1}{2}\, g \sum_{i\sigma} (z_\sigma\, S^z_i\, n_{i\sigma} + S^\sigma_i\, c^+_{i-\sigma}\, c_{i\sigma}) \quad (3)$$

g is the intraatomic sf-exchange constant. The Hamiltonian of Eq (1) describes a non-trivial many body problem that is generally not exactly solvable. However, there are a couple of exactly solvable limiting cases that are discussed in Section 3.

3.Results

The sf-model of the previous section is rigidly solved in the zero bandwidth limit [2] and the case $(T = 0, n = 0)$ describing one electron in an otherwise empty conduction band [3]. It follows already from the molecular field approximation of the model that the magnetization as a function of temperature has the typical form of a Brillouin function

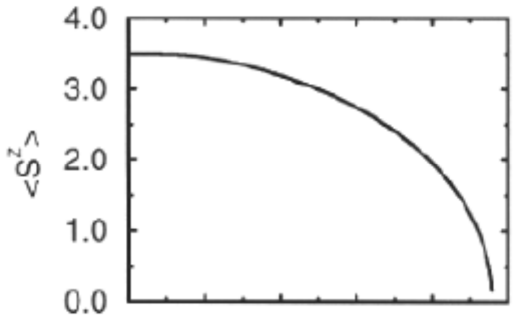

Fig 1: magnetization $\langle S^z \rangle\,(T)$ as a function of temperature in the case $n = 0$, i.e. empty conduction band.

with the saturation magnetization

$$\langle S^z \rangle \, (\, T = 0, n = 0) \; = S = \; {}^{7}/_{2}$$

The Curie temperature is the temperature where

$$\langle S^z \rangle \, (T = \; T_c) = 0$$

On the other hand, at finite band occupations n the saturation magnetization

$$\langle S^z \rangle \, (\, T = 0 \; , n \; \neq 0) \leq S \tag{4}$$

is reduced while the Curie temperature T_C is enhanced. This is due to the fact that according to the RKKY-interaction [4] the effective coupling between the localized magnetic moments is caused by the quasi-free conduction electrons of the semiconductor, so one may expect

$$k_B \, T_C \; \propto J_{ij}^{RKKY} \; \propto n_e^{\,4/3} \tag{5}$$

A similar increase of T_C as a function of n is also observed by the authors of reference [5]. W Nolting et al [6.7] combine the many body problem of the sf-model with a selfconsistent band structure calculation based on DFT to obtain highly realistic results for the Curie temperature T_C of ferromagnetic 4f-systems.

Obviously, the sf-model describes magnetism in magnetic semiconductors reasonably well. Furthermore, magnetic semiconductors combine all properties needed for both the storage and processing of information in one material. However, their $(n = 0)$ critical temperatures are generally too low. In that case the sf-model reduces to the Heisenberg Hamiltonian of Eq (2) and one obtains from a mean field approximation the following results

$$\rho_\sigma \, (E) = \; \rho_0 \, (\, E - U \, \langle n_{-\sigma} \rangle + \frac{1}{2} \, g z_\sigma \, \langle S^z \rangle \,)$$

The quasiparticle densities of state $\rho_\sigma \, (E)$ are rigidly shifted with respect to the free Bloch density $\rho_0 \, (E)$. At $T = \; T_C$ the two densities coincide, i.e.

$$\rho_\uparrow \, (E) = \; \rho_\downarrow \, (E) = \; \rho_0 \, (\, E - \frac{1}{2} \, U \, n)$$

and a paramagnetic state is obtained. This happens at the Curie temperature

$$k_B \, T_C = \; \frac{2}{3} \, S \, (S + 1) \, (\, z_1 \, J_1 + \; z_2 \, J_2 \,)$$

(6)

Here z_1, z_2 are the number of nearest and next nearest neighbors; J_1, J_2 are the corresponding exchange integrals. Eq (6) also qualitatively explains why a sufficient number of interactions are important regarding a ferromagnetic order of the magnetic moments and why in some systems of lower dimensions ferromagnetic solutions are according to the Mermin-Wagner theorem not possible (see reference [1]).

Experimental and theoretical values for the critical temperatures of EuX are listed in the table below.

Table 1: experimental and theoretical values for the critical temperatures of EuX.

X	Exp value for critical temperature	Theoretical value for critical temperature	Type of magnetism
O	66.8 K	86.6 K	ferromagnetic
S	16.6 K	21.5 K	ferromagnetic
Se	4.6 K	-4.0K	metamagnetic
Te	9.6 K	8.5 K	antiferromagnetic

While the experimental values are taken from ref [8] the theoretical calculations are based on a mean field approximation MFA of the Heisenberg model. Generally one observes the typically enhanced values in the MFA. Especially for $X = O, S$ very similar values for the critical temperature are cited in

ref [9]. For the antiferromagnet $EuTe$ Eq (6) yields the paramagnetic Curie temperature Θ which is negative and unequal to T_N. Again, very similar values for both T_N and Θ are also cited in ref [10].
Note that in EuSe the exchange integrals from nearest and next nearest neighbors compensate each other resulting in an antiferromagnetic state. However, ferromagnetic order may be induced by applying a moderate pressure of $0.5\ GPa$.

4.Applications

The EuX have become objects of interest regarding spintronics as the critical temperature T_C can generally be enhanced by applying pressure. The effect of pressure is a hybridization between the itinerant conduction band states and the localized 4f-states and this phenomenon is often described by the Anderson model [11]. As pressure also changes the lattice parameters of the solid, the authors of ref [12] use a density functional theory method with the LDA+U functional to calculate the critical temperature as a function of the lattice constant; values close to $200K$ are obtained.
On the other hand, in ferromagnetic metals spin dependent electron conduction can be explained from the band structure or density of states of the metal.

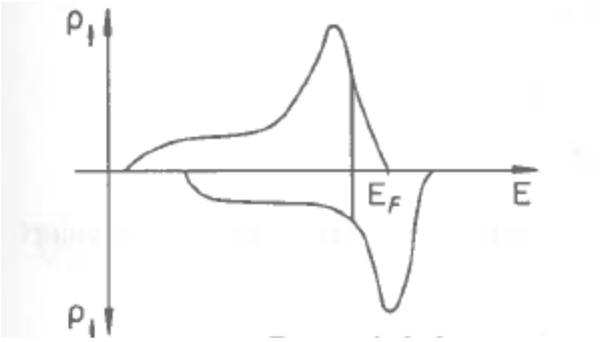

Both ↑ and ↓-bands are filled up to the Fermi energy ε_F. However, as the two bands are shifted against each other $n_\uparrow > n_\downarrow$ and therefore the spin polarization

$$P = \frac{n_\uparrow - n_\downarrow}{n_\uparrow + n_\downarrow} \leq 1$$

resulting in spin dependent currents. Spin polarizations close to 1 have indeed been calculated with the sf-model for small band occupations n and $T \leq T_c$ [13].
For the propagation of a spin polarized current through the interface between a ferromagnetic metal and a non-magnetic material the current must be injected through a magnetic tunnel junction MTJ. The MTJ consists of two layers of magnetic metals separated by a very thin insulating layer so that the electrons tunnel through the barrier. The tunneling current depends on the magnetization of the ferromagnetic layers and the tunnel resistance [14].
In hybrid metal/semiconductor structures a ferromagnetic metal with its high Curie temperature is combined with a non-magnetic semiconductor to enhance its magnetic properties. A thin layer of Fe is grown over GaAs doped with magnetic Mn-ions so that only a few percent of the Ga-atoms are replaced. The Fe lattice structure is nearly lattice matched to GaAs with a small lattice misfit

$$a_{Fe} \cong \frac{1}{2}\ a_{GaAs}$$

$$\eta = 0.014$$

allowing for epitaxial growth.

The magnetic properties of the Fe/GaAs hybrid structure have been studied extensively [15.16]. Both ab initio and Monte Carlo calculations show that the exchange interaction in Fe stabilizes ferromagnetism in a region of about four atomic layers across the interface. An RKKY type of interaction leads to an effective coupling between the Mn-ions which is ferromagnetic in nature. The induced magnetization in the semiconductor is opposite in direction to that of the iron. Furthermore, the Curie temperature depends on the carrier concentration. If n_e is low, then the coupling between the magnetic moments is weak and paramagnetism is observed. However, for carrier concentrations

$$n_e \cong 10^{20}\ cm^{-3} = \frac{1}{100}\ n_{metal} \rightarrow T_C \cong 200K$$

Curie temperatures close to room temperature are obtained. Similar results of high Curie temperatures in ferromagnetic semiconductors are reported in Co doped ZnO [17] and Mn doped $Pb_{1-x}Sn_xTe$ [18].

5 Summary and Conclusions

It has been shown in the previous sections that hybrid metal/semiconductor structures are interesting examples for spintronic devices and could result in significant gains regarding energy and time consumption as far as the exchange of information in electronic components is concerned. Then it is important to find ways to increase the critical temperature up to room temperature and the numerical results mentioned in the previous section are encouraging in this respect. Furthermore, the near perfect lattice match of Fe and $GaAs$ makes them promising applications for the development of multilayer functional devices. Note that for the devices to function very thin layers of only a few nm are required as the layer thickness must be smaller than the electron's mean free path $l \cong 10\ nm$ at room temperature.

Recent developments in spintronics have increased the capacity of computer hard disks and have extended the technology to mobile appliances. New concepts and ideas include magnetic memory MRAM, spin LED, and the giant magnetoresistance GMR devices [14].

References

[1] W. Nolting: Quantum Theory of Magnetism, Teubner (1986)
[2] W. Nolting and M. Matlak, phys stat sol (b) 123, 155 (1984)
[3] W. Nolting, U. Dubil, and M. Matlak, J. Phys. C 18, 3687 (1985)
[4] A.A. Rudermann and C. Kittel, Phys Rev 96, 99 (1954)
[5] V. Nolting and W. Nolting, phys stat sol (b) 149, 313 (1988)
[6] W. Nolting et al, Phys Rev B35, 7015 (1987)
[7] W. Nolting et al, Phys Rev B35, 7025 (1987)
[8] P. Larson and W.R.L. Lambrecht, J. Phys. Cond. Matter 18, 11333 (2006)
[9] X. Wan et al, arXiv:1003.2039v1, 10 March 2010
[10] A. Radomska and T. Balcerzak, Acta Physica Polonica 98, 83 (2000)
[11] P.W. Anderson, Phys Rev 124, 41 (1961)
[12] J. Kunes, W. Ku, and W.E. Pickett, J. Phys. Soc. Japan 74, 1408 (2005)
[13] W. Borgiel, W. Nolting, and G. Borstel, phys. Stat. sol (b) 136, 131 (1986)
[14] A. Fert, Rev. Mod. Phys. 80, 1517 (2008)
[15] C. Gould and L.W. Molenkamp, Physics 1, 43 (2008)
[16] F. Maccherozzi et al, Phys Rev Lett 101, 267201 (2008)
[17] K. Kittilstved et al, Phys Rev Lett 97, 37203 (2006)
[18] T. Story et al, Phys Rev Lett 56, 777 (1986)

Luminescence dynamics of $GdTaO_4$: Pr^{3+}.

LL Noto*, SS Pitale, OM Ntwaeaborwa and HC Swart*

Physics Department, University of the Free State, P. O. Box 339, Bloemfontein, 9300, South Africa

*Corresponding author: NotoLL@ufs.ac.za or SwartHC@ufs.ac.za

Abstract. A red glowing $GdTaO_4$ doped with Pr^{3+} phosphor with major emission coming from the $^1D_2 \rightarrow {}^3H_4$ and $^3P_0 \rightarrow {}^3F_2$ transitions, was prepared via the solid state route at 1200 ^oC. The X-ray diffraction pattern confirmed that the phosphor crystallized and formed a well known fergusonite structure phase of $GdTaO_4$ corresponding to the ICSD 415433 standard file. The diffuse reflectance spectrum showed the absorption peaks corresponding to TaO_4 charge transfer, and direct excitation of Pr^{3+} and Gd^{3+}. The photoluminescence emission spectrum consisted only with peaks from Pr^{3+}, suggesting that there was energy transfer from TaO_4 and Gd^{3+} to Pr^{3+}. The phosphorescence life time of the phosphor was estimated from the phosphorescence decay curve to be approximately 10 min.

Keywords: Red emitting phosphor, Pr^{3+}emission, long afterglow phosphor

1. Introduction

The $GdTaO_4$ compound exhibits a fergusonite structure, and it is classified under the distorted scheelites [1]. The $LnTaO_4$ (Ln = Ce, Gd, La, Y and Lu) group can absorb X-ray photons in the absence of a dopant, and re-emit a broad emission that is in the blue region of the electromagnetic spectrum. The broad emission is attributed to the TaO^{4-} group charge transfer [1,2]. The photoluminescence (PL) of Tb^{3+} and Eu^{3+} doped $GdTaO_4$ has been reported by Blasse *et al*. [1]. This achievement opens up a research opportunity to investigate the properties of other rare earth ions doped in $GdTaO_4$, to prepare a variety of phosphors that can be used in light emitting devices of different types. Since one of the major pursuit in phosphor research is to develop red phosphors that is close to that of an ideal red color with CIE coordinates (0.63, 0.33), Pr^{3+} doped $GdTaO_4$ has emerged as a potential red light emitting phosphor. Pr^{3+} was chosen because it emits red light with CIE color coordinates (0.68, 0.31) that are close to that of an ideal red color, as reported for $CaTiO_3$:Pr^{3+} [3,4].
The luminescent dynamics of trivalent Pr^{3+} ion were previously studied in several other host materials, such as $LiYF_4$ [5], $YAlO_3$ [6], etc. In such materials the emission is a result of electron transition from the lowest manifold of the 4f5d state to the 4f ($^3H_4$ level) states, and thus leading to an up conversion process. The pumping of carriers to the 4f5d state in $YAlO_3$ is aided by the wide band gap of the material and its strong crystal field. These lead to the 4f5d state to be well positioned in the energy band gap of the material [6]. In our previous study [7], we reported a single red emission from Pr^{3+} doped in $CaTiO_3$ at 613 nm wavelength due to the $^1D_2 \rightarrow {}^3H_4$ transition. They attributed the single red emission to metal-to-metal charge transfer (*Intervalence charge transfer*), which leads to a complete depopulation of carriers in the $^3P_0$ level by crossing it over to the $^1D_2$ level.

Pr^{3+} doped $GdTaO_4$ is a potential long persistent red emitting phosphor because it is chemically stable [1] and it can therefore be used in fabrication of devices that can be used in medical diagnostics, emergency and traffic signage at night [8]. The long afterglow observed in these materials is aided by the existence of defect levels that have the capacity to temporally store the energy of the excited carriers and liberate it after a certain period of time which may last for more than ten hours [8,9] after stopping the excitation.

The role of red phosphors with a persistent afterglow seems crucial in the modern world, and it becomes necessary for researchers in luminescent studies to develop such phosphors. In our laboratory we are studying the preparation and optical properties of red glowing phosphors with the view of increasing their intensity and enhancing their afterglow. In the present paper, we report luminescent dynamics of Pr^{3+} doped $GdTaO_4$ phosphor and its decay characteristics. In addition, we present a possible mechanism of energy transfer from TaO_4 and Gd^{3+} to enhance red emission of Pr^{3+}.

2. Experiments

$GdTaO_4$ doped with 0.5 mol% of Pr^{3+} was prepared by solid state chemical reaction route at 1200 ^oC for 4 h. The compound was prepared in the presence of Li_2SO_4 that was acting as a fluxing agent, as suggested by Hristea at al [10], in order to achieve complete reaction. The phosphor was prepared by stoichiometrically mixing Gd_2O_3, Ta_2O_5 and $PrCl_3$ into a slurry using ethanol, in the presence of 30 wt% of Li_2SO_4. This was then dried in an oven at 120 ^oC for 10 h. The dried mixture was baked in a furnace at 1200 ^oC for 4 h, and the final product ($Gd_{0.995}TaO_4$:$0.005Pr^{3+}$) was cooled to room temperature and washed with distilled water to remove the excess Li_2SO_4.

The phase purity and structure of $GdTaO_4$:Pr^{3+} were analysed using the X-ray diffractometer (AXS D8 Advance X-ray diffractometer (XRD)), and the morphology of the particles was analysed using Scanning Electron Microscopy (SEM) (Shimadzu SSX-550, Kyoto, Japan). The photoluminescent (PL) properties of the phosphor were measured using the Varian Carry-Eclipse fluorescence spectrometer, and the diffuse reflectance was measured using the PerkinElmer Lambda 950 UV/VIS absorption spectrometer. The phosphorescence lifetime measurements were conducted using the Thermoluminescence (TL) spectrometer TL 10091, Nucleonix spectrometer.

3. Results and Discussion

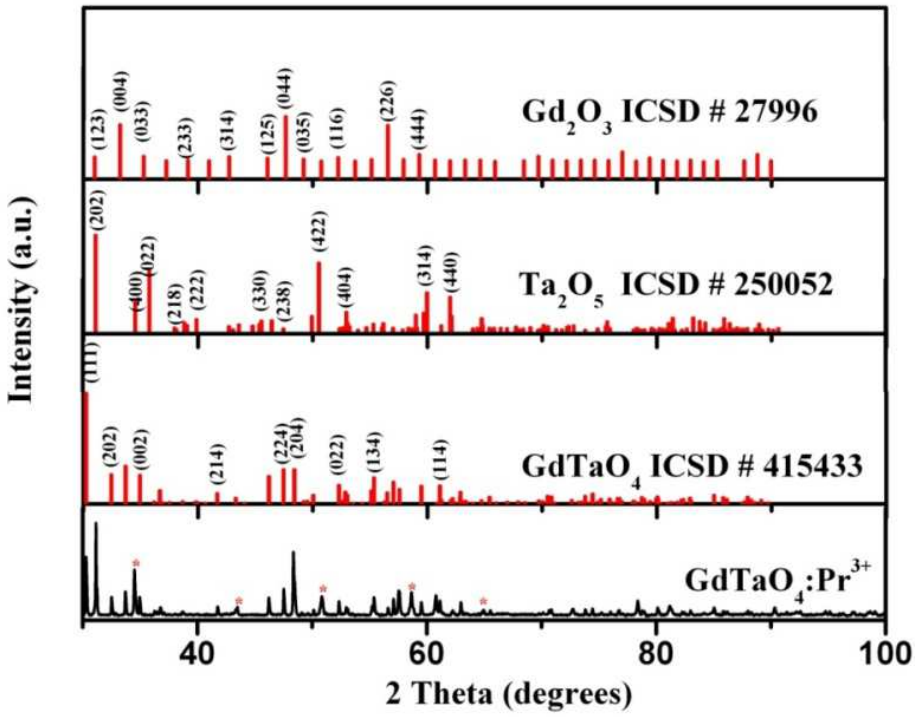

Figure 1: XRD patterns of $GdTaO_4$:Pr^{3+}

The state of the phase purity illustrated with the XRD pattern (fig. 1) of the prepared $GdTaO_4$ compound doped with Pr^{3+} matches closely with that of the fergusonite structure of the $GdTaO_4$

standard file (ICSD 415433). The impurity phases (arising from incomplete reaction of precursors) are marked with asterisks in figure 1. The particle morphology of the compound suggests that the particles are of different irregular shapes and have different sizes. Distinguishably are the sharp edges of the particles shown in the SEM image (fig. 2),

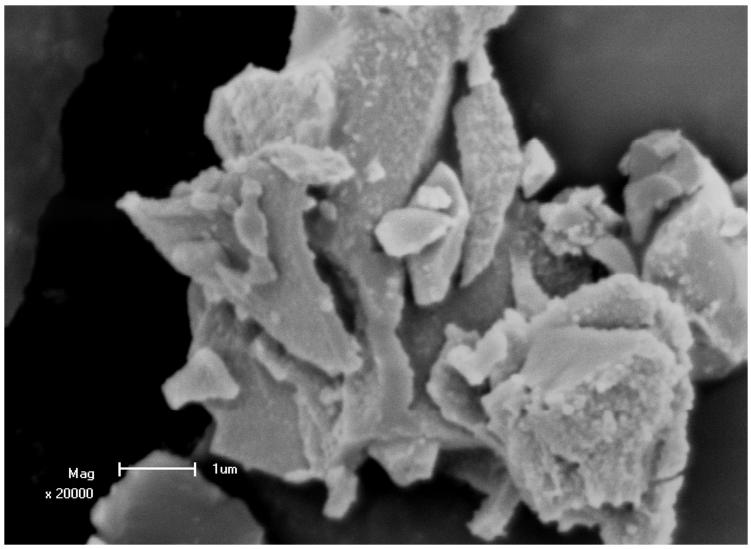

Figure 2: The SEM image of $GdTaO_4:Pr^{3+}$

The diffuse reflectance spectrum of $GdTaO_4:Pr^{3+}$ (fig. 3) shows that the major absorption of the phosphor material comes from band to band excitation at 245 nm. At lower wavelengths are 4f → 4f5d state excitations. There are also 4f → 4f absorptions that correspond to $^3H_4 \rightarrow {}^3P_{2,1}$, $^1I_6$, $^3P_0$ transitions of Pr^{3+} around 450 to 490 nm, and also the $^3H_4 \rightarrow {}^1D_2$ transition of Pr^{3+} around 600 nm [11,12]. There is a prominent charge transfer (CT) to the TaO_4 group at 285 nm [1,10] and there are absorptions at 272 and 279 nm which correspond to the $^8S \rightarrow {}^6I_j$, ^6P_j transitions of Gd^{3+} absorption centers [1].

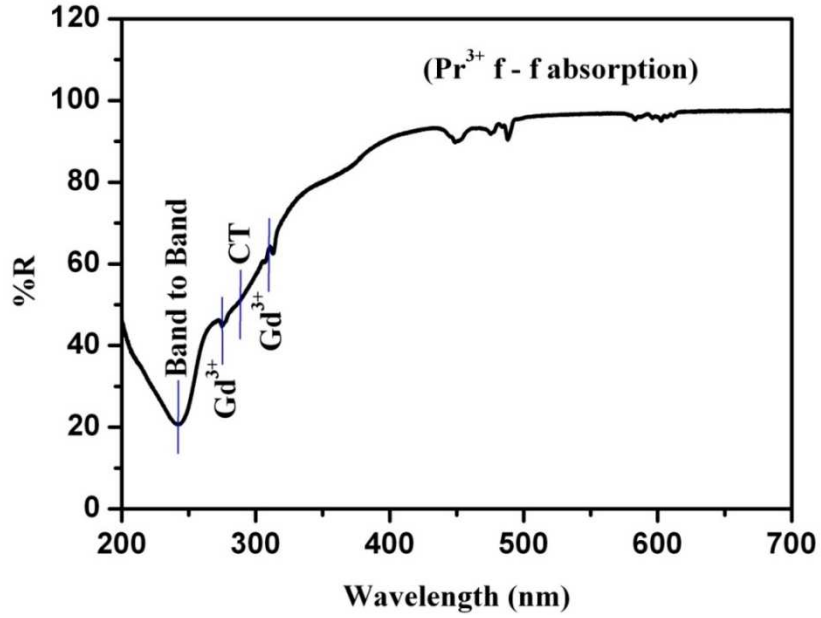

Figure 3: Diffuse reflectance spectrum of $GdTaO_4:Pr^{3+}$

The PL spectrum (fig. 4) of the phosphor was recorded using a Varian Cary Eclipse Fluorescence spectrometer at room temperature by exciting with a 245 nm wavelength using a monochromated xenon lamp as an excitation source. This excitation wavelength according to the diffuse reflectance spectrum should give maximum electron excitation to the conduction band [11]. From the spectrum, the blue and red emissions are observed, and the red emission is more intense than the blue emission. The blue emission peaks at 490 and 511 nm correspond to $^3P_0 \rightarrow {}^3H_4, {}^3F_2$ transitions of Pr^+ respectively. The red emission peaks at 610 and 630 nm corresponds to the $^1D_2 \rightarrow {}^3H_4$ transitions of Pr^{3+} [11].

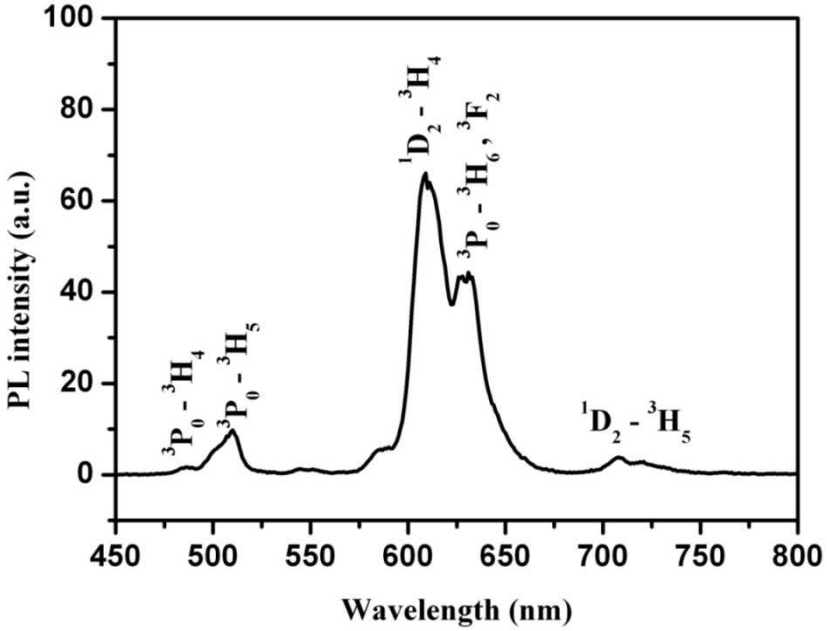

Figure 4: The photoluminescence spectrum measured at room temperature

The phosphorescence lifetime measurements were carried out using a TL spectrometer system by fixing the temperature at 30 ^oC, and pumping the carriers to the conduction band from the valence band for 5 minutes. The phosphorescent decay curve is composed of two exponential components that can be fitted using the second order exponential equation (eq. 1) [12]:

$$\boldsymbol{I(t) = Ae^{-t/\tau 1} + Be^{-t/\tau 2}} \qquad \textbf{[1]}$$

where ***I(t)*** is the luminescence intensity, ***A*** and ***B*** are constants and ***t*** is the time [12]. The first term (eq. 1) describes the fast component (fig. 5) that is attributed to the lifetime of Pr^{3+} emission with a lifetime ($\boldsymbol{\tau_1}$) equal to 64 ± 1 secs. The second term describes (eq. 1) the slow component (fig. 5) and is attributed to the lifetime of the emission coming from the electron trap levels, and its lifetime ($\boldsymbol{\tau_2}$) is 620 ± 63 secs. [12]

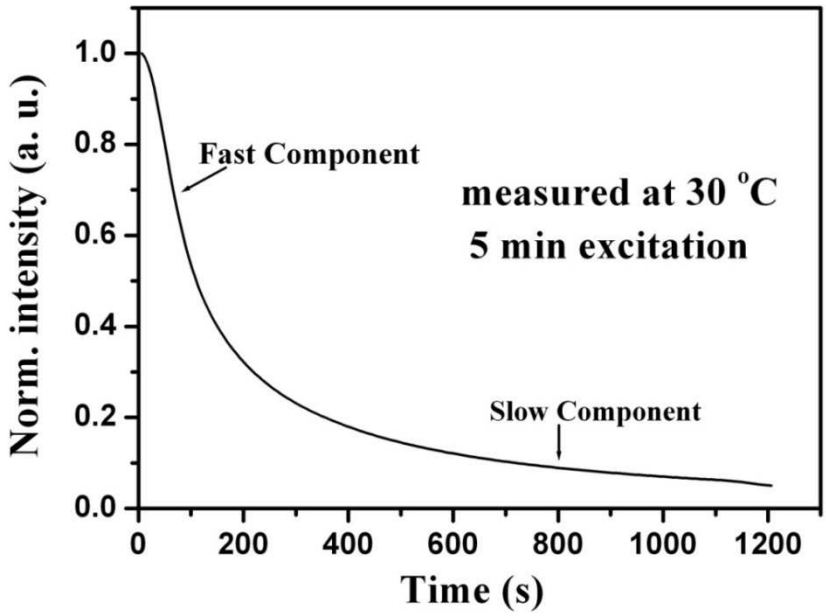

Figure 5: The phosphorescence lifetime spectrum measure at 30 °C

An explanation leading to the energy transfer and the phosphorescence decay time is illustrated using the mechanism of luminescence in figure 6. As observed from the diffuse reflectance spectra (fig. 3), there is a charge transfer to the TaO_4 group of $GdTaO_4$ and absorption by Gd^{3+} upon exciting the material [1, 10]. However from the PL spectrum (fig. 4) there is only an emission coming from Pr^{3+}. From these results we speculate that the absorbed energy by the TaO_4 group is transferred to the Gd^{3+} because the absorption of Gd^{3+} overlaps with the emission of the TaO_4 group [1]. The energy captured by Gd^{3+} states is then transferred to Pr^{3+} luminescent state and hence we only observe the emission from Pr^{3+} (fig. 5).

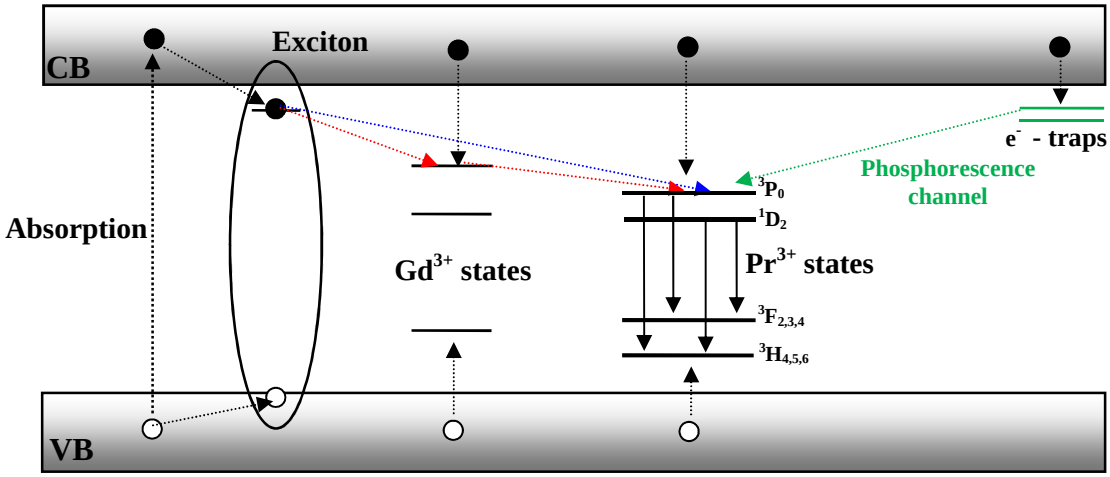

Figure 6: The phosphorescence and energy transfer mechanism

The oxide compounds in general have oxygen defects and amongst them are oxygen vacancies with different orientations. The different orientations result different trap energy distributions [13,16,17]. The shallow electron traps (fig. 6) in the material are responsible for the long afterglow luminescence, and the emission lifetime resulting from the electrons that were trapped is represented in figure 5. The electrons trapped within deeper traps are suitable to reveal the energy distribution of the traps using thermoluminescence spectroscopy [14–17].

4. Conclusion

$GdTaO_4$ doped with Pr^{3+} phosphor was prepared via the solid state route at 1200 ^oC for 4 hours. The XRD pattern of the final compound matched with the standard (ISCD 415433) file and it showed the presence of the unreacted reagent phases. Upon excitation, the diffuse reflectance shows absorption by TaO_4, Pr^{3+} and Gd^{3+} and the PL shows emission only corresponding to Pr^{3+} transitions and thus we speculate that there was energy transfer from TaO_4 and Gd^{3+} to Pr^{3+}. The phosphorescence life time of the phosphor was estimated to be 10 min.

Acknowledgement

The authors send gratitude to the National Research Foundation (NRF) for funding the project and the University of Free State Physics (Physics department, Center for microscopy and Geology department) for the research techniques used in this study.

Reference

[1] Blasse G, Bril A, 1970 J. Lumin. **3** 109
[2] Gu M, Xu XX, Liu X, Qiu L, Zhang R, 2005 J. Sol-gel Sci.Tech. **17** 152
[3] Zhang X, Cao C, Zhang C, Xie S, Xu G, J. Zhang, X. Wang, 2010 Mater. Res. Bull. **45** 1832
[4] Deren PJ, Pazik R, Strek W, Boutinaud P, Mahiou R, 2008 J. Alloys Compd. **451** 595
[5] Piper WW, Deluca JA, Ham FS, 1974 J. Lumin. **8** 344
[6] Nicolas S, Laroche M, Girard S, Moncorge R, Guyot Y, Joubert MF, Descroix E, Petrosyan AG, 1999 J. Phys.: Condens. Matter **11** 7937
[7] Noto LL, Pitale SS, Terblans JJ, Ntwaeaborwa OM, Swart HC, 2012 Physca B **407** 1517
[8] Pan Z, Lu YY, Liu F, 2012 Nature Mater. **11** DOI:10.1038/NMAT3173
[9] Aitasalo T, Hölsä J, Jungner H, Lastusaari M, Niittykoski J, 2006 J.Phys. Chem. B, **110** 4589
[10] Hristea A, Popovici EJ, Muresan L, Stefan M, Grecu R, Johnsson A, Boman M, 2009 J Alloys. Compd. **471** 524.
[11] Boutinaud P, Pinel E, Dubois M, Vink AP, Mahiou R, 2005 J. Lumin. **111** 69
[12] Diallo PT, Boutinaud P, Mahiou R, Cousseins JC, 1997 J. Phys. Stat. Sol. (a) **160** 255
[13] Ricci D, Bano G, Pacchioni G, 2003 Physical Review B **68** 224105
[14] Popovici EJ, Nazarov M, Muresan L, Noh DY, Bica E, Morar M, Arellano I, Indrea E, 2009 Phys. Proc. **2** 185
[15] Nyman BJ, Bjorketun ME, Wahnstrom G, 2011 J. Sol. Stat. Ionics **189** 19
[16] Deren PJ, Pazik R, Strek W, Bautinaud P, Mahiou R, 2008 J. Alloy Compd. **451** 595
[17] Diallo PT, Boutinaud P, Mahiou R, Cousseins JC, 1997 J. Phys. Stat. Sol. (a) **160** 255

Structural and thermodynamic properties of point defects in tin-dioxide (SnO_2)

JN Ntimane, TE Mosuang[1], KE Rammutla[1]

1. Department of Physics and Geology, University of Limpopo, Private Bag X 1106, Sovenga, 0727, Polokwane, South Africa

E-mail: thuto.mosuang@ul.ac.za

Abstract. Tin-dioxide ceramics have been intensively studied in recent years because of their potential in sensing and fuel cells. The present work uses classical molecular dynamics simulations focused on the role of defects in tin-dioxide. The total energy of the NPT Hoover ensemble at various temperatures has been calculated in order to determine the effects of oxygen vacancy and Ti substitutional defect in tin-dioxide. The results obtained showed an energy increase with temperature which was constantly compared with experiments. The radial distribution functions for the structures suggest the transformation of anatase to rutile tin-dioxide at high temperature.

1. Introduction

Structural and thermodynamic properties of metal oxide materials like tin-dioxide (SnO_2) play crucial role as semiconducting sensors and electronic devices. The manifestation of intrinsic bulk and surface defect levels and the origin of extrinsic defect levels are of practical significance in the functioning property of these materials [1-4]. The well-known reflectivity and conductivity property of SnO_2 are influenced by intrinsic native defects. In general, SnO_2 defects show up as oxygen vacancies. These introduce energy levels into the energy gap of the material causing the n-type conduction of states filled near the conduction band minimum [2,3]. For effective use as sensors and semiconductors, these materials must have good transmittance of the visible light and resistivity well below 10^{-3} Ωcm [4].

A great deal of experimental investigation has been performed on various forms of SnO_2 including the current nanoscale studies. Jones *et al* [3] performed some scanning tunnelling microscopy measurements on the surface structure whilst Cox *et al* [4] performed ion-scattering spectroscopy together with ultraviolet photoelectron measurements on the surface of SnO_2 to understand the oxygen vacancy defect in the conductivity of SnO_2. Now advanced computer softwares based on empirical and first principle calculations make it possible to study the bulk, surface, and nanostructures of this material. Such development permits formation of an atomistic image of semiconduction and sensing mechanisms. Noteworthy, the first principle calculations are limited to zero temperature, although high temperature environments are responsible for a number of kinetic factors observed in thin films, surfaces, and nanoparticles [4,5]. Subsequently, metal oxide sensors work at elevated temperatures, which also influence the impurity adsorption and catalytic processes in the material matrix [6]. Through the molecular dynamics approach for the defects in SnO_2, simulations at high temperatures can be achieved with ease.

The aim of this paper is to highlight some notable structural and thermodynamic properties obtained when anatase SnO_2 is subjected to oxygen (O) vacancy defect and titanium (Ti) substitutional defect. As Ti has same valency as Sn and TiO_2 is a competing material with SnO_2 on a variety of properties, it would be of great interest to observe Ti behaviour in SnO_2 material environment. The empirical molecular dynamics using the Buckingham potentials has been used through the simulations. Hopefully these results will provide an atomistic understanding of the role of defects in semiconducting sensors.

1. Computational details

Empirical molecular dynamics (MD) has been used to model the anatase SnO_2 and the related defects. A tetragonal space group $I4_1/amd$ SnO_2 unit cell has been repeated periodically in 3 dimensions to make a supercell with 192 Sn atoms and 384 O atoms. The oxygen parameter for anatase is 0.2066 Å and there are four Sn-O distance of 1.937 Å and two of 1.964 Å [7]. In the case of an oxygen vacancy defect on oxygen atom has been removed to make 383 O atoms. A Sn atom has also been replaced by a Ti atom in order for a substitutional Ti defect to materialize.

The material was modelled using the Buckingham potentials [8]. The DL-POLY package [8] has been used to perform all the empirical bond-order molecular dynamics calculations of SnO_2. A supercell with a 7.29 Å cutoff for forces on atoms, 576 atoms, and a sufficiently larger number grid points for the fast Fourier transformations (kmax1=6, kmax2=6, and kmax3=12) has been used for anatase SnO_2 throughout the calculations. The ewald convergence parameter of 0.3975 for anatase, on a Noose-Hoover NPT ensemble allowing the simulation supercell to change has been applied. The thermostat relaxation was set at 0.1 whilst the barostat was at 0.5. The simulation was allowed to run for more than 100 000 steps, with a simulation time step of 0.001ps. The controlled experimental crystal structure for anatase SnO_2 is according to Cromer and Herrington [7]. The material as is used for the molecular dynamics (MD) modeling is described by its lattice parameters as listed in Table 1, and a set of parameters required for the Buckingham potential are taken from AV Bandura *et al.* [9] and P Amstrong *et al*. [10]. Energy parameters were determined so as to reproduce the observed crystallographic structures of anatase SnO_2 and the accompanying dopants.

Table 1. The lattice parameters and relative sites for O atom and Sn-O bonds [7].

	this work	experiments
a (Å)	3.8263	3.7845
b (Å)	11.3194	9.5143
u	0.208	0.2066
Sn-O (Å)	4 x 2.1, 2 x 2.0	4 x 1.937, 2 x 1.964

2. Results and discussion

In Table 1, the simulated lattice parameters of anatase SnO_2 are shown. The results show that the two-body Buckingham potential reproduce the crystallographic structures within the experimental results.

In this paper the thermodynamic properties of anatase SnO_2 together with oxygen vacancy defect (V_O) in anatase SnO_2 and a Ti subsititutional defect (Ti_{Sn}) in anatase SnO_2 are being explored. The calculations have been performed above SnO_2 Debye temperature of 570 K by Tuerkes *et al*. [11] and 620 K by Bachmann *et al.* [12]. Subsequently the MD treats the motion of atoms classically; above the Debye temperature quantum mechanical effects can be neglected. So the average of the two, Debye temperatures was estimated at 595 K. Figure 1 shows the volume of anatase SnO_2, V_O, and Ti_{Sn} as functions of temperature above the SnO_2 Debye temperature. From the plots it can be seen that Ti_{Sn} curve has the lowest volume throughout the temperature range. This suggests that the presence of Ti substitutional defect in SnO_2 could assist in reduction of grain growth as argued by Rumyantseva *et al.* [13]. The volume thermal expansion coefficient for anatase SnO_2 was calculated to be 8.08 x 10^{-6} K^{-1},

of which differs by a few orders from the measured valued of 11.7 x 10^{-6} K^{-1} by Peercy and Morosin [14]. Of course it should also be noted that Peercy and Morosin Raman measurements were done on a rutile SnO_2 structure.

The specific heat of anatase SnO_2 has also been calculated with the increasing volume. This is obtained from the temperature derivative of the total energy of the system. Figure 2 shows the said plot of energy against temperature for anatase SnO_2, oxygen vacancy V_O, substitutional Ti_{Sn}. The specific heat calculated is 3.41 k_B which differ by about 12% from the Dulong-Petit's law of solids at high temperatures. But even the measured values seem to be more offline with the value 6.32 k_B [15]. It can be seen on the plots that substitutional Ti_{Sn} has the lowest energy, which suggest a good dopant for enhanced conductivity. Likewise, the oxygen vacancy V_O and the anatase SnO_2 curve intersect around 3000 K, which suggest an anticipated high temperature transition to the rutile SnO_2 phase in agreement with the Fan and Reid [16] measurements.

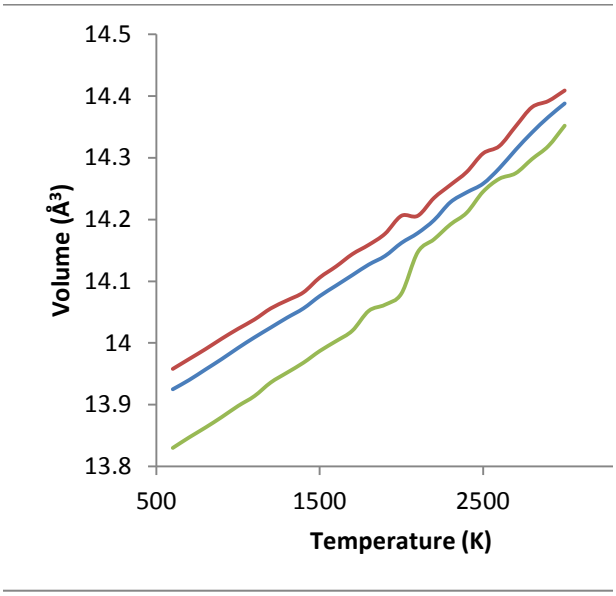

Figure 1. Volume as function of temperature for anatase SnO_2. blue curve is anatase SnO_2, red curve is V_O, and green curve is Ti_{Sn}.

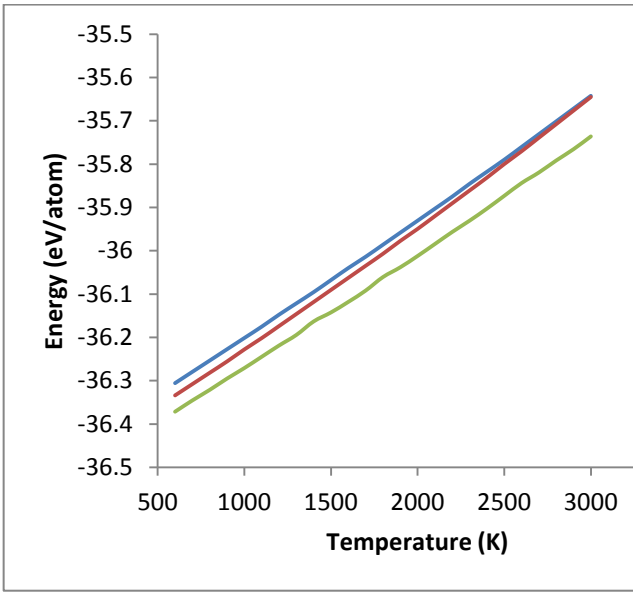

Figure 2. Energy as function of temperature for anatase SnO_2. blue curve is anatase SnO_2, red curve is V_O, and green curve is Ti_{Sn}.

In order to further check the stability of anatase SnO_2 and its two defects at various temperatures within the Buckingham potential, the radial distribution functions of SnO_2 at 300 K and 5000 K are presented in Figure 3 and 4. The peaks show the most probable distances between the atoms concerned. Furthermore, Figure 4 and 5 show that at 5000 K, the peak positions for anatase SnO_2 look the same as that of the rutile SnO_2 at 300 K, with notable peak shifts in the rutile SnO_2 [17]. The same form of peak positions is experienced with the substitutional Ti_{Sn} defect in anatase SnO_2 as shown in Figure 6. This suggest a probable phase transition from anatase to rutile SnO_2 in agreement with the first principle calculations of Yanlu Li *et al.* [18] and the experiments of Bachmann et al. [12] and Fan and Reid [16]. On the other hand these calculations show stability and transferability of the Buckingham potentials in structural analysis of materials.

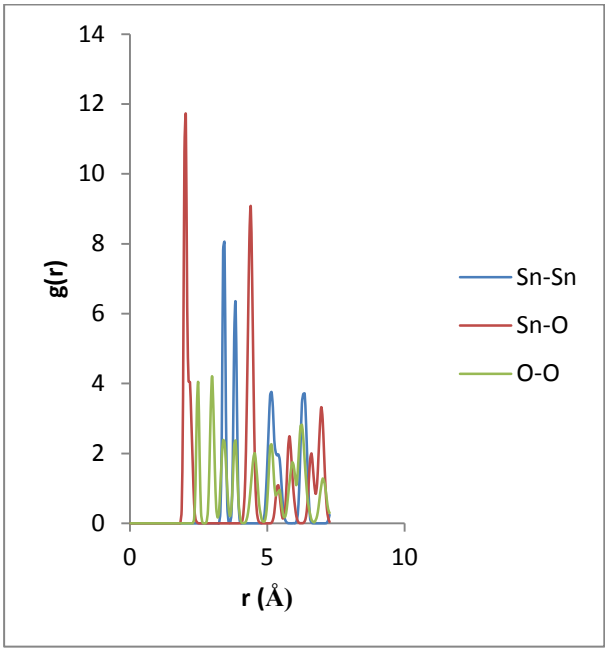

Figure 3. Radial distribution function of anatase SnO_2 at 300 K.

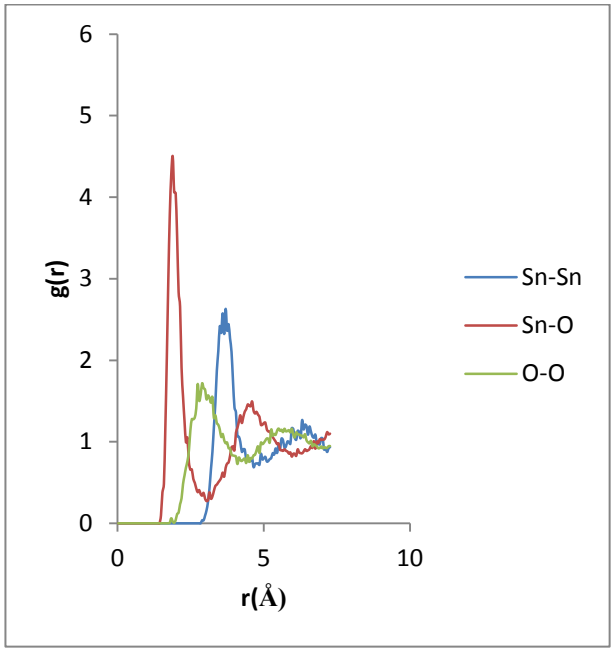

Figure 4. Radial distribution function of anatase SnO_2 at 5000 K.

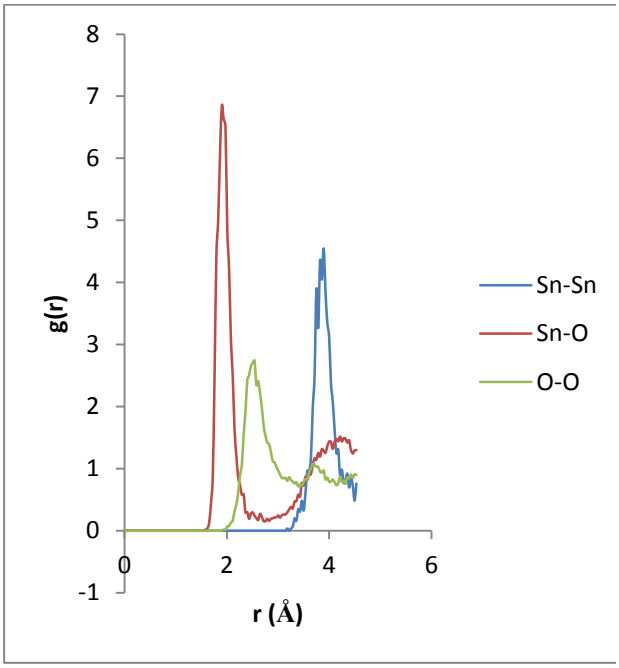

Figure 5. Radial distribution function of rutile SnO_2 at 300 K.

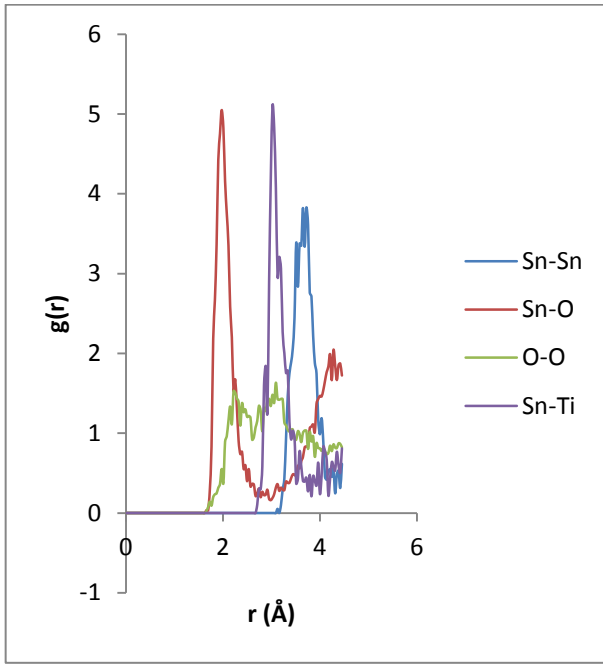

Figure 6. Radial distribution function of Ti substitutional defect in anatase SnO_2 at 1000 K.

4. Conclusion

Anatase SnO_2, oxygen vacancy and Ti substitutional defect in anatase SnO_2 have been modelled with molecular dynamics simulation using the Buckingham potential to investigate their structural and thermodynamic properties. The radial distribution curves and the energy-temperature graph suggest phase transformation at temperatures around 3000 K. Ti substitutional defect in anatase SnO_2 has the lowest energy and lowest volume which could improve its semiconducting properties at a controlled nanocrystalline growth. The volume thermal expansion coefficient is of the same order as the measured results. The specific heat capacity is of the same order with the Dulong-Petit law of solids at high temperatures.

5. Acknowledgements

IBSA, NRF and UL are thanked for their financial support. CHPC is thanked for their computational facilities.

References

[1] Godinho KG, Walsh A and Watson GW 2009 *J. Phys. Chem.* C **113** 439
[2] Hosono H 2007 *Thin solid Films* **515** 6000
[3] Eastwood PG, Claypole TC, Watson J, Coles GSV 1993 *Meas. Sci. Technol*. **4** 524
[4] Kim H, Gilmore CM, Pique A, Horwitz JS, Mattoussi H, Murata H, Kafafi ZH, Chrisey DB 1999 *J. Appl. Phys.* **86** 6451
[5] Lantto V, Rantala TT and Rantala TS 2001 *Journal of the European Ceramic Society* **21** 1961
[6] Jones FH, Dixon R, Foord JS, Edgell RG and Pethica JB 1997 *Surface Science* **376** 367
[7] Cox DF, Fryberger TB and Semancik S 1988 *Phys. Rev. B* **38** 2072
[8] Freeman CM and Catlow CRA 1990 *J. Solid State Chem.* **85** 65
[9] Bandura AV, Sofo JO and Kubicki JD 2006 *Journal of Chemistry* B **110** 8386
[10] Hines RI, Allan NL and Flavell WR 1996 *J. Chem. Soc., Faraday Trans.* **92** 2057
[11] Rantala TS, Rantala TT, Lantto V 2000 *Sens. Actuators B* **65** 375
[12] Cromer DT and Herrington K 1955 *Contribution from the national Lead Co., Titanium division* **77** 4708
[13] Smith W, Forester TR and Todorov IT 2009 *DL_POLY_2 User Manual*, STFC Daresbury Laboratory, Daresbury, Warrington WA4 4AD, Cheshire, UK
[14] Amstrong P, Knieke PC, Mackovic M, Frank G, Hartmaier A, Goken M and Peukert W 2003 *Acta Materialia* **57** 3060
[15] Tuerkes P, Pluntke Ch and Morosin D 1973 *Journal of Physics* C **13** 4941
[16] Bachmann KJ, Hsu FSL and Remeika JP 1981 *Physica Status Solidi* (a) **67** K39
[17] Rumyantseva MN, Sefonova OV, Boulova MN, Ryabova LI and Gas'kov AM 2003 *Russian Chemical Bulletin* **52** 1217
[18] Peercy PS and Morosin D *1973 Physical Review* B **7** 2779
[19] D'Ans-Lax:Taschenbuch f. Chemiker u. Physiker, Vol 1, Berlin, Heidelburg, New York: Spring 1967
[20] Fan H and Reid SA 2003 *Chemistry of Materials* **15** 564
[21] Ntimane JN, Mosuang TE and KE Rammutla 2011 *Proceedings of the SAIP2011* 268
[22] Li Y, Fan W, Sun H, Cheng X, Li P, Zhao X, Hao J and Jiang M 2010 *J. Phys. Chem.* A 114 1052

Synthesis and Characterisation of Ag- Cu-Doped Nano TiO_2

OO Nubi[1], KE Rammutla[1] and TE Mosuang[1]

[1]Department of Physics and Geology, University of Limpopo, South Africa

Erasmus.rammutla@ul.ac.za

Abstract. TiO_2 nanopowders, single and double doped with Ag and Cu, were prepared using the sol-gel method, with titanium isopropoxide as the precursor. For comparison, an undoped sample was also prepared. The synthesised samples were calcined to a temperature of 300°C and characterised by X-ray diffraction (XRD), Raman and scanning electron microscopy (SEM) techniques. The single-doped powders (as well as the undoped sample) featured only the anatase phase. The co-doped powder was found to be constituted by anatase and brookite phases. The results suggest that multiple doping of titania may favour a two-phase structure at lower temperatures than single doped powders.

1. Introduction

Nanomaterials, in general, are receiving a wide attention because of their unique physical and chemical properties. Nanosized titanium dioxide (Titania, TiO_2), in particular, is of special interest in scientific research and technological applications. Thus, extensive studies of the electric, magnetic, catalytic and electrochemical properties of TiO_2 have been conducted [1-4]. Its high surface area contributes to its optical properties and is a key factor in its photocatalytic capability [5].

TiO_2 is known to exist in three major natural crystalline polymorphs or phases namely, rutile (R), anatase (A) and brookite (B), of which anatase and brookite are metastable states – at all temperatures – that transform to rutile upon heat treatment. Brookite is rarely studied as it is difficult to synthesize [5]. Other phases that are of little significance in research and technological applications have been reported in literature[6].

In general, the various methods used in synthesising crystalline TiO_2 primarily yield the anatase phase [7]. The structure of the resulting nanoparticles is closely related to the preparation method. The sol-gel technique, being simple and of low equipment requirement, is often used to synthesise amorphous oxide of titanium which is subsequently transformed into crystalline anatase by heat treatment [8].

It is of significant interest to understand the conditions that affect the transition from one phase to another; particularly for high-temperature applications, in which phase transformation may affect the properties and performance of devices. The efficiency of nanosized TiO_2 in applications is greatly influenced by electronic modification techniques such as doping [9]. Several studies have recently investigated the effect of doping TiO_2 with metal impurities by chemical synthesis.[9] Factors that are influenced by doping include dopant concentration, distribution and the d-electronic configuration, as well as the crystallite size of TiO_2.[10] It has been noted that the simultaneous introduction of two or more atoms into TiO_2 structures, as well as the mixture of phases, can significantly improve photocatalytic activity and other peculiar characteristics[11-14] over single element doping.

This study is aimed at examining the effect of metal double-doping on the structural properties of TiO_2 nanopowders, synthesized by the sol-gel method. The structural properties are investigated using x-ray diffraction (XRD), Raman spectroscopy and scanning electron microscopy (SEM) techniques.

2. Experimental

2.1. *Synthesis (Sample Preparation)*

Three doped TiO_2 samples were prepared, namely Ag-doped, Cu-doped and Ag and Cu co-doped. A fourth sample (Pure-TiO_2) that excluded any doping was also synthesised. The dopant levels were 5% by weight each. Analytical reagent grade chemicals and the sol-gel technique were used in the preparation of samples. Tetraisopropyl Orthotitanate (Titanium (IV) Isopropoxide or $Ti\{OCH(CH_3)_2\}_4$) was used as a precursor of TiO_2, Silver Nitrate ($AgNO_3$) for Ag and Cupric chloride (Copper(II) Chloride or $CuCl_2$) for Cu. The dopants were prepared by first dissolving the solids in water. 10 ml of ethanol was then added to the required amount of each precursor. For the doped samples the dopant solution was added dropwise to the Titanium Isopropoxide, with vigorous stirring for up to 1 hour. The precipitate (xerogel) was further diluted with 30 ml water, filtered and left to dry at room temperature for 16 hours. Calcination of the samples was done at 300^{o}C for 1 hour before being ground to powders.

2.2. *Characterisation*

Powder diffractogram (XRD) data were obtained with Xpert-Pro diffractometer using Cu Kα radiation (1.5406 Å). Crystallite sizes, $D_{(hkl)}$, were estimated with the Debye-Scherrer equation:

$$_{hkl)} = \frac{0.9\lambda}{\beta_{\ hkl)} \cos\theta}$$

For quantitative analyses of the samples, the most intense peaks of the individual phases, (101) and (200) for anatase and (110) and (211) for rutile, were considered [12]. Lattice parameters were calculated from Bragg's law, $2d_{(hkl)} \sin\theta = n\lambda$, and the formula for the crystal system:

$$\frac{1}{d^2_{\ hkl)}} = \frac{h^2}{a^2} + \frac{k^2}{b^2} + \frac{l^2}{c^2}\ ,$$

in which anatase and rutile systems are tetragonal ($a = b \neq c$) while the brookite is an orthorhombic system ($a \neq b \neq c$).

The phase content (mass fraction f_x) of each sample was determined from the integrated intensities I_A, I_R and I_B of the respective peaks of anatase (101), rutile (110) and brookite (121) as [15]:

$$f_A = \frac{k_A I_A}{k_A I_A + I_R + k_B I_B}$$
$$f_R = \frac{I_R}{k_A I_A + I_R + k_B I_B}$$
$$f_B = \frac{k_B I_B}{k_A I_A + I_R + k_B I_B},$$

where the coefficients I_R and I_B assume the values 0.886 and 2.721.

Raman spectra from 50 to 1200 cm^{-1} were recorded by a spectrometer equipped with a He-Ne laser source and a charge-coupled device (CCD) detector. Micrographs of the samples were obtained with a scanning electron microscope (SEM).

3. Results and discussion

3.1. XRD

Figure 1 displays XRD patterns of the four samples – undoped Pure-TiO_2, Ag-doped TiO_2, Cu-doped TiO_2 and Ag/Cu co-doped TiO_2. All samples were heat treated at 300°C for 1 hour. Single-doped samples display the same anatase patterns as the Pure-TiO_2 but with reduced intensities. The Ag-doped sample shows stronger attenuation than the Cu-doped. However, the double-doped powder exhibits the brookite phase, in addition to the anatase. The unit cell parameters (Table 1) suggest that the TiO_2 lattice is not deformed by doping. Further, the crystallite sizes of doped powders are smaller than that of the "Pure" sample.

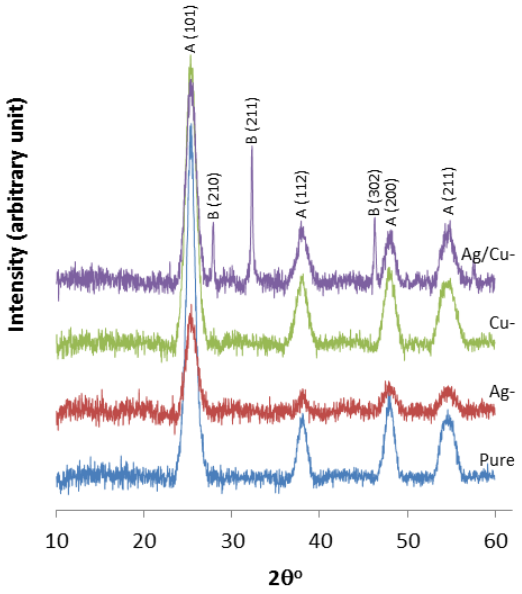

Figure 1. XRD patterns of undoped (Pure), Ag-doped, Cu-doped and Ag/Cu co-doped TiO_2, calcined at 300°C.

Table 1. Crystallite size and lattice parameters of undoped, single-doped and co-doped TiO_2, calcined at 300°C.

Sample	Phase	Crystallite size (nm)	Lattice Parameters (Å)		
			a	*b*	*c*
Pure	A	8.39	3.80	3.80	9.10
Ag-doped	A	7.02	3.83	3.83	8.77
Cu-doped	A	6.54	3.79	3.79	9.44
Ag/Cu-doped	A	6.93	3.80	3.80	9.11

3.2. Raman

The Raman shifts for the four powders are shown in Figure 2(a). Characteristic bands for anatase (153, 399, 519 and 639 cm^{-1} [16]) are presented for all samples. In Figure 2(b), the brookite phase that was revealed by the XRD results for the co-doped sample (Ag/Cu-doped) is confirmed by the Raman peaks (identified with vertical dotted lines).

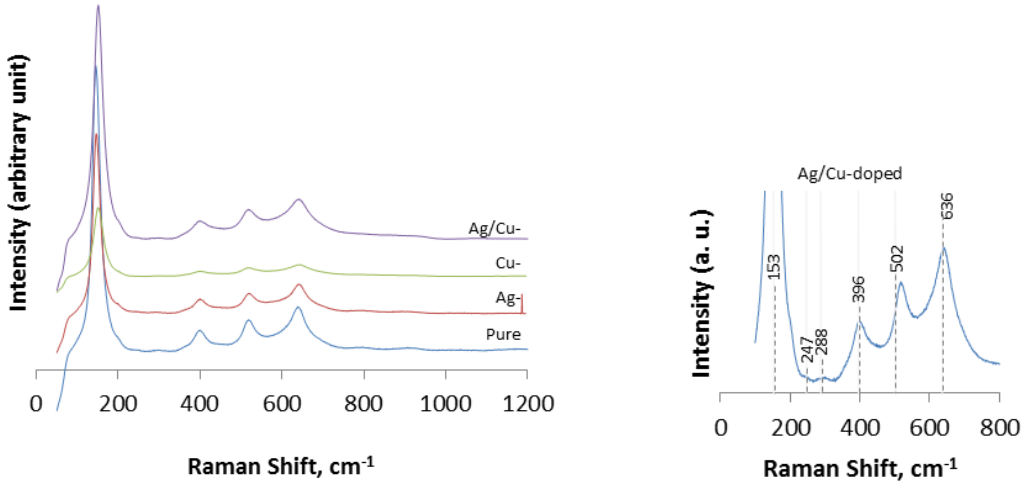

(a) (b)

Figure 2. (a) Raman spectra of undoped (Pure), Ag-doped, Cu-doped and Ag/Cu co-doped TiO_2, calcined at 300°C. (b) Brookite peaks in the Raman spectra of the Ag/Cu co-doped TiO_2.

3.3. SEM

The morphology of the samples is displayed in the SEM micrographs of Figure 3. The undoped sample displays spherical shapes, while the images of the doped powders feature irregularly-shaped, aggregated particles. Intra-particle pores are indicated by the pores within the aggregates, while the voids between the aggregates themselves are the inter-particle pores [17].

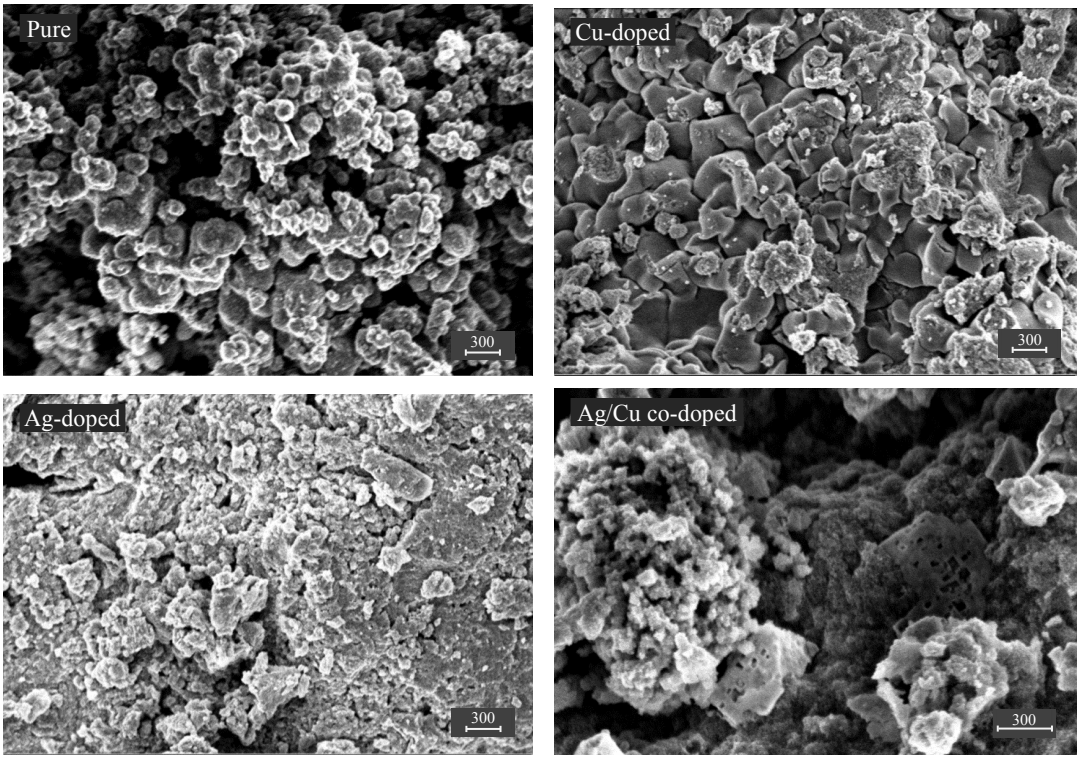

Figure 3. SEM micrographs of undoped, single-doped and co-doped TiO_2 samples. The scales are in nm.

4. Conclusions

The crystallisation of the brookite phase of titania was achieved at low temperatures (< 300^{o}C) through the introduction of multiple dopants into the TiO_2 structure. In contrast to single doping, co-doping of TiO_2 favoured a two-phased (anatase and brookite) structure without high temperature heat treatment. Single-doped samples display the same anatase patterns as the Pure-TiO_2 but with reduced intensities which results from the reduced particle sizes. The results suggest that the Ag dopant particles reside on the surface of the TiO_2 nanocrystals while Cu is incorporated into the titania matrix.

5. Acknowledgements

The authors would like to express their gratitude to NRF and University of Limpopo for financial support and CSIR's Centre for Nanostructured Materials for experimental resources.

References

[1] S-D Mo, WY Ching, Phys. Rev. B 51, (1995), 19
[2] C Hua, S Duoa, T Liua, J Xianga, M Li, Appl. Surf. Sci. (2010), doi:10.1016/j.apsusc. 11. 110
[3] JC Colmenares, MA Aramedia, A Marinas, JM Marinas, FJ Urbano, Applied Catalysis A: General 306 (2006) 120–127
[4] J-G Yu, JC Yu, B Cheng, SK Hark, K Iu, Journal of Solid State Chemistry 174 (2003) 372–380
[5] A. Beltrán, L Gracia, and J Andrés, J. Phys. Chem. B 110, (2006) 23417-23423
[6] D.A.H. Hanaor, C.C. Sorrell, J. Mater. Sci (2011) 46:855-874
[7] H Shin, HS Jung, KS Hong, JK Lee, J Solid State Chem (2005) 178:15
[8] QR Sheng, Y Cong, S Yua, JL Zhang, M Anpo, Microporous Mesoporous Mater. 95 (2006) 220
[9] P Yang, C Lu, N Hua, Y Du, Materials Letters 57 (2002) 794–801
[10] W Choi, A Termin, MR Hoffmann, J. Phys. Chem. 98 (1994) 13669
[11] D Chen, Z Jiang, J Geng, Q Wang, and D Yang, Ind. Eng. Chem. Res. 46, (2007) 2741-2746
[12] HP Klug, LE Alexander, (1975). J. Appl. Crystallogr, 8 (1975) 573-574
[13] MC Yam, F Chen, Zhang JL and M Anpo J Phys Chem B (2005) 109:8673
[14] V Stengl, S Bakardjieva and J Bludska, J. Mater. Sci. (2011) 46:3523
[15] H Zhang and J F Banfield, Journal of Physical ChemistryB, vol. 104, no. 15, (2000) 3481–3487
[16] Y Hu, H-L Tsai, C-L Huang, Journal of the European Ceramic Society, 23 (2003) 691–696
[17] J Kim, KC Song, S Foncillas, SE Pratsinis, J. Eur. Ceram. Soc. 21 (2001) 2863–2872

Reactive DC sputter deposition and charactersation of AlN thin films

T G Nyawo[1] and O M Ndwandwe[1]

[1]Department of Physics and Engineering, University of Zululand, Private Bag X1001, Kwa-Dlangezwa, 3886, South Africa

Email: NdwandweO@unizulu.ac.za

Abstract. Thin films of Aluminium Nitride (AlN) have been deposited on Si wafers using RF reactive sputter deposition in a nitrogen ambient. AlN is a wide bandgap semiconductor suitable for deep ultraviolet optoelectronics. The films have been characterized using Atomic Force Microscopy (AFM), Rutherford Backscattering Spectrometry (RBS), Scanning Electron Microscopy (SEM) and the oxygen content has been profiled using resonant RBS. The films were found to be smooth and uniform and adhere well to the Si substrate.

1. Introduction

Aluminium nitride is a semiconducting material with a bandgap of 6.2 eV making it suitable for deep ultraviolet optoelectronics. It has a high thermal conductivity which ranges from 70 to 285 $W.m^{-1}.K^{-1}$ depending on whether it is polycrystalline or a single crystal [1]. Many techniques have been used to deposit AlN on various substrates. The most popular method of depositing AlN films is by reactive RF sputtering in a nitrogen atmosphere [2,3,4,5,6]. Other techniques that have been used to deposit AlN are chemical vapour deposition [7], laser chemical vapour deposition [8], molecular beam epitaxy and pulsed laser ablation [3].

In this work we wanted to deposit AlN using reactive sputtering, study its surface using AFM and SEM and also use both RBS and resonant RBS to study both composition and possible incorporation of oxygen in these crystals as we could not find any reference to the use resonant RBS to study oxidation of AlN.

2. Experimental procedure

Silicon wafers were cut into squares of edge 12 mm, chemically cleaned in an ultrasonic bath and then rinsed in de-ionized water. The chemicals used to clean the substrate wafers were methanol, acetone, trichloroethylene, acetone and finally methanol, before using distilled water. The wafers were then dried and loaded into a sputtering system. The sputtering machine used is an AJA Orion 5 Sputtering System. Once good vacuum was achieved the chamber of the sputtering system was pre-heated at 600 ^{o}C for one hour to drive out any moisture and also to degas (remove oxygen from its walls). At the start of the experiment, before introducing any gas, the chamber had a base pressure of $2x10^{-7}$ Torr. The process gas

used to sputter the aluminium was argon introduced at a flow rate of 6 sccm (Standard Cubic Centimeters per Minute). The reactive gas used to obtain AlN was nitrogen introduced at a flow rate of 6 sccm. Both gases were high purity gases from AFROX (~99.98% pure). The aluminium target used was a disc of 2 inch diameter, 0.250 inch in thickness and had a purity of 99.999%. The target to substrate distance was 34 mm. The substrate was rotated in order to obtain a uniform film. The deposition was done for a period of two hours while maintaining a pressure of $3x10^{-3}$ Torr inside the chamber. After deposition the samples were left in the chamber for one hour to cool. Dry nitrogen was used to break vacuum, thus eliminating condensation inside the chamber as well as oxygen contamination.

3. Results and discussion

3.1. AFM results

Figure 1: AFM image showing a smooth AlN surface.

Figure 1 shows an image obtained from the as deposited film of AlN. It is seen from the image that the sample surface appears smooth.

3.2. Normal RBS

The samples obtained had a uniform colour, looked smooth and showed no signs of peeling (see figure 1). Rutherford Backscattering Spectrometry (RBS) was done using charged helium atoms accelerated to an energy of 2 MeV. The RUMP (Rutherord Universal Manipulation Program) software code was used to determine the Al:N stoichiometric ratio of deposited layers and to find layer thicknesses of the film.

Figure 2 shows RBS spectra of AlN on silicon. Normally it is not easy to analyse a sample using RBS if the mass of the two elements in the sample are close to each other. In this case Al is close to Si of the substrate. However Al (an element slightly lighter than Si) has been deposited on top of Si. The overlap between the spectra of the two creates an observed peak seen at the higher energy end of the spectrum (see figure 2). It is this bump which helps us to do the analysis. The surface positions of the elements Si and Al

are marked by means of arrows on the graph. These are positions at which alpha particles scattered on the surface will be recorded. Surface positions of both N and O have been shown also. RBS results show that the thickness of the AlN film deposited using RF magnetron sputtering at an energy of 60 W for two hours is about 1 400 Å. It seen from the other spectrum that the thickness of the sample deposited at RF magnetron power of 130 W is very close to that of the other sample. RF sputter deposition is less efficient when compared to DC magnetron deposition, in general. The gas flow rates of nitrogen and argon during the deposition of both samples were equal at 6 sccm.

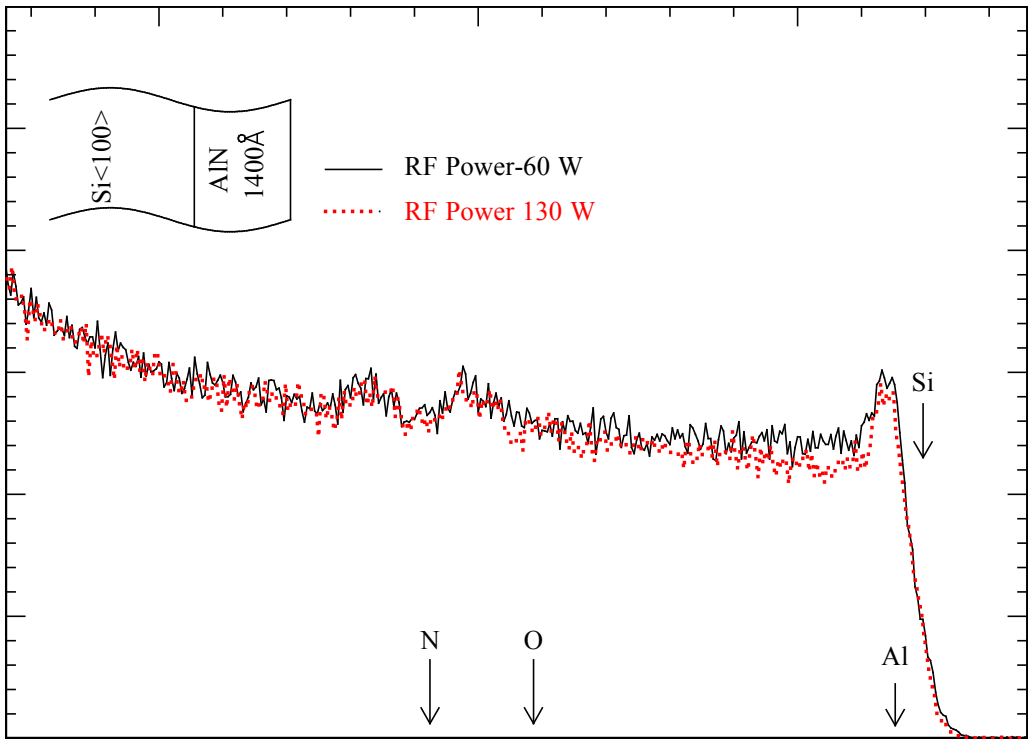

Figure 2: RBS spectra obtained from samples deposited at an RF magnetron power of 60 W and 130 W respectively for a period of 2 hrs. The argon and nitrogen flow rates were 4 sccm and 10 sccm respectively for both samples. The film thickness was found to be 1 400 Å. It is also obvious from both spectra that the samples have oxygen. The chamber pressure was maintained at $3x10^{-3}$ Torr.

Both depositions were done at room temperature; figure 2 shows the presence of oxygen on both samples. It shows that the amount of oxygen is almost the same in both samples.

We found using RUMP simulation that the ratio of Al:N is close to unity (i.e. we do have AlN, possibly oxidized).

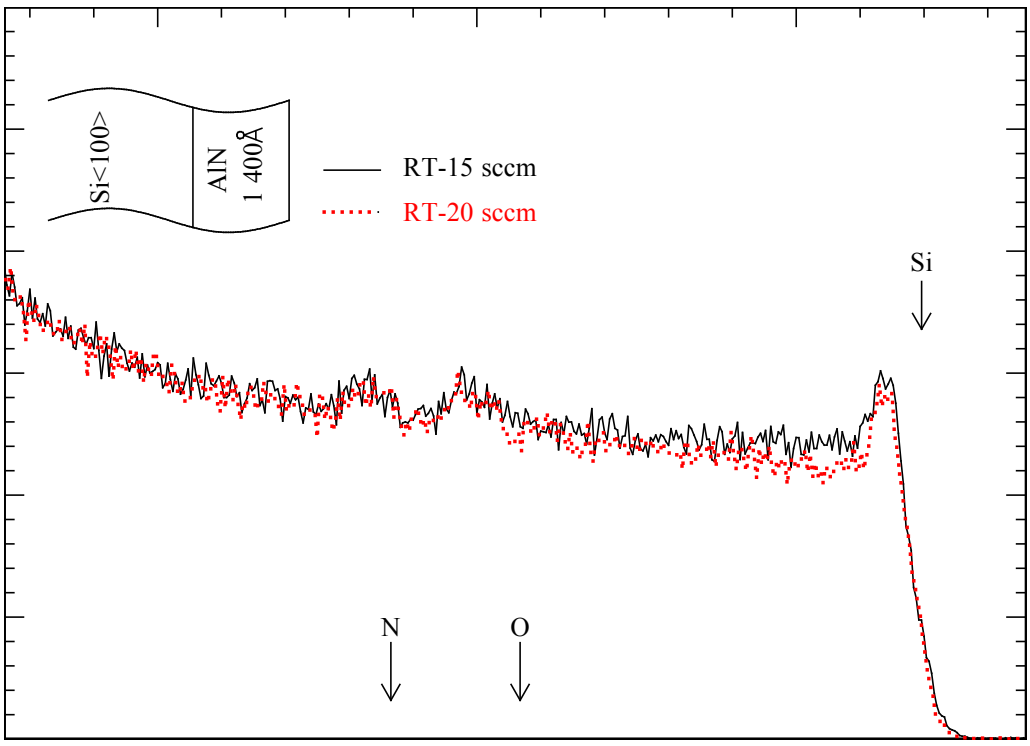

Figure 3: RBS spectra of samples deposited using RF magnetron power of 130 W for a period of 2 hrs. In an attempt to reduce oxygen contamination the flow rate of nitrogen was raised to 15 and 20 sccm for the two samples. It is difficult to tell whether the amount of oxygen has been reduced from these results. Sample thicknesses were found to be the same as before.

In an attempt to reduce oxygen contamination or its inclusion within the film, we increased the nitrogen flow rates to 15 sccm and 20 sccm for the two samples spectra shown in figure 3. The flow rate of argon was kept at 6 sccm and the chamber pressure was maintained at 3×10^{-3} Torr. The deposition was done for a period of two hours. It is noticed from figure 3 that the thickness of both samples remain at 1 400 Å. This is to be expected since sputtering results are fairly reproducible. The same amount of material for a given element will be deposited if the same power and time duration is used. On analyzing the data using RUMP, we could not find any difference in oxygen amounts for the two samples deposited using different nitrogen flow rates.

We decided to use resonant oxygen scattering to enhance the oxygen peak.

3.3 Resonant RBS

If the energy of the oncoming alpha particles exceeds the Coulomb barrier the alphas begin to interact with the nucleus of the target atom resulting in non-Rutherford backscattering. In this case the scattering cross section may increase resulting in an enhanced scattering yield. We used the process $^{16}O(^4He; ^4He)^{16}O$ inside a van De Graaf accelerator with He^{2+} ions of kinetic energy 3.05 MeV at a scattering angle of 165° and a sample tilt of 10° (to avoid channeling effects).

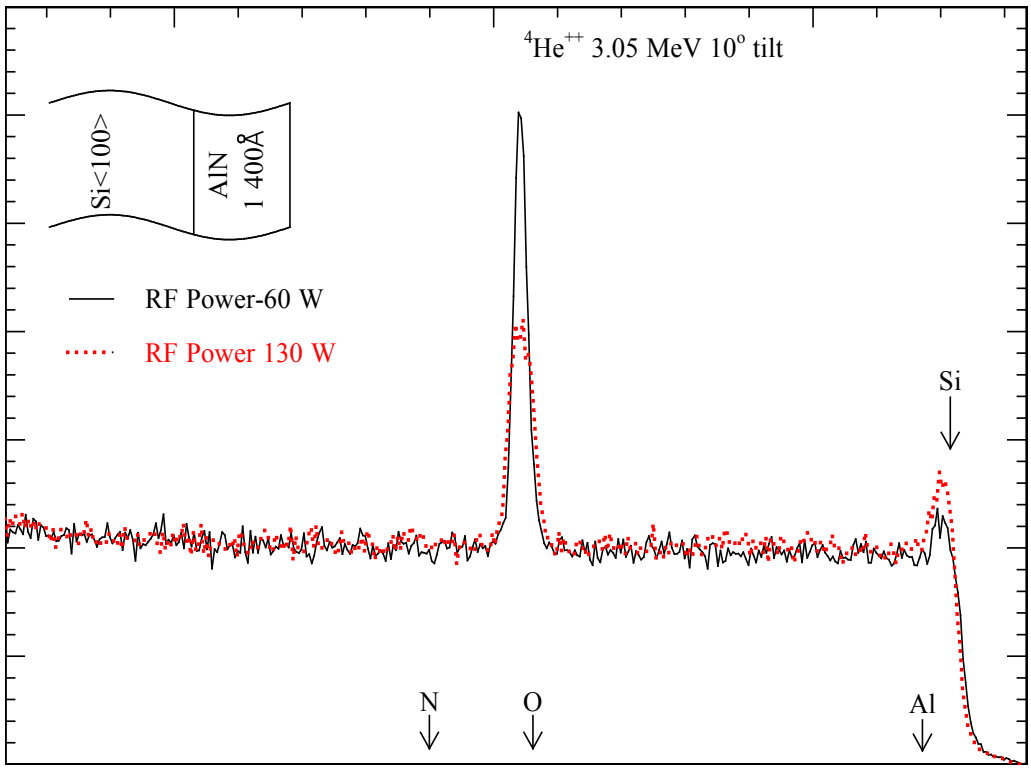

Figure 4: Backscattering with 3.05 MeV alphas. The spectra is that of samples used to obtain figure 3 (at 2 MeV). We note now the enhanced oxygen peak. Notice that there is more oxygen in the sample deposited using magnetron power of 60 W compared to that of 130 W.

The spectra shown in figure 4 was obtained by backscattering 3.05 MeV alpha particles on two samples, one obtained at magnetron power of 60 W, while the other at 130 W (they are the same samples investigated at 2 MeV in figure 3). Since the alphas scatter at resonance on oxygen at an energy of 3.05 MeV, the oxygen peak in the spectra is enhanced. We therefore notice that there is much more oxygen in the sample obtained using 60 W when compared to that in which 130 W was used. The peaks belonging to N are however even lower (compare these in both figure 3 and figure 4). It does not mean there is less nitrogen but simply because the surface barrier detectors used are less efficient at higher energies. Note also that nitrogen is not at resonance at this energy (3.05 MeV). Comparing the area under the RBS curves for the oxygen peak we find that there is 23.6% more oxygen in the sample deposited at 60 W when compared to that deposited at 130 W.

4. Summary and conclusion.

We have sputter deposited films of AlN using RF sputtering where the reactive gas used is nitrogen. We have found that RF sputtering is a suitable method to make films of AlN. The sputter rates are however low and thicker films can only be made over longer time periods. AFM analysis has shown that the resulting films are smooth, show no signs of peeling and are adherent on the Si substrate. We have used RBS to determine sample thicknesses. It also allowed us to find out the ratio of Al:N, which was found to be close to unity (meaning AlN films deposition achieved). We however serendipitously found signs of oxidation. We found resonant RBS to be a suitable tool to analyse samples that had oxidized. In trying to find the source of oxidation, it was discovered that higher sputter rates (higher RF power) lead to lower oxygen contamination. We also found that higher flow rates are better and lead to lower oxidation. The source of the oxidation is possibly the chamber itself.

References

[1] Chen H, Jian S, Kao H, Chen M and Huang G 2011. *Epitaxial growth of non-polar a-plane AlN films by low temperature sputtering using ZnO buffer layers*, Thin Solid Films, **519** 5090-5094.

[2] Umeda K, Takeuchi M, Yamada H, Kubo R and Yoshino Y 2006. *Improvement of thickness uniformity and crystallinity of AlN films*, Vacuum **80** 658-661.

[3] Cheng H, Sun Y, Zhang J X, Zhang Y B, Yuan S and Hing P 2003. *AlN films deposited under various nitrogen concentrations by RF reactive sputtering*, Journal of Crystal Growth, **254** 46-54.

[4] Lee S, Yoon K, Cheong D and Lee J 2003. *Relationship between residual stress and structural properties of AlN films deposited by RF reactive sputtering,* Thin Solid Films, **435** 193-198.

[5] Muhl S, Zapien J A, Mendez J M and Andrade E 1997. *Aluminium nitride films prepared by reactive magnetron sputtering*, Journal of Physics:D. Applied Physics.No15, **30** 2147- 2152.

[6] Carlotti G, Gubbiotti G, Hickernell F S, Liaw H M and Sosino G 1997. *Comparative study of the elastic properties of polycrystalline aluminium nitride films*, Thin Solid Films, **310** 34-38.

[7] Dobrynin A V 1999. *Thermoelastic strain and plastic yielding in aluminium nitride on sapphire,* Journal of Applied Physics, issue 3, **85** 1876-1883.

[8] Radhakrishnan G 1995. *Properties of AlN films grown at 350 K by gas-phase excimer laser photolysis,* Journal of Applied Physics, Issue 10, **78** 6000-6006.

Modification of glassy carbon under strontium ion implantation

O. Odutemowo, J.B malherebe, D.F Langa, A.J Botha, L.Prinsloo1, E. Wendler, W.Wesch, P.Chakraborty, E.F de silveira

Department of Physics, University of Pretoria, 0002, Pretoria, South Africa

E-mail: u12052613@tuks.co.za

Abstract. The effect of annealing on the surface morphology and on the diffusion of strontium ions implanted into glassy carbon is reported. Glassy carbon (GC) was implanted with strontium ions at an energy of 360 keV and a fluence of 2×10^{16} ions/cm^{2}at room temperature. The sample was isochronally annealed in vacuum for 1h at 200 ^{o}C, 300 ^{o}C and 400 ^{o}C respectively. Rutherford backscattering spectroscopy, Raman spectroscopy and scanning electron microscopy (SEM) were used to investigate and monitor changes in the sample. There was no visible diffusion of strontium after the sample was annealed at 200 ^{o}C for 1h but after annealing at 300 ^{o}C and 400 ^{o}C respectively, the diffusion of Sr towards the surface of the GC was observed with a distinct Sr peak forming on the surface of the GC at 400 ^{o}C. The Raman spectra showed that implantation of strontium damaged the structure of the glassy carbon but some of the damage was annealed out after heat treatment. SEM images of the sample showed that there is little change in the surface structure of the GC both after implantation and annealing.

1. Introduction

The difficulty of radiation leakage from nuclear reactors during accident conditions, waste storage and management has made nuclear power unpopular around the world. One of the major features of the Pebble Bed Modular Reactor (PBMR) is its ability to contain radioactive fission products within the Tristructural-Isotropic (TRISO) fuel particles [1]. However, there is still a need to store spent fuels i.e. fission products. These fission products are extremely dangerous if they escape into the environment, therefore it is important that they are stored in containers or storage made of a suitable material.

Glassy carbon (GC) is a nuclear material with very distinct characteristics. It is a disordered form of carbon with high temperature resistance, high hardness and strength and chemical stability even in extreme environments [2]. Glassy carbon is also unaffected by nearly all acids and cannot be graphitized even at very high temperature [2,3]. Because of these characteristics, there is a need to investigate the modification of the structure and diffusion behavior of fission products in glassy carbon. This is to determine if glassy carbon will be a good diffusion barrier and storage material for nuclear fission products.

In this research, Strontium was implanted in glassy carbon (Sigradur® G) and the diffusion mechanism and structural modification was studied.

2. Experimental Procedures

The glassy carbon was polished with 1μm diamond solution and then implanted with $^{84}Sr^{+}$ at energy of 360 keV and a fluence of 2×10^{16} ions/cm^2 at room temperature.

The sample was then cut into small pieces of about 5 mm × 5 mm. A piece was vacuum annealed isochronally at 200 ºC, 300 ºC and 400 ºC for 1h. The diffusion pattern and distribution was determined by Rutherford Backscattering spectroscopy (RBS), using helium particles with energies between 1.4 and 1.6 Mev. Raman spectroscopy and the Scanning electron microscope (SEM) were then employed to investigate the effect of implantation and annealing on the microstructure of the Glassy Carbon.

3. Results and Discussion

The Raman (D and G) peaks of the polished Glassy Carbon were very distinct and clearly resolved-see figure 1. However, after implantation, merging of the two peaks was noticed. This indicates that the glassy carbon was damaged due to the implantation of strontium at room temperature. The peaks reappeared after the sample was annealed; this implies that some of the damage was annealed out. the Although still merged, the peaks became slightly more prominent after the sample was annealed out; this implies that only some of the damage was annealed out.

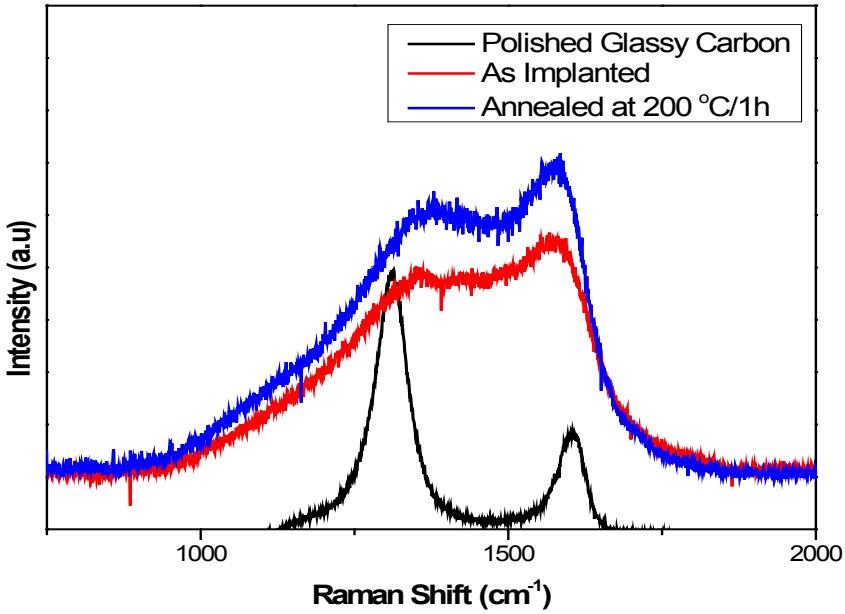

Figure 1. Non- normalized spectra of glassy carbon after different heat treatment.

Because surface topography can affect RBS spectra, especially where broadening of peaks are of interest, we investigated the topography of our samples before analysis using SEM. Figure 2 show that the SEM images of the polished GC, as-implanted GC and the vacuum annealed GC. The polished GC has lots of mechanical scratches due to polishing. These scratches were reduced and the surface appeared smoother after implantation. However, after annealing the samples, the scratch marks reappeared and became more prominent compared to the as-implanted images. This was perhaps due to the sputtering of the lose carbons sitting on the surface of the GC during polishing. The polishing marks were still small enough to affect the RBS spectra.

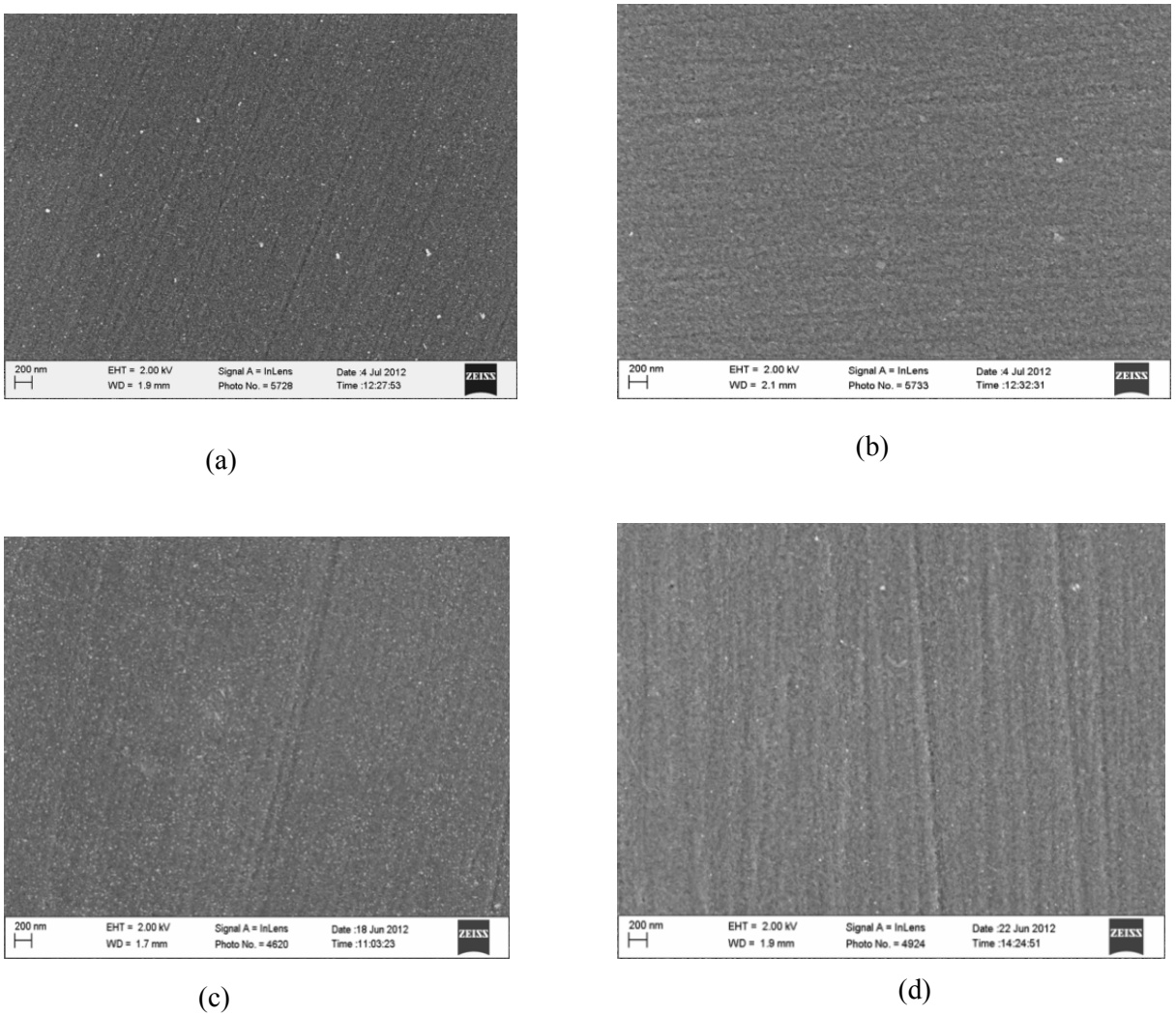

Figure 2. SEM images of strontium implanted GC. (a) Polished. (b) As-implanted. (c) Implanted and annealed at 300 ^{o}C for 1h. (d) Implanted and annealed at 400 ^{o}C for 1h.

Figure 3 illustrates the experimental profile and SRIM simulation [4] of GC implanted with strontium ions at room temperature. Also shown in Fig.2 is an edgeworth distribution fit to the experimental data. The experimental projected range of 231 nm was slightly lower than the theoretical estimate by SRIM of 271 nm. This discrepancy might be due to the inaccurate energy loss data used for the conversion of the RBS channels to depth and/or due to inaccurate interatomic potentials used in SRIM for glassy carbon.

Due to lack of suitable experimental values, data for graphite was used instead of glassy carbon. The projected range straggling was about 22 % higher than it was predicted by SRIM. The kurtosis (β) and skewness (γ) of the implanted distribution was almost Gaussian (β=3;γ = 0.036) for the SRIM and (β=2.5; γ = -0.5) for the experimental values. The negative gamma value derived from the experimental data showed that the implanted strontium peak was skewed to the left. This shows that even during implantation, there was already diffusion of strontium towards the surface of the GC.

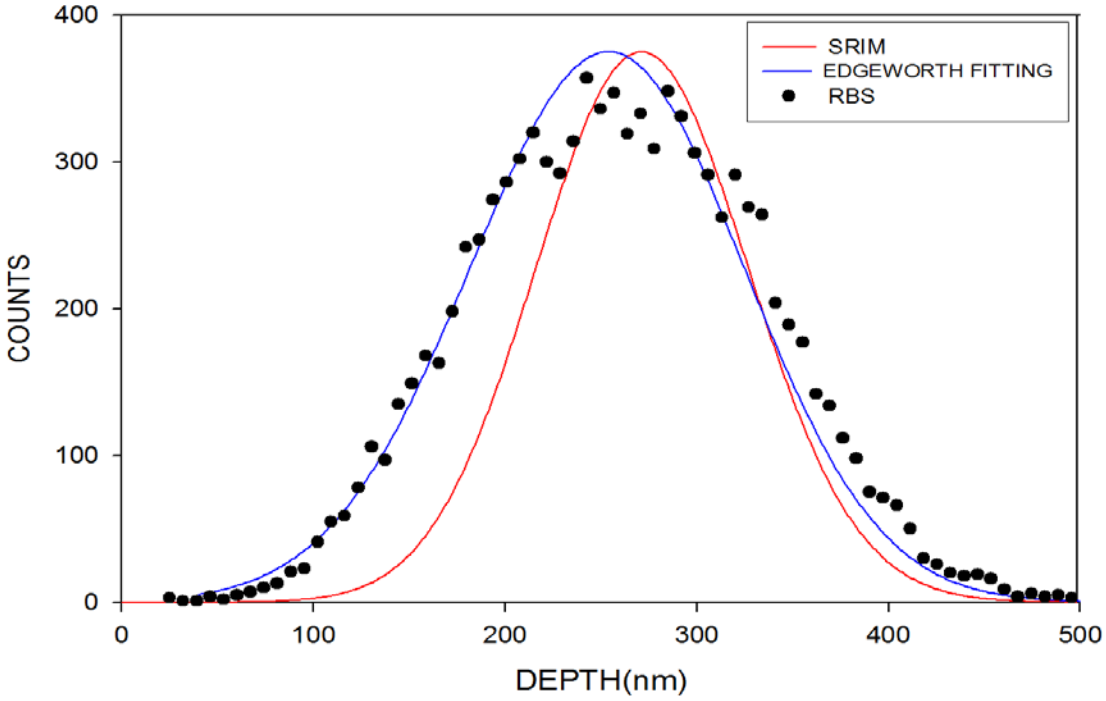

Figure. 3. RBS spectrum of the as-implanted strontium peak compared to a SRIM simulation.

The RBS spectra of vacuum annealed GC implanted with strontium are shown in Figure 4. After annealing the Sr-implanted glassy carbon at 200 ^{o}C for 1h, no change in the RBS spectrum for the strontium wasdetected and the strontium peak remained approximately Gaussian. This indicates that no visible diffusion of the Sr occurred. After further isochronal annealing for 1 h of the sample to 300 ^{o}C and 400 ^{o}C respectively, the Sr profile became broader and skewed towards the surface of the GC. A distinct strontium peak was formed on the surface of the GC after annealing at 400 ^{o}C. No broadening of the Sr profile towards the bulk of the GC was observed for both of these annealing temperatures. This indicates that diffusion of the implanted Sr occurred only towards the surface of the GC and not into the bulk of the glassy carbon. Since one can expect that most of the radiation damage induced by the bombarded Sr ions will roughly correspond to the implanted Sr profile, this diffusion towards the surface of the glassy carbon is an indication that the diffusion of strontium in glassy carbon was induced by the radiation damage. The Raman results confirmed that some damage remained in the glassy carbon after annealing allowing this radiation-induced diffusion to occur.

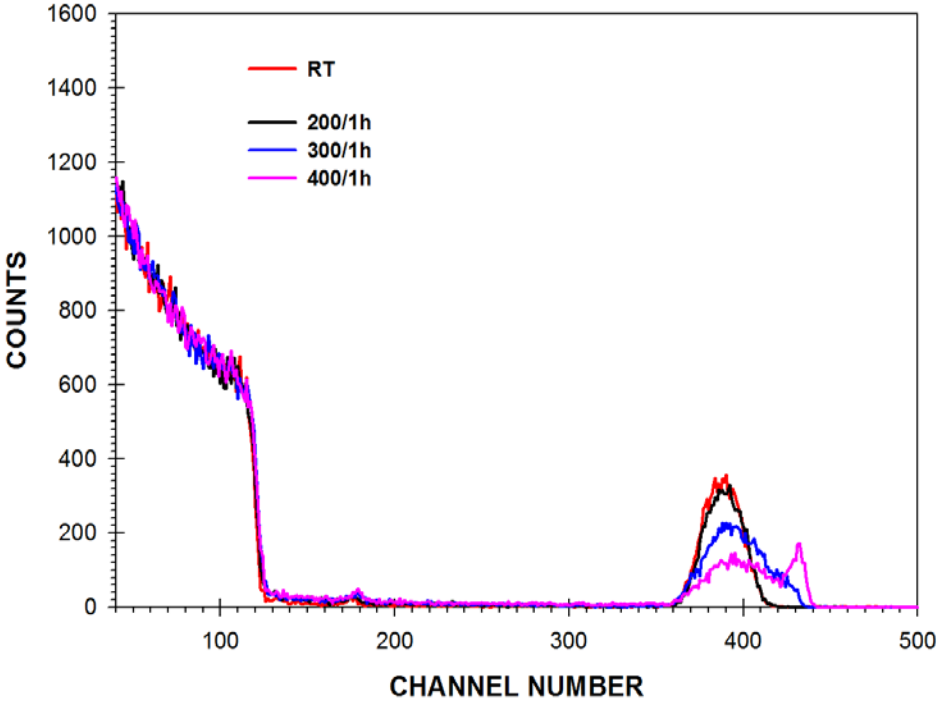

Figure. 4. RBS spectrum of the vacuum annealed GC implanted with strontium.

4. Conclusion

360 keV Sr ions were implated into glassy carbon to a fluence of 2×10^{16} ions/cm^2 at room temperature. Raman spectroscopy was used to investigate the effects of implantation and heat treatment on the structure of the glassy carbon. It was observed that the sample bcame damaged after implantation with Sr-ions. After implantation, the Raman peaks (D and G) of the glassy carbon merged, signifying damage in the material. After annealing at 200 ºC, the peaks reappeared although they were not as prominent as in the un-implanted glassy carbon. The reappearance of these peaks indicates that some of the damage was annealed out after heat treatment of the sample.

The diffusion of strontium implanted in glassy carbon was also investigated using RBS. Diffusion towards the surface of the glassy carbon occured at 300 ºC and 400 ºC. At 400 ºC, a distinct strontium peak formed on the surface. This diffusion/segregation towards the surface is probably due to radiation-induced diffusion. SEM investigations of the samples showed that the topography of the surface was small enough not to affect the RBS spectra.

References

[1] J. B. Malherbe, E. Friedland, N.G. van der Berg, *Ion beam analysis of materials in the PBMR rector. Nucl. Instrum.* Methods Phys. Res. **B 266** (2008) 1373-1377

[2] P.J.F. Harris, *Fullerene– related structure of commercial Glassy Carbon.* Philos. Mag. **84** (2009) 3159-3167.

[3] M.P. Manoharan, H. Lee, R. Rajagopalan, H.C. Foley, M.A. Haque, *Elastic properties of 4-6 nm thick Glassy Carbon thin films.* NanoscaleRes. Lett.**5** (2010) 14–19.

[4] J.F. Zieglar, SRIM 2010 computer code, www.srim.org , 20 July, 2012.

I-V-T and DLTS characteristics of e-beam deposited W/Pd Schottky contacts on 4H-SiC

A T Paradzah, M J Legodi, F D Auret, M W Diale and W E Meyer

Department of Physics, University of Pretoria, Private Bag X20, Hatfield 0028 Pretoria

Alexander.Paradzah@up.ac.za

Abstract. We report on the characteristics of W/Pd Schottky contacts deposited on 4H-SiC. I-V-T measurements indicate a deviation from thermionic emission (*TE*) theory in the 40 K to 100 K temperature range, suggesting an inhomogeneous Schottky barrier at the interface. This observed deviation could be due to the surface damage caused by e-beam deposition. Both the Schottky barrier height (Φ_{BO}) and the diode ideality factor (n) exhibited anomalous behaviour in the low doped (7.1×10^{15} cm^{-3}) and highly doped (1.96×10^{16} cm^{-3}) samples. In the 1.96×10^{16} cm^{-3} doped sample, we typically observed $1.50\ eV \leq \Phi_{BO} \leq 0.89\ eV$ and $1.1 \leq n \leq 4.3$ in the temperature range 340 K to 40 K. The inhomogeneous Schottky barrier was satisfactorily described by a Gaussian distribution with mean, $\Phi_{BO} = 1.73$ eV, and standard deviation, $\sigma_s = 0.09$ eV. Current conduction was predominantly *TE* for $T > 140$ K and was increasingly of thermionic-field-emission (*TFE*) character below 140 K. Deep level transient spectroscopy (DLTS) reveals the presence of two prominent peaks located at 0.096 eV and 0.607 eV below the conduction band minima, E_C. We detect, on the sample with a doping density of 7.1×10^{15} cm^{-3} (but not on the higher doped sample), two extra peaks with activation enthalpies of 0.160 eV and 0.121 eV which, we attribute to the e-beam metallization damage.

1. Introduction

The wide bandgap, high-thermal conductivity, high-breakdown field, and robust mechanical properties of SiC make it an attractive material for high- temperature, high-power, and high-frequency electronic devices [1-2]. The 4H polytype of SiC has generated much interest recently because of its outstanding electronic properties. It is a promising semiconductor for ionizing radiation detectors as well as for devices that operate in high temperatures and harsh radiation fields due to its wide bandgap [3-4]. Despite the material's high quality physical and electronic properties, SiC devices critically depend on the quality of the metal contacts formed, for example, Schottky contacts i.e., the types of metals used and fabrication factors such as surface cleaning and metallization processes. The quality of a Schottky diode is directly related to the barrier height. A high Schottky barrier height limits the amount of current as fewer charge carriers will have sufficient energy to overcome the barrier and a small barrier height can lead to large amounts of undesired leakage currents. In this work we investigate the behavior of a tungsten contact on n-type 4H-SiC. According to the Schottky-Mott theory, the Schottky

barrier height (Φ_{BO}) is defined as $\Phi_{BO} = \Phi_m - \chi$ [5] where Φ_m is the metal work function and χ is the semiconductor electron affinity. χ = 3.3 eV for SiC and Φ_m = 4.55 eV for tungsten, then the theoretical barrier height is 1.25 eV. However, SBH's of practical Schottky diodes are complicated affairs as they also depend on other factors such as the surface morphology of the underlying semiconductor, its doping density, the details of the metal-semiconductor (MS) interface and the metallization process. The theoretical value is therefore difficult to achieve in practice. The metallization process can also introduce electrically active defects in a material. Knowledge of these defects is vital because electrically active defects can either enhance or degrade device performance by altering the doping concentrations and carrier lifetimes [6-7]. It is thus important to identify, understand and possibly control these defects to enhance device operation [6-8]. In this study we use I-V-T methods to determine the Schottky barrier height and ideality factors of W/Pd contacts on SiC samples of different doping densities. This gives us insight into the nature of Schottky junction formed and its characteristics over a wide temperature range. From DLTS, we describe the electrically active defects that are associated with the metallization damage.

2. Experimental procedure

Samples of 4H-SiC with doping densities 7.1 × 10^{15} cm^{-3} and 1.96 × 10^{16} cm^{-3} were degreased by boiling in trichloroethylene followed by a boil in isopropyl alcohol and rinses in 18 MΩ cm de-ionized water. The native oxide layer on the samples was removed by dipping them in 40% HF solution before a final rinse in de-ionized water and a blow dry in N_2. Low resistance Ni ohmic contacts were deposited on the sample backsides by joule evaporation. The ohmic contacts are 300 nm thick and were annealed in a tube furnace, in flowing Argon gas at 950 °C for 10 minutes. The samples were then rinsed in deionised water and dipped in HF before W/Pd Schottky contacts with relative thickness of 15 nm and 35 nm, and 0.6 mm diameter were e-beam deposited through a metal contact mask. Current-voltage-temperature measurements in the temperature range 20 K to 380 K were carried out in a Helium cryostat. DLTS measurements were performed using a Laplace-DLTS National Instruments DAQ system.

3. Results and discussion

Unless or otherwise stated, all the experimental data are from the 7.1×10^{15} cm^{-3} specimens. Figure 1 shows the semi-logarithmic forward current-voltage characteristics of a typical 7.1×10^{15} cm^{-3} doped sample. The high temperature curves are linear over many orders of magnitude indicating the dominance of the *TE* mechanism. The curves below 140 K show two distinct linear regions. The low voltage "knees" are possibly due to the effect of recombination-generation of carriers in the space charge region and defect-assisted tunneling of charges through the barrier [9]. The curves corresponding to temperatures higher than 140 K are linear – in agreement with the *TE* theory.

According to the *TE* theory, the total majority carrier current, *I*, through a Schottky barrier diode (SBD) may be expressed as [9-10] $I = I_O \exp\left(q\left(V - IR_S\right)/nkT\right)\left[1 - \exp\left(q\left(V - IR_S\right)/kT\right)\right]$, where $I_O = AA^* \exp\left(-q\Phi_{BO}/kT\right)$ is the saturation current, q is the electronic charge, A^* the effective Richardson constant, A the effective diode area, T the absolute temperature, Φ_{BO} the zero bias barrier height, k the Boltzmann constant, V the bias voltage, n the ideality factor and R_s the series resistance. An ideality factor, n is introduced to describe the deviation of the experimental I - V results from the ideal *TE* model and is given by: $n = \left(q/kT\right)\left(dV/d\ln I\right)^{-1}$. The linear part of the curves of Figure (1)

thus gives the values of n from the gradient. Figure 2 shows variation of experimental n and Φ_{BO} with temperature.

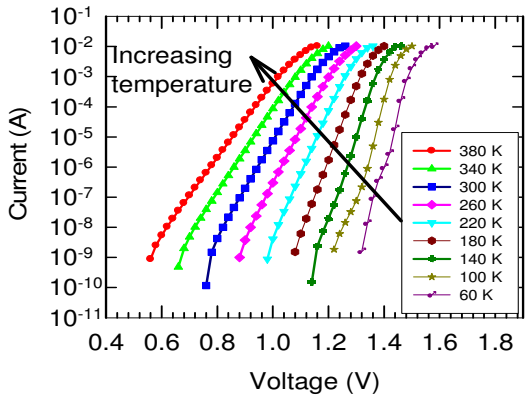

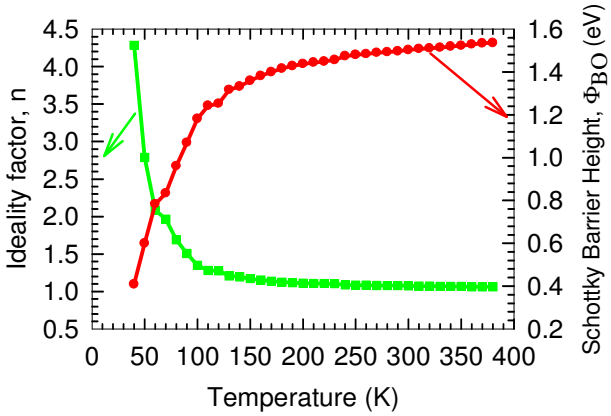

Figure 1 Selected forward *I-V* characteristics in the 60 K – 340 K range for the 7.1×10^{15} cn^{-3} sample.

Figure 2. Dependency of ideality factor and barrier height on temperature in the range 40 K – 380 K

The ideality factor decreases from 4.3 at 40 K to 1.1 at 380 K while Φ_{BO} increases from 0.89 eV at 40 K to 1.50 eV at 380 K. The graph shows that both n and Φ_{BO} have a strong reciprocal dependence on temperature for lower temperatures. This dependency is clearly in two distinct temperature regions where the change in n and Φ_{BO} is more pronounced for $T < 140$ K and less so for $T > 140$ K. For the 1.96×10^{16} cm^{-3} specimen, n decreases from 4.68 at 40 K to 1.09 at 340 K while Φ_{BO} increases from 0.253 eV to 1.42 eV in the same temperature range. Table 1 shows the changes in n and Φ_{BO} with temperature for the two differently doped samples. Since the only variable in the two samples is the doping density, it can be concluded that at any given temperature, Φ_{BO} decreases while n increases with increasing doping density which is in agreement with results of previous studies [11-12]. One can also conclude that lowly doped samples produce better quality SBD characteristics.

Table 1. Variation of n and Φ_{BO} with temperature for selected temperature values.

	7.1×10^{15} cm^{-3}		1.96×10^{16} cm^{-3}	
T (K)	n	Φ_{B0} (eV)	n	Φ_{B0} (eV)
40	4.2860	0.4090	4.68	0.363
50	2.789	0.6000	3.625	0.461
60	2.0860	0.7830	2.918	0.566
300	1.0750	1.5030	1.086	1.442

3.1. The Richardson constant

The Richardson plot is used to determine the effective barrier height and the Richardson constant. A plot of ln (I_o / T^2) versus (1 / T) should give a straight line with a slope corresponding to $q\Phi_{BO}/k$ and the intercept should give *ln AA**. From the Richardson plot, Figure 4(b), *A** has been calculated as 13.2×10^{-3} A cm^{-2} K^{-2} a value that is way too smaller than the expected value of 149 A cm^{-2} K^{-2}. The effective barrier height was calculated to be 0.59 eV. The deviation of the value of *A** from the theoretical value cannot be explained by the thermionic emission diffusion (*TED*) model [12]. Instead, the existence of barrier fluctuations at the interface between the *MS* interface is suggested as the possible cause of the anomalies [13]. Other possible causes of the deviations include existence of crystal defects, image force lowering, effects of tunneling current through the potential barrier, non-uniformity in the interfacial charges, and spatial distribution of the doping atoms [12,14-15].

3.2 Barrier height inhomogeneity analysis and the modified Richardson plot

If a Gaussian distribution of SBH's is assumed, a plot of Φ_{ap} *vs.* $1/2kT$, Figure 4 (a) should give a straight line whose intercept corresponds to Φ_{BO} while its gradient gives σ_{so}^2.

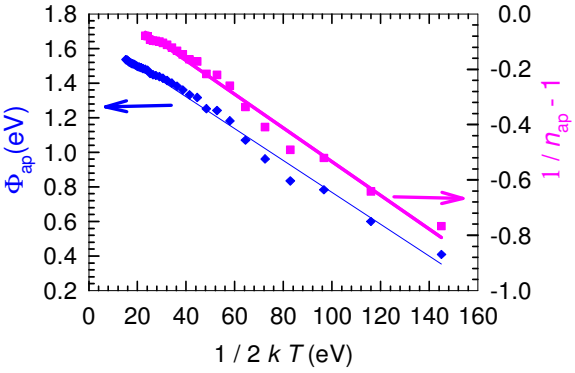

Figure 4(a). Graph of $1/n_{ap}$ -1 and Φ_{ap} vs. 1/2kT for the determination of ρ_2, ρ_3, and σ_{so}

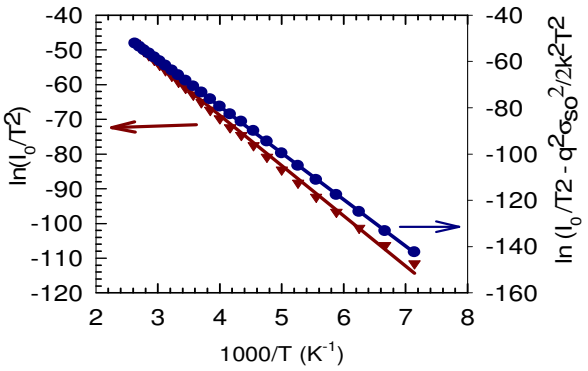

Figure 4(b). The Richardson plot of and the modified Richardson plot

Values of 0.56 eV and 0.09 eV are obtained from the plot for Φ_{BO} and σ_{so} respectively. Figure 4(a) also shows a plot of $1/n_{ap} - 1$ vs. $1/2kT$ which yields a straight line with an intercept that corresponds to ρ_2 while the gradient gives ρ_3. ρ_2 is found to be -0.53 and ρ_3 is -0.006. The straight line nature of the plot confirms that the ideality in the *I-V* curves represents the voltage deformation of the barrier height at the MS interface [16]. σ_{so} is used to modify the conventional Richardson plot which is constructed from $\ln\left(I_0/T^2\right) - q^2\sigma_{so}^2/2k^2T^2 = \ln AA^* - q\Phi_{BO}/kT$ through a plot of $\ln I_0/T^2 - q^2\sigma_{so}^2/2k^2T^2$ vs. $1/T$.

Figure 4(b) gives an intercept equivalent to *lnAA** and a gradient corresponding to Φ_{BO}. *A** is found to be 25.5Acm^{-2}K^{-2} and Φ_{BO} is obtained as1.734 eV. The value of *A** obtained from Figure 4(b) is still not close to the theoretical value. The reason is likely that a more complicated distribution is needed, say a double Gaussian, as can be seen by the clearly non linearity of Figure 4(a).

3.3 DLTS analysis of e-beam induced defect.

Figure 5(a) shows the DLTS spectrum of the 7.1×10^{15} cm^{-3} doped material after e-beam deposition. The spectrum reveals the presence of two prominent peaks at 0.09 eV and 0.67 eV. The shallower defect is the Nitrogen donor and the deeper level is the Z1/Z2 defect complex. Two additional peaks at 0.12 eV and 0.16 eV are also observed.

Figure 5(b) is the Arrhenius plot of log T^2/e vs. $1000/T$. It shows the levels detected by DLTS measurements recorded at a quiescent reverse bias of -1 V, a forward filling pulse of 0.2 V and a rate window of 1000 s^{-1}.

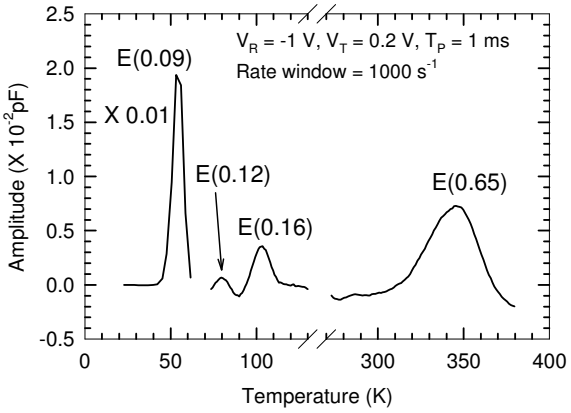

Figure5 (a). DLTS Spectra obtained at 1000 s^{-1} rate window. E (0.09) is scaled down by a factor of a thousand.

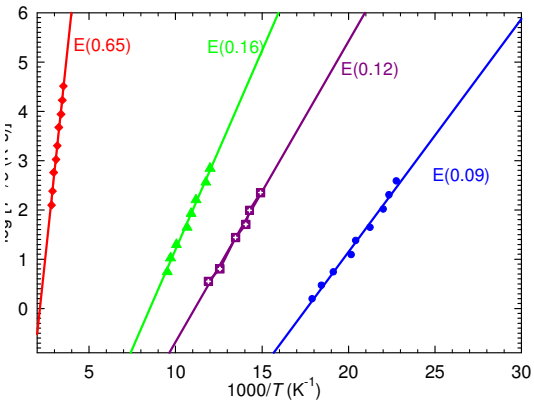

Figure 5 (b). The corresponding Arrhenius plots for the DLTS defects.

Table 2 below summarizes the properties of the detected defects in terms of the activation energies, the peak temperature and the apparent capture cross sections.

Table 2. Activation energies and apparent capture cross sections of identified defects. The spectra were recorded at a rate window of 1000 s^{-1}.

Defect	Activation energy (eV)	Capture cross section (cm^2)	T_{peak} (K)
E(0.09)	0.09	5.87×10^{-14}	55
E(0.12)	0.12	1.77×10^{-15}	70
E(0.16)	0.16	2.09×10^{-15}	110
E(0.65)	0.65	5.67×10^{-16}	350

The electron beam induced defects, (E_C – 0.160) eV and (E_C – 0.121) eV below the conduction band edge, have average concentrations of 3×10^{11} cm^{-3} and 1×10^{12} cm^{-3} respectively. These two peaks were not detected in the sample with resistively evaporated Schottky contacts. Also, we only detect these peaks in the 7.1×10^{15} cm^{-3} doped sample and not in the 1.96×10^{16} cm^{-3} doped sample.

4. Conclusion

I-V-T measurements of W/Pd Schottky contacts on n-4H SiC have shown that current transport below 140 K is not *TE* dominated. The anomalous temperature dependencies of n and Φ_{BO}; and, the very small Richardson constant obtained from the conventional the Richardson plot suggests an inhomogeneous MS interface. A modified Richardson constant ($25.5 Acm^{-2}K^{-2}$) was also not close to the expected value (149 $Acm^{-2}K^{-2}$) and a mean Schottky barrier height of 1.7 eV, was obtained from considering the inhomogeneities to be Gaussian distributed. DLTS measurements reveal the existence of two prominent peaks with activation energies of 0.09 eV and 0.67 eV. Two additional peaks with activation energies of 0.12 eV and 0.16 eV which we attribute to the e-beam metallization process and are dopant concentration dependent, are reported in this work.

Acknowledgements

We acknowledge the financial assistance by the South African National Research Foundation and colleague Sergio Coelho for the e-beam metallization.

References

[1] W. Harrell, J. Zhang, K. Poole, J. Electronic Materials, **31** 10 (2002) 1090-1095(6)
[2] S. Chang, S. Wang, K. Uang, B. Lion, Solid-State Electronics 49 (2005) 1937-1941
[3] J. Grant, W. Cunningham, A. Blue, V. O'Shea, J. Vaitkus, E. Gaubas, M. Rahman, Nuclear Instru. & Methods in Phys. Reaserch A546 (2005) 213-217
[4] V. Kazukauskas, J. V. Vaitkus Opto-Electronics Review 12 (4) 377-382
[5] F. Nava, A. Castaldini, A. Cavallini, P. Errani, V. Cindro IEEE Trans. On Nucl. Scie. 538 5 (2006) 2977-2982
[6] F. C. Beyer, C. Hemmingson, H. Pedersen, A. Henry, E. Janzen, J. Isoya, N. Morishita, T. Ohshima J. Appl. Phys. 109 103703 (2011)
[7] A. Castaldini, A. Cavallini, L. Rigutti, F. Nava, S. Ferrero, F. Giorgis, J. Appl. Phys. 98 0503706 (2005)
[8] P. B. Klein, B. V. Shanabrook, S. W. Huh, A.Y. Polyakov, M. Skowronski, J. J. Sumakeris, M. J. Oloughlin, Appl. Phys. Lett. 88 052110 (2006)
[9] S. M. Sze, Physics of Semiconductor devices, 2nd Edn. John Wiley and sons, New York, 1981
[10] E. H. Rhoderick, R. H. Williams, Metal – Semiconductor Contacts, Claredon Press, Oxford University Press, Oxford 1988 19
[11] M. K. Hudait, S. B. Krupanidhi, Physica B 307 (2001) 125-137
[12] S. K Noh, K. N. Jeon, S. E. Park, S. I. Ban, C. R. Lee, S. J. Son, K. Y. Lim, H. J. Lee (1999) *Sae MulliSae Mulli* 39 (4) p. 271-276
[13] T. Tung, Phys. Rev. B 45 (1992) 13509
[14] R. F. Schimitsdorf, T. U. Kampen, W. Monch, Surf. Sci. 324 (1995) 249
[15] B. Abay, G. Cankaya, H. S. Guder, H. Efeoglu and Y. K. Yogurtcu, J. Semicond. Sci. Technol.18 (2003) 75-81
[16] J. H. Werner, H. H. Guttler. J. Appl. Phys 69 (1991) 1522

A set-up to study the formation of proton-induced primary defects in wide band-gap semiconductors at cryogenic temperatures by space charge spectroscopy

Matthias Schmidt[1], Johan Janse van Rensburg[1], Hannes de Meyer[1], Walter E. Meyer[1], Danie F. Auret[1], Florian Schmidt[2], Holger von Wenckstern[2]

1 Department of Physics, University of Pretoria, Private bag X20, 0028 Hatfield, South Africa
2 Universität Leipzig, Institut für Experimentelle Physik II, Halbleiterphysik, Linnéstraße 5, 04103 Leipzig, Germany

E-mail: schmidt.matthias@matschmi.de

Abstract. We report on a new set-up to investigate electronic states of primary proton-bombardment-induced defects in wide band-gap semiconductors at cryogenic temperatures. The set-up consists of an ion accelerator with a vacuum chamber and a cryostat aligned in the beam-line. The defect studies are carried out in the same chamber by space charge spectroscopy such that no room temperature annealing of the sample is required between introduction and investigation of the defects. In contrast to existing facilities of this type, the sample can be optically excited in addition. This allows for photo-ionisation experiments like photo-capacitance spectroscopy or optical deep-level transient spectroscopy. These methods are essential for the investigation of electronic states of primary defects which anneal below room temperature since they allow for scanning for defect states in the entire band-gap at any temperature. First results measured on a zinc oxide thin film sample are presented.

1. Introduction

Lattice defects or impurities often introduce electronic states into the band-gap of semiconductors. Thereby, even in concentrations of less than 1 ppm, they strongly influence the concentration of free charge carriers in the material. This in turn affects macroscopic properties like conductivity and optical absorption. Thus, understanding the electronic properties of defects and their formation is a precondition for every semiconductor application.

Studying defects experimentally is usually divided into two tasks: Firstly, the controlled incorporation of impurities into the material; secondly their detection. Bombarding semiconductors with high energy protons has been proven to induce lattice defects in the crystal, in particular vacancies and interstitial atoms. These can then be investigated by space charge spectroscopy (SCS) which is known to be a powerful tool to detect and characterise electronic states of defects in low concentrations.

In this paper we describe our recently built set-up for in-situ studies of electronic defect states induced by proton bombardment into wide-band-gap semiconductors. In particular it is possible to induce as well as to characterise primary defects at cryogenic temperatures ($T \approx 20\,\mathrm{K}$) without heating the sample to room temperature between these experiments. This is crucial

since primary defects can be highly mobile, like for instance the mono-vacancy or the self-interstitial in silicon [1]. They may anneal-out or form defect-complexes even below room temperature. The detection and characterisation of the electronic defect states of these levels can in principle be carried out by established space charge spectroscopic methods like deep-level transient spectroscopy (DLTS). However, in a DLTS experiment the temperature-dependence of the thermal emission rate $e^{\mathrm{th}}_{\mathrm{n,p}}$ of charge carriers (electrons or holes, respectively) from localised states into the bands is measured. For a point defect in a non-degenerate semiconductor it is given by [2]

$$e^{\mathrm{th}}_{\mathrm{n,p}} \propto \sigma_{\mathrm{n,p}} T^2 \exp\left(-\frac{E_{\mathrm{a}}}{k_{\mathrm{B}} T}\right), \tag{1}$$

where T is the sample temperature and k_{B} is Boltzmann's constant. From Eq. 1 it can be seen that levels deep in the band-gap cannot be investigated at low temperatures because $e^{\mathrm{th}}_{\mathrm{n,p}}$ is too low to be conveniently measured since such levels usually exhibit high thermal activation energies E_{a} and small charge carrier capture cross-sections $\sigma_{\mathrm{n,p}}$. The problem is that in the case of primary defects, the increase in temperature necessary to detect their electronic states by SCS can lead to an anneal-out of the defect itself.

Our approach to overcoming this problem is to conduct SCS experiments in which the photo-ionisation of the electronic defect states is measured instead of their thermal ionisation. These experiments have in common that the sample is illuminated with monochromatic light. The rate at which a trapped charge carrier is optically emitted into either the conduction or the valence band is measured as a capacitance transient. The optical emission rates are almost independent of the sample temperature but depend on the photon flux $\Phi(h\nu)$ as well as the photo-ionisation cross-section spectrum $\sigma^{\mathrm{o}}_{\mathrm{n,p}}(h\nu)$ of the defect state [3]

$$e^{\mathrm{o}}_{\mathrm{n,p}} = \sigma^{\mathrm{o}}_{\mathrm{n,p}}(h\nu)\Phi(h\nu). \tag{2}$$

$\Phi(h\nu)$ is given by the spectrum of the light source. Our new set-up therefore enables us to induce lattice defects into a semiconductor and to investigate the entire band-gap for their electronic states at low temperatures.

Wide band-gap semiconductors are promising materials for opto-electronic devices operating in the near ultra-violet spectral range. The semiconductor zinc oxide (ZnO) exhibits a band-gap of 3.4 eV at 2 K [4]. It is considered to be radiation-hard [5, 6] which makes it an interesting material for UV sensors in harsh environments, e.g., in satellites. In this paper we present first results of SCS measurements on proton-induced primary defects in a ZnO thin film. These results suggest that the observed radiation-hardness of ZnO at room temperature is mainly due to an anneal-out of primary defects even at a temperature of 120 K.

2. Description of the set-up

Our set-up (Fig. 1a) consists of a Van-de-Graaff accelerator suitable for the acceleration of protons and alpha-particles up to energies of 2 MeV. Aligned in the beam-line of the accelerator is a high vacuum chamber with a closed-cycle helium cryostat suitable for the temperature range from 20 K to 380 K. The temperature is measured by a Lakeshore 340 temperature controller using a calibrated silicon diode. The sample is mounted on the cold-finger of the cryostat. Attached to the vacuum chamber is an electrical feed-through which allows the conduction of electrical measurements, in particular space charge spectroscopy. Capacitance transients and the admittance of the sample are measured by an Agilent 4284A LCR meter or a Boonton 7200 capacitance bridge and are recorded by a PC.

The feature that makes our set-up unique is the possibility of simultaneous optical excitation. Light stemming from a 1000 W Hg/Xe arc lamp is passed through a Cornerstone 284 (0.25 m) grating monochromator (line density 600 lines/mm). After the monochromatisation an optical

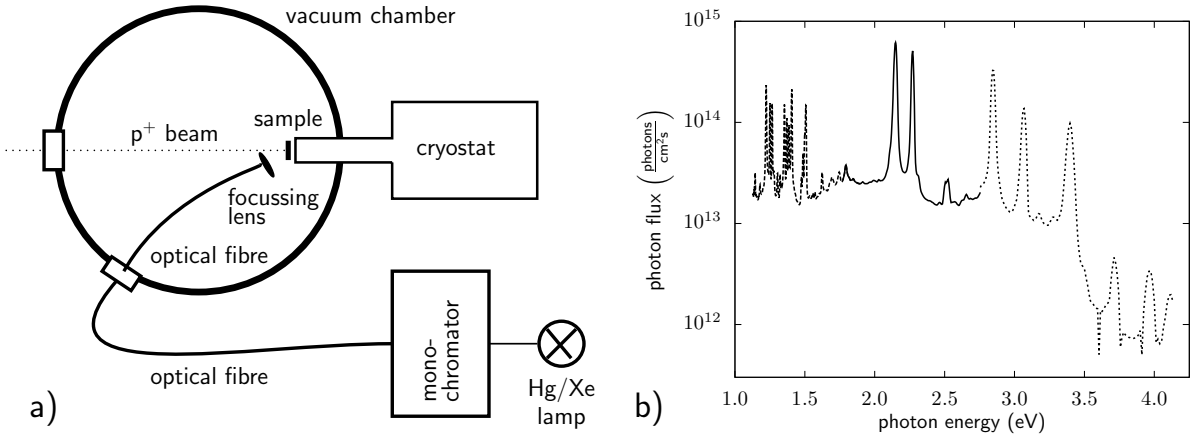

Figure 1. a) Sketch of the set-up. b) Spectral dependence of the photon flux on the sample measured by a calibrated silicon photo-detector. The different line-styles indicate the ranges, in which different filters were used. The monochromator slits were opened by 1mm resulting in a spectral resolution of approximately $\Delta\lambda = 5\,\mathrm{nm}$.

fibre guides the light into the vacuum chamber where it is focussed onto the sample. The optical set-up is suitable for the wavelength range from 1100nm to 300nm. The photon-flux on the sample was measured as a function of the wavelength using a calibrated silicon photo-detector (Gamma Scientific FlexOptometer), see Fig. 1b.

3. Samples

The proton-bombardment measurements were conducted on ZnO thin film Schottky diodes. Details of the sample preparation are discussed in [7] and [8]. On an *a*-plane sapphire substrate an approximately 200 nm thick layer of highly aluminium doped, metallically conducting ZnO was grown by pulsed laser deposition (PLD). This layer serves as the ohmic back contact of the samples. Subsequently a nominally undoped layer of ZnO (thickness 1500 nm) was pulsed laser deposited. This is the material in which the defect studies were carried out. The Schottky contacts were then fabricated from resistively evaporated palladium (thickness 9 nm).

4. First results

The results presented in this section have already been published in one of the PhD thesis of one of the authors (M.S.) [9]. In order to get a feeling for which defects are induced by high-energy proton bombardment of ZnO and which amongst them are stable up to room temperature or anneal out even at cryogenic temperatures respectively, we bombarded a ZnO Schottky contact at 20 K with 1.6 MeV protons. The proton fluence amounted to $6 \times 10^{13}\,\mathrm{cm}^{-2}$. Due to the lattice damage caused by the collisions of protons with the host atoms, the sample became highly resistive after the bombardment and the capacitance dropped to zero. The temperature was slowly increased and at approximately 120 K primary defects began to anneal out resulting in an increase of the sample capacitance. A further increase in temperature resulted in a strong increase of the capacitance[1]. At room temperature the capacitance of the proton-bombarded sample was only slightly smaller than in the as-grown state. From a subsequent capacitance-temperature measurement in which the capacitance of the sample did not drop to zero for $T < 120\,\mathrm{K}$ it can be concluded that the observed strong increase of the capacitance after the

[1] Unfortunately one of the pins used to contact the sample lost contact at 220 K.

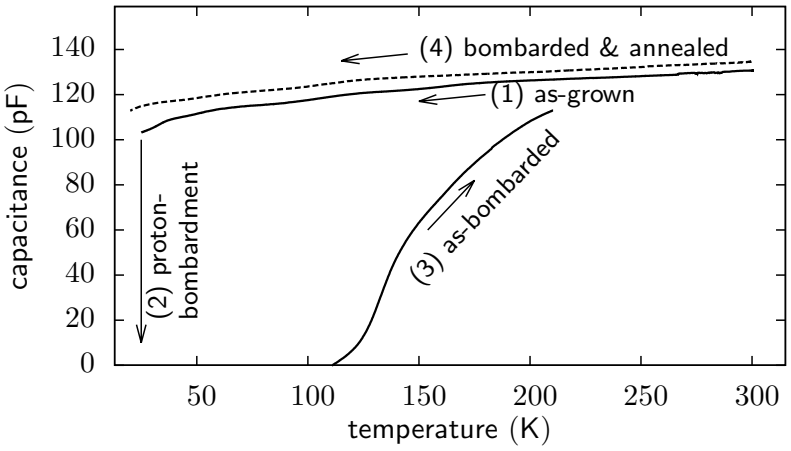

Figure 2. Capacitance vs. temperature measured on a ZnO Schottky contact during a temperature cycle: (1) As-grown sample was cooled from room temperature to 20 K. (2) Sample was bombarded with 1.6 MeV protons, fluence: $6 \times 10^{13}\,\mathrm{cm}^{-2}$. (3) Temperature was increased to 300 K. (4) Sample cooled to 20 K. During the cycle the sample was reverse biased at 2.5 V.

bombardment indeed stemmed from an annealing out of primary defects. The cooling cycle is depicted in Fig. 2.

Electronic defect states induced by proton-bombardment, which are stable up to room temperature were investigated by capacitance-voltage spectroscopy (CV) and DLTS. Therefore different Schottky contacts on the ZnO thin film sample were proton-bombarded (1.6 MeV) at different fluences ranging from $2 \times 10^{13}\,\mathrm{cm}^{-2}$ to $3 \times 10^{14}\,\mathrm{cm}^{-2}$. Using van Opdorp's method [10], the depth profiles of the net doping density were determined from the CV data:

fluence (cm^{-2})	N_{net} (cm^{-3})
0	4×10^{16}
2×10^{13}	5×10^{16}
6×10^{13}	5×10^{16}
1×10^{14}	3×10^{16}
3×10^{14}	4×10^{16}

Obviously, within the error bars of the experiment, the net doping density was not significantly changed by the proton bombardment. This in turn means that most of the lattice damage anneals out immediately after the bombardment and that furthermore the number of induced stable donors equals that of the induced stable acceptors.

In order to study the impact of the proton bombardment on deep-levels in the upper third of the ZnO band-gap, DLTS measurements were performed on those samples subsequent to the CV measurements. The DLTS measurements were conducted using 1 ms filling pulses that almost flattened the bands. During the recording of the capacitance transients, the samples were reverse biased at 2.5 V. The resulting spectra are depicted in Fig. 3(a) and reveal the presence of the well-known deep-levels E1 and E3 [11], T2 [12] and E4 [11, 13]. Evidently the concentrations of T2 and E3 are not affected by the proton bombardment of the samples. The concentration of E1 is slightly increased after the bombardment. But the DLTS peak height is almost equal in all bombarded samples, independent of the fluence. However, the E4 concentration[2] –which

[2] Here E4 is assumed to be almost uniformly distributed in the space charge region. First optical capacitance-voltage measurements [9] however hint at E4 concentrations gradients towards the bulk in the samples.

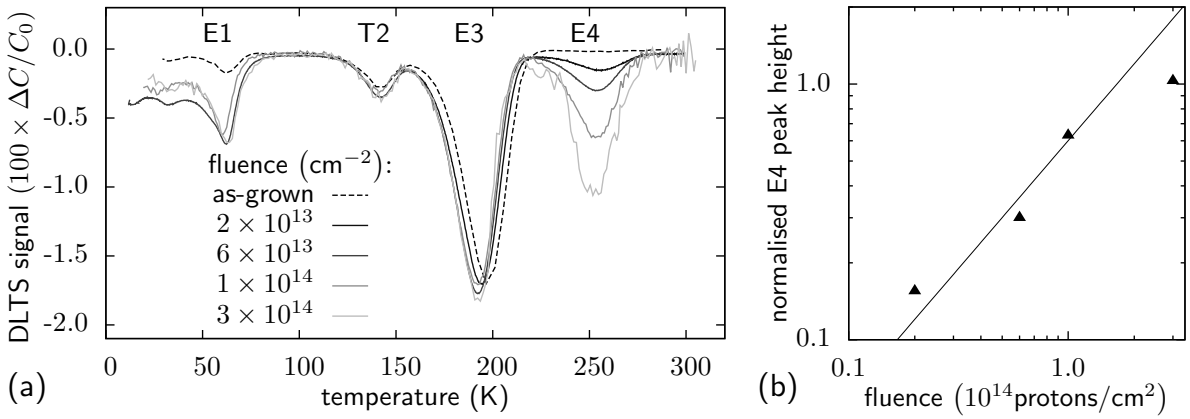

Figure 3. (a) Deep-level transient spectroscopy measurements on 1.6 MeV proton-bombarded Schottky contacts on a ZnO thin film sample (rate window: 200 Hz). Obviously the E4 deep-level is induced by the bombardment. (b) Determination of the E4 introduction rate from the E4 DLTS peak height (normalised on the maximum peak height). The straight line is a linear fit to the data which suggests an E4 introduction rate of 3 cm^{-1}. (For the linear regression only the E4 concentrations measured for fluences up to 10^{14} cm^{-2} were considered. The introduction rate for E4 decreases for larger fluences.)

was not traceable in the as-grown sample– increases almost linearly with increasing fluence up to 5×10^{14} cm^{-3}. In the following we want to elaborate on this deep-level.
A straight line fitted to the DLTS peak height vs. fluence data and intersecting the origin yields an E4 introduction rate of approximately 3 cm^{-1}, see Fig. 3(b). This is very close to the value of 2.4 cm^{-1} reported by Auret *et al.* [5, 6] for the proton-bombardment-induced deep-level EP1. Employing standard Arrhenius evaluation of the temperature-dependent thermal emission rate for electrons, the E4 activation energy and the high-temperature limit of the electron capture cross-section were determined to 540 meV and 2×10^{-13} cm^2, respectively. Again these values agree well with activation energy and high-temperature limit of the electron capture cross-section for the EP1 defect. Since the formation of vacancies can be expected during the proton bombardment, our finding that E4 is proton-induced also supports the suggestion by Frank *et al.* [13] that E4 is a state of the oxygen vacancy.

5. Conclusions

In this paper we have presented our new set-up suitable for the in-situ investigation of primary, proton bombardment induced electronic defect states by means of space charge spectroscopy. Owing to the possibility of conducting the proton irradiations and the defect studies in the same vacuum chamber as well as being capable of optically exciting the sample during space charge spectroscopic experiments, the set-up enables us to scan the *entire* band-gap of a wide-band-gap semiconductor for defect states. This means that no unintentional annealing step between the introduction of defects by high-energy protons at cryogenic temperatures and their investigation is necessary and thus an annealing out of primary defects can be avoided. First measurements on Pd/ZnO thin film Schottky diodes were performed and show that the previously observed radiation-hardness of ZnO mainly results from an anneal-out of radiation damage even at temperatures as low as $\approx$ 120 K. Room-temperature capacitance-voltage measurements on 1.6 MeV proton-bombarded Pd/ZnO Schottky diodes confirmed that the net doping density

was not significantly changed by the protons for fluences up to $3 \times 10^{14}\,\mathrm{cm}^{-2}$. However, DLTS experiments on the same samples revealed that the E4 deep-level is induced by the protons and is stable at room temperature. This is in line with previous observations on proton-bombarded ZnO single crystals[3] [5, 6, 14].

Acknowledgments

The authors wish to thank the mechanical workshop of the Department of Physics at the University of Pretoria for the fabrication of numerous parts of the set-up. To H. Hochmuth, M. Lorenz and M. Grundmann we are much obliged for the growth of the ZnO thin film sample. The authors are indebted to Deutsches Zentrum für Luft- und Raumfahrt e.V. for the financial support. Matthias Schmidt was funded by the Postdoctoral Fellowship Program of the University of Pretoria. We thank two referees for their thorough review of the manuscript and highly appreciate their comments and suggestions. This work is based upon research supported by the National Research Foundation (NRF). Any opinion, findings and conclusions or recommendations expressed in this material are those of the author(s) and therefore the NRF does not accept any liability in regard thereto.

References

[1] G.D. Watkins. *Intrinsic Defects in Silicon.* Mat. Sci. Semicon. Proc. **3** 227–235 (2000).

[2] P. Blood and J.W. Orton. *The Electrical Characterization of Semiconductors: Majority Carriers and Electron States*, volume 1. Academic Press, US, 1992.

[3] S. Brehme and R. Pickenhain. *A simple method for the determination of both photoionization and photoneutralization cross-sections of deep levels by optical DLTS.* Phys. Status Solidi A, **88** K63 (1985).

[4] C. Bundesmann, R. Schmidt-Grund, and M. Schubert. *Optical properties of ZnO and related compounds.* In K. Elmer, A. Klein, and B. Rech, editors, *Transparent Conductive Zinc Oxide*, pages 77 – 122. Springer Berlin, Germany, 2008.

[5] F.D. Auret, S.A. Goodman, M. Hayes, M.J. Legodi, H.A. van Laarhoven, and D.C. Look. *Electrical characterization of 1.8 MeV proton-bombarded ZnO.* Appl. Phys. Lett., **79** 3074–3076 (2001).

[6] F.D. Auret , S.A. Goodman , M. Hayes , M.J. Legodi1 , H.A. van Laarhoven, and D.C. Look *The inuence of high energy proton bombardment on the electrical and defect properties of single-crystal ZnO* J. Phys., **13** 8989–8999 (2001).

[7] M. Lorenz. *Pulsed laser deposition of ZnO-based thin films.* In K. Elmer, A. Klein, and B. Rech, editors, *Transparent Conductive Zinc Oxide*, pages 77–122, Springer Berlin, Germany, 2008.

[8] H. von Wenckstern, G. Biehne, R. A. Rahman, H. Hochmuth, M. Lorenz, and M. Grundmann. *Mean barrier height of Pd Schottky contacts on ZnO thin lms.* Appl. Phys. Lett., **88** 092102 (2006).

[9] Matthias Schmidt, *Space Charge Spectroscopy Applied to Defect Studies in Zinc Oxide Thin Films*, PhD thesis, Universität Leipzig, Germany (2012).

[10] C. van Opdorp. *Evaluation of doping proles from capacitance measurements.* Solid State Electron., **11** 397 (1968).

[11] F.D. Auret, S.A. Goodman, M.J. Legodi, W.E. Meyer, and D.C. Look. *Electrical characterization of vapor-phase-grown single-crystal ZnO.* Appl. Phys. Lett., **80** 1340–1342, (2002).

[12] M. Schmidt, M. Ellguth, R. Karsthof, H. v. Wenckstern, R. Pickenhain, M. Grundmann, G. Brauer, F.C.C. Ling, *On the T2 trap in zinc oxide thin films*, Phys. Status Solidi **249** 588–595 (2012).

[13] T. Frank, G. Pensl, R. Tena-Zaera *et al. Energetically deep defect centers in vapor-phase grown zinc oxide.* Appl. Phys. A, **88** 141–145 (2007).

[14] A.Y. Polyakov, N.B. Smirnov, A.V. Govorkov *et al. Proton implantation effects on electrical and recombination properties of undoped ZnO.* J. Appl. Phys., **94** 2895–2900 (2003).

[15] M. Ellguth, M. Schmidt, R. Pickenhain, H. v. Wenckstern, M. Grundmann, *Characterization of point defects in ZnO thin films by optical deep level transient spectroscopy*, Phys. Status Solidi **248** 941–949 (2011).

[3] In [5, 6] the deep-level was labelled EP1. However, it exhibits a similar Arrhenius plot of its temperature-dependent electron emission rate as the E4 level. Furthermore we found (not shown here) that the proton-induced deep-level we detected in this study can be photo-ionised and exhibits the same optical threshold as reported by Ellguth *et al.* [15] for the E4 level. Therefore it is highly probable that EP1 and E4 are identical.

A new white light emitting nanophosphor

Shaat SKK[1,2], Swart HC[1] and Ntwaeaborwa OM[1,*]

[1] Department of Physics, University of the Free State, Bloemfontein, ZA9300, South Africa.
[2] Department of Physics, Islamic University, P. O. Box 108, Gaza, Palestine.
* Corresponding author: ntwaeab@ufs.ac.za

Abstract. White light was produced from $CaAl_2O_4$ nanophosphor co-doped with $Tb^{3+}$and Eu^{3+}. The short time and low temperature reaction combustion route was used to synthesize $CaAl_2O_4:Tb^{3+},Eu^{3+}$ nanophosphors using metal nitrates precursors and urea as fuel. The crystalline structure and particle morphology were determined using X-ray diffraction and Scanning electron microscopy, respectively. The optical properties were studied by photoluminescence (PL) spectroscopy and the UV-Vis spectrometer in the range 800-200 nm. The excitation spectra were recorded by monitoring the three main emissions, namely blue at 438 nm, green at 543 nm and red at 617 nm. 227 nm was found to be the most suitable excitation wavelength to generate, simultaneously, blue and green emission from Tb^{3+} and red emission from Eu^{3+} whose combination constituted white light. The blue and green were respectively attributed to the 4f-4f transitions of Tb^{3+} by $^5D_3 – {}^7F_{J\ (J= 6-2)}$ and $^5D_4 \rightarrow {}^7F_{J\ (J = 0-6)}$ while the red emission was attributed to $^5D_0 \rightarrow {}^7F_{J\ (J=0-4)}$ transitions of Eu^{3+}. Preliminary results on the structure and PL properties of this phosphor are reported.

1. Introduction

Scientists and researchers are conducting research in search for suitable host lattices that can be used to prepare phosphors for solid state lighting. The host must, among other things, be chemically and thermally stable. Alkali earth aluminates with a general formula MAl_2O_4 (M = Ba, Ca or Sr) are widely used as hosts for trivalent rare-earth (Dy^{3+}, Nd^{3+}, etc) and divalent europium (Eu^{2+}) ions for the preparation of light emitting materials (phosphors) with persistent luminescence. Aluminates are more chemically stable, environmentally friendly [1] and they can be easily produced cost-effectively. Therefore the study of the preparation and characterization of aluminates based phosphors is growing rapidly. Phosphors such as $SrAl_2O_4:Eu^{2+}$, $CaAl_2O_4:Eu^{2+}$ and $BaAl_2O_4:Eu^{2+}$ phosphors, co-activated with different rare-earths (Dy^{3+},Nd^{3+}, Pr^{3+}) have been reported [2]. These phosphors are usually produced cost-effectively, at relatively low temperature and a short reaction time by the combustion method using metal nitrates as starting materials and urea as a fuel. White light in many practical applications is generated by combining currently three available colours blue, green and red phosphor in appropriate ratios. For example, in traditional white light emitting diodes (LEDs), white light is generated by combining a lnGaN-based blue diode with a yellow phosphor such as YAG:Ce^{3+} or by combining a UV chip with a three converter system of red, green and blue phosphors. Furthermore, white light from fluorescent lamps is produced from combining tri-colour phosphors which emit blue, green and red light upon excitation by ultraviolet radiation. Shaat et al, [3] produced white light from $Ca_xSr_{(1-x)}Al_2O_4:Tb^{3+},Eu^{3+}$ nanocrystalline phosphor for application in solid state lighting devices such as fluorescent lamps and LEDs. In this study, a potential white light emitting nanocrystalline phosphor was prepared by co-doping terbium (Tb^{3+}) and europium (Eu^{3+}) in a calcium aluminate ($CaAl_2O_4$) host.

2. Experimental

2.1 Sample Preparation

A combustion method was used to prepare Tb^{3+} and Eu^{3+} single and co-doped $CaAl_2O_4$ nanophosphor. The metal nitrates of $Ca(NO_3)_2.4H_2O$, $Al(NO_3)_3.9H_2O$, $Tb(NO_3)_3.5H_2O$, $Eu(NO_3)_3.5H_2O$ and urea

$CO(NH_2)_2$ of AR grade purchased from Merck, South Africa were used as starting materials (precursors) and were used as obtained without further purification. The distilled water was used to dissolve the precursors with vigorous stirring at 50°C for 0.3 hr until the solution became clear. The resulting solution was transferred to a muffle furnace maintained at 450±10% °C. The transparent solution started to boil and undergo dehydration, followed by decomposition and large amounts of gases (nitrogen, ammonia and oxides of carbon) escaping. White foamy and voluminous ash was produced after spontaneous ignition occurred and underwent smouldering combustion with enormous swelling. The combustion reaction was completed in ~5 minutes. The product was cooled to room temperature and the ashes were ground gently into fine powders. The powders were characterized without any further post-preparation treatment.

2.2 Experimental Techniques

The crystalline structure of $CaAl_2O_4:Tb^{3+};Eu^{3+}$ was analysed using a Bruker D8 ADVANCE powder diffractometer with Cu K radiation, =1.5406Å. The optical properties were characterized by UV-Vis spectroscopy (Lambda 950) and the Varian Cary Eclipse fluorescence spectrophotometer. PL (excitation and emission) were measured for 3 different samples namely: $CaAl_2O_4:Tb^{3+}$, $CaAl_2O_4:Eu^{3+}$ and $CaAl_2O_4:Tb^{3+};Eu^{3+}$ with different excitation wavelengths**.** All measurements were carried out at room temperature and atmospheric pressure.

3. Analysis and results discussion

3.1. XRD Study

Figure 1 shows the X-ray diffraction (XRD) patterns of $CaAl_2O_4:Tb^{3+};Eu^{3+}$ nanophosphor. The patterns correspond to the standard monoclinic structure of $CaAl_2O_4$ in JCPDS file No. 70-0134. The diffraction peak at 2θ=25.34° was indexed as the (012) peak of Al_2O_3 [4] which was possibly formed during an unwanted reaction between Al^{3+} and O^{2-} from the precursors. The Debye-Scherrer relation was used to estimate the average particle size for the (220) diffraction peak and was found to be ~16 nm. The calculated lattice parameters are a = 8.71 A° , b = 8.084 A° , c = 15.23 A° with and = 90° but . ° which are in a good agreement with the standard monoclinic $CaAl_2O_4$ referenced in JCPDS file No. 70-0134 (a = 8.700 A° , b = 8.092 A° , c = 15.19 A° with and = 90° but . °).

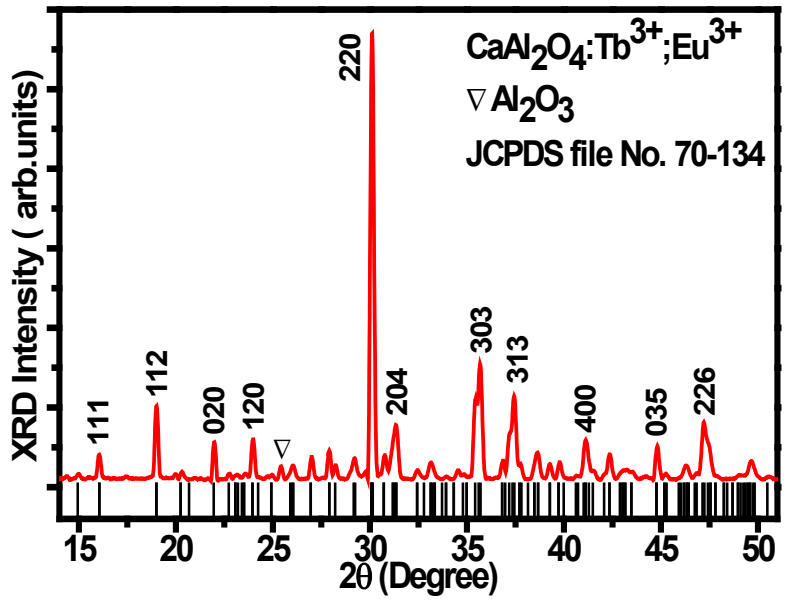

Figure 1. XRD spectrum of $CaAl_2O_4:Tb^{3+};Eu^{3+}$ nano-phosphors.

3.2. SEM micrograph study

Figure 2(a-b) show the SEM micrograph images of the as-prepared monoclinic $CaAl_2O_4:Tb^{3+};Eu^{3+}$ nanophosphor with two different magnifications. The foamy and agglomerate particle nature of the powder is clear in figure 2(a-b). The foamy structure of $CaAl_2O_4:Tb^{3+};Eu^{3+}$ reflects the inherent nature of the combustion process. Figure 2 (a-b) shows an irregular shape with a lot of voids and pores of the surface of the powder, which may be formed by the evolved gases during combustion reaction.

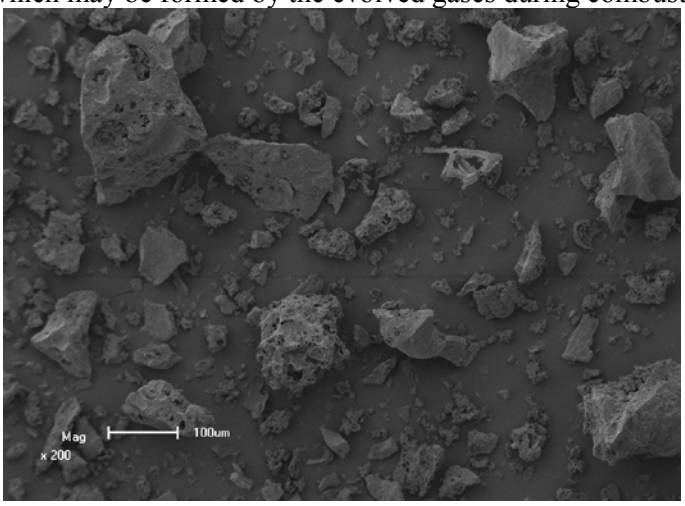

(a)

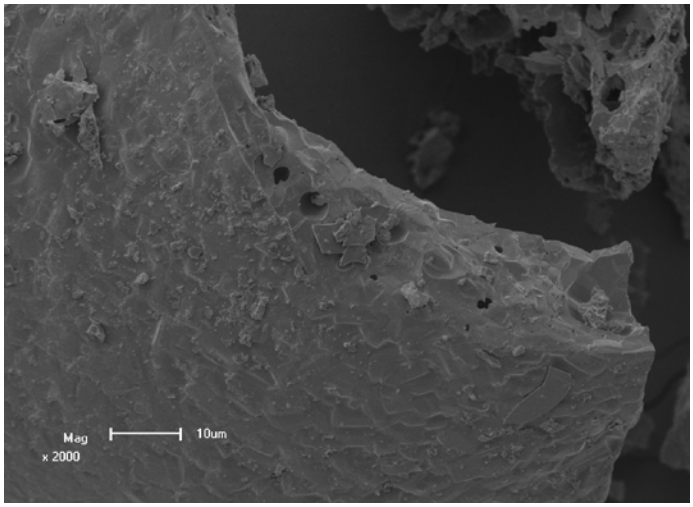

(b)

Figure 2(a-b). SEM micrograph images of the $CaAl_2O_4:Tb^{3+};Eu^{3+}$ nanophosphor.

3.3 UV-Vis study

Figure 3 shows the diffuse reflectance spectrum of the $CaAl_2O_4:Tb^{3+};Eu^{3+}$ nanophosphor. Two clear changes in the slope of the reflectance spectrum are seen at 213 nm and 330 nm. The peak observed at 213 nm is attributed to the interband transition of $CaAl_2O_4$ [5]. The peak near 330 nm was assigned to the O^{2-}-Eu^{3+} charge transfer band [6]. The band gap energy of the $CaAl_2O_4:Tb^{3+};Eu^{3+}$ was estimated from a plot of $(\alpha E)^2$ versus photon energy E shown in figure 4. The band gap energy was estimated from the linear part of the straight line to the $(\alpha E)^2 = 0$ axis and by extrapolating was found to be 5.3±0.1eV. This result is close to the value of 5.78 reported in ref. [7].

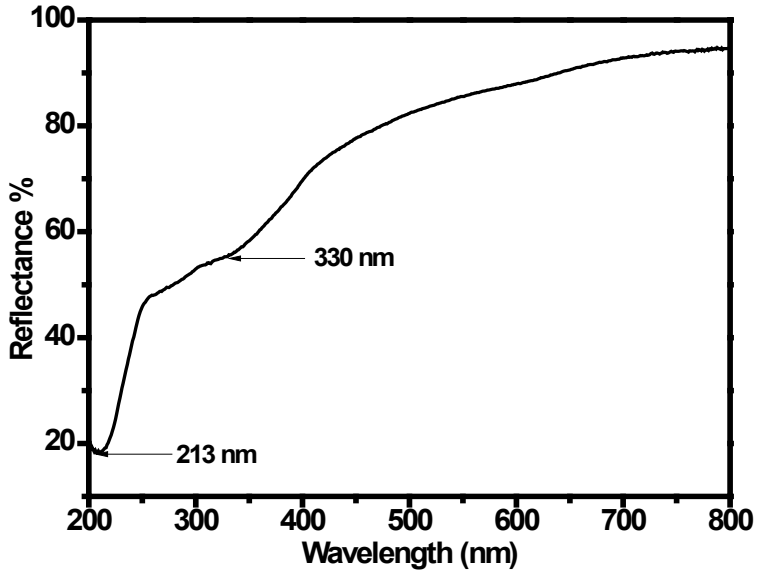

Figure 3. Diffuse reflectance spectrum of the $CaAl_2O_4;Tb^{3+};Eu^{3+}$ nanophosphor.

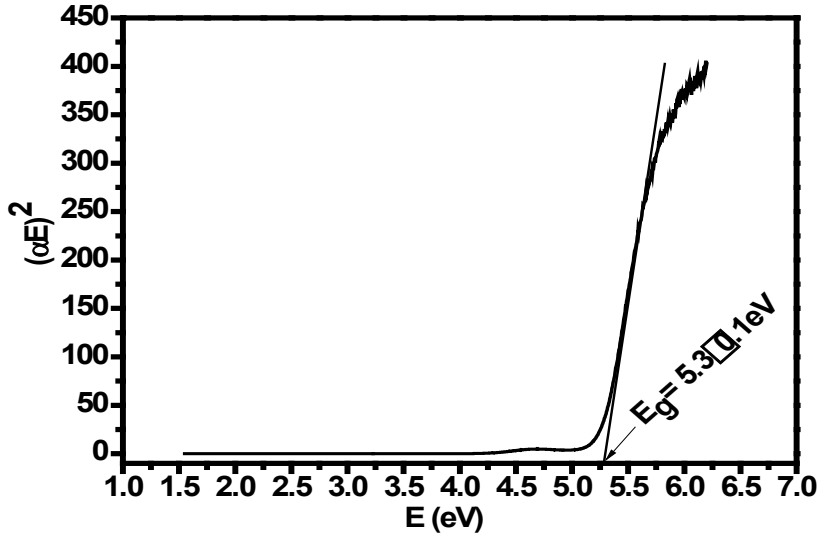

Figure 4. Plots of $(\alpha h\nu)^2$ versus photon energy ($h\nu$) to determine the band gap energy of the $CaAl_2O_4;Tb^{3+};Eu^{3+}$ nanophosphor.

3.3. Photoluminescence study

Photoluminescence (PL) excitation spectrum of $CaAl_2O_4:Tb^{3+},Eu^{3+}$ nanophosphor is shown in figure 5. The excitation spectra were recorded for three different emissions at 437 and 543 nm from Tb^{3+} and 617 nm from Eu^{3+}. There are two major peaks located at 227 and 237 nm due to direct excitation of Tb^{3+} and are assigned to the 4f→5d transitions [8.9]. The excitation peak at ~240 nm are due to $Eu^{3+}\rightarrow O^{2-}$ charge transfer transitions resulting from transfer of electrons from O^{2-} ($2p^6$) orbitals to the $4f^7$ and $4f^6$ states [10]. The PL emission spectrum of the $CaAl_2O_4:Tb^{3+},Eu^{3+}$ nanophosphor observed when exciting the phosphor at 227 nm is shown in figure 6. The PL emission spectra of Tb^{3+} and Eu^{3+} single doped $CaAl_2O_4$ also were recorded when exciting the phosphors at 227 nm are shown in the insets. The PL emission spectra of $CaAl_2O_4:Tb^{3+}$ consists of major green emission at 543 nm due to the $^5D_4\rightarrow{}^7F_5$ transitions of Tb^{3+} and minor emissions at 380 nm (violet), 416 nm (blue), and 437 nm (blue) due to the $^5D_3\rightarrow{}^7F_J$ (J = 6,5,4) transitions of Tb^{3+}. The PL emission spectrum of the $CaAl_2O_4:Eu^{3+}$ in the other inset consist of major red emission at 617 nm due to the $^5D_0\rightarrow{}^7F_2$ electric

dipole transitions of Eu^{3+} and minor emission at 593 nm due to magnetic dipole transitions of Eu^{3+} [11]. The PL emission spectrum of the $CaAl_2O_4:Tb^{3+},Eu^{3+}$ nanophosphor exhibits white light which is a result of simultaneous emissions of blue and green light from Tb^{3+}, and red light from Eu^{3+}. When exciting at the wavelength of 227 nm (i.e. the point where the excitation spectra of the 543 and 617 nm emissions overlap as shown in Fig. 5) there is a slight increase in the 542 nm peak intensity and a slight decrease in the 617 nm peak intensity indicating that Tb^{3+} and Eu^{3+} where excited simultaneously resulting in simultaneous emissions from both ions.

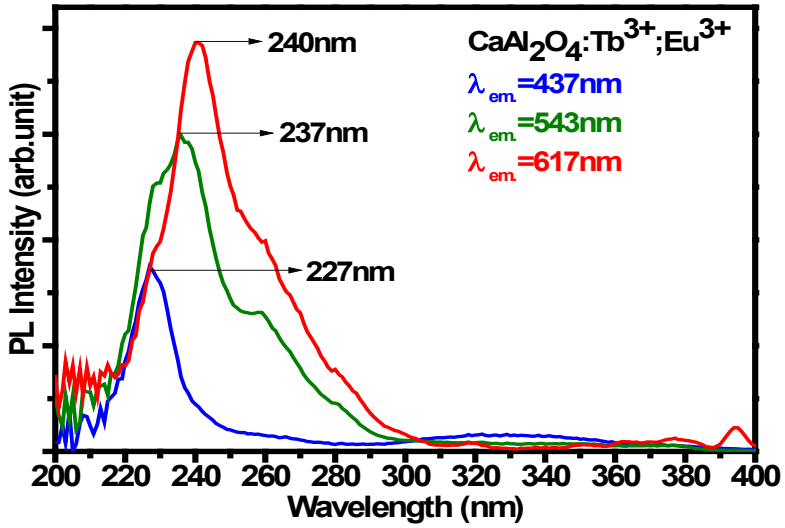

Figure 5: PL excitation spectra of $CaAl_2O_4:Tb^{3+};Eu^{3+}$ nanophosphor.

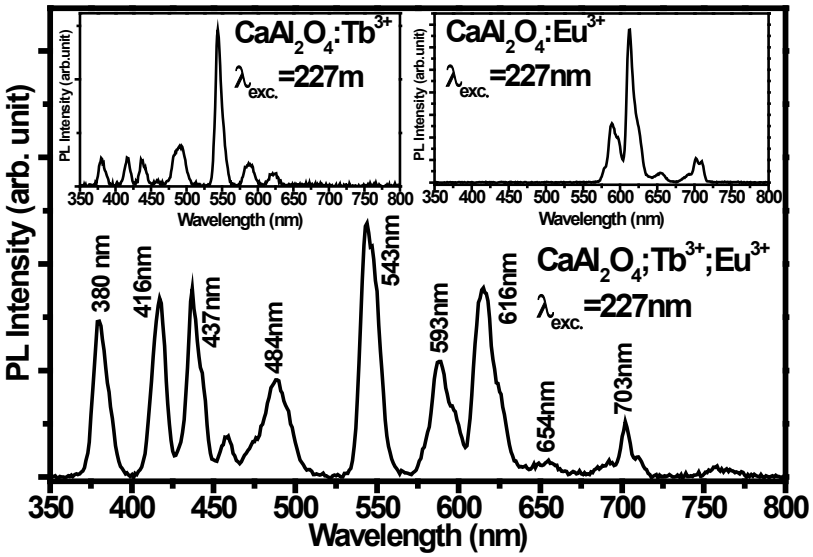

Figure 6: PL emission spectrum of $CaAl_2O_4:Tb^{3+};Eu^{3+}$ nanophosphor and the two insets are the PL emission spectra of $CaAl_2O_4:Tb^{3+}$ and $CaAl_2O_4:Eu^{3+}$. All were excited at 227 nm.

Figure 7 depicts the CIE diagram and the chromaticity coordinates for the (a) $CaAl_2O_4:Tb^{3+}$, (b) $CaAl_2O_4:Eu^{3+}$ and (c) $CaAl_2O_4:Tb^{3+},Eu^{3+}$. The calculated chromaticity coordinates for the white light emitted from $CaAl_2O_4:Tb^{3+},Eu^{3+}$ nanophosphor are given by x = 0.354, y = 0.337, which is in agreement with the chromaticity coordinates of standard white light (x = 0.333, y = 0.333) [12]. Also shown in the figure are the chromaticity coordinates of the red $CaAl_2O_4:Eu^{3+}$ given by x = 0.637, y = 0.360 and the green $CaAl_2O_4:Tb^{3+}$ given by x = 0.286, y = 0.477.

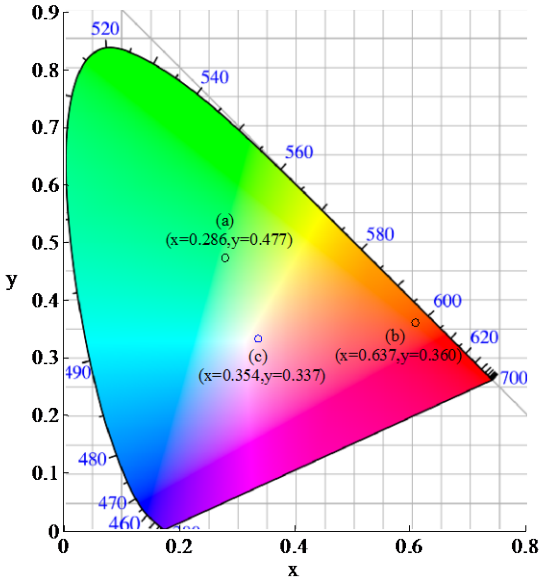

Figure 7: The CIE diagram and the chromaticity coordinates of (**a**) $CaAl_2O_4:Tb^{3+}$ at (x = 0.286, y = 0.477), (**b**) $CaAl_2O_4:Eu^{3+}$ at (x = 0.637, y = 0.360) and (**c**) $CaAl_2O_4:Tb^{3+};Eu^{3+}$ at (x = 0.354, y = 0.337).

4. Conclusion

In conclusion, a new potential white light emitting $CaAl_2O_4:Tb^{3+};Eu^{3+}$ nanophosphor was synthesized using the combustion method. The structure of the phosphors is consistent with standard monoclinic $CaAl_2O_4$. The SEM images confirm the irregular particle shape that was produced from the combustion reaction. The estimated band gap energy agrees with the other measured values. Furthermore, PL excitation spectrum confirmed that the excitation through absorption of the 4f→5d transitions of Tb^{3+} and charge transfer transitions of O^{2-}→Eu^{3+} which agreed with different studies. Finally, the white light occurred after excitation by photons of sufficiently high energy which come from 4f→5d transitions of Tb^{3+} and O^{2-}→Eu^{3+}. This materials has the potential application in different types of light emitting devices such as laser phosphor display (LPD), field emission displays (FEDs), fluorescent lamps and phosphor panel displays (PDP).

Acknowledgement

The authors send gratitude to the National Research Foundation (NRF) for funding the project.

References

[1] Mothudi BM, Ntwaeaborwa OM., Pitale SS and Swart HC 2010 *Journal of Alloys and Compounds* **508** 262.
[2] Eeckhout KV, Philippe FS and Poelman D 2010 *Materials* **3** 2536.
[3] Shaat S K K, Hendrik S C and Odireleng MN 2012 *Optical Materials Express* **2** 962.
[4] Rivas Mercury JM, De Aza AH and Pena P 2005 *Journal of the European Ceramic Society* **25** 3269.
[5] Kunimoto T, Kakehi K, Yoshimatsu R, Honda S, Ohmi K and Tanaka S 2002 *UVSOR Act Rep* **2001** 116.
[6] Bohdan P, Marek G, Benedykt K, Yuriy O, Oleksandr S, Dmitriy K and Andrew P 2010 *Optica Applicata* **2** 413.
[7] Bo L, Chaoshu S and Zeming Q 2005 Applied Physics Letters **86** 191111.
[8] Martínez-Martínez R, Àlvarez E, Spanghini A, Falcony C and Caldiño U 2010 *Materials Research Society* **25(3)** 484.
[9] Wang D, Yang P, Cheng Z, Wang W, Hou Z, Dai Y, Li C and Lin J 2012 Journal of Colloid and Interface Science **365** 320.
[10] Stanislava J, Linda S, Guillaume R, Yaroslav F, Damien B, Philippe B 2007 *Journal of Physics and Chemistry of Solids* **68** 1147.
[11] Grobelna and Bojarski 2009 *Journal of Non-Crystalline Solids* **355** 2309.
[12] Fan S, Yu C, He D, Wang X and Hu L 2012 Optical Materials Express **26** 765.

Annealing Effect on Nanostructures VO_2 and Potential Application as Gas Sensor Device

A. Simo[1, 3], R. Madjoe[3], B.T. Sone[1], L. Kotsedi[1], B.Mwakikunga[2], M. Maaza[1, 4]
[1]Nanosciences African Network, Nanoscience Laboratories, Materials Research Dept., iThemba LABS-National Research Foundation, PO Box 722, Somerset West 7129,
[2]DST/CSIR National Centre for Nano-Structured Materials, Pretoria, South Africa
[3]Physics Dept., University of Western Cape, Belleville, South Africa
[4]Faculty of Sciences, Pretoria-Tshwane University of Technology, Private Bag X 680, Pretoria, South Africa.

E-mail: simo@tlabs.ac.za

Abstract. In this study we present the synthesis of nanoplatelets VO_2 (A) by the hydrothermolysis method. The prepared samples were subjected to an annealing treatment in argon and nitrogen gas ambience at 500˚ C for 3hours. This was done to study the effect of heat catalyst on the atomic structure and vibrational modes of the material. The composition and nanostructure were analysed using Raman spectroscopy. The differential scanning calorimetry analysis showed that the crystallization temperature of the annealed samples shifted to approximately 67 ˚C transition temperature of VO_2 (M). This properties of the synthesized material resulted in efficient gas sensing of hydrogen gas at 50 ˚C.

1. Introduction

Interesting physical properties and potential device applications have drawn much attention of one dimensional nanoscale materials since the discovery of carbon nanotubes [1]. Different kinds of materials have been successfully synthesized including the fabrication of nanometer scale electronic devices with a variety of functions. Furthermore, as the demand for fabrication of special nanoplatelets structures increase, development of a method not only for synthesizing but also for modifying the properties of as-synthesized nanoplatelets is becoming increasingly important. For example excellent H_2 sensors need high surface to volume ratio for quickest response at low operating temperature and high surface interactions with H_2 [13]. VO_2 tetragonal [VO_2 (A)] is based on an oxygen bcc lattice with vanadium in the octahedral where the oxygen atoms are mainly aligned along one direction [2, 3] as seen in figure 1. It possesses a tetragonal structure with P42/nmc and can be directly transformed to VO_2 monoclinic [VO_2 (M)] under annealing treatment. Although there have been some reports on the synthesis of VO_2 (A), no reports on the synthesis of nanoplates VO_2 (A) + VO_2 (M) structures and on their annealing effect and direct application as gas sensing have been done. In the present study we use bulk V_2O_5 as the precursor material and hydrothermally reduce it to metastable VO_2 (A) nanoplates using simple aliphatic alcohols and aldehydes simultaneously as the reducing and structure-directing agents. Subsequently an annealing process is used to transform the VO_2 (A) nanostructures to monoclinic VO_2 (M) under Argon gas and compare to the one annealed under Nitrogen. VO_2 (A) is the thermodynamically stable phase compared with VO_2 (B) and is much more stable than VO_2 (R) (

VO_2 (R) and VO_2 (B) represent the polymorphic phases in VO_2 system where VO_2 (R) present a reversible phase transition at 68˚ C) according to the calculations principles using the hybrid function HSE06. VO_2 (A) possesses a density of 4.035 g/cm^3 and band gap energy of 0.21eV. See the crystalline structure on figure 1a).

2. Experimental techniques

All the reagents were of analytical grade and used without further purification. 0.75ml of Sulfuric acid H_2SO_4 (Kimix, 98%) followed by the drop-wise addition of 0.25ml of $N_2H_2 \cdot 2H_2O$ (Merck) were added into an aqueous suspension (10 mL) containing 0.45g of V_2O_5 (Alfa Aesar). After being warmed at 95˚C while stirring, the solution changes from yellow to green, then green to blue, characteristic of the presence of V^{+4} ions in the solution, finally blue to gray[7]. For the H_2 gas sensing experiments, a standard in-situ 2 contact points-based system was used. The cold pressed VO_2(A) nanobelt pellet was squeezed between two Al electrodes and a Si substrate wafer while the whole was interfaced to a heating stage (25-170 °C).

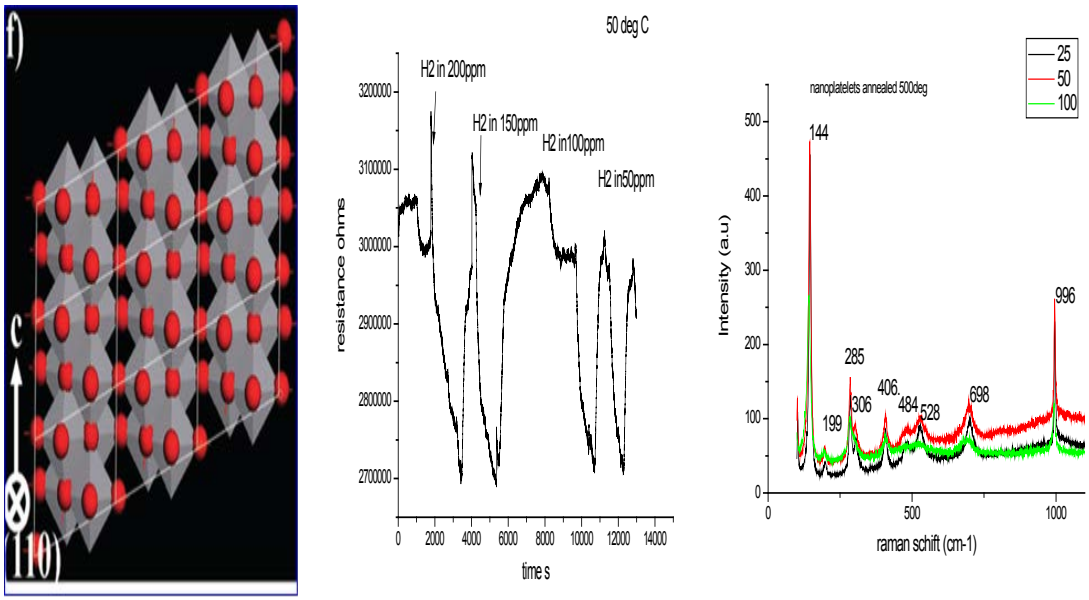

a) b) c)

Figure 1: a) Arrangement of VO_6 octahedra in real crystalline structure in (010) of VO_2 (A), b) various responses at room temperature for different H_2 concentrations in dry air, c) Raman spectra collected for nanoplateletsVO_2 annealed at differents output power 25mW, 50mW and 100mW.

3. Results and discussion

3.1 gas sensing properties

The gas sensing properties of VO_2 nano-platelets has been investigated at room temperature in N_2 dry air at different pressures of H_2 gas using the conductometric sensor signal. The increase in the resistivity is due to the injection of the H_2 gas describing the charge transfer with the material and because the low temperature favors the adsorption of negatively-charged hydroxyl species according to the equation below [4]:

$$H_2 + O_2 + 2e \rightarrow 2OH^- \qquad (1) \qquad \text{(Below 100 ˚ C)}$$

Intrinsic oxygen atoms trap the electron in the n-type VO_2 (A) metal reducing the charge carrier density in a depletion region close to the surface due to the band bending at the surface [5]. Depletion regions occur between grains giving higher resistance. A wide variety of events occur when a molecule impinges upon a surface. It may be reflected with no loss of energy or it may suffer a redistribution of momentum and be diffracted by the surface again with no loss of energy. In the case where the hydrogen molecules lose sufficient quantity of energy they become effectively bound to the surface with strength depending on the kinds of atoms involved. The resistance underwent a drastic drop when the gas is shut off exhibiting n-type semiconductor characteristic of VO_2 (A). This whole process responsive behavior has been qualified as conduction type inversion n-to-p of the sensing material whose conduction is surface trap limited owing to the high surface to volume ratio of this material [6]. Nanoparticles have appreciable fraction of their atom at the surface as the data. A number of properties of materials composed of nanometer sized grains depend strongly on the surface area. The specific surface area of a catalyst is customarily reported in the units of the square meter per gram. ρ is the density expressed in g/cm^3, d is the diameter and V the volume. A cylinder of diameter d and length L has a Volume $\pi d^2L/4$ and $A=2\pi rL$. Hence the surface area is given by:

$$S = \text{area}/\rho V = A/\rho V, \text{ and } S\ (m^2/g) = 4\times10^3/\rho d \quad \text{for } d \ll L. \quad (2)$$

This relation is justified for nanowires, nanosheet or nanoplate. The recovery response is rapidly restored after injection of the gas. This proved the good stability of the gas sensor with high surface to volume ratio. Figure1 c) presents Raman response of VO_2 (M) annealed under N_2 at room temperature giving structural information of the material, obtained by excitation of continuous wave laser light with a 514.5 nm line from argon ion. It is possible to identify the in situ molecule and to determine the amount of the molecule present in the sample. Most molecules at rest prior to interaction with the laser and at room temperature are likely to be in the ground vibrational state.

Table1. Size Variation from 20-500 nm obtained giving different surface area ratio:

Size (nm)	20	30	60	70	80	95	120	150	500
S (m^2/g)	19826.52	33.04	16.52	14.16	12.39	10.44	8.26	6.61	1.98

Therefore the majority of Raman scattering will be Stokes Raman scattering. The ratio of the intensities of the Stokes and anti-Stokes scattering is dependent on the number of molecules in the ground and excited vibrational levels. We notice that the output power at 50 mW was the best choice providing the best spectral resolution of the full width at half maximum. The spectrum presents some raman lines of V_2O_5 which are very close to the lines of VO_2: 144cm^{-1}, 199 cm^{-1}, 306 cm^{-1}, 406 cm^{-1}. We note that the change of the surface stoichiometry oxidation induced by a local heating at 100 mW (lowering of the vibration modes) may be responsible for the change of Raman line position. Hence nanoscale interactions occur at the surface which present small amount of V_2O_5.

3.2 Morphological studies and elemental analysis

The morphology of the synthesized crystals was observed by A Tecnai G2 F20X-Twin MAT field emission high resolution transmission electron microscope (HR TEM) operated at 200 KV Field emission used to investigate the atomic structure and the presence of different oxidation state of the nanocrystals equipped with an elemental EDAX system. As typically reported on figure 2, the surface morphology of the samples exhibit one dimensional nanoplatelet structures. This was found to be correlated to the V_2O_5 initial concentration and the high surface-energy liable with chemical reactions of the medium and becauseV_2O_5 crystallizes in an orthorhombic structure comprising layers of [VO_5] square pyramids sharing edges and corners with a structure only weakly bound along the

crystallographic b axis, which enables the facile intercalation of different molecular species within the interlayer sites [8]. The dimension of the crystallites is in the range of 20 nm to 150 nm for the as-prepared material and around 50-500 nm for the annealed sample. That means that annealing temperature induces significant grain growth promoting twin formation in larger grains. The elemental composition of the material acquired from the X-rays emitted shows that the elemental composition is only constitute of vanadium atoms and oxygen with high intensity showing the nucleation of grains and crystallization of the particles.

3.3 DSC Analysis and structural study of as-synthesized material

The metal insulator phase transformation has been studied via DSC on cooling and on heating. See figure 3. The isotherms that occur during the thermal cycling explain the kinetics of the phase transformation of the system. In both samples (as-synthesized and annealed), two peaks were detected during the experiment from room temperature to 110°C at 10 °C/min with the presence of a flowing of nitrogen gas at 5 ml/min. The as prepared presents a big hysteresis in order of 9 °C comparing to the one anneal with 6.7 °C. This is due to the particle size of the material. The as synthesized material peaks transition is due to the presence of slightly metallic atoms inserted in the tetragonal metastable domains for the VO_2 (A). The insulator to metallic transition in the annealed sample occurs at 67.1°C with an enthalpy of -3.596 W/g related to the exothermic peak where the crystallization of the material occur and the metallic to insulator transition occurs at 60.4°C with an enthalpy of 3.1W/g transition, only 85.28 % recovery of the monoclinic phase with a giving hysteresis of 6.7°C in peaks temperature between heating and cooling different from the literature which can be assigned to the stress in the sample. Changes in enthalpies of transformation are attributed to elastic stored energy and to some untransformed rutile phase [9, 14] that we determine as percolative phenomena.

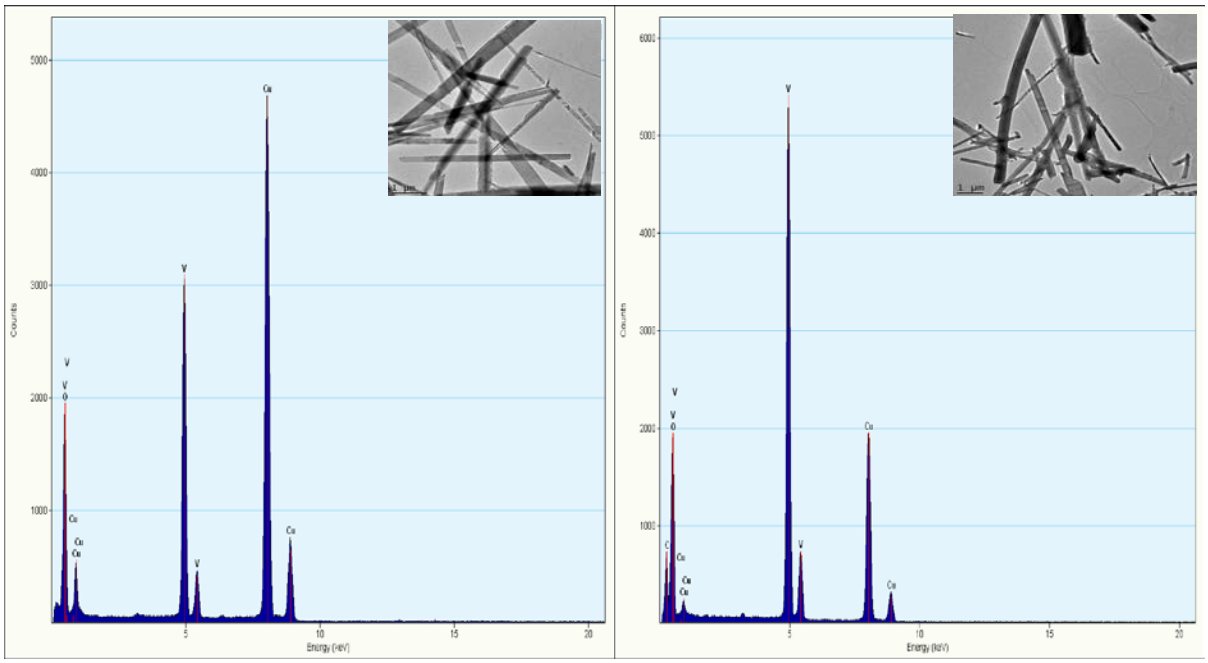

Figure 2. High magnification Transmission electron microscopy images and EDX spectra of VO_2 as-synthesized and anneal nanoplatelets.

The kinetics phenomena occur at different times. The well crystallized material after annealing present the transition temperature from VO_2(M) to VO_2 (R) taking place after 10 min and stop after 18 min while in the as-synthesized sample only few metallic domain transit to VO_2 (R) just for 2 min approximately. Hence the ultrafast of the metal to insulator transition is proportional to the density of

atoms intending to nucleate upon annealing temperature. Multiple physical phases or domains with dimensions of nanometres to micrometres can coexist in these materials at temperatures where a pure phase is expected. Making use of the properties of correlated electron materials in device applications will require the ability to control domain structures and phase transitions in these materials [11]. Measures of the temperatures and heat flows associated with transitions in the material as a function of time and temperature in a controlled atmosphere (N_2) were obtained via Differential Scanning Calorimetry (DSC).

The grain structure measured with the Software Image J presented in figure 4 shows that the grain size is smaller for high interspacing lattice for as-synthesized material approximately 0.400-0.600 nm ([110]) while for annealed sample the grain junction is shrinked and the intespacing become smaller 0.300 nm reducing residual stresses and optimization of the uniformity of the sample. The determination of the material phase and crystallinity was done using XRD crystallography. The majority of the peaks are indexed as VO_2 (A) according to a JCPDS card 00-042-0876. The lattice parameters a and c are 8.45000 Å and 7.68600 Å respectively and Z=16. The space group is P42/nmc. Figure 5 reveals sharp peaks and intense diffraction with a preferential orientation along (110) which demonstrates that the sample is well crystallized without impurities and we note also the presence of some peaks belonging to VO_2 (M) with a weak intensity. It has been demonstrated that the distortion of the VO_6 octahedra in the low temperature VO_2 (A) phase is similar to the monoclinic VO_2 (M) phase [12].

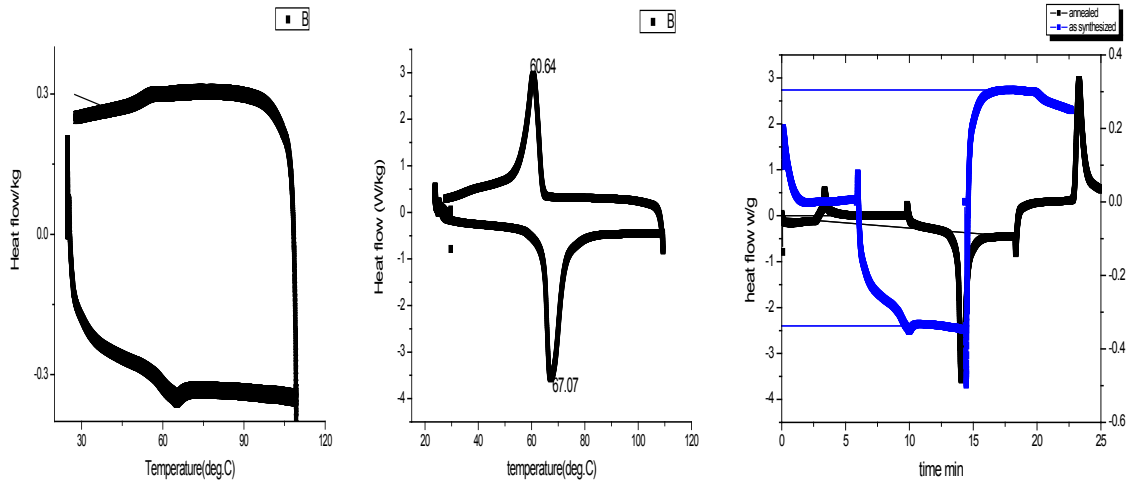

Figure 3. DSC curve showing the reversible phase transformation in the material during the thermal cycling in as synthesized material VO_2 (A) and VO_2 (M) and kinetics effects of both samples.

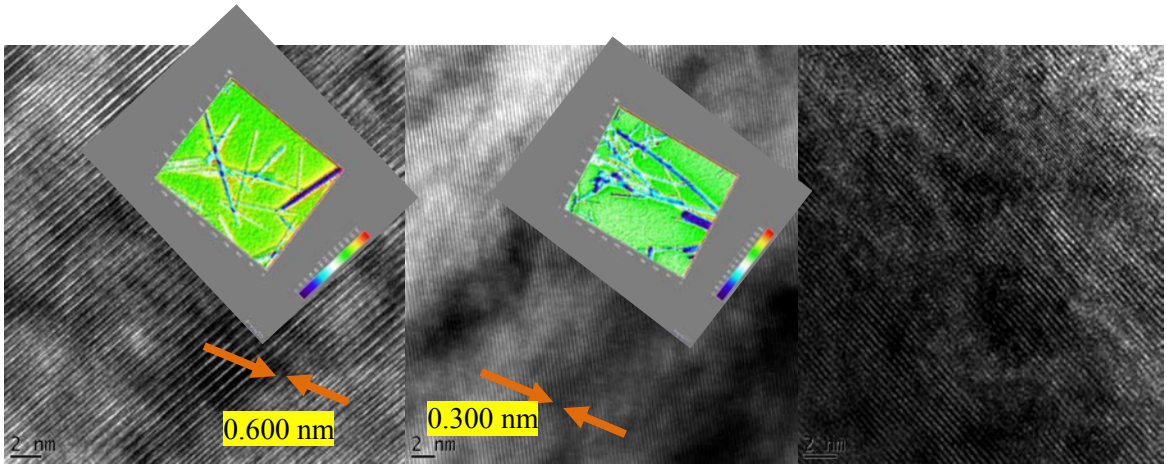

As-synthesized Argon treatment N_2 annealing

Figure 4. Grains structure observed at different annealing gas as indicated

After annealing at 500 °C, the (110) peak decreases in intensity when the material has been annealed under Nitrogen while it is completely vanished under Argon. The nanostructures exhibit two crystallographic structures: stable monoclinic and metastable tetragonal. Generally two main processes determined the phase transformation in annealing process: annealing temperature and time and interfacial stress. Here we see that the complete phase transformation is only possible with an annealing under Argon gas which is inert and act as gas purifier to prevent oxidation from the vanadium oxide, comparatively to the one under Nitrogen which interacts with the material and delays the metal insulator phase transition. The surface region appears as an imperfect region due to the presence of high surface region to volume ratio meaning that the number of atoms on the surface is comparable to the one inside the particles where atoms relax inside the normal lattices sites. The surface structure of nanoplatelet indicating interior of nanoplatelets as synthesized and annealed respectively presents highly surface active atoms with high surface energy where transition begins upon thermal treatment.

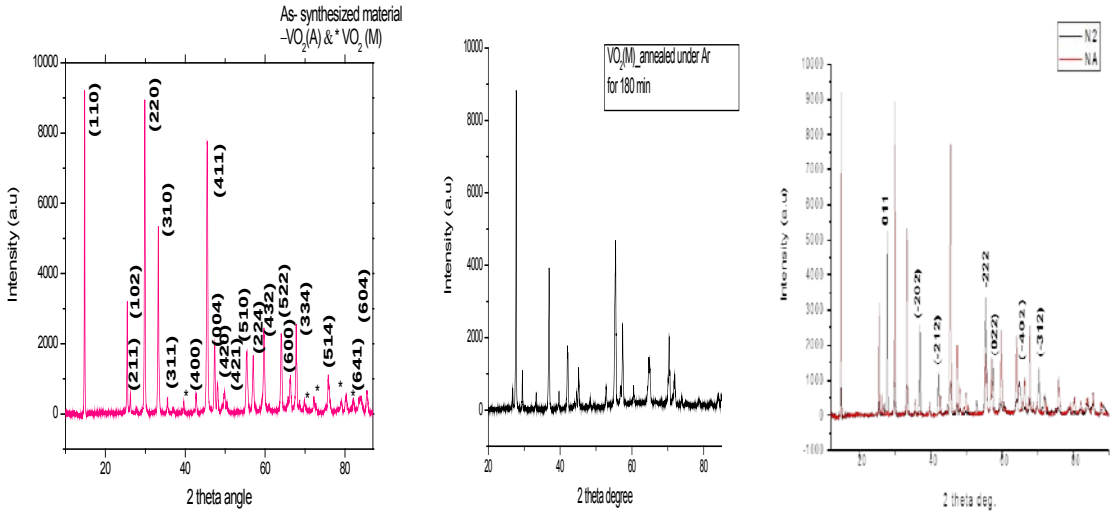

a) b) c)

Figure 5. Typical room temperature indexed X-rays diffraction of the as-synthesized a) annealed under Argon b) and annealed under Nitrogen c) nanostructures materials.

4. Conclusion

In summary, nanoplatelets VO_2 (A) nano-crystals was well synthesized by hydrothermal process with a percentage of crystallinity of 89%, presenting high surface to volume ratio due to the smallest size of the particles. The annealing treatment under N_2 gas and Ar gas gives good insight of internal transformation taking place in the material. The annealing under Argon gas appears preferable due to the optimum crystallization and purity of the material comparatively to the one under Nitrogen which interacts with the material and delays the metal insulator phase transition. Additionally, the as-synthesized material was discovered for the first time to be applicable as gas sensing device at room temperature under H_2. As future work the optimization of the nanoscale structure to enhance the sensitivity of the material is required and the testing of the annealing sample under same conditions and operating at differents temperatures to follow the effect of annealing time and annealing temperature on the electronical properties are highly demanded for the development of the gas sensing device.

Acknowledgements

This work was sponsored by the OWSDW with iThemba LABS-MRD/ National Research Foundation of South Africa, Tshwane University of Technology and the Council for Scientific and Industrial Research in South Africa, as well as the Abdus Salam ICTP-Trieste, Italy.

References

[1] Hyoun W K, Seung H S, Jong W L , Chongmu L , Sae C J 2008 *Optical Materials* **30** 1221-1224

[2] Leroux C, Nihoul G, Tendeloo G V 1998 Physica *Review* B **57** 9

[3] Zhang S, Shang B, Yan J, Yan W, Wei S and Xie Y 2011 *Phys.Chem.Chem. Phys*. **13** 15873-15881

[4] Koch C C *Nanostructured Materials Processing, Properties and Potential Applications* 2002 (Noyes Publications/William Andrew Publishing)

[5] Bochenkov V V E, Sergeev G B *Metal Oxide Nanostructures and their Applications Department of Chemistry* 2010 p 31-52

[6] Huang J and Wan Q *Review Sensors* 2009 9903-9924

[7] Simo A, Edomwonyi-Out L C, Madjoe R and Maaza M 2012. *Direct Synthesis of Pure Radiative VO_2 (M) Plate Like Structures via Hydrothermolysis at Low Temperature*. MRS Proceedings, 1406

[8] Whittaker L, Zhang H and Banerjee S, *J. Mater. Chem.* 2009 **19** 2968

[9] Tselev A, Strelcov E, Luk'yanchuk I, Budai J, Tischler J, Ivanov I, Jones K, Proksch K Kalininand S, Kolmakov A *Nano Lett* 2009 **10** 2003-2011

[10] Nag J, Haglund R F, Payzant E and More K, *Cond-Mat* 2010 3876

[11] Cao J, Ertekin E, Srinivasan V, Fan W, Huang S, Zheng H, Yim J W L, Khana D R, Ogletree D F, Grossmanand J,Wu J C, *Nature Nanotechnology* 2009 **4** 732

[12] Zhang S, Shang B, Yan J, Yan W, Wei S and Xie Y *Phys.Chem.Chem.Phys*. 2011 **13** 15873-15881

[13] Ou J Z, Yaacob M H, Campbell J L, Breedon M, Kalantar-zadeh K and Wlodarski W *Sensors and Actuators B* 2012 **1–6** 166–167

[14] Bai H, Berkhan M and Cortie M B, *PROCEEDINGS – 31ST ANNUAL CONDENSED MATTER AND MATERIALS MEETING* – 2007

Structural and optical properties of nanostructured tungsten trioxide thin films prepared by aqueous chemical growth

B T Sone [1,2], C Nlagamandla[1], T. Malwela [3], R Bucher [1], E Iwuoha[2] and M Maaza [1]

[1]NANOAFNET-Africa Nanocentre, Materials Research Department,iThemba LABS, P.O. Box 722, Somerset West,7129, South Africa.
[2]Chemistry Department, University of the Western Cape, Bellville, South Africa.
[3]National Centre for Nanostructured Materials, CSIR, P.O. Box 395, Pretoria, South Africa.

Email: sonebert@tlabs.ac.za, sonebert@gmail.com

Abstract. Crystalline thin solid films of WO_3 have been prepared on Corning glass and FTO through the low temperature, wet chemistry method of Aqueous Chemical Growth. SEM images of the thin films produced show that the surface morphology of the films is influenced by the kind of substrate used for the synthesis. While nanoplatelet-containing flower-like structures were consistently obtained on the Corning glass substrates, nanorod-containing urchin-like structures were consistently produced on the F-doped SnO_2-glass substrates. Structural characterization of the different thin films synthesized on both substrates was carried out using XRD, TEM, HRTEM and SAED. These showed that the films produced were made up of WO_3 in the monoclinic, cubic and hexagonal phase depending on what heat-treatment procedures the different substrates were subjected to post-synthesis. The quantum confinement effect is clearly demonstrated in the thin films on Corning glass as the optical band gap calculated for these films was seen to undergo a blue shift from the theoretical values of 2,7eV in the bulk to values of 3.18eV, 3.93eV, and 4.12eV at the nano/microscale.

1. Introduction

WO_3 is a wide band gap, 2.7eV, n-type semiconductor metal oxide (SMO) [1,8] that has been widely investigated for its gas sensing, electrochromic, gasochromic and catalytic properties[1,2,8]. It finds applications in a wide variety of devices which include among others optical switching devices, optical data storage devices, smart windows and gas sensors [1,2, 5].

WO_3 is more widely used in the form of thin films and coatings than bulk and has been prepared in this form using both physical and chemical methods which include pulsed laser deposition, electron beam evaporation, radio frequency magnetron sputtering, electrospinning, spray pyrolysis, thermal evaporation, chemical vapour deposition, sol-gel chemistry, hydrothermal synthesis[5,8]. The physical deposition techniques are generally energy intensive, costly, not easily scaled-up, are known to lead to the formation of amorphous films and coatings, but are more tunable in terms of determining film and surface coating thickness. The soft chemistry techniques are known to be less costly, less energy intensive, result in crystalline thin films but are less tunable in terms of determining film thickness. We have recently used,

for the first time, the soft-chemistry technique of Aqueous Chemical Growth (ACG) [3,4] to prepare, at low temperature (95˚C), WO_3 thin films on Corning Glass (CG) and F-doped SnO_2-Glass (FTO) substrates. ACG is a low temperature, soft-chemistry, environmentally benign technique that offers the possibility of building well-ordered, highly crystalline metal oxide thin films over a wide variety of substrates with large array, by using metal salts of desired metal oxides in aqueous media [3,4]. By varying pH, concentration and time of synthesis, it is possible to influence the structure of the films produced.

2. Experimental

Pale yellow acidic solutions of Peroxotungstic acid (PTA), iso-propanol and de-ionised water with 0.2< pH < 2.5 were prepared through slight modification of a method used in [5] for the synthesis of electrospun WO_3-PVP nanofibres on aluminium. Corning glass and FTO substrates (1 mm thick), cleaned by sequential ultrasonication in solutions of MeOH, acetone and de-ionised water for periods of 5 min each, then dried with N_2, were then placed at an angle 70˚ to the horizontal, in Schott® bottles containing the acidified mixture. These were then tightly sealed and placed in a pre-heated (90-95˚C) laboratory oven for 6-24h. The as-synthesized thin films grown on both substrates were generally greenish-yellow in color or whitish. Once removed, these were washed and dried in air after which calcination in air at 500˚C, for 1-2h, rendered them yellowish-green and strongly adhered to the substrate surface.

The morphology of the thin films' surfaces, the structures therein and chemical analysis of the surfaces was determined using Scanning Electron Microscopy (SEM) measurements performed on a LEO-Stereo Scan 440 Scanning Electron Microscope coupled to a unit for Electron Dispersive X-Ray Spectroscopy (EDX). Crystal structure was ascertained by X-Ray Diffraction (XRD) on a BRUKER AXS D8 Advance X-Ray Diffractometer equipped with a Cu Kα monochromator, at wavelength, λ= 1.540315 nm. To ascertain the morphology as well as the crystallinity of the structures produced Transmission Electron Microscopy (TEM) was carried out on Field Emission Gun-TEM with an accelerating voltage of 200kV, while High Resolution TEM (HRTEM) and Selected Area Electron Diffraction (SAED) were carried out on a TECNAI F20 FEG-TEM. Absorption and Transmission spectra of WO_3 thin films were measured in the UV-Visible-Near IR range (200-1100 nm) using a CECIL 2000 Spectrophotometer with the incident beam at the normal to the substrates.

3. Results & Discussions

3.1. Surface Morphology by Scanning Electron Microscopy and Chemical analysis by EDX

SEM revealed that for ACG carried out on Corning glass substrates, nanoplatelet structures were consistently and primarily formed with thicknesses in the 80-250 nm range and widths/diameters in the 1-2μm range. Also observed in figure 1(a) were nanorods/nanobelts 30-50 nm thick and tens of microns long. In some of the thin films, as in that grown at pH = 0.23 (figure 1(a)), the nanoplatelets assembled to form hierarchically ordered super structures bearing resemblance to desert roses. In other thin films, as in that grown at pH = 0.44, 0.91 (figure 1(b) and (c)), the nanoplatelets were observed to be vertically oriented away from the surface of the glass substrate. On the other hand for ACG carried out on FTO, urchin-like microspheres (figure 2(a) and (b)) were regularly formed as opposed to nanoplatelets. These urchin-like microspherical structures consisted of a sphere-like central core, several microns thick, covered with hair-like protrusions with dimensions in the nanorange. EDX (figures 1(d) and 2(c)) carried out on both samples showed that the films consisted mainly of W and Oxygen. An evaluation of the atomic % of both atoms suggests that WO_3 on the ACG samples in CG is in the 1:4 ratio. This suggests the possibility of the formation of oxygen vacancies in the WO_3 lattice particularly after annealing in air at 500˚C. EDX on the FTO-based samples (figure 2(c)) shows alongside W and O, the presence of Sn which

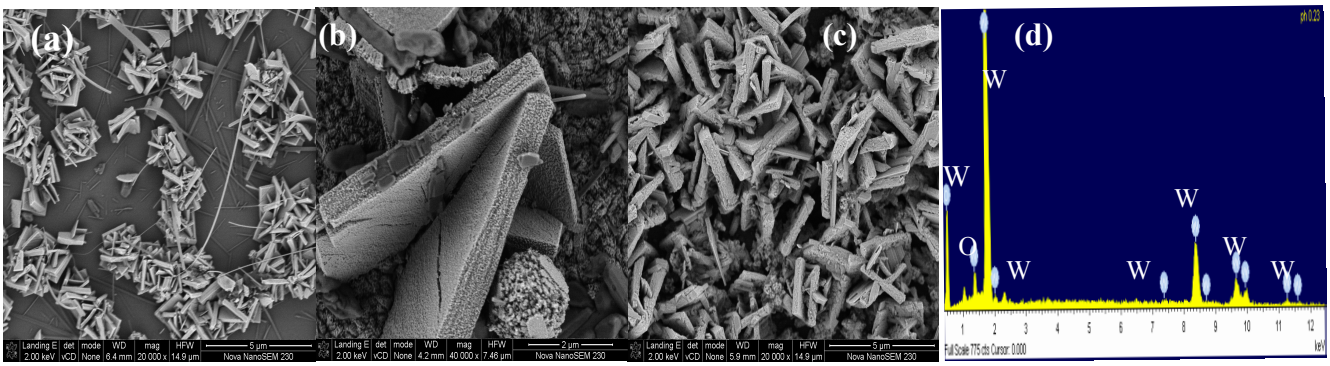

Figure 1.SEM of WO_3 on Corning glass prepared at (a) pH=0.23; (b) pH=0.44; (c) pH=0.91; (d)EDX spectrum of WO_3 on CG.

must come from the F-SnO_2 layer. We believe that the morphology of the films produced on FTO is influenced by the crystalline nature of the F-doped SnO_2 layer. As a result of the influence of the crystalline SnO_2 substrate the lattice parameters for WO_3 thin films on FTO may not be consistent with that of the bulk phase[6].

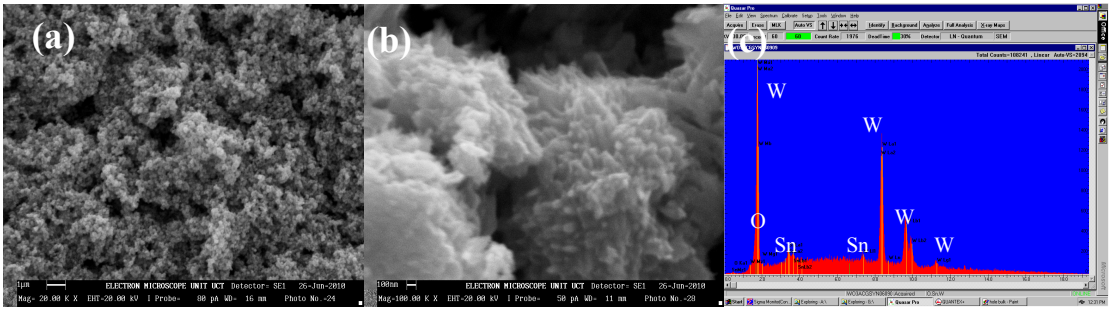

Figure 2 (a) and (b). SEM micrograph of WO_3 thin film on FTO; (c) WO_3 EDX spectrum of WO_3 on FTO.

3.2. Crystal structure determination by X-Ray Diffraction (XRD),TEM, HRTEM and SAED

XRD analysis of the WO_3-ACG samples on CG and FTO showed WO_3 the thin films to be in the monoclinic, cubic, and hexagonal phases. Peaks of WO_3 in the hexagonal phase, figure 3(b), could be indexed to JCPDS Card No. 033-1387 and had reflections of high intensity in the (100), (001), (110), (111) (201), (220), (202), (400), (401) planes. The height and narrowness of the peaks suggest that the WO_3 thin film, pH = 0.91, was highly crystalline. WO_3 in this thin film was in the cubic phase and could be indexed to the JCPDS Card No. 041-0905 with reflections in the (100), (110) planes and preferred orientation in the (100) plane. Using the Debye-Scherrer formula the grain size of the WO_3 thin film, pH = 0.23 was estimated to be ~ 8nm while that of the thin films at pH = 0.44 and 0.91 was estimated to be 17nm.

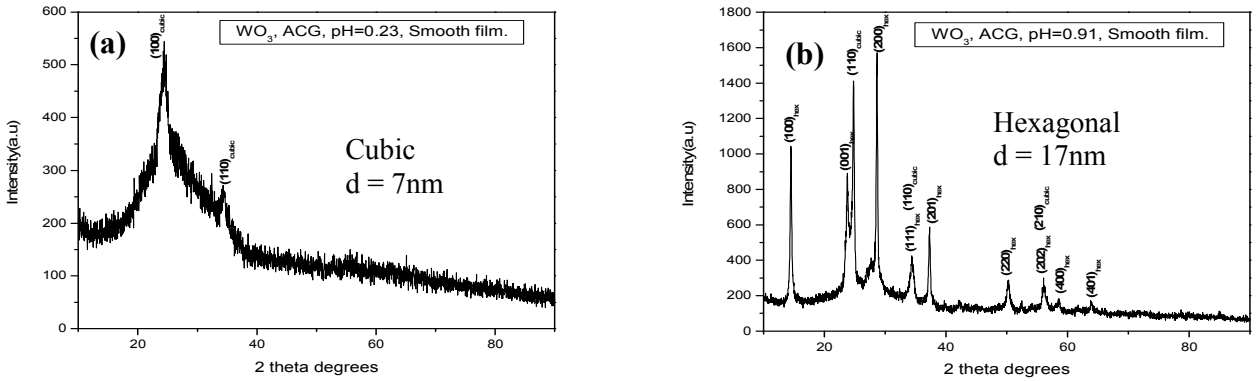

Figure 3. (a) XRD of WO_3 on C. glass at pH=0.23, pH = 0.91; (b). XRD of WO_3-ACG on FTO

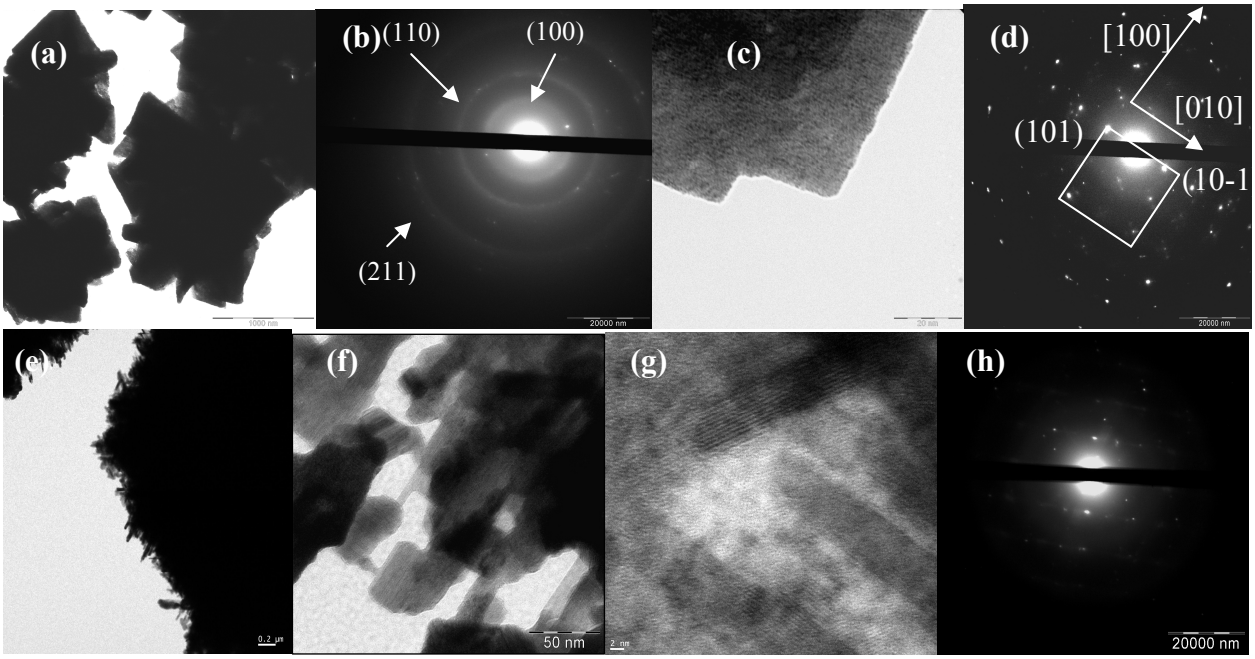

Figure 4. (a) TEM image of WO_3 nanoplatelets on CG; (b) SAED for WO_3 nanoplatelets on CG showing the poly- crystalline nature of film; (c) Higher magnification of WO_3 nanoplatelets on CG; (d) SAED of single crystal WO_3 nanoplatelets on CG; (e) TEM of WO_3 microsphere on FTO; (f). TEM of nanorods grown on WO_3 microsphere; (g) HRTEM nanorods on microsphere; (h) SAED on single crystal of WO_3 nanorod on microsphere.

TEM (figure 4(a) and 4(c)) carried out on the WO_3 thin film on Glass, pH = 0.23, showed the nanoplatelet-like structures. SAED (figure 4(b)) on an agglomeration of nanoplatelets showed through the existence of concentric rings that could be indexed to the (100), (110) and (211) planes of WO_3 of the cubic phase, the polycrystalline nature of the films. SAED (figure 4(d)) showed diffraction spots emanating from a single crystal of the WO_3 nanoplatelets in the cubic phase; alignment in of the planes in the [100] and [010] direction was clearly visible. Reflections from the (100) and the (110) could be

indexed. TEM (figure 4(e)) on WO_3 urchin-like microspheres showed the thick nature of the spheres, impermeable to the electron beam. The hair-like nanorods were however thin enough to be imaged using TEM (figure 4(f)) and HRTEM (figure 4(g)), from which the lattice fringes in the nano-rod like structures could be observed and was calculated to be 2.52 nm - a value which corresponds to the interplanar spacing $d_{(202)}$ in monoclinic phase of WO_3 grown on FTO. WO_3 grown on FTO was polymorphic showing the existence of WO_3 in both the monoclinic and hexagonal phase (XRD not shown here), this possibly as a result of the heating that took place at 400˚C for 0.5-1h, allowing for the transition in part of WO_3 in the monoclinic phase to WO_3 in the hexagonal phase [6]. Note the two different directions of growth in the HRTEM micrograph of the hair like structures in WO_3 on FTO. SAED on one of the nanorods (figure 4(h)) shows the diffraction spots from a single crystal of the WO_3 hair-like nanorod. Note the streaking in the diffraction patterns which may be attributed to the existence of planar defects and domains within the hair-like protrusions[6].

3.4. Optical properties of WO_3 thin films on Corning Glass prepared by ACG

The WO_3 samples on CG and FTO were evaluated for their optical properties in the UV-VIS-NIR region. Film thickness determined using FIB-SEM was estimated at 2 µm for the thin film on CG and 3µm for the film on FTO. The cut-off wavelength for the thin films on CG produced at pH = 0.23, 0.44, 0.91, lay at the edge of the UV-Visible boundary, 320, 420 and 334 nm respectively. By using the Tauc's relation for indirect semicondictors (equation (1)), (absorption coefficient*$h\upsilon$)$^{1/2}$ vs $h\upsilon$ (photon energy) was plotted; where α = absorption coefficient; A is a constant associated to fundamental band-band transitions constant in the optical frequency range; $h\upsilon$ = energy of the incident photons and E_g = optical band gap or electronic band gap.

$$(\alpha h\upsilon) = A(h\upsilon - E_g)^{1/2} \quad (1)$$

$$\alpha = 1/d[\ln (1/T)] \quad (2)$$

E_g which corresponds to indirect transition of photons/electrons between the valence and the conduction band in WO_3 was obtained by extrapolating the linear plot of the curve near the onset of

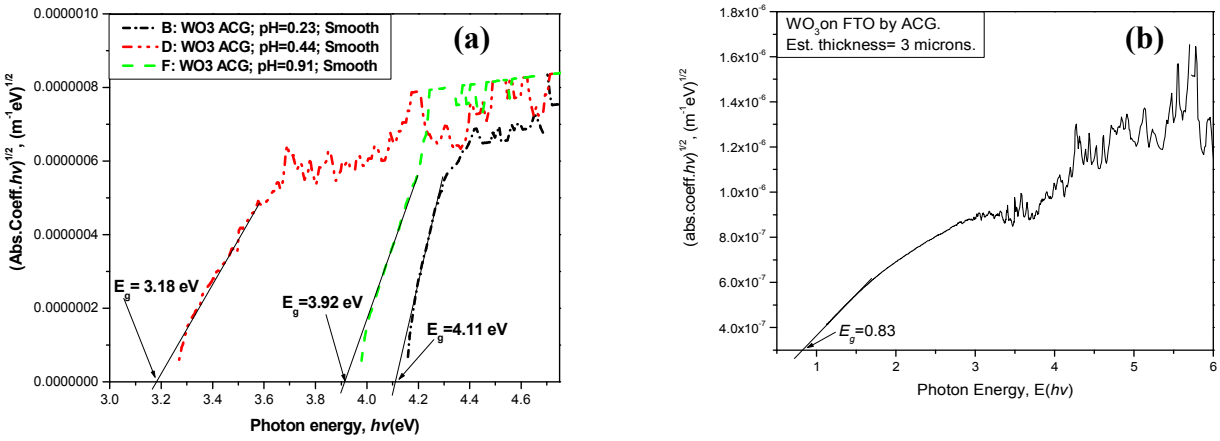

Figure 5. (a) Optical band gap calculation of WO_3 on CG; (b) Optical band gap for WO_3 thin film on FTO.

the absorption edge so that it touched the x-axis at the point where $(\alpha hv)^{1/2} = 0$. The absorption coefficient, α, of the film was calculated using the relation in equation (2), where d is the thickness of the film as estimated by SEM and T is the % transmittance of the film. E_g for the thin film, prepared at pH = 0.44, with thickness 4μm, was calculated to be 3.18eV (see figure 4(a)) while for the thin films prepared at pH =0.23 and 0.91, the optical band gap was calculated to be 4.11 eV and 3.92 eV respectively. The strong linear relationship between $(\alpha hv)^{1/2}$ and photon energy of the incident light, $E_g = hv$, shows that WO_3 is an indirect band gap material. The blue shift observed in the optical band gap can be explained as being a result of the quantum confinement effect that takes place when the size of bulk WO_3 is reduced to the nanoscale. The optical band gap for the WO_3 thin film on FTO (figure 5b) is calculated to be E_g= 0.83 based on UV-Vis-NIR transmission spectrum not shown here. The thin films of WO_3 on Corning glass with their array of closely packed, their reduced grain size in the nanoscale, their vertically oriented nanoplatelets and hierarchical desert rose-like nanostructures should alongside the dense but disordered distribution of microspheres on FTO, offer large surface areas with high porosity that offer increased pathways for gas diffusion making them applicable in gas sensing, electrochromic devices and possibly catalysis [6,7]. The thin films on FTO can be employed as electrochromic material in optical switching devices and smart windows.

4. Conclusion

ACG was used to prepare WO_3 thin films on Corning glass and FTO. SEM and TEM confirm the formation of nanoplatelet and urchin-like structures of WO_3 on the respective substrates. XRD, HRTEM and SAED showed that WO_3 existed in the cubic, hexagonal and monoclinic phase within the films. Average crystallite size for WO_3 in the films on CG was as small as 8 nm. This is less than the Bohr radius of WO_3 and may explaining in part the blue shift in E_g from 2.7eV in the bulk to 3.18eV, 3.92 eV, 4.11 eV in the WO_3 thin film on CG prepared at pH=0.44, 0.91 and 0.23 respectively. The other factors that may influence the final value for the optical band gap of the films is the film thickness as well as reflectance from the films which was not taken into consideration when calculating the absorption coefficients.

Acknowledgements

The financial support of iThemba LABS and Nanoscience Africa Network (NANOAFNET) is hereby acknowledged.

References

[1] Chaudhari G N, Bende A M, Bodade A B, Patil S S, Sapkal V S 2006 *Sensors and Actuators B* **115** 297-302

[2] Deepa M, Srivastava A K, Sharma S N, Govind and Shivaprasad S M 2008 *Applied Surface Science* **254** 2342-2352

[3] Vayssieres L, Hagfeldt A, and Lindquist S E 2000 *Pure Applied Chemistry* **72** 47-52

[4] Lionel Vayssieres 2004 *International Journal of Nanotechnology* **1** No.1/2 1-41

[5] Xiaofeng L, Xincai L, Zhang W, Wang C., Wei Y 2006 *Journal of Colloid and Interface Science* **298** 996-999

[6] LeGore L J, Lad R J, Moulzolf S C, Vetelino J F, Frederick B G, Kenik E A 2009 *Thin Solid films* **406** 79-86

[7] Solis J L, Sauko S, Kish L, Granqvist C G, Lantto V 2001 *Thin Solid Films* **391** 255-360

[8] Xie G, Yu J, Chen X, Jiang Y 2007 *Sensors and Actuators B* **123** 909-914

Structural, electronic and optical properties of gold nitrides

Mohammed S H Suleiman[1,2] and Daniel P Joubert[1]

School of Physics, University of the Witwatersrand, Johannesburg, South Africa
Department of Physics, Sudan University of Science and Technology, Khartoum, Sudan

E-mail: suleiman@aims.ac.za (M Suleiman)

Abstract. The atomic and electronic structures of AuN, AuN_2 and Au_3N are investigated using first-principles density-functional theory (DFT). We studied cohesive energy vs. volume data for a wide range of possible structures of these nitrides. Obtained data was fitted to Birch-Murnaghan third-order equation of state (EOS) so as to identify the most likely candidates for the true crystal structure in this subset of the infinite parameter space, and to determine their equilibrium structural parameters. The analysis of the electronic properties was achieved by the calculations of the band structure and the total and partial density of states (DOS). Some possible pressure-induced structural and electronic phase transitions have been pointed out. Further, we performed G_0W_0 calculations within the the random-phase approximation (RPA) to the dielectric tensor to investigate the optical spectra. Obtained results were compared with theory and with experiment.

1. Introduction

In 2002, Šiller and co-workers [1] reported direct observation of the formation the of Au_xN compound for the first time. Since then, single crystal and polycrystalline gold nitrides have been prepared with different methods [2, 3], and many theoretical [4, 5, 6, 7] and experimental [4, 8, 2, 9, 10] investigations on the structural and physical properties of gold nitride have been published. It turned out that gold nitride possesses interesting properties which may lead to potential practical applications [11].

So far, the most significant finding may be that of Šiller et. al [8] who, in 2005, reported the production of metallic large area gold nitride films which are $\sim 50\%$ harder than pure gold films produced under similar conditions, making the gold nitride ideal for use in large-scale applications in coatings and in electronics. Moreover, the possibility of patterning gold nitride film surfaces by electron/photon beam lithography was confirmed [11].

From their experimental observations and *ab initio* calculations, Krishnamurthy *et al.* [4] suggested the possiblity of formation of more than one gold nitride phase. Although theoretical calculations have predicted several possible structures for AuN, AuN_2 and Au_3N, none of these agrees with experiment [2]. In the current first-principles study, we consider AuN, AuN_2 and Au_3N formulas in possible crystal structures. AuN is investigated in the following nine structures: NaCl (B1) structure, CsCl (B2) structure, the hexagonal structure of BN (B_k), the hexagonal structure of WC (B_h), wurtzite structure (B4), cooperite structure (B17), and the face-centered orthorhombic structure of TlF (B24). AuN_2 was investigated in the following four structures: fluorite structure (C1), pyrite structure (C2), marcasite structure (C18), and

the simple monoclinc structure of $CoSb_2$. While for Au_3N, the following five structures were considered: the fcc structure of $AlFe_3$ ($D0_3$), the simple cubic structure of Cr_3Si (A15), the anti-ReO_3 structure ($D0_9$), and the sc structure of Cu_3Au ($L1_2$).

2. Calculation methods

Our electronic structure calculations were based on spin density functional theory (SDFT) [12, 13] within the projector augmented wave (PAW) method [14, 15] in which scalar kinematic relativistic effects are incorporated via mass-velocity and Darwin corrections in the construction of the pseudo-potentials, as implemented in VASP package [16, 17]. In solving Kohn-Sham (KS) equations [18]

$$\left\{ -\frac{\hbar^2}{2m_e}\nabla^2 + \int d\mathbf{r}' \frac{n(\mathbf{r}')}{|\mathbf{r}-\mathbf{r}'|} + V_{ext}(\mathbf{r}) + V_{XC}^{\sigma,\mathbf{k}}[n(\mathbf{r})] \right\} \psi_i^{\sigma,\mathbf{k}}(\mathbf{r}) = \epsilon_i^{\sigma,\mathbf{k}} \psi_i^{\sigma,\mathbf{k}}(\mathbf{r}), \tag{1}$$

the pseudo part of the KS one-electron spin orbitals $\psi_i^{\sigma,\mathbf{k}}(\mathbf{r})$ are expanded on a basis set of plane-waves (PWs) with energy cut-off $E_{cut} = 600$ eV. $\mathbf{\Gamma}$-centered Monkhorst-Pack meshes [19] were used to sample the first Brillouin zone (BZ), and the Perdew-Burke-Ernzerhof (PBE) parametrization [20] of the generalized gradient approximation (GGA) [21] was used for the exchange-correlation (XC) potentials. For static calculations of the total electronic energy and the density of state (DOS), partial occupancies were set using the tetrahedron method with Blöchl corrections, while in the geometry relaxation, the smearing method of Methfessel-Paxton (MP) was followed.

To study the energy-volume $E(V)$ equation of state (EOS), and to determine the equilibrium parameters of each structure, we make isotropic variations of the cell volume while ions with free internal parameters were allowed to search for local minima on the Born-Oppenheimer potential hyper-surface [22], following the implemented conjugate-gradient (CG) algorithm, untill all Hellmann-Feynman force components [23] on each ion were smaller than $1 \times 10^{-2} eV/\mathring{A}$. The obtained cohesive energies E_{coh}, as a function of volume V per atom, were fitted to a Birch-Murnaghan 3rd-order equation of state (EOS) [24], and the equilibrium volume V_0, the equilibrium cohesive energy E_0, the equilibrium bulk modulus B_0 and its pressure derivative B_0' were determined by a least-squares method.

In order to improve the calculated electronic structure, and to investigate the optical spectra, we carried out G_0W_0 calculations [25, 26] within the random-phase approximation (RPA) to the dielectric tensor. From the real $\varepsilon_{re}(\omega)$ and the imaginary $\varepsilon_{im}(\omega)$ parts of this frequency-dependent microscopic dielectric tensor we derive the frequency-dependent absorption coefficient $\alpha(\omega)$, reflectivity $R(\omega)$, refractive index $n(\omega)$, and energy-loss spectrum $L(\omega)$.

3. Results and discussions

3.1. Equation of states and structural properties

In Fig. (1), $E_{coh}(V)$ curves are displayed. It is clear that the simple tetragonal structure of cooperite (B17) would be the energetically most stable structure of AuN (Fig. 1(a)). This structure was theoretically predicted to be the ground-state structure of PtN [27], and we found it to be the most stable structure of CuN as well [28]. Kanoun and Said [6] studied the $E(V)$ EOS for AuN in the B1, B2, B3 and B4 structures. Within this parameter sub-space, the relative stabilities they arrived at agree in general with ours, however Fig. 1(a) shows that B4 is prefered against B3 and only at low pressures, while they predicted that B3 is always more stable than B4.

In the AuN_2 series, the least symmetric simple $CoSb_2$ monoclinc structure is found to be the most stable (Fig. 1(b)). This agrees with the conclusion of Ref. [7] where it is suggested that

AuN_2 may be synthesized at extreme conditions (higher pressure and temperature) and/or it may have other Au:N stoichiometric ratios.

Fig. 1(c) shows that $D0_9$ is the most stable in the studied Au_3N series. $D0_9$ structure is known to be the structure of the synthesized Cu_3N. Krishnamurthy *et al.* [4] studied all these Au_3N structures and found $D0_9$ to be the most stable. Yet, they identified a triclinic crystal structure with 1.0 eV per Au_3N unit below that of $D0_9$.

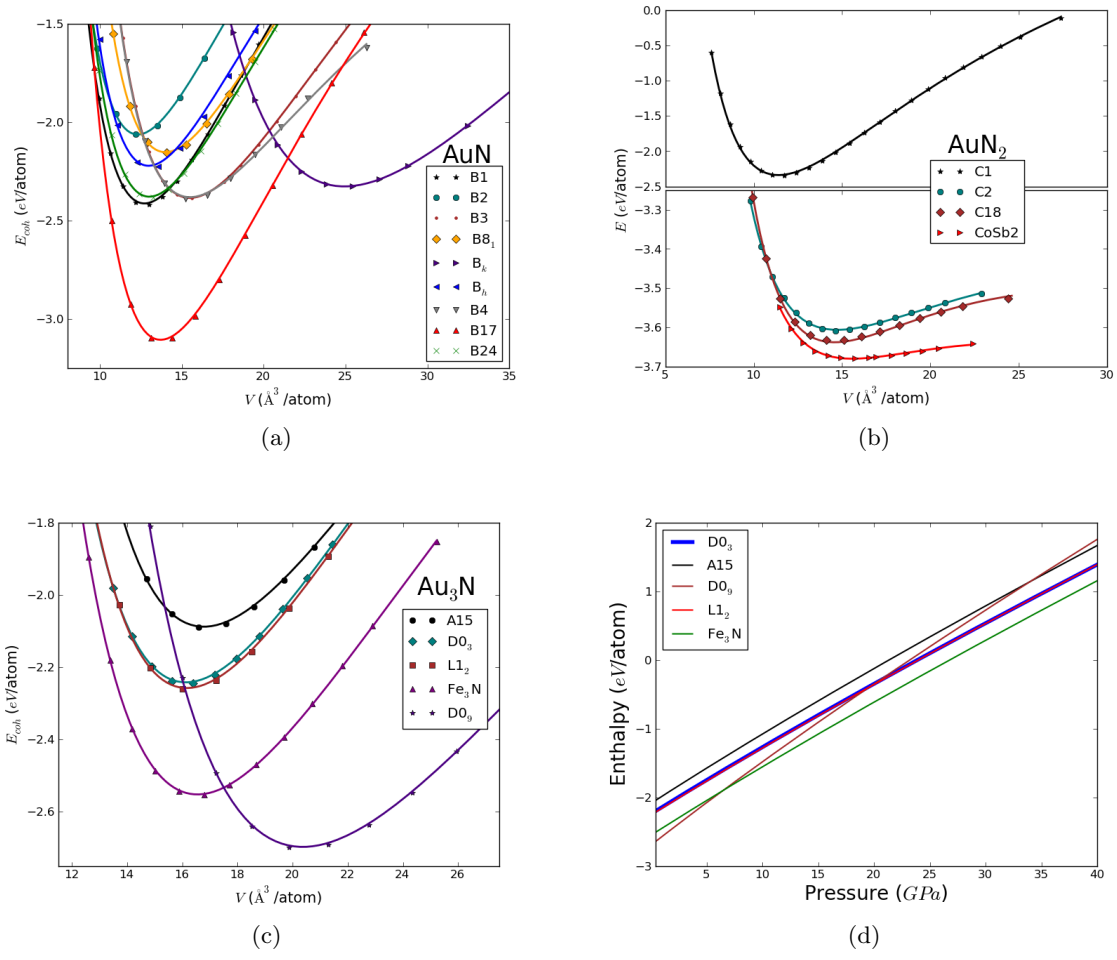

Figure 1: (Color online.) Cohesive energy $E_{\rm coh}(eV/\text{atom})$ versus atomic volume V (Å^3/atom) for (a) AuN in nine different structural phases, (b) for AuN_2 in four different structural phases, (c) for Au_3N in five different structural phases; (d) and enthalpy versus pressure for Au_3N in the five structures.

In table 1, we present some of our obtained equilibrium structural parameters and compare them with some previous theoretical calculations.

3.2. Pressure-induced phase transitions

Enthalpy-pressure relations for Au_3N in the considered structures are displayed in Fig. (1(d)). A point at which enthalpies $H = E_{coh}(V) + PV$ of two structures are equal defines the transition

Table 1. Calculated zero-pressure structural properties of some of the studied phases of AuN, AuN_2 and Au_3N**:** Lattice constants ($a(\mathring{A})$, $b(\mathring{A})$, $c(\mathring{A})$ and $\beta(^\circ)$), equilibrium atomic volume $V_0(\mathring{A}^3/\text{atom})$, cohesive energy $E_{\text{coh}}(eV/\text{atom})$, bulk modulus B_0 (GPa) and its pressure derivative B_0'. The cited data are of previous DFT calculations.

Phase	a(Å)	b(Å)	c(Å)	$\beta(^\circ)$	V_0 (Å^3/atom)	$E_{\text{coh}}(eV/\text{atom})$	B_0 (GPa)	B_0'
AuN(B17)	3.149	–	5.543	–	13.74	-3.115	176.8	5.3
$AuN_2(CoSb_2)$	6.011	5.869	10.656	151.2	15.64	-3.679	12.0	9.0
	8.149 [7]	5.350 [7]	5.361 [7]	131.09 [7]	14.68 [7]	–	–	–
AuN_2(C18)	5.162	–	–	–	11.46	-2.346	195.1	4.9
	5.144 [5]	–	–	–	15.11 [7]	–	198 [5]	
$Au_3N(D0_9)$	4.335	–	–	–	20.38	-2.702	95.4	5.5
	4.239 [4]	–	–	–	–	–	–	–

pressure P_t, where transition from the phase with higher enthalpy to the phase with lower enthalpy may occur.

Fig. (1(d)) shows that a transition from $D0_9$ phase to the Fe_3N phase would take place at a very low pressure $\sim$ 6.3 GPa; and it is clear that the $D0_9$ phase is favourable only at low pressures below $\sim$ 6.3 GPa, while the Fe_3N hexagonal structure of Ni_3N is favoured at higher pressures . Fig. (1(d)) also reveals that $L1_2$ and $D0_3$ phases may co-exist over a wide range of pressure and that they are both favoured over $D0_9$ phase at pressures higher than $\sim$ 20 GPa, while A15 would be favoured over $D0_9$ only at pressures higher than $\sim$ 33 GPa.

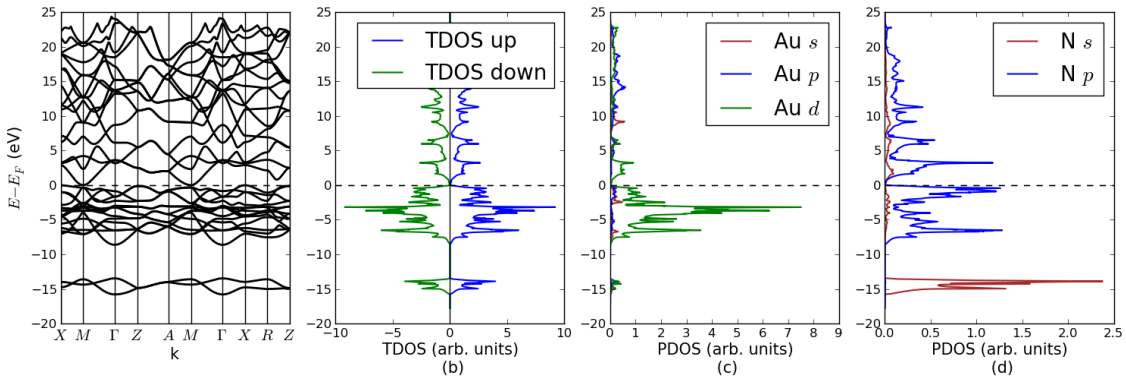

Figure 2: (Color online.) DFT calculated electronic structure for AuN in the B17 structure: **(a)** electronic band structure along the high-symmetry **k**-points. The coordinates of the labeled points w.r.t. the reciprocal lattice primitive vectors are: $X(0.0, 0.5, 0.0)$, $M(0.5, 0.5, 0.0)$, $\Gamma(0.0, 0.0, 0.0)$, $Z(0.0, 0.0, 0.5)$, $A(0.5, 0.5, 0.5)$ and $R(0.0, 0.5, 0.5)$; **(b)** spin-projected total density of states (TDOS); **(c)** partial density of states (PDOS) of Au(s, p, d) orbitals in AuN; and **(d)** PDOS of N(s, p) orbitals in AuN.

3.3. Electronic properties

The DFT(GGA) calculated electronic band structures for AuN(B17) and $Au_3N(D0_9)$ and their correponding total and partial DOS are displayed in Fig. 2 and Fig. 3, respectively. Although it might not be clear on the graph, AuN(B17) shows a very small 0.013 eV $(X - M)$ indirect DFT band gap. Krishnamurthy *et al.* [4] predicted $Au_3N(D0_9)$ to be an indirect band-gap

semiconductor, but they did not give a value. Fig. 3 shows that it is indeed a semiconductor with an $(R-X)$ indirect DFT band gap of 0.139 eV GGA value. According to the fact that the produced gold nitrides are metallic, the $D0_9$ structure may not be the true candidate for the most likely stoichiometry, Au_3N.

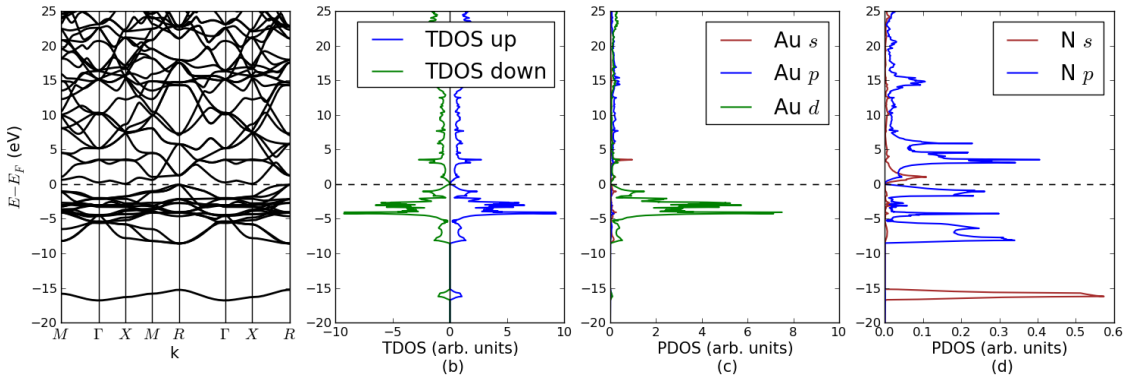

Figure 3: (Color online.) DFT calculated electronic structure for Au_3N in the $D0_9$ structure: **(a)** electronic band structure along the high-symmetry **k**-points. The coordinates of the labeled points w.r.t. the reciprocal lattice basis vectors are: $M(0.5, 0.5, 0.0)$, $\Gamma(0.0, 0.0, 0.0)$, $X(0.0, 0.5, 0.0)$ and $R(0.5, 0.5, 0.5)$; **(b)** spin-projected total density of states (TDOS); **(c)** partial density of states (PDOS) of $Au(s, p, d)$ orbitals in Au_3N; and **(d)** PDOS of $N(s, p)$ orbitals in Au_3N.

3.4. Optical properties

Fig. 4 displays the real and the imaginary parts of the frequency-dependent dielectric function $\varepsilon_{\mathrm{RPA}}(\omega)$ of $Au_3N(D0_9)$ and the corresponding derived optical constants within the visible spectrum. It is clear from the absorption coefficient $\alpha(\omega)$ spectrum that G_0W_0 calculations give a band gap of $\sim 1\ eV$, which is a significant correction to the obtained DFT value.

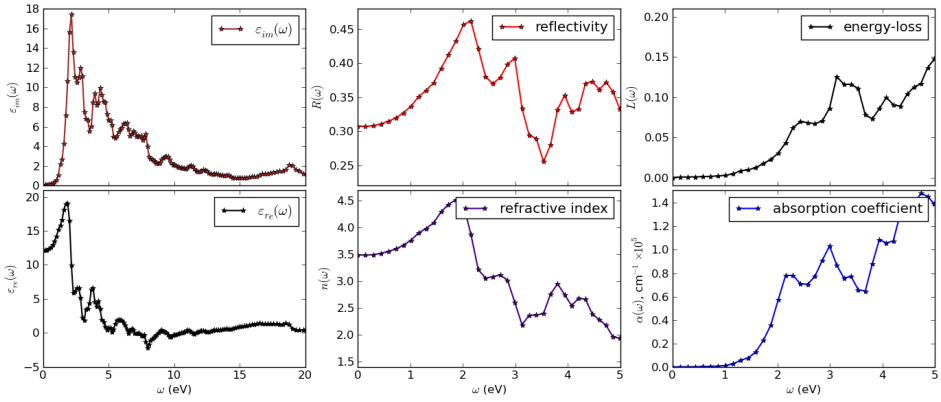

Figure 4: (Color online.) The real and the imaginary parts of the frequency-dependent dielectric function of and the corresponding optical constants of $Au_3N(D0_9)$.

4. Summary

We have applied first-principles methods to investigate the structural, electronic and optical properties of some possible stoichiometries and crystal structures of gold nitrides. The metallic B17, $CoSb_2$ and the semiconducting $D0_9$ phases have been found to be the energetically most stable structures in the studied AuN, AuN_2 and Au_3N series, respectively. The GW calculated optical spectra confirmed the semiconducting nature of $D0_9(Au_3N)$ and corrected the DFT calculated band gap. Obtained results show good agreement with previous studies.

Acknowledgments

Suleiman would like to thank Dr. Mahlaga P. Molepo for his valuable discussions and support. Many thanks to Mr. Ross McIntosh for his comments.

References

[1] Šiller L, Hunt M, Brown J, Coquel J M and Rudolf P 2002 *Surface Science* **513** 78 – 82 ISSN 0039-6028
[2] Alves L, Hase T P A, Hunt M R C, Brieva A C and Šiller L 2008 *Journal of Applied Physics* **104** 113527 (pages 5)
[3] Šiller L, Alves L, Brieva A, Butenko Y and Hunt M 2009 *Topics in Catalysis* **52**(11) 1604–1610 ISSN 1022-5528 10.1007/s11244-009-9281-6
[4] Krishnamurthy S, Montalti M, Wardle M G, Shaw M J, Briddon P R, Svensson K, Hunt M R C and Šiller L 2004 *Physical Review B* **70**(4) 045414
[5] Yu R and Zhang X F 2005 *Physical Review B* **72**(5) 054103
[6] Kanoun M and Goumri-Said S 2007 *Physics Letters A* **362** 73 – 83 ISSN 0375-9601
[7] Chen W, Tse J and Jiang J 2010 *Solid State Communications* **150** 181 – 186 ISSN 0038-1098
[8] Šiller L, Peltekis N, Krishnamurthy S, Chao Y, Bull S J and Hunt M R C 2005 *Applied Physics Letters* **86** 221912 (pages 3)
[9] Quintero J H, Ospina R, Crdenas O O, Alzate G I and Devia A 2008 *Physica Scripta* **2008** 014013
[10] Brieva A C, Alves L, Krishnamurthy S and Siller L 2009 *Journal of Applied Physics* **105** 054302 (pages 4)
[11] Butenko Y, Alves L, Brieva A, Yang J, Krishnamurthy S and Šiller L 2006 *Chemical Physics Letters* **430** 89 – 92 ISSN 0009-2614
[12] von Barth U and Hedin L 1972 *Journal of Physics C: Solid State Physics* **5** 1629–1642
[13] Pant M and Rajagopal A 1972 *Solid State Communications* **10** 1157 – 1160 ISSN 0038-1098
[14] Blöchl P E 1994 *Physical Review B* **50**(24) 17953–17979
[15] Kresse G and Joubert D P 1999 *Physical Review B* **59**(3) 1758–1775
[16] Kresse G and Hafner J 1993 *Physical Review B* **47**(1) 558–561
[17] Kresse G and Hafner J 1994 *Physical Review B* **49**(20) 14251–14269
[18] Kohn W and Sham L J 1965 *Physical Review* **140**(4A) A1133–A1138
[19] Monkhorst H J and Pack J D 1976 *Physical Review B* **13**(12) 5188–5192
[20] Perdew J P, Burke K and Ernzerhof M 1996 *Physical Review Letters* **77**(18) 3865–3868
[21] Becke A D 1988 *Physical Review A* **38**(6) 3098–3100
[22] Born M and Oppenheimer J R 1927 *Annalen der Physik* **84** 457–484
[23] Feynman R P 1939 *Physical Review* **56**(4) 340–343
[24] Birch F 1947 *Physical Review* **71**(11) 809–824
[25] Hedin L 1965 *Physical Review* **139**(3A) A796–A823
[26] Shishkin M and Kresse G 2006 *Physical Review B* **74**(3) 035101
[27] von Appen J, Lumey M W and Dronskowski R 2006 *Angewandte Chemie International Edition* **45** 4365–4368 ISSN 1521-3773
[28] Suleiman M S H, Molepo M P and Joubert D P 2012 *ArXiv e-prints* (*Preprint* 1211.0179)

Investigation of Radiation Damage and Diffusion of Xenon Implanted in 6H-SiC

T.T. Thabethe[1], T.T Hlatswayo[1], J.B. Malherbe[1], E Wendler[2], W. Wesch[2], P Chakraborty[3], & EF da Silveira[4]

[1]Department of Physics, University of Pretoria, Pretoria, 0002, South Africa

[2]Institute for Institut für Festkörperphysik, Friedrich-Schiller University Jena, Jena, Germany

[3]Saha Institute of Nuclear Physics, Bidhannagar, Kolkata 700 064, India

[4]Physics Department, Pontifícia Universidade Católica do Rio de Janeiro, 22453-900 Rio de Janeiro, Brazil

E-mail: thabby.theo@gmail.com

Abstract. Radiation damage and diffusion behaviour of xenon implanted in 6H-SiC has been investigated using Rutherford backscattering spectrometry (RBS) and channelling techniques. Implantation at 600ºC caused the 6H-SiC to retain its crystallinity but with some damage in the implanted region. Vacuum-annealing of radiation damage was performed for 5h in the range 1000 to 1500ºC in steps of 100ºC. There was no diffusion detected during annealing from 1000ºC to 1400ºC; only a shift of the xenon profile towards the surface was observed at 1400ºC, perhaps due to thermal etching. Diffusion was observed at the annealing temperature of 1500ºC also with a shift towards the surface.

1. Introduction

In modern high temperature nuclear reactors, silicon carbide (SiC) is used as the main diffusion barrier for the fission products in the coated fuel called TRISO particles. In the TRISO particle, pyrolytic carbon and SiC layers retain most of the important fission products like xenon, krypton and cesium effectively at temperatures up to 1000ºC, with the release of silver raising doubts on the effectiveness of SiC layer [1].

Previous studies [2, 3] have shown that room temperature implantation of heavy ions into single crystal 6H-SiC causes the SiC to become amorphous. However, the SiC remains crystalline with many point defects and dislocation loops (damage) for 400 to 600ºC implantations. The recovery of SiC material upon annealing depends on both the amount of damage created during implantation as well as the annealing temperature [4].

K Fukuda *et al.* [2] suggested that the release of Xe at annealing temperatures below 1200ºC was due to interstitial diffusion and release of Xe from trapping sites (vacancies and dislocation loops). At temperatures ranging from 1200ºC to 1400ºC, grain boundary diffusion was the dominant mechanism, while above 1400ºC the release is governed by the normal volume diffusion without any hindrance of trapping effects [2].

In this study two phenomena in single crystal 6H-SiC implanted by 360 keV Xenon ions are studied using Rutherford Backscattering Spectroscopy (RBS) and channelling:

- Radiation damage: it's annealing behaviour at annealing temperatures ranging from 1000°C to 1500°C.
- Diffusion of xenon in 6H-SiC at these annealing temperatures.

2. Experimental Procedure

Xenon ions were implanted in a single crystalline wafer (6H-SiC) with 360keV at 600°C with a fluence of 1×10^{16} cm^{-2}. A normal incident angle was tilted 7° off to reduce channelling. To prevent beam induced target heating, the dose rate was kept below 10^{13} cm^{-2} s^{-1} .The sample was vacuum annealed in a computer control Webb 77 graphite furnace at different temperatures for the same time, of 5h. Depth profiles were obtained by Rutherford backscattering spectrometry (RBS) using α-particles with 1.6MeV. The same set up was use to investigate radiation damage of 6H-SiC sample by channelling spectroscopy.

3. Results and Discussion

Implantation of 6H-SiC at 600°C retained the crystallinity of 6H-SiC with some damage remaining in the implanted region. The damaged region is indicated by the broad peak around 150nm in the RBS spectra compared with the unimplanted sample as shown in Figures 1 and 2. Figure 1 shows that the implanted xenon created damage near the surface of 6H-SiC. It also shows that the xenon peak corresponded with the damage peak. During implantation the xenon atoms were mobile due to their

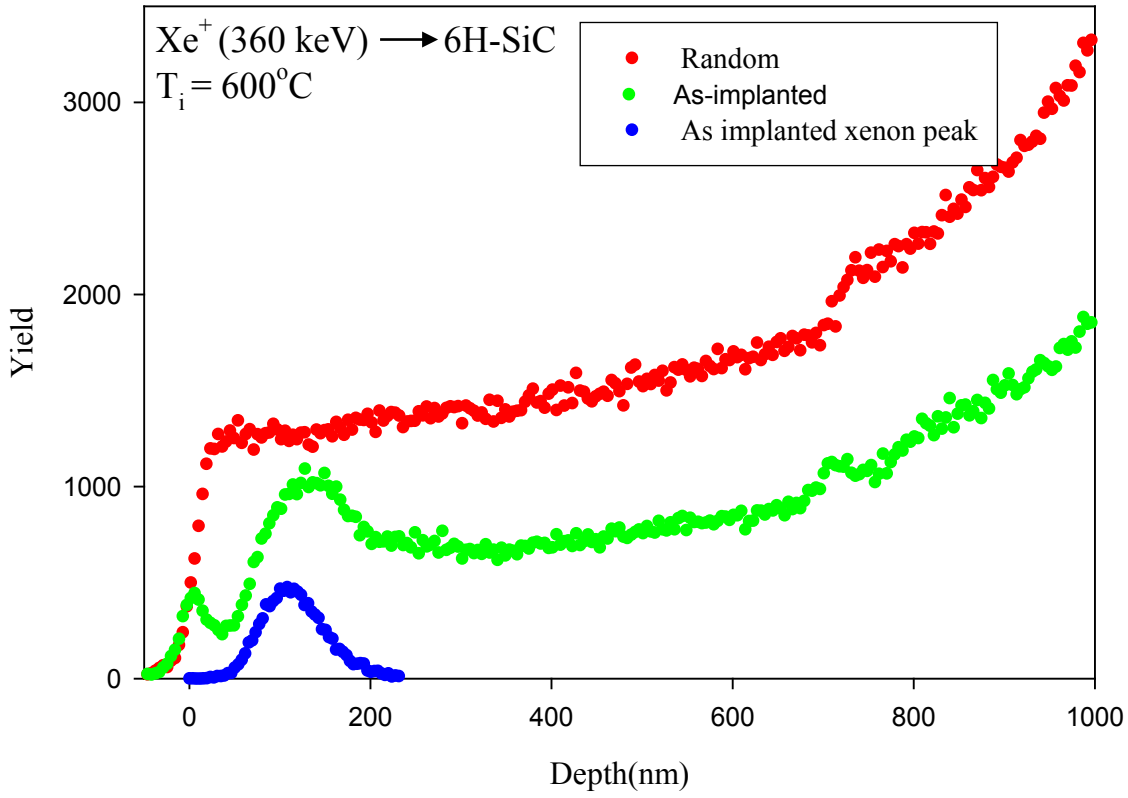

Figure 1. The random and aligned Rutherford backscattering spectra of 6H-SiC implanted at 600°C compared with the as-implanted xenon peak.

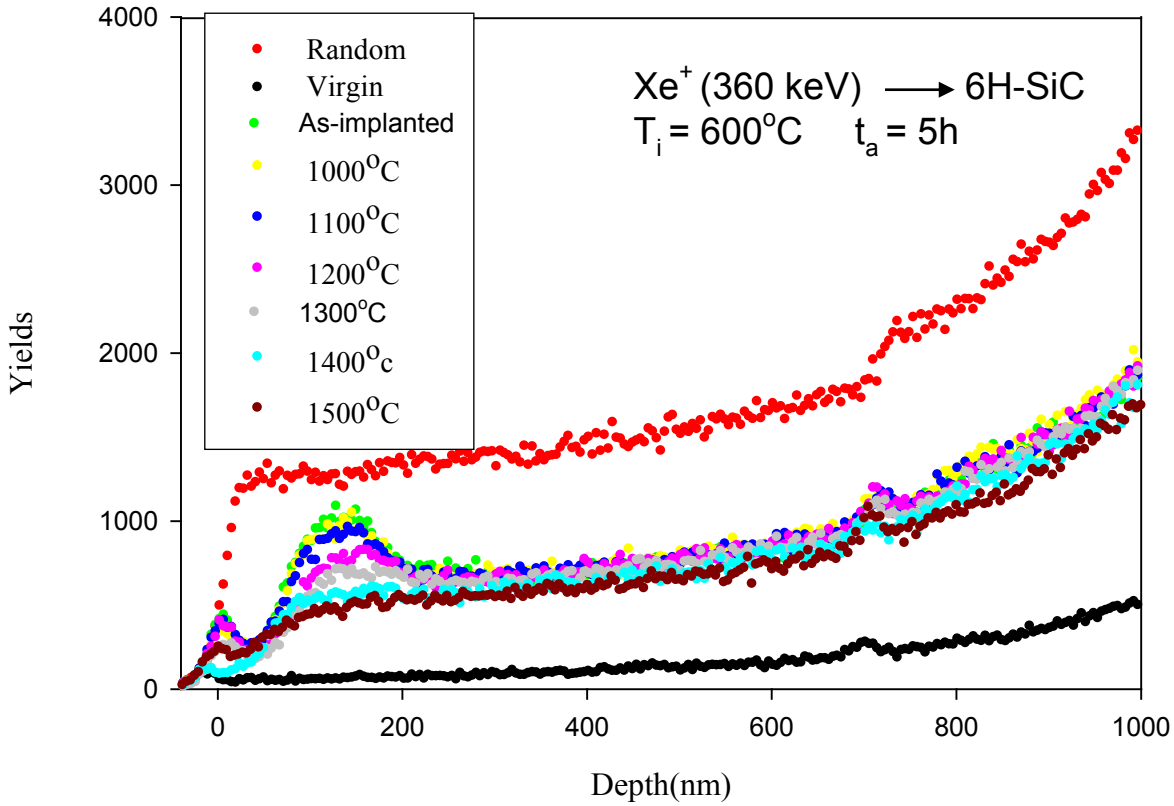

Figure 2. Random and aligned Rutherford backscattering spectra of 6H-SiC implanted at 600ºC and submitted to isochronal annealing of 5h.

high energy, which enables them to displace atoms causing radiation damage. The results show the radiation hardness of SiC during implantation at high temperatures. Similar radiation hardness of SiC was reported for heavy implanted ions at temperatures above 400ºC [4].

Isochronal annealing of the sample implanted at 600ºC from 1000ºC to 1400ºC for 5h caused some annealing of the radiation damage with retention of some defects. This was the result of the defects annealing into dislocation loops and other extended defects during the first annealing cycle that are hard to anneal out. The annealing of some defects is indicated by the reduction of the broad peak around 150nm (Figure 2). At 1500ºC the damage pick disappears but the virgin spectrum was still not achieved due to retained implanted Xe and some damage.

The projected range of 360 keV xenon ions implanted at room temperature agreed, within experimental error and within the accuracy of SRIM11, with the SRIM11 prediction, with the room temperature implantation being slightly deeper. The projected range straggling ΔR_P was also slightly larger due to experimental error and/or channelling. The skewness and kurtosis of the implanted profile were nearly equal to the SRIM11 predictions.

Table 1. Projected range values obtained from Genplot [5] by fitting experimental values to the Edgeworth distribution, and from SRIM11[6].

	23ºC	**600ºC**	**SRIM11**
R_p (nm)	112.4	113.8	101
ΔR_p(nm)	28.7	35.3	24.0
Skewness	0.4	0.6	0.1
Kurtosis	2.7	3.0	2.6

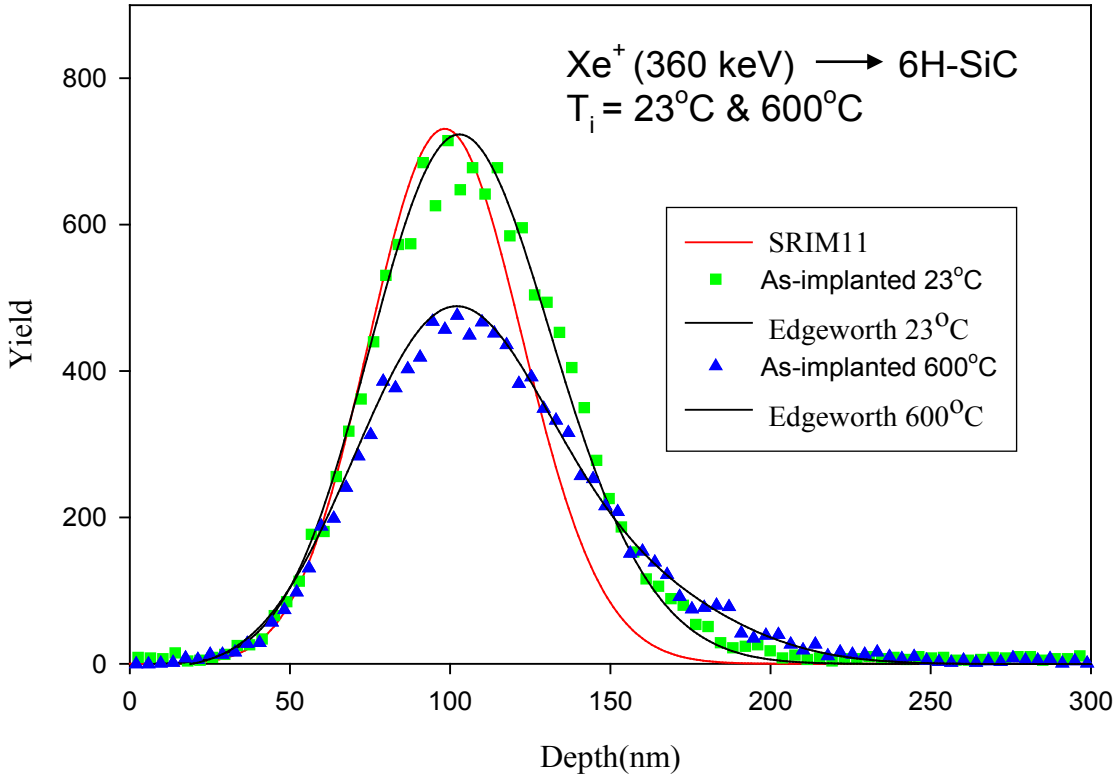

Figure 3: Xenon profile in 6H-SiC implanted at different temperatures compared to SRIM11 prediction.

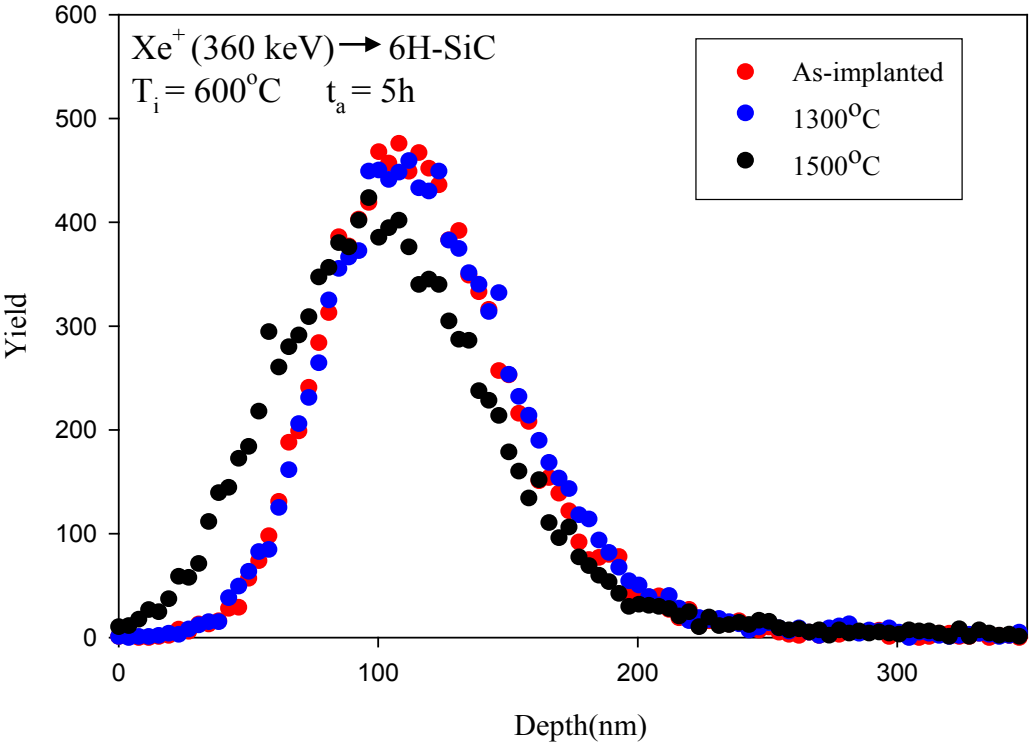

Figure 4: Xenon depth profile in 6H-SiC implanted at 600°C after isochronal annealing.

Table 2. The projected range R_P and projected range straggling ΔR_P values obtained from Genplot by fitting a Gaussian distribution to the experimental data.

Temperature (ºC)	Rp(nm)	ΔRp(nm)
Un-annealed	113.8	35.3
1000	111.0	34.3
1100	114.9	34.5
1200	119.0	36.8
1300	115.8	35.8
1400	90.2	35.3
1500	95.9	42.5

Comparing the Xe RBS spectra for implantation at 600ºC to the room temperature implanted samples showed that a signified loss of xenon took place during implantation at 600ºC, i.e. there was a reduction of the xenon peak area under the curve and a broadening of the implanted profile (i.e. an increase in ΔR_p). This loss was probably due to radiation-induced diffusion.

From Table 2 and Figure 4 the RBS spectra showed no broadening of the xenon peak for isochronal (5h) annealing from 1000ºC to 1300ºC. Thus no diffusion is taking place at these temperatures. At 1400ºC xenon tended to shift towards the surface perhaps due to thermal etching, with no sign of any broadening of the Xe peak, i.e. no diffusion taking place.

Annealing at 1500ºC for 5h caused the xenon profile to shift towards the surface accompanied by a broadening of the peak, indicating that diffusion was taking place at this temperature.

4. Summary

Radiation damage created in 6H-SiC by bombardment of 360 keV xenon ions at a substrate temperature of 600ºC was investigated using RBS channelling. It was found that the implantation of xenon at 600ºC caused the 6H-SiC to retain its crystallinity with some distortions near the surface region. Vacuum-annealing of radiation damage was performed for 5h in the range 1000 to 1500ºC in steps of 100 ºC. Annealing of the radiation damage took place with the increase in annealing temperatures. The rate of annealing out of the damage depended on the temperature of annealing i.e. At 1000ºC small amount of damage was annealed out while at 1500ºC the damage was almost completely annealed out. Thus at 1500ºC the damage pick disappears but the virgin spectrum still not achieved due to retained Xe and damage.

For comparison with SRIM11 predition, we found that RBS-measured room temperature implantation profile agreed within the experimental error with the SRIM11 simulated profile. Comparing the 600ºC implantation profile with the room temperature implanted profile indicated that diffusion took place during implantation and there was loss of the implanted species.

No diffusion took place in the annealing temperature range of 1000 to 1300ºC. At 1400ºC, a shift of the xenon profile towards the surface, which might be due to thermal etching, was observed. Annealing at a temperature of 1500ºC, showed a shift towards the surface accompanied by broadening and reduction of the xenon peak, indicated that diffusion taking place.

References

[1] H.J. MacLean, “Silver Transport in CVD Silicon Carbide’’, PhD thesis, MIT, Department of Nuclear Engineering, June 2004.
[2] K. Fukuda and K. Iwamoto, J. Mater. Sci. 11 (1976) 522.
[3] T.T. Hlatshwayo, J.B. Malherbe, N.G. van der Berg, A,J. Botha and P. Chakraborty, Nucl. Instr. Meth. B 273 (2012) 61-64.
[4] T. Bus, A. van Veen, A. Shiryaev, A.V. Fedorov, H. Schut, F.D. Tichelaar and J. Sietsma. Mater. Sci. Eng. B 102 (2003) 269-276.
[5] http://www.genplot.com, 4 November 2009.
[6] J.F. Ziegler, SRIM 2010 computer code, www.srim.org.

Energy transfer from Ce^{3+} to Tb^{3+} in low quartz and amorphous SiO_2 hosts

K.G. Tshabalala[1,2], H C Swart[2] and O.M. Ntwaeaborwa[2,3]

[1]Department of Physics, University of the Free State (Qwaqwa Campus), Private Bag X 13,Phutaditjhaba 9866, South Africa

[2]Department of Physics, University of the Free State, IB51, Box 339, Bloemfontein 9300, South Africa

E-mail: ntwaeab@ufs.ac.za

Abstract. Low quartz and amorphous Ce^{3+}-Tb^{3+} co-activated SiO_2 phosphors were synthesized by a solution combustion using urea as a fuel. The objective of this study was to compare the efficiency of energy transfer from Ce^{3+} to Tb^{3+} in low quartz and amorphous SiO_2 hosts. As confirmed by X-ray diffraction (XRD) data, SiO_2 was produced as either low quartz or amorphous phase. The photoluminescence (PL) data showed that the green emission of Tb^{3+} at 543 nm was sensitized by Ce^{3+}, i.e. there was energy transfer from Ce^{3+} to Tb^{3+} resulting in an improvement of the green line emission due to the $^5D_4 \rightarrow {}^7F_5$ transitions of Tb^{3+} ions. Possible mechanism of UV down-converted green emission due to energy transfer from Ce^{3+} to Tb^{3+} is discussed.

1. Introduction

Silica is widely used in many fields such as medium layer and silicon-based photoelectron material for its excellent chemical stability, thermal stability as well as interfacial combination with a silicon semiconductor. However, taking into consideration that SiO_2 can be generated in the form of crystalline and amorphous, it has stimulated a long history of experimental and theoretical investigations. SiO_2 doped with metal ions can also be studied as a luminescence material. The rare earth or transition metal ions [1-4] are often used as activator ions to enhance the luminescent properties of silica for their unique electronic structures. For example, Tb^{3+} ions due to their extensive use as materials for fabricating various optical re-radiators and cathodoluminescent screens when incorporated into glasses have created great interest by many researchers [5,6]. However, the problem of enhancing the light output of Tb^{3+} - containing glasses upon UV excitation still remains unresolved. The reason is that the light output of these materials is limited by the occurrence of intense absorption bands in the high-frequency range due to $4f^8 \rightarrow 4f^7(^8S_{7/2})5d^1(T_2)$ and $4f^7(^8S_{7/2})5d^1(E)$ inter-configurational transitions [7] and a relatively low efficiency of excitation transfer from the luminescence sensitizers. In this work we synthesized low quartz and amorphous SiO_2 hosts doped with Ce^{3+} and Tb^{3+} ions in an attempt to solve the problem through the comparative study on their structures and spectroscopic properties. In particular, we focus the attention in the performance of the energy transfer from Ce^{3+} to Tb^{3+} in low quartz and amorphous phases.

[3] Corresponding Author: ntwaeab@ufs.ac.za

2. Experimental procedure

Nano sized pure SiO_2, singly doped SiO_2 with Ce and Tb, and SiO_2 co-doped samples with ($Ce3^+$/ Tb^{3+}) were prepared by a solution combustion method as described in reference [8]. Silicic acid ($SiO_2 \cdot nH_2O$) and ammonium nitrate (NH_4NO_3) were used as the starting materials, urea (CH_4N_2O) was used as fuel and both cerium and terbium nitrates were used as dopant precusors. All the samples prepared were annealed in a reducing atmosphere of 4% H_2 / 96% Ar mixture at an elevated temperature of 1 000 °C for 2 hours. The phase purity and crystallinity of the powder samples was characterized by X-ray powder diffraction (XRD). XRD measurements were carried out a Bruker D8 Advanced powder diffractometer with Cu-Kα radiation (λ = 1.5418 Å) in the 2θ range from 10° to 80°. The morphology of the prepared nanoparticles was analyzed by scanning electron microscopy (SEM) using Shimadzu model ZU SSX−550 Superscan. The photoluminescence (PL) properties of the powder phosphors were characterized using a Cary Eclipse fluorescence spectrophotometer.

3. Results and discussion

3.1. X-ray diffraction

The XRD patterns of the pure SiO_2 and singly doped SiO_2: *x*mol% Tb^{3+} (x = 1, 4), SiO_2:2mol%Ce^{3+} and co-doped SiO_2: 2mol%Ce^{3+}, *x*mol%Tb^{3+} (x =1,4) powders prepared from Combustion are shown in figure 1. The undoped SiO_2 and singly doped SiO_2: *x*mol%Tb^{3+} (x =1,4) patterns show only a broad peak around 2θ = 23.6°. On the other hand, a singly doped SiO_2: 2mol%Ce^{3+} co-doped samples show a broad peak and some small signatures emanating from low quartz silica. The observed peaks were assigned by comparing the JCPDS database file no 86-1565, which is the characteristics diffraction pattern of the low quartz's phase of a SiO_2 glassy matrix. Figure 2 shows the XRD patterns of the sol-gel derived pure SiO_2 and singly doped SiO_2: *x*mol% Tb^{3+} (x = 1, 4), SiO_2:2mol%Ce^{3+} and co-doped SiO_2: 2mol%Ce^{3+}, *x*mol%Tb^{3+} (x =1,4) powder phosphors. The observed broad peak from a pure SiO_2 and a singly doped SiO_2: *x*mol% Tb^{3+} (x = 1, 4) at 2θ = 23.6° is similar to the XRD pattern shown in Figure 1. The only exception here is that pure SiO_2 derived from sol-gel is completely amorphous when is compared with pure SiO_2 derived from combustion of which has a peak shift towards lower angle suggesting that it was crystalline. Singly doped SiO_2: *x*mol% Tb^{3+} (x = 1, 4) have a broad peak respectively, and there is a shift towards a lower angle observed and this suggests that material is crystalline. For SiO_2: 2mol%Ce^{3+} and co-doped SiO_2: 2mol%Ce^{3+}, *x*mol%Tb^{3+} (x =1,4) the XRD data confirmed that all the powder samples crystallize in a low quartz after heat treatment.

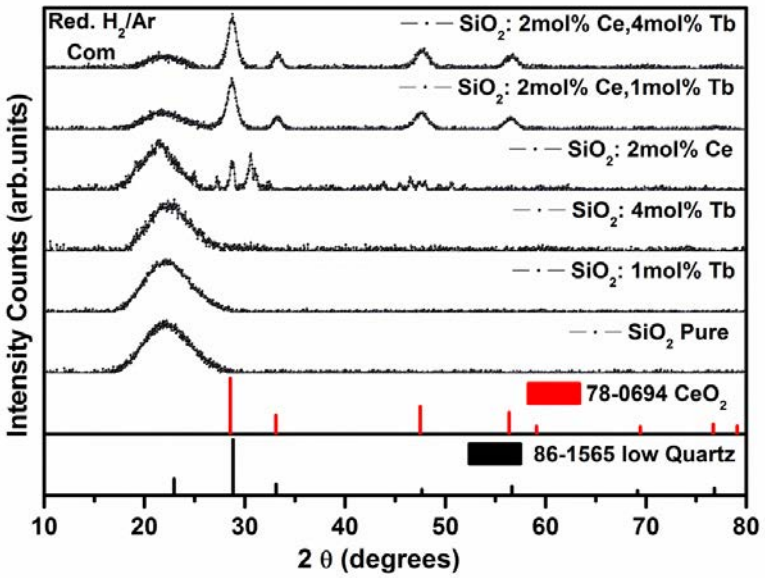

Figure 1 Room Temperature XRD patterns of (as cast) pure SiO_2 and a singly doped SiO_2: *x* mol%Tb^{3+} (*x* = 1, 2), SiO_2: 2mol%Ce^{3+} and co-doped SiO_2: 2mol%Ce^{3+}, *x*mol%Tb^{3+} (*x*= 1,4) from combustion derived route.

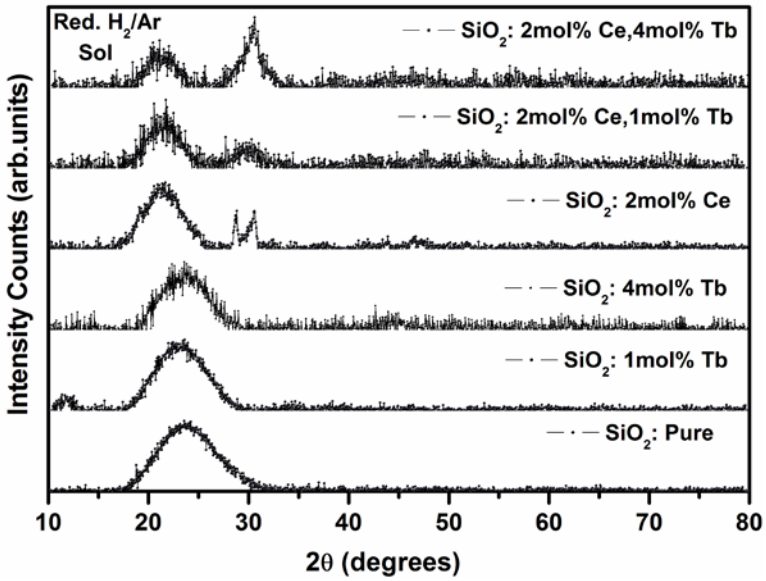

Figure 2 Room Temperature XRD patterns of (as cast) pure SiO_2 and a singly doped SiO_2: *x* mol%Tb^{3+} (*x* = 1, 2), SiO_2: 2mol%Ce^{3+} and co-doped SiO_2: 2mol%Ce^{3+}, *x*mol%Tb^{3+} (*x*= 1,4) from Sol-gel derived route.

3.2. Scanning electron microscopy (SEM)

Figure 3 shows a general morphology of the (a) SiO_2:2mol% Ce and SiO_2:2mol% Ce, 1mol% Tb respectively. The SEM image in figure 3 (a) shows the agglomerated SiO_2:Ce with small particles appearing circular, confirming spherical shapes. However, in figure 3 (b) the particles are relatively smaller than shown in (a), which suggest that the Terbium incorporation interferes with the crystal growth [9].

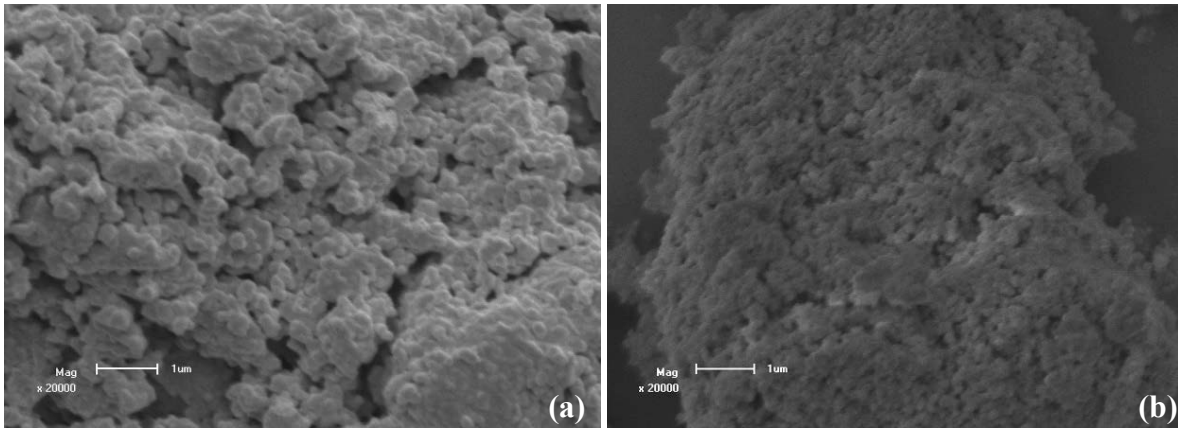

Figure 3 SEM images of the (a) SiO_2:2mol%Ce and (b) SiO_2:2mol%Ce,1mol%Tb samples

3.3. Photoluminescence studies

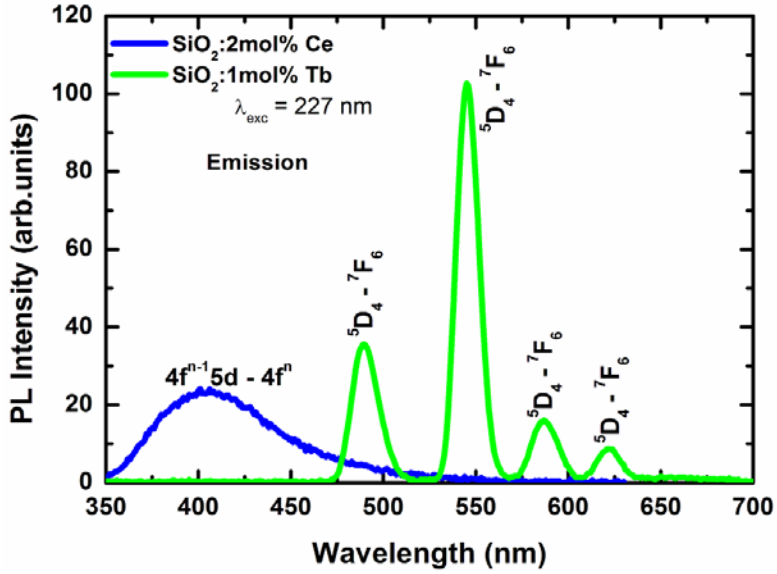

Figure 4 PL emission spectra SiO_2:2 mol% Ce and SiO_2:1mol% Tb (λ_{exc} = 227 nm).

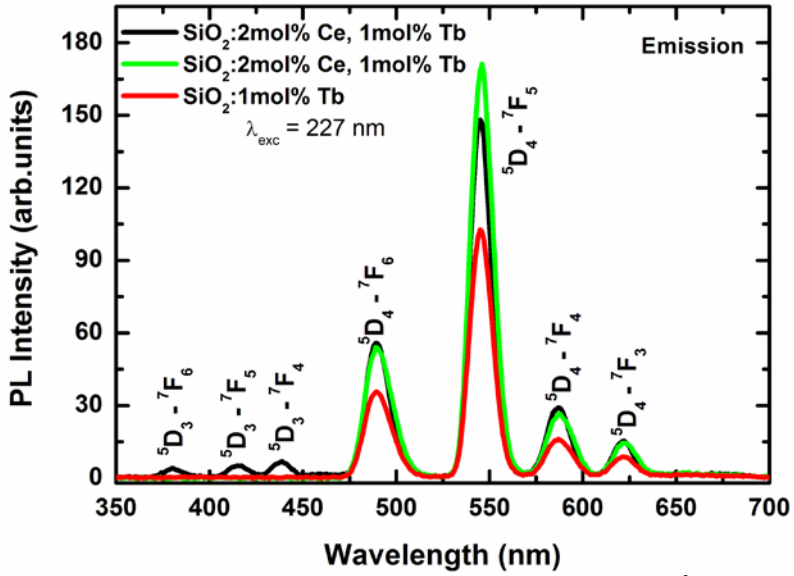

Figure 5 PL emission spectra of SiO_2 singly doped with 1 mol%Tb^{3+} and co-doped with 2Ce^{3+} and 1Tb^{3+} in mol% under excitation at 227 nm. Corresponding transitions are indicated.

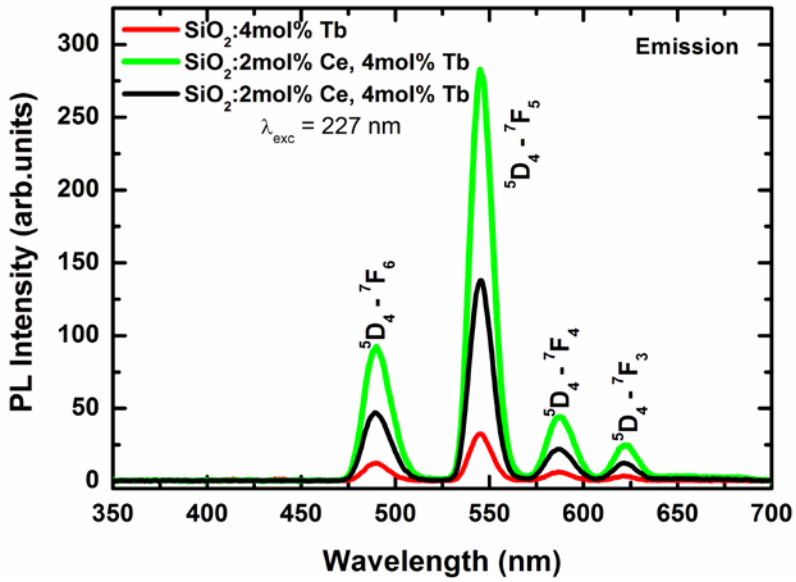

Figure 6 PL emission spectra of SiO_2 singly doped 4 mol%Tb^{3+} and co-doped with 2Ce^{3+} and 4Tb^{3+} in mol% under excitation at 227 nm. Corresponding transitions are indicated.

Figure 4 exhibit the PL emission spectra of the reduced singly doped SiO_2:2mol% Ce^{3+} and SiO_2:1mol% Tb^{3+} respectively. The emission from singly doped SiO_2:2mol% Ce^{3+} at 402 nm is consistent with the 400 nm emission ascribed to Ce^{3+} ions as reported by Kroon *et al* [10]. On the other hand, PL emission corresponding to Tb^{3+} characteristics show sharp emission peaks from upper-laying levels, i.e., $^5D_4 \rightarrow {}^7F_{6,5,4,3}$ at 488, 543, 585 and 620 nm, respectively. These peaks match well with emissions from Tb^{3+} ions into nanocrystalline silica, confirming their incorporation into the system, according to the previous results obtained by the authors using sol–gel derived SiO_2 doped with Tb^{3+} [11]. Figure 5 and 6 respectively, focuses mainly on the samples obtained as low quartz after some heat treatment in a reduced atmosphere with 2 mol% of Ce^{3+} ions while varying the concentration of Tb^{3+} ions. In particular, samples

exhibiting low quartz were derived from Combustion route while that derived from sol-gel route became crystalline after heat treatment was supplied. Therefore, the rest of the paper is designed to compare the performance of Ce^{3+} and Tb^{3+} into low quartz and amorphous SiO_2 hosts through energy transfer (ET) efficiency studies. In figure 5 the PL emission (λ_{exc} = 227 nm) spectra of the co-doped SiO_2: Ce^{3+}, Tb^{3+} and singly doped SiO_2: $Tb^{3+}$are compared. It can be noted that all characteristic emission peaks of Tb^{3+} ions from $^5D_3 \rightarrow {}^7F_{J\ (J\ =\ 6,5,4)}$ to $^5D_4 \rightarrow {}^7F_{J\ (J=6,5,4,3)}$ are well pronounced from the low quartz matrix, confirming their incorporation into nanocrystals as shown in section 3.2. However, the intensity of the emission at 543 nm in SiO_2:Ce^{3+}, Tb^{3+} derived from nanocrystals silica due to some heat treatment was much bigger than that of a singly doped SiO_2:Tb^{3+}. The excitation wavelength 227 nm used here is attributed to the absorption spectrum of the Ce(IV) valence states as a series of excitonic excitations from orbitals of atoms that surround tetravalent cerium into a silica matrix [12]. Therefore, taking a look at a broad cerium emission (350 – 500 nm) in Figure 4 in comparison to the co-doped systems represented in Figure 5 and 6 respectively, we can conclude that the energy transfer from Ce^{3+} to Tb^{3+} took place. Furthermore, the intensity of the Ce^{3+} as seen from Figure 4 decreases completely in a co-doped SiO_2: Ce,Tb however increases the Tb^{3+} emission when the Tb^{3+} content is enlarged i.e (from 1 to 4 mol% Tb^{3+}). As a result, the energy transfer rate from Ce^{3+} to Tb^{3+} is the best in amorphous nanocrystalline SiO_2 host instead of amorphous.

4. Conclusions

SiO_2, SiO_2:Ce, SiO_2:Tb and SiO_2:Ce,Tb powders were successfully synthesized through combustion and sol-gel routes and latter reduced in a mixture of 4% H_2 / 96% Ar at 1 000 °C for 2 hr. The structural and spectroscopic study in Ce^{3+} and Tb^{3+} single and co-doped SiO_2 has been carried out. The XRD data confirmed that the samples crystallized after some heat treatment from a reducing atmosphere. The SEM images showed the agglomerated platelet-like particles of SiO_2:Ce with encrusted with small spheroidal particles. Due to the incorporation of Ce^{3+} and Tb^{3+} ions in the silica hosts, energy transfer from Ce^{3+} to Tb^{3+} ions was observed. The transfer rate was more efficient in low quartz than amorphous host. Thus, the maximum energy transfer was observed from the sample co-doped with 2mol%Ce^{3+} and 4mol%Tb^{3+}.

Acknowledgements

This work is supported by South African National Research Foundation (NRF), and Nanomaterials Cluster fund of the University of the Free State. The author would like to extend his thanks to Prof. FB Dejene for the use of his laboratory and chemicals during the sample preparations.

References

[1] Chryssou CE, Kenyon AJ and Pitt CW 2001 *Mater. Sci. Eng.* **B 81** 16
[2] Ferrari M and Armellini C 2000 *J. Sol-Gel Sci. Technol* **19** 569
[3] Morita M, Kajiyama S , Kai T, Rau D and Sakurai T 2001 *J. Lumin*. **94** 91
[4] Garcia MA, Borsella E, Paje SE, Llopis J, Villegas MA and Polloni R 2001 *J. Lumin*. **93** 253
[5] Maciel GS, Biswas A and Prasad PN 2000 *Opt. Commun.* **178** 65
[6] Martin GS, Yanes AC, Mendez-Ramos J, Torres ME and Rodriguez VD 2001 *J. Appl. Phys.* **89** (5) 2520
[7] Arbuzov VI, Ya. Grabovaskins V, Kovaleva NS, Rogulis UT and Tolstoĭ 1988 *Opt. Spectrosc.* **65** 555
[8] Nagpure IM, Pitale SS, Kumar V, Ntwaeaborwa OM, Terblans JJ and Swart HC 2011 *Materials Research Bulletin* **46** 23604
[9] Lu Xi-Hong, Li Gao-Ren, Yu Xian-Lan and Tong Ye-Xiang 2008 *Electrochemical and Solid-State letters* **11** (9) K86
[10] Kroon RE, Seed Ahmed HAA, Ntwaeaborwa OM, Koao LF, Nagpure IM, Gusowski MA, Botha JR and Swart HC 2011 *Physica **B*** 407 1596
[11] Seed Ahmed HAA, Ntwaeaborwa OM, Gusowski MA, Botha JR and Kroon RE 2012 *Physica **B*** 407 1654
[12] Efimov AM, Ignat'ev AI, Nikonorov NV and Postnikov ES 2011 *Optics and Spectroscopy* **111** 432

Effects of annealing temperature on the optical properties of ZnO

M.A. Tshabalala[2], B.F. Dejene[1*], O.M. Ntwaeaborwa[2], H.C. Swart[2*]

[1]Physics Department, University of the Free State, Private Bag X13, Phuthaditjhaba, 9866, South Africa

[2]Physics Department, University of the Free State, P. O. Box 339, Bloemfontein, 9300, South Africa

[*]Corresponding author: Dejenebf@qwa.ufs.ac.za or SwartHC@ufs.ac.za

Abstract The optical properties of ZnO nanoparticles synthesised using a sol-gel method and water as a solvent are reported. The effects of annealing at different temperatures (300, 400, 500 and 600 °C) on the optical properties were investigated. The scanning electron microscopy images indicate that ZnO nanoflakes were synthesized. The X-ray diffraction (XRD) peaks were indexed as the hexagonal wurtzite structure of ZnO referenced in JCPDS 36-1451. The photoluminescent (PL) emission peaks were observed at 381, 423, 486 and 535 nm. From the UV-Vis spectra the vacancy energy level was determined and the effect of the post-preparation annealing temperature on the energy level is illustrated. The vacancy energy level of ZnO was shown to decrease from 2.63 to 2.20 eV with increasing annealing temperature.

1. Introduction

Nanostructured ZnO semiconductor has drawn enormous attention due to its unique optical properties and its variety of application in, among other things, sensors, photonics and optoelectronics [1]. Different research groups worldwide are studying the optical properties of the ZnO nanostructures with different morphologies. Some properties of ZnO nanostructures change after annealing at different temperatures [2]. Different wet chemistry methods and different solvents are used to prepare ZnO with different particle morphologies. In this study, ZnO nanoparticles were synthesized using the sol-gel method and water as a solvent. Water is a dipolar, amphiprotic solvent with a high dielectric constant and, as a consequence, most salts dissolve readily in water. The zinc cation is soluble in water and growth is controlled by the diffusion of Zn^{2+} ions in the ethanol-rich layer [3]. In this report nanostructure ZnO particles were prepared by adding NaOH into the aqueous solution of $Zn(CH_3COO)_2.2H_2O$ (zinc acetate). The aim of this work was to investigate the effect of annealing temperature on the optical properties of ZnO nanoparticles.

2. Experimental

ZnO nanoparticles were prepared by dissolving 4.4g of zinc acetate [Zn $(CH_3COO)_2.2H_2O$] in 100 ml of water (0.2 M) using vigorous stirring until the solution turned clear (transparent) and was cooled in ice water. Then 3.2 g of NaOH was dissolved in 130 ml of water (0.8 M) in an ultrasonic bath and was also cooled in ice water. This solution was slowly added to the transparent Zn^{2+}solution using vigorous stirring at room temperature for 1 hour before centrifuging. The unwanted CH_3COO^- and Na^+ ions were removed by washing the precipitate repeatedly with deionised water. The precipitate was then dried at 60°C for an hour and then annealed in air at 600 °C, 500 °C, 400 °C and 300 °C for 1 hour.

The X-ray diffraction (XRD) patterns were recorded using a D8 Bruker Advanced AXS GmbH X-ray diffractometer (XRD).The room temperature photoluminescence (PL) of the samples was measured using a He–Cd laser (325 nm) as excitation sources The particle morphology of was analyzed using a Shimadzu Superscan SSX-550 scanning electron microscope (SEM) operated at 20 kV and also equipped with energy dispersive X-ray spectroscopy (EDS). Optical absorption measurements were carried out using a Perkin Elmer Lamb 950 UV-visible spectrophotometer (UV).

3. Results and Discussion

3.1. Structure

Figures 1 a) shows the SEM micrographs of the as prepared ZnO nanoparticles b) and c) depict the highly agglomerated ZnO nanoflakes resulting from overlapping of small particles when calcined at 300 °C and 600 °C respectively. The post-preparation annealing temperature was shown to play an important role on the surface, the growth and the shape of the ZnO nanoparticles. The XRD patterns consistent with the well-known wurtzite ZnO (JCPDS file No. 36-1451) are shown in Figure 2. The peak intensities especially the (101) diffraction increased with increasing annealing temperature. The as grown ZnO shows to be crystalline with a grain size of 33 nm. The ZnO nanoparticles become more crystalline with an increase in the annealing temperature. The strong and narrow diffraction peaks at high annealing temperature point to the crystallinity and grain sizes. The grain sizes for the annealing temperatures 300, 400, 500 and 600 °C were determined to be 38, 38, 44 and 46 nm.

Table 1. The calculated grain sizes of the ZnO nanostructure annealed at various temperature.

Temperature (°C)	***Grain size (nm)***
As grown	*33*
300	*38*
400	*38*
500	*44*
600	*46*

3.2. Optical properties

The PL emission spectra of the ZnO nanoflakes at various annealing temperatures (300, 400, 500, 600 °C), shown in figure 3 consist of four emission peaks, these are a strong blue emission at ~423 nm, a blue-green emission at ~486 nm, and a weak green emission at 535 nm. The 423 nm peak can be attributed to the interstitial zinc or oxygen [4]. The weak green emission of the ZnO prepared presumably due to the vacancies or defects that are intrinsic to most synthesis methods, and this emission is a result of capturing of a photo-generated hole by the oxygen vacancy [5]. The presence of oxygen vacancies (V_o), zinc vacancies (V_{Zn}) and interstitial zinc (Zn_i) have been attributed to corresponding to the green emission of ZnO [6]. The spectra of ZnO annealed at 300, 400, 500 and 600 °C shows a strong emission peak at ~381 nm, it is well known that the UV emission peak (381 nm) originates from the near band-edge emission from the recombination of free excitons [7]. The weak blue-green emissions at 486 nm might be due to surface defects in the ZnO powder as in the case of ZnO nanowires reported by Wang and Gao [8]. An increase on the annealing temperature is known to move the oxygen and zinc atoms from interstitial to lattice sites [9]. The PL intensity reduction was observed in figure 3 and the nanoparticles grain size increase was detected by XRD, as shown in

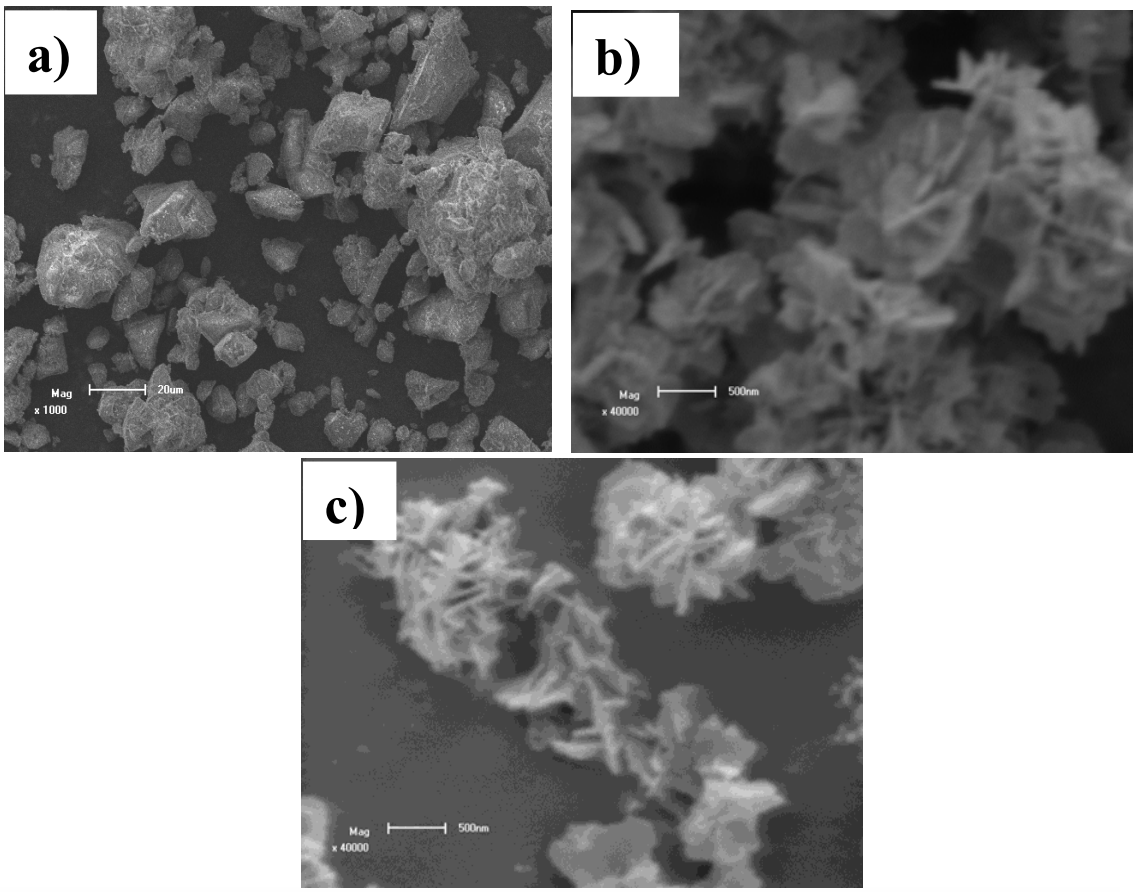

Figure 1: SEM images of ZnO nanoparticles at different temperatures of a) as prepared b) 300 °C and c) 600 °C.

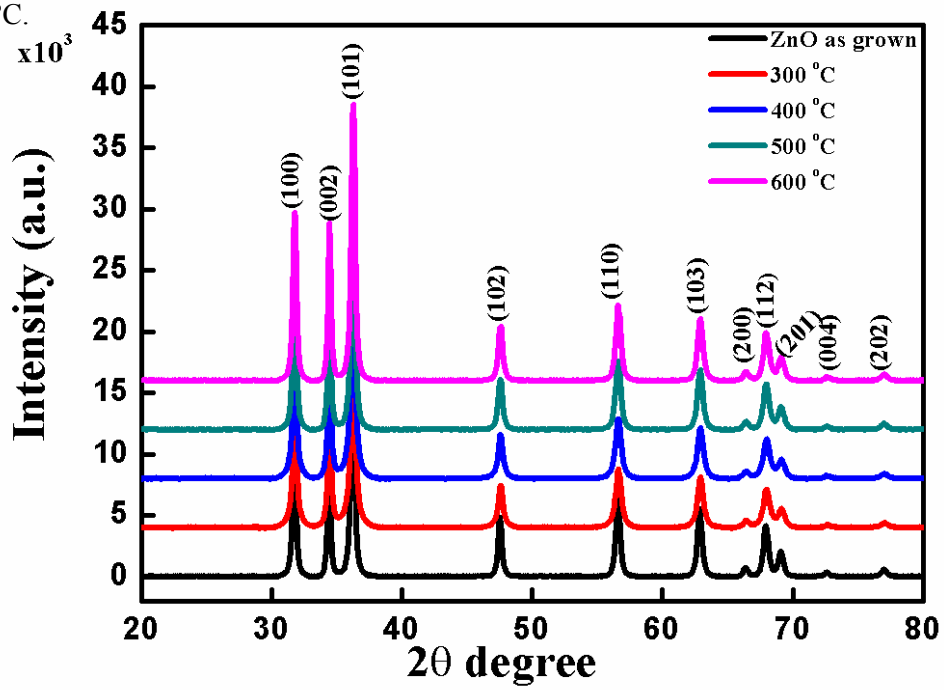

Figure 2: XRD patterns of ZnO prepared at different annealing temperatures: 300, 400, 500 and 600°C.

figure 2. The decrease in PL intensity can be attributed to the dependence of the PL spectra on the number and distribution of the defects in the grains which will change with an increase in annealing temperature and size of the nanoparticles.

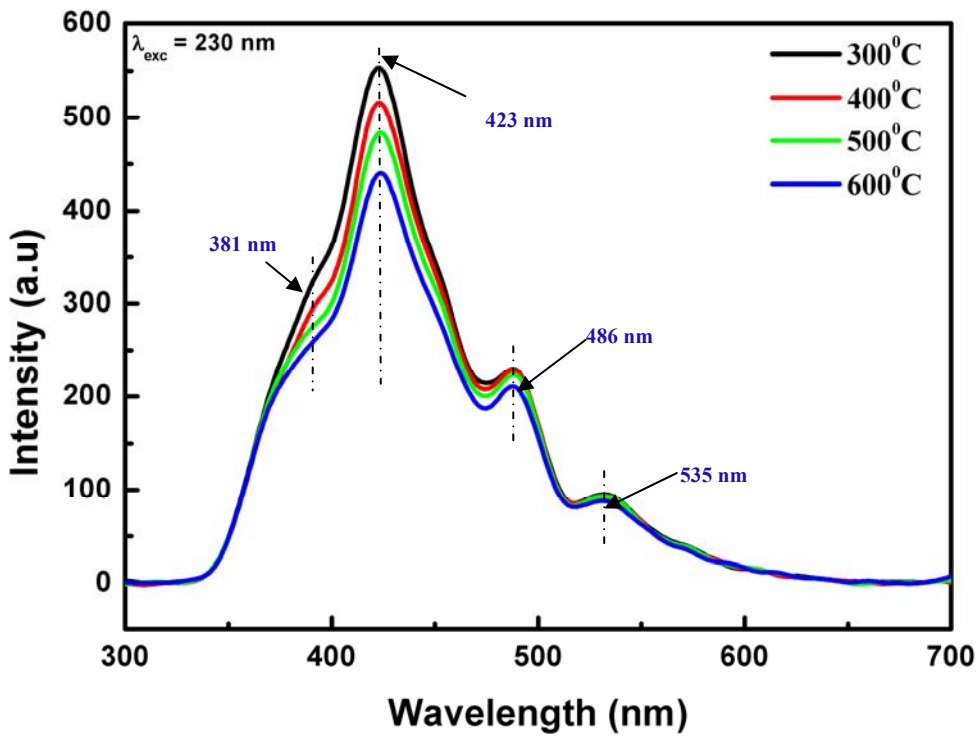

Figure 3: PL emission spectra of ZnO prepared annealed at various temperatures.

The UV absorption spectra showed the absorption peak centred at 375 nm at an annealing temperature of 300, 400, 500 and 600 °C (Figure 4). It is known that the bulk ZnO has an absorption band edge at ~3.30 eV in the UV-visible spectrum [10]. The absorption peak intensity at 375 nm decreased with increasing annealing temperature. Figure 4(b) shows the $(\alpha hv)^2$ plots (where α is absorption coefficient and *hv* is the photon energy) as a function of *hv*. ZnO nanoflakes/flower annealed at 300 °C has an energy of 2.63 eV, annealed at 400 °C has an energy of 2.43 eV, annealed at 500 °C has an energy of 2.23 eV, and annealed at 600 °C has an energy of 2.20 eV. These values are too low to be an indication of the band gap energies but rather an indication of the vacancy/defect energy levels. This is highly speculative at this stage and need more investigation in future. This shows that an increase in the annealing temperature decreased the vacancy energy level. The decrease in the vacancy energy levels of ZnO nanoflakes as annealing temperature increases may be attributed to the defects that are in the ZnO powder. The decrease in the vacancy/defect energy levels when the temperature increased may be explained by the effects of the increase in grain size from the agglomeration of nanoparticles. This shifting of the levels may also be the effect of the lattice thermal expansion which is related to the change of electron energies with the volume. That is, the variation of Eg with temperature may be attributed to a shift in the relative positions of the valance and conduction bands due to the temperature dependence of the dilation of the lattice.

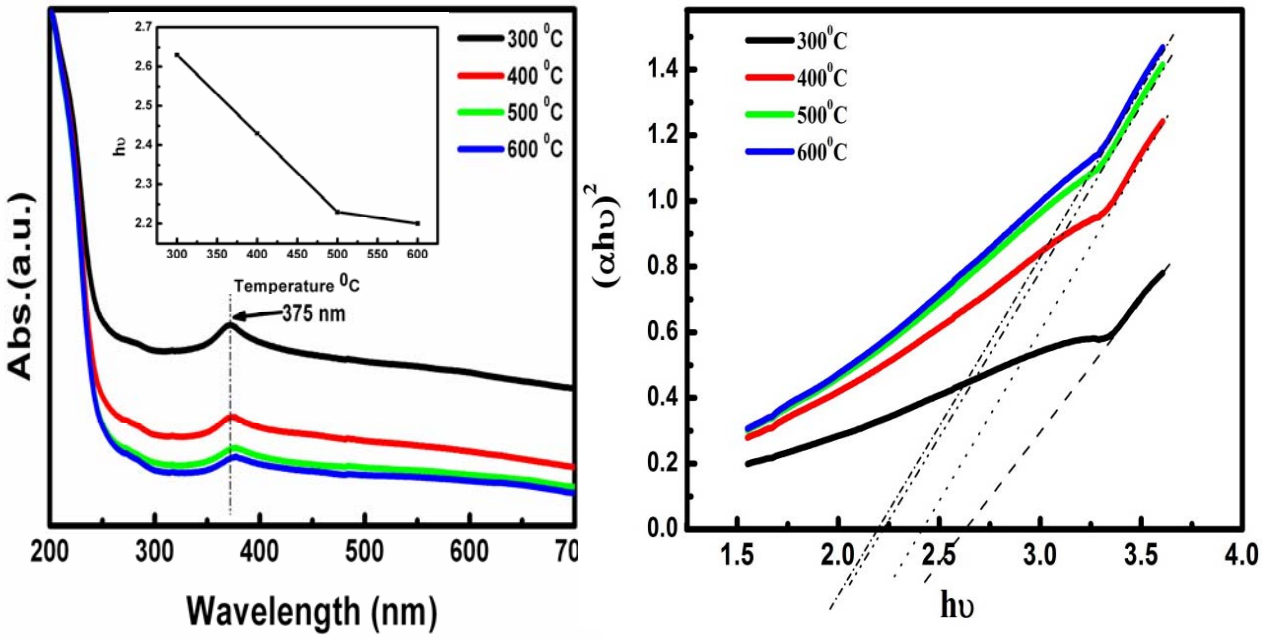

Figure 4: (a) Absorption spectra of ZnO nanoparticles prepared with water annealed at different temperatures (b) Plots of $(\alpha h\nu)^2$ versus photon energy ($h\nu$) at different temperatures.

4. Conclusion

ZnO nanostructures were successfully prepared using water as a solvent by a sol-gel process. The effects of annealing temperatures on the optical properties were investigated. SEM images showed that agglomerated nanoflakes/flowers of ZnO were synthesized. The photoluminescence emission intensity was influenced by various temperatures. The UV-vis absorption exhibited absorption peaks at 375 nm which was shown to decrease with an increase in annealing temperature. The vacancy energy levels of the ZnO decreased with an increase in the annealing temperatures.

Acknowledgement

The financial support of the National Research Foundation (NRF) and the University of Free State is acknowledged.

Reference

[1] Sun L, Li Y, Miyatake N, Sue H, 2007 *J. Sol-Gel Sci Technol* **43** 237-243
[2] Yousefi R, Kamluddin B, 2012 *Solid State Sciences* **12** 252-256
[3] Hsieh C, 2007 *J. Chinese Chem. Soc.* **54** 31-34
[4] Choi K, Kang T, Oh S G, 2012 *Materials Letters* **75** 240-243
[5] Maensiri S, Masingboon C, Promarak V and Seraphin S, 2007 *Opt. Mat,* **29** 1700-1705
[6] Wang J B, Shuang D, Zhong X L, Yan H L, 2007 *Materials Science in Semiconductor Processing* **10** 97-102
[7] Bu I Y Y, Yan C C, 2012 *Superlattices and Microstructures* **51**745-753
[8] Wang J, Gao L, 2004 *Solid State Commun.* **132** 269-271
[9] Vishwas N, Rao M K, Gowda K V A, Chakradhar R P S, 2010 *Spectrochimica Acta Part* A **77** 330-333
[10] Yiamsawas D, Boonpavanitchakul K, Kangwansupamonkon W, 2009 *J. Microscopy Society of Thailand* **23** 75-78

The effect of temperature on the calculated bulk vacancy formation energy in Al and Cu

C. van der Walt[1] **, HC Swart and JJ Terblans**[2]
Department of Physics, University of the Free State, PO Box 339, Bloemfontein, South Africa

E-mail address: terblansjj@ufs.ac.za

Abstract. The bulk vacancy formation energies (E_v) were calculated for Al and Cu single crystals in a molecular dynamics simulation. The Sutton-Chen many-body potential was used to calculate the vacancy formation energies for the single crystal with the surface orientations of (111), (100) and (110) at temperatures ranging from 0 K to below the simulated melting temperatures. The values obtained for vacancy formation energies at 0 K compared well to values obtained from literature and exhibited E_v values that reflect the respective surface stabilities. The (111) surface has the greatest stability and had the highest bulk vacancy formation energy, followed by the (100) surface, and finally the (110) surface showed the greatest instability and had the lowest bulk vacancy formation energy. The E_v values at higher temperatures show surface instability, particularly in Cu(110), where it is caused by an adatom layer that forms on the surface at temperatures well below melting point. A general trend of a decrease of vacancy formation energy was observed for increasing temperature.

1. Introduction

The vacancy formation energy is an important factor in atomic transport, and is of fundamental importance in diffusion kinetics. The vacancy formation energy, (E_v) has been shown to be dependent on surface orientation in both Al and Cu. [1,2] What has not yet been extensively studied is the effect of temperature on these vacancy formation energies, but with the use of density functional theory (DFT) it has been shown for Pt, Pd and Mo that the vacancy formation energy increases with temperature. [3]

Although modern quantum mechanical calculations can more accurately simulate these interactions, calculations are costly in time and limited in the number of atoms they are able to handle. The code used for the calculations in this article was new code written by the authors as was the previous Sutton-Chen calculations [1,2] which was only conducted at 0 K. The new code is able to investigate the effects of temperature and can handle larger calculations of several thousand atoms, well beyond the capabilities of quantum mechanics calculations, in conditions that can more closely approximate bulk materials. The method of modelling surface binding energies to determine the effect of temperature on surface orientations is also new.

Perfect crystals of Al and Cu were simulated with the use of an embedded atom potential developed by Sutton and Chen. [4] The crystals were simulated with surface orientations of (100), (110) and (111) at a range of temperatures. The Sutton–Chen potential (U_i) is an embedded atom potential with a many-body term that uses particle densities in FCC metals and can determine pair wise distributions. The total energy of the simulated crystal (U^{total}) can be calculated by using

[1] Main author
[2] To whom any correspondence should be addressed.

$$U = \sum_i U_i = \varepsilon \sum_i \left[\tfrac{1}{2} \sum_{i \neq j} \tfrac{1}{2} V\left(r_{ij}\right) - c\sqrt{\rho_i} \right] \tag{1}$$

Where is an energy parameter and c is a dimensionless parameter. V is the pairwise repulsive potential and $_i$ is a density like term;

$$V\left(r_{ij}\right) = \left(\frac{a}{r_{ij}}\right)^n \tag{2}$$

$$\rho_i = \sum_{i \neq j} \phi\left(r_{ij}\right) = \sum_{i \neq j} \left(\frac{a}{r_{ij}}\right)^m \tag{3}$$

with r_{ij} the distance between atoms i and j, a is the lattice constant, n a positive integer that determines the repulsive potential and m is a positive integer that determines the range of the repulsive potential such that $n > m$. The parameters that were used for Al and Cu are those published by Sutton and Chen, which are listed in Table 1.

Table 1. The Sutton–Chen parameters for Al and Cu. [4]

Element	ε (eV)	a (A°)	c	n	m
Al	3.3147×10^{-2}	4.05	16.399	7	6
Cu	1.2382×10^{-2}	3.61	39.432	9	6

2. Calculations

Using the Schottky mechanism to describe the vacancy formation energy (E_v) has been defined as finding the difference between the energy needed to remove an atom from inside the crystal volume and the energy obtained from adding an atom to the crystal surface. [1,2,5]

$$E_v = E_{coh}^{(\text{Bulk})} - E_{coh}^{(\text{surface})} \tag{4}$$

Here $E_{coh}^{(\text{Bulk})}$ is the cohesive binding energy for an atom in the bulk of a crystal and $E_{coh}^{(\text{surface})}$ is the binding energy for the added atom (adatom) on the surface. To calculate the bulk vacancy formation energy (E_v), the total energy (U^{total}) for a perfect crystal the Sutton–Chen potential needs to be calculated. Single crystals of Al and Cu with different surface orientations were simulated as shown in figure 2. Each of the crystals, Al(100), Al(110), Al(111), Cu(100), Cu(110) and Cu (111) with 1944 atoms each was simulated. The crystals each had six layers of 18 x 18 atoms. The corresponding vacancy formation energies were calculated at temperatures ranging from 0K at 100K intervals to a temperature below their respective melting points and compared. A Berendsen thermostat regulated the system temperatures with a coupling constant τ of 0.05 ps.

A standard cut-off distance of 2.5 was used and the time step used was 0.001 ps. Using the Sutton–Chen empirical many-body potential and the Verlet leapfrog integration method, the interactive forces between the atoms were calculated and the crystal structures were allowed to relax for 20 000 steps and the total energy (U^{total}) was then obtained. A vacancy was then created and moved to a distance of 1 m from the crystal surface to approximate infinity. The total energy (U^{total}) of the crystal with a vacancy was then measured again. The difference between these two total crystal energies is the bulk cohesive binding energy $E_{coh}^{(\text{Bulk})}$.

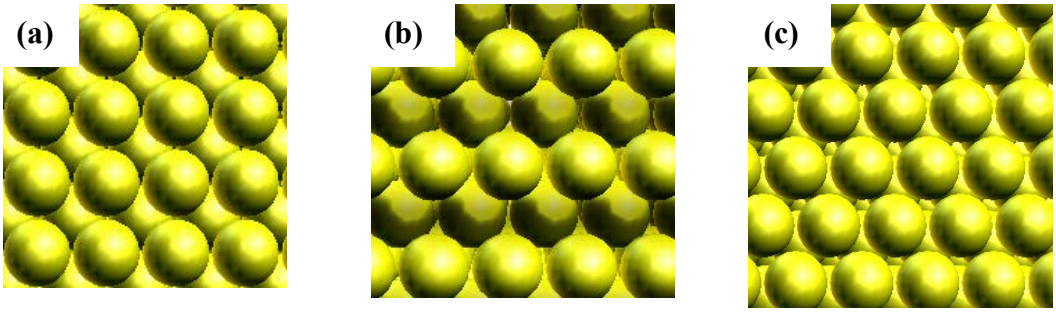

Figure 1. shows schematics of the three different surface orientations of the bulk crystals: (100) in 2(a), (110) in 2(b) and (111) in 2(c).

To find the cohesive surface binding energy for the adatom $E_{coh}^{(\text{surface})}$, the total energy ($U^{total}$) was calculated for the same crystal setup, where the adatom was moved closer to the surface to a distance x from the surface. The energy difference between the two crystal total energy (U^{total}) where the adatom is at infinity from the surface, and where the adatom is a distance x from the surface, is equivalent to the binding energy between the adatom and the surface with the adatom at a distance x from the surface. The adatom was moved closer to the surface and each time this energy difference was measured until a maximum binding energy for an adatom on a surface was found. Figure 1 shows the calculated potential energy curve as the adatom is moved closer to Cu(100), Cu(110) and Cu(111) surfaces.

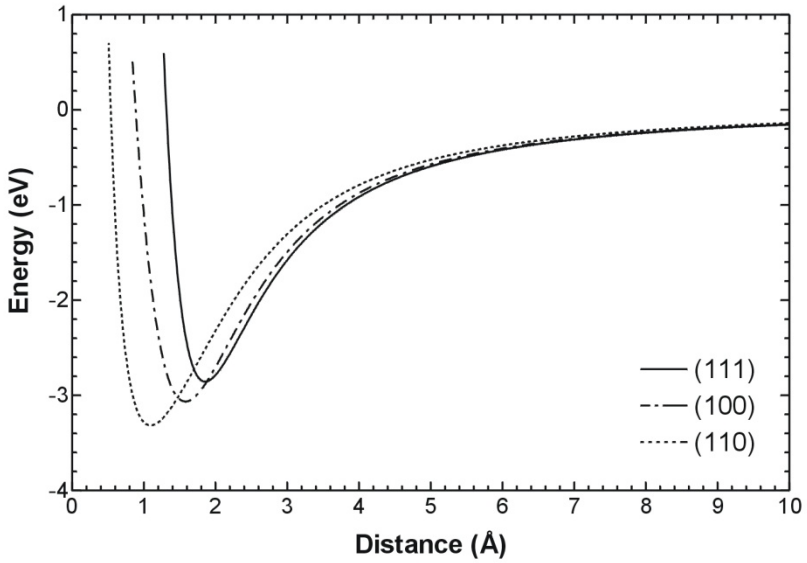

Figure 2. A potential energy curve of a single atom added to Cu(100), Cu(110) and Cu(111) orientated surfaces respectively.

The surface binding energies were measured for the points most likely to bond an atom on the surface. Preferred binding sites were chosen as the points with the lowest maximum surface binding energy. Using likely bonding sites, the average surface binding energy for each crystal was determined for each of the various temperatures. The binding energies were measured five times over time to obtain a good average of the surface binding energy for each temperature.

3. Results And Discussions

As described in section 2, the binding energies for adatoms added onto Al(111), Al(100) and Al(110), and Cu(100), Cu(110) and Cu(111) surfaces were calculated. The values obtained for the maximum surface binding energies on each point of the surface was plotted in a contour plot for selected temperatures of Cu and is shown in figure 3. To find the best binding sites, the binding energy of preferred binding sites were averaged. The results for the calculated surface binding energies for Cu and Al at 0 K are summarized in Table 2 and compared to values from literature. The values of 3.09 eV, 3.14 eV and 2.96 eV for Al(100), Al (110) and Al(111) respectively correspond very well with the values of 2.81 eV, 2.94 eV and 2.65 eV from the literature. [2] The values calculated the surface binding energies in low index Cu also compare very well. [1]

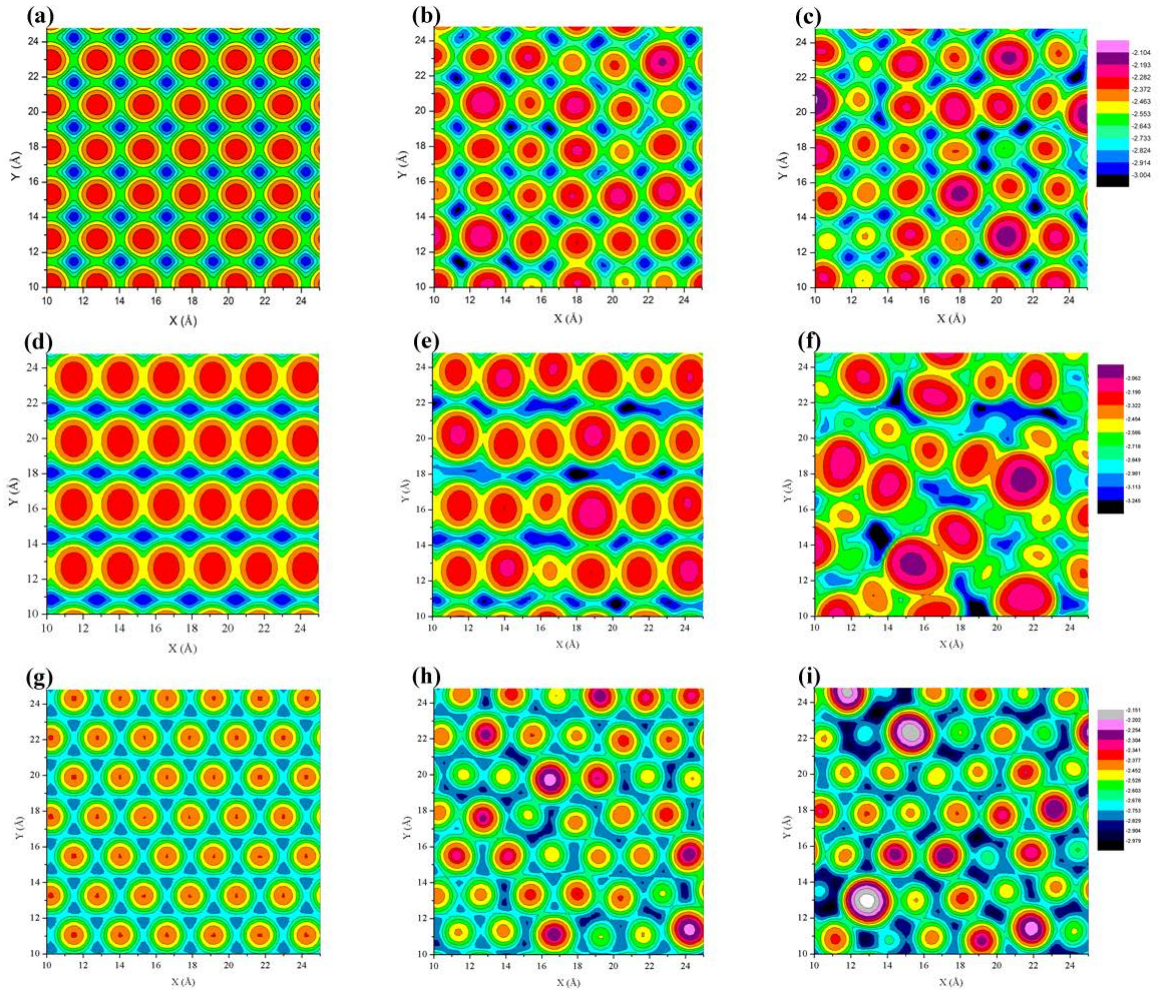

Figure 3. A contour plot was drawn showing the surface binding energies of the adatom on the Cu(100) surface at 0 K in 3(a), at 400 K in 3(b) and at 800 K 3(c). The corresponding binding energies measured for each point on the Cu(110) bulk crystal surface is shown in figure 3(d-f) and the plots of Cu(111) can be seen in figure 3(g-i).

From the cohesive surface binding energy for the adatom $E_{coh}^{(\text{surface})}$ and the bulk cohesive binding energy $E_{coh}^{(\text{Bulk})}$ the bulk vacancy formation energy (E_v) was calculated. The same process as described

in section 2 was repeated for 0 K and the results of the bulk vacancy formation energy (E_v) was also tabulated in table 2, along with values from literature.

Table 2. Summary of the calculated surface binding energies and the calculated bulk vacancy formation energies compared results from literature.

Surface	Calculated E_v (eV/atom)	E_v from literature (eV/atom)	Calculated $E_{coh}^{(surface)}$ (eV/atom)	$E_{coh}^{(surface)}$ from literature (eV/atom)
Al(100)	0.67	0.50 [2]	3.09	2.81 [2]
Al(110)	0.58	0.37 [2]	3.14	2.94 [2]
Al(111)	0.78	0.66 [2]	2.96	2.65 [2]
Cu(100)	1.35	1.34 [1]	2.99	3.05 [1]
Cu(110)	1.07	1.07 [1]	3.22	3.32 [1]
Cu(111)	1.52	1.54 [1]	2.81	2.85 [1]

The calculated E_v's of 1.52 eV for Cu(111), 1.35eV for Cu(100) and 1.07 eV for Cu(110) correspond well to the literature values of 1.54 eV for Cu(111), 1.34eV for Cu(100) and 1.07 eV for Cu(110), and there is a good agreement between the calculated and literature values of the Al E_v's.
The calculations were repeated for crystals at higher temperatures. The Cu crystals were simulated at temperatures ranging in 100 K steps from 0 K up to 1000 K. At high temperatures various surface effects were observed, especially in Cu(110), which exhibited roughening and the formation of an adlayer as can be seen in figure 3(f). Previous work in literature with the embedded atom model simulating Cu(110) surface also showed the formation of an adlayer at 900 K through a generation of vacancies, and surface premelting at 80 K below the simulated bulk melting point. [6] Another study used a semi-empirical potential based on the tight-binding method to study the thermal behaviour of low index copper surfaces. [7] It was found in Cu(110) that above 700 K an adlayer formed due to adatom/vacancy formation, which lead to roughening and premelting of the Cu(110) surface. The Cu (100) surface showed disordering above 800 K, whereas the Cu(111) surface was observed to be the most stable with an ordered surface observed for high temperatures. The bulk vacancy formation energies for Cu at various temperatures is shown in figure 4, and shows a general trend of decreasing vacancy formation energy with increasing temperature. Further the error also increases with increasing temperature, which would suggest that the crystal simulated may have been too small as the roughening in the surface at higher temperatures causes a greater spread in surface binding energies, and that more sampling should be done in future calculations.

The Sutton-Chen potential used to simulate the Al crystals showed melting of the surface at very low temperatures. Although the melting temperature of Al is found at 660 K, melting was found to occur at temperatures as low as 400 K. This underestimation of the melting temperature in Al has been observed before in thermodynamic studies of Al clusters and bulk simulations. [8–12] The Al surface was further found to premelt at temperatures below its melting temperature. [13] Al crystals were simulated for temperatures ranging up to 300 K and the resulting calculated vacancy formation energies (E_v) are shown in figure 5.

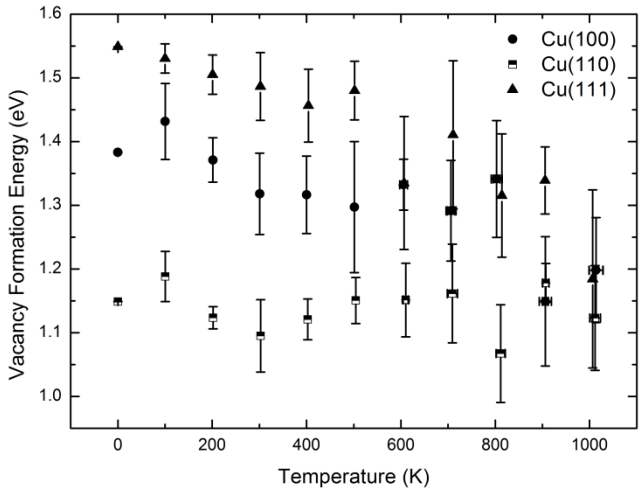

Figure 4. The vacancy formation energies (E_v) obtained for temperatures from 0 K to 1000K for Cu(100), Cu(110) and Cu(111) orientated surfaces.

In both materials, the bulk vacancy formation energy of the (111) surface crystals was larger than that of the (100) surface crystals, and that the bulk vacancy formation energy of the (100) surface crystals was found to be larger than that of the (110) surface crystals. The values calculated the vacancy formation energy of Schottky defects in low index Al and Cu compare very well to values found in the literature. As the temperature increased the E_v's tended to decrease, indicating a tendency for more vacancies to form at higher temperatures, which confirms observations.

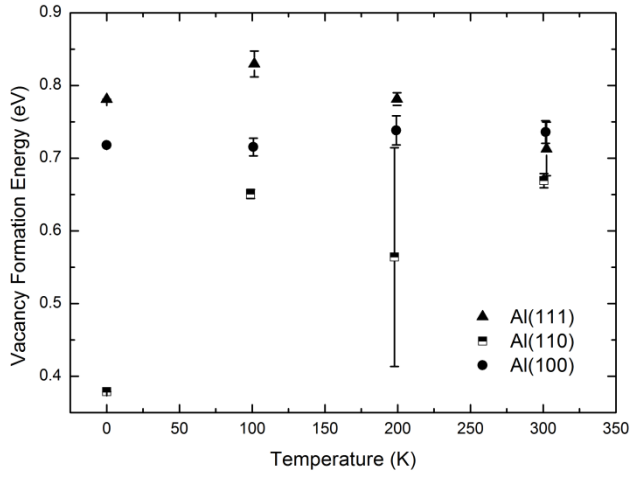

Figure 5. The effect of temperature on the vacancy formation energy in Al(111), Al(110) and Al(100).

4. Conclusion

Cu (100), (110) and (111), and Al (100), (110) and (111) bulk crystals were successfully simulated using the Sutton-Chen Potential. The bulk and surface cohesive energies for each of these crystals were measured at temperatures ranging from 0 K to 1000 K for Cu and 0 K to 300 K for Al. The Al melting temperature was underestimated by the Sutton-Chen potential and premelting in the surface was also observed. The Sutton-Chen also underestimates the melting temperature in Cu and surface

effects such as a surface adlayer were observed. This effect was especially pronounced in Cu(110). Generally with temperature increase, the vacancy formation energy was found to decrease.

Acknowledgments
Funding from the University of the Free State and the NRF is gratefully acknowledged.

5. References

[1] Terblans J J 2002 *Surf. Interface Anal*. **33** 767–770
[2] Terblans J J 2003 *Surf. Interface Anal*. **35** 548–551
[3] Mattsson T R and Mattsson A E 2002 *Phys. Rev*. B. **66** 214110
[4] Sutton A P and Chen J 1990 *Phil. Mag. Lett.* **61** 139–146
[5] Terblans J J, Erasmus W J, Viljoen E C and du Plessis J 1999 *Surf. Interface Anal*. **28** 70
[6] Barnett R N and Landman U 1991 *Phys. Rev*. B. **44** 3226
[7] Resende F J, Carvalho V E, Costa B V and de Castilho C M C 2004 *Braz. J. Phys.* **34** 414–8
[8] Puri P and Yang V 2007 *J. Phys. Chem.* C **111** 11776-11783
[9] Ozgen S and Duruk E 2004 *Mater. Lett.* **58** 1071– 1075
[10] Stoltze P, Norskov J K and Landman U 1988 *Phys. Rev. Lett.* **61** 440–3
[11] Qi Y and Krajewski P E 2007 *Acta Mater.* **55** 1555–63
[12] Budi A, Henry D J, Gale J D and Yarovsky I 2009 *J. Phys.: Condens. Matter* **21** 144206
[13] Ojwang' J G O, van Santen R, Kramer G J, van Duin A C T and Goddard III W A 2008 *J. Chem. Phys*. **129** 244506–14

The influence of working atmosphere on $Y_3(Al,Ga)_5O_{12}$:Tb thin films grown with the PLD technique

A Yousif [1,2], HC Swart[1], OM Ntwaeaborwa[1] and E Coetsee[1]
[1]Physics Department, University of the Free State, P.O. Box 339, Bloemfontein, ZA 9300, South Africa.
[2]Physics Department, Faculty of Education, University of Khartoum, P.O. Box 321, Postal Code 11115, Omdurman, Sudan.

swarthc@ufs.ac.za, Tel: +27(0)514012926, Fax: +27(0)514013507

Abstract. $Y_3(Al,Ga)_5O_{12}$:Tb thin films were grown on Si (100) substrates using the pulsed laser deposition technique. The influence of working atmosphere (base pressure, O_2, Ar and N_2) on morphology and structure of the thin films were investigated by Atomic force microscopy (AFM) and X-ray diffraction (XRD), respectively. Auger electron spectroscopy (AES) was employed to analyze the surface chemical composition of the films and the Auger data confirmed the presence of all major elements, namely Yttrium (Y), Aluminum (Al), Gallium (Ga) and Oxygen (O) present in the $Y_3(Al,Ga)_5O_{12}$:Tb phosphor. The brightest emission was observed from the film which was deposited in the O_2 atmosphere, indicating that oxygen is the best working atmosphere for growing the $Y_3(Al,Ga)_5O_{12}$:Tb thin films. AES also shows the differences in atomic concentration of the different films in comparison with that of the phosphor powder. The concentration of the elements of the O_2 atmosphere thin film was more similar to the elemental concentration of the powder itself.

1. Introduction

Pulsed laser deposition (PLD) is a widely used technique to grow thin films for a variety of applications. The major advantage of the PLD is the ability to transfer the material stoichiometry from a multi-component ablation target to a growing film [1-3]. However, it is well known that such favourable results do not occur under all experimental conditions. Therefore different deposition parameters for each kind of material need to be optimized to get the films with the desired properties. Parameters that may play a role are target-substrate distance, different working atmosphere, substrate temperature, laser pulse energy density and pulse repetition rate [2, 4]. Compared to phosphor powders that are widely used in conventional displays, thin phosphor films in general have advantages such as superior thermal conductivity, a high degree of uniformity, a better thermal adhesion to the substrate. In addition, the uniform thickness combined with smoother surface morphology and smaller grain size makes it possible to obtain smaller pixel spot size for achieving higher resolution [5]. Yttrium aluminium garnet $Y_3Al_5O_{12}$ material has been widely studied for different applications, by changing the dopants, the materials can be used to produce phosphors for a full-color display. In this paper we, however, only focus on the Tb doped $Y_3(Al,Ga)_5O_{12}$. It can withstand a high-energy electron

beam and has been considered as an ideal candidate to prepare display phosphors [6,7]. The brightness and the saturation characteristics of $Y_3Al_5O_{12}$:Tb were improved by the replacement of a portion of Al with Ga resulting in a $Y_3(Al,Ga)_5O_{12}$:Tb phosphor, that shows very good cathodoluminescent (CL) stability, during prolonged electron bombardment, indicating that, it is a promising phosphor candidate for field emission displays (FEDs) or other light emitting devices [7]. Thin films of $Y_3Al_5O_{12}$:Tb phosphor have already been fabricated by the PLD technique and has been proposed for practical application [1] but there are no reports on $Y_3(Al,Ga)_5O_{12}$:Tb thin films fabricated by PLD. In this study all the deposition parameters were kept constant except the working atmosphere. The working atmospheres used were base pressure, oxygen, and argon and nitrogen pressures.

2. Experiment

Phosphor powder of $Y_3(Al,Ga)_5O_{12}$:Tb, obtained from Phosphor Technology [8] was directly pressed without binders into a homemade sample holder and was used as an ablation target. The target was annealed at 600 ^oC for 2 hrs in air and was then placed inside the PLD system on a rotating target holder. Si (100) wafers were ultrasonically cleaned sequentially in ethanol for 15 min, were transferred to an ultrasonic water bath and then dry blown with nitrogen (N_2) gas. The films deposited in the different gas atmospheres were then deposited after the deposition chamber was evacuated to a base pressure of 1.4×10^{-6} m bar and then backfilled to a deposition pressure of 2.7×10^{-2} m bar for each gas (O_2, N_2 and Ar), except for the film deposited at the base pressure, where the chamber pressure was 6.6×10^{-6} m bar during the deposition process. A Nd:YAG 266 nm pulsed laser was used to ablate the phosphor pellet in the different working atmosphere. The laser frequency and fluence were 10 Hz and 0.767 J/cm^2 respectively. The substrate temperature was fixed at 400 ^oC and the target to substrate distance was 6 cm. X-ray diffraction (XRD) analysis was carried out using a Bruker AXS D8ADVANCE diffractometer, using a Cu K_α (1.5406 Å) radiation in the 2θ range from 15^o–50^o, with a counting time of 1 s for each step size of 0.015^o. Photoluminescent (PL) properties of the thin films were measured using a Carry eclipse spectrophotometer at room temperature using a monochromatized Xenon flash lamp as an excitation source. The surface morphology and roughness were examined by atomic force microscopy (AFM) with a Shimadzu SPM-9600 set in contact mode. The root mean square (RMS) roughness values were calculated from the height values from the AFM images using commercially available software. Chemical composition analyses and depth profiles were carried out using a PHI 700 nano scanning Auger electron microprobe (NanoSAM), surveys were done with 25 kV 10 nA electron beam, a 2 kV Ar ion gun was used and the sputtering rate was 27 nm/min.

3. Results and discussion

3.1 Structural, morphology and chemical composition analysis

Figure 1 shows the XRD patterns of $Y_3(Al,Ga)_5O_{12}$:Tb powder and the films grown in the different working atmospheres. For the films prepared at base pressure and in Ar and N_2 broad diffraction peaks located at 2θ=29.55^o were observed, indicating that amorphous structures were formed during the deposition process. The XRD from the O_2 layer only shows the (420) peak of $Y_3(Al,Ga)_5O_{12}$ [7] and peaks which are labelled with an asterisk (*) can be associated with diffraction from the Si substrate. The deposition layer therefore has a 420 preferential orientation. The substrate peaks are not consistent but have been obtained in several other measurements in the past. It, however, did not have any effect on the outcome and interpretation of our results and might be from the impurity dopands in the Si itself. The XRD of the Ar sample also has a (420) peak. Jiwei et al. [9], Jong-Ho Park et al. [11] and Naohiro et al. [12] reported that some peaks of the Y_2O_3:Tb cubic structure are in the range of these broad peaks.

Figure 2(a)-(d) shows three dimensional AFM images of the films. The film grown in base pressure in Figure 2 (a) shows undefined grain boundaries and a uniform surface with root mean square (RMS) roughness around 6 nm. The RMS was calculated without inserting the larger defect in the surface that can be seen in the figure. On the contrary, Figure 2 (b) presents the surface of the film

grown in the O_2 atmosphere, where big agglomerated grains with defined grain boundaries and roughness of about 30 nm were obtained. Figure 2(c) exhibits the surface topography of the Ar atmosphere thin film showing a smooth surface between spaced bigger grains with roughness of about 12 nm. The roughness of the N_2 film shown in Figure 2 (d), is about 5 nm with a well defined grain distribution but it seems that the film was not continuous. It can be concluded that the surface roughness, grain shape and size were influenced by the deposition environment.

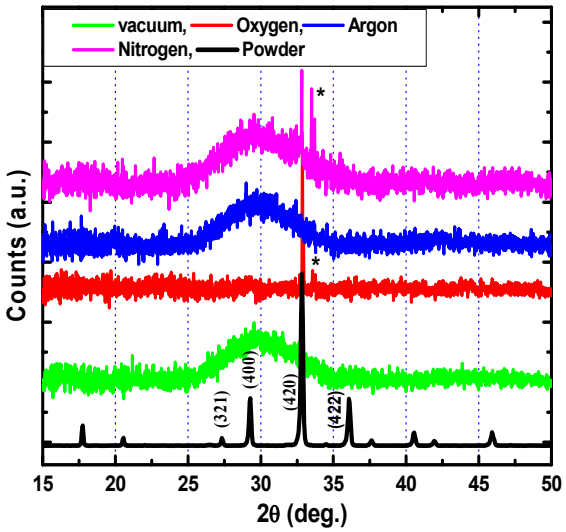

Figure 1. XRD spectra of $Y_3(Al,Ga)_5O_{12}$:Tb phosphor powder and thin films grown in different working atmosphere.

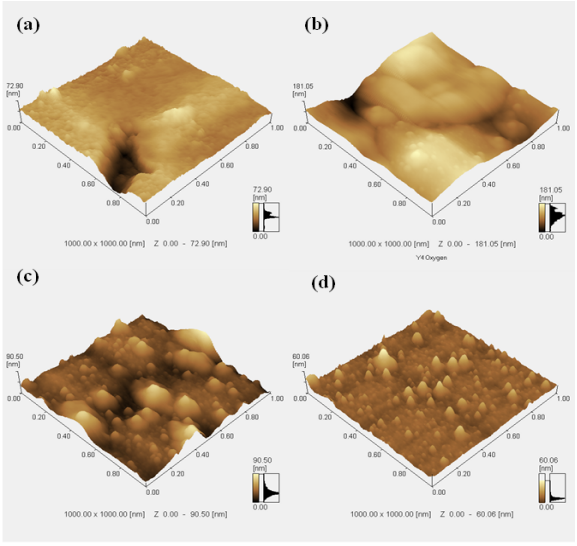

Figure 2. Three dimensional AFM images, for the thin film surfaces, grown in (a) base, (b) O_2, (c) Ar and (d) N_2 atmosphere.

The surface morphology of the films prepared in the different working atmosphere, can be seen from the SEM images in Figure 3(a)-(d). Figure 4 (a)-(i) show the AES spectra of (1) the $Y_3(Al,Ga)_5O_{12}$:Tb powder (2-4) the thin films that were grown in base pressure, (5) O_2, (6) Ar and (7) N_2 pressure. The spectra were recorded at the indicated positions on the SEM images. Spherical particles appeared on the smooth surface of the $Y_3(Al,Ga)_5O_{12}$:Tb films. Some areas of the substrate's surface were not completely covered with the thin film that was prepared in base pressure, Figure 4 (a). It can probably be referred to as the Volmer–Weber growth mode [13] where the energy due to the creation of interface is higher than the surface energy of the substrate and film. On the contrary, all the other substrate surfaces were covered with the deposited material for the films that were grown in (b) O_2, (c) Ar and (d) N_2. The AES spectra in Figure 4 confirm the presence of all the major elements, namely Yttrium (Y), Aluminium (Al), Gallium (Ga) and Oxygen (O) in the $Y_3(Al,Ga)_5O_{12}$:Tb phosphor target and in the thin films [1,7].

Figure 5 (a)-(d) show the compositional depth profiles of the thin film layers grown at (a) base pressure, (b) in O_2, (c) in Ar and (d) in N_2. The difference in atomic concentration, of films deposited in the different atmospheres, of each chemical element determined from the middle of the films is presented in table 1. The film grown in the O_2 atmosphere is enriched in oxygen with respect to the films grown at the base, Ar and N_2 atmospheres. It seems that during transport of the ablation material a depletion of some of the oxygen occurred. In the presence of the O_2 atmosphere, however, some of these are replaced leading to a thin film stoichiometry that is most similar to the original phosphor as shown in figure 6(a) and table 1. The thickness of the films were determined from the AES depth profiles to be approximately 55, 45, 40 and 30 nm for the films prepared in the base pressure, O_2, Ar and N_2 atmospheres respectively.

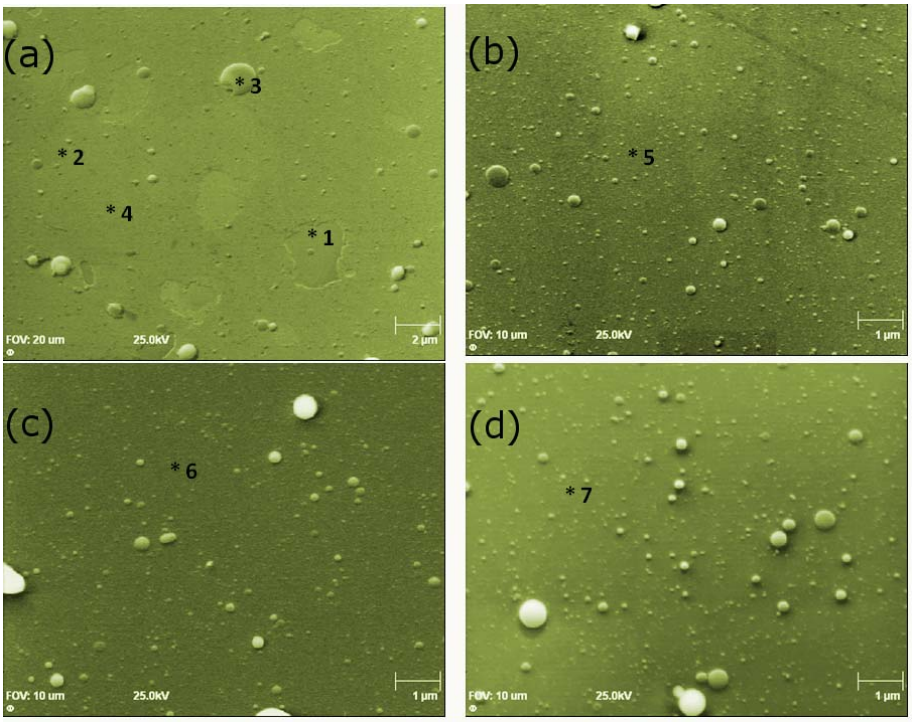

Figure 3. SEM images, for the thin film surfaces, grown in (a) base, (b) O_2, (c) Ar and (d) N_2 pressure, numbers 1-7 indicate where AES spectra were drawn - see also figure 4.

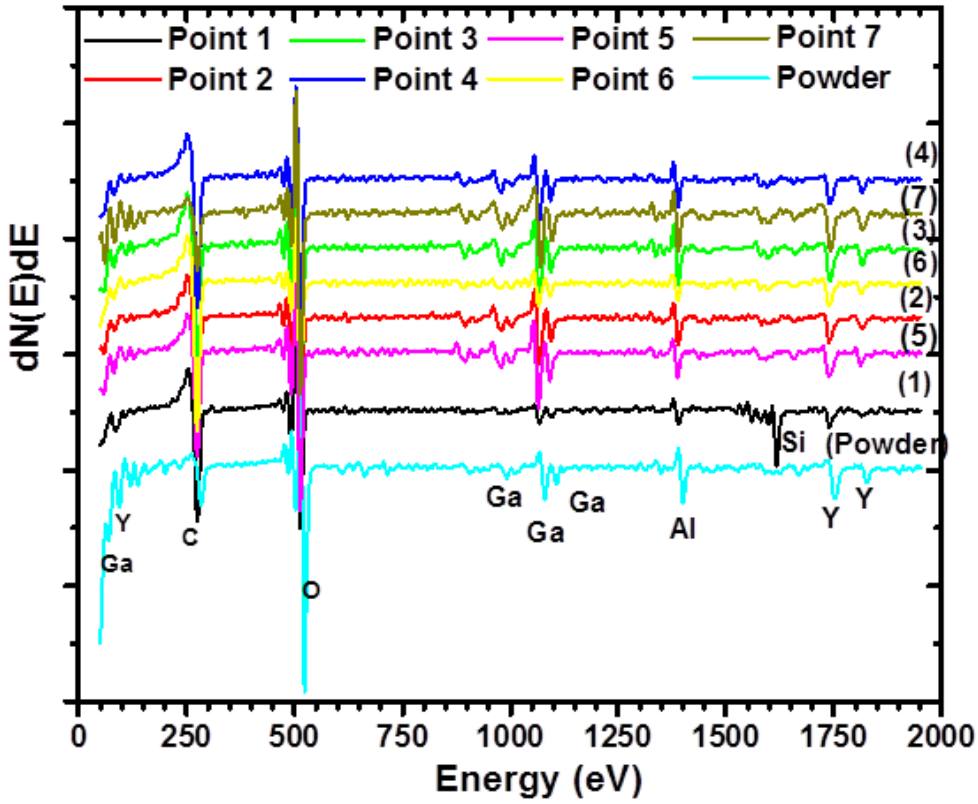

Figure 4. Different AES spectra of $Y_3(Al,Ga)_5O_{12}$:Tb powder (a) and thin films grown in base pressure (b-e), (f) O_2, (g)Ar and (i) N_2 atmospheres.

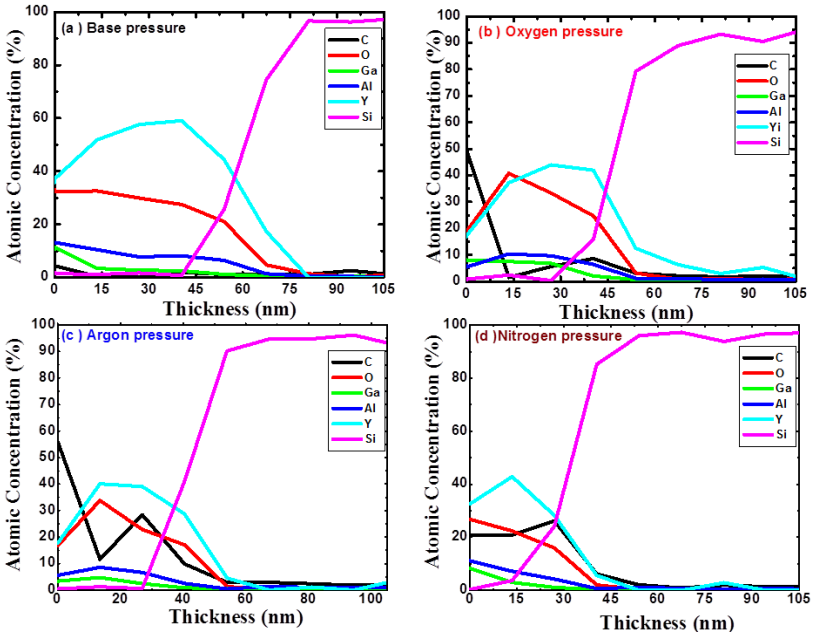

Figure 5. Depth profiles of the thin films structures, that were grown in (a) base, (b) O_2, (c) Ar and (d) N_2 atmospheres.

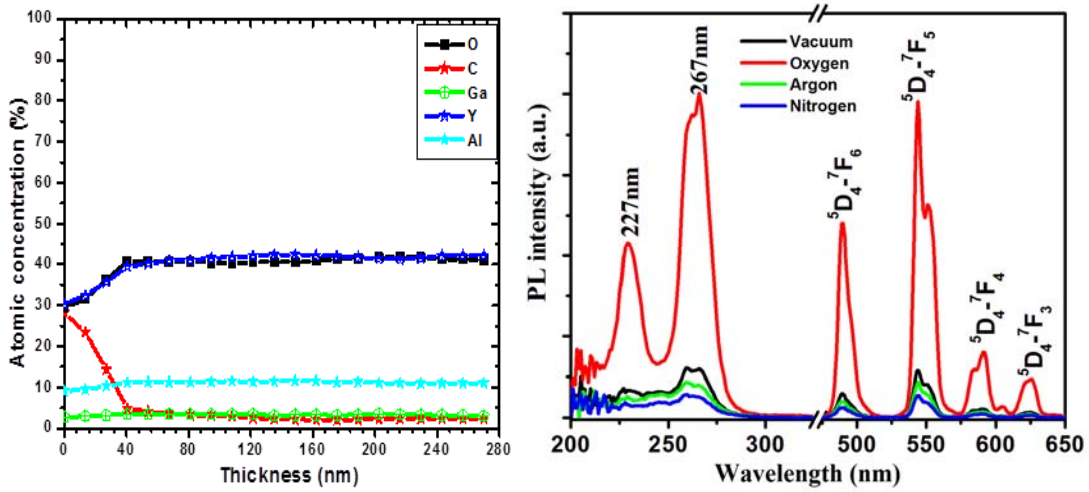

Figure 6 (a). Depth profile of the phosphor powder (b) PL emission and excitation of $Y_3(Al,Ga)_5O_{12}$:Tb thin films grown in different working atmosphere (Excitation measured at an emission wavelength of 544 nm; emission measured at an excitation wavelength of 267 nm.).

3.2 Photoluminescence (PL)

The PL emission characteristics for the thin films are illustrated in Figure 6(b). They all show typical emission spectra of Tb^{3+} ions due to the 5d-4f transitions from the excited $^5D_4$ level to ^5F_j (j=6-4) levels of the ground state with the main peak at a wavelength of 544 nm ($^5D_4 \rightarrow {}^7F_5$) and minor peaks at 489 nm ($^5D_4 \rightarrow {}^7F_6$), 561 nm ($^5D_4 \rightarrow {}^7F_4$) and 625 nm ($^5D_4 \rightarrow {}^7F_3$) [7,10]. The effect of different working atmosphere on the intensity can clearly be noticed in Figure 6(b). The highest luminescent emission intensity was obtained from the thin film grown in the O_2 working atmosphere.

Table 1: Atomic concentrations determined from the middle of the thin film layers deposited in the different working atmosphere

Working atmosphere	Atomic concentrations (%)					
	O	Y	Al	Ga	C	Si
Base pressure	30	57	8	3	0.2	1.5
Oxygen	37	40	10	7	4	1
Argon	28	40	7	4	20	1
Nitrogen	23	41	8	3	21	3
Powder	42	40	12	4	2	

4. Conclusion

Our results show that there is a clear correlation among the deposition atmosphere, structural properties of the thin films and their luminescent properties. The highest luminescent emission intensity was obtained from the film grown in the O_2 working atmosphere. Deposition in vacuum gives a smoother surface with roughness value around 6 nm and deposition in oxygen gave big agglomerated grains with defined grain boundaries and roughness of about 30 nm. Good luminescence was obtained from the Ga added $Y_3(Al,Ga)_5O_{12}$:Tb thin films.

Acknowledgment

We would like to thank the African Laser Center (ALC) and the University of the Free State for financial support and the National Laser Center for allowing us to use their PLD system.

References

[1] Hirata GA, Lopez OA, Shea LE, Yi JY, CheeksT, McKittrick J,Siqueiros J, Avalos-Borja M, Esparza A, Falcony C 1996 *J. Vac. Sci. Technol* A **14** 1694-1696.
[2] HEGDE M S 2001 J. *Indian Acad. Sci.* **113** 445–458.
[3] Arnold, Craig B, Michael J Aziz 1999 *J. Appl. Phys.* A **69** S23-S27.
[4] Haugan T, Barnes P N, Brunke L, Maartense I, Murphy J 2003 *J. Physica C* **397** 47–57.
[5] Jia P Y, Lin J, Han X M, Yu M 2005 *Thin Solid Films* **483** 122– 129
[6] Yun Chan Kanga, Wuled Lenggoroa I, Seung Bin Parkb, Kikuo Okuyama 2000 *Materials Research Bulletin* **35** 789–798.
[7] Yousif A, Swart HC, Ntwaeaborwa O M 2012 *Appl. Sur. Sci.* **258** 6495– 6503.
[8] http://www.phosphor-technology.com/products/crt.htm [Accessed 24 April 2012].
[9] Jiwei Wang, Hongwei Song, Baojuan Sun, Xinguang Ren, Baojiu Chen, Wu Xu 2003 *J. Ch. Phy. Let.* **379** *507*–511
[10] Guifang Li,Quanxi Cao, Zhimin Li, Yunxia Huang, Yunge Wei, Junyan Shi 2009 *J. Allo. Comp.* **485** 561-564.
[11] Jong-Ho Park , Nam Gwon Back, Min-Gi Kwak, Byeong-Eog Jun, Byung-Chun Choi, Byung-Kee Moon, Jung-Hyun Jeong, Soung-Soo Yi, Jeong-Bae Kim 2007 *J. Mat. Sci. Engin. C* **27** 998–1001.
[12] Naohiro Ishiwada, Toshihisa Ueda, Takeshi Yokomori 2011 *J. Lumin.* **26** 381–389.
[13] Eason John R 2007 *Pulsed Laser Deposition of Thin Films Applications-led Growth of Functional Material* Wiley & Sons, Hoboken, New Jersey.

Division B – Nuclear, Particle and Radiation Physics

Linking nuclear masses with nucleon separation energies

S Karataglidis[1], K Amos[1,2], L Canton[3], P R Fraser[2,3], J P Svenne[4], and D van der Knijff[2]

[1] Department of Physics, University of Johannesburg, P.O. Box 524 Auckland Park, 2006, South Africa
[2] School of Physics, University of Melbourne, Victoria 3010, Australia
[3] Istituto Nazionale di Fisica Nucleare, Sezione di Padova, Padova I-35131, Italia
[4] Department of Physics and Astronomy, University of Manitoba, and Winnipeg Institute for Theoretical Physics, Winnipeg, Manitoba, Canada R3T 2N2

E-mail: [1]stevenka@uj.ac.za

Abstract. With the growing interest in masses of nuclei near the drip lines, and especially for those beyond the drip lines, we take a survey of mirror systems near the drip lines, where one of the mirror pair is unbound. Various methods are followed by which their masses may be determined. As an example, we consider the mass of ^{17}Na, and its energy relative to the p+^{16}Ne threshold.

1. Introduction

There is much interest in extending the knowledge of nuclear masses beyond the valley of stability. However, many of the masses of the exotic nuclei, especially those near or beyond the drip lines, are not known, and may never be known, given the limited availability of beams at Radioactive Ion Beam (RIB) Facilities, and even less information is available with regards to their spectra. So one looks to theory, such as the Multi-Channel Algebraic Scattering (MCAS) Theory [1] to fill in the gaps. With that theory, states in ^{15}F were predicted [2] from studies of low-energy p+^{14}O scattering. Those states were subsequently found in experiment [3].

Herein, we are interested in determining masses of exotic nuclei in three ways. The first method is to use mass formulae for nuclei within an isobar multiplet. That approach is (largely) model-independent. The second method relies on using the mirror system, which may have a well-measured spectrum, in determining the properties of the system in question. (Such was done to determine the spectrum of ^{15}F [2].) The third is to find trends among the known (measured) values from which to extrapolate to the drip lines. This last method serves as a guide to the more theoretic approaches.

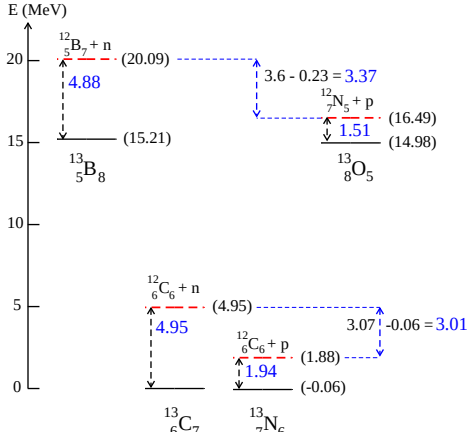

Figure 1. The mass-13 systems. All energies are relative to the ground state of ^{13}C.

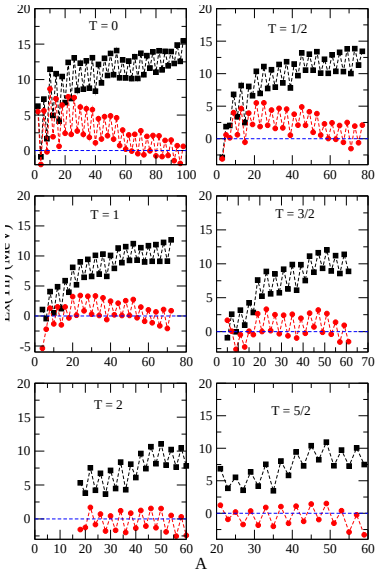

Figure 2. Excitation energies of particle-emission thresholds, $Th(nX)$ (squares) and $Th(pY)$ (circles). (The connecting lines are only a guide.)

2. Ground state energy and scattering threshold data brought together

For two mirror nuclei ${}^{A}_{(\pi=Z)}X_{(\nu=N)}$ and ${}^{A}_{(\pi=N)}Y_{(\nu=Z)}$, the energies (in MeV) of the nucleon plus nucleus thresholds are

$$\begin{aligned} Th(nX) &= E(n{+}X) - E_{\text{g.s.}}\left[{}^{(A+1)}_{(\pi=Z)}X_{(\nu=N+1)},\right] \\ Th(pY) &= E(p{+}Y) - E_{\text{g.s.}}\left[{}^{(A+1)}_{(\pi=Z+1)}W_{(\nu=N)}\right]; \\ \Delta(Th) &= Th(nX) - Th(pY). \end{aligned} \tag{1}$$

In Fig. 1 we show a plot of the various energies for the mass-13 systems, relative to the ground state of ^{13}C. The data were taken from the Ame2003 compilation [4]. We also evaluated the excitation energies of nucleon-emission thresholds in pairs of mirror systems, which are displayed in Fig. 2 for all nuclei with known mass and with core nucleus isospin $T < 3$. Negative values correspond to those nuclei which lie beyond the drip line, and are mostly proton emissive systems.

The associated $\Delta(Th)$ are plotted in Fig. 3. Therein the curves are results for $T = 0$ core nuclei ($N = Z = \frac{A}{2}$) with a proton, determined from

$$\Delta(Th) = \frac{\alpha Z\hbar c}{R} = \frac{197.3269602}{137.035999679}\ Z\ \frac{1}{R}. \tag{2}$$

where [5]

$$R = c_1\ A^{\frac{1}{3}} + c_2\ A^{-\frac{2}{3}}\ + r_p. \tag{3}$$

Ref. [5] gives $c_1 = 0.94$ and $c_2 = 2.81$ fm. The dashed curve in Fig. 3 was obtained with $r_p = 0.5$ fm, while the solid curve was obtained without any proton radius correction. For the latter, the resulting fitted curve gave values $c_1 = 1.07585$ fm and $c_2 = 1.95514$ fm.

The comparisons of the light mass results ($A \leq 20$) are shown on a larger scale in Fig 4. The two results give very good representations of data save one point: that of the mirror pair

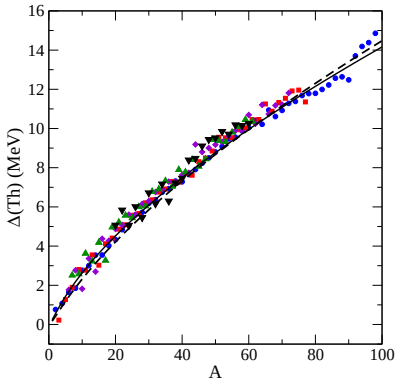

Figure 3. $\Delta(Th)$ plotted against the mass number of the core nuclei for isospins $T \leq 2$. The nuclear isospins are shown by circles ($T = 0$), squares ($T = \frac{1}{2}$), diamonds ($T = 1$), up-triangles ($T = \frac{3}{2}$), and down-triangles ($T = 2$).

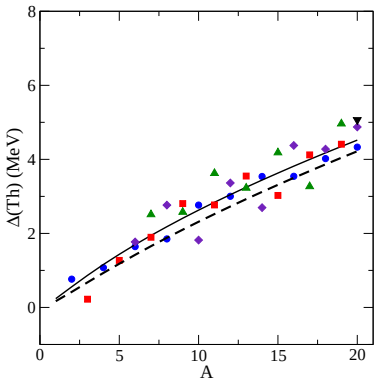

Figure 4. The Coulomb shifts $\Delta(Th)$ for the light mass core nuclei. Notation is as used with Fig. 3

.

^{19}N–^{19}Mg. Both those nuclei are represented by a neutron coupled to ^{18}N and a proton coupled to ^{18}Na, respectively, and there is very little information available for both ^{18}Na and ^{19}Mg, both lying beyond the proton drip line.

3. Mass Equations

Kelson and Garvey [8] gave a formula to relate masses of isobars, namely

$$M(A, T_z = -T) - M(A, T_z = T) = \sum_x \left[M(A + x, T_z = -1/2) - M(Z + x, T_z = 1/2) \right], \quad (4)$$

where $-(2T - 1) \leq x \leq (2T - 1)$. Using experimentally known masses, they predicted results for nuclei with atomic numbers 4 to 22. Reasonable results were obtained for nuclei that are not weakly bound using this prescription.

Antony *et al.* [9] proposed another mass formula to specify isobaric mass multiplet energies for $A < 40$, for which they considered multiplets with $T \leq 2$. The energy (in MeV) of a generic (less-stable) ground-state nucleus is given with respect to that of a more stable one, taken as a 'base', *viz.*

$$\epsilon = \epsilon(Z, A) = E(Z, A) - E(Z_s, A)$$
$$E(Z, A) = M_{Z,A} - ZM_{\rm H} - (A - Z)M_{\rm n} - 0.6Z(Z - 1)A^{\frac{1}{3}}, \quad (5)$$

where Z_s is the charge of the base nucleus, $M_{\rm n}$ is the mass of the neutron, and $M_{\rm H}$ is the mass energy of the hydrogen atom. The last term is a correction for the Coulomb energy.

Using data from Ame2003 [4], we have used Eq. (5) to estimate gap energies between the ground-states within isobars with members of mass 6 to 19. Values of those estimates are shown in Table 1. There is a close pairing of the ground-state energies of nuclei within each set of isobars according to their isospin - an effect that has been noted before [9]. We plot the energy differences between ground states of isospin pairs, $D_T = \epsilon(Z, A) - \epsilon(A - Z, A)$, with $Z < A - Z$ in Fig. 5. For the three separate isospin values, the trend is for the energy differences of the pairs to decrease as mass increases. However, strong deviations do occur for some masses within each isospin set.

Table 1. Ground state gap energies (in MeV) of light mass isobars determined using Eq. (5).

Base	A	Z	$\epsilon(Z,A)$	Base	A	Z	$\epsilon(Z,A)$
	6	1	28.19		7	2	11.66
^{6}Li	6	2	4.05	^{7}Li	7	4	−0.24
	6	4	3.09		7	5	10.13
	8	2	28.09		9	2	30.91
^{8}Be	8	3	17.02		9	3	14.55
	8	5	16.36	^{9}Be	9	5	−0.46
	8	6	26.32		9	6	13.93
	10	2	39.42				
	10	3	23.33		11	3	34.34
^{10}B	10	4	2.00		11	4	12.88
	10	6	1.64	^{11}B	11	6	0.07
	10	7	22.18		11	7	11.26
	12	4	28.23				
^{12}C	12	5	15.21		13	5	15.21
	12	7	14.97	^{13}C	13	7	−0.06
	12	8	26.80		13	8	14.92
	14	5	24.72		15	5	32.66
^{14}N	14	6	2.36		15	6	11.91
	14	8	2.40	^{15}N	15	8	0.13
					15	9	10.94
	16	6	23.06		17	6	26.35
^{16}O	16	7	12.97		17	7	11.16
	16	9	12.39	^{17}O	17	9	−0.19
	16	10	22.20		17	10	10.90
	18	6	31.32		19	6	41.00
	18	7	17.54		19	7	22.53
^{18}F	18	8	1.23		19	8	7.64
	18	10	1.10	^{19}F	19	10	−0.03
					19	11	7.43

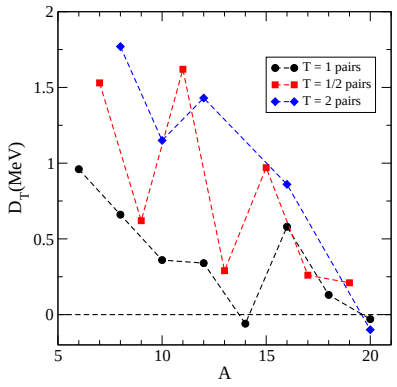

Figure 5. The energy differences between mirror ground-state energies calculated using Eq. (5).

Table 2. Mass-17 system properties deduced from inversion of Eq. (5). The base system defining $E(Z_s, A)$ is ^{17}O. All energies are in units of MeV and masses are in atomic mass units.

	$\epsilon(Z,A)$	$M_{Z,A}$	$Th(nX)$	$Th(pY)$
^{17}C	26.35	17.02259	0.73	23.33
^{17}N	11.16	17.00845	5.88	13.11
^{17}O	0.0	16.99914	4.14	13.78
^{17}F	−0.19	17.00209	16.8	0.60
^{17}Ne	10.92	17.01778	15.6	1.49
^{17}Na	25.5(1.0)	17.03752(107)	26.8(1.0)	−3.66(1.0)

Table 3. Predicted ground state energies of ^{17}Na relative to the p+^{16}Ne threshold (in MeV).

System.	KG_{old}	KG_{new}	Antony	cluster	MCAS
3.3(8)	3.65	4.28	3.66(1.0)	2.4	1.03

4. The case of ^{17}Na

^{17}C and ^{17}Na are a mirror pair of current interest [12, 13] but there is very little actually known about ^{17}Na. An early tabulation of nuclear masses [14] estimates the mass excess for ^{17}Na at values of 35.61, 35.81, and 35.84 MeV.

From Figs. 3 and 4 we estimate the ground state of ^{17}Na, relative to the p+^{17}Ne threshold, to be 3.3 ± 0.8 MeV. Kelson and Garvey [8] find mass excesses of 35.61 MeV and 24.67 MeV for ^{17}Na and ^{16}Ne, respectively, with the proton threshold to be 3.65 MeV. However, using the masses of Ame2003 in Eq. (4), we obtain a mass excess of 35.56 MeV for ^{17}Na. The measured mass excess for ^{16}Ne is 23.996 MeV and the proton mass excess is 7.288 MeV, giving a value for the proton threshold of 4.28 MeV.

By inverting Eq. (5), we can find masses for exotic nuclei. For mass-17 nuclei, those are listed in Table 2, with data taken from Refs. [4] and [10, 11]. The agreement is excellent. Given the close pairing of the ground state energies for nuclei of the same T within an isobar multiplet, and noting from Fig. 5 that as T increases, so does the gap between these ground states, we estimate the gap between the $T = \frac{5}{2}$ ^{17}C and ^{17}Na ground states to be around 1 MeV. Then, since the gap energy between ^{17}C and ^{17}O ground states is 26.54 MeV, we can assume a gap energy for ^{17}Na above ^{17}O to be 25.5±1.0 MeV. Thus, the last unknown in the equation, the atomic mass of ^{17}Na, is estimated as 17.03752 ±0.00107, which is 3.66 ± 1.0 MeV above the proton-^{16}Ne threshold. These values are slightly higher than those obtained using a microscopic cluster model [12]. And the results from MCAS [16] suggest a much lower value. All results are summarized in Table 3, and the differences may be due to the treatment of Coulomb effects.

5. Conclusions

A systematic study to predict the ground state energies of exotic nuclei has been presented. It is based upon examining the nucleon removal thresholds for mirror systems across the existing tabulated data for light-mass nuclei. A strong correlation in the data is found and does well for a wide range of masses, with variations from observed values usually being a few hundred keV and largest for the highest T-values. However, there are exceptional points with differences of

up to an MeV.

We used the result from the systematic method and results from two mass formulae to estimate the mass of the unbound ^{17}Na. The systematics suggest a ground state of 3.3 ± 0.8 MeV above the proton-^{16}Ne threshold, in accord with predictions from mass formulae. And considering the differences in model predictions for the ground state energy, there is a need for a direct measurement of ^{17}Na.

SK acknowledges support from the National Research Foundation of South Africa. JPS acknowledges support from the National Sciences and Engineering Research Council (NSERC) of Canada. PRF acknowledges funds from the Dipartimento di Fisica e Astronomia dell'Università di Padova and PRIN research project 2009TWL3MX.

References

[1] Amos K, Canton L, Pisent G, Svenne J P and van der Knijff D 2003 *Nucl. Phys.* **A728** 65
[2] Canton L, Pisent G, Svenne J P, Amos K and Karataglidis S 2006 *Phys. Rev. Lett.* **96** 072502
[3] Mukha I *et al.* 2009 *Phys. Rev. C* **79** 061301(R)
[4] Audi G, Wapstra A H and Thibault C 2003 *Nucl. Phys.* **A729** 337
[5] Dieperink A E L and Isacker P V 2009 *Eur. Phys. J. A* **42** 269
[6] Ogawa K, Nakada H, Hino S and Motegi R 2000 *Riken Review* **26** 99
[7] Lenzi S M and Bentley M A 2009 *Lect. Notes Phys.* **764** 57
[8] Kelson I and Garvey G T 1966 *Phys. Lett.* **23** 689
[9] Antony M S, Britz J, Bueb J B and Pape A 1985 *At. Data and Nucl. Data Tables* **33** 447
[10] Tilley D R, Weller H R and Cheves C M 1993 *Nucl. Phys.* **A564** 1
[11] Tilley D R *et al.* 1998 *Nucl. Phys.* **A636** 155 and from *www.tunl.duke.edu/nucldata*
[12] Timofeyuk N K and Descouvemont P 2010 *Phys. Rev. C.* **81** 051301(R)
[13] Fortune H T, Lacaze A and Sherr R 2010 *Phys. Rev. C* **82** 034312
[14] Wapstra A H, Audi G and Hoekstra R 1988 *At. Data and Nucl. Data Tables* **39** 281
[15] Fraser P R, Amos K, Canton L, Pisent G, Karataglidis S, Svenne J P and van der Knijff D 2008 *Phys. Rev. Lett.* **101** 242501
[16] Amos K, Canton L, Fraser P R, Karataglidis S, Svenne J P and van der Knijff D 2012 *Nucl. Phys.* **A879** 132
[17] Goldberg V Z *et al.* 2004 *Phys. Rev. C* **69** 031302(R)
[18] Guo F Q *et al.* 2005 *Phys. Rev. C* **72** 034312

Search for the Higgs boson to 4 leptons "decay channel" through new gauge bosons

P. Ntsoele[1], M. Aurousseau[1], S. H. Connell[1], K. A. Assamagan[1,2]

[1]University of Johannesburg, Johannesburg, South Africa
[2]Brookhaven National Laboratory, Upton, NY, USA

E-mail: pntsoele@uj.ac.za, mathieua@uj.ac.za

Abstract. The $H \rightarrow ZZ^{(*)} \rightarrow 4l$ channel has long been known to be the dominant discovery channel for the Standard Model (SM) Higgs boson with the ATLAS detector, thanks to its clean signature of 4 isolated leptons. However, some Hidden Valley (HV) scenarios predict the existence of a new sector with Higgs and gauge bosons (Z'). The Higgs boson could therefore decay to a pair of Z' through the mixing between the Standard Model (SM) and the HV sectors. In this study, prospects for a Higgs discovery in the decay channel $H \rightarrow Z'Z' \rightarrow 4l$ (where l can either be an electron or a muon) is being investigated. This channel has both a clean signature and a potentially large branching ratio for a low mass Higgs boson ($m_H < 200$ GeV/c^2). The Z' bosons in the present model can have a mass as low as 5 GeV/c^2, and decay preferably to SM fermions (leptons or light quarks) with a very narrow width. The $H \rightarrow Z'Z' \rightarrow 4l$ channel can be explored a similar way to the standard $H \rightarrow ZZ^{(*)} \rightarrow 4l$ channel, by changing the constraints on the dilepton invariant mass. Based on the study of 9 benchmark points, we developed a new algorithm to select our signal and reject the SM background, by constraining the two dilepton pairs to have the same mass within a certain window. The dominant backgrounds are also studied. Perspectives on this new approach with the ATLAS experiment are presented.

1. Introduction

The Higgs boson, long considered to be the last missing piece of the Standard Model (SM) of Particle Physics, was recently discovered in 2012. In the low-mass region, the Higgs boson was mainly searched for through its decay to two photons ($H \rightarrow \gamma\gamma$) or to four leptons through Z bosons ($H \rightarrow ZZ^{(*)} \rightarrow 4l$): these channels suffer from a relatively low branching ratio (BR) but have a very clean experimental signature. Recent results from the LHC experiments ATLAS [1] and CMS [2] in these channels seem to indicate a Higgs-like new particle at a mass of about 126 GeV/c^2 [3, 4]. This work reports on an analysis method in the search for a Higgs boson decaying to four leptons through new light gauge bosons ($H \rightarrow Z'Z' \rightarrow 4l$), with the ATLAS detector. The leptons considered here are electrons and muons. We will focus on the low-mass region ($m_H < 200$ GeV/c^2). Although in this study we consider all final states (4 electrons, 4 muons, 2 electrons plus 2 muons), we will present results concerning the 4-muon channel (4μ) only.

2. Theoretical framework

2.1. Abelian Hidden Sector model

Some Abelian Hidden Sector models [5] predict the existence of new Higgs and gauge bosons (Z'). The process $H \rightarrow Z'Z'$ is made possible through the kinetic mixing between the SM

and Hidden sectors. The mass of the new gauge boson Z' is not constrained by the model and the particle can be as light as a few GeV/c^2. It is weakly coupled to SM fermions so that the model is compatible with previous experimental data (from the LEP experiments), but the decay $Z' \to ll$ is allowed with a possibly large BR. These arguments make the search for a Higgs boson decaying to 4 leptons through a pair of Z' bosons relevant in the low-mass region: it benefits from the clean experimental signature of the "golden" channel and is accessible with minimal changes to the standard $H \to ZZ^{(*)} \to 4l$ analysis.

Although this study mainly focuses on one particular model, it should be noted that the search for low-mass resonances is also motivated by other models, such as "dark Z" models [6].

2.2. Signal event simulation

For this analysis, events were simulated with the MadGraph event generator [7], interfaced with Pythia [8] for parton showering, and then passed through the simulation of the ATLAS detector [9]. The event generation was made consistently with the Abelian Hidden Sector model of Ref. [5]. Several benchmark points were considered, as shown in Table 1. For the first points (light H and Z'), we see that we can expect to see several hundreds of $H \to Z'Z' \to 4l$ events in the data already collected in 2011 (about 5 fb^{-1}), or to exclude the model.

Table 1. Benchmark Points generated with MadGraph and the corresponding cross-sections (σ) times branching ratio (BR) at $\sqrt{s} = 7$ TeV.

H mass [GeV/c^2]	120	120	120	130	130	130	150	250
Z' mass [GeV/c^2]	5	20	50	5	20	50	50	100
$\sigma(gg \to H) \times BR(H \to Z'Z' \to 4l)$ [pb]	1.61	1.20	0.70	1.27	0.95	0.54	0.34	0.0004

For each point, 30000 events were generated. These events are used to optimize the analysis algorithm, in particular maximize the signal event selection and the background rejection. This analysis is based on events simulating 7-TeV collisions in the conditions of the 2011 data-taking period.

2.3. Backgrounds

In this study, the irreducible background is composed of events with 4 leptons in the final state. The dominant one is the direct $pp \to ZZ^{(*)} \to 4l$ production, but other processes can produce this final state (in particular events containing J/ψ mesons). There is also a background which can be reduced with the particle identification. These are events containing leptons and jets faking leptons, such as the processes $(Z \to ll)$+jets and $t\bar{t}$.

Besides this, there is a non-physical background coming from the final state topology: when selecting 4 leptons, several combinations are possible and the "wrong" combinations form the combinatorial background. We will see that this analysis also aims at reducing the contribution of this background.

3. Experimental setup

3.1. The LHC and the ATLAS Detector

The ATLAS detector [1] is a multi-purpose detector installed at the LHC[1], 100 m underground. The detector is composed of various sub-detectors. Going outwards from the beam-line, the sub-detectors are the Inner Tracking Detector (ID), the Electromagnetic (EM) calorimetry system,

[1] The Large Hadron Collider (LHC) is a proton-proton collider located at CERN, in Switzerland. It has provided $p-p$ collisions at a center-of-mass energy $\sqrt{s} = 7$ TeV in 2010 and 2011, and at $\sqrt{s} = 8$ TeV since 2012.

the Hadronic calorimetry system, and the Muon Spectrometer. A complete description of the ATLAS detector and its components can be found in Ref. [1].

3.2. Muon reconstruction

Muons in the ATLAS detector are reconstructed primarily from the tracks they leave in the trackers (ID and MS). The magnetic fields allow a precise measurement of the particle momentum. In order to maximize the acceptance of the analysis, three types of reconstructed muons are considered:

- combined: from a track in the ID and a matching track in the MS;
- standalone : from a track in the MS only; and
- calorimetric : from the energy deposit in the EM calorimeter.

4. The $H \rightarrow Z'Z' \rightarrow 4\mu$ analysis: optimization of analysis algorithm

4.1. Event pre-selection

Given the huge amount of data provided by the LHC and recorded by ATLAS, an event pre-selection is needed. The pre-selection is aimed at maximizing the integrated luminosity by removing luminosity blocks[2] with detector defects or misbehavior. To ensure that a hard event took place, only events with at least one reconstructed collision vertex with three associated tracks are kept. Finally, and most importantly, the selection is made on the high-level trigger system. For the 4μ final state, it is required that the events fired a single or di-muon trigger. Details about the triggers in this search can be found in Ref. [10].

4.2. Four-muon events

Among the pre-selected events, we select events with 4 muons, by applying several cuts on the particle identification, kinematics (transverse momentum p_T, pseudo-rapidity η), track quality and projectivity of the muon candidates. All possible quadruplets of leptons are kept at that stage. It is required that within a quadruplet, there are two pairs of same-sign, opposite-charge leptons. Additional kinematic cuts are applied, in particular the leading lepton should have $p_T > 20$ GeV/c, the subleasing lepton $p_T > 15$ GeV/c, the third lepton $p_T > 10$ GeV/c, and the fourth lepton $p_T > 7$ GeV/c, and that the reconstructed leptons match the triggered objects. A cut on the invariant mass of the lepton pairs is then applied, and is described in the next subsection as it is the central point of this analysis. The final cuts applied are separation between the leptons, calorimetric and track isolation, and the significance of the impact parameter. More details about this procedure can be found in Ref. [10] on which this analysis is based.

4.3. Optimization of the analysis: invariant mass cut

The cut on the invariant mass of the lepton pairs is optimized in order to maximize signal efficiency and background rejection. Unlike for a "standard" $H \rightarrow ZZ^{(*)} \rightarrow 4l$ analysis, where the known SM Z mass can be used as a constraint on the dilepton system, here we will use the fact that the two dilepton systems of a quadruplet must have the same mass within a window. This study is based on the benchmark points presented above, and the results will be shown for the points with a Higgs mass at 120 GeV/c^2 and a Z' mass at 5 GeV/c^2 and at 50 GeV/c^2. The background considered is the dominant direct ZZ production.

In the following, we will consider quadruplets selected after the kinematic cuts mentioned above. In all cases, only one quadruplet was selected, which means in the 4μ case that there are

[2] A luminosity block (LB) is a collection of events for which the data-taking conditions are constant. It is the unit of the Data Quality assessment.

two possible combinations for the dilepton pairs (combinatorial background). The lepton pairs within a quadruplet are labelled Z_1 and Z_2. The choice of the first and second pair is arbitrary.

Figure 1 shows the invariant mass distribution for the $H \rightarrow Z'Z' \rightarrow 4\mu$ signal (red solid line) and the ZZ background (black solid line) for the lepton pairs of the selected quadruplets.

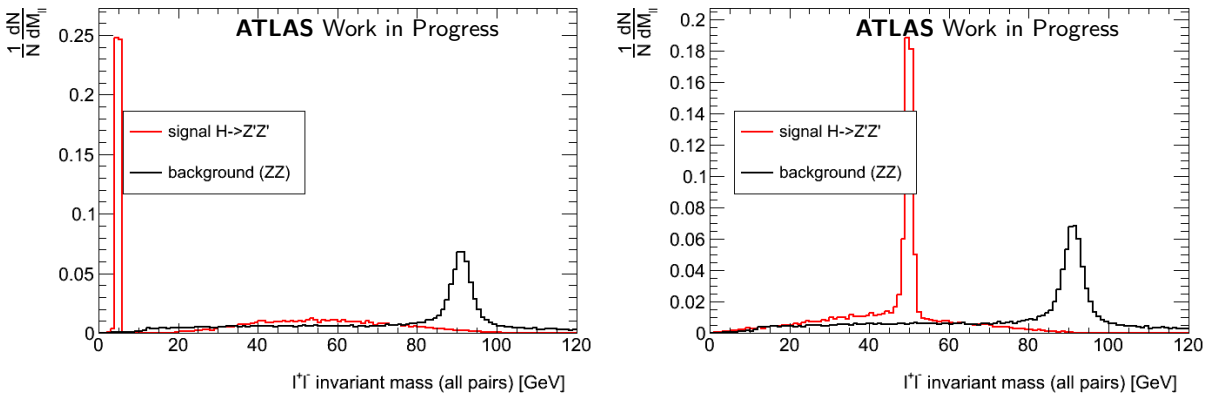

Figure 1. Dilepton invariant mass distribution for $H \rightarrow Z'Z' \rightarrow 4\mu$ signal (red) and ZZ background (black). All distributions are normalized to unity. The generated signal Higgs mass is $m_H = 120$ GeV/c^2. The generated Z' mass is $m_{Z'} = 5$ GeV/c^2 (left), and $m_{Z'} = 50$ GeV/c^2 (right).

It has to be noted that the signal distribution is narrower than the background distribution. Since all combinations are represented in this figure, each event provides 4 entries (2 pairs per quadruplet, and 2 possible quadruplet combinations). The combinatorial background is clearly visible in the tails of the distributions, adding an almost continuous distribution. The case of the combinatorial background is treated in section 4.4.

Figure 2 shows the invariant mass difference between the lepton pairs of the same selected quadruplets, again for the $H \rightarrow Z'Z' \rightarrow 4\mu$ signal (red solid line) and the ZZ background (black solid line).

The distribution is again sharper for signal than for background. Several cuts on $|M_{Z_1} - M_{Z_2}|$ are tested, from 5 GeV/c^2 to 50 GeV/c^2. In each case, the relative efficiency of the cut is measured, *i.e.* the ratio of the number of events after and before the cut. The measured efficiencies are represented by dots for the signal (red) and the background (black). For the lightest Z' (Fig. 2 (left)), the signal efficiency is 100% already for the smallest value of the cut. In the second case ($m_{Z'} = 5$ GeV/c^2, Fig. 2 (right)), the signal efficiency reaches 100% for larger values of the cut. In both cases, the background rejection is high for a cut at 5 GeV/c^2.

4.4. Combinatorial background

As mentioned earlier, the non-physical (combinatorial) background must also be removed. Figure 3 shows the mass distribution of the same selected lepton pairs, for $H \rightarrow Z'Z' \rightarrow 4\mu$ signal. The contribution of the truth-matched pairs, *i.e.* muons coming from the same Z' identified using the Monte-Carlo truth information, is shown in red, while the combinatorial background is shown in blue ("wrong pairs").

This translates to the $|M_{Z_1} - M_{Z_2}|$ distribution as an almost continuous background, as shown on Fig. 4. It appears clearly that setting the cut at the lowest available threshold (5 GeV/c^2) will reduce the combinatorial background as well.

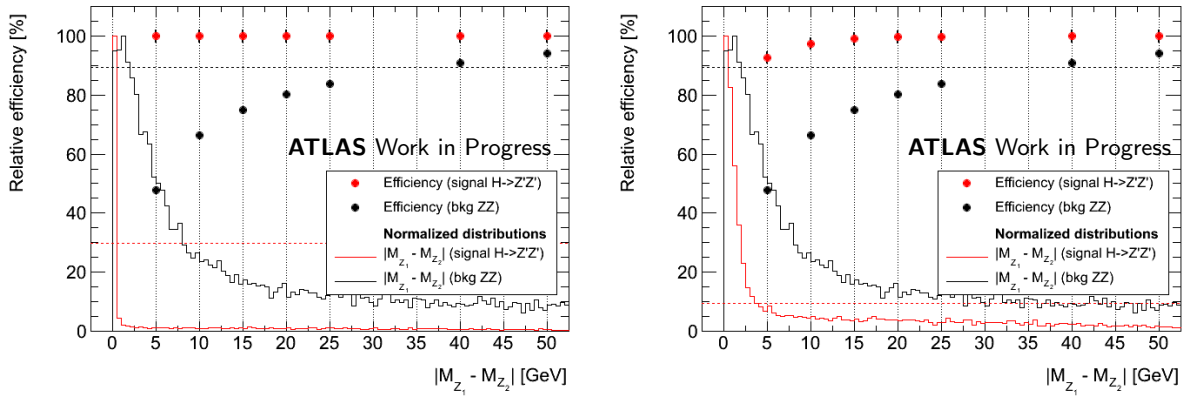

Figure 2. Difference between the invariant masses of the selected lepton pairs for $H \rightarrow Z'Z' \rightarrow 4\mu$ signal (red line) and ZZ background (black line), normalized to unity. The dots represent in each case the relative efficiency of the $|M_{Z_1} - M_{Z_2}|$ cut, for the cut threshold ranging from 5 GeV/c^2 to 50 GeV/c^2. The generated signal Higgs mass is $m_H = 120$ GeV/c^2. The generated Z' mass is $m_{Z'} = 5$ GeV/c^2 (left), and $m_{Z'} = 50$ GeV/c^2 (right).

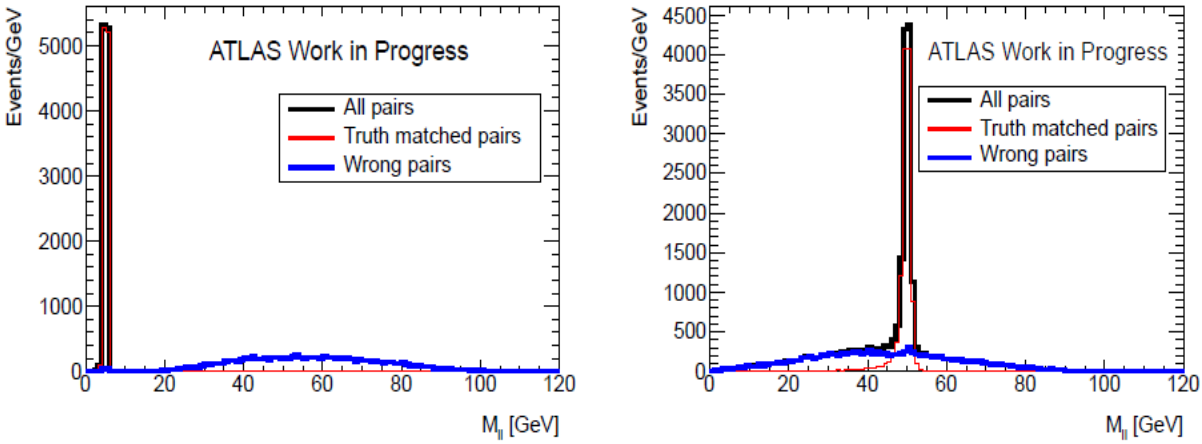

Figure 3. Dilepton invariant mass distribution for $H \rightarrow Z'Z' \rightarrow 4\mu$ signal. The truth-matched pairs are shown in red, while the combinatorial background is shown in blue (the black curve is the total). The generated signal Higgs mass is $m_H = 120$ GeV/c^2. The generated Z' mass is $m_{Z'} = 5$ GeV/c^2 (left), and $m_{Z'} = 50$ GeV/c^2 (right).

5. Conclusions

Using a set of simulated events, the analysis algorithm for $H \rightarrow Z'Z' \rightarrow 4l$ has been derived, based on the official standard $H \rightarrow ZZ^{(*)} \rightarrow 4l$ analysis of the ATLAS collaboration [10]. This includes in particular the definition of a cut which examines the difference between the invariant masses of the selected lepton pairs, in order to reject both the physical irreducible background (direct ZZ production) and the combinatorial background. The study presented here in the 4μ final state, has also been conducted for the other possible final states ($4e$ and $2e2\mu$) and leads to similar results. A cut value at 5 GeV/c^2 seems optimal in terms of signal efficiency and background rejection.

An extension of this study is in progress, to include a new model ("dark Z" model [6], with new gauge bosons of very low mass, from a few MeV/c^2 to a few GeV/c^2) and a new intermediate state ($H \rightarrow ZZ' \rightarrow 4l$). This requires a new approach of the analysis strategy, as the dilepton

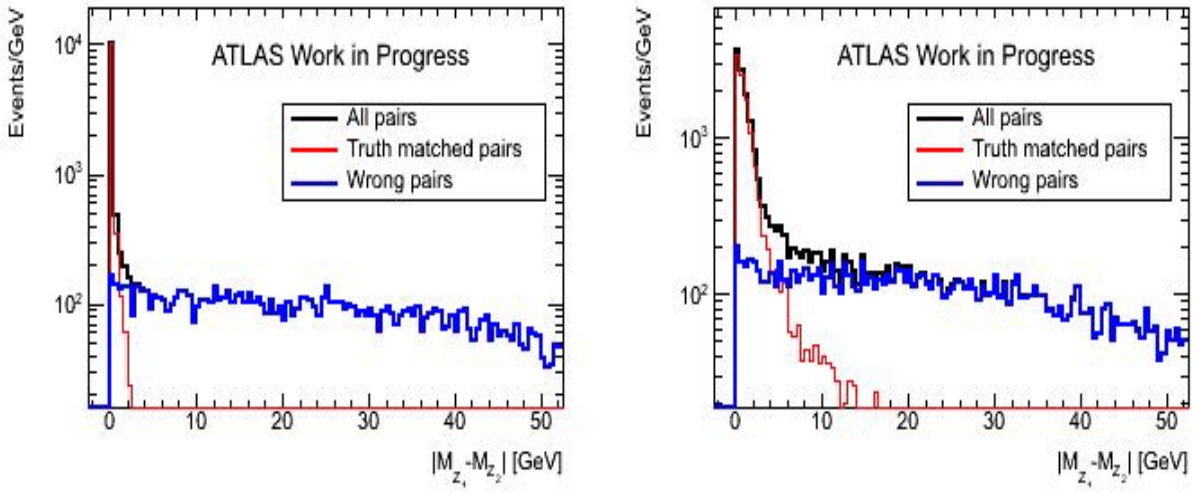

Figure 4. Difference between the invariant masses of the selected lepton pairs for $H \rightarrow Z'Z' \rightarrow 4\mu$ signal. The truth-matched pairs are shown in red, while the combinatorial background is shown in blue (the black curve is the total). The generated signal Higgs mass is $m_H = 120$ GeV/c^2. The generated Z' mass is $m_{Z'} = 5$ GeV/c^2 (left), and $m_{Z'} = 50$ GeV/c^2 (right).

systems will have a different invariant mass.

This analysis on simulated events shall be completed using the conditions of the 2012 data-taking period, before proceeding to the analysis of the combined 2011 and 2012 datasets. We estimate that with only the data already collected in 2011, corresponding to an integrated luminosity of about 5 fb^{-1}, several hundreds of events in the low mass region should already be produced. We therefore expect to draw an exclusion limit even before the end of the LHC run.

6. Acknowledgements

We would like to thank S. Jung and J. Wells for their explanations about their Z' model (Ref. [5]). This work has received the support from the South African National Research Foundation, the South-Africa-CERN consortium, the University of Johannesburg, Brookhaven National Laboratory and the US Department of Energy.

References

[1] The ATLAS Collaboration 2008 *Journal of Instrumentation JINST* **3** S08003
[2] The CMS Collaboration 2008 *Journal of Instrumentation JINST* **3** S08004
[3] The ATLAS Collaboration 2012 *ATLAS-CONF-2012-093*
[4] The CMS Collaboration 2012 *CMS-PAS-HIG-12-020*
[5] Gopalakrishna S, Jung S and Wells J 2008 *Arxiv preprint arXiv:0801.3456*
[6] Davoudiasl H, Lee H S and Marciano W J 2012 *Arxiv preprint arXiv:1203.2947*
[7] Alwall J, Demin P, Visscher S, Frederix R, Herquet M, Maltoni F, Plehn T, Rainwater D and Stelzer T 2007 *Journal of High Energy Physics* **2007** 028
[8] Sjöstrand T *et al.* 2001 *Computer Phys. Commun.* **135** 238
[9] The ATLAS Collaboration 2010 *ATLAS-SOFT-2010-01-004* Submitted to Eur. Phys. J. C (*Preprint* 1005.4568)
[10] The ATLAS Collaboration 2012 *Arxiv preprint arXiv:1202.1415*

Characterization of Incomplete Fusion Reaction with AFRODITE and DIAMANT

B. G. Maqabuka[1,2], S. M. Mullins[2], R. A. Bark[2], S. Bogolomov[3], S. H. Connell[1], A. Efremov[3], I. Kuti[4], E. A. Lawrie[2], J. J. Lawrie[2], S. N. T. Majola[2], J. Molnár[4], S. H. T. Murray[2], B. Nyakó [4], P. Papka[5], R. Thomae[2]

[1]Department of Physics, University of Johannesburg, Johannesburg, South Africa
[2]iThemba LABS, National Research Foundation, South Africa
[3]Joint Institute for Nuclear Research, Dubna, Russian Federation
[4]Institute for Nuclear research "ATOMKI", Debrecen, Hungary
[5]Department of Physics, University of Stellenbosch, Stellenbosch, South Africa

E-mail: bmaqabuka77@gmail.com

Abstract.

This project concerns the nuclear reaction ^{7}Li + ^{176}Yb at 50 MeV which was carried-out using the AFRODITE and DIAMANT facility of detectors at iThemba LABS, Cape town. A ^{7}Li nucleus is considered suitable for the breakup fusion (incomplete fusion) reaction because of its well developed cluster structure of an α-particle and *triton* which are weakly bound in this nucleus. One of the fragments may be captured by the target while the other escapes at the beam velocity. Light charged-particles (alphas, tritons, deuterons and protons) were detected with the DIAMANT (CsI) array in coincidence with gamma-rays detected by the AFRODITE (HPGe) spectrometer. The project involves data processing to produce charged-particle-gated gamma-gamma coincidence matrices which are analysed with the RADWARE software package [1]. The intensity ratios as function of spin for the proton to triton-gated matrices populating ^{178}Hf nucleus were extracted. Insights could be developed into the incomplete fusion reaction mechanisms initiated by the breakup of the incident ^{7}Li projectile.

1. Introduction

In this work we investigate the incomplete fusion (IFC) mechanism following the breakup of ^{7}Li projectiles incident on a target of ^{176}Yb, by looking at the ^{178}Hf isotope populated through (^{6}He, 4n) and (^{4}He, 2n) exit channels. This nucleus is located in the region of deformation near $A = 180$. This region is characterised by collective rotational behaviour which coexists with intrinsic quasiparticle modes of excitation as a means with which to form the yrast line. These quasiparticle states have large K values which arise as a result of the large angular momentum projections (Ω) of the single-particle orbitals on the nuclear symmetry z-axis. Electromagnetic transitions of multipolarity λ between high K states are forbidden if ΔK is greater than the multipolarity, λ of the photon. This causes the excited quasiparticle states to be isomeric in character. Bands built on these metastable states are decoupled from the level scheme below, due to the isomeric nature (i.e. having long lifetimes) of these bandhead states. This makes it difficult to assign these bands to a particular isomer, and indeed to the nucleus itself.

However, studies done by Mullins *et al.* [2, 3], show that there is a distinct correlation between the relative gamma-ray intensities of the product nuclei when selected by alpha/triton-particles detected at forward or middle/backward angles. These relative yields can be a useful tool in the assignment of the unknown transitions to their associated bands and also to the particular nucleus itself. We investigate these correlations in gamma-ray intensity ratios by looking at the various bands of ^{178}Hf nucleus populated through forward gated proton or triton-particles, i.e. taking a ratio of the (^{6}He, 4n) to (^{4}He, 2n) exit channels.

2. EXPERIMENTAL TECHNIQUES

The measurements were carried out with a beam of ^{7}Li ions incident on the target, which was supplied at an energy of 50 MeV by the iThemba LABS separated sector cyclotron . A self-supporting metallic foil (of 4.6 mg/cm^2 thickness) of ^{176}Yb, which is isotopically enriched to 95%, was used as a target. States in ^{178}Hf were populated via two possible exit channels (^{6}He, 4n) and (^{4}He, 2n). The *proton* and α-particle yields came from breakup of the beam, ^{7}Li $\longrightarrow$ ^{6}He + ^{1}H or ^{7}Li $\longrightarrow$ ^{4}He + ^{3}H respectively. This process is called incomplete fusion or "massive transfer" [4, 5] reaction process, and it is believed to occur for collisions detected forward of the grazing angle. During the fusion reaction process, a weakly-bound projectile such as ^{7}Li may break-up into two clusters as mentioned above, and fusion of one of the fragments and the target occurs. This results in an anisotropic distribution of the emitted particles. According to Dracoulis *et al.* [6], the presence of incomplete fusion enhancing the anisotropy in the angular distribution of emitted particles, produces different intensities of γ-transitions when in coincidence with particles detected at backward and forward angles (yield ratios) for the isotopes produced in a heavy-ion reaction.

The measurements were performed with the AFRODITE spectrometer in conjunction with a compact array of charged-particle detectors, DIAMANT. The AFRODITE spectrometer is an array consisting of two sets of High Purity Germanium (HPGe)detectors, which are the clover (for high energy gamma-rays) and Low Energy Photon Spectrometer (LEPS) detectors [7]. In this experiment 8 clover detectors were used, with 4 placed at 90°and the rest at 135°with respect to the beam. The DIAMANT is a 4π array of light charged-particle (CsI) scintillation detectors coupled to photo-diodes [8]. It was developed to be used as an ancillary detector used inside large gamma-ray spectrometers to identify the light charged particles emitted in heavy-ion induced reactions. It was placed around the target position at the center of the AFRODITE γ-ray array. This was the arrangement that was used to collect time correlated particle-γ-γ coincidences when the ^{176}Yb target foil was bombarded with ^{7}Li ions.

In order to reduce the amount of scattered beam incident on the particle detectors, the detectors were shielded with $\sim$46 mg/cm^2 aluminium absorber foils. A ^{152}Eu source was used for the energy and efficiency calibration of the HPGe detectors.

3. DATA ANALYSIS

Time-correlated particle-γ -γ coincidence data were sorted off-line into particle-gated E$_\gamma$ -E$_\gamma$ matrices with same time conditions. The full-background subtracted projection spectra in coincidence with a (a) proton and (b) triton particle (Fig. 1), show γ-rays from the ground state band (GSB) of ^{178}Hf, the γ-rays are clearly visible up to spin 12$^+$. The level scheme for ^{178}Hf extracted from the triton gated spectrum is given in Fig. 2 [2]. There are no new states established in this work.

The main analysis was carried out with two matrices; one matrix proton-gated i.e. (^{6}He, 4n) exit channel and the other triton-gated i.e. (^{4}He, 2n) exit channel, both at forward angles covering angles up to a maximum of $\sim$60°with respect to the beam axis. The proton gated matrix contained $\sim 3.7 \times 10^6$ counts and the triton gated matrix had $\sim 6.5 \times 10^6$ counts. Ratios of γ-γ coincidence intensities of the form (proton/triton)$_{\texttt{forward}}\gamma - \gamma$ were generated, and were

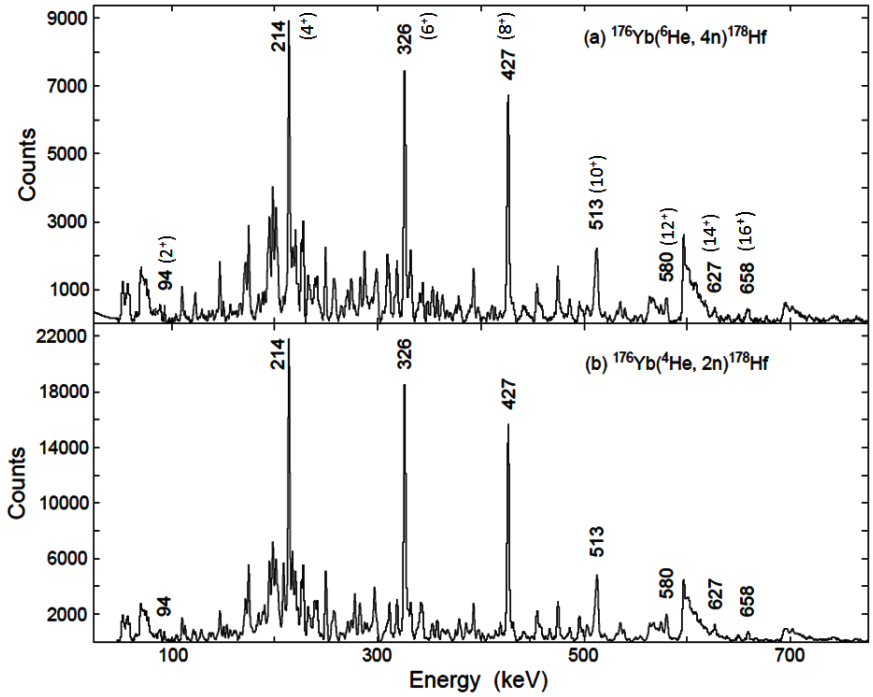

Figure 1. Total background-subtracted projection spectra of the ^{7}Li + ^{176}Yb reaction from a 2-dimensional symmetric $\gamma - \gamma$ matrix, with (a) proton tagged spectrum and (b) triton tagged spectrum.

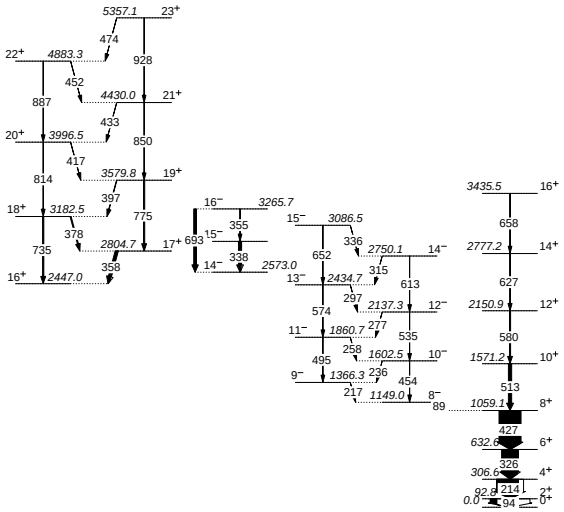

Figure 2. A partial level scheme of ^{178}Hf [2] extracted from the spectrum in Fig. 1(b), produced through ^{176}Yb(^{4}He,2n)^{178}Hf exit channel of this experiment.

plotted as a function of spin for each of the various bands GSB, $K^\pi = 8^-$, $K^\pi = 14^-$ and $K^\pi = 16^+$ band of the ^{178}Hf isotope, Fig. 3. From the plot, all bands i.e. GSB, $K^\pi = 8^-$, $K^\pi = 14^-$ and $K^\pi = 16^+$ show no change in the proton-triton intensity ratio with increase in angular momentum. The yield ratios are spin independent. However, when bands are compared, there are observable differences. The GSB and $K^\pi = 8^-$ bands show relatively low yield ratios compared to $K^\pi = 14^-$ and $K^\pi = 16^+$ bands. The $K^\pi = 16^+$ band has a further higher yield ratio compared to the $K^\pi = 14^-$ band. The rise in the (proton/triton) intensity ratio at higher spins can be attributed to the differences in mass of the fused fragments, with ^{6}He being 50% more massive than ^{4}He. The less mass-asymmetric the beam/target combination for a given compound nucleus, the higher the maximum angular momentum that can be induced into the system. At high spin, ^{176}Yb show a relatively high cross-section for incomplete fusion with ^{6}He as compared to ^{4}He (the alpha particle).

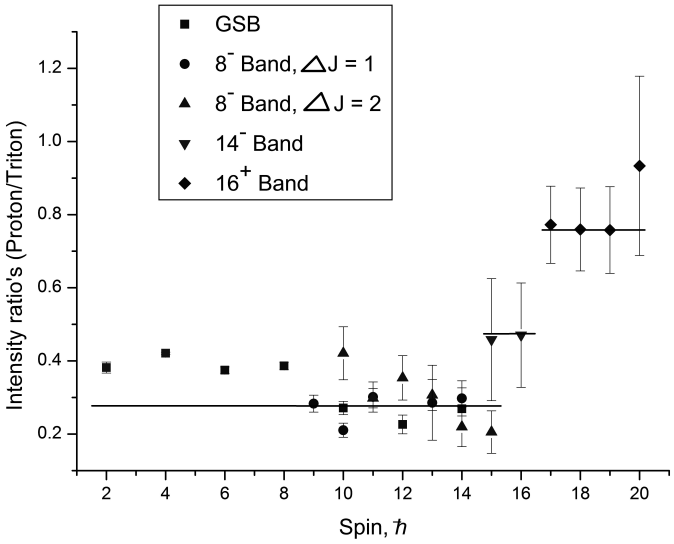

Figure 3. Intensity ratios of the proton to triton-gated gamma-ray yields as a function of spin for $K^\pi = 0^+$ (Ground-State Band), $K^\pi = 8^-$, $K^\pi = 14^-$ and $K^\pi = 16^+$ bands in ^{178}Hf. The lines are drawn to guide the eye.

4. Conclusions

The experimental signatures of incomplete fusion reactions are the observation of strongly forward-peaked charged particles, with a ^{7}Li beam; protons, deuterons, tritons and alphas with much higher energies than observed in conventional fusion-evaporation reactions. These charged particles have been used for a very efficient channel selection. It has been possible to extract the level scheme exclusive to a particular channel for the production of the ^{178}Hf. The relative cross section for various reaction channels could therefore be extracted. There are variations observed between the proton/triton at forward angles and the angular momentum of the residual nucleus, with the different bands showing no change in the yield ratios (proton-triton), but when bands are compared, there are differences. This work has therefore produced data which gives insight to the reaction mechanisms for incomplete fusion processes.

References

[1] D. C. Radford. ESCL8R and LEVIT8R: Software for interactive graphical analysis of HPGe coincidence data sets. *Nuclear Instruments and Methods in Physics Research* ***A***, 361:297–305, 1995.

[2] S. M. Mullins, G. D. Dracoulis, A. P. Byrne, T. R. McGoram, S. Bayer, W. A. Seale, and F. G. Kondev. Rotational band on the 31 yr 16^+ isomer in ^{178}Hf. *Physics Letters B*, 1997.

[3] S. M. Mullins, A. P. Byrne, G. D. Dracoulis, T. R. McGoram, and W. A. Seale. High-spin and rotational states in the stable nucleus ^{177}Hf: Evidence for reaction-dependent spin population. *Physical Review C*, 1998.

[4] T. Fukuda T. Shimoda H. Hiruta T. Inamura, M. Ishihara. Gamma-rays from an incomplete fusion reaction induced by 95 Mev ^{14}N. *Physics Letters*, 68B(1):51–54, 1977.

[5] J. van Driel S. Gonggrip D. C. J. M. Hageman R. V. F. Janssens J. Lukasiak R. H. Siemssen S. Y. van der Werf J. Wilczynski, K. Siwek-Wilczynska. Binary l-matched reactions in ^{14}N + ^{159}Tb collisions. *Nuclear Physics* ***A***, 373:109–140, 1982.

[6] G. D. Dracoulis, A. P. Byrne, T. Kibedi, T. R. McGoram, and S. M. Mullins. Incomplete fusion as a spectroscopic tool. *J. Phys. G: Nucl. Part. Phys.*, 23:1191–1202, 1997.

[7] R. T. Newman, J. J. Lawrie, B. R. S. Babu, M. S. Fetea, S. V. Fortsch, J. V. Nangaleswaran, D. A. Raave, C. Rigollet, J. F. Sharp-Schafer, C. J. Stevens, F. D. Smith, G. F. Steyn, C. V. Wikner, D. G. Aschman, R. Beetge, R. W. Fearick, G. K. Mabala, S. Murray, D. G. Roux, W. Whittaker, and N. J. Ncapayi. Proceedings of Balkan School on Nuclear Physics. *Balkan Physics Letter*, 1998.

[8] J. Gal, G. Hegyesi, J. Molnar, B.M. Nyako, G. Kalinka, J.N. Scheurer, M.M. Aleonard, J.F. Chemin, J.L. Pedroza, K. Juhasz, and V.F.E. Pucknell. The VXI electronics of the DIAMANT particle detector array. *Nuclear Instruments and Methods in Physics Research A*, 516:502–510, 2004.

A new negative parity band in ^{72}Ge

D G Roux, K R Henninger

Department of Physics and Electronics, Rhodes University, Grahamstown.

E-mail: d.roux@ru.ac.za

R A Bark, S Bvumbi, E A Gueorguieva-Lawrie, S M Mullins, S H T Murray, S S Ntshangase, L P Masiteng, and O Shirinda

Ithemba LABS, Somerset West.

Abstract. High-spin states in the nucleus ^{72}Ge were investigated via the ^{70}Zn(α,2n)^{72}Ge reaction at a beam energy of 30 MeV, using the AFRODITE spectrometer. One of the many extensions to the previously existing level scheme included a new, negative-parity, even-spin band. This band is likely the unfavoured signature partner of the band built on the previously-known $I^\pi = 3^-$ state at 2515 keV. The two negative-parity bands are interpreted as involving an aligned octupole vibration which evolves to a four-quasiparticle structure at higher spins. This brief paper presents spectroscopic evidence for the new band, summarizes the spin-parity assignments, and discusses the proposed configuration.

1. Introduction

The ^{72}Ge nucleus is superbly endowed with interesting physics. The yrast band defies description in any one theoretical model, being neither strictly vibrational, nor rotational, and yet the nucleus displays both quadrupole and octupole collective excitations. It exhibits shape coexistence: the spherical, excited 0_2^+ state at 690 keV coexists with the prolate deformed 0_1^+ ground state. In fact the 0_2^+ state is the lowest in the mass region, and lies substantially beneath the first collective 2^+ state at 834 keV. Further, mean-field calculations [1] had predicted the occurrence of tetrahedral magic numbers at N or $Z = 32, 40$. This would make ^{72}Ge, with $Z = 32$ and $N = 40$, a prime tetrahedral candidate. The present investigation was geared to search for tetrahedral states. None were found [2].

The present work, however, details the discovery of a new negative parity band in this nucleus, and its interpretation, in terms of a $\lambda = 3$ octupule excitation. ^{72}Ge has a moderate ground-state prolate deformation of β_2=0.24 [3]. At such a deformation, the proton Fermi surface lies close to two orbitals of opposite parity, namely one of $p_{3/2}$ parentage, and the unique parity $g_{9/2}$ orbital. The scattering of nucleons between such $\Delta j = \Delta \ell = 3$ orbitals is known to give rise to large octupole matrix elements and consequently large octupole correlations, and these are associated with a reflection-asymmetric nuclear shape. The presence of a large number of 3^- terms in the wave function lowers the energy of the 3^- state. This is indeed true for ^{72}Ge, where the previously known 3^-, 2515 keV state is located at the local energy minimum. Octupole excitations have negative parity, and may exist in $K = 0, 1, 2, 3$ forms. They are characterized by strong E1 and /or E3 transitions to the ground state band.

2. Experimental methods and analysis

High spin states in ^{72}Ge were populated via the ^{70}Zn(α,2n)^{72}Ge reaction at a beam energy of 30 MeV, using a self-supporting ^{70}Zn target foil of thickness 5 mg/cm^2. The K=200 separated sector cyclotron facility of Ithemba LABS was used to accelerate the pulsed beam with 58 ns between beam bursts. At an incident energy of 30 MeV the dominant residual nuclei were found to be ^{72}Ge (93%) and ^{70}Ge (3%), where the figures in parentheses denote an approximate percentage of the total cross section. The data also included γ-rays emitted following the Coulomb excitation of ^{70}Zn (4%).

Coincident γ-rays were measured with the AFRODITE [4] spectrometer array comprising nine Compton-suppressed Clover detectors and five four-fold segmented Low Energy Photon Spectrometers (LEPS). The Clovers were positioned in two rings, at 90° relative to the beam direction (five Clovers) and at 135° (four Clovers). The LEPS data were not used in the analysis. The master event trigger demanded a two-or-higher-fold coincidence between any of the detectors, in coincidence with the radio frequency signal from the cyclotron. The coincidence time window was set to 150 ns. Under these conditions, and during some 50 hours of beam time, a data set of ∼868 million coincident events was acquired.

In the off-line analysis, the raw event data from the Clover detectors were sorted into Radware-compatible [5] matrices. These included the matrices used in the coincidence analysis, and also the Polarization and Directional Correlation from Oriented states (PDCO) analysis.

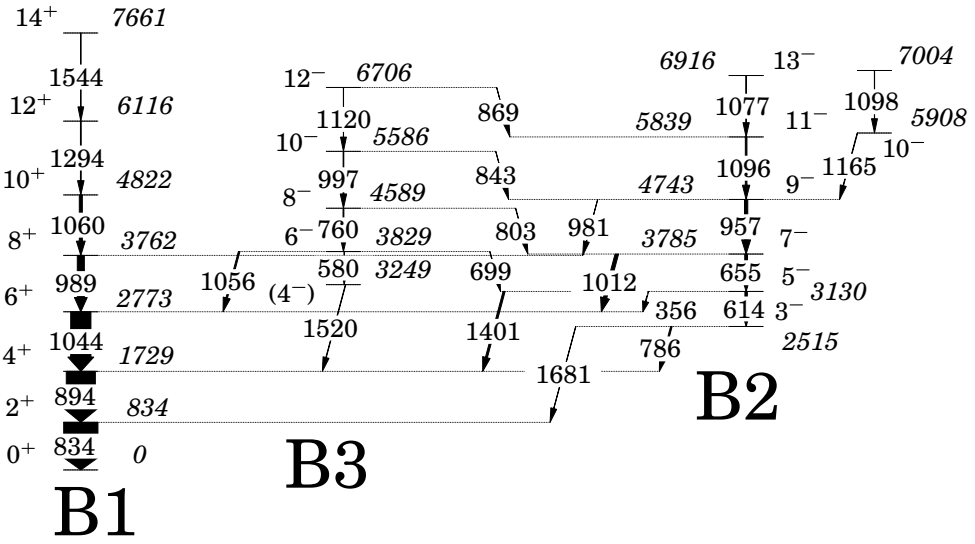

Figure 1. Partial decay scheme for ^{72}Ge, showing only the yrast band (Band 1) and the two negative parity bands. Arrow widths indicate transition intensities; uncertain I^π values appear in parentheses; the energies are in keV.

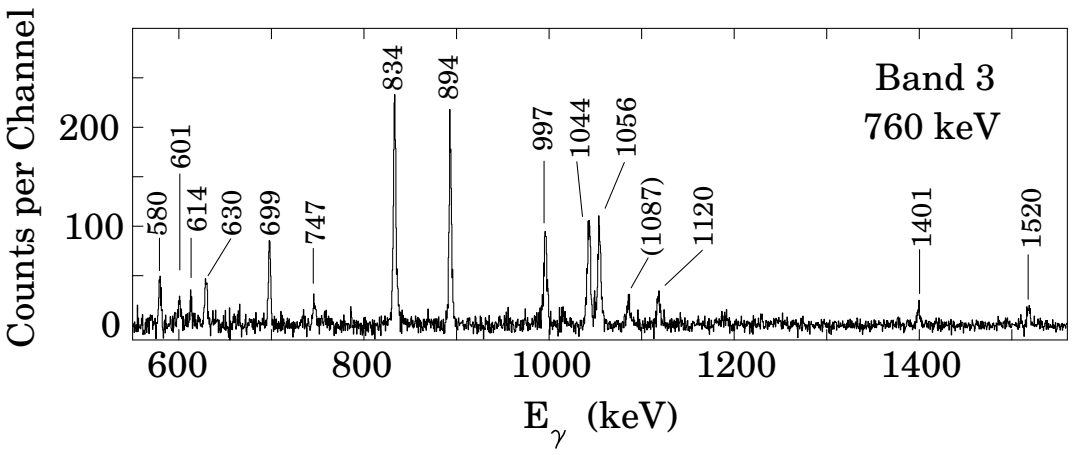

Figure 2. A coincidence spectrum obtained by setting an energy gate on the Clover-Clover matrix at 760 keV. All of the labelled γ-ray peaks could be included in the level scheme, except the one in parentheses. The spectrum clearly shows the transitions linking Bands 2 and 3, below the gating transition. The 630 and 747 keV transitions are not included in Fig. 1.

3. The level scheme

The partial level scheme shown in Fig. 1 displays only the yrast band and the two negative parity bands discussed in this paper. The yrast band and Band 2 were previously known, although the uppermost transition in each is new. Band 3 is observed for the first time. A detailed discussion of the construction of the level scheme may be found in the full paper [2] which is currently in press, and thus only a brief summary is given here of the placement, and of the spin-parity assignments, of Band 3.

The coincidence spectrum displayed in Fig. 2 provides experimental evidence for the placement of Band 3. It shows the γ-rays in coincidence with one of the band members, the 760 keV γ-ray, which feeds the 3829 keV level. In the spectrum one can see not only all the remaining observed band members (580, 997, 1120 keV), but also the links (1056 and 1520 keV) to the yrast band, the decay out (699 keV) of the 3829 keV level to Band 2, the decay out (748 keV) of the same level to one of the positive parity bands (omitted from the level scheme) and the lowest three yrast transitions (834, 894, 1044 keV) below 6_1^+. No transitions *above* 6_1^+ in the yrast band are present in the spectrum. This is proof that the 1056 keV transition which links Band 3 and the yrast band must feed the 6_1^+ yrast level.

The spins and parity of Band 3 were assigned following a thorough PDCO analysis of the linking transitions to Bands 1 and 2, and also of transitions within the band. First of all, the character of the decay-out transitions to levels in Band 2, for which I^π are already known [6], was established. For example, the R_{DCO} values for two of the linking transitions, 699 and 803 keV,

are respectively 0.37(5) and 0.46(9). When these were compared with theoretical predictions, they were found to be consistent *only* with mixed M1/E2 character. The respective polarization anisotropies $P = +9(13)\%, -28(22)\%$ are also consistent with this interpretation, in which $P < 0$ is expected. This established the parity of Band 2 as negative, and the respective spin-parity of the 3829 and 4589 keV states as 6^- and 8^-. In fact the spin-parity of all levels in Band 3, except for the 3249 keV level, could be established by PDCO analysis. Although it was not possible to firmly establish whether the 3249 keV level is 4^- or 5^+, we tentatively assigned it 4^- after considering the alignments shown in Fig. 3C, which suggest that it may indeed be a band member.

4. Interpretation of the negative parity bands

In order to understand the physics of Band 2, it is instructive to compare it with an analogous structure in the N=40 isotone ^{74}Se, which also displays an odd-spin, negative parity band (Band 5 in reference [7]). Band 2 and its isotonic analogue display similarities but also important differences, and both may hold clues to its structure. Among the similarities are the respective band-head excitation energies $E(3^-)$, 2515 and 2349 keV, and initial alignments of $\sim 2.5\hbar$, as shown in Fig. 3A. Further, the decay out of the respective 3^- states have considerable $B(E3)$ strength: 9.2 W.u. for ^{74}Se [7] and 23.7 (51) W.u. for ^{72}Ge [8]. This is a fingerprint of high octupole collectivity. It is therefore likely that Band 2 is an octupole rotational band, like its partner in ^{74}Se. Indeed, the doubly-even Ge isotopes are systematically observed to exhibit octupole vibrational 3_1^- states, for example ^{70,74,76}Ge [9, 10].

The ^{74}Se analogue was interpreted by Döring *et al.* [7] in terms of octupole and 2-qp excitations. It is natural to ask, in view of these strong similarities, whether Band 2 can also be given this interpretation. However several differences between the bands suggest non-identical structures. For example, the significantly larger $B(E3)$ strength for Band 2 suggests greater octupole collectivity than ^{74}Se. The alignments and also the kinematic moments of inertia of these two octupole bands were plotted in Fig. 3 to highlight some of the differences between the isotones. Differences are evident between both the alignments (Fig. 3A), and the kinematic moments of inertia (Fig. 3B). For example, below the AB crossing, the ^{74}Se octupole band maintains an alignment of $\sim 3\hbar$ greater than that of the ^{74}Se yrast band. In ^{72}Ge, however, the alignment of Band 2 displays an upbend at ~ 0.25 MeV, where it changes from $\sim 2.5\hbar$ to $\sim 5\hbar$ greater than the yrast alignment. The kinematic moment of inertia of Band 2 shows an upbend at the same frequency, whereas that of the ^{74}Se analogue is flat. This indicates a structural change in Band 2 at ~ 0.25 MeV which is not exhibited by the ^{74}Se octupole band. This change is also reflected in the plot of the static moment of inertia of Band 2, at $(\hbar\omega)^2 \simeq 0.1$ MeV^2, as shown in reference [2].

We therefore propose that the bottom of Band 2 is an aligned octupole vibration. At higher rotational frequencies, between ~ 0.25 and ~ 0.5 MeV, the wavefunction changes to involve 2 quasiparticles. This accounts for the large $\sim 5\hbar$ difference in alignment between the yrast band and Band 2. The quasiparticles cannot be the A or B neutrons, because at ~ 0.5 MeV the band undergoes the AB crossing, and presumably evolves to a 4-qp structure. The ^{74}Se analogue of this band was also given the 2qp→4qp interpretation [7]. It is not clear to what extent the octupole vibrational character persists to high spins.

We now consider how to interpret the new band, Band 3. At low spins, Fig. 3(C) shows that the alignment patterns of Band 3 and Band 2 are nearly parallel suggesting a common underlying intrinsic configuration. Further, the moments of inertia of these two bands are almost identical below the upbend (in Band 2), as may be seen in the full paper [2]. This may also be expected for bands with similar configurations. In both cases the moments of inertia are significantly larger than that of the yrast band. This may be due to a larger deformation or reduced pairing associated with the proposed 2-qp configuration. The two bands are connected

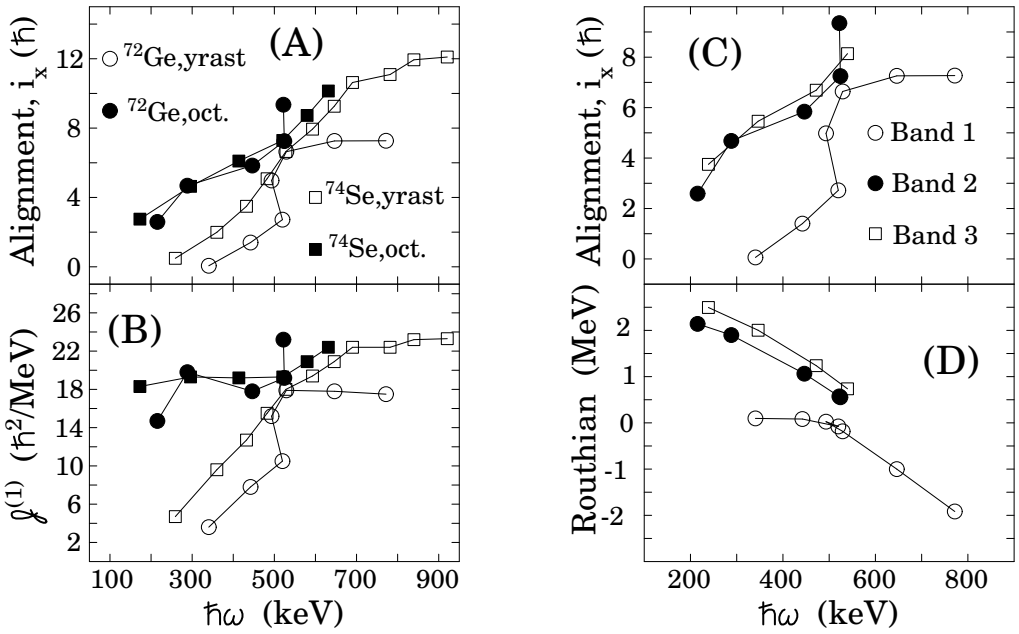

Figure 3. On the left are the alignments (panel A) and kinematic moments of inertia (panel B) of the yrast and octupole bands of the isotones ^{72}Ge and ^{74}Se. These are, respectively, Bands 1 and 2 of ^{72}Ge, and Bands 2 and 5 of ^{74}Se, in reference [7]. On the right are the alignments (panel C) and routhians (panel D) of the yrast band (Band 1) and negative parity Bands 2 and 3 of ^{72}Ge. The chosen Harris parameters, $J_0 = 3.0$ MeV^{-1} and $J_1 = 8.5\ \hbar^4$MeV^{-3}, imposed zero alignment on the first data point of Band 1. Therefore the ordinate denotes relative alignment.

by several $\Delta I = 1$, $M1/E2$ transitions, commonly observed in signature-partner bands. Fig. 3(D) shows that the experimental routhians of the band lie above those of Band 2, with an energy splitting of $\sim$0.42 MeV at frequency 250 keV, and they lie about 2.4 MeV above those of the yrast band. We therefore interpret this even-spin band as the hitherto unobserved $\alpha = 0$, unfavoured signature partner of Band 2.

5. Summary

In this paper we have presented one of several facets of the spectroscopy of the nucleus ^{72}Ge, namely a new negative-parity $\alpha = 0$ band. It is likely that this band and the previously known $\alpha = 1$ negative-parity band are a signature partner pair, the new band being the unfavoured partner. We have interpreted these structures as a rotation-aligned octupole vibration coupled at intermediate spins to 2-qp, and probably evolving to a 4-qp excitation above a rotational frequency of 0.5 MeV. The further evolution of this band with increasing spin awaits investigation.

References

[1] Dudek J, Gozdz A, Schunck N and Miskiewicz M, Phys. Rev. Lett **88**, 252502 (2002).
[2] Roux D G, Henninger K R, Bark R A, Bvumbi S, Gueorguieva-Lawrie E A, Lawrie J J, Mullins S M M, Murray S H T, Ntshangase S S, Masiteng L P and Shirinda O, in press.
[3] Raman S, Nestor C W and Tikkanen P, Atomic Data and Nuclear Data Tables **78**, 1 - 128 (2001).

[4] Newman R T*et al.*, Balkan Phys. Lett. Special Issue, 182 (1998).
[5] Radford D C, Nucl. Instr. Meth. **A361**, 297 (1995).
[6] Morand C, Bruandet J F, Chambon B, Dauchy A, Drain D, Giorni A and Chan T U, Nucl. Phys. **A313**, 45-76 (1979).
[7] Döring J, Johns G D, Riley M A, Tabor S L, Sun Y and Sheikh J A, Phys. Rev. C **57**, 2912 (1998).
[8] Spear R H, At. Data Nucl. Data Tables **42**, 55 (1989).
[9] Ballester F, Casal E and England J B A, Nucl. Phys. **A490**, 227 - 244 (1988).
[10] Chu D, Hsieh S T and Chiang H C, Phys. Rev. C **47**, 183 (1993).

Division C – Photonics

The role of low intensity laser irradiation on collagen production in diabetic wounded fibroblast cells *in vitro*

S M Ayuk, N N Houreld and H Abrahamse[1]

[1]Laser Research Centre, Faculty of Health Sciences, University of Johannesburg, P.O. Box 17011, Doornfontein, Johannesburg, 2028, South Africa

Tel: +27 11 559-6406 Fax +27 11 559-6884

Email: habrahamse@uj.ac.za

Abstract. *Background*: Collagen Type I (Col-I) is a major component of the extracellular matrix (ECM) and is important in wound healing processes. Several studies have shown that Low Intensity Laser Irradiation (LILI) biostimulates Col-I synthesis both *in vitro* and *in vivo*. Diabetic patients are known to suffer from slow-to-heal wounds and collagen production in these patients is impaired. This study aimed to determine if LILI affects collagen production and related cellular responses in an *in vitro* diabetic wounded fibroblast model. *Method*: This study was performed on isolated human skin fibroblasts. Different cell models namely; normal and diabetic wounded were used. Cells were irradiated with 5 J/cm^2 at a wavelength of 660 nm and incubated for 48 or 72 hours. Non-irradiated cells (0 J/cm^2) were used as controls. Biological responses were assessed. Cellular viability (Trypan blue), morphology (Bright Field Microscopy), proliferation (VisionBlue Quick Cell Proliferation Assay), and Col-I (Enzyme Linked Immunoabsorbent Assay, ELISA) were assessed. *Results:* Diabetic wounded cells irradiated with 5 J/cm^2 at 660 nm showed a significant increase in cell migration, viability, proliferation and Col-I. *Conclusion*: This study shows that LILI stimulates Col-I synthesis in diabetic wound healing *in vitro* at 660 nm.

1. Introduction

Impaired wound healing stands as a major diabetic complication and non-healing ulcers remain a serious problem in public health and clinical practice. It is common to note that out of about 15% of people with diabetic foot ulcers (DFUs), 3% suffer from lower limb amputation [1]. Wound healing comprises of a series of composite biological processes summarized in three phases namely inflammation, proliferation and tissue remodeling. These phases involves cytokines, chemokines, clotting factors, various cells and growth factors [2, 3] that must occur in the correct order, at a given time and at favorable intensities to ensure proper healing [4]. Fibroblasts secrete Col-I and other types of collagen which make up the major protein found in the ECM, provides structural scaffold of the cell that maintains the cell integrity and tensile strength in wound healing [5-7]. Studies have shown that diabetes affects collagen production as well as wound healing [8].

In the visible and Near Infra-Red (NIR) spectral range, Low Intensity Laser Irradiation (LILI) is known to accelerate wound healing processes in cell culture, *in vivo* and animal models [9, 10] at different wavelengths and doses [11]. This process is non-invasive and is achieved at wavelengths between 500-1,100 nm and power outputs of 10-200 mW during treatment [10]. Even though LILI is widely used in medical practice, however, there are disputable views on the use of
treatment specifications since there is not enough scientific evidence and guidelines. More so, there is a need for these specifications to be stabilized under optimal conditions in both animal models and clinical practice; hence there is need for more research [12]. The purpose of this study is to determine

[1] To whom all correspondence should be addressed.

if LILI affects collagen production and related cellular responses in an *in vitro* diabetic wounded fibroblast model at 660 nm with a fluence of 5 J/cm^2.

2. Methods

2.1 Cell Culture and Laser Irradiation

In this study, unstressed, "normal" (N) and diabetic wounded (DW) cell models were utilized. Using standardized culture methods [13-16] isolated human skin fibroblast cells (Academic ethics Committee, Clearance Reference Number: 01/06, University of Johannesburg) were regularly cultured. Approximately 6 x 10^5 cells were seeded into 3.3 cm diameter culture plates containing 3 ml complete media and incubated overnight for the cells to attach. Prior to irradiation, a central scratch was created from a confluent cellular monolayer by using a 1 ml sterile disposable pipette to mimic a wounded model [17]. An *in vitro* diabetic wounded model was also established [18]. The normal cells were used as controls. Cells were irradiated using 660 nm diode laser (RGBlase, TECIRL-100G-650SMA, Fremont, California, USA) with a continuous wave emission, 92.8 mW power output, 9.1 cm^2 spot size, 10.22 mW/cm^2, and the cells were exposed to laser irradiation for 8 min 9 s in order to achieve a fluence of 5 J/cm^2 (Figure 1). The effects of laser irradiation on cellular responses for cellular morphology (time lapse), viability (Trypan blue exclusion test), proliferation (MTT and Vision Blue assay) and collagen production (Enzyme Linked Immunosorbent Assay, ELISA) were observed after 48 h and 72 h (Table 1). All lasers were supplied and set up by the National Laser Centre (NLC), Council for Scientific and Industrial Research (CSIR) of South Africa. Irradiations were performed four times (n=4) and each biochemical assay was done in duplicate and the mean used.

3. Results

Table 1. Summary of the methodology and results. Trypan blue was used to determine cellular percentage viability. Irradiated diabetic wounded (DW) cells showed a significant increase in viability compared to non-irradiated normal (N) and DW cells. The Vision Blue™ quick proliferation assay and MTT assay was used to measure cell proliferation. Proliferation of irradiated DW cells was significantly increased at 48 h as compared to both non-irradiated N and DW cells, and decreased at 72 h as compared to non-irradiated N and DW cells.

Method		**48 h**			**72 h**		
		N 0 J/cm^2	**DW 0 J/ cm^2**	**DW 5 J/cm^2**	**N 0 J/cm^2**	**DW 0 J/cm^2**	**DW 5 J/cm^2**
Trypan blue exclusion test	Viability (%)	95 ± 0.8	94 ± 1.8	97 ± 0.1*	83 ± 0.2	94 ± 0.3***	93 ± 0.1***†
Proliferation MTT (Cell Titre Non-Radioactive Proliferation Assay)	Absorbance$_{550}$ nm	0.163 ± 1.32	0.19 ± 7.5***	0.2 ± 4.8***†††	0.23 ± 3.6	0.31 ± 5.5***	0.26 ± 3.8***†††
Vision Blue (VisionBlue™ Quick Cell Proliferation Assay)	Excitation/ Emission Absorbance$_{560/595}$ nm	193 ± 413	225 ± 1513***	237 ± 114***†††	157 ± 0.3	237 ± 222***	213 ± 86***†††

*P<0.05, and ***P<0.001, compared to normal 0 J/cm^2
†P<0.05 and ††† P<0.001, compared to diabetic wounded 0 J/cm^2
± SE

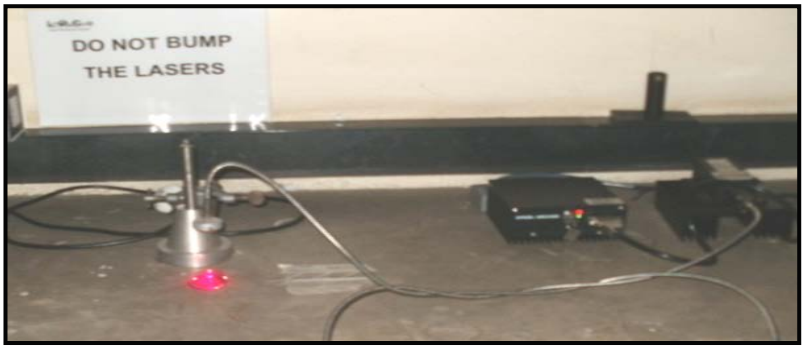

Figure 1. Cells were irradiated from above via fiber optics at a distance which produced a beam area of 9.1 cm^2.

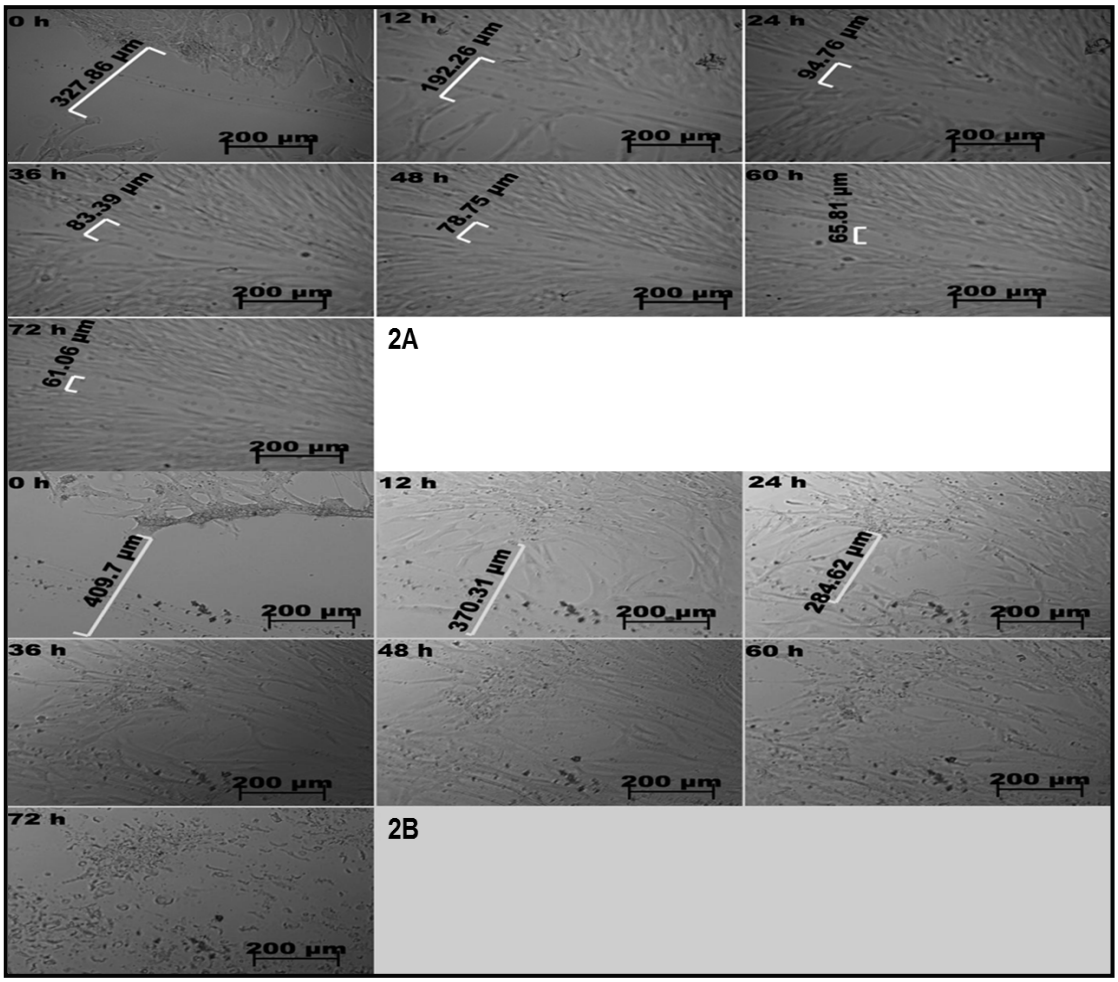

Figure 2. Cellular morphology and migration was assessed over 72 h in non-irradiated (2A) and ir radiated diabetic wounded (2B) cells using time lapse microscopy. Irradiated diabetic wounded cells showed an increase in cell migration and 'wound healing' towards the central scratch compared to non-irradiated diabetic wounded cells. Irradiated diabetic wounded cells showed a decrease in the width of the central scratch from 409.7 µm to 370.31 µm at 12 h and by 36 h the central scratch was closed.

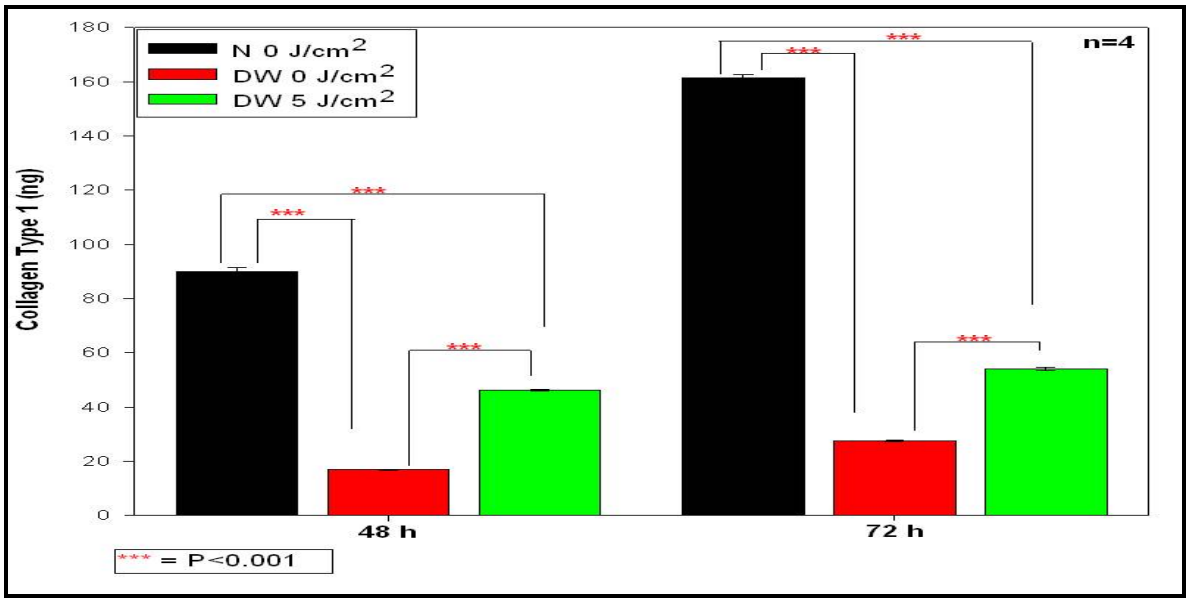

Figure 3. The effect of collagen production was assessed, in normal (N) and diabetic wounded (DW) isolated skin fibroblast cells irradiated with 660 nm at 5 J/cm^2 *in vitro* using ELISA. Non-irradiated N cells (N 0 J/cm^2) and DW cells (0 J/cm^2) were used as controls. There was a significant increase in irradiated DW cells (5 J/cm^2) compared to DW 0 J/cm^2 ($P<0.001$) and a significant decrease compared to the N 0 J/cm^2. Significant probability is shown as *** $P<0.001$.

4. Discussion and Conclusion

Cell migration, viability, and proliferation are various aspects that are affected by LILI *in vivo* and *in vitro* [19]. In this study, irradiated diabetic wounded cells showed an increase in cell migration, and proliferation compared to non-irradiated diabetic wounded cells, with no changes in morphology, however the time lapse showed a decrease in migration over time which is due to contact inhibition (Figure 2). It is important to note here that the variation in the initial central scratch size did not significantly affect the results obtained. This is in line with studies performed by other researchers [20 - 23] who showed that a central scratch could induce a wound environment *in vitro*, even if only 5-10% of the cell surface is affected. The decrease seen in viability and proliferation at 72 h in irradiated diabetic wounded cells correlates with the time-lapse images, and this decrease is due to contact inhibition, this is where cells growth is inhibited when they encounter another cell and 100% confluence has been reached. Col-I increased in irradiated diabetic wounded cells compared to non-irradiated cells at 48 h and 72 h (Figure 3). Normal cells also showed a significant increase compared to diabetic wounded cells. According to Karu (2003) [24], LILI is thought to enhance these biological processes. Increase in cell proliferation could possibly have occurred through changes in the mitochondrial respiratory chain as a primary response to healing leading to increased ATP production [11, 25, 26]. This in turn affects RNA synthesis and changes the expression of various proteins [27, 28]. However in a diabetic situation the process is impaired due to disturbed cell migration. As a result of this disorder, there is poor synthesis of growth factors and vasodilator agents [29].

These results showed that LILI increase Col-I production at 660 nm at a fluence of 5 J/cm^2. These findings are in agreement with Silveira and colleagues (2011) [11] who also observed that LILI produced a stimulatory effect in an animal model at 1 and 3 J/cm^2 [30, 31]. Their study further confirmed that shorter wavelengths and energy densities between 1-5 J/cm^2 increase the tensile force of tendons and speed up collagen production compared to higher energy densities and wavelengths [11].

In conclusion, this study adds to evidence that the effect of LILI is time dependent and more so stimulates Col-I synthesis in diabetic wound healing *in vitro* at 660 nm.

5. Acknowledgement
Many thanks to the National Research Foundation (NRF) South Africa, the University of Johannesburg (UJ), the National Laser Centre (NLC), Council for Scientific and Industrial Research (CSIR) South Africa, and the African Laser Centre (ALC) South Africa who supported this project.

References

[1] Boulton A J, Vileikyte L, Ragnarson T G and Apelqvist J 2005 *Lancet* **366** 1719
[2] Henry G. and Garner W.L. 2003. *Surg Clin North Am*. **83** 483
[3] Cross K.J and Mustoe T.A. 2003 Surg Clin North Am. **83** 531
[4] Mathieu D, Linke J-C, Wattel F. 2006 pp. 401-427.
[5] Ottani V, Raspanti M and Ruggeri A. 2001 *Micron* **32** 251
[6] Rhee S. 2009 *Exp. Mol. Med*. **41** 858
[7] Campos A C, Groth A K and Branco A B. 2008 *Curr Opin Clin Nutr Metab Care.* **11** 281
[8] Cruz J W, Oliveira M A, Hohman T C and Fortes Z B 2000 *Eur. J. Pharmacol*. **391** 163
[9] Huang Y Y, Chen A C H, Carroll J D and Hamblin M R 2009 *Dose Response* **7** 358
[10] Hawkins Evans D and Abrahamse H 2009 *Proceedings of BioS (BO109) SPIE-Photonics West (SPIE, Bellingham, WA)* Paper 7165-8
[11] Silveira P C L, Silva L A, Freitas P T, Latini A, Pinho R A 2011 *Lasers Med Sci* **26** 125
[12] Silva Junior A N, Pinheiro A L, Oliveira M G, Weismann R, Ramalho L M and Nicolau R A 2002 *J. Clin. Laser Med. Surg*. **20** 83
[13] Hawkins D and Abrahamse H 2005 *J Photomed Laser Surg* **23** 251
[14] Hawkins D and Abrahamse H 2006 *J Photomed Laser Surg* **24** 715
[15] Hawkins D and Abrahamse H 2007 *J Laser Appl* **19** 74
[16] Houreld N and Abrahamse H 2010 *Diabetes Technol Ther*. **12** 971
[17] Rigau J, Sun C, Trelles M A and Berns M 1996 *Proc SPIE* **2630** 38
[18] Houreld N and Abrahamse H 2007 *Photomed Laser Surg* 2007 **25** 78
[19] Xu X, Zhao X, Liu T C Y and Pan H 2008 *Photomed Laser Surg* **26** 197
[20] Cory G 2011 *Mol Biol* **769** 25
[21] Goetsch K P and Niesler C U *Anal Biochem* **411** 158
[22] Liang C-C, Park A Y and Guan J-L 2007 *Nat Protoc* **2** 329
[23] Zungu I L, Hawkins Evans D, Houreld N and Abrahamse H 2007 *Afr J of Biochem Res* **1** 60
[24] Karu T 2003 *Biomedical Photonics Handbook* 2003 **48** 1
[25] Hashmi J T, Huang Y-Y, Osmani B Z, Sharma S K, Naeser M A and Hamblin M R 2010 **2** S292 [26] Houreld N N, Masha R T and Abrahamse H 2012 *Lasers Surg Med* **44** 429
[27] Lavi R, Shainberg A, Friedmann H, Shneyvays V, Rickover O, Eichler M, Kaplan D and Lubart R 2003 *J Biol Chem* **278** 40917
[28] Gavish L, Asher Y, Becker Y and Kleinman Y 2004 *Lasers Surg Med* **35** 369
[29] Kofler S, Nickel T and Weis M 2005 *Clinical sci*. **108** 205
[30] Maiya G A, Kumar P and Rao L 2005 *Photomed Laser Surg* **23** 187
[31] Carvalho P T, Mazzer N, Reis F A, Belchior A C and Silva I S 2006 *Acta Cir Bras* **21** 176

Compensating Birefringence Effects in Optical Fibre for Polarisation Encoded QKD

S Pillay[1], A R Mirza[1, 2], T B Gibbon[3]and F Petruccione[1, 2, 4]

[1] Quantum Research Group, School of Physics, University of KwaZulu-Natal, Private Bag X54001, Durban 4000, South Africa
[2]QZN Technology, Innovation Centre, Howard College Campus, University of KwaZulu-Natal, South Africa
[3]Department of Physics, Nelson Mandela Metropolitan University (NMMU), Port Elizabeth, South Africa
[4]National Institute for Theoretical Physics, South Africa

E-mail: 206507614@ukzn.ac.za

Abstract. Fibre optic cables provide a convenient channel to implement QKD. In order to implement any polarisation encoded protocols, the state of polarisation of photons must be maintained within the fibre channel. Birefringence due to impurities in the fibre or environmental stresses causes the polarisation of light to be altered when passed through a fibre. If the fibre is fixed and the environment is unchanged, the environmental stresses result in a unique and constant change of polarisation. This can be compensated by rotating the polarisation of each photon appropriately before being measured. If the fibre is subjected to variable conditions, the change in the state of polarisation of photons must be monitored and adjustments must be made at suitable time intervals. These changes can be observed using a test signal and the effects may be compensated with the use of a polarisation controller. While orthogonal states are corrected, protocols such as BB84 and B92 use non-orthogonal basis sets, hence two compensators must be used. However, we propose that by using an appropriate search algorithm, the polarisation controller can isolate the plane on the Poincaré sphere that passes through both bases, thus compensating non-orthogonal states with one device.

1. Introduction

With the increase in global data traffic in recent years, secure communications has become essential. Cryptography ensures the security of such data by using cryptographic protocols to generate a unique and secret key to encode the data during transmission. Conventional methods of encryption rely on the complexity of a mathematical algorithm to secure the key [1].While currently effective, advancements in mathematics and computing may compromise some aspects of conventional cryptography. Quantum Key Distribution (QKD) relies on the laws of physics, and not the complexity of a numerical algorithm, to ensure the security of the key, therefore it is not vulnerable to technological advances [2]. In order to gain unauthorized information about the cryptographic key the eavesdropper will have to measure or copy a part of the signal. These processes violate the laws of quantum mechanics, in particular the Heisenberg Uncertainty principle [3] and the 'No Cloning' theorem [4]. These two laws ensure that any interception by an eavesdropper will result in a noticeably high error rate in the

transmission of the key. The mutual information between the sender and the eavesdropper may increase due to limitations in the implementation of QKD as a result of background noise and imperfections in the apparatus. This sets an upper bound for the quantum bit error rate of the system. If the error rate is found to be above this threshold, an eavesdropper is assumed and the key is discarded [5].

The data transferred between the transmitter and receiver is in the form of a quantum two-level system (qubit). The qubit state is shown as a linear superposition of two basis states, denoted by $|0\rangle$ and $|1\rangle$. This paper will focus on polarization encoded QKD schemes. In this case, the basis states are implemented as states of polarization (SOP), e.g. $|0\rangle$ may represent a vertically polarised state and $|1\rangle$ may represent a horizontally polarised state [6]. QKD protocols such as BB84 [6] and B92 [7] can be implemented through polarization encoding. These protocols utilise two non-orthogonal polarisation bases, e.g. the rectilinear basis and the diagonal basis. For this example, the resulting qubits are the four available States of Polarisation (SOP): vertical, horizontal, right diagonal and left diagonal. In the case of the B92 protocol, only one state from each basis is needed.

2. A fibre quantum channel

QKD protocols can be easily implemented over a fibre optic link. Light propagates through fibre by means of the processes of total internal reflection and waveguide refraction [8], hence it has the advantage of being independent of a line of sight connection between the transmitter and receiver. A fibre link for QKD is however, not suitable for distances longer than 200 km [9, 10]. This would require a quantum amplifier, which is not yet developed. Impurities and manufacturing errors in the fibre absorb photons which causes a minimum loss of 0.2 dBm per km. Therefore, the qubits become too weak to measure after long distances [11]. Coupling a fibre channel to a free space channel would allow for greater transmission distances since free space has a lower attenuation. It would also allow for various mediums of communication to be used in one meshed network. In order to implement such a setup, it is necessary to establish an untrusted interface between the fibre network and the free space network. It is easier to implement polarization encoding over a free space channel since the atmosphere is not birefringent, therefore, polarization encoding must also be implemented through fibre. This poses a problem since a standard single mode fibre optic cable is not able to maintain the SOP of light that is transmitted through it due to birefringence [12]. Birefringence refers to the refractive differences between orthogonal components of the SOP of light. This causes the SOP of light to be rotated as it is transmitted through fibre and this effect must be compensated in order to accurately measure the transmitted qubits. Additionally, any changes in the surrounding environment will alter the birefringence of the fibre, so compensation of the SOPs must be done in real time [13].

3. Compensating for the changes in SOP

In order to compensate for the changes in SOP caused by the fibre channel, the SOP of each photon at the transmission wavelength must be rotated back to its original state. This is done by passing the photons through a polarisation controller. The fibre squeezers of the polarisation controller simultaneously bend the fibre to induce a ‘reverse rotation’ of the SOP of each photon. Since each photon in the quantum signal has a unique SOP, the polarisation controller will have to adjust each one separately. This, however, poses two concerns. Firstly, the polarisation controller must be able to compensate each photon without prior knowledge of what each respective SOP is. This is necessary in order to maintain the security of the QKD protocol being utilised. Secondly, polarisation controllers must not measure the SOP of any photons, since this will destroy the encoded information before Bob can receive it. This means that the polarisation controller cannot measure the current SOP and then make adjustments to it accordingly. Instead, the setting for the polarisation controller must be independently determined prior to the QKD transmission and any adjustments made to the SOPs of

photons must be done passively. In order to determine the correct polarisation controller setting, test pulses must be deployed into the system using either time division multiplexing or wavelength division multiplexing. The polarisation controller must be adjusted to compensate the test pulses and thereby passively compensate the quantum signal.

A good example of this implementation is found in [11]. This setup requires four SOPs however, two polarisation controllers are utilised to compensate these four states. This is because the compensation of one state will automatically correct its orthogonal state. This is shown by applying the Jones matrix that represents one of the phase retarders in a polarisation controller to the Jones vector of a chosen SOP [8]. As an example, equation (1) shows the Jones matrix of a quarter wave plate with its fast axis aligned vertically applied to a quarter wave plate.

$$e^{i\frac{\pi}{4}}\begin{bmatrix}1 & 0\\ 0 & -i\end{bmatrix}\begin{bmatrix}0\\ 1\end{bmatrix} = e^{i\frac{\pi}{4}}\begin{bmatrix}0\\ -i\end{bmatrix} \quad (1)$$

Equation (2) shows the same calculation done with a horizontal SOP.

$$e^{i\frac{\pi}{4}}\begin{bmatrix}1 & 0\\ 0 & -i\end{bmatrix}\begin{bmatrix}1\\ 0\end{bmatrix} = e^{i\frac{\pi}{4}}\begin{bmatrix}1\\ 0\end{bmatrix} \quad (2)$$

The resulting vectors in equations (1) and (2) are orthogonal and similar results can be obtained using other sets of orthogonal SOPs. This shows that when two orthogonal SOPs undergo the same transformation using a phase retarder, the resulting vectors will also be orthogonal. Therefore, if a polarisation controller is set to correct for the vertical SOP, the horizontal SOP will undergo the same changes and will also be compensated. Therefore, only one polarisation controller is required per basis.

4. Using one polarisation controller to compensate for both bases

In the proposed scheme, shown in Figure 1, only one polarisation controller is required. In this case, the polarisation controller is in the form of a polarisation locker. The polarisation locker includes many internal piezoelectric polarisation controllers which are driven by an in-line polarimeter and digital signal processor which form an internal feedback loop as shown in Figure 2 [14]. The locker can be pre-programmed so that all output SOPs are fixed. The internal polarimeter will measure the output SOPs and communicate the adjustments that need to be made to the polarisation controller via the feedback loop. Using this method, the polarisation locker is able to 'lock' onto a specified SOP. Alternatively, the user can manually increment the value of the SOP along a grid superimposed onto the Poincaré sphere to a specific value.

The locker is used to isolate one point on the Poincaré sphere and fix all incoming light to that SOP. In this setup, the locker is used in a time division multiplexed scheme and a test signal is used to achieve the settings for the locker. The quantum signal is periodically stopped to allow the test signal through the quantum channel. The test signal must have only one SOP e.g. vertical. The SOP locker is then used to return the SOP back to vertical after it undergoes changes in the quantum channel. This would compensate the horizontal SOP as well. Since only one SOP locker is used in this setup, the locker must also compensate the diagonal SOPs. This can only be done if the locker is used to isolate the plane on the Poincaré sphere that passes through all four SOPs being used in the QKD transmission [15]. This is shown in Figure 3. A step search must be used on the locker to correctly identify the plane on which all four SOPs exist. Usually, the locker fixes on one point on the Poincaré sphere, but this point can lie on any path. If the path is specified as the equatorial plane of the sphere,

all four SOPs will be correctly compensated. Thus, allowing for polarisation compensation with just one polarisation controller. This method has been implemented manually and has shown successful results. The single photon detection rates measured in this setup corresponded well to the initial SOPs set by the transmitter. The detector measuring the initial SOP obtained a maximum detection rate and the detector measuring the orthogonal SOP obtained only dark counts which correspond to a zero reading.

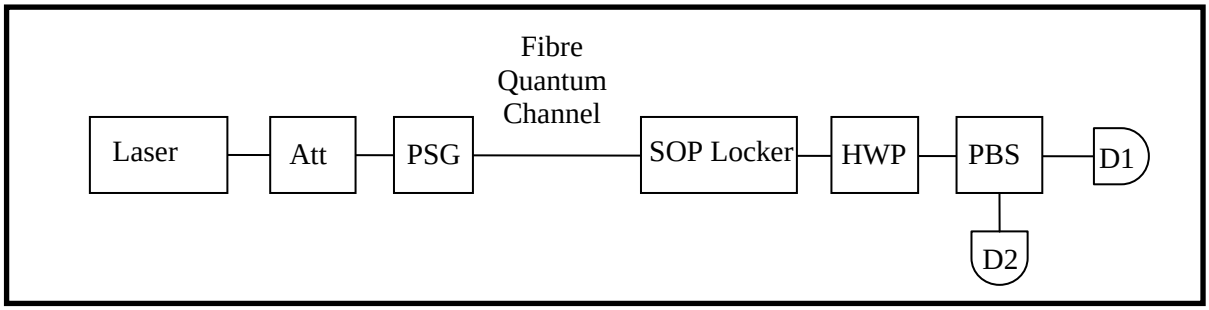

Figure 1: The proposed setup for a polarization encoded QKD scheme. The laser pulses are first passed through an optical attenuator (Att) which creates pseudo-single photons. Each photon is then assigned an SOP with the polarization state generator (PSG) and is transmitted through the quantum channel to the receiver. The receiver then uses the SOP locker to compensate for changes in polarization. A half wave plate (HWP) is used to select the basis in which the receiver will measure each photon and finally, the photons are separated at a polarization beam splitter (PBS) to be measured at one of two detectors.

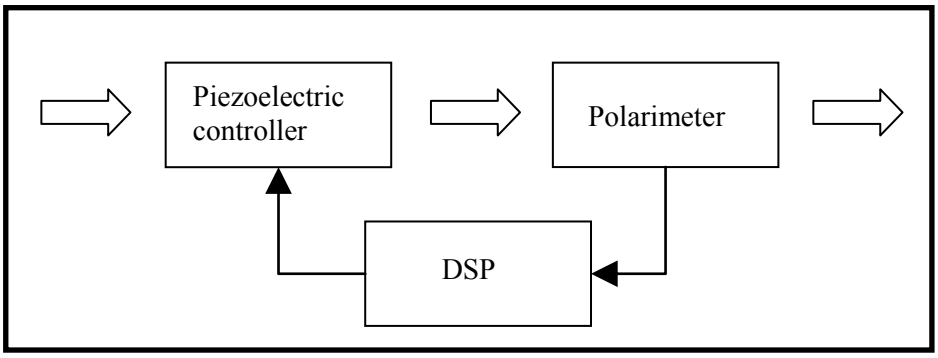

Figure 2: The internal loop of an SOP locker.

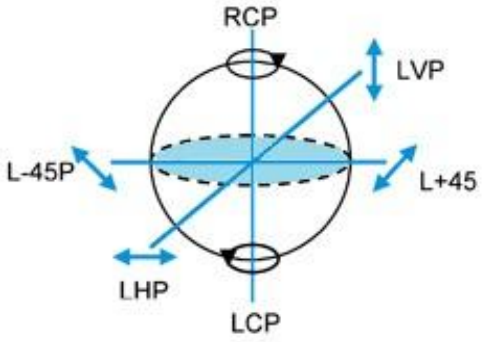

Figure 3 : A diagram of the Poincaré sphere highlighting the equatorial plane which passes through the four linear SOPs. The SOP locker is used to isolate this plane and rotate all SOPs back to their original form.

5. Conclusion

In order to effectively implement polarisation encoded quantum key distribution in fibre optic cables, the birefringence effects of fibre must first be overcome. In order to correct for birefringence, the changes in SOP caused by fibre must first be monitored. A time division multiplexed scheme can be used to test the changes in SOP and polarisation controllers can be used to compensate these changes. In order to use just one polarisation controller, a polarisation locker can be used to isolate the plane on the Poincaré sphere on which both the non-orthogonal bases are located. By using an appropriate search algorithm, the SOP locker can locate this plane and effectively compensate both bases. Future work will focus on automating the search algorithm and integrating it into the QKD system so that polarisation encoded QKD can be implemented in fibre.

Acknowledgements

This work is based on research supported by the South African Research Chair Initiative of the Department of Science and Technology and National Research Foundation.

References

[1] Diffie W and Hellman M E 1976New Directions in Cryptography *IEEE Trans. on Info. Theory* **IT-22** 644-654

[2] Gisin N, Ribordy G, Tittel W and Zbinden H 2002 Quantum Cryptography *Review of Modern Physics* **74**, 145

[3] Krane K 1996 *Modern Physics* (New York: John Wiley& Sons)

[4] Wootters W K and Zurek W H 1982 A Single Quantum Cannot Be Cloned *Nature* **299** 802-803

[5] Capraro I 2008 Advanced Techniques in Free Space Quantum Communication PhD Thesis University of Padua 33-34

[6] Bennet C and Brassard G1984 Quantum cryptography:Public Key Distribution and Coin Tossing*Proc. of IEEE International Conference on Computers Systems and Signal Processing* 175-179

[7] Bennet C 1992 Quantum Cryptography Using Two Nonorthogonal States *Physical Review Letters* **68** 3121-3124

[8] Hecht E 2001 *Optics* (Reading, MA: Addison-Wesley)

[9] Hubel H, Vanner M R, Lederer T, Blauensteiner B, Lorunser T, Poppe A and Zeilinger A 2007 High-fidelity Transmission of Polarization Encoded Qubits from an Entangled Source over 100 km of Fiber *Optics Express* **15** 7853-62

[10] Hughes R J, Morgan G L and Peterson C G, 2000 Quantum Key Distribution Over a 48 km Optical Fibre Network *Journal of Modern Optics* **47** 533-547

[11] Xavier G B, Walenta N, Vilela de Faria G, Temporo G P, Gisin N, Zbinden H and von der Weid J P 2009 Experimental Polarization Encoded Quantum Key Distribution over Optical Fibres with Real-time Continuous Birefringence Compensation *New Journal of Physics* **11** 045015

[12] [Online]www.lunatechnologies.com/files/22pmdweb.pdf

[13] Xavier GB, Vilela de Faria G, Temporo G P and von der Weid J P 2008 Full polarization control for fiber optical quantum communication systems using polarization encoding *Optics Exress* **16** 1867-1873

[14] [Online] http://www.thorlabs.com/newgrouppage9.cfm?objectgroup_id=1769

[15] [Online] spie.org/x32375.xml

A novel 2-D$^+$ magneto-optical trap configuration for cold atoms

M. Semonyo[1], S. Dlamini[1], M. J. Morrissey[1] and F. Petruccione[1,2]

[1] Quantum Research Group, School of Chemistry & Physics, University of KwaZulu-Natal, Westville, Durban, South Africa.
[2] National Institute for Theoretical Physics, School of Chemistry & Physics, University of KwaZulu-Natal, Westville, Durban, South Africa.

E-mail: Semonyo@ukzn.ac.za

Abstract. Presented in this paper is a proposed novel coil configuration for a 2-D$^+$ magneto-optical trap. The design is based on the cancellation of magnetic fields along a common radial axis of two pairs of coils positioned orthogonal to eachother in order to create a zero magnetic field along this axis while maintaining a sharp linear gradient along the other axes. This novel design is more compact than standard methods and achieves the same magnetic field properties with less electrical power consumption.

1. Introduction

The field of cold and ultra-cold quantum gases has lead to many significant breakthroughs in numerous fields of physics such as quantum optics, solid-state physics, precision measurement and metrology [1]. In order to create a Bose-Einstein Condensate (BEC) it is crucial to do so within an ultra-high vacuum environment to reduce the background collisions and thus extend the lifetime of the condensate. It is therefore common to create a double chamber system whereby atoms are first pre-cooled in a chamber with a high atomic background density and subsequently transferred into a separate chamber where there are no background atoms, and thus there is less loss of atoms due to thermal collisions. In this second chamber the atoms are again trapped and further cooled to form the Bose-Einstein condensate.

Many techniques have been experimentally implemented to transfer pre-cooled atoms between the chambers. Techniques such as Zeeman-slowers were initially implemented with great success. In this regime a thermal atom beam emerges from an 'oven' and is decelerated by a counter-propagating laser beam, while the changing Doppler shift, due to the reduced speed of the atoms, is compensated by an inhomogeneous magnetic field along the deceleration path [2]. More recently, techniques such as a low velocity intense source (LVIS), which rely on the optical cooling, have been used. In this method, a 3-D magneto-optical trap (MOT) is created with a small hole drilled on one of the retro-reflecting mirrors in order to produce a flux of low velocity atom beam [3]. Other techniques rely more on the magnetic transfer of atoms, which involves creating a 3-D MOT in the high-pressure chamber and magnetically guiding it into the low vacuum chamber. This can be performed by using moving coils [4], a series of fixed coils [5] or a magnetic wave-guide [6].

Today, the 2-D$^+$ MOT is the most popular technique to pre-cool and transfer atoms. It is compact, robust, relatively easy to setup and results in an intense flux of atoms entering the BEC chamber. In this paper we present a novel coil configuration for the 2-D$^+$ MOT which provides the same magnetic field as standard configurations but does so with less electrical power consumption. The novel coil configuration also leads to an overall more compact system and thus there are less stringent demands on the design of the vacuum system. This setup is an adaption of a previous MOT experiment which has been built in UKZN [7]. At this point it should be noted that this is a proposed setup and that it is

not yet a reality. Also presented this paper is a brief overview of the entire experiment.

2. Experimental Setup

Bose-Einstein Condensation physics is one of the most multidisciplinary topics in physics. These experiments require ultra-high vacuum (UHV) technology, laser frequency stabilisation, high quantum efficiency imaging systems, high power magnetic coils, a sophisticated timing system as well as the associated state-of-the-art electronics. Given that the main focus of the paper is the 2-D$^+$ MOT, only the vacuum system, the laser system and the 2-D$^+$ itself will be presented.

2.1. Vacuum System

The final stage in creating a BEC is evaporative cooling which relies on elastic collisions between trapped atoms for re-thermalisation. Given that the process of magnetic trapping and evaporative cooling can take over 40 seconds, these procedures must be performed in very low vacuum environment to prevent large atom losses due to background collisions. On the other hand, to create a MOT with a large number of atoms, which is one of the first steps in creating a BEC, a relatively high background pressure of rubidium atoms is required. It is for this reason that our vacuum system is partitioned into two different chambers, which are separated by a differential pumping hole (DPH). The high-pressure side is referred to as the 2-D MOT section and is shown on the left-hand side of figure 1 whereas the low-pressure side is referred to as the BEC section and shown on the right-hand side of figure 1. The DPH that separates these two sections has a diameter of 2 mm and a length of 26 mm. This is large enough to allow the atom beam from the 2-D$^+$ MOT to pass through unobstructed with minimal atom loss and small enough to allow the two vacuum sections to maintain a differential pressure of three orders of magnitude. Both vacuum sections contain a chamber where optical access is provided by optical viewports, which allow the cooling, optical pumping and imaging beams to interact with the atom cloud.

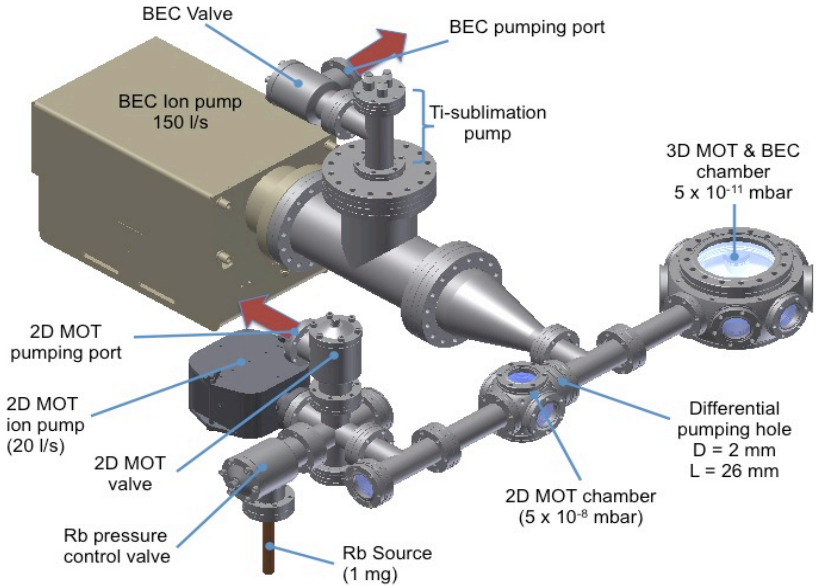

Figure 1: Illustration of the current vacuum system at UKZN.

An ion pump in each vacuum section maintains the UHV that is achieved during the bake-out procedure where the vacuum is heated to ~350°C for two weeks. During this process the out-gassed materials are removed using two turbo-molecular pumps which are backed-up by a single rotary vain pump. There is also a titanium sublimation pump which can be used to decrease the base pressure if it rises due to continuous use. This pump creates a very thin porous layer of titanium on the vacuum internal surface which absorbs background gases and thus reduces the vacuum pressure.

The 2-D MOT section contains a 1 mg ampule of rubidium which constantly out-gases and thus fills this side of the vacuum system with rubidium vapour resulting in the pressure of ~$5x10^{-8}$ mbar. This pressure can be controlled using the 'Rb pressure control valve' as indicated in figure 1. These thermal background atoms are cooled using the laser cooling beams and a novel coil configuration combined together in the form of a 2-D^+ MOT. The atoms are then optically pushed through the DPH into the low pressure section of ~$5x10^{-11}$ mbar where they enter the BEC chamber and are again cooled in the form of a 3-D MOT and will eventually form the BEC.

2.2. Laser System

Figure 2 (a) shows the hyperfine structure of the $5^2S_{1/2} \rightarrow 5^2P_{3/2}$ Rb-87 transition as well as the required laser frequencies necessary to build a BEC experiment. There are four main frequencies necessary in such an experiment, namely, the cooling, imaging, optical pumping, and repumping frequencies. Figure 2 (b) gives the general schematic implemented to derive and distribute these beams. As can be seen, the various sections are coupled together using polarisation maintaining (PM) optical fibres which allow the beams to be easily transported around the experiment.

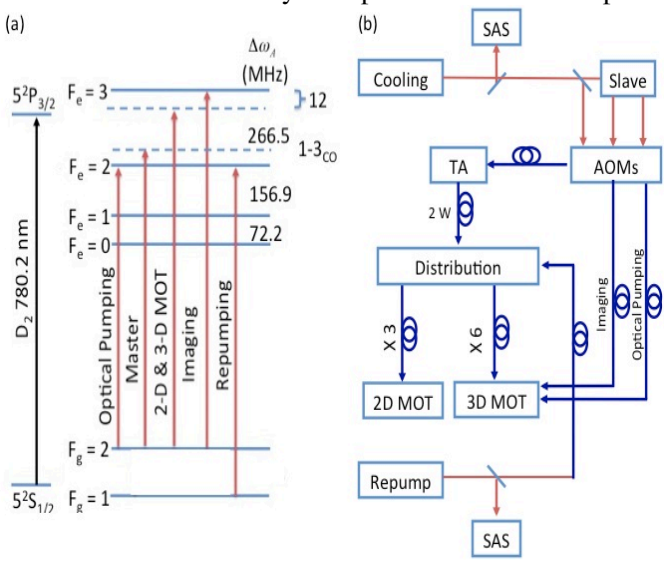

Figure 2: (a) The hyperfine structure of ^{87}Rb with all the necessary optical transitions and corresponding frequencies shown. (b) A block diagram showing an overview of the laser system layout.

The master cooling laser provides the initial seed power for the cooling, imaging and optical pumping beams as shown in figure 2 (b). A small percentage of the laser output is directed to a saturated absorption spectroscopy setup where the lasers is locked to the $F_g = 2 \rightarrow F_e = (1\text{-}3)_{CO}$ crossover peak of the Rb-87 D_2 line. A detuning of 12 MHz from the $F_g = 2 \rightarrow F_e = 3$ cooling transition, which compensates for the Doppler shift, is provided via an acousto-optical modulator (AOM) in a double pass configuration. Given that the correct frequency has been generated for the cooling process, 10 - 20 mW of optical power is injected into a tapered amplifier (TA) which generates a up to 2 W output beam at this frequency. This beam is then sent to a distribution board where a series of waveplates and polarisation beam-splitters divide the beam into its various beam components. Three beams are required for the 2-D^+ MOT and six beams are required for the 3-D MOT. These are coupled to polarisation maintaining (PM) optical fibre and sent directly to the experiment. In addition to the cooling beams, we require a repumping beam in order to keep the atom resonant with the cooling laser. This is performed using a separate ECDL locked to the $F_g = 1 \rightarrow F_e = 2$ transition. The repump beam is then sent to the beam distribution section where it is coupled to the MOT fibres.

To perform the tasks of absorption imaging and optical pumping, an additional two frequencies are derived from the master cooling laser. Given that our cooling laser has a low output power we use a slave laser to provide power for these beams. The slave laser is injected with 2 mW of master power and thus its output is of the same frequency. Two separate AOMs are used to shift the imaging and optical pumping frequencies to their relevant transition. The imaging beam is shifted on resonance with the $F_g = 2 \rightarrow F_e = 3$ cooling transition and the optica pumping beam is shifted to the $F_g = 2 \rightarrow F_e = 2$ transition. These beams are coupled to fibre and then sent directly to the experiment.

3. A Novel 2-D Magneto-Optical trap

A 2-D MOT cools and traps atoms in two spatial dimensions allowing atoms to move freely along the remaining axis. This is done by using elliptical beams, which perform laser cooling in two spatial dimensions, in combination with a magnetic field which traps the atoms in the same two spatial dimensions. Thus atoms are trapped in two dimensions but are free to move along the third spatial dimension. A 2-D$^+$ MOT is an extension of this where a low powered push beam is used to preferentially push the atoms in one particular direction along the untrapped axis. This creates a high flux of cold atoms in this axis, which enter the BEC chamber.

3.1. The 2-D MOT Magnetic Fields

The magnetic field required to create a 2-D MOT is a linear quadrupole field. This field can be produced using four equally spaced straight current carring bars in a rectangular arrangement with currents flowing in alternate directions for neighbouring bars. In practice this is can be performed using either one or two pairs [8] of rectangular coils in anti-Helmholtz configuration as shown on figure 3 (a) and (b). These coils create a linear gradient on the x- and y- axis but a zero magnetic flied along the z-axis. In the case where one coil pair is used, the short end bars of the rectangular coils create a magnetic field that can disrupt or shorten the length of the zero magnetic field along the z-axis. This effect can be eliminated by increasing the length of the coils along the z-axis, but this results in an increase in electrical power consumption. In the case of two coil pairs, again there is an increase in electrical consumption due to the addition of two extra coils, but the magnetic field gradient is double that of a single pair and the field generated by the end bars cancel each other allowing the length of the coils to be shorter. The magnetic field created by the rectangular coils, B_{rect}, can be written as $B_{rect} = \alpha_{rect}(x,-y,0)$ where α_{rect} is the over all axial gradients in the x- and y-axis.

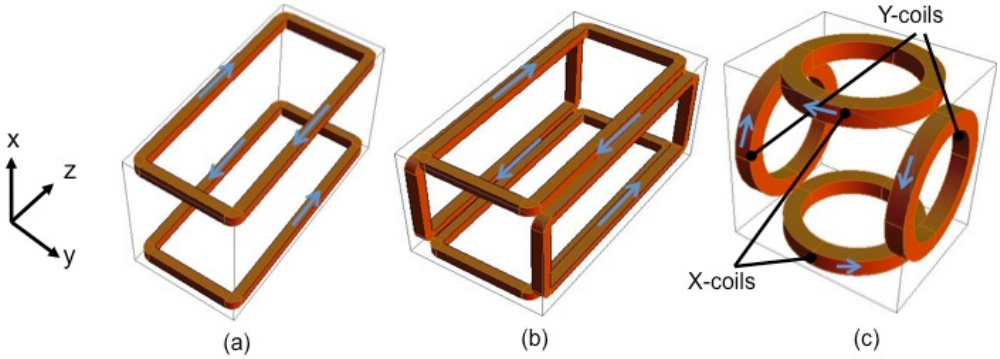

Figure 3: Illustrations of coil configurations for the 2-D MOT.

Figure 3(c) illustrates our novel coil configuration for generating the same magnetic field. This consists of two pairs of circular coils in anti-Helmholtz configuration. A single pair of circular coils in anti-Helmholtz configuration creates a spherical quadrupole field where the gradient in the axial direction is twice that of the radial axes. Thus the magnetic field, B, created by each individual pair of coils, is given by $B_{x-coil} = \alpha_x(x,-y/2,-z/2)$ and $B_{y-coil} = \alpha_y(x/2,-y,z/2)$, where α represents the axial

gradient of that specific coil pair. The total magnetic field generated by the two pairs of coils, B_{tot}, is the sum of each of the individual coil pairs and is thus given by

$$B_{tot} = \left[\left(\alpha_x + \alpha_y/2\right)x, \left(-\alpha_x/2 - \alpha_y\right)y, \left(\alpha_x/2 - \alpha_y/2\right)z\right] \quad (1)$$

From this equation it is clear that the axial gradient of one coil pair adds with the radial gradient of the other coil pairs in both the x- and y-axis. However, in the z-axis, both radial fields generated by the individual pair subtract from each other. Thus, if both coils are the same and have identical gradients, $1.5\alpha_x = 1.5\alpha_y = \alpha_{tot}$, a zero magnetic field is created along the z-axis. The individual and combined effect of the coils for all spatial dimensions can be clearly seen on examination of figure 4(a). In this case equation 1 becomes B_{tot} $B_{tot} = \alpha_{tot}(x, y, 0)$ which is of the same format as the standard 2-D MOT coils. Contour plots of the magnetic field can be seen in figure 4 (b), where the zero magnetic field along the z-axis can be clearly seen in the z-x plot and the spherical quadrupole field can be seen in the x-y plot.

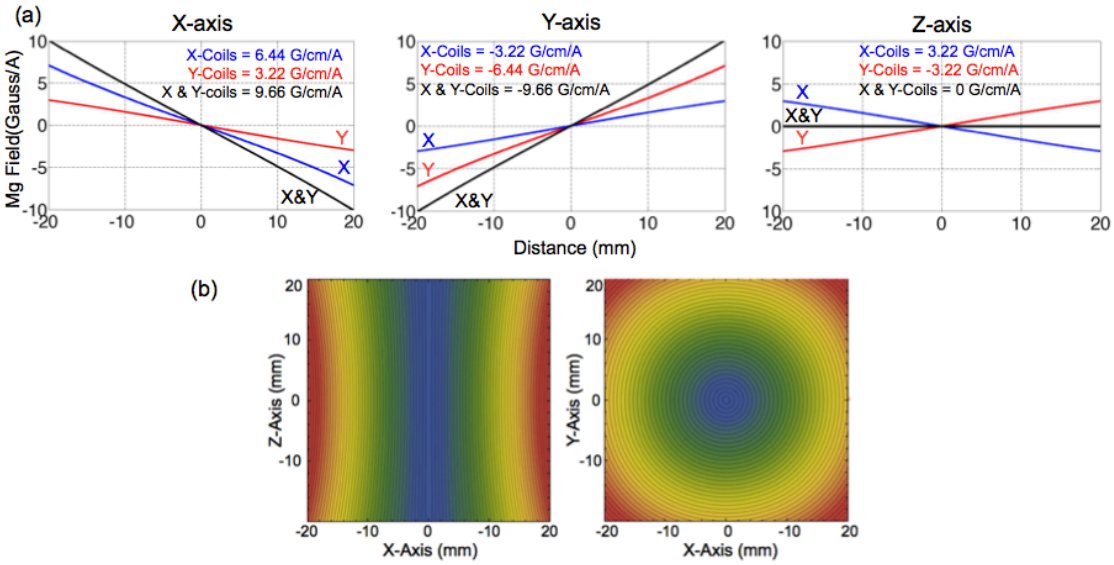

Figure 4: (a) Line plots and (b) contour plots of the magnetic fields created by the circular 2-D MOT coils in the respective axes.

Bolpasi *et al* [9] use a similar coil configuration to create a linear quadrupole magnetic field as part of an Ioffe Pritchard trap replacing the usual race-track shaped Ioffe bars with the two pairs of circular coils. In this case the authors present a plot of the magnetic field gradient per unit power as a function of varying coil length which is a direct measure of the efficiency of the coil configuration. From this analysis it is clear that the higher gradients per unit power are achieved for the smaller coil length. In fact, compared to the circular configuration, coils of typical length can lose up to 60% of its gradient per unit power. This also applies for the above mentioned novel configuration for the 2-D MOT.

3.2 The Complete 2-D⁺ MOT

The derivation of the optical power for the 2-D$^+$ MOT, as well its associated frequency relative to an atomic transition is briefly explained in section 2.2. This optical power arrives to the vacuum chamber via PM fibres. On exiting the fibre the beam expands freely and is then collimated using a convex lens creating a beam with a circular cross-section. This beam is then polarised using a quarter wave-plate to create the σ^+/σ^- polarised light necessary for laser cooling. The polarised beam is expanded in one dimension using a spherical cylindrical concave lens and collimated again using a large cylindrical convex lens. This results in a 68 x 17 mm beam which is cut to 40 x 17 mm (which is the optical

access limitation of the vacuum view-ports) which gives a more even power distribution along the larger dimension. The expansion of both the 2-D$^+$ MOT beams can be seen in figure 5(a). Also shown is the mechanical housing of the optics which makes the entire beam system easy to align. With the aid of standard optical components these beams are aligned to intersect perpendicular to each other at the geometrical centre of the 2-D MOT chamber. The complete optical and magnetic coil combination is illustrated in figure 5(b).

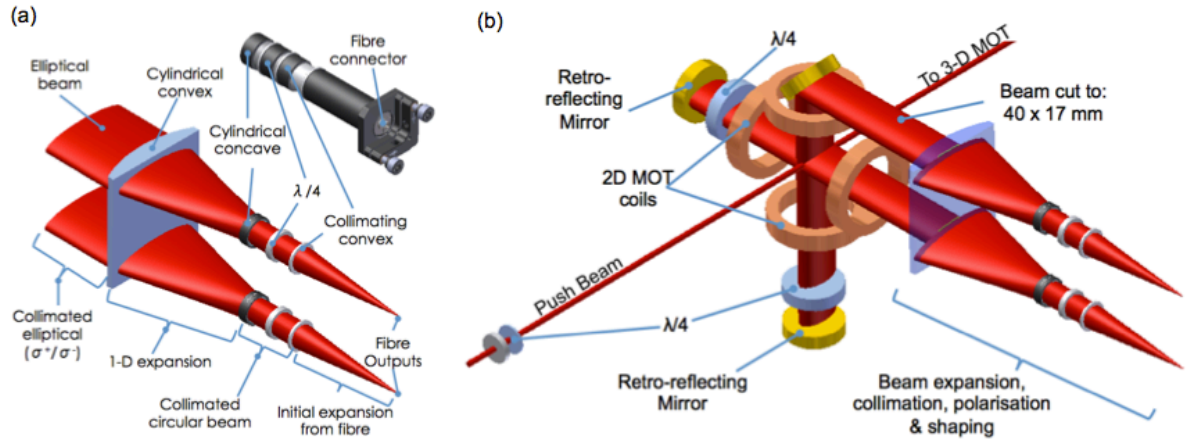

Figure 5: (a) the expansion of the 2-D MOT beam. (b) Illustration showing the magnetic coils and the 2-D$^+$ MOT beam configuration.

4. Conclusion and Outlook

Presented here is a novel coil configuration of a 2-D MOT. We have given a mathematical description of the magnetic field showing that it is of the same format as the more traditional rectangular coils. Also presented are the vacuum and laser system in order to give a clearer overview of the entire setup. This coil configuration allows the 2-D MOT to be compact and efficient in terms of creating an adequate magnetic field gradient with low power consumption. The atomic flux created by the 2-D$^+$ MOT will serve as a supply for a 3-D MOT whose atoms will eventually form Africa's first BEC.

References

[1] Bertoldi A, Lamporesi G, Cacciapuotia L, de Angelisb M, Fattoric M, Petelskid T, Peterse A, Prevedellif M, Stuhlerc J and Tinog G M 2006 *Eur. Phys. J. D* **40**, 271-279 v

[2] van der Stam K M R, van Ooijen E D, Meppelink R and Vogel J M 2007, *Rev. Sci. Instrum* **78**, 013102

[3] Lu Z T, Corwin K L, Renn M J, Anderson M H, Cornell E A and Wieman C E 1996 *Phys. Rev. Lett.* 77, 3331–3334

[4] Nakagawa K, Suzuki Y, Horikoshi M and Kim J B 2005 *Appl. Phys. B* 81, 791-794

[5] Greiner M, Bloch I, Hansch T and Esslinger T 2001, *Phys. Rev. A* 63, 031401

[6] Leanhardt A E, Chikkatur A P, Kielpinski D, Shin Y, Gustavson T L, Ketterle W and Pritchard D E 2002 *Phys. Rev. Lett.* **89**, 040401

[7] Semonyo M, Rehn M, and Petruccione F 2011 In Proceedings of SAIP2011, the 56th Annual Conference of the South African Institute of Physics

[8] Conroy RS, Xiao Y, Vengalattore M, Rooijakkers W, and Prentiss M 2003 *Optics Communications*, 226

[9] Bolpasi V, Grucker J, Morrissey M J, and von Klitzing W 2012, *J. Phys. B: At. Mol. Opt. Phys.* 45, 235301.

Realization of B92 QKD protocol using id3100 Clavis^2 system

Makhamisa Senekane[1], Abdul Mirza[1], Mhlambululi Mafu[1] and Francesco Petruccione[1,2]

[1] Centre for Quantum Technology, School of Chemistry and Physics, University of KwaZulu-Natal, P/Bag X54001 Durban, South Africa
[2] National Institute for Theoretical Physics (NITheP), University of KwaZulu-Natal, P/Bag X54001 Durban, South Africa

E-mail: 211560527@stu.ukzn.ac.za, mirzaa@ukzn.ac.za, 209526077@stu.ukzn.ac.za, petruccione@ukzn.ac.za

Abstract. Quantum key distribution is an encryption technique for securely exchanging a bit string (known as a key) between two communicating parties, traditionally known as Alice, the sender and Bob, the receiver, in the presence of an eavesdropper, Eve. This technique is based on two laws of quantum mechanics, namely the Uncertainty Principle and the no-cloning theorem. The first operational quantum key distribution protocol known as the BB84 protocol was developed by Charles Bennett and Gilles Brassard. Since then, various QKD protocols have been developed. Examples include B92, SARG04 and six state protocols. Currently, BB84 forms the most established protocol and therefore is the most widely used protocol. However, since the B92 protocol uses two quantum states, as opposed to BB84's four, it requires less resources for its implementation. Despite the B92 protocol being simpler to implement than the BB84 protocol, surprisingly this advantage has not been fully exploited. Therefore, in this paper we investigate the feasibility of implementing the B92 protocol by using the id3100 Clavis^2 system from idQuantique.

1. Introduction

Cryptography is the art of transforming information into something unintelligible to anyone other than the intended recipient [1]. It provides communication between legitimate parties in the presence of an adversary. Therefore, the goal of cryptography is to transmit information from the sender to the receiver in such a way that the information sent could not be intercepted/modified by an eavesdropper.

There are two main branches of cryptography, namely secret- (symmetric-) key cryptography and public- (asymmetric-) key cryptography [2]. For practical purposes, since it is difficult to distribute keys using secret-key cryptography, public-key cryptography is widely used in conventional cryptosystems. The main problem of public-key cryptosystems is that they can be undermined by advances in technology and mathematical algorithms; since their security is conditioned on the assumption that Eve would have limited computational power and that some mathematical functions (one-way functions) are difficult to compute [3]. It is here that quantum mechanics offers a solution in the form of quantum key distribution (QKD). Unlike conventional cryptographic protocols, whose security is based on unproven assumptions

concerning mathematical complexities, QKD's theoretical unconditional security is based on the fundamental laws of quantum mechanics.

The remainder of this paper is divided into three sections. Section 2 provides some background information on the BB84 protocol, the B92 protocol, the "Plug and Play" optical scheme and the Clavis^2 system. This is followed by Section 3 which explains explains the implementation of the B92 protocol on the Clavis^2 system. Lastly, Section 4 concludes this paper.

2. Background Information

QKD allows two users to establish an identical and purely random sequence of bits at two different locations while also allowing for the detection of an eavesdropper [4]. This string of bits is used as a one-time pad for cryptographic purposes. QKD security is based on the fact that it is theoretically impossible to gain information about non-orthogonal quantum states without disturbing these states [5, 6, 7, 8, 3, 9].

QKD protocols can be classified into two types [10]:

- Prepare and Measure schemes: Alice prepares a quantum signal according to her basis and bit values and sends them through a quantum channel to Bob, whom upon reception, measures them. Examples of Prepare and Measure schemes are BB84 [5], B92 [11] and SARG04 [12] protocols.
- Entanglement-based schemes: an entangled source emits a pair of entangled signals, and this pair is then measured by Alice and Bob separately. An example of entanglement-based protocol is the one which was proposed by Artur Ekert in 1991 (E91) [13].

QKD uses two communication channels, namely:

- Quantum channel: which is used for key exchange between Alice and Bob, this channel uses the laws of quantum mechanics to reveal (if any) the presence of Eve.
- Classical channel: which is used to perform classical post-processing tasks such as sifting, error correction and privacy amplification.

2.1. BB84 Protocol

The BB84 protocol is the first QKD scheme that has been proposed [5, 3]. It encodes a quantum state (usually a single photon polarization) using two non-orthogonal bases, namely rectilinear and diagonal bases, with four polarization states (0°, 90°, 45° and 135°). The Uncertainty Principle dictates that if a measurement (on Bob's side) is performed in a different basis from the one in which it was prepared (by Alice), then such a measurement would yield a random outcome and such a state would be disturbed. This means that Eve's presence would introduce errors which could be detected [14, 15]. On the other hand, if Bob's measurement basis is the same as Alice's preparation basis, then such a quantum bit (qubit) would be used to generate a raw key [3].

As already stated, the BB84 protocol uses two channels: one for quantum key exchange (quantum channel) and one for classical post-processing (classical channel). The steps which are followed for quantum key exchange between Alice and Bob are [5, 8, 14]:

- Alice generates a qubit sequence and sends it to Bob, randomly choosing which basis to use to represent such a sequence.
- Bob randomly measures the polarization of the incoming sequence of quantum states by using any of the bases.

The second and last stage of the BB84 protocol is a classical post-processing procedure which uses the classical channel. This stage involves [5, 8, 14]: sifting, error correction and privacy

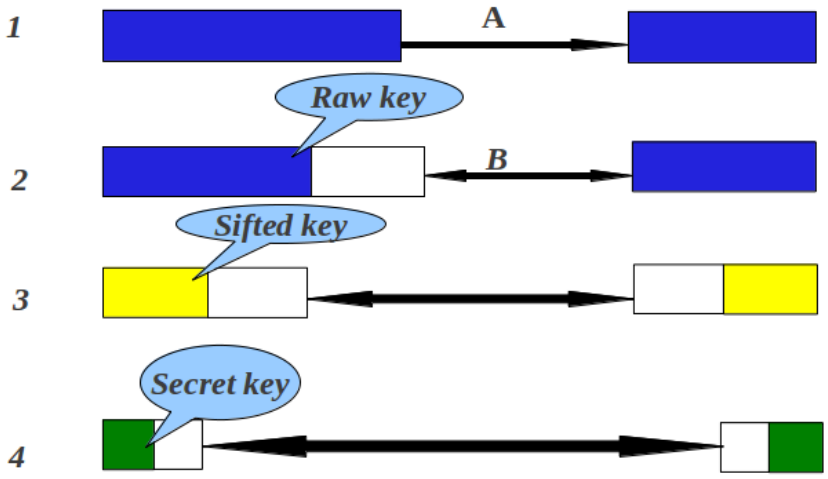

Figure 1. Key generation stages in BB84 protocol. A: Quantum channel, B: public channel, 1: Qubit transmission, 2: After sifting, 3: After error correction, 4: After privacy amplification.

amplification. Figure 1 shows the stages of the BB84 protocol and reductions in key length due to sifting, error correction and privacy amplification.

2.2. B92 Protocol

The B92 protocol forms a simpler version of the BB84 protocol [16]. It is a two-state protocol (it uses two non-orthogonal quantum states) which was proposed by Charles Bennett in 1992. It is based on the fact that two non-orthogonal quantum states are sufficient to guarantee the detection of an eavesdropper.

In the B92 protocol, quantum key exchange stage for B92 is implemented as follows:

- Alice randomly generates a qubit sequence and sends it using any of the two non-orthogonal states.
- Bob randomly chooses the time-slots (instances) to measure the incoming qubit sequence.

The classical post-processing procedure is similar to that of the BB84 protocol. However, the subtle difference lies in the sifting step. In this step Alice and Bob compare their time-slots in order to generate a raw key unlike in BB84 protocol where Alice and Bob compare their bases. Bob communicates to Alice the time-slots he used to determine non-erasures [8], and Alice compares those time-slots to hers. They both record time-slots where non-erasures were detected, and use bits corresponding to those slots as a raw key. The other steps (error correction and privacy amplification) of B92 are the same as those of BB84.

2.3. "Plug and Play" Scheme

QKD can be implemented by using either free-space or optical fibers as a quantum channel. Free-space QKD systems are easier to design and are also resistant to birefringence [3]. However, optical fibers (using phase coding) constitute the frequently used quantum channel for QKD applications. Of the phase coding schemes, the most commonly used (for commercial applications) is the "Plug and Play" scheme [1].

The "Plug and Play" scheme for quantum key distribution was first introduced by Muller *et al.* in 1997 [17]. Basically, this scheme features Bob sending a classical signal to Alice in order to initiate a key exchange session. Alice then attenuates (to an average of a single photon per pulse)

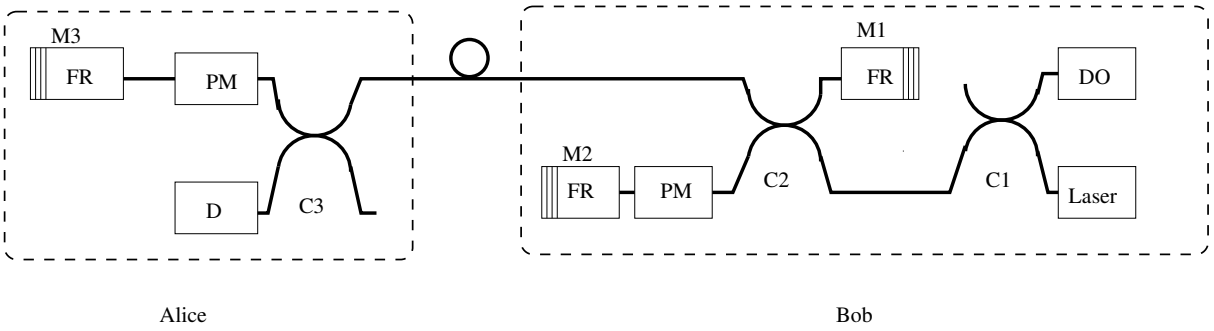

Figure 2. "Plug and Play" system. DO: single photon detector, C1, C2 & C3: fibre couplers, PM: phase modulator, FR: Faraday rotator, M1, M2 & M3: mirror, D_A: classical detector.

and encodes the received signal and sends it back to Bob, who then performs a measurement. The major advantage of "Plug and Play" systems is that they do not require additional optical adjustments during operation. Figure 2 shows a typical "Plug and Play" scheme.

2.4. Clavis^2 System

The Clavis^2 system is a QKD research platform used for deploying a "Plug and Play" scheme. It is a product of idQuantique from Geneva, Switzerland. It uses a proprietary auto-compensating optical platform which guarantees a low quantum bit error rate (QBER). Currently, this system supports BB84 and SARG04 protocols only. Figure 3 shows the set-up of the Clavis^2 system which we used for the implementation of the B92 protocol.

3. B92 on a Clavis^2 System

Usually, the B92 protocol is implemented using frequency coding scheme [1, 18]. However, these schemes do not enjoy any commercial success because of difficulties involved with deploying optical networks based on them. Also, the security of this scheme has not been studied in depth [1].

We take advantage of the commercial success and ease of deployment of "Plug and Play" scheme to implement the B92 protocol. This implementation does not alter the hardware of the Clavis^2 system, but alters Alice's preparation process (by using two quantum states instead of four), Bob's measurement process (using two quantum states instead of four) and sifting (using comparison of time-slots instead of comparisons of the bases). The two sifting processes are equally feasible because in order to extract the key the BB84 and SARG protocol uses comparisons of bases and states respectively whilst the B92 protocol uses erasures. However, this difference in the sifting process only determines which protocol can suit a particular implementation but it cannot be used to directly compare the efficiency between different protocols.

In order to compare the B92 protocol and the other two standard protocols (BB84 and SARG04), we use the raw key length and the QBER. The QBER forms one of the most important parameters when investigating the security of a protocol. The QBER is the fraction of positions where Alice's and Bob's string values differ [3]. The QBER forms a direct measure for the secrecy of the shared string. If the QBER is above a certain threshold, the two parties abort the protocol, otherwise they apply a post-processing scheme to distill the secret key from the raw key. Therefore, the higher the QBER, the lower the raw key length (fraction of correlated bit strings) which the two legitimate parties share. This means that the protocol only allows a small fraction of errors to occur in order for the two parties to establish a shared secret key, thus making the implementation of the protocol less efficient. The theoretical QBER is given as

Figure 3. Clavis^2 QKD system in our laboratory at the University of KwaZulu-Natal. Bob's side is on the left while Alice's side is on the right.

Cycle	Protocol	Raw Key Length (Frames)	Theoretical QBER (%)
1	BB84	12804	0.72
2	BB84	13443	0.72
3	BB84	13692	0.72
1	B92	12636	0.68
2	B92	13023	0.68
3	B92	12835	0.68
1	SARG04	13329	1.25
2	SARG04	12492	1.25
3	SARG04	13143	1.25

Table 1. A comparison of BB84, SARG04 and B92 protocols using raw key length and theoretical QBER.

[3]

$$QBER = R_{\text{error}}/R_{\text{sift}}, \tag{1}$$

where $R_{\text{sift}} = 1/2R_{\text{raw}}$ is the sifted key rate and R_{error} is the rate of getting a wrong signal on Bob's side.

The theoretical QBER values and raw key length were compared among the three Prepare and Measure protocols; BB84, B92 and SARG04 protocols. Each protocol session was executed for three cycles, with each cycle running for 100 seconds. Table 1 summarizes the findings. From

Table 1, it can be observed that the B92 has the lowest theoretical QBER. However, it is also observed that the raw key of the B92 protocol generated is the shortest of the three compared protocols. This observation also agrees with theory [19].

4. Conclusion

We have demonstrated the realization of the B92 QKD protocol using the id3100 Clavis^2 system without modifying the Clavis^2 hardware. Prior to our work, the system only supported two protocols, namely BB84 and SARG04 protocols. Based on the results obtained (shown in Table 1), the B92 displays raw key length and theoretical QBER comparable to BB84 and SARG04 protocols, which implies that it is feasible and efficient to implement the B92 protocol on the Clavis^2 system. As expected, the B92 displays a lower key rate as compared to BB84 and SARG04 protocols. However, an advantage of such an implementation is that the B92 protocol requires less resources and when compared to the other two protocols. The security analysis of this approach is left for future work.

Acknowledgments

This work is based on research supported by the South African Research Chair Initiative of the Department of Science and Technology and National Research Foundation.

References

[1] Makarov V 2007 *Quantum cryptography and quantum cryptanalysis* Ph.D. thesis Norwegian University of Science And Technology
[2] Lo H and Lütkenhaus N 2007 *arXiv:0702202*
[3] Gisin N, Ribordy G, Tittel W and Zbinden H 2002 *Reviews of Modern Physics* **74** 145–195
[4] Scarani V, Bechmann-Pasquinucci H, Cerf N J, Dušek M, Lütkenhaus N and Peev M 2009 *Reviews of Modern Physics* **81** 1301
[5] Bennett C and Brassard G 1984 *Proceedings of IEEE International Conference on Computers, Systems and Signal Processing* vol 175 (Bangalore, India) pp 175–179
[6] Alleaume R, Bouda J, Branciard C, Debuisschert T, Dianati M, Gisin N, Godfrey M, Grangier P, Langer T, Leverrier A *et al.* 2007 *arXiv:0701168*
[7] Qi B, Qian L and Lo H 2010 *arXiv:1002.1237*
[8] Lomonaco S 1999 *Cryptologia* **23** 1–41
[9] Bennett C, Bessette F, Brassard G, Salvail L and Smolin J 1992 *Journal of Cryptology* **5** 3–28
[10] Fung C, Ma X and Chau H 2010 *Physical Review A* **81** 012318
[11] Bennett C 1992 *Physical Review Letters* **68** 3121–3124
[12] Scarani V, Acin A, Ribordy G and Gisin N 2004 *Physical Review Letters* **92** 57901
[13] Ekert A 1991 *Physical Review Letters* **67** 661–663
[14] Kollmitzer C and Pivk M 2010 *Applied Quantum Cryptography* vol 797 (Springer Verlag)
[15] Zeng G 2010 *Quantum Private Communication* (Springer)
[16] Desurvire E 2009 *Classical and Quantum Information Theory* (Cambridge University Press)
[17] Muller A, Herzog T, Huttner B, Tittel W, Zbinden H and Gisin N 1997 *Applied Physics Letters* **70** 793
[18] Kumar P and Prabhakar A 2009 *IEEE Journal of Quantum Electronics* **45** 149–156
[19] Christandl M, Renner R and Ekert A 2004 *arXiv:0402131v2*

Ability of a mixture of sulfonated Zinc-phthalocyanine ($ZnPcS_{mix}$) to induce cellular death in human breast cancer cells (MCF-7) using laser irradiation

I M Tynga, N N Houreld and H Abrahamse[1]

Laser Research Centre, Faculty of Health Sciences, University of Johannesburg, P.O. Box 17011, Doornfontein, South Africa, 2028, Tel: 27(0)115596406

Email: habrahamse@uj.ac.za

Abstract. *Background:* Breast cancer is the most diagnosed and the leading cancer for women worldwide. Photodynamic therapy (PDT) is a light induced chemotherapy process; used for cancer treatment. This study aimed to determine the effects of $ZnPcS_{mix}$ on MCF-7cells and identify the mode of cell death induced by PDT using the optimum $ZnPcS_{mix}$ concentration and laser fluency. *Methods:* The ability of a mixture of sulfonated Zinc-phthalocyanine ($ZnPcS_{mix}$) to induce death in MCF-7 cells was determined after the following techniques and assays were performed: subcellular localization (fluorescence microscopy), viability (trypan blue staining and adenosine triphosphate, ATP, luminescence), proliferation (alamarBlue assay) and cytotoxicity (Lactate Dehydrogenase, LDH). The mode of cell death was determined by flow cytometry (Annexin-V). *Results:* Mitochondrial, lysosomal and Golgi apparatus were the cellular primary localization sites of $ZnPcS_{mix}$. The optimal parameters were identified as 0.5 µM of $ZnPcS_{mix}$ at 10 J/cm^2 and treated cells showed a 50% decrease in cell viability, low proliferation and high cytotoxicity. More than 90% of cells were apoptotic and nuclear fragmentation occurred after treatment. *Conclusion:* The treatment is an effective method to induce cell death in MCF-7 cells and apoptosis was the main mode of cell death. $ZnPcS_{mix}$ mediated PDT may be considered for designing a more effective cancer treatment.

1. Introduction

Cancer refers to a genetic disorder that is the second cause of death worldwide after heart-related conditions [1]. Many types of cancer exist and cancer of the breast accounts for 23% of cancer cases. Breast cancer is the most diagnosed and the leading cause of mortality among women worldwide [2,3]. It is believed that cancer can be overcome through research, which aims to identify and develop anti-cancer means to deal with the condition.

Photodynamic therapy (PDT) is a cancer target therapy, which uses a photochemotherapeutic agent, also known as a photosensitizer (PS), in conjunction with laser irradiation to induce cancer cell death. The administration of PS and its incorporation into body tissues is done in a selective manner so that cancerous tissues are mainly affected. The activation of PS is the second step which is done through laser irradiation at a specific wavelength, which is dependent on the PS. Activated PS is excited and

promoted from the ground state to a higher level of energy, known as the singlet state, which reacts with oxygen and gives rise to free radical species to destroy tissue [4,5]. Phthalocyanines are a second generation family of PSs that contain a central atom. The atom ensures not only high triplet state quantum yields but also a prolonged lifespan in this state [6,7].

In this study, the photosensitizing capabilities of $ZnPcS_{mix}$ were assessed and a dose dependent study on a breast cancer cell line (MCF-7) was done. The mode of cell death was also determined.

2. Methods

MCF-7 cells are derived from a human breast cancer cell line and were first isolated from a Sexagenarian lady at the Barbara Ann Karmanos Cancer Institute in Detroit. The MCF-7 breast cancer cell line (ATCC: HTB 22) is an adherent cell line and commercially available. MCF-7 cells were grown as a monolayer and attached to the bottom of cell culture flasks. Cells were grown to 85% confluence in 25 ml complete DMEM (Gibco Invitrogen Corporation, 41966). DMEM was supplemented with 10% (v/v) FBS (Gibco Invitrogen Corporation, 10106), 1% (v/v) penicillin-streptomycin (PAA Laboratories GmbH, P11-010) and 1 µg/ml Amphotericin B (PAA Laboratories GmbH, P11-001) in an 85% humidified atmosphere at 37°C and 5% CO_2. The cells were incubated at 37°C, in 5% CO_2 and 85% humidity throughout the study and frequently observed to monitor cell growth. Ethics approval was obtained from the Faculty of Health Sciences Academic Ethics committee of the University of Johannesburg to perform this study (AEC58/01-2010). Cells were seeded at a concentration of 6 x 10^5 cells in 3 ml culture media into 3.3 cm diameter culture dishes and incubated for 4 h to allow cells to attach. Cell cultures were divided into 4 groups (G): G1 was an unirradiated control with no $ZnPcS_{mix}$, G2 contained $ZnPcS_{mix}$ but was not irradiated and G3 was irradiated but contained no $ZnPcS_{mix}$. G4 was irradiated and contained $ZnPcS_{mix}$. The last group of cells (G4) were treated using one of the 4 concentrations of $ZnPcS_{mix}$ and one of the three laser fluences to monitor PDT. All laser irradiations were done in a dark room. A 680 nm diode laser was used with an output power of 45 mW. The laser irradiation was delivered to the cells at a distance and the irradiance spot size was 9.1 cm^2 covering the exact surface of the culture dish. Cells were irradiated for 16 min 50 s, 33 min 40 s and 50 min 30 s in order to receive a fluence of 5, 10 and 15 J/cm^2 respectively. All samples were incubated for 24 h and thereafter dose response was determined. *Cell viability:* All cells were stained with 0.4% trypan blue and percentage viability was determined. ATP present in each sample was quantified by recording the luminescence signal. *Cell proliferation:* Cells were treated with 10% alamarBlue and absorbances were detected at 550 nm. *Cytotoxicity:* Membrane integrity was assessed and LDH was measured at 490 nm [8]. *Fluorescence staining:* G2 cells were stained with 4',6-diamidino-2-phenylindole (DAPI) and either mitotracker or lysotracker before being examined [8]. *Cell death*: PDT cells (0.5 µM $ZnPcS_{mix}$; 10 J/cm^2) were treated with annexin-V and Propidium iodide (PI) before cell death was measured [9]. Significant differences were indicated as * $p<0.05$, ** $p<0.01$ and *** $p<0.001$ were considered at the 95th percentile.

3. Results and Discussion

Cell Viability: Trypan blue exclusion test was done to obtain the proportion of viable and damaged cells in different treated cell population. Laser irradiated or cells that contained $ZnPcS_{mix}$ alone maintain high percentage viability and do not differ much from the percentage viability of the untreated control cells. However, PDT-treated cells differ as the percentage viability significantly decreased ($p< 0.1$ and 0.01) when higher $ZnPcS_{mix}$ concentrations (0.5 and 1 µM) coupled with at least 10 J/cm^2 of laser fluence were used.

ATP did not vary when compared to the untreated control and a similar observation was done for cells that contained $ZnPcS_{mix}$ alone or only irradiated cells as no statistically significance was seen. PDT

cells treated with at least 0.1 µM concentration of $ZnPcS_{mix}$, showed major ATP depletion ($p<0.1$; 0.01 and 0.001) in a dose dependent pattern (figure 1).

Cell proliferation: AlamarBlue assay was performed to determine the degree of cell proliferation. Decrease in cell proliferation was observed with all treated cells and no statistical significance was noted with cells that irradiated or contained $ZnPcS_{mix}$ alone. When compared to control MCF-7 cells, significant decrease ($p<0.1$ and 0.01) in cell proliferation was mostly observed when 0.5 and 1 µM $ZnPcS_{mix}$ was used in PDT treated cells (figure 2).

Cytotoxicity: The assay was performed and the level of LDH released into the culture media was taken into consideration to elucidate cell damage especially cell membrane damages subsequent to $ZnPcS_{mix}$-mediated PDT applied to MCF-7 cells. After 24h of incubation, PDT induced an increase in cell membrane damage as a rise in the level of LDH significantly detected ($p<0.1$ and 0.01) in each sample when compared to the untreated MCF-7 cell control (figure 2).

Photosensitizer localization: Figure 3 shows successful $ZnPcS_{mix}$ cellular uptake, cell staining (blue DAPI, green mito- and lyso-tracker) as well as the initial subcellular localization of $ZnPcS_{mix}$ in MCF-7 cells after less than 1 h incubation. In the merged picture of both cases, there is an overlapping of red $ZnPcS_{mix}$ and green lyso-/mito-tracker colour giving rise to an intermediate yellowish tint, but no evidence of an overlapping between the red and blue DAPI colouration as both dyes are separately identified in the merged image.

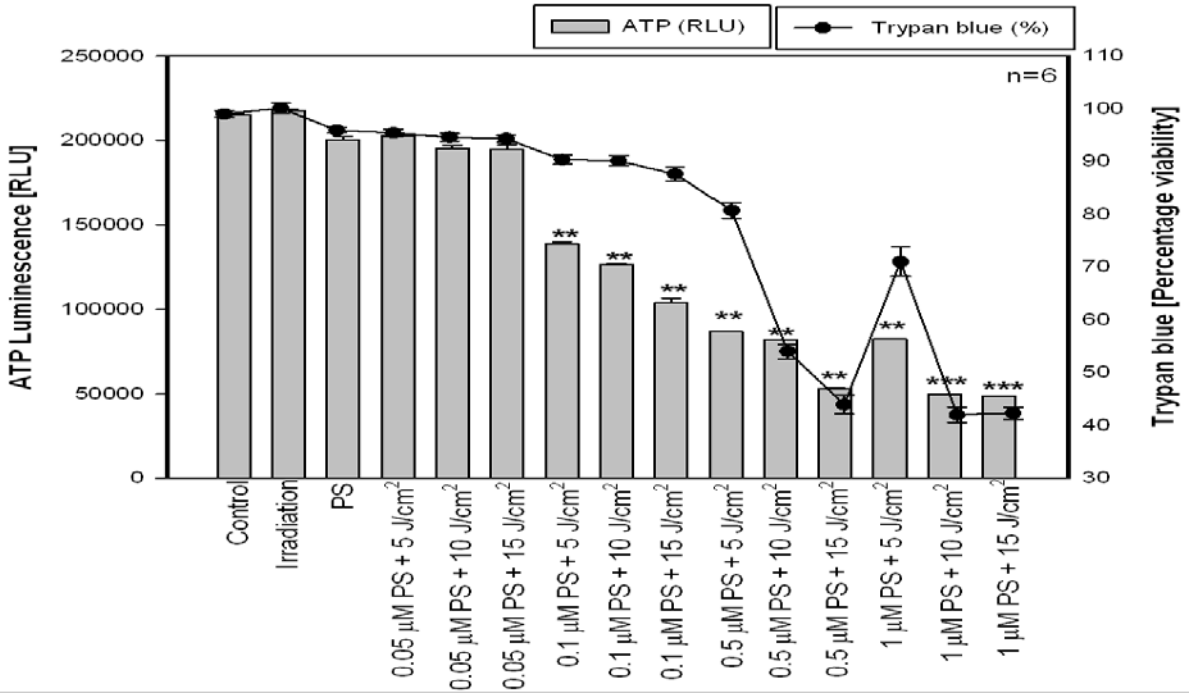

Figure 1: Decrease in ATP luminescence (measured in relative light units, RLU) and trypan blue percentage viability is seen with all PDT samples and no significant change was observed with irradiation- and PS-treated samples. Statistical differences were indicated as * ($p<0.1$),** ($p<0.01$) and *** ($p<0.001$) and compared to the reference control group.

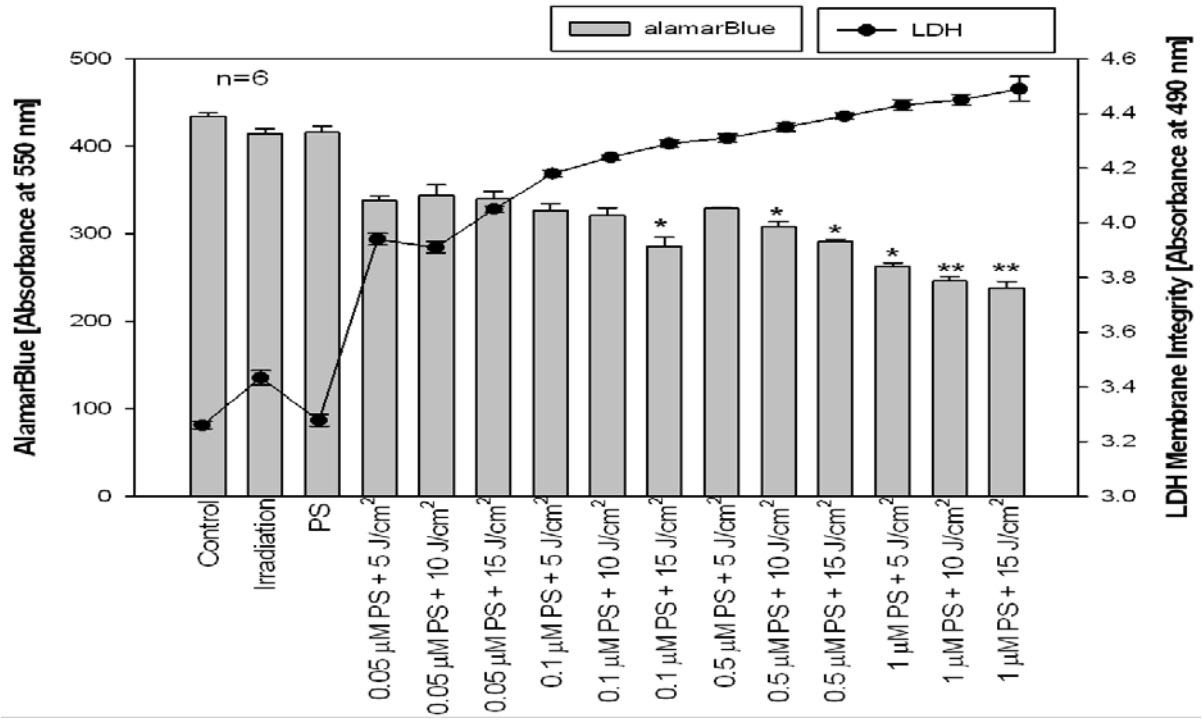

Figure 2: The cytodamage was significant with all PDT samples (LDH) and PDT treated cells have a slow proliferation rate (alamarBlue). Statistical significances are expressed * ($p<0.1$),** ($p<0.01$) and *** ($p<0.001$)and compared to the control group. No major change was identified with irradiated and PS-treated samples.

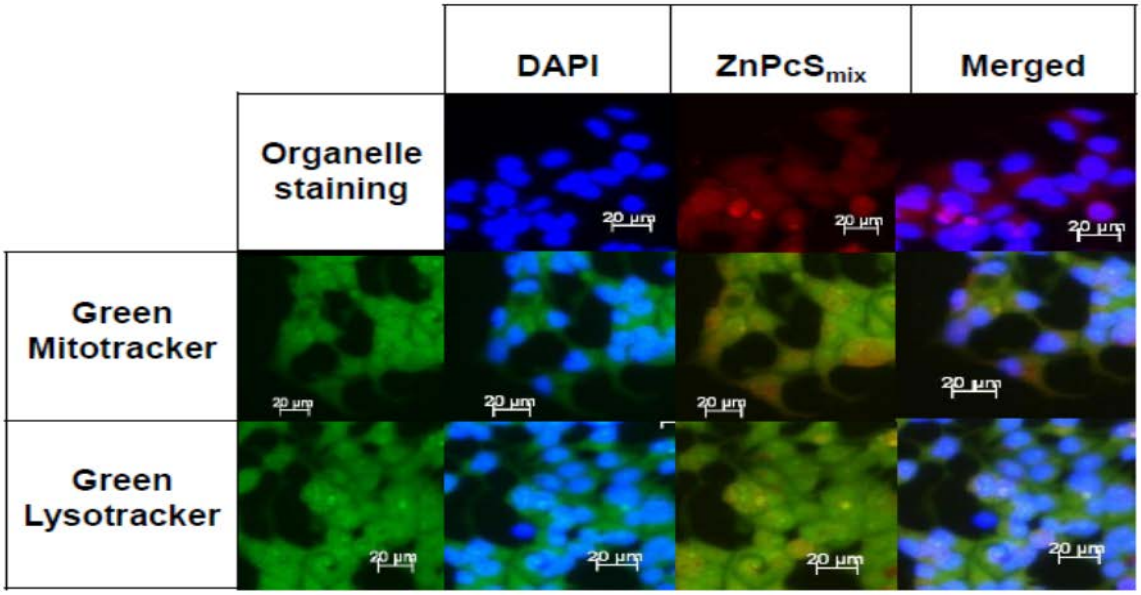

Figure 3: Blue DAPI is a dye that stains the nuclei, green mitotracker and green lysotracker stain mitochondria and lysosomes, respectively. Red $ZnPcS_{mix}$ localizes in both mitochondria and lysosomes as the intermediate yellow between green and red and not in nuclei (superimposed images). The PS localizes also in the perinuclear regions, which correspond to the golgi apparatus.

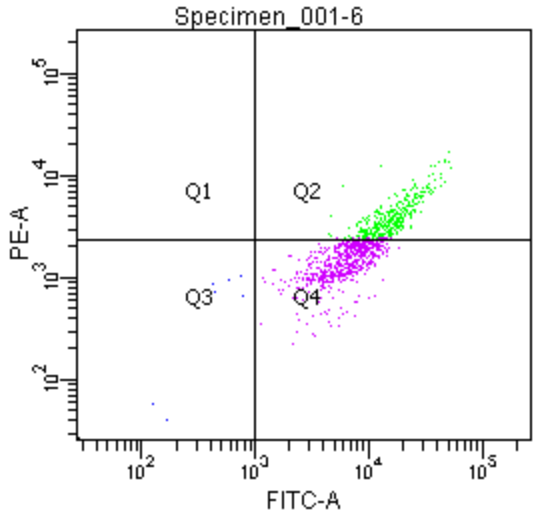

Figure 4: Flow cytometry analysis shows that 37% of cells were in the early apoptotic stage and 64.3% in the late apoptotic cells after PDT.

Fluorescence images reveal that $ZnPcS_{mix}$ localizes at perinuclear sites, which corresponds to the Golgi apparatus and this finding concurs with the work done by [10,11]. Mitochondria and lysosomes are the primary sites of $ZnPcS_{mix}$, as red and green fluorescence merged to give the observed intermediate yellow fluorescence. It was shown that a similar Zinc (II) phthalocyanine localizes in the lysosomes and phthalocyanine delivery to the lysosomes is done via endocytosis [10]. Moreover, these lysosome localized-PSs accumulate in microzomes and in the mitochondria [11,12]. Mitochondria are important organelles in cellular energy metabolism and are important role-players in cell death. Under stress, release of mitochondrial proteins trigger cascades responsible for the changes to cell structure and functions resulting in apoptosis. Like any phthalocyanine, $ZnPcS_{mix}$ has a strong tendency to aggregate, is taken up and retained in the organelles of tumor cells, where upon light activation they induce cell death [13]. At higher concentrations, $ZnPcS_{mix}$ induces cell membrane damage following PDT and trypan blue dye entered cells through these damaged membranes. At the same concentration, the produced toxic derivative prevents the activities of mitochondrial energy metabolic enzymes and therefore decreases ATP levels. $ZnPcS_{mix}$ localized in golgi apparatus and mitochondria, might affect both protein and energy synthesis. Decreases in both percentage viability and ATP level was observed with A549 human lung cancer cells after PDT using a similar PS [8]. The drop in ATP levels correlate with the decrease in the proliferation of cancer cells. Cancer cells are high consumers of energy, less energy is available to cancer cells to perform their activities such as cell division. Wong and co-workers [14] reported a decrease in proliferation with FaDu hypopharyngeal carcinoma cells. These decreases might be due to the absence of sensitivity of PDT samples to cell stimulating factors.

This study has identified 0.5 μM $ZnPcS_{mix}$ and 10 J/cm^2 as the PDT condition that induced approximately 50% of cell death in MCF-7 cells. The quasi totality of cells was found to be apoptotic with the majority in their late apoptotic stage. Tomecka and colleagues [15] reported that 32-65% of G361 tumor cells were undergoing apoptosis and early apoptosis occurred between 8-15 h after PDT treatment using ZnTPPS4 as a sensitizer. Chen and collaborators [16] also found out that PDT using motexafin Lutetium induces up to 35 % increase in the apoptosis of vascular cells. It was reported that the cell death is dependent on the cell line, photosensitising agent, and/or experimental conditions.

4. Conclusion

$ZnPcS_{mix}$ localizes in mitochondria, lysosomes and at the perinuclear sites, which correspond to the golgi apparatus and induced cytotoxic reactions leading to apoptotic like cell death responses. About 99 % of dead cells and nuclear fragmentation (not shown) were observed after $ZnPcS_{mix}$ mediated PDT treatment. This sensitizer at concentrations from 0.5 μM has demonstrated to be an effective inducer of cell death.

5. Acknowledgments

This work was conducted at the Laser Research Centre of the University of Johannesburg and supported by all the African Laser Centre, National Research Foundation and Medical research Council of South Africa. We thank Prof. Tebello Nyokong (Department of chemistry, Rhodes University, South Africa) for the synthesis and supply of the PS and both the National Laser Centre of the Council for Scientific and Industrial Research of South Africa is acknowledged for the supply and maintenance of lasers.

6. References

[1] Calin M A and Parasca S V 2006. *J Optoelectron Adv M* **8(3)**:1173-1179.
[2] van Zyl S, van der Merwe L J, Walsh C M, van Rooyen C and Groenewald AJ 2012 *PHCFM* **4(1)**:1-10
[3] Benn C A 2009 www.Health24.com/woman/medical accessed on 31 March 2010
[4] Castano A P, Demidora T N and Hamblin M R. 2004 *Photodiagn Photodyn* **1**:279-293.
[5] Mroz P, Szokalska A, Wu M X and Hamblin M R 2010 *J Pone* **5(12)**: 15194-15201.
[6] Ogunsipe A, Chen J Y and Nyokong T 2004 *New J Chem* **28**:822-827.
[7] Kessel D and Oleinick N L 2010 *Methods Mol Biol* **635**:35-4
[8] Manoto S L and Abrahamse H 2011 *Lasers in Med Sci* **43**: 333-342.
[9] Van Engeland M, Nieland L J W, Ramaekers F C S, Schutte B and Reutelingsperger C P M 1998 *Cytometry* **31**:1–9.
[10] Wood S R, Holroyd J A and Brown S B 1997 *Photochem Photobiol B* **65(3)**:397-402
[11] Fabrics C, Valduga G, Miotto G, Borsetto L, Jori G, GarbisaI J and Reddi E 2001 *Cancer Res* **61(20)**:7495
[12] Kessel D, Luo Y, Deng Y and Chang C K 1997. Photochem and Photobiol **65(3)**: 422-426
[13] Ochsner R 1997 *J Photochem and Photobiol* **39**: 1-18
[14] Wong T W, Tracey E, Oseroff A R and Baumann H 2003 *Cancer Res* **63**:3812-3818
[15] Tomecka M, Kolarova H, Dzubak P, Bajgar R, Macecek J, Nevrelova P, Tomankova K and Strnad M 2005 *Scrita Medica* **78 (4)**: 205–210
[16] Chen Z, Woodburn KW, Shi C, Adelman D C, Rogers C and Simon D I 2001 *Arterioscler Thromb Vasc Biol* **21(5)**: 759–64.

Global DNA methylation status of colorectal cancer cells exposed to photodynamic therapy

L Vorster, N Houreld and H Abrahamse[1]
Laser Research Centre, Faculty of Health Sciences, University of Johannesburg, P.O. Box 17011, Doornfontein, Johannesburg, 2028, South Africa Tel: +27 11 559-6406 Fax +27 11 559-6884,
e-mail: habrahamse@uj.ac.za

Abstract. *Aim:* Photodynamic therapy (PDT) is the use of low intensity laser irradiation (LILI) in conjunction with a photosensitiser (PS), in this instance Zinc (II) Phthalocyanine (ZnPc), to treat cancer cells. A single wavelength is used to activate the PS, which in turn causes changes in cellular functions. DNA methhylation is an epigenetic regulator. The methylation status of a gene determines if it is expressed or silenced. This study aims to determine if DNA methylation has an effect on the effectiveness of PDT. *Method:* Cancer cells, demethylated with aza-5-dc and normal, were exposed to PDT with different incubation times. Cell viability, proliferation and morphology were measured. *Results:* Cells that underwent PDT and aza-5-dc treatment showed a statistically significant decrease in viability when compared to control cells. A significant decrease was also shown when cells, demethylated with a high concentration of aza-5-dc were compared to cells exposed to PDT. *Conclusion:* The DNA methylation status of cells does have an effect on PDT effectiveness.

1. Introduction

DNA methylation is a chemical change to the DNA, without changing the sequence. Hypermethylation normally leads to the silencing of genes and hypomethylation leads to over expression [1-3]**.** DNA methylation is not only an epigenetic regulator, but also contributes to the tertiary structure of the DNA double helix [4,5]. DNA methylation occurs when a methyl group (CH_3) is covalently added to the 5' position of a cytosine that is part of a CpG di-nucleotide. This methylation is normally found in cytosine and guanine rich regions in the genome called CpG islands [6,7]. Recent studies have shown that the use of a demethylating agent with chemotherapy on a therapy resistant brain tumour increased the chemosensitivity [5]. Low intensity laser irradiation (LILI), also known as photobiostimulation, has been used for various medical treatments. This involves the use of a single wavelength of light that emits no sound, heat or vibration to stimulate cells. Photodynamic therapy (PDT) is the use of LILI in conjunction with a photosensitiser (PS). The PS is activated by the LILI and it generates reactive oxygen species (ROS) that destroys the cells. In recent years a significant amount of research has gone into the use of metallophthalocyanine (MPc) as PSs [8].

2. Methodology

Colorectal ademocarcinoma cells (CaCo2, ATCC HTB-37) were cultured in minimum essential media Eagle (Sigma M2279) until confluent. After confluence was achieved, cells were treated with aza-5-dc (Sigma A3656) to demethylate the cells at 0.1 μM and 3 μM. Demethylated cells were then seeded into 3.3 cm diameter culture plates and incubated for either 3 or 24 h with 20 μM Zinc phthalocyanine (ZnPc). When seeded into small plates for irradiation two groups were made with different incubation times of the PS, 3 h and 24 h. Cells were then irradiated with 5 J/cm^2 at 680 nm (43.0 mW; 5.03 mW/cm^2; 16.5 min; 990 s). Viability was determined using Trypan Blue staining in conjunction with the Countess Automated Cell Counter (Invitrogen C10227). Cell proliferation was measured using the AlamarBlue-stain and the Victor^3 multi-label plate reader (PerkinElmer). Cell morphology was viewed using inverted light microscopy.

3. Results and Discussion

3.1 Morphology

Morphological changes were observed as shown in figure 1. In the group that underwent PDT treatment and 3h incubation, cells became rounded and started to detach from the plate surface while the 24 h incubation group showed signs of severe structural damage. The control groups (Control, PS, aza-0.1 and aza-3) showed almost no morphological changes. An interesting observation is the vacuoles in the cells. Cells exposed to a high concentration of aza-5-dc (group aza-3 in figure 1) showed a decrease in these vacuoles.

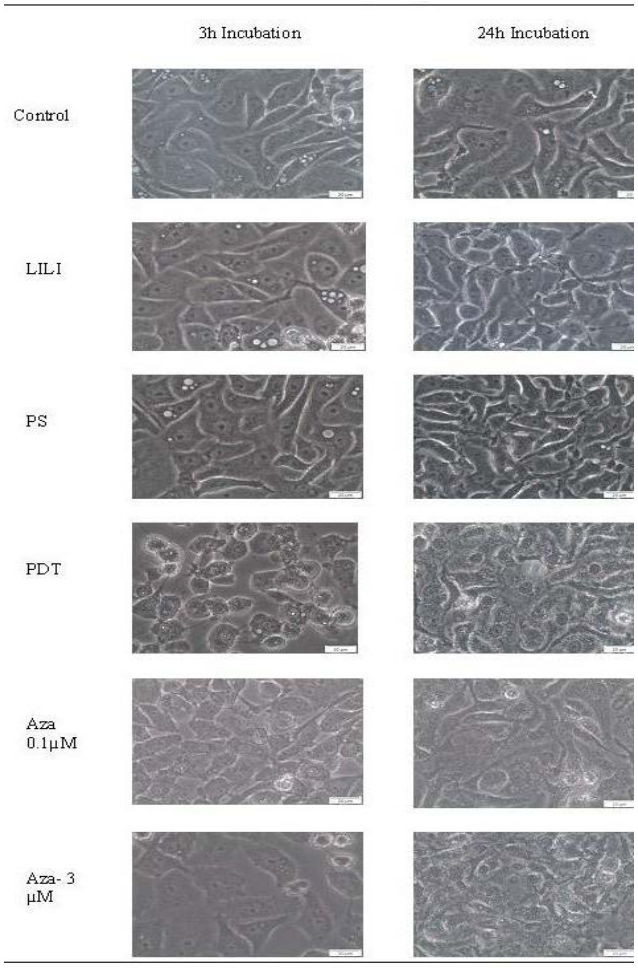

Figure 1: Morphological changes in the different groups. Groups that served as control are LILI: cells exposed to laser irradiation; PS: cells treated with the photosensitiser. PDT: cells that were treated with PDT. Aza-0.1: cells treated with a low concentration (0.1μM) aza-5-dc. Aza-3: cells treated with a high concentration (3 μM) aza-5-dc.

3.2 Viability and proliferation

Cells exposed to PDT showed a statistical significant decrease in viability when compared to the control at both 3 and 24 h ($P < 0.05$ and $P < 0.001$ respectively) as shown in figure 2a and 2b. In the 24h incubation group, demethylated cells showed a significant difference when compared to the control, but less than the PDT group, while for the 3h incubation group the opposite effect was observed. However when comparing the PDT group to the demethylated groups, no significant difference was seen, which correlates with the results found by Patties *et. al.*[5]. The cells exposed to a high concentration of aza-5-dc and PDT showed a significant difference when compared to the demethylated cells not exposed to PDT, albeit it was still had a less significant effect than the PDT group. The viability results show that PDT significantly decreases the viability of cells when incubated with the PS for 24h. DNA methylation did not affect PDT when incubated for 24 h. This can be due to the fact that the DNA repair mechanisms had time to work before PDT was administered. Another factor that can play a role in the effectiveness of the aza-5-dc and PDT is the stage of the cell cycle the cells were in [9]. No significant statistical difference was found with the AlamarBlue proliferation assay (results not shown).

(a) (b)

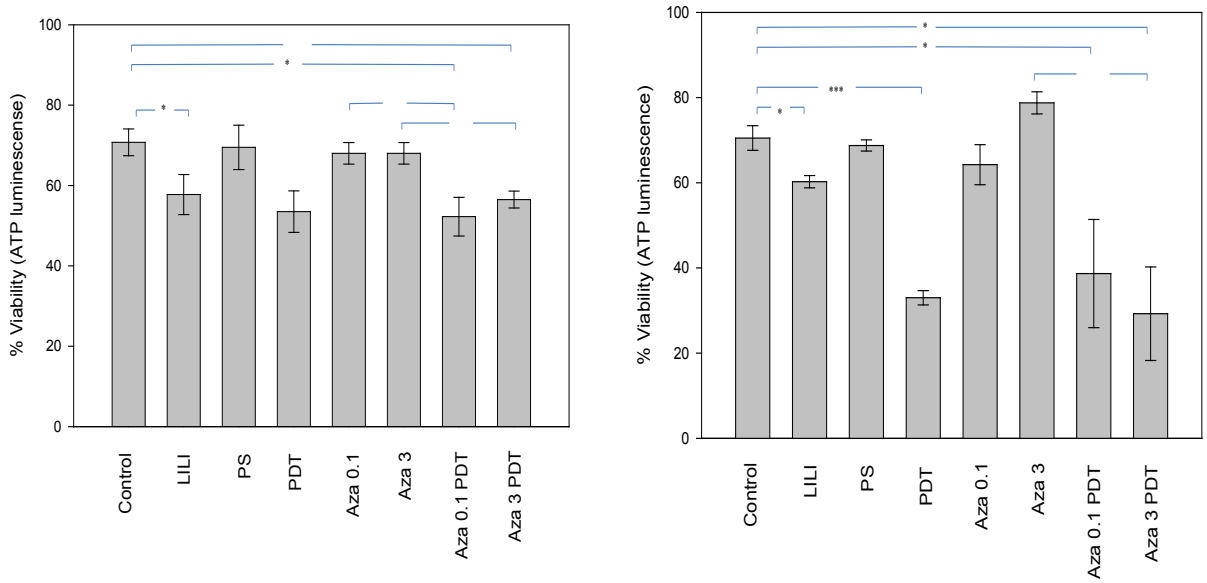

Figure 2(a) and (b): CaCo2 cells were treated with different concentrations of demethylser, aza-5-dc (Aza-0.1 and Aza-3), and incubated with ZnPc for 3 (a) or 24 (b) h. Cells were then irradiated at 660 nm with 5 J/cm2 (PDT). Cells which were not treated (control), irradiated only (LILI), or incubated with ZnPc but not irradiated (PS) served as controls. Statistical significances are shown as *P<0.05, **P<0.01 and *** P<0.001.

4. Conclusion

From these results, it can be concluded that DNA methylation status does affect the effectiveness of PDT, but it is dependent on the incubation time with the PS. If cells are left to incubate for too long, demethylation has no effect on PDT effectiveness and this is possibly due to activation of cellular DNA repair mechanisms. These results have also shown that CaCo2 cells are sensitive to treatment with 20 μM ZnPc and irradiated to a wavelength of 660 nm and a fluence of 5 J/cm^2.

References

[1] Partha M, Signal R (2004) DNA methylation and cancer. *Journal of Clinical Oncology* **22(22):** 4632-4642

[2] Wilson A S, et al. (2006) DNA hypermethylation and human disease. *Biochimica et Biophysia Acta* DOI: 1016/j.bbcan200608007

[3] Robertson C A, Hawkins Evans D, Abrahamse H (2009) Photodynamic therapy (PDT): a short review on cellular mechanisms and cancer research applications. *Journal of Photochemistry and Photobiology B: Biology* **96:** 1-8

[4] Mroz P, Hamblin M (2009) Combination of PDT and a DNA demethylating agent produces anti-tumour immune response in a mouse tumour model. *Proc SPIE* **7380:** 73800H-1 – 73800H-9

[5] Patties I, *et al.* (2009) Additive Effects of 5-Aza-2'-deoxycytidine and Irradiation on Clonogenic Survival of Human Medulloblastoma Cell Lines. *Strahlentherapie und Onkologie* **185:**331–338

[6] Portella A, Esteller M (2010) Epigenetic modification and human disease . *Nature Biotechnology* (**28**)10: 1057 -1068

[7] Lorincs M C, *et al.*(2004) Intragenic DNA methylation alters chromatin structure and elongation efficiency in mammalian cells. *Nature Structural & Molecular Biology* **11**: 1068 – 1075

[8] Robertson C A, Abrahamse H (2010) The In Vitro PDT Efficacy of a Novel Metallophthalocyanine (MPc) Derivative and Established 5-ALA Photosensitizing Dyes Against Human Metastatic Melanoma Cells. *Lasers in Surgery and Medicine* **42**:766–776

[9] Wyld L, *et. al.*(1998) Cell cycle phase influences tumour cell sensitivity to aminolaevulinic acid-induced photodynamic therapy in vitro. *British Journal of Cancer* **78**(1): 50 – 55

Division D1 - Astrophysics

The Effect of Different Magnetospheric Structures on Predictions of Gamma-ray Pulsar Light Curves

M Breed[1], C Venter[1], A K Harding[2], T J Johnson[3]

[1]Centre for Space Research, North-West University, Potchefstroom Campus, Private Bag X6001, Potchefstroom, 2520, South-Africa

[2]Astrophysics Science Division, NASA Goddard Space Flight Center, Greenbelt, MD 20771, USA

[3]NRC Fellow, High-Energy Space Environment Branch, Naval Research Laboratory

E-mail: 20574266@nwu.ac.za

Abstract. The second pulsar catalogue of the *Fermi* Large Area Telescope (LAT) will contain in excess of 100 gamma-ray pulsars. The light curves (LCs) of these pulsars exhibit a variety of shapes, and also different relative phase lags with respect to their radio pulses, hinting at distinct underlying emission properties (e.g., inclination and observer angles) for the individual pulsars. Detailed geometric modelling of the radio and gamma-ray LCs may provide constraints on the B-field structure and emission geometry. We used different B-field solutions, including the static vacuum dipole and the retarded vacuum dipole, in conjunction with an existing geometric modelling code, and constructed radiation sky maps and LCs for several different pulsar parameters. Standard emission geometries were assumed, namely the two-pole caustic (TPC) and outer gap (OG) models. The sky maps and LCs of the various B-field and radiation model combinations were compared to study their effect on the resulting LCs. As an application, we compared our model LCs with *Fermi* LAT data for the Vela pulsar, and inferred the most probable configuration in this case, thereby constraining Vela's high-altitude magnetic structure and system geometry.

1. Introduction

Pulsars are considered to be cosmic lighthouses that rotate at tremendous rates and are highly magnetized neutron stars (NS) [1]. The fact that pulsars are embedded in such extreme conditions make them valuable laboratories for studying a wide range of topics, including: nuclear physics, plasma physics, electrodynamics, magnetohydrodynamics (MHD), and general relativistic physics [2]. Pulsars emit radiation across the electromagnetic spectrum, including radio, optical, X-ray and gamma (γ) rays [1]. We focus on γ-ray pulsars, specifically the Vela pulsar, which was detected [3] by the *Fermi* Large Area Telescope (LAT) [4]. The Vela pulsar is the brightest persistent GeV source. *Fermi* was launched in 2008 and has discovered in excess of 100 γ-ray pulsars. The LAT has a very large field of view of 2.4 sr which enables it to observe 20% of the sky at any instant, scanning the entire sky in a time frame of a few hours.

1.1. Geometric pulsar models

There are several models which can be used for the modelling of high-energy (HE) emission from pulsars. These models include the two-pole caustic (TPC) (the slot gap (SG) [5] model may

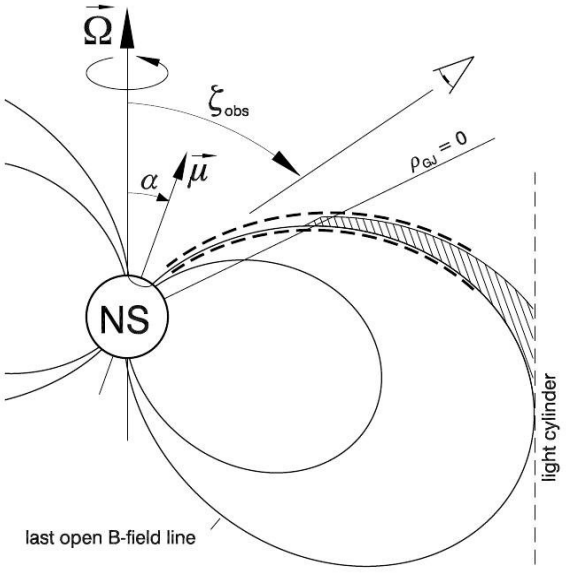

Figure 1. A schematic representation of geometric pulsar models. The TPC emission region extends from $R_{\rm NS}$ (NS radius) up to $R_{\rm LC}$ (light cylinder radius), OG region from $R_{\rm NCS}$ (null charge surface radius) to $R_{\rm LC}$, and the PSPC from $R_{\rm NS}$ to $R_{\rm LC}$ [covering the full open volume region].

be its physical representation) model [6], outer gap (OG) model [7],[8] and pair-starved polar cap (PSPC) model [9]. Figure 1 illustrates these geometric pulsar models, and their emission regions [6].

Consider an ($\vec{\Omega}$, $\vec{\mu}$) plane, with $\vec{\mu}$ (the magnetic moment) inclined by an angle α with respect to the rotation axis $\vec{\Omega}$ (the angular velocity). The observer's viewing angle ζ is the angle between the observer's line of sight and the rotation axis. The gap region is defined as the region where the relativistic particles originate and particle acceleration takes place. The emissivity of HE photons within this gap region is assumed to be uniform in the co-rotating frame and the γ-rays are expected to be emitted tangentially to the local magnetic field in this frame [10]. The gap region for the TPC model extends from the surface of the NS along the entire length of the last closed magnetic field lines, up to the light cylinder, as indicated by the dashed lines in Figure 1. For the OG model, the gap region extends from the null-charge surface (NCS), where the Goldreich-Julian charge density is $\rho_{GJ} = 0$ [11], to the light cylinder, as indicated by the shaded region (the emission region may be located at slightly smaller co-latitudes compared to the TPC). The PSPC is the gap region that extends from the surface of the NS to the light cylinder over the full open volume [9].

1.2. Assumed magnetospheric structure

The magnetospheric structures studied in this paper include the static [12] and retarded vacuum dipole [13]. The (aligned) static dipole is a special case of the retarded dipole and is described by the following B-field equations in terms of spherical coordinates in the laboratory frame:

$$B_{\rm st,r} = \frac{2\mu}{r^3}\cos\theta \tag{1}$$

$$B_{\mathrm{st},\theta} = \frac{\mu}{r^3}\sin\theta. \tag{2}$$

The retarded dipole is described by the following B-field equations [14]:

$$B_{\mathrm{ret,r}} = \frac{2\mu}{r^3}[\cos\alpha\cos\theta + \sin\alpha\sin\theta(r_{\mathrm{n}}\sin\lambda + \cos\lambda)] \tag{3}$$

$$B_{\mathrm{ret},\phi} = -\frac{\mu}{r^3}\sin\alpha[(r_{\mathrm{n}}^2 - 1)\sin\lambda + r_{\mathrm{n}}\cos\lambda] \tag{4}$$

$$B_{\mathrm{ret},\theta} = \frac{\mu}{r^3}(\cos\alpha\sin\theta + \sin\alpha\cos\theta[-r_{\mathrm{n}}\sin\lambda + (r_{\mathrm{n}}^2 - 1)\cos\lambda]) \tag{5}$$

$$\lambda = r_{\mathrm{n}} + \phi - \Omega t \tag{6}$$

$$r_{\mathrm{n}} = \frac{r}{R_{\mathrm{LC}}}. \tag{7}$$

By setting r_{n} equal to zero the retarded field simplifies to the general (non-aligned) static dipole, with r the radial distance. The static dipole field is studied for numerous reasons. Two of them are: (1) calculations are simpler for this B-field, and (2) when the results for the static dipole are compared to those for the other B-fields, the importance of the near-R_{LC} distortions in the B-fields for predicted radiation characteristics can be gauged [15].

In this paper we will study the impact of different magnetospheric structures on the predictions of γ-ray pulsar LCs. The layout is as follows: §2 describes the method we used to construct sky maps, LCs, and χ^2 contour plots for the different combinations of the two B-fields and two geometric models. Section 3 contains our results, §4 our discussions and §5 contains the conclusions and future aims.

2. Method

We used an existing geometric modelling code [10] in which different B-field solutions and geometric models are implemented. We constructed sky maps, which are defined as the intensity per solid angle as a function of phase and ζ, and LCs for the B-field and radiation model combinations, using a 5° resolution for α and ζ. LCs are obtained by making a constant-ζ cut through each sky map.

Table 1. Best-fit (α, ζ) values for the Vela pulsar.

		Our model		Reference fit [16]		Radio polarization [17]	
Combination	$\log_{10}\chi^2$	$\alpha(^\circ)$	$\zeta(^\circ)$	$\alpha(^\circ)$	$\zeta\ (^\circ)$	$\alpha(^\circ)$	$\zeta\ (^\circ)$
Static Dipole:							
TPC	15.3	60	85				
OG	6.4	65	85				
Retarded Dipole:							
TPC	15.7	70	55	62–68	64		
OG	1.3	80	70	75	64		
						53	59.5

After the preparation of the sky maps and LCs, a statistical method for finding the best fits is applied. We used a χ^2 method to compare our model LCs with *Fermi* LAT data for the Vela pulsar:

$$\chi^2 = \sum_{i=1}^{N} \frac{(Y_{\mathrm{d,i}} - Y_{\mathrm{m,i}})^2}{Y_{\mathrm{m,i}}}, \tag{8}$$

with $Y_{\mathrm{m,i}}$ the model (relative flux) value and $Y_{\mathrm{d,i}}$ the measured number of counts (relative units) in each phase bin. First we lowered the model LCs resolution, so that both the model and data have the same amount of bins N. Next, we smoothed the data using a Gaussian kernel density estimator (KDE). The data are treated as being cyclic. For computational efficiency, we aligned the maximum peaks of the model and data before calculating $\chi^2(\alpha, \zeta)$. A contour plot of χ^2 is shown in panel (b) of Figure 4.

3. Results

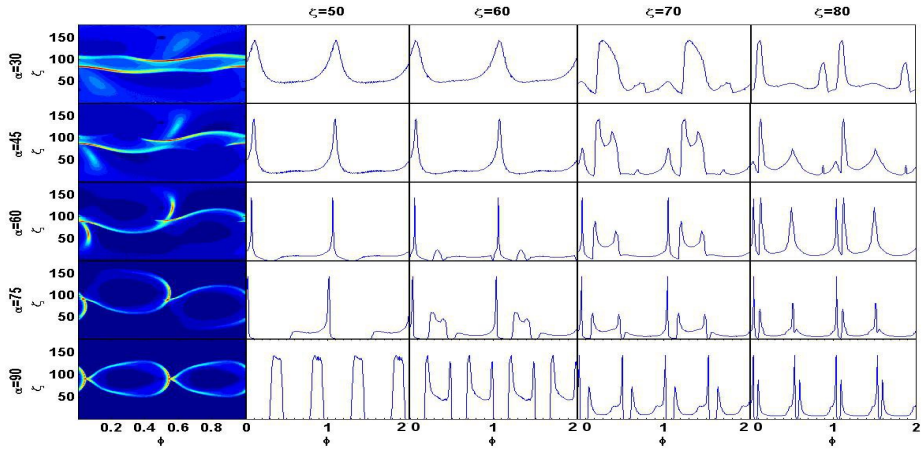

Figure 2. The sky maps (left) and LCs (right) as predicted from the TPC model using the static dipole field for different α and ζ values (deg).

As an example, we show the sky maps and their corresponding LCs for the TPC model, for both the static and retarded dipole fields (Figure 2 and 3). We used a maximum gap radius of $R_{\mathrm{max}} = 1.2R_{\mathrm{LC}}$ for both the TPC and OG cases. There are different LCs on the right of each sky map corresponding to different ζ-cuts. In both the figures there appear two dark circles, the PCs, followed by two sharp, bright regions near it, called the main caustics, on the sky map. The caustic structure is qualitatively different between the two cases, leading to differences in the resulting LCs. The caustics seem wider and more pronounced in the retarded dipole case. A thin line of emission, due to the 'notch' [14] is also visible in the latter case. For large α the caustics extend over a larger range in ζ for the retarded case compared to the static case. The OG models are not visible at all angle combinations and thus do not fill all phase space. This is due to emission that occurs below the null charge surface for the TPC model, but not for the OG model. The TPC model LCs also exhibit relatively more off-pulse emission. The LCs in the OG models are due to emission from only one pole, while both poles are visible in the TPC model.

The different model LCs are fitted to the Vela data of *Fermi* LAT and for each model, we constructed a χ^2 contour plot which indicates the best possible fit. The white marker on the

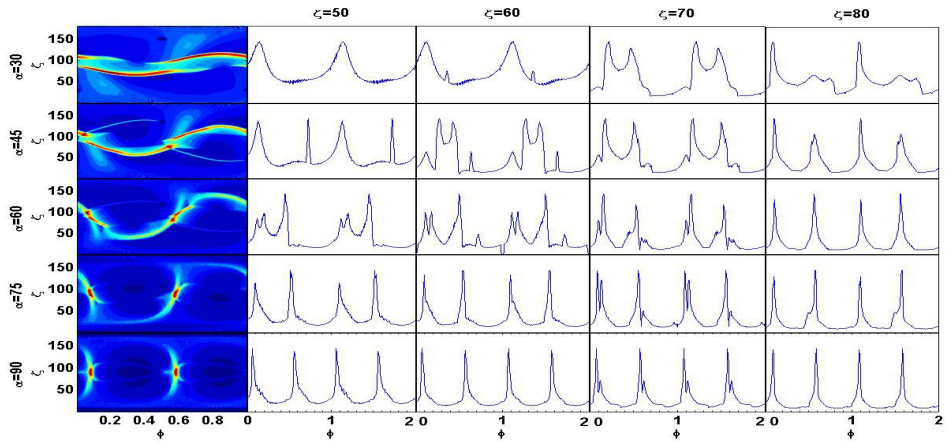

Figure 3. The sky maps (left) and LCs (right) as predicted from the TPC model using the retarded dipole field for different α and ζ values (deg).

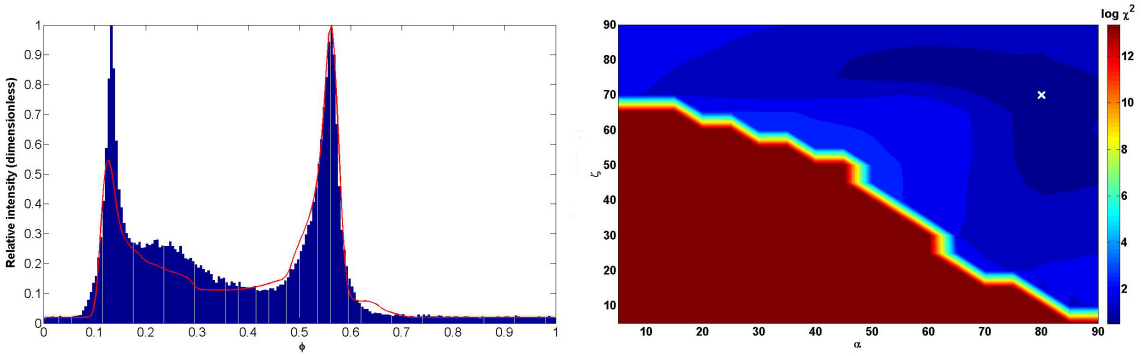

Figure 4. Panel (a) indicates our best-fit LC for Vela (see Table 1). Panel (b) shows the contour plot for $\chi^2(\alpha, \zeta)$, indicating the best-fit solution.

contour plot (Figure 4, panel (b)) indicates the minimum value of $\log_{10}\chi^2$ and these values are shown in Table 1. The first column shows our different combinations of magnetic field and geometric model, the second indicates the minimum value of $\log_{10}\chi^2$, and the third and fourth columns indicate the best-fit α and ζ from our models. These are for the 5° resolution. We will estimate more rigorous errors on these values in future. The fifth column contains the derived ζ values from the pulsar wind nebula (PWN) torus fitting with α constrained [18]. The last two columns are derived from fits of the rotating vector model to the radio polarization angle (PA) versus phase ϕ [19]. The best-fit model LC to the Vela LC is shown in Figure 4, panel (a). Our best fit is close to values inferred from these independent studies.

4. Conclusions and future work

We have studied the effect of different magnetic fields on gamma-ray LC characteristics. We utilized the static and retarded vacuum dipole solutions, in combination with the TPC and OG geometries. It is evident that the magnetospheric structure and emission geometry determine the pulsar visibility and also the γ-ray pulse shape. We applied our models to the Vela pulsar and found a best fit from the OG model using the retarded dipole field, for $(\alpha, \zeta) = (80^\circ, 70^\circ)$.

This is reasonably close to the value of $(\alpha, \zeta) = (75°, 64°)$ inferred by [16]. In future, we will implement an additional magnetic field solution, the offset dipole [20] and study the effect of this solution on the predicted pulsar LCs.

Acknowledgments
This work is supported by the South African National Research Foundation (NRF). A.K.H. acknowledges the support from the NASA Astrophysics Theory Program. C.V., T.J.J., and A.K.H. acknowledge support from the *Fermi* Guest Investigator Program.

References

[1] Chaisson E and McMillan S 2002 *Astronomy Today 4th Ed*, pp 569–70
[2] Becker W, Gil J A, and Rudak B 2007 *Proc. XXVIth IAU Gen. Ass. Ed K A van der Hucht* **14** 1–30
[3] Abdo A A *et al.* 2009 *Astrophys. J.* **696** 1084–93
[4] Atwood W B *et al.* 2009 *Astrophys. J.* **697** 1071–102
[5] Muslimov A G and Harding A K 2004 *Astrophys. J.* **606** 1143–53
[6] Dyks J and Rudak B 2003 *Astrophys. J.* **598** 1201–06
[7] Romani R W 1996 *Astrophys. J.* **470** 469–78
[8] Cheng K S, Ho C and Ruderman M 1986 *Astrophys. J.* **300** 500–21
[9] Harding A K, Usov V V and Muslimov A G 2005 *Astrophys. J.* **622** 531–43
[10] Dyks J, Harding A K and Rudak B 2004 *Astrophys. J.* **606** 1125–42
[11] Goldreich P and Julian W H 1969 *Astrophys. J.* **157** 869–80
[12] Griffiths D J 2008 *Introduction to Electrodynamics 3rd Ed*, p 246
[13] Deutsch A J 1955 *Ann. d'Astrophys.* **18** 1–10
[14] Dyks J and Harding A K 2004 *Astrophys. J.* **614** 869–80
[15] Dyks J and Harding A K 2004 *Astrophys. J.* **606** 1125–42
[16] Watters K P, Romani R W, Weltevrede P and Johnston S 2009 *Astrophys. J.* **695** 1289–301
[17] Johnston S *et al.* 2005 *MNRAS* **364** 1397–412
[18] Ng C -Y and Romani R W 2008 *Astrophys. J* **673** 411–417
[19] Radhakrishnan V and Cooke D J 1969 *Astrophys. L.* **3** 225–9
[20] Harding A K and Muslimov A G 2011 *Astrophys. J.* **726** L10

Pulsation mode identification for B stars recently discovered in the Galaxy and the LMC

CA Engelbrecht[1] , C Ulusoy[1] , T Gülmez[1] & FAM Frescura[2]

[1]Department of Physics, University of Johannesburg, PO Box 524, Auckland Park 2006, Johannesburg. [2]School of Physics, University of the Witwatersrand, Private Bag 3, WITS 2050, Johannesburg.

E-mail: chrise@uj.ac.za

Abstract. Following the announcement of potential B star pulsators discovered in OGLE data on the LMC [1], and in ASAS-3 data on Galactic stars [2], various long-term photometric campaigns on a variety of B stars have been conducted by the authors since late 2009. This paper summarises the recent results of these campaigns.

1. The motive for pulsation mode identification

A sustained increase in the breadth and depth of observational data on stellar behaviour has made it clear that current models of stellar structure and evolution need significant refinements (see, for example, recent reviews by Christensen-Dalsgaard and Christensen-Dalsgaard & Houdek [3]). The field of asteroseismology provides valuable tools for achieving this. This is in large part due to the rapid increase in both the quantity and the quality of observational data on pulsating stars, as a result of extensive ground-based surveys such as OGLE and ASAS [4] and dedicated space telescopes (MOST, CoRoT, *Kepler* and BRITE – [5]), as well as the increase in computing power that now allows fully 3-D simulations of stellar interiors to be performed [6]. Since the vibrational properties of any physical medium depend very sensitively on fine details of the interior structure and the physical dimensions of the medium, and measurements in the time domain can be made particularly precisely, a study of the vibrations of stars can provide remarkably detailed knowledge of their structure and interior dynamics. An essential prerequisite for this process to succeed is the determination of the modal identities of the periodic signals detected in stars.

2. The motive for studying B stars

Early B stars are very likely to become progenitors of supernovae that will produce a neutron star as the core remnant. A precise understanding of early B stars is essential for a precise understanding of the formation and character of the lower-mass population of core-collapse supernovae. The degree of uncertainty in our present descriptions of stellar structure and evolution is illustrated in a recent paper [7], where the mass value of a classical Cepheid variable, determined from traditional evolutionary models, was shown to be approximately 20% in error. Equally dramatic improvements in our understanding of the detailed structure and evolutionary timescales of B stars are possible. Such improvements will have a significant impact on our understanding of the formation of supernovae, and also on our understanding of the formation and character of pulsars. Supernovae play an important role

in the study of a wide variety of astrophysical and cosmological problems, while pulsars are set to play a key role in the science programmes of MeerKAT and the SKA. Furthermore, main-sequence B stars form part of the continuum of stellar classes on the sequence, from red dwarfs through to super-massive stars, and are important to understand in their own right.

3. Our projects

Early B stars show dominant pulsations with periods in the range 3 – 8 hours. Many of the pulsation modes have relatively low amplitudes, requiring extensive observation to raise the signal-to-noise ratio to sufficient levels. Early B stars that display such pulsations are classified as Beta Cephei stars (after the prototype). Two of the most important questions about early B stars that invite an asteroseismological answer are: i) What are the precise boundaries of the *instability strip* (in the HR diagram) associated with Beta Cephei-type pulsations; ii) How low can the *iron-group metal content* in a main-sequence early B star go before pulsations become quenched? Since it is the iron-group elements that enable the kappa-mechanism to drive pulsations in early B stars, the width and length of the B-star instability strip is heavily dependent on *metallicity*. However, the detailed nature of this dependence is not clear. Following the announcement of potential pulsations in B stars discovered in OGLE data on the LMC [1], and in ASAS-3 data on Galactic stars [2], the reliability of current theoretical models of B stars in correctly quantifying the connection between metallicity and pulsational behavior in early B stars has come under question. This has prompted us to embark on a long-term observational project to bring quantitative evidence of the connection between metallicity and pulsation to the fore.

We report here on the results of two projects aimed at exploring an observational correlation between metallicity and pulsation: Both projects involve detailed, long-term observational studies, necessary to determine frequencies, amplitudes and phases of multiple pulsation modes in each star with sufficient precision to make a clear identification of mode type.

One project focuses on open clusters in the Galaxy, the other on the Large Magellanic Cloud (LMC). We have obtained 6 weeks of UBVI photometry on pulsating stars in the open cluster NGC6200, spanning a total observing period of 11 months between July 2010 and May 2011. These data were obtained with the UCTCCD operating on the 0.75-m telescope of the South African Astronomical Observatory (SAAO) at Sutherland, as well as with the STE4 CCD operating on the 1.0-m telescope at the same site. We have also obtained 4 weeks of UBVI photometry on three distinct 5 arcmin x 5 arcmin fields in the LMC, over a period spanning from December 2010 to March 2012. All of these data were obtained with the STE4 CCD camera operating on the 1.0-m telescope at Sutherland. Theoretical pulsation models of B stars predict that the respective amplitudes of any particular pulsation mode, as detected through various filters, depend quite strongly on the median wavelength of the filters. The amplitudes further depend quite sensitively on fundamental stellar parameters such as metallicity, mass and age, as well as on values of stellar opacity and stellar composition spectra. Consequently, a precise determination of pulsation amplitudes in each of the U, B V and I filters may be compared with theoretically predicted values for various combinations of the aforementioned parameters.

4. Results

A well-sampled light curve (obtained through the V filter) of one of the pulsating B stars in NGC 6200 appears in figure 1. One full pulsation period covers the range between the two maxima in the curve. The "stillstand" phase on the ascending leg of the light curve is a rare feature and is reminiscent of the high-amplitude Beta Cephei pulsator, BW Vul. The stillstand is a phenomenological feature that is seen in light curves as well radial velocity curves of a few Beta Cephei stars. In figure 1, it appears between the values 0.55 and 0.60 of the fractional day. The theoretical explanation for the stillstand in BW Vul is based on the motions of opacity-driven shocks through the stellar envelope. A key finding is that the model only works for exceptionally high values of metallicity [9]. It will be interesting to determine whether the same holds for the star we have discovered in NGC6200.

The Lomb-Scargle periodogram for the same star's V data is depicted in figure 2. The aliasing envelopes corresponding to a number of Beta-Cephei-type pulsations can be clearly seen.
Finally, the relative amplitudes of the strongest pulsation found in this star, as detected through the U, B, V and I filters respectively, are shown superimposed on a grid of plots of predicted amplitude ratios for various evolutionary stages of a 15 solar-mass star in figure 3. Each of the coloured, "ribbon-like" features corresponds to a specific spherical harmonic degree of the pulsation mode (ℓ = 0, 1, 2 and 4 resepctively). Each evolutionary stage considered produces a single 'line' of each colour; the spread of evolutionary age considered results in the 'broadening' of the various lines into coloured 'bands'. The observed amplitudes (indicated by black dots with vertical error bars) correspond very well to predictions for the radial mode (the red band).

A similar treatment of the second strongest pulsation in this star implies that it is a quadrupole (ℓ = 2) mode.

A somewhat sterner observational challenge was posed by the B stars in the LMC, with average V magnitudes around 16.5, as opposed to magnitudes of 9.5 for the stars in NGC6200. Preliminary results obtained from the analysis of only 2.5 weeks of data are very encouraging. Lomb-Scargle periodograms of 2.5 weeks of V data for one of the fainter targets in the LMC are shown in figures 4 and 5. The highest peaks seen in these two periodograms correspond to the strongest two Beta Cephei-type pulsations in this star. The four-sigma (in the classical statistical sense) detection thresholds are shown. This is a common detection threshold applied in confirming the presence of pulsation in a star (although it is sometimes incorrectly applied in the literature). Once analysis of the full dataset is completed, we expect at least a third (and perhaps a fourth) distinct pulsation to be detected above this threshold.

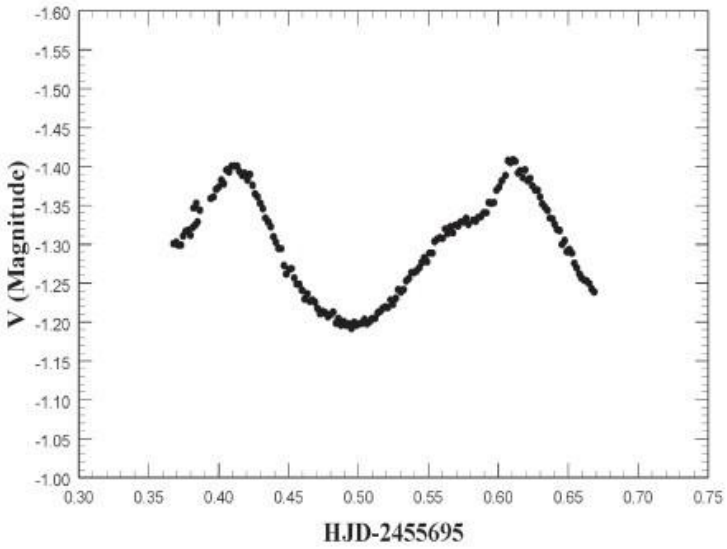

Figure 1. Light curve of the pulsating B star in NGC 6200 in the Johnson V filter. The abscissa records time in fractions of a day, while the ordinate records the V magnitude relative to an arbitrary zero-point.

5. Conclusions

We have shown that a 6-week multi-colour observing programme on a 1.0-m class telescope allows us to glean relative (in UBVI) pulsation amplitudes from pulsating B stars in open clusters with sufficient precision to perform photometric mode identification. We have also confirmed that multiple pulsation periods can successfully be gleaned from 4-week observing campaigns on pulsating B stars in the LMC. We anticipate that longer observing campaigns on stars in the LMC will also allow photometric pulsation mode identification. Spectroscopy obtained with the Southern African Large

telescope (SALT) will be used to explore the correlation (if any) of metal content in the detected pulsating B stars with their pulsation characteristics.

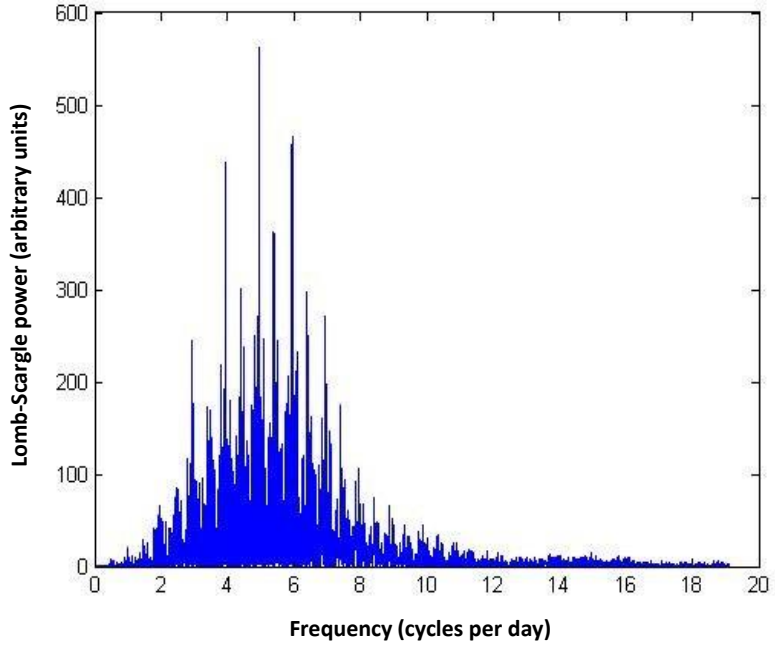

Figure 2. Periodogram of V data obtained for the pulsating B star in NGC 6200 reported here.

.

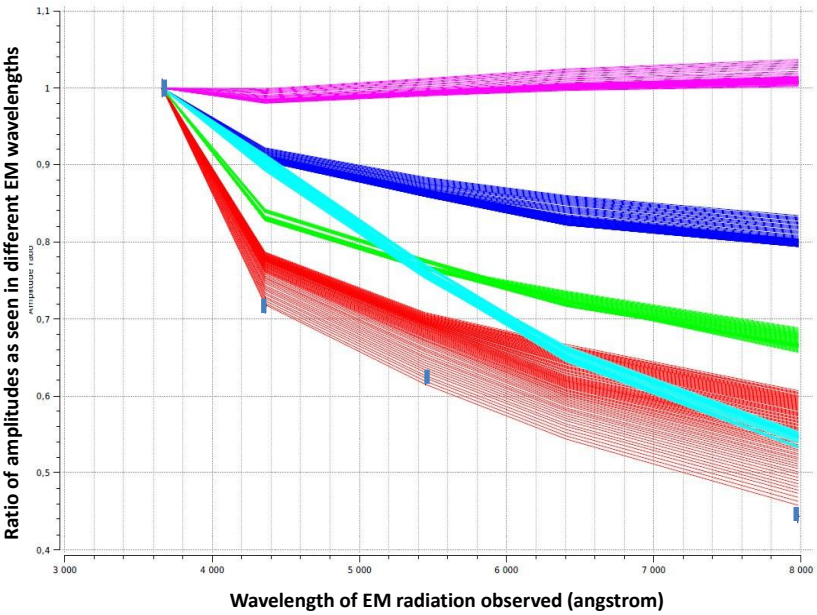

Figure 3. Observed pulsation amplitude ratios (small vertical bars) for the same pulsating B star in NGC6200, superimposed on ratios for various theoretical models computed for a 15 solar-mass star.

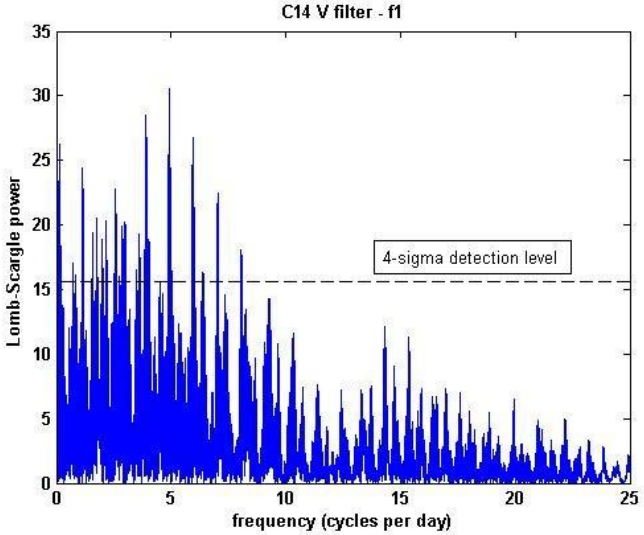

Figure 4. Lomb-Scargle periodogram for target C14 in the LMC, after subtraction of a least-squares fit of a 3-day period (related to the sampling of the observations) - from 2.5 weeks of data. The primary pulsation mode in this star is represented by the tallest peak in the periodogram.

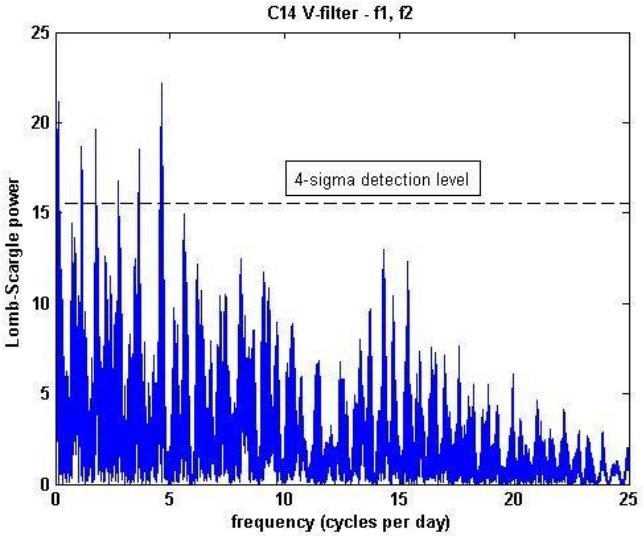

Figure 5. Lomb-Scargle periodogram for target C14 in the LMC, after subtraction of a combined least-squares fit of the 3-day period and the primary pulsation period from 2.5 weeks of data. T he secondary pulsation mode in this star is represented by the tallest peak in the periodogram.

Acknowledgments
The National Research Foundation and the University of Johannesburg's Central Research Fund as well as its Faculty of Science are thanked for providing financial support for this project. The Director of SAAO is thanked for awarding sufficient observing time on the 1.0-m and 1.9-m telescopes in support of thisproject.

References

[1] Pigulski A and Kolaczkowski Z 2002 *Astronomy & Astrophysics* **388** 88
Kolaczkowski Z and Pigulski A 2006 *Memorie della Società Astronomica Italiana* **77** 336
[2] Pigulski A and Pojmanski G 2008 *Astronomy & Astrophysics* **477** 917
[3] Christensen-Dalsgaard J 2010 *Astronomische Nachrichten* **331** 866;
Christensen-Dalsgaard J and Houdek G 2010 *Astrophysics and Space Science* **328** 51
[4] Udalski A et al. 1997 *Acta Astronomica* **47** 319;
Pojmanski G 1997 *Acta Astronomica* **47** 467
[5] Walker G et al. 2003 *Publications of the Astronomical Society of the Pacific* **115**, 1023 ;
Baglin, A. et al. 2007 *AIP Conference Proceedings* **895** 201;
Karoff C et al. 2009 *Mon Not R Astron Soc*, **399** 914;
Kuschnig, R. and Weiss, W. 2009 *Communications in Asteroseismology* **158** 351
[6] Meakin CA and Arnett D 2007 *The Astrophysical Journal* **667**, 448
[7] Pietrzynski G et al. 2010 *Nature* **468** 542
[8] Fokin A et al. 2004 *Astronomy and Astrophysics* **426** 687

The central stellar populations of brightest cluster galaxies

D N Groenewald[1] **and S I Loubser**[1]

[1] Centre for Space Research, North–West University, Potchefstroom, 2520, South–Africa

E-mail: 20569513@nwu.ac.za

Abstract. In this paper we investigate the central stellar populations of brightest cluster galaxies (BCGs), more specifically to determine whether the stellar populations (SPs) can shed any light on the formation and evolution of these galaxies. The high signal-to-noise ratio, long-slit spectra of a sample of BCGs were fitted against the Pegase.HR and Vazdekis-Miles synthesis stellar population models of the *ULySS* software package. We use the full spectrum fitting abilities of *ULySS* and fit each spectrum against a single stellar population (SSP) and a composite stellar population (CSP). The CSPs generally consists of 2 or 3 SSPs that can be divided into young, intermediate and old aged components. Monte-Carlo simulations are used to assess the relevance of the solutions, and χ^2-maps aid in the selection of the most probable star formation histories of the BCGs. We investigate whether any correlations can be found between the derived parameters and the internal properties of the galaxies and the properties of the host clusters, more specifically whether the presence of cooling flows (CFs) have any detectable influence on the stellar population components of the galaxies. Considering clusters with CFs, we find an indication that BCGs located closer to the cluster centres consists of intermediate aged SPs while those located further away generally consists of older aged SPs. For the clusters without CFs, the BCGs located closer to the centres generally consists of intermediate and old aged SPs while those located further away consists of old aged SPs. From the fact that both clusters with and without CFs experienced star formation epochs, may indicate that at least some of the star formation, but not all of the activities might be due to the presence of CFs.

1. Introduction

The centre of galaxy clusters contain rather unique, massive and luminous galaxies. The most luminous and massive of these early-type galaxies (ETGs) are called *brightest cluster galaxies* (BCGs) and are located very close to or at the centre of the clusters. BCGs have luminosities of $\sim 10L_\star$ with $L_\star = 1.0 \times 10^{10} h^2 L_\odot$ and a mass of $\sim 10^{13}\, M_\odot$ [1]. It was suggested by [2] that these BCGs are well-aligned with the host cluster galaxy distribution, which implies that the BCGs are located at the bottom of the cluster gravitational potential well. This indicates that the origin of BCGs are closely related to the formation of the host cluster because it is widely accepted that the stars have settled to the bottom of these potential wells. Initially it was thought that the special location of BCGs could be regarded as the cause for the properties that distinguished BCGs from ordinary galaxies [3] but it was later found that BCGs dominate the massive end of the galaxy luminous function [4], which in turn implies that the properties of these galaxies can be influenced by their large mass as well as by the environment of the host cluster. This further complicates the formation and evolution theories of BCGs [5]. It was proposed by [6] that the location of the BCGs at the bottom of these potential wells are responsible for the distinct properties of these galaxies, for example the high luminosities, the diffuse and extended structures of these galaxies. These properties in turn indicates that the formation and evolution of these galaxies are closely linked to that of their parent clusters, but the mechanisms behind these formations are still not fully understood.

The formation theories of BCGs are summarised by [2] as follows:

(i) Theory 1: Star formation due to *cooling flows* (CFs) are expected to occur in the dense, cool centres of X–ray clusters [7]. These CFs present researchers with a plausible formation theory since clusters with CFs have extremely high luminosities and large central galaxies, but the connection between the cooling of the X–ray gas and the formation of the BCGs is still not clear. It was stated by [6] that BCGs are more frequently found in the centre of clusters containing CFs. This implies that if the density in the core of the clusters are high enough, then stars will form at the bottom of the gravitational well. The presence of blue cores and ultraviolet excess in some BCGs are taken as an indication of recent star formation [8, 9, 10, 4] but this is inconsistent with the fact that these galaxies have red photometric colors, which implies that BCGs contain old stellar populations.

(ii) Theory 2: A second theory is called *galactic cannibalism*, which is the accretion of existing galaxies through dynamical friction and tidal stripping. This theory was first proposed by [11] and developed by [12]. Through this process, a central galaxy is formed through the mergers/capturing of less massive objects [13]. [14] found that tidal stripping reduced the mass of the clusters to such a degree that the timescales over which the dynamical friction took place were too long to be considered a viable formation theory. The study conducted by [15] found that the stars in BCGs formed very early on in the formation of these galaxies. By using numerical simulations, [16] found that BCGs, contained in clusters with redshifts higher than $z \sim 1$ experienced a significant number of mergers. The nature of these mergers were dissipationless, therefore no new stars were formed during these mergers and the BCGs are expected to consist of old stellar populations.

(iii) Theory 3: [17] proposed another theory – primordial origin, also known as *galaxy merging*. This process took place in the early history of the formation of the cluster, as predicted by the hierarchical cosmological models. The failures of the galactic cannibalism theory pointed to the fact that BCGs must have had an earlier origin than that determined through the dynamical friction timescales. This meant that mergers could have taken place during the collapse of a cosmological hierarchy and therefore offered up another formation theory [2] i.e. that galaxies were formed through the merger of smaller objects that were dragged into the centres of the clusters by dynamical friction. A study conducted by [15] found that most of the stars in BCGs formed very early on in the star formation histories (SFHs) of the BCGs and that mergers took place in the final stages of the BCG evolution where nearly all the gas was converted into stars. Hence, these mergers were dissipationless and no significant star formation are expected to take place in the BCGs.

Studies regarding the SFHs of BCGs are further complicated due to several aspects:

(i) It is difficult to find progenitors of these ETGs by means of direct observations, which is a tough requirement to satisfy even with the current generation of telescopes because large amounts of observational time is needed [13].

(ii) The properties used in the analysis of the formation histories of these ETGs are effected by the high mass of these galaxies and also by the cluster environment [18].

It is for these reasons that researchers were forced to divert to other methods to obtain meaningful information about the SFHs of the BCGs, more specifically to study the SFHs of nearby galaxies by analysing the stellar populations of these galaxies in terms of their ages and metallicities ([Fe/H]).

Little is known about the properties of the stellar populations of BCGs [19]. A study was recently undertaken by [3] in which 625 brightest group and cluster galaxies was taken from the Sloan Digital Sky Survey; their stellar population properties were compared with those of elliptical galaxies with the same mass. This study can be regarded as a point of reference in the investigation of stellar populations in BCGs. However, this study did not include any spatial information about the BCGs. The merger history of a galaxy determines the kinematical and stellar population properties and these properties can be used in an analysis of the formation history of the galaxies.

In this paper we investigate whether any correlations can be found between the derived parameters and the internal properties of the galaxies and the properties of the host clusters, more specifically whether the presence of CFs have any detectable influence on the stellar population components of the galaxies.

2. Sample Selection and Observations

2.1. Sample

The sample of galaxies analysed in this paper is based on the sample of BCGs analyzed by [20], where they initially selected cD galaxies (a special sub–class of BCGs) by using astronomical databases, for example the NASA/IPAC Extragalactic Database (NED)[1] and literature. For a more detailed description of the methods used in identifying these cD galaxies and for the BCG sample identification, refer to [20] and [13]. In summary, the sample consist of 41 galaxies where:

(i) [20] contained 31 BCGs, as classified by either NED (classified as cD galaxies in the morphological notes or in notes from previous observations) and/or have surface brightness profiles breaking the de Vaucouleurs law ($r^{\frac{1}{4}}$). In addition, NGC 4946 (an elliptical galaxy) was also observed with the same instrumental setup as the BCGs and included in the sample. Here it should be noted that only the galaxies, observed with the Gemini Telescopes (GTs) were included in the BCG sample studied in this paper.

(ii) [13] contained eight additional BCGs which were observed with the Gemini South Telescope during July 2007 to January 2008.

Here we note that we refer to the galaxies contained in the sample as the BCG sample.

2.2. Observations

Please refer to [20] for the GT observation setup used to observe the galaxies in the BCG sample.

3. Method

High signal-to-noise ratio, long-slit spectra for the sample were obtained on the GTs. Out of this sample, 31 galaxies lacked emission line and ten galaxies showed the presence of weak emission lines (hereafter referred to as emission galaxies). The spectra of the emission galaxies were analysed with the GANDALF routine [21] to accurately separate the stellar and emission line contributions to the observed spectra.

The method followed for this data analysis, is the same as outlined in [22]. In summary: Each galaxy in the sample was fitted against the *ULySS* software which contains the Pegase.HR (P.HR) and Vazdekis-Miles synthesis stellar population models. The models were elaborated on by defining additional fitting parameters, i.e. the error spectra, velocity dispersions, redshifts, line spread functions and a wavelength of (3800, 6000) Å were chosen to include all the important spectral feature elements, for example H_β and Fe5270. Each observed spectrum was fitted against a single stellar population (SSP) as well as composite stellar population (CSP). The CSP models were limited to three star formation epochs (refer back to [22] for more detail on why this was done). Monte-Carlo simulations were then used to assess the relevance of the solutions and thereby aided in the selection of the most probable SFHs of the respective BCGs. The χ^2-statistical test assisted in choosing the most probable SSP model, more specifically whether the BCGs could be presented more accurately by a SSP or CSP model.

4. Results and Discussions

NGC 6173 was excluded from further analysis because the observed spectrum provided a visibly poor fit to the models. As previously determined in [22], the analysis indicated that the P.HR model gave the most accurate representation of the SFHs for the majority of the BCGs. The results obtained from this

[1] `http://www.ipac.caltech.edu/`.

model showed that at least some of the galaxies in the sample underwent periods of recent star formation and could therefore be represented by CSPs. This in turn indicated that the BCGs had a more complex evolution than first thought.

The derived parameters were tested against the internal galaxy properties (the velocity dispersions and absolute K-band magnitudes) and the properties of the host cluster environment (the X–ray temperatures, luminosities, offsets and CFs) to determine whether any correlations could be derived to shed light on the formation and evolution of the BCGs. The internal galaxy and host cluster properties used in these comparison can be found in table 7 of [13].

In table 1 the clusters in the sample with CFs are given. The other clusters in the sample either did not have CFs or no indication in the literature could be found to suggest that CFs were present.

Table 1. The clusters in the sample that have CFs. Columns 1 and 2 give the names of the BCGs and host clusters while Column 3 gives the references to the literature from which this conclusion was derived.

Object name	Cluster	Ref.
ESO349-010	A4059	[24, 6, 27]
ESO488-027	A0548	[28]
ESO541-013	A0133	[24, 26, 27, 28]
GSC555700266	A1837	[28]
IC1101	A2029	[24, 26, 27, 28]
IC5358	A4038	[24]
MCG-02-12-039	A0496	[6, 26, 28]
NGC 1399	RBS454	[28]
NGC 2832	A0779	[28]
NGC 3311	A1060	[24, 28]
NGC 6160	A2197	[25, 28]
PGC026269	A0780	[6]
PGC044257	A1644	[28]
PGC072804	A2670	[28]

The young aged stellar populations were characterised by the ages – 2.0 $<$ Log(Age) $<$ 0.0 Gyr, the intermediate aged stellar populations by 0.0 $\leqslant$ Log(Age) $<$ 0.8 Gyr and the old aged stellar populations by the ages 0.8 $\leqslant$ Log(Age) $<$ 1.3 Gyr.

No clear correlations could be derived between the ages and [Fe/H] of the BCGs (represented by 1 and 2 SSPs) and the (i) velocity dispersions of the BCGs and the host clusters and (ii) the absolute K–band magnitudes of the galaxies. This was also true for the X–ray luminosities and the temperatures.

In the sample it was found that 14/40 clusters contained CFs (see table 1). Ten of the cluster with CFs had BCGs which could accurately be represented by 1 SSP and were comprised of intermediate stellar populations (ISPs). The remaining four clusters with CFs had BCGs that could be represented by 2 SSPs and were comprised out of ISPs and old stellar populations.

In figure 1, the age of the BCGs in clusters with (black) and without CFs (cyan) are compared against the offset between the BCG and the X–ray peak of the clusters. Considering only the clusters with CFs, it can be seen that BCGs located closer to the cluster centres consist of intermediate aged SPs while those located further away generally consists of older aged SPs. For the clusters without CFs, it follows that the BCGs located closer to the centres consists of intermediate and old aged SPs while those located further away consists of old aged SPs. From the fact that both clusters with and without CFs experienced star formation epochs, may indicate that at least some of the star formation, but not all of the activities might be due to the presence of CFs.

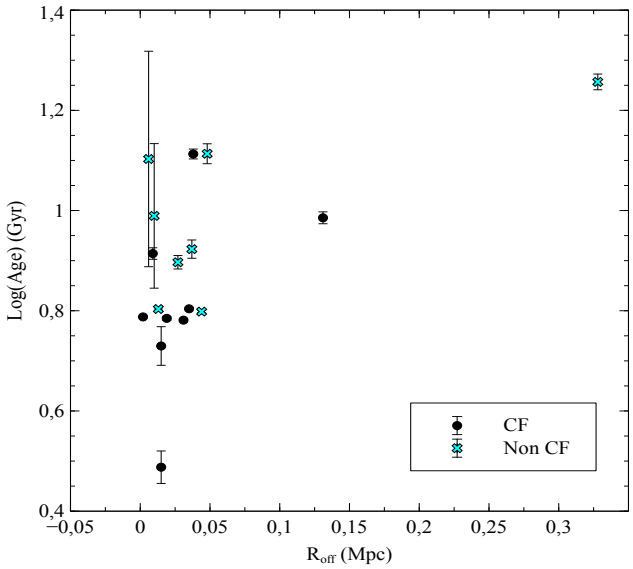

Figure 1. Age versus the X–ray offset for the clusters with and without CFs, containing BCGs which SFHs can be represented by 1 SSP.

The BCGs in clusters with CFs were located at higher X–ray luminosities than those in clusters without CFs. [30] found that very luminous systems harbored very massive CFs and contributed more than 70% of the cluster's bolometric luminosity.

5. Conclusions

Several studies, i.e. [29, 4, 30] have proposed possible sources for the gas fuelling the star formation detected in some BCGs, for example: (i) CFs, (ii) the re-use of matter ejected in stellar ejections and (iii) the accretion of other stellar matter i.e satellites. It has long since puzzled astronomers as to whether there existed a connection between the presence of these CFs and the star formation epochs in these BCGs.

Our sample contained 14 clusters with CFs. The BCGs in these clusters can be represented by ISPs and old stellar populations. From the fact that the majority (10/14) of the clusters with CF contained intermediate or young BCGs, indicated that a possible connection might exist between the presence of the CFs and recent star formation periods. As both clusters with and without CFs contains intermediate aged BCGs, this suggests that both types of clusters experienced star formation epochs. This in turn indicates that not all the star formation activities in these clusters might be explained due to the presence of CFs. [20] suggested that the gas fuelling the star formation activity in these galaxies had to originate from mergers because the merging/capturing of less massive galaxies are enhanced due to the unique location of the BCGs in the cluster potential well.

Acknowledgments

The financial assistance of the South African Square Kilometre Array Project towards this research is hereby acknowledged. Opinions expressed and conclusions presented, are those of the authors and are not necessarily to be attributed to the National Research Foundation.

References

[1] Katayama H, Hayashida K I, Takahara F and Fujita Y 2003 *Astrophys. J.* **585** 687–93
[2] Dubinski J 1998 *Astrophys. J.* **502** 141–9
[3] Von der Linden A, Best P N, Kauffmann G and White S D M 2007 *Mon. Not. R. Astron. Soc.* **379** 867–93

[4] Liu F S, Mao S and Meng X M 2012 *Mon. Not. R. Astron. Soc.* in press
[5] Brough S, Proctor R, Forbes D A, Couch W J, Collins C A, Burke D J and Mann R G 2007 *Mon. Not. R. Astron. Soc.* **378** 1507–30
[6] Edwards L O V, Hudson M J, Balogh M L and Smith R J 2007 *Mon. Not. R. Astron. Soc.* **379** 100–10
[7] Fabian A C 1994 *Annu. Rev. Astron. Astrophys.* **32** 277–318
[8] Bildfell C, Hoekstra H, Babul A and Mahdavi A 2008 *Mon. Not. R. Astron. Soc.* **389** 1637–54
[9] Crawford C S, Allen S W, Ebeling H, Edge A C and Fabian A C 1999 *Mon. Not. R. Astron. Soc.* **306** 857–96
[10] McNamara B R, Rafferty D A, Bîrzan L, Steiner J, Wise M W, Nulsen P E J, Carilli C L, Ryan R and Sharma M 2006 *Astrophys. J.* **648** 164–75
[11] Ostriker J P and Tremaine S D 1975 *Astrophys. J.* **202** L113–7
[12] Ostriker J P and Hausman M A 1977 *Astrophys. J.* **21** L125–9
[13] Loubser S I, Sánchez-Blázquez P, Sansom A E and Soechting I K 2009 *Mon. Not. R. Astron. Soc.* **398** 133–56
[14] Merritt D 1985 *Astrophys. J.* **289** 18–32
[15] De Lucia G and Blaizot J 2007 *Mon. Not. R. Astron. Soc.* **375** 2–14
[16] Gao L, Loeb A, Peebles P J E, White S D M and Jenkins A 2004 *Astrophys. J.* **614** 17–25
[17] Merritt D 1983 *Astrophys. J.* **264** 24–48
[18] Barrena R, Girardi M, Boschin W and Mardirossian F 2012 *Astron. Astrophys.* in press
[19] Loubser S I 2009 PhD thesis Univ. Central Lancashire
[20] Loubser S I, Sánchez-Blázquez P, Sansom A E, Soechting I K and Bromage G E 2008 *Mon. Not. R. Astron. Soc.* **391** 1009–28
[21] Sarzi M, Falcón-Barroso J, Davies R L, Bacon R, Bureau M, Cappellari M, de Zeeuw P T, Emsellem E, Fathi K, Krajnović D, Kuntschner H, McDermid R M and Peletier R F 2006 *Mon. Not. R. Astron. Soc.* **366** 1151–200
[22] Viljoen D N and Loubser S I 2011 Brightest Cluster Galaxies Simple or composite stellar populations? *Proc. J. Phys.: Conf. Series* (University of South Africa, Pretoria, 2011)
[23] Du W, Luo A L, Prugniel Ph, Liang Y C and Zhao Y H 2010 *Mon. Not. R. Astron. Soc.* **409** 567–81
[24] Chen Y, Reiprich T H, Bohringer H, Ikebe Y and Zhang Y Y 2007 *Astron. Astrophys.* **466** 805–12
[25] Giovannini G, Liuzzo E and Giroletti M 2008 *Proc. Approaching Micro–Arcsecond Resolution with VSOP–2: Astrophysics and Technology* ed Y Hagiwara et al.
[26] McCarthy I G, Balogh M L, Babul A, Poole G B and Horner D J 2004 *Astrophys. J.* **613** 811–30
[27] Rafferty D A, McNamara B R, Nulsen P E J and Wise M W 2006 *Astrophys. J.* **652** 216–31
[28] White D A, Jones C and Forman W 1997 *Mon. Not. R. Astron. Soc.* **292** 419
[29] Edge A C, Stewart G C and Fabian A C 1992 *Mon. Not. R. Astron. Soc.* **258** 177–88
[30] Peres C B, Fabian A C, Edge A C, Allen S W, Johnstone R M and White D A 1998 *Mon. Not. R. Astron. Soc.* **298** 416–32

The detailed nature of active central cluster galaxies

S. I. Loubser

Centre for Space Research, North-West University, Potchefstroom 2520, South Africa

E-mail: Ilani.Loubser@nwu.ac.za

Abstract. We present detailed integral field unit (IFU) observations of the central few kiloparsecs of the ionised nebulae surrounding four active central cluster galaxies (CCGs) in cooling flow clusters (Abell 0496, 0780, 1644 and 2052). Our sample consists of CCGs with Hα filaments, and have existing data from the X-ray to radio wavelength regimes available, but lacked the detailed optical emission-line (and simultaneous absorption line) data over a broad wavelength range to probe the dominant ionisation processes, excitation sources, morphology and kinematics of the hot gas (as well as the morphology and kinematics of the stars). This, combined with the other multiwavelength data, will form a complete view of the different phases (hot and cold gas and stars) and how they interact in the processes of star formation and feedback detected in central galaxies in cooling flow clusters, as well as the influence of the host cluster. Here, in this proceedings, we will introduce the observations and derive the optical dust extinction maps of the four nebulae.

1. Introduction

Decades ago, elliptical galaxies were thought to contain very little, if any, gas. Studies of galaxy formation, therefore, often focussed on the stellar properties, however we now know that a large fraction of the baryonic mass in massive galaxies is believe to be in diffuse form. Thus a complete view of galaxy formation necessarily incorporates both the stars and hot gas and an understanding of the processes by which these phases interact (McCarthy et al. 2010).

Cooling-flow clusters are common in the local Universe and massive central cluster galaxies (CCGs) are often found at the centres of these systems (Edwards et al. 2007). If the central cluster density is high enough, intracluster gas can condense and form stars at the bottom of the potential well. Since the radiative cooling times for intracluster gas are short enough that gas can cool and settle to the cluster centre (Edge, Stewart & Fabian 1992), it has been suggested that cD envelopes may arise from the gradual deposition of this cool gas. The lack of widespread detection of iron lines expected from cluster gas cooling below 1 – 2 keV in *XMM-Newton* observations of cool-core clusters contradicted the model that these young stars are formed in cooling flows. However, it is possible that star formation is ongoing in cool-core clusters at a much reduced rate (Bildfell et al. 2008).

Previous studies have reported several examples of ongoing star formation in CCGs, in particular those hosted by cooling-flow clusters (Crawford et al. 1999; Edwards et al. 2007; Bildfell et al. 2008; Loubser et al. 2009). However, the origin of the gas fuelling this star formation is not yet known. Possible explanations include processes involving cooling flows or cold gas deposited during a merging event (Bildfell et al. 2008). These processes will leave different imprints in the dynamical properties, the detailed chemical abundances, and the star formation

Object	Cluster	Redshift z	Linear scale (kpc/arcsec)	R_{off} (Mpc)	Exposure Time (seconds)	Foreground extinction (mag) $E(B\text{-}V)_{gal}$
MCG-02-12-039	Abell 0496	0.0329	0.654	0.031	7×1800	0.140
PGC026269	Abell 0780	0.0539	1.059	0.015	6×1800	0.042
PGC044257	Abell 1644	0.0474	0.935	0.009	6×1800	0.071
UGC09799	Abell 2052	0.0345	0.685	0.038	6×1800	0.037

Table 1. CCGs observed with the GMOS-IFU on the Gemini South telescope. All four galaxies show extended Hα emission (McDonald et al. 2010). The values for R_{off} (the projected distance between the centre of the optical CCG and the X-ray peak of the cluster) are from Edwards et al. (2007), with the exception of PGC044257 which is from Peres et al. (1998).

histories of these galaxies, which can be studied using high-quality spectroscopy (Loubser et al. 2008; 2012).

As cooling flow models predict more cooled gas than is observed (Bohringer et al. 2001), it is possible that the mass deposited into the molecular clouds is heated by one of several processes - hot young stellar populations, radio-loud AGN, X-rays or heat conduction from the intracluster medium itself, shocks and turbulent mixing layers, and cosmic rays. Therefore, only a small fraction of the cooled gas is detected (Crawford et al. 2005). Thus, CCGs lie at the interface where it is crucial to understand the role of feedback and accretion in star formation. Within these cooling-flow CCGs, cool molecular clouds, warm ionized hydrogen, and the cooling intracluster medium are related. A complete view of the star formation process incorporates the stars with the gas and an understanding of the processes by which these phases interact, and therefore, requires information from several wavelength regimes.

2. Sample

We have chosen our sample of active CCGs from the Hα imaging presented in McDonald et al. (2010). From their 23 cooling flow clusters, we selected all the clusters with clearly detected Hα in their centres (albeit filamentary, extended or nuclear emission). In addition, all of these central galaxies have optical imaging, near-IR (2MASS) and UV (Galex data) available. Thereafter, we selected all the central galaxies with detailed X-ray (Chandra) data, as well as VLA 1.4 GHz fluxes, available. This resulted in a sub-sample of 10 galaxies. The four of these galaxies that we observed with the GMOS IFU are shown in Figure 1.

The rest-wavelength range of the emission lines of interest is 4860–6720 Å (Hβ to [SII]λ6720). The ratio of the forbidden [NII]λ6584 to Hα line will depend on the metallicity of the gas, the form of the ionising radiation, and the star formation rate. The relative strength of the [OIII]λ5007 and Hβ lines reveals further excitation mechanism and gas metallicity information. The role of AGN photo-ionisation is confined to the central 2 – 3 arcsec of active, massive elliptical galaxies (Sarzi et al. 2006). Thus, IFU observations are ideal and will also allow us to study the 2D-distribution of the ionising radiation. In addition to the information from the emission lines, we are able to extract the underlying stellar absorption spectra using the improved GANDALF code (Sarzi et al. 2006). Thus, the kinematics and morphology of the hot ionised gas and stellar components can be correlated. The amount of new stars in the CCGs can be quantified using stellar population models, and be directly comparing to the cooling flows in the clusters.

3. Observations and data reduction

The data were obtained with the GMOS-IFU on the Gemini South telescope in semester 2011A (February to July 2011). The GMOS-IFU in 1-slit mode was used and allowed us to map at least a 3 kpc wide region in the centre of the target galaxies with a simultaneus coverage of

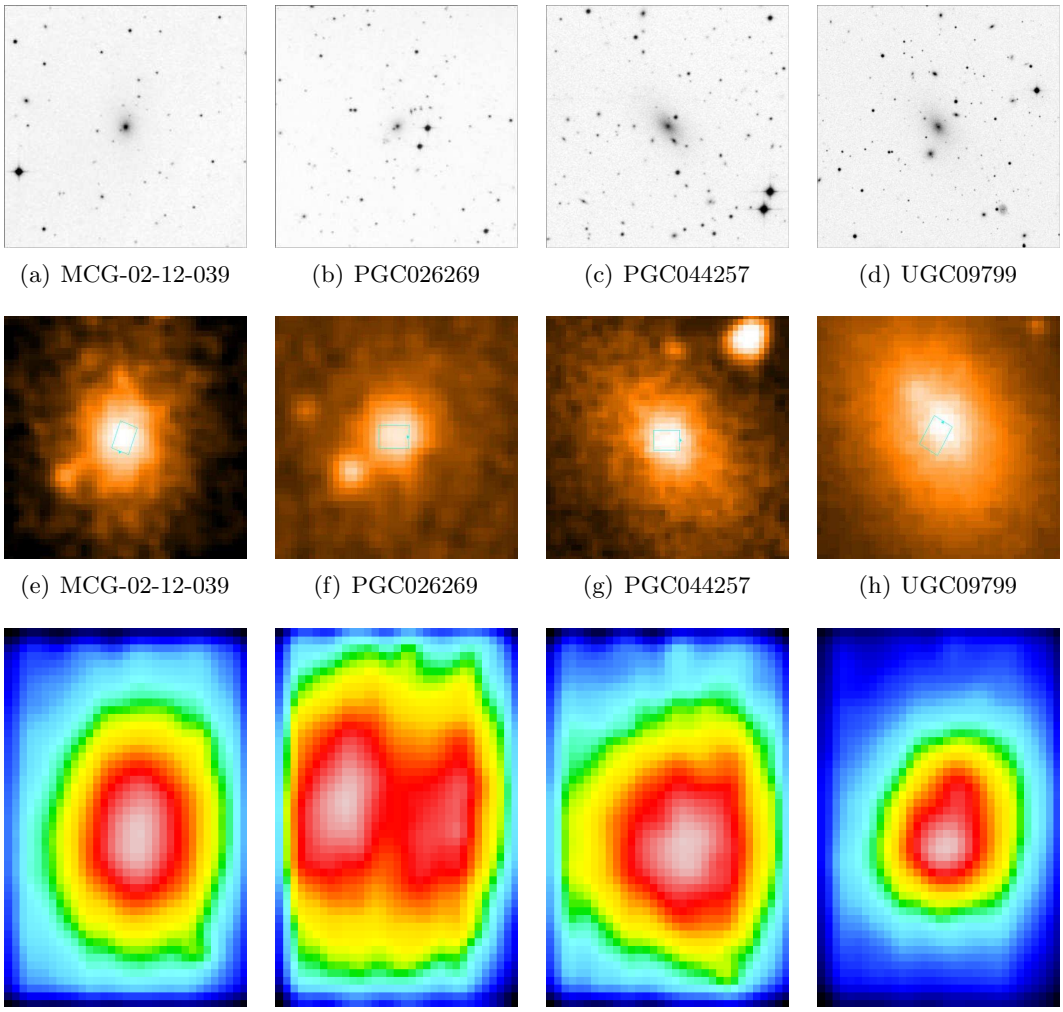

(a) MCG-02-12-039 (b) PGC026269 (c) PGC044257 (d) UGC09799

(e) MCG-02-12-039 (f) PGC026269 (g) PGC044257 (h) UGC09799

(i) MCG-02-12-039 (j) PGC026269 (k) PGC044257 (l) UGC09799

Figure 1. DSS images of the four targets (east to the left). The upper plots show 8 × 8 arcmin field-of-views (FoV), and the middle plots show the targets with the 5 × 3.5 arcsec IFU FoV overlayed. The images are orientated with North at the top and East left, and the top of the IFU FoV is indicated with a blue arrow. The lower plots show continuum images made from the IFU cubes (width of 50 Å at 6350 Å), smoothed spatially with a Gaussian with width 3 spaxels (which corresponds to 0.3 arcsec) and using the SAURON colourmap.

the 4600–6800 Å range in the target rest frame (using the B600 grating) with a single pointing. Detailed observation and data reduction procedures will be given in Loubser et al. (in prep).

The reduced 2D data arrays were transformed back to a physical coordinate grid (x, y, λ datacube) before scientific analysis, while also correcting for atmospheric dispersion. The latter causes the position of a target within the IFU field to vary with wavelength. This correction was necessary as data were taken at different airmasses throughout the observing nights. Each hexagonal spaxel (spatial element) was 0.2 arcsec, and this was subsampled onto a rectangular grid of 0.1 arcsec per spaxel when the separate exposures were combined. The exposures were combined using a centroid algorithm to calculate the shifting in x and y, and also shifting in λ for the exposures at two different wavelength settings. The cubes were also converted into RSS (row-stacked spectra) for further data reductions in IDL (Interactive Data Language). Each

spaxel was averaged with its eight neighbouring spaxels, which is effectively smoothing over 0.3 arcsecs - this is still slightly undersampled compared to the average seeing, but only larger regions will be analysed further.

4. Line measurements and internal extinction

To accurately measure the emission-line fluxes of the CCG spectra, we use a combination of the PPXF (Cappellari & Emsellem 2004) and GANDALF (Sarzi et al. 2006) routines[1]. Gandalf version 1.5 was used as it enables a reddening correction to be performed, and it encorporates errors. This code treats the emission lines as additional Gaussian templates, and solves linearly at each step for their amplitudes and the optimal combination of stellar templates, which are convolved by the best stellar line-of-sight velocity distribution. The stellar continuum and emission lines are fitted simultaneously. All 985 stars of the MILES stellar library (Sánchez-Blázquez et al. 2006) were used as stellar templates to automatically include α-enhancement in the derived optimal template. The Hα and [NII]λ6583 lines were fitted first, and the kinematics of all the other lines were tied to these lines, following the procedure described in Sarzi et al. (2006). However, in cases where the emission of the other lines (example Hβ) were strong enough to measure velocity and velocity dispersion, this was calculated independently as there is no a priori reason to expect the kinematics measured from the [NII]λ6583 and Hβ lines to be the same (as they can originate in different regions). After the kinematics are fixed, a Gaussian template is constructed for each emission line at each iteration, and the best linear combination of both stellar and emission-line templates (with positive weights) is determined. This is done without assuming line ratios, except in the case of doublets where their relative strength is fixed by the ratio of the corresponding transition probabilities. We have adapted the GANDALF code to apply it to the GMOS-IFU cubes for a longer wavelength range. All 1617 spaxels were collapsed together to obtain a 1D spectrum per cube, thereafter all 985 stars for the MILES library were used to create a global optimal template for each galaxy. This global optimal template (and the stars it consisted of – to account for varying weights over the spatial region) was then applied to all 1617 spectra per cube.

Some ellipticals contain dust in the centre that can be patchy, uniform or filamentary (Laine et al. 2003). The long wavelength range of the spectra allows GANDALF to constrain the amount of reddening using the observed decrement of the Balmer lines, which can be set to have an intrinsic decrement consistent with the recombination theory by treating the lines as a multiplet. The physical constraints on the emission from the higher-order Balmer lines also ensures the strength of the corresponding absorption features is correctly estimated.

It uses the dust models by Calzetti et al. (2000) to return the flux attenuation values at the desired wavelength for any given $E(B-V)$ value (optional, see below). The Balmer decrement assumes a case B recombination for a density of 100 cm^{-3} and a temperature of 10^4 K, resulting in the predicted Hα/Hβ ratio of 2.86 (Osterbrock 1989). The code can adopt either a single dust component, affecting both the stellar continuum and the emission-line fluxes, or include a second dust component that affects only the emission-line templates.

The parameter $E(B-V)$, i.e. the colour excess between 4350 Å and 5550 Å, for the galactic extinction for each of the four galaxies was taken from the NED database (Schlegel, Finkbeiner & Davis 1998), and ranged between 0.037 and 0.140 mag. The parameter R_V, i.e. the ratio of the absolute extinction at 5550 Å (A_V) to the colour excess $E(B-V)$, was taken as 3.1 for the interstellar medium (Cardelli, Clayton & Mathis 1989). The total extinction is then given by:

$$E(B-V)_{total} = \frac{2.177}{-0.37R} \times (\log \frac{I_{0H\alpha}}{I_{0H\beta}} - \log \frac{I_{H\alpha}}{I_{H\beta}})$$

[1] We make use of the corresponding PPXF and GANDALF IDL codes which can be retrieved at http:/www.leidenuniv.nl/sauron/.

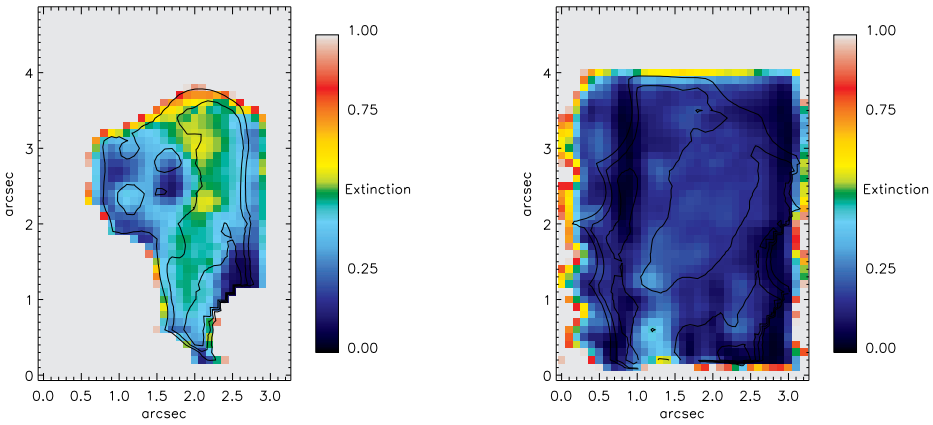

(a) MCG-02-12-039 (b) PGC026269

Figure 2. Total extinction of MCG-02-12-039 and PGC026269. The extinction was smoothed over 0.3 arcseconds, and is only plotted where the velocity dispersion of the Hα line is less than 500 km s^{-1} (to avoid spaxels where the Hα line could not be separated from the NII lines), and it is only plotted where the A/N ratio of the Hα line is higher than 3. The Hα flux contours are overplotted at 1 magnitude apart.

The theoretical Hα/Hβ flux ratio of 2.86 may not be the ideal value to use for Seyfert-type galaxies, but the actual value is debated. It is often assumed that the Hα emission in these systems is enhanced due to collisional processes, and several authors use a value R_V of 3.1 (Osterbrock 1989), although other values have also been determined (Binette et al. 1990 calculate a value of 3.4). The total extinction measured from the Balmer decrement are shown in Figures 2 and 3. The extinction was smoothed over 0.3 arcseconds, and is only plotted where the velocity dispersion of the Hα line is less than 500 km s^{-1} (to avoid spaxels where the Hα line could not be separated from the bordering NII lines), and it is only plotted where the amplitude-to-noise (A/N) ratio of the Hα line is higher than 3 (as defined in Sarzi et al. (2006).

Figures 2 and 3 and shows very low extinction mostly, but some morphological features can be seen in MCG-02-12-039 and UGC09799. In particular, high values of $E(B-V)_{internal}$ can be seen in UGC09799 (once $E(B-V)_{gal}$ (Table 1) is subtracted from $E(B-V)_{total}$ (given in the maps)). The galactic extinction of PGC044257 is $E(B-V)_{gal} = 0.071$ mag, and from long-slit spectra, Crawford et al. (1999) derived the total extinction as 0.46 to 0.63 mag. This agrees with the extinction we derived for the very centre of the galaxy in Figure 3, but on average our spatially resolved extinction is slightly lower. The galactic extinction $E(B-V)_{gal}$ of UGC09799 is 0.037 mag, and Crawford et al. (1999) derived an integrated internal extinction of $E(B-V)$ of 0.22 mag for the centre of this galaxy. This corresponds very well to what we derived and plotted in Figure 3, although we find that some regions shows much higher internal extinction. The values of extinction determined here may be slightly overestimated due to the choice of intrinsic Hα/Hβ flux used.

5. Future work

We are currently measuring the kinematics of the gas and stellar components, and correlating them with each other. Now that we can also measure reddening-corrected fluxes, we can also derive the line ratios to help us determine the ionisation mechanisms. We are continuing the observational program, and a further five of the ten galaxies in the subsample (with confirmed Hα emission and detailed auxillary data already available) have already been observed with

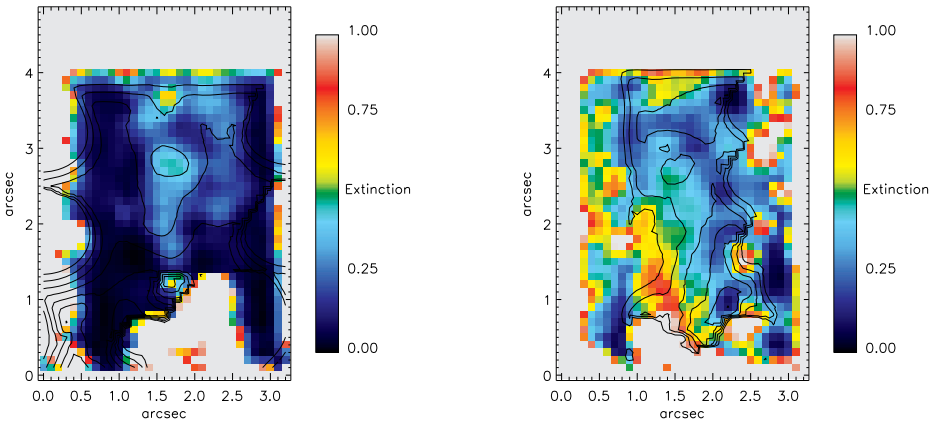

(a) PGC044257 (b) UGC09799

Figure 3. Total extinction of PGC044257 and UGC09799. See caption of Figure 2 for explanation.

long-slit spectroscopy on SALT (the Southern African Large Telescope).

Acknowledgments
SIL is financially supported by the South African National Research Foundation. Based on observations obtained on the Gemini South telescope.

References

[1] Bildfell C, Hoekstra H, Babul A and Mahdavi A 2008 *MNRAS* **389** 1637
[2] Binette L, Raga A C, Calvet N and Canto J 1990 *PASP* **102** 723
[3] Bohringer H et al 2001 *A&A* **365** 181
[4] Calzetti D, Armus L, Bohlin R C, Kinney A L, Koornneef J and Storchi-Bergmann T 2000 *ApJ* **533** 682
[5] Cappellari M and Emsellem E 2004 *PASP* **116** 138
[6] Cardelli J A, Clayton G C and Mathis J S 1989 *ApJ* **345** 245
[7] Crawford C S, Allen S W, Ebeling H, Edge A C and Fabian A C 1999 *MNRAS* **306** 857
[8] Crawford C S, Hatch N A, Fabian A C and Sanders J S 2005 *MNRAS* **363** 216
[9] Edge A C, Stewart G C and Fabian A C 1992 *MNRAS* **258** 177
[10] Edwards L O V, Hudson M J, Balogh M L and Smith R J 2007 *MNRAS* **379** 100
[11] Laine S, Van der Marel R P, Lauer T R, Postman M, O'Dea C P and Owen F N 2003 *AJ* **125** 478
[12] Loubser S I, Sansom A E, Sánchez-Blázquez, P Soechting I K and Bromage G 2008 *MNRAS* **391** 1009
[13] Loubser S I, Sánchez-Blázquez P, Sansom A E and Soechting I K 2009 *MNRAS* **398** 133
[14] Loubser S I and Sánchez-Blázquez P 2012 *MNRAS* **in print**
[15] McCarthy I G et al 2010 *MNRAS* **406** 822
[16] McDonald M, Veilleux S, Rupke D S N and Mushotzky R 2010 *ApJ* **721** 1262
[17] Osterbrock D E 1989 *Astrophysics of gaseous nebulae and active galactic nuclei* (University Science Books, Mill Valley CA)
[18] Peres C B, Fabian A C, Edge A C, Allen S W, Johnstone R M and White D A 1998 *MNRAS* **298** 416
[19] Sánchez-Blázquez P et al 2006 *MNRAS* **371** 703
[20] Sarzi M et al 2006 *MNRAS* **366** 1151
[21] Schlegel D J, Finkbeiner D P and Davis M 1998 *ApJ* **500** 525

A search for optical counterparts of the complex Vela X system

T E Marubini[1], R R Sefako[2], C Venter[1], and O C de Jager[1]

[1]North-West University, Potchefstroom Campus, Private Bag X6001, Potchefstroom, 2520, South Africa

[2]South African Astronomical Observatory, P.O. Box 25, Sutherland, 6920, South Africa

E-mail: 21610126@nwu.ac.za

Abstract. The pulsar wind nebula (PWN) associated with the Vela pulsar is a bright source in the radio, X-ray and gamma-ray bands, but not in the optical. This source is very near, lying at a distance of 290 pc, as inferred from the radio and optical parallax measurements of the pulsar. Knowledge of the brightness and structure of the Vela PWN in optical is important in order to constrain the underlying particle spectrum (and possibly the B-field properties and particle losses) associated with this extended source. We use results from the Digital Sky Survey, as well as results obtained using the SAAO 1.0 m telescope equipped with an imaging CCD (STE4) and BV filters, in an attempt to measure optical radiation from Vela X. To enlarge our field of view, we constructed a mosaic consisting of 3×3 frames around the pulsar position. We present spectral measurements from the *High Energy Stereoscopic System (H.E.S.S.)*, *Fermi Large Area Telescope (LAT)*, *ASCA*, *Hubble Space Telescope (HST)*, *Very Large Telescope (VLT)*, *New Technology Telescope (NTT)*, and *Wilkinson Microwave Anisotropy Probe (WMAP)*, in addition to our optical results. Using these data, we investigate whether or not the radio synchrotron component can be smoothly extrapolated to the optical band. This would constrain the electron population to consist of either a single or multiple components, representing a significant advancement in our understanding of this complex multiwavelength source.

1. Introduction

Vela X has been a very enigmatic source since its discovery, and its true nature has been the subject of debate for many years before its verification as a Crab-like pulsar wind nebula (PWN; see Section 1.1). It is a very rich source, and has been studied extensively in all wavebands. The complex system includes the PWN (Section 1.2), Vela supernova remnant (SNR; Section 1.3), and the well-known Vela pulsar (Section 1.4), with each of the wavebands giving a unique window on the intricate properties of this source.

In this paper, we describe our efforts to detect optical emission from the Vela X plerion. This is a crucial piece of the puzzle needed to constrain important properties, such as the leptonic injection spectrum, B-field, or diffusion coefficient, all of which impact on the broadband spectral emission of Vela X.

In Section 2 we describe our data accumulation, analysis and results, while we discuss our conclusions in Section 3.

1.1. Discovery and identification

Since the detection of Vela X, a disagreement raged between various authors as to the true nature of this source. Three strong nonthermal radio sources of enhanced brightness temperature have been observed [39] and designated Vela X, Vela Y, and Vela Z. To determine the nature of these sources several authors have tried to find their spectral indices [31, 32, 44, 33, 15]. A controversy among two groups ([31, 33] vs. [44]) erupted. The first group claimed that there was no significant difference between the indices of Vela X and Vela YZ, and concluded that Vela X was associated with the Vela supernova remnant (SNR). Conversely, the second group maintained that Vela YZ exhibited a steeper index than that of Vela X, and concluded that Vela YZ is part of the shell SNR, while Vela X was a plerion (defined as a Crab-like PWN, a filled-centre SNR). To solve this mystery, the spectral indices were remeasured [15] and the free-free absorption at 85 MHz estimated. The plerion classification was thus confirmed. Vela X was furthermore found to consist of a network of fine, overlapping, linear, synchrotron-emitting filaments ubiquitous in other plerions [16]. The plerion identification was clinched by showing that there are significant morphological differences between the nebula and the shell filaments [6]. Spectral indices for Vela X, Vela Y, and Vela Z have been obtained [4] which were consistent with a spherical SNR containing a central plerion. We therefore conclude that Vela X is a plerion.

1.2. Multiwavelength properties of the Vela PWN

Two radio lobes oriented about the spin axis of the pulsar between the energy 1.4 GHz−8.5 GHz have been uncovered [26], in agreement with models where the emission is driven by particles from its magnetic poles. They also found that the northern lobe exhibited a bright edge, while the southern lobe was more diffuse. Radio emission from two lobes around the pulsar between the energy 2.4 GHz−5 GHz was next measured [12], the lobes differing in size and brightness, with the radio emission starting where the X-ray emission stops. The orientation of the 31 GHz PWN is in agreement with that of the radio lobes observed at higher resolution and at lower frequencies [17].

A marginal detection of an optical counterpart to the compact Vela X-ray nebula was claimed [36]. Much deeper upper limits of 28.1 *HST* mag arcsec^{-2} for the inner nebula, and $28.0 - 28.5$ *HST* mag arcsec^{-2} for the outer nebula have subsequently been found [29]. An optical plerionic excess for Vela has been observed [40], as well as an Hα feature at the bow shock of Vela, and also an apparent excess around the pulsar position in R band.

The X-ray source 2U 0832.45 was detected above 9σ [23], being less than $1^\circ.2$ in extent. Various authors found spectral indices ranging from $\Gamma = 1.7 - 2.17$ for different regions of the Vela X plerion. A compact X-ray nebula with extension $\sim 1'$ was measured [36], as well as an emission region extending from the pulsar in the southwestern direction out to $3'$. An X-ray emitting "jet" (cocoon) originating at the pulsar, with a size of $45' \times 12'$, extending towards the south-southwest was next observed [27]. The cocoon's X-ray spectrum was similar to the spectrum of the surrounding Vela SNR [28]. Displacement and flux changes in various jet substructures have been observed [37], as well as a hint of a counterjet with a position angle of 130°, measured east of north, and aligned to within $8^\circ \pm 5^\circ$ with the proper motion vector. Two arcs of emission around the pulsar, surrounded by diffuse emission in a "kidney-bean shape" were seen [19]. A two-component X-ray spectrum consisting of a thermal and a nonthermal component have been inferred [24]. The spectrum was steepening with distance, rather than softening, which may be caused by the crushing of the cocoon against the PWN, leading to adiabatic heating that hardens the spectrum.

An unpulsed power-law spectrum with a steep photon index of $\Gamma = 1.6 \pm 0.5$ in the energy range between 0.06 MeV and 0.4 MeV was obtained [8, 9, 41]. These results are consistent with an extrapolation of the $\sim E^{-1.7}$ spectrum of the $1'$ compact nebula. An index of $\Gamma = 2.2$ below 20 keV, with a significant steepening above ∼20 keV ($\Gamma = 2.7$), and a hardening above ∼ 60 keV

to meet the index of $\Gamma = 1.8$ for the *OSSE* spectrum (corresponding to the $1'$ compact nebula) have been obtained [41]. The Vela X region to the south of the Vela pulsar has been observed with the High Energy Stereoscopic System (H.E.S.S.) [3], yielding a fit spectrum between 550 GeV and 65 TeV with a photon index of $\Gamma = 1.45 \pm 0.09_{\rm stat} \pm 0.2_{\rm sys}$ and an exponential cutoff energy of $13.8 \pm 2.3_{\rm stat} \pm 4.1_{\rm sys}$ TeV for an integration region of $0^\circ.8$. The best-fit intrinsic width of the very high energy (VHE) source was $0^\circ.48 \times 0^\circ.36$ (i.e., 58×43 arcmin^2 vs. the X-ray size of 42×12 arcmin^2). *AGILE* detected a source in the off-pulse window of the Vela pulsar at $\sim 5.9\sigma$ significance, with a flux of $(3.5 \pm 0.7)\ \times 10^{-7}$ cm^{-2} s^{-1} above 100 MeV, located $\sim 0^\circ.5$ southwest of the pulsar and having an extent of $1^\circ.5 \times 1^\circ$ [38]. The *Fermi* Large Area Telescope (LAT) detected γ-ray emission at the 14σ level from a $2^\circ \times 3^\circ$ area south of the Vela pulsar [2]. They found that the flux is significantly spatially extended, with a best-fit radius of $0^\circ.88 \pm 0^\circ.12$ for a uniform disc morphology. The spectrum is well described by a power-law with a spectral index of $2.41 \pm 0.09 \pm 0.15$.

1.3. Multiwavelength properties of the Vela supernova remnant (SNR)

The total-power radio image of Vela exhibits many filaments and loop-like structures, and the northern side of the SNR displays a pair of bright concentric arcs, defining the northern edge of the shell [14]. On the southern edge, the emission fades smoothly into the background. The centre of the X-ray shell coincides with the centre of the optical SNR [30]. An optical region covered by the Vela SNR filaments was found [42] having a diameter of $270'$. These filaments occur more densely near the region of Vela X and do not appear to correspond to the radio hot spots. The Vela SNR is interacting with a corner of the observed HI shell at its northwestern border, and it was suggested that this interacting may be responsible for various local bright ultraviolet (UV) and optical arches and filaments, and also for the off-centre position of the Vela pulsar [13]. Far ultraviolet (FUV) emission was detected from the Vela SNR, subtending $\sim 8^\circ$ [34]. A faint X-ray shell was seen [5], which is described by a circle of $\sim 8^\circ.3$ diameter, showing that the pulsar is $\sim 25'$ from the centre of the SNR. These authors also observed six extended X-ray features located outside the blast wave front having conal shapes.

1.4. Multiwavelength properties of the Vela pulsar

The Vela pulsar is a rotation-powered neutron star (NS). Its discovery [25] revealed a period of $P = 89$ ms and a period derivative of $\dot{P} = 1.25 \times 10^{-13}$ s s^{-1}, which implies an age of $\sim$11 000 yrs and a spin-down luminosity of $\dot{E} = 7 \times 10^{36}$ erg s^{-1} [24]. The Vela pulsar emission in all wavelengths is less than 2×10^{-4} that of the Crab [43]. A pointlike object in infrared (IR), the likely counterpart of the Vela pulsar, was found [7], and it was noted that the multiwavelength spectrum of the Vela pulsar reveals a steep flux increase towards the IR. A pointlike object coinciding with the pulsar in the energy range 0.1 keV to 4.5 keV has been found [18]. Thermal X-ray radiation was seen from the vicinity of the Vela pulsar [35]. A power-law with spectral index of $\Gamma = 1.5 \pm 0.3$ for the soft component, and $\Gamma = 2.7 \pm 0.4$ for the harder component between the energy range 0.2 keV to 8.0 keV was found [37]. A spectrum described by a power-law with a spectral index of 1.89 ± 0.06 in the energy range between 50 MeV and 3 GeV was obtained [21], and they concluded that there was no evidence of a steady γ-ray emission from the direction of the pulsar. An average flux of $(7.8 \times 1.0) \times 10^{-6}$ photons cm^{-2} s^{-1} was detected [22] and obtained a power-law spectrum with index $\Gamma = -1.70 \pm 0.02$ (30 MeV to 2 GeV). *Fermi* found a phase-averaged power-law index of $\gamma = 1.51^{+0.05}_{-0.04}$, with an exponential cutoff at $E_{\rm c} = 2.9 \pm 0.1$ GeV [1]. An upper limit to the pulsed emission from the pulsar of $(3.7 \pm 0.7) \times 10^{-13}$ photons cm^{-2} s^{-1} was found above 2.5 TeV [45].

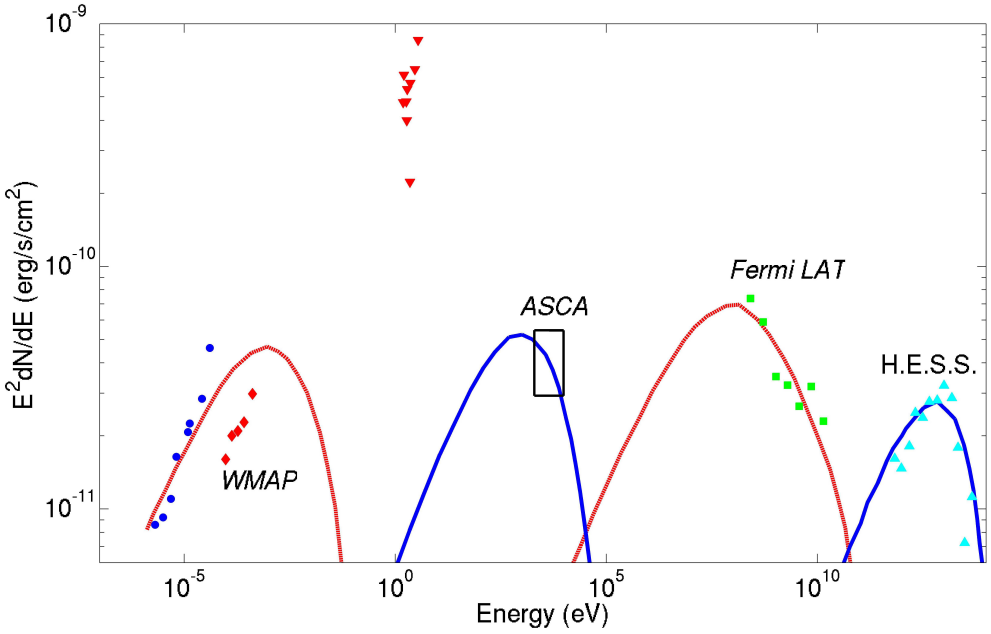

Figure 1. Spectral energy density plot of Vela X. Data and models are taken from [20]. The optical upper limits (red triangles) have been calculated using [29]. The red dashed lines are for the extended radio nebula (ERN) while the blue lines are for the cocoon.

2. Data analysis and results

We have used the 1.0 m telescope at SAAO and collected data during February 2010 and March 2011. We took nine $5.3' \times 5.3'$ images about the Vela pulsar, and constructed a mosaic consisting of 3×3 frames. The raw data of the illuminated detector of a 512×512 pixel chip (STE) were trimmed to 510×510 to avoid gaps in the data. An overlap from frame to frame of about $1'$ was allowed and averages were taken at positions where overlapping occurred. We next rebinned our data to obtain a final trimmed image consisting of 70 rows and 72 columns, taking averages of smaller bins making up the new larger bins so as to decrease fluctuations in our data.

First, we attempted to resolve optical structure in our image mosaic. We removed the bright (mostly foreground) stars by hand, replacing them by the average background level. Different regions around the pulsar have slightly different backgrounds. The emission levels of a number of pixels with a very large number of counts were also replaced with the local background level to smooth out the image. Some excess emission is seen near the southern radio lobe position. This is suspected to be as a result of bright stars that were not clearly removed, but could also be the hints of the optical counterparts of Vela X.

We next proceeded to obtain upper limits. We constructed a circular source centred on the pulsar position, and by eye limited its size so as to exclude most of the obvious foreground stars. This yielded a source encompassing about 340 arcsec^2. From the number of counts DN included by this source circle during our $\tau = 120$ s long observation, we found an upper limit on the magnitude using [1]

$$m' = -2.5 \log_{10} \left(\frac{DN}{\tau} \right) + m_0, \tag{1}$$

with m_0 the zero point magnitudes of the telescope. The zero point magnitudes of the 1.0 m SAAO telescope are 22.0 for the B band, and 22.4 for the V band. Using standard stars, we

[1] www.stsci.edu/instruments/wfpc2/Wfpc2_dhb/wfpc2_ch52.html

next corrected our magnitudes as follows

$$m = 1.03m' - 0.8. \tag{2}$$

Finally, we calculated the implied flux using

$$F_\nu = F_{\nu,0}10^{-0.4m}. \tag{3}$$

We used $F_{\nu,0} = 4\ 260$ Jy for the B filter, and $F_{\nu,0} = 3\ 640$ Jy for the V filter. To derive an upper limit for the full cocoon size, we scaled our flux to extend over an area of 45×12 arcmin^2, making the implicit assumption that the background is roughly similar for the region centred on the pulsar and the cocoon region. Our νF_ν upper limits are $\sim 9.6 \times 10^{-8}$ erg s^{-1} cm^{-2} for the B filter, and $\sim 7.5 \times 10^{-8}$ erg s^{-1} cm^{-2} for the V filter.

In order to compare with other optical studies, we converted *U, B, V, R,* and *I* upper limits found [29] using *Hubble Space Telescope (HST)*, *New Technology Telescope (NTT)*, and *Very Large Telescope (VLT)* to νF_ν values assuming the optical source size to be the same as that of the X-ray cocoon. These upper limits are indicated as red triangles in Figure 1, along with multiwavelength data and models for the broadband spectrum of Vela X [20].

3. Conclusions

The search for the Vela X PWN in optical is crucial to understand its morphology and how energy is distributed throughout the multiwavelength spectrum. It is a challenge to resolve the extended structure of Vela X in the optical waveband, given that many sources contribute to the background radiation, as well as its apparent intrinsic faintness.

We only observed a background level of optical emission near the Vela pulsar position, and there is no structure visible that could be associated with a possible Vela X optical counterpart, apart from some hints of brighter emission near the position of the southern radio lobe. However, this may be due to bright stars that were not cleanly removed. Our νF_ν upper limits of $\sim 10^{-7}$ erg s^{-1} cm^{-2} are clearly not constraining for a multiwavelength model of Vela X's emission.

We note that our upper limits suffer from several observational factors that introduce uncertainties. Removal of bright or even fainter unresolved point sources remain problematic. Our integration times were also very short. Furthermore, the field of view of the telescope is too small to capture the full extension of the source, and we had to use a method of mosaicing several single images to obtain one large image that encapsulates the probable extension of the optical source. Changing conditions between the constituent frames add complexity and uncertainty to our analysis.

Neither our optical limits nor those of others prove to be constraining for the spectral model of Vela X. Barring the gamma-ray data for the moment, one may model the radio, optical and X-ray data with either a single or double synchrotron component, implying either a single or multi-component electron spectrum interacting with the PWN B-field. However, the *Fermi* and H.E.S.S. data are consistent with a two-component leptonic interpretation [2], first put forward by [10] and subsequently elaborated on by [11]. A second model [20] invokes a single electron population, but then assumes different diffusive properties for the $2^\circ \times 3^\circ$ extended radio nebula (ERN) and $45' \times 12'$ cocoon regions (although the H.E.S.S. "coccoon" is quite more extensive). The particles are assumed to be contained within the ERN until the reverse shock from the SNR interacts with the ERN, and diffusive transport starts to take place. Older particles escape then from the ERN, while newly-injected particles are thought to suffer significant cooling in the high-B-field region near the pulsar before being injected into the low-B-field cocoon. Within such a scenario, each substructure (the ERN and cocoon) is responsible for different components of the multiwavelength spectrum (radio and GeV vs. X-ray and TeV). In essence, this is a different

way of constructing a two-component electron injection spectrum. Our optical limits are not violated by these models, although the available limits support the idea of particle escape from the ERN (i.e., a lower synchrotron flux component). Deeper optical observations as well as refined modelling should continue to enhance our understanding of this complex source.

References

[1] Abdo A A *et al.* 2009 *Astrophys. J.* **696** 1084
[2] Abdo A A *et al.* 2010 *Astrophys. J.* **713** 146
[3] Aharonian F *et al.* 2006 *Astron. Astrophys.* **448** L43
[4] Alvarez H, Aparici J, May J and Reich P 2001 *Astron. Astrophys.* **372** 636
[5] Aschenbach B, Egger R and Trümper J 1995 *Nature* **373** 587
[6] Bietenholz M F, Frail, D A and Hankins T H 1991 *Astrophys. J.* **376** L41
[7] Danilenko A A, Zyuzin D A, Shibanov Y A and Zharikov S V 2011 *Mon. Not. Royal Astron. Soc.* **415** 867
[8] De Jager O C, Harding A K, Sreekumar P and Strickman M 1996 *Astron. Astrophys.* **120** C441
[9] De Jager O C, Harding A K and Strickman M S 1996 *Astrophys. J.* **460** 729
[10] De Jager O C 2007 *Astrophys. J.* **658** 1177
[11] De Jager O C, Slane P O and LaMassa S 2008 *Astrophys. J.* **689** L125
[12] Dodson R, Lewis D, McConnell D and Deshpande A A 2003 *Mon. Not. Royal Astron. Soc.* **343** 116
[13] Dubner G, Giacani E, Cappa de Nicolau C and Reynoso E 1992 *Astron. Astrophys. Suppl.* **96** 505
[14] Duncan A R, Stewart R T, Haynes R F and Jones K L 1996, *Mon. Not. Royal Astron. Soc.* **280** 252
[15] Dwarakanath K S 1991 *J. Astrophys. Astron.* **12** 199
[16] Frail D A, Bietenholz M F, Markwardt C B, and Ögelman H. 1997 *Astrophys. J.* **475** 224
[17] Hales A S *et al.* 2004 *Astrophys. J.* **613** 977
[18] Harnden J F R, Grant P D, Seward F D and Kahn S M 1985 *Astrophys. J.* **299** 828
[19] Helfand D J, Gotthelf E V and Halpern J P 2001 *Astrophys. J.* **556** 380
[20] Hinton JA, Funk S, Parsons R D and Ohm S 2011 *Astrophys. J.* **743** L7
[21] Kanbach G *et al.* 1980 *Astron. Astrophys.* **90** 163
[22] Kanbach G *et al.* 1994 *Astron. Astrophys.* **289** 855
[23] Kellogg E, Tananbaum H, Harnden J F R, Gursky H, Giacconi R and Grindlay J 1973 *Astrophys. J.* **183** 935
[24] LaMassa S M, Slane P O and De Jager O C 2008 *Astrophys. J.* **689** L121
[25] Large M I, Vaughan A E and Mills B Y 1968 *Nature* **220** 340
[26] Lewis D, Dodson R, McConnell D and Deshpande A 2002 *Neutron Stars in Supernova Remnants, Astron. Soc. Pac. Conf. Ser. ed P O Slane and B M Gaensler* **27** 191
[27] Markwardt C B and Ögelman H B 1995 *Nature* **375** 40
[28] Markwardt C B and Ögelman H B 1997 *Astrophys. J.* **480** L13
[29] Mignani R P, De Luca A, Kargaltsev O, Pavlov G G, Zaggia S, Caraveo P A and Becker W 2003 *Astrophys. J.* **594** 419
[30] Miller E W 1973 *PASP* **85** 764
[31] Milne D K 1968 *Australian J. Phys.* **21** 201
[32] Milne D K 1980 *Astron. Astrophys.* **81** 293
[33] Milne D K and Manchester R N 1986 *Astron. Astrophys.* **167** 117
[34] Nishikida K *et al.* 2006 *Astrophys. J.* **644** L171
[35] Ogelman H, Koch-Miramond L and Auriere M 1989 *Astrophys. J.* **342** L83
[36] Ogelman H and Zimmermann H-U 1989 *Astrophys. J.* **214** 179
[37] Pavlov G G, Zavlin V E, Sanwal D, Burwitz V and Garmire G P 2001 *Astrophys. J.* **552** L129
[38] Pellizzoni A *et al.* 2010 *Science* **327** 663
[39] Rishbeth H 1958 *Australian J. Phys.* **11** 550
[40] Sefako R R 2002 *PhD thesis* Potchefstroomse Universiteit vir Christelike Hoër Onderwys
[41] Strickman M, De Jager O and Harding A K 1996 *Astron. Astrophys.* **120** C449
[42] Van den Bergh S, Marscher A P and Terzian Y 1973 *Astrophys. J.* **26** 19
[43] Wallace P T *et al.* 1977 *Nature* **266** 692
[44] Weiler K W and Panagia N 1980 *Astron. Astrophys.* **90** 269
[45] Yoshikoshi T *et al.* 1997 *Astrophys. J.*, **487** L65

To Pulse or not to Pulse? That is the question.

C T Middleton and C A Engelbrecht

Department of Physics, University of Johannesburg
PO Box 524, Auckland Park, 2006, South Africa

Email: cmiddleton@uj.ac.za, chrise@uj.ac.za

Abstract.
We present reduction and analysis of two eclipsing Algol-type binary systems from data obtained by the *Kepler* Satellite. KIC star A with parameters more indicative of an evolved Algol system (q = 0.36; $T_{Primary}$ = 7300K, $T_{Secondary}$ = 4900K) shows no pulsation of the primary component of any description, whilst KIC star B, a theoretically less evolved system (q = 0.105; $T_{Primary}$ = 7950K, $T_{Secondary}$ = 4800K) shows strong pulsation frequencies down to a level of 8 x 10^{-4} magnitudes. We suggest possible reasons for the lack of pulsation in KIC A and address the shortfalls in our understanding of Algol systems.

Introduction; Oscillating Eclipsing Algols
Algol systems are a class of eclipsing binary stars. The designation of an 'Algol system' is used specifically to refer to eclipsing binary systems which are young enough that neither component has yet become degenerate, but close (and old) enough that some mass transfer of one component to another has already taken place. In some Algol systems, one of the components has been found to undergo stellar pulsation. All pulsating Algols detected and analysed thus far lie inside the classical δ Scuti star instability strip, very close to the ZAMS [1]. These authors also adopted the oEA (oscillating EA) designation for mass accreting, pulsating components in Algols. Rapid Mass Transfer or Accretion (RMT/RMA) evolutionary stages see low-mass progenitors of oEA stars accreting a large portion of mass from Roche lobe overflow of the formerly massive secondary component. These stars have by now evolved rapidly - on thermal time scales - to higher mass and luminosity. They are presently situated close to the ZAMS on the HR diagram, in the hot end of the classical instability strip. They are of spectral type A– F, and are at a slow mass accretion (SMA) stage in their evolution. SMA maintains a thermal imbalance and ensures a slow evolution along the MS towards higher masses and earlier spectral type. In the mass accretion process they do not follow standard evolutionary tracks of normal main-sequence (MS) or post-MS δ Scuti stars.

1. The *Kepler* Satellite

Launched in March 2009, the *Kepler* satellite is NASA's first mission designed to identify Earth- and smaller-sized planets [2].The satellite has a 0.95 meter Schmidt telescope with 42 CCD's having a fixed field of view of 105 square degrees aimed at the constellations of Cygnus and Lyra. The design made it possible to continuously monitor the brightness of ~150 000 stars during the first year and thereafter reduced to 100 000 stars as the mission drew to a close. The results are extremely high quality light curves of interest in both planet detection and asteroseismology. Of significance is that the CCDs are not designed to take pictures. The images are intentionally de-focussed to 10 arc seconds to improve photometric precision [3]

The instruments collect data in the 430-890 nanometre range, with a dynamic range of 9^{th} to 16^{th} magnitude stars and a near 100% duty cycle. The duty cycle is not 100% as the telescope is rolled every 90 days to maintain the sun on the solar arrays and the radiator pointed into deep space.

From May 12 2009, *Kepler* observed ~150 000 stars for close on four years. The observing intervals were 29.4 minutes (Long Cadence) for the primary purpose of detecting planetary transits. Only 512 targets were sampled at 1 minute intervals to support asteroseismic characteristics [4]. Of particular importance is that *Kepler* was required to obtain a signal to noise ratio (S/N) of 4:1 for an 84 parts per million (ppm) deep, 6.5 hour transit of a G2V star. The implications of this are that the noise on the 6.5 hour intervals must be below 20 ppm, which is to include stellar variability

contributions.

2. Candidate selection

KIC A and KIC B were selected from a group of eclipsing binary stars initially identified by the *Kepler* Asteroseismic Science Consortium (KASC) and made available by the ninth working group (Binary stars). At the time of selection the pulsation characteristics of the binary pairs were not evident in the available light curves. These pulsations only became apparent after the initial binary model had been subtracted from ten quarters (i.e 2.5 years) of *Kepler* data.

3. KIC A and KIC B

3.1 KIC A

3.1.1 Light curves

The best fit initial binary model (solid line superimposed on the phased data - figure 1) was generated in Binary Maker 3 [5] with minor adjustments in Phoebe (Physics of Eclipsing binaries) – [6]. Derived parameters, whilst not unique (without accurate mass ratios from spectroscopy), give the mass ratio of the components as $q = 0.36$, while $T_1 = 7300$ K and $T_2 = 4900$ K.

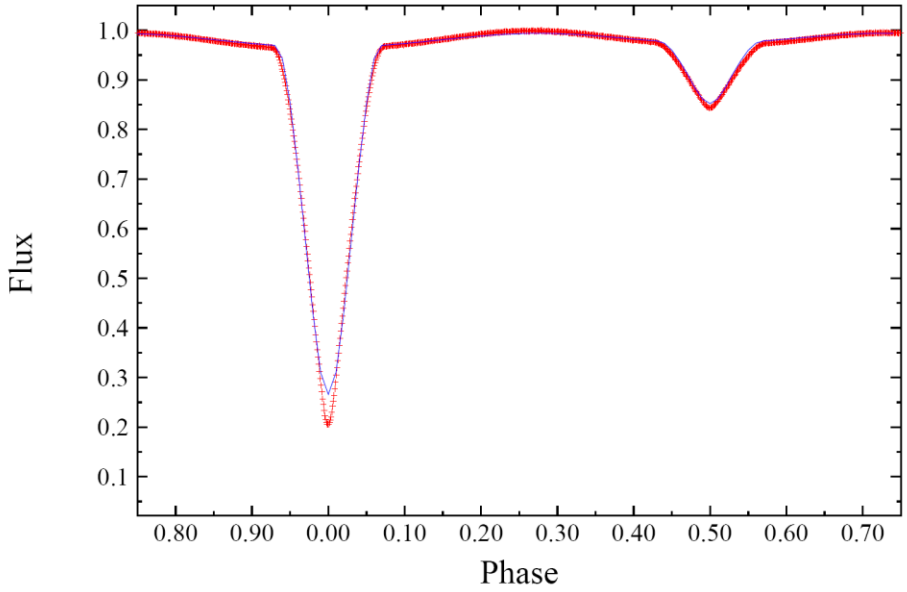

Figure 1: Phased flux for KIC A with binary fit superimposed. 'Phase" refers to the phase of the binary orbit, while 'Flux' is a measure of intensity.

3.1.2. Looking for pulsations

An iterative procedure was followed to separate the binary signal from any potential pulsation signatures in the light curve. Residuals were created by subtracting the binary model from all ten quarters of detrended data. The process converged upon a stable model after three iterations.

Two standard packages for binary system analysis, viz. Binary Maker 3 (BM3) and PHOEBE, were employed for the task. Figure 2 shows a small section of the residuals generated by removal of the synthetic curve from the first ten quarters of data using the first binary model.

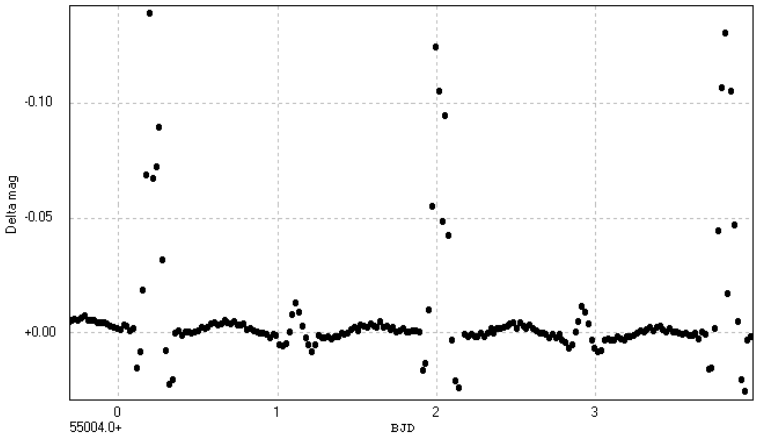

Figure 2: A section of the residuals generated by subtracting the first PHOEBE-generated binary model from the detrended data. The abscissa is indexed in days relative to Baryocentric Julian Date 2455004.

3.1.3. Pulsation signatures

The initial periodogram of the residuals from KIC A, after consecutive refinement of the binary model, is shown in figure 3.

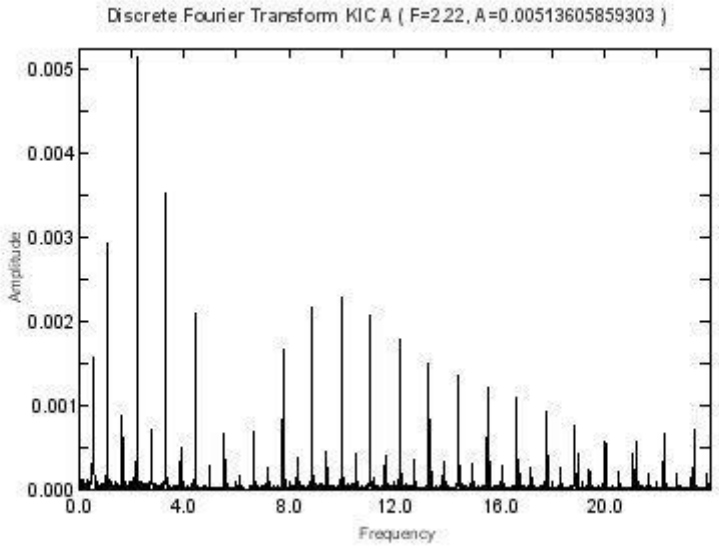

Figure 3: The initial Discrete Fourier Transform (DFT) periodogram of the residuals from KIC A, after consecutive refinement of the binary model.

If there are detectable pulsations present in one of the components of the system, corresponding peaks will appear in the periodogram. However, Figure 3 only shows the expected decaying envelope of Fourier components associated with the binary orbit. When a sine function with the orbital frequency (and ampltide and phase determined by a least-squares fit) is subtracted from these residuals, the periodogram shown in Figure 4 is obtained. A Fourier envelope is still visible, though much reduced in amplitude.

3.2 KIC B

3.2.1 Light curves

The best fit initial binary model (solid line superimposed on the phased data - figure 5) was generated in Binary Maker 3, with minor subsequent adjustments then applied with PHOEBE. The fit is here shown against magnitude, and illustrates the contrast with the flux fit that was shown for KIC A in Figure 1. Derived parameters of the best fit, whilst not unique (without accurate mass ratios from spectroscopy), give the mass ratio q = 0.105, angle of inclination of the orbit i = 70.8 degrees, effective temperature of the primary T_1 = 7950 K and that of the secondary T_2 = 4800 K.

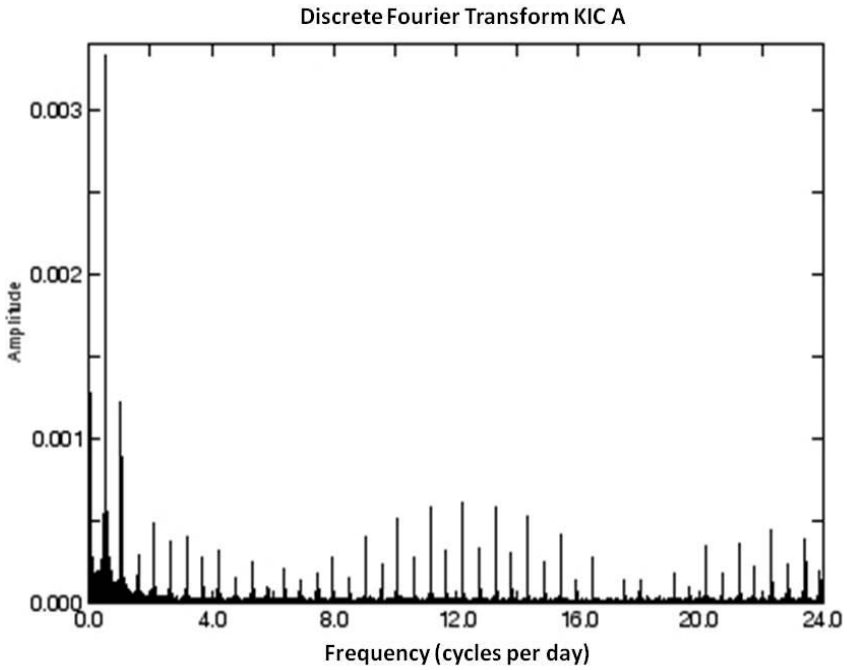

Figure 4: The DFT periodogram of the residuals from KIC A after removal of a sine curve with the orbital frequency

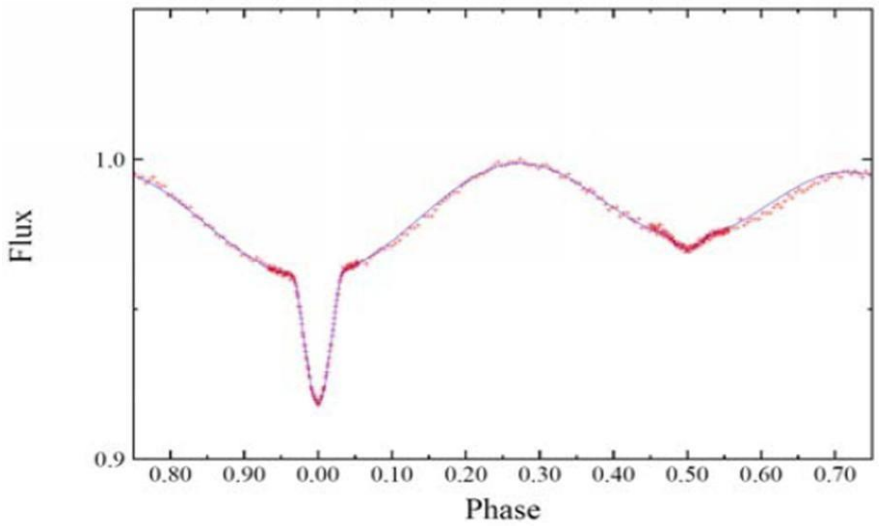

Figure 5: Phased flux for KIC B with binary fit superimposed. 'Phase" refers to the phase of the binary orbit, while 'Flux' is in magnitudes.

3.2.2. Looking for pulsations

As alluded to above, we followed an iterative process, where the residuals obtained - after subtraction of the initial binary fit – are tested for periodic signals. If any are found, a least-squares fit of harmonic components with these periods is subtracted from the original data and a binary fit is performed once again. This cyclic procedure is continued until no further changes occur (i.e. the procedure has converged to a stable solution). The residuals obtained after subtraction of this final (convergent) binary solution are then interrogated for any remaining periodic signals, beyond the obvious declining envelope of harmonic overtones (i.e. the Fourier components) of the orbital period.

3.2.3. Pulsation signatures

The periodogram obtained for the residuals after subtraction of the initial binary fit is shown in Figure 6. Compare this with the behaviour of KIC A as shown in Figure 4. Although there is still a remnant of the binary period and a few low-order harmonics, a separate periodicity at about 15 cycles per day is clearly evident. This is a classic (albeit new!) pulsation signature in an Algol system.

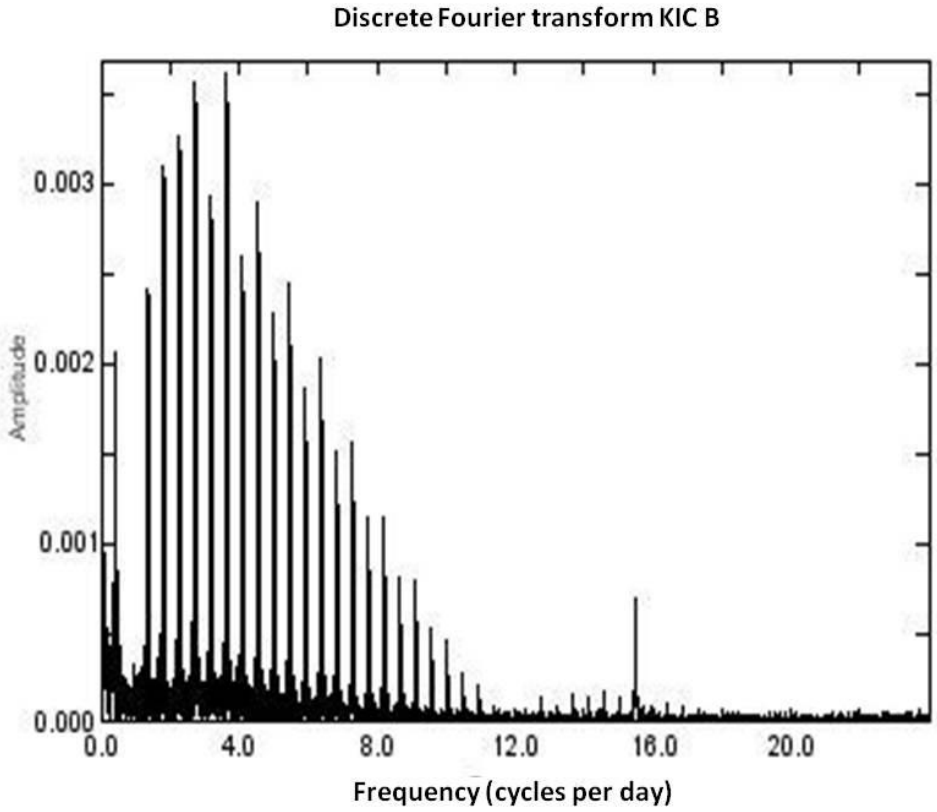

Figure 6: DFT Periodogram of residuals obtained after subtraction of first binary fit for KIC B and after removal of a sine curve with the orbital frequency

3.2.4 Binary: Pulsation resonances

When comparing the pulsation signal obtained from the residuals of the final, convergent fit, with the orbital period, it transpires that $f_{pulsation} : f_{orbit} = 34$. It can not yet be theoretically proven that the pulsation is actually driven by a resonance with the orbital period, but it is a compelling possibility that requires pulsation modelling of the primary star in this system to be confirmed (the secondary is too cool and small to be pulsating with a period of 15 c/d). Spectroscopy of this star is currently being analysed with this goal in mind.

4 Discussion and Conclusion

We have shown the results of a search for pulsations conducted in two very similar Algol systems, observed contemporaneously with the same instrument. KIC A shows no evidence of pulsations while KIC B shows a clear pulsation signal at 15 c/d, which is also 34 x the orbital frequency. In order to ascertain the reason for this difference, we first need to obtain radial-velocity time series for the two systems to pin down the actual masses more accurately and appropriate spectroscopy to determine the effective temperatures of the components, so that a satisfactory comparison with stellar pulsation models may be made. Spectra for KIC B have already been obtained and are being analysed at present. We hope to also obtain spectra for KIC A. Once the masses of the components have been accurately obtained, we shall proceed to modelling of the respective primary components' pulsation behaviour. The existence of an actual pulsation:rotation resonance (and the causes thereof) may then be considered.

We speculate that one or more of the following causes might be responsible for the difference in behaviour that has been reported above: i) The primary in KIC A falls just outside the classical instability strip and pulsations are therefore damped in the interior. This conjecture can be tested once detailed spectra of KIC A have been obtained; ii) Both KIC A and KIC B fall outside the classical instability strip, but the presence of a companion allows driving of the 15 c/d pulsation seen in KIC B to overcome the normal damping effects; iii) A sufficiently high rate of mass transfer might inhibit pulsations in KIC A. Improved modelling of Algol systems will be required to test the latter two conjectures.

A few dozen similar systems have been selected from the *Kepler* database and are undergoing similar analysis at present.

References

[1] Mkrtichian DE et al. 2002 *ASP Conference Series* **259** 96
[2] Borucki WJ et al. 2010 *Science* **327** 977
[3] Koch D et al. 2010 *38thCospar Scientific Assembly* (Bremen, Germany) 4
[4] Gilliland RL et al. 2010 *The Astrophysical Journal* **713** L160
[5] Bradstreet D 2005 *Society for Astronomical Sciences24th Annual Symposium on Telescope Science* (Society for Astronomical Sciences) 23
[6] Prsa A 2006 Phoebe Scientific Reference *Online Manual* www.phoebe-project.org

Modelling Stellar Convection

S L Moonsamy[1], F A M Frescura[1], C A Engelbrecht[2]

[1]School of Physics, University of the Witwatersrand, Private Bag 3, WITS 2050, Johannesburg, South Africa
[2]Department of Physics, University of Johannesburg, PO Box 524, Auckland Park 2006, Johannesburg, South Africa

E-mail: sashin.moonsamy@gmail.com

Abstract. We briefly review Mixing Length Theory and comment on its effectiveness in modelling stellar convection.

1. Introduction

Computer models of stellar structure have been severely hampered by several key problems. These include the description of stellar convection, the inclusion of non-linear effects in stellar pulsation, and the effect of rapid rotation on the pulsation modes [1]. To date, these problems have been inadequately addressed by replacing the full theory by highly simplified versions thereof. In particular, current models of stellar structure do not incorporate in a realistic way one of the key features of real stars: turbulent convection.

The modelling and theoretical understanding of this phenomenon has proven to be a considerable challenge to both theorists and observers. However, during the last two decades, rapid advances in computer technology coupled with observational data of an unprecedented resolution and accuracy has permitted a new look at the field.

Until recently, stellar models have relied almost exclusively on a semi-phenomenological theory of stellar convection, known as mixing-length theory (MLT) [2]. While having served as a useful model of the convective process, MLT is however not without its flaws. The theory is littered with seemingly arbitrary parameters which have been the source of some disagreement in the literature [3]. One of the major sources of uncertainty in MLT is the value to be used for the mixing-length itself.

Recent work in the field has suggested that this theory underestimates hugely the rate of energy transport through the stellar material [4]. This has far reaching consequences since the predicted rate of energy transport impacts severely on the evolution of stars, their ages and lifetimes and consequently also on our understanding of the evolution and structure of galaxies and of the cosmos.

The purpose of this paper is to review the essential ingredients of mixing length theory and consider its role in our present understanding of the structure and evolution of stars.

2. Basic Formalism

In MLT, the convection zone is treated as if it consisted of groups of "average" convective elements. This replaces the conceptually difficult situation, involving eddies of different shapes,

sizes, velocities and lifetimes, that actually occurs inside these zones since each of the "average" convective elements are assumed to have the same physical properties at a given radial distance r from the stellar centre.

Convective elements are assumed to form as a result of instabilities or perturbations in the stellar fluid. Once formed, they will rise or fall under the action of bouyancy forces through a characteristic distance known as the mixing length, before losing their identity and merging with the surrounding fluid. In this sense, the mixing length for a given convective element is its "mean free path" in the convective motion. The elements may of course also exchange heat with their surroundings via radiation as a result of temperature imbalances.

According to Gough [5]: *"It is as a result of ignoring different combinations of these processes, approximating the remaining ones in slightly different ways, and making different assumptions about the geometry of the flow that different mixing length models have emerged."* The differences in these models have not been stressed in the literature since in almost all cases they result in formulae for the advection of heat through the stellar interior that are essentially the same up to factors of order unity. They do however become apparent in situations where the convectively unstable region is not static, such as in studies of stellar pulsation. Some authors ([6], [7]) have proposed a different picture of convection based on cells consisting of rising and falling columns of fluid surrounded by a rising or falling cylinder of fluid. It has however been shown that this amounts to little more than thinking of pairs of rising and falling elements as a single entity in the MLT picture [5].

3. Assumptions

The assumptions of MLT may be stated formally as follows:

- On average, each convective element is assumed to travel through a distance λ, the mixing length, before dissipating into the surroundings. Note that in general $\lambda = \lambda(r)$.
- The mixing length is assumed to be much shorter than any scale length associated with the structure of the star.
- The precise shape of the elements is not specified, but they are all assumed to possess the same characteristic dimension. This characteristic dimension will be taken to be of the same order as the mixing length.
- All convective elements at a given radial distance r from the centre of the star are assumed to convect at the same *average* speed $\overline{v}$, which is taken to be the speed of upward and downward moving elements averaged over both the mixing length and the surface defined by r. Note that $\overline{v} = \overline{v}(r)$.
- Each element is assumed to maintain a state of complete pressure equilibrium with its surroundings as it rises or falls. This means that each material element at a given distance r from the stellar centre is at exactly the same value of pressure. This assumption implies that $\overline{v}$ should never exceed the local sound speed, v_s, in the mixing length approach. Were this to happen, the assumption of complete pressure equilibration would not be very realistic, since the mechanical adjustment time t_p is of the order λ/v_s whereas the mean eddy lifetime t is of the order of $\lambda/\overline{v}$. Hence $t_p/t \sim \overline{v}/v_s$ which means that $\overline{v} < v_s$ in order for $t_p < t$.
- The star is assumed to be in a steady state. The amount of matter rising at each level is thus, at each time, the same as the amount sinking. This assumption is equivalent to that of hydrostatic equilibrium throughout the star.
- The effects of magnetic fields and rotation are ignored as well as all acoustic phenomena.
- Temperature and density differences between the element and its surroundings are assumed to be small.

- The effects of turbulent pressure on the the convective process are neglected. It will be shown that this is a reasonable assumption to make provided that the convection is subsonic.

4. Noteworthy Issues

The above assumptions represent an extreme simplification of the convective processes that occur in the stellar interior. The constraints represented by these assumptions are all derived from laboratory based simulations of convection and may not be applicable to the much more complicated situations encountered in the interiors of stars. In fact, it can be shown that in practice, MLT ends up violating one of its own assumptions. This failure is traceable to the fact that the MLT assumptions are essentially equivalent to what is known as the Boussinesq Approximation. This approximation assumes that the fluid is almost incompressible, and that variations in its temperature and density may be ignored except insofar as they give rise to the buoyancy forces that drive convection. While the Boussinesq Approximation has been shown to work very well in laboratory situations where the size of the fluid system is much smaller than any of the associated scale heights, it turns out, that when applied to stars, reasonable results are obtained only if the mixing length is chosen to be approximately equal to the pressure (or some other) scale height characteristic of the star.

To make matters worse, the question as to which scale height is the most physically significant with regard to the mixing length theory is still unresolved. It is customary to set $\lambda = \alpha H$ where H is usually taken to be either the pressure or density scale height and α is a free parameter. Use of the density scale height may however lead to difficulties when studying the stellar surface since it becomes negative in the case of density inversion. It has also been suggested by Faulkner et al. [8] that the temperature scale height be used in certain applications. Most authors tend to adopt the pressure scale height for the sake of convenience.

There is also another troublesome feature present in the assumptions. Using the virial theorem, one can easily show that the average value of the pressure scale height in a star is of the same order of magnitude as the stellar radius, R, so that $\lambda \approx H_p \approx R$. Now if the size of the element is assumed to be of the same order as the mixing length, then this suggests that it does not get very far before mixing.

Furthermore, if the cross-sections of rising and falling gas columns were originally equal in a convective layer, then the rising gas must have expanded by a factor of e after moving through a pressure scale height, in order to maintain a state of pressure equilibrium with the surroundings. This means that after a distance comparable to H_p there is very little room left for the falling gas plumes. But we require that the amount of material falling be equal to the amount which is rising. The only way in which this can happen is if some of the rising gas elements are dragged down by the falling material. Thus, for any given layer, a large percentage of the falling matter must have been taken out of the rising columns. There is however, no satisfactory method for computing these percentages.

Lastly, our entire picture of convective heat transfer would have to be drastically modified in order to account properly for situations involving supersonic convection. In the absence of a theory which can accurately account for these effects, we will force v_s to be the upper limit of v, so that should the equations of MLT ever yield a value of $v > v_s$ at some point in a convection zone we would simply set $v/vs = 1$. This assumption is arbitrary and ad hoc. The results obtained using it are likely to be incorrect, both due to fundamental crudity of MLT and the fact that the theory may not even be applicable at all in such regions.

5. Discussion

The mixing-length treatment has been proven to be fairly adequate when building stellar models whose sole purpose is the description of the salient features of stellar evolution. But it has well known shortcomings in specific applications. Almost all versions of MLT approximate the

equations of motion in the manner set out by Boussinesq [9]. The Boussinesq approximation is known to be valid only when the mixing-length is much less than the pressure and density scale heights, and implies in particular that the motion is subsonic. However, there is a disagreement between stellar models and observations unless the mixing length is of the same order as these scale heights, so the theory is internally inconsistent. Moreover, the energy equation does not admit terms such as viscous heating which can be important in deep layers, even when the motion is subsonic [5]. It also appears that supersonic convective velocities may be achieved in certain classes of variable stars, making the generation of acoustic energy an important effect. If the flux of acoustic energy becomes a significant proportion of the total flux, then pulsational effects can no longer be ignored. This is not something that can be described within the Boussinesq regime since it does not allow for the possibility of acoustic waves.

Another major deficiency of the MLT is that it describes the convective heat flux in terms of the local properties of the fluid. This makes it particularly inadequate for studies of non-local effects such as convective overshoot, which is known to play a significant role in almost all stages of stellar evolution. Moreover, MLT provides little information about the dynamical properties of convection apart from the mean size of the convective eddies and their turnover time.

MLT is therefore inadequate when dealing with:

- The description of photospheric and subphotospheric layers.
- Convective overshoot and penetration.
- The coupling between convection and pulsation.
- The interaction between convection and rotation.
- The generation and transport of magnetic fields in stars.

A number of papers in the literature have started to remedy the situation. Alternate prescriptions for the treatment of convection in the stellar interior have for example been proposed by Canuto and Mazittelli [4], who claim that the MLT can be significantly improved by considering the full spectrum of eddies with the appropriate convective flux distributions. Recently, more sophisticated models which not only include the turbulent pressure but the full Reynolds stress and other higher order moments in the velocity and temperature fluctuations have also received attention [10], [11].

It remains to be seen whether the use of more sophisticated closure models based on higher order moments will result in predictions that are in better agreement with observation than the MLT. This is now becoming an area of active research and it is hoped that the development of these models will provide a solution to some of the severe limitations present in MLT.

References

[1] Weiss A 2002 *E.S.A. S.P.* **485**, 57
[2] Bohm-Vitense, E 1958 *Z. Astrophys.* **46**, 108
[3] Mazzitelli I. 1999 *A.S.P.C.* **173**, 77
[4] Canuto V M and Mazzitelli I 1991 *Ap. J.* **370**, 295
[5] Gough D O 1977 *Ap. J.* **214**, 196
[6] Plaskett H H 1936 *M. N. R. A. S.* **96**, 402
[7] Opik E J 1950 *M. N. R. A. S.* **110**, 559
[8] Faulkner J, Griffiths K and Hoyle F 1965 *M.N.R.A.S.* **129**, 323
[9] Boussinesq J 1903 *Theorie Analytique de la Chaleur*, **vol. II**, (Gauthier-Villars)
[10] Canuto V M 1992 *Ap. J.* **392**, 218
[11] Canuto V M 1993 *Ap. J.* **416**, 331

Periodic X-ray modulations in Supersoft X-ray Sources[1]

A Odendaal[1], PJ Meintjes[1], PA Charles[2] and AF Rajoelimanana[3,4]

[1]Department of Physics, University of the Free State, P.O. Box 339, Bloemfontein, 9300, South Africa
[2]School of Physics and Astronomy, Southampton University, Southampton SO17 1BJ
[3]South African Astronomical Observatory, P.O. Box 9, Observatory, 7935, South Africa
[4]Astrophysics, Cosmology and Gravity Centre (ACGC), University of Cape Town, Private Bag X3, Rondebosch, 7701, South Africa

E-mail: WinkA@ufs.ac.za

Abstract. The supersoft source CAL 83 is often considered to be the prototype of its class. We report the discovery of modulations at a period of ∼67 s in *XMM-Newton* X-ray data of CAL 83. This may be the spin period of a highly spun-up white dwarf, which is to be further investigated with follow-up observations in both the X-ray and optical wavebands. The supersoft source SMC 13 has an orbital period of ∼4.1 h. SMC 13 was reported in the literature to exhibit orbital modulation in its X-ray flux, as inferred from its folded *ROSAT* light curve. We report the confirmation of this orbital modulation from three *Chandra* data sets, each providing continuous coverage of ∼2.7 complete orbital cycles.

1. Introduction

Supersoft X-ray sources (SSS) form a highly luminous ($\sim 10^{36}$-10^{38} erg s^{-1}) class of objects that emit more than ∼90% of their energy below 0.5 keV. SSS were first observed with the *Einstein X-ray Observatory* (Long et al. 1981, Seward and Mitchell 1981) and further discoveries by *ROSAT* established them as a distinct class of objects (Trümper et al. 1991). Typical effective temperatures range between ∼15-80 eV (see Kahabka and van den Heuvel (2006) for a recent review on SSS).

It was shown by van den Heuvel et al. (1992) that the low effective temperatures and high luminosities of these sources can be explained by the nuclear burning of hydrogen on the surface of a white dwarf accreting material on the thermal time scale of the donor. The accretion rate required for steady nuclear burning is $\sim 10^{-7} M_{\odot}$ yr^{-1}, which can be sustained if the donor mass is comparable to or greater than the white dwarf mass (Paczyński 1971, Savonije 1983). Many SSS are also believed to contain accretion discs.

Recent analysis of archived data of the binary supersoft sources CAL 83 and SMC 13 showed strong modulations in the X-ray waveband. We report preliminary results of the timing analysis performed on these data, based on the results obtained during the M.Sc. research of Odendaal (2012).

[1] Based on observations obtained with *XMM-Newton*, an ESA science mission with instruments and contributions directly funded by ESA Member States and NASA, as well as observations from the *Chandra Data Archive*.

2. CAL 83 in the Large Magellanic Cloud

2.1. Observations and data calibration

CAL 83 has been observed by *XMM-Newton* several times from April 2000 to May 2009. The X-ray data were recorded with the three EPIC detectors (MOS1, MOS2 and PN) and the RGS. The data sets were calibrated by following standard data reduction procedures with the *XMM-Newton* Science Analysis System[2], Version 11.0. The arrival times in the event files were corrected to the solar system barycentre (TDB system). From each calibrated event file, a light curve with a binning of 10 s was created from the source photons in the 0.15-2.5 keV range.

2.2. Timing analysis

Each of the CAL 83 X-ray light curves were detrended by subtracting the mean and dividing by the standard deviation. The task SCARGLE in the Starlink PERIOD package[3] was subsequently utilized to create a Lomb-Scargle (LS) periodogram from each detrended light curve (Scargle 1982).

A power peak at a $\gtrsim 2\sigma$ level near 15 mHz ($P \sim 67$ s) was found in the EPIC PN (the most sensitive of the 5 detectors) periodograms of 6 of the observations. These periodograms are shown in figure 1. The EPIC MOS periodograms of some of these observations have a very weak feature near ∼67 s. The periodicity was not detected in the RGS periodograms.

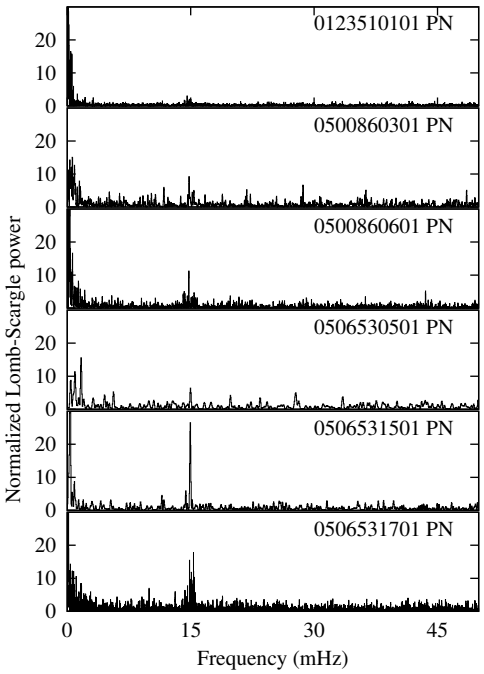

Figure 1. LS periodograms of EPIC PN observations exhibiting ∼67 s periodicity.

The EPIC PN data of the 6 data sets exhibiting the periodicity were reanalysed by subdividing the longer data sets into shorter light curves and creating a similar LS periodogram for each. The results from the segments exhibiting the periodicity are summarized in table 1. The error bars on the period values were determined by the intrinsic Fourier resolution of each periodogram, which gives an error of $P^2/2T$ to each side of each period peak, where P is the period, and T the total length of the light curve.

It is evident from table 1 that the detected period varies over a range of several seconds. The power of the peak is also highly variable for the different periodograms. No obvious correlation was found between the mean count rate and peak power, although it was noted that the period was not detected in data sets where the EPIC PN count rate was below 1 count/s.

2.3. Discussion

The exact origin of the ∼67 s period is still under investigation. As the periodicity was found in the X-ray data, it is associated with the white dwarf. The fact that the modulation at ∼67 s is present in different data sets spanning over about 9 years possibly rules out short-lived quasi-periodic oscillations. A very promising possibility is that the periodicity represents the spin period of a magnetized white dwarf in CAL 83. The period is reminiscent of the short white

[2] `http://xmm.esa.int/sas/`

[3] `http://www.starlink.rl.ac.uk/star/docs/sun167.htx/sun167.html`

Table 1. Timing analysis of the CAL 83 *XMM-Newton* PN light curves exhibiting a ∼67 s periodicity. "Peak power" refers to normalized power from Lomb-Scargle periodogram.

Obs ID	Length (s)	BJD (middle)	Period (s)	Peak power	Mean PN counts/s	Principal investigator
0123510101	5000	2451657.95459	68.6 ± 0.5	7.8	7.3	Fred Jansen
	5000	2451658.06917	67.9 ± 0.5	9.8	5.9	
	5000	2451658.12704	67.2 ± 0.5	5.2	6.7	
	5000	2451658.24162	67.2 ± 0.5	12.5	3.4	
	5000	2451658.29949	66.3 ± 0.4	7.7	3.0	
0500860301	5240	2454288.51696	65.0 ± 0.4	7.8	6.9	Thierry Lanz
	5240	2454288.57761	67.5 ± 0.4	8.6	6.8	
0500860601	5010	2454429.44780	67.8 ± 0.5	5.1	5.9	
	5010	2454429.56378	67.8 ± 0.5	9.3	6.9	
	5010	2454429.62176	69.9 ± 0.5	10.6	7.2	
0506530501	4600	2454573.12196	66.8 ± 0.5	6.6	2.1	Robert Schwarz
0506531501	6480	2454691.16206	66.9 ± 0.3	27.6	9.3	
0506531701	4570	2454981.86631	67.6 ± 0.5	7.8	8.8	
	4570	2454981.91920	66.6 ± 0.5	10.5	8.7	
	4570	2454981.97210	66.1 ± 0.5	15.9	9.2	
	4570	2454982.02499	64.9 ± 0.5	6.4	9.4	
	4570	2454982.07788	64.9 ± 0.5	5.5	7.9	
	4570	2454982.13078	67.3 ± 0.5	8.5	10.0	
	4570	2454982.18367	67.6 ± 0.5	4.7	9.8	
	4570	2454982.23657	66.1 ± 0.5	6.9	9.8	
	4570	2454982.28946	65.4 ± 0.5	15.6	8.9	
	4540	2454982.34224	65.3 ± 0.5	16.5	9.2	

dwarf spin periods in the cataclysmic variables AE Aqr (∼33 s), V533 Her (63.633 s) and DQ Her (142 s) (Norton et al. 2004).

If it does represent the white dwarf spin period, one would expect the detected period to have exactly the same value in different data sets. However, it must be kept in mind that, although the arrival times have been corrected to the solar system barycentre, the orbital motion of the white dwarf will also modulate the detected spin period. This possibility is still under investigation.

Consistent modulations in other supersoft sources that have been ascribed to the spin period of a magnetized white dwarf are e.g. the 217.7 s pulsations in the source XMMU J004252.5+411540 in M31 (Trudolyubov and Priedhorsky 2008), and the 1110 s pulsations in Nova M31N 2007-12b (Pietsch et al. 2011). The recurrent nova RS Oph exhibited an unstable ∼35 s periodicity during the supersoft phase after its 2006 outburst (see Osborne et al. (2011) and references therein). The favoured explanation of this variable modulation is the possibility of non-radial oscillations caused by nuclear burning instabilities. It may be that the ∼67 s X-ray periodicity in CAL 83 is due to a similar effect.

3. SMC 13 in the Small Magellanic Cloud

The orbital period of SMC 13 was first reported by Schmidtke et al. (1994), but the most recent orbital ephemeris is that of van Teeseling et al. (1998) (with the number on the left denoting the time of minimum light, and the one on the right the orbital period of 0.1719260±0.0000007 days):

$$T_0 = \text{HJD } 2450434.1320 \pm 0.0006 \quad + \quad 0.1719260E \pm 0.0000007 \text{ d} .$$

Kahabka (1995) reported the discovery of orbital modulation in the *ROSAT* data of SMC 13, and Kahabka (1996) determined the *ROSAT* period to be 4.123 h (0.1718 d).

Table 2. Archived *Chandra* X-ray observations of SMC 13.

Obs ID	Instrument	Start date & time (UT)	Exposure time (s)	PI
4535	ACIS-S3	2005-01-30 16:56:17	40 140	J. Greiner
7456	HRC-S+LETG	2007-02-12 18:25:16	40 190	T. Lanz
8519	HRC-S+LETG	2007-02-18 00:42:08	42 670	T. Lanz

3.1. Observations and data calibration

We discuss 3 archived *Chandra X-ray Observatory* observations of SMC 13, which are summarized in table 2. The calibration of the data was carried out by following standard data reduction and processing procedures with the CIAO software[4], Version 4.3, using Version 4.4.5 of the CALDB (CIAO Calibration Database). The arrival times in the calibrated event files of the three observations were corrected to the solar system barycentre (TDB system).

3.2. Timing analysis

The PERIOD task SCARGLE was used to search for an orbital period in the *Chandra* X-ray light curves around the period of 4.123 h found by Kahabka (1996) in the *ROSAT* data. Each of the three Lomb-Scargle periodograms exhibited a strong power peak at the approximate position of the orbital period. However, the uncertainty in the peak positions was very high due to the relatively short length of the individual data sets. Therefore the X-ray modulation could be constrained to nothing better than 4.44 ± 0.89 h with the separate observations.

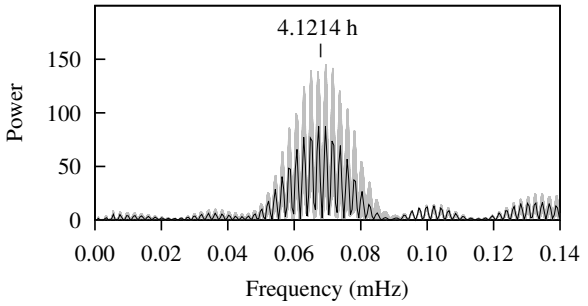

Figure 2. Lomb-Scargle periodograms of combined SMC 13 *Chandra* light curves. Black: Obs 7456 and 8519. Gray: Obs 4535, 7456 and 8519.

To obtain a higher period resolution, two additional Lomb-Scargle periodograms were created (see figure 2 for the region around the strongest peak): one by combining all three observations, and the other by combining only the observations of February 2007 (Obs 7456 and 8519). The presence of numerous alias peaks is evident, as well as possible harmonics of the orbital period. The strongest peak in the 2007 periodogram was determined to be at a period of 4.12 ± 0.06 h. The position of this (relatively broad) peak was then used to choose the appropriate peak on the high time-resolution periodogram obtained by combining all three data sets, yielding a period of 4.1214 ± 0.0005 h. The error value was calculated with the method described in Section 2.2, considering the total time from the start of Obs 4535 to the end of Obs 8519.

The *ROSAT* light curves of Kahabka (1996) in the soft (S: 0.1-0.25 keV) and hard (H: 0.26-0.50 keV) energy bands, as well as the hardness ratio, folded on the ephemeris of Schmidtke et al. (1994) are shown in figure 3.

The intrinsic energy resolution of the ACIS-S detector was used to create two similar *Chandra* light curves: one in the soft band (S: 0.100-0.250 keV) and one in the hard band (H: 0.251-0.500 keV). For both the *ROSAT* and the *Chandra* light curves, the hardness ratio was calculated as HR=(H-S)/(H+S). The soft, hard and HR light curves of observation 4535 were folded on the newly determined period by making use of the task **efold** in the Xronos Timing Analysis Software Package[5], using the time of minimum light of the third minimum of the Obs 4535 light curve (BJD 2453401.5682), and these are provided in figure 4.

[4] `http://cxc.harvard.edu/ciao/index.html`

[5] See the Xronos User's Guide (HEASARC 2009) for more information.

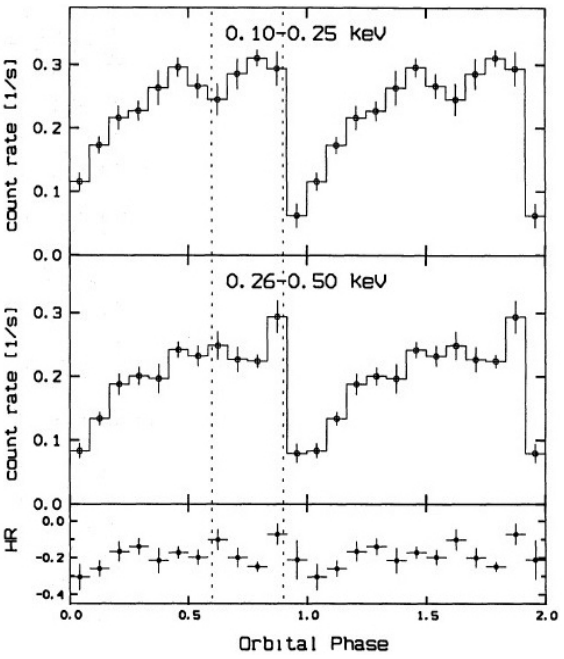

Figure 3. *ROSAT* light curves of SMC 13, folded on 4.123 h with respect to the epoch Nov. 3.105, 1994. (Adopted from Kahabka (1996, figure 3).)

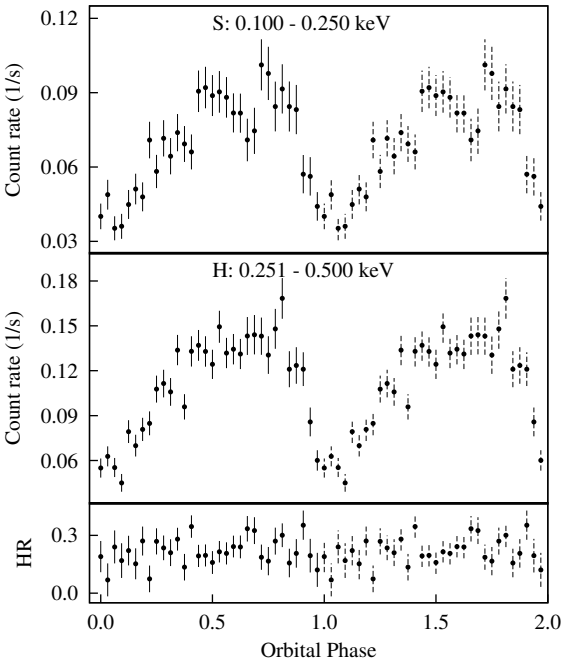

Figure 4. *Chandra* ACIS light curves of SMC 13, folded on $P_{\rm orb} = 4.1214$ h with respect to the third minimum in the data set.

3.3. Discussion

Because the time of minimum in the *ROSAT* light curve is largely defined by only three data points, Crampton et al. (1997) mentioned the possibility that these few minima might be caused by the system being in a low state at some epochs, rather than by orbital modulation. However, each of the *Chandra* data sets constitutes an uninterrupted observation of the source for a duration of ∼2.7 full orbital periods, and the orbital modulation is clearly evident.

The orbital period of 4.1214 ± 0.0005 h determined from the combined data set is very close to the $P_{\rm orb} = 4.126224 \pm 0.000017$ h determined by van Teeseling et al. (1998) from photometrical data, although not included in its error ranges. However, the aliasing effects arising from the long time gaps between the *Chandra* observations made it very difficult to choose the appropriate peak, therefore the van Teeseling et al. (1998) period is considered to be more reliable.

Comparison of the folded *ROSAT* and *Chandra* light curves in figure 3 and figure 4 shows that they exhibit the same sharp, asymmetric form. As pointed out by Kahabka (1996), there seems to be a second dip at $\phi = 0.6$ in the 0.1-0.25 keV (S) band in addition to the main minimum at $\phi \sim 0.9$-1.1 in the ROSAT data, which is not present in the 0.26-0.50 keV (H) band. This is also visible in the *Chandra* light curves. The large amplitude variation may be ascribed to the eclipse of the primary taking place in a high inclination system. If this is the case, the fact that the eclipse is not total indicates that there is an extended emitting region. The structure of the light curve may be the result of variable absorption in the system, possibly by an accretion disc edge. As mentioned below, Kahabka (1996) also considered the possibility of SMC 13 being a polar-like system.

The hardness ratios (HR) for the 2 detectors can not be compared directly, as the H and S counts depend on detector sensitivity. However, there does seem to be an increase in HR during the minor dip, and just before the major dip for both *ROSAT* and *Chandra*. It is also interesting to note that the count rate in the H band correlates with the variations in HR. The favoured

explanation of Kahabka (1996) for this HR modulation is that it may be due to temperature variations, as an increase in temperature would result in an increase in both the HR and the count rate. Kahabka (1996) suggested that a changing observed temperature can be explained if the white dwarf is magnetized, as this would result in a changing viewing angle of the polar caps or an accretion column at the polar caps.

From figure 3, it appears that the X-ray modulation is in phase with the orbital motion. On the other hand, Schmidtke et al. (1996) found that the X-ray minimum occurs about 0.25 of an orbital cycle earlier than the optical minimum, according to their ephemeris. However, folding the *Chandra* light curves through the orbital ephemeris of van Teeseling et al. (1998) showed that the X-ray minima approximately coincides with the optical minimum. Therefore a more in-depth analysis of the orbital period and ephemeris in conjunction with previous observations of SMC 13 needs to be carried out. In particular, simultaneous optical and X-ray observations are needed to clarify the relative phasing of the minima in these wavebands. If the minima they do not coincide, it can indicate a situation where the main sources of X-ray and optical flux respectively are not aligned and therefore not eclipsed simultaneously, for example with the X-rays being brightest close to the compact object, and an optically bright "hot spot" where the accreting stream hit an accretion disc rim.

Probing periodicities in supersoft sources can therefore be instrumental in understanding these systems. With timing analysis, orbital and spin periods and also various types of quasi-periodic signals can be detected and can provide information on the orbital parameters and component masses, as well as the nature of the compact object and accretion process.

Acknowledgments

The financial assistance of the South African Square Kilometre Array Project towards this research is hereby acknowledged. Opinions expressed and conclusions arrived at, are those of the author and are not necessarily to be attributed to the NRF. We would like to thank the principal investigators of the archived X-ray data for the opportunity to analyse the data, as well as Frank Haberl for his comments on the periodicity detected in CAL 83.

References

Crampton D, Hutchings J B, Cowley A P and Schmidtke P C 1997 *ApJ* **489**, 903–11.

HEASARC 2009 *Xronos: A Timing Analysis Software Package. User's Guide Version 5.22*. Available at: `http://heasarc.gsfc.nasa.gov/docs/xanadu/xronos/`.

Kahabka P 1995 *in* H. Böhringer et al, ed., 'Seventeenth Texas Symposium on Relativistic Astrophysics and Cosmology' Vol. 759 of *Annals of the New York Academy of Sciences* p. 324.

Kahabka P 1996 *A&A* **306**, 795–802.

Kahabka P and van den Heuvel E P J 2006 Cambridge University Press New York chapter 11, pp. 461–74.

Long K S, Helfand D J and Grabelsky D A 1981 *ApJ* **248**, 925–44.

Norton A J, Wynn G A and Somerscales R V 2004 *ApJ* **614**, 349–57.

Odendaal A 2012 A Multi-Wavelength Study of Super Soft X-ray Sources in the Magellanic Clouds Master's thesis University of the Free State Bloemfontein.

Osborne J P et al. 2011 *ApJ* **727**, 124–33.

Paczyński B 1971 *ARA&A* **9**, 183–208.

Pietsch W, Henze M, Haberl F, Hernanz M, Sala G, Hartmann D H and Della Valle M 2011 *A&A* **531**, A22.

Savonije J 1983 *in* W. H. G. Lewin & E. P. J. van den Heuvel, ed., 'Accretion-Driven Stellar X-ray Sources' pp. 343–66.

Scargle J D 1982 *ApJ* **263**, 835–853.

Schmidtke P C, Cowley A P, McGrath T K, Hutchings J B and Crampton D 1994 *IAU Circulars* **6107**, 1.

Schmidtke P C, Cowley A P, McGrath T K, Hutchings J B and Crampton D 1996 *AJ* **111**, 788–93.

Seward F D and Mitchell M 1981 *ApJ* **243**, 736–43.

Trudolyubov S P and Priedhorsky W C 2008 *ApJ* **676**, 1218–25.

Trümper J et al. 1991 *Nature* **349**, 579–83.

van den Heuvel E P J, Bhattacharya D, Nomoto K and Rappaport S A 1992 *A&A* **262**, 97–105.

van Teeseling A, Reinsch K, Pakull M W and Beuermann K 1998 *A&A* **338**, 947–56.

Modelling the stellar soft-photon energy density profile of globular clusters

P L Prinsloo[1], C Venter[1], I Büsching[1] and A Kopp[1,2]

[1] Centre for Space Research, North-West University, Potchefstroom Campus, Private Bag X6001, Potchefstroom 2520, South Africa

[2] Institut für Experimentelle und Angewandte Physik, Christian-Albrechts-Universität zu Kiel, Leibnizstrasse 11, 24118 Kiel, Germany

E-mail: 21696764@nwu.ac.za

Abstract. Recent observations by the *Fermi* Large Area Telescope (LAT) and the High Energy Stereoscopic System (H.E.S.S.) have revealed globular clusters (GC) to be sources of high-energy (HE) and very-high-energy (VHE) γ-rays. It has been suggested that the presence of large numbers of millisecond pulsars (MSPs) within these clusters may be either directly responsible for these γ-ray fluxes through emission of pulsed curvature radiation, or indirectly through the injection of relativistic leptons into the cluster. These relativistic particles are plausibly re-accelerated in shocks, created by the collision of stellar winds, before interacting with the soft-photon radiation field set up by the stellar population of the host cluster. Inverse Compton (IC) scattering then produces γ-radiation in the TeV band. In order to calculate the IC spectrum, an accurate profile for the energy density of the soft-photon field is required. We construct such a profile by deriving a radially-dependent expression for the stellar energy density, and then solve it numerically. As a next step, the average energy density values for three different regions of the cluster (demarcated by its core, half-mass, and tidal radii) are determined, which we consequently import into an existing radiation code to predict the TeV γ-ray spectrum. As an application, we consider the case of Terzan 5, boasting a population of 34 radio MSPs, and compare our predicted spectrum with that measured by H.E.S.S.

1. Introduction

Globular clusters (GC) are large spherical collections of roughly a hundred thousand to a million gravitationally bound stars [1]. The cluster cores contain the more massive stars and have very high stellar densities, creating favourable conditions for binary interaction [2]. Expressions for the mass density profile of a GC can be constructed using Michie-King multi-mass models, for example [3]

$$\rho(r) = \rho_0 \begin{cases} 1 & r < r_\mathrm{c} \\ (r_\mathrm{c}/r)^2 & r_\mathrm{c} < r < r_\mathrm{h} \\ (r_\mathrm{c} r_\mathrm{h})^2/r^4 & r_\mathrm{h} < r < r_\mathrm{t}, \end{cases} \tag{1}$$

where r is the radial distance from the GC centre, r_c is the core radius, r_h the half-mass radius, r_t the tidal radius, and ρ_0 a normalisation constant. It would appear as if GCs are suitable to host large populations of millisecond pulsars (MSPs), since GCs are found to harbour a great number of stellar binary members [4, 5]. Also, GCs are ancient objects with mean ages of

12.8±1.0 Gyr [6], so that one would expect them to contain many evolved stellar products. In fact, the presence of 144 pulsars in 28 different clusters has been established to date[1], although it has been predicted that there may be as many as a few hundred MSPs in cluster centres [7].

Recent observations have revealed several GCs to be sources of HE and VHE[2] γ-radiation. The Large Area Telescope (LAT) aboard the *Fermi* Gamma-ray Space Telescope, for instance, detected γ-ray emission from clusters such as 47 Tucanae and Terzan 5 (Ter5) [9, 10, 11, 12]. Ter5 was also revealed by the ground-based High Energy Stereoscopic System (H.E.S.S.) as a source of VHE γ-radiation [13]. Since GCs are known hosts of MSPs, these ancient stars are thought to be responsible for the γ-ray fluxes. Ter5, in particular, hosts the largest known number of radio MSPs of all GCs with a population[1] of 34, and also boasts one of the highest central densities and stellar collision rates [14]. It is situated at a distance of 5.9 kpc from Earth [15], has core, half-mass, and tidal radii of $0.15'$, $0.52'$ and $4.6'$ respectively, a total luminosity of $8{\times}10^5 L_\odot$ [14], and is expected to harbour as many as 200 MSPs [16, 11].

One particular manner in which the energy of pulsars dissipates is through the ejection of particles in the form of relativistic pulsar winds [17]. These are thought to be accelerated to relativistic speeds either within the magnetosphere of the MSP [18], or in relativistic shocks caused by the collision of pulsar winds [19]. Although such particles are expected to account for a very small fraction of a pulsar's spin-down luminosity, with an energy conversion efficiency of as little as $\eta \sim 0.01$ [20], they are plausibly responsible for emission in the TeV band [8]. The relevant radiation mechanism is thought to be inverse Compton (IC) scattering[3] where relativistic leptons upscatter soft (or low-energy) photons to γ-rays. The IC-emissivity $Q_{\mathrm{comp},j}$, related to the scattered photon spectrum per incident electron, is [22],

$$Q_{\mathrm{comp},j}(E_\gamma) = 4\pi \int_0^\infty n_j(\epsilon, r) d\epsilon \times \int_{E_{\mathrm{e,thresh}}}^{E_{\mathrm{e,max}}} J_{\mathrm{e}}(E_{\mathrm{e}}) F(\epsilon, E_\gamma, E_{\mathrm{e}})\, dE_{\mathrm{e}}, \tag{2}$$

with E_γ the upscattered photon energy, and E_{e} the electron energy (the limits of the rightmost integral signify the threshold and maximum electron energy). Here the J_{e} component is a steady-state particle spectrum related to the lepton injection spectrum, which is in turn related to the pulsar spin-down luminosity, and also entails the particle transport. The F component in equation (2) relates to the cross-section of the interaction. See [23, 22] for more details. What is of interest for the purposes of this paper is the n_j component, which is the photon number density, with subscript j corresponding to one of three soft-photon components (cosmic microwave background (CMB), infrared (IR) or starlight). For a blackbody, it is given by [22],

$$n_j(\epsilon) = \frac{15 U_j}{(\pi k T_j)^4} \frac{\epsilon^2}{e^{(\epsilon/kT_j)} - 1}. \tag{3}$$

Here ϵ represents the initial energy of the photon before scattering, k is the Boltzmann constant, and T_j and U_j respectively represent the temperature and energy density corresponding to each soft photon component. In an environment such as that created by GCs, one would expect the vast stellar populations to induce a prominent starlight component with high energy density U, which decreases with increasing distance from the cluster centre, similar to the stellar population density.

In some models, the energy density has been represented by average values within two zones, demarcated by the cluster centre, the core and half-mass radii [18, 20]. It is the objective of this paper to construct a radially-dependent expression for the stellar soft-photon energy density of

[1] See www.naic.edu/∼pfreire/GCpsr.html, doa: 1 Dec. 2014.
[2] HE: High-energy $E > 100$ MeV, VHE: Very-high-energy $E > 100$ GeV [8].
[3] For an alternative interpretation, see [21].

a GC (Section 2), and to solve it numerically for the case of Ter5 (Section 3). We then use this profile to predict the γ-radiation spectrum of MSPs within Ter5 (Section 3) whilst regarding IC scattering as the predominant radiation mechanism. Following this, comparisons can be made with the predicted spectra of other models (Section 3-4).

2. Constructing the energy density profile

We assume that the stars in a GC radiate as blackbodies. By integrating the specific intensity, $I_\nu = (2h\nu^3/c^2)(\exp(h\nu/kT)-1)^{-1}$ [1] with units $\mathrm{erg\,s^{-1}\,cm^{-2}\,Hz^{-1}\,sr^{-1}}$ and T the temperature, over all frequencies, one obtains the total intensity, $I = 4\sigma T^4/\pi$, with $\sigma = (2k^4\pi^5)/(15h^3c^2)$ the Stefan-Boltzmann constant, h the Planck constant, and c the speed of light. The energy density due to a single star is therefore $u_\mathrm{s} = (4\pi/c)I$. We next scale u_s by a factor $(\bar{R}^2/d^2)$ to compensate for the distance to the star (d) as well as its total radiating surface area ($\propto \bar{R}^2$, with $\bar{R}$ the average stellar radius). By replacing d with the separation distance $|\mathbf{r}-\mathbf{r}'|$ between the contributing source at radius r' and an observer within the cluster at radius r (with the GC centre at the origin), and assuming identical properties for all stars (with average stellar mass $\bar{m} \approx M_\odot$, and $M_\odot$ the solar mass), we can calculate the total energy density profile as

$$u(r) = \int u_\mathrm{s} N(r')\,dr' = \int u_\mathrm{s}\frac{\rho(r')}{\bar{m}}\,dV', \tag{4}$$

where $dN = N(r')\,dr'$ is the number of stars in the interval $(r', r'+dr')$, which is equivalent to $\rho(r')dV'/\bar{m}$ when assuming spherical symmetry. Using axial symmetry, the cosine rule, and making the substitution $p(\theta) = r'^2 + r^2 - 2r'r\cos\theta$, we finally obtain

$$u(r) = \frac{8\pi^2R^2}{c}\frac{I}{\bar{m}}\frac{1}{r}\int_0^{r_t}\rho(r')r'\ln\left(\frac{|r'+r|}{|r'-r|}\right)dr'. \tag{5}$$

For $\rho(r')$, we use equation (1), and normalise this by setting the total cluster mass $M_\mathrm{total} = N_\mathrm{total}\bar{m} = \int\rho(r)\,dV = 4\pi\int\rho(r)r^2\,dr$, where $N_\mathrm{tot} = L_\mathrm{tot}/L_\odot$ is the total number of stars in the cluster. Here L_tot is the total GC luminosity, and all stars are assumed to have $L \approx L_\odot$ (as a first approximation;[19]), with $L_\odot$ the solar luminosity. We can then express the central mass-density ρ_0 in terms of measurable cluster parameters and solve the integral in equation (5) numerically.

3. Results and discussion

A general proportionality relation of $u \propto N_\mathrm{tot}R^2T^4$ can be deduced for the energy density from equation (5). This effectively means that doubling either the total number of stars, the stellar radius, or the stellar temperature will result in an energy density increase of factor 2, 4 or 16 respectively. Notice that the energy-density, according to this model, shows no dependence on the mean stellar mass. This is because the central mass-density ρ_0, which was determined by normalising equation (1), contains a factor $\bar{m}$ which cancels with that contained in the denominator of equation (5). Furthermore, solving equation (5) numerically, using the measured parameters for Ter5 and assuming solar properties for its stars, an energy density profile is obtained as shown by the solid black curve in Figure 1. This energy density profile is then divided into three discrete zones [4], as shown in Figure 1. The average energy densities for each of these three zones are obtained as 1.1×10^4, 6.3×10^3, and 170 $\mathrm{eV\,cm^{-3}}$, which are consequently imported into an existing radiation code [18] to calculate the resulting IC spectrum. The temperature and energy density of the CMB are chosen as 2.76 K and 0.27 $\mathrm{eV\,cm^{-3}}$,

[4] This is adequate for the current application; however, we have used the full expression when preforming detailed transport calculations involving many zones [24].

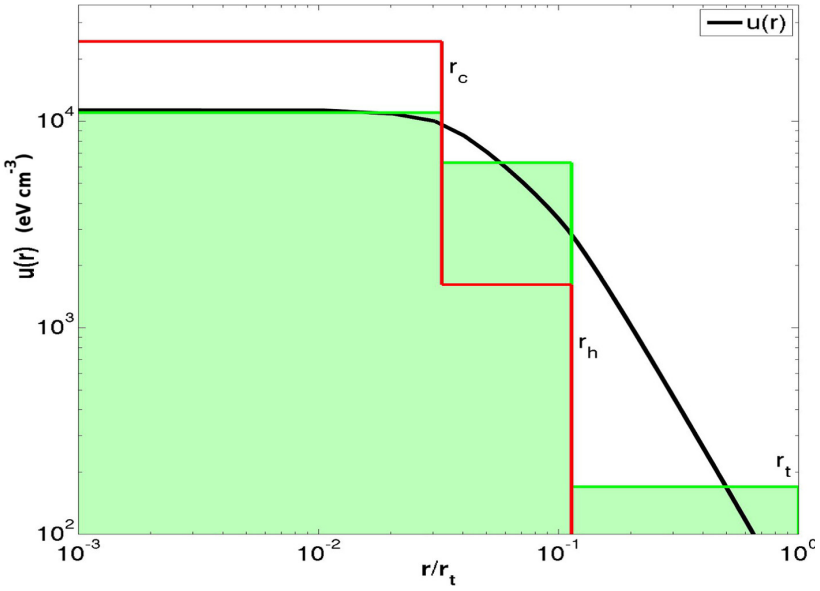

Figure 1. Comparison of energy densities calculated for Ter5. The average energy densities for three regions (shown in green), demarcated by the core, half-mass and tidal radii, are calculated from the energy-density profile (solid black line) of Ter5. Shown in red are the average energy densities for two zones used by [20, 18].

and the cluster magnetic field strength as 1 μG. A number of 8×10^5 stars is deduced from the total cluster luminosity, while the distance and cluster radii are taken as mentioned in Section 1. Regarding the injection spectrum, a power law is assumed and the minimum and maximum particle energies taken as 0.1 GeV and 100 TeV respectively, with a spectral index of 1.6. Furthermore, the number of MSPs is taken as 100, the average spin-down luminosity $\langle \dot{E} \rangle$ as $2 \times 10^{34}\,\mathrm{erg\,s^{-1}}$ and the particle conversion efficiency η as 1%. Having used all of these parameters, we obtain Figure 2.

The resultant spectrum obtained from the contribution from only two zones is indicated with a faint blue line (see Figure 2), and does not differ much from the result by [20] (shown in dark green). The small difference stems from a difference in the average energy density values used. However, with the inclusion of the third zone (of which the contribution is shown with the top faint red line), the resultant spectrum (thick, solid blue line) is shaped in such a way that it can be well aligned to fit the H.E.S.S. data. For the best alignment however, it is necessary to scale the spectrum up by a factor 3, which means that if the IC-spectra depends roughly on the product $N_{\mathrm{tot}}\, N_{\mathrm{MSP}}\, \eta_{\mathrm{p}}\, \langle \dot{E}_{\mathrm{rot}} \rangle$, then the total number of stars and MSPs, the energy conversion efficiency and the spin-down luminosity must each be scaled in such a manner that a resultant increase of factor 3 occurs.

4. Conclusions

It has been argued that GCs, having a high number of stars in late evolutionary stages and a high binary encounter rate, are suitable to host large populations of MSPs. In addition, GCs have been revealed by the *Fermi* LAT and H.E.S.S. as sources of HE and VHE γ-radiation. Such γ-ray emissions have been modelled to arise from the IC scattering of stellar soft photons due to interactions with relativistic particles injected by MSPs. As part of the calculation of the IC spectrum, it was necessary to construct a radially-dependent expression for the soft photon energy density of GCs. We derived this expression analytically, normalised it, and then solved

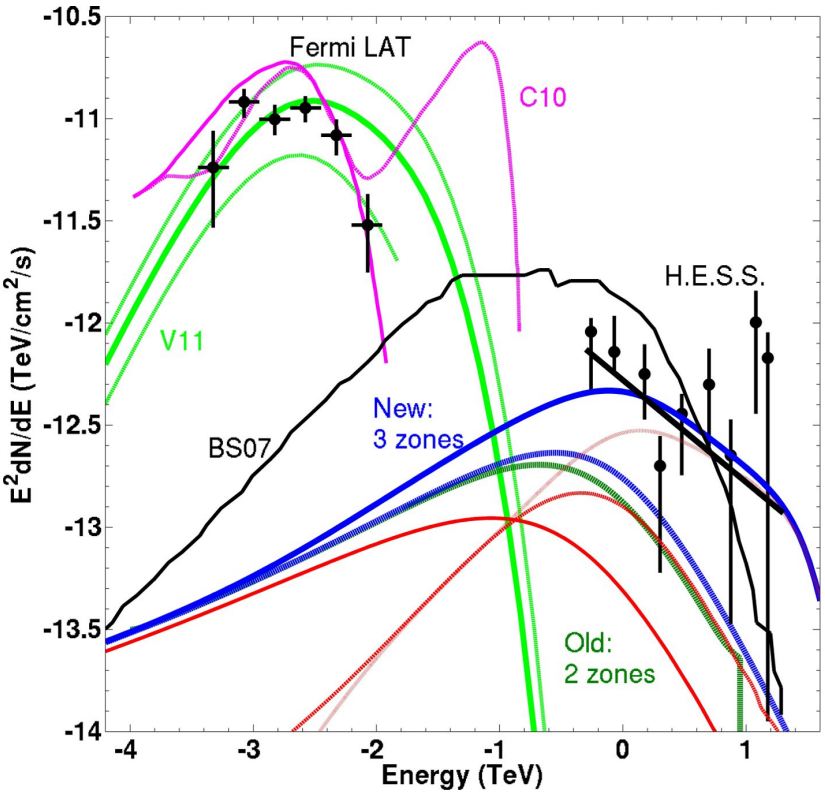

Figure 2. Predicted γ-ray spectra for Ter5. Here, the contributions to the IC spectrum of the energy densities for the three zones constructed in this paper are shown in red, and their collective contribution with a solid, bright blue line. The faint blue line shows the collective contribution of the first two zones constructed in this paper. Take note that these spectra have been scaled up by a factor of three so that the resultant spectrum is better aligned with the H.E.S.S. data. Furthermore, the IC spectrum obtained by [20] is shown in dark green and is labelled 'Old: 2 Zones', while a scaled prediction of [19] is shown in black with label 'BS07'. The lime green and magenta lines (labelled V11 and C10) are the spectra calculated for the HE band [25, 26].

it numerically for the parameters of the GC Ter5. Having divided the profile for Ter5 into three zones (while awaiting more refined particle transport calculations which would allow us to use a greater number of zones), we calculated an average energy density for each zone and consequently used these values to predict the IC spectrum of Ter5. The resultant spectrum was compared to that generated by earlier models as well as to H.E.S.S. data. We found that the predicted spectrum provides a good fit to the H.E.S.S. data if scaled up by a factor 3. This factor may be obtained by, for example, scaling $N_{\rm tot}, N_{\rm MSP}, \eta_{\rm p}$ and $\langle \dot{E}_{\rm rot} \rangle$ each by a factor of roughly 1.3. It can be concluded that the addition of the third zone greatly improved the model's performance when comparing our IC spectrum with those of models that included fewer zones.

Our results can be expanded in a number of ways. When calculating $u(r)$, Hertzsprung-Russel diagrams may be consulted to find a more realistic mass distribution of GC stars. Also, we may generalise $u(r)$ by considering the radii and temperatures of individual stars, and not using average values for the whole population. The energy density can be derived again for asymmetrically distributed sources, and the soft photon contribution of the Galactic background should be taken into account as well [26]. In addition, the surface brightness profile implied by equation (1) should be compared to the observed optical surface brightness to assess the validity

of this equation. Furthermore, possible ways of improving the IC calculation include constructing a cluster magnetic field profile and using refined transport equations for a better modelling of the evolution of the particle injection spectrum. The latter will allow the average energy densities of a greater number of zones to be imported into the radiation code without loss of stability. This might further strengthen the correspondence of the predicted IC spectrum with observational data.

Acknowledgements
This research is based upon work supported by the South African National Research Foundation.

References

[1] Tayler R J 1994 *The Stars: Their Structure and Evolution* (Cambridge University Press)
[2] Pooley D and Hut P 2006 *IAU Joint Discussion* vol 14 p 34
[3] Kuranov A G and Postnov K A 2006 *Astron. Lett.* **32** 393–405
[4] Alpar M A, Cheng A F, Ruderman M A and Shaham J 1982 *Nature* **300** 728–30
[5] Camilo F and Rasio F A 2005 *Binary Radio Pulsars* (*ASP Conf. Ser.* vol 328) ed Rasio F A and Stairs I H p 147
[6] Krauss L M 2000 *Physics Reports* **333** 33–45
[7] Tavani M 1993 *Astrophys. J* **407** 135–41
[8] Bednarek W 2011 *High-Energy Emission from Pulsars and their Systems* ed Torres D F and Rea N pp 185–205
[9] Abdo A A *et al.* 2009 *Science* **326** 1512–6
[10] Abdo A A *et al.* 2010 *Astron. Astrophys.* **524** A75
[11] Kong A K H, Hui C Y and Cheng K S 2010 *Astrophys. J* **712** L36–9
[12] Tam P H T, Kong A K H, Hui C Y, Cheng K S, Li C and Lu T N 2011 *Astrophys. J* **729** 90–7
[13] Abramowski A *et al.* 2011 *Astron. Astrophys.* **531** L18–22
[14] Lanzoni B *et al.* 2010 *Astrophys. J* **717** 653–7
[15] Valenti E, Ferraro F R and Origlia L 2007 *Astron. J* **133** 1287–301
[16] Fruchter A S and Goss W M 2000 *Astrophys. J* **536** 865–74
[17] Reynolds S P and Chevalier R A 1984 *Astrophys. J* **278** 630–48
[18] Venter C, De Jager O C and Clapson A C 2009 *Astrophys. J* **696** L52–5
[19] Bednarek W and Sitarek J 2007 *Mon. Not. R. Astron. Soc.* **377** 920–30
[20] Venter C and de Jager O C 2008 *AIP Conf. Ser.* vol 1085 ed Aharonian F A *et al.* pp 277–80
[21] Venter C, Büsching I, Kopp A, Clapson A C and de Jager O C *These proceedings*
[22] Zhang L, Chen S B and Fang J 2008 *Astrophys. J* **676** 1210–7
[23] Blumenthal G R and Gould R J 1970 *Rev. Mod. Phys.* **42** 237–71
[24] Kopp A, Venter C, Büsching I and de Jager O C 2013 *Astrophys. J* **779** 126–37
[25] Venter C, de Jager O C, Kopp A and Büsching I 2011 *Fermi Symp. Proc., eConf C110509* (*Preprint* `arXiv:1111.1289`)
[26] Cheng K S, Chernyshov D O, Dogiel V A, Hui C Y and Kong A K H 2010 *Astrophys. J* **723** 1219–30

Extragalactic large-scale structures in the northern Zone of Avoidance

M Ramatsoku[1], R C Kraan-Korteweg[1], A C Schröder[2] and W van Driel[3]

[1]Astrophysics, Cosmology and Gravity Centre (ACGC), Department of Astronomy, University of Cape Town, Private Bag X3, Rondebosch 7701, South Africa.
[2]South African Astronomical Observatory (SAAO), PO Box 9, 7935 Observatory, Cape Town, South Africa.
[3]GEPI, Observatoire de Paris, CNRS, Universit Paris Diderot, 5 place Jules Janssen, 92190 Meudon, France.

E-mail: mpati.ramatsoku@ast.uct.ac.za, kraan@ast.uct.ac.za, anja@hartrao.ac.za, wim.vandriel@obspm.fr

Abstract. We used the Nançay Radio Telescope (NRT) to measure the 21 cm line emission of near-infrared bright galaxies in the northern Zone of Avoidance (ZoA) without previous redshift determinations. We selected galaxies with extinction-corrected magnitudes $K_s^o \leq 11\overset{\mathrm{m}}{.}25$ from the 2MASS Extended Source Catalog. These data will complement the existing 2MASS Redshift Survey (2MRS; first data release) as well as the ongoing 2MASS Tully-Fisher survey, both of which exclude the inner ZoA ($|b| < 5°$), where the identification of galaxy candidates is the hardest. Of the ∼1000 identified 2MASX galaxy candidates we have so far detected 252 to our 3.0 mJy rms sensitivity limit and the velocity limit of 10500 km s^{-1}. The resulting redshift distribution reveals various new structures that were hitherto uncharted. They seem to form part of the larger Perseus-Pisces Supercluster (PPS). The most conspicuous is a ridge at about $\ell \approx 160°$,$v \approx 6500$ km s^{-1}. Within this wall-like structure, two strong radio galaxies (3C 129 and 3C 129.1) are embedded which lie at the same distance as the ridge. They seem to form part of an X-ray cluster. Another prominent filament has been identified crossing the ZoA at $\ell \approx 90°$, hence suggesting the second Perseus-Pisces arm is more extended than previously thought.

1. Introduction

Dust extinction and high stellar densities in the Galactic Plane block a large fraction of the sky resulting in the so-called Zone of Avoidance (ZoA) [1]. Compared to the optical, the near-infrared (NIR) is much less affected by the dust obscuration. A whole-sky near-infrared (JHK) imaging survey exists in the form of the 2-Micron All Sky Survey (2MASS)[2]. The resulting extended source catalogue, 2MASX, with its 1.6 million sources complete to $K_s \leq 13\overset{\mathrm{m}}{.}5$ [3], provides the most uniform and deep NIR sample of the whole sky. Although 2MASX suffers little from dust extinction, there remains an "NIR ZoA" caused by stellar crowding around the Galactic bulge ($\ell \lesssim \pm 90°$) [1].

To analyse the large-scale galaxy distribution over the entire sky, the optical 2MASS Redshift Survey (2MRS) was started about a decade ago. The first data release is complete to $K_s^o = 11\overset{\mathrm{m}}{.}25$ [4], the second to $K_s^o = 11\overset{\mathrm{m}}{.}75$ [5]. Both versions do exclude, however, the inner ZoA ($|b| \leq 5°$)

because of the inherent difficulties in getting good signal-to-noise (SNR) optical spectra for these heavily obscured galaxies. While the 2MRS is currently the deepest "whole-sky" redshift survey for mapping large-scale structures, and studying the dynamics in the nearby Universe and the CMB dipole [6], the lack of redshift data in the ZoA remains an obstacle. This also holds for the 2MASS Tully Fisher survey (2MTF) which uses a subsample of sufficiently inclined 2MASX spiral galaxies to study cosmic flow fields [7].

To improve on this we have started a project to systematically observe in H I all likely 2MASX galaxies in the "2MRS ZoA" without previous redshift information. The line emission from neutral hydrogen (H I) at the radio wavelength of 21 cm can travel unhindered through the thickest dust layers of the Milky Way. Targeting ZoA galaxies with a radio telescope will therefore allow us to obtain redshifts for gas-rich 2MASS galaxies. We used the 100m-class Nançay Radio Telescope (NRT) for pointed observations of all ZoA galaxies with Dec $> -39°$. We were particularly interested in filling in the northern ZoA because – contrary to the southern ZoA – most of the northern ZoA has not been surveyed in any systematic way before. For the southern hemisphere a blind H I survey has been performed with the Parkes Multi-Beam receiver (HIZOA) which covers $|b| < 5°$ for the longitude range $196° \leq \ell \leq 52°$ out to velocities of 12700 km s^{-1} (rms $\approx$ 6 mJy)[8], [9]. For the remaining ZoA ($196° \gtrsim \ell \gtrsim 52°$) hardly any data are available (see e.g. the top panel of Fig.1).

2. Filling in the redshift gap in the ZoA

2.1. Sample selection

To start filling in the northern redshift gap we first extracted all extended sources from 2MASX with $|b| \leq 10°$ and extinction-corrected magnitudes $K_s^o \leq 11\overset{\mathrm{m}}{.}25$, i.e., the completeness limit of the first 2MRS catalogue and the 2MTF. Of the 4743 extended sources accessible to the NRT (Dec $> -39°$), we classified 2546 sources as clear galaxies (plus 42 as possible galaxies) by visually inspecting the Digitized Sky Survey (DSS)[1] images in the B_J, R and I bands, the 2MASS J and K-bands, as well as the 2MASX colour images. From that sample we excluded galaxies that already had redshift measurements by cross-correlating our catalogue with NED and unpublished data sets like 2MRS (Macri, priv comm), HIZOA (Kraan-Korteweg et al, priv comm), etc.

The final NRT target sample consists of ∼1000 near-infrared bright galaxy candidates in the ZoA ($-20° \lesssim \ell \lesssim 270°$; $|b| \leq 10°$); the great majority ($\gtrsim 83\%$) of them are located in the $|b| < 5°$ strip. We have already used 1200 hours of observing time with the NRT for pointed observations of these objects since mid-2009.

2.2. Observations and data reduction

The galaxy candidates were observed with the NRT in position-switching mode. Pairs of equal-duration ON/OFF-source integrations were made, with the OFF-source position $20'$ east of the target. Candidates were typically observed for 40-minute long periods till an rms noise level of 3.0 mJy was reached. Because none of the target galaxies have prior redshift information, the auto-correlator was set to cover a radial velocity range of -500 to 10500 km s^{-1}. The original resolution is 2.6 km s^{-1}, which is later smoothed to 18 km s^{-1} for further analysis. Observations were made simultaneously in two linear polarizations, to gain sensitivity. Data reduction and Radio Frequency Interference (RFI) recognition and mitigation were performed using the NAPS and SIR data reduction packages, developed by the NRT staff.

[1] http://stdatu.stsci.edu/dss/

2.3. Results

From July 2009 to March 2012, we observed 926 out of the total of 1000 target galaxies to an rms level of 3.0 mJy. The resulting spectra were first inspected by eye by one of us for the signature of redshifted Galactic H I-emission. The reliability of all potential H I detections was then assessed independently by three other team members, followed by an adjudication by another team member. Clear detections, and non-detections which had reached our target rms noise level of 3.0 mJy were filed as such, whereas marginal or possible detections were tagged for re-observation, whose results were continuously updated.

This has led to 252 solid detections so far out of the 926 observed targets, i.e., a detection rate of 27%. This is a respectable detection rate given that no pre-selection was made according to morphological type (which is not straightforward in the NIR, nor in the ZoA). The mean rms in the final spectra was found to be 2.9 mJy. The 252 detected H I profiles have a peak signal-to-noise ratio $\gtrsim 5.0$.

A reliable detection was found to have a typical linewidth- and flux-dependent signal-to-noise ratio as defined in the Arecibo Legacy Fast ALFA survey of $\mathrm{SNR}_{ALFALFA} > 6.0$ [10]. Detections with $5.0 \lesssim \mathrm{SNR}_{ALFALFA} \lesssim 6.0$ typically were adjudicated as marginal.

3. Resulting large-scale structures

While we find galaxies over the entire observed redshift range, the majority lie within $2000-8000\,\mathrm{km\,s^{-1}}$. The velocity histogram (not shown here) shows a clear peak at $6000\,\mathrm{km\,s^{-1}}$, probably due to the prevalence of galaxies connected to the Perseus-Pisces Supercluster (PPS) described below. There is a noticeable drop-off in detections around $\sim 8000\,\mathrm{km\,s^{-1}}$ which is due to a combination of recurring RFI at $v > 8500\,\mathrm{km\,s^{-1}}$ and limited telescope sensitivity.

The new H I detections are distributed almost symmetrically about the Galactic equator, irrespective of Galactic latitude b (see the middle panel of Fig. 1), confirming that the detection rate is independent of extinction and star density.

To investigate the large-scale structures revealed by these new detections we plot in Fig. 1 their spatial distribution in Galactic coordinates centred on the northern Milky Way. It includes 2MRS data up to latitudes of $|b| \geq 15^\circ$ to test for continuity of the newly identified features with previously known structures (filaments, walls, voids) at higher Galactic latitudes. The outlined rectangular region demarcates the NRT survey area.

The top panel shows the 2MRS galaxies with $K_s^o \leq 11\overset{\mathrm{m}}{.}25$, as well as data in the $|b| \lesssim 5^\circ$ strip from the Zcat ($K_s^o \leq 11\overset{\mathrm{m}}{.}25$) compilation by Huchra (priv comm). The middle panel displays the distribution of the 252 NIR-bright 2MASX galaxies detected with the NRT. In the bottom panel the new detections have been merged with previously known data of objects to the $K_s^o \leq 11\overset{\mathrm{m}}{.}25$ completeness limit. In all three panels galaxies are colour-coded by velocity: the $300-2500\,\mathrm{km\,s^{-1}}$ velocity range is shown in cyan, $2500-5000\,\mathrm{km\,s^{-1}}$ in blue, $5000-7500\,\mathrm{km\,s^{-1}}$ in black and the $7500-10000\,\mathrm{km\,s^{-1}}$ range in green. The black and blue colours coincide with the approximate velocity range of the PPS.

When comparing the bottom and top panels (i.e., the status before and after the NRT observations) the power of revealing previously unknown large-scale structures in the ZoA through H I observations of intrinsically bright (extinction-corrected) NIR galaxies is quite obvious. Several prominent filaments and walls are now seen to cross the ZoA which were previously not – or at most marginally – visible. The most obvious filamentary structures cross the Galactic Plane at $\ell \approx 90^\circ$ (Cygnus), $\ell \approx 135^\circ$ (Cassiopeia), $\ell \approx 160^\circ$ (Perseus), $\ell \approx 180^\circ$, as well as the Puppis filament at $\ell \approx 240^\circ$ [11]. An underdense region of galaxies is apparent at $\ell \approx 120^\circ$ and $-2^\circ \lesssim b \lesssim 5^\circ$, stretching from $cz \approx 4000$ to $7000\,\mathrm{km\,s^{-1}}$. The 2MASX finds no galaxies in regions of high stellar densities, such as around the Galactic Bulge, therefore the ZoA for $\ell \lesssim 30^\circ$ remains unsampled. In the next sections we will discuss only two of the most striking newly revealed features in more detail, namely the ones at $\ell \approx 90^\circ$ and $\ell \approx 160^\circ$.

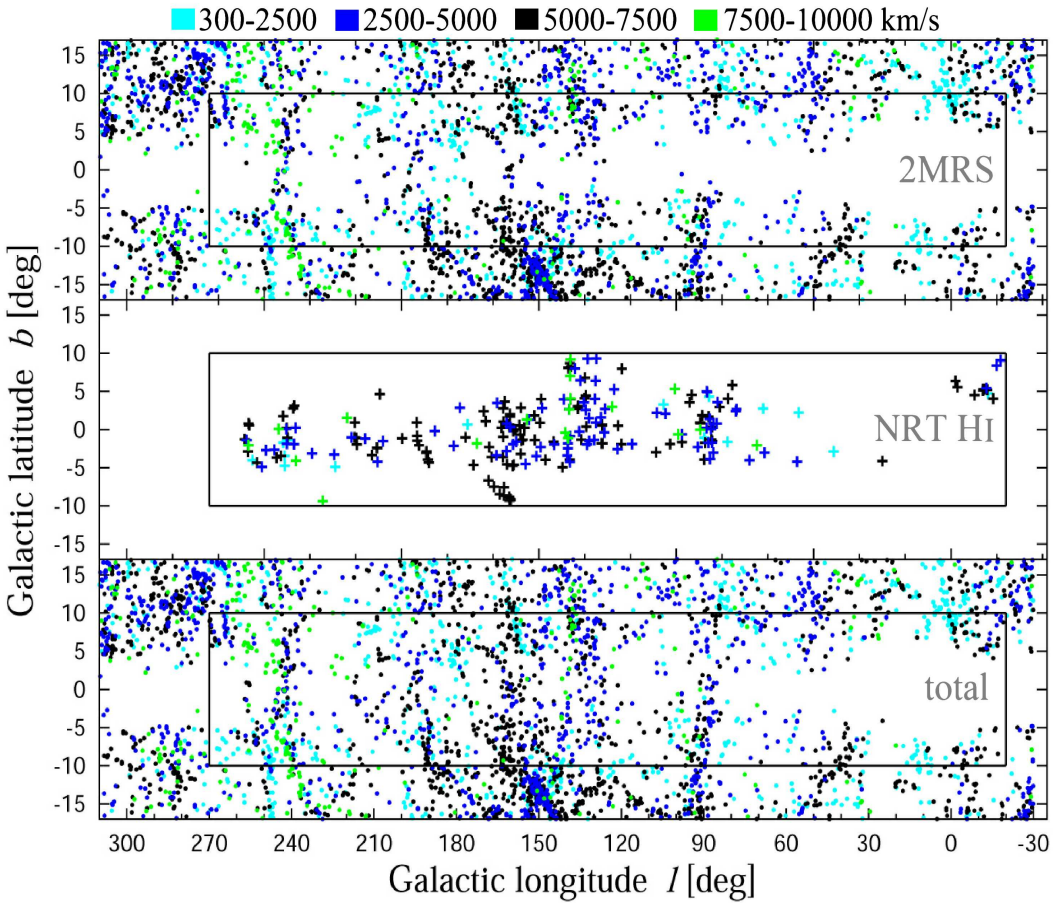

Figure 1. The spatial distribution of galaxies in Galactic coordinates in the ZoA, showing large-scale structure filaments and voids. The survey area explored with the NRT is marked by the black rectangle. Galaxies are colour-coded by their velocity range, as shown at the top: the $300-2500\,\mathrm{km\,s^{-1}}$ velocity range is shown in cyan, $2500-5000\,\mathrm{km\,s^{-1}}$ in blue, $5000-7500\,\mathrm{km\,s^{-1}}$ in black and the $7500-10\,000\,\mathrm{km\,s^{-1}}$ range in green. The top panel shows the 2MRS galaxies ($K_s^o \leq 11\overset{\mathrm{m}}{.}25$) with known redshifts from Zcat (Huchra, priv comm) for low-latitude 2MASX galaxies. The middle panel displays the H I-detections obtained by us with the NRT. The bottom panel shows the combined data and emphasizes the links with previously known structures.

3.1. The Perseus extension of the second Perseus-Pisces arm

The first region of interest is seen in the constellation of Cygnus around $\ell \approx 90°$. It shows a very prominent filament that can be traced from below the Plane at $\ell, b \approx 90°, -10°$ extending up to the other side of the ZoA at a slight angle to $\ell, b \approx 100°, -10°$. This filament seems to form part of the second (eastern) PPS arm that emanates southwards from the Perseus A 426 cluster (ℓ,b) $\approx$ (150°,-13°), then bends backwards towards the Galactic plane (at about $\ell, b \approx 110°, -30°$; not shown here) and re-enters the plot at about $\ell, b \approx 80°, -15°$. Most previous studies of the PPS assumed it to kind of stop and dissolve around $\ell, b \approx 90°, -10°$ as no signature was found of it in earlier optical galaxy searches [12], nor any indication of a continuation on the other side of the obscuring ZoA band. Our data clearly confirms such a continuation. It implies the eastern Perseus-Pisces chain to be considerably larger than evidenced in any previous survey of the PPS complex.

3.2. A potentially massive cluster

The second prominent feature is a concentration of H I-detections at $\ell \approx 160^\circ$ right in the middle of the ZoA ($b = 0\overset{\circ}{.}5$). It lies within a nearly vertical (in Fig. 1) wall-like structure (at $v \approx 6000 \pm 1000\,\mathrm{km\,s^{-1}}$ in velocity space) and can be traced across the full width of the ZoA. It is interesting to note that within this wall, at the core of the galaxy concentration, we find two very strong radio galaxies. Their position and redshifts (6236 and 6655 km s^{-1} respectively; [13]) confirm that they reside inside the galaxy concentration. These are the head-tail radio source (3C 129) and the double-lobed giant elliptical radio galaxy (3C 129.1). The presence of such radio sources with bent lobe morphology usually is indicative of a rich cluster environment.

Focardi et al (1984) [14] were the first to put forward the idea of an extension of the PPS Complex across the ZoA towards the northern Galactic hemisphere that would link the Perseus cluster (A 426; $\ell, b, v \simeq 150^\circ, -13^\circ, 5000\,\mathrm{km\,s^{-1}}$) to Abell 569 ($\ell, b, v \simeq 168^\circ, 23^\circ, 5800\,\mathrm{km\,s^{-1}}$). It would traverse the Galactic Plane at the location of the two bright radio galaxies, which also coincides with the location where Weinberger (1980) ([15]) found an excess of galaxies in his early optical search (at $\ell \approx 160^\circ$). This connection has been much debated over the years (e.g., [16], [17], [18]), but no conclusive results were found due to the lack of (redshift) data in this dust-enshrouded region.

The suspicion that 3C 129 and 3C 129.1 form part of a massive cluster was later substantiated through the identification of the X-ray cluster CIZA J0450.0+4501 ([19]). The radio sources lie within the X-ray emission of the CIZA cluster and are at the same distance. With an X-ray luminosity of $L_\mathrm{X} = 1.89 \times 10^{44}\ \mathrm{h_{50}^{-2}erg\ s^{-1}}$ this cluster is not among the brightest X-ray sources in ROSAT. For comparison, its flux is about 20% that of the Norma cluster A 3627, the central cluster of the Great Attractor [20] – which, as an aside, also hosts 2 radio sources, the central one a wide-angle tail source and the other also a head-tail source. With regards to the X-ray flux it should be noted, however, that the intervening high gas column density ($N_H \gtrsim 10^{21}\ \mathrm{cm^{-2}}$) in the Galaxy may well have reduced the flux of the low energy X-ray photons in the ROSAT $0.1 - 2.4$ keV band, resulting in an underestimate of its luminosity. The cluster might therefore be more massive than its X-ray luminosity suggests. Despite its possible connection with the wider PPS complex, it has not received much attention since.

4. Conclusions and future perspectives

The 252 H I detections in this previously unexplored northern region of the ZoA have revealed new and interesting structures that are clearly associated with the Perseus Pisces Supercluster. These new structures at $\ell \approx 90^\circ$ and $\ell \approx 160^\circ$ seem to imply that the PPS is more extended than previously thought and potentially much more massive, with the newly identified cluster in the $\ell \approx 160^\circ$ filament described in Sect. 3.2. This may well have implications for our understanding of the dynamics and flow-fields observed in this region, such as the tug of war between the PPS and the Great Attactor [21, 22, 23] .

To learn more about the $\ell \approx 160^\circ$ cluster's role in, and its mass contribution to the PPS, and its relation to the observed local flow fields, we recently put in a proposal – and have been allocated time - to conduct a deep H I imaging survey over a $2\overset{\circ}{.}4 \times 2\overset{\circ}{.}4$ area (mosaicked) around this cluster with the Westerbork Synthesis Radio Telescope (WSRT).

Acknowledgements

This work is based upon research supported by the National Research Foundation and Department of Science and Technology. MR is grateful for the bursary provided by the South African SKA Project Office. This publication makes use of data products from the Two Micron All Sky Survey, which is a joint project of the University of Massachusetts and the Infrared Processing and Analysis Center, funded by the National Aeronautics and Space Administration and the National Science Foundation.

The anatomy of γ-ray pulsar light curves

A S Seyffert[1], C Venter[1], T J Johnson[2] and A K Harding[3]

[1] Centre for Space Research, North-West University, Potchefstroom Campus, Private Bag X6001, Potchefstroom 2520, South Africa
[2] NRC Fellow, High-Energy Space Environment Branch, Naval Research Laboratory
[3] Astrophysics Science Division, NASA Goddard Space Flight Center, Greenbelt, MD 20771, USA

E-mail: 20126999@nwu.ac.za

Abstract. To obtain constraints on the inclination angle (α, between the magnetic and rotation axes) and observer angle (ζ, line-of-sight relative to the rotation axis) of a γ-ray pulsar from its observed light curve (LC), we make use of geometric models detailing the position and extent of emission regions (acceleration gaps) located in the magnetosphere. We do this by generating a sky map of the relative emission intensity for a range of α, and at each α extracting a set of LCs covering the entire range of ζ. This effectively yields an atlas of LCs characterised by a specific set of model parameters, such as pulsar period, gap width and position, and radial gap extent. This atlas can then be used to obtain fits to observed pulsar LCs (including rough errors on α and ζ) by eye through a systematic search of the possible (α,ζ) solution space. In the case of radio-loud γ-ray pulsars, significantly better constraints on the viewing geometry (α and ζ values) can be obtained by doing this not only for the observed γ-ray LC, but concurrently for the observed radio LC. This multiwavelength approach has been used successfully to obtain constraints on the viewing geometries of 6 LAT pulsars [1]. It is crucial, however, to understand how the set of model parameters which characterizes an LC atlas, influences the shapes and properties of the LCs contained in that atlas, since such an understanding enables improved parameter constraints, and directs future model refinement. A simple first approach is to vary these parameters and study the changes they bring about in the LCs. This approach proves useful in some respects (and is indeed adequate for understanding the LC atlases produced by the relatively simple radio models). However, due to the complex structure of many of the produced γ-ray LCs (sometimes displaying up to 4 individual peaks), this approach doesn't give a comprehensive enough understanding of how all the LCs are produced in terms of the underlying magnetospheric structure and accelerator geometry. In this paper we explore a second approach to investigating the interplay between the model parameters and the LC atlas. In this approach we do not attempt to understand how the set of model parameters influences the LC shapes directly, but rather, more fundamentally, investigate how the set of model parameters affects the sky maps from which the latter are extracted. This allows us to also recognise structure within the atlas itself, as we are now able to attribute certain features of the LCs to specific features on the sky map, meaning that we not only understand how the structure of single LCs come about, but how their structure changes as we move through (α,ζ)-space, and why.

1. Introduction

The Large Area Telescope (LAT) is the primary instrument on the *Fermi Gamma-ray Space Telescope* mission which was launched on 11 June 2008. LAT is an imaging, wide field-of-view, high-energy γ-ray telescope covering the energy range from 20 MeV to $>$ 300 GeV. The LAT

continuously scans the sky in an ever improving all-sky survey, taking advantage of it's large field-of-view and high sensitivity to scan the entire sky every three hours. One of the important products to date of this all-sky survey is the first LAT catalogue of γ-ray pulsars [2] produced using the first six months of LAT data, and increasing the number of known γ-ray pulsars from at least 6 [3] to 46. The second LAT γ-ray pulsar catalogue is due to be published soon, and will push the number of known[1] γ-ray pulsars to over 100. This dramatic increase has opened up a whole new population of pulsars, with exciting possibilities for multiwavelength studies [4].

We have previously obtained fits to 6 LAT pulsar light curves (LCs) using geometric LC predictions to concurrently fit both radio and γ-ray data [5].

1.1. The geometric pulsar models

We use an idealized picture of the pulsar system, wherein the magnetic field has a retarded dipole structure [6] and the γ-ray emission originates in regions of the magnetosphere (referred to as 'gaps') where the local charge density is sufficiently lower than the Goldreich-Julian charge density [7]. These gaps facilitate particle acceleration and radiation. We assume that there are constant-emissivity emission layers embedded within the gaps in the pulsar's corotating frame. The location and geometry of these emission layers determine the shape of the γ-ray LCs, and there exist multiple models describing their geometry.

Two such models for the geometry of the γ-ray emission regions are the outer gap (OG, [8]) and two-pole caustic (TPC, [9]) models. In both the OG and TPC models emissions are produced by accelerated charged particles moving within narrow gaps along the last open magnetic field lines (the field lines which close at the light cylinder). In the OG model, radiation originates above the null charge surface (where the Goldreich-Julian charge density changes sign) and *interior to* (closer to the magnetic axis) the last open magnetic field lines. The TPC gap starts at the stellar surface and extends *along* the last open field lines up to near the light cylinder, where the corotation speed approaches the speed of light. The special relativistic effects of aberration and time-of-flight delays, which become important in regions far from the stellar surface (especially near the light cylinder), together with the curvature of the magnetic field lines, cause the radiation to form caustics (accumulated emission in narrow phase bands). These caustics are detected as peaks in the observed γ-ray LCs [9, 10].

1.2. Phaseplots and LCs

The tool we use to visualise the emission of the pulsars is called a phaseplot, and is an equirectangular projection skymap of the emission of the pulsar with the phase at which the emission is observed, ϕ, on the horizontal axis, and ζ on the vertical axis. For each point in the (ϕ, ζ) space it gives the relative intensity of the emission per solid angle which would be observed if the line-of-sight to the observer would pass through that point. On this phaseplot the pulsar makes one full rotation around its rotation axis, and the equator of the NS is at $\zeta = 90°$. To find out what an observer would see during the course of the period we can obtain an LC from this phaseplot by taking a cut at a constant ζ through the phaseplot. Fig. 2 shows an example of a phaseplot (for the TPC case) for a pulsar with an inclination angle of $\alpha = 50°$, accompanied by an LC extracted from it using such a cut (designated by the yellow line through the phaseplot). Both the phaseplot and LC are independently normalised so their respective maxima are 1.

2. Obtaining LC fits

To obtain fits to the observed pulsar LCs we need to consider the entire domain of α and ζ at the very least, keeping the other parameters fixed. To most effectively do this we generate 'atlases',

[1] https://confluence.slac.stanford.edu/display/GLAMCOG/Public+List+of+LAT-Detected+Gamma-Ray+Pulsars

consisting of a set of model LCs covering the (α, ζ) domain at a chosen resolution, i.e., a grid of LCs sampling the two-dimensional parameter space evenly. The data are then compared to this atlas (for our purposes this is done by eye) and the best-fit (α, ζ) are then inferred.

This fitting process has proven to be effective in a multiwavelength arena with concurrent fitting of both radio and γ-ray light curves yielding well-constrained best-fit parameters for a number of radio-loud γ-ray pulsars [1]. In the case of by-eye fitting the effectiveness and usefulness of this process is quite dependent on the level of the qualitative knowledge available about the behaviour of the produced atlas of LCs when model parameters other than α and ζ are varied. This knowledge can be best garnered by performing parameter studies on the models focusing on the relevant parameters.

2.1. Performing parameter studies: radio models vs. γ-ray models

To perform parameter studies using these phaseplots and LCs it is convenient to investigate the interplay between the parameters and the LC atlas. In the case of the simpler conal radio models this approach proves very effective and a lot can be learned from doing such parameter studies. The γ-ray models yield considerably more complex phaseplots, and as such, more convoluted LC atlases. This means that to obtain useful knowledge from these parameter studies we need to adjust our approach accordingly.

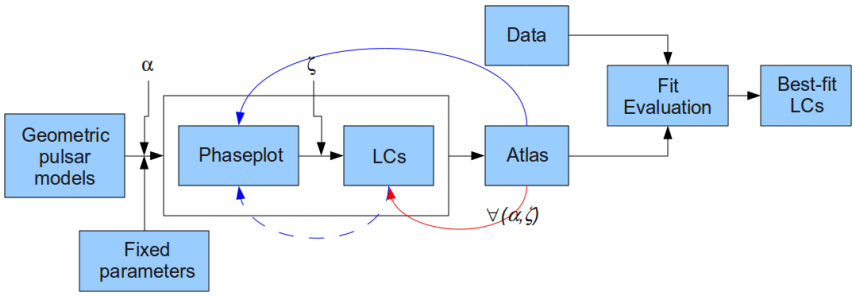

Figure 1. The process whereby fits to observed LCs can be obtained from geometric models.

Fig. 1 shows a schematic representation of the process used to obtain fits to the radio and γ-ray LCs. The red arrow illustrates the established methodology of understanding the influence the parameters have on the LC atlas, by examining the LCs directly. The blue arrows illustrate the proposed methodology wherein the influence of the model parameters on the LC atlas is understood by examining the effects of the model parameters on the structure of the phaseplots from which the LC atlas is generated.

3. Re-examining the LCs and phaseplots

Fig. 2 shows how the different features on the phaseplot can be associated with the peaks seen on the LC. In this case (the TPC model with $\alpha = 50°$ and $\zeta = 70°$) the two main peaks on the LC are produced by cutting the caustic (marked C on the phaseplot) above its lowest point (around $\zeta = 50°$), thus intersecting it twice. The earlier (at lower ϕ) of these two peaks also includes emission from the so-called 'overlap region' (where the directions of many of the rotationally distorted magnetic field lines are such that their emission overlaps; marked O on the phaseplot). The LC furthermore includes four smaller peaks, one preceding the earliest large peak, one between the two large peaks, and two following the later large peak. The earliest of the four is associated with the so-called 'dynamical caustic' (marked D on the phaseplot), and is the dominant peak for LCs produced cutting below (at smaller ζ) the lowest point of the

caustic. The second and fourth peaks of the four smaller peaks are associated with the caustic itself, respectively being produced by very high altitude emission (where the magnetic field is most distorted), and by the small tail of the caustic (both encircled). The third of the four smaller peaks is produced by the line on the phaseplot associated with the so-called 'notch' in the rim of the neutron star's polar cap at the surface.

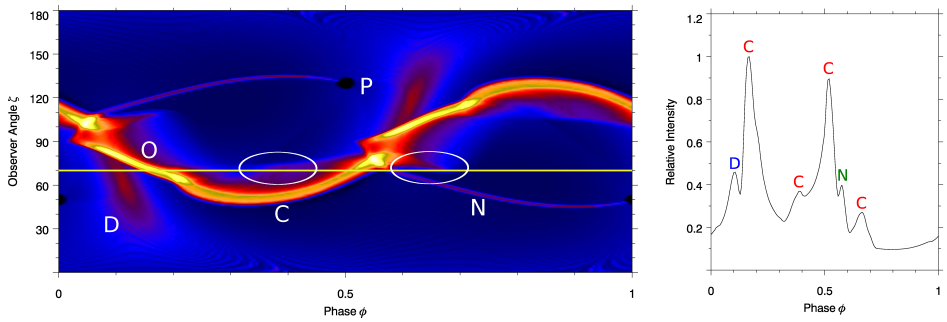

Figure 2. A phaseplot generated by the TPC model with $\alpha = 50°$ and cut at $\zeta = 70°$. *C* denotes the main caustic, *D* denotes the secondary caustic, *P* denotes the polar cap, and *N* denotes the notch line.

Thus, we see that the parts of an extracted LC can be understood in terms of the features on the phaseplot which generate them. This means that the hard work of understanding how the LCs change under changes in the underlying parameter set, shifts to having to understand how the structure of the phaseplots change under changes in the underlying parameters. There are mainly 5 features on the phaseplot we need to account for, namely:

The *main caustic, C*: This feature is the result of bunching of emission directions occurring due to aberration and time-of-flight effects.

The *secondary (dynamical) caustic, D*: This feature is brought about purely through the effects of aberration and time-of-flight, and at higher α merges with the above caustics. This feature is accompanied by a spreading of emission directions in the rest of the rotation ((ϕ, ζ) between $(0.3, 50°)$ and $(1, 0°)$; a *trough*).

The *polar cap*: The polar cap is delimited by the footpoints of the last magnetic field lines to close within the light cylinder. Due to the screening of the electric field above the polar cap by the particles produced in the pair cascade, no γ-ray radiation is expected above the polar cap. In LCs cutting this feature a very sharp fall in emission intensity can be observed at the appropriate phases.

The *overlap region*: This region is where the distortion of the magnetic field under the rotation of the pulsar causes emission directions to overlap. It is associated with the notch in the polar cap rim.

The *notch line*: This line on the phaseplot is a result of the bunching of emission directions due to the bunching of the magnetic field lines of the pulsar.

4. Revisiting the Atlas

4.1. A single phaseplot

The LC atlas is produced by generating a phaseplot for each step in the range of possible α, and for each of those phaseplots cutting it at each step in the range of possible ζ (see Sec. 2). Fig. 3 shows the same phaseplot as is used in Fig. 2, for multiple ζ cuts. The colours of the dots indicate which feature on the phaseplot the LC peaks are associated with.

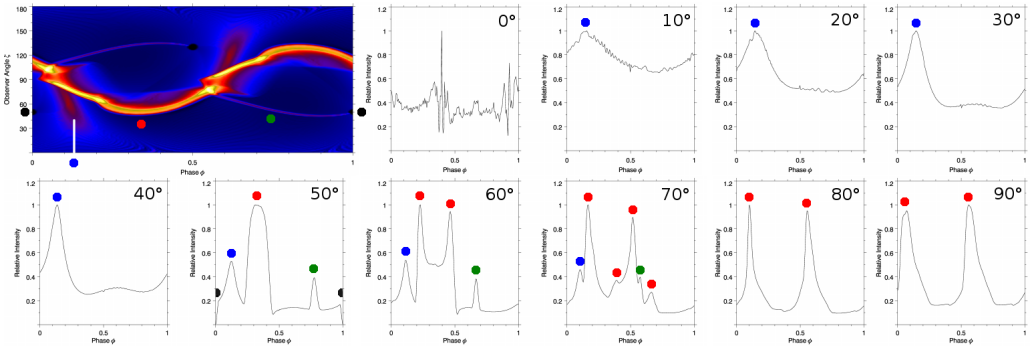

Figure 3. The set of LCs produced by cutting the same phaseplot (as in Figs. **??** and **??**) at successively higher ζ, starting at $\zeta = 0°$, and going as high as $\zeta = 90°$. Note that the phaseplot is symmetric under a 0.5 shift in phase accompanied by a reflection about the equator due to the symmetry of the pulsar's magnetic field (between hemispheres). This means that cuts above $\zeta = 90°$ are redundant.

We can now very clearly see the structure of the phaseplot reflected in the set of LCs produced from it. We see that at $\zeta \leq 40°$ the only dominant peak is associated with the secondary caustic (blue dots), except for $\zeta = 0°$, where the LC is entirely made up of low level emission. At $\zeta = 50°$ we see that (besides coincidentally cutting through the polar cap (black dots) and seeing the accompanying dip in intensity at $\phi = 0$ and 1) the main caustic (red dots) suddenly becomes the dominant feature on the LC as we cut it tangentially at its lowest point. Furthermore, we also see the notch line (green dots) for the first time. From $\zeta = 60°$ onward we see that predominantly two-peaked profiles are produced as we are now cutting the caustic above its lowest point and our line-of-sight is intersecting with it twice. At $\zeta = 80°$ and $90°$ we see pure two-peaked profiles. Notice the movement of the peak associated with the notch line moving toward earlier phases as we increase ζ until its effect becomes lost under the intense emission coming from the caustic. Also, notice that the separation between the two dominant peaks ($\triangle$) steadily increases to almost 0.5 in ϕ as we progressively cut higher above the lowest point of the caustic.

4.2. The entire set of phaseplots

Looking at Fig. 4 we see that the intuition we have built up enables us to very easily pin down some major attributes of the structure of the atlas which would be produced under a certain set of model parameters (see caption for details).

We start with a flat and relatively featureless phaseplot at $\alpha = 0°$ with the structure of the magnetic field being the only factor determining the structure of the phaseplot. At $\alpha = 30°$ we see the main and secondary caustics starting to form, as well as the polar cap. We expect to see very few two-peaked profiles, and predominantly profiles with a single early peak associated with the secondary caustic. The secondary caustics are much more prominently visible at $\alpha = 60°$, and we can see the notch line and associated overlap region making their appearance. The main caustics are more extremely curved, and the main and secondary caustics have started to merge. Here we expect to see a much larger number of two-peaked profiles, as well as some very complicated profiles between $\alpha = 50°$ and $80°$, having multiple additional small peaks due to the cut intersecting many of the minor features on the phaseplot.

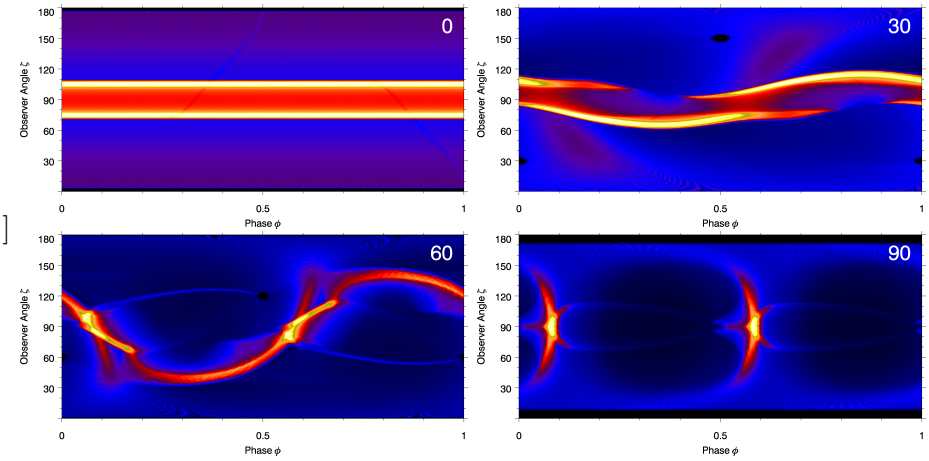

Figure 4. Phaseplots for α between 0° and 90° with a resolution of 30° in both α and ζ for the TPC model. Period - 160 ms; Gap width - 5% (the gap extends from the last open field line toward the magnetic field axis 5% of the polar cap radius); Radial gap extent - 1.2 $R_{\rm LC}$ (the light cylinder radius).

At $\alpha = 90°$ the (now merged) caustics dominate the atlas, yielding a very large range of two-peaked profiles with very large separations between the peaks ($\triangle \sim 0.5$ in phase). Here the high altitude emissions produce a significant wing (around $(\phi, \zeta) = (0.5, 90°)$) leading the caustic at higher ζ, producing LCs with broader peaks.

5. Discussion and Conclusions

In this paper we have illustrated how an understanding of the structure of the phaseplots generated by geometric pulsar models can translate into an understanding of the structure of the resulting LC atlas. Moreover, this understanding also allows us to more easily and effectively understand how changes in the model parameters can affect the LC atlas by understanding how they affect the phaseplots. This approach also allows us to effectively interpret obtained LC fits upon inspection in terms of the features contributing to the best-fit LC, and thus make more successful use of the obtained LC fit in, e.g., predicting at which altitudes the relevant radiation originates.

Acknowledgments

This research is based upon work supported by the South African National Research Foundation. A.K.H. acknowledges support from the NASA Astrophysics Theory Program. C.V., T.J.J., and A.K.H. acknowledge support from the Fermi Guest Investigator Program.

References

[1] Seyffert A S, Venter C, Harding A K, Johnson T J *Proc. of The 56th Ann. SAIP Conf.* 531–36
[2] Abdo A A et al. 2010 *Astrophys. J.* **715** 429–57
[3] Thompson D J 2001 *AIP Conf. Series* **558** 103–14
[4] Weltevrede P et al. 2010 *Astrophys. J.* **708** 1426–41
[5] Seyffert A S, Venter C, Harding A K, Johnson T J *Proc. of The 25th Biann. TEXAS Conf.*
[6] Deutsch A J 1955 *Ann. d'Astrophys.* **18** 1–10
[7] Goldreich P and Julian W H 1969 *Astrophys. J.* **157** 869–80
[8] Cheng K S, Ho C and Ruderman M 1986 *Astrophys. J.* **300** 500–21
[9] Dyks J and Rudak B 2003 *Astrophys. J.* **598** 1201–6
[10] Morini M 1983 *Mon. Not. R. Astron. Soc.* **202** 495–510

References

[1] Kraan-Korteweg R C 2005 *Reviews in Modern Astronomy* (*Reviews in Modern Astronomy* vol 18) ed S Röser pp 48–75

[2] Skrutskie M F, Cutri R M, Stiening R, Weinberg M D, Schneider S, Carpenter J M, Beichman C, Capps R, Chester T, Elias J, Huchra J, Liebert J, Lonsdale C, Monet D G, Price S, Seitzer P, Jarrett T, Kirkpatrick J D, Gizis J E, Howard E, Evans T, Fowler J, Fullmer L, Hurt R, Light R, Kopan E L, Marsh K A, McCallon H L, Tam R, Van Dyk S and Wheelock S 2006 *AJ* **131** 1163–1183

[3] Jarrett T H, Chester T, Cutri R, Schneider S E and Huchra J P 2003 *AJ* **125** 525–554

[4] Huchra J, Jarrett T, Skrutskie M, Cutri R, Schneider S, Macri L, Steining R, Mader J, Martimbeau N and George T 2005 *Nearby Large-Scale Structures and the Zone of Avoidance* (*ASP conf.* vol 329) ed A P Fairall & P A Woudt p 135

[5] Huchra J P, Macri L M, Masters K L, Jarrett T H, Berlind P, Calkins M, Crook A C, Cutri R, Erdoğdu P, Falco E, George T, Hutcheson C M, Lahav O, Mader J, Mink J D, Martimbeau N, Schneider S, Skrutskie M, Tokarz S and Westover M 2012 *ApJS* **199** 26

[6] Kraan-Korteweg R C and Lahav O 2000 A&A Rev. **10** 211–261

[7] Masters K L, Springob C M and Huchra J P 2008 *AJ* **135** 1738–1748

[8] Henning P A, Springob C M, Minchin R F, Momjian E, Catinella B, McIntyre T, Day F, Muller E, Koribalski B, Rosenberg J L, Schneider S, Staveley-Smith L and van Driel W 2010 *AJ* **139** 2130–2147

[9] Donley J L, Staveley-Smith L, Kraan-Korteweg R C, Islas-Islas J M, Schröder A, Henning P A, Koribalski B, Mader S and Stewart I 2005 *AJ* **129** 220–238

[10] Saintonge A 2007 *AJ* **133** 2087–2096

[11] Kraan-Korteweg R C and Huchtmeier W K 1992 A&A **266** 150–166

[12] Seeberger R, Huchtmeier W K and Weinberger R 1994 A&A **286** 17–24

[13] Spinrad H 1975 *ApJL* **199** L1

[14] Focardi P, Marano B and Vettolani G 1984 A&A **136** 178–180

[15] Weinberger R 1980 A&AS **40** 123–127

[16] Chamaraux P, Cayatte V, Balkowski C and Fontanelli P 1990 A&A **229** 340–350

[17] Lu N Y and Freudling W 1995 *ApJ* **449** 527

[18] Pantoja C A, Altschuler D R, Giovanardi C and Giovanelli R 1997 *AJ* **113** 905–936

[19] Ebeling H, Edge A C, Bohringer H, Allen S W, Crawford C S, Fabian A C, Voges W and Huchra J P 1998 *MNRAS* **301** 881–914

[20] Kraan-Korteweg R C, Woudt P A, Cayatte V, Fairall A P, Balkowski C and Henning P A 1996 *Nature* **379** 519–521

[21] Scharf C, Hoffman Y, Lahav O and Lynden-Bell D 1992 *MNRAS* **256** 229–237

[22] van de Weygaert R and Hoffman Y 2000 *Cosmic Flows Workshop* (*Astronomical Society of the Pacific Conference Series* vol 201) ed Courteau S and Willick J p 169 (*Preprint* `astro-ph/9909103`)

[23] Erdoğdu P, Huchra J P, Lahav O, Colless M, Cutri R M, Falco E, George T, Jarrett T, Jones D H, Kochanek C S, Macri L, Mader J, Martimbeau N, Pahre M, Parker Q, Rassat A and Saunders W 2006 *MNRAS* **368** 1515–1526 (*Preprint* `astro-ph/0507166`)

Glow-in-the-dark globular clusters: modelling their multiwavelength lanterns

C Venter[1], I Buesching[1], A Kopp[2], A-C Clapson[3], and O C de Jager[1]

[1]Centre for Space Research, North-West University, Potchefstroom Campus, Private Bag X6001, Potchefstroom 2520, South Africa

[2]Institut für Experimentelle und Angewandte Physik, Christian-Albrechts-Universität zu Kiel, Leibnizstrasse 11, 24118 Kiel, Germany

[3]Max-Planck-Institut für Kernphysik, PO Box 103980, 69029 Heidelberg, Germany

Abstract. Globular clusters (GCs) are astronomical tapestries embroidered with an abundance of exotic stellar-type objects. Their high age promises a rich harvest of evolved stellar products, while the deep potential wells and high mass densities at their centres probably facilitate the formation of multiple-member stellar systems via increased stellar encounter rates. The ubiquity of low-mass X-ray binaries, thought to be the progenitors of millisecond pulsars (MSPs), explain the large number of observed GC radio pulsars and X-ray counterparts. The *Fermi* Large Area Telescope (LAT) recently unveiled the first γ-ray GC pulsar (PSR J1823−3021A). The first observations of GCs in the GeV and TeV bands furthermore created much excitement, and in view of the above, it seems natural to explain these high-energy lanterns by investigating an MSP origin. An MSP population is expected to radiate several pulsed spectral components in the radio through γ-ray wavebands, in addition to being sources of relativistic particles. The latter may interact with background photons in the clusters producing TeV excesses, while they may also radiate synchrotron photons as they traverse the cluster magnetic field. We present multiwavelength modelling results for Terzan 5. We also briefly discuss some alternative interpretations for the observed GC γ-ray signals.

1. Introduction

There are about 150 Galactic globular clusters (GCs), ancient spherical arrangements of 10^5-10^6 stars bound by their mutual gravity. The peculiar properties of these objects have been useful in diverse astrophysical disciplines such as cosmology, galaxy formation, stellar evolution and dynamics, and binary and variable stars [22]. Empirical correlations between (i) the number of low-mass X-ray binaries (LMXRBs) – the progenitors of millisecond pulsars (MSPs) – and the two-body stellar encounter rate [33], and between (ii) the number of MSPs ($N_{\rm MSP}$) and this same encounter rate [2, 24], provide evidence for a dynamical formation of such GC stellar objects. Encounter rates may in turn be enhanced by the high core densities of GCs [43], leading to relatively large numbers of LMXRBs and MSPs in GCs. These sources may be directly or indirectly responsible for, or contribute to, the multiwavelength emission seen from GCs. This paper discusses the multiwavelength observations and modelling of GCs, but with a strong focus on the γ-ray waveband.

2. Multiwavelength pieces of the puzzle

GCs have now plausibly been detected in all energy domains [1]. There are various examples: surface brightness profile measurements in the optical and infrared which facilitate King-model-type fits [37] that in turn allow, e.g., inference of structural parameters; discoveries of embedded radio MSPs [35], X-ray MSPs, LMXRBs, white dwarfs (WDs), and main-sequence binaries [19]; extended radio emission [13]; and the high-energy (HE) and very-high-energy (VHE) detections discussed below.

2.1. GCs by the dozen: Fermi Large Area Telescope (LAT) results

Just over a year into the *Fermi* mission, detection of 47 Tucanae at a 17σ level was claimed, making this the first GC to be detected in γ-rays [1]. The spectrum was consistent with being an accumulation of several individual MSPs' pulsed spectra (for an alternative interpretation, see Section 4.2), with the measured luminosity constraining the 47 Tucanae MSP population to ~ 60. However, no pulsations from individual MSPs were found. This was followed by the detection of Terzan 5 [26], as well as several (plausibly ~ 6) other GCs [2], including M 28, NGC 6388, and Omega Cen. Another 3 detections and 3 GC candidates were claimed [36], bringing the total number of HE GCs to about a dozen [30].

2.2. The shy waveband: VHE observations

In contrast to the HE successes, TeV observations have only been able to uncover an excess in the direction of, but offset from the centre of, Terzan 5 [3] (with a probability of a chance coincidence of $\sim 10^{-4}$). The extended VHE source reaches beyond the cluster's tidal radius, exhibiting a power-law spectrum with a photon index of $2.5 \pm 0.3_{\rm stat} \pm 0.2_{\rm sys}$ that implies an integral flux of $(1.2 \pm 0.3) \times 10^{-12}$ cm^{-2} s^{-1} above 440 GeV. Only upper limits exist on other GC positions: 47 Tuc [6], M 13 [7, 29], M 5 and M 15 [4, 29], and NGC 6388 [4].

2.3. Diffuse X-rays

Diffuse X-rays have been reported for M 22, Omega Cen, 47 Tucanae [23, 28], M 80, NGC 6266, NGC 6752, and M 5 [31]. This emission has been interpreted [28] as being due to the formation of bow shocks which result from the GC motion through the Galactic halo plasma, since it appears to be associated with GCs with high proper motions and large accumulations of internal gas [31]. However, the clumpy structure observed near NGC 6752 exhibits a hard non-thermal spectrum as well as a radio counterpart, and may be due to bremsstrahlung by shock-accelerated electrons hitting nearby gas clouds, while unresolved X-ray sources may contribute to, or even dominate, diffuse X-ray radiation from GCs in general [15]. Diffuse X-ray emission has also been observed from Terzan 5 (1–7 keV), peaking at the centre and decreasing smoothly outwards [15], probably of a non-thermal origin (e.g., synchrotron radiation – SR). A follow-up search for diffuse X-rays from six HE GCs yielded no significant emission above the background level [16]. Within the MSP scenario that this paper focuses on, SR is expected to be produced by relativistic leptons that escape from a population of MSPs inside GCs and interact with the GC magnetic field [38]. Using the diffuse X-ray profile [15], the diffusion coefficient of these particles may be constrained [12, 27]. One can also probe the magnitude and profile of the cluster's magnetic field.

3. Message from the most powerful γ-ray MSP

The *Fermi* detection [17] of the most powerful (and likely youngest) γ-ray MSP to date, PSR J1823−3021A in NGC 6624, which is also the first firm[1] detection of a γ-ray MSP in a GC, allows constraints on the underlying mechanism of HE GC emission (Section 2.1). Using

[1] *AGILE* claimed a 4σ detection of PSR J1824−2452 in M 28 [32]. This was only later confirmed by *Fermi* [25].

the measured γ-ray light curve, one may define an 'off-pulse window' – a range in the cyclic normalized phase coordinate where the pulse is believed to be 'switched off' ($0.07 < \phi < 0.60$ and $0.67 < \phi < 0.90$ in this case). Selecting off-pulse γ-rays only, one can then constrain the level of emission from other sources (e.g., other GC MSPs) or from the background. This technique is also used when searching for steady emission from putative pulsar wind nebulae surrounding younger pulsars [5]. *Fermi* did not detect any GeV point sources in the off-pulse window of PSR J1823−3021A. A previous estimate [2, 36] assigned ~ 100 γ-ray MSPs to this cluster. We now know that this extraordinarily powerful MSP accounts for almost all of NGC 6624's HE emission and the off-pulse flux upper limit constrains the number of additional 'ordinary' GC MSPs to < 32. This implies that, at least for NGC 6624, the HE emission must be predominantly due to pulsed emission, believed to be magnetospheric curvature radiation (CR; Section 4.1). Any unpulsed emission (e.g., due to inverse Compton (IC) scattering) is severely constrained in this case (Section 4.2). Although this supports a pulsed origin for HE emission in other GCs, one can only speculate as to the general validity, given the plausible differences in MSP population properties and environments between GCs.

4. Successes and challenges of the γ-ray MSP population model

4.1. Pulsed HE emission

The fact that *Fermi* has detected several GCs exhibiting spectra that are very reminiscent of pulsar spectra (hard power law with exponential cutoff at a few GeV) leads to the notion that a population of MSPs hosted within the GC may be cumulatively responsible for this HE emission [2], strengthened by the discovery of γ-rays from PSR J1823−3021A (see Section 3). Indeed, this had been predicted [21, 39, 40] shortly before the discovery of 47 Tucanae in the HE band [1]. The pulsed emission arises from particles being accelerated by electric fields inside the MSP magnetospheres, and suffering CR losses as they move along curved magnetic field lines, before being ejected beyond the light cylinder. Predictions for 47 Tucanae were reasonably close to the measured spectrum, and implied a population size of ~ 50 members [42], but overpredicted the spectral cutoff by a factor ~ 2, suggesting some revision of the model (e.g., a lower electric field or smaller curvature radius may be needed; this may be attained by newer magnetospheric structures and different charge density properties). The predicted spectrum was also too hard [40]. It has to be borne in mind, however, that a pair-starved electric field has been assumed in these calculations. Subsequent light curve modelling of several γ-ray MSPs [41] suggests that the bulk of this population may have screened electric fields, a possibility not considered previously within the standard assumption of MSP magnetospheres consisting of dipolar magnetic fields [20].

4.2. Unpulsed HE emission

As an alternative to the CR mechanism, an IC scenario was considered to explain the HE fluxes seen by *Fermi* [12]. The model solves a cosmic-ray diffusion equation (using a slightly different stellar photon energy density profile than [8]), and predicts that the bulk of the HE radiation comes from a region beyond the GC core (contrary to the findings of [8]), so that GCs should be extended HE sources. The *Fermi* flux may be reproduced for some combinations of model parameters in this scenario. This model also predicts spectral components that should be visible in the VHE domain in some cases. Such unpulsed IC components seem less dominant, however, in the case of the cluster NGC 6624, as explained in Section 3.

4.3. Unpulsed VHE emission

In addition to being sources of pulsed photons, MSPs may also produce leptons with energies of up to a few TeV [11]. These leptons escape from the magnetospheres and may be reaccelerated in shocks formed by collisions of stellar winds in the cluster core [8, 9]. The leptons may

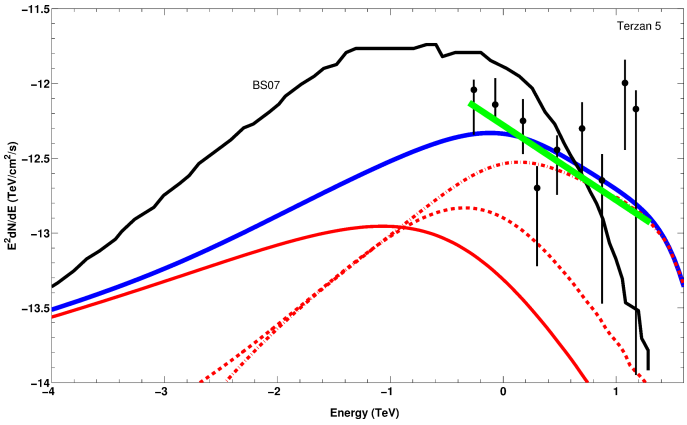

Figure 1. Predicted IC spectrum in the MSP scenario. The black solid line labelled BS07 is scaled from [8], while the thick blue solid line represents the sum of the IC emission from three zones lying at increasing radii from the GC centre (indicated by the lower solid, dashed, and dashed-dotted red lines). We assumed a power-law lepton injection spectrum with minimum energy of 100 MeV, maximum energy of 100 TeV, photon index of 1.6, cluster field of 1 μG, and total power of 2×10^{34} erg s^{-1} (e.g., $N_{\rm MSP} = 100$ if the conversion efficiency of spin-down power to particle power is 1%). We also introduced a factor 3 scaling. This implies a larger value of $N_{\rm MSP}$, number of cluster stars ($N_{\rm star} > 8 \times 10^5$), average stellar radius ($R > 10^6$ cm), stellar temperature ($T > 6\,000$ K), or smaller GC distance ($d < 5.9$ kpc), or a combination of these [34]. The green line and data points are from H.E.S.S. results [3].

then upscatter bright starlight and cosmic microwave background (CMB) photons to very high energies, leading to an unpulsed VHE spectral component, which gives an independent constraint[2] (vs. pulsed emission) on $N_{\rm MSP}$ (depending on the cluster magnetic field and diffusion coefficient) [40]. It was found that 47 Tucanae and Terzan 5 may be visible for H.E.S.S., depending on model parameters [8, 40]. Using the H.E.S.S. upper limits on the VHE γ-ray emission from 47 Tucanae, we could infer a population of $\sim 30 - 40$ MSPs, given a cluster magnetic field of $B \sim 10\mu$G (but quite larger for $B < 5\,\mu$G or $B > 30\mu$G).

We have now extended our calculations for Terzan 5 (Figure 1), including a third large emission zone extending up to the tidal radius, a full calculation of the energy density profile [34], and assuming a power-law injection spectrum for the leptons. It has been expected that, since the stellar energy density profile is strongly peaked at the centre of the GC, the TeV flux should follow a similar profile, as the IC process depends on this target soft photon field [14]. However, even though the energy density drops steeply as one leaves the core region, the much larger size of the halo traps the particles for much longer, where they interact with the low-energy-density field. This increase in residence time outweighs the drop in soft photon energy density and emission from this region dominates the VHE spectrum in our model.

4.4. Challenges

Typical constraints derived from the measured GeV energy fluxes on $N_{\rm MSP}$ are not always so restrictive, given uncertainties in energy flux, GC distance, and average MSP beaming factors. This means that the level of the pulsed CR flux predictions is somewhat uncertain. Lack of evidence for spectral cutoffs around a few GeV for some GCs also challenge the cumulative CR interpretation for the HE GC emission [10, 36]. Concerning VHE models, refinement of the soft

[2] We are assuming that the number of visible HE MSPs $N_{\rm vis} \approx N_{\rm MSP}$.

photon energy density profile (e.g., adding a Galactic component [12]), cluster magnetic field profile, and particle transport calculations may be needed. The peculiar asymmetric, offset VHE source seen in coincidence with Terzan 5 also challenges a simplistic MSP scenario, but may be introduced by several factors, including a small MSP population at relatively large distances from the centre, formation of MSPs near the tidal radius in addition to the core [36], non-spherical photon target fields, proper motion of the GC, and an asymmetric diffusion coefficient [12]. Source extension, morphology, spectrum and energetics will continue to constrain GC models.

5. Other sides of the VHE coin: alternative explanations

5.1. Explosive energy: a short γ-ray burst (GRB) relic in Terzan 5?

Long GRBs (> 2 s), signalling the death of massive stars [18], have been invoked as a possible origin for some of the many unidentified TeV sources observed by H.E.S.S. [3]. Similarly, the scenario of the VHE emission from Terzan 5 being due to the remnant of a short (< 2 s), powerful GRB (thought to be due to a compact binary merger [18]) has been put forward [14]. The main argument relies on the fact that the high-density environments of ancient GCs are conducive to the formation of compact binaries, and that the merger of the members (e.g., two neutron stars) may accelerate hadronic cosmic rays. The latter may interact with ambient target nuclei and decay into γ-rays via the π^0 channel. It was shown that for a target density of $n \sim 0.1$ cm^{-3}, and a broken power-law cosmic-ray spectral shape with spectral index of 2.0 below 5 TeV, the total energy of hadrons of $E \approx 10^{51}$ ergs may possibly be supplied by ultrarelativistic blast waves converting a significant part of the kinetic energy to cosmic ray particle energy. A break in the γ-ray spectrum in the GeV / TeV range would support such a scenario. The putative remnant age of $\sim 10^4$ yr (estimated from the TeV source extension and depending on the hadron diffusion coefficient) corresponds roughly to the estimated rate of short bursts in the Milky Way (~ 1 event per 10^4 yr, depending on the burst beaming factor) in the event of relatively slow diffusion. In this scenario, electrons accelerated by the blast wave scatter the stellar photons to produce diffuse non-thermal X-ray emission. Additional predicted signatures are faint thermal X-rays from hot thermal plasma in the remnant, faint nuclear line emission from radio-active decay of heavy nuclei ejected during the merger, and faint ionization lines following from interaction of the GRB afterglow with the interstellar medium.

5.2. Distant cousins: a partly WD origin?

Instead of MSPs, a population of fast-rotating, magnetized WDs contained within GCs has been investigated as being responsible for (part of) the HE and VHE signals [10]. An estimate involving the initial mass function implies that the number of all WDs in a GC may be as high as $\sim 10^5$, dominating the MSP population by a factor of a few hundred. The evolutionary behaviour of the non-accreting WD energetics is furthermore very similar to the case of rotation-powered pulsars, although the typical surface magnetic fields may be lower ($\sim 10^8$ G vs. 10^{8-9} G), rotational periods much longer (~ 100 s vs. 5 ms), masses similar ($\sim 0.8 M_\odot \approx 1.4 M_\odot$), and radii larger ($\sim 5 \times 10^8$ cm vs. 10^6 cm). These parameters suggest that a single WD may have injected electrons with a power of up to $\sim 10^{28}$ erg s^{-1} (vs. $\sim 10^{32}$ erg s^{-1} for an MSP), but this would be less in the case of magnetic field decay. In addition, WDs created by WD-WD mergers in compact binary systems (having larger masses, smaller radii, and shorter periods than non-accreting WDs) may also contribute to the observed γ-ray flux, but at a much lower level (a factor ~ 10). It has been shown [10] that a few thousand WDs that have been created uniformly during the GC lifetime may produce a detectable VHE signal via upscattering of CMB and stellar soft photon fields (assuming mono-energetic electron injection spectra, and different models for WD formation, evolution, and magnetic field decay, and also depending on the electron acceleration process).

6. Conclusion

We have discussed GCs as multiwavelength objects, focusing on their γ-ray properties. Although some models have proven reasonable, inevitable refinement is due in the wake of observations that are increasing both in quality and quantity.

Acknowledgments

This research is based upon work supported by the South African National Research Foundation.

References

[1] Abdo A A *et al.* 2009 *Science* **325** 845–8
[2] Abdo A A *et al.* 2010 *Astron. & Astrophys.* **524** A75
[3] Abramowski A *et al.* 2011 *Astron. Astrophys.* **531** L18–22
[4] Abramowski A *et al.* 2011 *Astrophys. J.* **735** 12–9
[5] Ackermann M *et al.* 2011 *Astrophys. J.* **726** 35–51
[6] Aharonian F *et al.* 2009 *Astron. Astrophys* **499** 273–7
[7] Anderhub H *et al.* 2009 *Astrophys. J.* **702** 266–9
[8] Bednarek W and Sitarek J 2007 *Mon. Not. Royal Astron. Soc.* **377** 920–30
[9] Bednarek W 2011 *High-Energy Emission from Pulsars and their Systems: Proc. 1st Session Sant Cugat Forum of Astrophys.* ed N Rea and D F Torres pp 185–205 arXiv:1009.1694
[10] Bednarek W 2012 *J. Phys. G: Nucl. Part. Phys.* **39** 065001
[11] Büsching I, Venter C and de Jager O C 2008 *Adv. Space Res.* **42** 497–503
[12] Cheng K S *et al.* 2010 *ApJ* **723** 1219–30
[13] Clapson A-C, Domainko W F, Jamrozy M, Dyrda M and Eger P 2011 *Astron. Astrophys.* **532** A47
[14] Domainko W F 2011 *Astron. Astrophys.* **533** L5–8
[15] Eger P, Domainko, W F and Clapson, A-C 2010 *Astron. Astrophys.* **513** A66
[16] Eger P and Domainko W F 2012 *Astron. Astrophys.* **540** A17
[17] Freire P C C *et al.* 2011 *Science* **334** 1107–10
[18] Gehrels N *et al.* 2005 *Nature* **437** 851–4
[19] Grindlay J E, Heinke C, Edmonds P D and Murray S S 2001 *Science* **292** 2290–5
[20] Harding A K, Muslimov A G and Zhang B 2002 *Astrophys. J.* **576** 366–75
[21] Harding A K, Usov V V and Muslimov A G 2005 *Astrophys. J.* **622** 531–43
[22] Harris W E 1996 *Astron. J.* **112** 1487–8
[23] Hartwick F D A, Grindlay J E and Cowley A P 1982 *Astrophys. J.* **254** L11–3
[24] Hui C Y, Cheng K S and Taam R E 2010 *Astrophys. J.* **714** 1149–54
[25] Johnson T J *et al.* 2013 *Astrophys. J.* **778** 106–17
[26] Kong A K H, Hui C Y and Cheng K S 2010 *Astrophys. J.* **712** L36–9
[27] Kopp A, Venter C, Buescing, I, de Jager, O C 2013 *Astrophys. J.* **779** 126–37
[28] Krockenberger M and Grindlay J E 1995 *Astrophys. J.* **451** 200–9
[29] McCutcheon M *et al.* 2009 *Proc. 31st ICRC, Lodz, Poland* arXiv:0907.4974
[30] Nolan, P L *et al.* 2012 *Astrophys. J. Suppl. Ser.* **199** 31–76
[31] Okada Y, Kokubun M, Yuasa T and Makishima K 2007 *Publ. Astron. Soc. Japan* **59** 727–42
[32] Pellizzoni A *et al.* 2009 *Astrophys. J.* **695** L115–9
[33] Pooley D *et al. Astrophys. J.* **591** L131–4
[34] Prinsloo L P, Venter C, Buesching I and Kopp A *these proceedings*
[35] Ransom S M 2008 *40 Years of Pulsars: Millisecond Pulsars, Magnetars and More, AIP Conf. Ser., ed C Bassa, Z Wang, A Cumming, V M Kaspi* **983** pp 415–23
[36] Tam P H T *et al.* 2011 *Astrophys. J.* **729** 90–7
[37] Trager S C, King I R and Djorgovski S 1995 *Astron. J.* **109** 218–41
[38] Venter C and de Jager O C 2008 *AIP Conf. Ser.* **1085** 277–80
[39] Venter C and de Jager O C 2008, *Astrophys. J.* **680** L125–8
[40] Venter C *et al.* 2009 *Astrophys. J.* **696** L52–5
[41] Venter C *et al.* 2009 *Astrophys. J.* **707** 800–22
[42] Venter C, de Jager O C, Kopp A and Büsching I 2011 *2011 Fermi Symp. Proc. eConf C110509* arXiv:1111.1289
[43] Verbunt F and Hut P 1987 *IAU Symposium ed D J Helfand and J-H Huang* **125** 187–96

Seyfert 2 galaxies with unusually wide nebular lines

H Winkler, T Chauke

Dept. Physics, University of Johannesburg, PO Box 524, Auckland Park, 2006

hwinkler@uj.ac.za

Abstract. We report on a set of AGN that match the Seyfert 2 galaxy classification criteria, but display unusually wide "narrow" lines, with the 4959 Å and 5007 Å nebular lines overlapping with each other. This spectral line broadening is in most cases evidence of a complex profile with multiple components. It indicates an unusual narrow line region with diverse gas clouds and a range of velocity systems. We list 14 such objects with these characteristics identified in a set of Sloan Digital Sky Survey spectra. We measure the strengths of all lines visible in the spectrum, and attempt to fit multiple Gaussian profiles to the nebular lines. We quantify the line parameters of all multiple velocity systems discovered. We compare the spectral characteristics of our sample with those of other, 'conventional' type 2 Seyferts and attempt to determine whether other systematic spectral differences exist. We consider whether the investigated sample constitutes a clear sub-class of the Seyfert 2 population. In conclusion we offer possible explanations for the unusual line profiles.

1. Introduction

Seyfert 2 galaxies are characterised by a nuclear emission line spectrum marked by [O III] 5007 Å and 4959 Å (the so-called nebular lines) that are significantly stronger than the Hβ line, and [N II] 6583 Å of a similar strength as Hα. In contrast to the related Seyfert 1 galaxies, type 2 nuclei display no overt signs of broadened hydrogen and helium lines [1]. It has however been established that a significant fraction of type 2 Seyferts, including the 'prototype' NGC 1068, do in fact contain a broad line region that is mostly hidden behind dust [2].

The nebular lines, along with other 'narrow' lines in Seyfert spectra, form relatively far from the central black hole whose immediate surroundings generate the ionising radiation responsible for the emission lines. The dynamics of the narrow emission line region manifests itself in the line profile, and hence the study of the profiles of prominent spectral features such as the nebular lines has been a favoured method to map the outer parts of a Seyfert nucleus [3, 4, 5]. In some instances the line profile was shown to be asymmetric and broader than expected. Indeed, the nebular lines in the NGC 1068 nuclear spectrum are so wide that they partly overlap [2].

In this work we investigate a set of Seyfert 2 galaxies characterised by unusually wide nebular lines with complex profiles. We attempt to identify individual components making up these profiles and measure the relative strengths of other lines in the spectrum. We compare the properties thus determined to a sample of Seyfert 2s that do not show evidence of nebular line complexity. We probe possible systematic differences between the samples, and explore possible causes of the complex line profile. We determine whether there are sufficient grounds for assigning the objects studied to a new sub-class of Seyferts.

2. Spectral data reductions

2.1. Identification of sample

During the course of a programme initiated by one of us to classify AGN observed by the Sloan Digital Sky Survey (SDSS) [6], a number of spectra were identified that matched the typical Seyfert 2 spectral line ratio criteria ([O III] 5007 Å >> H-beta, [N II] 6583 Å ~ H-alpha) [7]. Some of these spectra were however noted to be unusual, as their nebular lines exhibited a complex profile, to the extent where these lines partly overlapped. An example of the spectrum of such an object is illustrated in figure 1 below.

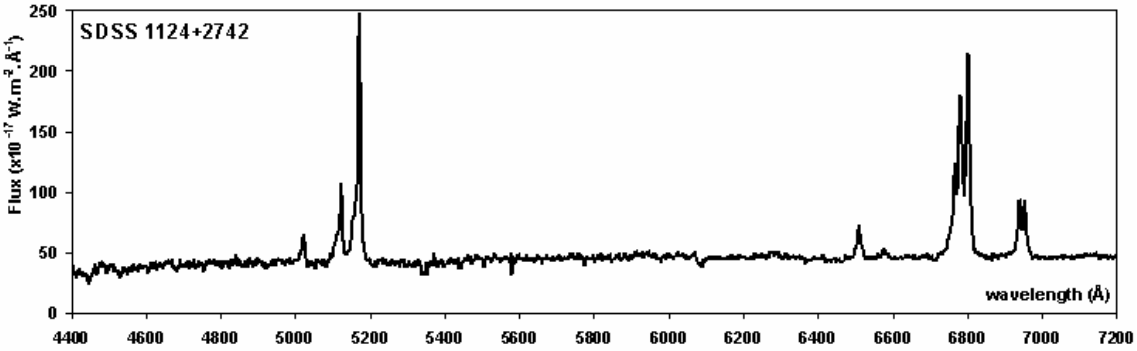

Figure 1. Example of a spectrum of a Seyfert 2 galaxy with wide nebular lines. Note that the 4959 Å and 5007 Å lines (redshifted into the range 5100-5200 Å in the diagram above) overlap each other.

We resolved to study this potential sub-class of Seyfert galaxies further, and identified 12 objects from the SDSS spectral collection that met the overlapping nebular line profile criterion. These are listed in table 1. We also chose five objects with regular Seyfert 2 spectra to act as a comparison sample. The details of the comparison sample are given in table 2.

Table 1. List of AGN of the class identified

code	R.A.(2000)	Dec(2000)	*z*
A	02h08m23.8s	–00 20 00	0.074
B	08h11m21.4s	+40 54 51	0.067
C	08h13m47.5s	+49 41 10	0.094
D	09h18m07.5s	+34 39 45	0.097
E	10h56m38.9s	+14 19 30	0.081
F	11h24m23.9s	+27 42 45	0.032
G	11h47m19.9s	+07 52 43	0.083
H	12h17m27.8s	+15 54 13	0.084
I	12h17m41.9s	+03 46 31	0.080
J	14h48m38.5s	+10 55 36	0.089
K	14h50m18.7s	+12 06 46	0.098
L	15h11m41.3s	+05 18 10	0.084

Table 2. Comparison sample

code	R.A.(2000)	Dec(2000)	*z*
M	00h17m41.8s	+00 07 53	0.070
N	02h02m23.7s	+12 47 17	0.086
O	07h37m15.8s	+31 31 11	0.027
P	10h22m12.6s	+38 37 43	0.056
Q	14h24m05.5s	+01 47 57	0.056

2.2. Spectral reductions

Electronic wavelength- and flux-calibrated spectra were downloaded from the SDSS website. The spectra were then converted to the target's rest frame by eliminating the redshift. High resolution representations of the spectral region spanning the 4959 Å, 5007 Å nebular lines are shown in figure 2.

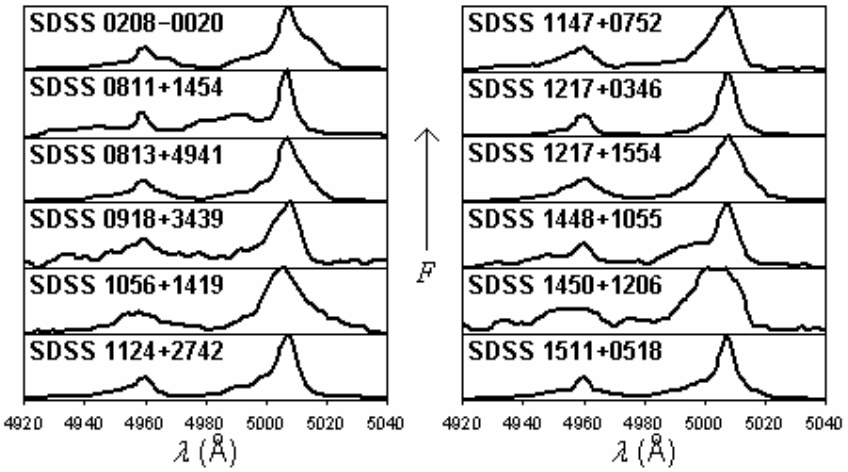

Figure 2. The profiles of the [O III] 4959 Å, 5007 Å lines. The vertical scale in each case ranges from the lowest to the highest values in the displayed wavelength window.

2.3. Spectral line strengths

To systematically compare the relative strengths of the emission lines in each spectrum, we adopted a new procedure to parameterise SDSS AGN spectra. In essence, this procedure measures $\Phi(\lambda)$, the integrated flux for each line over the wavelength range corresponding to a velocity offset $|\Delta v| < 380$ km/s relative to the galaxy's recession velocity (corresponding to 5 SDSS wavelength bins on either side of the peak).

3. Spectral line analysis

3.1. Asymmetry index

The asymmetry of a spectral line may be quantified according to the procedures of Heckman et al [3] or Whittle [4]. The latter method is based on the area under a curve, and is thus less appropriate when spectral lines overlap. We hence preferred the Heckman et al procedure, as it only requires the identification of the wavelengths where the spectral lines reach 20% ($\lambda_{B,20}$ on the blue side, $\lambda_{R,20}$ on the red side) and 80% of its maximum. $\lambda_{C,80}$ is the midpoint between $\lambda_{B,80}$ and $\lambda_{R,20}$ (see figure 3).

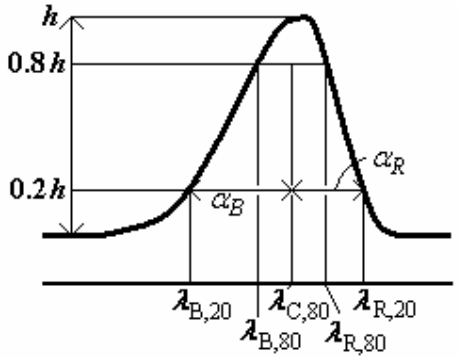

Figure 3. Diagram to illustrate the definition of the Heckman et al [3] asymmetry index.

The Asymmetry index at 20% peak height is then defined by

$$AI_{20} = \frac{\alpha_B - \alpha_R}{\alpha_B + \alpha_R} = \frac{(\lambda_{C,80} - \lambda_{B,20}) - (\lambda_{R,20} - \lambda_{C,80})}{(\lambda_{C,80} - \lambda_{B,20}) + (\lambda_{R,20} - \lambda_{C,80})} = \frac{\lambda_{B,80} + \lambda_{R,80} - \lambda_{B,20} - \lambda_{R,20}}{\lambda_{R,20} - \lambda_{B,20}}.$$

This asymmetry index is listed for all objects studied in table 3.

Table 3. Measured parameters for the Seyfert 2 galaxies studied here.

code	AI_{20}	1st cmp. FWHM	2nd cmp. offset	2nd cmp. FWHM	ρ_{3727}	ρ_{3868}	ρ_{4686}	ρ_{4861}	ρ_{6583}	ρ_{6300}	ρ_{6725}
A	0.02	380	360	1400	1.28	0.97	-	0.99	1.61	0.77	1.41
B	-	320	930	1800	1.90	1.22	-	-	1.81	1.23	1.89
C	0.13	350	60	1200	1.41	0.83	0.33	-	-	1.10	1.53
D	0.89	300	210	800	1.85	1.38	1.12	-	2.83	1.34	2.05
E	–0.45	600	–180	1500	1.96	0.92	-	-	2.32	1.65	2.32
F	1.75	350	270	1200	1.50	0.94	0.26	1.18	2.03	1.22	1.78
G	0.69	330	270	800	1.55	1.15	0.61	1.52	2.08	1.02	1.66
H	0.35	330	140	1100	1.62	1.13	0.44	0.84	1.92	0.97	1.62
I	0.59	510	120	1400	1.23	1.01	0.45	0.70	1.93	0.89	1.39
J	2.95	390	630	1200	1.76	1.16	-	-	2.52	1.26	1.89
K	0.47	400	570	900	2.13	1.16	-	-	2.71	1.53	2.11
L	0.39	310	250	1500	1.38	1.02	0.66	1.72	-	0.97	1.50
M	–0.34	340	-	-	1.36	0.93	0.40	0.80	1.90	0.87	1.43
N	–0.28	350	-	-	1.05	0.87	0.52	1.05	1.45	0.43	1.10
O	–0.28	330	-	-	1.12	0.88	0.34	0.73	1.64	0.69	1.35
P	0.26	220	-	-	1.45	0.95	-	-	1.28	0.75	1.22
Q	1.29	300	-	-	1.49	0.96	0.60	–0.07	1.68	0.74	1.48

3.2. Line positions and widths

We fitted multiple Gaussian profiles to the nebular lines and to the region around Hα. These take the mathematical form

$$F(\lambda) = F(\lambda_0)\exp\left(-\frac{(\lambda-\lambda_0)^2}{2\sigma^2}\right)$$

where λ_0 is the peak wavelength, $F(\lambda_0)$ is the peak flux and the full width at half-maximum (FWHM) corresponds to 2.355σ.

We first fitted Gaussians with widths corresponding to a common velocity and peak wavelengths corresponding to identical recession velocities to the [O III], [N II] and Hα lines. We constrained the peak heights of the two nebular lines, and of the two [N II] lines, to stick to the theoretical 3:1 ratio. We then fitted a second component (of corresponding widths and peak ratio) to the nebular lines. We also found that we required a further, broader component at Hα to obtain a reasonable match with the observed profile. Details of the parameters obtained through these fits are also given in table 3, and an example of the fitted profiles may be viewed in figure 4.

3.3. Spectral parameters

Table 3 also lists the ratio of diagnostically significant [7] other spectral lines ([O II] 3727 Å, [Ne III] 3868 Å, He II 4686 Å, H I 4861 Å, [N II] 6583 Å, [O I] 6300 Å and the [S II] 6725 Å doublet) relative to the stronger 5007 Å nebular line. These are represented in terms of the parameter ρ_λ = 2 + log[Φ(λ)/Φ(5007)]. Note that for the [S II] doublet we use Φ(6725) = Φ(6716) + Φ(6731).

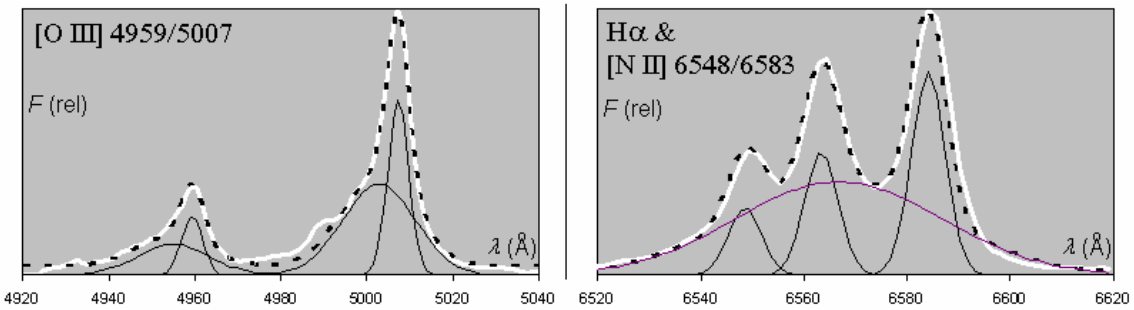

Figure 4. Gaussian components for the nebular lines ([O III] 5007 Å and 4959 Å), Hα and the nitrogen lines [N II] 6583 Å and 6548 Å (black solid line), for the galaxy SDSS 1124+2742. The dashed line represents the sum of the Gaussian components, while the white line is the actual data. The vertical range and scale are adjusted to span the lowest value and highest peak in the wavelength range viewed.

4. Discussion

4.1. Spectral comparison with other Seyfert 2 galaxies

To evaluate whether significant spectral parameter differences exist between the sample of objects with broadened nebular lines (codes A-L in table 3) and the control sample (codes M-Q), we performed Student's t-tests with the values for the asymmetry parameters, widths and line ratios.

At the 95% confidence level, we find significant differences between the samples for the line ratio parameters ρ_{3727}, ρ_{3868}, ρ_{6300} and ρ_{6725}, but not for the widths, the asymmetry indexes or ρ_{4686}. At the same time, we note a wide spread in all parameters for the objects coded A-L, whereas there is more uniformity in the control sample.

4.2. A new sub-class of Seyfert galaxies?

The findings of this study confirm that the Seyfert 2 galaxies with broad nebular lines do not constitute a homogeneous group. Some of the objects studied are definitely unusual, and warrant further investigation. However, unless similar features are detected in several other objects, these cannot be defined as a new Seyfert sub-class.

4.3. Explaining the complex profiles

In most cases the asymmetries and second components identified point to at least parts of the emission line regions being blue-shifted compared to the system velocity. This signifies gas moving towards Earth. We also note that a broad-line component in Hα was fitted in all objects investigated. Although this component was usually too weak to have been evident in a low-resolution view of the spectrum, it does support the view that type 2 Seyferts are nothing but broad-line objects with a highly obscured nucleus, meaning that the broad component is generally too faint to be detected.

It is thus plausible for many of the objects in our sample the Earthwards moving gas is part of a jet, and that the outflow in the opposite direction is not visible due to obscuration by dust. We may also draw on previous high angular resolution studies of the closest and brightest AGN known with overlapping nebular lines, NGC 1068 [8], and another well-known Seyfert 2, NGC 5643 [9]. These studies reveal clumps of matter that to some extent suggest a bi-conical structure with matter outflow, though other mechanisms cannot be entirely excluded.

Alternatively, another possible explanation is that the SDSS spectra have combined the spectra of two interacting galaxies with emission lines, possibly even Seyfert nucleus pairs [10].

In either event, the objects studied here all display a complex narrow-line region structure, and the more abnormal ones would make good candidates for more in-depth study using high-resolution imaging, polarimetry or radio observations.

Acknowledgements
This paper utilized data from the Sloan Digital Sky Survey (SDSS). Funding for the SDSS and SDSS-II has been provided by the Alfred P. Sloan Foundation, the Participating Institutions, the National Science Foundation, the U.S. Department of Energy, the National Aeronautics and Space Administration, the Japanese Monbukagakusho, the Max Planck Society, and the Higher Education Funding Council for England. The SDSS Web Site is http://www.sdss.org/.

The SDSS is managed by the Astrophysical Research Consortium for the Participating Institutions. The Participating Institutions are the American Museum of Natural History, Astrophysical Institute Potsdam, University of Basel, University of Cambridge, Case Western Reserve University, University of Chicago, Drexel University, Fermilab, the Institute for Advanced Study, the Japan Participation Group, Johns Hopkins University, the Joint Institute for Nuclear Astrophysics, the Kavli Institute for Particle Astrophysics and Cosmology, the Korean Scientist Group, the Chinese Academy of Sciences (LAMOST), Los Alamos National Laboratory, the Max-Planck-Institute for Astronomy (MPIA), the Max-Planck-Institute for Astrophysics (MPA), New Mexico State University, Ohio State University, University of Pittsburgh, University of Portsmouth, Princeton University, the United States Naval Observatory, and the University of Washington.

References

[1] Osterbrock D E and Ferland G J 2006 *Astrophysics of Gaseous Nebulae and Active Galactic Nuclei* 2nd Ed. (University Science Books, Sausalito, California)
[2] Antonucci R R J and Miller J S 1985 *Astrophys. J.* **297**, 621
[3] Heckman T M, Miley G K, van Breugel W J M and Butcher H R 1981 *Astrophys J* **247** 403
[4] Whittle M 1985 *Monthly Notices Roy. Astron. Soc.* **213** 1
[5] Busko I C and Steiner J E 1988 *Monthly Notices Roy. Astron. Soc.* **232** 525
[6] Abazajian K, Adelman J, Agueros M, et al. 2003 *Astron J.* **126** 2081
[7] Baldwin J A, Phillips M M and Terlevich R 1981 *Publ. Ast. Soc. Pacific* **93** 5
[8] Ozaki S 2009 *Publ. Ast. Soc. Japan* **61** 259
[9] Simpson C, Wilson A S, Bower G, et al. 1997 *Astrophys. J.* **474** 121
[10] Liu X, Shen Y, Strauss MA and Greene J E 2010 *Astrophys. J.* **708** 427

Lower and Upper thermosphere wind variations during magnetically quiet days

W.T. Sivla and H. McCreadie

School of Chemistry and Physics, University of Kwazulu-Natal, P/Bag X54001, Durban 4000, South Africa

E-mail: sivla_w@yahoo.com

Abstract. Wind variations in the lower and upper thermosphere have been compared during a magnetic quiet period. The mesosphere/lower thermosphere and thermospheric F-regions are dynamically coupled through thermospheric winds, tides and waves. The regular fluctuations in the earth's magnetic field on quiet days are caused by dynamo-induced currents which flow in the ionosphere/thermosphere system. This paper presents simultaneous mesosphere/lower thermosphere and upper thermospheric region wind observations during a quiet magnetic period using data from TIMED and CHAMP satellites. The upper thermospheric winds from two time local sectors are observed to be faster than the lower thermospheric winds.

1. Introduction

Based on thermal considerations the thermosphere is the layer located above the mesosphere. The thermosphere lies above the mesopause at above an approximate height of 90 km. The thermosphere ends at the boundary with the exosphere, approximately 500-700 km, where atoms can escape freely from the atmosphere (Kane, 2005). Unlike the mesosphere, temperature increases with height in the thermosphere. The thermosphere is often considered in a first approximation as a linear stable dissipative oscillatory system, which suppresses the small-scale and short- term structures more effectively than the large-scale and long-term ones (Kazimirovsky,2005). Much of the sun's X-rays and UV radiations are absorbed in the thermosphere. These radiations, in addition to ionizing radiations from outer space, ionize neutral species in the mesosphere and thermosphere forming the ionosphere. The ionosphere extends from about 60 to 800 km, and using electron density is subdivided into; the D region (70-90 km), E-region (90-150 km) and F-region (150-700 km). The terrestrial thermosphere and ionosphere form the most variable part of the Earth's atmosphere (Kazimirovsky and Vergasova, 2009).

Pressure gradients resulting from diurnal and latitudinal variations of neutral gas heating together with Coriolis effect, generate meridional and zonal winds in the earth's upper atmosphere. Ion drag resulting from collisions between ions and the neutral particles contributes in establishing the general pattern of the winds especially in the F-region thermosphere. The effect of molecular diffusion in the thermosphere becomes important at heights above about 110 km. Above this height there is rapid decrease in the densities of heavier molecular species.

The general heating for the Thermosphere-Ionosphere system comes from the interaction of the solar UV photons and energetic particles. Ion drag which brings about differential motion between the neutrals and ionized species is also an energy source for the thermosphere. Frictional heating of the

neutrals and ions in the high latitudes caused by electric field driven currents is a major source of heat at the high latitudes. Figure 1 below shows the energy changes that take place between the thermosphere/Ionosphere system and the surroundings. Ions and atoms which are likely products from photoionisation and dissociation, and electron impact and ionization may be converted to different species in the thermosphere. These species may eventually recombine in reactions which are exothermic.

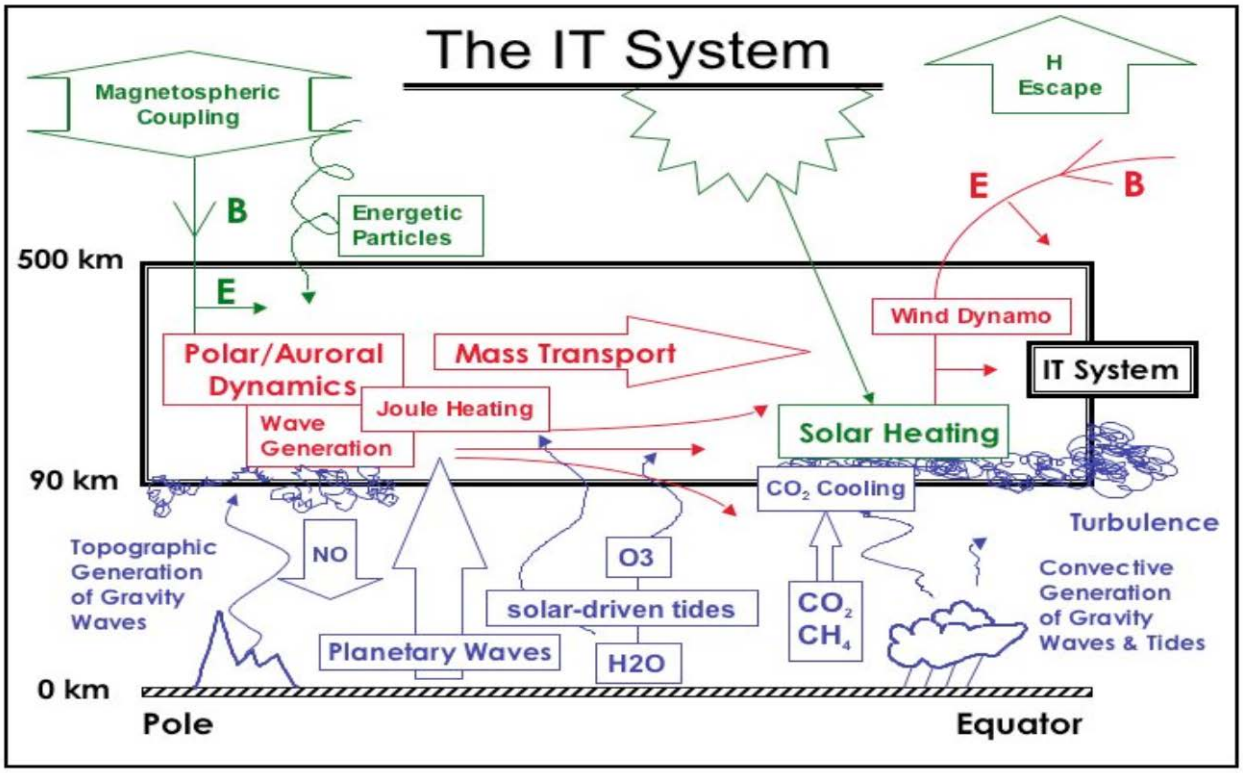

Figure 1. Energy input, conversion and transport processes in the Ionosphere-Thermosphere system (Forbes, 2007).

During periods of moderate and intense geomagnetic activity, the effects of tides and gravity waves which originate from the lower layer of the atmosphere, the troposphere, on the upper thermosphere may be masked by geomagnetic disturbances propagating from the high to the low latitudes. Thermospheric wind variation studies in the lower and upper thermosphere at quiet times will likely improve our understanding of the extent to which tides and gravity waves can influence the dynamics of the upper thermosphere. The aim of this paper is an attempt to compare wind variation in the lower and upper thermospheric regions during a quiet period using satellite data. Wind data for the month of September, 2003 from the TIMED and CHAMP satellites has been used for this study. The month of September, 2003 was a relatively quiet month. Quiet time disturbances (Q-disturbances) can either be positive or negative. Positive Q-disturbances occur under slightly enhanced auroral activity when high latitude heating increases and damps the solar driven poleward thermospheric circulation (Mikhailov et al., 2009). Negative Q-disturbances occur under so called ground state of the thermosphere which corresponds to very low geomagnetic activity with an unconstrained solar-driven thermospheric circulation characterized relatively strong daytime poleward wind and relatively low atomic oxygen concentrations at middle and sub-auroral latitudes (Mikhailov et al., 2007a).

The lower and upper thermospheres with the embedded ionosphere form a coupled system. Influences that originate at one height have influences elsewhere in the system. Ionospheric dynamo is

driven by neutral winds, but operations of these winds in the E and F-layers are different. The E-layer and F-layer dynamos are linked by geomagnetic field lines, which act as highly conducting 'wires' because electrons can move freely along them to neutralize parallel electric field (Rishbeth, 1997).

2. Data Sources

The TIMED Doppler Interferometer (TIDI) is a wind measuring instrument on board the TIMED satellite. It measures horizontal vector wind speeds in the mesosphere and lower thermosphere from an altitude of 70 km to 120 km. The TIDI telescopes perform limb scan simultaneously in four orthogonal directions: two at 45^0 forward but on either side of the spacecraft's velocity vector and two at 45^0 rearward of the spacecraft (Talaat et al., 2003). An image of the TIDI geometry is shown in figure 2 below. The TIMED satellite orbits an altitude of 625 km and the total inclination is 74.1^0; TIDI measures the horizontal vector wind field with an accuracy of 3 m/s and a vertical resolution of 2 km (Killeen et al., 2006). TIDI measures wind by measuring the Doppler shift of the atmospheric emission features.

Thermospheric wind is obtained from the 'Spatial Tri-axial Accelerometer for Research' (STAR) on board the Challenging Mini-Payload Satellite (CHAMP). The STAR accelerometer measures the non-gravitational accelerations acting on the satellite. Figure 3 shows the STAR and spacecraft reference frames. The orbital plane of the low Earth orbiting (LEO) spacecraft precesses by 1h of local time (LT) in 11 days, thus after 131 days all local times are covered (Ritter et al., 2010). Sutton et al. (2007) adapted the method used by Liu et al. (2006) to process the accelerometer dataset into density and wind datasets. During the month of September, 2003 the CHAMP satellite altitude varied between 390 km and 425 km. This range falls within the F-region of the embedded ionosphere.

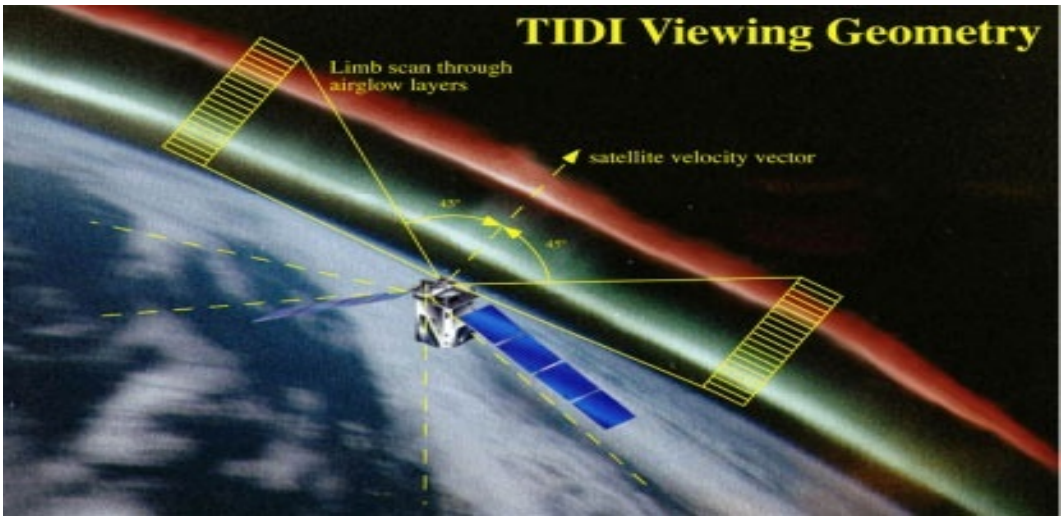

Figure 2. Illustration of TIDI viewing geometry (Killeen, 2002).

3. Results and Discussion

The solar and geophysical conditions that prevailed during the period of study, the month of September 2003, are shown in figure 4. The Dst index represents the axially symmetric disturbance magnetic field from large-scale magnetospheric current systems observed at the dipole equator on the Earth's surface (Ritter et al.,2004). The Dst index varied between 35nT and -67nT during the period of study. The global Kp index is the mean value of the disturbance geomagnetic levels observed at 13 selected mid-latitude stations during three-hour time intervals. According to a quasi-logarithmic scale it covers the range from 0 to 9. The highest Kp index values are recorded between 15^{th} and 20^{th}. The highest Ap value is observed within these days. The geomagnetic planetary index, Ap, gives a measure

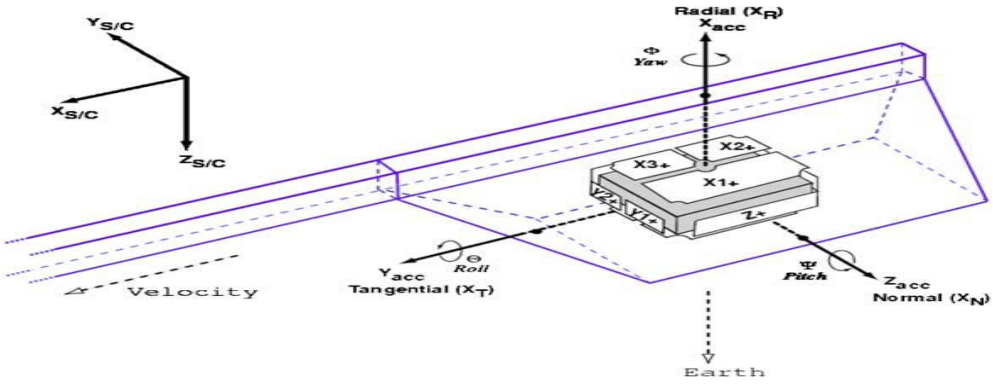

Figure 3. The STAR reference frame with respect to the fixed Spacecraft frame (Bruinsma et al., 2003).

of the level of geomagnetic activity over the entire Earth, for a given day. It is the daily average of the 3-hourly ap index, derived from the 3-hourly Kp values.

The solar flux (F10.7) varied with minimum values of about 90 s.f.u and maximun values going up to about 140 s.f.u recorded towards month end.

Figure 5 shows the latitudinal variation of the zonal and meridional winds with local time and (a),(b) and(c) represent zonal wind distributions at 90 km, 100 km and 110 km respectively and (d), (e) and (f) represent meridional wind distributions at 90 km,100 km and 110 km respectively and likewise figure 6 shows the zonal wind distribution in the upper thermospheric during the early morning sector and late afternoon sector. The meridional wind illustrates clear latitudinal structures. The winds are generally equatorwards for most of the day. Polewards winds are observed for the most of the evening to morning hours. At high latitudes in the northern hemisphere strong equatorward winds are experienced with speeds going above 150 m/s. Speeds up to 250 m/s are experienced at 90 km altitude. The zonal winds do not show any clearly defined structure at 90 and 100 km altitudes.

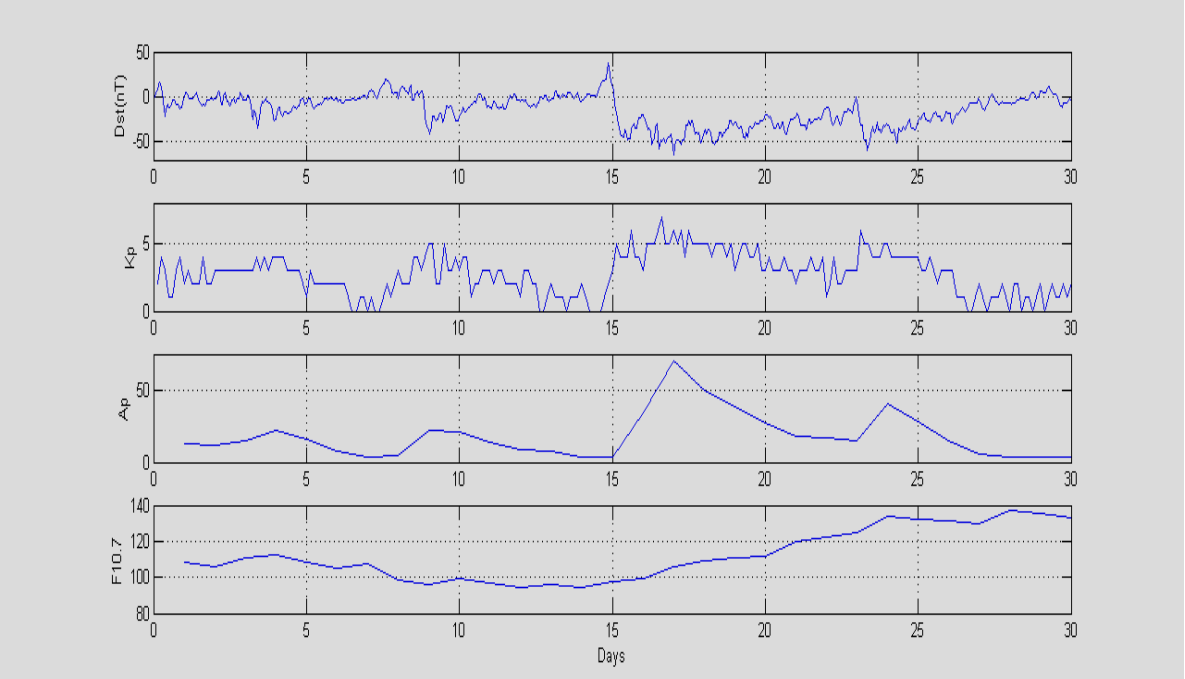

Figure 4. Solar (F10.7) and geomagnetic activity (Dst, Kp and Ap) conditions during the month of September 2003.

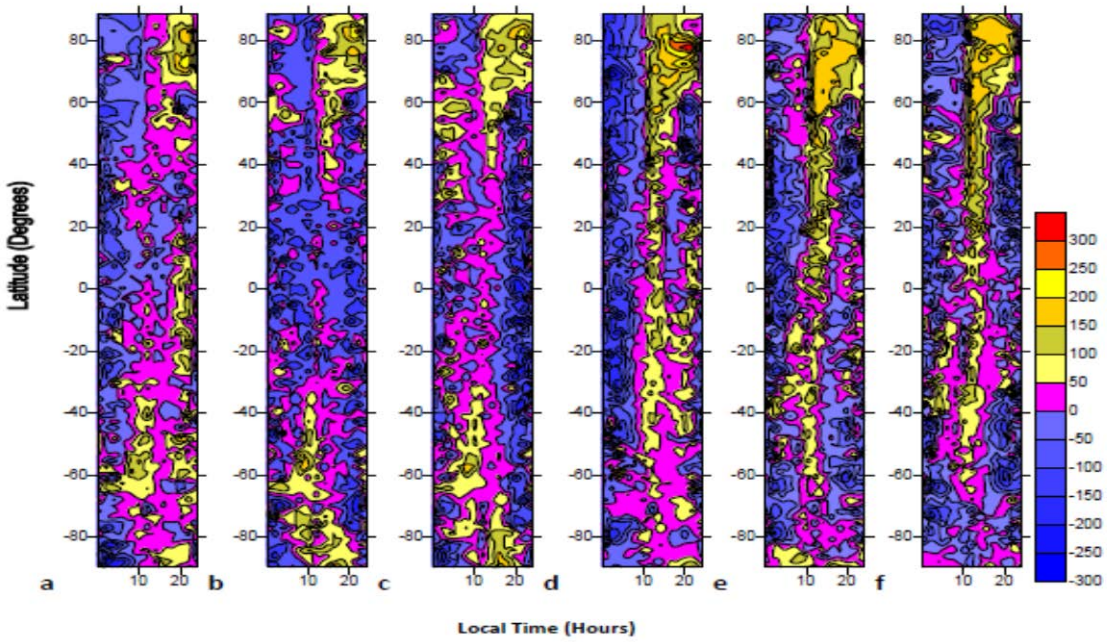

Figure 5. Zonal wind speed distribution at (a) 90 km (b) 100 km (c) 110 km and meridional wind distribution at (d) 90 km (e) 100 km (f) 110 km. The negative westward wind speeds for zonal winds indicate westward winds, while negative wind speeds for meridional winds indicate poleward winds. The colour codes in the bar represent the wind speed in m/s.

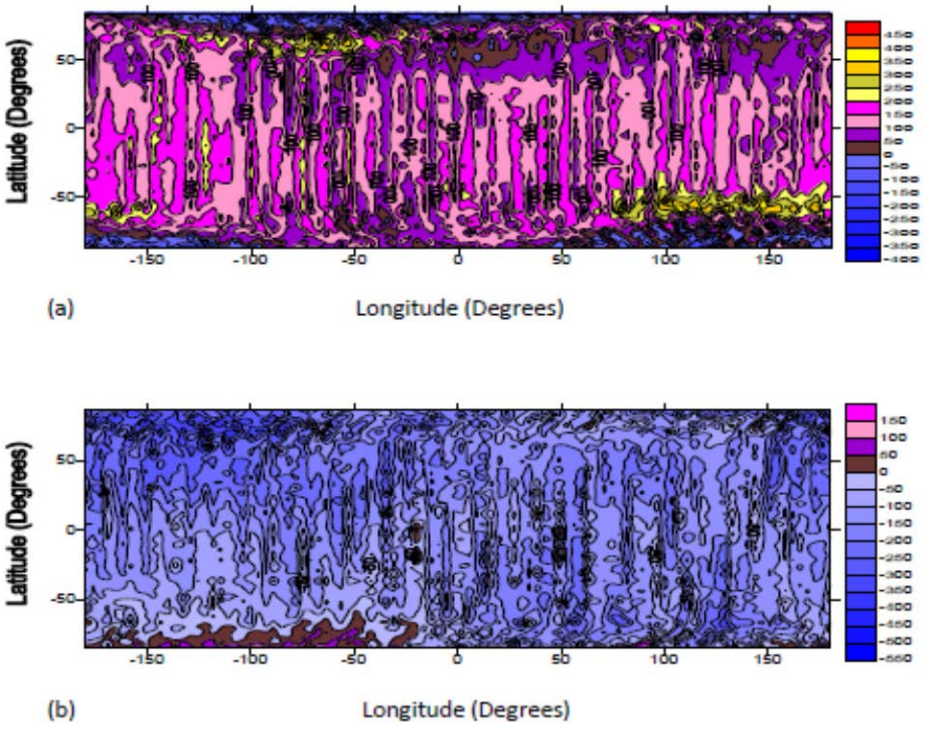

Figure 6. Latitude/longitude distribution of zonal wind speed from CHAMP at two local time sectors. (a) 1500-1900, (b) 0300-0700. The negative westward wind speeds for zonal winds indicate westward winds. The colour codes in the bar represent the wind speed in m/s.

At high latitudes in the northern hemisphere evening winds are eastwards with speeds going above 150 m/s. At 90 km altitude pre-dawn winds are westwards (towards west) with speeds in excess of 200 km experienced in some locations. The CHAMP zonal winds are westward during the morning hours as shown in the local time sector (0300-07000) figure in 6b.

Early morning winds in this local time sector within the longitude band (-50 to -150 degrees) in the southern hemisphere high latitude are eastward (towards east) with speeds less than 50 m/s. Also within this longitude band in the North Pole winds with speeds up to 350 m/s are observed in the west direction. Wind direction in the afternoon to early evening local time sector (1500-1900) is generally westwards.

Under magnetically quiet conditions at mid-latitudes, meridional winds in the lower thermosphere are generally equatorward (towards equator) during daytime and poleward (towards poles) at night (Balan et al., 2004). From the distribution in figure 5 (d) to (f), there is some agreement as the meridional winds presented in the lower thermosphere seem to follow this pattern. The F-region zonal winds in the mid-latitudes are generally westward before local noon and eastward in the afternoon, with a nighttime transition that occurs during the early morning hours in local winter and near midnight in local summer (Roble, 1983). Our winds in the presented sectors agree with this variation. The E-layer and F-layer wind systems are very different, the F-layer winds being generally faster and having less vertical structure than E-layer winds, because of the greater molecular viscosity (Rishbeth, 1997). From our distributions in figures 5 and 6 zonal winds in the upper thermosphere as observed in the two local time sectors are faster than the E-region winds observed by the TIMED satellite.

The lower thermosphere dynamics at quiet times is different from what is observed at the F-region. In addition to the difference with optical depth, the lower thermosphere is strongly influenced by tides, gravity waves and planetary waves from the lower atmosphere. In the F-region circulation is primarily governed by solar EUV heating at low and middle latitudes, at high latitudes it is strongly controlled by ion drifts associated with magnetospheric convection (Roble, 1983). Under very quiet geomagnetic conditions, clear thermospheric and ionospheric signatures of magnetospheric processes are only seen at high geomagnetic latitudes (Rees, 1995).

4. Summary and Conclusion

During magnetically quiet times, meridional wind in the lower thermosphere is generally equatorward during daytime and poleward at night. The zonal winds in the lower thermosphere are generally westward at night. Early morning local time sector upper thermospheric zonal winds are westward, while the late afternoon local time winds are eastwards.

The upper thermosphere winds in the early morning and late afternoon local time sectors are faster than zonal winds in the lower thermosphere. The datasets used may not reveal a good comparison as data is obtained from the two satellites by two different methods. Upper themospheric winds from CHAMP are derived from the accelerometer readings while Lower thermospheric winds are obtained from the TIMED Doppler interferometer. There is need to consider the plasma effect and the field line structure.

Simultaneous measurements need to be carried out at several points in the thermosphere to overcome the uncertainty associated with single satellite measurements.

5. Acknowledgements

The authors are indebted to Professor J.M. Forbes and Dr. E. Sutton of the Department of Aerospace Engineering Sciences, University of Colorado for the CHAMP wind dataset (version 2.0) and to the TIMED team for the TIDI wind dataset.

References

Balan, N., kawamura, S., Nakamura, T., Yamamoto, M., Fukao, S., Igarashi, K., Maruyama, T., Shiokawa, K.,Otsuka, Y.,Ogawa T., Alleyne H., Watanabe, S., and Murayama,Y.(2004), Simultaneous mesosphere/lower thermosphere and thermospheric F-region observations during magnetic storms, *J. Geopys. Res.,* 109(A04308), doi: 10.1029/2003JA009982.

Bruinsma, S.,Tamagnan, D., Biancale, R.(2003); Atmospheric densities derived from CHAMP/STAR accelerometer observations*, Planet. Space sci.*, 52, 297-312.

Forbes, J.M.(2007):Dynamics of the Thermosphere. *J. Meteorol. Soc. of Jpn.* ,85B, 193-213.

Kane,R.P. (2005), Sun-Earth relation: Historical development and present status-A brief review, *Advances in Space research*,35,866-881.

Kazimirovsky,E.S.,Kokourov,V.D.,Vergasova,G.V.(2006),Dynamical climatology of the upper mesosphere, lower thermosphere and ionosphere. *Surveys in Geophysics*, 27, 211-255.

Kazimirovsky,E.S. and Vergasova,G,V.(2009), Mesospheric, lower thermospheric dynamics and external forcing effects: A review, *Indian Journal of Radio and Space Science*,38,7-36.

Killeen, T.L., Wu, Q., Solomon S.C., Ortland, D.A., Skinner, W.R., Niciejewski, N.J., and Gell, D.A.(2006), ''TIMED Doppler Interferometer: Overview and recent results'', *J. Geophys. Res.*, 111, A10S01, doi: 10.1029/2005JA011484.

Killeen, T.L. (2002), 'Timed Doppler Interferometer',
(http://download.hao.ucar.edu/archive/tidi/docs/overview.pdf).

Liu, H., Luhr, H.,Watanabe, S.,Kohler,W.,Henize,V.,and Visser, P.(2006): Zonal Winds in the equatorial Upper Atmosphere: Decomposing the solar flux, geomagnetic activity, and seasonal dependencies, *J. Geophys. Res*., A07307, doi: 10.1029/2005JA011415.

Mikhailov, A.,Depueva, A.H.,Depuev, V.H.(2009),Quiet time F2-layer disturbances: seasonal variations of the occurrence in the daytime sector, *Ann. Geophys*.,27,329-337.

Mikhailov,A. H., Depuev, V.H. and Depuev,A.H.(2007a): Synchronous NmF2 and NmE daytime variations as a key to the mechanism of quiet-time F2-layer disturbances, *Ann. Geophys.*,25,483-493.

Rishbeth,H.(1997), The ionospheric E-layer and F-layer dynamos-a tutorial review, *J. atmos. Sol. Terr. Phys*.,59,1873-1880.

Ritter, p., Luhr, H., and Doornbos, E. (2010),Substorm-related thermospheric density and wind disturbances derived from CHAMP observations, *Ann. Geophys*.,28,1207-1220.

Ritter,P.,Luhr,H.,Maus,S. and Viljanen, A.(2004),High-latitude ionospheric currents during very quiet times: their characteristics and predictability, Ann. Geophys.,22,2001-2014.

Roble, R.G.,(1983), Dynamics of earth's thermosphere, *Rev. Geophys. Space phys.,* Vol. 21, No.2, 217-233.

Sutton,E.K., Nerem,R.S. and Forbes, J.M.(2007), Density and winds in the thermosphere deduced from accelerometer data, *presented as paper 6170 at the AIAA/AAS Astrodynamics specialist conference and Exhibit,Keystone,CO,21-24 August,2006.*

Talaat, E.R., Yee,J.,Christensen A.B., Killeen, T.L.,Russell III,J.M.,and Woods, T.N.(2003),TIMED science: First light: John Hopkins *APL Technical Digest*, Vol.24,No.2.

Division D2 – Space Science

Extracting growth rates from a Particle-In-Cell simulation

Etienne J. Koen[2,3], Andrew B. Collier[4,5], Shimul K. Maharaj[1]

[1]SANSA Space Science, Hermanus, South Africa
[2]Space Advisory Company, Somerset West, South Africa
[3]The Royal Institute of Technology, Stockholm, Sweden
[4]University of KwaZulu-Natal, Durban, South Africa
[5]Exegetic Analytics, Durban, South Africa

E-mail: koenej@gmail.com

Abstract. Using a Particle-In-Cell simulation, the characteristics of electrostatic waves are investigated in a plasma containing 3 electron components (hot, cold and beam electrons) and a cold ion population. Three electrostatic modes are excited, namely electron plasma, electron acoustic and beam driven waves. These modes have a broad frequency spectrum and have been associated with intense broadband electrostatic noise observed in the Earth's auroral zone. The growth rates of the beam mode is studied by constructing a growth rate curve from the electric field data. The beam mode is found to have a high growth rate for an intermediate range of wave numbers while it is damped elsewhere.

1. Introduction

The electron acoustic mode may be present in a plasma containing two electron components of different temperature [1]. An electron beam can drive this mode unstable over a wide range of parameters [2, 3]. The nonlinear properties of the electron acoustic instability for upstream foreshock conditions have been observed in the magnetospheric cusp [4], the upstream bowshock [5, 6], the magnetotail plasma sheet [7], the auroral zone [8] and Saturn's magnetosphere [9]. Free energy sources such as electron beams have also been observed in the polar cap and auroral zone, together with the coexistence of warm and cold plasma populations [10].The electrostatic waves excited in such a system may explain the broadband electrostatic noise observed in this region. In addition to electron acoustic waves, electron plasma waves are also excited by the electron beam [11].

Previously a theoretical study has been made of the electron acoustic mode found containing three electron components [3]. Recently the study has been extended to investigate the nonlinear regime of such a system using a PIC simulation [12]. The system contained warm and cold electron populations with roughly equal densities and a low density electron beam with a large streaming speed compared to the warm and cold electron populations. In such a scenario, the beam mode was found to dominate the wave spectrum being most intense at intermediate wave numbers. Electron plasma waves were found to be weakly damped at low wave numbers while electron acoustic waves were found to be damped over most of the wave number spectrum.

It is quite common to construct a dispersion diagram using the electric field data from a PIC simulation to study the dispersion characteristics of different wave modes. These dispersion

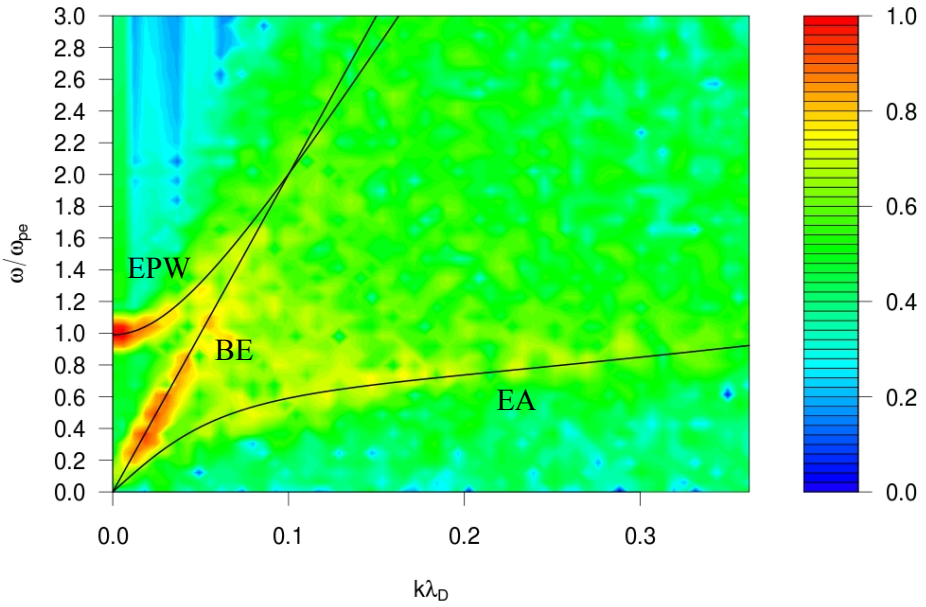

Figure 1. The ω–k diagrams at 1200–1302.4 $\omega_{pe}t$. EPW, EA, and BE curves indicate the theoretical dispersion relations for the electron plasma, electron acoustic, and beam wave modes, respectively

diagrams have been found to successfully reproduce the theoretical curves for different wave modes (Figure 1). The diagram also gives a representation of the damping or growth for the different wave modes. However, these dispersion diagrams, showing the amplitudes for the modes, either gives a snapshot for the whole simulation or a small fixed period within the simulation. Thus, one is limited to only make comparisons of one wave mode's average amplitude to another in most scenarios.

In theoretical studies of plasma waves, a dispersion curve together with a growth rate curve is required to give a complete picture of the wave characteristics. The growth rate curve gives information on the damping or growth of the wave mode whereas the dispersion diagram gives information on the dispersion characteristics. The aim of this work is to extend the analysis of the beam mode previously performed [12] by constructing a growth rate curve from the electric field data.

2. Theoretical Model

An unmagnetised plasma with one ion and three electron components is considered. Ions are treated as massive (therefore motionless) and are only included to form a neutral background. The electron components consist of hot, cold, and beam electrons. The initial velocity distributions of the particles are assumed to be Maxwellian with the beam electrons having a streaming speed v_b. The total unperturbed density is $n_{e0} = n_{c0} + n_{h0} + n_{b0}$ where n_{c0}, n_{h0}, and n_{b0} are the cold, hot, and beam electron equilibrium densities, respectively. The plasma

frequency for component j is

$$\omega_{pj} = \left(\frac{n_j e^2}{m_e \epsilon_0} \right)^{1/2}. \quad (1)$$

Similarly, the Debye length is

$$\lambda_{Dj} = \left(\frac{\epsilon_0 k_B T_j}{n_j e^2} \right)^{1/2}, \quad (2)$$

where T_j is the temperature of component j.

In such a plasma, the dispersion relation takes the form [13]

$$1 + \frac{2}{k^2 \lambda_{Dc}^2} [1 + \zeta_c Z(\zeta_c)] + \frac{2}{k^2 \lambda_{Dh}^2} [1 + \zeta_h Z(\zeta_h)] + \frac{2}{k^2 \lambda_{Db}^2} [1 + \zeta_b Z(\zeta_b)] = 0, \quad (3)$$

where $\zeta_c = \omega / k v_{Tc}$, $\zeta_h = \omega / k v_{Th}$ and $\zeta_b = (\omega - k u_d / k v_{Tb})$ with v_{Tj} being the thermal velocity of component j. $Z(\zeta)$ is the plasma dispersion function [14].

When the streaming speed of the beam electrons becomes sufficiently large and $n_b \ll n_{e0}$, Eq. (3) can be approximated by [15]

$$\omega = \frac{k v_b}{1 + n_b / n_{e0}} \approx k v_b, \quad (4)$$

which is the beam wave mode. This is also the mode of interest for this study of the construction of the growth rate curve.

3. Simulation

A 1D electrostatic PIC simulation was used to solve Maxwell's equations [16]. Particle charge densities, ρ, were projected onto a grid. The fields were updated based on the particle distribution using the discrete form of Poisson's equation.

The particle positions and velocities were then advanced by a small time step using the most recent fields. Periodic boundary conditions were applied. The densities were normalized to the total unperturbed electron density n_{e0}. Velocities were expressed in units of thermal velocity of cold electrons v_{Tc}. The space and time (x and t) were normalized to cold electron Debye length $\lambda_{Dc} = (\epsilon_0 k_B T_c / n_{c0} e^2)^{1/2}$ and to the inverse of the total electron plasma frequency $\omega_{pe} = (n_0 e^2 / m_e \epsilon_0)^{1/2}$. The electric field and potential were normalized to $m_e \omega_{pe} v_{Tc} / e$ and $k_B T_c / e \epsilon_0$.

The combined number of particles employed for the hot and cold electrons was 2×10^6 and the number of beam electrons was allocated by the ratio of beam to cold electrons, n_b / n_c. The simulation uses 1024 grid cells with a grid spacing of λ_D (the total electron Debye length). A fixed time step of $0.01 \omega_{pe}^{-1}$ is used throughout the simulation.

Fig. 1 shows a ω–k (dispersion) diagram, which was obtained by Fourier transforming the electric field E_x in space and time for the quasi-equilibrium stage $\omega_{pe} t$ = 1200–1302.4. The frequencies are normalised to ω_{pe}. The theoretical dispersion relation curves overlaid on the ω–k diagram are based on parameters of the unperturbed plasma. The waves and particles interact through Landau damping, changing the unperturbed parameters of the plasma and waves.

4. Growth rate analysis

The growth rate curve was constructed by analysing unique ω–k areas every time step along the beam mode's dispersion curve. The time window for each dispersion diagram at each time step was $\omega_{pe} t = 50$. When analysing a portion of the dispersion diagram it produces a series of amplitudes with time. From this series of amplitudes an exponential curve is fitted by using

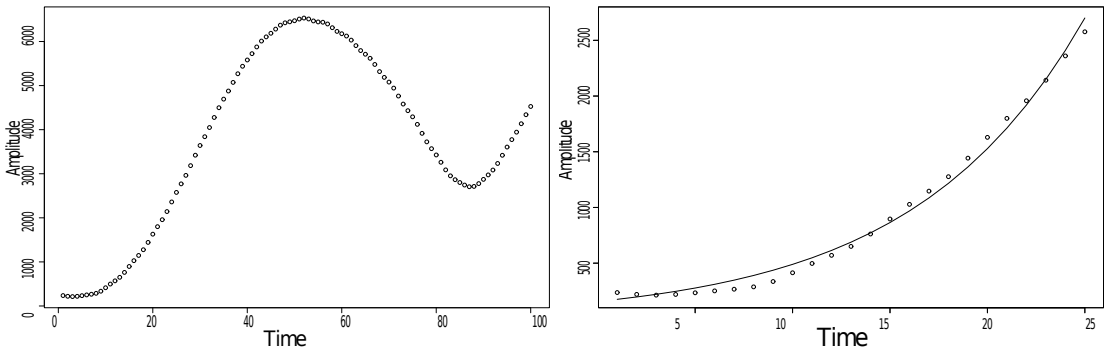

Figure 2. Example of time series of amplitudes extracted for $\omega/\omega_{pe} = 0.4$ and $k\lambda_D = 0.02$ for the whole simulation (Left) and the initial part of the same simulation with an exponential function fitted to the data (Right).

the nonlinear least squares method (Figure 2). The exponential curve has the form $y = Ae^{\gamma t}$ where γ refers to the growth rate parameter in the complex wave function $\omega = \omega_r + i\gamma$. Here γ corresponds to the growth rate of the wave mode.

Figure 3 shows the growth rate curve for a range of wave numbers for the beam mode. The range of wave numbers extends from $k\lambda_D = 0.006$–0.072. This range was chosen to exclude the coupling effects of the electron acoustic mode with the beam mode. Figure 3 shows that there is a region, $k\lambda_D = 0.018$–0.048 for which the beam mode will be weakly damped. At greater and smaller wave numbers the beam mode will be damped.

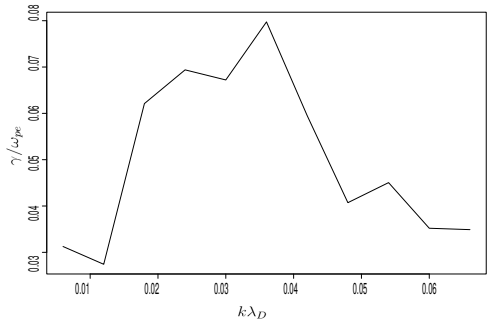

Figure 3. Growth rate diagram constructed from coefficients of exponential curves fitted to a series of amplitudes for different wave numbers.

Summary and conclusions

PIC simulations is a simulation tool based on kinetic theory which enables one to study wave dispersion by constructing a dispersion diagram from the electric field data. These diagrams give information of the dispersion characteristics of the wave modes at a specific time for a time window. By using a fixed time window and advancing the time of analysis, a growth rate diagram can be constructed that gives the growth rates of a given wave mode at different wave number intervals. The growth rate diagram together with the dispersion diagram now gives a more complete picture of both the dispersion and growth characteristics of the wave modes.

The beam mode in a plasma containing hot, cold and beam electrons was investigated. It was found that the beam mode has a strong growth rate in the region of $k\lambda_D = 0.006$–0.072 while the mode is damped at smaller and larger wave numbers.

References

[1] Watanabe K and Taniuti T 1977 *Journal of the Physical Society of Japan* **43** 1819–1820
[2] Tokar R L and Gary S P 1984 *Geophysical Research Letters* **11** 1180
[3] Gary P S and Tokar L R 1985 *Physics of Fluids* **28** 2439
[4] Roth I and Hudson M K 1986 *Journal of Geophysical Research* **91** 8001
[5] Thomsen M F, Barr H C, Gary S P, Feldman W C and Cole T 1983 *Journal of Geophysical Research* **88** 3035
[6] Mace R L and Hellberg M A 1993 *Journal of Geophysical Research* **98** 5881
[7] Ashour-Abdalla M and Okuda H 1986 *Journal of Geophysical Research* **13** 366
[8] Sotnikov V I, Schriver D and Ashour-Abdalla M 1995 *Journal of Geophysical Research* **100** 765
[9] Koen E J, Collier A B and Maharaj S K 2012 *Physics of Plasmas* **042102**
[10] Winningham J D, Yasuhara F, Akasofu S I and Heikkila W J 1975 *Journal of Geophysical Research* **80** 3148
[11] Matsukiyo S, A T R and Scholer M 2004 *Journal of Geophysical Research* **109** A06212 ISSN 0148-0227
[12] Koen E J, Collier A B and Maharaj S K 2012 *Physics of Plasmas* **042101**
[13] Schriver D, Ashour-Abdalla M, Sotnikov V, Hellinger P, Fiala V, Bingham R and Mangeney A 2000 *Journal of Geophysical Research* **105** 12919–12927
[14] Stix T 1992 *Waves in Plasmas* (American Institute of Physics) ISBN 9780883188590
[15] Treumann R and Baumjohann W 1997 *Advanced Space Plasma Physics* (Imperial College Press) ISBN 9781860940262
[16] Birdsall C K and Langdon A B 2004 *Plasma Simulation via Computer Simulation* Series in Plasma Physics (Taylor & Francis Group)

Effects of slant angle and illumination angle on MTF estimations

L M Vhengani, D Griffith and M Lysko

Council for Scientific and Industrial Research, Defence Peace Safety and Security, Pretoria, South Africa

E-mail: Lvhengani@csir.co.za

Abstract. Modulation Transfer Function (MTF) is a measure of the spatial resolution of an optical imaging system. For Earth Observation (EO) imaging systems in space, continuous MTF assessment is crucial for data quality. Several techniques of measuring MTF exist and some are still in development. MTF assessment techniques include the use of slanted knife-edge targets, point source techniques that make use of convex mirrors or xenon lamps and pulse methods that use linear features such as bridges. All these techniques have been successfully used to assess the MTF of imaging systems aboard the Ikonos, Landsat and QuickBird satellites. Laboratory experiments were conducted to evaluate the effect of slant angle of the knife-edge target and the effect of light illumination angle on the MTF result. MTF results were computed using a standard method according to ISO 12233. This paper will report the results of these laboratory experiments.

1. Introduction

The image quality of earth observation satellites strongly depends on the Modulation Transfer Function (MTF) of the system. Practically, MTF is a metric quantifying the sharpness of the reconstructed image. By definition, MTF is the normalized magnitude of the Fourier Transform of the system Point Spread Function (PSF) [1] as shown in Equation (1). PSF is the system response to a point source. In order to comply with the (ISO) standard, MTF is measured at Nyquist frequency [3]. Nyquist frequency is half of the sampling rate of a signal.

$$MTF = \left|\mathcal{F}\{PSF(x,y)\}\right| \tag{1}$$

The development process of a satellite system incorporates testing and calibration before the satellite is launched into space. The Modulation Transfer Function (MTF) of an imaging system of a satellite is one of the characteristics that are assessed before the satellite is launched into orbit. However, the vigorous nature of launch and the effects of space such as high radiation and extreme temperatures may alter the characteristics of the imaging system including MTF. Hence the MTF of an imaging system must be continuously characterized on-orbit [2].

Multiple methods have been used to determine the MTF of earth observation satellite imagers. These include the use of knife-edge (shown in Figure 1 and Figure 2) [3], pulse (lines) and point source (spot lights and convex mirrors) targets [4]. The use of knife-edge targets is one the most commonly used methods [5]. When using the knife-edge approach, the first step is to determine the required geometry (size and orientation) of the knife-edge target. This is highly dependent on the

spatial resolution and orbit of the satellite. The second step is to image the target on a clear day free of clouds. The third step is image processing.

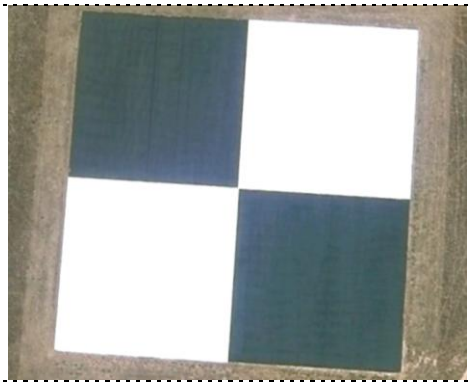

Figure 1. A knife-edge target for measuring the MTF of satellite imaging systems.

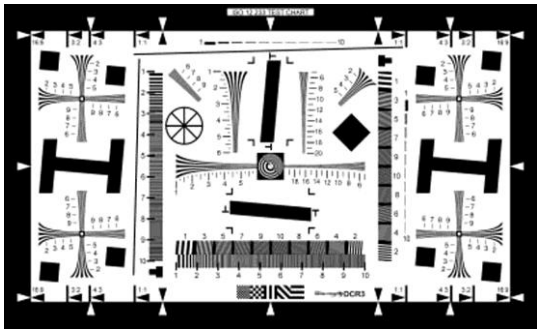

Figure 2. ISO 12233 chart for measuring the MTF of imaging systems.

Image processing steps involve detecting the edge in order to compute the Edge Spread Function (ESF). The ESF is the system response to a high contrast edge. The first derivative of the ESF generates the Line Spread Function (LSF), which is the system response to a high contrast line as shown in Figure 3. Quantitatively, the LSF is the 2-dimensional PSF integrated over one dimension and thereby reduced to a function of a single dimension [5]. The normalized magnitude of the Fourier Transform of the LSF produces the MTF of the imaging system.

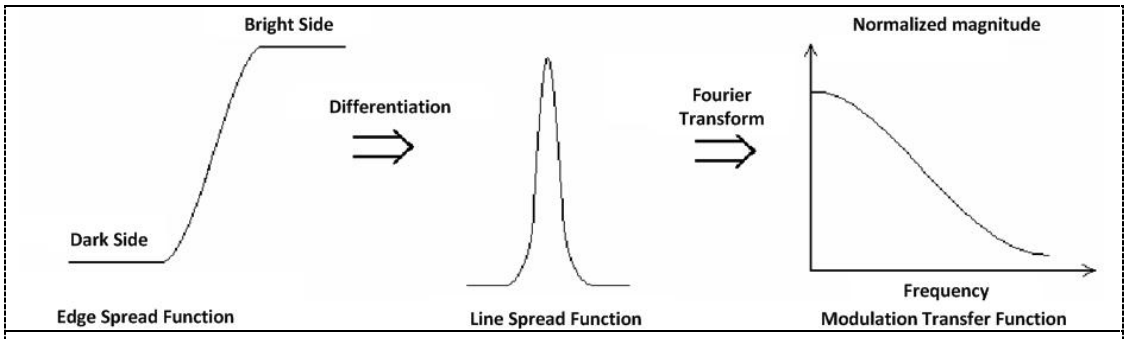

Figure 3. Computation of the Modulation Transfer Function using the knife-edge target.

2. Methodology

The objective of this study is to assess the effects of edge slant angle and illumination angle on the estimated MTF. To achieve this objective, two laboratory experiments were set up and these are explained in detail in the following subsections.

2.1. Effects of slant angle

A knife-edge test target was used to test the effects of varying edge slant angle on the estimated MTF. The laboratory arrangement of the knife-edge and camera is shown in Figure 4. The standard laboratory (fixed) fluorescent lamps were used as light sources. Images of the knife-edge target were captured while varying the inclination angle of the knife-edge target by rotating the target about an axis perpendicular to the target surface. Results of this experiment are shown in Figure 6 and Figure 7.

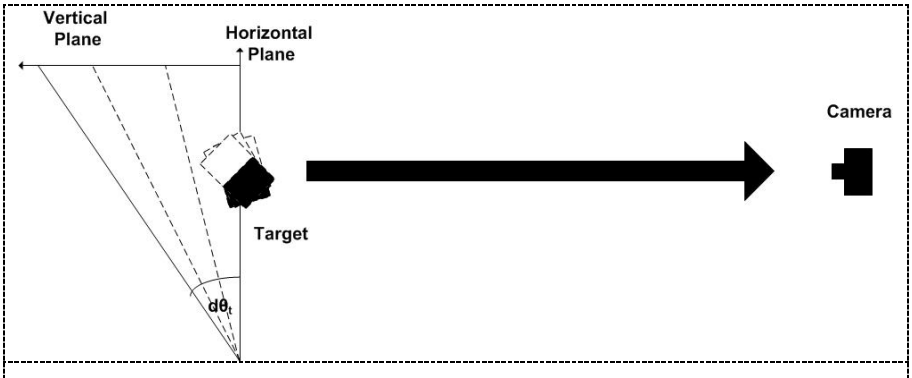

Figure 4. Setup for the experiment for evaluating the effect of varying the slant angle of the knife-edge target on estimated MTF.

The challenge of this experiment was that the operator manually changed the inclination angle. This may not introduce an uncertainty, but the change in slant angle d(θ) was not constant. It was also noted that the iris of the imaging system was in most cases adjusted during initial setup of each measurement. After each measurement, the knife-edge target was replaced with the ISO 12233 MTF target (shown in Figure 2) and its image was captured using the same camera and same laboratory settings.

2.2. Effects of illumination angle

In this setup, instead of fixed fluorescent lamps, a moveable lamp was used as a light source. Images of the fixed inclined knife-edge target were captured while varying the illumination angle of the light source. Figure 5 below, gives an illustration of the arrangement of the slanted knife-edge target, lamp and the camera. The results of this experiment are shown in Figure 7.

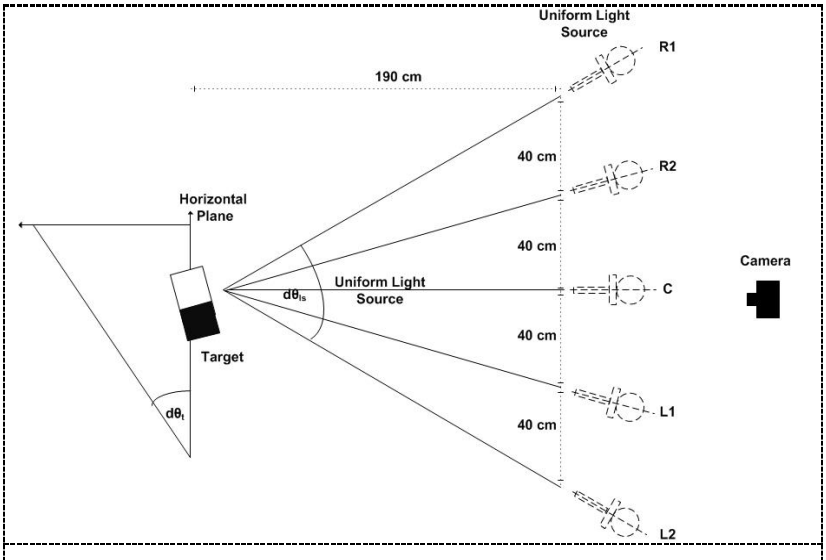

Figure 5. Setup for the experiment for evaluating the effects illumination angle on estimated MTF

The challenge for this laboratory set-up was the limitation of space, which limited the extent to which the illumination angle could be varied. The lamp was also moved manually and this might introduce an uncertainty since the pointing direction towards the target will be different each time the

lamp is moved. Nonetheless, the distance between the light source and the target was considered small and therefore the effects of pointing were assumed negligible.

3. Results and discussions

This section gives a summary discussion of results. Plots shown in Figure 3 and Figure 4 below illustrate the relationship between the inclination angle the resulting MTF at Nyquist frequency. These plots illustrate that there is relationship between the inclination angle of the knife-edge target and the resulting MTF estimate at Nyquist frequency.

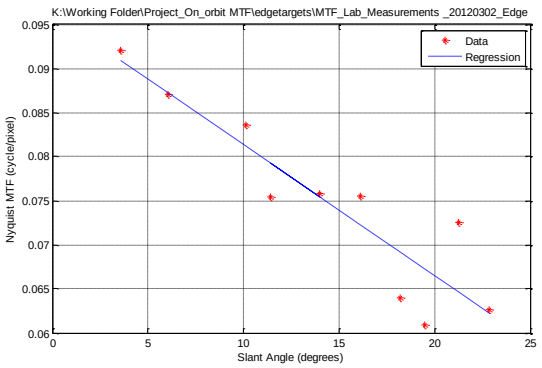

Figure 6. Regression of positive slant angle and MTF at Nyquist Frequency.

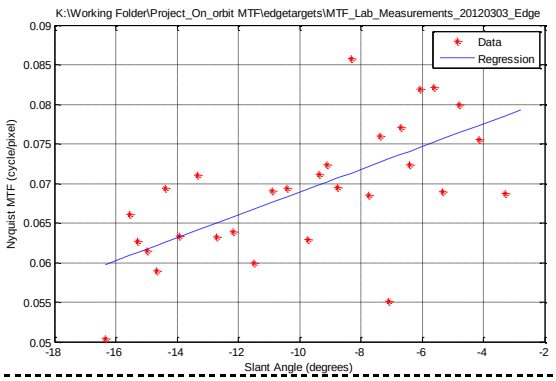

Figure 7. Regression of negative slant angle and MTF at Nyquist Frequency.

The relationship between the edge slant angle and MTF estimate was assumed linear and the derived regression equations from the plots in Figure 6 and Figure 7 are shown in equation(2) and equation(3) respectively. The reason for different regression equations could be attributed to different settings of the imaging system's iris. These plots show that as the slant angle moves away from perfect alignment with the pixel array, the estimated MTF at Nyquist frequency is reduced. Table 1 shows the MTF results of the ISO target that were used to verify the regression equations. The predicted Nyquist MTF values are within 5 % of the Nyquist MTF results yielded using ISO targets as shown in Table 1.

$$y = -0.0015x + 0.0962 \tag{2}$$

$$y = 0.0014x + 0.0833 \tag{3}$$

Table 1. ISO target Nyquist Frequency MTF.

Regression Equation	Correlation Coefficient	ISO Image Angle	ISO Image MTF at Nyquist Frequency	Predicted MTF at Nyquist Frequency	Percentage Error (%)
2	-0.914	-5.6625	0.0885	0.0878	0.7956
3	0.668	-4.8562	0.0794	0.0763	3.982

The plot shown in Figure 8 below displays the average Nyquist frequency MTF corresponding to different illumination angles. As illustrated in Figure 5, 'C' is the illumination at nadir (centre), 'L2' and 'R1' represent the illumination from the extremes (Left and Right) of the target. These results indicate that the estimated MTF at Nyquist frequency is highest when the illumination direction is orthogonal to the target and decreases as the light source is moved away from orthogonality.

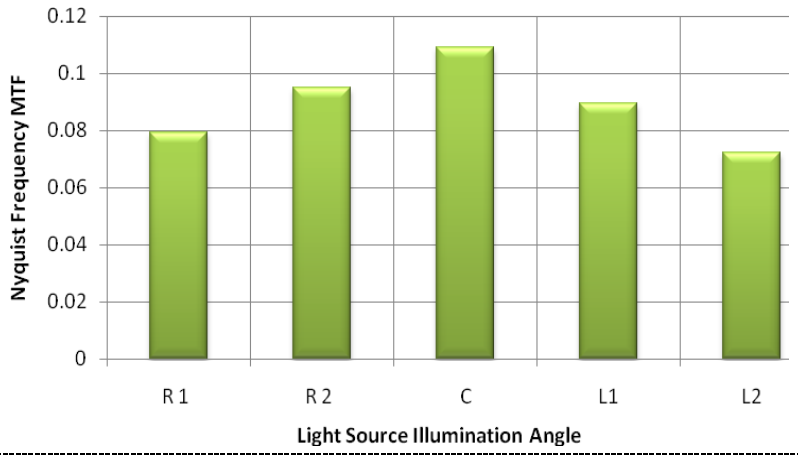

Figure 8. Light Source Angle and Average MTF at Nyquist Frequency.

Results obtained in both experiments are important for the study of system MTF. These results indicate that the estimated MTF of the same imaging system will be different when measured under different conditions.

4. Conclusions and recommendations

After analyzing the data, it was observed that lower absolute edge slant angles relative to the satellite cross-track direction tend to increase the estimate of the MTF at Nyquist and higher angles tend to decrease the estimate of the MTF at Nyquist. It was also observed that the MTF at Nyquist frequency is high (maximum) when the illumination angle is orthogonal. This means that the MTF at Nyquist frequency decreases as the angle of illumination diverges from orthogonality.

With reference to these observations it can be concluded that the angle of inclination and the illumination angle may add an uncertainty to the estimated MTF. The uncertainty was not quantified. However, the derived regression equations demonstrate this argument.

The recommendations are that the uncertainty due to the light source illumination angle imply that on-orbit MTF estimations must be done at consistent acquisition solar and sensor geometry and that any estimated MTF must be accompanied with information on the sun illumination angle and the inclination angle of the knife-edge target with respect system's sample grid.

The underlying mechanism resulting in these variations in the MTF estimate should also be investigated. Another effect worthy of investigation is the variation in the MTF estimate caused by edge targets that deviate from straightness.

References

[1] Choi T 2002 IKONOS Satellite on-orbit Modulation Transfer Function (MTF) measurements using edge and pulse method.

[2] Vhengani L M, Griffith D and Lysko M 2010 Campaign for vicarious calibration of SumbandilaSat in Argentina, in Proceedings of SAIP2011, the 56th Annual Conference of the South African Institute of Physics, edited by Basson I and Botha A E (University of South Africa, Pretoria, 2011), pp. 555-560. ISBN: 978-1-86888-688-3. Available online at http:\\www.saip.org.za

[3] ISO 12233:2000 Photography - Electronic still-picture cameras – Resolution measurements', International Organisation for Standardization

[4] Rangaswamy M K 2003 Two-dimensional on-orbit Modulation Transfer Function analysis using convex mirror array.

[5] Li X; Jiang X; Zhou C; Gao C and Xi X 2010 An analysis of the knife-edge method for on-orbit MTF estimation of optical sensors, International Journal of Remote Sensing **31**, 4995-5010

Division E – Physics Education

Active Learning in Thermal and Statistical Physics at the University of the Witwatersrand

Jonathan M. Keartland

School of Physics, University of the Witwatersrand, WITS 2050, South Africa

E-mail: jonathan.keartland@wits.ac.za

Abstract. Active learning techniques have been employed in the 2nd and 3rd year Thermal and Statistical Physics modules since 2009. The introduction of these methods has resulted in increased student participation during lectures, and improved student performance in both modules. This paper reports on an ongoing evaluation of active learning initiatives in these two modules, and compares and contrasts student performance in, and attitudes to, modules at 2nd and 3rd year level that are not presented using active learning. The study suggests that active learning has the potential to improve student performance and understanding in higher level courses, and that this approach may benefit experienced physics instructors in teaching concepts that are traditionally regarded as difficult by students.

1. Introduction

Active learning (AL) strategies have the potential to improve student learning, and hence their performance in assignments, tests and examinations in all spheres of education. They include active engagement, collaborative learning, and problem-based learning, as well as the provision of regular feedback to the student cohort. Prince [1] has produced an illuminating review of the research on the efficacy of using AL techniques in university teaching. While his conclusions are largely positive, he cautions that empirical evidence for improvement may be less clear-cut than might be hoped and expected. Felder [2] points out that recent cognitive research provides more convincing evidence that these strategies improve student learning. For example, the book by Ambrose *et al* [3] deals extensively with the processes by which students learn, and the seven strategies they propose for effective or smart learning provide strong support for the implementation of AL.

While the primary focus of research on the use of AL in physics classrooms has been on first year or freshman courses [4], they have been employed in intermediate and upper-level courses [5]. AL strategies in higher level Thermal and Statistical Physics courses has been the subject of recent studies by Loverude [6, 7] and Christensen *et al* [8], where the focus has been on developing and evaluating specific AL materials. Lopez and Gross [9] have applied AL in a graduate Space Weather Modeling summer school, while Wiljhelm *et al* [10] have used AL in teaching the Physics of Medical Imaging.

AL techniques have been employed in the School of Physics at the University of the Witwatersrand (WITS) in the 2nd and 3rd Year Thermal and Statistical Physics modules since 2009. A recent report [11] on the effect of introducing these into the 3rd Year Statistical Physics module has suggested that students have embraced the deployment of these techniques, and that an improvement in student performance has resulted from applying these strategies. This paper reports on several student evaluations of lecturer performance (SELP) surveys, an analysis of student performance over a

number of years in the 3rd Year module, and a comparison of student performance in the four components of the Physics II course during 2011. It is concluded that AL has had a positive impact on student attitude and performance, and that AL should be considered by experienced and successful physics lecturers who teach intermediate and advanced level courses. For those that may be interested in trying out these techniques, Felder and Brent [12] provide an engaging and informative short paper on the benefits and potential pitfalls of introducing AL in their lectures.

2. The 2nd and 3rd Year Physics Courses at WITS

2.1. Physics II

The Physics II course is divided into two modules. Both modules have a laboratory component. The PHYS2001 module (taught in the first semester) has two theory components – Classical Mechanics and Modern Physics. PHYS2002 (offered in the second semester) also has two theory components – Electrodynamics and Thermal Physics. Each theory component is presented by a different instructor.

2.2. Physics III

The Physics III course is divided into five modules, one of which is the laboratory module and includes a major project. The other four (theory and lecture-based) modules focus on Quantum Mechanics (PHYS3000), Applications of Quantum Mechanics (PHYS3001), Statistical Physics (PHYS3002) and Waves and Modern Optics (PHYS3003). Each theory module is presented by a different instructor.

3. Details of Active Learning Strategies Employed in Thermal and Statistical Physics

Details of the AL techniques employed during the lectures have been given in a previous paper [11], and it is not necessary to present these in detail here. To recap briefly, these are Lecture Activities and Co-operative Learning, Minute Papers and Responses, Conceptual Questions and Active Tutorials. In addition to these strategies students are provided with regular set assignments which contribute to their final mark, and one test and one examination form the bulk of the final mark for the module. It is important to note that students were explicitly told that AL techniques were being employed, and that their use was based on substantive and convincing education research.

4. SELP Surveys

Regular SELP surveys have been administered in the Statistical Physics module of Physics III. The multiple response evaluation employed is the standard Strongly Agree (10), Agree (7.5), Neutral (5), and Disagree (2.5), Strongly Disagree (0) scoring method. In order to make sense of the data provided in Table 1, it is necessary to provide some background to the manner in which the course was taught in the three years surveyed. In 2005 the course was taught using the traditional ‘chalk-and-talk’ method, as opposed to the more modern trend of using a computer-generated presentation and data projector. This was the first time the author had taught the course, but student reaction was largely positive. AL was introduced in 2009, and the two surveys from 2009 and 2012 show a marked improvement in several key factors. It is interesting to note that efforts to engage the students in discussion (‘Lecturer encourages audience participation’) were recognized by the student cohort of 2005. While the 2012 class appear, as a collective, to be less comfortable about participating in class discussions, the lower score appears to have been the result of two students who felt strongly on the matter. The 2012 class were the first group surveyed who had also been taught using AL in their 2nd Year. Comments received in the open-ended questions in both the 2009 and 2012 surveys indicated that the students have collectively and individually given their approval to AL. Examples from the 2009 survey include the following:

- The minute papers are a very nice addition. It is really nice to have a lecturer that clearly puts so much effort in. Thanks.

- I found the activities really good; you learn while you do them and can't go lazy on your attention. They made lectures more enjoyable. I also looked forward to the tut sessions, and the minute paper responses are appreciated.

Similar comments came from the 2012 survey, some of which suggested possible improvements to the course:

- The minute papers and lecture activities have been pivotal to my understanding of the course material. Going through the tutorials myself has always added value to my understanding. Minute papers help clarify points which were unclear in the previous lecture.
- Assign a roster for the active tutorials rather than asking for volunteers as it can be intimidating when you call for volunteers and no-one is willing to stick their neck out.
- The most valuable part of the course is the lecture activities, because they give us the chance to apply the concepts immediately. I think this helps us retain the information presented longer.

Table 1. A comparison of three Student Assessment of Lecturer Performance surveys undertaken over the period during which the Statistical Physics III module has been lectured by the author. Active Learning was introduced during 2009.

Assertion	Score		
	2005	2009	2012
Lecturer makes the purpose of the lecture clear	9.32	9.29	8.75
Lecturer stimulates interest in the subject	8.86	9.11	9.38
Lecturer is always well-prepared for class	9.09	10.00	9.84
Lecturer is available for consultation	8.18	9.29	9.06
Lecturer encourages audience participation	10.00	9.29	9.69
Lecturer communicates effectively	9.09	8.93	9.38
Lecturer chooses and organizes material well	7.95	8.93	9.53
Lecturer pitches lectures at an appropriate level	9.32	9.11	8.92
I gained a good understanding of concepts and principles	7.73	8.58	8.14
I was motivated to do extra work	7.50	8.04	8.30
I feel comfortable about participating actively in class	8.18	8.58	7.84
The lecturer welcomes independent thinking	8.86	8.93	9.06
The lecturer is approachable for individual questions	9.09	9.65	9.08
The lecturer has enthusiasm for the subject	8.64	9.83	9.69
Instructions and assessment criteria are clear and specific	8.41	9.29	9.06
Lecturer makes digressions which add interest	7.27	9.47	8.28
Lecturer links the lecture to other parts of the course	9.32	9.47	9.06
Lecturer summarizes the main points effectively	9.09	8.93	9.69
Lecturer gets feedback on student understanding	8.86	9.65	9.69
Lecturer's grasp of my level of knowledge is realistic	8.41	8.40	8.28
Lecturer is clear and understandable in his explanations	8.41	9.11	9.06
Lecturer shows thorough knowledge of his subject	8.64	9.47	10.00
Average Score	8.65	9.15	9.08

The 2012 survey included an additional section designed to probe student reaction to specific AL strategies, impressions of the assessment of the assignments, and student use of the on-line resources

provided on the course website that was developed and introduced in 2012. The results of this section of the survey are presented in Table 2. While student reaction to the minute papers and lecture activities are overwhelmingly positive, the active tutorials are less popular (as may be expected from the small selection of student responses noted above). Use of the course website and the on-line textbook [13] was disappointing, but the students obviously regard the website as a vital component of their learning experience. It should be noted that the on-line textbook has been used as the primary reference text by the students since 2005, and that the two courses are structured with this textbook in mind.

Table 2. The results of a student survey administered in March 2012 designed to probe student attitudes to specific active learning initiatives, and to gauge use of the course website, and the on-line textbook used for the course. The results of the survey are discussed in the text.

Assertion	Score
Assignments were marked fairly and returned promptly	9.84
Minute Papers are a valuable part of the course	9.53
I use the Minute Papers to highlight difficult material	9.06
Lecture Activities are a valuable part of the course	10.00
Lecture Activities help to develop problem solving skills	9.38
I like the Active Tutorial sessions	7.50
I use the course website regularly	7.20
The course website is a valuable resource	8.77
I have used the on-line textbook of the course website	5.03
The on-line textbook is relevant to the course	6.89

5. Comparison of Student Performance – with and without Active Learning

As Prince [1] has pointed out, a full endorsement of AL requires empirical evidence that student performance has significantly improved as a result of their implementation. In this section an analysis of student performance in courses taught with and without AL is presented.

Table 3. Performance of the students in 3rd Year Statistical Physics over a period of eight years. The same lecturer has taught the module in each of these years. Active learning was introduced in 2009, and student performance has significantly improved from 2009 onwards.

Year	Exam Average (%)	Final Average (%)	Pass Rate (%)
2005	60	62	71
2006	58	62	94
2007	56	59	71
2008	64	65	93
2009	76	75	100
2010	73	74	100
2011	74	75	84
2012	79	81	94

Student performance in the Statistical Physics module over a period of eight years is summarized in Table 3. In the years 2005-2008 the course did not include AL methods. The data presented show a dramatic increase in both the exam performance, and in the final mark for the module. These results are statistically significant, and provide concrete evidence that AL improves both continual assessment, and retention of the course material under exam conditions. While it may be argued that improved performance may be the result of the instructor becoming more competent, this is countered by the excellent results of the 2005 SELP. An identical analysis of the 2nd Year Thermal Physics results over a shorter period shows a similar dramatic improvement in student performance when the course component was presented using AL.

Table 4. A comparison of the general student performance in Physics II by course component during 2011. It is clear that Thermal Physics is the only component in which student performance in the Exam and in other activities is comparable. While the connection between active learning and student performance is clear, there are other factors involved. These are discussed in the text.

	Component A		Component B		Component C		Thermal Physics	
	Exam	Class Record	Exam	Class Record	Exam	Class Record	Exam	Class Record
Average (%)	40	65	39	58	41	75	68	73
Pass Rate (%)	34	75	28	50	36	88	84	89

A comparison of student performance in 2nd Year Physics during 2011 over the four components is presented in Table 4. Before proceeding with an analysis of the data presented it is important to take cognizance of the following observations. Components A and C are more demanding of the students' mathematical skills, and student performance in these topics has traditionally been poorer than that in Thermal Physics, which may be considered as less demanding. The class record performance in Component C is excellent, and this is probably due to the progressive continuous assessment policy of the lecturer concerned. In addition, Components A and B are examined during the same exam, as are Component C and Thermal Physics. Students therefore have the option of spending more time on "easy" material during the exam. It is clear, even when taking these considerations into account, that the exam and class record performance is comparable in the Thermal Physics component, while exam performance is significantly lower in the other three components. This is strong evidence that students are retaining the material presented in the Thermal Physics lectures more effectively than they do in the other components, and is arguably further empirical evidence that the implementation of AL raises student marks in a statistically significant manner. A similar comparison of student performance in the modules of the 3rd Year Physics course shows that the Statistical Physics module has, on average, a better correlation between exam and class record performance, and that the students consistently perform better in this module than they do in the other three theory-based modules.

Finally, the analysis of individual results for students over all years and for both modules provides some additional relevant insights. The most capable students over the years have consistently obtained marks in excess of 90 %, with the best mark usually being in excess of 95 %. It would appear that these students have the ability and motivation to perform exceptionally whatever strategies the lecturer employs. It is the students in the mid-range who appear to benefit most from AL, and it is these students that boost the overall class performance. It is perhaps obvious, but nevertheless worth noting that the small number of students who fail the course after the introduction of AL are students who do not attend the lectures.

6. Conclusions

Active learning (AL) techniques are now well-established in the 2nd and 3rd Year Thermal and Statistical Physics modules presented at WITS. It has been shown that these techniques have been

accepted with noticeable enthusiasm by the students taking these courses, and that student surveys show that the students have recognized that the techniques have improved the lecture room experience. It is interesting that the student response in open-ended responses echo the opinion of those involved in educational research as to why these techniques result in effective learning.

A comparison of student performance in the Statistical Physics module, over a number of years, provides statistically significant evidence that AL improves student performance in this particular module. It would appear that all students benefit from AL, particularly students in the mid-range of performance, while it is clear that those who do not attend lectures are invariably those that prove to be at risk of failing the modules.

A comparison of student performance in the different course components across the 2nd Year of study in 2011 provides compelling evidence that students retain the presented material more effectively when AL methods are used extensively, although it is recognized that other factors certainly play a role in student performance.

This study suggests that experienced physics instructors who are responsible for intermediate and advanced level courses should consider employing AL techniques in their lectures. In addition to the obvious benefit of providing students with an improved service, the employment of AL (particularly the use of minute papers) allows the instructor to reflect immediately on whether important points are recognized by the students, and what material the students are having difficulty comprehending.

Acknowledgements
The author wishes to thank Richard M. Felder for his inspiration, encouragement, and helpful discussions in implementing the active learning teaching strategies described in this paper.

References

[1] Prince M 2004 *Jounal of Engineering Education* **1** 223-231
[2] Felder R M 2011 *private communication*
[3] Ambrose S A, Bridges M W, DiPietro M, Lovett M C and Norman M K 2010 *How learning works: Seven research-based principles for smart teaching* (Jossey-Bass, San Francisco)
[4] Thacker B A 2003 *Rep. Prog. Phys* **66** 1833-1864
[5] Meltzer D E and Thornton R K 2012 *Am. J. Phys.* **80** 478-496
[6] Loverude M E 2009 *AIPConf. Proc.* **1179** 189-192
[7] Loverude M E 2010 *AIPConf. Proc.* **1289** 213-216
[8] Christensen W M, Meltzer D E and Ogilvie C E 2009 *Am. J. Phys.* **77** 907-917
[9] Lopez R E and Gross N A 2008 *Advances in Space Research* **42** 1864-1868
[10] Wiljhelm J E, Pihl M J, Lonsdale M N and Jensen M 2008 *Medical Engineering and Physics* **30** 607-614
[11] Keartland J M 2011 *Proceedings of SAIP2011*, the 56th Annual Conference of the South African Institute of Physics ed Basson I and Botha A (University of South Africa, Pretoria) pp 585-590 ISBN 978-1-86888-688-3
[12] Felder R M and Brent R 2009 *ASQ Higher Education Brief* **2(4)** available online at http://www4.ncsu.edu/unity/lockers/users/f/felder/public/Papers/ALpaper%28ASQ%29.pdf
[13] Gould H and Tobochnik J 2010 *Statistical and Thermal Physics* available online at http://stp.clarku.edu/notes/

Physics III Laboratory Module at the University of the Witwatersrand

Jonathan M. Keartland

School of Physics, University of the Witwatersrand, WITS 2050, South Africa

E-mail: jonathan.keartland@wits.ac.za

Abstract. One of the problems facing experimental physicists at the University of the Witwatersrand is the small number of home-grown graduate students opting for experimental physics projects when deciding to pursue higher degrees in the School of Physics. It has been suggested that the reason for this may lie in the structure and curriculum of the undergraduate laboratory courses. The curriculum for the Physics III Laboratory module at the University of the Witwatersrand is well-established, and has followed a particular format for approximately a decade. A new module co-ordinator was appointed at the beginning of 2011, and it was decided to review the curriculum, and actively make changes if this was required. Accordingly, a comprehensive student survey was presented to the student cohort towards the end of 2011. The results of the survey highlighted several issues which have the potential to make experimental physics unattractive. During 2012 several changes were made to the course in response to the survey, and their efficacy is at present being monitored carefully. Results of a follow-up survey and details of the measures taken to address some of the student concerns will be presented.

1. Introduction

The experimental component of an undergraduate Physics Major curriculum should ideally introduce the student to Experimental Physics as an integral part of the subject, and students should be made aware of the vital role that Experimental Physics plays in the development of the discipline. During the last ten years it has become increasingly clear that the Physics Major curriculum may not be achieving one of its secondary goals – that of providing the School of Physics at the University of the Witwatersrand (WITS) with a cohort of enthusiastic and motivated graduate students opting for experimental projects. The reasons for this are not immediately clear, and the matter has been discussed informally in various forums. It has been suggested that students are "turned off" Experimental Physics by the present curriculum, and this paper reports on the first steps in an ongoing critical assessment of the present state of the curriculum.

The development of curricula for high school and first year experimental physics courses has received a great deal of attention from specialists in Physics Education. A review of the literature shows, however, that reports examining senior laboratory courses [1, 2], or the development of a coherent laboratory curriculum for a Physics Major stream, are rare.

The 3rd Year Physics course at WITS is made up of five modules. They are Quantum Mechanics III (PHYS3000), Applications of Quantum, Mechanics III (PHYS3001), Statistical Physics (PHYS3002), Waves and Modern Optics III (PHYS3003), and Advanced Experimental Physics and Project III (PHYS3006). In terms of calculating the final mark for the course, the laboratory module (PHYS3006) is worth 28 points and the other four (theory-based) modules are worth 11 points each.

2. The PHYS3006 Module

The PHYS3006 module consists of four broad areas of activity. Each of these areas of activity are discussed in this section.

2.1. Set Experiments (30 % of the final mark for the module)

Eight Set Experiments are offered, and each student will do five of these experiments during the course of one teaching quarter. Students do the experiments as individuals, and are assisted by a demonstrator assigned to the experiment. Students are supplied with a handout giving the details of each experiment (handouts to all set experiments are distributed at the start of the relevant teaching quarter), and take the experimental data during the course of one afternoon. Laboratory reports are due one week after the experiment, and the students are required to make use of the library, on-line resources, data-fitting packages and a word processing package to produce the final laboratory report. The reports are typically between eight and fifteen pages long, depending on the experiment. The students are supplied with a rubric, which gives details of the marks allocated to each section of a typical laboratory report. The demonstrator responsible for the experiment marks the completed report.

2.1.1. *Michelson Laser Interferometer.* The objective of this experiment is to introduce students to the principle of interferometery and its application to relative displacement measurement. The experiment is done on a high quality optical table.

2.1.2. *Optical Diffraction.* The experiment introduces the student to advanced optical spectroscopy, including Fourier transforms. The relationship between optical spectroscopy and electron and X-ray spectroscopy is emphasized.

2.1.3. *Temperature dependence of the resistance of a metal and a semi-conductor.* Students investigate the temperature dependence of the resistance of the two samples in the temperature range 100 K – 300 K. Elementary band structure concepts are introduced through analysis of the experimental data, and students are required to calibrate a thermocouple.

2.1.4. *Magnetic Resonance.* Students measure the g-factor of the proton and the electron using continuous wave nuclear magnetic resonance and electron paramagnetic resonance respectively. The natural line-width of the resonance lines is emphasized.

2.1.5. *Lecher Wires.* This experiment introduces students to the transmission of electromagnetic waves along transmission lines. They obtain the velocity of the waves, determine the properties of the transmission lines, and examine the properties of a standing electromagnetic wave.

2.1.6. *X-ray Spectroscopy.* Students are introduced to X-rays, and a calcite crystal is used to investigate the X-ray spectrum produced by a copper tube in a research-quality diffractometer. This is followed up by a study of some powder samples using the K_α copper line.

2.1.7. *γ-ray Spectroscopy.* The objective of this experiment is to introduce the student to some of the techniques used in nuclear physics data capture, while providing an introduction to basic nuclear physics. A modern computer-based Multi Channel Analyzer is used to capture γ-ray spectra, and analysis is done using computer-based data fitting packages.

2.1.8. *Radio Astronomy.* Students make use of equipment based on the principles of Radio Astronomy to study the microwave spectrum of the sun. A simple arrangement involving standard satellite receiver dishes is used.

2.2. Electronics Experiments (20 % of the final mark for the module)

Students are introduced to electronics during the 2nd Year, and this part of the PHYS3006 module is an extension of the 2nd Year course to transistors and digital electronics. In total five experiments are completed involving a number of circuits. Two demonstrators are assigned to the electronics experiments, the students work individually, and part of the mark assigned to each experiment is based on an in-lab assessment of the circuits built.

2.2.1. *Introduction to Electronics.* This experiment is designed to introduce the students to the experimental apparatus (which differs noticeably from the equipment used in the 2nd Year). Potential divider, and low and high pass filters circuits are constructed and tested.

2.2.2. *Transistors.* The use of transistors in amplifier circuits is presented. The students build and test four circuits involving transistors, including an audio amplifier.

2.2.3. *Introduction to Digital Electronics.* Students are introduced to building TTL logic circuits using diodes. Three diode logic circuits are built and tested, including a cascaded OR and AND configuration.

2.2.4. *Gates and Flip-Flops.* Integrated circuits are introduced in this series of four circuits. The use of gates and flip-flops in real devices is emphasized.

2.2.5. *Counters, Encoder and Decoder.* Two circuits are built and tested in this experiment. These are a Programmable Divide-by-N Counter and a Binary Encoder. Details of a possible decoder circuit are also provided.

2.3. Specialist Lectures and Essays (10 % of the final mark for the module)
During the 3rd and 4th quarter two afternoons are devoted to lectures that are presented by research specialists. In 2011, for example, lectures were presented on Experimental Nuclear Physics and Superconductivity. The lectures included an introduction to the relevant fundamental concepts, and to recent research results and the experimental techniques employed. Students were required to listen, take notes and then write an essay of not less than two pages on the lecture. This exercise is designed to enhance the critical listening and writing skills of the students.

2.4. Major Project (40 % of the final mark for the module)
The major project is done during one teaching quarter. The aim of the project is to introduce the student to the research interests of the School of Physics, but they are didactic rather than research-based. The projects may be exclusively experimental, computational or theoretical in nature, or may be a combination of two or more. Projects are offered by research-active staff of the School and associated entities. Projects are intended to develop the following attributes that are necessary for a young scientist: critical reading of the literature; analytical, experimental, computational and theoretical skills (depending on the focus of the project); written and oral communication skills.

2.4.1. *Choice of a Project.* Students are required to approach at least three potential supervisors before making a final choice of project. A list of potential supervisors and their contact details is provided, and students are encouraged to find out the research interests of the staff by using web resources.

2.4.2. *Quality Control.* During the third week of the relevant teaching the course co-ordinator meets with each of the students who are busy with their project. During this meeting the course co-ordinator ensures that the supervisor and the student have a decent working relationship, that the project is proceeding within the time constraints, and that the student has a reasonable idea of what they are required to do.

2.4.3. *Project Report.* The students submit a written project report in the first week of the teaching quarter following the quarter in which they completed the project. The report should follow the layout of a long scientific paper, and they are usually between twenty and forty pages long. The supervisor marks the report following suggested guidelines. The report counts 25 % of the final module mark.

2.4.4. *Oral Presentation.* During the final teaching quarter several afternoons are set aside for oral project presentations. All members of staff are invited to the presentations, and each staff member allocates a mark to the presentation based on the quality of the presentation, familiarity with the work they are presenting, and the student's response to questions posed by the audience. A discussion of the projects by staff members follows, and the final mark for the oral presentation is an average of the marks submitted by the staff members present. The oral counts 15 % of the final module mark.

3. Student Assessment Survey conducted at the end of 2011

The PHYS3006 module has been run along the lines outlined in Section 2 for a number of years. During 2010 I was appointed to co-ordinate the course, effective from the beginning of 2011. Mindful of the desire to evaluate and modify the laboratory curriculum for the Major stream, I administered an official University Student Assessment Survey towards the end of my first year as co-ordinator (September 2011). The survey consisted of 24 multiple response assertions based on a standard Strongly Agree (10), Agree (7.5), Neutral (5), and Disagree (2.5), Strongly Disagree (0) scoring method. In addition, there were three open-ended questions as follows:

- Which aspects of the course were most valuable?
- Which aspects of the course were least valuable?
- Any suggestions about how to improve the course for next year?

Table 1. Results of the student survey of the PHYS3006 module administered during September 2011. The results are discussed in the text.

Statement	Score
The course is effectively administered	7.70
Laboratory reports require a reasonable amount of time and effort	6.40
Laboratory reports are marked fairly	5.63
Marked laboratory reports are returned promptly	5.00
Demonstrators have a constructive attitude	7.00
The research project was very stimulating	8.00
The feedback sessions on projects are valuable	7.10
The project assisted me to improve my data analysis skills	7.60
The project improved my ability to write concisely and clearly	7.20
Mark allocation reflects the right emphasis in the course	6.30
I would recommend this module to other students	6.60
The department has a positive image amongst students	7.30

The results for a selection of the multiple response assertions are tabulated in Table 1. It is clear from these results that students attach great value to the major project. This is corroborated by the responses to the open-ended questions where the project was highlighted as the most valuable aspect of the course (18/25 students). The electronics experiments were highlighted as one of the least valuable aspects of the course by a large minority of students (10/25 students). A significant number of students mentioned that a short background course related to the electronics component would improve the impact of the electronics experiments, while others suggested that a short electronics

project would improve the module. The low scores for the two items related to the fair marking and prompt return of laboratory reports (see Table 1) is of grave concern, and these were further highlighted in the responses to the open-ended questions.. A more structured method of handling report submission and marking was suggested by several students, as was the lack of comments by demonstrators on marked reports. Despite the problems with the marking and returning of set experiment reports, the set experiments were identified as a valuable aspect of the course (10/25 students).

4. Changes made to the PHYS3006 module for 2012

Two significant changes were introduced for 2012. These are an automated system for the submission and return of the reports for the set experiments, and the introduction of a small electronics project. Brief details of submission procedure are given in this section. The electronics project will be done in the second half of 2012, and will not be discussed in this paper.

4.1. Set Experiment Report Submission Procedure and Assessment

An automated web-based application was developed for the submission and return of reports, in response to the concerns raised by students in 2011 concerning the marking and returning of set experiment reports. Students are able to access the application using their favourite web browser from any location with an internet connection. They are able to upload a PDF file containing their lab report, and direct it to a particular demonstrator. Once the report is successfully uploaded the date and time of submission and the details of the student and demonstrator concerned are recorded in the database back-end to the application. The report file is stored on the web server, and an electronic copy is emailed to the demonstrator for marking. Demonstrators use Adobe Acrobat Reader to add comments to the submitted report, and save the changes to the document. The demonstrator uploads the marked report using the web application, and during this process fills in a mark schedule (including comments) for the report. The student receives both the marked lab report and a PDF version of the mark schedule, and both documents are stored on the web-server.

Table 2. Results of the student survey of the PHYS3006 module administered during May 2012. This survey follows some of the interventions introduced during 2012. The results are discussed in the text.

Statement	Score
The laboratory course is effectively administered	8.93
Set experiments are a valuable part of the course	8.39
The time and effort required to produce lab reports is reasonable	6.15
I like the submission procedure for the set experiments	9.82
The submission procedure works effectively	9.82
The electronics experiments are a valuable part of the course	6.25
The handouts for the electronics experiments are adequate	5.54
The demonstrators for the electronics course are effective	7.86
The theoretical background provided for the electronics component is adequate	4.82
The electronics component would be improved by a series of lectures	8.39
The electronics learned will be of future practical use	5.36
I would recommend this module to other students	6.43
The School of Physics has a positive image amongst students	7.32
I intend to pursue a career in experimental physics	5.18

5. Mid-year Student Assessment – May 2012

As part of the ongoing evaluation of the course a further student survey was administered following the conclusion of the first semester of the module in May 2012. The survey is designed to evaluate the changes that were introduced to the submission and return of the set experiment reports, to probe further the issues that the students appear to have with the electronics course, to probe student impressions of each of the set experiments, and to elicit student impressions of the demonstrators responsible for each experiment. The results of the survey as they relate to administration, the set experiments as a whole, the report submission procedure, and the electronics experiments are tabulated in Table 2. It is clear from the survey that the set experiments are regarded as a valuable aspect of the course, and that both the administration of the course and the submission procedure have the approval of the students. The problems raised by the student cohort of 2011 regarding electronics experiments are echoed by those of 2012, with the handouts and theoretical background once again receiving low scores. The high score obtained for the suggestion that some theoretical background be provided for the electronics experiments indicates that this should be addressed for 2013. This conclusion is supported by comments made in the open-ended questions.

Table 3. A summary of the student survey of May 2012 for each of the Set Experiments. The results are discussed in the text.

Statement	Experiment							
	1	2	3	4	5	6	7	8
Demonstrator provided sufficient information to do the experiment	7.81	8.44	9.06	8.61	8.33	7.50	8.61	6.43
Handouts adequate	6.88	7.50	7.50	7.22	5.56	6.39	7.78	6.07
Equipment adequate	4.06	6.88	9.38	6.94	8.89	8.06	8.61	5.71
Fundamental physics was learned	7.50	7.81	9.44	8.33	9.17	8.06	8.61	5.36
Demonstrator provided lab report guidance	5.94	8.13	9.06	8.06	8.89	5.28	7.22	3.93
Report marked fairly	7.50	5.50	8.75	8.21	8.75	5.31	6.88	2.50
Report returned promptly	1.50	3.93	8.75	8.57	6.88	3.06	4.17	0.00
Experiment increased interest in experimental physics	5.63	6.43	6.88	5.56	6.67	5.83	5.28	3.21

A section for each of the set experiments was included in the survey. These results are displayed in Table 3. While an appreciable number of the experiments are being demonstrated adequately with adequate equipment, there are worrying issues raised with regard to equipment, documentation and demonstrating for several experiments. These issues must be addressed for 2013. Praise and criticism for particular demonstrators in the open-ended section underline the results shown in Table 3.

6. Conclusions

A description of, and an ongoing evaluation of, the Advanced Experimental Physics and Project III (PHYS3006) module offered at WITS has been presented. It is clear that changes were, and still are, required to the module so that it offers students both a high-quality well-taught module, and an excellent impression of experimental physics. The work described is part of a re-development of the Physics Major Laboratory Curriculum at WITS.

References

[1] Zwickl B M, Finkelstein N and Lewandowski H J 2012 *Am. J. Phys* **81** 63-70
[2] Zwickl B M, Finkelstein N and Lewandowski H J 2012 *AIP Conf. Proc.* **1413** 391-394

Our Galaxy and Venus in Setswana as a Tool in (Astro)Physics Education

Lerothodi Leeuw[1]

[1] College of Graduate Studies, University of South Africa, P.O.Box 392, UNISA, 0003, South Africa

E-mail: lerothodi@alum.mit.edu

Abstract. Excitedly awaiting the Square Kilometre Array (SKA), the world's largest radio telescope, being built primarily in Southern Africa, and the full scientific operations of the Southern African Large Telescope (SALT), and the very faint and distant celestial objects these telescopes will observe, we present an exemplary lesson of our Galaxy and Venus in the Setswana the Setswana language of Southern Africa. This short paper opens the window to the potential benefits of such a lesson as a teaching tool in (astro)physics education, that may be one of the methods useful for spuring an increased number of young Southern Africans to consider a study of the night sky and careers to use these power telescopes at their doorsteps. The presentation showcases an example for broadening access and understanding of astrophysical concepts and exposing a relatively unpublicized astronomical interest of the Batswana people, and local Southern African people in general.

1. Introduction

For many generations, Africans, like many people across the globe, used their natural astronomical instrument, the human eye, to observe, comment on, and name celestial objects that interested them (cf. Leeuw 2007, 2014). Most of these objects are very bright and relatively nearby to Earth and can thus be seen by eye, without requiring the use sophisticated or expensive tools. On the other hand, most of modern astronomy uses data from large telescopes, and its study can deal with the very faintest and most distant observable objects in the Universe.

The scholarly study of modern astronomy and its teaching in schools and universities is done almost exclusively in English, which is its assumed international and standard language and certainly of most scientific journals. Such an approach is often built on a notion that interest in the subject is primarily Western and that there is no similar interest in the local Southern African cultures. This approach can alienate some local learners or, at least, miss the opportunity to build on what learners may know, particularly those who may already have some home taught knowledge of the night sky from their own cultures.

In anticipation of the world's largest radio telescope, the Square Kilometre Array (SKA), and its smaller predecessor, the MeerKAT, being built primarily in Southern Africa, the full scientific operations of Southern African Large Telescope (SALT), and the very faint and distant celestial objects they telescopes will observe by a large number of scientist that should include an increased number of local ones, this paper presents our Galaxy and Venus in the Setswana language of Southern Africa (SA), as a teaching tool in introductory (astro)physics education. The lesson showcases our Galaxy, the conglomeration of stars of which our Sun is a part, and

Venus, the brightest and nearest astronomical body from Earth after the Sun and Moon. The idea is to explore the potential benefits of this exemplary lesson in (1) broadening access and understanding of scientific concepts by local students and non-specialists and (2) exposing a relatively unpublicized astronomical interest of the Batswana people, or Southern African people in general.

2. Our Galaxy, the Milky Way or Molagodimo

Figure 1 shows a photographic mosaic of our Galaxy, the Milky Way, or *Molagodimo* made by astrophotographer Axel Mellinger between 1997 and 2000. Our Galaxy as seen by the human eye, or an optical camera, is a myriad of patterns, i.e. a multitude of stars among dark patches of dust and gas, that astronomers now understand is forming new stars. Indeed, for the night sky and stars, there is a riddle in the Setswana language of Southern African that says, *mosese ya ga mmakgathi, maranthatha* or "the dress of the painter (a female one) is a myriad patterns." This Setswana riddle demonstrates an old, though refreshing interest in the stars and night sky by the Batswana – a fascination that is deeply woven in the language and culture of the people of Southern Africa, riddled with idiom, poetry, indirect or evasive speech and educational potential. *Mosese*, or literally a dress, is also poetically used to mean a woman, in Setswana. It is coincident that the beautiful patterns of this dress or a woman, is partly made so by stars and cosmic dust, out of which future stars are born. The beauty of the coincidence lies in that *mosese*, or a woman, bears children, and in Setswana culture traditionally cares for them, making a great analogy of the Galaxy, with its stars and dust from which future stars will be born.

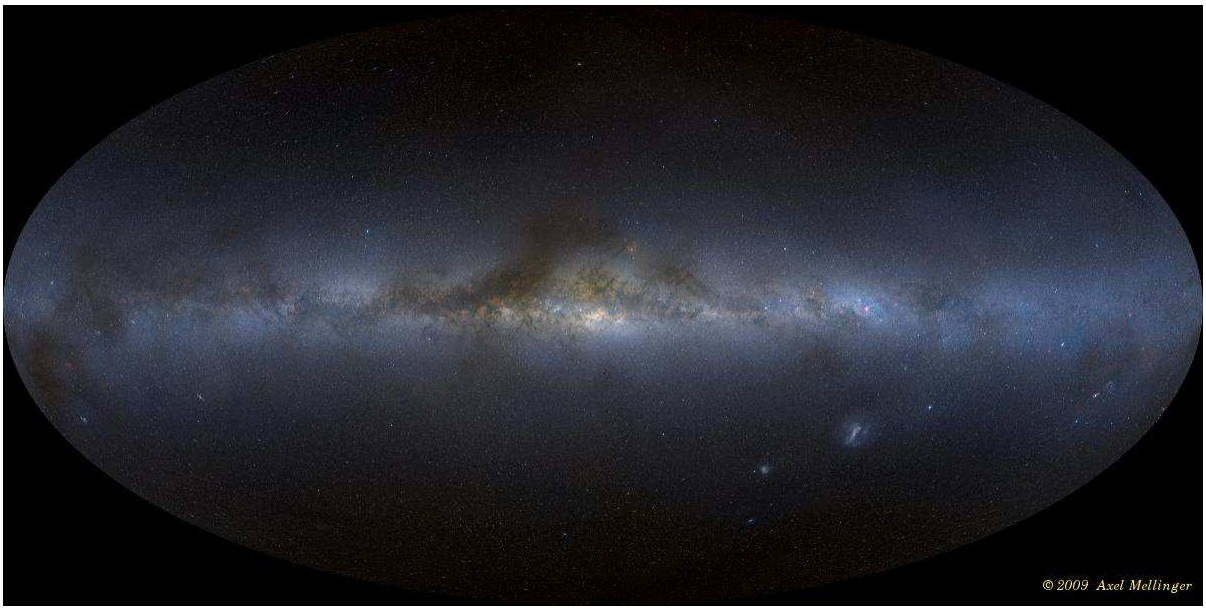

Figure 1. A panoramaic mosaic of the night sky made by Axel Mellinger from dark-sky locations in South Africa, Texas, and Michigan, using the three optical digital photography colours or filters *RGB* (Mellinger 2009). The map, with our Milky Way Galaxy or *Molagodimo* in the centre of the image, is plotted in a Hammer-Aitoff projection, which is an equal-area map of an equatorial form and shows the central disk of the Milky Way with its multitude of stars and dust that will form future stars. As well as stars, dust, and nebulae in our Galaxy, the Milky Way's bright neighbour galaxies Andromeda and Magellanic Clouds are also shown in this map off the central part.

The Setswana name of our Milky Way Galaxy itself or *Molagodimo*, means the path (or

mola) above (or *godimo*). Like the meaning of "way", in the Milky Way, it is called path both in English and Setswana because the Galaxy, as seen from Earth, looks like a path. This is because Earth and our Sun, around which we revolve, sit inside a disk-like part of the Galaxy. This disk is made of a concentration of stars interlaced with dust and is the main stellar component of the Galaxy. In fact, we sit about two-thirds from the centre of this disk-like part of the Galaxy; and, when looking along the direction of this disk from the location of the Earth, the disk or, if you like, the Galaxy itself, looks like a path. Both these simple English and Setswana names of our Galaxy therefore tell about the main disk component of the Galaxy and how it appears from Earth. The projection of the Galaxy as would be seen in the Northern and Southern Hemispheres respectively on the left and right of the picture in Figure 2.

3. Venus, the "Evening or Morning Star"

Venus, the goddess of love and beauty - according to Greek Mythology, is the third brightest celestial object in sky, after the Sun and Moon. In Setswana, Venus is *Kopadilalelo* (or, seeker of evening meals) as seen at sunset or *Mphatlalatsane* (or, the brilliant one) as seen at sunrise. The inner planets, Mercury and Venus, always appear in the West or East with the Sun - never opposite to it. Mercury is dimmer and only visible a few weeks a year, so the brighter Venus, is the one called the "Evening or Morning Star", by the Batswana and many across the globe, depending on when it is sighted in the sky.

Figure 2. A NASA true-colour image of Venus, the "Evening or Morning Star"

Venus does not appear as the "Evening and Morning Stars" on the same day in the sky. In fact, the periods of appearance as evening and morning stars respectively last around nine months, with other smaller periods in between. Viewed through a small telescope (e.g. by Galileo in 1610 when he observed these phases), Venus has phases; and, when it is at its brightest, it is in a phase of a crescent, a few say they have resolved by naked eye or seen make shadows.

The orbital (i.e., period versus stars from outside Earth) and Synoptic (i.e., period versus Sun from moving Earth) periods of Venus are 225 and 584 Earth days. Now, 225×13 is about 8×584 is 5×365. Thus, Venus orbits the Sun 13 times in 8 Earth years, passing Earth 5 times. The synoptic cycle of Venus takes 584 Earth days, about 263 continuously as evening star and then morning one, and 8 and 50d ays in between on the near- and far-side from the sun. Thus the reason Venus was thought of as two separate celestial objects by the Batswana and many across the globe.

Venus is the second-closest planet to the Sun, orbiting it every 224.7 Earth days. Its mean surface temperature is 735 K or 460 °C. Venus has few impact craters, demonstrating that the

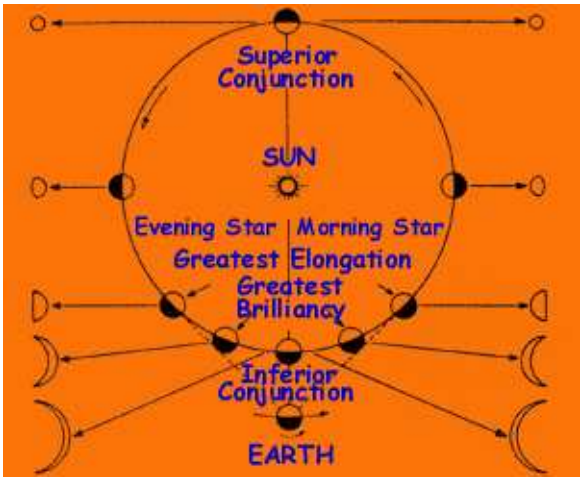

Figure 3. The relative positions of Venus, its apparent size and phases and the Earth are indicated on the diagram, which has been simplified by keeping the Earth's position fixed (http://www.absoluteaxarquia.com/nightsky/venus.html).

surface is relatively young (about 0.5 billion years) and perhaps, how Earth was when young. Classified as a terrestrial planet, it is sometimes called Earth's "sister planet" because they are similar in size, gravity, and bulk composition. Classified as a terrestrial planet, Venus is sometimes called Earth's "sister planet" because they are similar in size, gravity, and bulk composition. Perhaps because of its age and temperature, Venus can be though of as Earth, younger and hotter or more temperamental sister or as the Batswana call it, *Kopadilalelo* (or, young, seeker of evening meals, the bringer of night) as seen at sunset or *Mphatlalatsane*, (or, the brighter , bearer of dawn) as seen at sunrise – the forerunner of night or day time.

Figure 4. A NASA image showing the relative sizes of Mercury, Venus, Earth, and Mars, shown respectively from left to right.

4. References

1. Leeuw, L., AFRICAN SKIES/CIEUX AFRICAINS, No. 11, July 2007, pp. 19-20
2. Leeuw, L., Multilingual Universities in South Africa, edited by Liesel Hibbert and Christa van der Walt, published by Multilingual Matters, 2014, pp. 167
3. Mellinger, A., Publications of the Astronomical Society of the Pacific (PASP), Vol. 121, No. 885 (November 2009), pp. 1180-1187
4. http://www.absoluteaxarquia.com/nightsky/venus.html

How much do first year physics students really understand? An entry-level test.

P Molefe, B M Sondezi-Mhlungu and H Winkler

University of Johannesburg (UJ), P.O. BOX 524, Auckland Park, 2006.

Email: pmolefe@uj.ac.za

Abstract: The intake of first-year physics students in Higher Education Institutions has grown considerably over the last four years, and there has been even greater increase in student diversity. In order to academically support these students effectively, and to ensure the subject they take remains relevant, the academic preparedness of these students must be determined. For these reasons, the University of Johannesburg lecturers for first year physics introduced, at the beginning of the year in 2012, a physics skills test to determine the level of incoming students' understanding of basic–mechanics. This paper presents and discusses the main misconceptions that students have on the concepts assumed to be a prior knowledge as they enter their first year physics course. From this study some recommendations will be suggested.

1. Introduction

Pure BSc and engineering students at the University of Johannesburg (UJ) enroll for a standard calculus- based Physics course which serves as an introduction to their degree. Failure to obtain a satisfactory pass mark of 50% in a such course renders them ineligible to embark upon their degree of choice leading to the significant attrition experienced in science and engineering faculties at the university level. Globally, industry demands an increasing number of Science, Engineering and Technology (SET) graduates (Smaill, Godfrey, & Rowe, 2007). However, the number of secondary school students well prepared for studying SET at university level is shrinking in many countries (Smaill, Godfrey, & Rowe, 2007). In South Africa there is an increase in the number of students pursuing studies in SET but there is relatively low first semester completion rates by students entering first year university studies. At UJ the first semester of the first year of study is one of the major factors for early drop-out from university, since a pass in this semester is the pre-requisite to enroll for second semester. In order to support these students effectively, and to ensure the course remains relevant, their academic preparedness must be determined. However, recent changes in South African (SA) school curriculum and how national examinations are conducted have made this difficult (Yeld, 2009,Jansen& Phakati, 2011). For example, in the past all students who chose to study mathematics and physical science in their secondary schooling were required to study standard grade (SG) or higher grade (HG). In the recent years, only one grade paper is written by all students, and it makes it difficult to determine their preparedness.

Physics 1(Introductory physics), mechanics, is part of the compulsory module for all incoming first year science and engineering students at UJ. For a fundamental introductory mechanics course at university level the topics to be studied include areas such as kinematics, dynamics, Newton's Law of motion, work and energy, impulse and momentum, and rotational motion. Four hundred and twenty six (426) and three hundred and six (306) students enrolled in the three year and four year program, respectively. To enroll for a three year program the student must have obtained a minimum of 60% overall mark and for a four year program the student needs a

minimum of 50% overall mark from the National Senior Certificate (NSC) results. Since the inception of the National Curriculum Statement (NCS) and introduction of NSC in high school in 2006 the number of students achieving university entrance scores has increased. A total of 496090 candidates sat for the matriculation exams in 2011, 70% of whom passed. Of those who wrote exams, 24.3% qualified for university study (DoE, 2011). The University of Johannesburg experienced more students registering for science and engineering courses in the last three year see table 1.

More than half of students registering for module 1 in semester 1 at UJ do not enroll for module 2 in semester 2, due to various personal reasons. It has been observed that some of those enrolled in physics for a four year program do not pass the first module of physics or fail one or more other modules. Other reasons that some students from a three year program fail to qualify to write examinations and some of those that manage to write don't do well in them. As means of establishing the readiness of the students in respective physics program, a physics skills (diagnostic) test was given to first year students and administered in February 2012 (see Table 1 below).

Subject Codes	2008	2009	2010	2011	2012
PHY1(3year)	332	461	374	483	426
PHY1A1E(4Year)	128	207	169	454	306
Total	460	668	543	937	732

Table 1: A table showing the total number of students enrolled for physics year-one.

The lecturers were greatly surprised by the extent to which students' misconceptions in mechanics were revealed. The development of the physics skill test was informed by previous years' first class and semester tests results obtained by students in physics three year and four year programs, respectively.

Physics Skills Test (PST)

A physics skills test has been designed for students entering the mechanics module in the first semester of introductory physics first year. The test consists of a 20 multiple choice questions related to basic understanding of the principles of Mechanics, Waves and Thermodynamics (which the student should have learned in the high school physical science). Each question tests knowledge that the student is expected to be able to produce without special preparation, and that should be well understood by him/her. For example the student might be asked to execute a vector sum or evaluate the magnitude and direction of the vector.

2. Methodology

The physics skills test were given to two different groups of 2012 first year physics students: one being part of a three year degree program and the other being drawn from a four year degree program. The test consisted of 20 multiple choice questions and was administered for a one hour period at the beginning of the first quarter. The test was administered to a total of 423 participants of physics 1 students UJ from 732 registered students. The participants were divided according to the programmes they enrolled into and it must be mentioned that not all the students wrote the test. The three year (n= 157) passed their grade 12 physical science with 60% or

above, while the four year group (n = 266) only passed their grade 12 physical science with marks in the range of 50-60%. The test was written by students at their convenience over a period of a week in the beginning of the second week of their semester on the Electronic Learning Media (Edulink) platform. Each student attempting the questions needed to login and finish test in an hour.

3. Results and Discussion

The Physics Skills Test, Initial Analysis

The physics skills test has been given to two different groups of 2012 first year physics, that is, three year degree and four year degree programmes. The total number of students completed the 20 question test are 157 and 266, respectively. Test statistics reveals that the time allocated to the test appeared to be sufficient, as a significant number of students finished the test with adequate time to spare. Other students however made full use of the allocated hour working on their answers. Mark histograms are provided in Figures 1 below.

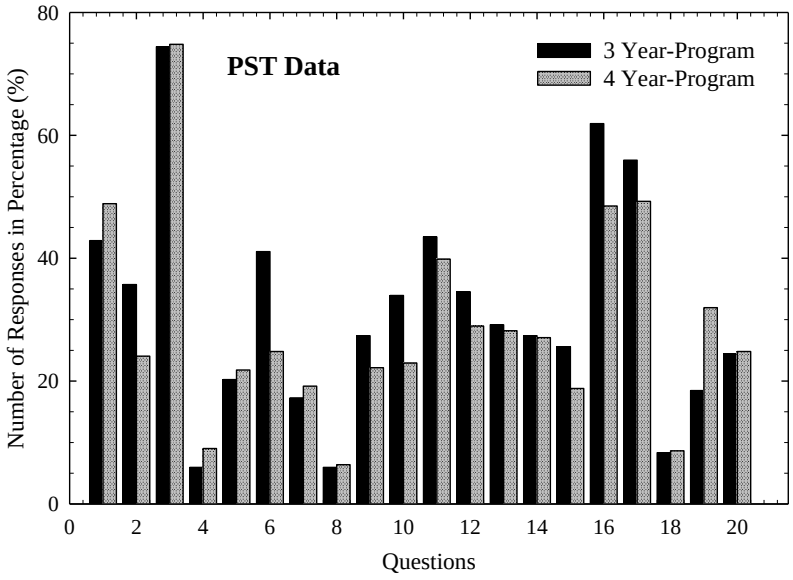

Figure 1: Mark the histogram(s) for 2012 Physics Skills Test

Figure 1 confirms that for most questions the correct response rate is low, showing a lack of understanding of the pre-conceived physical science concepts. Both groups (3-year and 4-year programs) did not show much difference in terms of their averages which were calculated to be 32% and 29% for a 3-year and 4-year program, respectively.

This indicates that certain simple pre-knowledge skills, which the test assumes students can execute, will often be incorrectly answered. To enable us to interpret these results, some of the questions were selected for in-depth analysis to provide understanding to some of the misconceptions the students had.

A close look at some of vector questions

Analysis of selected PST questions

In question 8 shown below, the results were of considerable concern, as they revealed significant misunderstandings of a fundamental and elementary concept. Only 6% of the students gave option (E), the correct answer. By contrast, 42% thought the answer was option (C). Clearly the misconception outlined above is well-established and widespread. This indicates that a significant (based on which statistical package?) percentage of students from both groups does not have a conceptual understanding of the definition of a vector and vector addition. They cannot make use of the Cartesian plane (axes) to determine the magnitude and directions of vectors. Of course, they would have an idea of definition of a vector quantity and knowledge of resultant vector.

Q8: In the diagram below you are looking at a mass on a frictionless surface from above. Three forces act on the mass as illustrated in the diagram. $F_3 > F_2$ and $F_2 > F_1$. The magnitude of the resultant force acting on the mass will be:

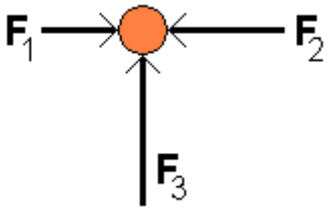

A	B	C	D	E	F	G	H
$F_3 - F_2 - F_1$	$F_3 + F_1 - F_2$	$F_3 + F_2 - F_1$	F_3	Slightly bigger than F_3	$F_1 + F_2 + F_3$	I do not know the answer because I do not understand the Physics in this question.	I do not know the answer because I do not understand some of the words used in this question

Q.11: Five boxes are tied together by identical strings and tied to a ceiling by another string identical to the others (see diagram). The large box in the diagram is also heavier than the others, and the smallest box is the lightest. Which string is most likely to break?

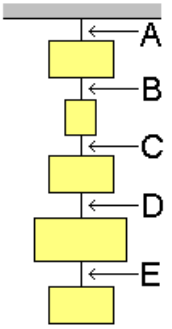

A	B	C	D	E	F	G	H
where the top box is tied to the ceiling	just above the small box	just below the small box	just above the big box	just below the big box	All strings A-E are equally likely to break	I do not know the answer because I do not understand the Physics in this question	I do not know the answer because I do not understand some of the words used in this question

In question 11, only 46% of the students gave option (A), the correct answer. 24% thought the answer was option (D). This indicates that a significant percentage of students do not have a conceptual understanding of tension and weight. The misunderstanding of weight is revealed by the answer (D) showing that this group thinks that the bigger the box means more weight applied on the string just above it. About 10% of students thought the answer was (C), their reasoning could be that they thought the sum of the masses of the boxes below the small box will give more weight and more stress on the string just below the small box.

Q13: A person carrying a box with a weight W (W = mg) is walking up the hill from point X, along the flat top, and then down to Y. What is the work done by the person for the entire trip from X to Y?

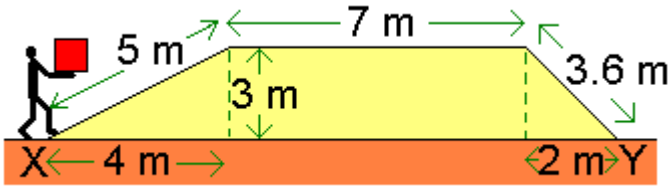

A	B	C	D	E	F	G	H
zero	3*W* Joules	5*W* Joules	6*W* Joules	13*W* Joules	All strings 15.6*W* Joules	I do not know the answer because I do not understand the Physics in this question	I do not know the answer because I do not understand some of the words used in this question

In question 13 above a disappointing 31% of students gave the correct option (A) as the answer. 17% of students thought (E) is the correct answer, presumably as in the figure above students just added all x-axis values to get a displacement (13 m). A small percentage (8%) gave option (D), apparently adding the 4 m and 2 m in the x-direction to get the displacement. It seems as if they realized that at the end of the journey the displacement in the y-direction is zero. Clearly, students know the definition of work-done (W= Fcosθ.s) but do not have a clear understanding of the calculation of displacement in relation to the above given diagram. Only 31% managed to realize that displacement is zero. Literature shows that students still hold misunderstanding about vector addition even after they have been taught vector addition (Wutchana & Emarat, 2011).

Q15: This question relates to the same physical setup as in the previous question. The small box X moves with speed *v* and kinetic energy E_0 on a smooth horizontal surface towards the heavier stationary box Y. After the boxes rebound, X moves to the left with a kinetic energy E_X and Y moves to the right with a kinetic energy E_Y. Some heat is generated during the collision. What is always true about the relationship between E_0, E_X and E_Y?

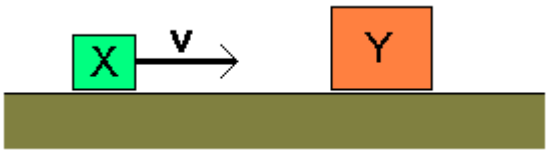

A	B	C	D	E	F	G	H
$E_0 > E_X + E_Y$	$E_0 = E_X + E_Y$	$E_0 = E_Y - E_X$	$E_0 = E_X - E_Y$	$E_0 < E_Y - E_X$	$E_0 < E_X - E_Y$	I do not know the answer because I do not understand the Physics in this question.	I do not know the answer because I do not understand some of the words used in this question

While a simple knowledge of conservation of energy may have helped 27% of students to the correct answer (A) for the questions illustrated below, 52% of students opted for (C) or (D) and arrived at quite nonsensical results through blindly relying on the definition of conservation energy without considering the loss of energy through some heat generated during the collision. They could have noticed a loss of energy but lacked the skill to determine the correct answer.

4. Conclusion and Recommendations

The physics skills (diagnostic) term test was disappointing but also enlightening. It appears to indicate that most of the class either had not understood or had forgotten much of the basic physics they were supposed to have covered in high school. The recent NCS introduction of NSC for high-school qualification may have led teachers to adopt a more learner-centred teaching style which, in turn, encouraged students to adopt a more fragmented approach to their learning.

More remarkably, success rates for many of the individual questions corresponded very closely between the two samples. The test shows that the NSC results may not be used to place students to a particular group, since students produced similar and, at times, identical statistics. The physics skills (diagnostic) test acted as a "wake-up call" and led to behavioural changes on the part of many students and to some modification of the course teaching style. A question-by-question analysis has proven valuable, with the most significant feature to emerge from the analysis being the basic (pre-tertiary) level at which the misconceptions occurred.
This study recommends that some intervention be made early in the year and the amount of time allocated to understanding of basic mechanics concepts be increased because the mechanics concepts are the core in introductory first year physics. We hope that the recommendations would enhance pass rates and throughput and hence more students would as a result progress to the second semester of their first year.

5. Acknowledgements

The authors acknowledge the assistance from the department of physics at large.

References

DoE. (2011). *National Senior Certificate Examination Results.* Pretoria: Government Printer.
Jansen, J. (2011, 01 12). Results don't add up. *Times Live. Availble at : www.timeslive.co.za/opinion/article847919.ece/results-dont-add-up? Service=print* .
Jansen, J. (2011, January 12). *Times Live*. Retrieved fromwww.timeslive.co.za/opinion/article847919.ece/Results-dont-add-up? Service=print.
Molefe, P; Sondzi-Mhlungu, B.M. (2011). The transition from high-school physics to first year physics: How much well prepared are sour students? *Proceeding of the South African Institute of Physics* (pp. 614-618). Pretoria: University of South Africa.
Phakati, B. (2011). *Umalusi defends adjustments. Business Day Online*. Retrieved from www.businessday.co.za/articles/Content.aspx?id=131918
Smaill, C., Godfrey, E., & Rowe, G. B. (2007). Transition from final-year high school physics and mathematics to first-year electrical engineering: a work in progress. *In Eigthteenth Annual Conference of the Australasian for Engineering Education.* Melbourne, Australia.
Wutchana, U., & Emarat, N. (2011). Students' Understanding of Graphical Vector Addition in One and Two. *Eurasian J. Phys. Chem. Educ., 3(2)* , 102-111.
Yeld, N. (2009). *National Benchmark Test Project. (Workshop presented at the University of Johannesburg on 13 June.* Johannesburg: University of Johannesburg.

Investigating the causes of unsatisfactory performance on the section involving vectors in basic mechanic

P Molefe and B M Sondezi

University of Johannesburg (UJ), P.O. BOX 524, Auckland Park, 2006.

Email: pmolefe@uj.ac.za

Abstract: First year physics lecturers report difficulties with students' learning of concepts and skills associated with solutions of basic mechanics problems. From a basic vector definition: a vector is a quantity with both magnitude and direction that is represented geometrically by a directed line (length of the line representing the magnitude; and an arrow representing the direction of a vector). The use of vectors in both forces and equilibrium concepts illustrated by free-body diagrams, are basics to all mechanics problems. Despite this, it apparently remains a difficult area for a significant number of students, even in the later years of their degree. Therefore, attention to this section at first year level is crucial as it forms a solid foundation to the mechanics and their related topics. It has been observed that students' response before an assessment is always positive, whilst the assessment results show poor performance, which are the sources of concerns. The results of the investigation in this regard seem to suggest that students have insufficient knowledge and understanding of magnitude, direction, and the significance of free-body diagrams in resolving the related forces into components. In addition, students also seem to encounter difficulties in using trigonometric ratios.

1. Introduction

The Physics lecturers at the University of Johannesburg (UJ) has engaged in a short term, short scale investigation of students understanding of vectors. In this study, we examined the ability of students to determine and use qualitatively the magnitude and direction of the vector from knowledge of drawing a free-body diagram. From a basic vector definition a vector is a quantity with both magnitude and direction that is represented geometrically by a directed line (length of the line representing the magnitude; and an arrow representing the direction of a vector). The use of vectors in both forces and equilibrium concepts illustrated by free-body diagrams, are basics to all mechanics problems. In his report Knight (1995) [1] emphasized that the vector nature of forces, fields, and kinematics quantities requires that students have a good grasp of basic vector concepts if they are to be successful in mastering even introductory level physics. The fundamental concept of Newtonian mechanics is force, and forces are vectors, they must be added using vector addition to determine the net force along the axis of motion.

Dealing with vector quantities is somehow more complicated, than dealing with scalar as more mathematical manipulations are required. A fundamental introductory mechanics course at university level needs to include topics areas such as kinematics, dynamics, Newton's Law of motion, work and energy, impulse and momentum, and rotational motion. In order to have a well-founded understanding of the concepts presented in these topics, a basic understanding for the drawing a free-body diagram and its interpretation is needed.

Student learning is our primary criterion for determining teaching effectiveness. Poynter (2005) [2] in their study indicated that, "in spite of clear instruction in procedures for vector addition, many students tend to forget to draw final side of the triangle (resultant) when calculating the vector sum, or have difficulties when vectors are in non-standard positions". Literature indicates that a quarter of students who had completed a calculus-based physics course and a half of students who had completed an algebra-based physics course could not add vectors in two dimensions [4]. In the study by Shaffer [3] he found that in some cases, inability to perform basic vector operations is the obstacle. They also found that in many instances, the difficulties are fundamentally conceptual, rather than mathematical.
Studies referred to above suggest that students seem to have their own ways of conceptualizing the vector concept. Despite most students' previous exposure to vector concepts, there are still misconceptions and difficulties related to vectors. These studies suggest that instructors in introductory physics course must give explicit consideration to students' familiarity with the learning of vectors.
The aim of this study was to investigate the causes of unsatisfactory performance on the section involving vectors in basic mechanics. The objective of this study was to examine the ability of students to determine and use qualitatively the magnitude and direction of the vector from knowledge required to draw a free-body diagram. The questions of the assessment test were designed to measure students' basic level knowledge on of vectors; it incorporated a drawing of a free-body diagram, the addition of vectors algebraically and graphically, the expression of vectors in terms of magnitude and direction, the use of trigonometric functions to calculate the direction of the vectors.
All students who participated in this study have obtained Admission Point Score in the range of 50-60% in physical science in their National Senior Certificate (NSC). Most students were enrolled for engineering degree(s), others science degree with physics as their major with mathematics being the other enrolled course, whilst some were not doing mathematics 1.

2. Methodology

A general pre physics skills test of 20 multiple choice questions was given to students in the beginning of the course to check if the students possess the basic knowledge of vectors that will allow them to understand fundamental mechanics topics. Five questions of the 20 multiple choice questions were designed to measure students' knowledge of basic level of vectors, these questions were based on kinematics, algebraic addition of vectors and, expressing vectors in terms of magnitude and direction. In addition similar question including problem solving questions were given to students throughout the course. Also students were finally given familiar questions in the final semester examination in order to determine whether conceptual understanding had been gained.

The tests were administered to 290 four year curriculum physics 1 students from the University of Johannesburg (UJ). Only 266 students wrote the physics skills test (PST) and only 269 managed to write the final exam. The examination was marked by two lecturers and was moderated by the internal examiner from the physics department. Four questions from the exam were chosen for this study, a multiple choice question, a conceptual understanding question and two questions needing a correct free-body diagram and calculation of the direction of motion.

3. Results and Discussion

Initial Analysis

Q8: In the diagram below you are looking at a mass on a frictionless surface from above. Three forces act on the mass as illustrated in the diagram. $F_3 > F_2$ and $F_2 > F_1$. The magnitude of the resultant force acting on the mass will be:

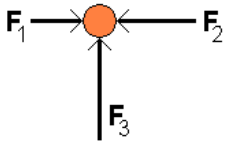

A	B	C	D	E	F	G	H
$\mathbf{F_3 - F_2 - F_1}$	$\mathbf{F_3 + F_1 - F_2}$	$\mathbf{F_3 + F_2 - F_1}$	$\mathbf{F_3}$	Slightly bigger than F_3	$\mathbf{F_1 + F_2 + F_3}$	I do not know the answer because I do not understand the Physics in this question.	I do not know the answer because I do not understand some of the words used in this question

Question used early in the physics skills test investigation about the knowledge of vectors. The analysis of question 8 in this test was specifically investigating the students' knowledge of vector addition and understanding of Newton's second law. This question revealed that 94% of students from high school had misconceptions of fundamental and elementary concepts. Only 6% of the students gave option (E), the correct answer. This indicates that a significant percentage of students do not have a conceptual understanding of the definition of a vector and vector addition. They cannot make use of the Cartesian plane (axes) to determine the magnitude and directions of vectors. Of course, they would have an idea of definition of a vector quantity and knowledge of resultant vector. The histograms of the class tests (vector question) performance are presented in fig.1. Encouraging features of these histograms is the high percentage of the students passing vector question in class test (CT2). It is evident from both graphs that students perform better on the question in CT2 compared to (class test 1) CT1.

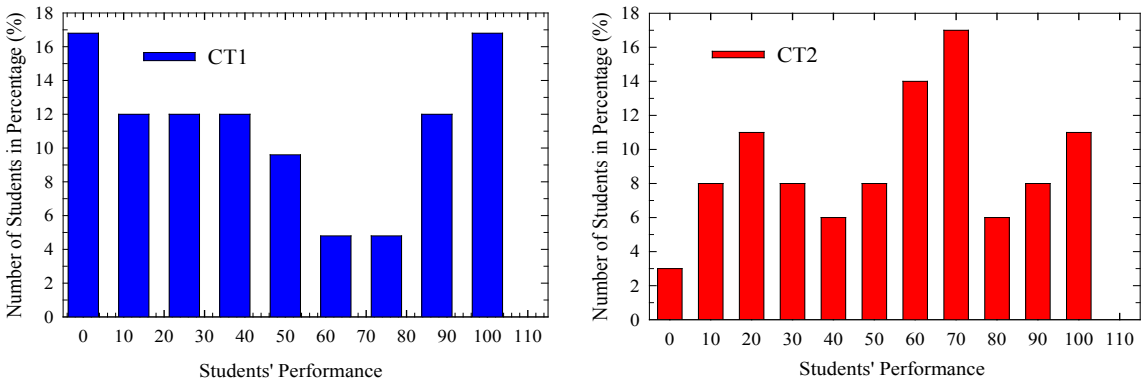

Students seem to be gaining confidence and were expected to do well in the semester tests. This was derived from the observed improvement in the vectors related questions in their class tests results. Surprisingly, observations in fig.2 paint a different picture; the results are very poor as compared to performance in CT2.

Of particular relevance to similar questions given to the students in different assessments in this module, performance in the semester tests reveals that students either just achieved a pass or failed. Even after been given a problem on vectors in every assessment, students had difficulties in drawing the free-body diagram and calculating the direction of acceleration of motion. In fig.4 assessment 3, only half of the students were very successful in answering/drawing the correct free-body diagram and only 82.3% of those successfully answered assessment 4 correctly. It was also observed that in general, many students were not able to draw the correct free-body diagrams and consequently could not resolve vectors in their component form. As a result they could not add or subtract vectors graphically and qualitatively as reflected by students' performance shown in fig.4.

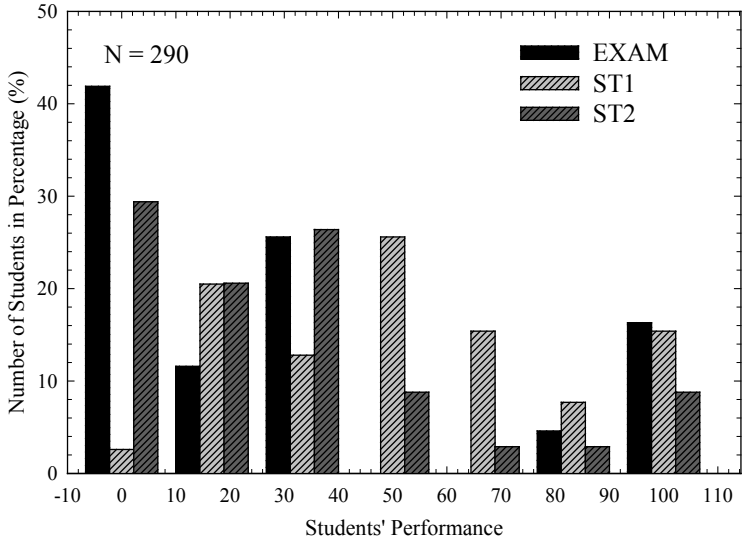

Figure 2: A histogram showing the students' performance versus the number of students in percentage of correct students' responses in respective questions given in different assessments.

A close look at some of vector questions and students responses (%) in figure 3.

Figure 3: Questions used in the assessment 3, 4 & 5. Fig.3 (a) students were asked to draw a free-body diagram before calculating the direction of acceleration of motion. Fig.3 (b) there was no hint given for drawing a free-body diagram before calculating the horizontal acceleration.

A multiple choice question is as follows:

Two vectors **A** and **B** are added together to form a vector **C**. The relationship between the magnitudes of the vectors is given by $A + B = C$. Which one of the following statements concerning these vectors is true?

A. **A** and **B** *must be displacements*.
B. **A** and **B** *must have equal lengths.*
C. ***A*** *and* ***B*** *must point in opposite directions.*
D. ***A*** *and* ***B*** *must point in the same direction.*
E. ***A*** *and* ***B*** *must be at right angles to* each other.

In the above question given to the students in the assessments 1 shown in fig.4 shows that students improved in their conceptual understanding with almost 51% of students giving option (D) the correct answer. Though there is improvement, 49% of students do not have a conceptual understanding of addition of vectors.
With reference to the conceptual question given to students, it is revealed that students gained understanding of addition of vectors and calculation of the resultant vector. The 69.4% of them managed to explain their correct answer, which was positive given that in the early investigation question only 6% of them chose the correct answer.

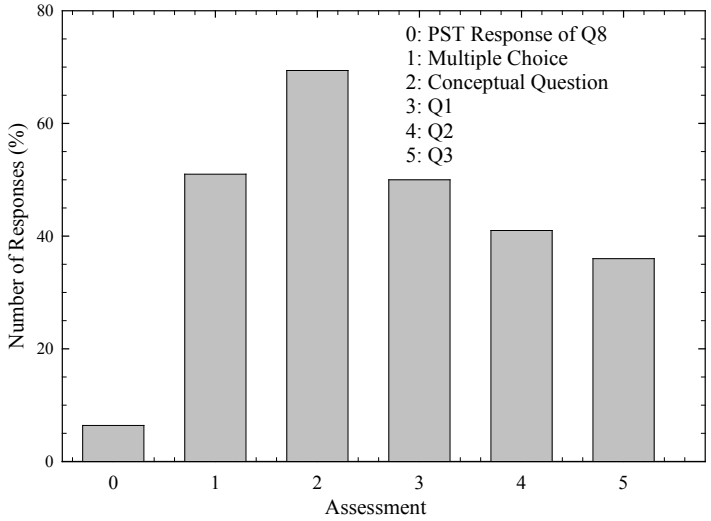

Figure 4: A histogram showing the percentage of correct students' responses in respective questions given in different assessments.

In assessment 3 students were asked to draw a free-body diagram of fig.3 (a) and answer assessment 4 related to assessment 3. It must be mentioned that though almost 50% drew the correct free-body diagram, less than 41% of students assessed managed to answer assessment 4 correctly see fig. 4. Fig.3 (b) was given to students for assessment 5; this question was testing the same skill. In this question students were not guided to draw the free-body diagram before they could calculate the magnitude and direction of acceleration in motion. It was observed that 36% of the students knew that they must draw a free-body diagram and calculated the correct magnitude and direction of motion. In both assessments (4 and 5); some students seemed to be recalling memorized definition of summations of vectors, apparently not understanding how to represent that from the free-body diagram and failed to get the correct magnitude and direction of the vector.

4. Conclusion and Recommendations

In the course taught by the authors, we have made modifications to the content of the course and to the questions that were specifically intended to improve students understanding of vectors in mechanics. Although the degree obtained from the modification and the results of students vary, none of the modifications have been more than moderately successful. One consistent result has been to increase

the fraction of students who attempted answering vector related questions in the exam, to employ the use of free-body diagrams and vectors calculating net force and acceleration of the motion.

This study recommends that some intervention be made early in the year and the amount of time allocated to understanding of basic mechanics concepts be increased because the mechanics concepts are the core in introductory first year physics.

As a result of this investigation, we have become more aware of the degree to which the application of a free-body diagram is a challenge to students. As this study progresses, we hope to learn more about the nature of students difficulties with regards to vectors.

5. Acknowledgements

The authors acknowledge the assistance from the department of physics at large.

References

[1] Knight, R.D. (1995). Vector knowledge of beginning physics students. *The Physics Teacher*.**33**, 74-76.

[2] Poynter A, & Tall, D. (2005). Relating Theories to Practice in the teaching of mathematics.

[3] Shaffer, P.S & McDermott, L.C. (2005). A research-based approach to improving students understanding of the vector nature of kinematics concepts. *American Association of Physics Teachers.* **73** (10), 921-931.

[4] Nguyen, N., & Meltzer, D., (2003). Relating theories to practice in the teaching of mathematics. (*in preparation*).

[5] Mhlongo, M.R. (2011). The pre-knowledge of the physics I students on vectors. *Proceedings of the South African Institute of Physics,* University of South Africa (pp.608-6613).

Curriculum reform – Does it provide the divide between developed and developing countries?

Sam Ramaila, Padmanabhan Nair, Leelakrishna Reddy

Physics Department, University of Johannesburg, Johannesburg

E-mail: samr@uj.ac.za

Abstract Globalisation is an inevitable and inescapable phenomenal reality. Global imperatives dictate the level of growth and development in various emerging economies across the globe. Over the years, many countries embarked upon educational reforms to serve as catalysts for economic development. Given this scenario, this article provides a comparative analysis of secondary education Physics curricula in selected countries with a view to meaningfully evaluate the level of depth up to which each curriculum extends. Analysis of secondary education Physics curricula of selected countries reveals striking distinctive features that serve to provide the structural differentiation with regard to these curricula. In addition, further detailed elucidation on the nature and structural coherence of each curriculum is subsequently provided in order to make sense of any correlation that could be possible between curriculum reform and economic growth of selected countries.

1. Introduction

Curriculum reform has been a key area of concern for both developed and developing countries in a bid to consolidate the structural imperatives that characterise their education systems. While most developed and developing countries have made substantial progress in overhauling their education systems, secondary education in particular remains a weak link in the education chain in many countries [1]. It is against this background that this article unpacks the secondary education Physics curricula of selected countries as its primary focus in order to provide a comparative analysis in terms of distinguishing features.

2. Secondary education reform

Secondary education in the Asia-Pacific region has been characterized by rapid expansion in response to an increasing demand for skilled manpower, economic growth and strong private requirements [1]. Consequently, some of the varied approaches adopted by different countries in this region in developing the structure of secondary education included diversifying the curriculum, financing institutions and student support and assessing student-learning performance. Curriculum reform was the major driving force in the improvement of the quality of secondary education in the Asia-Pacific region. Some of the detailed strategies that were developed to adequately address curriculum reform include the improvement of the quality and scope of vocational education, strengthening science and technology education, developing competence in information technology skills by introducing or expanding the use of information technology in the classroom, as well as focusing on the teaching of a

wide range of cognitive, social and personality skills so as to develop the capacity for flexibility, problem-solving, creativity, initiative and life-long learning [2].

While secondary education reform process in Eastern Europe was largely influenced by political and economic factors, the rules of the game that resulted in good educational outcomes under Communism are changing [3]. In the main, educational change in this region can be described in terms of four key characteristics [4]: (a) depolarization of education (i.e., the end of the ideological control of the system); (b) breaking down of the state monopoly in education by allowing private and denominational schools to be established; (c) increased choices in schooling options; and (d) decentralization in the management and administration of the education system (in particular the emergence of school autonomy).

Although the education systems in Latin America and the Caribbean were characterised by relatively high enrolment rates at the primary and secondary levels during the latter part of the 20th century, there were significant problems with regard to quality and relevance of instruction [5]. In fact, the system was bedevilled by a bimodal distribution of enrolment [6], which provided a skewed picture in terms of both school and university attendance and completion. The revamping of secondary education in this region primarily focused on aspects such as curriculum structure, teacher training, student evaluation, development of technological infrastructure and management [7].

Arab States also undertook a series of educational reforms to overhaul their education systems. While educational reform in the Arab States was previously aimed at the elimination of high illiteracy rate, the education reform policies have of late been geared towards quality and equity in education [8]. In addition, educational reforms in this region reflected different sources of funding for education [9]. This scenario is in stark contrast with educational reform initiatives in other countries.

Secondary education reform in Sub-Saharan Africa has also been an area of increased focus over many years. The quality of education in this region was eroded by a skewed provision of resources in favour of basic and higher education at the expense of secondary education [10]. In response to this predicament, several African countries embarked on secondary education reforms and South Africa is no exception. Suffice to say that substantial growth in secondary education in this region was characterized by a general shift in emphasis from vocational training to general secondary education [11].

3. Theoretical framework

Analysis of secondary education Physics curricula of selected countries in this article is underpinned by a Product-Process Framework [12] provided in Figure 1 below. This framework consists of three continuums. The first continuum,[Product (Dimension 1): Broad conceptual content versus Descriptive factual content], is used to identify the organisation of content. The second continuum, [Product (Dimension 2): Pure content versus Socially applied content], is used to identify the nature of Physics content. The third continuum, [Process dimension: Intellectual process skills versus Practical process skills], is used to identify the skills valued in the Physics curricula. Data was sourced from policy documents characterising education reforms in the respective countries involved in this inquiry.

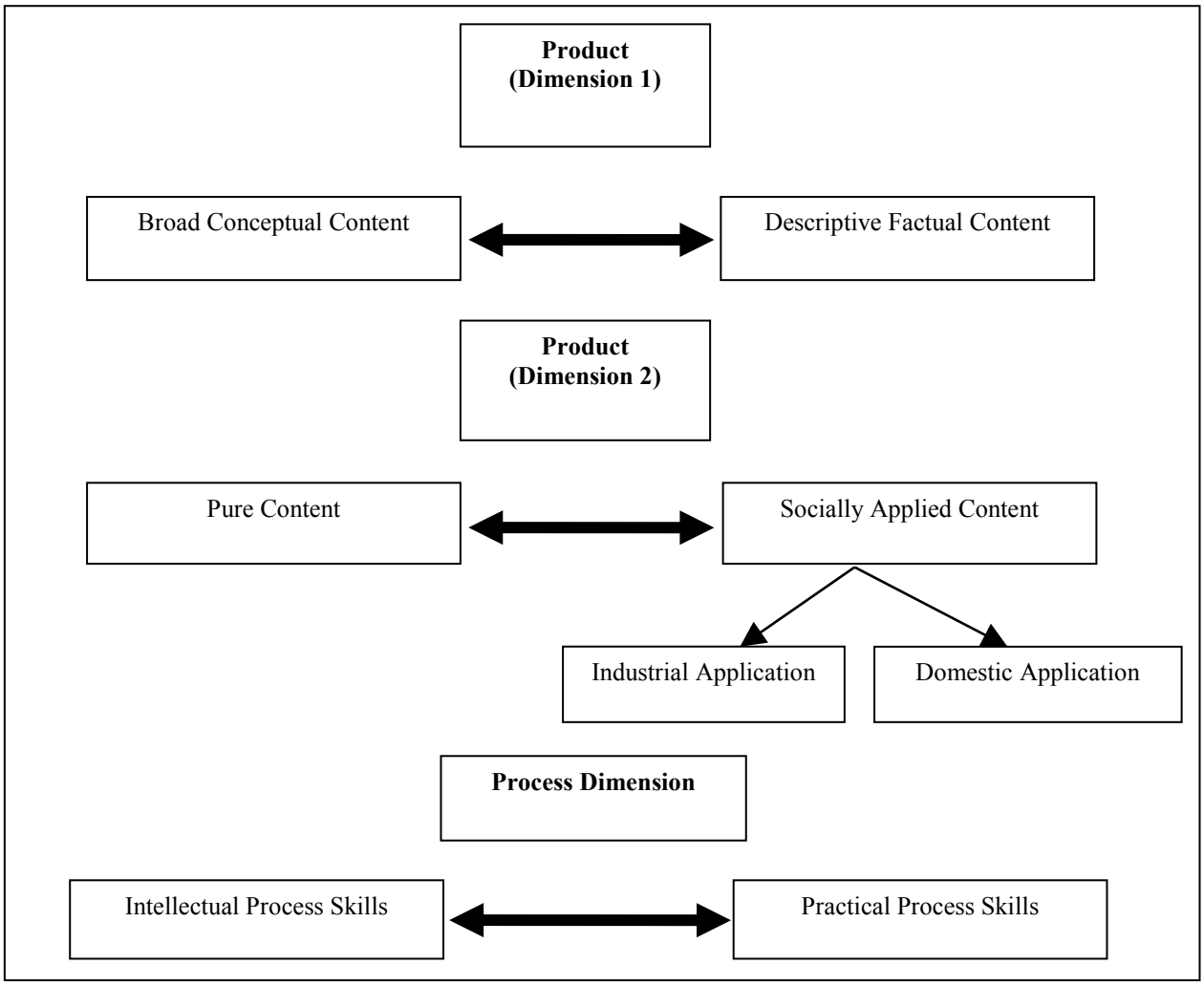

Figure 1. Bailey's (1978) Product-Process Framework.

4. Analysis of secondary education Physics curricula of selected countries

The countries selected for comparative analysis of secondary education Physics curriculum are India (Asia- Pacific), Ghana and South Africa (Sub-Saharan Africa). This comparative analysis is motivated by the fact that both India and Ghana made significant strides in terms of sustainable economic growth and overall development.

4.1. South Africa

The structure of the curriculum content in relation to the South African secondary education Physical Sciences curriculum [13] is depicted in Table 1.

Table 1. South African secondary education Physical Sciences curriculum

STRUCTURE OF THE SYLLABUS: SOUTH AFRICAN SECONDARY EDUCATION PHYSICAL SCIENCES CURRICULUM
GRADE 11 AND GRADE 12
Mechanics Waves, Sound and Light Electricity and Magnetism Matter and Materials Systems Chemistry Change Chemistry

The South African Physical Sciences curriculum seeks to prepare learners for future learning, specialist learning, employment, citizenship, holistic development, socio-economic development and environmental management by developing competences in the following three focus areas: scientific inquiry and problem solving in a variety of scientific, technological, socio-economic and environmental contexts (Intellectual Process Skills); the construction and application of scientific and technological knowledge(Practical Process Skills); and the nature of science and its relationship to technology, society and the environment (Industrial Application and Domestic Application) [13].

The South African Physical Sciences curriculum is characterised by six core knowledge areas: two with a Chemistry focus – Systems and Change; three with a Physics focus – Mechanics; Waves, Sound and Light; Electricity and Magnetism; and one with an integrated focus – Matter and Materials [13].A major structural deficiency of the South African secondary education Physical Sciences curriculum is that it does not make provision for Physics and Chemistry to be taught as separate components despite repeated calls to do so. While the curriculum provides opportunities for learners to perform practical work, this is not augmented as a logical imperative by a clear practical assessment process to evaluate the practical skills acquired by the learners.

4.2. India

The structure of the syllabus pertaining to the Indian secondary education Physics curriculum [14] is illustrated in Table 2 below.

Table 2. Indian secondary education Physics curriculum

STRUCTURE OF THE SYLLABUS: INDIAN SECONDARY EDUCATION PHYSICS CURRICULUM	
CLASS XI (THEORY)	**CLASS XII (THEORY)**
Physical World and Measurement Kinematics Laws of Motion Work, Energy and Power Motion of System of particles and Rigid Body Gravitation Properties of Bulk Matter Thermodynamics Behaviour of Perfect Gas and Kinetic Theory of gases Oscillations and Waves	Electrostatics Current Electricity Magnetic effect of current and Magnetism Electromagnetic Induction and Alternating current Electromagnetic Waves Optics Dual Nature of Matter Atoms and Nuclei Electronic Devices Communication Systems

In terms of broad conceptual content, the curriculum provides more emphasis on basic conceptual understanding of the content through detailed description of factual content. Furthermore, the curriculum exposes the learners to different processes used in Physics-related industrial and technological applications (Industrial Application). The Domestic Application component of the curriculum is not clearly articulated though. The curriculum provides opportunities for Intellectual Process Skills as it promotes the development of process-skills and experimental, observational, manipulative, decision making and investigatory skills in the learners. In terms of Practical Process Skills, every learner is afforded the opportunity to perform 10 experiments (5 from each section) and 8 activities (4 from each section) during the academic year. In addition, two demonstration experiments must be performed by the teacher with participation of learners with learners maintaining a record of these demonstration experiments. This is augmented by a Practical Examination based on a clearly defined evaluation scheme. The striking characteristic feature with regard to the Indian secondary education Physics curriculum is that Physics and Chemistry are treated as two separate components and this is in stark contrast to the South African secondary education Physical Sciences curriculum. On close scrutiny, the level of depth of the Indian secondary education Physics curriculum reveals that Physics topics taught at university in South Africa are covered at secondary school in India.

4.3. Ghana

Ghana represents in this particular context West African countries which have historically embraced the British A Level and O Level Physics curricula [15]. The structure of the syllabus pertaining to the A Level and O Level Physics curricula is provided in Table 3 below.

Table 3. A Level Physics and O Level Physics

STRUCTURE OF THE SYLLABUS	
A LEVEL PHYSICS	**O LEVEL PHYSICS**
General Physics Newtonian mechanics Matter Oscillations and waves Electricity and magnetism Modern Physics Gathering and communicating information	General Physics Newtonian mechanics Mass, Weight and Density Turning Effect of Forces Deformation Pressure ENERGY AND THERMAL PHYSICS Temperature Thermal Properties of Matter Kinetic Model of Matter WAVES Light Electromagnetic Spectrum Sound ELECTRICITY AND MAGNETISM Magnetism and Electromagnetism Static Electricity Current Electricity D.C. Circuits Practical Electricity Electromagnetism Electromagnetic Induction Introductory Electronics Electronic Systems ATOMIC PHYSICS Radioactivity The Nuclear Atom

It is appropriate to indicate at the outset that the A Level and O Level Physics curricula make provision for a Practical Assessment (Practical Process Skills) designed to assess the learner's competence in those practical skills which can realistically be assessed within the context of a formal test of limited duration. The learners pursue a comprehensive course in practical Physics throughout the time during which they are being taught the theoretical content. In line with broad conceptual content imperatives, the curriculum provides a thorough introduction to the study of Physics and scientific methods through detailed description of factual content. In addressing the need for Intellectual Process Skills, these curricula make provision for the development of skills (such as accuracy and precision, objectivity, integrity, the skills of inquiry, initiative and inventiveness) and abilities that are relevant to the safe practice of science and to everyday life (Domestic Application).In addition, these curricula also strive to enable learners to become confident citizens in a technological world (Industrial Application) and to take an informed interest in matters of scientific importance such as the promotion of the use of Information Technology (IT) as an aid to experiments and as a tool for the interpretation of experimental and theoretical results(Practical Process Skills). The A Level and O Level Physics curricula cover the curriculum content in sufficient depth far superior than the South African secondary education Physical Sciences curriculum does. As is the case with the Indian secondary education Physics curriculum, the A Level and O Level Physics curricula make provision for Physics and Chemistry to be taught as two separate components.

5. Economic growth levels of selected countries

Economic considerations paint a rather interesting picture with regard to the countries selected. More specifically, India's average quarterly gross domestic product (GDP) growth rate stood at 7.45% during the period 2000-2011 [16]. In addition, the per capita GDP growth rate doubled from 3.7% (1980-1991) to the current 7.3% [17]. India's real GDP growth averaged 7.3% per annum between 2000-2001 and 2007-2008 [18]. Another remarkable feature is that India's annual average GDP growth stood at 6.6% during the period 1990-2010 [18]. Ghana posted an average annual GDP growth rate of 5% over the past ten years [19]. South Africa's average quarterly GDP growth rate stood at 3.32% during the period 1993-2011 while its average annual GDP growth rate was 3.26% during the period 1994-2011 [16]. The average real GDP growth rate was 3.0% during the period 1995-2004 [20]. Clearly, South Africa's economic performance was far below par during the period under review as compared to India and Ghana. South Africa faces a real challenge to generate acceptable levels of economic growth as an integral part of the global community of nations. Can South Africa overcome this critical challenge without making significant reforms to curriculum particularly the Physical Sciences National Curriculum Statement? There appears to be a healthy correlation between economic growth level and the structure of the secondary education Physics curricula in India and Ghana and it is indeed imperative for South Africa to follow suit.

6. Recommendations

All things considered, South Africa has a moral obligation to harness its potential in order to develop and strengthen its competitive edge in the global arena. This can possibly be accomplished through epoch-making and crucial steps such as undertaking significant and far-reaching curriculum reforms in a bid to develop the much needed human capital for meaningful competitive advantage. Efforts at beneficiation of available mineral resources in South Africa can hardly yield any positive results given the nature of the curriculum particularly the inherently shallow secondary education Physical Sciences National Curriculum Statement when viewed against similar curricula elsewhere.

7. Conclusion

The level of development in the countries involved in this inquiry appears to be a function of the quality of education reforms. It is imperative for South Africa in particular to consolidate its education reforms in order to realise meaningful human capital development.

8. Acknowledgements
The authors would like to express sincere gratitude to colleagues in the Physics Department at the University of Johannesburg for providing assistance during the course of this undertaking.

9. References

[1] National Institute for Educational Research (NIER). (1995). *Reorienting Secondary Education in Asia and the Pacific*. Report of a regional seminar.
[2] Byron, I. (1999). *An Overview of Country reports on Curriculum Development in South and South-East* Asia. Available: http://www.ibe.unesco.org/National/China/chicoune.htm.
[3] World Bank. (2000). *Improving Education and Reforming Education Systems in Central and Eastern Europe and the Commonwealth of Independent States*. Available: http://www.worldbank.org/eca/eca.nsf.
[4] Cerych, L. (1997). Educational reforms in central and Eastern Europe: Processes and outcomes. *European Journal of Education*, **32**(1), 75-96.
[5] Torres, C.A. & Puiggrós, A. (1995). The state and public education in Latin America. *Comparative Education Review*, **39** (1), 1-27.
[6] Arnove, R.F., Torres, A., Franz, S., & Morse, K. (1997). A political sociology of education and development in Latin America.In Y.W. Bradshaw. (Ed.), *Education in Comparative Perspective*. New York: E.J. Brill.
[7] Inter-American Development Bank (IDB). (2000). *Reforming Primary and Secondary Education in Latin America and the Caribbean: An IDB Strategy*.
[8] Eeghen, W. (2000). *Education and Economic Growth in Middle, East and North Africa.* Available: http://www.worldbank.org/wbi/mdf/mdf1/edecmen.htm.
[9] World Bank. (1997). *World Development Report*. Washington, DC: World Bank.
[10] UNESCO. (1999). *Reforming Secondary Education Consortium*. Available: http://www.unesco.org.
[11] World Bank. (2000). *World Education Report 2000*. Available: http://www.worldbank.org.
[12] Bailey, R.F. (1978). *A Study of Secondary School Chemistry Courses in Victoria, 1932 – 1972*. Unpublished M.Ed Thesis, Monash University, Melbourne.
[13] Department of Education (DoE). (2003). *National Curriculum Statement Grades 10-12 (General) Physical Sciences.* Government Printer: Pretoria.
[14] Department of School Education & Literacy. (2012. *Schools Curriculum*. India
[15] Cambridge International Examinations. *University of Cambridge syllabi for A-Level and O-Level Physics*. Cambridge, United Kingdom
[16] http://www.tradingeconomics.com
[17] http://www.OECD.org
[18] http://www.Eastasiaforum.org
[19] http://www.Ghanaembassy.org
[20] http://www.ber.ac.za

An informal teaching of light and lasers through the CSIR-NLC PULSE programme

L. Shikwambana, T. du Plooy and P. Motalane

CSIR National Laser Centre, P.O Box 395, Pretoria 0001, South Africa

Email: lshikwambana@csir.co.za

Abstract. In this paper we report on the outreach activities taking place at the CSIR-National laser centre. The centre has an outreach programme called PULSE which focuses on creating laser awareness. The awareness is carried out in a relaxed manner and the presentations done in an informal way. Visual stimulation is the most used mechanism to give the teaching. Here we also report on the method we use to give the presentations.

1. Introduction

PULSE stands for Public Understanding of Laser Science and Engineering. This is a programme that is run at the CSIR-National laser centre (NLC). The objectives of the programme are: (1) to create awareness to the students, learners, teachers and the general public about the state of photonics in South Africa and the world. (2) To teach learners in an informal way about light and lasers. (3) To teach learners to follow their dream of innovation, and the excitement of science. The programme was initiated to help learners understand the principles of light and lasers better so they can see the various applications of these concepts in real life. To also show learners the various careers and opportunities there are in laser science and engineering.

The PULSE team usually conducts the presentations at national science events such as Scifest Africa, Sasol TechnoX and Science-tube to name a few. But we also visit schools and host schools at the NLC. The aim of the programme is not to teach learners aboutlight and lasers, as this done at schools and universities, but to show the learners visually and practically the laws of light and the principle operation of a laser.

In this paper we discuss the impact the programme has made over the years and we also discuss the method we use to present the concepts of light and laser.

2. Background

The PULSE programme was established in 2002 at the CSIR-NLC to create awareness to laser related activities both nationally and internationally. The CSIR-NLC saw that learners and students lacked knowledge on photonics activities that are happening worldwide and hence took it upon themselves to convey the message since they are already in the discipline. Our staff that gave the talks to the students and learners used to be our engineers or scientists. But recently we have found that our audience relate better with our student researchers and engineers because of the age difference. At the moment our student researchers are the ones driving this programme.

With more of the student researchers helping out we have seen an increase in the numbers of learners reached by the programme. As can be seen from Figure 1(a), there was an increase in 2008 to 2009 in the number of learners reached. From 2009 to 2011 a steady number of learners has been reached. The number of learners shown in Figure 1(a) includes the number of learners reached by the science centres we support. Figure 1(b) shows the estimated number of learners reached by only the PULSE team.

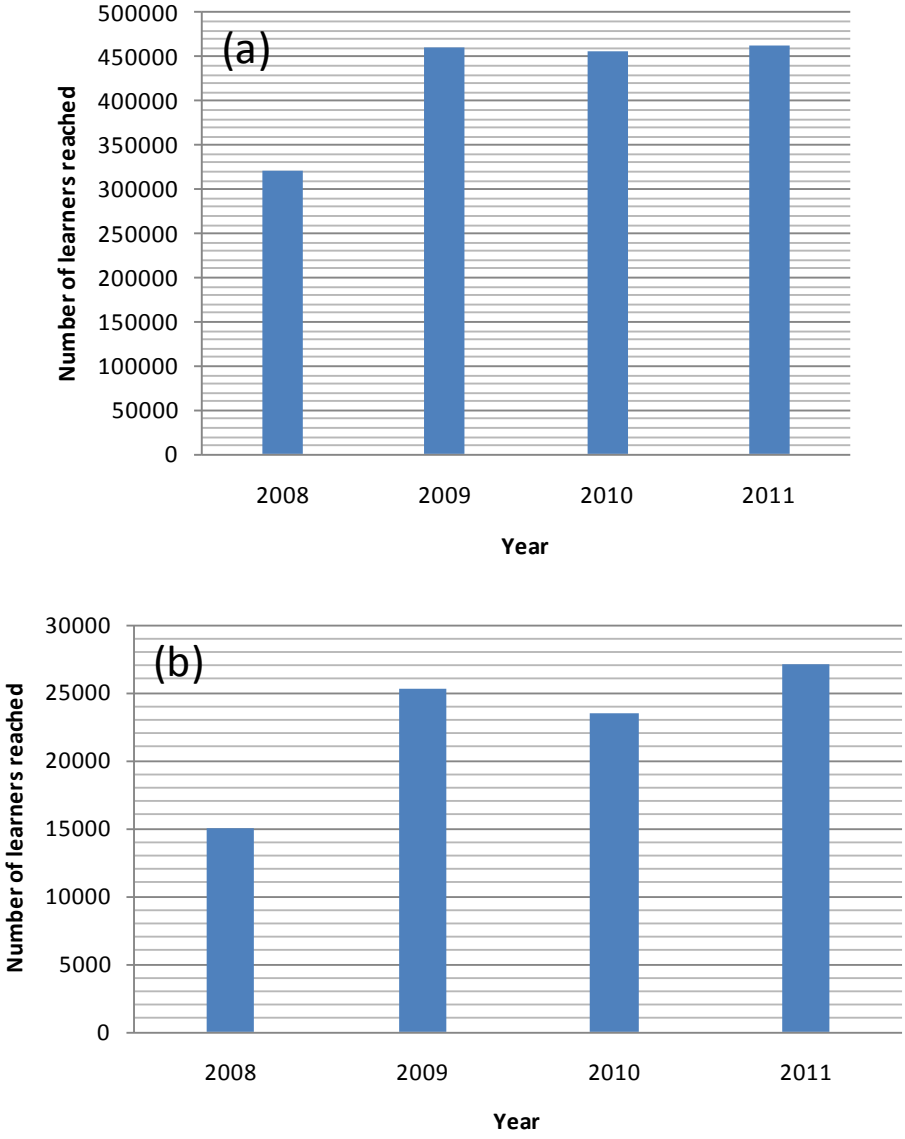

Figure 1. Graphs showing the impact of the PULSE programme (a) the number includes learners in science centres supported by PULSE and (b) excludes the number of learners from the science centres.

3. Method

The majority of the content used in our presentation is light and laser related. We use a lot of videos and diagrams to illustrate concepts. Some of the light concepts covered by our presentation include:

- Laws of light: reflection, refraction, dispersion and diffraction
- Sources of light
- The nature of light

Under the heading 'Laws of light' we show a video on each of the laws and give a real live scenario on where this is found. As a way of example if we where to discuss refraction, we would first define what refraction is, Figure 2(a), then we would show a video of refraction, Figure 2(b), and show a picture where one could find this laws in everyday live, Figure 2(c).

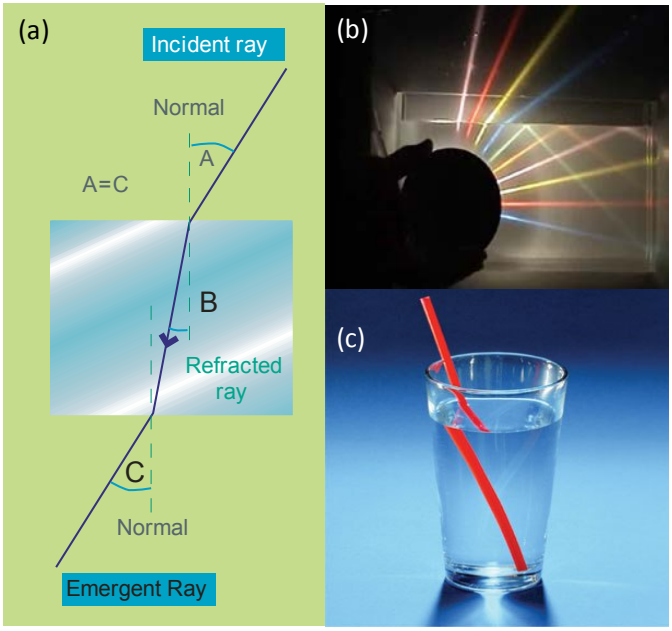

Figure 2. A picture illustrating how the concept of refraction is taught through the PULSE programme: (a) Defining the concept refraction, (b) a video showing how refraction occurs and (c) an everyday example of refraction.

For the sources of light part of the presentation we usually ask the learners to tell us where we get light from. This is the most interactive part of the talk as we give out prices to learners who give the correct answers or those really close to the correct answer. From the presentations we have given in the past we have seen that after this part of the presentation learners tend to be freer and start asking and answering questions. So for this reason we decided to start with this part of the presentation to make the learner more comfortable early in the presentation.

In the nature of light part of the presentation we discuss the dual nature of light. We tell the learners that light behaves both as a wave and as a particle. We also explain to them that particles of light are called photons and these photons have an energy described by the equation

$$E = hf \tag{1}$$

where E is the energy, h is Planck's constant and f is the frequency of the photon.

After we finish discussing light, we then move on to discuss lasers. Our layout of this part is as follows:

- What is a laser
- Spontaneous emission
- Stimulated emission
- How does a laser work
- Laser applications

We first define what a laser is and tell learners that the word laser is an acronym. We also tell learners that in order to understand how a laser works they need to know the Bohr's model of the atom and the

concept of spontaneous emission. So we start by discussing how spontaneous emission occurs, Figure 3(a). Then we move on to discuss stimulated emission, Figure 3(b). Both these concepts are discussed using animations.

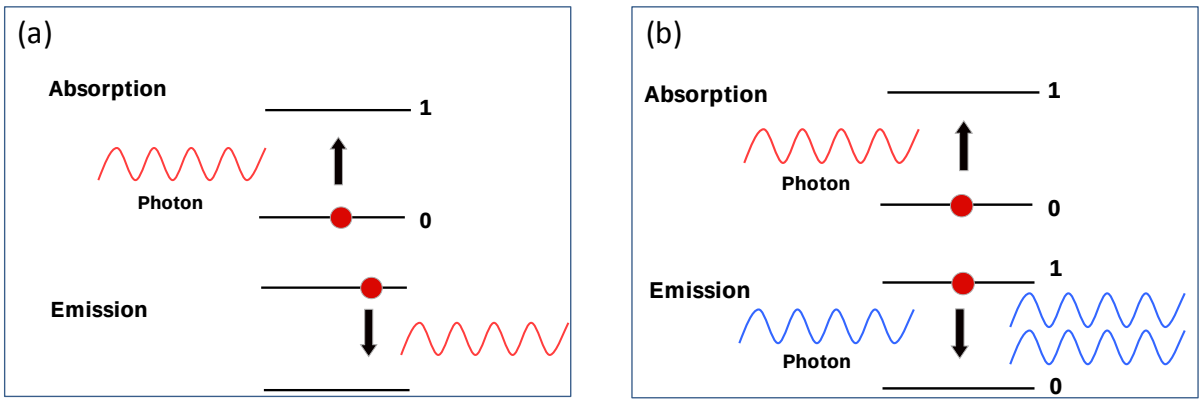

Figure 3. A diagram illustrating (a) spontaneous emission and (b) stimulated emission.

We explain how a laser works by showing the learners a video animation we developed. The animation basically shows the three components needed to build a laser. In the animation the components are put together in a particular way to produce a functional laser. Figure 4 shows the components needed to build a laser.

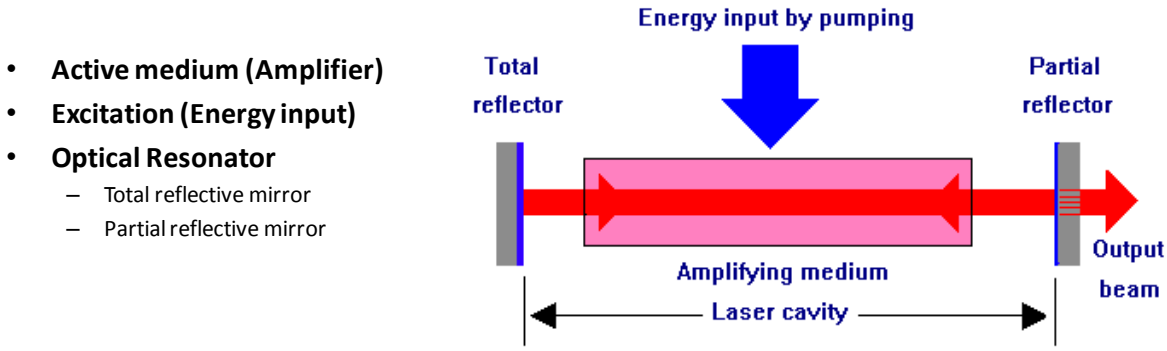

Figure 4. A diagram showing the three components need to build a laser. These components are an active medium, input energy and an optical resonator.

Before we show the different laser applications we first show them the main differences between laser light and normal white light. Figure 5 is a diagram we use to show these differences.

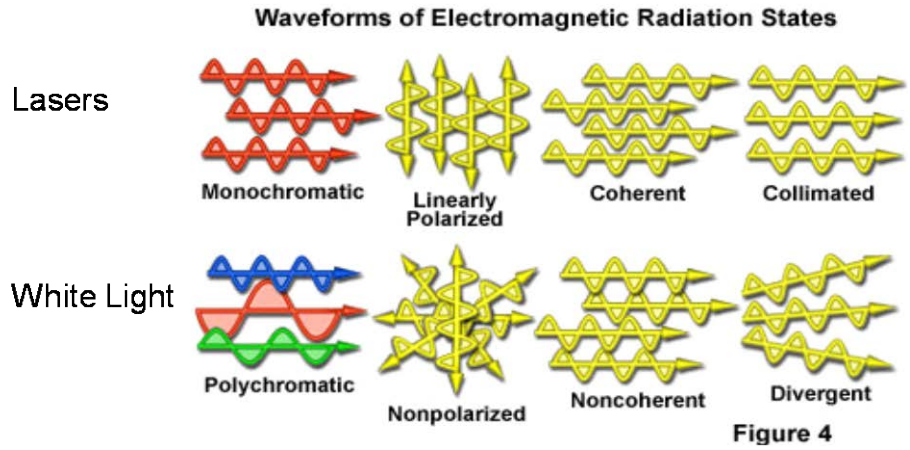

Figure 5. A picture showing the differences between white light and laser light.

When discussing the different laser applications we only show videos. The applications we discuss are in military, industry, medicine, commercial and research. As a way of example, when we discuss industrial applications we will show videos of cutting, drilling, welding, marking and laser machining. We also show them really samples that we produced by these techniques.

4. Discussion and conclusion

The aim of our presentation is to stimulate interest to the learners in the field of photonics. We hope to achieve this by showing visually and by the learners seeing for themselves what light and lasers can do. The feedback from the learners has been positive as most of them say the presentation has made them understand some concepts better. The only down side to this presentation is that it mostly caters for grade 11 and 12 learners. Although some grade 10 learners can follow, most of them say they have not covered this topic (of light) in school. When it comes to the laser application part everyone enjoys it and can follow as it is just videos. They are all amazed at the different things lasers can be used for, even things they use in their everyday life such a dvd player.

Based on the feedback we get from the learners we think our programme is making a difference in helping learners to understand some concepts of light. We would however like to reach the younger grades as well, so we are at the working on a presentation to cater of them.

5. Acknowledgement

PULSE will like to thank the students and the researchers at the CSIR-National Laser Centre for taking their time and helping out with the various outreach activities.

Is Foundation Provision the solution to the first year students' performance?

B M Sondezi, P Molefe

University of Johannesburg (UJ), P.O. Box 524, Auckland Park, 2006

Email: bmsondezi@uj.ac.za

Abstract: An introduction of Foundation Provision Programme (FPP) in the physics content of first year physics at the University of Johannesburg (UJ) has shown an observable improvement in the performance of the students. It was observed that one of the major sources of difficulty experienced by students in understanding physics concepts were due to the lack of mathematical skills which are not fully developed as they exit Further Education and Training (FET) level. An introduction of the mathematical concepts within the physics content at the beginning of main physics syllabus at UJ for a four-year programme was observed to produce improved results. However, at the beginning of 2012 the content of the first section of FPP was introduced within the physics content as compared to what was done and reported in the previous year. This simultaneous assimilation of both physics and mathematical basic concepts was observed and analyzed and the recommendation of the better method is suggested based on the students' performances in the first term of 2011 and 2012, respectively.

1. Introduction

Science, Engineering and Technology (SET) have become essential in the development of the country in all its facets. It has been observed over the past few years that students entering university for degree studies in their respective fields experience considerable level of difficulty. Inadequate understanding of basic mathematics and physics concepts has been identified as a critical deficiency characterizing the performance of SET first year university students. In an endeavour to bring a necessary intervention to the understanding of the basic concepts related to mathematics and physical science, a four year program at the UJ introduced topics that focus on the fundamentals of these courses. As it was identified in the previous years that in understanding physics, students lack basic mathematics, therefore the Foundation Provision Programme (FPP) was established in the year 2010 (Sondezi-Mhlungu, 2011). FPP tried to bridge the gaps between the high school basic concepts and those expected to be well understood when entering first year of university. In 2010, the first three months (term) of the first semester (first half of the year) was dedicated towards bringing about these necessary basic mathematical concepts and techniques needed in solving physics related problems. In 2011, the duration was increased from a term to a semester with an aim of increasing the performance of the students and the understanding of the physics concepts thereof. It was observed that the results did not show any significant difference, as they showed comparable averages of students' performances at the end of the semester. It was then decided that for the year 2012, FPP would be offered in a manner that the focus will be more on the physics topics. Basic mathematics was still

offered in the context of physics. The pace was retained to be as slow as possible to allow simultaneous assimilation of both mathematics and physics concepts.

Definition of phrases and terms

Semester Mark: Contribution of all the assessment marks obtained by a students in one semester. This mark comprises of all assessments undertaken in a semester, that is, the combination of class tests, tutorial tests, homeworks and practical mark.

Average Module Mark: Final mark obtained after the contribution of the semester mark and the exam mark.

Module Pass Rate: This is the percentage obtained by considering the number of students who participated in a given examination. The total number of students passing the exam divided by the number of students allowed to write the exam, gives a pass rate of that particular group.

Throughput: This is the percentage of the number of students who passed the module divided by the total number of students who initially registered for the course.

2. Methodology

The four year degree program at UJ sees the enrolment of various groupings of students; ranging from pure BSc. students, BEng. students and BOptom. students. The physics FPP for 2012 covered basic mathematics concepts in physics contexts, that is, straight line graphs whereby these were taught in the context of graphs of motion, position versus time graphs, velocity versus time graphs and other associated concepts. Basic trigonometry was used in the context of understanding vectors and forces. Students were taught the technique of resolving vectors from the understanding of trigonometric ratios. Continuous assessment was monitored to establish their understanding and the build up towards the exam. Other topics covered in this module were motion in two dimension (building up from the understanding of one dimension, linear graphs and related concepts); Newton's laws; including the proper drawing of free-body diagrams; work and energy and impulse and momentum, waves and sound. After the implementation of these interventions in the four year degree program, a closer look at the performance of the students with the aim of assessing the program was undertaken. These observations of the students' performance in their first semester from 2010 to 2012 was looked at and the findings are listed in tables 1, 2 and 3.

3. Results and discussion

Table 1 contains the information regarding the overall picture of the students, from the students' intake into the module, the students allowed to write the exam, the module pass rate and throughput numbers of the module. The information in this table show that 90%, 89% and 95% of the students qualified to write the exam in the year 2010, 2011 and 2012, respectively. It is important to mention that a student at UJ, requires only 40% of the theory mark and 50% of the practical mark to be allowed into the exam. Table 2 lists the outcomes of the students' marks outputs as analysed from the students' progress from the time of enrolment to the final exam written. Despite the fact that almost equal percentage of students qualified to write an exam in 2010 and 2011 (≈ 90%); we observe the difference in the exam pass rate (59% and 64% obtained in 2010 and 2011, respectively). This

difference can be attributed to both the content and duration of FPP (one term in 2010 and a semester in 2011). This therefore suggests that, time for simulating the content learnt is of utmost importance for the proper learning of the content. Although the exam pass rate of students in 2012 is even much lower as compared to those obtained from two previous years, we still observe exactly the same throughput (67%) as obtained in 2011. This is an indication that, incorporating mathematics suitable for the understanding of Physics concepts was more relevant than to teach pure mathematical concepts away from Physics.

Table 1: Mark groupings of students' performances in the years 2010, 2011 and 2012.

	2010	**2011**	**2012**
Students in module	174	481	306
Students admitted to the exam	156 (90%)	428 (89%)	290 (95%)
Students refused admission to the exam	18 (10%)	53 (11%)	16 (5%)
Students who attended exam	155 (89%)	418 (87%)	269 (88%)
Number of absentees from exam	1 (0.6%)	10 (2.1%)	21 (7%)
Students who passed exam	92 (53%)	268 (56 %)	139 (5%)
Students who passed the module	108 (62%)	324 (67%)	205 (67%)

Table 2: Mark groupings of students' performances in the years 2010, 2011 and 2012; data represented in percentage.

		2010 (%)	**2011 (%)**	**2012 (%)**
1	Average semester mark	57	54	59
2	Average final exam mark	52	54	50
3	Exam pass rate	59	64	52
4	Average module mark	52	50	52
5	Module pass rate	70	78	76
6	Throughput	62	67	67

This consistency in the throughput (in 2011 and 2012) is as a result of the average semester mark of the year 2012 is 59%; which is a bit higher than those obtained from the other two years whilst keeping the exam mark comparable with those in the previous years. It is rather important to note that the module pass rate obtained from the years 2011 and 2012 is $\geq$ 70% (obtained in 2010) which is a good indication of the success of the program. The minimum of 70% obtained in 2010 as opposed to 78% and 76% obtained in 2011 and 2012, respectively, is achieved due to time spent in the program (term (2010) and semester (2011 and 2012)). The histogram in Figure 1, graphically represents these data and it is clear that there is a correlation between the duration of FPP (three months) and the performance of the students. The introduction of mathematical concepts within the physics context are presumed to be beneficial towards the understanding of the physics at this level. This is an indication that pure basic mathematics concepts (which initially involved pure algebra and basic trigonometry) are not a direct necessity in bringing the understanding of the physics concepts, but a strategy of incorporating necessary mathematics within the physics content are a necessary tools to tackle physics

related problems. Despite the difference in the throughput and the module pass rate obtained in respective years, it is observed that the average final exam mark (≈ 52%) and average module mark (≈ 50%) are constant throughout this three year duration.

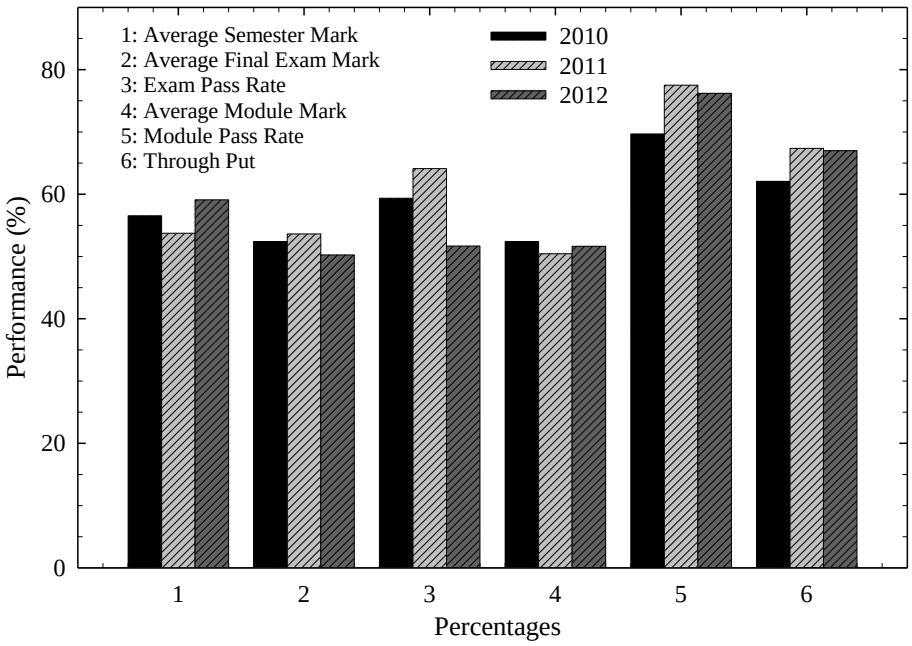

Figure 1: A histogram representing students' marks distribution in percentages of the total contribution towards students' promotion, for 2010, 2011 and 2012, respectively.

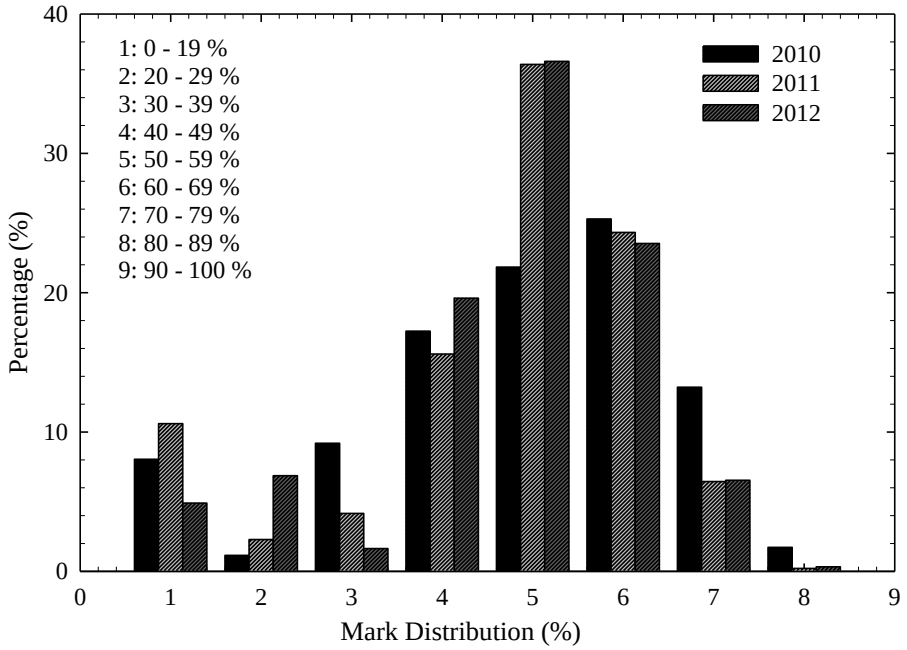

Figure 2: A histogram representing students' marks distribution for 2010, 2011 and 2012, respectively.

Table 3: Distribution of students' performance in the final examinations during the years 2010, 2011 and 2012; data represented in percentage.

		2010 (%)	**2011 (%)**	**2012 (%)**
1	0-19	9	11	5
2	20-29	2	2	7
3	30-39	10	4	2
4	40-49	17	16	20
5	50-59	21	36	37
6	60-69	25	24	24
7	70-79	14	6	7
8	80-89	2	0	0
9	90-100	0	0	0

It is of ultimate importance to determine the distribution of the final performance of the students in these years. A mark distribution of the performance of students at the end of the module; is listed in Table 3 and graphically represented in the form of a histogram in Figure 2.

The distribution of 2010 performance is seen to be more towards lower percentages as compared to the other two following years (2011 and 2012). Almost 38% of the students in 2010 obtained less than a pass mark (50%), 33% of these in 2011 and 34% of students got less than a pass mark in 2012. Although there is a significant difference in these percentages of the students passing the module, between the 2010 and (2011/2012) percentages, the average marks obtained in these years are almost similar (50%). This suggests that the average marks cannot be an accurate indicator of the performance of the students in terms of the module pass rate and the throughput.

4. Conclusion and Recommendations

The results across the two groups (2011 and 2012 groups) were very similar. These observations lead to the conclusion that students enrolling for Physics as part of their courses, need some basic mathematical skills. For Physics module(s), these skills must be incorporated within the course itself. This was established from the comparison of the 2011 and 2012 results. It was revealed that teaching mathematics outside the context of Physics does not give better results, instead the results are similar to the results where these concepts were learnt within the Physics concepts. This programme has revealed that students get a chance to assimilate necessary concepts over some time and they gain confidence in solving Physics related problems. The results obtained in 2010 indicates that the students' performance is a bit lower due to the lack of the treatment of basic concepts which incorporate mathematical skills and Physics related problem solving skills. The time spent in making sure that students grasp these concepts is very important.

This study recommends that, some intervention be made early in the year and the amount of time allocated to understanding of basic mechanics concepts be increased because the mechanics concepts

are the core in introductory first year physics. We hope that the recommendations will enhance maximum pass rate and throughput and hence more students will enrol for physics in the second semester of their first year.

5. Acknowledgements

The authors acknowledge the assistance received from the members of Physics Department at University of Johannesburg.

References

[1] Sondezi-Mhlungu B M and Molefe P, Foundation Provision: Any Difference in Student's Performance? (2011) *56th Annual Conference of South African Institute of Physics Proceedings.*

Division F – Applied Physics

Effects of impurities and defects on the performances of synthetic diamond crystals when used as radiation sensors for medical applications

N Ade[1,3], T L Nam[1] and S H Mhlanga[2]

[1]School of Physics, Radiation and Health Physics Unit and DST/NRF Centre of Excellence in Strong Materials, University of the Witwatersrand, Private Bag 3, Wits 2050, Johannesburg, South Africa.
[2]Department of Radiation Sciences, Division of Medical Physics, Charlotte Maxeke Johannesburg Academic Hospital, Private Bag X39, Johannesburg, 2000, South Africa.

E-mail: leroinicholson@yahoo.ca

Abstract. Diamond is attractive for medical applications due to its remarkable dosimetric properties. The dosimetric performance of a diamond crystal to radiation is however well recognised to be dependent on the types of defects and impurity levels within the crystal, and to date their influence on the performance of synthetic diamonds when subjected to low-energy X-rays and high-energy electron therapy beams has not been fully investigated. This study was therefore aimed at evaluating the dosimetric performances of synthetic diamonds when used as radiation sensors for both radiation types by highlighting some of the defect/impurity types that either enhance or degrade detector performance in order to select suitable crystals. The sensitivities of synthetic diamond crystals of various types (HPHT and CVD diamonds of optical grade (OG) and detector grade (DG)) were evaluated and compared based on their defect/impurity levels. The results of the study showed that the HPHT and OG diamonds had much higher levels of single substitutional nitrogen (N_s) impurities and were less sensitive compared to DG diamonds. The sensitivities of the diamond crystals to radiation were largely influenced, in particular by N_s impurities which act as recombination centres and degrade crystal performance in this study suggesting that N_s levels ought to be the foremost criteria used in the selection of a sensor material. As DG CVD diamonds have very low N_s impurities such crystals should be the radiation sensors of choice for medical applications.

1. Introduction

Diamond is attractive for medical applications due to its unique physical and dosimetric properties such as bio-compatibility, high sensitivity, high spatial resolution, non-toxicity, and more cost effective as it was shown in a previous study [1] that a single synthetic diamond probe could perform effectively in both low-energy X-rays and megavoltage electron beams. The dosimetric performance of a diamond crystal to radiation is however well recognized to be dependent on the types of defects and impurity levels present within the crystal - most arguably nitrogen - [2-6] , and to date their

[3] To whom any correspondence should be addressed.

influence on the performance of synthetic diamond crystals when subjected to low-energy X-rays and high-energy electron therapy beams has not been fully investigated. In addition, different types and grades of synthetic diamonds exist – single crystal high-pressure/high-temperature (HPHT) diamond, single crystal (SC) chemical vapour deposition (CVD) diamond and polycrystalline CVD diamonds of detector grade (DG) and optical grade (OG) qualities – all of which perform differently and the reason is yet to be determined. This study was therefore aimed at evaluating the dosimetric performances (i.t.o. sensitivity values) of synthetic diamond crystals when used as radiation sensors for the above mentioned radiation types by highlighting some of the defect/impurity types that either enhance or degrade detector performance in order to select suitable crystals.

It should be noted that the use of natural diamond for medical applications is limited by the high cost and long delivery times, due to the scarcity of suitable stones [5], [7].

2. Experimental Details

Five commercially available synthetic diamond crystals of various types were investigated. These included one single crystal HPHT sample of dimensions 7.90 x 6.38 x 0.96 mm^3 and four polycrystalline CVD diamond samples (two DG (DGA1 and DGA2) and two OG (OGA1 and OGA2) samples) each of dimensions 5.0 x 5.0 x 1.0 mm^3. The opposite surfaces of each of the diamonds have been metallised as reported in a previous study [1] to provide the necessary ohmic contacts for voltage biasing and acquisition of the ionization signal. For quality control and the determination of defect/impurity types, the crystals were characterised using Raman spectroscopy and electron spin resonance (ESR). The Raman spectra were acquired using a Jobin-Yvon T64000 Raman spectrometer with the 514.5 nm line of an Ar^+ laser as excitation source. The ESR measurements were carried out with a Bruker ESP300E ESP spectrometer in a similar procedure as reported by this group [8].

The dosimetric responses of the diamond crystals to low-energy X-rays (25-32 kV_p) from a Senographe 500T mammography X-ray machine, and a 12 MeV electron therapy beam produced by a clinical linear accelerator (Siemens Primus) at the Charlotte Maxeke Johannesburg Academic Hospital (CMJAH) were measured. Each diamond crystal, biased at +50 V was encapsulated in, a probe housing as described in a previous work [1] and the probe, placed in its customised Perspex phantom was connected to a PTW-Freiburg UNIDOS E electrometer system operated manually in the 'charge' mode. The charge measured by the electrometer is defined as the response of the probe.

3. Results and Discussion

3.1. Raman Spectroscopy and ESR

Raman spectroscopy, which evaluates the material quality of diamond crystals showed only the characteristic diamond Raman peak at 1332 cm^{-1} over a linear background with no evidence of non-diamond component for all the crystals. The measured Raman widths (full-width-at-half-maximum (FWHM)) were 2.27±0.04, 2.60±0.13, 2.55±0.09, 2.56±0.09 and 2.41±0.06cm^{-1} for the HPHT, DGA1, DGA2, OGA1 and OGA2 crystals respectively. As the Raman width is an indication of the crystalline quality of diamond [9], i.e. a measure of the concentration of defects (such as point defects, crystal defects, grain boundaries, etc) it implies the HPHT sample having the smallest width (2.27 cm^{-1}) is the least defective crystal, and DGA1 having the broadest width (2.60 cm^{-1}) is the most defective crystal. The drawback of Raman spectroscopy is that it does not isolate defect types responsible for the inhomogeneous broadening of the diamond Raman peak.

Nitrogen, which is a commonly observed impurity in diamond, affects its electrical, optical and mechanical properties. It has been established that single substitutional nitrogen (N_s) is responsible for many performance characteristics of diamond radiation detectors [10]. ESR, which determines the concentration of N_s ([N_s]) gave values of 130, 3.5, 5, 42.9 and 71±2 ppm for the HPHT, DGA1, DGA2, OGA1 and OGA2 samples respectively. The much higher levels of N_s impurities of the HPHT and OG crystals compared to the DG samples observed in this study could be attributed to the technique normally used to grow diamond by the HPHT method and as for the OG crystals, we have

been informed that nitrogen is intentionally introduced during the growth of CVD OG diamond (private communication).

3.2. Dosimetric response of the diamond crystals – dose linearity and sensitivity

The linear response of a detector's signal with absorbed dose is a stringent requirement for medical applications. Dosimetric measurements for linearity evaluation and sensitivities determination included measurement of the response of each crystal as a function of absorbed dose on exposure to mammography X-rays and a 12 MeV electron therapy beam as shown in figures 1 and 2 respectively. Since X-ray tube peak kilovoltage (kV_p) and current-time product (tube loading, mAs) are two determinants of patient dose in mammography, with patient dose increasing either with an increase in kV_p or mAs, the absorbed dose was measured (with a PTW-Diados mammography detector – Type T60005 0735) as a function of kV_p (25 – 32 kV_p) at a constant tube loading of 200 mAs at the nominal distances used in routine mammography. For the 12 MeV electron beam, the measurements were done positioning the diamond probe in the Perspex phantom at the depth of dose maximum, d_{max} = 2.5 cm, at 100 cm source-to-phantom surface distance with an applicator defined field size of 10 x 10 cm^2 and the absorbed dose, (measured with a 0.6 cc Farmer-type ion chamber) was varied from 1.0 to 5.0 Gy by varying the number of monitor units from 100 to 500 using a dose rate of 3 Gy/min.

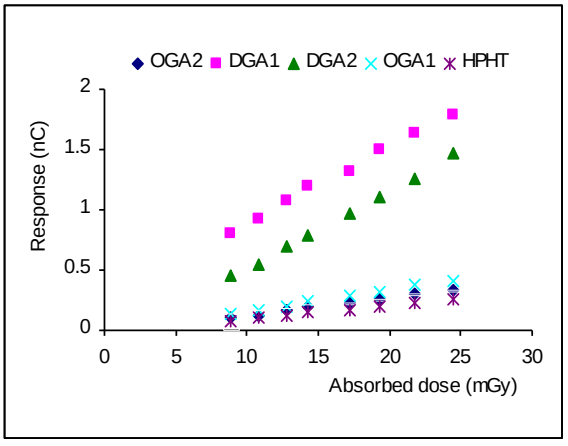

Figure 1. Response of the diamonds with absorbed dose at 200 mAs tube loading.

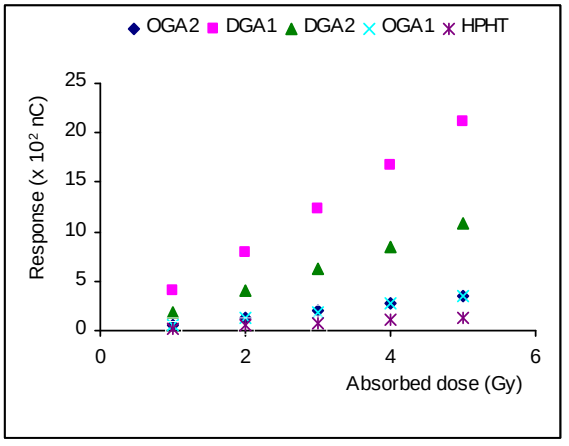

Figure 2. Response of the diamonds with absorbed dose for a 12 MeV electron beam.

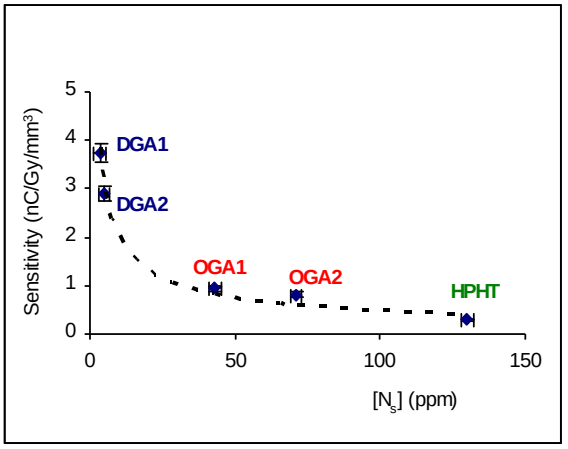

Figure 3. Variation of sensitivities (for the kV_p X-rays) of the diamonds with [N_s].

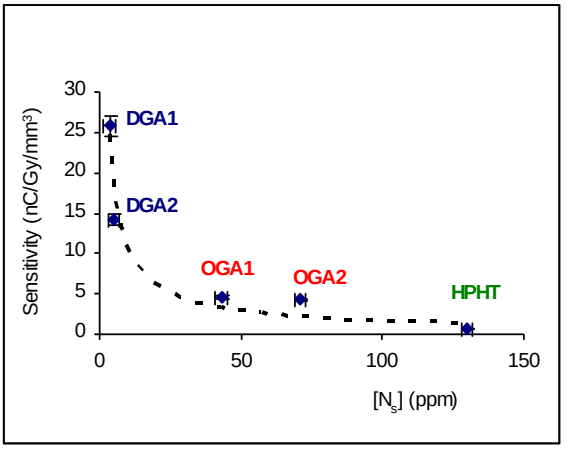

Figure 4. Variation of sensitivities (for the 12 MeV electrons) of the diamonds with [N_s].

As the sensitivity of a detector is defined as the collected charge, corrected for leakage, per unit absorbed dose and sensing volume [11], the slopes of the linear fits of figures 1 and 2 gave sensitivity values between 0.3 to 4 nC/Gy/mm^3 for X-rays and 0.7 to 26 nC/Gy/mm^3 for electron beams, where the detector volume of each crystal has been calculated as the product of the active area and thickness.

3.3. The role of impurity and defect levels of the diamond crystals

3.3.1. *Variation of sensitivities of the diamond crystals with [N_s]*. Figures 3 and 4 show the variation of sensitivities measured in X-rays and electron beams respectively of the diamond crystals with [N_s]. Both figures show similar trends or relationship between sensitivity and [N_s], with sensitivity decreasing as [N_s] increases. This is related to the observation that diamonds with N_s have high recombination efficiency which compromises the response [3]. Hence the figures show in general that N_s impurities in diamond act as recombination centres and degrade crystal performance (by reducing its sensitivity) when used as a radiation dosimeter. It is seen that the HPHT diamond with the highest [N_s] is the least sensitive while DGA1 with the lowest [N_s] is the most sensitive.

3.2.2. Variation of sensitivities of the crystals with defect levels. The sensitivities of the crystals were found to increase with Raman broadening (figures 5 and 6). As stated earlier, the Raman width indicates the presence and concentration of defects within a diamond crystal. Due to the presence of two inter-playing parameters, namely Ns impurities which act as recombination centres, and defect concentration, related to Raman width, the sensitivities of the crystals were then evaluated in terms of the ratio of Raman width to [N_s] in order to rule out the effect of [N_s]. Figures 7 and 8 show the variation of sensitivities measured in X-rays and electron beams respectively of the diamond crystals with Raman width per [N_s]. The increase in the sensitivity values of the crystals with the presence of defects could be attributed to one or a combination of two effects: the concentration of defects within the crystals and/or an increase in the interaction cross-section of diamond to radiation produced by the as yet unidentified defects within the crystals. Both effects result in the creation of more charge carriers suggesting in general that pure crystals or crystals with fewer defect levels may not function effectively as diamond radiation sensors. The particularly observed higher sensitivity of DGA1 to electron beams (causing the curve to deviate from linearity) could be attributed to the greater presence of a particular defect on the surface rather than within the crystal bulk making it more sensitive to electrons compared to X-rays.

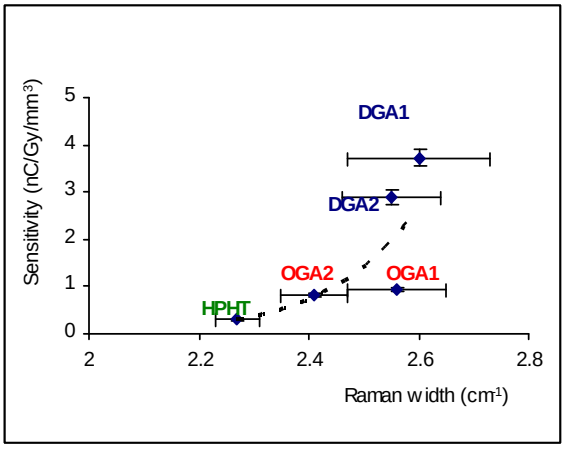

Figure 5: Variation of sensitivities (for the kVp X-rays) of the diamond crystals with Raman width.

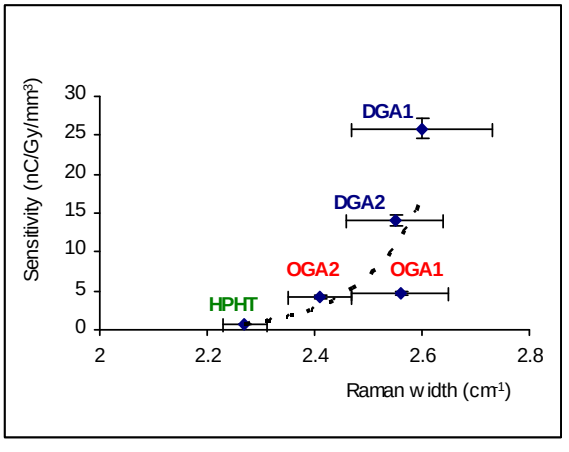

Figure 6: Variation of sensitivities (for the 12 MeV electron beam) of the diamond crystals with Raman width.

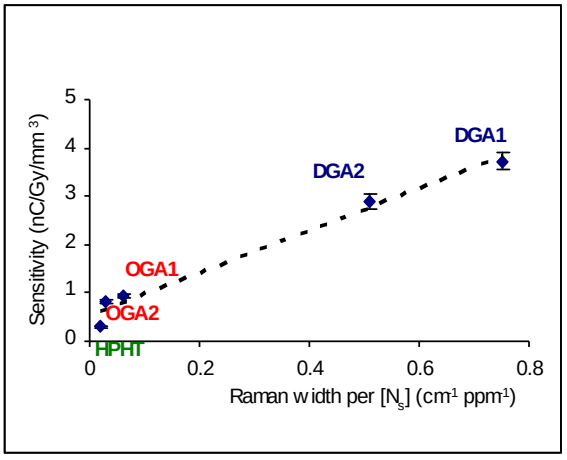

Figure 7: Variation of sensitivities (for the kVp X-rays) of the diamond crystals with Raman width per [N_s].

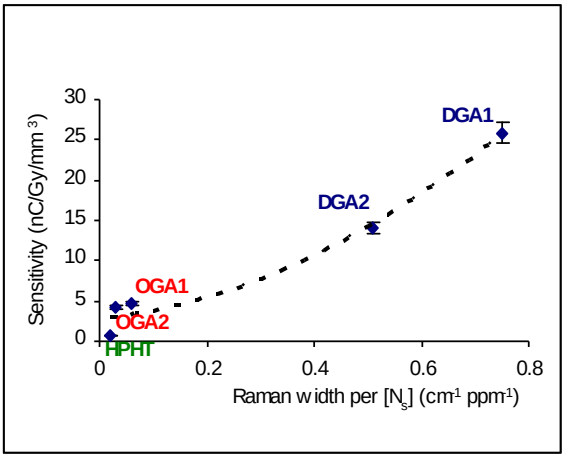

Figure 8: Variation of sensitivities (for the 12 MeV electron beam) of the diamond crystals with Raman width per [N_s].

4. Conclusions

In this study the HPHT and OG diamonds were found to have much higher levels of N_s impurities and were less sensitive compared to DG diamonds. The study has established that a diamond crystal with fewer defect levels may not function effectively as a radiation detector as the sensitivities of the diamond crystals were found to increase with defect density. The study thus concludes that once the defect type is identified, diamond could be selected or perhaps tailored made with defect and impurity levels which when used as radiation dosimeters could display optimum response. The sensitivities of the diamond crystals were largely influenced, in particular by N_s impurities which act as recombination centres and degrade crystal performance in this study suggesting that N_s levels ought to be the foremost criteria used in the selection of a sensor material. As DG CVD diamonds have very low N_s impurities such crystals should be the radiation sensors of choice for medical applications.

Acknowledgements

This project is ongoing and the support of the Department of Science and Technology and National Research Foundation of South Africa are hereby acknowledged. Our sincere thanks go to Dr R. Erasmus and Prof J. van Wyk for Raman spectroscopy and ESR measurements, respectively.

References

[1] Ade N, Nam, T L and Assiamah M 2012 *Radiat. Phys. Chem*. **81** 232.
[2] Keddy R L, Nam, T L and Burns R C 1988 *Carbon* **26** 345.
[3] Nam T L PhD Thesis,University of the Witwatersrand, Johannesburg, 1989.
[4] Yacoot A, Moore M and Makepeace A 1990 *Phys. Med. Biol.* **35** 1409.
[5] Guerrero M G, Tromson D, Rebisz M, Mer C, Bazin B and Bergonzo P 2004 *Diamond Relat. Mater.* **13** 2046.
[6] Mavunda R D, Zakari Y I, Nam T L and Keddy R J 2008 Appl. *Radiat. Isot.* **66** 1128.
[7] Fidanzio A, Azario L, Venanzi C, Pinzari F and Piermattei A 2002 *Nucl. Instrum. Methods Phys. Res.* A **479** 661.
[8] Assiamah M PhD Thesis, University of the Witwatersrand, Johannesburg, 2004.
[9] Faggio G, Marinelli M, Messina G, Milani E, Paoletti A, Santangelo S and Verona-Rinati G 1999 *Microsystem Technologies* **6** 23.
[10] Nam T L, Karfunkel U, Keddy R J and Every A G 1991 *Radiat. Eff. Def. Solids* **116** 233.
[11] Górka B, Fernandez-Varea, J M, Panettieri V and Nilsson B 2008 *Nucl. Instrum. Methods Phys. Res.* A **593** 578.

Gasification characteristics of sugarcane bagasse

[1]Anthony Anukam, [2]Edson Meyer, [1]Omobola Okoh and [2]Sampson Mamphweli

University of Fort Hare, [1]Chemistry Department, [2]Institute of Technology

Private Bag X1314, Alice 5700.

e-mail:aanukam@ufh.ac.za

Abstract. Sugarcane bagasse is a residue that results from the crushing of sugarcane in the sugar industry. Among the various agricultural crop residues, sugarcane bagasse is the most abundant lignocellulosic material in tropical and sub-tropical countries including South Africa. Bagasse is a renewable feedstock that can be used for power generation and manufacturing cellulosic ethanol. In the sugarcane industries the bagasse is mainly burnt inefficiently in boilers that provide the heating for the industry. This project seeks to investigate the possibility of gasifying sugarcane bagasse as an efficient conversion technology. Proximate and ultimate analysis of sugarcane bagasse was conducted after which the results were used to conduct computer simulation of the mass and energy balance during gasification. This paper presents the proximate and ultimate analysis as well as the computer simulation results.

1 Introduction

The development of sustainable renewable energy technologies for their use in current and new power plants is of utmost importance now, more than ever before due to several reasons. Some of these reasons include energy security and availability, independence from foreign oils and reduction of greenhouse gas emissions to provide a cleaner environment for better health, plant and animal life. These reasons are precepts for the development of alternative and sustainable energy technologies. Among the various agricultural crop residues, sugarcane bagasse is the most abundant lignocellulosic material in tropical and sub-tropical countries including South Africa. Sugarcane bagasse is a residue produced in large quantities by sugar and alcohol industries. In general, 1 ton of sugarcane generates 280 kg of bagasse, and about 54 million dry tons of bagasse is produced annually throughout the world [1].

In South Africa approximately 6 million tons of bagasse is produced annually [2]. Most large and medium sized mills can use up to 75% of this bagasse onsite to generate heat and electricity [3]. Epithelial cells, vessels, and parenchyma as well as fiber bundles are part of the structural elements contained in sugarcane bagasse [4]. Bagasse holds promise as a fuel source since it can produce more than enough heat energy to supply the needs of a common sugar mill. It is a renewable feedstock that can be used for power generation and manufacturing cellulosic ethanol, and if efficiently utilized, it could generate excess electricity that could be sold to the utility company or any other third party or even be exported [5].

Gasification of sugarcane bagasse provides part of the solution towards sustainable renewable energy sources. Gasification is a process that converts organic or fossil based carbonaceous materials into carbon monoxide, hydrogen, methane and carbon dioxide. This is achieved by reacting the material at high temperatures, usually above 1000°C, in the presence of a limited amount of oxygen and/or steam. The resulting syngas or producer gas has a heating value in the range of 4-6 MJ/kg. The clean syngas from bagasse can be used in stationary gas turbines. The advantage of gasification is that using the syngas is potentially more efficient than direct combustion of the original fuel because it can be combusted at higher temperatures or even in fuel cells, so that the thermodynamic upper limit to the efficiency defined

by Carnot's rule is higher or not applicable [5]. Gasification of sugarcane bagasse produces the same amount of CO_2 as it consumes during its growth rendering it carbon neutral [6]. However limited data is available on the efficient conversion of bagasse to clean syngas. The aim of this study is to investigate the possibility of gasifying sugarcane bagasse as an efficient conversion technology.

2 Research Methodology

Samples of sugarcane bagasse (SB) were obtained from TSB sugar, South Africa and were preserved to prevent contamination. The bagasse was dried at 105°C in a furnace for 4 hours. The dried sugarcane bagasse was ground using a cryogenic grinder to size range of 100 μm as required by the analytical instruments used to characterize bagasse. The bagasse, after grinding was preserved in a sample container for further analysis. The characterization methods involved proximate analysis, which gave the amount of fixed carbon, volatile and ash contents as well as moisture content of bagasse. These were determined from the thermo gravimetric curves in Figure 1, and were undertaken at two different heating rates (15°C/min and 20°C/min). Apart from providing information about proximate analysis, the essence of analysis using the thermo gravimetric analyzer (TGA) was to establish the thermal stability and the gasification temperature of sugarcane bagasse since the study is dealing with gasification which is a high temperature process.

The ultimate analysis of bagasse was determined using a carbon, hydrogen, nitrogen and sulfur (CHNS) analyzer, which is an instrument used to determine, in weight percentage, the concentration of these elements. The analyzer is restricted only to the analysis of these elements. The weight percentage of oxygen is usually obtained by difference. The higher heating value (HHV) of bagasse was measured using a bomb calorimeter (CAL2K Model). Analyses were undertaken in triplicates using each of the techniques (TGA, CHNS and Calorimeter) and an average value was calculated. A downdraft biomass gasification program developed by Jayah et al, 2003 [7] was used to undertake computer simulation of the gasification process of sugarcane bagasse. Table 1 shows the parameters used during simulations. The moisture content of the material was varied between 2.14%, 7.14% and 15.0% respectively. Gas profiles were obtained after computer simulation of the gasification process and were used to calculate the gas heating value from the percentage composition of the combustible gases in the syngas using the following equation [8]:

$$HV_{gas} = \left(\frac{(CO_{vol} \times HVCO) + (H_{2vol} \times HVH_2) + (CH_{4vol} \times HVCH_4)}{100\%} \right) \quad [1]$$

where HV_{gas} is the gas heating value in MJ/kg, CO_{vol} is the volume concentration of carbon monoxide gas in percentage, $HVCO$ is the heating value of carbon monoxide gas (usually 12.64 MJ/kg by standard [9], H_{2vol} is the volume concentration of hydrogen gas in percentage, HVH_2 is the heating value of hydrogen gas (10.1 MJ/kg by standard [10], CH_{4vol} is the volume concentration of methane gas in percentage, $HVCH_4$ is the heating value of methane gas (38 MJ/kg by standard measurement [9]. The heating values of the combustible gases were obtained from the standard gas table.

The conversion efficiency of the gasification process was calculated from the heating value of the gas obtained from equation 1.1 and that of the feedstock which was measured and found to be 17.8 MJ/kg. This was calculated from equation 2 [8]:

$$\eta = \left[\left(\frac{HV_{gas} \times 2}{HV_{fuel}} \right) \times 100 \right] \quad [2]$$

where η is the efficiency of the gasifier, and HV_{fuel} is the heating value of the fuel (sugarcane bagasse).

Table 1. Parameters used during gasification simulation

Fuel properties	**Value**	**Gasifier operating conditions**	**Value**
Carbon (%)	44.1	Throat diameter (cm)	25.5
Hydrogen (%)	5.7	Throat angle (°)	30
Oxygen (%)	47.7	Insulation thickness (cm)	17.5
Nitrogen (%)	0.20	Thermal conductivity (W/cm K)	2.8
Fixed carbon (%)	18.19	Temperature of input air (K)	300
Bulk density (g/cm^3)	0.178	Air input (kg/hr)	44.5
Diameter of SB particle (cm)	14.3	Heat loss (%)	12.8
Moisture content	1.14 (%)		

The values for the fuel properties in Table 1 are as measured from the material (bagasse) except for the particle diameter (14.3) which was assumed to be unground based on the maximum/minimum allowable size for a downdraft gasifier system. In terms of thermodynamics and mass transfer in the conversion process, the particle size of the material is of prime importance and severely affects the thermochemical conversion of the material to the desired product; therefore, smaller particle diameter results in increased conversion efficiency due to larger surface area per unit weight of the material and larger pore sizes which facilitates faster rates of heat transfer and gasification [11]. However, the effect of particle diameter (on the conversion efficiency of the gasification process of sugarcane bagasse) was varied in another study and published in a peer reviewed journal.

3 Results and discussion

3.1 Sugarcane bagasse proximate and ultimate analysis

Table 2 presents the proximate analysis of sugarcane bagasse under study at 15°C/min and 20°C/min heating rates. The maximum temperatures reached were approximately 670°C and 488°C for the 15 and 20°C/min heating rates respectively.

Table 2. Proximate analysis of SB at 15°C/min and 20°C/min heating rates

Components	**% Composition @ 15°C/min**	**% Composition @ 20°C/min**
Moisture Content	2.14	3.62
Volatile Matter Content	58.02	68.4
Fixed Carbon	19.25	18.19
Ash	-	0.53

No ash composition was observed for the 15°C/min heating rate due to the fact that the maximum temperature reached was not enough for complete combustion and determination of ash content. At 20°C/min heating rate, an ash content of 0.53% was observed which is typical of biomass materials. The

ash content and its composition are important factors for biomass use in thermochemical processing due to its catalytic activity [12]. It is also evident from table 2 that the heating rate influences the rate of volatile evolution from the material as volatile matter content increased from 58.02% at 15°C/min heating rate to 68.4% at 20°C/min heating rate. The ultimate analysis of SB is presented in table 3. It can be observed from the table that sugarcane bagasse contains more oxygen than carbon, which is typical of biomass materials.

Table 3. Ultimate analysis of sugarcane bagasse

Chemical Components	Composition (%)
N	0.20
C	44.1
H	5.7
S	2.3
O	47.7

The ratio of the products formed during gasification of biomass is influenced by the chemical composition of the biomass feedstock and the operating conditions of the gasifier [13].

3.2 Thermogravimetric analysis

Figure 1 shows the TGA plot for sugarcane bagasse under study at 15°C/min and 20°C/min heating rates under nitrogen atmosphere. This was obtained using a thermo gravimetric analyzer which was used to observe the weight loss of the sample as a function of temperature.

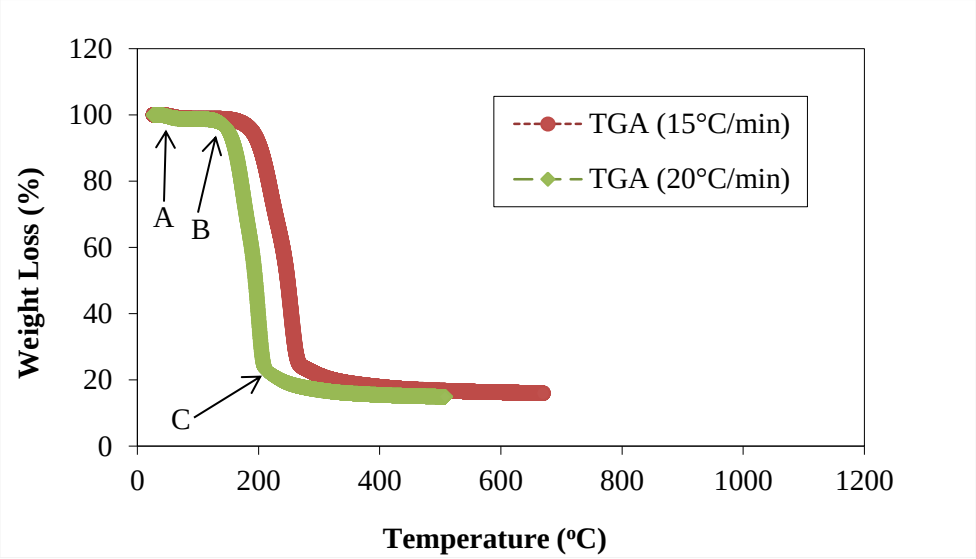

Figure 1. TGA curve of SB at 15°C/min and 20°C/min heating rates

In general, three distinct weight loss stages could be noticed. In the first stage (A), a slight weight loss is noticed from the material at both heating rates, and indicated by an arrow, which reflects the loss of

moisture from the material at temperatures approximately 27°C. This slight weight loss in stage A is due to the fact that the material was dried before the TGA analysis. A rapid weight loss is observed in stage B at temperatures slightly above 130°C which reflects the loss of volatiles from the material, resulting from the major components (cellulose, hemicellulose and lignin) of the material [14]. The degradation of hemicellulose typically occurs in the temperature range 100-230°C while cellulose decomposes at a higher temperature range of 200-300°C (B). The weight loss of the material continued up to stage C where there is a much lower rate of weight loss than in stage B, which corresponds partly to the end of cellulose degradation and partly to the starting of degradation of heavier volatiles and formation of char. Lignin degradation also continues in this region [14]. This analysis is based on the heating rate of the sample at 20°C/min. A rapid weight loss of the material occurred also in stage B at a much higher temperature range (approximately 189°C) for the 15°C/min heating rate, which means that the rate of decomposition of the material is dependent on the heating rate. The last weight loss stage at 15°C/min heating rate also occurred at a much higher temperature range (273°C) as compared to the 20°C/min heating rate.

3.2 Gasification simulation results

The higher heating value of the material was measured and found to be 17.8 MJ/kg, which was used during calculation of the conversion efficiency of the gasification process. Moisture content was varied between 2.14, 7.14 and 15% respectively in order to establish its effect on the volume of the syngas produced after computer simulation. Figure 2 shows the gas volumes and percentage difference obtained during gasification simulation using the gasifier operating parameters presented in Table 1.

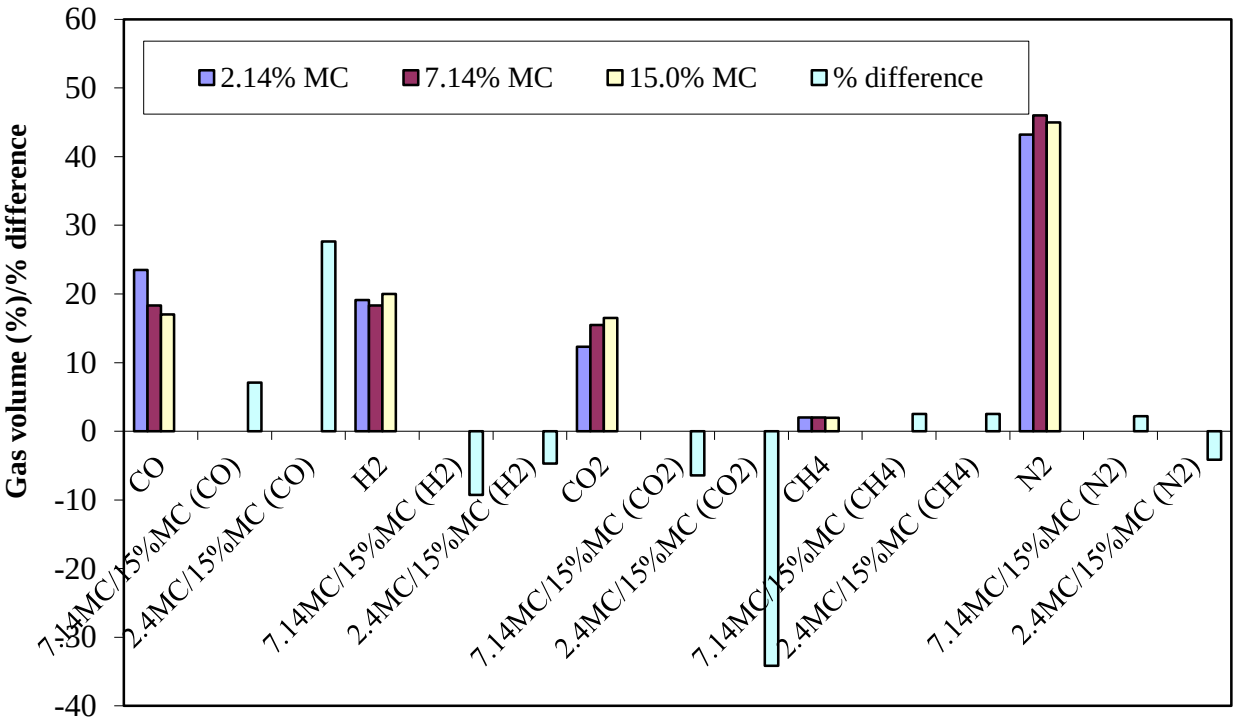

Figure 2. Gas volumes obtained through computer simulation

The major part of the syngas is formed through reduction reactions in the reduction zone of the biomass gasifier, most of which are endothermic reactions. The reactions are as follows [15]:

Boudouard reaction

$$CO_2 + C \rightleftharpoons 2CO \qquad -164.9 \text{ kJ/mol} \qquad (3)$$

Water-gas reaction

$$C + H_2O \rightleftharpoons C + H_2 \qquad + 122.6 \text{ kJ/mol} \qquad (4)$$

Water shift reaction

$$C + H_2 \rightleftharpoons CO + H_2O \qquad + 42.3 \text{ kJ/mol} \qquad (5)$$

Methane production reaction

$$C + 2H_2 \rightleftharpoons CH_4 \qquad + 75 \text{ kJ/mol} \qquad (6)$$

The volume of carbon monoxide was found to be higher (27% by difference) when the moisture content of bagasse was low (2.14%) compared to when it was higher (7.14% and 15% respectively). This can be attributed to the fact that heat is not consumed during the drying of the feedstock; it is rather available for the reduction reactions to take place. The hydrogen content was found to be higher when the moisture content of the bagasse was assumed to be higher (15%). This is because of the availability of moisture for the water-gas reaction to take place. However the reduction in carbon monoxide implied a reduction in conversion efficiency and the gain in hydrogen could not compensate for the loss in CO content. The volume of the combustible gases in the syngas largely influences the gas heating value. This in turn influences the conversion efficiency of the gasification process because the gas heating value is directly proportional to the conversion efficiency of the gasifier. Figure 3 shows the simulated gasifier conversion efficiency. The Boudouard reaction in equation 3 is a reaction named after a French chemist, and involve the disproportionation of carbon monoxide to carbon dioxide and carbon. The reaction is exothermic because energy is released in the process [16, 17, 18].

The effect of moisture content on the conversion efficiency of the gasification process of sugarcane bagasse was also determined by varying the moisture content from 2.14, 7.14 and 15% respectively. This was established after computer simulation of the gasification process. Figure 3 presents a plot of the impact of moisture content on the conversion efficiency of the gasification process of bagasse.

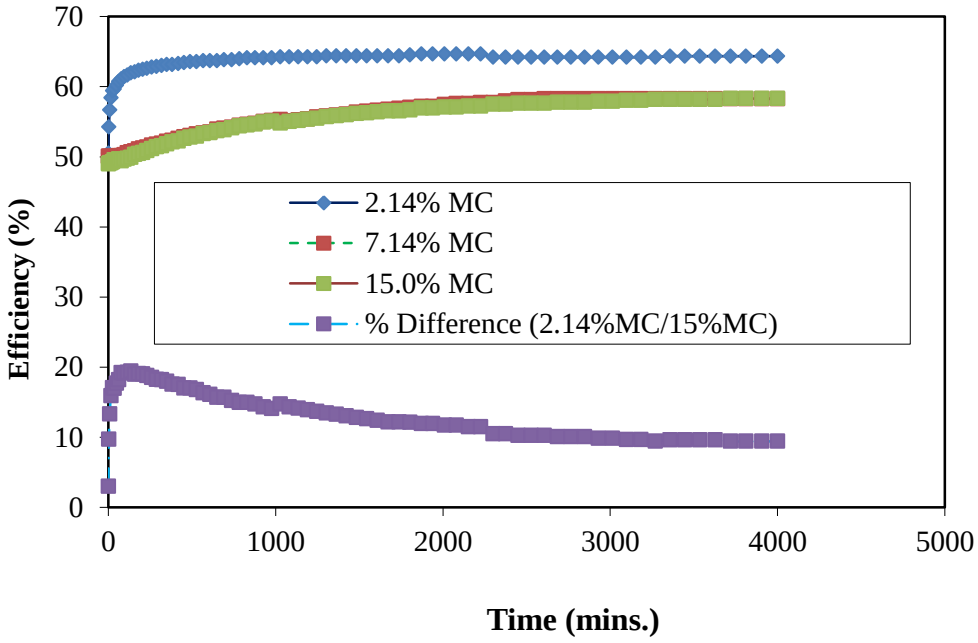

Figure 3. Computer simulation of the conversion efficiency of the sugarcane bagasse

The impact of moisture content on the conversion efficiency of the gasification process of bagasse is evident in Figure 3. As moisture content increases, conversion efficiency decreases considerably as evident. Optimum conversion efficiency (61%) was achieved at low moisture content of 2.14%. The implication for this is that the chemical reactions that favour the production of carbon monoxide during gasification of sugarcane bagasse should be optimized. This observation could also be explained by the reaction kinetics. A high quantity of energy is consumed during the drying process of the material and the energy is no longer available for reduction reactions to take place (equations 3-6). However, at higher moisture contents (7.14% and 15% respectively), the low oxidation temperature inhibiting the rate of reaction is compensated by a high water (H_2O) concentration which accelerates the water – gas shift reaction (equations 4 and 5). The percentage difference between 2.14% and 15% moisture contents is approximately 20% in terms of efficiency. This value is significantly higher when compared to that of 7.14% and 15% moisture contents. This means that material moisture content has an important influence on the efficiency of a gasification process.

4 Conclusion

The paper investigated the possibility of gasifying sugarcane bagasse as an efficient conversion technology, establishing the effect of moisture content on the syngas volume and conversion efficiency of the gasification process of bagasse. Results indicated that moisture content has an important influence on the volume of the product gas as well as on the conversion efficiency of the gasification process. Thermal analysis of the material also established the gasification temperature of bagasse which was approximately 700°C. The degradation behaviour of the material was also determined using the TGA which indicated that rapid decomposition of the material occurred between the temperature ranges of 200-400°C at both heating rates (15 and 20°C/min). The composition of sugarcane bagasse, as evident in Table 2, is comparable with what is found in the literature and suggests that bagasse is a suitable feedstock for gasification because of its high volatile matter content as well as its low ash composition including its low moisture content. The oxygen composition in Table 3 is about 8.16% more than the composition of carbon, as a result, higher reactivity of the material under much less severe operating gasification conditions is expected which is typical of biomass materials.

5 References

[1] Cerqueira D, Rodrigues G, Meireles C. Optimization of sugarcane bagasse cellulose acetylation. Carbohyd. Polym (2007) 69: Pp. 579-582.

[2] Sugar Milling Research Institute. Sugarcane bagasse. Proc S Afr Sug Technol Ass (2008) 81: Pp. 266-273.

[3] Zandersons J., Kokorevics A., Gravitis J., Zhurinsh A., Bikovens A., Tardenaka A. Spince B. Studies of the Brazillian sugarcane bagasse carbonization process and products properties. Biomass and Bioenergy (1999) 17: Pp. 209-219.

[4] Sanjuan R., Anzaldo J., Vargas J., Turrado J., Patt R. Morphological and Chemical Composition of Pith and Fibres from Mexican Sugarcane Bagasse. Holzals Roh-und Werkstoff (2001) 59: Pp. 447-450.

[5] Ahmed I., Gupta A. Sugarcane bagasse gasification: Global reaction mechanism of syngas evolution. Elsevier. Applied Energy (2012) 91: Pp. 75-81.

[6] Ahmed I, Gupta A. Sugarcane bagasse gasification: Global reaction mechanism of syngas evolution. Applied Energy (2012) 91: Pp. 75-81.

[7] Jayah T, Aye L, Fuller R, Stewart D. Computer simulation of a downdraft wood gasifier for tea drying. Biomass and Bioenergy (2003) 25(4):Pp. 459-469.

[8] Mamphweli S, Meyer E. Implementation of the biomass gasification project for community empowerment at Melani village, Eastern Cape, South Africa. Renewable Energy (2009) 34 (12): Pp. 2923-2927.

[9] Bjerketvedt D., Bakke J., Wingerden K. (1997). Gas explosion handbook. J. hazardous Mater; 52: Pp. 1-150.

[10] Fossum M. and Beyer R. Co-combustion: Biomass fuel gas and natural gas (1998). SINTEF Energy Research, Trondheim.

[11] A. Anukam, S. Mamphweli, E. Meyer, O. Okoh, "Computer simulation of the mass and 324 energy balance during gasification of sugarcane bagasse", Journal of Energy, vol. (2014). Article 325 ID 713054.

[12] Bridgwater A. The technical and economic feasibility of biomass gasification for power generation. Fuel (1995) 74 (5): Pp. 631-55.

[13] Chandrakant T. Biomass Gasification – Technology and Utilisation. Humanity Development Library, (2002). Artes Institute, Glucksburg, Germany. www.pssurvival.com. Last accessed November 2012.

[14] Biagini E., Barontini F., Tognotti L. Devolatilization of biomass fuels and biomass components studied by TG/FTIR technique. Industrial and Engineering Chemistry Research (2006) 45: Pp. 4486-4493.

[15] Kumar A., Wang L., Dzenis Y., Jones D., Hanna M. Thermogravimetric characterization of corn stover as gasification and pyrolysis feedstock. Biomass and Bioenergy (2008) 32: Pp. 460-467.

[16] Highman C, Van der Burgt M. Gasification. 1st ed. USA: Gulf Professional; (2003).

[17] Andre´ RN, Pinto F, Franco C, Dias M, Gulyurtlu I, Matos MAA, et al. Fluidised bed co-gasification of coal and olive oil industry wastes. Fuel (2005);84(12-13):1635-44.

[18] Fermoso J. Pressure co-gasification of coal and biomass for the production of hydrogen. University of Oviedo; (2009).

Investigation of the design aspects on the performance of a LCPV system

MA Benecke[1,2],EE van Dyk[1],FJ Vorster[1]

Abstract. This paper addresses the procedures that need to be considered when designing an optical and electrical sub-system of a low concentrator photovoltaic (LCPV) module. CPV systems make use of optical elements and solar tracking to concentrate solar flux onto a photovoltaic (PV) receiver. The performance of the concentrator module is highly dependent on the configuration and alignment of the optical elements in the system. In this study a LCPV module was constructed to satisfy a certain set of predetermined boundary conditions. This LCPV module has a geometric concentration ratio of 5.3 X. Various design considerations were taken into account to optimise the configuration of the photovoltaic receiver of the module. The LCPV module was then characterised with respect to optical design and electrical performance.

1. Introduction.

Concentrator Photovoltaics (CPV) is one of the technologies that have attracted a renewed interest due to the increased search for the use of non-fossil fuel based sources of energy to mitigate environmentally damaging effects of using fossil fuel for electricity production. CPV modules are a cost effective alternative to flat-plate photovoltaic (PV) modules since they concentrate sunlight onto small efficient solar cells [1].

In low concentration photovoltaics (LCPV), solar cells are subjected to higher irradiance levels than conventional flat-plate cells. The electrical output, and hence efficiency of a LCPV module is dependent on three factors; the amount of irradiance, uniformity of illumination across the solar cells and PV receiver temperature. These factors are interdependent and need careful consideration when deigning an LCPV module.

Three subsystems can be identified in CPV modules, namely optical, thermal and electrical. This paper discusses the design aspects and characterisation of the optical sub-system as well as electrical sub-system of a LCPV concentrator. By optimising the aperture area of the LCPV concentrator while still maintaining a uniform illumination intensity across the solar cells, the electrical performance can be maximised.

In theory it is assumed that an optical concentrator produces a perfectly uniform illumination profile, but in reality this is not the case due to a number of factors. The concentration level obtained is an average of the concentration profile impinging upon the solar cell [2]. It is important that the optical elements in the system create a uniform illumination profile across the solar receiver as far as possible. A non

[1]Department of Physics, Nelson Mandela Metropolitan University, P. O. Box 77000, Port Elizabeth, South Africa

[2] Corresponding AuthorsEmail: s207039151@live.nmmu.ac.za

uniform illumination profile from an optical concentrator generates a 2 dimensional temperature gradient on the receiver surface which affects the power output of the solar receiver.

Previous research resulted in the construction of a V-trough concentrator reaching 2.4 X concentration [3]. One of the main problems with the vertical receiver system was that the distance between the facetted reflector element and the receiver emphasized the effects of small misallignments of optical elements [4].

An initial design that had to satisfy a predetermined set of boundary conditions was introduced to improve on the V-trough concentrator system.

2. Theoretical Framework.

Due to difficulty in obtaining a uniform illumination intensity distribution in the aforementioned vertical receiver design an alternative design was sought, with an emphasis on the module cross-sectional aspect ratio that must be kept as low as possible and keeping in mind the uniformity of the intensity profile across the PV receiver.

The predetermined set of boundary conditions that had to be satisfied were:

- Module profile to have a low cross-sectional aspect ratio.
- Facetted reflector as concentrator element.
- Light incident on the receiver must be as perpindicular as possible to the incident light from the reflection facets.
- Reflector element symmetrical around receiever.
- Beams incident on opposite ends of facet to be reflected to opposite ends of the receiver.

A mathematical model was constructed in Optica 3 [5] for this design. From initial testing and prototypes it was found that a horizontal face down receiver system was the more feasible design. Figure 1 shows an illustration of the horizontal receiver design traced in Optica 3. The receiver pairs are also labeled in the figure.

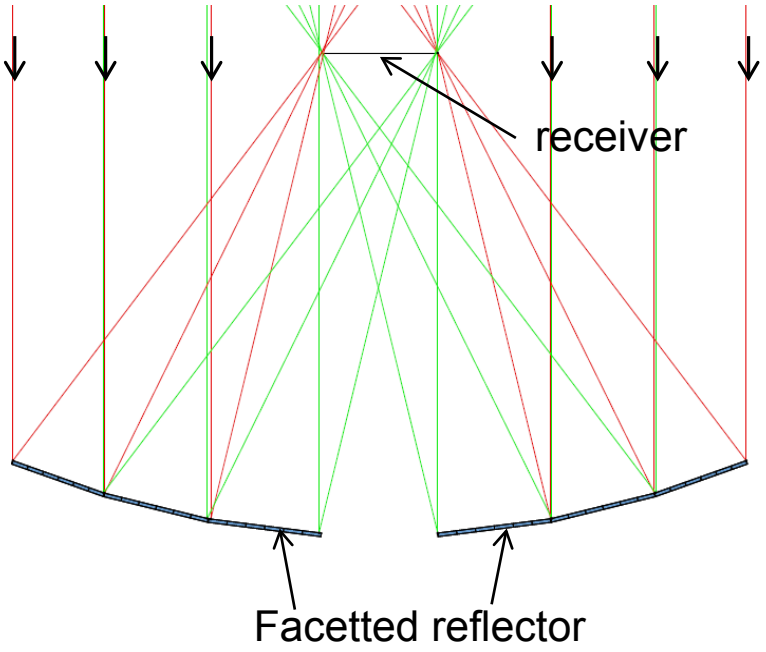

Figure 1: Illustration of horizontal receiver design with ray tracing.

3. Experimental.

A horizontal receiver LCPV prototype module was constructed and characterised with respect to optical and electrical performance. For optical characterisation the intensity profiles were obtained by investigating the contribution of each facet pair and compared to the theoretical contribution. Verification of illumination intensity and uniformity on the receiver plane was done by making use photography and image analysis using Image J software [6]. Image J analysis software also facilitated the extractof line scans from the intensity profiles.

For electrical characterisation various cell string configurations used as the PV receiver for the concentrator system were evaluated. These include 3, 4, 6 and 8 cell string receivers. The cell material was cut to ensure that the total area of cell material remained constant. Electrical output parameters were measured at 1 sun (1000 W/m^2) and under concentration using an Agilent Current-Voltage (I-V) tracer.

4. Results and Discussions

4.1. Optical characterisation

Figure 2 shows a photograph of the horizontal receiver LCPV module. The inset in the figure shows the PV receiver under concentrated illumination. A typical illumination profile such as that seen in the inset was recorded and is shown in figure 3. This type of profile was used to evaluate the optical performance of the respective reflector pairs (1; 2 and 3) as illustrated in figure 1. The effective concentration for each pair is listed in table 1 and typical line scans extracted from an intensity profile map, like that shown in figure 3, are shown in figure 4.

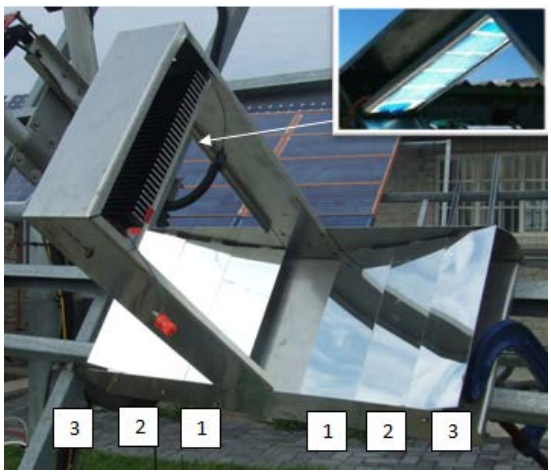

Figure 2. Photograph of horizontal receiver concentrator system.

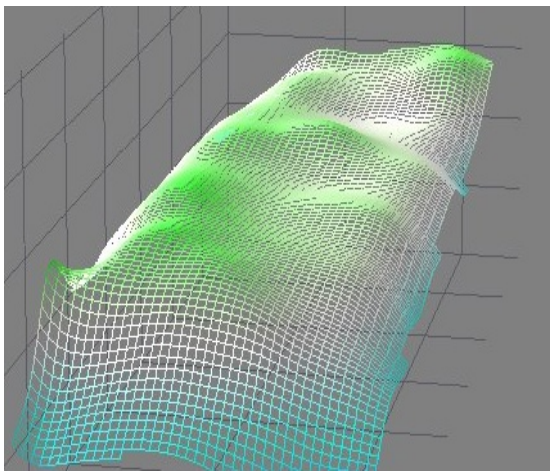

Figure 3. Intensity profile obtained from LCPV module.

Table 1. Theoretical and experimental contribution of each facet pair.

Facet Pair	Measured Concentration	Theoretical Concentration
First	1.96	1.96
Second	1.65	1.84
Third	1.52	1.68

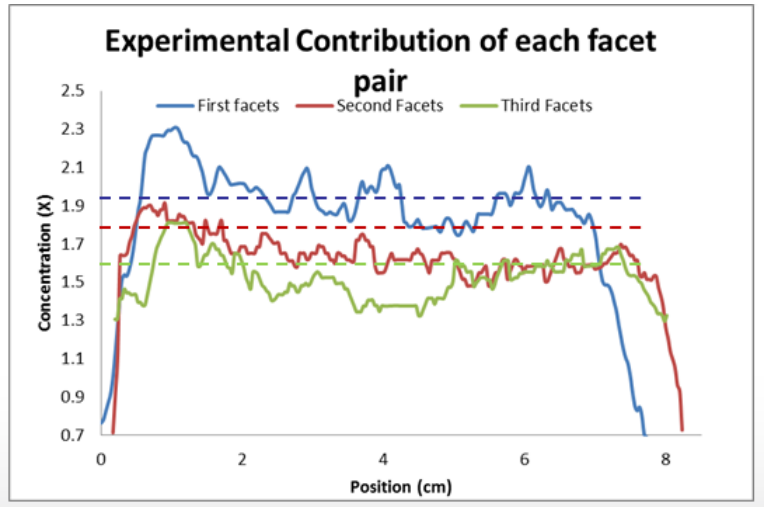

Figure 4. Line scans obtained from intensity profiles of each facet pair.

From the data it can be seen that the contributions closely resemble the expected theoretical values. The reasons for the second and third facet pair not reaching the expected contribution are due to lensing effects of the facets as well as some illumination missing the receiver. Although the illumination profile uniformity is much improved for this design, compared to the vertical receiver system, further optimization is required.

4.2. Electrical characterisation

The different cell string configurations were tested in the concentrator systemand the I-V characteristics measured under one-sun and concentration are shown in in figures 5, 6, 7 and 8. The performance parameters are also listed in the figures. Also shown in each figure is a schematic of the PV receiver, illustrating the number of cells and the fact that the total effective receiver area remains constant.

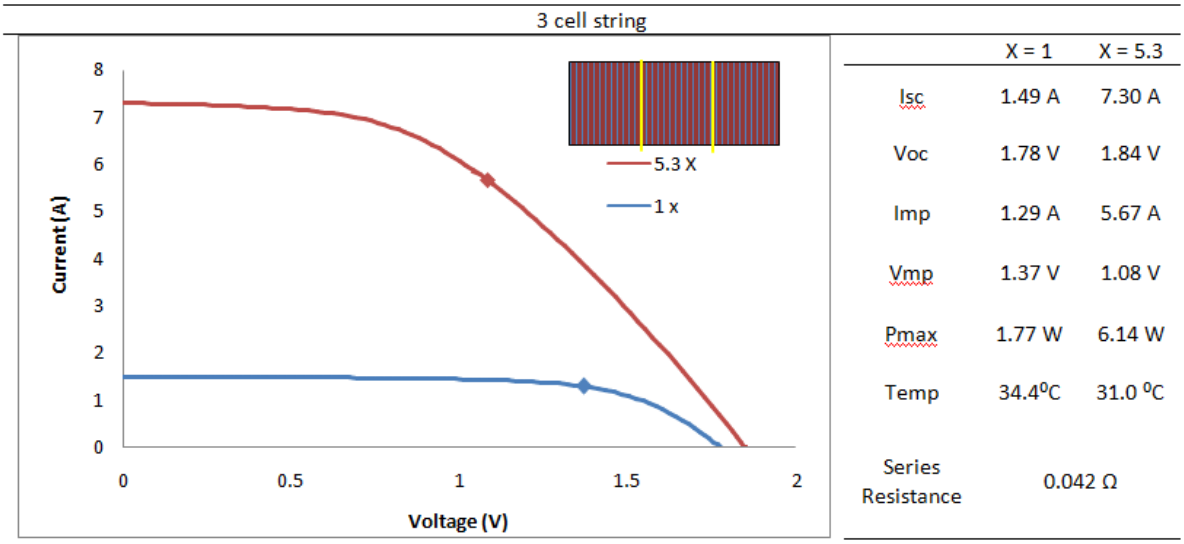

	X = 1	X = 5.3
Isc	1.49 A	7.30 A
Voc	1.78 V	1.84 V
Imp	1.29 A	5.67 A
Vmp	1.37 V	1.08 V
Pmax	1.77 W	6.14 W
Temp	34.4°C	31.0 °C
Series Resistance	0.042 Ω	

Figure 5. I-V characteristic of 3 cell string configuration with electrical parameters.

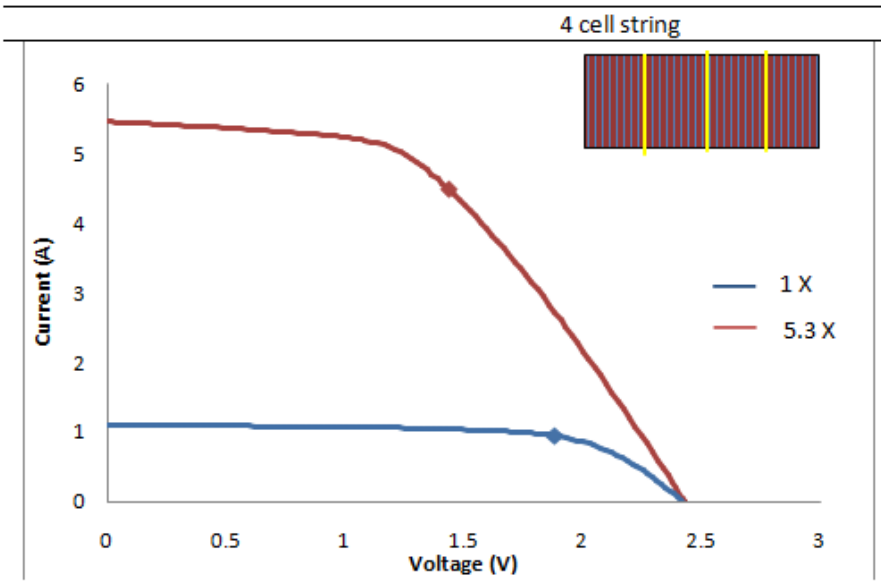

	X = 1	X = 5.3
Isc	1.10 A	5.50 A
Voc	2.42 V	2.43 V
Imp	0.94 A	4.49 A
Vmp	1.88 V	1.43 V
Pmax	1.78 W	6.45 W
Temp	28°C	32 °C
Series Resistance	0.04 Ω	

Figure 6. I-V characteristic of 4 cell string configuration with electrical parameters.

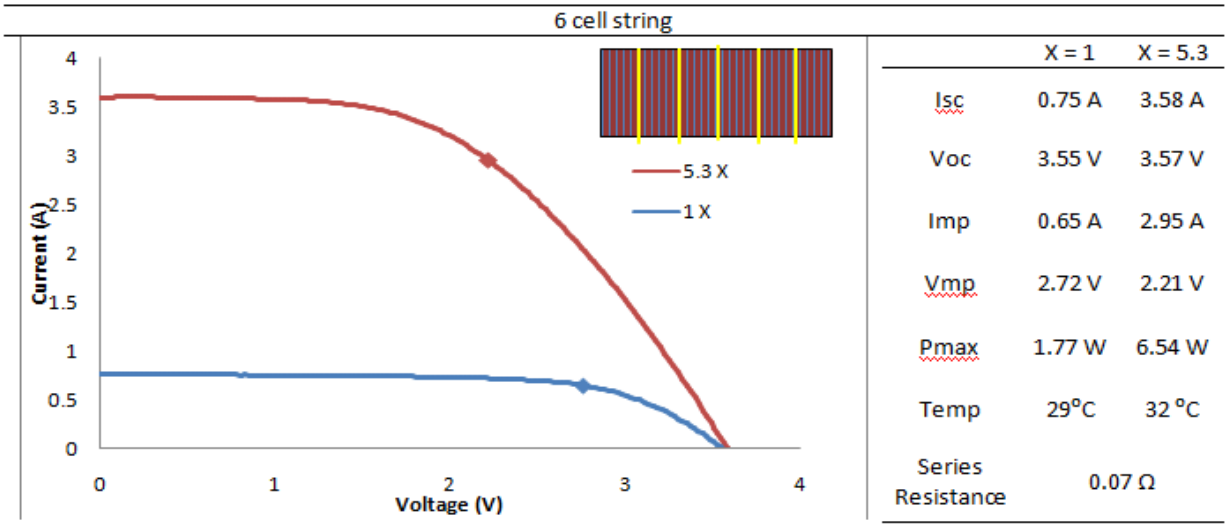

Figure 7. I-V characteristic of 6 cell string configuration with electrical parameters.

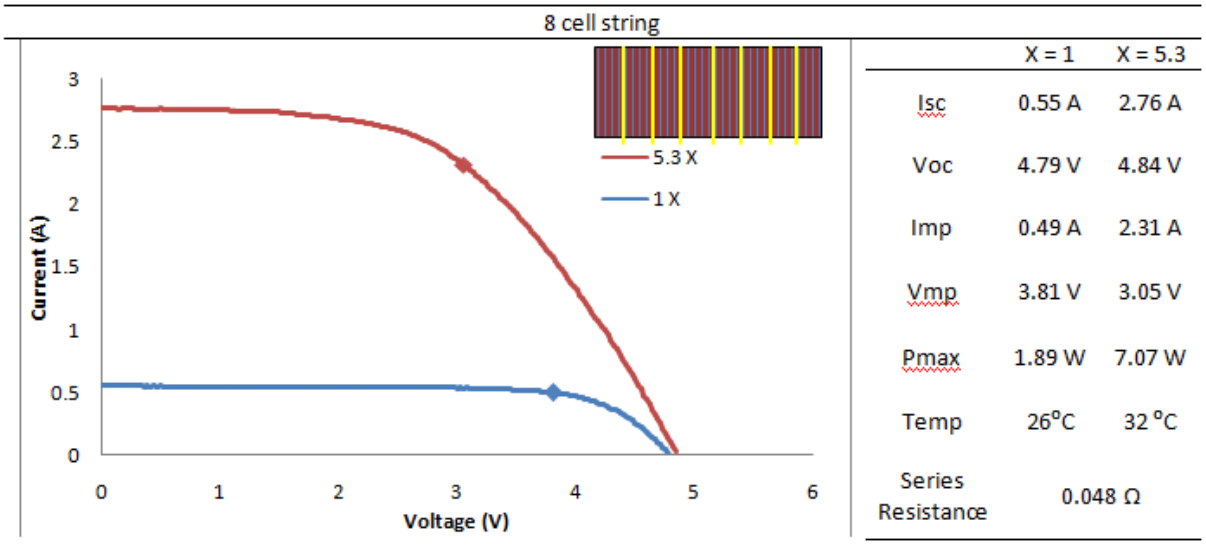

Figure 8. I-V characteristic of 8 cell string configuration with electrical parameters.

Table 2, shown below, illustrates the concentration factors achieved on short circuit current with each cell string configuration using the LCPV module.

Table 2. Concentration factors obtained for each cell string configuration.

PV receiver	Concentration Factor ($Isc_{(Concentration)}/Isc_{(one\text{-}sun)}$)
3	4.90
4	5.01
6	4.80
8	5.01

From the results it can be seen that the highest concentration factors were obtained for the 4 and 8 cell string configurations reaching 5.01 X concentration. The 3 and 6 cell string configuration reached concentration factors of 4.8 and 4.9 respectively. Theoretically 5.3 X was expected due to the geometrical concentration factor of the LCPV module, but this does not take into account optical losses and misallignment of optical elements. A comparison was made of the fillfactor as well as maximum power of each receiver under one-sun conditions as well as under concentration.

These 4 different cell string configurations were used to obtain the optimal receiver for a LCPV module. Figure 10 illustrates the different fill factors obtained for each cell string configuration. Figure 9 illustrates the maximum power obtained from each cell string configuration.

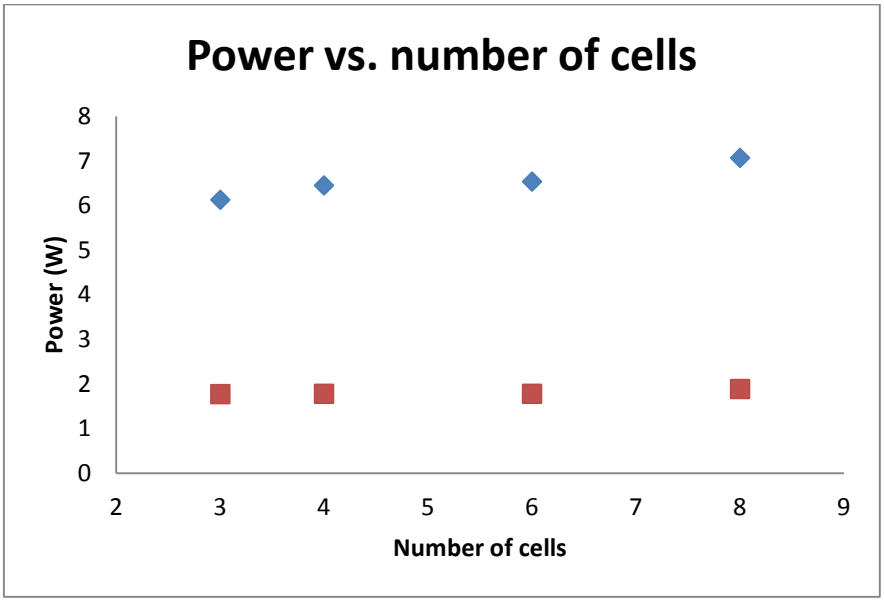

Figure 9. Relationship between Pmax and the number of cells in the string configuration.

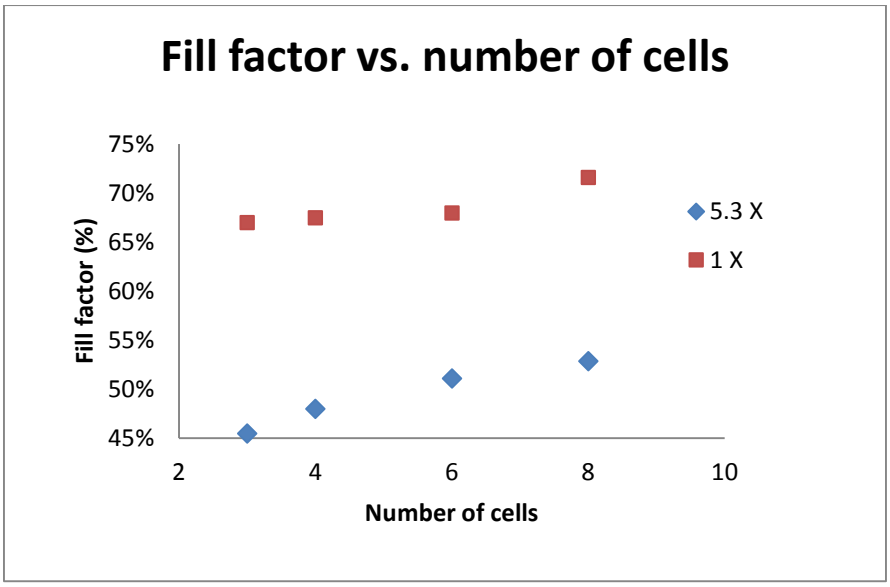

Figure 10. Relationship between fill factor and the number of cells in the string configuration.

From figure 10 it can be seen that the cell string configuration with the most cells connected in series obtained the highest fill factor. As the cell sizes increased and the number of cells connected in series decreased so did the fill factor decrease, this was observed under one-sun as well as under concentrated illumination. Figure 9 shows that the 8 cell string configuration obtained the best maximum power. The results illustrate that low current-high voltage cells yield a higher power and fill factor under one-sun and under concentration. Low current-high voltage receivers that yield better electrical performance is more ideal in a LCPV system. One of the reasons for them being more suiteable for LCPV purposes is that under concentration the current increases drastically, which in effect will lead to increase in resistive losses. These resistive losses decreases maximum power as well as fill factor obtained from the concentrator system.

5. Conclusions

A Horizontal receiver LCPV module was constructed to improve on previous prototype designs that were constructed, such as the V-trough concentrator [3] and vertical receiver LCPV module [4]. The results illustrate the feasibility of the optical design and that it can be used to improve on the V-trough concentrator design as well as the vertical receiver LCPV module.

An optical characterization was done on the LCPV module by investigating the illumination profile of the module as well as contributions of each reflection facet pair. Optical losses and misalignment of optical elements lead to a reduction in concentration levels and thus performance. The optical losses and misallignment of optical elements also cause non-uniformities in the illumination profile of the LCPV module. These non-uniformities in the illumination profile caused by optical misallignments can lead to cell mismatch in the PV receiver, which will cause loss in electrical performance of the module.

Various string configurations and cell matching techniques were implemented under the electrical characterization of the LCPV module. Theoretically a geometric concentration factor of 5.3 X was expected, where experimentally close to 5 X were obtained with each PV receiver. It is important to note that this theoretical geometrical concentration factor does not account for optical losses of the reflective material etc. It was found that higher fill factors and maximum power can be obtained by using low current-high voltage cell string configurations when the total PV receiver area is kept constant.

6. References

[1] A. Luque and S. Hegedus 2008 *Handbook of Photovoltaic Science and Engineering* (Wiley-VCH).

[2] A. Luque and V. Andreev 2007 *Concentrator Photovoltaics* (Springer-Verlag, Berlin Heidelberg).

[3] B.A. Butler, E.E. van Dyk and F.J. Vorster 2010 *Investigation of Low Concentration Photovoltaic Modules and Systems* (MSc dissertation NMMU Port Elizabeth).

[4] M.A. Benecke, E.E. van Dyk and F.J. Vorster 2012 *Optical design of low concentrator photovoltaic modules* (1st SASEC Conference 2012 paper)

[5] *Wolfram, MathematicaOptica 3.0*, http://www.opticasoftware.com/store/index.php, 31/10/2011

[6] *Image J*, http://rsbweb.nih.gov/ij/, 10/11/2011

Morphological and luminescent properties of $Y_3(AlGa)_5O_{12}$:Ce3+ powder phosphor.

S T S Dlamini, H C Swart [1]and O M Ntwaeaborwa
Department of Physics, University of the Free State, P. O. Box 339, Bloemfontein, ZA-9300, South Africa
E-mail: SwartHC@ufs.ac.za

Abstract. The morphological and luminescent properties of Y_3 $(AlGa)_5O_{12}:Ce^{3+}$ powder phosphor were investigated. Scanning Electron Microscopy revealed the phosphor's agglomerated particles with a size ranging from 0.4µm to 1.4µm. The X-ray diffraction indicated a cubic polycrystalline phosphor with an average crystal size of 80 nm. Luminescent properties include the emission wavelength at 512 nm which was also used to approximate the Al/Ga ratio within the crystal. Photoluminescence data also revealed that the addition of the Ga into the YAG:Ce^{3+} matrix caused a blue-shift in the emission spectra. The UV-VUV excitation and emission spectra of the $Y_3(AlGa)_5O_{12}:Ce^{3+}$ were also recorded and an energy diagram was constructed from the values.

1. Introduction

Cerium-doped yttrium aluminum garnet ($Y_3Al_5O_{12}:Ce^{3+}$ or YAG:Ce^{3+}) is used in several applications such as solid state lighting and displays. The Ce^{3+} ion is responsible for a nanosecond decay time and an intense emission at a visible wavelength range. Most phosphors have been developed for the use in fluorescent tubes or compact fluorescent lamps (CFLs) that use UV radiation, but yet they have not been optimized for the use in light emitting diodes (LEDs) that emit in the visible spectrum range. The first basic commercially available white LED is based on an InGaN chip emitting blue light at a wavelength of 460 nm that is coated with a YAG:Ce^{3+} phosphor layer that converted some of the blue light into yellow light which is combined to a rather cool white light [1]. This is good for many applications (e.g., displays and lighting in cars), but the quality of light is not good enough for home lighting, for which a warmer white light containing some red light is desirable. Some of the Al in the YAG:Ce^{3+}, is often replaced with Ga^{3+} to form $Y_3(AlGa)_5O_{12}:Ce^{3+}$ due to the similarity in cation size to get the red light component in LEDs [2]. Knowing properties of this phosphor in detail could lead to the application of this phosphor in manufacturing of LEDs for home lighting. In this work the $Y_3(AlGa)_5O_{12}:Ce^{3+}$ powder phosphor is characterized with different techniques.

2. Experimental

In this study a commercial $Y_3(AlGa)_5O_{12}:Ce^{3+}$ powder phosphor was obtained from Phosphor Technology with CIE coordinates: (x= 0.306, y=0.521) [3]. By using X-ray Diffraction (XRD) the powder was characterized for its phase purity and crystalinity. A Bruker AXS D8ADVANCE X-ray diffractometer was used to carry out the XRD analysis. Scanning electron microscope (SEM) images of the powder were captured using a Shimadzu Superscan SSX-500 SEM system. Photoluminescence (PL) properties of the phosphor were recorded using the Carry eclipse spectrophotometer at room temperature with a monochromatized Xenon flash lamp as an excitation source. The UV-VUV excitation and emission spectra of the $Y_3(AlGa)_5O_{12}:Ce^{3+}$ were recorded between 100 to 330 nm and 252 nm, respectively, by using the UV-VUV synchrotron radiation facility at the SUPERLUMI beamline I of HASYLAB (Hamburger Synchrotron strahlungslabor) at DESY (Deutsches Elektronen-

[1] To whom any correspondence should be addressed

Synchrotron, Hamburg, Germany) [4]. The spectra were recorded at room temperature. The setup consisted of a 2-m McPherson type primary (excitation) monochromator with a resolution up to 0.02 nm. The UV-VUV excitation spectra were corrected for the variation in the incident flux of the excitation beam using the excitation spectrum of sodium salicylate as a standard.

3. Results

The XRD pattern of $Y_3(AlGa)_5O_{12}:Ce^{3+}$ reveals a cubic polycrystalline phase with the main peak centered at $2\theta = 32.9°$. The pattern corresponds to the cubic phase in the reference data ICSD No 029250. Using Scherrer's equation and the XRD peaks, the average crystal size of the phosphor was estimated to be around 80 nm.

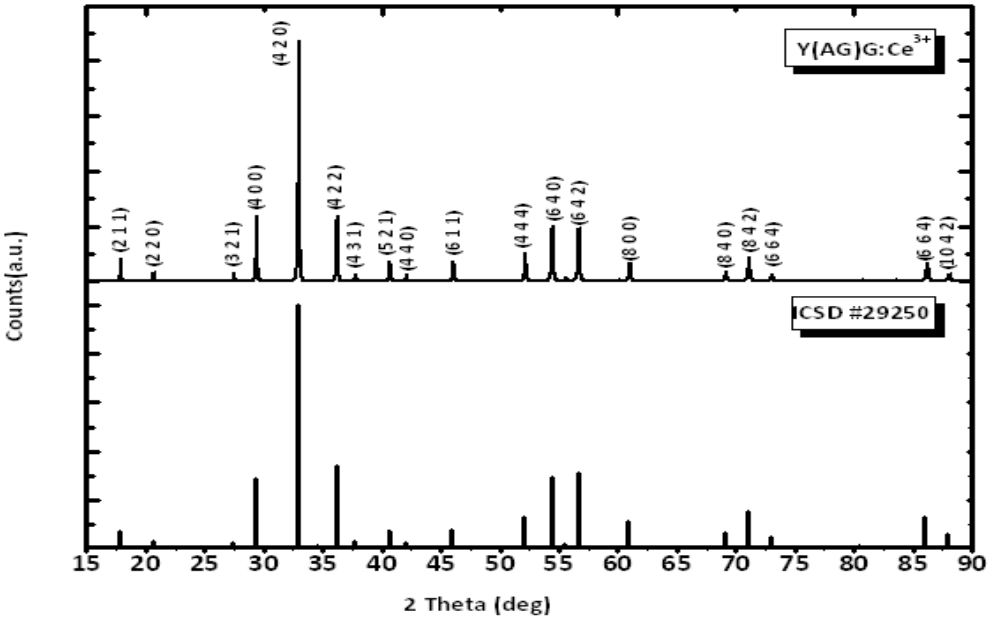

Figure 1. XRD pattern of phosphor and the ISCD reference profile.

The microstructure of $Y_3(AlGa)_5O_{12}:Ce^{3+}$ was characterized from SEM micrographs. As shown in the images, $Y_3(AlGa)_5O_{12}:Ce^{3+}$ phosphor was made up of an agglomeration of faceted spherical particles. The particle sizes were ranging from 0.5 µm to 1.4 µm.

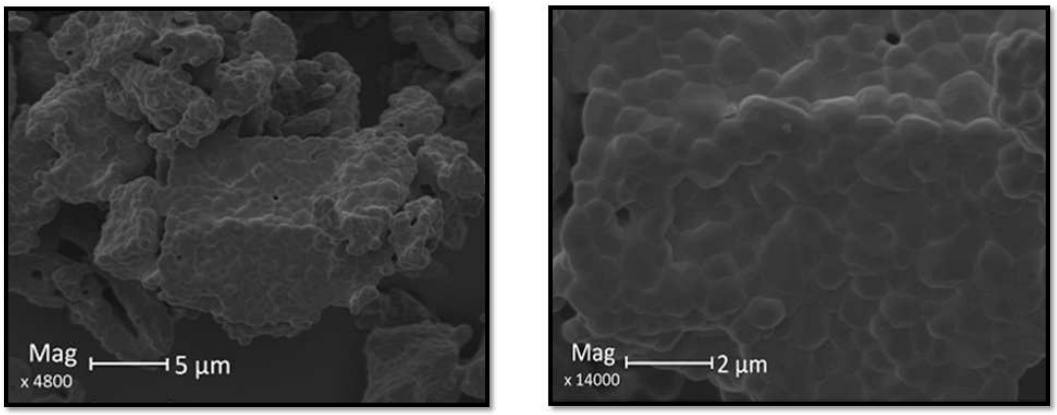

Figure 2. SEM images of the commercially obtained $Y_3(AlGa)_5O_{12}:Ce^{3+}$ phosphor.

The PL excitation and emission spectra of the $Y_3(AlGa)_5O_{12}:Ce^{3+}$ phosphor are shown in figure 3. The excitation peaks are due to the 4f to 5d transitions of electrons in the Ce^{3+} ion and the emission spectra is attributed to the de-excitation of these electron from the lowest 5d level to the field split 4f levels. Shifts in the PL emission spectra are an indication of structural changes caused by the substitution of Al with Ga in the phosphor host. Table 1 shows emission data with different concentrations of Ga in the Ce^{3+} doped garnets [2]. From the table and the PL spectra in figure 3 it can be estimated that there is roughly 60% Ga and 40% Al in the $Y_3(AlGa)_5O_{12}:Ce^{3+}$ crystal structure and also table 1 shows the shift in the emission and excitation wavelength as Al is substituted for Ga within the phosphor host. When Al^{3+} is substituted with Ga^{3+}, the Ga-O bonds re-adjust due to the difference in atomic radius of Ga^{3+} which is larger than Al^{3+}. The schematics of the relative arrangement of Y, O, Al and Ga were drawn using the diamond crystal software [5] and are shown in figure 4. The Y/Ce ions are surrounded by O^{2-} ions in the dodecahedral arrangement. The Al^{3+} and Ga^{3+} are surrounded by O^{2-} ions in a tetrahedral and octahedral arrangement. Ultimately, the substitution of Ga into the YAG lattice resulting in a decompression of oxygen atoms directly coordinated to the Ce^{3+} atom and the structure becomes more cubic. This change in structure directly affects the 5d orbitals of the Ce^{3+} and likewise the PL characteristics [2].

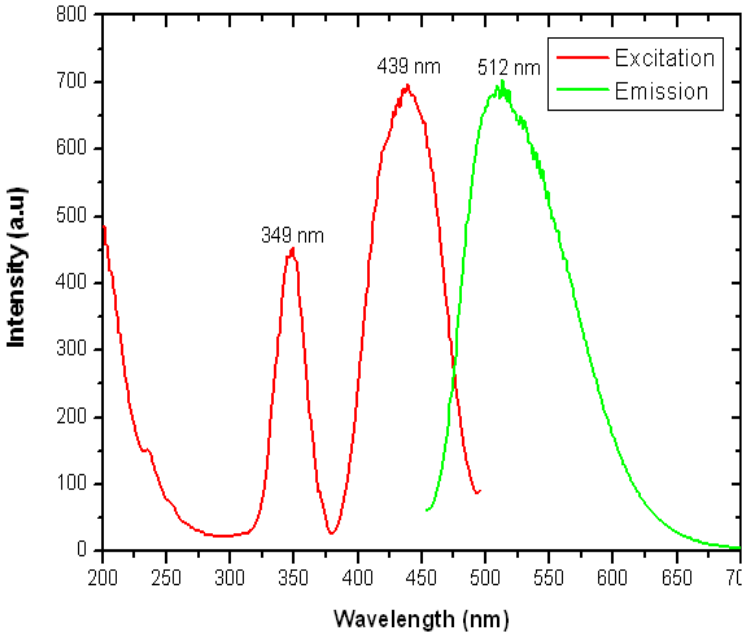

Figure 3. PL spectra of $Y_3(Al,Ga)O_{12}:Ce^{3+}$

Table 1. Spectroscopic and structural properties of Ce^{3+} doped garnets [3]

Host	λex(nm)	λem(nm)
$Y_3Al_5O_{12}$	457	540
$Y_3Al_4GaO_{12}$	447	527
$Y_3Al_3Ga_2O_{12}$	440	523
$Y_3Al_2Ga_3O_{12}$	430	512
$Y_3AlGa_4O_{12}$	422	504

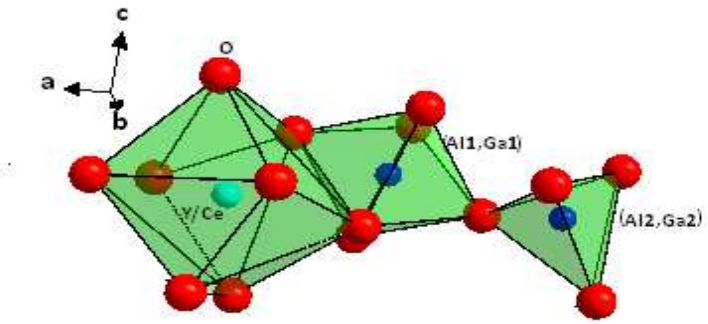

Figure 4. The relative arrangement of Y, O, Al and Ga in $Y_3(AlGa)_5O_{12}:Ce^{3+}$

Figure 5 shows the relative placement of the 5d orbitals in $Y_3Al_5O_{12}:Ce^{3+}$ (YAG: Ce^{3+}) and $Y_3(AlGa)_5O_{12}:Ce^{3+}$ (YAGG:Ce^{3+}). Electrons are excited to the E" state of the 5d orbital and are emitted from the E' state. The splitting of the E" and E' states is determined by the crystal field around the Ce^{3+} atom. In unsubstituted YAG, the oxygen atoms around the Ce^{3+} atom are highly compressed and form a non cubic structure. The splitting of the E" and E' states increases as the oxygen atoms are further distorted from the cubic structure. As Ga is substituted into YAG, oxygen atoms surrounding the Ce^{3+} atom are decompressed and form a cubic structure. As a result, the splitting between the E" and E' states decreases with the Ga content. Consequently, the samples with Ga have noticeably shorter emission wavelengths (higher energy) [6].

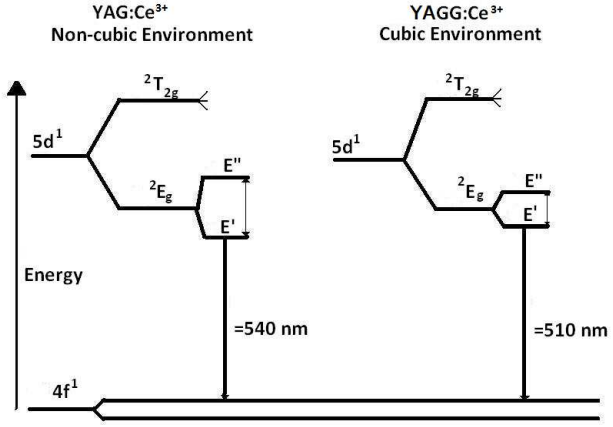

Figure 5. Energy level diagram for YAG: Ce^{3+} and YAGG:Ce^{3+} (not drawn to scale)[6]

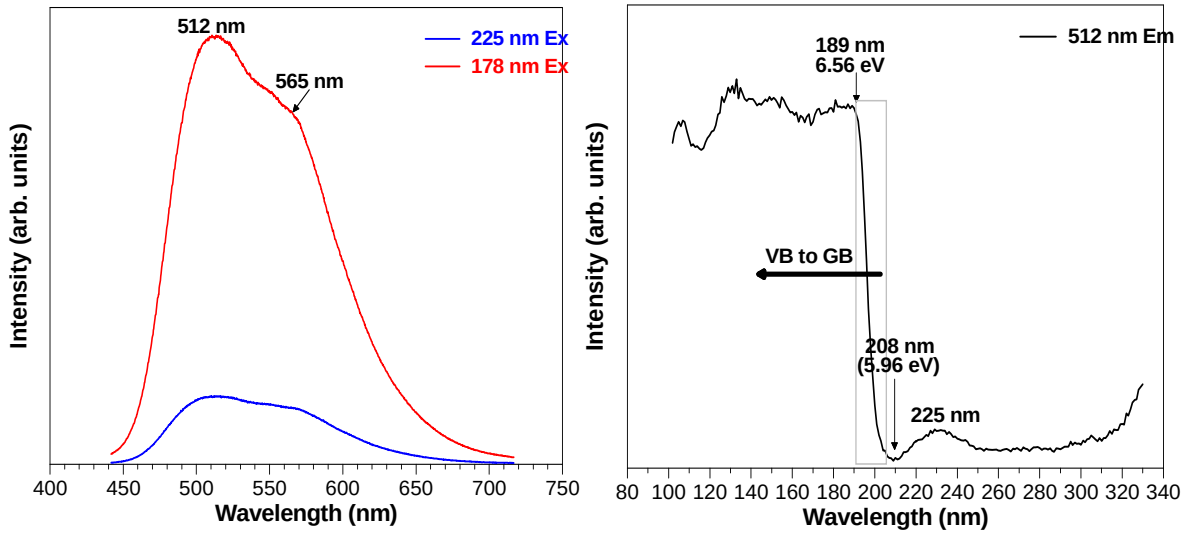

Figure 6. The emission and excitation spectra of the $Y_3(AlGa)_5O_{12}:Ce^{3+}$ phosphor measured with an excitation wavelengths of 178 and 225 nm and at an emission wavelength of 512 nm.

At room temperature, undoped YAG has a transmission window from the end of the lattice multiphonon bands at 4.2 µm to the beginning of the UV region at about 300 nm. Consequently YAG

is transparent and colorless in the visible range. YAG's optical band gap is in the order of 6.6 eV, with the valence band comprised of filled oxygen 2p orbitals, and the conduction band comprised of empty yttrium 4d orbitals. The UV absorption between 300 nm and the band edge at 190 nm varies dramatically from crystal to crystal [7]. YAG:Ce^{3+} mainly belongs to the luminescent materials with individual luminescent centers. The Ce^{3+} ion has only one electron in the 4f state. The ground state is split into a $^2F_{5/2}$ and a $^2F_{7/2}$ level by the spin-orbit interactions. The first excited state originates from the 5d state, which interacts strongly with the host lattice due to the large spatial extent of the 5d wave function. Thus the crystal-field interaction dominates over the spin-orbit interaction and the 4f to 5d transitions are parity and spin allowed [8]. When a Ce^{3+} ion enters exclusively one specific lattice site, its 5d state will be split into 2–5 different components depending on the site symmetry [9]. The 5 d state may also split into several more components if present in more than one lattice position with different site symmetry. Coetsee et. al. [10] found that the cathodoluminescent (CL) and PL emission spectra for Y_2SiO_5:Ce^{3+} phosphor powder due to the Ce^{3+} ions were attributed to the two different sites (A1 and A2) of the Ce^{3+} ion in the host matrix and the difference in the orientation of the neighbor ions in the complex crystal structure. Each Ce^{3+} site gave rise to transitions from the 5d to the two (therefore two peaks) 4f energy levels ($^2F_{5/2}$ and $^2F_{7/2}$ due to crystal field splitting). For the understanding of the lanthanide fd structure, knowledge about the excitation spectrum of the Ce^{3+} ion in a certain host lattice is very important. The Ce^{3+} ion has the $4f^1$ configuration, and irradiation with UV radiation will excite this 4f electron into a 5d orbital, leaving the 4f shell empty. Therefore, the excitation spectrum of Ce^{3+} will give direct information on the crystal-field splitting of the 5d orbitals. A similar crystal-field splitting is expected for all rare-earth ions in the same host lattice. The crystal-field splitting of the 5d states dominates the structure in the fd excitation spectra, even in the more complex rare-earth ions with more than one 4f electron. [11].

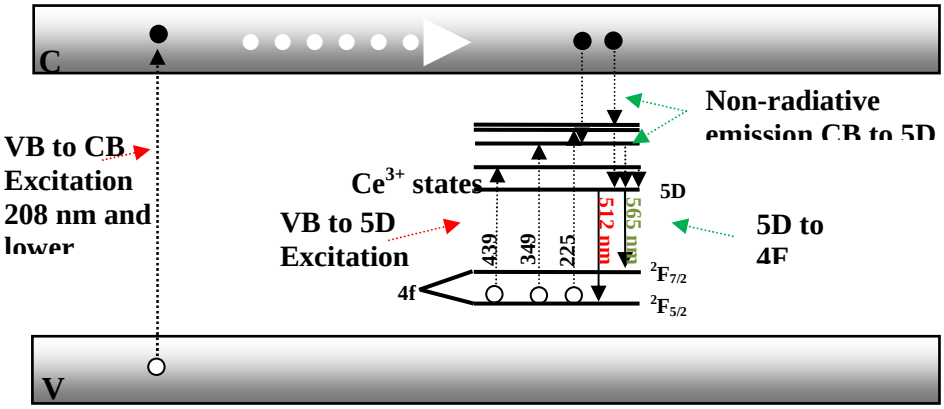

Figure 7. The energy diagram of the $Y_3(AlGa)_5O_{12}$:Ce^{3+} phosphor showing the excitation and emission as compiled from the emission and excitation spectra.

The emission spectra of $Y_3(AlGa)_5O_{12}$:Ce^{3+} were obtained under excitation of the host at 178 nm and 225 nm at room temperature (Figure. 6). Except for the intensity difference the spectra are identical with a broad peak consisting of two peaks at around 512 and 565 nm. These peaks are from the de-excitation of electrons from the lowest 5d level to the field split 4f ($^2F_{5/2}$ and a $^2F_{7/2}$) levels. Similar emission spectra were obtained with excitation wavelengths of 349 and 439 nm, figure. 3. The two emission peaks confirm the arrangement of the atoms in which the Ce^{3+} can only occupied one site position, as shown in figure 4. The excitation spectra shown in Figure 3 and 6 were measured from the 512 nm emission. Excitation peaks were obtained at 349, 439, 225 and 189 nm. The last peak started to increase from 209 nm up to 189 nm is assigned to the host-related absorption, since many phosphors show host-related absorptions around this spectral range [9]. In this case it is an indication of the band gap absorption of the $Y_3(AlGa)_5O_{12}$ between 5.96 eV (208 nm) and 6.56 eV (189 nm). The

other excitation peaks clearly indicate the excitation peaks of the 4f ($^2F_{7/2}$) to 5D levels. It is therefore clear that the Ce^{3+} is excited via the conduction band as well as in the Ce^{3+} ion itself. A summary of the energy levels of Ce^{3+} in the $Y_3(AlGa)_5O_{12}$ is given in figure 8 as obtained and compiled from the measured excitation and emission spectra. The Ce^{3+} energy values of the 5d lines obtained from this study compared very well with that obtained by Tomiki et. al. [12]. The values from Tomiki are: 460 nm (2.695 eV); 340 nm (3.643 eV); 266 nm (4.66 eV); 228 nm (5.44 eV) and 204 nm (6.07 eV).

4. Conclusions.

Ga substitution induced changes in the crystal structure of $Y_3Al_5O_{12}:Ce^{3+}$, these changes are observed in the morphological and luminescence properties. Samples with Ga have noticeably shorter emission wavelength (higher energy) and the absorption wavelengths are longer (lower energy). The excitation peaks indicated that Ce^{3+} is excited via the conduction band as well as in the Ce^{3+} ion itself. The two emission peaks confirmed the arrangement of the atom in which the Ce^{3+} can only occupy one lattice site position.

Acknowledgements.

For UV-VUV measurements, a special thanks to the synchrotron radiation facility at the SUPERLUMI beam line I of HASYLAB (Hamburger Synchrotron strahlungslabor) at DESY (Deutsches Elektronen-Synchrotron, Hamburg, Germany). The National Research Foundation and the University of the Free State for financial support.

References

[1] Schotter P, Schmidt R and Schneider J 1997 *Appl. Phys*. A **64** 417-418

[2] Wu J L, Gundiah G and Cheetham A K 2007 *Chem. Phys. Lett.* **441** pp 250-254

[3] http://www.phosphor-technology.com/products/crt.htm [Accessed 29 May 2012].

[4] HASYLAB, Beamline I: SUPERLUMI, http://hasylab.desy.de/facilities/doris_iii/beamlines/ i_superlumi [Accessed January 2012]

[5] K. Brandenburg, DIAMOND-3.0e, Visual crystal structure information System, Crystal Impact distribution, Bonn, Germany, 1998

[6] Hansel R, Allison S and Walker G 2010 *J Mater Sci.* **45** 146-150

[7] Kuo J and Chen W 1987 The electrical and optical properties of doped Yttrium Aluminium Garnets (PhD Thesis University of California, Berkeley) p 77

[8] Xin F, Zhao S, Xu S, Jia G, Deng D, Wang H and Huang L 2012 **30**(1) 21-24.

[9] Wang Y, Zhang J, Hou D, Liang H, Dorenbos P, Sun S and Tao Y 2012 *Optical Materials* **34** 1214–1218

[10] Coetsee E, Terblans J J, Ntwaeaborwa O M and Swart H C 2009 *Phys. B* **404** (22) 4426 - 4430.

[11] van Pieterson L, Reid M F, Wegh R T, Soverna S and Meijerink A 2002, *Phys. Rev.* B **65** 045113

[12] Tomiki T, Akamine H, Gushiken M, Kinjoh Y, Miyazato M, Miyazato T, Toyokawa N, Hiraoka M, Hirata N, Ganaha Y and Futemma T 1991 *J. Phys. Soc.* **60**(7) 2437– 2445

Prediction of aerodynamic loads in arbitrary manoeuvre: identifying flow regimes

I M A Gledhill[1]
DPSS, CSIR, PO Box 395,
Pretoria 0001 South Africa

E-mail: igledhil@csir.co.za

Abstract. Aerodynamic loads on aircraft are usually predicted at present by performing calculations in the body frame attached to the moving object. The assumption of Galilean invariance underlies the transform, and breaks down when arbitrary manoeuvre is to be modelled. A general framework for transformation between arbitrary accelerating frames has been provided by Löfgren [1], and extended by Forsberg [2]. A numerical scheme has been implemented in the inertial, or absolute, frame for computational purposes, and the implementation has been validated and applied to test cases [3] in a finite-volume formulation [4]. However, we still need to characterise flow regimes for exploration of accelerating flows. For this purpose Forsberg's transformation is used, with explicit expansion of the force terms in the relative frame, to derive dimensionless parameters which may be used as a guide to flow behaviour under limited conditions. In this paper, loads on a generic store modelled with the absolute frame Computational Fluid Dynamics capability are shown and compared with the insight gained from the theory. The store is a rolling hemisphere-cylinder with fins and strakes. Disruption of the fin aerodynamics by vortices originating on the strakes is the subject of interest, and this study suggests a way forward in understanding strake-fin interaction.

1. Introduction

There is an increasing need to predict aerodynamic loads on manoeuvring aircraft. Usually, analyses of geometrically complex configurations have been carried out using numerical solutions of discrete approximations to the Navier-Stokes equations in a body frame attached to a moving object. This is usually an inertial frame. Rotating transforms of the Navier-Stokes equations are well known [5][6][7], but a general model in an arbitrarily accelerating frame has been provided by Löfgren [1]. Based on this formulation, a general expression of the Navier-Stokes equations in an inertial (or absolute) frame, and in the non-inertial (or relative) frame, was developed by Forsberg [2] and extended to include gravity by Gledhill and Nordström [8].

The Forsberg formulation allowed the merits of numerical implementation in the absolute and relative frames to be compared [2]. The relative frame has the disadvantage that a set of source terms depending on translational acceleration, rotational velocity, and rotational acceleration, appear. Each of these terms must be treated numerically, and each term must be verified and validated. In addition, source terms may increase the stiffness of the matrix to be solved in the numerical implementation, posing problems that require attention within the solver itself.

[1] To whom any correspondence should be addressed.

By contrast, all that implementation in the absolute frame requires that the coordinates of the grid points are able to change with time. This has already been implemented in codes in mesh-deforming codes and is related to the ALE (Arbitrary Lagrangian-Eulerian) formulation. The major difference between ALE codes and the present formulation is that boundary conditions must be modified for arbitrary deformation in the case of far field boundaries.

It is also noted that inertial frame expression provides results in the inertial frame itself, while the aeronautical community traditionally evaluates results in the body frame (the relative frame) of the aircraft.

Previous work largely falls into three categories, with the exception of the more general acceleration models of Inoue *et al.* [9], and those of Roohani and Skews [10] which use source terms in the Navier-Stokes equations. Where deformations and translations are on the same typical length scale as the object in flight, existing methods have been successfully applied; this group includes aeroelastic models, control surface deflection models, modelling of dynamic models in wind tunnels, and the release of stores from aircraft [11-13]. Work on the numerical prediction of dynamic derivatives falls in the second category [14-16], while the third category covers the constant rotation models of turbines, fans, and geophysical flows.

The interest in extending the field to arbitrary manoeuvre arises primarily because of the increased agility of missiles and aircraft, but the methods are applicable to any accelerating fluid. Practical examples are now arising in which significant acceleration takes place during flight; fifth generation missiles such as A-Darter execute turns at 100g, where g is the acceleration due to gravity, and thrust from propulsion systems may approach 500g. In the present paper, interest is focussed on the generation and propagation of vortices along the length of the body of a missile. Part of the emergence of the new field is the exploration of the conditions under which acceleration is a negligible effect, and those in which acceleration is considered to be significant.

Many missiles in current use either have canards which generate strong vortices, or strakes at the nose or along the length of the body, or experience the formation of body vortices at high angles of attack. It is common practice at present to use the guidance system to correct any small effects at the rear fins. As manoeuvrability increases, it becomes desirable to have reliable predictions of these effects. The positions of axial vortices are usually the subject of modelling or experiment, and in accelerating flow little is understood of their dynamics. In this paper, the effects of vortex generation along strakes is demonstrated, the theory is summarised, and the main features of this complicated but realistic case are used to develop an approach to understanding the vortex dynamics. It is unlikely that a missile configuration of the kind used here would be subjected to the roll rate which is used to generate the vortices used for illustration, but the intention is to exaggerate the effect and then to change the roll rate, applying a significant angular acceleration about the long axis of the missile.

2. Theory

Notation is introduced to distinguish between vectors in viewed in ', and *vice versa*. A general vector a with components in viewed in , is denoted by $\breve{a}$ when viewed from '. For example, if a is constant in time but ' rotates, $\breve{a}$ must have rotating components $\breve{a}$ in ' (fig. 1).

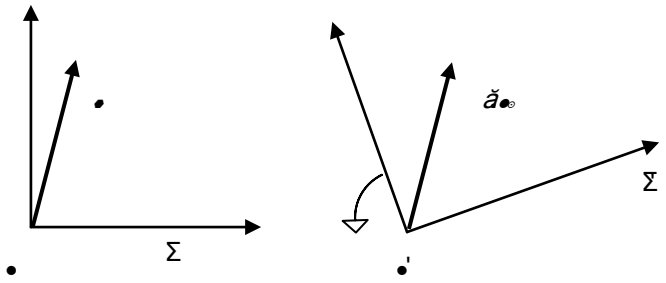

Figure 1. Vector a has constant components in , and varying components in '.

A vector $\underline{a}$ with components in ' viewed in ' is denoted by $\hat{\underline{a}}$ when viewed from . The rotation of ' relative to is denoted by the transform U. Then

$$\hat{\underline{a}} = U \cdot \underline{a}, \ldots \breve{a} = U^{-1} \cdot a = U^{t} \cdot a, \ldots \det(U) = +1 \tag{1}$$

Let the displacement of the origin O' of ' from the origin O of be denoted by r. Then a displacement vector x is related to $\underline{x}$ by

$$x = r + \mathrm{U} \cdot \underline{x} \tag{2}$$

For time derivatives we are able [2] to define a rotation vector by

$$\omega \times (U \cdot \underline{a}) = \frac{\partial U}{\partial t} \cdot \underline{a} \tag{3}$$

Differentiating with respect to time we obtain absolute and relative velocities respectively:

$$\begin{aligned} v &= \dot{r} + U \cdot (v + \breve{\omega} \times \underline{x}) = \dot{r} + \hat{\underline{v}} + \breve{\omega} \times \underline{x} \\ \underline{v} &= -\dot{r} + \breve{v} - \breve{\omega} \times \underline{x} \end{aligned} \tag{4}$$

The relative velocity field $\underline{u}$ between the two frames is defined by

$$\underline{u} = \breve{v} - \underline{v} \tag{5}$$

which leads to

$$\dot{\underline{u}} = \dot{\breve{r}} + \breve{\omega} \times \underline{x} \tag{6}$$

Spatial derivatives and frame transformations can then be derived [2]. Note that density and pressure are invariant under transformation [1]. The general integral form for a conserved tensor quantity ρa in a moving control volume can be written [2] as

$$\frac{\partial}{\partial t}\int_V \rho a dV + \oint_{\partial V} (\rho a \hat{\underline{v}} + F_a) \cdot d\hat{\underline{S}} = \int_V Q_a dV \tag{7}$$

For present purposes, viscous terms have been neglected. Here ρ is density, F_a is the non-convective flux term, $d\hat{\underline{S}}$ are surface normals for volume V, and Q_a are volume source terms. The mass continuity equation is obtained with $a = 1$ and $Q_a = 0$:

$$\frac{\partial}{\partial t}\int_V \rho dV + \oint_{\partial V} \rho \hat{\underline{v}} \cdot d\hat{\underline{S}} = 0 \tag{8}$$

In the absolute frame

$$\frac{\partial}{\partial t}\int_V \rho dV + \oint_{\partial V} \rho (v - \hat{\underline{u}}) \cdot d\hat{\underline{S}} = 0 \tag{9}$$

or equivalently in the relative frame

$$\frac{\partial}{\partial t}\int_V \rho dV + \oint_{\partial V} \rho \underline{v} \cdot d\underline{S} = 0 \tag{10}$$

Gravity is then included in order to show the way in which the Froude number and the Rossby number (defined below) appear [8]. For the momentum conservation equation $a = v$ in the inertial frame, $F_a = pI$ where p is pressure and I is the identity matrix, and $Q_a = -\rho g$ where g is the acceleration due to gravity. No other external forces are present. Here, the vector product with components $[a \otimes b]_{ij} = a_i b_j$ has been used. In the absolute frame

$$\frac{\partial}{\partial t}\int_V \rho v dV + \oint_{\partial V} (\rho v \otimes (v - \hat{\underline{u}}) + pI) \cdot d\hat{\underline{S}} = -\int_V \rho g dV \tag{10}$$

and in the relative frame

$$\frac{\partial}{\partial t}\int_V \rho \breve{v} dV + \oint_{\partial V} (\rho \breve{v} \otimes \underline{v} + pI) \cdot d\underline{S} = -\int_V \rho g dV \tag{11}$$

In order to examine the momentum equation in Σ', we substitute $v = U \cdot \breve{v}$ from (1) and use the expansions [2]

$$\nabla \cdot (\rho \underline{v} \otimes \underline{u}) = \underline{u} \nabla \cdot (\rho \underline{v}) + \rho \underline{v} \cdot \nabla \underline{u} \tag{12}$$

and

$$\frac{\partial}{\partial t}(\rho \underline{u}) = \underline{u} \cdot \nabla \rho \underline{u} + \rho \breve{u} \tag{13}$$

(with all spatial derivatives taken in Σ'). Then [2]

$$\frac{\partial}{\partial t}\int_V \rho \underline{v} dV + \oint_{\partial V} (\rho \underline{v} \otimes \underline{v} + pI) \cdot d\underline{S} = -\int_V \rho (\frac{\partial \breve{r}}{\partial t} + \frac{\partial \breve{\omega}}{\partial t} \times \underline{x} + 2\breve{\omega} \times \underline{v} + \breve{\omega} \times (\breve{\omega} \times \underline{x}) + g) dV \tag{14}$$

The source terms in the non-inertial frame

$$Q'_a = -\rho \dot{\breve{r}} - \rho \dot{\breve{\omega}} \times \underline{x} - 2\rho \breve{\omega} \times \underline{v} - \rho \breve{\omega} \times (\breve{\omega} \times \underline{x}) - \rho g \tag{15}$$

can be interpreted as the fictitious effects of Batchelor [6] and Greenspan [7]. They can also be non-dimensionalised with a typical velocity in the relative frame *v*, angular velocity Ω, density, and length *L* [8]. If $r(t)$ does not revolve, so that all rotation is expressed by *U*, then the first term captures heave, thrust and other translational acceleration terms and is characterised by $L\ddot{r}/\underline{v}^2$. The second term incorporates angular acceleration effects and is characterised by $L^2\dot{\Omega}/v^2$, where *L* can be used to characterise $\underline{x}$ from the rotation radius. The third term denotes Coriolis effects and is characterised by the inverse of the Rossby number $1/Ro = 2L\Omega/v$. The fourth term, characterised by $L^2\Omega^2/v^2$, denotes centrifugal effects in the non-inertial frame. The final buoyancy term is characterised by the inverse of the Froude number, $1/Fr = Lg/v^2$. If viscous forces had been included, the inverse of the Reynolds number would appear as the associated dimensionless number.

Conservation of internal energy *e* can be treated in the same way. However, the behaviour of fluids is highly non-linear, and dimensionless numbers have limited usefulness.

3. Numerical implementation

The absolute frame formulation has been implemented in the codes Euranus and carried over to Edge [4]. Edge is a Navier-Stokes solver, running on unstructured grids, with cell-centred finite volumes and a dual grid implementation. It employs symmetric or upwind Total Variation Diminishing (TVD) flux splitting. The code is based on space conserving grid stretching originally for mode-coupled aeroelasticity, but which proved very useful for the absolute frame. Boundary conditions have been modified for the absolute frame implementation. Second order central differencing is applied in space, and is stabilised with Jameson artificial dissipation. A 5-stage Runge-Kutta time integration scheme is used with implicit time stepping. The time step, based on earlier investigations, is 2 x 10^{-4} s, with 3 to 10 inner iterations. The domain is initialised with the boundary conditions and is allowed to reach a steady state. Residuals and aerodynamic loads are monitored to check convergence.

4. Test case

The purpose of the test case is to begin the investigation of strake or canard vortices on fin aerodynamics, particularly in cases of significant manoeuvre. The intention is to perturb the strake vortices and monitor the effect on the fins. An airframe used for the present example cases is a hemisphere-cylinder of total length L = 2 m and diameter 0.1 m (fig. 2). The *x* axis is oriented from nose to base along the length of the missile; the origin is at the half-length. Fins with rectangular profiles and planforms are positioned at 0.75 m$\leq$ $x \leq$ 0.85 m and extend to 0.15 m from the axis; the fins are approximately 1 mm thick. Strakes of 1 mm thickness extend from the front of the cylinder to the fins and may be removed for assessment of the strake effects. The calculation domain extends to 18 m in each direction. A structured grid extends between the inner surfaces, at which slip boundary

conditions are applied, to the far field, at which Riemann boundary conditions are used to reduce the reflection of flow features.

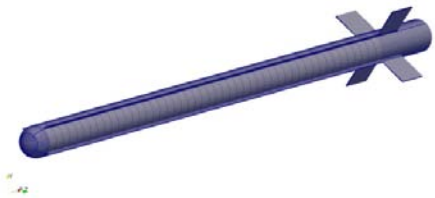

Figure 2. Surface grid on solid surfaces

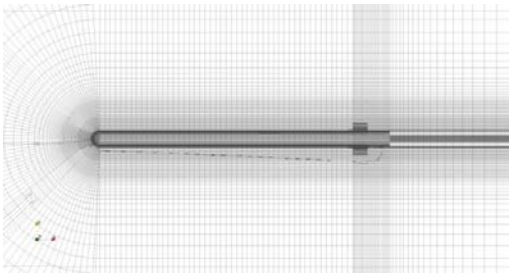

Figure 3. Grid on $z = 0$ plane

Far field conditions are p = 10 kPa, T = 300 K, and all velocity components zero. The missile and grid move at -600 ms^{-1} or a Mach number of ~1.9. A roll rate of Ω = 235.6 s^{-1} along the x axis is prescribed. For this investigation, no viscosity is modelled, and the Navier-Stokes equations reduce to the Euler equations. From $1/Ro = 2L\Omega/v \approx 2$ (taking L=0.06 m near the vortex structures, and $v = L\Omega$) it may be expected that Coriolis effects are present but not dominant; and since $L^2\Omega^2/v^2 \approx 1$ it is expected that centrifugal effects are similarly present.

x = 0 m	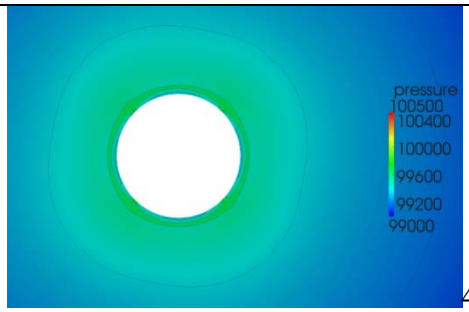 4a	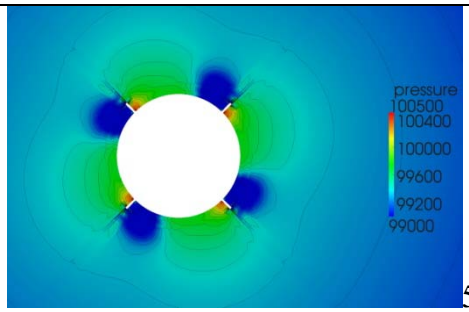 5a
x = 0.75 m	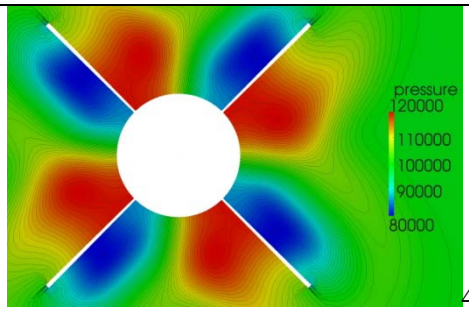 4b	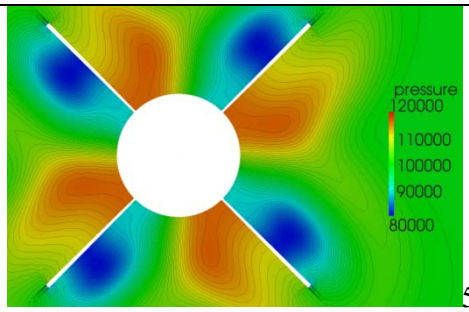 5b
	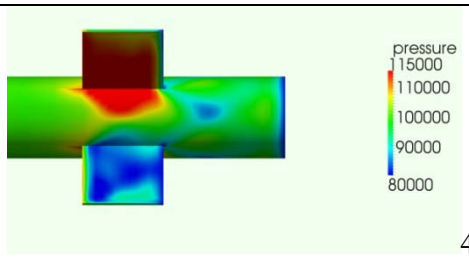 4c	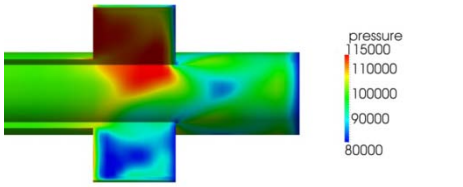 5c
	Figure 4. Pressure without strakes, Pa	**Figure 5.** Pressure with strakes, Pa

In fig. 4 and fig. 5, pressure contours are compared for the cases with and without strakes. The formation of vortices along the strakes (Fig. 5a) leads to a different structure of the pressure field at the fins (figs. 4b, 5b). Pressure footprints on the fins (figs. 4c, 5c) differ on the forward surface of the leeward fin.

5. Discussion and Conclusions

A framework for the theory of accelerating flow has been summarised, and it has been shown that the relative size of contributing terms may be estimated in terms of dimensionless constants. A test case with complex vortex flow has been demonstrated for a Rossby number of ~0.5 and the comparable dimensionless number for centrifugal effects of ~1. In this regime these effects are therefore expected to be present. Pressure is conserved between inertial and non-inertial frames, and a comparison of contours for a missile with strakes and one with shows the presence of vortices along the strakes, and the consequent change of flow field at the fins.

This case can be used as a basis for a study of the effect of roll acceleration on the configuration. A significant effect should be achievable for $L^2\dot{\Omega}/v^2 >> 1$. If the sign of Ω is reversed over a period of about 2 ms, this number is ~ 60, and this estimation indicates that the effect should be significant. Experience with the complexity of the strakes body flow field indicates that it may also be advantageous to model the effect for two wings without intervening solids, and to move these wings independently.

References

[1] Löfgren P 2000. FFA, The Swedish Aeronautical Institute, FFAP-B-066

[2] Forsberg K 2000. FFA, The Swedish Aeronautical Institute, Report

[3] Gledhill I M A *et al.* 2009. *Aerospace Science and Technology* **13** 197-203

[4] Eliasson P and Nordström J 1995. FFA, The Swedish Aeronautical Institute FFA-TN 1995-39

[5] Landau L D and Lifshitz E M 1959. *Fluid Mechanics* (Oxford: Pergamon Press)

[6] Batchelor G K 1967. *An Introduction to Fluid Dynamics* (Cambridge: Cambridge University Press)

[7] Greenspan H P 1968. *The Theory of Rotating Fluids* (Cambridge: Cambridge University Press)

[8] Gledhill I M A and Nordström J 2011. *Int. Aerospace Symp. of South Africa Conference Pretoria Sept. 2011*

[9] Inoue O *et al.* 1997. *Fluid Dynamics Research* **21** 413-416

[10] Roohani H and Skews B W 2009. *Shock Waves* **2** 1065-1070

[11] Murman S M *et al.* 2002. *American Institute of Aeronautics and Astronautics* AIAA-2002-2798

[12] Naidoo K and Skews B W 2009. *Shock Waves Proc* **2** 1377-1382

[13] Cenko A *et al.* 2000. *American Institute of Aeronautics and Astronautics* AIAA-2000-0795

[14] Weinacht P and Sturek W B 1988. USA Leadership Corps TR BRL-TR-2931

[15] Cornier J *et al.* 2000. *ECCOMAS* Barcelone Spain Sept. 2000

[16] Hirt C W *et al.* 1972. *J. Comp. Phys.* **14** 227-254

[17] Eliasson P 2001. FOI, The Swedish Defence Research Agency FOI-R-0298-SE

Measurement and simulation of neutron beam fluence spectra

M Herbert[1], R Nchodu[2] and P Maleka[3]

[1]Physics Department University of the Western Cape, Modderdam road, Bellville, 7535, South Africa
[2]Physics Department University of Cape Town, Rondebosch, Cape Town, 7700, South Africa
[3]iThemba LABS (Laboratory for Accelerator Based Sceince), PO Box 722, Somerset West 7129, South Africa

msherbert@uwc.ca.za

Abstract. This paper reports on work done at the neutron time-of-flight facility at the iThemba LABS in South Africa. Neutron beams of energy up to ~ 64 MeV were produced by bombarding a pulsed beam of 66 MeV protons from the iThemba LABS separated sector cyclotron onto either a Li (1.0 mm) metal target or a Be (10.0 mm) metal target or a graphite (10.0 mm) target. The Li, Be and C neutron beam fluence spectra were measured with an NE213 detector using the time-of-flight technique. The results from the time-of-flight measurements were compared with Monte Carlo simulations using the MCNPX code.

1. Introduction

Knowledge of fast neutron beam fluence spectra are of interest in various nuclear applications namely radiotherapy for the treatment of cancer [1]; radiobiology, studying the biological effectiveness of neutrons [2] and radiation protection at nuclear research facilities namely the iThemba LABS. The latter one is of importance because neutron fields encountered around high-energy accelerators like iThemba LABS are characterised by broad spectral distribution ranging from thermal energies to several hundred MeV. Monitoring these neutron fields and determining their fluence spectra pose a challenge for radiation protection [3]. In principle, these fluence spectra can either be calculated by Monte Carlo Methods or measured experimentally [4].

There are a number of difficulties that are involved in carrying out either the calculations or experiments, especially at energies above 20 MeV. One in particular, which limits the accuracy of the predictions of the calculations is the degree to which the required reaction cross-sections are known [5]. This applies particularly to the energy region above 20 MeV where the non-elastic contribution to the reaction cross-section is significant and have either not been measured or are not correctly calculated by present nuclear models. There are a variety of methods that can be used to measure neutron beam fluence spectra [5]. At energies above 20 MeV, the techniques include time-of-flight, recoil spectrometry, threshold (activation or fission) spectrometry and methods based on neutron moderation. Of these methods the time-of-flight is the most accurate and it is widely used for measuring neutron beam fluence spectra.

The purpose of this paper is to report on work done at the neutron time-of-flight facility at the iThemba LABS in South Africa. Neutron beams of energy up to ~ 64 MeV were produced by bombarding a pulsed beam of 66 MeV protons from the iThemba LABS separated sector cyclotron onto either a Li (1.0 mm) metal target or a Be (10.0 mm) metal target or a graphite (10.0 mm) target. The Li, Be and C neutron beam fluence spectra were measured with an NE213 detector using the time-of-flight technique. The results from the time-of-flight measurements and Monte Carlo simulations of the measurements using the MCNPX code are presented, compared and discussed [6].

2. Experimental procedures and Data analysis

Experiments were conducted at the neutron time of flight facility at the iThemba LABS in Faure, outside Cape Town, South Africa. Fig. 1 is a schematic diagram showing the details of the beam line in the neutron vault, the shielding in the experimental area and the positions of the detectors including the neutron monitor.

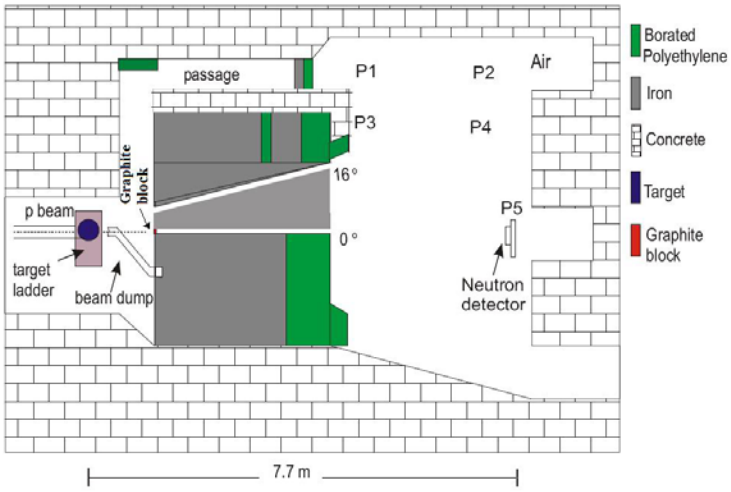

Fig.1: Schematic diagram showing the details of the beam line in the neutron vault. Note the borated blocks are not part of the current neutron vault.

Neutrons were produced by bombarding either a Li metal target (thickness 1 mm) or a Be metal target (thickness 10 mm) or a graphite target (thickness 10 mm) with a pulsed beam of 66 MeV protons from the iThemba LABS separated sector cyclotron. A 2 m thick shielding wall (concrete and iron) separated the experimental area from the target. A circular aperture (25 mm diameter) in the wall provided a collimated neutron beam at angle 0° to the proton beam direction. The neutron beam profile measured at the end of the neutron flight path of 7.7 was found to be uniform within 5% over a circular area of diameter 50 mm. Measurements of the neutron beams were taken with an NE213 liquid scintillator of 25 mm diameter x 25 mm at a distance of 7.7 m away from the target. The NE213 scintillator was equipped with a LINK pulse shape discriminator to suppress gamma rays and to select only events such as n-p elastic scattering or all heavier particles resulting from neutron interaction in the scintillator [7].

The neutron energy spectra for the respective targets were obtained in the offline analysis from the measurements of time-of-flight, T and pulse height, L by the NE213 detector as follows. The neutron energy was determined from T. This information with T and L measurements were used to determine the neutron detection efficiency of the NE213 detector as a function of neutron energy with reference to the n-p elastic scattering cross-section as described by Brooks and Klein [5]. The neutron detection efficiency of the NE213 detector was determined for 31 equally spaced 2 MeV neutron energies

ranging from 6 MeV to 66 MeV. The response functions of the NE 213 detector were determined at each one of the 31 neutron energies from the data from each target. From each one of response functions the number of n-p elastic scattering events corresponding to each one of the 31 neutron energies was determined. The ratio of the number n-p elastic scattering events at energy E to the neutron detection efficiency at E give the number of neutrons at E measured in the detector relative to the n-p elastic scattering cross-section at E. The number of neutrons incident on the detector for each one of the neutron energies was determined in this manner for each one of the experimental measurements. The neutron fleunce for the beam of each target is given by the ratios of numbers of neutrons measured at each one of the energies to the area of the NE213 detector.

The measurements carried out in this work were simulated using the Monte Carlo code MCNPX. The Monte Carlo code MCNPX is widely used in nuclear physics for simulating the transport of particles through matter. MCNPX describes the physics of the nuclear interactions that take place by using: (a) evaluated nuclear data libraries or (b) various physics models, including intranuclear cascade models [8] where libraries are not available [9]. In this work the simulations were carried out in two stages. First, the proton transport through the beam line onto the target was carried out and the neutrons produced were calculated at a position 10 cm along the 0 degree beam line from the target. In these simulations the proton beam was modelled as a pencil beam. In the second stage the neutrons produced were transported along the 0 degree line to the position of the NE213 detector in the vault at 7.7 m.

3. Results and discussion

The neutron fluence spectra measured are compared to the predictions of Monte Carlo calculations using the code. To facilitate comparison between the spectra, the integral fluence of each calculated spectra were normalised to the same integral fleunce as that of its corresponding measured spectra. The results obtained are display in Figure 2 (a) – (c). The solid line histograms indicate the measurements obtained from time-of-flight with the NE213 scintillator detector while the dotted line histograms are the results from the MCNPX Monte Carlo code.

Overall the Monte Carlo calculations reproduce all the main features in the measured spectra, namely the peaks in the measured spectra as well as the shape of the measured spectra. The agreement between the calculated and measured spectra of the Be- and C targets are better than the agreement between calculated and measured spectra of the Li-target. The disagreements observed between the calculated and measured spectra might be as a result of how the proton beam and the target thickness was modelled in the Monte Carlo calculations. The above will be investigated in future. However, overall the research indicates that the Monte Carlo calculations and measurements agree well. Hence, the Monte Carlo code MCNPX is a viable way to predict neutron fleunce of neutron fields encountered around high-energy accelerators like iThemba LABS.

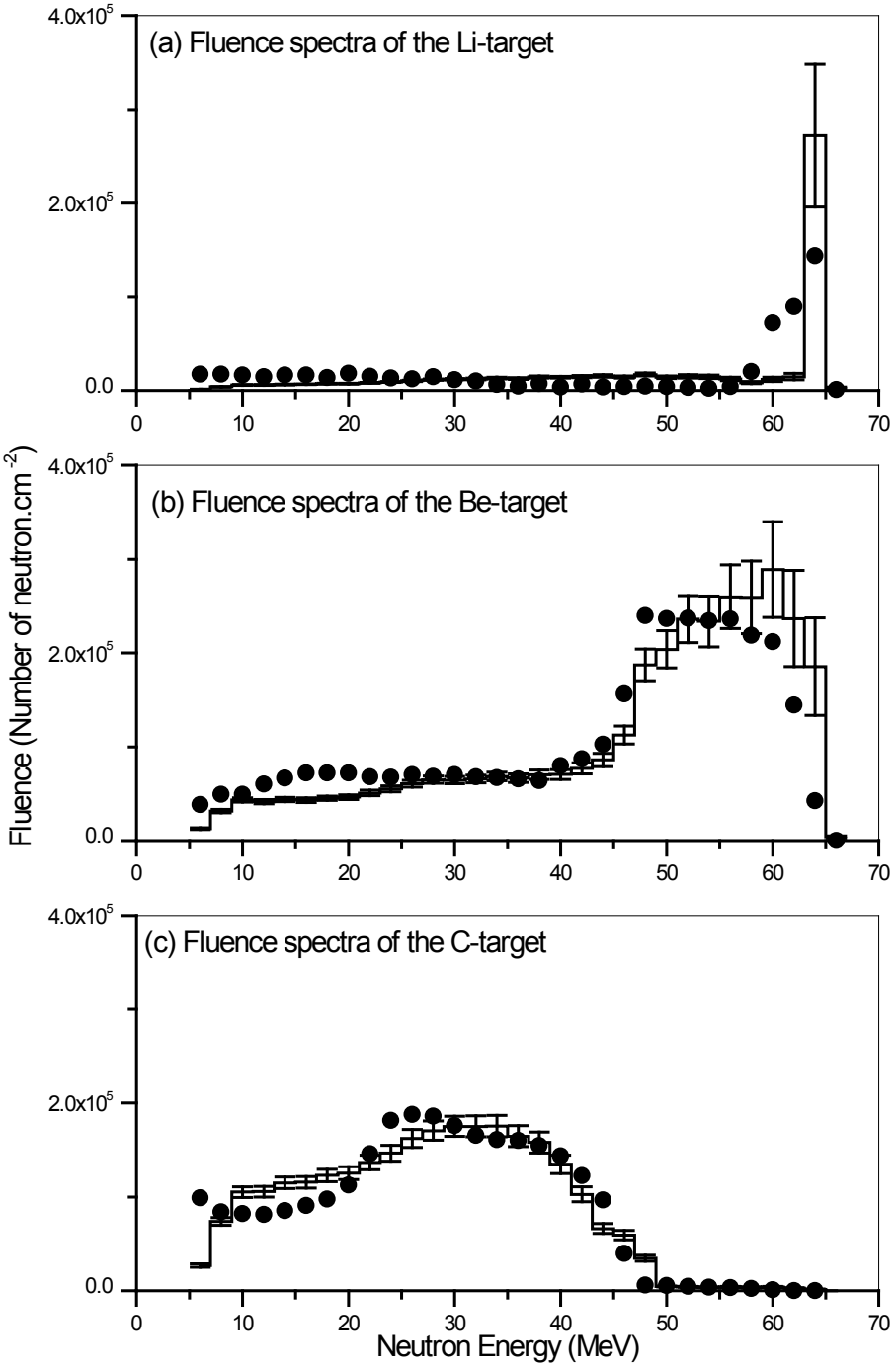

Fig 2(a) -(c): Monte Carlo calculated fluenc spectra (solid circles) compared with fluence spectra (histograms) measured by time-of flight.

4. References

[1] Herbert M 2009. *Determination of neutron energy spectra inside a water phantom irradiated by neutrons of energy up to 64 MeV*. PhD Thesis, Unpublished, University of Cape Town.

[2] Nolte R, Mhlbradt K, Meulders J, Stephan G, Haney M and Schmid E. *RBE of Quasi-monoenergetic 60 MeV Neutron Radiation for the Induction of Dicentric Chromosomes in Human Lymphocytes.* Radiation and environmental biophysics, **44**(3), 201-209.

[3] Taniguchi S, Nakamura T, Nunomiya T, Iwase H, Yonai S, Sasaki S, Rokni S, Liu, J, Kase K and Roesler S 2003. ..... Nuc.Instru. and Meth **A503**, 595

[4] Bohm T, Deluca P, Cox L, Maughan R, Jones D and Lennox A 1999. *Monte Carlo calculations to characterize the source for neutron therapy facilities*. Med. Phys. **26,** 783-792.

[5] Brooks F and Klein H 2002, *Neutron spectrometry- historical review and present status*, Nucl. Instr. Meth. **A476,** 1-1.

[6] Hughes H, Prael R and Little R 1997. *MCNPX- The LAHET/MCNP code merge*. X- Division research note XTM-RN(U) 97-012, LA-UR- 97- 4891, Los Alamos National Laboratory.

[7] Adams J and White G 1978. *A versatile pulse shapes discriminator for charge particle separation and its application to fast neutron time of flight spectroscopy*. Nucl. Instr. and Meth, **156,** 459-476.

[8] Bertini H 1969, *Intranuclear-cascade calculation of the secondary nucleon spectra from nucleon-nucleus interactions in the energy range 340 to 2900 MeV and comparison with experiment*. Phys. Rev **188**, 1711-1730.

[9] Rose P 1991, *ENDF-201: ENDF/B-VI Summary Documantation.* Report BNL-NCS-17541, Brookhaven National Laboratory.

Kinetic analysis of biomass/sorbent blends for gasification purposes

A.I Mabuda, N.S Mamphweli and E.L Meyer
University of Fort Hare, Institution of Technology, Alice, 5700
e-mail: amabuda@ufh.ac.za

Abstract. Biomass is one of the main renewable energy sources and coupled with a carbon dioxide adsorbent material such as calcium oxide sorbent it increases the biomass conversion efficiency during gasification. Kinetic study of materials is vital to the assessment of parameters including the feasibility, design, and scaling of industrial biomass conversion applications. This study aims to investigate the thermal degradation behavior of thermochemical conversion of biomass/sorbent blends in order to choose the ratio that result in higher conversion efficiency during gasification. Thermal stability is the stability of material to resist change in physical shape as its temperature changes. Thermogravimetric analysis (TGA) was employed to determine the thermal stability and kinetics of biomass and sorbent mixtures of pine wood, calcium oxide (CaO) and magnesium oxide (MgO), which will ultimately determine the gasification characteristics of the blends. A mixture of 75 % pine wood and 12.5 % CaO and 12.5 % MgO resulted in the highest thermal stability compared to others. For this reason this mixture was found to be the one suitable for gasification. The thermal analyses obtained for the different blends are presented and discussed in detail in this paper.

1 Introduction

Biomass is recognized as one of the major sources of renewable energy [1]. Biomass pyrolysis can be classified as a heterogeneous chemical reaction and can be affected by changes in reaction geometry and by interfacial diffusion of reactants and products [2, 3]. The progress of heterogeneous reactions could not be studied using the concentration of biomass components since these values may vary over time; the mentioned variation is a difference between homogeneous and heterogeneous reactions [4]. However, pyrolytic decompositions of biomass are best described considering independent parallel reactions, assuming the presence of pseudo-components [2].

Pyrolysis is a fundamental thermochemical conversion process that can be used to transform biomass directly into gaseous and liquid fuels. Pyrolysis is also an important step in combustion and gasification processes. The reaction dynamics and chemical kinetics of heterogeneous processes can be affected by three key elements [3]. In this regard, a thorough understanding of pyrolysis kinetics is vital to the assessment of items including the feasibility, design, and scaling of industrial biomass conversion applications [5, 6]. Table 1 presents a series of chemical reactions that occur during the conversion of biomass into useful products in a gasification system [7].

Table 1: Gasification reactions.

Reaction type	Heat of reaction	Equation
Oxidation reactions		
$C + O_2 \rightarrow CO_2$	-394 kJ/mol	(1)
$C + ½O_2 \rightarrow CO$	-284 kJ/mol	(2)
$H_2 + ½O_2 \rightarrow H_2O$	-242 kJ/mol	(3)
$CH_4 + 2O_2 \leftrightarrow CO_2 + 2H_2O$	+803 kJ/mol	(4)
Reduction reactions		
$C + CO_2 \leftrightarrow 2CO$	+172 kJ/mol	(5)
$C + H_2O \leftrightarrow CO + H_2$	+131 kJ/mol	(6)
$C + 2H_2 \leftrightarrow CH_4$	+74.8 kJ/mol	(7)
$C + ½O_2 \rightarrow CO$	-111 kJ/mol	(8)
Shift reaction		
$CO + H_2O \leftrightarrow CO_2 + H_2$	+41.2 kJ/mol	(9)
Methanization reaction		
$2CO + 2H_2 \rightarrow CH_4 + CO_2$	-247 kJ/mol	(10)

$CO + 3H_2 \leftrightarrow CH_4 + H_2O$	+206 kJ/mol	(11)
$CO_2 + 4H_2 \rightarrow CH_4 + 2H_2O$	-165 kJ/mol	(12)
Steam reactions		
$CH_4 + H_2O \leftrightarrow CO + 2H_2$	+206 kJ/mol	(13)
$CH_4 + ½O_2 \rightarrow CO + 2H_2$	+36 kJ/mol	(14)

Thermogravimetric analysis (TGA) provides an excellent tool that may provide insight regarding the kinetics of heterogeneous reactions. However, it cannot be overstressed that the kinetic data obtained from a single thermo-analytical technique, does not provide the necessary and sufficient evidence to draw mechanistic conclusions about a solid state decomposition process [8]. The kinetic behavior of a given heterogeneous reaction system may change during the process and so it is possible that the complete reaction mechanism cannot be represented suitably by a single specific kinetic model [9].

The purpose of this paper is to evaluate the thermal stability of various biomass/sorbent blends using the TGA method and to determine kinetic parameters (activation energy, *E* and pre-exponential factor, *A*) using the model-free (Isoconversional) approach.

2 Methodology

TGA measurements were carried out with biomass and biomass/sorbent blends. The experiments were carried out in a nitrogen atmosphere with the flow rate maintained at 20 ml/min. Biomass (wood) was coarse ground to 250 μm and mixed with calcium oxide (CaO) and magnesium oxide (MgO). CaO and MgO powders were used without further preparation. The mixtures of biomass and sorbents are presented in Table 2.

Table 2: The mixture of wood, CaO and MgO materials

Method	Wood (%)	CaO (%)	MgO (%)	CaO.MgO (%)
I	75	12.5	12.5	25
II	90	5	5	10

The TGA measurements were conducted at different heating rates of 10 °C, 15 °C and 20 °C/min in a temperature range of 20 °C to 700 °C. The proximate and ultimate analysis of biomass is shown in Table 3. The kinetic parameters were determined using the model-free, Kissinger method.

Table 3: Proximate and ultimate analysis of wood

Proximate analysis	(wt. %)	Ultimate analysis	(wt. %)
Volatile matter	68	Carbon	47.5
Moisture content	8	Hydrogen	6.5
Fixed carbon	24	Nitrogen	0.1
Ash content	0.3	Oxygen[1]	45.9

[1]calculated by difference

2.1 Isoconversional methods

The majority of kinetic methods used in the area of thermal analysis considers the rate to be a function of only two variables, *T* and α [10]:

$$\frac{d\alpha}{dt} = k(T)f(\alpha) \tag{15}$$

where $k(T)$ is the rate constant and $f(\alpha)$ is the reaction model. The temperature dependence of equation (15) is given by Arrhenius equation:

$$k(T) = Ae^{\left(-\frac{E}{RT}\right)} \tag{16}$$

where T is the absolute temperature in K, R is the universal gas constant, A is the frequency factor, or pre-exponential, and E is the activation energy of the reaction. The extent of reaction, α, can be defined either as the mass fraction of biomass substrate that has decomposed or as the mass fraction of volatiles evolved and can be expressed as shown below:

$$\alpha = \frac{W_0 - W}{W_0 - W_f} \tag{17}$$

where W is the mass of substrate present at any time t, W_0 is the initial substrate mass, W_f is the final mass of solids (i.e., residue and unreacted substrate) remaining after the reaction.

The Kissinger method is a model free method, which allows obtaining the kinetic parameters of a solid-state reaction without knowing the reaction mechanism. Kissinger [12] developed a model-free, non-isothermal method with no need to calculate E for each conversion value in order to evaluate kinetic parameters. This method allows to obtain the value of the activation energy from a plot of Ln (β/T_m^2) against $1000/T_m$ for a series of experiments at different heating rates, β (°C/min), where T_m is the temperature peak of the DTG curve. The equation is the following:

$$\ln\left(\frac{\beta}{T_m^2}\right) = ln\left(\frac{AR}{E}\right) - \frac{E}{RT_m} \tag{18}$$

The activation energy can be calculated from the slope of the plot, which is equal to $-E/R$ and the pre-exponential factor from the intercept of the plot, which is equal to ln(AR/E).

3 Results and Discussions

Figure 1 shows the TGA curves of biomass and biomass/sorbent blends at the heating rate of 20 ^{o}C/min. The initial thermal degradation for all curves is due to water vaporization below 100 °C. This is then followed by a rapid weight loss due to devolatilisation, between the temperature range of 100 °C and 400 °C. After devolatilisation/pyrolysis of the biomass and biomass/sorbent samples, the remaining material consist mainly of char and carbonates, respectively. These data were limited to devolitilisation process up to 700 ºC, although the reactions were still taking place up to 900 ºC where the char and carbonates mass remains constants after 800 º C. The small decomposition peak appear at temperatures 550 °C and 650 °C in the case of 25% CaO.MgO mixture, it can be attributed to the carbonation of $CaCO_3$, through which CaO can absorb the released CO_2 to form $CaCO_3$ product [13]. This figure shows that 25% CaO.MgO is the most thermally stable compared to other samples. This helps with the selection of the end use application, which helps to predict the performance of a material and improve its quality. Wood and 10% CaO.MgO blend decomposes by 7.5 and 8.55 %/°C after 600 °C respectively. Whereas 25% CaO.MgO blend loses weight at a low rate of 2.69 %/°C after this temperature. For this reason the 25% CaO.MgO sample was chosen for kinetic study and its results were compared with wood sample.

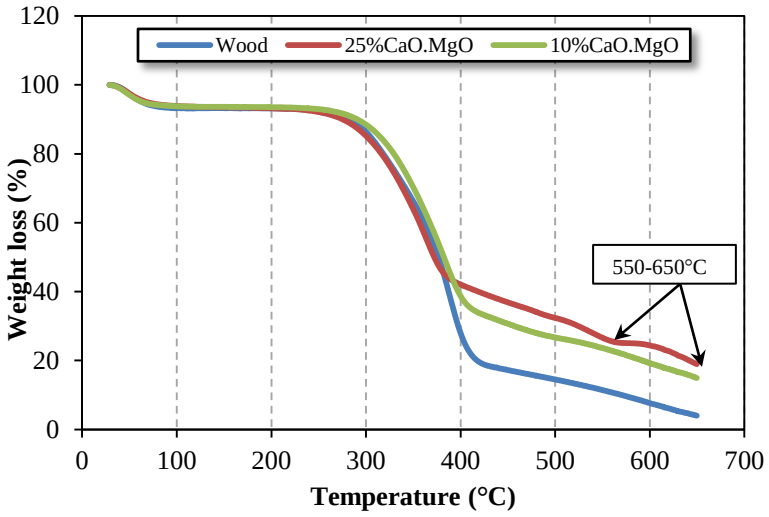

Figure 1: Thermal degradation of wood and blends at the heating rate of 20 °C/min.

Figures 2 shows the TGA curves of wood (solid lines) and wood with 25% CaO.MgO blend (dashed lines) at different heating rates of 10 °C/min, 15 °C/min and 20 °C/min, respectively. It is known that the heating rate affects both locations of the TGA curve and maximum decomposition rate [14]. As can be observed from both graphs, there is a shift in weight loss lines caused by decreased heating rate implying that the reaction is slowing down. At higher heating rates, individual weight losses are reached at lower temperatures. Again, during the measurements, at a lower heating rate, a larger instantaneous thermal energy is provided in the system and a longer time is required for the purge gas to reach equilibrium with the temperature of the furnace [15]. At a lower heating rate of 10 °C/min, 25% CaO.MgO blend shifted to higher temperature compared to wood. This means the temperature needed for this blend to decompose is 4.55 % higher than wood. Whereas the higher heating rate has a short reaction time and the temperature needed for the sample to decompose is lower. This also causes the maximum rate curve to shift to the right [16]. This can be a result of heat and mass transfer limitations. Which implies that the temperature in the furnace space can be a bit higher as the temperature of a particle and the rate of devolatilisation is higher than the release of volatiles [15]. It also implies that at a higher temperature the volatiles are released and are more likely to deposition reactions [17].

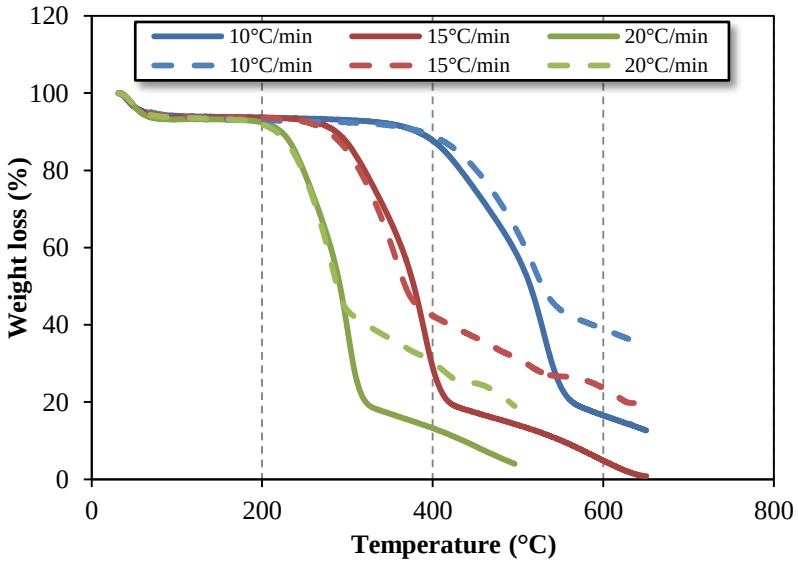

Figure 2: Thermal degradation of wood (solid lines) and wood with 25% CaO.MgO blend (dashed lines) at various heating rates

The kinetics parameters were obtained from model-free, non-isothermal TGA data and require a set of experimental tests at different heating rates. The heating rates were 10 °C/min, 15 °C/min and 20 °C/min as shown from Figure 2. Figure 3 shows the Kissinger plot of $\ln(\beta / T_m^2)$ versus $1000/T_m$ (K^{-1}) of the decomposition process for wood (blue plot) and 25% CaO.MgO blend (red plot) respectively. A linear fit to the data enabled the determination of E and A as per equation (18).

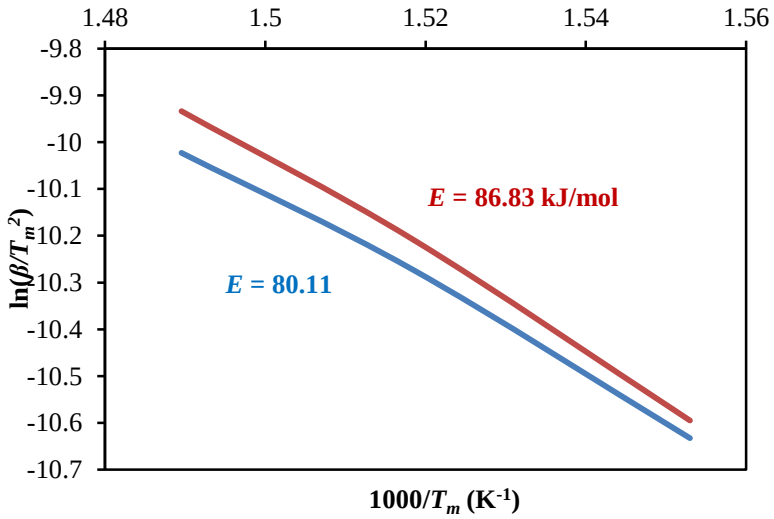

Figure 3: Plots of $\ln(\beta/T_m^2)$ versus $1000/T_m$ of wood sample (blue plot) and 25% CaO.MgO blend (red plot) for the heating rates of 10 °C/min, 15 °C/min and 20 °C/min

The results obtained from TGA were elaborated according to model-free method to calculate the kinetic parameters. The activation energy (E) and the pre-exponential factor (A) of wood and 25% CaO.MgO samples were calculated from Eq. (18) where T_m is a temperature which corresponds to the maximum weight loss peaks calculated from DTG curve. The peak temperatures were 370.9 °C, 385.6 °C, and 398.3 °C corresponding to 10 °C/min, 15 °C/min and 20°C/min heating rates, respectively. The correlation coefficient (R^2) for both wood and 25% CaO.MgO blend is 99.7%.

Table 4 presents the results for activation energy (E) and pre-exponential factor (A) obtained from this method. The activation energy obtained is 80.11 and 86.83 kJ/mol, and pre-exponential factor is 7.38 x 10^5 and 2.91 x 10^6 min^{-1} for wood and 25% CaO.MgO blend, respectively. This means that the reaction mechanism is not the same (8.39 % difference) for the decomposition process. The study [15] reported that the heating rate, the type of biomass tested and the atmosphere in which thermal degradation takes place, have significant effects on the thermal degradation rates and, therefore, on the activation energies. The results presented herein are in the agreement with the latter statement.

Table 4: Kinetic parameters (E and A) obtained by Kissinger method.

Samples	***E* (kJ/mol)**	**Δ*E* (%)**	***A* (min^{-1})**
Wood	80.11	—	7.38 x 10^5
25% CaO.MgO	86.83	8.39	2.91 x 10^6

4 Conclusions

There was a significant difference (59 %) in weight loss between the biomass and biomass with sorbent mixture (25% CaO.MgO) at higher temperature (400-650 °C), which implies that the wood with sorbents have a better thermal stability compared to pure wood. The activation energy (E) and the pre-exponential factor (A) for wood and 25% CaO.MgO blend were 80.11 and 86.83 kJ/mol and 7.38 x 10^5 and 2.91 x 10^6 min^{-1} respectively. The energy of the blend is 8.39 % higher than the biomass, which implies that the blend requires more energy to react and would thus gasify at higher

temperatures and release more energy than pure biomass materials. The released energy is due to the exothermic reaction whereby CaO absorbs CO_2 during the water-gas shift reaction in the gasifier. The resultant energy can be used by other endothermic reactions in the gasifier and for external use purposes.

5 References:

[1] Bridgwater V., Meier D., Radlein D. *Organic Geochemistry* **30** (1999) 1479-1493.
[2] Song Hu, Andreas Jess, Minhou Xu. *Fuel* **86** (2007) 2778–2788.
[3] John E. White,W. James Catallo, Benjamin L. Legendre. *Journal of Analytical and Applied Pyrolysis* **91** (2011) 1–33.
[4] Ozawa T. Bull *Chem Soc Jpn* 1965; **38:**1881–6.
[5] Raveendran K., Ganesh A., Khilar K.C. *Fuel* **75** (1996) 987–998.
[6] Sensoz S., Can M., Energy Sources. *Utilization, and Environmental Effects* **24** (2002) 347–355.
[7] Ruiz, A. J., Juarez, C. M., Morales, P. M., Munoz, P., Mendivil, A. M. *Renewable and Sustainable Energy Reviews*, 18, (2013) pp. 174–183.
[8] Vyazovkin S., Wight C.A. *International Reviews in Physical Chemistry* **17** (1998) 407–433.
[9] Galwey A.K., Brown M.E. *Thermochimica Acta* **386** (2002) 91–98.
[10] Vyazovkin S., Alan K. Burnham, José M. Criadoc, Luis A. Pérez-Maqueda, Popescu C., Sbirrazzuoli N. *Thermochimica Acta* **520** (2011) 1–19.
[11] H.L. Friedman, Journal of Polymer Science. Part C: *Polymer Symposia* **6** (1964) 183–195.
[12] Kissinger H., 1956. *Journal of Research of the National Bureau of Standards, Vol*.**57**, No 4, pp. 217-221.
[13] Biagini E., Barontini F., and Tognotti L 2006. *Ind. Eng. Chem. Res.,* **45** 4486–4493.
[14] Slopiecka K., Bartocci P., Fantozzi F. *3rd International Conference on Applied Energy* - 16-18 May 2011 - Perugia, Italy, pages 1687-1698.
[15] Gašparovič L., Koreňová Z., Jelemenský Ľ. *Chemical Papers* **64** (2) 174–181 (2010).
[16] Quan C., Li A., Gao N., 2009. *Waste Management*, Vol.**29**, No 8, pp. 2353-236.
[17] Bliek A., Van Poelje W. M., Van Swaaij W. P. M., van Beckum F. P. H., 1985. A*lChE Journal* (Vol. **31**, No. 10), pages 1666-1681.

Influence of the motion of aerospace systems on the polarization angle of qubits for free space QKD

M Mariola[1], A Mirza[1] and F Petruccione[1,2]

[1]University of KwaZulu-Natal, Westville Campus, Durban, South Africa
[2]National Institute for Theoretical Physics, South Africa

E-mail: mmspazio@libero.it

Abstract. Quantum cryptography allows private key exchange between the transmitter system, called Alice, and receiver system, called Bob. The key must be sent as a sequence of single photons and must be appropriately polarized. A photon sent with a horizontal base polarization must be received with the same base polarization. The polarization of the photon in free space, especially for satellite communication does not change enough to be a problem in our system. However, the change of directions of an aerospace system does require the system to be able to compensate for the relative rotations between Alice and Bob. In the case of satellite communications, the tracking angle can be deduced from the orbital parameter. For an atmospheric vehicle, a particular system to hold the contact between the transmitter and receiver is required. This proceeding shows some possible solution for a robust solution for a robust compensation.

1. Introduction

From the oldest to the newest cryptography systems, the fundamental security is related in terms of the key exchange used to decrypt and encrypt the message. The keys can be of public or private domain and when it comes to quantum cryptography it refers to the exchange of private keys, where the key for coding and encoding is the same. Using this kind of system, the receiver and the transmitter must be sure that the key is not interceptable from an eventual eavesdropper, that from this moment we'll call Eve. The quantum cryptography is guaranteed by the no-cloning theorem [2] such that the key is received without any interception from Eve and it is possible to send the encrypted message by using the public channel. The key will be formed by bit sequence called quantum bit (qubit) which is obtained by a reading of the quantum state of the corpuscle. As known for this kind of communication, qubits are sent as a sequence of photons [3]. Briefly, the qubit will be sent and received by using two non-orthogonal bases (vertical and horizontal). Alice and Bob separately and randomly decide which polarizing base they use to receive or transmit the photon. If Alice uses a different base from that of Bob which he used to receive the qubit, this would result in the loss of one bit of the key but they know that in that time interval Bob received one qubit. When the transmission is complete, Alice and Bob will compare some received qubits with the same base used (that will be removed from the key). If there are important statistic differences, this means that Eve was present in the channel and it is not possible to send the message. From this brief discussion Alice and Bob must be synchronized, be spatially aligned [4] and with polarizers of the receiver and transmitter collimated.

2. Tracking system

It was shown that it's possible to obtain a quantum cryptography system in free space between two stationary points on the ground [5]. In aerospace systems, it is not possible to have two stationary units because the relative position of the transmitter and receiver change continuously with time. The communication systems must guarantee the optical link between Alice and Bob. This can be achieved by the GPS system or a system that uses the radio or laser signals.

2.1. GPS system

By using a GPS, Alice and Bob, knowing their positions and altitude, can send their location's data one after each other. Alice and Bob knowing their relative positions in space are able to align and send the key. One of the advantages of this system is that the same GPS signal can be used to synchronize the qubit transmission. This system is not independent from the other systems and it is possible to have Doppler problem [4] in some case.

2.2. Radio signal system

The system proposed to use a radio signal to send the encrypted message [4], synchronizes the qubit and for tracking as shown in Figure 1. The system resolves the Doppler effect and the system is completely autonomous. The radio signal is however transmitted from aerospace system which means an increase of the power budget on board of aerospace vehicle.

2.3. Laser tracking system

The system uses a laser with a different wavelength to the laser used for qubit exchange. This tracking laser signal is sent from Alice and received at Bob. In the system shown in the Figure 1, the laser signal will be detected at sensor 1 and sensor 2. As the same signal is received with varying phases by the sensors, it is possible to extract a voltage signal from the phase comparator circuit which is used to control the orientation of an aerospace vehicle. Bob must send another radio or laser signal to control the tracking of Alice. The laser used for the tracking can also be used for the synchronization of the key exchange and also as a beam reference for the collimation of the polarizer.

2.4. Tracking scheme

Using the system suggested in §2.3, suppose Alice is the satellite system that is not aligned with the Earth station, Bob. Photosensor 1 detects the signal at a varying time with respect photosensor 2. The signal in the channel 1 (CH1) has a different phase with respect to the signal detected in channel 2 (CH2). The phase difference provides the voltage difference which is able to drive the control tracking system. An example is shown in Figure 1. By using a pulsed laser beam as tracking signal, if the satellite is not aligned with the ground station, a phase difference will exist. In this proceeding, the phase sensor is shown like a XOR port. From the measured phase difference in output of the logical port, we have an impulse sequence through a filter which is converted to a voltage difference that is able to control the tracking. In this particular scheme, the filter can be a low-pass filter. The phase difference received between channel 1 and channel 2 is:

$$\Delta\phi = \frac{2\pi}{\lambda}(\lambda - d\sin(\alpha)), \tag{1}$$

where, $\Delta\phi$ is the phase difference between the received signal and λ is the wavelength of the signal. The precision of tracking depends on the frequency, the distance d and the reactivity of the electronic circuits at high frequency.

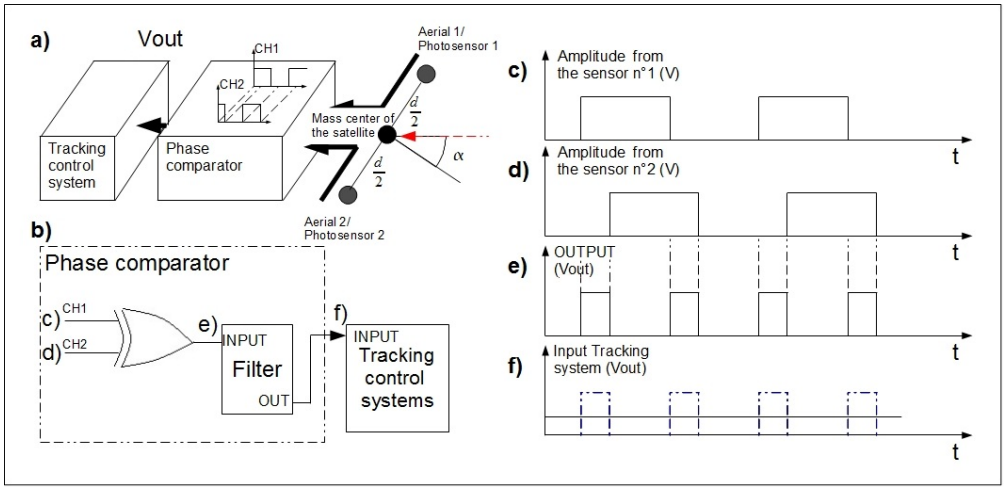

Figure 1. The figure shows the scheme for tracking between Alice and Bob.

3. Quantum cryptography for satellite communication

The tracking scheme shown in the Figure 1 can be used for any kind of aerospace systems. Once the systems are accurately tracked, it is necessary to adjust the angle of the polarizers of the receiver and the transmitter. The polarization of the photon does not change drastically [6]. By considering Alice as a satellite, and the horizontal base of the polarizer parallel at the orbital plane, it is possible to know the polarization received on the ground station by using a function of the longitude μ and latitude λ. In this simulation we consider a low orbit of 300 km and 0 degree between the Greenwich and the Aries constellation. These conditions are at the initial time when the satellite crosses over the descendent node. The ground trace is calculated by considering the rotation motion of the Earth. The ground trace is given by the formulas:

$$\sin(\lambda) = \sin(\phi)\sin(\beta), \tag{2}$$

where $\phi = \phi(t)$ is the angle between the position of the satellite and the line of nodes, β is the angle between the equatorial plane and the projection of the satellite's orbit on the Earth surface. The longitude, μ, is given by,

$$\mu = \mu_\Omega + \omega_E \Delta t - \arcsin\frac{\cos(\phi)}{\cos(\lambda)}, \tag{3}$$

where $\mu_\Omega = -25$ degrees is the angle between the line of nodes and Greenwich, Δt is the change in time, and ω_E is the Earth's angular speed.
In Figure 2 the polarizer's angle θ is calculated from the nodes line until 1 rad. The angle θ, represents the angle between the line of horizontal base of the polarizer (parallel to the orbital plane) and the equatorial plane. The simulation considers the equatorial plane as the reference plane. On the ground trace the additional phase per period is due to the rotation of the Earth.

4. Aerosystem to Aerosystem links

A link between two aerosystems is realizable without a complicated orientation control system of the aerosystem because it is possible to exploit the aerodynamics forces. The synchronism by the laser is particularly easy if two vehicles fly at the same altitude and are sufficiency close since this will prevent the multipath [4]. In the previous section, it is possible to calculate the polarizer's angles during the orbit evolution, but in this case the change in relative position

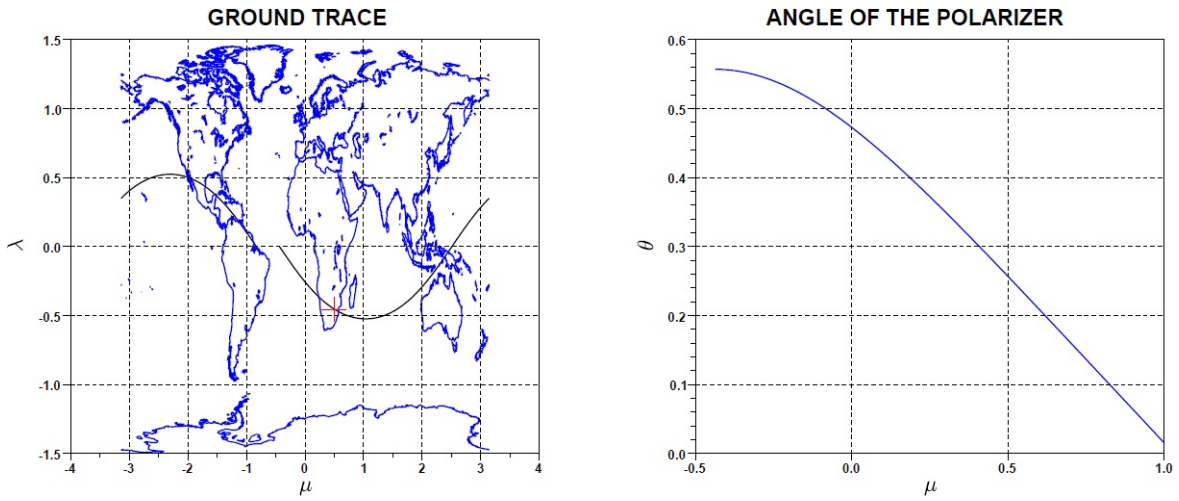

Figure 2. Angle of polarizer θ in function of the longitude μ. It is possible to observe from the first chart the simulation which considers the satellite that crosses the geographical position of Johannesburg.

between Alice and Bob is random and it is impossible to predict the orientation of the polarizers of Alice and Bob during the flight. To resolve this problem, the communications systems must have the appropriate polarization compensation controls.

5. Satellite to satellite

As the satellite orbit is predictable, it is possible to know the relative position of the satellites. In the satellite to satellite link, the direction of the link and the position of the polarizers are either known or it possible by the use of an appropriate systems of tracking and collimation.

6. Possible solutions

Other experiments show the possibility of using a beam laser reference which is able to hold a correct polarization angle between Alice and Bob [7]. A possible circuit for this is shown in Figure 3. Bob has two optical receivers, one for the quantum channel and another for the polarization control. The intensity of the polarized light I_0 through the Polaroid foil at an angle of θ from polarization axis has a final intensity according to the formula [8]:

$$I(\theta) = I_0 \cos^2(\theta). \tag{4}$$

The hypothetical scheme is shown in Figure 3. Suppose that Bob receives a beam laser reference with an angle α between $\frac{\pi}{4}$ and $\frac{\pi}{2}$, the intensities received at P1 and P2 (see Figure 3) are respectively:

$$I_{P1} = \cos^2(\alpha) \tag{5}$$

$$I_{P2} = \cos^2(\frac{\pi}{4} + \alpha). \tag{6}$$

The output is measured as a proportion of voltage to the intensity of light. The signal difference $V_{OUT} = V(I_{P1}) - V(I_{P2}) > 0$ dictates the drive turn of the polarizer until the difference is zero. This system is generic, but necessary observations must be made by considering the limit it uses. If the wavelength of the laser beam is much different from the wavelength of the photon, the aerosystems must have the same altitude and are limited to be close to each other. As shown in Figure 4, Alice sends the quantum key to Bob 1 and the laser beam and photon

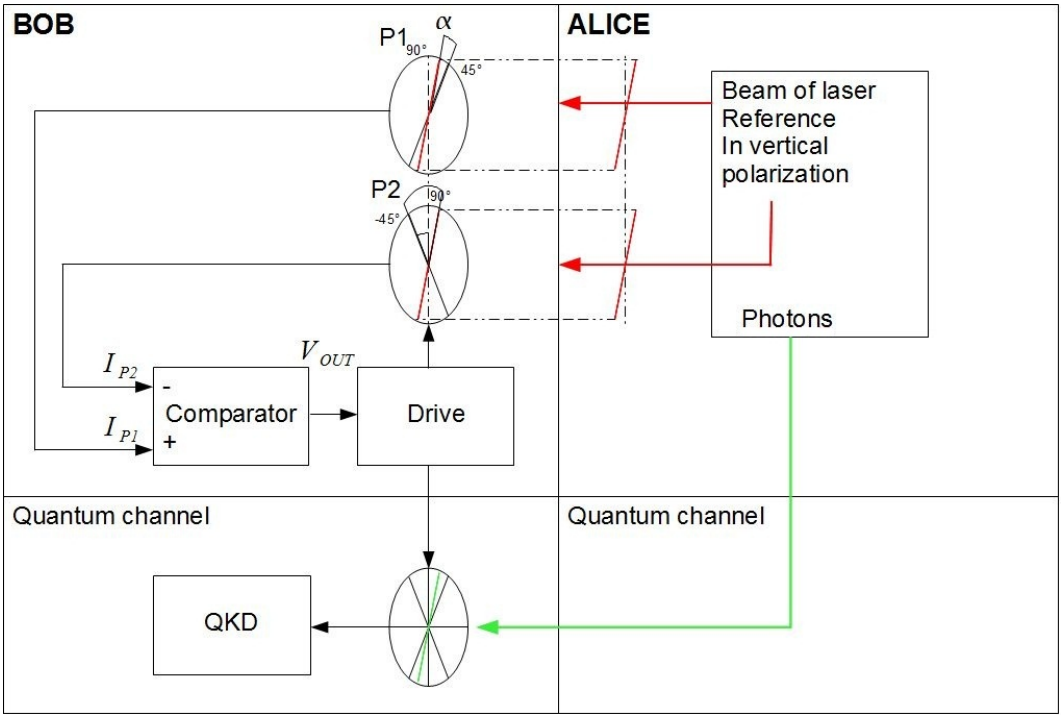

Figure 3. Scheme of the circuit to track the polarization angle of Alice and Bob.

have different wavelengths. By dividing the atmosphere into layers, where the state atmosphere parameters remains constant, the communication is possible without any problems. If Alice sends the message to Bob 2, the laser beam and the photons cross different atmospherics layers and follow different paths due to refractive indexes. It is possible to enhance the solution, if the value of wavelength of the laser beam is near to the wavelength of the photons, but this will lead to noise which is received by Bob. In this case the laser beam must be off when Alice sends the photons or the laser beam must be spatially far from the path of photons. This kind of system can be used for ground to aerospace vehicle links as well.

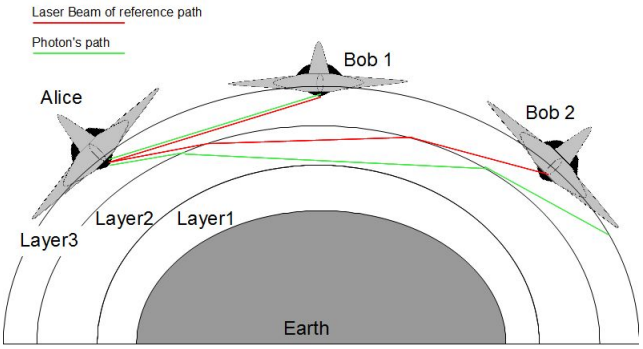

Figure 4. Consider the link between Alice and Bob. If the link propagates through a single layer of the atmosphere, minimal diffraction occurs, hence the green laser and the red laser (Single photon) have the similar paths as illustrated with Bob 1. The link to Bob 2 propagates through various layers of the atmosphere and due to chromatic dispersion the lasers follow different paths.

7. Conclusion

The QKD for satellite communications can be made possible from the knowledge of the orbital parameters. It is also possible to use the radio signal or laser signal to provide the synchronization between the earth station and the satellite or between two generic aerospace systems. If the system uses the laser beam to collimate the polarizer, the same signal can be used for tracking and synchronizing Alice and Bob for any kind of link. By considering Alice as satellite, this offers an advantage for not complicating the orientation control system and also makes it possible to improve the key generation rate [9]. For QKD, the proposed method of using the radio signal to synchronize Alice and Bob and the laser beam reference to control the polarization during the flight of Alice and Bob is seen to be the most elegant solution. This is seen from the fact that if the power budget for satellite is high it is necessary to use the simulation proposed in §3, but in our case it is not necessary to use it. This further shows the efficiency of our system.

Acknowledgments

This work is based on research supported by the South African Research Chair Initiative of the Department of Science and Technology and National Research Foundation.

References

[1] Salvador E 2007 *Appunti di crittografia complementi al modulo 3 del laboratorio una introduzione all'algebra moderna* (Torino: Universita' degli studi di Torino)
[2] Bonzio S Galeazzi S 2011 *Dalla crittografia classica alla crittografia quantistica* (Firenze: Unifi)
[3] Bennett C and Brassard G 1984 *Quantum cryptography: public key distribution and coin tossing* Proc of IEEE International conference on computer systems and signal processing 175-179
[4] Mariola M Mirza A Petruccione F 2011 *Quantum cryptography for satellite communication* Proc of SAIP 403-408
[5] Ursin R Tiefenbacher F Schmitt-Manderbach T Weier H Scheild T Lindenthal M Blauensteiner B Jennewein T Perdigues T Trojek P Ömer B Fürst M Meyenburg M Rarity J Sodnik Z Barbieri C Weinfurter H Zeilinger A 2007 Entaglement-based quantum communication over 144 km *Nature physics* **3** 481-486
[6] Bonato C Aspelmeyer Jennewein T Pernechele C Villoresi P Zeilinger A 2006 Influence of satellite motion on polarization qubits in a Space-Harth quantum communication link *Optics express* **14** 10058-10059
[7] Toyoshima M Takenaka H Shoji Y Takayama Y Takeoka M Fujiwara M Sasaki Polarization-basis tracking scheme in satellite quantum key distribution International Journal of Optics **2011** 5-6
[8] Di Pierro A *Quantum Computing* http://oldweb.ct.infn.it/ terrasi/LezioniQC-05.pdf
[9] Bonato C Tomaello A, Da Deppo V, Naletto G, Villoresi P *Feasibility of satellite quantum key distribution* Department of Information Engineering, University of Padova CNR-INFM LUXOR, New Journal of Physics **20 2009**

Design of a high-resolution PID temperature controller for use in a low-cost thermoluminescence system

M Mbongo[1] and R O Ocaya[2]

[1,2]Department of Physics, University of the free State, P. Bag X13 Phuthaditjhaba 9866

E-mail: mbongom@qwa.ufs.ac.za

Abstract. The operation of an associated low-cost thermoluminescence (TL) system [1] necessitated the design and construction of a precision temperature controller. The temperature controller is presented separately since it is a crucial aspect of the TL system. The overarching design condition was a tightly controllable temperature regime with a resolution of about $\pm 0.5^{\circ}$C. The system was designed in such a way that an embedded controller formed around the PIC18f2520 heats up a sample holder to a specified temperature in optimal time while monitoring the temperature. The control algorithm was then written to ramp the temperature through the desired range of temperature between 25 and 700°C. The output of the PID controller was made to drive a resistive heater element or plant, modelled as a low-delay component owing to the small size of the sample holder. A mathematical model of the plant was obtained, simulated within MATLAB and the optimal controller found. The results of the simulation were then used to design an algorithm for the PIC controller. It was initially thought that the demands of controlling the temperature necessitated an additional PIC controller separate from one that would handle USB communications and general control. However, the responses of the temperature controller and optimal design of the overall user interface software and PIC firmware eliminated that need. The performance of the constructed PID controller was verified over the temperature range of 100°C to 400°C. While the PID controller has been designed specifically for usage in the TL system, it can be adapted with minimal adjustments to many other laboratory processes where fine temperature control is required.

1. Introduction

To facilitate their practical studies of thermoluminescence (TL) several independent researchers have offered alternative solutions to commercial instrumentation with the main impetus being low cost, simplicity of usage or suitability for their specific purposes [2, 3, 4, 5, 6, 7]. While TL is simple in principle, in practice there are many technical instrumentation challenges that must be identified and solved. The control of temperature over wide ranges (though typically below 400°C) with good measurement resolution and accuracy for the small dimensioned samples can be difficult, more so if the samples are in powder form. Other issues stem from nonlinearities, output drift, detector correlation errors and so on. The alternatives encountered in the literature have diverse attributes, for example arbitrary, wide range heating, profiled excitation such as logarithmic heating, "automatic" control of heating, and even open-loop "bang-bang" servos. The heating apparatus themselves are just as varied as are the intensity sensing apparatus also. Several of the foregoing designs have used third-party hardware proportional-integral (PI)

or proportional-integral-derivative (PID) control of the heating element. Notwithstanding this detraction from true low-cost, our point of contention in this article is that our own experiences with the open-loop, small heater "plant" have shown that a reported temperature regulation technique often can not have the claimed accuracy, even at the lowest heating rates [1]. For example, in [2], the stated temperature accuracy is erroneously the bit resolution of the analog to digital converter (ADC) itself in open-loop. In this article we report on a design of a temperature controller using a digital PID algorithm implemented as part of the firmware of the PIC18F2520 controller. The output element is a 100 watt resistive soldering iron driven directly by a 2SK3115 power MOSFET using pulse-width modulation (PWM) at 10 kHz, with temperature feedback provided by a k-type thermocouple referenced to ambient temperature. The heater power is derived from a locally built toroidal mains transformer rectified to supply direct current of 0.6 amperes at 180 volts. Varying the duty cycle in the algorithm from 0 to nearly 100% allows a wide range of temperature for the small heater. We report on the considerations of the design, ranging from the identification of the open-loop heater plant to optimization simulations and then to the coding of the digital algorithm. Finally, we present experimental data obtained from actual performance of the heating arrangement for a typical heating run.

2. System identification

2.1. The heater and feedback arrangement

A full description of the overall TL system can be found in [1]. For the purposes of designing the temperature controller and a digital PID algorithm, only a small part of the overall system will suffice. That is, the aluminium sample holder, a type K-thermocouple (Chromel-Alumel) for temperature feedback, and the ambient-compensated temperature conditioning circuit. The K-type thermocouple has an effective Seebeck coefficient of about 41μV per degree change in temperature. A system is considered to be open-loop if a control signal sent out simply hopes to achieve a desired action, known as the set point, without any sense of what the instantaneous value of the action actually is. In the present context it can be looked at as the heater simply being turned on in some manner without temperature feedback. It is important to know the various time parameters of the open-loop plant associated with certain types of control input. For example, the times associated with the attainment of a new steady state when a control input is suddenly changed from one value to another. Loosely speaking, these responses convey a sense of the "sluggishness" of the plant and ultimately how best to ply its input. The thermocouple circuit used was built around the low-cost LM324N quad operational amplifier (OPAmp) shown Figure 1. External offset trimming and room-temperature compensation using the LM35CZ device were used to improve temperature measurement accuracy. The sample holder is an aluminium block of $2.5\times1.7\times0.5$ cm^3 to which the k-type thermocouple was affixed using a pressing metal plate and screws. A 100W resistive heating source was implemented simply using a commercial pen-type soldering iron with a tip long and narrow enough to be inserted tightly into a compatible hole drilled into the sample holder.

2.2. The software PID temperature controller

In PID temperature control the drive control signal, $u(t)$, to the heating element is derived from the feedback from past and present temperature [9]. The controller first determines the error difference signal $e(t)$ that indicates the difference between the target and the current temperature. It then generates a control signal that is a sum of three quantities, one proportional to $e(t)$, another dependent on the time accumulated (integral) error and another dependent on how fast the error is changing with time i.e. the error derivative. Mathematically,

$$u(t) = K_p e(t) + \frac{K_p}{T_i}\int_0^t e(t)dt + K_p T_d \frac{de(t)}{dt}, \tag{1}$$

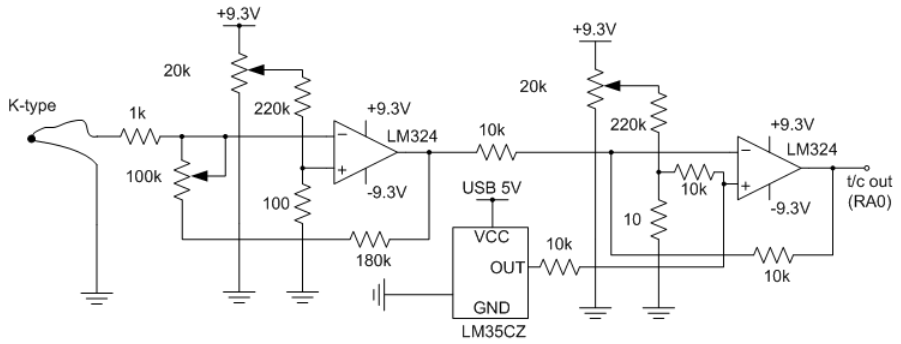

Figure 1. The temperature measurement circuit based on a K-type thermocouple.

where K_p is the proportional gain, T_i and T_d are the integral and derivative time constants respectively. Tranforming Equation 1 and defining a common forward gain K_p in Laplace transform space gives the PID controller:

$$C(s) = K_p\Big[1 + \frac{1}{T_I} + T_D s\Big] \tag{2}$$

Figure 2 shows the PWM actuator used. The gate of the MOSFET was driven at a software generated 10 kHz, forming the input of the controlled plant. Therefore, an input is subsequently any fixed amplitude (i.e. 5V), 10 kHz gate input distinguishable from other inputs by its duty-cycle only. A true "unit step" input was then a duty-cycle change from 0 to 100%. In practice a smaller step range can also be used to characterize the plant. To implement Equation 1, the time constants T_i and T_d were determined using the Ziegler and Nichols tuning method (ZNM) [8, 10] on the open-loop plant. Converting the system to z-transform space allowed digital implementation on the PIC18f2520 micro-controller.

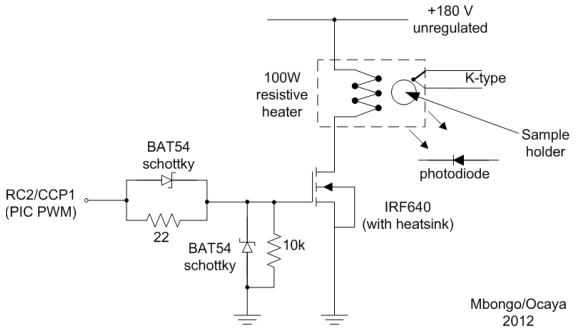

Figure 2. Diagram of the PWM heater driver.

2.3. Realization of a discrete PID controller

The Ziegler-Nichols method can be used in both open and closed loop configurations to ascertain the parameters of a plant thereby enabling a reasonable controller to be defined. In the present work the response to a step input on the open-loop plant was found to be sufficient. According to ZNM the open-loop unit step response, $G(s)$, can be approximated by the Laplace transform

$$G(s) = \frac{K\ e^{-sT_d}}{sT_1 + 1} \tag{3}$$

with the parameters K (d.c. forward gain), T_d and T_1 as in Figure 3. By direct experimentation

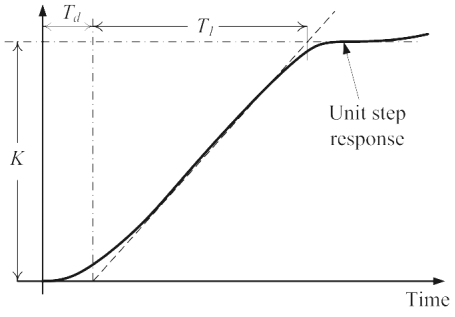

Figure 3. Parameters of interest in Ziegler-Nichols open loop tuning.

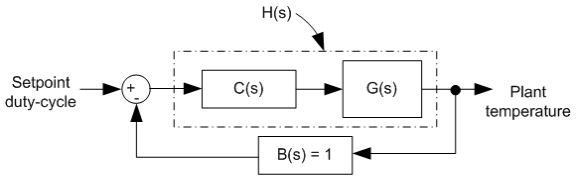

Figure 4. Block diagram of the implemented temperature controller. The closed-loop function can be written as $H(s)$=$C(s)G(s)$.

the parameters for the heater plant (sample holder and heating arrangement) were estimated graphically to be T_d=4.0s, K=4.4 and T_1=184s. The ZNM method suggests that the parameters of Equation 2 for a starting PID controller for the plant response in Equation 3 are:

$$K_p = \frac{1.2T_1}{KT_d} \approx 1.882, \qquad T_I = 2T_d = 150\text{s} \quad \text{and} \qquad T_D = \frac{1}{2}T_d \approx 6.67\text{s}. \tag{4}$$

Substitution of the parameters in Equation 4 into Equation 2 gives a PID controller $C(s)$ that has good transient response.

$$C(s) = 12.55\Big[\frac{s^2 + 0.15s + 0.001}{s}\Big]. \tag{5}$$

The MATLAB/Simulink model shown in Figure 5 was obtained from $H(s)$=$C(s)G(s)$ as shown in Figure 8. The transport delay block models the delay T_d in Equation 3. To implement the

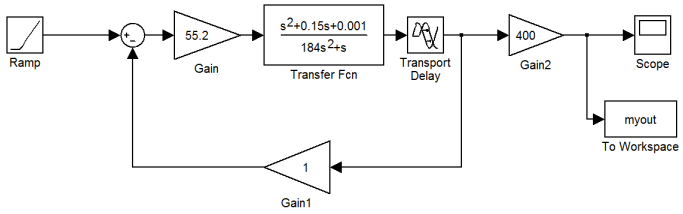

Figure 5. MATLAB/Simulink model of the closed-loop system that gives good transient performance. The input shown is a linear ramp with input duty cycle starting from 0 to 100%.

controller using a digital PID algorithm running on the PIC18f2520 firmware, it was necessary to convert the controller to the sampled time domain. The techniques of the z-transform were readily applied [11], though a full description of the technique is beyond the present scope. The PID controller in Equation 2 has the "velocity" z-transform form in sampled time $t \in 0, T, 2T, \ldots$ given by

$$C(z) = K_p\left[1 + \frac{T}{T_I(1-z^{-1})} + T_D\frac{(1-z^{-1})}{T}\right] = a + \frac{b}{1-z^{-1}} + c(1-z^{-1}), \tag{6}$$

where $a{=}K_p$, $b{=}K_pT/T_I$ and $c{=}K_pT_D/T$. The parameter T is the sampling interval of the converter. It is roughly equal to the firmware looping or polling time. The result is the parallel PID implementation in Figure 6 which can readily be coded into the microcontroller firmware. The controller output $u(kT)$ is the PWM MOSFET gate drive. The sampled PID equations,

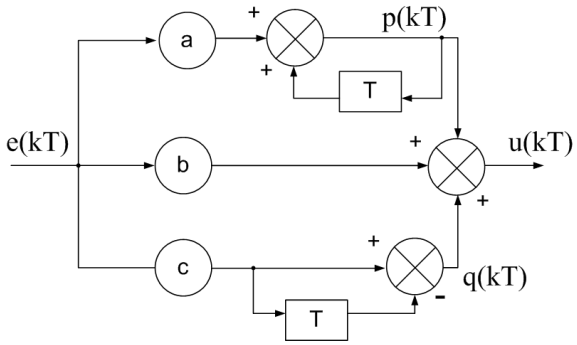

Figure 6. Parallel implementation of the PID TL-system heater controller.

Equations 7, were implemented on the PIC device in mikroC code [12].

$$\begin{aligned} p(kT) &= b\ e(kT) + p(kT-T) \\ q(kT) &= c\ e(kT) - c\ e(kT-T) \\ u(kT) &= p\ e(kT) + a\ e(kT) + q(kT) \end{aligned} \tag{7}$$

3. Results

The goal of creating a TL-instrument using common components has been largely met. Figure 7 shows the observed heating open-loop response of the small plant versus the MATLAB simulated function. From this information a good PID controller can then be derived and implemented

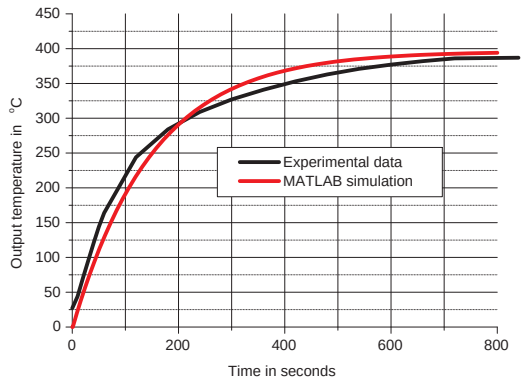

Figure 7. Experimental and simulated open-loop unit step response based on Equation 3.

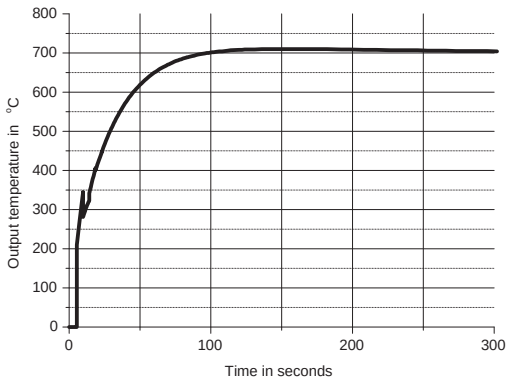

Figure 8. Closed-loop unit step response under scaling showing good transient response.

digitally in the microcontroller firmware, with a response typified by Figure 8. Linear heating was possible by ramping the control input from the software through the output range. Heating rate is known to affect observed results [13] and control of the heating rate is therefore needed. Figure 9 shows the typical output of the closed-loop plant in response to ramping duty-cycle input. Simulations show that rates exceeding 20°C/min are possible with the designed controller.

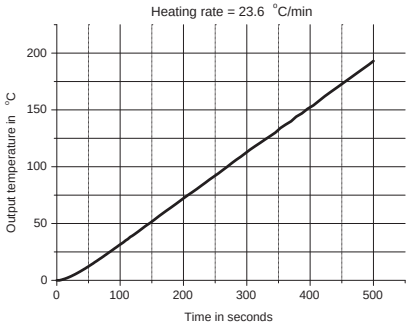

Figure 9. PID response of the system showing linear heating with a ramped duty-cycle input of 0.06 per min with Pearson's coefficient of linearity R^2=0.999.

4. Conclusions

We have presented the temperature controller in a low-cost TL-instrument. We show how the transfer function of a physically small heating plant can be determined for fine temperature control. Precise characterizations of the actual heating arrangement are usually not fully described in similar TL instruments in the literature, and many of the comparable TL systems surveyed use open-loop methods at the cost of finer temperature control. We outline the closed-loop PID and heater circuitry, ambient-temperature compensation mechanism and showed how this leads to greater temperature resolution. The digital PID algorithm was then derived and implemented in PIC microcontroller firmware. A linear heating regime with variable heating rates were obtained by ramping the control input from the software through the output range, with attained heating rates exceeding 20°C/min. The use of the digital PID algorithm allowed ease of tuning the controller by allowing minor adjusting the parameters in the firmware. Finally, the present approach to low-cost TL instrument design is significant in many respects and ultimately allow higher accuracy and finesse in glow peak separation on the temperature axis. The scope for future work with respect to temperature control remains to write algorithms for arbitrary heating regimes that can be invoked from the graphical user interface of the control program.

References

[1] Mbongo M and Ocaya R O 2012, *A low-cost thermoluminescence system for use with .net computing environments. (Submitted to SAIP 2012).*
[2] Neelamegam P, Padmanabhan K and Selvasekarapandiang S 1992 *Meas. Sci. Technol.* **3** 581
[3] Molina P, Santiago M, Caselli E, Lester M and Spano F 2002 *Meas. Sci. Technol.* **13** N16
[4] Bhatnagar R, Saxena P, Vora H S, Dubey V K, Sarangpani K K, Shirke N D and Bhattacharjee S K 2002 *Meas. Sci. Technol.* **10** 2017
[5] Lyamayev V I 2006 *Meas. Sci. Technol.* **17** N75
[6] Neelamegam P and Rajendranb A 2006 *JINST* **1** T05001
[7] Quilty J W, Robinson J, Appleby G A and Edgar A 2007 *Rev Sci Instrum.* **78**(8):083905
[8] Ziegler J G and Nichols N B (1942). *Optimum settings for automatic controllers.* Trans. of the ASME. **64**.
[9] Ibrahim D, *Microcontroller based temperature monitoring and control*, Newnes 2002, ISBN 978-0750-655569.
[10] Åström K J and Hägglund Tore, *PID Controllers-Theory, Design, and Tuning*, 2^{nd} edition, ISA, 1995.
[11] Stroud K A, *Advanced Engineering Mathematics*, 4^{th} ed., Industrial Press, NY, 2003.
[12] MikroElektronika, *mikroC Pro for PIC Microcontrollers, mikroC Pro v3.2*, http://www.mikroElektronika.com (last accessed August 2011).
[13] Kitis G, Spiropulu M, Papadopoulos J and Charalambous S (1993), Nuclear Instr. & Methods in Physics Research Section B, **73** (3), pp 367372 DOI: 10.1016/0168-583X(93)95753-R

Optimization of biogas by co-digestion using a field-scale bath digester

P Mukumba[1], G Makaka[1], S Mamphweli[2], E Meyer[2]
University of Fort Hare, [1]Physics Department, [2]Institute of Technology, Private Bag X1314, Alice 5700.

E-mail: pmukumba@ufh.ac.za

Abstract. Biogas technology converts organic wastes into biogas, which consists of about 80% methane. The digester effluent after digestion can be used as manure. Co-digestion of organic wastes involve mixing of various substrates in varying proportions. The investigation was carried out using a field batch biogas digester. Fresh goat dung and horse dung were collected from the University of Fort Hare Honey dale farm. The latter substrates were analyzed for total solids (TS), volatile solids (VS), total alkalinity (TA) and calorific value (CV) before they were co-digested in a bath biogas digester in different mixing ratios. The biogas composition for each sample was analysed using a Non-Dispersive Infrared gas sensor, which detects methane gas up to 100% volume. The study found that a mixing ratio with 40% horse dung and 60% goat dung produced biogas with the highest methane yield. Therefore, biogas yield was influenced by variations in mixing ratios as well as waste types used.

1. Introduction

South African economy is highly dependent on fuel fuels, with coal accounting for about 90% of electricity generation. Fossil fuels have many negative impacts on the environment, which include, environmental degradation, climate change and human health problems (Elaiyaraju and Partha, 2012). After the ratification of UNFCCC and Kyoto Protocol respectively in August 1997 and July 2002, the South African government embarked upon numerous projects related to climate change, including projects that have been intended as measures to reduce greenhouse gases (Mwakasonda 2007). One measure taken by the country to reduce greenhouse gas emissions was anaerobic digestion by use of biogas digesters in rural areas. Anaerobic digestion is the production of biogas mainly methane from organic wastes in complete absence of oxygen by anaerobic aerobes such as acetogens, acidogens and methanogens.

Numerous studies have been conducted by several researchers in order to optimize biogas yield in anaerobic digestion (Iyagba *et al.,* 2009; Li *et al.,* 2011; Misi 2001; Mukumba *et al.,* 2011; Uzodinma *et al.,* 2009). These studies established that using co-substrates in anaerobic digestion system improves the biogas yield due to positive synergisms established in the digestion medium and supply of missing nutrients by the co-substrates. The co-digestion of organic wastes involves mixing of various substrates in varying proportions (Misi, 2001*).*

The aim of the paper is to optimize biogas production by co-digestion. The biogas digester substrates used for co-digestion were goat dung and horse dung. These wastes were co-digested at different mixing ratios.

2. Methodology

2.1. Source of substrate and mixing proportions

Fresh goat dung and horse dung were collected from University of Fort Hare Honey dale farm. The goat dung was in form of pellets. The goat dung and horse dung were mixed in different proportions. Table 1 shows the mixing proportions for horse dung and goat dung. Lime was added to each prepared sample to inhibit pH fluctuations within the biogas digester.

Table 1. Mixing proportions for horse dung and goat dung

Treatment	% of horse dung	% of goat dung
A	0	100
B	40	60
C	50	50
D	60	40
E	75	25
F	100	0

2.2. Substrate parameters

Before mixing the substrates, the following parameters for the substrates were determined, pH, total solids (TS), volatile solids (VS), ammonia-nitrogen (NH_4 - N), total alkalinity (TA), temperature (T) and caloric value (CV). All the analytical determinations were performed according to the standard methods for examination of water and waste water (ALPHA, 2005). The temperature of slurry was measured by type-K thermocouple, while the digital pH meter measured the influent and effluent pH.

2.3. Biogas analysis

The biogas composition was analysed by the biogas analyser. The biogas analyser consisted of Non-Dispersive Infrared sensor for sensing methane and carbon dioxide and Palladium/Nickel sensor for sensing hydrogen and hydrogen sulphide. Figure 1 shows the biogas data acquisition system that includes a biogas analyser.

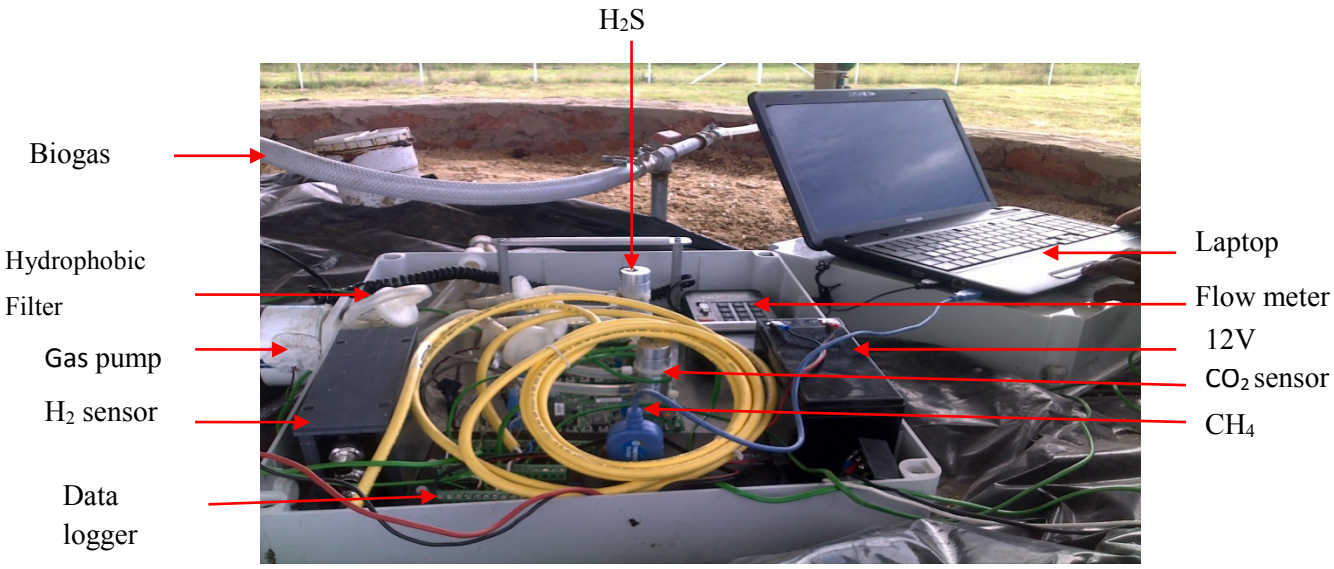

Figure 1. The data acquisition system

The data for biogas composition was recorded by a CR1000 data logger at a time interval of 2 minutes. The biogas analyser and the CR1000 data logger were powdered by a 12 V DC battery that was connected to a 20 W photovoltaic module. The biogas was carried to the flow meter where the production of the biogas was measured. A CR1000 data logger was interfaced to a laptop computer used to download data. The ambient, biogas, sawdust and slurry temperature sensors were connected to the data logger. The 12V battery was connected to the solar photovoltaic module via the battery regulator. The battery regulator prevented the 12V battery from excessive charging and discharging.

3. Results and discussions

Substrate characteristics of the horse dung and goat dung are shown in Table 2. The horse dung had less volatile solids than the goat dung. The TS/VS ratio of donkey dung was 72.11 and for goat dung was 64.16. Karim *et al.,* 2005, found that as the TS/VS ratio is increases, the amount of methane production increases. The goat dung had a higher pH than horse dung.

Table 2. Substrate characteristics for goat and horse dung

Parameter	Goat dung	Horse dung
Total solids (mg/L)	642796.16	269515.67
Total solids (%)	64.28	26.95
Volatile solids (mg/L)	463500.53	172934.47
Volatile solids (%)	72.12	64.16
Total solids/ volatile solids (%)	72.11	64.16
Total alkalinity (mg/L)	62136-65789	62361-65897
pH [average]	7.75-7.82	7.34-7.36
Calorific value (MJ/g)	27.28	26.40
Ammonia-nitrogen (mg/L)	175-226	232-250

Table 3 shows substrate parameters for horse dung and goat dung in different mixing ratios. There were variations of methane content among different treatments. Goat dung had a biogas composition with higher methane yield than horse dung. Co-digestion of goat dung and horse dung at different mixing ratios increased methane content in biogas. The 40% horse dung and 60% goat dung had the highest methane yield of 60-75%. The 50% horse dung and 50% goat dung also produced biogas of high methane yield content of 58-75%. The 75% horse dung and 25% goat dung had the lowest methane yield for all the co-substrates used between 55-65%.

Table 3. Composition of biogas for different substrates with different mixing ratios

	0%,horse 100%,goat dung	40% horse,60% goat dung	50% horse,50% goat dung	60% horse, 40% goat dung.	75% horse, 25% goat dung	100% horse, 0% goat dung
CH_4%	45-58	60-75	58-75	55-73	55-65	40-55
CO_2%	30-45	25-35	30-40	28-40	30-45	40-50
H_2S%	trace	trace	trace	trace	trace	Trace
H_2% + other gases	1-10	1-6	1-6	1-6	1-6	1-8

Biogas yields for different samples with different mixing ratios are shown in Figures 2 and 3. Figure 2 shows biogas yield for goat dung and horse dung. The biogas production started soon after seeding the biogas digester with active inoculums, and kept increasing until reaching the peak and then began to decline. The retention time was 23 days for the trials. The goat dung produced the highest biogas yield of 900 litres on day 12, while horse dung produced the highest biogas yield of 813 litres on day 13. There was difference of 87 litres between the two peaks of cow dung and horse dung. The cumulative biogas yield of cow up to the peak was 4670.19 litres. This was 63% of the total biogas yield within a hydraulic retention period of 23 days. However, cumulative biogas yield of horse dung up to the peak was 4492.52 litres. This was 63% of the total biogas yield within a hydraulic retention period. For goat dung, as from day 13, there was a decrease in biogas production until the production levels off, while for horse dung, biogas production decreased as from day 14. On average, the biogas production from goat dung was 336 L/day and for horse dung was 324 L/day. It was observed that in all trials there was very low gas production after a retention time of 20 days. This indicated that the gas content within the substrate was almost given off.

Goat dung had slightly a higher biogas yield than horse dung. This has been attributed by its high TS/VS ratio. Goat dung is easily biodegradable as compared to horse dung. Theoretically, horse dung produces more biogas than goat dung because of its carbon/nitrogen ratio of 25:1. Horse dung does not have the right bacteria in their guts to digest cellulose in plant material unlike goat dung. The dung is made of indigestible matter. The subsidiary peaks in the gas production in horse dung are a result of the presence of high lignin and cellulose in the wastes which are resistant to enzymatic degradation and hence, biogas production is low. There are more peaks for mono-digestion than when horse dung is digested with other wastes. Pre-treatment of horse dung by use of grinding would greatly increase biogas production thereby minimizing these peaks. Minor peaks are seen on mono-digestion on goat dung. Biogas production increased when goat dung and horse dung were co-digested together at different mixing ratios. This is consistent with other researches that stated that more than one kind of substrate could establish positive synergism in the biogas digester (Iyagba *et al.*, 2009; Li *et al.*, 2011; Misi 2001; Mukumba *et al.*, 2011; Uzodinma *et al.*, 2009).

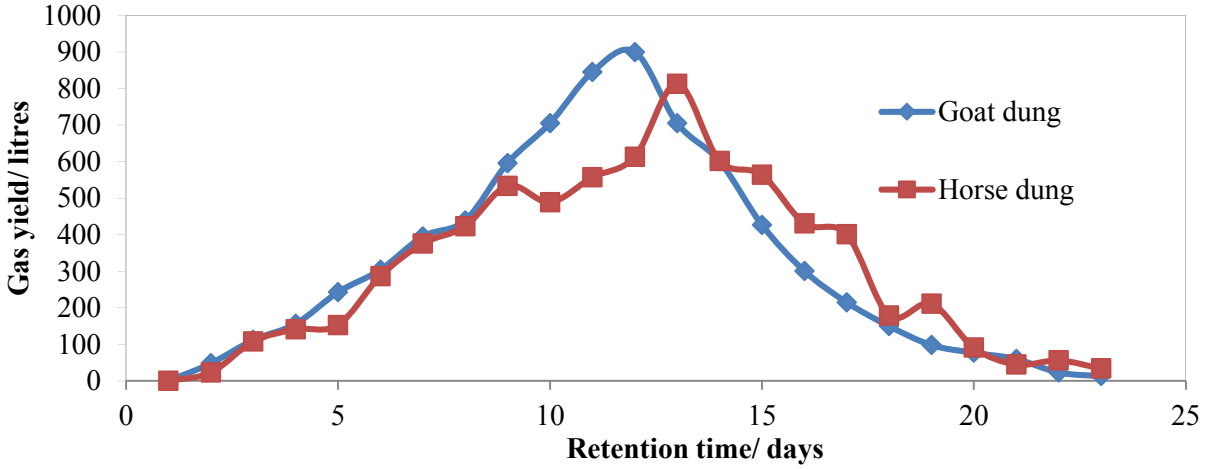

Figure 2. Biogas yield for horse and goat dung

Figure 3 shows biogas production in litres for co-digestion of 40% horse dung and 60% goat dung, 50% horse dung and 50% goat dung, 60% horse dung and 40% goat dung, 75% horse dung and 25% goat dung. The highest biogas yield was made up of 40% horse dung and 60% goat dung. This was followed by the treatment made up of 50% horse dung and 50% goat dung. The mixing ratio of 75% horse dung and 25% goat dung produced the lowest biogas yield. This was attributed by an unstable pH resulting in

poor buffering, thus lowering biogas production. The retention time for the co-digested trials was 23 days. The mixing ratio of 60% horse dung and 40 % goat dung produced a peak cumulative biogas yield of 64% in 11 days which was 6044 litres while the mixing ratio of 75% horse dung and 25 % goat dung, produced cumulative biogas yield of 5825 litres in 12 days. However, the mixing ratio 50% horse dung and 50% goat dung produced cumulative biogas yield within the first 11 days which was 61% of the total biogas yield which was 6498 litres. For the 40% horse dung and 60% goat dung, the maximum biogas yield was 6776 litres which was 62% of the total biogas yield attained in the first 10 days. However, for all the co-substrates used there was a decrease in biogas production until the production levels off.

The average biogas production per day, for the 60% horse dung and 40 % goat dung, for the 75% horse dung and 25 % goat dung, for the 50% horse dung and 50% goat dung and for the 40% horse dung and 60% goat were 429 litres, 401 litres, 484 litres and 500 litres respectively.

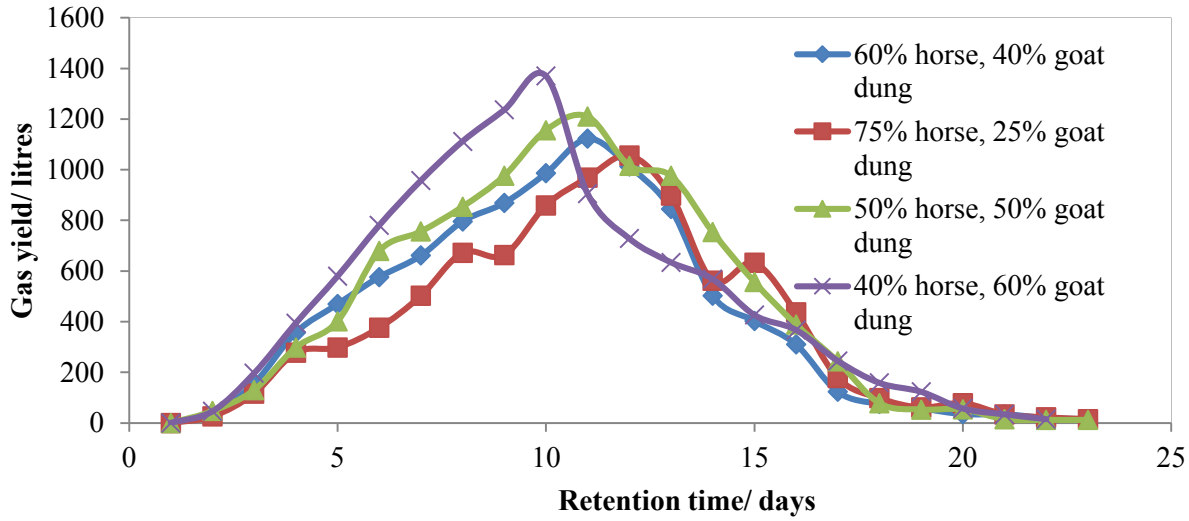

Figure 3. Biogas yield for the treatments

The co-digestion of 40% horse dung and 60% goat dung produced the highest biogas with the highest methane content. The co-digestion of 40% horse dung and 60% goat dung produced the higher yield of methane content of 60-75% than previous studies on co-digestion of horse dung with sludge that produced biogas with a methane yield of about 67% (Agayev and Egurglu 2011). Horse dung has a carbon: nitrogen ratio of 25:1 (Fulford, 2001), while goat dung has a ratio of 12:1 (Nijaguna, 2002). This means horse dung has a high carbon-nitrogen ratio than goat dung. Therefore, co-digestion of horse dung and goat dung increases biogas yield due to supply of mixing nutrients to the co-substrates.

Treatment made up of 60% horse dung and 40% donkey dung had few subsidiary peaks than the treatment made up of 75% horse dung and 25% goat dung. The peaks are an indication of high ligninostic material in horse dung that disturbed methanogenesis processes. It was observed that increase in lignin-cellulosic wastes resulted in unstable pH which is associated with poor buffering causing volatile fatty acids accumulation. Consequently, biomethation processes were affected due to the increase in acids which could not all be taken up by the methanogens. This increased acidic conditions of the methanogens. Hydrolysis and acidifying micro-organisms prefer an acid environment (pH 4.5 to 6.0). However, methanogens prefer neutral conditions with pH between 6.8 and 7.5. Most methanogens will die if pH is below 6.6. Therefore, to produce more biogas from horse dung, pretreatment techniques such as grinding of the dung to increase its biodegradability should be applied. In all digestion trials the temperature ranges between 29 - 33 °C.

4. Conclusion

There were variations in methane content for different treatments. The highest biogas yield with the highest methane content was obtained from mixing ratio 40% horse dung and 60% goat dung. However, the mixing ratio of 75% horse dung and 25% goat dung produced the lowest biogas with the lowest methane yield. It can be concluded that co-digestion horse dung and goat dung greatly increases biogas. However, for higher biogas yields, pre-treatment of horse dung is required before co-digestion. Analysis of the results reveals that biogas potential can be enhanced by addition of lime (calcium oxide) that inhibits pH fluctuations especially when horse dung is used as a co-substrate.

5. References

[1] Agegev E and Ugurlu A 2011 Biogas production from co-digestion of horse manure and waste sewage sludge *June 13-14 technol. conf.*

[2] American Public Health Association (ALPHA) 2005 *Standard methods for Examination of Water and Waste Water* (Washington DC: WEF)

[3] Elaiyaraju P and Partha N 2012 Biogas production from co-digestion of orange peel waste and jatropha de-oiled cake in an anaerobic batch reactor. *African J. of Biotechnology* **11** 3339-3345

[4] Fulford D 2001*Running a Biogas Programme* (UK: ITDG Publishing)

[5] Han M J Behera S K and Park H S 2012 Anaerobic co-digestion of food waste leachate and piggery wastewater for methane production: Statistical optimization of key process parameters *J. of Chemical Technology and Biotechnology*

[6] Hill D T and Botte J P 2000 Methane Production from the Low Solid Concentration liquid Swine Waste using Convectional Anaerobic Fermentation *Bioresource Technology* **74** 241

[7] Iyagba E l, Mangibo I A and Mohammad 2009 The study of cow dung as co-substrate with rice husk in biogas production *Scientific Research and Essay* **4** 861-866

[8] Karim K, Hoffmann R, Klasson T and Al-Dahhan 2005 Anaerobic Digestion of Animal Waste, Waste strength versus impact of mixing *Bioresource, Technol*. **96** 1771-1781

[9] Kshirgar M P, Arora A and Chandra H 2010 Estimation of anaerobic co-digestion potential of Agricultural waste in India and comparative financial analysis *International J. of sustainable energy* **31** 175-188

[10] Li J, Jha A K, He J, Ban Q, Chang S and Wang W Assessment of dry anaerobic co-digestion of cow dung with waste water sludge on biogas yield and bio-degradability *International J. of Physical Sciences* **6** 3679-3688

[11] Misi S N 2001 *Anaerobic Co-digestion of Agro-industrial Wastes for Optimum Biogas Production*, PhD Thesis, University of Birmingham

[12] Mukumba P, Makaka G and Mamphweli S 2011 Batch anaerobic co-digestion of cow dung and donkey manure *Proc. of SAIP 2011 SA Institute of Phys.* 701-706

[13] Mwakasonda S A 2007 *South Africa Low Carbon Scenario Report* (University of Cape Town: Energy Research Centre)

[14] Naomichi N and Yutaka N 2007, Recent development of anaerobic digestion processes for energy recovery from wastes *J. Biosci. Bioeng* **103** 105-112

[15] Nijaguna B T 2002 *Biogas Technology* (New Delhi: New Age International (P) Limited, Publishers)

[16] Uzodinma E O, Ofoelule A U, Eze J I, Mbaaeyi I and Onwuka N D Effect of some organic wastes on biogas yield from carbonated soft drinks sludge *Sci. Res. Essays* **3** 401-405

VCSEL Technology for Square Kilometre Array (SKA) Optical Fibre Network

E. K. Rotich Kipnoo, D. Waswa, A. W. R. Leitch and T. B Gibbon

Physics Department, Nelson Mandela Metropolitan University, P. O. Box 77000, Port Elizabeth 6031, South Africa. Tel: +27 41-504-2141; Fax: +27 41-504-2573.

Email: Enoch.Rotich@live.nmmu.ac.za

Abstract. For the first time, we propose the use of Vertical Cavity Surface Emitting Lasers (VCSELs) within the optical fibre network supporting data collection and transmission for Square Kilometre Array (SKA) in South Africa. We have theoretically demonstrated VCSEL transmission over typical SKA required distances. We show that VCSELs are ideal for per-channel transmission rates of 2.5 Gb/s, 5 Gb/s and 10 Gb/s within SKA project. It is found that Bit Error Rate (BER) decreases with increase in power. This work is valuable in providing SKA with a VCSEL technology, option for extremely high network performance at reasonable cost.

1. Introduction

Square Kilometre Array (SKA) Radio Telescope in South Africa will be the most powerful radio astronomy project that will allow us to understand the physics and the evolution of the universe and its structures as well as new aspects of astrophysics, like the origin of extremely high-energy particles, cosmic jets, black holes, and the structure and evolution of magnetic fields in cosmic structures, which will probably be addressed for the very first time [1]. Its design, construction and operation at Karoo region of the Northern Cape is to be completed in 2025. A major component of the SKA telescope array will be an extensive array of approximately 3,000 antennas. Half of these will be concentrated in a 5 km diameter central region, and the rest will be distributed out to 3,000 km from this central concentration. The Karoo project specification demands high sensitivity with fast survey speeds on a very well calibrated instrument to achieve the necessary observational performance. The proposed implementation is summarized in table 1[2]. This proposed scheme constitutes 4.192 Pb/s (10^{15} bits per second) of data collected for transmission and eventual processing at Cape Town ~300 km away (Fig. 1). Square Kilometre Array (SKA) South Africa demands high transmission rates at reasonable cost because of enormous data rates. This calls for the most efficient means of data transmission. For the first time, we propose the use of Vertical Cavity Surface Emitting Lasers (VCSELs) within the optical fibre network supporting data collection and transmission.

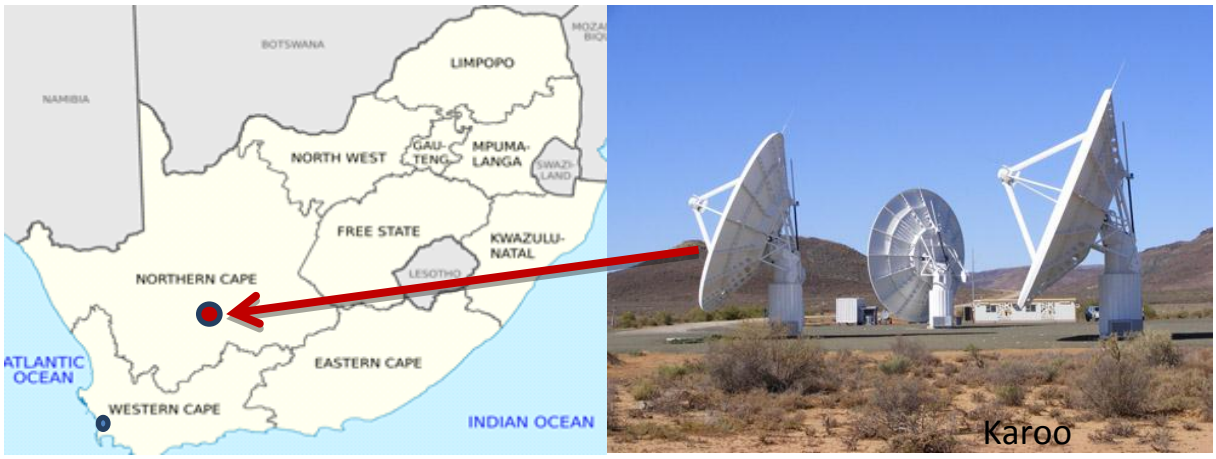

Figure 1: Map of South Africa indicating the proposed Karoo SKA site.

VCSELs are high performing, energy efficient optical sources ideal for relatively short distance high speed optical communication networks. VCSELs offer high bandwidth, single mode operation within C-L bands, wavelength tunabilities, the convenience of direct modulation and energy efficiency at low drive currents. VCSEL operation is however limited by wavelength chirp and chromatic dispersion [3]. In this study, we demonstrate VCSEL transmission over typical SKA required distances over ideal per-channel transmission rates of 2.5 Gb/s, 5 Gb/s and 10 Gb/s within SKA project.

Table 1: Proposed SKA implementation showing antennae characteristics and distribution [2]

Freq. Range	**Collector**	**Sensitivity**	**Number/size**	**Distribution**
0.07-0.45 GHz	Aperture array (AA-lo)	4,000 m^2/K at 100 MHz	250 arrays, Diameter 180 m	66 % within core 5km diameter, rest spread out to 180 km radius
0.4-1.4 GHz	Aperture array (AA-hi)	10,000 m^2/K at 800 MHz	250 arrays, Diameter 56 m	
1.2-10 GHz	Dishes with wideband single pixel feed (SD-WBSPF)	5,000 m^2/K at 1.4 GHz	1,200 dishes, Diameter 15 m	50 % within core 5 km diameter, 25 % between core and 180 km, 25 % between 180 km and 500 km radius.

2. Theory

VCSELs are semiconductor lasers with a monolithic laser resonator, where the emitted light leaves the device in a direction perpendicular to the chip surface as shown in Fig. 2. The cavity is realized with two semi-conductor Bragg mirrors between which there is an active region with (typically) several quantum wells and a total thickness of only a few micrometers. The active region is electrically pumped with a few tens of milliwatts and generates an output power in the range from 0.5 to 5 mW (-3.01 to 6.99 dBm), or higher powers for multimode devices. The current is often applied through a ring electrode, through which the output beam can be extracted, and the current is confined to the region of the resonator mode using electrically conductive (doped) mirror layers with isolating material around them [4].

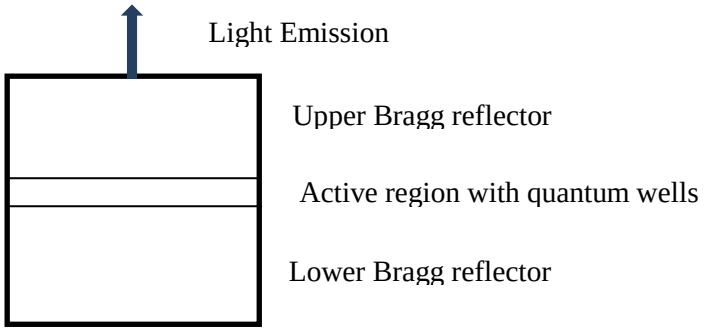

Figure 2: Schematic structure of a VCSEL

VCSELs have been studied for use in fibre-optic networks and as optical interconnects [5] [6]. The major advantages of the VCSEL are; compatibility with low-cost wafer scale fabrication and testing methods, high-volume, lower-cost manufacturing and compatibility with most active optical devices. The VCSEL has other attractive characteristics that make it well suited for use in fibre-optic systems. These include a circularly shaped output beam for high coupling efficiency, high modulation bandwidths at low current levels, single mode operation, low power consumption and the potential for producing integrated modules and arrays on wafer [5]. However, chirp and chromatic dispersion is a limitation. Frequency chirping is defined as the instantaneous change of the central wavelength or optical frequency υ in response to variations in optical power i.e. residual frequency modulation of an amplitude modulated optical wave. The instantaneous frequency chirp can be expressed as [7] [8]

$$\Delta\nu(t) = -\frac{\alpha}{4\pi}\left(\frac{d}{dt}\ln P(t) + kP(t)\right) \ldots\ldots\ldots (1)$$

where P(t) is the instantaneous optical power, and α is the linewidth enhancement factor and the κ parameter are constants. The κ parameter is related to the non-linear gain and depends on the geometry of the device. The first term describes transient chirp relating to the time derivative of the changing instantaneous optical power with rising and falling pulse edges. The second term describes adiabatic chirp relating to the instantaneous optical power itself. Chirp has generally been avoided in Non-Return-to- Zero (NRZ) systems because it increases the optical bandwidth and hence the effects of Group Velocity Dispersion (GVD). Mitigation techniques include; introduction of an offset between the VCSEL wavelength and Array Waveguide Grating (AWG) channel as a way of reducing chirp-related dispersion penalty [3] and phase modulation prior to launch as a countermeasure against the deleterious effects of the fibre nonlinearity [9].

3. Research design

The schematic diagram for the simulation using VPI transmission Maker & VPI component Maker is as shown in fig. 3. The VCSEL is modulated at various bit rates (2.5, 5 and 10 Gb/s) by a Non-Return-to- Zero (NRZ) Pseudo-Random Binary Sequence (PRBS) signal and propagated over a single mode fibre. On –Off Keying (OOK) receiver was used. During Bit Error Rate (BER) measurements, attenuator (Att.) was used to vary the receiver input power and to fix input power to the detector.

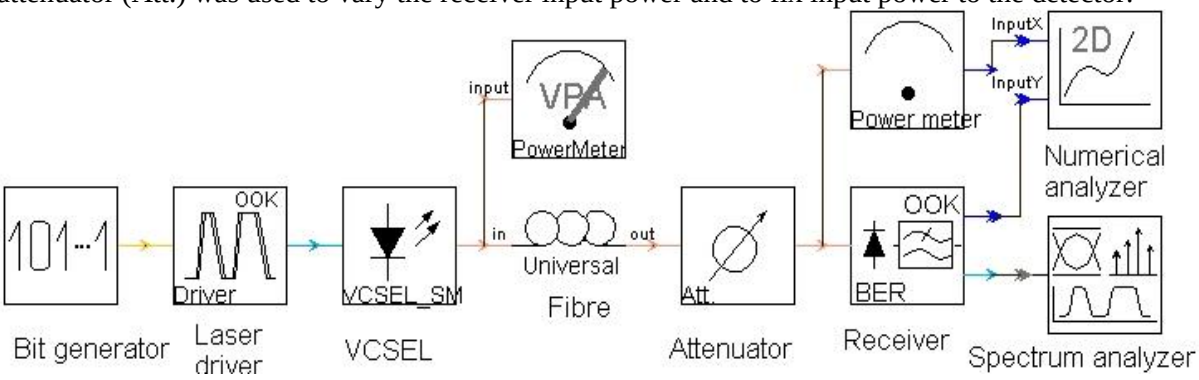

Figure 3: Simulation set up showing BER measurement.

The length of the fibre is varied from 1.4 km, 5 km, 7.5 km and 10 km and the dispersion penalties established.

4. Results and discussion

Efficient VCSELs have high output power (above 0 dBm), high extinction ratio and low chirp. Fig.4 presents the VCSEL characterization i.e. output power verses bias current. The unmodulated bias current was set to 9 mA giving an output power of 1.09 mW (0.37 dBm). The threshold lasing bias is 3 mA.

Modulation currents, I_{pp} (off '0' - on '1') in VCSELs defines its optimum performance. I_{pp} (off-on) was adjusted to 5 mA (7-12 mA), 7 mA (7-14 mA), 9 mA (6-15 mA) and 11 mA (5-16 mA) and the corresponding eye diagrams obtained were as shown in fig. 5. The Extinction Ratio (ER) values are 14.8 dB, 7.6 dB, 5.3 dB and 4.2 dB for I_{pp}; 11 mA, 9 mA, 7 mA and 5 mA respectively. An increase in modulation current increases the chirp and ER and vice versa.

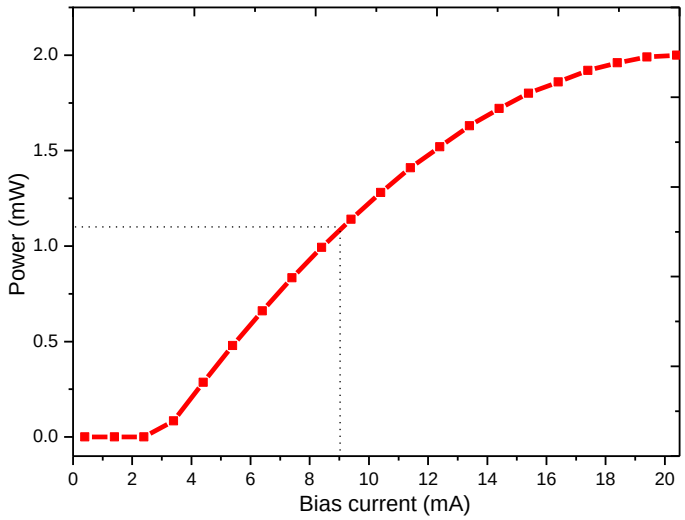

Figure 4: Unmodulated VCSEL output power as a function of bias current

Modulation current of 9 mA (off '0' - on '1'; 6mA and 15 mA) was set and the BER measurements for 2.5 Gb/s, 5 Gb/s and 10 Gb/s taken. At 10 Gb/s transmission, an acceptable bit error rate threshold of BER<10^{-9} is achieved at an optical sensitivity of -23.05 dBm, -22.66 dBm, -21.59 dBm, and -17.88 dBm for back to back, 1.4 km, 5 km, 7.5 km and 10 km respectively as shown in fig. 6(a). Hence the fibre dispersion introduces a power budget penalty of 0.37 dB, 1.47 dB, 2.52 dB and 5.17 dB respectively.

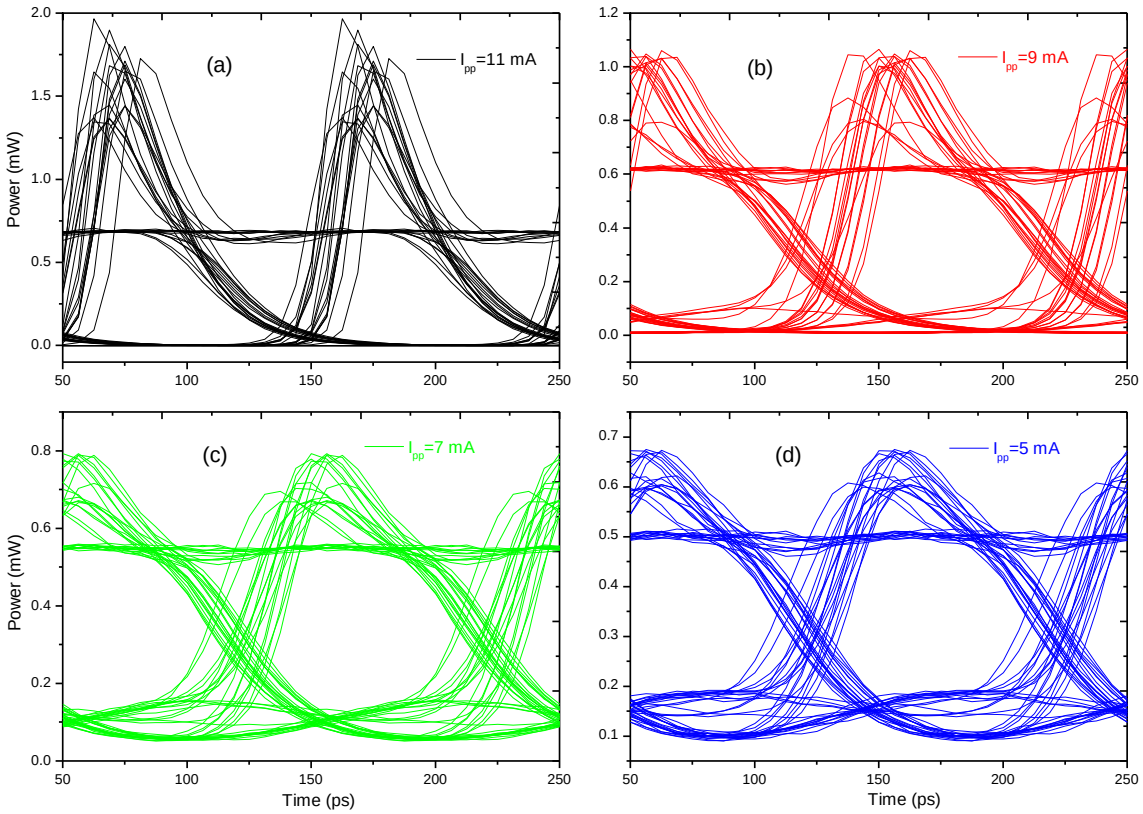

Figure 5: Eye diagrams for various modulation currents; (a) 11 mA (b) 9 mA (c) 7 mA (d) 5 mA.

Transmission penalty increases with increase in fibre length. Fig. 6 (b) gives the transmission penalty for the various bit rates, then penalty increases with increase in bit rate. Therefore, the findings of this study agree with acceptable penalty budget of 3-5 dB for a typical network design.

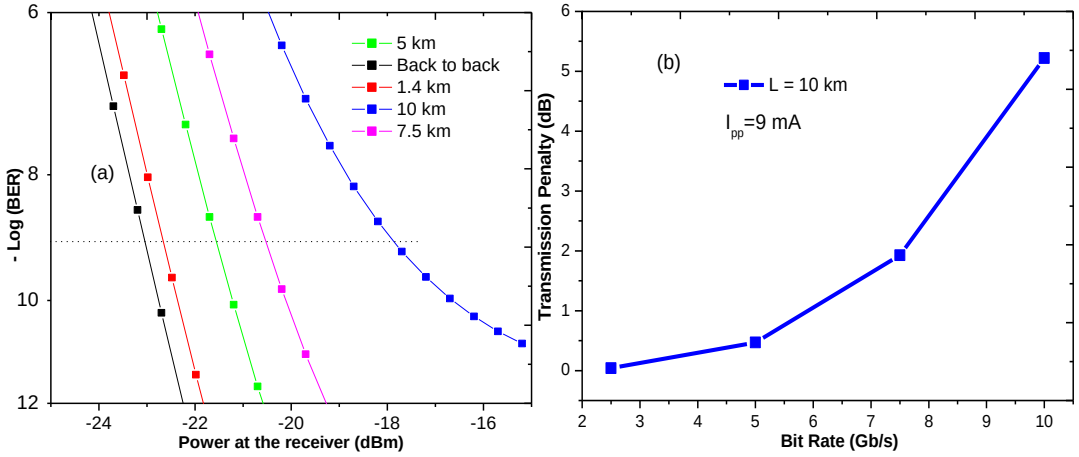

Figure 6: (a) VCSEL BER at various fibre lengths (Reference BER =10^{-9}) (b) Transmission penalties at different bit rates.

5. Conclusion

We have shown that VCSELs are ideal for up to 10 Gb/s transmission over 10 Km fibre length. Dispersion penalties of 0.038 dB, 1.47 dB and 5.17 dB for 2.5 Gb/s, 5 Gb/s and 10 Gb/s respectively over 10 km fibre length were realized. This work is valuable in providing SKA with an option for extremely high network performance for the enormous data.

6. Acknowledgement

We are grateful for Research Funding from: Telkom, Dartcom, Ingoma, NRF, CSIR, THRIP, and Scholarship Funding from SKA/NRF.

References

[1]. http://www.ska.ac.za//index.php
[2]. The SKADS Teams, *Aperture Arrays for the SKA: the SKADS White Paper***,** Design Study 8 Task 1 Deliverable 0.5 Rev.:0.91, 17 March 2010.
[3]. T.B. Gibbon, K. Prince, T.T. Pham, A. Tatarczak, C. Neumeyr, E. Rönneberg, M. Ortsiefer, "VCSEL transmission at 10 Gb/s for 20 km single mode fibre WDM-PON without dispersion compensation or injection locking"*Elsevier. Opt. Fib. tech*. 17, pg 41-45 (2011).
[4]. R. Paschotta, *Encyclopaedia of Laser Physics and Technology*, Straus, Morlenbach, 2008.
[5]. A. Karim, S. Bjorlin, J. Piprek and J. E. Bowers., "Long-wavelength vertical-cavity lasers and amplifiers", *IEEE J. Sel. Top. Quant. Electron.* **6**, 1244 (2000).
[6]. T.B. Gibbon, K. Prince, C. Neumeyr, E. Rönneberg, M. Ortsiefer and I. T. Monroy, "10 Gb/s 1550 nm VCSEL transmission over 23.6 km single mode fibre with no dispersion compensation and no injection locking for WDM PONs", *Proceedings Optical Fibre Communication Conference & Exposition and the National Fibre Optic Engineers Conference*, San Diego, CA, USA, (2010).
[7]. T. L. Koch, R. A. Linke, "Effect of nonlinear gain reduction on semiconductor laser wavelength chirping*", Appl. Phys. Lett.*, vol.48, no.10, pp.613-615, Mar 1986.
[8]. L. Bjerkan, A. Rgyset, L. Hafskjaer, and D. Myhre, "Measurement of Laser Parameters for Simulation of High-speed Fibre optic Systems," *J. of Lightwave Tech.*, Vol. 14, No. 5, pg 839-850 (1996).
[9]. S. T. Cundiff, B. C. Collings, L. Boivin, M. C. Nuss, K. Bergman, W. H. Knox,and S. G. Evangelides, Jr "Propagation of Highly Chirped Pulses in Fibre-Optic Communications Systems" , *J. of Lightwave Tech.*, Vol.17, No. 5, pg 811-816 (1999).

Confined single- and multiple-jet impingement heat transfer in helium-cooled beam window assemblies at a cyclotron facility

G F Steyn and C Vermeulen

iThemba Laboratory for Accelerator-Based Sciences, Faure, Somerset West 7129, South Africa

Email: deon@tlabs.ac.za

Abstract. The thermal modelling of the helium-cooled beam-window assemblies on the radionuclide production bombardment stations at iThemba LABS is described based on a dimensional analysis description of convection heat transfer utilizing turbulent submerged jets. It is concluded that these windows remain relatively cool even when bombarded with proton beams having the maximum design intensity. The reasons why helium is the preferred coolant are also discussed, partly based on a comparison with the cooling properties of other gasses.

1. Introduction

At iThemba LABS, radionuclide production targets are irradiated outside the beamline vacuum in order to facilitate rapid target transfers after bombardment and to preserve the cyclotron vacuum. This approach is followed by several other such facilities in the world. The relevant beamlines are provided with beam exit windows consisting of two closely-spaced thin metal foils cooled by a suitable gas flowing between them. These gas-cooled double-foil windows are thin enough to cause minimal beam energy degradation but provide a strong enough barrier to maintain the vacuum behind it for extended periods of time. They do have a finite life-time due to radiation damage, however, but a window typically lasts many months and sometimes even several years.

Figure 1 shows the vertical beam target station (VBTS) at iThemba LABS as well as its helium-cooled beam window assembly. This bombardment station is used for the production of long-lived radionuclides with beams of the highest intensity delivered by the separated sector cyclotron (SSC). Circularly swept proton beams of 66 MeV with intensities up to 300 μA are delivered to this facility. The sweep frequency is 3 kHz. A typical beam profile is shown in figure 2, obtained by analysing an autoradiogram made on radiochromic film [1] with an open source version of the software package DoseLab. The beam profile is very well represented by a rotating Gaussian function truncated at twice the full width at half maximum (FWHM) value. Such Gaussian functions are therefore used to model the beam.

The thermal modelling of such windows is the topic of this presentation. The calculation of temperature profiles for a window foil under bombardment is relatively straightforward and is based in this work on the finite difference approach described in Ref. [2]. For such calculations to be meaningful, however, the input data provided should be trustworthy. Convection heat-transfer coefficients, for example, are sometimes problematic to determine accurately. Values deduced from

measurements as well as calculations based on dimensional analysis [3] are often inconsistent and differences by up to an order of magnitude are not uncommon [4,5].

Recently Gagnon et al. [6] obtained good agreement between measurements and calculations of the thermal behaviour of water-cooled metal targets, using forced convection heat-transfer coefficients predicted from the equations derived in a dimensional analysis study of heat transfer by means of submerged liquid jets. The original study [4] employed Freon (R-113) as cooling medium. Gagnon et al. applied – with brute force – the derived formalism of Ref. [4] to water-cooled targets and obtained surprisingly good results. This prompted us to investigate the same approach for helium-cooled beam windows, in particular because some experimental values for the convection heat-transfer coefficient obtained from a simulated window assembly [2] are available, which would permit a direct comparison. Furthermore, there was a need to have a fresh look at the thermal behaviour of beam windows on all the bombardment stations for radionuclide production at iThemba LABS in view of a programme to increase production capacity by increasing the beam intensity. Two bombardment stations for horizontal beams are shown in figure 3: The "Elephant" is used for the production of short-lived medical radionuclides (such as ^{67}Ga, ^{81}Rb and ^{123}I) using batch targetry, while "Babe" is dedicated to semi-permanent targetry (currently housing an enriched [^{18}O]H_2O target for ^{18}F production). As for the VBTS, circularly swept beams (but with a smaller sweep radius) are also delivered to the Elephant but the beam to the Babe station is not swept. Thus, the beam characteristics at the three bombardment stations are different and it would be interesting to compare the thermal behaviour of the beam windows under maximum bombardment conditions as it pertains to each station. Some of the properties of the beam and window assemblies are summarized in Table 1.

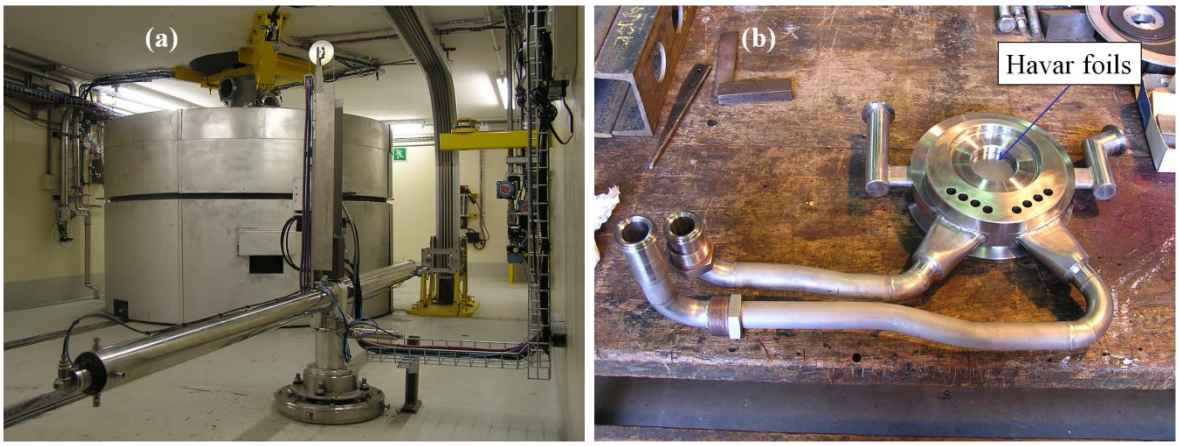

Figure 1. (a) The vertical beam target station (VBTS) at iThemba LABS for the production of long-lived radionuclides such as ^{22}Na, ^{68}Ge and ^{82}Sr. **(b)** A beam window assembly of the VBTS.

2. Jet impingement heat transfer

The methods of dimensional analysis are most often employed to derive expressions for the convection heat-transfer coefficient by searching for correlations between an appropriate set of dimensionless quantities such that it reproduces the measured data. Generally, the dependent variable is expressed as a power-law monomial function of the independent variables in dimensionless form, as this guarantees dimensional homogeneity [3]:

$$Q = \alpha A_{therm}^{a} \cdot B_{therm}^{b} \cdots X_{geom}^{x} \cdot Y_{geom}^{y} \cdots, \tag{1}$$

where A_{therm}, B_{therm}, X_{geom}, Y_{geom}, etc., are thermal and geometrical quantities in dimensionless form, respectively, while α, a, b, x, y, etc., are real numbers. First, we will consider the case of a single jet.

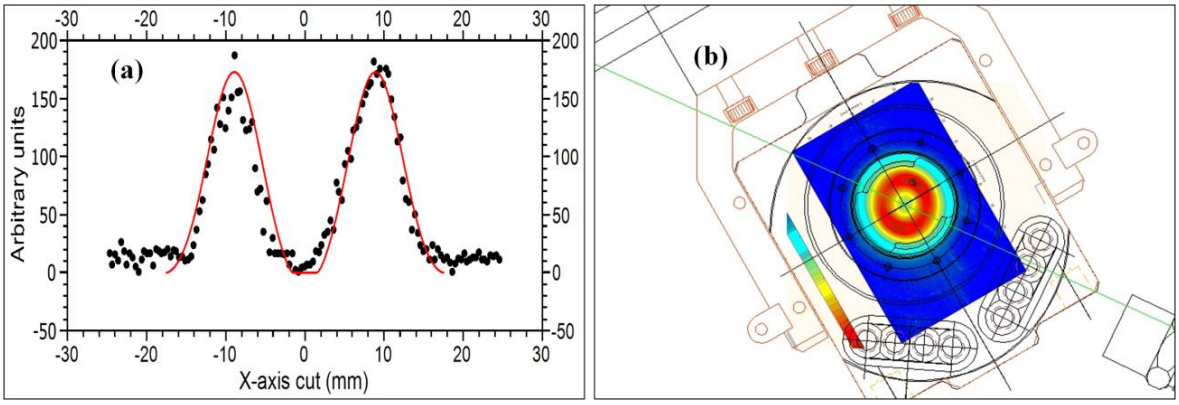

Figure 2. (a) Measured VBTS beam profile (symbols) obtained from an autoradiogram analysed with the DoseLab software (see text). The curve is a cross section through a rotating Gaussian function truncated at 2 x FWHM. **(b)** The autoradiogram overlayed on a VBTS target holder.

In this work, all jets are assumed to have circular orifices. Chang et al. [4] obtained the following expression for the stagnation point Nusselt number, $Nu(0)$, a dimensionless form of the convection heat-transfer coefficient which will be explained below:

$$Nu(0) = 0.660 Re_j^{0.574} Pr^{0.4} (z/d_j)^{-0.106}, \tag{2}$$

where Re_j is a Reynolds number evaluated with the characteristic length taken (by convention) as the exit nozzle diameter, Pr is the Prandtl number, z is the distance between the nozzle exit and the point of impact on the heated surface, and d_j is the nozzle exit diameter. The dimensionless groups are given by

$$Nu = \frac{hx}{k}; \qquad Re = \frac{\rho v x}{\mu}; \qquad Pr = \frac{c_p \mu}{k}; \tag{3}$$

where h is the convection heat-transfer coefficient, k is the thermal conductivity of the coolant, x is a characteristic length (which is taken here as the nozzle exit diameter d_j , as already mentioned), ρ is the density of the coolant, v is its bulk flow velocity, μ is its dynamic viscosity and c_p is its specific heat. The Reynolds number is a measure of the ratio of inertial forces to viscous forces in the coolant medium – the higher the Reynolds number the more turbulent the flow. The Prandtl number is a ratio of the magnitudes of the diffusion of momentum and diffusion of heat in the coolant medium. Thus, the heat-transfer coefficient can be evaluated as it is the only unknown quantity. Note that this applies only to the stagnation point (i.e. the point of impact). There is a radial decrease in the value of the Nusselt number away from the stagnation point. A local average Nusselt number for a region within a radius r from the stagnation point is given by

$$\begin{aligned} \overline{Nu}(r)/Nu(0) &= [1 + 0.1147(r/d_j)^{1.81}]^{-1} \quad \text{for} \quad r/d_j \le 1.25; \\ \overline{Nu}(r)/Nu(0) &= 1.0632(r/d_j)^{-0.62} \quad \text{for} \quad r/d_j > 1.25. \end{aligned} \tag{4}$$

A local average heat-transfer coefficient is then given by

$$\bar{h} = \frac{\overline{Nu}(r) k}{d_j}. \tag{5}$$

The data of Ref. [4] were not extensive enough to find a general description for multi-jet heat transfer. In that study, results from a 25 jet set-up arranged in a 5 x 5 matrix was extensively compared to the single-jet results and some interesting conclusions drawn. No significant additional dependence on the pitch-to-jet diameter ratio, p/d, was found, however, an inclusive dependence already exists in equation 4. A weak dependence was found on the z/d_j ratio from plots of $\overline{Nu}(r)_{multi-jet} / \overline{Nu}(r)_{single-jet}$ versus z/d_j, leading to an overall expression as follows:

$$\overline{Nu}(r)_{multi-jet} = C(z/d_j)^{-0.116}\overline{Nu}(r)_{single-jet}, \tag{6}$$

where C is a constant found to have a value of $C = 1.667$ for that particular case.

In our study, we followed a slightly different approach which gave quite similar results. Assuming that N equispaced jets have mass flow rates of $1/N$ of the total flow rate, a local radial region for each jet can be defined by partitioning the surface to be cooled accordingly:

$$r_l = \sqrt{\frac{A_h}{\pi N}}, \tag{7}$$

where A_h is the area of the heated surface. Average local Nusselt numbers using this radius can then be obtained from equation 4. The combined effect of reducing the jet diameter, which naturally follows if we increase their number while keeping the total flow rate constant, as well as reducing the effective radius in equation [4] leads to an increase of the heat-transfer coefficient.

The approach outlined above is believed to be conservative as it essentially assumes individual jets to act independently of neighbouring impinging jets. In real situations, however, there is interference between the jets due to the viscosity of the coolant medium. According to Ref. [4], this reduces the strength of the jet potential cores and the values of the heat-transfer coefficient at the stagnation points. Nevertheless, the interaction of the jets with each other leads to increased turbulence, hence increased effective Reynolds numbers, which leads to an overall increase in convection heat transfer.

Table 1. Typical properties of the beam and He-cooled window assemblies.

	VBTS	**Elephant**	**Babe**
Beam direction	vertical	horizontal	horizontal
Beam sweep radius	10 mm	3 mm	nil (no sweeping)
Beam sweep frequency	3 kHz	450 Hz	450 Hz
Beam diameter (2 x FWHM)[a]	10 mm	8 mm	8 mm
Maximum design beam current	300 µA	100 µA	50 µA
Window collimator diameter	36 mm	16 mm	16 mm
Target collimator diameter[b]	none	none	9 mm
Window diameter	50 mm	20 mm	20 mm
Inner window foil thickness	75 µm	25 µm	25 µm
Outer window foil thickness	50 µm	25 µm	25 µm
He bulk pressure (temperature)	1.25 bar (25 ºC)	1.25 bar (25 ºC)	1.25 bar (25 ºC)
He bulk volume flow rate[c]	125 m^3/h	125 m^3/h	125 m^3/h
He jet flow velocity	138 m/s	217 m/s	217 m/s
Number of jets	20	1	1
Effective jet exit diameter	4 mm	14.27 mm	14.27 mm

[a] Diameter of the unswept beam, assuming a Gaussian shape of width twice the full width at half maximum.

[b] Not required on the Elephant and VBTS. Necessary to reshape the degraded beam for the $H_2{}^{18}O$ target.

[c] Delivered by a positive displacement rotary compressor.

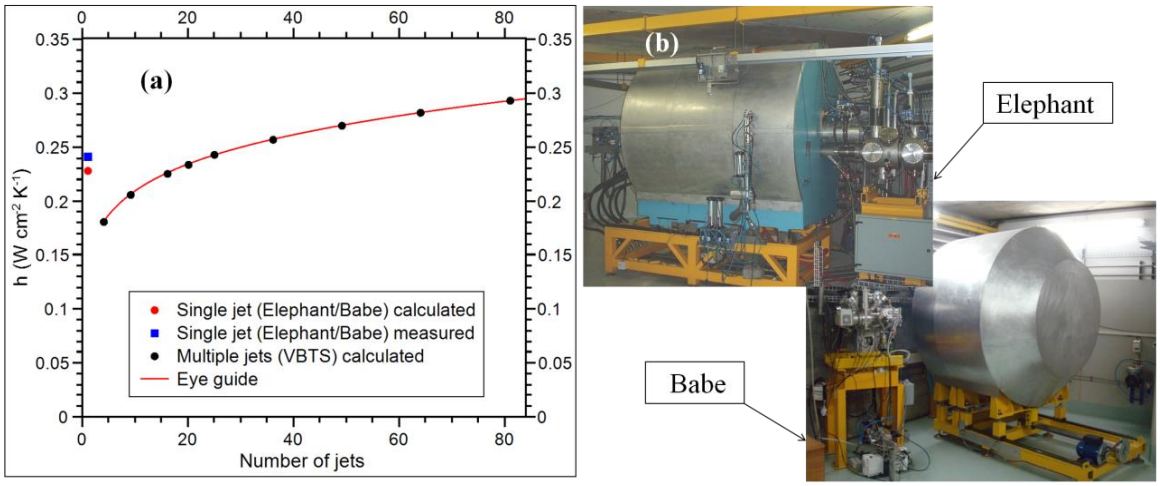

Figure 3. (a) Measured and calculated convection heat-transfer coefficients (see text). (b) The two horizontal beam target stations for radionuclide production at iThemba LABS.

3. Results and conclusions

Calculated and measured convection heat-transfer coefficients for single-jet helium cooling of the beam windows of the two horizontal-beam stations (the Elephant and Babe window assemblies are similar) are shown in figure 3. The calculated value of 0.228 W cm^{-2} K^{-1} is quite close to the measured value of 0.24 W cm^{-2} K^{-1}. For the VBTS, which has 4 times larger windows, a multi-jet configuration was chosen to achieve similar cooling with the same helium flow rate. With the same flow rate but by increasing the number of jets, the cooling becomes more efficient, as shown in figure 3. The final VBTS window design employs 20 jets. In all cases, the helium flow rate is nominally 125 m^3/h at a pressure of 1.25 bar at room temperature (25 ºC assumed in all calculations – see Table 1). This gives a linear gas velocity of about 217 m/s for Babe/Elephant windows and 138 m/s for VBTS windows. Figure 3 (a) shows that very similar values of the convection heat-transfer coefficient are obtained for the Elephant/Babe windows and the VBTS if 20 jets are employed, even though the He flow rate is lower in the latter case. It was also found that the two approaches outlined for calculating multi-jet heat transfer coefficients give values not differing by more than 10% for the case of Ref. [4].

Figure 4 (a) shows calculated temperature profiles for the Havar beam windows of all stations using typical beam profiles and maximum design beam intensities (50 µA for Babe, 100 µA for the Elephant and 300 µA for the VBTS). A conservative, slightly lower value of h = 0.2 W cm^{-2} K^{-1} has been adopted for all the calculations. Havar is a Co-Cr-Ni-based super alloy which can be used safely up to temperatures of 700 ºC (its melting point is 1480 ºC) thus one can conclude that these windows are operating at relatively cool temperatures. The windows of Babe become the hottest as that beam is not swept but the maximum temperature is still below 250 ºC. All windows will rapidly melt if the helium cooling fails (i.e. when $h \rightarrow 0$) while the bombardment continues. If the beam sweeping falls away, Elephant windows will survive but VBTS windows will melt.

Finally, figure 4 (b) compares different gasses as coolant. It is evident that the lighter gasses are better for this application. While hydrogen has the best cooling properties, it will be too dangerous to use for window cooling due to its highly flammable properties, thus helium is the cooling gas of choice. An additional advantage of helium is that its interactions with the energetic protons of the beam do not lead to a build-up of radioactive activation products in the cooling system, something which would have been unavoidable if e.g. R22 Freon in the gas phase was used.

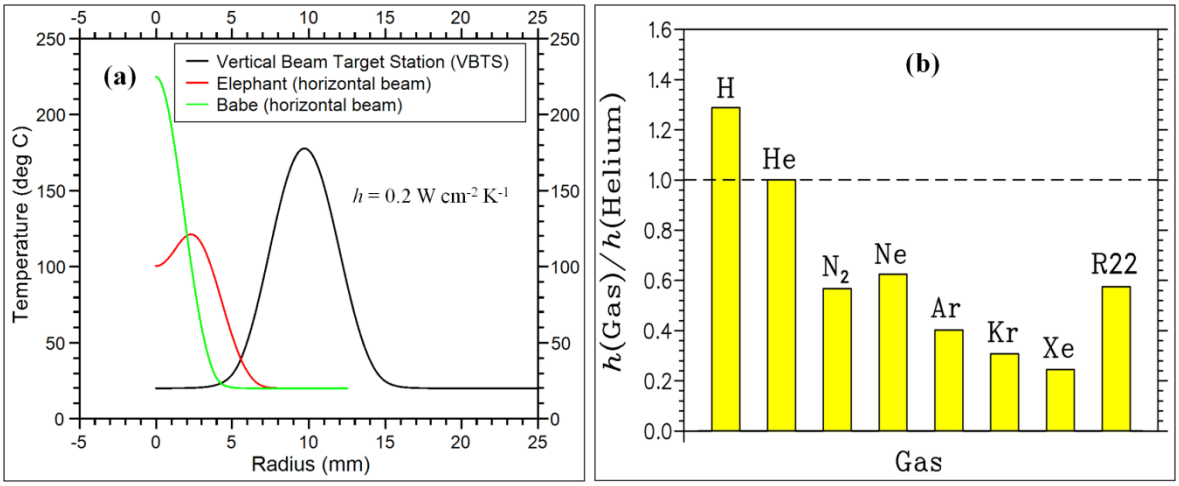

Figure 4. (a) Calculated temperature profiles for beam window foils under bombardment with maximum design beam intensity. **(b)** Ratios of convection heat-transfer coefficients for various gasses as coolants (relative to helium).

References

[1] Dempsey J, Low D, Mutic S, Markman J, Kirov A, Nussbaum G and Williamson J 2000 Validation of a precision radiochromic film dosimetry system for quantitative two-dimensional imaging of acute exposure dose distributions *Med. Phys.* **27** 2462–2476

[2] Steyn G F, Nortier F M and Mills S J 1990 Helium cooling of a double-foil window for external cyclotron beams *Nucl. Instrum. and Meth.* **A 292** 35–44

[3] Sonin A A 2001 The Physical Basis of Dimensional Analysis 2nd Edition (MIT, Cambridge, USA) p 1–57

[4] Chang C T, Kojasoy G, Landis F and Downing S 1995 Confined single-and multiple-jet impingement heat transfer – I. Turbulent submerged liquid jets *Int. J. Heat Mass Transfer* **38** 833–842

[5] Steyn G F and Stevens C J 1996 The importance of thermal entrance effects in gas-cooled beam windows for radioisotope production targets *Nucl. Instrum. and Meth.* **A 373** 10–17

[6] Gagnon K, Wilson J S and McQuarrie S A 2010 Thermal modelling of a solid cyclotron target using finite element analysis: An experimental validation *Proc. 13th Int. Workshop on Targetry and Target Chemistry, WTTC 13* (Roskilde, Denmark) 010. Available from URL <www.triumf.ca/wttc/>

Production of ^{18}F by proton bombardment of ^{18}O-enriched water targets under saturation conditions

G F Steyn and C Vermeulen

iThemba Laboratory for Accelerator-Based Sciences, Faure, Somerset West 7129, South Africa

Email: deon@tlabs.ac.za

Abstract. Single-cavity, boiling-water targets are commonly used for the production of the PET radionuclide ^{18}F, utilizing the ^{18}O(p,n)^{18}F reaction on ^{18}O-enriched water. At iThemba LABS, two such target systems are in routine use. Monte Carlo simulations were performed by means of the radiation transport code MCNPX in order to investigate alternative target configurations with the aim to improve the production efficiency with a degraded beam from the separated-sector cyclotron. A configuration is presented where most of the energy degradation of a 66 MeV primary proton beam down to the recommended energy of 18 MeV is achieved in the cooling water. With the improved target system, 80% of the incident beam reaches the ^{18}O-water cavity, in contrast to the 25% typically obtained with the initial target configuration. A simple model is also presented that reproduces the pressure versus beam-current characteristics of several different closed-cavity boiling-water targets surprisingly well. An assumption of the model is that the majority of the system operates at saturation conditions as given by the standard steam tables. It has only one free parameter, namely an overall heat-transfer coefficient, which is also called an *h*-factor. This parameter can be determined by adjusting its value until a good agreement with measured data is obtained. In this way, values of *h* have been determined for a number of different targets with volumes ranging from 0.5 cm^3 to 5 cm^3. Even though the target sizes differ by an order of magnitude, the *h*-factor remains nearly constant. This gives the model predictive power.

1. Introduction

The radionuclide ^{18}F is extensively utilized in positron emission tomography (PET). Its use is not only limited to oncology but also important in fields such as neurology, cardiology and pharmacology. In addition, non-medical applications of PET are becoming increasingly important. A group at the University of Cape Town, for example, uses PET technology for positron emission particle tracking (PEPT) [1]. Fluorine-18 is routinely produced at iThemba LABS, mainly as a service to the South African medical community, utilizing the ^{18}O(p,n)^{18}F reaction on ^{18}O-enriched water targets.

Currently, iThemba LABS utilizes beams from both the separated sector cyclotron (SSC) and a dedicated 11 MeV PET cyclotron for ^{18}F production. The target system on the SSC became operational in 2005 and production with the PET cyclotron commenced in 2012. While the bulk of the production is nowadays done with the smaller PET cyclotron and its targetry, regular productions are still being scheduled on the SSC in order to keep both systems in good operational condition. This is done to prevent disruptions in the ^{18}F production programme (e.g. during shutdowns for accelerator maintenance or when unforeseen breakdowns occur) ensuring a continuous and reliable supply.

The main aim of this paper is to discuss two aspects of the targetry. The first deals with problems associated with radial beam spread, which is particularly severe when utilizing a degraded beam from the SSC to achieve the energies required for ^{18}F production. The second concerns the observation that saturation conditions are maintained inside the target cavities during bombardment. This, we believe, is relevant not only to water targets but also to other closed-cavity liquid targets. The focus is therefore on the SSC water targetry but the lessons learnt are relevant to other target systems as well, in particular where the incident beam has to be degraded to match the requirements of the target system.

The radial beam spread, which affects the ratio of protons penetrating the water cavity versus those lost upstream on degrader and collimator units, were studied by means of extensive Monte Carlo radiation transport calculations as well as separate beam current measurements on various electrically isolated targetry components. Simulations with the code MCNPX [2] assisted in improving the target geometry and significantly enhancing the efficiency of beam utilization, which will be shown below.

The conditions inside boiling-water cavities during bombardment were studied by measuring their pressure versus beam current characteristics. It is shown that a very simple model reproduces these characteristics quite well. In addition to the results for the SSC target in use at iThemba LABS, calculations are also presented for two other target systems described in the literature, giving results for cavity sizes ranging from 0.5 cm^3 to 5 cm^3.

2. Targetry and Monte Carlo simulations

A commercial stand-alone target (SAT) and processing system for activated [^{18}O]H_2O was purchased for use on the SSC. There was, however, a compatibility issue concerning the proton beam energy that had to be resolved. A proton beam of 18 MeV was specified for the SAT system but the routine radionuclide production programme was based on proton beams of 66 MeV, shared with neutron therapy. The cyclotron schedule could not accommodate energy changes between 66 MeV and 18 MeV several times per week (one energy change typically takes between 4 and 6 hours). Thus, the beam energy had to be degraded from 66 MeV down to an average of 18 MeV.

A simplified schematic diagram of the initial target configuration is shown in figure 1. The target cavity for [^{18}O]H_2O is cylindrical and elongated with a volume of 2.3 mL. The beam is stopped in the target water. A helium-cooled, double-foil Havar window is employed to contain the target water at the beam entrance side of the cavity. Just upstream of the cavity is a conical collimator, supplied by the commercial manufacturer. Its function is to stop scattered beam particles emerging from the aluminium degrader on a relatively large water-cooled surface and to allow only a well-defined degraded beam into the target cavity. Note that, for the sake of clarity, figure 1 does not show certain details such as the cooling channels of the degrader and collimator units.

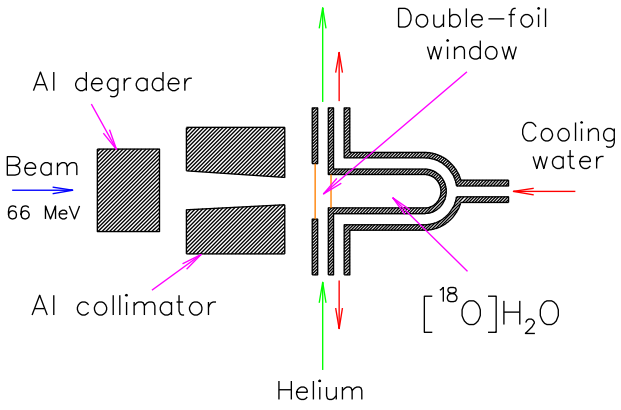

Figure 1. A simplified schematic diagram of the initial configuration of the ^{18}O–enriched water target for ^{18}F production with a 66 MeV primary proton beam delivered by the SSC.

The performance of this beautifully constructed target was rather disappointing, however, as it turned out to be impossible to get more than 25% of the protons into the Nb target cavity under well-optimized beam conditions, i.e. three quarters of the beam was stopped by the collimator. Simulations of the beam and targetry were subsequently performed by means of the Monte Carlo code MCNPX in an attempt to better understand this behavior and to improve the targetry.

MCNPX Version 2.7.0 [2] was used for the Monte Carlo simulations. The beam was modelled with realistic values of the emittance in two orthogonal directions normal to the beam axis downstream of the last focusing quadrupole (ε_x = 14 π-mm-mrad and ε_y = 5 π-mm-mrad), drift length upstream of the target (150 cm) and beam spot at the target position (2 to 3 mm FWHM). It was found that the beam profile at the entrance to the target cavity was rather insensitive to the exact choice of beam parameters upstream of the degrader as long as the values remained realistic. By means of the Monte Carlo simulations, various alternative target configurations were investigated as well as the effect of small changes in the degraded beam energy. Concerning the latter, it is interesting to look at the relevant integral yield curve [3] for the production of ^{18}F but expressed as the yield per unit energy deposited by the beam in the target water. This is shown in figure 2. A maximum is evident at 14 MeV. In principle, this should be the optimum incident energy from a thermal point of view because the challenge is to remove a significant amount of heat from quite a small volume with very limited heat-transfer surfaces. As the 66 MeV beam had to be downgraded by a rather a large amount, it was eventually decided to retain the nominal energy of 18 MeV as specified by the commercial supplier.

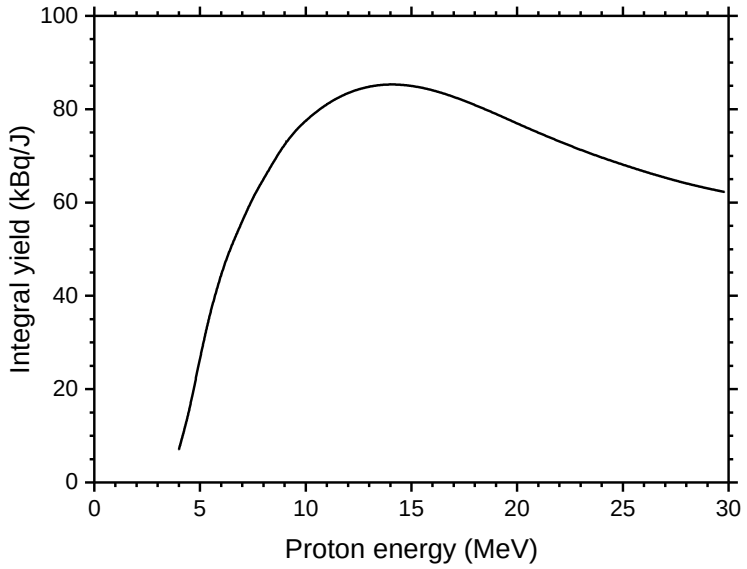

Figure 2. Integral yield per unit energy deposited by the beam in the water cavity, plotted as a function of incident energy. Note that the beam is stopped inside the target water.

A full account of all the simulations performed will not be given here. Various possibilities exist to improve the configuration of figure 1, in particular by reducing the length of the elongated collimator. Finally, a configuration was adopted where most of the beam degrading is done in the cooling water (at a high flow rate of 30 L/min) in close proximity to the target cavity. Also, the collimator was reduced considerably in length and machined to be an integral part of a single degrader/collimator unit. The final configuration is shown schematically in figure 3. The collimator has a 10 mm diameter and that of the target cavity is 11.5 mm. Using the cooling water for degrading purposes has an additional advantage, namely that a large fraction of residual radioactivity induced in the degrader can be transported away with the water to an ion exchanger located in a convenient location outside the vault. This helps to reduce the radiation dose to staff doing routine target maintenance in the vault.

Figure 4 shows the fraction of the incident beam at a penetration depth corresponding to the entrance of the target cavity, as a function of radius, obtained by means of MCNPX simulations. In these particular simulations, the degraders were retained but the collimators were removed in order to study the overall radial beam spread. In both cases, 1 000 000 primary protons were tracked. Since no secondary photons and neutrons needed to be tracked, the execution time of the code was quite short (< 30 min) on a standard high-end PC, in spite of creating a large number of event histories. The improvement in beam efficiency of the modified target configuration is evident. Excellent agreement between Monte Carlo simulations and results from beam current measurements on the major targetry components was obtained. In a typical production run, about 20% of the beam is usually measured on the combined degrader/collimator unit and 80% on the Nb target cavity. Also, by utilizing a mesh tally on the inside surface of the Nb cavity, it was possible to determine that > 99% of the collimated proton beam entering the cavity stopped in the target water without escaping to the Nb wall. (Concerning figure 4, note that the inner radius of the cylindrical part of the target cavity is 5.75 mm).

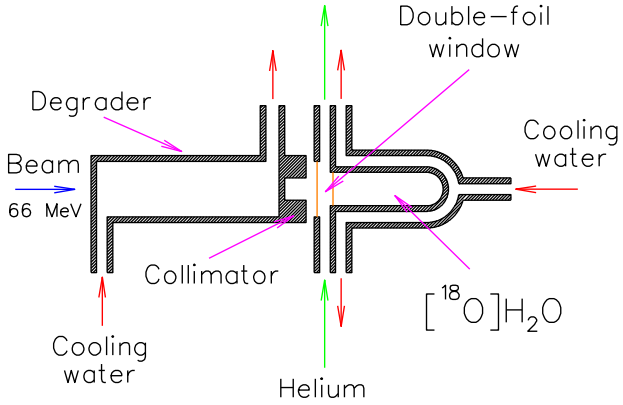

Figure 3. Simplified schematic diagram of the final configuration of the ^{18}O–enriched water target for ^{18}F production with a 66 MeV primary proton beam delivered by the SSC.

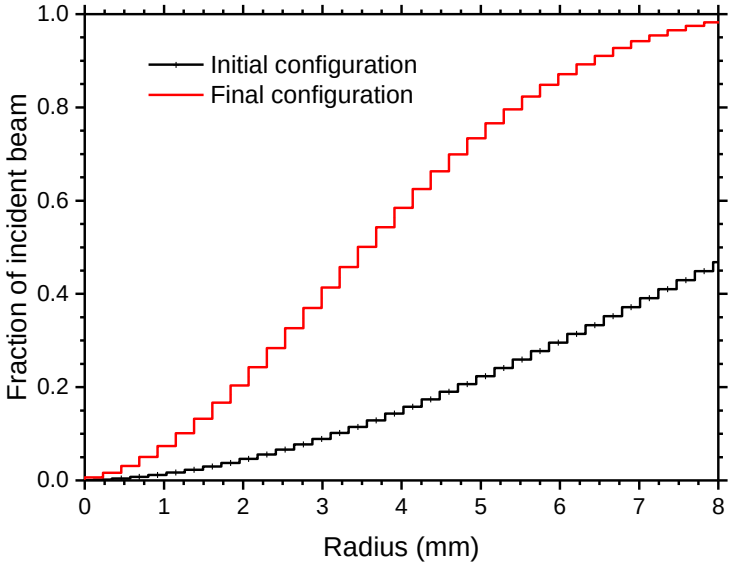

Figure 4. MCNPX predictions of the fraction of the incident beam reaching the entrance plane of the ^{18}O–enriched water target cavity, plotted as a function of the radius around the beam axis. Here the mesh tally was placed on the plane of the inner Havar foil and the degraders were removed.

3. Boiling and saturation conditions

At iThemba LABS, measurements of the target pressure versus the beam current were performed on a 2.3 mL single-cavity, boiling-water target. A calibrated piezoresistive transducer with a response time of about 1 ms was used for the pressure measurements. An EG&G CD 1010 current digitizer was used to measure current on the target cavity (Nb insert) and a Keithley 485 electrometer to measure current on the degrader/collimator. These values were logged on a PC using the LabVIEW code [4] for data acquisition. The results are shown in figure 5. Also shown in figure 5 are published measured results for a much smaller cylindrical target cavity with a volume of 0.5 mL, operating at a proton beam energy of 13 MeV [5], as well as for a larger conically-shaped cavity with a volume of 5 mL [6]. The measurements are compared with calculations based on a simple model, described below.

The model assumes that the bulk of the ^{18}O-enriched target water has a constant temperature, which is the same as the inner wall temperature of the cavity, T_w. It is further assumed that saturation conditions are being maintained during bombardment. Both assumptions are being justified by referring to the work of Alvord et al. [7]. These authors pointed out that elevated pressures and temperatures in excess of saturation conditions may exist in a water target during bombardment. However, as long as the rate of condensation matches the rate of vaporization, the bulk of the system should remain at saturation conditions. Superheated regions are therefore likely to form but also likely to rapidly disappear, typically on the scale of a few milliseconds for such small volumes. The boiling process is generally quite complex, enhanced by radiation-induced nucleation. This, however, introduces fast mixing mechanisms in the water volume. Large temperature gradients can therefore only briefly exist under these very ebullient boiling conditions.

A second simplification is to neglect the temperature difference across the target chamber wall, which is only justified if the wall is thin (e.g. 1 mm thick Nb). A further assumption is that a single, overall convective heat-transfer coefficient can be applied, which is considered to be constant over the entire water-cooled surface. Here we take as the heat-transfer surface the inner cavity surface opposite the outer surface of the Nb insert directly in contact with the cooling water. The energy balance between the beam heating and the convection heat transfer (Newton's law of cooling) is given by

$$I_b \Delta E = hA(T_w - T_0), \tag{1}$$

where I_b is the beam intensity, ΔE is the energy window of the target (which is the same as the incident energy if the beam is stopped in the target water), h is the convective heat-transfer coefficient, A is the inner cavity surface through which the heat has to be transferred from the target-water volume to the cooling water, and T_0 is the cooling-water temperature.

The saturated vapor pressure versus temperature of water is a characteristic curve, given by the steam tables [8]. It can be written as

$$P = f(T) \quad \text{or} \quad T = f^{-1}(P). \tag{2}$$

Assuming the bulk of the system at saturation conditions, substitution of (1) into (2) gives

$$P = f(T_w) = f\left[\left(\frac{\Delta E}{hA}\right) I_b + T_0\right]. \tag{3}$$

The function f can be conveniently represented by a polynomial fitted through the tabulated values. The only unknown in equation (3) is the overall convective heat-transfer coefficient, h. Our approach was to adjust h until a good visual fit with a set of measured data was obtained. The results are shown in figure 5 and the values of h as well as other relevant quantities are presented in table 1.

A very good agreement between the measurements and calculations is evident in figure 5 for the 2.3 mL and 5 mL targets. In the case of the 0.5 mL target of reference [5], only one measured value

was available, nevertheless, the extracted value of *h* is in good quantitative agreement with the other two cases, as shown in table 1. The extracted *h*-factors are indeed remarkably similar, even though the target volumes differ by an order of magnitude.

It is evident from equation (3) that the target performance in terms of the maximum operational beam current for a given beam energy and a maximum pressure (and hence the corresponding yield) can be improved by increasing the heat-transfer surface (A), the heat-transfer coefficient (h) and by reducing the cooling-water temperature (T_0). At a typical operational pressure of 30 bar, the saturated water temperature is 234 °C, thus by using chilled cooling water at, say, 15 °C only a small performance increase of about 7% will be obtained compared to using cooling water at an average temperature of 30 °C (i.e. room temperature). It will also be difficult to significantly increase the overall heat-transfer coefficient by increasing the cooling-water flow rate. High flow rates are normally employed and care must be taken as further increases may cause adverse effects, e.g. too large forces on components and cavitation with damage potential. Thus, the only viable way to significantly increase target performance is to increase the surface from which the heat can be removed. This leads to an increase in the target volume. As the enriched ^{18}O-water is quite expensive, some judgment call needs to be made, depending on operational needs. This is not the same for all producers. For this reason, commercial suppliers nowadays offer their clients a range of target sizes with volumes typically ranging between 2 and 10 cm^3.

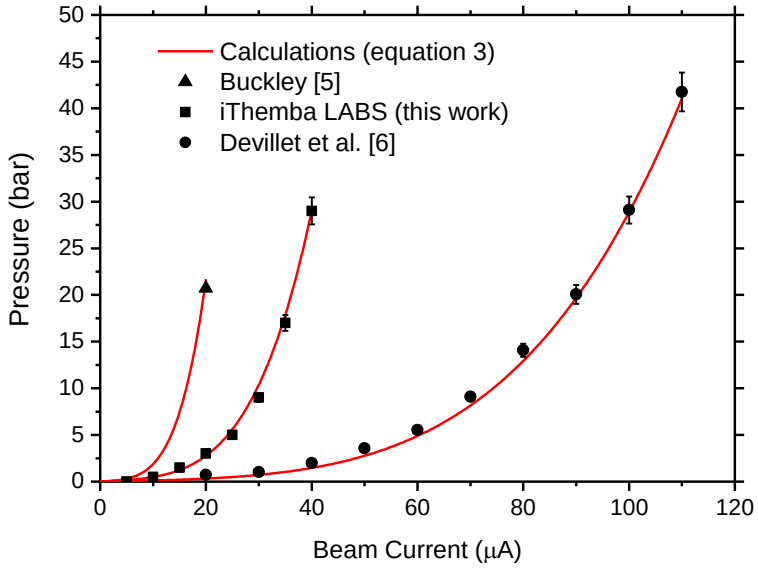

Figure 5. Pressure versus beam current for several ^{18}O-enriched water targets, as indicated. Error bars are shown where they exceed the symbol size.

Table 1. Values extracted for the overall heat-transfer coefficient (h) and other relevant quantities of the targets investigated.

Target	Energy window [ΔE] (MeV)	Cavity volume (cm^3)	Heat-transfer surface [A] (cm^2)	Cooling-water temperature [T_0] (°C)	h (W.cm^{-2}.°C^{-1})
Reference [5]	13	0.5	2.70	20	0.49
This work	18	2.3	6.56	30	0.54
Reference [6]	18	5.0	18.59	30	0.48

4. Other considerations

Single-cavity, boiling-water targets are vulnerable to sudden increases in beam current as bulk vaporization can lead to destructive pressure spikes. An interlock condition set on the target pressure is therefore essential. The calibrated piezoresistive transducer used for the pressure measurements at iThemba LABS has a rapid response time of about 1 ms and is a necessary component of the beam interlock system.

As the primary beam energy from the SSC is 66 MeV, the primary activation of the targetry as well as the secondary neutron activation of the immediate vicinity is far more severe than what is typical for a PET facility based on a small medical cyclotron. The target is therefore well shielded during bombardment, similar to all the other radionuclide production targets on SSC beamlines at iThemba LABS. Figure 6 shows the target and a dedicated bombardment station for semi-permanent targets.

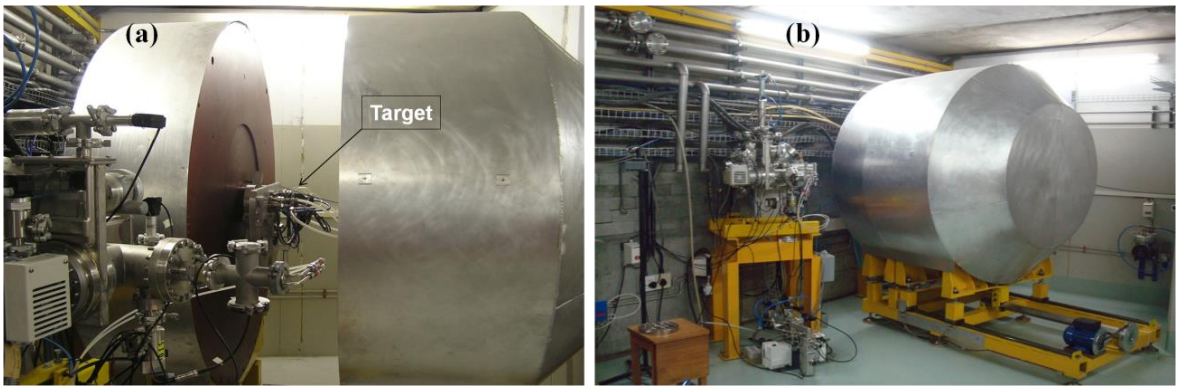

Figure 6. (a) The shielding of the bombardment station in an open position, showing the location of the target on the beamline. **(b)** The bombardment station in beam-ready state.

5. Summary and conclusion

The SSC target system described above has now been in routine use for the production of ^{18}F at iThemba LABS for several years. It operates in the boiling regime with the majority of the system at saturation conditions. By keeping it in routine use on the SSC conjointly with a new 11 MeV PET cyclotron and its dedicated targetry, a year-round supply of ^{18}F can be maintained.

The Monte Carlo radiation transport code MCNPX has proved to be an extremely useful tool in gaining an understanding on target systems under irradiation conditions. It is possible to simulate the proton beam very precisely with the latest version of the code (Version 2.7.0) and the radial beam spread as a function of penetration depth is found to be in excellent agreement with experimental observations. Simulations of the 66 MeV proton beam from the SSC and the entire ^{18}O-enriched water-target system allowed us to investigate alternative configurations of the degrader and collimator. Finally, it proved to be advantageous to combine them in a single unit and use cooling water for most of the required energy degradation (down to an average energy of 18 MeV).

A study of the pressure inside a water target versus the applied beam current indicated that saturation conditions are indeed maintained. This made it possible to reproduce the pressure versus beam-current characteristics of a number of different targets, under their respective operational conditions, with a rather simple model. The values extracted for the overall heat-transfer coefficient, which is the only free parameter of the model, are quite similar in magnitude for a number of target systems with volumes differing by an order of magnitude. This is interpreted as as evidence that the model has predictive power. It may be useful to apply to other liquid targets as well.

The monitoring of the pressure inside a closed-cavity, boiling-water target, by means of a transducer with a fast response time, is strongly advisable for inclusion in the beam interlock system.

If an upper pressure limit is exceeded, the bombardment should terminate immediately. Lastly, the use of a degraded beam for the purpose of ^{18}F production, as implemented on the SSC of iThemba LABS, requires local shielding in close proximity to the target. This is not a requirement for a production facility based on a dedicated low-energy PET cyclotron.

References

[1] Volkwyn T S, Buffler A, Govender I, Franzidis J –P, Morrison A J, Odo A, van der Meulen N P and Vermeulen C 2011 Studies of the effect of tracer activity on time-averaged positron emission particle tracking measurements on tumbling mills at PEPT Cape Town *Minerals Engineering* **24** 261–266

[2] Pelowitz D B (ed) 2011 MCNPX User's Manual Version 2.7.0 *Los Alamos National Laboratory Report LA-CP-07-1473* (Los Alamos, USA)

[3] Takács S, Tárkányi F, Hermanne A and Paviotti de Corcuera R 2003 Validation and upgrading of the recommended cross section data of charged particle reactions used for production of PET radioisotopes *Nucl. Instr. and Meth.* B **211** 169–189; EXFOR entry D4111 subentry D4111006

[4] Orgen P J, Jones T P, Paul J and Thomas P 1996 Laboratory interfacing using the LabVIEW software package *Journal of Chemical Education (ACS)* **73** 1115–1116

[5] Buckley K 2006 ^{18}O Water target design for production of ^{18}F *TRIUMF Design Note TRI-DN-06-07* (TRIUMF, Vancouver, Canada) pp 1–6

[6] Devillet F, Geerts J-M, Ghyoot M, Kral E, Michaux O, Nactergal B, Nuttens V, Courtyn J, Mooij R, and Perk L 2013 Performance of IBA new conical shaped niobium [^{18}O] water targets *Proceedings 20th International Conference on Cyclotrons and their Applications* (Vancouver, Canada, ISBN 978-3-95450-128-1) WEPSH043 pp 1–3

[7] Alvord C W, Ruggles A E and West C D 2008 Calculation of attainable superheats and predicted embryonic flux rates in commercial water isotope targets *Appl. Radiat. Isot.* **66** 1781–1787

[8] Lemmon E W 2010 Thermophysical properties of water and steam *CRC Handbook of Physics and Chemistry 90th Edition* (Lide D R (ed) CRC Press, Boca Raton, FL, USA) pp 6-1–6-4

Mathematical modelling of the coefficient of performance of a Carnot's Air source heat pump water heater

Stephen L.Tangwe, Michael Simon and Edson L. Meyer
Fort Hare Institute of Technology, University of Fort Hare, Alice, Eastern Cape, South Africa
Phone:+277406022086, Fax:+27 (0) 40 653 0665, e-mail: stangwe@ufh.ac.za

Abstract. In South Africa, there is an ongoing constraint on the electricity supply at the national grid to meet the demand. Eskom is implementing various measures such as the Integrated Demand Management (IDM) and the encouragement of the use of efficient energy devices like air source heat pump (ASHP) water heater for replacement of high electrical energy consumption utility (conventional geysers) in sanitary hot water production. The ASHP water heater market is fast gaining maturity. A critical mathematical model can lead to performance optimization of the system that will further result in the conservation of energy and significant reduction in global warming potential. ASHP is an electro-mechanical device that operates on the principles of vapour compression refrigerant cycle. The ASHP water heater comprises of an ASHP and a hot water storage tank. A data acquisition system (DAS) monitors the temperature at the evaporator, condenser, hot water and the ambient temperature in the vicinity of the evaporator. This work focuses on using the mathematical equation for the Coefficient of Performance (COP) of an ideal Carnot's heat pump (CHP) water heater and writing basic computation in M-file of Matlab and Simulinks software to model this system based on two reservoir temperatures, viz., evaporator temperatures (Tevp) of -10°C to 40°C (equivalent to ambient temperature, Ta) and condenser temperatures (Tcon) at 65°C, 85°C and 95°C (equal set point temperature of hot water in the tank of 50°C, 55°C and 60°C). From the modelling results it can be deduced that at 0°C Tevp, the COP is 4.2 and 2.7 respectively with the set temperatures of 55°C. Above 27°C Tevp, the rate of change of COP increased exponentially for CHP but is constant at 0.01/°C for practical ASHP. Finally the paper will present an analytical comparison of CHP water heater to practical ASHP water heater for hot water temperature set at 55°C.

1. Introduction

Hot water heating constitutes a significant percentage of energy consumption in industrial, commercial and residential sectors worldwide. In South Africa, water heating is the largest residential use of energy, with up to 50% of monthly electricity consumption being used for this purpose (Meyer and Tshimankinda, 1998). Eskom strategic plan outlook for 2010 to 2030 show over 20% reduction of electricity production from coal (Digest of SA Energy statistics, 2009). To achieve this goal, an urgent need of the use of energy efficiency technology such as smart use of heat pump for sanitary hot water is encouraged. Eskom is embarking in rolling out rebate program of 65,580 units of residential ASHP water heater still March 2013(Eskom, 2010) in a bid to promote the use of this technology by residential end users. ASHP can be categorized into integrated or 'drop in' system and retrofit or split type. Each of this type is divided into single or one passed circulation system and a multi-passed or recirculation system. The key components of the heat pump unit are the evaporator coil, vapour compressor, heat rejection condenser and an expansion valve. ASHP water heater provides hot water at 40 to 100 percent of the rate of electric resistance units and 30 to 50 percent of the rate of gas units, but require warm ambient temperatures and a large heat pump or storage tank to provide a constant flow of hot water (Bodzin, 1997). The characteristics of a heat pump that enables it provide such a very high efficiency of 300% is called coefficient of performance (COP) (De Swardt *et al.,* 2000). The COP of ASHP water heater depends on various parameters including components design, heating load cycle, thermo-physical properties of the working fluids, relative humidity and air speed through the duct space. The instantaneous, seasonal or annual COP can be calculated using simulation with TRNSYS software package (Kline *et al.,* 1999), components testing (Morrison, 1977) and mathematical modelling (Itoe *et al.,*1999).

2. Fundamental principles of ASHP water heater

The schematic diagram in figure 1 shows the full designed and components of the ASHP water heater

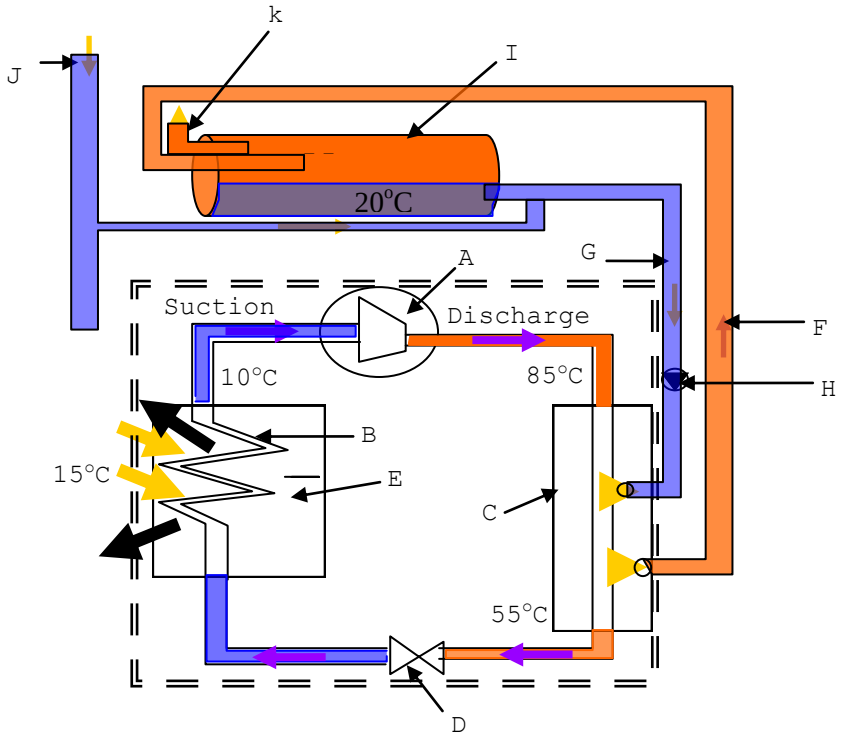

Key features
A= Vapour compressor
B=Evaporator coil
C=Condenser
D=Expansion valve
E=Fan
F=ASHP outlet pipe
G=ASHP inlet pipe
H=water pump
I=Storage tank
J=Incoming cold water
K=Hot water supply

Figure 1: A shows a schematic diagram of an ASHP water heater

During a heating load cycle, the ASHP undergo a vapour compression refrigerant cycle (VCRC) and this cycle can only be achieved by electrical energy input to drive the compressor for a CHP and for a practical ASHP energy is needed to run the pump and the fan showed in figure 1. The low pressure and temperature refrigerant extract aero-thermal energy from the ambient air and this low pressure vapour flow to the compressor where it is compressed and discharged as super-heated gas. The thermal energy absorbed by the gas is rejected at the condenser unit while incoming cold water is heated to hot water set temperature. The fluid finally flow passed an expansion valve where it pressure and temperature drop. The complete process involved in the cycle is showed in the temperature and entropy as well as pressure and enthalpy graphs. From the graphs the COP of the heat pump is calculated. At the evaporator the process is isothermal, while at the compressor is isentropic. Also, for the condenser the process is isobaric and at the expansion valve is isenthalpic. The figure 2 and 3 illustrated the graphs of the various processes provided the thermo-physical fluid is a pure refrigerant.

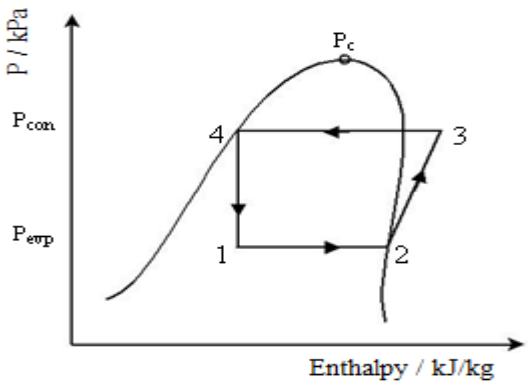

Figure 2: Pressure versus enthalpy graph

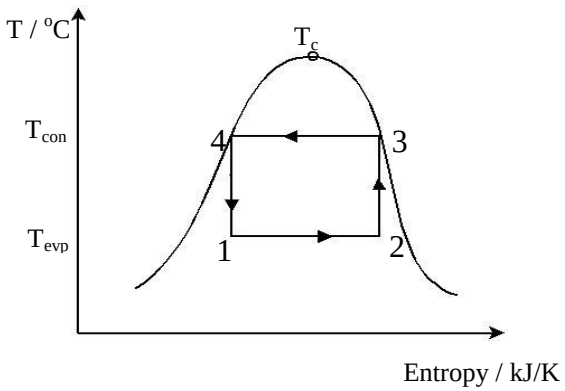

Figure 3: Temperature versus entropy graph

The analysis of the processes involved in each section of the two figures is explained below: where h and s are specific enthalpy and specific entropy of the system, respectively, E_{in} is input electrical energy and Q_{out} is the useful heat gain. In order to understand and mathematically represent the processes taking place in the evaporator, compressor, condenser and expansion valve sections of the heat pump, a set of equations (1- 8) were deduced. Analyzing figure 2, the process 1 to 2 occurred in the evaporator and the heat gain was calculated using equation 1.

$$\Delta Q = mh_2 - mh_1 \quad (1)$$

Process 2 to 3 occurred at the compressor and heat gain was calculated as shown in equation 1

$$\Delta Q = mh_3 - mh_2 \quad (2)$$

Process 3 to 4 occurred in the condenser and the heat rejected was calculated using equation 3

$$\Delta Q = mh_3 - mh_4 \quad (3)$$

Process 4 to 1 occurred in the expansion valve and enthalpy change was calculated as shown in equation 4

$$\Delta Q = mh_4 - mh_1 = 0 \quad (4)$$

Using the definition of COP in terms of energy factor, equation 5 was obtained

$$COP = \frac{Q_{out}}{E_{in}} \quad (5)$$

From equation 5, both energies (Q_{out}, output thermal energy and E_{in}, input electrical energy) can be expressed in terms of h to give equation 6.

$$COP = \frac{m(h_3 - h_1)}{m(h_3 - h_2)} = \frac{h_3 - h_4}{h_3 - h_2} \quad (6)$$

The COP could also be derived from figure 3 and by using the first law of thermodynamics. The COP can be defined by equation 7

$$COP = \frac{s_2 T_{con} - s_1 T_{con}}{(s_2 T_{con} - s_1 T_{con}) - (s_2 T_{evp} - s_1 T_{evp})} \quad (7)$$

Simplifying equation 7 gives equation 8

$$COP = \frac{T_{con}}{T_{con} - T_{evp}} \quad (8)$$

Both the evaporator and condenser temperatures were expressed in Kelvin (K). Equation 8 was the COP formulation applied to the CHP water heater. Based on this equation, a computational programme which modeled the COP variation with temperature lift (T_{con}-T_{evp}) was generated from the M-file script of the MATLAB software.

3. Methodology

3.1 Development of programme code to modelled Carnot's ASHP water heater COP

The basic programme is computed upon key assumptions that evaporator and ambient temperature are equal and the thermodynamic fluid is a pure refrigerant. All comments are expressed with % and are not executed by the programme. The programme is run for condenser set temperatures at 65 ^{o}C, 85 ^{o}C and 95 ^{o}C corresponding to hot water temperatures of 50 ^{o}C, 55 ^{o}C and 60 ^{o}C for a domestic ASHP water heater. This programme used the "for loop" and show that Carnot's COP increases linearly with

ambient temperature from 0 ^{o}C to 20 ^{o}C at 0.04/ ^{o}C and above this range increases exponentially. The code is shown below.

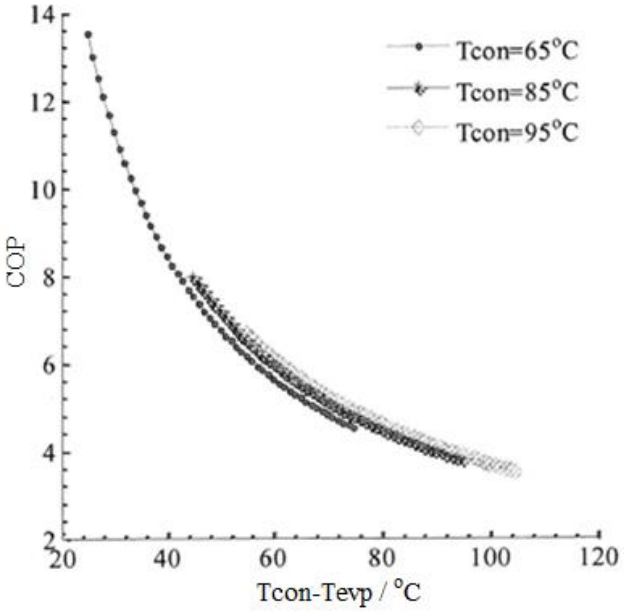


```
% COP of Carnot's heat pump as function of evaporator and condenser temperature
% Ambient temperature range (Ta) is approximated to Tevp.
% Tevp = Evaporator temperature in K
% Tcon = Condenser temperature in K
% Th = Hot water set point temperature in °C
T0 = 273; % Temperature conversion factor
Tcons = ['r.-';'b*-';'gd-';'mx-']; % set color for Tcon
x=1; % Initializing color to start count
Ta = -10:1:43; % Annual ambient temperature in °C
Tevp = Ta+T0; % Tevp range in K
for T_H = 85:5:100; % condenser temperature in °C
Tcon = T_H+T0;
hold on     % generate various graphs
COP = Tcon/(Tcon-Tevp);
Plot((Tcon-Tevp), COP,Tcons(x,1:end))
x = x+1;
end
```

Figure 4: COP versus temperature lift

From graphs generated in figure 4, the COP increases with a decreased in temperature lift.

3.2 Mathematical modelling of practical ASHP water heater

The equation 9 and 10 are the Morrison COP correlation with temperature that was used to mathematically modelled the practical ASHP water heater.

$$COP = a_1 + a_2(T_t - T_a)\left\lfloor \frac{T_t - T_w}{T_t - T_a} \right\rfloor \quad (9)$$

$$COP = a_1 + a_2(T_t - T_a) \quad (10)$$

Equation 10 is a constrain equation to optimized the COP, and the constants a_1 and a_2 were determined for T_t = 50 ^{o}C, T_t = 55 ^{o}C, and T_t = 60 ^{o}C. Figure 5 presents the modelled COP for these different temperatures.

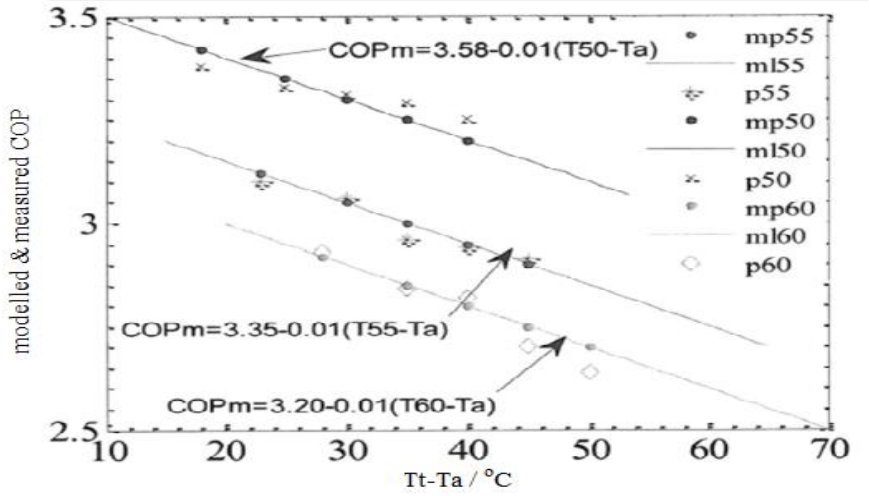

Figure 5: Shows measured and modelled COP against (Tt-Ta)

The line plots with solid markers show the modelled equations of the COP while the scatter marker points represent the calculated COP at the specific hot water temperature as well as relative humidity and ambient temperature.

3.3 Methodology for determination of input parameters

The computation of the COP using mathematical modelling from Matlab and Simulink software was performed for a typical week baseline profile of a 3 kW convectional 150 L geyser installed in a domestic residence (occupied by four adults and two children) of middle class at Fort Bueafort, South Africa. The geyser was installed to operate without interruption for 24 h on a daily basis. Figure 6 and 7 illustrate the DAS and a full schematic set up. Figure 6 and 7 illustrate the DAS and the full schematic block diagram of the metering transducers and sensors employed in the set up parameters. The main electric power consumption and total current drawn to the building was measured by power track 1. Power track 1 was installed on the main distribution board with the positive voltage cable (red) and the negative voltage cable (black) connected to the live and neutral lines of the mains. The current transformer (CT) of the power tack was placed on the live. Power track 2 was placed to the line supplying current to the geyser and measured the current and total power utilized by the 150 L, 3 kW combinational geyser. The power track is configured to log every 1 minute. All the temperature sensors were thermistor resistance sensors. Temperature sensor 1 was placed at the cold water inlet pipe to the geyser well insulated. Similarly, the temperature sensors 2, 3 and 4 measured the hot water temperatures for the outlet hot water from the geyser, hot water to the bathroom and kitchen respectively. Flow meter (T-Minol 130) was placed in close proximity to temperature 2 on the hot water pipe and measured the flow rate of the hot water drawn in number of counts per minute and was logged. The relative humidity and ambient temperature sensor measured the relative humidity and ambient temperature. The Hobo NRC-U30 data logger was used to logged counts for the volume of water drawn, various temperatures and the relative humidity and ambient temperature.

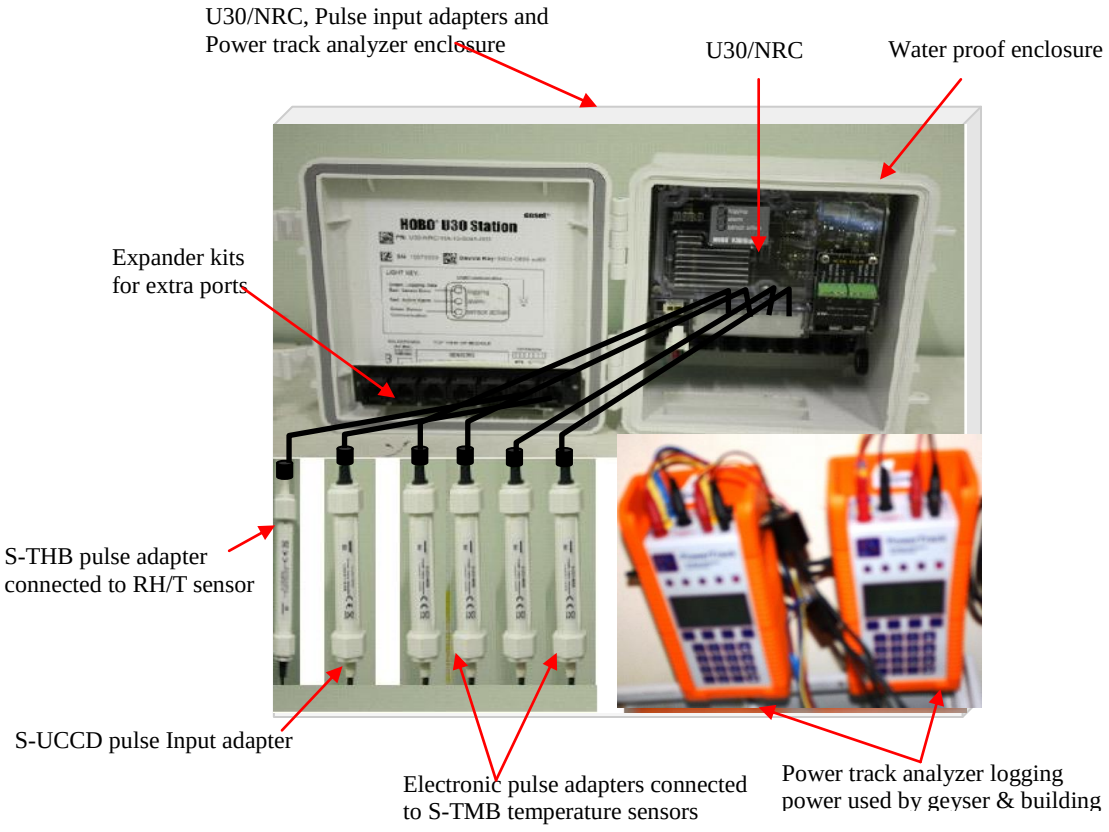

Figure 6: DAS for the experimental set up.

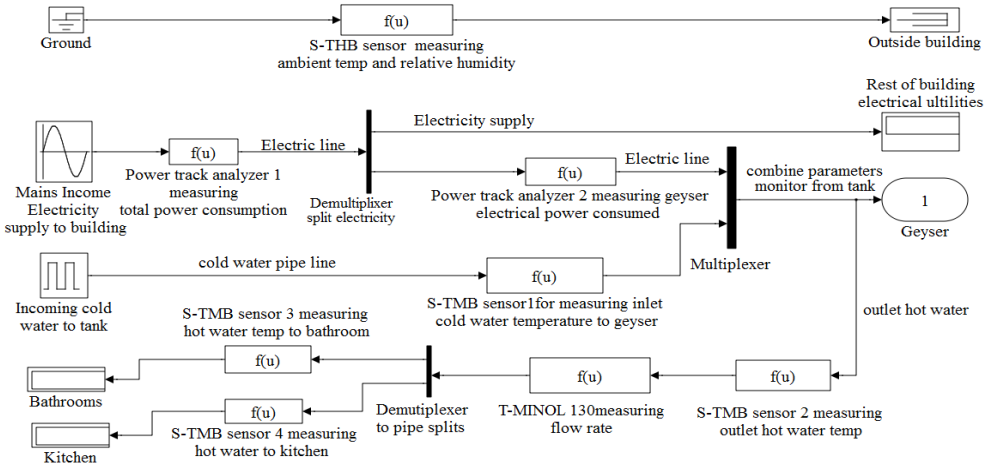

Figure 7: Schematic layout of the full installation set up

3.3.1 Data acquisition system

The research actually employed power track analyzers which recorded and logged voltages, current and power consumption in 1 minute interval. The U30-NRC logger was used to log all the temperature sensors, flow meter and the relative humidity and ambient temperature sensors measured data.

4.0 Results and discussion

4.1 Experimental determination of the baseline

A baseline is needed as a real reference to justified the energy savings when retrofitting geyser with ASHP. Again is needed to calculate the input energy to be used in the simulation model. A typical week profile was considered and used in the development of the modelled. From the data, the building power usage, geyser power consumes and hot water drawn off was determined for a typical week over a 24 h shown in table 1.

Table 1: Average typical week energy and hot water consumption

Days of the week	Volume of water drawn off (L)	Average maximum power (kw)		Total energy consumption (kWh)	
		Building	Geyer	Building	Geyer
Monday	287.690	5.305	2.063	28.696	17.424
Tuesday	283.905	2.850	2.013	28.499	15.742
Wednesday	405.038	3.125	2.040	34.176	21.376
Thursday	344.471	4.051	2.092	31.839	21.375
Friday	348.257	2.551	2.003	30.737	19.604
Saturday	370.969	3.655	2.043	38.774	20.002
Sunday	393.682	3.119	2.034	33.177	19.582

From the table 1, the capacity of daily hot water drawn for the average week day and average week end was 333 L and 382 L. This indicates significant electrical energy consumption and hence favoured the retrofit of geyser with ASHP.

4.2 Simulation model using Simulink

Figure 8 shows the simulation application used to modelled the COP of the propose retrofit geyser with an ASHP.

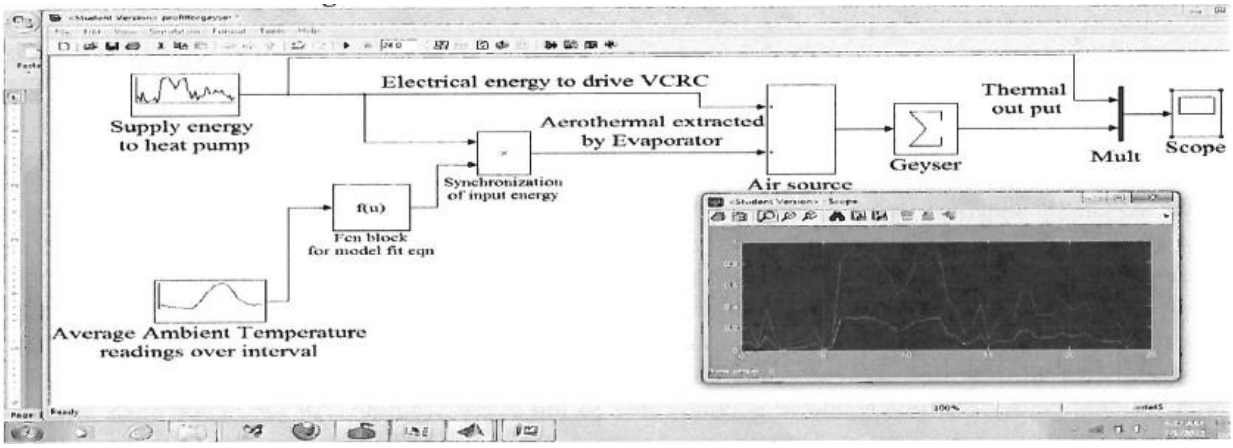

Figure 8: Illustrate the simulation architectural and programming sequence used in modelling the system COP

The input parameters (energy used by ASHP and ambient temperature) over 30 minutes interval are loaded to the two sources. The function block (f(u)) contain the modelling equation while the summation block act as heat pump extracting aero-thermal energy at the evaporator and electrical energy via compressor for CHP and additional energy used by fan and pump for ASHP water heater. The both input and output are displaced on the oscilloscope.

4.3 Average week energy and ambient condition variation

The figure 9, 10, 11 and 12 show the energies, ambient temperature and relative humidity for an average week day and week end profiles.

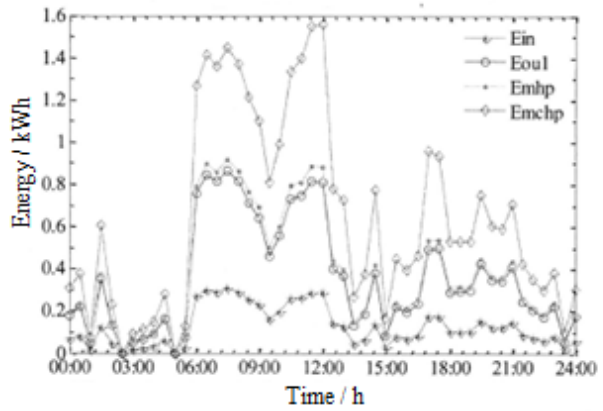

Figure 9: A typical week day energy profiles

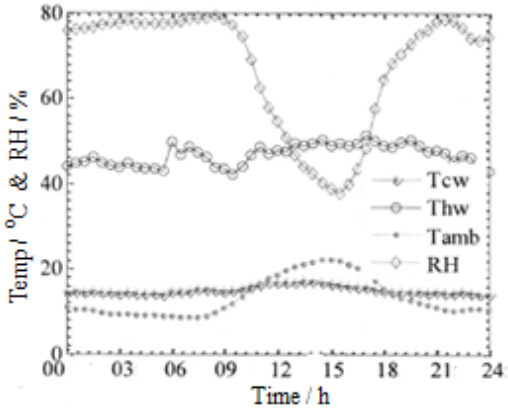

Figure 10:A typical week day energy profiles

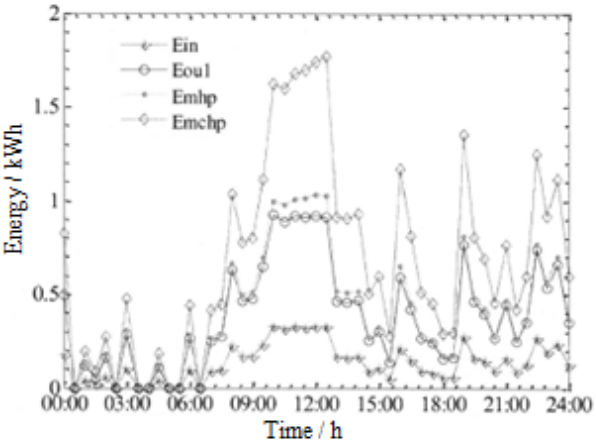

Figure 11: A typical week end energy profiles

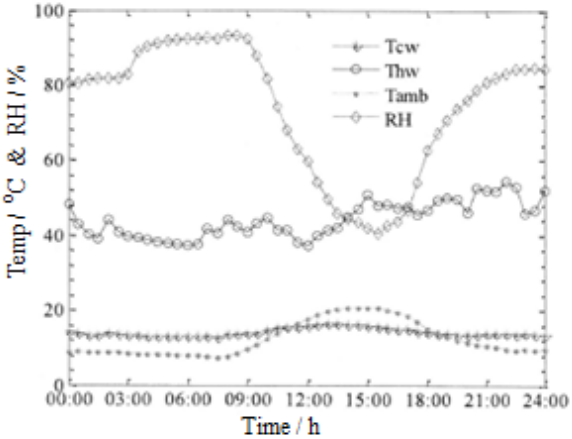

Figure 12: A typical week end energy profiles

The both energy profiles for the typical week day and week end follows a common dynamics and is classified into three time zones. Between 00:00 to 05:30, there is no hot water drawn, and energy (8% of total) used up is to compensate for standby losses, and hot water set temperature is almost constant. During the period the relative humidity is very high since ambient temperature is low. Between 06:00 to 11:00, the demand is high and over 60% of total energy is utilized and average COP of the modelled system is 3.008 and the CHP COP is 5.110. From 12:00 to 18:00, an average COP of 3.011 is achieved due to the increase in ambient temperature although the relative humidity is low. From the profiles of week day and week end, it was depicted that there was negligible variation of the system COP (above 3) and CHP COP (about 5) owing to the relative constant ambient temperature recorded throughout the week.

5.0 Conclusion

The modelled COP of the practical ASHP water heater was comparable to the experimental ASHP water heater with less than 0.03% error. Seasonal and annual COP can be accurately determined for ASHP water heater provided transient ambient temperatures and hot water temperatures are known. The ASHP water heater is an energy efficient technology for sanitary hot water production but compared to Carnot's system is below 65 % efficiency. Mathematically modelling and simulation of COP can be determined without actually measuring the primary factors (load cycle, inlet cold water temperature).

6.0 References

[1] Bodzin, S. (1997), "Air-to-Water Heat Pumps for the Home", Home Energy Magazine Online, July/August 1997

[2] Digest of South Africa Energy Statistics. Department of Energy, 2009

[3] Domestic water heating and water heater energy consumption in Canada, CBEEDAC, 2005

[4] Energy Management and conservation handbook (Nitin Goel, Thermo physical properties of refrigerants) CRC press (2008)

[5] G.L. Morrison, Anderson, T. and Behnia M. (2004). Seasonal performance rating of heat pump water heaters. Energy Conservation & Management. 76:147-152

[5] Ito S, Miura N and Wang K. (1999) Performance of a heat pump using direct expansion solar collectors. Solar Energy V65, 189-196

[7] Kline, S. A., et al. (2000). TRNSYS 15, A Transient system simulation program. University of Wisconsin Solar Energy

[8] MATLAB and Simulink software package (Math Work Corporation 2011b, version 7.12)

[9] Meyer, J.P., and M. Tshimankinda (1998), "Domestic Hot Water Consumption in South African Townhouses", Energy Conversion and Management, 39:7, 679-684

[10] www.eskom.co.za/home/about. Integrated Demand Management (Eskom, 2010)

Measurement of residual stress by diffraction techniques

AM Venter

Research and Development Division, Necsa Limited, South Africa

Corresponding author: Andrew.Venter@necsa.co.za

Abstract. Residual stresses present themselves as a two axed sword in material science applications. Compressive residual stresses offer beneficial conditions in applications where fatigue performance is required with it being able to mitigate crack initiation and propagation, whilst tensile residual stresses are generally considered to be detrimental. Non-destructive assessment of these stresses has become an essential requirement in high performance components where residual stress tailoring can render substantial improvements in the optimisation of component design. Strain scanning with diffraction techniques enables accurate investigation of the depth dependence by direct probing of the lattice plane spacing of the material microstructure. Complementary diffraction techniques are discussed and their application illustrated with results from a number of studies.

1. Introduction

The total stress that a component experiences in practical use is the vector sum of the applied and residual stresses. The applied stresses result from the loading forces in use and can be calculated to high precision. Residual stresses on the other hand result from the processing and manufacturing treatments of the material and are mostly only approximated qualitatively. Residual stresses in solids are defined as those stresses that are present in the material without it being subjected to an external force. They can be as high as the in situ yield stress of the material, and are subject to an internal force balance over the volume of the part. Macroscopic internal stresses in polycrystalline materials, which are homogenous over a large number of crystalline grains (micrometer to millimeter size), lead to local strains and stresses.

Diffraction based techniques enable accurate non-destructive measurement of the prevailing residual strain tensors from which the stress fields can be calculated in conjunction with the material elastic moduli [1-3]. Diffraction refers to the constructive interference of short wavelength radiation from the microstructure of a crystalline material as governed by the Bragg law $n\lambda = 2d^{hkl}\sin\theta^{hkl}$ where λ is the wavelength of the probing radiation, d^{hkl} is the interatomic spacing, θ^{hkl} the specular angle of diffraction with reference to the crystallographic lattice planes *hkl*. A limiting condition for diffraction to take place from crystal lattice planes is $\lambda \le 2d^{hkl}$, thus requiring wavelengths 1-3 Å in magnitude. Such wavelengths are offered by X-rays and thermal neutrons. X-rays are generated as low energy monochromatic beams from target tubes such as Cu, Co, Cr, etc. Each target tube has its own characteristic wavelength (energies smaller than 8 keV). Higher energy X-rays, 15-200 keV, are generated in synchrotron light sources. Thermal neutrons are generated in steady state research reactors or spallation sources. From a residual strain measurement perspective, each of these radiation

types present different penetration depths that enables depth selective non-destructive investigation. The penetration depths are governed by their fundamental interactions with matter. X-rays, having an interaction with the electron cloud of the material, have penetration depths that are proportional to the atomic number. In typical engineering materials the penetration depths are limited to 10 μm, i.e. presenting a near surface probe. Synchrotron X-rays are substantially more penetrating due to their higher energies. As an example 2 mm penetration into mild steel is achievable for energies larger than 60 keV. Thermal neutrons present a probe that is generally 1000 times more penetrating than normal X-rays for the transmission metal element series. Typically 40 mm steel can be penetrated. By defining a gauge volume with beam apertures, depth resolved investigations can be performed by systematic translation of the sample in a step-wise manner through the gauge volume.

Strain scanners are special derivatives of powder diffractometers that are devoted to the three-dimensional mapping of internal strains, by very precise measurement of the local lattice plane spacing deviations $\Delta d^{hkl}/d^{hkl}$ induced by these strains and stresses:

$$\Delta d^{hkl}/d^{hkl} = (\Delta\lambda/\lambda) - \cot\theta\Delta\theta$$

Constant wavelength strain scanners correspond to $\Delta\lambda = 0$ and pulsed instruments to $\Delta\theta = 0$. The strains determined in the laboratory coordinate system is related to the unknown strain components in the sample coordinate system using the transformation relation $\varepsilon'_{ij} = \alpha_{ik}\alpha_{jl}\varepsilon_{kl}$ where α_{ij} are the direction cosines between the coordinate systems. By orientating the specimen such that the diffraction vector is along the X'_3 coordinate axis in figure 1 the strain $\varepsilon_{\phi\varphi}$ in that direction can be determined

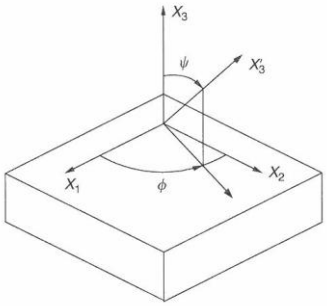

Figure1: Coordinate systems to measure stresses with diffraction. The sample coordinate system, X_i, is oriented by angles ϕ and φ to the sample coordinate system. X'_3 is the laboratory axis coordinate system.

$$\varepsilon_{\phi\varphi} = \frac{d_{\phi\varphi} - d_0}{d_0} = \varepsilon_{11}\cos^2\phi\sin^2\varphi + \varepsilon_{22}\sin^2\phi\sin^2\varphi + \varepsilon_{33}\cos^2\varphi + \varepsilon_{12}\sin 2\phi\sin^2\varphi$$
$$+ \varepsilon_{13}\cos\phi\sin 2\varphi + \varepsilon_{23}\sin\phi\sin 2\varphi$$

This equation relates the quantities measurable with diffraction, $d_{\phi\varphi}$ and d_0 (strain-free lattice parameter), to the unknown components of strain ε_{ij} in the material. Having determined the strain tensor, the stress tensor is obtained from Hooke's law

$$\sigma_{ij} = \frac{1}{1/2S_2}\left[\varepsilon_{ij} - \delta_{ij}\frac{S_1}{1/2S_2 + 3S_1}\varepsilon_{ii}\right]$$

where S_1 and $1/2S_2$ are the diffraction elastic constants.

Strain scanning with diffraction techniques is widely applied in materials characterization studies. This stems from the solid fundamentals in technique benchmarking employed and continuous expansion programs [4,5]. Diffraction furthermore enables investigation of different chemical phases in multi-phased materials. Examples from investigations that have been performed using X-rays, synchrotron light and neutrons are presented to illustrate potential applications. The investigations have been done at the Necsa facilities, supplemented with investigations at leading international facilities. The neutron strain scanner at Necsa is currently upgraded to offer capabilities of international standard to the South African research community.

2. Examples of applications

Examples are given of residual stress investigations in practical samples owing to their production / processing steps, supplemented by the characterization of a surface conditioning treatment deliberately applied to introduce a beneficial residual stress field rendering improved fatigue performance.

2.1. WC-Co coated substrates

Tungsten-carbide based *cermet* coatings with metallic cobalt binders, e.g. WC-Co, are frequently used when wear resistance, high surface hardness and low coefficient of friction similar to sintered carbide materials are required. In the industry, WC-Co coatings are typically deposited on substrates by the high-velocity oxygen-fuel, (HVOF) spraying process. In coated substrate systems, residual stresses are a superposition of contributions from the sample production history (cold work related to forging, rolling, extrusion), surface preparation (roughening through grit blasting) and the coating deposition process. Inherent to the nature of the HVOF coating deposition process, residual stresses due to the coatings arise from the impact, cooling, solidification and solid-state cooling of the splats, first onto the substrate and subsequently onto existing splats as the coating is built up layer by layer.

By combining the penetration depths of laboratory X-rays (Co-tube), high energy synchrotron radiation (80 – 200 keV white beam synchrotron X-rays from the ID15A instrument at the ESRF in energy dispersive mode) and thermal neutrons (KOWARI neutron strain scanner of the Bragg Institute, ANSTO) [11], depth resolved strain information was performed. Results are shown in figures 2-4.

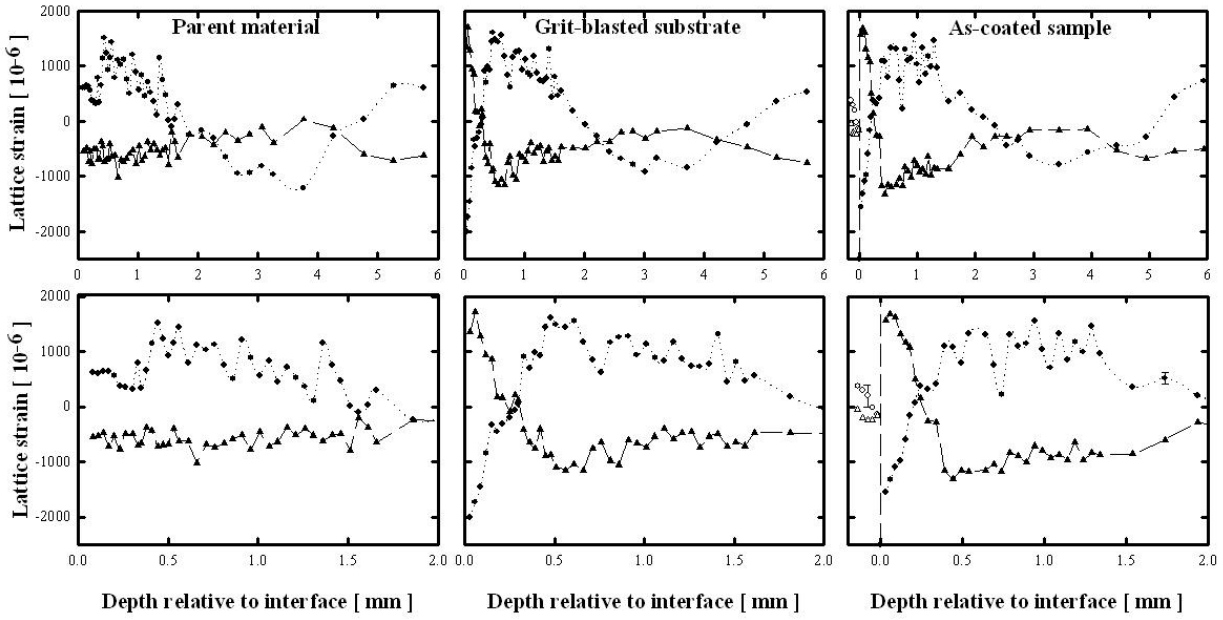

Figure 2: In-plane residual stress depth dependence determined from the lattice strain results of the (311) Cu and (101) WC Bragg peaks measured with synchrotron X-ray diffraction on a brass sample set. Results are for the parent material reference state (left set), the grit-blast substrate (centre set) and HVOF as-coated sample (right set) [6]. The near surface residual stress of the WC determined with laboratory X-rays (Co radiation) is also indicated [7]. The substrate coating interface is at 0 mm. The bottom sets of figures show an enlarged view of the results at the near-surface region. The error bars indicate the systematic error associated with the measurements. The lines connecting the symbols are guides to the eye. Legend: ●, substrate in-plane stress; ○,WC in-plane stress; ▲, WC near surface stress (laboratory X-rays).

Owing to the extremely small coating thickness of 200 μm (in sense of neutron diffraction stress experiment) measurements were done employing a fine through-thickness measurement mesh strategy with the aim to obtain the coating stress indirectly, i.e. through stress balance in the coating/substrate system. In addition, an attempt has been made to measure stresses in coatings directly. The two approaches gave a good countercheck on each other.

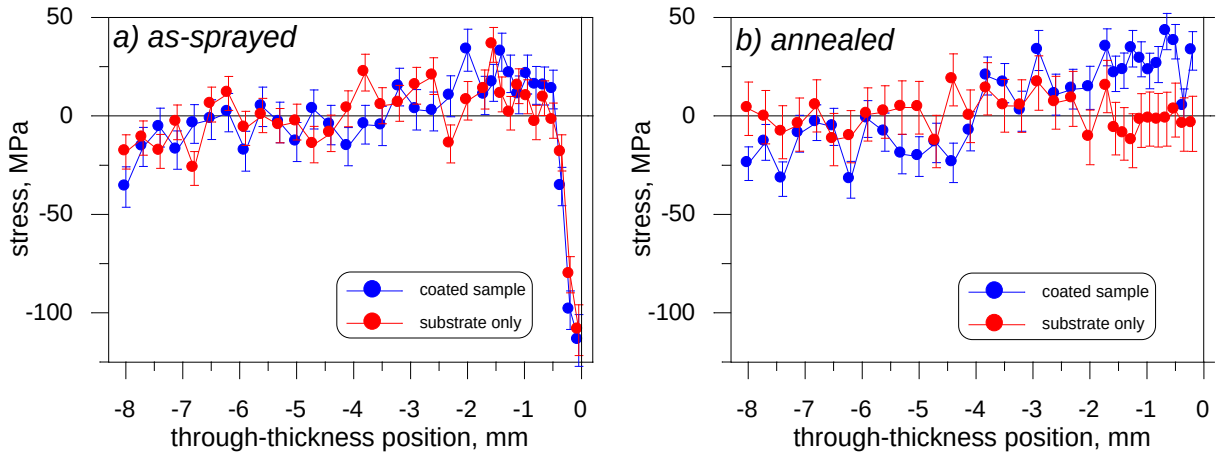

Figure 3. Experimentally measured through-thickness stress profiles for steel samples in a) as-sprayed and b) annealed conditions. Profiles measured in substrate only samples are also shown. [8]

Results of the stress profiles measured in a mild steel substrate series are shown in figure 4 as a comparison between the residual stress distributions observed from the as-coated and substrate-only samples, respectively for as-coated and annealed counterpart series. The differences between each set of profiles yield the stress purely due to the elastic effect from the WC coating.

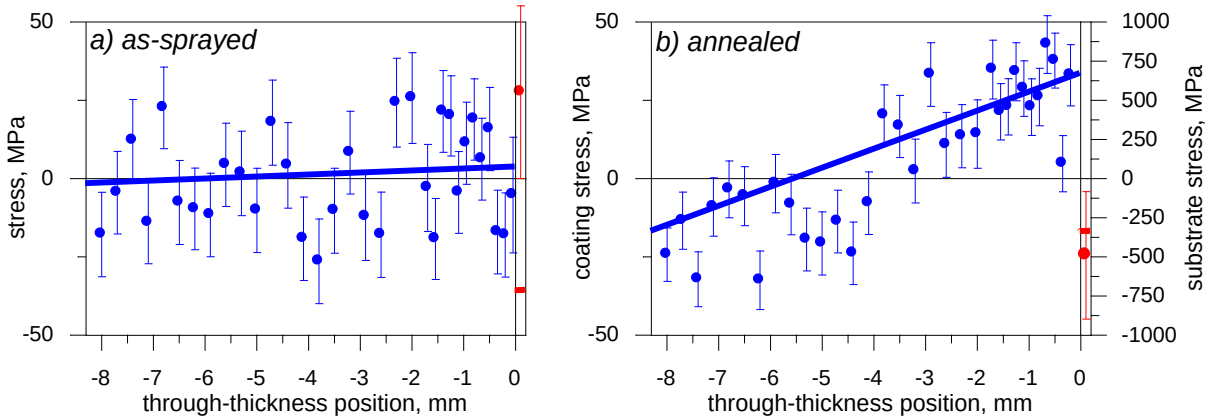

Figure 4. Experimentally determined through-thickness stress profiles for steel samples in a) as-sprayed and b) annealed conditions and model fit of the experimental data. [8]

2.2. Characterisation of production steps of cold cooled automotive undercarriage springs

Different approaches are followed with the manufacture of coil springs in the automotive industry today. Lately springs is manufactured using the cold coil forming process in which the feeder rod material is heat treated in advance, off line, and the coiling operation done at much lower temperature. By reducing the time the material has to be processed at high temperatures, excess of 900 °C, this leads to substantially lower manufacturing costs. The input material to the coiling process is thus

already in a fully tempered martensitic state that gives the material its strength and hardness. The coiling is done at room temperature followed by a low temperature stress annealing (380 °C) to reduce the detrimental effects associated with the cold working process. Figure 5 shows the residual stress components mapped across the diameter of the coil. Investigations have been performed on the KOWARI neutron strain scanner (Bragg Institute, ANSTO). To measure the interplay between the various production stages on the residual stress fields , the interior stresses were directly measured with the spring geometry intact to negate possible relaxation effects that may result from sectioning or application of other destructive approaches.

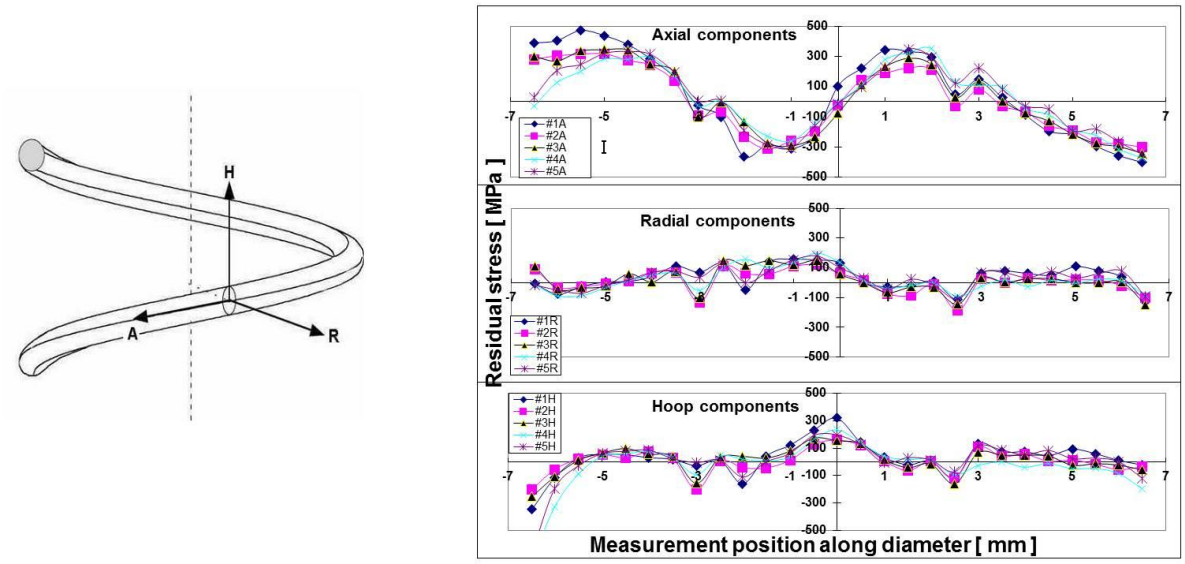

Figure 5: Results of the residual stresses measured along the centre line of cold coiled helical springs used in the motor vehicle industry. Samples have been extracted from sequential production steps: 1) Cold coiled from the fully tempered martensite state; 2) Low temperate tempering; 3) Hot setting; 4) Hot shot peening; 5) Cold shot peening.

2.3. Shot peened surfaces

Shot peening a surface treatment technique that is routinely used to introduce beneficial compressive residual stresses within the near-surface regions of components to mitigate against stress corrosion cracking and improves wear resistance. The technique comprises bombarding the sample surface with high speed pellets causing localised plastic deformation from which the restoring force captures a substantial compressive stress in the near-surface regions. The residual strain depth dependence was investigated using the 65 keV synchrotron beam at the ESRF on instrument ID31. Figure 6 show the in-surface residual strain fields existing at different regions in a specific sample geometry chosen to enable studying the influence of the underlying elastic material volume on the compressive residual stress conditions [9].

Conclusion

The complementary application of diffraction techniques using different radiation types to investigate various material systems have been presented. The examples show the capabilities to provide insight into the performance of materials from the characterisation of the inherent residual stresses. The neutron strain scanning technique is furthermore ideally suited to the study of in-situ loading response [10] with the investigations even possible at elevated or low temperatures to mimic the application conditions of materials in practical use.

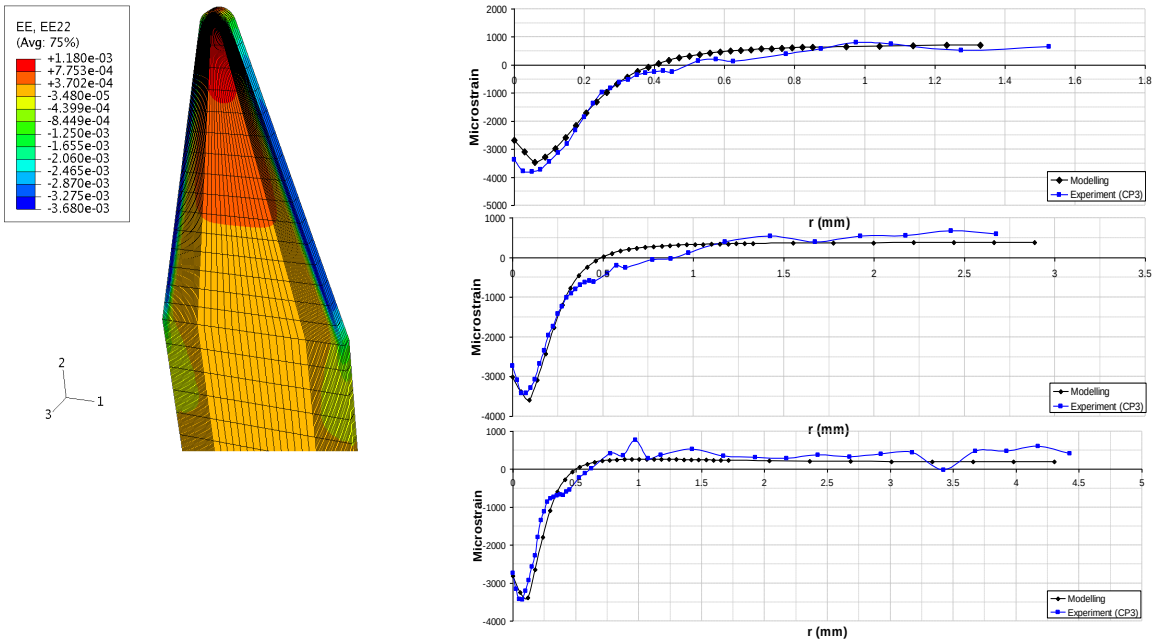

Figure 6: Depth dependence investigations of the in-plane residual strains in a shot peened sample with specifically geometry chosen to investigate the influence of the underlying elastic material volume on the beneficial compressive strains [9]. The depth dependence investigations have been performed with 65 keV synchrotron X-rays.

Acknowledgements

Access to leading strain scanning centres internationally is acknowledged. These include the European Synchrotron Radiation Facility (Grenoble, France), Australian Nuclear Science and Technology Organisation (Lucas Heights, Australia), LANSCE (Los Alamos, USA).

References

[1] *Introduction to the Characterization of Residual Stress by Neutron Diffraction*, Eds. MT Hutchings, PJ Withers, TM Holden and T Lorentzen, 2005, Taylor and Francis, ISBN 0-415-31000-8

[2] *Analysis of residual Stress by Diffraction using Neutron and Synchrotron Radiation*, Eds. ME Fitzpatrick and A Lodini, 2003 Taylor and Francis, ISBN 0-415-30397-4

[3] *Neutrons and Synchrotron Radiation in Engineering Materials Science*, Eds. W Reimers, AR Pyzalla, A Schreyer, H Clemens, 2008, Wiley-Vch Verlag GmbH & Co, ISBN 978-3-527-31533-8

[4] GA Webster (ed.), "Neutron Diffraction Measurements of Residual Stress in a Shrink-fit Ring and Plug" 2000 *VAMAS Report No. 38* ISSN 1016-2186

[5] C Ohms, RV Martins, O Uca, AG Youtsos, PJ Bouchard, M Smith, M Keavey, SK Bate, P Gilles, RC Wimpory, L Edwards 2008 *Proceedings of ASME PVP 2008* ASME, CD Publication, Order No. I795CD, ISBN 0-7918-3828-5

[6] AM Venter, T Pirling, T Buslaps, OP Oladijo, A Steuwer, TP Ntsoane, LA Cornish, N Sacks 2102 *Surface and Coatings Technology* **206** 4011

[7] OP Oladijo, AM Venter, LA Cornish, N Sacks 2012 *Surface and Coatings Technology*. In Press.

[8] AM Venter, V Luzin, D Hattingh 2012 *Material Science Forum*. Submitted for publication.

[9] TS Jun, AM Venter, AM Korsunsky 2011 *EXPERIMENTAL MECHANICS* **51** Issue: 2 165

[10] AD Krawitz, AM Venter, EF Drake, SB Luyckx, B Clausen 2009 *Int. Journal of Refractory Metals & Hard Materials* **27** 317

[11] A Brule, O Kirstein 2006 *Physica B* 385-386 1040

Division G – Theoretical and Computational Physics

Nonlocality arguments in the temporal Clauser-Horne-Shimony-Holt scenario

Sujit K Choudhary, Sandeep K Goyal, Thomas Konrad
School of Chemistry and Physics, University of KwaZulu-Natal, Durban 4000, South Africa.
E-mail: choudhary@ukzn.ac.za, goyal@ukzn.ac.za, konradt@ukzn.ac.za

Abstract. For testing the existence of superposition of macroscopically distinct quantum states, Leggett and Garg [Leggett A J, Garg A 1985 Phys. Rev. Lett. **54** 857], proposed an inequality based on the assumptions of 'macroscopic realism', 'noninvasive measurabilty' and 'induction'. These assumptions in a slightly different form have been used to derive a temporal version of Bell's inequality [Brukner C, Taylor S, Cheung S, Vedral V (e-print quant-ph/0402127)]. This inequality is violated in Quantum Mechanics and thus establishes nonlocality of quantum correlations in time. We compare various nonlocality arguments in this temporal scenario.

1. Introduction

Quantum mechanics is a mathematical theory for describing the physical world but it is probabilistic in nature. This may not be surprising, however. What is surprising is that (according to the Copenhagen interpretation) this probability is not the probability of some dynamical variable having a particular value in some state, rather it represents the probability of finding a particular value of the variable if that dynamical variable is measured. So what about the variables when the system is not subjected to any measurement; quantum mechanics remains mute in this regard. This interpretation generated numerous debates among physicists which resulted into the development of Hidden Variable Theories. The aim of hidden variable theories is to provide a formalism which, while being empirically equivalent to quantum mechanics, does not contain the intrinsic indeterminacy of quantum mechanics *i.e.*, in this theory quantum probabilities become epistemic, they arise due to our ignorance about hidden variables whose knowledge would give us the precise value of every observable.

In a much celebrated paper [1], J.S. Bell showed that this realistic viewpoint cannot explain some correlations predicted by quantum mechanics unless it assumes some signalling between the correlated events. Such correlations are called nonlocal. Bell showed this by means of an inequality, known as Bell's inequality [1]. Later, Hardy [2] gave an argument which also reveals the nonlocal character of Quantum Mechanics, but his argument, unlike Bell's argument, does not use inequalities involving expectation values. Afterwards, Cabello [3] introduced another logical structure to prove Bell's theorem, namely predictions of quantum mechanics are not compatible with the notion of local-realism, without inequality. Although, Cabello's logical structure was originally proposed for establishing nonlocality for three particle states, it was later exploited to establish nonlocality for a class of two-qubit mixed entangled state [4]. It is

noteworthy here that in contrast, there is no two-qubit mixed state which shows Hardy type nonlocality [5] whereas almost all pure entangled states of two-qubits do so (maximally entangled states are the exception) [6, 7]. Likewise, for almost all two-qubit pure entangled states other than maximally entangled ones, Cabello's nonlocality argument works and for these states, the maximum probability of success of this argument is 0.11 [8]. This is interesting, as for two-qubit states, the maximum success probability of Hardy's argument is known to be 0.09 [6, 9].

Although quantum theory predicts the existence of nonlocal correlations but these correlations cannot be exploited to communicate with a speed greater than that of the light in vacuum. But quantum theory is not the only nonlocal theory consistent with the relativistic causality [10]. Theories which predict nonlocal correlations and hence permit violation of Bells inequality but are constrained with the no signalling condition are called Generalized Nonlocal Theory (GNLT). Success probabilities of Hardy's and Cabello type arguments have also been compared in the framework of GNLT [11]. It has been shown there that for two two-level systems, success probabilities of both these arguments converge to a common maximum, 0.5.

Recently, the principle of nonviolation of information causality [12] has been proposed as one of the foundational principles of nature. Hardy and Cabello arguments have also been studied in the context of the above principle. Once again for two two-level systems, the success probabilities of these arguments converge to a common maximum, 0.20717 [13].

For testing the existence of superposition of macroscopically distinct quantum states, Leggett and Garg [14], proposed an inequality based on the assumptions of macroscopic realism, noninvasive measurabilty and induction. These assumptions in a slightly different form have been used to derive a temporal version of Bell's inequalities [15]. They are the constraints on certain combinations of temporal correlations for measurements of a single quantum system, which are performed at different times. These inequalities are violated in Quantum Mechanics and thereby give rise to the notion of *entanglement in time*. Recently, Hardy's argument has been studied in the temporal Bell-CHSH scenario [16]. It has been shown there that the maximum probability of success of this argument can assume up to 25%. We describe Cabello's argument in this temporal scenario as the probability of its success in revealing the time-nonlocal features of quantum states can be more than that of the Hardy's argument.

2. Temporal Bell-CHSH inequality

The temporal Bell inequalities are derived from the following two assumptions [15]

(i) *Realism*: The measurement results are determined by hidden properties, which the particles carry prior to and independent of observation, and

(ii) *Locality in time*: The result of a measurement performed at time t_2 is independent of any measurement performed at some earlier or later time t_1.

These assumptions are similar to the assumptions made by Leggett and Garg [14] in the context of testing superpositions of macroscopically distinct quantum states. But here these assumptions are more general in the sense that they do not necessarily demand the physical system under consideration to be macroscopic [17].

In the framework of a probabilistic theory, consider a physical system on which one of the two observers, Alice conducts the experiments of measuring any one (chosen at random) of the two $\{-1, +1\}$-valued random variables a_1 and a_2 whereas another observer Bob can run the experiments of measuring any one (chosen at random) of the two $\{-1, +1\}$-valued random variables b_1 and b_2 at a later time (this we call the temporal CHSH scenario).

Consider now the quantity B defined as:

$$B = a_1[b_1 + b_2] + a_2[b_1 - b_2].$$

In a realistic theory the value of the quantity B cannot be other than 2 or -2 if the theory is also local in time. After averaging this expression over many runs of the sequence of measurements, one obtains

$$-2 \leq \langle B \rangle \leq 2 \tag{1}$$

i.e.

$$|\langle a_1 b_1 \rangle + \langle a_1 b_2 \rangle + \langle a_2 b_1 \rangle - \langle a_2 b_2 \rangle| \leq 2. \tag{2}$$

This we call temporal Bell-CHSH inequality in analogy to the spatial one. As shown in [15], this inequality is violated in quantum mechanics if the system under consideration is a single spin-1/2 particle and observables a_1, a_2, b_1 and b_2 are the spin observables in directions given by the unit vectors $\tilde{a_1}$, $\tilde{a_2}$, $\tilde{b_1}$ and $\tilde{b_2}$ respectively where the spin directions are related as $\tilde{a_1} = \frac{1}{\sqrt{2}}(\tilde{b_1} + \tilde{b_2})$ and $\tilde{a_2} = \frac{1}{\sqrt{2}}(\tilde{b_1} - \tilde{b_2})$. In fact, for these observable settings the violation is maximum and it is equal to $2\sqrt{2}$. This may be called the temporal Tsirelson's bound [15, 18].

3. Temporal version of Hardy's argument

Consider the following four conditions in the above mentioned temporal CHSH scenario:

$$\left.\begin{array}{rcl} \text{Prob}(a_1 = +1,\ b_1 = +1) & = & 0, \\ \text{Prob}(a_2 = +1,\ b_1 = -1) & = & 0, \\ \text{Prob}(a_1 = -1,\ b_2 = +1) & = & 0, \\ \text{Prob}(a_2 = +1,\ b_2 = +1) & = & q \end{array}\right\} \text{(with } q > 0\text{)}. \tag{3}$$

The above four conditions together form the basis of Hardy's nonlocality argument. The last equation, for example, states that if Alice measures a_2 and Bob measures b_2 at some later time, then the probability that both will get $+1$ as their measurement results is q. These four conditions cannot be fulfilled simultaneously in a theory which is realistic and time-local [16, 19].

On the contrary, a qubit prepared in the state $|x+\rangle$ with the measurement setting $a_1 = -\sigma_x, a_2 = \sigma_y, b_1 = \sigma_y, b_2 = -\sigma_x$ satisfies all these conditions with $\text{Prob}(a_2 = 1, b_2 = 1) = 0.25$ which indeed is its optimal value [16]. Thus the temporal version of Hardy's proof is considerably stronger than its spatial analog where $\text{Prob}(a_2 = 1, b_2 = 1)$ can be no greater than 0.09. This fact has been recently verified in an experiment [19].

4. Cabello's argument in the temporal scenario

Cabello's conditions result by replacing the right hand side of the first condition of (3) with a nonzero probability p with $p < q$, and keeping the remaining three conditions the same.

It can easily be seen that these equations contradict local-realism if $0 \leq p < q$. To see this, let us consider those realistic (hidden variable) states for which $a_2 = +1$ and $b_2 = +1$. For these states, the second and the third equations in (3) tell that the values of a_1 and b_1 must be equal to $+1$. Thus according to the assumptions of *locality in time* and *realism* $\text{Prob}(a_1 = +1,\ b_1 = +1)$ should at least be equal to q. This contradicts the Cabello's argument as $p < q$. It should be noted here that $p = 0$ reduces this argument to Hardy's one. So by Cabello's argument, we specifically mean that the above argument is valid, even for nonzero p. The probability of success of this argument is measured by the difference in the two nonzero probabilities appearing in the argument, i.e. by $q - p$ [8]. As this argument is more relaxed than Hardy's argument, so we expect it to show a higher violation of timelocal-realism of quantum mechanics.

5. Discussion

We discussed various nonlocality arguments in the temporal scenario. In particular, we reviewed the Bell-like inequality, the Hardy and Cabello-like arguments. Hardy's argument has already been tested to be stronger in the temporal situation than its spatial version. As we have seen

that Cabello's argument is more relaxed than Hardy's argument, therefore we expect it to show a violation at least equal to Hardy's. In fact, we expect it to show a higher violation of timelocal-realism of quantum mechanics which will be subject of future study.

References

[1] Bell J S 1964 *Physics* **1** 195
[2] Hardy L 1992 *Phys. Rev. Lett.* **68** 2981
[3] Cabello A 2002 *Phys. Rev. A* **65** 032108
[4] Liang L M and Li C-Z 2005 *Phys. Lett. A* **335** 371
[5] Kar G 1997 *Phys. Rev. A* **56** 1023
[6] Hardy L 1993 *Phys. Rev. Lett.* **71** 1665
[7] Goldstein S 1994 *Phys. Rev. Lett.* **72** 1951
[8] Kunkri S, Choudhary S K, Ahanj A, Joag P 2006 *Phys. Rev. A* **73** 022346
[9] Jordan T F 1994 *Phys. Rev. A* **50** 62.
[10] Popescu S and Rohrlich D 1994 *Fond. Phys.* **24** 379
[11] Choudhary S K, Ghosh S , Kar G , Kunkri S, Rahaman R, Roy A 2010 *Quant. Inf. Comp.* **10** 0859
[12] Pawlowski M., Paterek T, Kaszlikowski D, Scarani V, Winter A, Zukowski M 2009 *Nature* **461** 1101
[13] Ahanj A, Kunkri S, Rai A, Rahaman R, Joag P S 2010 *Phys. Rev. A* **81** 032103
[14] Leggett A J, Garg A 1985 *Phys. Rev. Lett.* **54** 857
[15] Brukner C, Taylor S, Cheung S, Vedral V (*e-print* quantph/0402127)
[16] Fritz T 2010 *New Journal of Physics* **12** 083055
[17] Brukner C, Zukowski M (*e-print* quantph/0909.2611)
[18] Cirelson B S 1980 *Lett. Math. Phys.* **4** 93
[19] Fedrizzi A, Almeida M P, Broome M A, White A G, Barbieri M 2011 *Phys. Rev. Lett.* **106** 200402

Non-equilibrium steady state entanglement in a continuous variable system

A Ghesquière, I Sinayskiy, F Petruccione

Quantum Research Group, School of Physics, University of KwaZulu-Natal and National Institute for Theoretical Physics, Westville Campus, Durban, 4000, South Africa

E-mail: ghesquiere@ukzn.ac.za, sinayskiy@ukzn.ac.za, petruccione@ukzn.ac.za

Abstract. We examine an entangled bipartite state, where each particle is coupled to an independent reservoir. A difference in temperatures between the baths creates a non-equilibrium steady state. We investigate how the entanglement depends on the temperatures and the strength of the interaction. We find that the steady state does not exist for all values of the system parameters and offer an explanation for this behaviour.

1. Introduction

Dissipation effects induced by the coupling of an entangled quantum system to an environment, may yield various consequences for the entanglement within the system. As such, they have been widely studied in recent years and for a variety of systems. In [15], the authors studied non-equilibrium dissipation effects on a spin chain. Freitas and Paz have studied the dynamics of the Gaussian discord, a measure of quantum correlations, within a system of two oscillators sharing the same heat bath [7]. The effects of detuning the frequencies of two oscillators have also been examined [8].

Our system consists of two identical oscillators, coupled each to a reservoir with different coupling strengths. We keep the reservoirs at different temperatures, which creates a non-equilibrium situation. In many such situations, the steady state can be obtained explicitly and its properties analysed. As such, we examine the steady state behaviour of our bipartite system, particularly, that of its entanglement, so that we might understand the properties of the system in a non-equilibrium situation. Steady state entanglement is found to be difficult to obtain for a system interacting only locally with the environment it is strongly coupled to [12].

To determine the steady state, we use the Non-Rotating-Wave master equation, whose derivation can be found in [2, 9–11, 13]. We measure the entanglement using the logarithmic negativity, which is easy to compute using the covariance matrix formalism described in [1,3,14], which is particularly suited to the study of Gaussian states.

The stationary state is determined in Section 2. We will examine some results and offer some concluding remarks in Section 3.

2. Steady State

We study an entangled pair of identical oscillators, each one oscillating with frequency ω_0 and mass m, and coupled to its own heat bath. They have positions and momenta x_1, x_2, p_1 and

p_2. The oscillators are interacting linearly with each other with coupling strength κ. The total Hamiltonian reads as

$$H = \frac{p_1^2}{2m} + \frac{p_2^2}{2m} + \frac{m\omega_0^2}{2}(x_1^2 + x_2^2) + \kappa x_1 x_2 + \sum_j \left\{ \frac{p_j^2}{2m_j} + \frac{m_j\omega_j^2}{2}(q_j - x_1)^2 \right\} + \sum_k \left\{ \frac{p_k^2}{2m_k} + \frac{m_k\omega_k^2}{2}(q_k - x_2)^2 \right\}. \quad (1)$$

$q_{j,k}$ and $p_{j,k}$ are the baths' positions and momenta; ω's are the baths' oscillators frequencies and m_j and m_k are their masses. The interaction between the reservoirs and the particles is considered to be linear in their position; the Non-Rotating-Wave master equation for the system's density matrix ρ, in the quantum Brownian limit is written as [2, 9–11, 13]

$$\dot{\rho} = -\frac{i}{\hbar}[H_s, \rho] - \frac{i\gamma_1}{2\hbar}\left[x_1, [p_1, \rho]_+\right] - \frac{\gamma_1 kT_1}{\hbar^2}[x_1, [x_1, \rho]] - \frac{i\gamma_2}{2\hbar}\left[x_2, [p_2, \rho]_+\right] - \frac{\gamma_2 kT_2}{\hbar^2}[x_2, [x_2, \rho]], \quad (2)$$

where the T_i $(i = 1, 2)$ are the temperatures of the reservoirs, and the γ_i $(i = 1, 2)$ the coupling constants between the particles and their respective reservoirs. To study the entanglement, we will use the logarithmic negativity which may be expressed in terms of the covariance matrix as follows [16]

$$\mathcal{L}_{\mathcal{N}}(\rho) = -\sum_{i=1}^{n} \log_2(\min(1, |\lambda_i^{T_1}|))$$

where the λ's here are the symplectic eigenvalues of the covariance matrix, whose terms may be determined as $\Gamma_{jk} = 2\mathrm{Re}\,\mathrm{Tr}\left[\rho(\hat{R}_j - \langle\hat{R}_j\rangle)(\hat{R}_k - \langle\hat{R}_k\rangle)\right]$. The $\hat{R}$'s are the system's operators, e.g. $\hat{x}$ and $\hat{p}$. We note here that since we study a Gaussian state, we may determine the covariance matrix in terms of second moments only as $\Gamma_{jk} = 2\mathrm{Re}\,\mathrm{Tr}\left[\rho\hat{R}_j\hat{R}_k\right]$. We write a system of equations for the terms of the covariance matrix which yields the solution Γ_{ss} in the stationary limit

$$\begin{aligned}
\langle x_1^2\rangle &= \frac{-\gamma_1 kT_1(\gamma_2^2 m^2\omega_0^4 - \gamma_2^2\kappa^2 + \gamma_1\gamma_2 m^2\omega_0^4 + \kappa^2\omega_0^2) - \gamma_2 kT_2\kappa^2(\omega_0^2 + \gamma_1\gamma_2)}{(\kappa^2 - m^2\omega_0^4)(\gamma_1 + \gamma_2)(\gamma_1\gamma_2 m^2\omega_0^2 + \kappa^2)}, \\
\langle x_2^2\rangle &= \frac{-\gamma_1 kT_1\kappa^2(\omega_0^2 + \gamma_1\gamma_2) - \gamma_2 kT_2(\gamma_1^2 m^2\omega_0^4 - \gamma_1^2\kappa^2 + \gamma_1\gamma_2 m^2\omega_0^4 + \kappa^2\omega_0^2)}{(\kappa^2 - m^2\omega_0^4)(\gamma_1 + \gamma_2)(\gamma_1\gamma_2 m^2\omega_0^2 + \kappa^2)}, \\
\langle p_1^2\rangle &= \frac{\gamma_1 kT_1(\gamma_2^2 m^2\omega_0^2 + \gamma_1\gamma_2 m^2\omega_0^2 + \kappa^2) + \gamma_2 kT_2\kappa^2}{(\gamma_1 + \gamma_2)(\gamma_1\gamma_2 m^2\omega_0^2 + \kappa^2)}, \\
\langle p_2^2\rangle &= \frac{\gamma_1 kT_1\kappa^2 + \gamma_2 kT_2(\gamma_1^2 m^2\omega_0^2 + \gamma_1\gamma_2 m^2\omega_0^2 + \kappa^2)}{(\gamma_1 + \gamma_2)(\gamma_1\gamma_2 m^2\omega_0^2 + \kappa^2)}, \\
\langle x_1 x_2\rangle &= \frac{-\gamma_1 kT_1\kappa - \gamma_2 kT_2\kappa}{m(\gamma_1 + \gamma_2)(\kappa^2 - m^2\omega_0^4)}, \\
\langle x_1 p_2\rangle &= \langle p_2 x_1\rangle = -\langle x_2 p_1\rangle = -\langle p_1 x_2\rangle = \frac{\gamma_1 kT_1\gamma_2\kappa - \gamma_2 kT_2\gamma_1\kappa}{(\gamma_1 + \gamma_2)(\gamma_1\gamma_2 m^2\omega_0^2 + \kappa^2)},
\end{aligned} \quad (3)$$

and $\langle[x_1, p_1]_+\rangle = \langle[x_2, p_2]_+\rangle = \langle p_1 p_2\rangle = 0$. Using $[x, p] = i\hbar$, it is clear that $\mathrm{Re}[\langle x_i p_i\rangle] = \mathrm{Re}[\langle p_i x_i\rangle] = \frac{1}{2}\mathrm{Re}[\langle[x_i, p_i]_+\rangle] = 0$ $(i = 1, 2)$. The steady state covariance matrix can now be

witten as

$$\Gamma_{ss} = \begin{pmatrix} 2\langle x_1^2\rangle & 0 & 2\langle x_1 x_2\rangle & \langle x_1 p_2\rangle \\ 0 & 2\langle p_1^2\rangle & -\langle p_1 x_2\rangle & 0 \\ 2\langle x_2 x_1\rangle & -\langle x_2 p_1\rangle & 2\langle x_2^2\rangle & 0 \\ \langle p_2 x_1\rangle & 0 & 0 & 2\langle p_2^2\rangle \end{pmatrix} . \tag{4}$$

One can easily notice from (3) that there is a singularity at $\kappa = \pm m\omega_0^2$. The Quantum Langevin Equation [6] helps us to understand this. For simplicity, let us set $\gamma_1 = \gamma_2 = \gamma$ and apply the normal mode transformation $X_\pm = (x_1 \pm x_2)/\sqrt{2}$ so that in the high temperature memoryless case, that we consider, the Quantum Langevin Equation has the form

$$\begin{aligned} m\ddot{X}_+ + \gamma\dot{X}_+ + (m\omega_0^2 + \kappa)X_+ &= \Xi_+(t)\,, \\ m\ddot{X}_- + \gamma\dot{X}_- + (m\omega_0^2 - \kappa)X_- &= \Xi_-(t)\,, \end{aligned} \tag{5}$$

where $\Xi_\pm(t) = (\xi_1(t) \pm \xi_2(t))/\sqrt{2}$ and ξ_j are the random forces between the particles and their respective baths, with autocorrelation function given by

$$\frac{1}{2}\langle [\xi(t), \xi(t')]_+ \rangle = 2kT\gamma\delta(t - t')\,.$$

If $\kappa = \pm m\omega_0^2$, then one of the oscillators becomes effectively an unbounded classical Brownian particle. Such system will not reach a steady state.

3. Observations and concluding remarks

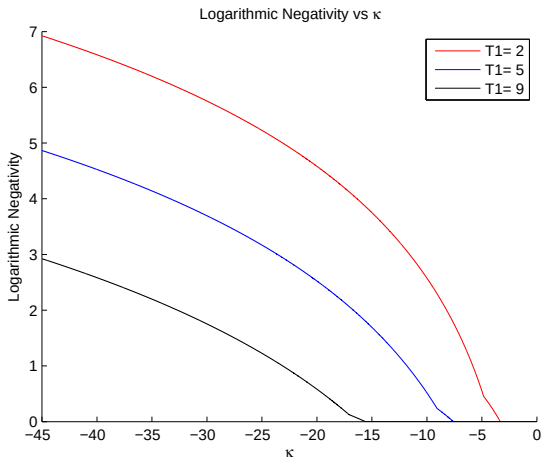

Figure 1: Logarithmic negativity versus κ for $T_2 = 5$, $\gamma_1 = 0.1$, $\gamma_2 = 0.1$, $m = 3$ and $\omega_0 = 0.5$.

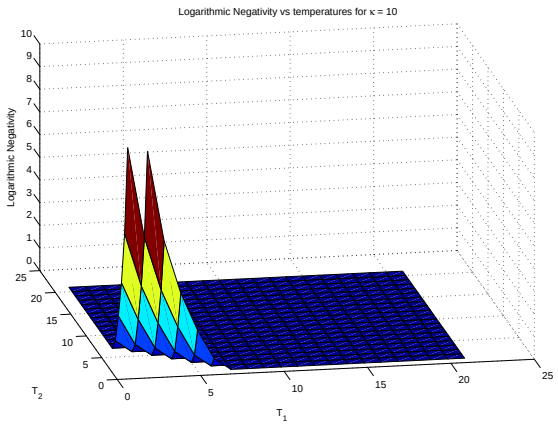

Figure 2: Logarithmic negativity versus the temperatures for $\kappa = 10$, $\gamma_1 = 0.1$, $\gamma_2 = 0.1$, $m = 3$ and $\omega_0 = 0.5$.

We observe on Figure 1, how the entanglement behaves, when plotted against κ for various temperatures. It is easily noticed that as κ approaches zero, the entanglement decreases. Furthermore, the entanglement is less as the temperature is higher. We observe on Figure 2 the effect of the temperatures on the entanglement for a given κ. It can be seen that as the temperatures increase, the entanglement vanishes. However, one may also notice on Figures 3 and 4 that the entanglement disappears for higher temperatures if κ is larger. This suggests

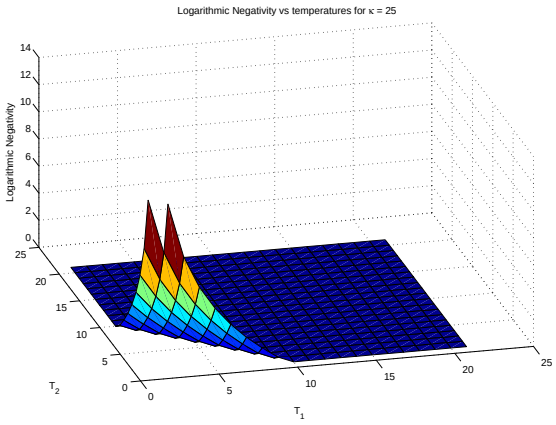

Figure 3: Logarithmic negativity versus the temperatures for $\kappa = 25$, $\gamma_1 = 0.1$, $\gamma_2 = 0.1$, $m = 3$ and $\omega_0 = 0.5$.

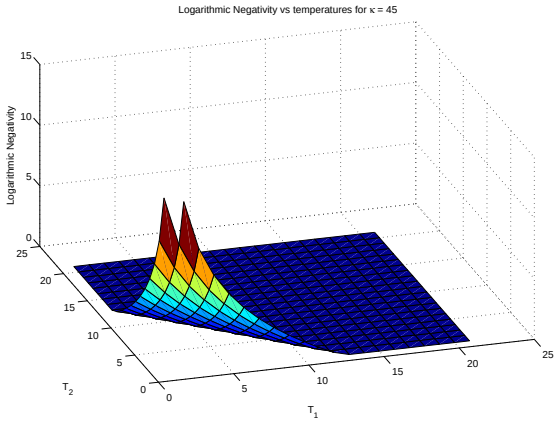

Figure 4: Logarithmic negativity versus the temperatures for $\kappa = 45$, $\gamma_1 = 0.1$, $\gamma_2 = 0.1$, $m = 3$ and $\omega_0 = 0.5$.

that a much stronger interaction is needed to counteract the effects of the temperatures. On the other hand, at $\kappa = 0$, there is no entanglement. Similar observations have been reported in [4, 5] and [11]. It may be worth noting that the steady state entanglement is that which is created through interaction between the system and their reservoirs. Indeed, it is also known as thermal entanglement and is independent of any initial entanglement the state may have been initially prepared with.

We have determined explicitly the steady state of a system of two oscillators, coupled to two independent reservoirs. However, we have shown that this solution does not exist for two particular values of system parameters. We have provided a simple explanation of the phenomenon. We have also shown that if the baths are at high temperatures, then the interaction between the particles must be strong in order for there to be steady state entanglement.

Acknowledgements
This work is based on research supported by the South African Research Chair Initiative of the Department of Science and Technology and National Research Foundation.

References

[1] J. Anders. *LANL e-print quant-ph/0610263*, 2003.
[2] H. P. Breuer and F. Petruccione. *The Theory of Open Quantum Systems*. Oxford: Oxford Press, 2002.
[3] J. Eisert and M. B. Plenio. *International Journal of Quantum Information*, 1:479, 2003.
[4] Z. Ficek and R. Tanás. *Physical Review A*, 74:024304, 2006.
[5] Z. Ficek and R. Tanás. *Physical Review A*, 77:054301, 2008.
[6] G. W. Ford, J. T. Lewis, and R. F. O'Connell. *Physical Review A*, 37:11, 1988.
[7] J. N. Freitas and J. P. Paz. *Physical Review A*, 85:032118, 2012.
[8] F. Galve, G. L. Giorgi, and R. Zambrini. *Physical Review A*, 81:062117, 2010.
[9] C. W. Gardiner and P. Zoller. *Quantum Noise*. Springer, 2nd enlarged edition edition, 2000.
[10] A. Ghesquière. *Entanglement in a Bipartite Gaussian State*. PhD thesis, available as LANL e-print quant-ph/1105.0564, 2009.
[11] A. Ghesquière and T. Dorlas. Entanglement of a two-particle gaussian state interacting with a heat bath. *Physics Letters A*, 377:1682, 2013.
[12] L. Hartmann, W. Dür, and H.-J. Briegel. *Physical Review A*, 74:052304, 2006.
[13] W. J. Munro and C. W. Gardiner. *Physical Review A*, 53:4, 1996.
[14] M. B. Plenio, J. Hartley, and J. Eisert. *New Journal of Physics*, 6:36, 2004.

[15] I. Sinaysky, D. Burgarth, and F. Petruccione. *Physical Review A*, 78:062301, 2008.
[16] G. Vidal and R. F. Werner. *Physical Review A*, 65:3, 2002.

Derivation of the quantum bit-error-rate for BB84 protocol based on the phase-covariant cloning machine

Mhlambululi Mafu[1], **Francesco Petruccione**[1,2]

[1] Centre for Quantum Technology, School of Chemistry and Physics, University of KwaZulu-Natal, P/Bag X54001 Durban, South Africa
[2] National Institute for Theoretical Physics (NITheP), KwaZulu-Natal, South Africa

E-mail: mafum@ukzn.ac.za, petruccione@ukzn.ac.za

Abstract. Based on the laws of physics, in particular the no-cloning theorem, quantum key distribution makes possible the distribution of a secret key between two legitimate parties commonly known as Alice and Bob. The third party known as an eavesdropper, Eve, can not clone the quantum states sent by Alice and then re-send a perfect copy to Bob without being detected. However, the phase-covariant cloning machine seems to be the best cloning machine for the BB84 quantum states but there is a trade-off between the quality of the clone and the amount of information that Eve can gain while the protocol remaining secure. By using the phase-covariant cloning machine to illustrate strategies performed by the eavesdropper, we arrive at the quantum bit-error-rate of 0.1464, which agrees with previous results.

1. Introduction

Quantum cryptography or more exactly quantum key distribution (QKD) provides the only physically secure and proven method for the transmission of a secret key between two distant parties, Alice and Bob, who are connected by an authenticated classical channel and an insecure quantum channel [1]. The security of QKD is based on the laws of physics rather than on the complicated mathematical algorithms to afford security [2, 3]. Specifically, QKD is based on the no-cloning theorem [4] which prohibits perfect cloning of an unknown quantum state with perfect fidelity and also on the Heisenberg uncertainty principle [5].

Wootters and Zurek showed that it is impossible to construct a device that will produce an exact copy of an arbitrary quantum state [4]. If perfect cloning was allowed then Eve would duplicate exact copies of the signal states being transmitted between legitimate parties. However imperfect cloning is possible, but it comes at a cost of being detected. For example, Eve can make a poor clone for herself and then send a perfect clone to Bob without being detected, but does not obtain much information about the key. On the contrary, she can make a perfect clone for herself and then send a poor copy to Bob. However, this affords her to obtain enough information but would reveal her presence to the legitimate parties.

In a QKD protocol, the quantum-bit-error-rate (QBER) refers to the fraction of positions where Alice's and Bob's bit strings differ. QBER is generally a direct measure for the secrecy of Alice and Bob's strings since any eavesdropping strategy would perturb the correlations between

them. For example, if the QBER is very high, the two parties abort the protocol or else they use the classical post-processing procedure to distill a secret key.

The security proof of the BB84 protocol [6] against arbitrary eavesdropping strategies was first shown in a complicated proof by Mayers [7]. Later, a simpler proof was shown by Lo and Chau [8]. However, their proof needs a quantum computer to implement it. A number of years later, Shor and Preskill generalized the ideas of Lo and Chau's security proof [8] and proposed a simpler proof for the BB84 protocol [9]. Many versions of security analysis have been derived for this protocol [10, 11, 12]. This protocol was first proven to be unconditionally secure by Inamori [13]. We highlight that this unconditional security proof also takes into account the finite-size key effects and this is immediate to practical implementations of the protocol.

There is a trade-off between the quality of the clone and the amount of information that Eve can gain about the key. Hence in this paper, our goal is to calculate an upper bound on the achievable information that Eve can gain but still the protocol remaining secure. In our derivation, we normalize clearly the states to be cloned in order to explicitly arrive at a QBER of 0.14644, which has been proven in various papers [14, 9].

2. BB84 Protocol

The BB84 protocol utilizes two communication channels between Alice and Bob. It consist first of a public classical channel where each party including the eavesdropper can listen to conversations but cannot change the contents of the message and, second of a quantum communication channel used for the transmission of quantum signals. However, the quantum communication channel is assumed to be insecure. This means that the eavesdropper has got all the resources needed to manipulate the signals. The protocol uses four quantum states $\{|0\rangle, |1\rangle, |+\rangle = \frac{1}{\sqrt{2}}(|0\rangle + |1\rangle), |-\rangle = \frac{1}{\sqrt{2}}(|0\rangle - |1\rangle)\}$. These basis states can be represented by any two-level quantum system, for example, by photon polarization and spin 1/2 systems. For linearly polarized photons, the first two states correspond to vertically ($\uparrow$) and horizontally polarized ($\rightarrow$) photons. For circularly polarized photons, the last two states correspond to polarization angles $45°$($\nearrow$) and $-45°$($\nwarrow$) with respect to the vertical axis. The states $|0\rangle$ and $|+\rangle$ represent bit value 0 while the states $|1\rangle$ and $|-\rangle$ represent bit value 1. The pairs $\{|0\rangle, |1\rangle\}$ and $\{|+\rangle, |-\rangle\}$ form two non-orthonormal and conjugate bases. The BB84 protocol consists of the following steps:

a) **Quantum Transmission Phase**

Alice randomly generates a bit string that she wants to send. For each bit, she randomly and independently chooses her encoding basis and prepares the states. She sends these prepared states via the insecure quantum channel. Upon receiving these states, Bob independently of Alice randomly chooses his measurements basis for each qubit he receives. Bob records his measurements bases and also the result of the measurements.

b) **Bases Announcement**

Alice and Bob communicate over the unjammable classical channel to compare the bit value of each basis, discarding those instances in which they used different bases. This step is called sifting. Statistically, this happens in half of the cases. The remaining sequence of bits forms the sifted key.

c) **Error estimation**

Ideally, in the absence of errors, the raw key should be identical between Alice and Bob meaning that Eve has no information and therefore the raw key becomes the secret key. Alice and Bob can check whether an eavesdropper was present or not by checking the difference between their keys (i.e., error rate) by comparing some randomly chosen bits. Let us assume that the error rate for measurements in both bases are the same

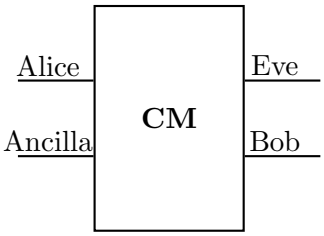

Figure 1. Eavesdropping by using a phase-covariant cloning machine. **CM** represents the cloning machine.

and equal to ε. If the calculated error rate is higher than some prescribed threshold they abort the protocol. Otherwise they have to perform classical post-processing and this is performed on the classical channel. At the end of this processing Alice and Bob share a truly secret key or nothing at all since they abort the protocol.

3. Description of the phase-covariant cloning machine

Regardless of the no-cloning theorem, the best eavesdropping strategy for the BB84 quantum states can be achieved by using the phase-covariant cloning machine [15]. This cloning machine consists of two inputs states labelled as Alice, $|0\rangle_a$ and ancilla $|Q_0\rangle_x$. These are states to be cloned. The cloning machine gives out a state which is sent to Bob, $|0\rangle_b$ and another to Eve, $|\bar{Q}_0\rangle_x$ which she keeps. This is shown in Figure 1.

We describe the behavior of an ideal quantum copying machine as

$$|s\rangle_a|Q\rangle_x \rightarrow |s\rangle_a|s\rangle_b|\bar{Q}\rangle_x, \tag{1}$$

where $|s\rangle_a$ represents the *in* state of the original mode to be copied, $|Q\rangle_x$ represents the *in* state of the copying machine, $|s\rangle_b$ represents the *out* state of the copy mode and $|\bar{Q}\rangle_x$ represents the final state of the copying machine.

The cloning machine can be described by the following transformation rules on the *in* states $|0\rangle_a$ and $|1\rangle_a$ as

$$|0\rangle_a|Q\rangle_x \rightarrow |0\rangle_a|0\rangle_b|Q_0\rangle_x, \tag{2}$$

and

$$|1\rangle_a|Q\rangle_x \rightarrow |1\rangle_a|1\rangle_b|Q_1\rangle_x. \tag{3}$$

We note that the basis vectors $|0\rangle_a$ and $|1\rangle_a$ can be perfectly cloned but others cannot be. Instead of using these quantum states $|0\rangle_a$ and $|1\rangle_a$ which can be copied ideally, we use the Pauli matrix **Y** to demonstrate what happens in a real scenario as

$$|0\rangle_a = \tfrac{1}{\sqrt{2}}(|0\rangle + i|1\rangle), \tag{4}$$

and

$$|1\rangle_a = \tfrac{1}{\sqrt{2}}(|0\rangle - i|1\rangle). \tag{5}$$

The action of the phase covariant cloning machine can now be described as follows

$$|0\rangle_a|Q_0\rangle_x \rightarrow |0\rangle_b|\bar{Q}_0\rangle_x, \tag{6}$$

$$|1\rangle_a|Q_0\rangle_x \rightarrow \cos\gamma|1\rangle_b|\bar{Q}_1\rangle_x + i\sin\gamma|0\rangle_b|\bar{Q}_0\rangle_x, \tag{7}$$

where $0 \leq \gamma \leq \pi/2$. We use the basis $\{|0\rangle, |1\rangle\}$ to explain how the cloning machine operates when various states are sent by the following operation

$$|a\rangle_\alpha|Q_0\rangle_x \rightarrow \sum_{b,c\in\{0,1\}} \zeta_{abc}|b\rangle_\beta|c\rangle_{\text{Eve}}, \tag{8}$$

with,

$$\zeta_{abc} = e^{i(a+b+c)\pi/2}((-1)^a + (-1)^b\cos\gamma + (-1)^c\sin\gamma), \tag{9}$$

where γ determines the quality of the two clones. If Bob measures a $|1\rangle$ when Alice has sent a $|0\rangle$ this results in an error in Alice's and Bob's key elements. We find that

$$\begin{aligned} |\zeta_{010}|^2 &= (1+\cos\gamma-\sin\gamma)^2 \\ &= 2+2\cos\gamma-2\sin\gamma-2\cos\gamma\sin\gamma, \end{aligned} \tag{10}$$

and

$$\begin{aligned} |\zeta_{011}|^2 &= (1-\cos\gamma-\sin\gamma)^2 \\ &= 2-2\cos\gamma-2\sin\gamma+2\cos\gamma\sin\gamma. \end{aligned} \tag{11}$$

Then, we can find the error probability by evaluating $|\zeta_{010}|^2 + |\zeta_{011}|^2$ as follows

$$\begin{aligned} |\zeta_{010}|^2 + |\zeta_{011}|^2 &= (1-\cos\gamma)^2(1-\cos\gamma)\sin\gamma + \sin^2\gamma \\ &\quad + (1-\cos\gamma)^2 - 2(1-\cos\gamma)\sin\gamma + \sin^2\gamma \\ &= 4(1-\cos\gamma). \end{aligned} \tag{12}$$

Now, our goal is to calculate the normalization constant where we use $|\psi\rangle = \sum_{b,c\in 0,1}\zeta_{abc}|b\rangle_\beta|c\rangle_{\text{Eve}}$, $a \in 0,1$ and the fact that $||\psi||^2 = \langle\psi|\psi\rangle$ and proceed as follows

$$\begin{aligned} |\psi\rangle &= \zeta_{a00}|0\rangle|0\rangle + \zeta_{a10}|1\rangle|0\rangle + \zeta_{a01}|0\rangle|1\rangle + \zeta_{a11}|1\rangle|1\rangle \\ \langle\psi| &= \zeta^*_{a00}\langle 0|\langle 0| + \zeta^*_{a10}\langle 1|\langle 0| + \zeta^*_{a01}\langle 0|\langle 1| + \zeta^*_{a11}\langle 1|\langle 1| \\ \langle\psi_{a=0}|\psi_{a=0}\rangle &= 2((1+\cos\gamma)^2+\sin^2\gamma) + 2((1-\cos\gamma)^2+\sin^2\gamma) \\ &= 8. \end{aligned} \tag{13}$$

The amount of error between Alice's and Bob's key elements can be obtained by evaluating the probability that Bob measures $|1\rangle$ although Alice sent the state $|0\rangle$. This is obtained by calculating the probability mass on the $|1\rangle_b$ state. This is the probability that Bob measures $|1\rangle$ exactly and we can calculate it as follows

$$\varepsilon = \sum_{c=0,1} |\zeta_{01c}|^2 = 4(1-\cos\gamma)/8 = (1-\cos\gamma)/2. \tag{14}$$

The degree of correlations between Alice and Bob can be quantified by the mutual information which is expressed as $I(A:B) = H(A) - H(A|B)$. The entropy of Alice's string A equals $H(A) = 1$ and the conditional entropy of A given B is given by $H(A|B) = h(\varepsilon)$. This can then be written as

$$\begin{aligned} I(A:B) &= H(A) - H(A|B) \\ &= 1 - h(\varepsilon) \\ &= 1 - h[(1-\cos\gamma)/2], \end{aligned} \tag{15}$$

where $h(\varepsilon) = -\varepsilon \log_2 \varepsilon - (1-\varepsilon)\log_2(1-\varepsilon)$ is the binary entropy function. The probability of Eve guessing a result can be found by calculating the probability on the $|1\rangle_{\text{Eve}}$ state which is

$$\varepsilon = \sum_{b=0,1} |\zeta_{0b1}|^2. \tag{16}$$

Also, by using $\zeta_{abc} = e^{i(a+b+c)\pi/2}((-1)^a + (-1)^b \cos\gamma + (-1)^c \sin\gamma)$ we find that,

$$\begin{aligned} |\zeta_{001}|^2 &= (1 + \cos\gamma - \sin\gamma)^2 \\ &= 2 + 2\cos\gamma - 2\sin\gamma - 2\cos\gamma\sin\gamma, \end{aligned} \tag{17}$$

$$\begin{aligned} |\zeta_{011}|^2 &= (1 - \cos\gamma - \sin\gamma)^2 \\ &= 2 - 2\cos\gamma - 2\sin\gamma + 2\cos\gamma\sin\gamma. \end{aligned} \tag{18}$$

We again find the error probability by evaluating $|\zeta_{010}|^2 + |\zeta_{011}|^2$ as follows

$$\begin{aligned} |\zeta_{001}|^2 + |\zeta_{011}|^2 &= 2 + 2\cos\gamma - 2\sin\gamma - 2\cos\gamma\sin\gamma \\ &\quad + 2 - 2\cos\gamma - 2\sin\gamma + 2\cos\gamma\sin\gamma \\ &= 4(1 - \sin\gamma). \end{aligned} \tag{19}$$

It can also be recognized that by using the same procedure as in Equation (13), the normalization is again calculated and found equal to $\langle\psi_{a=0}|\psi_{a=0}\rangle = 8$. Then, we can evaluate the error probability as

$$\varepsilon = \sum_{b=0,1} |\zeta_{0b1}|^2 = 4(1 - \sin\gamma)/8 = (1 - \sin\gamma)/2. \tag{20}$$

Again, the degree of correlations between Bob and Eve is quantified by the mutual information and is calculated as

$$\begin{aligned} I(B:E) &= H(B) - H(B|E) \\ &= 1 - h(\varepsilon) \\ &= 1 - h[(1 - \sin\gamma)/2]. \end{aligned} \tag{21}$$

In order to determine whether the channel is secure for communication, one must compare the mutual information between Alice and Bob, $I(A:B)$ and the minimum mutual information between each party and Eve. This gives us an expression for the secret fraction r and is expressed as

$$r = I(A:B) - \min(I_{AE}, I_{EB}), \tag{22}$$

The secret key fraction is expressed as $r = \ell/N$ where, ℓ is the length of the secret key to be extracted and N is the number of signals exchanged by Alice and Bob in a run of key exchange. In this scheme, the optimal mutual information between Alice and Bob is the same. We use the Csiszár-Körner bound [16] which is expressed as

$$\ell = I(A:B) - \max_{\text{Eve}} I(A:E). \tag{23}$$

In order to find the security bound for individual attacks we can express

$$I(A:E) = \max_{\text{Eve}} I(A:E), \tag{24}$$

and similarly $I(E:B)$ is defined in the same manner. The term $\max_{\text{Eve}}$ means that one must maximize the mutual information over Eve's strategies. Then the amount of information gained by the eavesdropper as a function of error rate can expressed as

$$\begin{aligned} I(A:E) &= 1 - h[(1-\sin\gamma)/2] \\ &= 1 - h[\tfrac{1}{2} - \sqrt{\varepsilon(1-\varepsilon)}], \end{aligned} \tag{25}$$

where $\varepsilon = (1-\cos\gamma)/2$ from Eq (14). In the case of $\gamma = \pi/4$, the two clones have the same quality. Therefore, if we take $\gamma = \pi/4$ (this is where we evaluate the minimum of $I(B:E) = I(A:E)$), this equation gives the upper bound on the bit-error-rate for the BB84 protocol by using one-way classical post-processing. The value of the QBER becomes $\varepsilon = 0.14644$ at which it is safe to extract a secret key. This is the limiting QBER at which the communication channel is considered to be secure for the generation of the security key. We note that this derived QBER value agrees with the previous results which appear in Refs. [14, 9].

4. Conclusion

Based on the above calculation, we recognize that the most dangerous eavesdropping attack can be realized with the aid of phase-covariant cloning machine, which was used to perfectly clone the quantum states of the BB84 protocol. This can also be interpreted via the complimentarity principle. If Bob receives the first clone and the second clone is the eavesdropper's copy then the more Eve knows Alice and Bob's signals, the less strongly their signals are correlated, thus leading to detection. This means the quantum bit-error-rate will be above 0.1464, so they abort the protocol because the channel is no longer secure for reliable communication.

Acknowledgments

This work is based on research supported by the South African Research Chair Initiative of the Department of Science and Technology and National Research Foundation.

References

[1] Scarani V, Bechmann-Pasquinucci H, Cerf N, Dušek M, Lütkenhaus N and Peev M 2009 *Rev. Mod. Phys.* **81** 1301
[2] Gisin N, Ribordy G, Tittel W and Zbinden H 2002 *Rev. Mod. Phys.* **74** 145–195
[3] Ekert A K 1991 *Phys. Rev. Lett.* **67**(6) 661–663
[4] Wooters W and Zurek W 1982 *Nature* **299** 802
[5] Busch P, Heinonen T and Lahti P 2007 *Physics Reports* **452** 155–176
[6] Bennett C and Brassard G 1984 *in Proceedings of IEEE International Conference on Computers, Systems and Signal Processing (IEEE, New York)* p 175
[7] Mayers D 2001 *J. Assoc. Comput. Mach.* **48** 351–406
[8] Lo H and Chau H 1999 *Science* **283** 2050–2056
[9] Shor P W and Preskill J 2000 *Phys. Rev. Lett.* **85** 441–444
[10] Xiangbin W 2005 *Phys. Rev. A* **71** 052328
[11] Gottesman D and Preskill J 2001 *Phys. Rev. A* **63** 022309
[12] Gottesman D and Lo H 2003 *IEEE Trans. Info. Theory* 457–475
[13] Inamori H, Lütkenhaus N and Mayers D 2007 *Eur. Phys. J. D* **41** 599–627
[14] Branciard C, Gisin N, Kraus B and Scarani V 2005 *Phys. Rev. A* **72** 32301
[15] Bruss D, Cinchetti M, Mauro G and Macchiavello C 2000 *Phys. Rev. A* **62** 12302
[16] Csiszár I and Korner J 1978 *IEEE Trans. Info. Theory* **24** 339–348

Upper bound to accessible information for the six-state quantum key distribution protocol

Mhlambululi Mafu[1], **Francesco Petruccione**[1,2]

[1] Centre for Quantum Technology, School of Chemistry and Physics, University of KwaZulu-Natal, P/Bag X54001 Durban, South Africa

[2] National Institute for Theoretical Physics (NITheP), University of KwaZulu-Natal, P/Bag X54001 Durban, South Africa

E-mail: 209526077@stu.ukzn.ac.za, petruccione@ukzn.ac.za

Abstract. It is necessary for any quantum key distribution protocol to have an unconditional security proof which is robust against any kind of attacks that are allowed by the laws of physics. This is the main advantage of quantum key distribution schemes over classical ones aiming to achieve the same task. We derive an upper bound on the achievable information that an eavesdropper may obtain. Instead of the known method of conditioning on the random variable, we express Eve's information about the raw key as a function of the error since it is related to the secret key function. The proposed method reproduces the upper bound that was derived previously.

1. Introduction

Quantum key distribution (QKD) allows two distant parties, traditionally known as Alice and Bob who are connected by an authenticated classical channel and insecure quantum channel to establish a secure random cryptographic key under the intervention of an eavesdropper, Eve [1]. However, there stands a theoretical challenging problem of determining the necessary conditions for security in QKD schemes. The main task for a security analysis is to figure out what the length of the final secure key is and perform hashing in order to obtain the final key. The lower and upper bounds on the secret key rate which involve entropies of two qubit density operators for the six-state protocol has been found [2]. The security of the protocol against optimal eavesdropping on noisy states has been studied [3, 4]. We highlight that the unconditional security proof of the six-state protocol has been shown in various papers [5, 6, 7].

In this paper our goal is to re-derive an upper bound on the achievable information that an eavesdropper may obtain about the key and also to improve the security threshold. We highlight that in order to improve the security threshold a known method of conditioning on the random variable is used for the BB84 protocol [8]. However, in this paper we apply it to the six-state protocol by expressing Eve's information about the raw key as a function of the error since it is related to the secret key function. The proposed method reproduces the upper bound that was derived previously. This maximum threshold in the secret key fraction is important in the QKD security of the protocol as it determines the maximum value in which the secret key can be extracted in the presence of an eavesdropper while the protocol remains secure.

2. The Six-state protocol

The six-state protocol makes use of three different encodings which are defined by the x basis $\{|0\rangle_x, |1\rangle_x\} := \{\frac{1}{2}(|0\rangle_z \pm |1\rangle)\}$, the y basis $\{|0\rangle_y, |1\rangle_y\} := \{\frac{1}{2}(|0\rangle_z \pm i|1\rangle)\}$ and the z basis as $\{|0\rangle_z, |1\rangle_z\}$. In this protocol, Alice randomly selects with equal probability ($p = 1/3$) the basis she uses and then sends the appropriate qubit to Bob in the base she chose. By making use of the classical channel, Alice announces to Bob which bases she used. In the event that Bob measures in Alice's basis (the sent qubit agrees with the measured qubit) they use these values to form the key.

Similarly, the six-state protocol [9] displays symmetry just like the BB84 protocol [10]. However, the six-state protocol is more symmetrical due to the fact that three bases span the full Bloch sphere (symmetrically distributed) as opposed to the BB84 where only a two-dimensional plane is spanned. In the six-state protocol only 1/3 of the qubits are kept and the rest discarded. For comparison in the BB84 protocol only 1/2 of the qubits are kept and the rest are discarded. Due to the symmetry in the six-state protocol, one can compute the bounds restricting consideration to collective attacks and the joint attacks such that the final state of Alice and Bob is Bell-diagonal as shown below

$$\rho_{AB} = \gamma_1|\phi^+\rangle\langle\phi^+| + \gamma_2|\phi^-\rangle\langle\phi^-| + \gamma_3|\psi^+\rangle\langle\psi^+| + \gamma_4|\psi^-\rangle\langle\psi^-|, \tag{1}$$

with $\gamma_1 + \gamma_2 + \gamma_3 + \gamma_4 = 1$, where the Bell states are defined as

$$|\phi^\pm\rangle = \tfrac{1}{\sqrt{2}}(|00\rangle \pm |11\rangle), \qquad |\psi^\pm\rangle = \tfrac{1}{\sqrt{2}}(|01\rangle \pm |10\rangle). \tag{2}$$

If we perform the substitution of Equation (2) into Equation (1) we proceed as follows

$$\begin{aligned}
\rho_{AB} &= \gamma_1|\phi^+\rangle\langle\phi^+| + \gamma_2|\phi^-\rangle\langle\phi^-| + \gamma_3|\psi^+\rangle\langle\psi^+| + \gamma_4|\psi^-\rangle\langle\psi^-| \\
&= \tfrac{\gamma_1}{2}(|00\rangle\langle 00| + |11\rangle\langle 11| + |00\rangle\langle 11| + |11\rangle\langle 00|) + \tfrac{\gamma_2}{2}(|00\rangle\langle 00| + |11\rangle\langle 11| - |00\rangle\langle 11| - |11\rangle\langle 00|) \\
&= \tfrac{\gamma_3}{2}(|01\rangle\langle 01| + |10\rangle\langle 10| + |10\rangle\langle 01| + |01\rangle\langle 10|) + \tfrac{\gamma_4}{2}(|01\rangle\langle 01| + |10\rangle\langle 10| - |10\rangle\langle 01| - |01\rangle\langle 10|) \\
&= (\tfrac{\gamma_1}{2} + \tfrac{\gamma_2}{2})(|00\rangle\langle 00| + |11\rangle\langle 11|) + (\tfrac{\gamma_1}{2} - \tfrac{\gamma_2}{2})(|00\rangle\langle 00| + |11\rangle\langle 11|) + (\tfrac{\gamma_3}{2} + \tfrac{\gamma_4}{2})(|01\rangle\langle 01| + |10\rangle\langle 10|) \\
&= (\tfrac{\gamma_1}{2} - \tfrac{\gamma_2}{2})(|00\rangle\langle 00| + |11\rangle\langle 11| + |00\rangle\langle 11|) + 2\varepsilon\frac{(|00\rangle\langle 00| + |11\rangle\langle 11|)}{4} + 2\varepsilon\frac{(|01\rangle\langle 01||10\rangle\langle 10|)}{4} \\
&= (\tfrac{\gamma_1}{2} - \tfrac{\gamma_2}{2})|\psi^+\rangle\langle\psi^+| + 2\varepsilon\tfrac{\mathbb{I}}{4} \\
&= (1 - 2\varepsilon)|\psi^+\rangle\langle\psi^+| + 2\varepsilon\tfrac{\mathbb{I}}{4}.
\end{aligned} \tag{3}$$

In order to simplify the last step we make use of the additional constraint on the eigenvalues, i.e., $\gamma_3 = \varepsilon - \gamma_2$ which it has been shown to yield $\gamma_1 = 1 - 3/2\varepsilon$ and $\gamma_i = \varepsilon/2$ for $i = \{2, 3, 4\}$. This corresponds to a security threshold of 6.8% when evaluated for the above state. The states $|\phi^\pm\rangle$ give perfect correlations in the z-basis, $|\psi^\pm\rangle$ give perfect anticorrelations in the x-basis where the probabilities $\sum_i \gamma_i = 1$. As we highlighted that in the original security proof [8] for the BB84 protocol, in order to improve this security threshold, a conditioning on the random variable, i.e., $W = X \otimes Y$ was performed. The random variable contains all the information about the error positions. However, in our derivation we express Eve's information about the raw key $I_E(\underline{\varepsilon})$ as a function of the error positions which appears to be more elegant.

In this protocol, the third basis is conjugate to the others. Since γ_3 and γ_4 bring perfect anticorrelations which is equivalent to the quantum bit-error-rate (QBER) in the z-basis then

$$\varepsilon_z = \gamma_3 + \gamma_4.$$

The constraints on the eigenvalues yield the error rates in the other bases such that

$$\gamma_2 = \varepsilon_x - \gamma_4,$$

and

$$\gamma_3 = \varepsilon_y - \gamma_2.$$

Eve's information can be calculated by using the Holevo bound which states that

$$I_E = S(\rho_E) - \tfrac{1}{2}S(\rho_{E|0}) - \tfrac{1}{2}S(\rho_{E|1}). \tag{4}$$

The entropy of the state after the purification of Eve, ρ_{AB} becomes

$$S(\rho_E) = S(\rho_{AB}) = H(\{\gamma_1, \gamma_2, \gamma_3, \gamma_4\}) \equiv H(\underline{\gamma}), \tag{5}$$

where H is the Shannon entropy. A purification $|\psi\rangle_{ABE} = \sum_i \sqrt{\gamma_i}|\phi_i\rangle_{AB}|e_i\rangle_E$ was used to calculate $\rho_{E|b}$, by using a change of notation for the Bell states, and $\langle e_i|e_j\rangle = \delta_{ij}$ where e_i and e_j are two orthonormal basis, we trace out Bob and then project Alice on $|+z\rangle$ for $b = 0$ and on $|-z\rangle$ for $b = 1$. Since there is no preference in this attack, because both values are equiprobable then

$$S(\rho_{E|0}) = S(\rho_{E|1}) = h(\varepsilon_z). \tag{6}$$

By substituting the relationship in Equation (4) and using Equation (5) we get

$$I_E(\underline{\gamma}) = H(\underline{\gamma}) - h(\varepsilon_z). \tag{7}$$

Using the above constraints we arrive at

$$\varepsilon_x - \varepsilon_y = \gamma_4 - \gamma_3.$$

We add this constraint to ε_z in order to eliminate γ_3 we get

$$\varepsilon_x - \varepsilon_y + \varepsilon_z = 2\gamma_4.$$

After dividing each term by ε_z we get

$$\frac{1 + (\varepsilon_x - \varepsilon_y)/\varepsilon_z}{2} = \gamma_4/\varepsilon_z.$$

Starting from the sum of probabilities ($\sum_i \gamma_i = 1$), we can express γ_1 in terms of the other constraints,

$$\begin{aligned} \gamma_1 &= 1 - (\gamma_2 + \gamma_3 + \gamma_4) \\ &= 1 - (\varepsilon_x + \varepsilon_y + \varepsilon_z)/2. \end{aligned} \tag{8}$$

However, in this proof, the error positions are still employed. Instead of conditioning on the random variable in order to increase the security threshold, the Eve's information about the raw key, $I_E(\underline{\varepsilon})$ is used in this derivation. If no error occurred, we obtain $h\left(\frac{\gamma_1}{1-\varepsilon_z}\right)$ and if an error occurred we obtain $h\left(\frac{\gamma_4}{\varepsilon_z}\right)$. By averaging over the four subsystems we obtain

$$I_E(\underline{\varepsilon}) = \varepsilon_z h\left(\frac{1 + (\varepsilon_x - \varepsilon_y)/\varepsilon_z}{2}\right) + (1 - \varepsilon_z)h\left(\frac{1 - (\varepsilon_x + \varepsilon_y + \varepsilon_z)/2}{1 - \varepsilon_z}\right). \tag{9}$$

Using the assumption for the depolarizing channel, where we use, $\varepsilon_x = \varepsilon_y = \varepsilon_z = \varepsilon$, then $I_E(\underline{\varepsilon})$

$$I_E(\underline{\varepsilon}) = \varepsilon + (1 - \varepsilon)h\left(\frac{1 - 3\varepsilon/2}{1 - \varepsilon}\right).$$

Using $r = 1 - h(\varepsilon) - I_E(\underline{\varepsilon})$ to find the secret fraction (one-way postprocessing, no preprocessing and perfect error correction) and then equating it to zero so that we can obtain the value for ε we arrive at

$$\varepsilon + h(\varepsilon) + (1 - \varepsilon)h\left(\frac{1 - 3\varepsilon/2}{1 - \varepsilon}\right) = 1. \tag{10}$$

Solving this equation gives us the lower bound on the bit error rate for the six state scheme using one-way classical post-processing. Thus, the bound on the bit error rate becomes $\varepsilon \approx 0.1261$.

3. Conclusion

We have derived the upper bounds to the accessible information for the six-state protocol without using the technique of conditioning on the random variable and we arrived at the same QBER. This value shows the limit to which the channel should be considered to be secure for the safe generation of a secret key. Above this value, the channel is insecure and the parties abort the protocol.

Acknowledgments

This work is based on research supported by the South African Research Chair Initiative of the Department of Science and Technology and National Research Foundation.

References

[1] Gisin N, Ribordy G, Tittel W and Zbinden H 2002 *Reviews of Modern Physics* **74** 145–195
[2] Renner R, Gisin N and Kraus B 2005 *Physical Review A* **72** 12332
[3] Shadman Z, Kampermann H, Meyer T and Bruss D 2008 *Arxiv preprint arXiv:0804.0587*
[4] Bruß D and Macchiavello C 2002 *Phys. Rev. Lett.* **88**(12) 127901 URL `http://link.aps.org/doi/10.1103/PhysRevLett.88.127901`
[5] Lo H 2001 *Arxiv preprint quant-ph/0102138*
[6] Kraus B, Gisin N and Renner R 2005 *Phys. Rev. Lett.* **95** 080501
[7] Gottesman D and Lo H 2003 *Information Theory, IEEE Transactions on* **49** 457–475 ISSN 0018-9448
[8] Christandl M, Renner R and Ekert A 2004 *Arxiv preprint quant-ph/0402131*
[9] Bruß D 1998 *Phys. Rev. Lett.* **81** 3018–3021
[10] Bennett C, Brassard G *et al.* 1984 *Proceedings of IEEE International Conference on Computers, Systems and Signal Processing* vol 175 (Bangalore, India)

Models of decoherence-assisted transport in quantum networks

Adriana Marais, Ilya Sinayskiy and Francesco Petruccione.

Quantum Research Group and National Institute for Theoretical Physics, School of Chemistry and Physics, University of KwaZulu-Natal, Durban, 4001, South Africa

E-mail: adrianamarais@gmail.com, sinayskiy@ukzn.ac.za, petruccione@ukzn.ac.za

Abstract. The dynamics of a quantum network under the influence of decoherence were studied. This work is a generalisation of previous research on decoherence-assisted transport in a dimer system [I. Sinayskiy, A. Marais, F. Petruccione and A. Ekert, Phys. Rev. Lett. 108, 020602 (2012)]. The model under investigation consists of a homogenous fully connected quantum network in contact with an environment of spins. Exact analytical expressions for the transition probabilities are obtained. It is shown that there exist well-defined ranges of parameters for which decoherent interaction with the environment assists energy transfer in the quantum network. This model of decoherence-assisted energy transfer is applied to energy transfer in the Fenna-Matthews-Olson complex.

1. Introduction

Recently, evidence of quantum coherence has been detected in biological systems at physiological temperature, including the photosynthetic light-harvesting complexes of a species of green sulphur bacteria [1] and two species of marine cryptophyte algae [2]; organisms well-adapted to photosynthesise under low-light conditions. Light-harvesting complexes act as antennas, absorbing photons and transferring the resulting excitation energy through a network of photoactive pigments held in well-defined orientations and configurations by a scaffold of proteins, to the reaction centre, where the secondary photosynthetic process of charge separation takes place. The electronic excitation energy transfer (EET) happens on a scale of picoseconds and with a quantum efficiency of over 95% [3]. The surprising phenomenon of quantum coherence in warm, noisy, complex and yet remarkably efficient energy transfer systems has led to discussion about the role of the protein environment in the energy transfer process and the degree to which it may contribute to this efficiency [4].

Modelling the complexity of the environment is a challenge. The protein-solvent environment interacts strongly with the pigments due to its polarity and as a result can have a significant effect on the quantum dynamics, which will therefore in general be non-Markovian [5]. Such non-Markovian effects have widely been taken into account [5, 6], but so far, all have been within spin-boson models of excitons within a protein medium. While any biological system is always in contact with a bosonic environment, interaction with a more structured environment such as a spin bath is more likely to assist quantum efficiency and also induces intrinsically non-Markovian dynamics [7].

With the aim of exact solvability, we investigate the relationship between environmental spin degrees of freedom and the efficiency of the EET process described by the Hamiltonian H_{ex}

$$H_{ex} = \sum_j E_j |j\rangle\langle j| + \sum_{i \neq j} V_{ij} |i\rangle\langle j|, \tag{1}$$

where the site energies of the pigments are given by E_j, and the EET couplings by V_{ij}. We review the case of the dimer system; generalise this model to a fully connected network; and finally apply this model to the Fenna-Matthews-Olson (FMO) antenna complex [10].

2. Dimer

For a dimer with Hamiltonian $H_d = \varepsilon_1|1\rangle\langle 1| + \varepsilon_2|2\rangle\langle 2| + J(|1\rangle\langle 2| + |2\rangle\langle 1|)$, the maximum transfer probability for a single excitation $\mathrm{Max}[P_{1\to 2}(t)]$ is given by $J^2/(J^2 + \Delta^2)$ where J is the amplitude of transition, and the detuning Δ is given in terms of the energy levels of the dimer as $(\varepsilon_2 - \varepsilon_1)/2$. Certain transfer is achieved when $\Delta = 0$ at time $t = \pi/(2J)$, or when there is resonance between the energy levels in the system.

In a recent article [8], it is shown that there exist well-defined ranges of parameters for which a purely decoherent interaction with environmental spins in a spin star configuration [7] assists energy transfer in the dimer system. For a dimer with each level coupled to a spin bath at zero temperature, the Hamiltonian of the total system is given by

$$H = H_d + H_B + H_I. \tag{2}$$

Each environment B_j consists of n_j spin-half particles

$$H_B = \sum_{j=1}^{2} H_{B_j} = \sum_{j=1}^{2} \sum_{k=1}^{n_j} \alpha_j \frac{\sigma_z^{k,j}}{2}, \tag{3}$$

where $\sigma_z^{k,j}$ are Pauli matrices. The purely decoherent interaction between each site j in the system and the corresponding spin bath is modelled by

$$H_I = \sum_{j=1}^{2} H_{I_j} = \sum_{j=1}^{2} \sum_{k=1}^{n_j} \gamma_j |j\rangle\langle j| \frac{\sigma_z^{k,j}}{2}. \tag{4}$$

The Hamiltonian of the environment H_B commutes with the Hamiltonian of interaction H_I and therefore the state of the total system is always in a product state of the network and the baths. As a result, the effective Hamiltonian for the total system with spin baths at zero temperature is given by

$$H = \sum_{j=1}^{2} \varepsilon'_j |j\rangle\langle j| + \sum_{\substack{i,j=1 \\ i \neq j}}^{2} J|i\rangle\langle j|, \tag{5}$$

where $\varepsilon'_j = \varepsilon_j - \gamma_j n_j/2$.

For the Hamiltonian H, the maximum transfer probability $\mathrm{Max}[P_{1\to 2}(t)]$ is given by $J^2/(J^2 + \Delta'^2)$ where in this case the detuning is given by $\Delta' = (\varepsilon'_2 - \varepsilon'_1)/2$, and ε'_j are the shifted energy levels of the dimer as a result of coupling with strength γ_j with each of the spin baths wit

number of spins n_j. Certain transfer is similarly achieved when $\Delta' = 0$, which in this case is possible for a wide range of the parameters γ_j and n_j.

This effect persists at physiological temperature, where transfer probabilities of nearly 90% can be achieved in the dimer at 300 K for biologically relevant parameters [8].

3. Fully-connected quantum network

For a fully connected network of N qubits interacting via homogeneous Heisenberg XX coupling with coupling strength $2J$ and with equal site energies ε, the effective Hamiltonian in the single excitation subspace is given by

$$H_N = \sum_{i=1}^{N} \varepsilon |i\rangle\langle i| + \sum_{\substack{i,j=1 \\ i\neq j}}^{N} J|i\rangle\langle j|. \tag{6}$$

By coupling $N-k$ of the sites in the fully connected network to independent spin environments in symmetric star configurations, the Hamiltonian of the total system is given by

$$H_k = H_N + H_B + H_I, \tag{7}$$

with H_B and H_I defined as previously, but with $j = 1, ..., N-k$. We can then write the effective Hamiltonian for the total system, with the baths arbitrarily coupled to the last $N-k$ sites, as

$$H_k = \sum_{j=1}^{k} \varepsilon |j\rangle\langle j| + \sum_{j=k+1}^{N} \varepsilon_j |j\rangle\langle j| + \sum_{\substack{i,j=1 \\ i\neq j}}^{N} J|i\rangle\langle j|, \tag{8}$$

where $\varepsilon_j = \varepsilon - \gamma_j n_j/2$.

In the case where $k = N$ and all levels have equal energy ε, the Hamiltonian H_N is given by Eq. (1). In this case the maximum probability of purely coherent transfer through the network is

$$\mathrm{Max}[P_{I\to F}(t)] = \frac{4}{N^2}, \tag{9}$$

at time $t = \pi/(NJ)$. Our study will focus on whether decoherent interaction between a fully-connected network and environmental spins can enhance energy transport through the network.

We analyse a range of cases where spin baths are added to the initial, final and intermediate network sites, and find that decoherent interaction with the spin baths in general increases transfer probability through the network, and furthermore that these effects persist at physiological temperature [9].

As an example, we consider here the case of coupling both the initial and final sites to spin baths, with Hamiltonian H_{N-2} given by Eq. (8) with $k = N-2$. In this case, it can be shown that when the shifted energy levels are equal, $\varepsilon_1 = \varepsilon_2$, there exist times for which the transfer probability is arbitrarily close to 1.

We now show that such an effect persists at physiological temperatures by considering the Hamiltonian H_{N-2} with spin baths at a temperature of 300 K coupled to the initial and final sites.

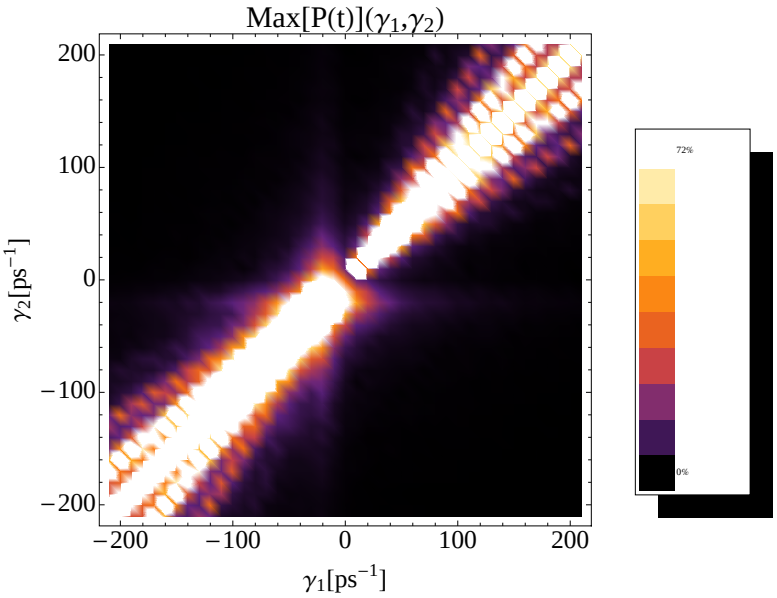

Figure 1. Graph of the maximum of the probability of transition $\mathrm{Max}[P_{I\to F}(t)]$ at 300 K in a 10-site fully connected homogeneous network, with isolated site energies $\varepsilon = 100\mathrm{ps}^{-1}$, and spin baths coupled to each of the initial and final sites, with $n_1 = n_2 = 10$ and bath energy parameter $\alpha_1 = \alpha_2 = 100\ \mathrm{ps}^{-1}$.

In this case the initial state of the bath is given by the canonical distribution

$$\rho_B(0) = \prod_{i=1}^{2} \frac{1}{Z_i} \mathrm{e}^{-\beta\alpha_i S_i^z}, \tag{10}$$

where Z_i is the partition function of the corresponding spin bath, β is the inverse temperature and S_i^z are collective spin bath operators, see [8] for details.

In Fig. 1 the maximum of the probability of transition $\mathrm{Max}[P_{I\to F}(t)]$ for such a system is plotted as a function of the coupling constants γ_1 and γ_2 with spin baths coupled to each of the initial and final sites. It can be seen that in regions where $\varepsilon_1 \approx \varepsilon_2 \neq \varepsilon$, transfer probabilities of up to 72% are achieved.

4. FMO complex

The first evidence of quantum coherence in photosynthetic antennas at physiological temperature was detected in green sulphur bacteria and cryptophyte algae [1, 2], both organisms able to photosynthesise efficiently at low light intensities. Green sulphur bacteria uniquely contain a complex called the Fenna-Matthews-Olson (FMO) complex [10], which mediates excitation energy transfer from the antenna to the reaction centre [11]. The site energies and optical transition energies for the FMO complex of *Chlorobium tepidum* used here were calculated by Adolphs and Renger [12]. Quantum coherent EET through the bare excitonic system without adding environmental contributions to the Hamiltonian H_{ex}^{FMO} happens with a low probability: for the transfer of the excitation from site 1 to site 3, the probability of transfer is just 4.2%.

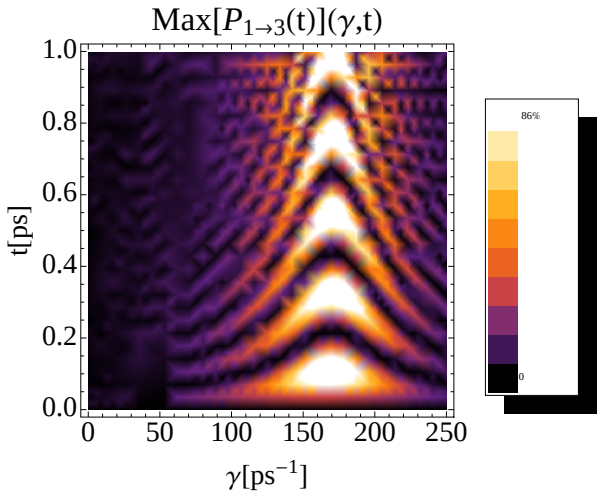

Figure 2. The probability of transfer $P_{1\to3}(\gamma, t)$ for the FMO complex with sites coupled to spin baths at 300 K with numbers of spins at each site $n_1 = 2, n_4 = 8$ and $n_{2,3,5,6,7} = 0$ and spin bath energy constant α=150 ps^{-1}. The maximum transfer probability is 86%.

We now investigate the effect of decoherent interaction with environmental spins at 300 K on the process of EET in the FMO complex.

With the spin baths at a temperature of 300 K, we calculate the maximum probability of transfer during the first picosecond, for equal environmental couplings γ between 0 and 250 ps^{-1} at each site. We find that for a total of 10 spins, distributed between the seven network sites as follows: $n_1 = 2, n_4 = 8$ and $n_{2,3,5,6,7} = 0$, and with spin bath energy constant α=150 ps^{-1}, the maximum transfer probability is 86% (see Fig. 2). This is a vast increase in the transfer probability from the case with no spin baths, where the probability is 4.2%. Therefore, in this case decoherence assists the efficiency of quantum coherent EET in the FMO complex.

5. Conclusion

The recent detection of quantum coherence in biological systems that are remarkably efficient in transferring excitation energy at physiological temperatures, has led to the investigation as to whether this coherence contributes to the efficiency. Here, we have investigated the influence of environmental spins on quantum coherent transfer. We have shown through the derivation of analytical expressions that the transfer probabilities through a fully connected quantum network are improved as a result of decoherent interaction with environmental spins, and that in some cases certain transfer can be achieved. Moreover, this effect is shown to persist at physiological temperatures. We apply this model to the FMO complex, and find that coupling the network sites with environmental spins at physiological temperature improves transport through the network for the considered case. These promising results motivate further study of biological transport systems where environmental spins may play an important role in the dynamics.

Acknowledgments

The authors would like to thank Artur Ekert and Alastair Kay for valuable and interesting discussions. This work is based upon research supported by the South African Research Chair Initiative of the Department of Science and Technology and National Research Foundation.

References

[1] G. Panitchayangkoon, D. Hayes, K. A. Fransted, J. R. Caram, E. Harel, J. Wen, R. E. Blankenship and G. S. Engel., Proc. Natl. Acad. Sci. U. S. A. 107, 12766 (2010).
[2] E. Collini, C.Y. Wong, K.E. Wilk, P.M G. Curmi, P. Brumer and G.D. Scholes, Nature 463, 08811 (2010).
[3] B. R. Green and W. W. Parson (Eds.), Light-harvesting Antennas in Photosynthesis (Kluwer Academic Press, Dordrecht, 2003).
[4] M. Mohseni et al., J. Chem. Phys. 129, 174106 (2008); M.B. Plenio and S.F. Huelga, New J. Phys. 10, 113019 (2008); K. Furuya, and G.J. Milburn, New J. Phys. 12, 083033 (2010); S. Lloyd and M. Mohseni, New J. Phys. 12, 075020 (2010); M. Sarovar et al., Nature Physics 6, 462 (2010); F. Caruso et al., Phys. Rev. A81, 062346 (2010); I. Kassal and A. Aspuru-Guzik, arXiv:1201.5202 (2012).
[5] A. Ishizaki and G. R. Fleming, J. Chem. Phys. 130, 234110 (2009); 130, 234111 (2009).
[6] V. I. Novoderezhkin and R. van Grondelle, Phys. Chem. Chem. Phys. 12, 7352 (2010).
[7] H.-P. Breuer, D. Burgarth, and F. Petruccione, Phys. Rev. B 70, 045323 (2004).
[8] I. Sinayskiy, A. Marais, F. Petruccione and A. Ekert, Phys. Rev. Lett. 108, 020602 (2012).
[9] A. Marais, I. Sinayskiy, F. Petruccione and A. Ekert (in preparation).
[10] R. E. Fenna and B. W. Matthews, Nature 258, 573 (1975).
[11] R. Blankenship, J. Olson and M. Miller, A.I.P.H. 2, 399 (2004).
[12] J. Adolphs and T. Renger, Biophys. J. 91, 2778 (2006).

Unsharp measurement in Quantum Mechanics and its application to monitor Rabi Oscillations

Sujit K. Choudhary[1] , **Hermann Uys**[2] & **Thomas Konrad**[1]
[1]School of Physics, University of KwaZulu-Natal, Durban 4000, South Africa.
[2] National Laser Centre, CSIR, Pretoria, South Africa.

E-mail: choudhary@ukzn.ac.za

Abstract. In recent years a generalized notion of quantum mechanical observables has been developed in terms of positive operator valued measure (POVM). The POVM formalism of observables captures features of quantum mechanics in a more comprehensive way than the standard formalism. Certain POVMs can be interpreted as unsharp quantum measurements. This article reviews the notion of unsharp measurement, its utility and experimental realization.

1. Introduction

Usual quantum measurements are projective measurements which project the initial state of a system onto one of the eigenstates of the observables being measured. For example in a measurement for spin along direction $\hat{r}$, the projectors onto the eigenstates are:

$$\hat{P}_{\pm} = \frac{1}{2}[\mathbb{I} \pm \hat{r}.\vec{\sigma}], \tag{1}$$

$\mathbb{I}$ denotes the identity operator and $\vec{\sigma} = (\hat{\sigma_x}, \hat{\sigma_y}, \hat{\sigma_z})$ is the usual Pauli-operator.

However, further progress had shown that the most general quantum measurements are given by positive operator valued measures (POVM) [1]. These generalized measurements allow us to describe any measurement that can be performed within the limits of quantum theory.

The POVM formalism of observables captures features of quantum mechanics in a more comprehensive way than the standard formalism. It is worth mentioning here that Bell could construct a Hidden Variable Theory for two dimensional quantum system by using standard observables but it has been shown recently that if one uses the formalism of generalized observables (i.e., the POVM formalism), then even for two dimensional quantum system, Gleasons theorem as well as the Kochen-Specker theorem hold [2, 3]. This formalism creates the possibility of certain joint measurements of complementary observables like position and momentum; spin along two different directions, etc., it has also been used to show that the CHSH expression should be bounded by $2\sqrt{2}$ for quantum systems to avoid superluminal signalling in quantum mechanics [4]. On the other hand, it is turning out to be very useful in controlling quantum systems [5, 6].

2. Generalized measurement in quantum mechanics

In this more general framework of quantum theory, the states of a quantum system are represented by positive trace class operators. Any observable is represented by a collection

of positive operators $\{E_i\}$ where $0 \leq E_i \leq \mathbb{I}$ for all i and $\sum E_i = \mathbb{I}$, $\mathbb{I}$ being the unit operator on the Hilbert space associated with the system. In a measurement of this observable for the state ρ (say), the probability of occurrence of the ith result is given by $Tr[\rho E_i]$. Unlike the case for projective measurement, knowing the operators $\{E_i\}$ is, in general, not enough to determine the state of the system after measurement; we further need to know the operators $\hat{M}_{ij}$'s constituting the POVM elements $\{E_i\}$. As an example, let $E_i = \sum_j M_{ij}^\dagger M_{ij}$, then after obtaining the outcome i, the state is $\rho \mapsto \rho' = \frac{1}{Tr[\rho E_i]} \sum_j M_{ij} \rho M_{ij}^\dagger$. This measurement does not preserve the purity of states in general, unless there is a single M_{ij} for each E_i and in that case the post measured state is given by $|\psi'\rangle = \frac{M_i|\psi\rangle}{\sqrt{\langle\psi|M_i^\dagger M_i|\psi\rangle}}$.

Let us consider the following operators:

$$\begin{aligned} \hat{M}_0 &= \sqrt{p_0}\,\hat{P}_+ + \sqrt{1-p_0}\,\hat{P}_- \\ \hat{M}_1 &= \sqrt{1-p_0}\,\hat{P}_+ + \sqrt{p_0}\,\hat{P}_- \end{aligned} \tag{2}$$

related via

$$M_0^\dagger M_0 + M_1^\dagger M_1 = \mathbb{I}, \tag{3}$$

and $0 \leq p_0 \leq 0.5$. The positive operators $M_i^\dagger M_i$, $(i \in 0, 1)$ constitute POVM elements and are interpreted as unsharp dichotomic observables (for example, spin observable of a spin-1/2 particle, energy of a two-level system etc.) [7, 8, 9], the measurement strength is parametrized by the quantity $\Delta p = (1 - p_0) - p_0 = 1 - 2p_0$. For $\Delta p = 1$, it represents the usual projective (sharp) measurement. The M_0 and M_1 (given in (2)) are diagonal in the basis corresponding to the projectors (1). This assures that the post-measurement state is again a superposition of these basis elements if we start with such a superposition and thus the post measurement state is not qualitatively different from the pre-measurement state. Moreover, these Kraus operators are minimal, in the sense that they cannot be further decomposed as a product of a unitary operator (other than the identity) and another operator. This minimality assures no unnecessary disturbance of the state due to the measurement as an unitary evolution does not add to our knowledge about the system.

3. Realization and application of unsharp measurement in monitoring Rabi Oscillations

Any POVM can be realized, in principle, by allowing the measured system to interact with an ancilla, and then doing a projective measurement on the ancilla. As will be shown elsewhere two ions of different species interacting with laser light and moving inside a linear trap provide a realistic system to implement the generalized measurement given by (2) on a qubit.

In order to monitor the dynamics of a qubit undergoing Rabi oscillations, we generally need an ensemble prepared in the initial state of the qubit. The oscillating Rabi-probabilities at a particular time t are then determined by performing projective measurements (at that time) of a dichotomic observable, having the two states of the qubit as its eigenstates, on each member of the ensemble. In order to know these probabilities at a different time, the procedure is repeated from the beginning. If, instead, we are supplied with only a single qubit, the above procedure of visualization fails. In such a situation, evolution of the system is tracked by performing a sequence of above said measurement (2) on the qubit with period τ [5]. It is assumed that the time it takes to execute each measurement is negligible compared to all other timescales of the system. In between measurements the system evolves through the Hamiltonian $H_R = \hbar\frac{\Omega_R}{2}\sigma_x$ (written in a frame rotating at the transition frequency (Ω_R) between its two internal states). At

$t = N\tau$, i.e., after N measurements the system is, up to the appropriate normalization constant, in the state

$$|\psi(N\tau)\rangle = M_{n_N} U M_{n_{N-1}} ... M_{n_1} U |\psi\rangle, \tag{4}$$

where $U = \exp\{-\frac{i}{\hbar} H_R \tau\}$. The overall strength of a sequence of measurements depends on the strength of a single measurement ($\Delta p = 2p_0 - 1$), together with its frequency. The influence of a sequential unsharp measurement on the state of the qubit is parametrized by a quantity $\gamma = \frac{(\Delta p)^2}{\tau}$ which can be identified by the inverse of the decoherence time of the system [10] when averaging over the measurement results. By decoherence time we mean the time after which the coherences of the system state falls to $1/e$ of its initial value on average.

The sequential measurement has a stronger influence on the state for a larger γ. The Hamiltonian dynamics of the system is characterized by the Rabi-frequency. For γ much larger than the Rabi-frequency, the disturbance by the measurement causes quantum jumps (a zeno type effect). Thus, in order not to disturb the original dynamics too much, we need to keep the measurement strength (γ) well below the Rabi-frequency.

In order to estimate the state of the system the same sequence of operators corresponding to the measured outcomes in Eq. (4) are applied to an initial guess $|\psi'\rangle$ which can be taken as an arbitrary state vector on the Bloch sphere and in between measurements the estimated state is assumed to evolve through the Hamiltonian H_R [11]. Interestingly, the estimate closely approximates the true state within a few Rabi cycles [5]. The idea of estimating the state by updating the initial guess with the outcomes obtained by doing continuous measurement on the actual system was first introduced by Diosi et al [11]. It was also shown there that ultimately the estimate converges to the actual state.

We gave a scheme to monitor the dynamics of a qubit without taking into account the noises present. Interestingly, the above estimation strategy still works with a reasonably high fidelity even in presence of noise. To estimate the state, the abovesaid sequence of unsharp measurement is again performed on the system and the same sequence of operators corresponding to the measured outcomes in Eq. (4) are applied to an arbitrary initial guess, but in between measurements the estimated state is assumed to evolve only through the Hamiltonian H_R since the experimenter does not know what the instantaneous values of the noise fields are. Interestingly enough, the estimate quickly approaches the real state with a reasonably high fidelity (fig 1)(though this time the fidelity is not unity) [5].

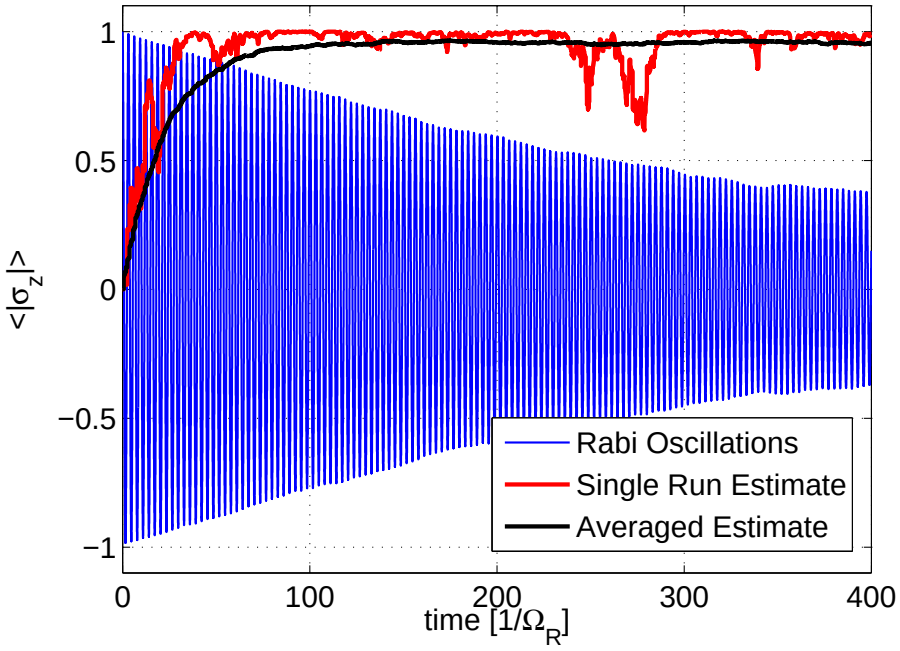

Figure 1. Wavefunction estimation in the presence of dephasing noise. The red line shows the estimation fidelty for a single run, while the black line gives the expected fidelity obtained by averaging over 1000 runs. The blue line demonstrates that the Rabi oscillations monotonically lose coherence in the absence of unsharp measurements [5] .

4. Conclusion

In conclusion, we have reviewed here the formulation of unsharp measurement in quantum mechanics and its utility in monitoring the dynamics of a single qubit undergoing Rabi oscillations.

[1] Peres A, *Quantum Theory: Concepts and Methods* (Kluwer, Dordrecht, 1993)
[2] Busch P 2003 *Phys. Rev. Lett.* **91** (120403)
[3] Cabello A 2003 *Phys. Rev. Lett.* **90** (190401)
[4] Choudhary S K , Kar G P, Kunkri S, Rahaman R 2007 *Phys.Lett. A* **371** (395)
[5] Uys H, Konrad T (*e-print* quantph/1111.4801)
[6] Ashhab S, Nori F 2010 *Phys. Rev. A* **82** (062103)
[7] Martens H, Muynck W M de 1990 *Found. Phys.* **8** 255
[8] Busch P 1986 *Phys. Rev. D* **33** 2253.
[9] Busch P 1987 *Found. Phys.* **12** (9)
[10] Audretsch J, Diosi L, Konrad T 2002 *Phys. Rev. A* **66** (022310)
[11] Diosi L, Konrad T, Scherer A, Audretsch J 2006 *J. Phys. A: Math Gen* **39** (L575)

Dissipative Dynamics of a Spinless Electron Strongly Interacting with an Environment of Spinless Electrons

Michael Mwalaba, Ilya Sinayskiy and Francesco Petruccione
National Institute for Theoretical Physics and Quantum Research Group, School of Chemistry and Physics, University of KwaZulu-Natal, Durban, South Africa

E-mail: sinaykiy@ukzn.ac.za

Abstract. We consider the dissipative dynamics of a spinless electron (fermion) strongly interacting with a finite bath of fermions. The fermionic environment is embedded in a bosonic Markovian bath. The master equation for the fermion interacting with the fermionic bath is derived. Based on the master equation for this system, the reduced dynamics and thermalization of the spinless electron is studied.

Understanding thermalization in complex quantum systems plays an important role in modern quantum statistical physics. The description of the mesoscopic system is important from both the experimental and the theoretical points of view. Recently, there has been a lot of interest in modeling steady state transport through quantum dots [1, 2, 3]. Typically, electrons in the quantum dot strongly interact with electrons in the surroundings (finite number degrees of freedom). In order to describe the interaction of the electron with the environment of electrons without restrictions on the strength of the electron-electron interactions we embed the whole system into a bosonic Markovian bath which will thermalize the subsystem of the electron interacting with the bath of electrons. In the present work we will not consider the spin-spin interaction between electrons, so that we will describe all electrons in this model as spinless fermions.

The studied system consists of a fermion interacting with a mesoscopic fermionic bath which is embedded into a Markovian bosonic bath. The total Hamiltonian of the system reads,

$$H = H_S + H_B + H_{SB}, \tag{1}$$

where H_S is the Hamiltonian of a fermion interacting with fermionic bath, i.e.,

$$H_S = \omega d^\dagger d + \sum_{i=1}^{N} \left(\epsilon c_i^\dagger c_i + g d c_i^\dagger + g d^\dagger c_i \right), \tag{2}$$

where $d^\dagger, d$ are creation and annihilation operators of the fermion of interest and $c_i^\dagger, c_i$ are creation and annihilation operators of fermions in the mesoscopic bath. All the operators $d^\dagger, c_i^\dagger$ satisfy standard anticommutation relations. The Hamiltonian of the bath H_B reads,

$$H_B = \sum_n \omega_n b_n^\dagger b_n, \tag{3}$$

where $b_n^\dagger, b_n$ are standard bosonic creation and annihilation operators. The Hamiltonian of interaction of the fermonic bath with the bosonic Markovian environment is denoted by H_{SB} and given by,

$$H_{SB} = \sum_{i=1}^{N} \sum_{n} g_n b_n c_i^\dagger + g_n^* b_n^\dagger c_i. \tag{4}$$

In order to derive the quantum master equation for the system it is convenient to diagonalize the Hamiltonian of the system H_S, as

$$H_S = \sum_{i=0}^{N} \lambda_i \xi_i^\dagger \xi_i, \tag{5}$$

where $\xi_i^\dagger, \xi_i$ are creation and annihilation operators of a new set of quasi-fermions satisfying standard anti-commutation relationships, i.e., $\{\xi_i, \xi_j^\dagger\}_+ = \delta_{i,j}$. The explicit expressions for $\xi_i^\dagger$ and λ_i read,

$$\xi_0^\dagger = \cos\theta d^\dagger + \frac{\sin\theta}{\sqrt{N}} \sum_{i=1}^{N} c_i^\dagger, \quad \lambda_0 = \frac{\omega+\epsilon}{2} + \frac{\Omega_N}{2}, \tag{6}$$

$$\xi_1^\dagger = -\sin\theta d^\dagger + \frac{\cos\theta}{\sqrt{N}} \sum_{i=1}^{N} c_i^\dagger, \quad \lambda_1 = \frac{\omega+\epsilon}{2} - \frac{\Omega_N}{2}, \tag{7}$$

and for $i = 2 \ldots N$

$$\xi_i^\dagger = \frac{1}{\sqrt{i(i-1)}} \sum_{k=1}^{i-1} c_k^\dagger - \sqrt{\frac{i-1}{i}} c_i^\dagger, \quad \lambda_i = \epsilon, \tag{8}$$

where the coefficients $\Omega_N, \cos\theta, \sin\theta$ read,

$$\Omega_N = \sqrt{4g^2 N + (\epsilon-\omega)^2}, \quad \cos\theta = \frac{2g\sqrt{N}}{\sqrt{\Omega_N\left(\Omega_N + (\epsilon-\omega)\right)}}, \quad \sin\theta = \sqrt{\frac{\Omega_N + (\epsilon-\omega)}{2\Omega_N}}. \tag{9}$$

Using the explicit expression for the diagonalized Hamiltonian of the system, the quantum Markov equation can be obtained from the general expression [4],

$$\frac{d}{dt}\rho_S(t) = -\int_0^\infty d\tau \mathrm{Tr}_B[H_{SB}^{(I)}(t), [H_{SB}^{(I)}(t-\tau), \rho_S(t) \otimes \rho_B(0)]]. \tag{10}$$

By the direct substitution of the interaction Hamiltonian into Eq. (10) and assuming that $|\lambda_0 - \lambda_1| \gg 1$ (this holds for $N \gg 1$), we obtain the following quantum master equation,

$$\frac{d}{dt}\rho_S = \sum_{i=0}^{1} \gamma_i^+ \left(\xi_i \rho_S \xi_i^\dagger - \frac{1}{2}\{\xi_i^\dagger \xi_i, \rho_S\}_+\right) + \gamma_i^- \left(\xi_i^\dagger \rho_S \xi_i - \frac{1}{2}\{\xi_i \xi_i^\dagger, \rho_S\}_+\right), \tag{11}$$

where the damping rates $\gamma_i^\pm$ are given by,

$$\gamma_0^\pm = \pi N \sin^2\theta J(\lambda_0)\left(\coth\frac{\beta\lambda_0}{2} \pm 1\right), \tag{12}$$

$$\gamma_1^\pm = \pi N \cos^2\theta J(\lambda_1)\left(\coth\frac{\beta\lambda_1}{2} \pm 1\right), \tag{13}$$

where $J(\omega)$ is the spectral density and β is the inverse temperature of the bosonic Markovian bath.

The obtained quantum master equation can be solved exactly and its solution can be presented with help of the Kraus representation,

$$\rho_S(t) = \sum_{i=0}^{1}\sum_{k=1}^{4} E_k^i(t)\rho_S(0)E_k^{i\dagger}(t), \tag{14}$$

where the Kraus operators are given by

$$E_0^i(t) = \frac{\cos\alpha_i}{\sqrt{2}}\left(\xi_i^\dagger\xi_i + f_i(t)\xi_i\xi_i^\dagger\right), \tag{15}$$

$$E_1^i(t) = \frac{\cos\alpha_i}{\sqrt{2}}g_i(t)\xi_i^\dagger, \tag{16}$$

$$E_2^i(t) = \frac{\sin\alpha_i}{\sqrt{2}}\left(\xi_i\xi_i^\dagger + f_i^*(t)\xi_i^\dagger\xi_i\right), \tag{17}$$

$$E_3^i(t) = \frac{\sin\alpha_i}{\sqrt{2}}g_i(t)\xi_i, \tag{18}$$

and

$$\cos\alpha_i = \sqrt{\frac{\gamma_i^-}{\gamma_i^+ + \gamma_i^-}}, \quad \sin\alpha_i = \sqrt{\frac{\gamma_i^+}{\gamma_i^+ + \gamma_i^-}}, \tag{19}$$

$$f_i(t) = \exp\left(-\frac{\gamma_i^+ + \gamma_i^-}{2}t - i\lambda_i t\right), \quad g_i(t) = \sqrt{1-|f_i(t)|^2}. \tag{20}$$

In the present work we will consider that initially there is a fermion of interest and no fermions in the mesoscopic bath, i.e.,

$$\rho_S(0) = d^\dagger|0\rangle\langle 0|d = \cos^2\theta\xi_0^\dagger|0\rangle\langle 0|\xi_0 + \sin^2\theta\xi_1^\dagger|0\rangle\langle 0|\xi_1 - \sin\theta\cos\theta\left(\xi_1^\dagger|0\rangle\langle 0|\xi_0 + \xi_0^\dagger|0\rangle\langle 0|\xi_1\right). \tag{21}$$

Using the explicit form of the Kraus operators and the initial conditions for the system, the density matrix can be obtained in the quasi-fermionic picture. After transformation to the original fermionic picture and tracing out the mesoscopic bath we obtain the explicit expression for the reduced dynamics of the electron of interest,

$$\rho_e(t) = \kappa(t)d^\dagger|0\rangle\langle 0|d + (1-\kappa(t))|0\rangle\langle 0|, \tag{22}$$

where

$$\kappa(t) = \cos^2\theta c_{00}(t) + \sin^2\theta c_{11}(t) + \sin^2\theta\cos^2\theta\mathrm{Re}\left(f_0(t) + f_1(t)\right) + w(t), \tag{23}$$

$$c_{00}(t) = \frac{\cos^2\theta}{2}\left(\cos^2\alpha_0 + \cos^2\alpha_1|f_1(t)|^2 + \sin^2\alpha_0|f_0(t)|^2 + \sin^2\alpha_1\right), \tag{24}$$

$$c_{11}(t) = \frac{\cos^2\theta}{2}\left(\cos^2\alpha_1 + \cos^2\alpha_0|f_0(t)|^2 + \sin^2\alpha_1|f_1(t)|^2 + \sin^2\alpha_0\right), \tag{25}$$

$$w(t) = \frac{1}{2}\left(\cos^2\alpha_0\sin^2\theta g_0^2(t) + \cos^2\alpha_1\cos^2\theta g_1^2(t)\right). \tag{26}$$

Based on the exact expression for the reduced density matrix we calculate the mean number of fermions, and it is clear that $\langle d^\dagger d\rangle = \kappa(t)$.

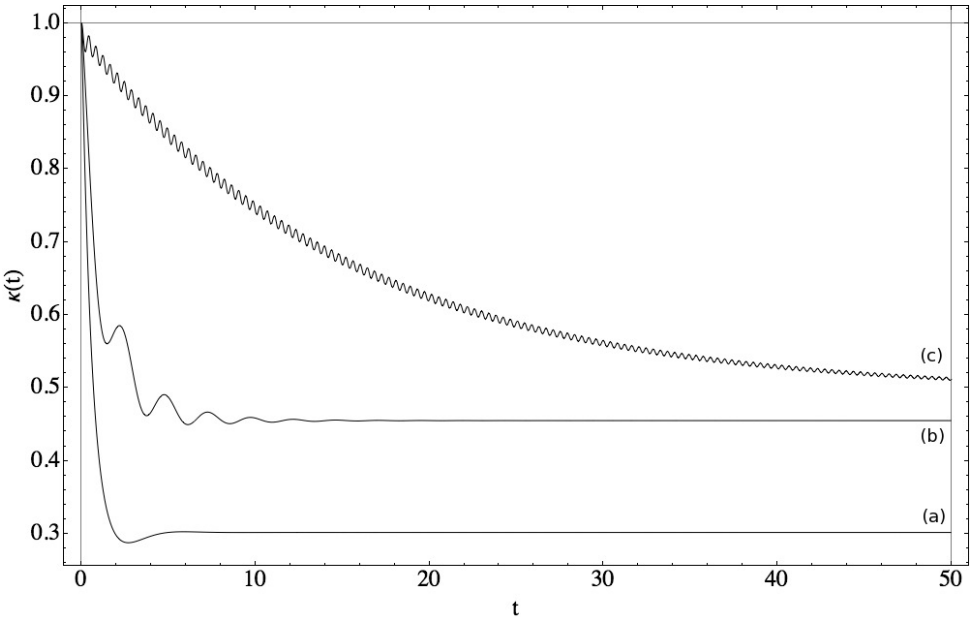

Figure 1. Time dependance of the mean number of fermions as a function of coupling strength to the mesoscopic bath. Curves (a), (b) and (c) correspond to 0.01, 0.1 and 1 values of the coupling strength g, respectively. The rest of the parameters are chosen to be the same for all three curves: $\epsilon = 1$, $\omega = 1.3$, $N = 200$, $J(\lambda_0)$=$J(\lambda_1)$=0.01 and $\beta = 10$.

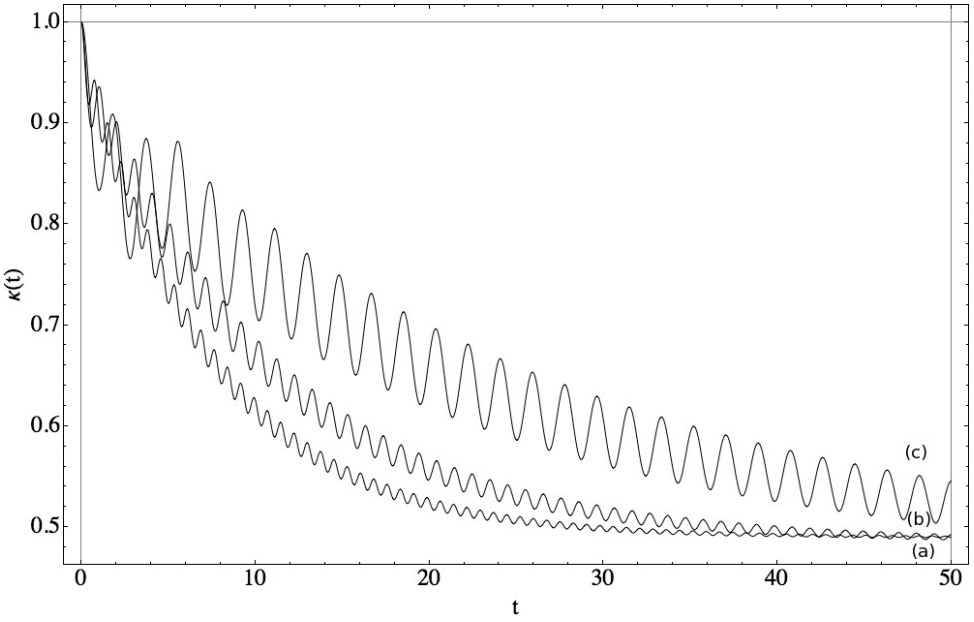

Figure 2. Time dependance of the mean number of the fermions as a function of the number of fermions in the mesoscopic bath. Curves (a), (b) and (c) correspond to 200, 100 and 20 number of fermions in the mesoscopic bath (N), respectively. The rest of the parameters are chosen to be the same for all three curves: $\epsilon = 1$, $\omega = 1.3$, $g = 0.5$, $J(\lambda_0)$=$J(\lambda_1)$=0.01 and $\beta = 10$.

In Fig. 1 and Fig. 2 the dynamics of the mean number is shown. In Fig. 1 we analyze

different regimes of the interaction between fermion and meso-reservoir of fermions. It is clear that in the weak coupling case (Fig. 1a) Markovian dissipation is observed, however, increasing the interaction strength (g) (Fig. 1b, Fig. 1c), the process of thermalization shows clear signs of non-Markovian behaviour. In Fig. 2 we analyze the influence of the number of fermions in the mesoscopic bath on the dynamics of the fermion. It is clear from the Fig. 2 that decreasing the number of fermions strongly influences the frequency of oscillations ($\sim \sqrt{N}$).

In conclusion, we derive and solve analytically the quantum master equation for the spinless electron interacting with a mesosopic bath of spinless electrons with restrictions on the system-bath interaction. We further analyze the dynamics of the reduced system. In the future we plan to take into account spin-spin interactions and consider more general initial conditions.

This work is based upon research supported by the South African Research Chair Initiative of the Department of Science and Technology and National Research Foundation.

References

[1] Ajisaka S *et al*, arXiv:1204.1321 (2012)
[2] Kosov DS, Prosen T and Zunkovic B, arXiv:1206.3450 (2012)
[3] Ajisaka S *et al*, arXiv: 1205.1167 (2012)
[4] Breuer H-P and Petruccione F 2002 *The Theory of Open Quantum Systems* (Oxford: Oxford University Press)

The ^{4}He(e,e' p)^{3}H reaction in the antisymmetrized molecular dynamics approach

G J Rampho[1], S A Sofianos[1], S Oryu[2]

[1] Department of Physics, University of South Africa, Pretoria 0003, South Africa
[2] Department of Physics, Tokyo University of Science, Noda, Chiba 278-8510, Japan

E-mail: ramphogj@gmail.com

Abstract. Electron-induced proton knock-out process from the ^{4}He nucleus is investigated. Bound states of the systems are described with the angular-momentum-projected and parity-projected antisymmetrized molecular dynamics wave functions. The nuclear Hamiltonian is constructed with a semi-realistic nucleon-nucleon potential. Non-relativistic nuclear charge and current operators are employed in calculating nuclear transition amplitudes. Final-state interactions are taken into account by the use of the Glauber approximation. It is found that the antisymmetrized molecular dynamics generates a very good description of experimental data at high momentum transfer.

1. Introduction

Quasielastic electron-nucleon scattering is a very useful tool to extract important information about nuclear structure [1]. This is based on the fact that the interaction of the electrons and nuclei is predominantly electromagnetic and the theory underlying electromagnetic interactions, quantum electrodynamics theory, is well understood. Furthermore, the electromagnetic interactions are a lot weaker than nuclear interactions, and thus can be treated as a small perturbation to the nuclear Hamiltonian. Therefore, only one-photon exchange processes are dominant. In the one-photon approximation the electron and nuclear structure functions factor out completely in the transition form factor. Therefore, the only input quantities requiring careful construction are the nuclear wave functions. In this work the antisymmetrized molecular dynamics (AMD) to construct wave functions for bound nuclear systems to study proton knock-out process ^{4}He(e, e' p)^{3}H.

The AMD approach was developed [2] from the Time-Dependent Cluster Model [3] for the study of fermionic systems. This approach combines Fermi-Dirac statistics with elementary quantum mechanics to treat the motion of particles in a system [4]. However, the model is not fully quantum mechanical and does not assume a shell structure for the system. The AMD approach was used to study the dynamics of heavy-ion collisions [5] and elastic proton-nucleus scattering [6]. Clustering in nuclei as well as angular distributions of scattered protons in proton-nucleus scattering can be explained by the AMD model [6]. Improved AMD wave functions have been shown to give satisfactory predictions of properties of few-body systems [7, 8]. In this work we use the parity-projected and angular-momentum-projected AMD [9].

In Section 2 key features of the AMD approach are summarized. In this section the construction of the wave function, the equations of motion of the variable parameters and the

variational technique used are briefly outlined. Basic features of the electron-nucleus scattering formalism are given in Section 3. In Section 4 the theoretical results are compared with some experimental data for the proton knock-out from the ^{4}He nucleus. Conclusions drawn are indicated in Section 5.

2. AMD Formalism

An AMD wave function describing a bound nuclear system of A nucleons is constructed as a Slater determinant

$$\Psi_{AMD}(\vec{\mathrm{S}}) \;=\; \frac{1}{\sqrt{A!}}\det[\,\phi_j(\alpha,\vec{s}_i),\chi_j(\vec{\sigma}_i),\xi_j(\vec{\tau}_i)\,] \tag{1}$$

where ϕ, χ and ξ are, respectively, the spatial, spin and isospin components of the single-particle wave functions. A wave function with definite parity (π) and total angular momentum (J), with total angular momentum projection (M) onto the quantization axis, is constructed from the AMD wave function as

$$\Psi^{J\pi}_{MK}(\vec{\mathrm{S}}) \;=\; \frac{1}{2}\,P^J_{MK}(\Omega)\,[\,1\pm P^\pi\,]\,\Psi_{AMD}(\vec{\mathrm{S}}) \tag{2}$$

where $P^J_{MK}(\Omega)$ is the angular momentum projection operator, P^π the parity projection operator and $\vec{\mathrm{S}}\equiv\{\vec{s}_1,\vec{s}_2,\vec{s}_3,\ldots,\vec{s}_A\}$. The angular momentum projection operator is defined by [10]

$$P^J_{MK}(\Omega) \;=\; \frac{2\,J+1}{8\,\pi^2}\int \mathrm{d}\Omega\, D^{J*}_{MK}(\Omega)\,\hat{R}(\Omega) \tag{3}$$

where $D^J_{MK}(\Omega)$ is the Wigner D-function, $\hat{R}(\Omega)$ the rotation operator and $\Omega\equiv\{\alpha,\beta,\gamma\}$ the Euler rotation angles.

The single nucleon wave functions are given by

$$\psi_i(\vec{r}_j) \;=\; \left(\frac{2\,\alpha}{\pi}\right)^{2/4}\exp\left[-\alpha\left(\vec{r}_j-\frac{\vec{s}_i(t)}{\sqrt{\alpha}}\right)^2+\frac{1}{2}\,\vec{s}_i^{\,2}(t)\right]\otimes\chi_i\otimes\xi_i \tag{4}$$

where $\chi_i\otimes\xi_i$ are time-independent spin-isospin states of the i-th nucleon. These states are compactly expressed in the form $\kappa_i=\{\,N\uparrow\ \text{or}\ N\downarrow\,\}$ for nucleon with spin-up or spin-down. The Gaussian width parameter α is a real constant and the variational parameter $\vec{s}(t)$ is complex. The time-dependent variational principle [5]

$$\delta\int_{t_1}^{t_2}\frac{\langle\,\Psi(\vec{S})\,|\,\mathrm{i}\hbar\,\frac{\partial}{\partial t}-H\,|\,\Psi(\vec{S})\,\rangle}{\langle\,\Psi(\vec{S})\,|\,\Psi(\vec{S})\,\rangle}\,\mathrm{d}t=0 \tag{5}$$

with the constraints

$$\delta\Psi(t_1)=\delta\Psi(t_2)=\delta\Psi^*(t_1)=\delta\Psi^*(t_2)=0\ . \tag{6}$$

is used to determine the dynamical equations for the variational parameters. The resulting equations are solved to minimizes the variational energy

$$E^{J\pm}_0(\vec{S},\vec{S}^*) \;=\; \frac{\langle\,\Psi^{J\pm}_{MK}(\vec{\mathrm{S}})|\,H\,|\Psi^{J\pm}_{MK}(\vec{\mathrm{S}})\,\rangle}{\langle\,\Psi^{J\pm}_{MK}(\vec{\mathrm{S}})|\Psi^{J\pm}_{MK}(\vec{\mathrm{S}})\,\rangle}\ . \tag{7}$$

of the nucleus and also determine the variational parameters. The Hamiltonian of the system is constructed with the AV4 NN potential including the $V_{C1}(r)$ Coulomb component [11]. The evaluation of the components of the energy expectation values is explained in Refs. [12, 13, 14].

The wave function describing a nucleon separation from a nucleus is written in the form [13]

$$\Psi_{\vec{S}}(\vec{r}_1,\vec{r}_2,\ldots,\vec{r}_A) \;=\; \frac{1}{\sqrt{A!}} \begin{vmatrix} \psi_1(\vec{r}_1) & \psi_2(\vec{r}_1) & \cdots & G(\vec{R})\,\overline{\psi}_A(\vec{r}_1) \\ \psi_1(\vec{r}_2) & \psi_2(\vec{r}_2) & \cdots & G(\vec{R})\,\overline{\psi}_A(\vec{r}_2) \\ \vdots & \vdots & \ddots & \vdots \\ \psi_1(\vec{r}_A) & \psi_2(\vec{r}_A) & \cdots & G(\vec{R})\,\overline{\psi}_A(\vec{r}_A) \end{vmatrix} \tag{8}$$

where nucleon A is the one ejected, $\vec{r}_i$ the position vector of the i-th nucleon and $\overline{\psi}_A(\vec{r})$ a plane wave. The $G(\vec{R})$ is the Glauber multiple-scattering operator which approximates the final state interaction (FSI). This operator is given by [15]

$$G(\vec{R}) = \prod_{j=1}^{A-1} \left[\, 1 - \Gamma(\vec{b}_A - \vec{b}_j)\,\theta(z_j - z_A) \,\right] \tag{9}$$

where $\theta(z)$ is the step function and $\Gamma(\vec{b})$ the nucleon-nucleon scattering profile function. The profile function is given by

$$\Gamma(\vec{b}) = \frac{\sigma_{NN}(1 - \mathrm{i}\,\epsilon_{NN})}{4\pi\,\beta_{NN}^2} \exp\left[-\frac{b^2}{2\beta_{NN}^2} \right]. \tag{10}$$

where the vector $\vec{B}$ is defined through the notation $\vec{r}_n = \vec{b}_n + \hat{\vec{q}}\,z_n$. The parameters σ_{NN}, ϵ_{NN} and β_{NN} are determined by fitting $\Gamma(\vec{b})$ to nucleon-nucleon scattering experimental data at some invariant energy. The first three terms of the Glauber operator considered in this work are illustrated in figure 1.

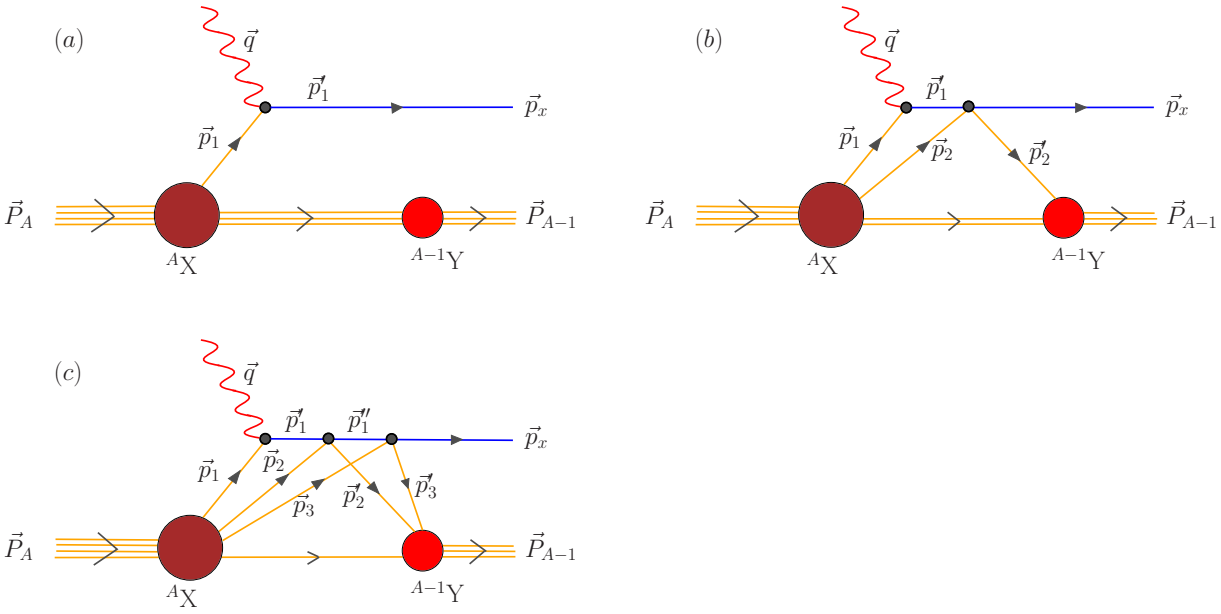

Figure 1. Feynman diagram vertex for a nucleon removal from the ^{A}X nucleus. The free nucleon (a) does not interact with the nucleons (b) interacts with single nucleons and (c) interacts with pairs of nucleons, in the recoil nucleus $^{A-1}$Y.

3. Inclusive Electron-nucleus scattering

Consider an electron with an initial energy $\mathcal{E}_i$ and momentum $\vec{k}_i$ interacting with a nucleus with initial energy E_i and momentum $\vec{P}_i$. The electron transfers a photon of energy and momentum $(\omega, \vec{q})$ to the nucleus and scatters with final energy and momentum $(\mathcal{E}_f, \vec{k}_f)$ at an angle θ_e. The final state of the nucleon system recoils with energy and momentum $(E_f, \vec{P}_f)$. In the case of a nucleon knock-out, the energy and momentum of the ejected nucleon are denoted by $(E_x, \vec{p}_x)$. The interaction of relativistic electrons with nuclei is well described by the impulse approximation.

The differential cross-section for inclusive electron-nucleus scattering, in the *one photon approximation*, is given by [1]

$$\frac{\mathrm{d}^2\sigma}{\mathrm{d}\mathcal{E}_f\,\mathrm{d}\Omega_e} = \sigma_M \left[\left(\frac{Q^2}{q^2}\right)^2 R_L(\omega,\vec{q}) + \left(\frac{Q^2}{2\,q^2} + \tan^2\frac{\theta_e}{2}\right) R_T(\omega,\vec{q}) \right] \tag{11}$$

where $Q^2 = q^2 - \omega^2$, σ_M is the Mott differential cross section and $R_L(\vec{q},\omega)$ ($R_T(\vec{q},\omega)$) the longitudinal (transverse) nuclear response function. The transverse response is given by

$$R_T(\vec{q},\omega) = \frac{1}{2\,J_i+1} \sum_f \left| \langle\, J_f^{\pi_f} M_f \,|\, \vec{j}_\perp(\vec{q},\omega) \,|\, J_i^{\pi_i} M_i \,\rangle \right|^2 \delta\,(\,\omega - \Delta E\,) \tag{12}$$

where $|\,J_i^{\pi_i} M_i\,\rangle$ is the initial state of the target nucleus with parity π_i, angular momentum J_i, angular momentum projection M_i along the quantization axis, and $\vec{j}_\perp(\vec{q},\omega)$ the components of the nuclear current operator that are perpendicular to $\vec{q}$. The coordinate system is oriented such that $\vec{q}$ is directed along the z-axis, which is also chosen to be the quantization axis. For the function $R_L(\vec{q},\omega)$ the nuclear charge operator $\rho(\vec{q},\omega)$ is used in the place of $\vec{j}_\perp(\vec{q},\omega)$. The delta function expresses the conservation of energy with $\Delta E = T_p + T_{A-1} + \Delta M$, where T_p (T_{A-1}) is the non-relativistic energy of the proton (recoil nucleus) and $\Delta M = M_A - M_{A-1} - M_x$ the separation energy of a proton (mass M_x) from the target nucleus (mass M_A). The nuclear charge and current operators used in this work are of the form [16]

$$\rho(\vec{q},\omega) \;=\; \frac{q}{Q}\,G_E^x(Q^2) + \frac{\mathrm{i}}{4\,M_x^2}\,\frac{2\,G_M^x(Q^2) - G_E^x(Q^2)}{\sqrt{1+\eta}}\,\vec{\sigma}_x\cdot\vec{q}\times\vec{p}_x \tag{13}$$

$$\vec{\mathrm{j}}(\vec{q},\omega) \;=\; \frac{\sqrt{\eta}}{q}\left[\Big(\,2\,G_E^x(Q^2) + \eta\,G_M^x(Q^2)\Big)\,\vec{p}_x - \mathrm{i}\,G_M^x(Q^2)\left(\,\vec{q}\times\vec{\sigma}_x + \frac{\omega}{2\,M_x}\,\vec{\hat{q}}\cdot\vec{\sigma}_x\;\vec{\hat{q}}\times\vec{p}_x\right)\right] \tag{14}$$

where $\vec{\hat{q}} = \vec{q}/|\vec{q}|$, $\eta = Q^2/4M_x^2$ and G_E^x (G_M^x) the nucleon Sachs electric (magnetic) form factor. For the Sachs form factors the phenomenological parametrization derived in Ref. [17] is adopted.

4. The ^{4}He(e,$e'\,p$)^{3}H reaction

The longitudinal and transverse response function for the inclusive ^{4}He(e,$e'\,p$)^{3}H process are calculated for the kinematics of the experimental results presented in reference [18]. To evaluate the response functions it is convenient to decompose the initial state of the target in the form

$$|\,J_i^{\pi_i} M_i\,\rangle_A = \sum_{m_p} \langle j_p m_p\, J_\mathrm{o} M_\mathrm{o} | J_i M_i\,\rangle [\,\Big|\,j_p^{\pi_p} m_p\,\Big\rangle \otimes |\,J_\mathrm{o}^{\pi_\mathrm{o}} M_\mathrm{o}\,\rangle_{A-1}\,] \tag{15}$$

where $|\,j_p^{\pi_p} m_p\,\rangle$ is the proton initial state and $\langle j_p m_p\, J_\mathrm{o} M_\mathrm{o} | J_i M_i\,\rangle$ Clebsch-Gordan coefficients. The theoretical results are compared with experimental data for $q = 300\,\mathrm{MeV/c}$, $q = 400$ MeV/c and $q = 500\,\mathrm{MeV/c}$ in figure 2. PWIA results are also shown and compared with the

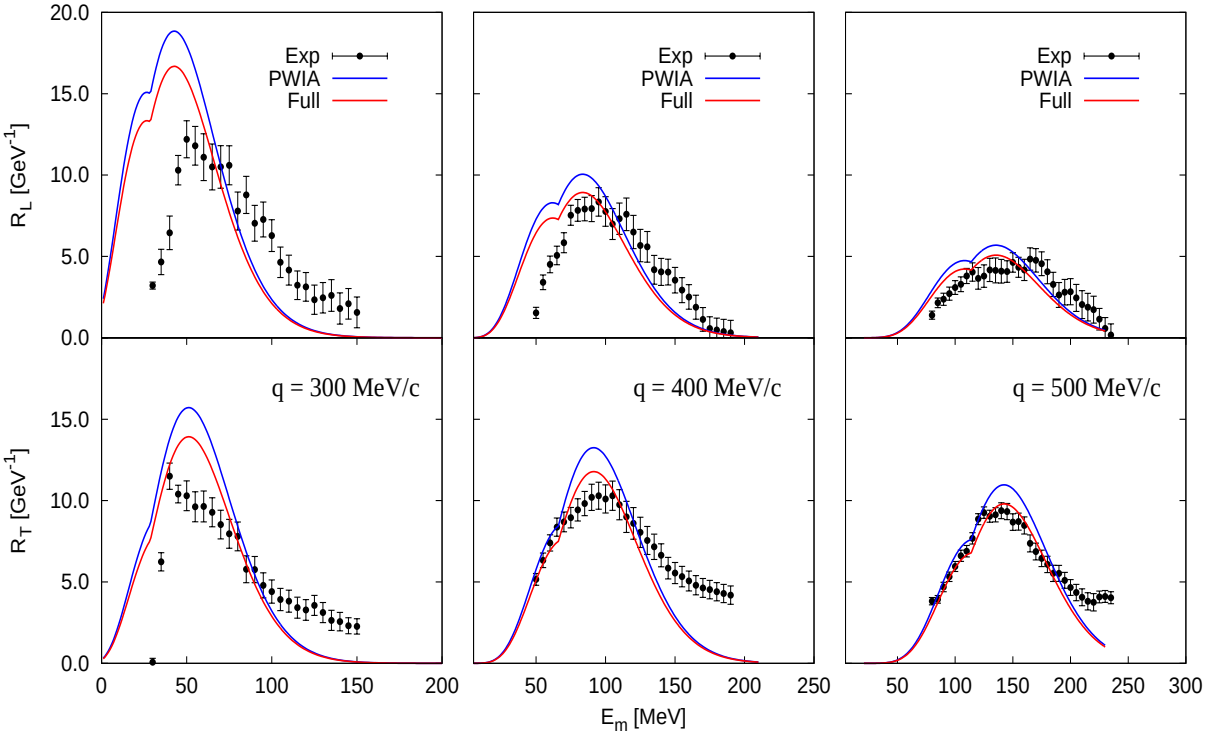

Figure 2. The longitudinal (R_L) and transverse (R_T) response function for the ^{4}He nucleus at $q = 400\,\mathrm{MeV/c}$, $q = 400\,\mathrm{MeV/c}$ and $q = 500\,\mathrm{MeV/c}$. The experimental data are from reference [18].

results that include FSIs. The results of the longitudinal response function $R_L(\vec{q},\omega)$ reproduce the general structure of the experimental data for all the values of q, with the size of the peak decreasing as q increases. For values of $E_m = \omega > 100\,\mathrm{MeV}$ the theoretical results reproduce the experimental data satisfactorily. However, for $\omega < 100\,\mathrm{MeV}$ the theoretical results overestimate the experimental data. The discrepancy between theory and experiment decreases as q increases. The contributions of the FSI to the theoretical response functions decrease the disparity between theory and experiment. The theoretical results for the transverse response functions $R_T(\vec{q},\omega)$ overestimate the experimental data at low energy transfers. The transverse response is generally well predicted. The AMD results are consistent with the theoretical results presented in reference [18]. In general, the theory fails to explain the experimental results for low energies. This is expected since the employed Glauber approximation is valid only at high energies.

5. Conclusions

The AMD approach was used to investigate the electron-induced proton knock-out process in the ^{4}He nucleus. FSI between the ejected proton and the recoil nucleus are included using the Glauber approximation. Transverse and longitudinal response function the two-body electrodisintegration at high missing momenta where calculated. The AMD results gave a very good description of the experimental data. It was observed that the inclusion of FSI in general, improves the agreement between theory and experiment. Furthermore, the AMD results are consistent with results obtained using other theoretical methods. Therefore, AMD provide a

simple yet accurate bound-state wave functions to of nuclear systems.

Acknowledgments
This work is part of a PhD thesis submitted to the University of South Africa.

References

[1] Benhar O, Day D, Sick I, 2008 *Rev. Mod. Phys.* **80** 189
[2] Horiuchi H 1991 *Nucl. Phys.* **A522** 257c
[3] Caurier E, Grammaticos B and Sami T 1982 *Phys. Lett.* **B109** 150
[4] Feldmeier H 1990 *Nucl. Phys.* **A515** 147
[5] Ono A, Horiuchi H, Maruyama T and Ohnishi A 1992 *Prog. Theor. Phys.* **87** 1185
[6] Tanaka E I, Ono A, Horiuchi H, Maruyama T and Engel A 1995 *Phys. Rev.* **C52** 316
[7] Togashi T, Kat$\overline{o}$ K 2007 *Prog. Theor. Phys.* **117** 189
[8] Watanabe T and Oryu S 2006 *Prog. Theor. Phys.* **116** 429
[9] Kanada-En'yo Y, Horiuchi H and Ono A 1995 *Phys. Rev.* **C52** 628
[10] Peierls R E and Yoccoz J 1957 *Proc. Phys. Soc.* **A70** 381
[11] Wiringa R B and Pieper S C 2002 *Phys. Rev. Lett.* **89** 182501-1
[12] Rampho G J 2011 *Few-Body Syst,* **50** 467
[13] Rampho G J 2010 *PhD Thesis*, University of South Africa, unpublished.
[14] Rampho G J, Sofianos S A, Oryu S, Watanabe T 2013 *Few-Body Syst.* **54** 455
[15] Morita H, Ciofi degli Atti C. Treleani D 1999 *Phys. Rev.* **C60** 034603-1
[16] Schiavilla R, Benhar O, Kievsky A, Marcucci L E, Viviani M 2005 *Phys. Rev.* **C72** 064003-1
[17] Friedrich J and Walcher Th 2003 *Eur. Phys. J.* **A17** 607
[18] von Reden K F, *et al*, 1990 *Phys. Rev.* **C41** 1084

The role of the initial system-bath correlations in the dynamics of open quantum systems

V Semin[1], I Sinayskiy[1,2], F Petruccione [1,2]

[1]Quantum Research Group, School of Chemistry and Physics, University of KwaZulu-Natal, Durban, 4001, South Africa
[2]National Institute for Theoretical Physics, University of KwaZulu-Natal, Durban, 4001, South Africa

E-mail: semin@ukzn.ac.za

Abstract. In the typical derivation of the master equation for the system interacting with a bath it is assumed that initially system and bath are uncorrelated. However, in many physical situations this is not the case. Here, we study the influence of the initial system-bath correlations on the dynamics of the system. As a toy model we will consider a particle with spin 1/2 interacting with a spin bath through an intermediate spin. On the one hand, we use the technique of correlated projection operators to construct a time convolutionless (TCL) master equation with an inhomogenous term and on the other hand we will solve exactly the equation for the evolution operator of the total system. This allows us not only to study the influence of the initial correlations on the system-bath dynamics, but also the influence of the initial system-bath correlations on the accuracy of TCL approach.

1. Introduction

In this paper, we study the reduced dynamics of a spin coupled to a spin bath through an intermediate spin. The main goals of this work are the following: Firstly, to use the exact solution of the studied model derived here to show the importance of initial system-bath correlations. Secondly, to demonstrate that in the case where initial system-bath correlations are present, a rigorously derived master equation will contain an inhomogeneous term which substantially affects the dynamics of the reduced system. Thirdly, by comparing the exact and approximate solutions of the master equation, to understand the limitations of the approximate correlated projector method in the presence of an inhomogeneous term in the quantum master equation.

2. Model

We consider the model of a central spin coupled to a spin bath through an intermediate spin. The interaction Hamiltonian is given by

$$H = H_{SI} + H_{IB}, \tag{1}$$

where

$$H_{SI} = \frac{\gamma}{2}\left(\sigma_+\tau_- + \sigma_-\tau_+\right)$$

is the Hamiltonian describing spin-spin interactions and $\sigma_\pm, \tau_\pm$ are the creation and annihilation operators for the central spin and the intermediate spin, respectively, while γ denotes the strength of the spin-spin interaction. In this work units are chosen such that $k_B = \hbar = 1$.

The interaction between the intermediate spin and the spin bath is described by

$$H_{IB} = \frac{\alpha}{2\sqrt{N}} \left(\tau_+ J_- + \tau_- J_+\right), \tag{2}$$

where $J_\pm = \sum_{i=1}^{N} \sigma_\pm^i$, where $\sigma_\pm^i$ are the creation and annihilation operators for the ith spin in the bath, α is the strength of interaction, and N denotes the number of bath spins. The factor $1/\sqrt{N}$ is introduced as usual [1] to obtain the correct behaviour in the thermodynamic limit $(N \to \infty)$.

3. Exact dynamics

To describe the exact dynamics of the total system we need to specify an initial state of the total system given by the density operator $\rho_{\text{tot}}(0)$, and to find an evolution operator of the total system $U(t)$ in an explicit form, as

$$U(t) = \exp[-iHt]. \tag{3}$$

With the knowledge of the evolution operator and the initial state of the total system, the reduced dynamics of the central spin can be found as

$$\rho^S(t) = \text{tr}_{IB}\{U(t)\rho_{\text{tot}}(0)U^\dagger(t)\}. \tag{4}$$

In this work, we will consider an initially correlated state between the central spin and the intermediate spin, while the rest of the bath is assumed to be unpolarized.

The initial state of the total system reads,

$$\rho_{\text{tot}}(0) = \rho_{SI}(0) \otimes \rho_B(0), \tag{5}$$

where the initial state $\rho_{SI}(0)$ is given by the generic X-like two-qubit density matrix, as

$$\rho_{SI}(0) = \begin{pmatrix} \rho_{11}^0 & 0 & 0 & \rho_{14}^0 \\ 0 & \rho_{22}^0 & \rho_{23}^0 & 0 \\ 0 & \rho_{32}^0 & \rho_{33}^0 & 0 \\ \rho_{41}^0 & 0 & 0 & \rho_{44}^0 \end{pmatrix}, \tag{6}$$

while $\rho_B(0)$ is the density matrix describing the bath of N unpolarized spin-1/2 particles, given by

$$\rho_B(0) = \frac{I_B}{2^N}. \tag{7}$$

The evolution operator in (4) can be found analytically from Schrödinger's equation $i\frac{\partial}{\partial t}U = HU$. Then, using Eq. (4), we derive the reduced density matrix of the central spin. The typical behaviour of the probability to find the central spin in the excited state for different initial correlations is shown in Fig. 1. The ρ_{11}^S in the Fig. 1 is just a matrix element of the reduced density matrix (4). To derive this element it is necessary to find dynamics of the ρ_{tot} and trace out degrees of freedom corresponding to the bath and the intermediate spin.

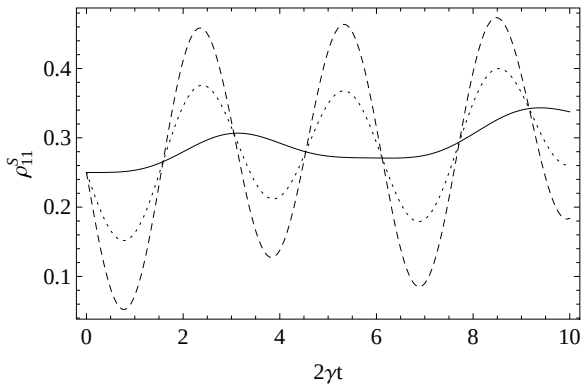

Figure 1. Exact solution for $\rho^0_{23} = \rho^0_{32} = 0$ (solid line), $\rho^0_{23} = -\rho^0_{32} = 0.2i$ (dashed line), $\rho^0_{23} = -\rho^0_{32} = 0.1i$ (dotted line). Other parameters: $N = 10$, $\rho^0_{11} = 0$, $\rho^0_{22} = 0.25$, $\rho^0_{33} = 0.25$, $\rho^0_{44} = 0.5$, $\alpha = \gamma/4$.

4. Time-convolutionless master equation

The idea behind applying projection operator techniques to open quantum systems is to consider the operation of tracing over the environment as a formal projection $\rho \mapsto \mathcal{P}\rho$ in the state space of the total system [2, 3]. The superoperator $\mathcal{P}$ has the property of a projection operator, that is $\mathcal{P}^2 = \mathcal{P}$, and the density matrix $\mathcal{P}\rho$ is said to be the relevant part of the density ρ of the total system. Correspondingly, a projector $\mathcal{I} - \mathcal{P}$ or $\rho \mapsto \mathcal{Q}\rho$ is defined as a projection onto the irrelevant part of the total density matrix.

An exact master equation for the relevant part of ρ is obtained by removing the dependence of the system's dynamics on the full history of the system, and formulating a time-local equation of motion, which is given by [2]

$$\frac{\partial}{\partial t}\mathcal{P}\rho(t) = \mathcal{K}(t)\mathcal{P}\rho(t) + \mathcal{I}(t)\mathcal{Q}\rho(0). \tag{8}$$

This equation is called the time-convolutionless (TCL) master equation, and $\mathcal{K}(t)$ is a time-dependent superoperator, which is referred to as the TCL generator. In general, the term proportional to $\mathcal{Q}\rho(0)$ on the right-hand side of Eq. (8) is called the inhomogeneous term.

The TCL generator and inhomogeneous term can be perturbatively expanded in powers of H. The expansion to second order is given by

$$\mathcal{K}(t) = \mathcal{P}\mathcal{L}(t)\mathcal{P} + \int_0^t ds\mathcal{P}\mathcal{L}(t)\mathcal{L}(s)\mathcal{P}, \tag{9}$$

$$\mathcal{I}(t) = \mathcal{P}\mathcal{L}(t)\mathcal{Q} + \int_0^t ds\mathcal{P}\mathcal{L}(t)\mathcal{L}(s)Q. \tag{10}$$

It was shown Fisher and Breuer [4], that a general class of projection superoperators can be represented as follows:

$$\mathcal{P}\rho = \sum_i \mathrm{tr}_E\{A_i\rho\} \otimes B_i, \tag{11}$$

where $\{A_i\}$ and $\{B_i\}$ are two sets of linearly independent Hermitian operators on $\mathcal{H}_E$ satisfying the relations

$$\mathrm{tr}_E\{B_iA_j\} \quad = \quad \delta_{ij}, \tag{12}$$

$$\sum_i (\mathrm{tr}_E B_i) A_i = I_E, \tag{13}$$

$$\sum_i A_i^T \otimes B_i \geq 0. \tag{14}$$

Once $\mathcal{P}$ is chosen, the dynamics of the open system is uniquely determined by the dynamical variables

$$\rho_i(t) = \mathrm{tr}_E\{A_i \rho(t)\}. \tag{15}$$

The connection to the reduced density matrix is simply given by

$$\rho_S(t) = \sum_i \rho_i(t), \tag{16}$$

and the normalization condition reads

$$\mathrm{tr}_S\, \rho_S(t) = \sum_i \mathrm{tr}_S\, \rho_i(t) = 1. \tag{17}$$

In this way, the correlation projection operator for our model is chosen as

$$\mathcal{P}\rho = \sum_{j=0,\frac{1}{2}}^{N/2} \sum_{m=-j}^{j} \mathrm{tr}_{IB}\left(\Pi_{jm}^{+}\rho\right) \otimes \frac{\Pi_{jm}^{+}}{N_j} + \sum_{j=0,\frac{1}{2}}^{N/2} \sum_{m=-j}^{j} \mathrm{tr}_{IB}\left(\Pi_{jm}^{-}\rho\right) \otimes \frac{\Pi_{jm}^{-}}{N_j}, \tag{18}$$

where $\Pi_{jm}^{\pm} = |\pm\rangle\langle\pm| \otimes |j,m\rangle\langle j,m|$. The $|\pm\rangle$ are eigenvectors, τ_z and $|j,m\rangle$ are eigenvectors of the bath operators J_z and J^2, with corresponding eigenvalues m and $j(j+1)$. It is convenient to introduce the notation

$$N_j = \mathrm{tr}\Pi_{jm}^{\pm} = \frac{2j+1}{\frac{N}{2}+j+1} \frac{N!}{(\frac{N}{2}+j)!\frac{N}{2}-j)!}. \tag{19}$$

Then, the TCL 2 master equation with projection operator (18) has the form of a system of coupled equations

$$\dot{r}_{jm} = -\frac{\alpha^2}{2N} b(j,-m)(r_{jm} - R_{jm-1})t - \frac{\gamma^2}{4}(r_{jm}\sigma^-\sigma^+ + \sigma^-\sigma^+ r_{jm} - 2\sigma^- R_{jm}\sigma^+)t + \Lambda_1 \tag{20}$$

$$\dot{R}_{jm} = -\frac{\alpha^2}{2N} b(j,m)(R_{jm} - r_{jm+1})t - \frac{\gamma^2}{4}(R_{jm}\sigma^+\sigma^- + \sigma^+\sigma^- R_{jm} - 2\sigma^+ r_{jm}\sigma^+)t + \Lambda_2, \tag{21}$$

where $b(j,m) = (j-m)(j+m+1)$, $R_{jm} = \mathrm{tr}_{IB}\left(\Pi_{jm}^{+}\rho\right)$, and $r_{jm} = \mathrm{tr}_{IB}\left(\Pi_{jm}^{-}\rho\right)$. The inhomogeneity is given by

$$\Lambda_1 = \begin{pmatrix} i\frac{\gamma}{2^{N+1}}(\rho_{23}^0 - \rho_{32}^0) & 0 \\ 0 & 0 \end{pmatrix}, \tag{22}$$

$$\Lambda_2 = \begin{pmatrix} 0 & 0 \\ 0 & -i\frac{\gamma}{2^{N+1}}(\rho_{23}^0 - \rho_{32}^0) \end{pmatrix}. \tag{23}$$

The exact dynamics of the probability to find the central spin in the excited state following from Eqs.(20)–(21) and Eqs. (22)–(23) is shown in Fig. 2.

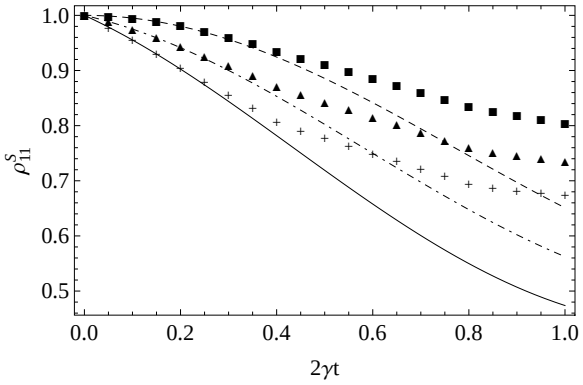

Figure 2. TCL 2 solution for $\rho_{23}^0 = 0.2i$, $\rho_{32}^0 = -0.2i$ (cross dot); for comparison, the solid curve is the exact solution; $\rho_{23}^0 = 0.1i$, $\rho_{32}^0 = -0.1i$ (triangle dot); for comparison, the dot-dashed curve is the exact solution; $\rho_{23}^0 = \rho_{32}^0 = 0$ (square dot); for comparison, the dashed curve is the exact solution. The other parameters are chosen as: $\alpha = \gamma/2$, $\rho_{11}^0 = \rho_{22}^0 = 0.5$, $\rho_{33}^0 = \rho_{44}^0 = 0$, $N = 30$.

5. Conclusion

We have found an exact solution for a simple spin system coupled to a spin bath through an intermediate spin. We have studied the dynamics of the system and have shown that the initial correlations between the central spin and the intermediate spin have a strong influence on the dynamics of the central spin. On the other hand, the dynamics of the central spin are weakly dependent on the number of bath spins. In addition to the exact solution, an approximate TCL 2 master equation was derived with the help of the projection correlation operator technique. The derived equation explicitly takes into account initial correlations between the central spin and the intermediate spin. The solution of the master equation was compared with the exact solution. It is shown that the approximate technique gives good results for short time dynamics.

[1] Hamdouni Y, Petruccione F 2007 *Phys. Rev.* B **76** 174306
[2] Breuer H-P and Petruccione F 2002 *The Theory of Open Quantum Systems* (Oxford: Oxford University Press)
[3] Richter M, Knorr A 2010 *Ann. Phys.* **325** 711
[4] Fisher J, Breuer H-P 2007 *Phys. Rev.* A **76** 052119

Molecular dynamics simulations of bilayer graphene structures

M Shai, TE Mosuang, KE Rammutla

Department of Physics and Geology, University of Limpopo, Private Bag x1106, Sovenga, 0727, Polokwane, South Africa

E-mail: Moshibudi.shai@ul.ac.za

Abstract. In this paper, the formulation of the Tersoff bond-order potential was used to study the structural and thermodynamics properties of bilayer graphene (BLG). The simulations were performed within a canonical (NVT) ensemble for structural properties and isothermal–isobaric ensemble (NPT) for thermodynamic properties. Each double layer is a hexagonal arrangement of carbon atoms at the corners to make up a two dimensional honeycomb sheet. One model consists of 64 carbons (graphene64); the other model has 256 carbon atoms (graphene256). Using the structural optimization and radial distribution functions, some equilibrium properties of these layered graphene structures are noted. Thermodynamic properties will be investigated to understand the behaviour of graphene at high temperatures.

1. Introduction

Graphene has sparked much interest in the field of condensed matter physics. It is atomically thin sheet of carbon arranged in a two dimensional honeycomb crystal [1]. The existence of graphene has since been explained by the idea that graphene has intrinsic roughness. The rippling of graphene makes it to be a nearly perfect two dimensional crystal in three dimensional spaces which is not forbidden [2]. Graphene is not only important new testing ground for fundamental physics such as relativistic quantum mechanics and low dimensional thermodynamics, but also have potential applications to nano-scale technology [3]. The carbon-carbon bond length of graphene is 1.42 Å with an interplanar spacing of 3.35 Å for bilayer graphene. Because of its unique structural, mechanical and electronically properties, it has stirred many scientists involved in the field to look forward to making a breakthrough in some new research areas.

Up to date research has revealed many possible applications in solar cell technology [4], sensors, liquid device and the fabrications of nanosized prototype transistors [5]. Similar to carbon nanotube [6], graphene is also a good candidate for usage as gas sensor materials to detect various molecules, ranging from gas phase molecules to some small bioactive molecules [7]. These desirable properties promise graphene to offer excellent short-circuit current-gain cutoff frequency for high frequency applications. Figure 1 and 2 shows two structures of bilayer graphene64 and bilayer graphene256. Both structures were varied at 300 K temperature using DL-POLY software and a program that is called a Viewer life.

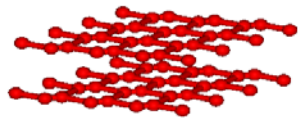

Figure 1. Bilayer graphene 64 atoms

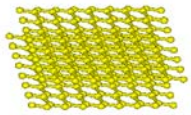

Figure 2. Bilayer graphene 256 atoms

2. Molecular dynamics

Molecular dynamics (MD) is a form of computer simulation in which atoms and molecules are allowed to interact for a period of time by approximations of known physics, giving a view of the motion of the particles. The leapfrog verlet method and Tersoff potential for molecular dynamics was used. Leapfrog integration is a simple method for integrating equations, particularly in the case of a dynamical system [4]. In this method position ($\vec{r}$) and force ($\vec{F}$) at time t are needed while the velocities ($\vec{v}$) are half a time step behind. We first advance the velocities to $t + \frac{\Delta t}{2}$ by

$$\vec{v}(t + \tfrac{\Delta t}{2}) = (\vec{v}t - \tfrac{\Delta t}{2})\vec{r}(t) + \Delta t \frac{\vec{f}(t)}{m}, \quad (1)$$

$$\vec{r}(t + \Delta t) = \vec{r}(\mathrm{t}) + \Delta t \vec{v}(t + \tfrac{\Delta t}{2}), \quad (2)$$

The velocity equation is executed first and generates a new mid-step velocity. This velocity is then used to calculate the new position. The velocity is calculated from

$$\vec{v}(t) = \left(\tfrac{1}{2}\right)\vec{v}\left(t + \tfrac{1}{2}\Delta t\right) + (\tfrac{1}{2})\vec{v}(t - \tfrac{1}{2}\Delta \mathrm{t}) \quad (3)$$

This leapfrog method also has the advantage that temperature scaling by velocity scaling is feasible [4]. The family of potentials developed by Tersoff are based on the concept of bond order: the strength of a bond between two atoms is not constant, but depends on the local environment (11). At first sight, a Tersoff potential has the appearance of a pair potential:

$$E = \sum_i E_i = \tfrac{1}{2}\sum_{i \neq j} V_{ij} \quad (4)$$

$$= \tfrac{1}{2}\sum_{ij} \emptyset_R\left(\vec{r}_{ij}\right) + \cdots + \tfrac{1}{2}\sum_{ij} B_{ij}\emptyset_A\left(\vec{r}_{ij}\right) + \cdots \quad (5)$$

Where the potential energy is decomposed into a site energy E_{ij} and a bonding energy V_{ij}, $\vec{r}_{ij}$ is the distance between atoms i and j, $\emptyset_R$ and $\emptyset_A$ means ``repulsive" and ``attractive" pair potential respectively.

$$\emptyset_R(\vec{r}_{ij}) = Ae^{(-\lambda_1 \vec{r}_{ij})} \quad (6)$$

$$\emptyset_A(\vec{r}_{ij}) = -Be^{(-\lambda_2 \vec{r}_{ij})} \quad (7)$$

3. Methodology

The molecular dynamics (MD) simulation is performed within a canonical NVT and NPT ensembles, using DL_POLY software [7]. The Newtonian equations of motion are integrated with a routine based on the leapfrog verlet algorithm with the time step of 1.0×10^{-3} s at a 0.0atm pressure. The temperature was varied from 300 K to 5000 K for calculating the radial distribution functions. For equilibrium properties we varied only the lattice constant at 300 K. All the equilibrium calculations were made at 300 K temperature. After 400 000 iterations, different average properties are separated. This step is very important and aims to calculate for each atom and generate at each time step, a new positions and velocities. After that a frequency distribution of atomic separations is produced to compute the pair distribution function, and other various properties which are computed along the trajectory of the

system in the phase space. Real space cut off and primary neighbour cut off was 2.68 Å. The structures were optimized at 300 K, by allowing the atomic positions, cell shape, and volume to relax.

4. Results and discussion

The calculation of radial distribution functions (rdf's) from molecular dynamics trajectory data is a common and computationally expensive analysis task. To test the reliability of the tersoff potential in describing graphene, we calculate the pair distribution function of $F(r)$ for graphene. From peak positions of $F(r)$, we can know the probable distance between the atoms. Figure 3 and 4 are rdf's of graphene64 and graphene256 respectively, the first peak which is the first nearest neighbour parameter appears at 1.43 Å for 300 K and 3000 K. At 5000 K which is above melting point of graphene, the first nearest neighbour parameter increases to 1.46 Å for graphene64 and 1.48 Å for graphene256. The second peak which is the second nearest neighbour parameter appears at 2.48 Å for 300 K and 3000 K.

At 5000 K the second nearest neighbour parameter increases to 2.50 Å for graphene64 and 2.56 Å for graphene256. When the temperature increases, the base of the peaks increases and the height decreases. The first peak is associated with the bond length of graphene which is 1.42 Å, and the second peak is associated with the lattice parameter of graphene which is 2.46 Å [10]. The results for both models at 5000 K, shows that, above the melting point of BLG the bond length and lattice constant changes. These results of the rdf's of graphene are in agreement with both the theoretical calculations and the experimental [10, 13, 14].

4.1. Equilibrium properties of bilayer of graphene (BLG)

The two graphs are for energy as a function of volume and energy as a function of lattice constant for graphene64 and graphene256 respectively. Since the two graphs behave similar and we can calculate the same things using them, we decided to take one for lattice constant and one for volume.

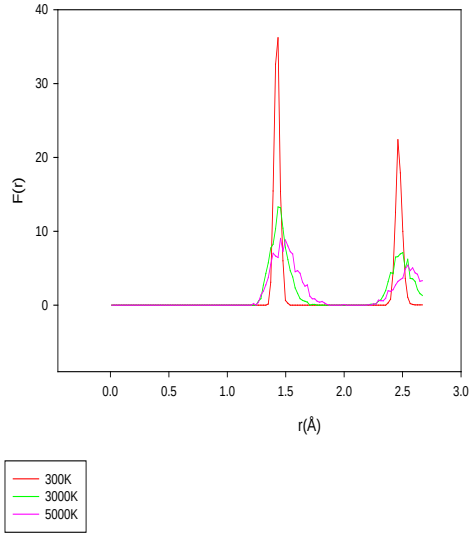

Figure 3. The radial distribution functions of graphene64

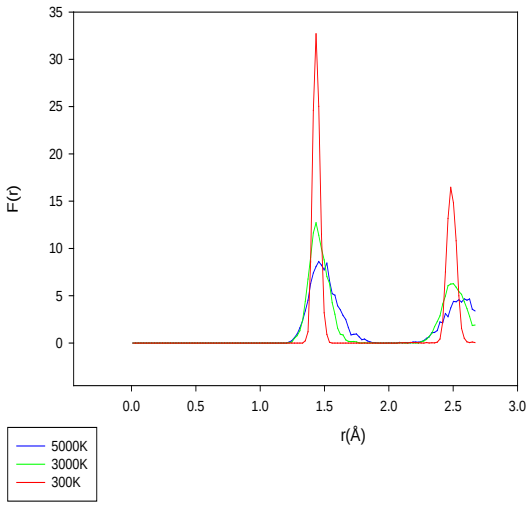

Figure 4. The radial distribution functions of graphene256.

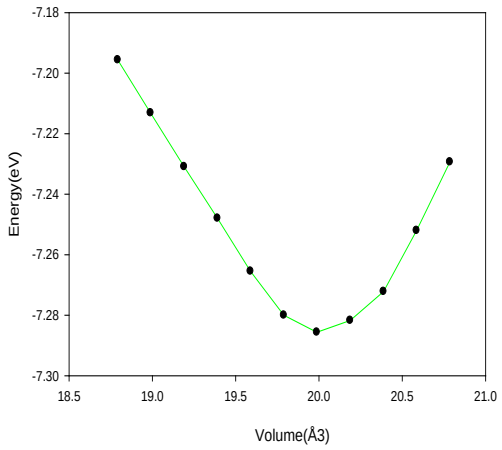

Figure 5. Energy as a function of volume.

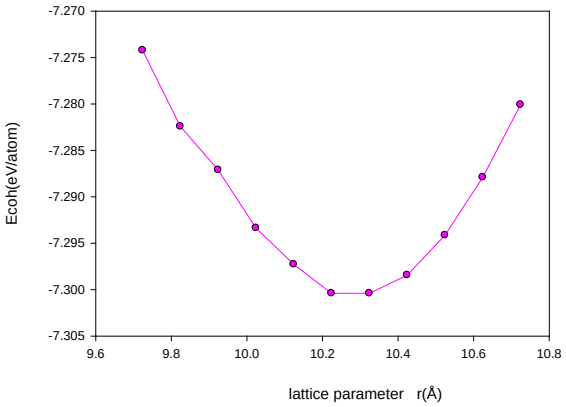

Figure 6. Energy as a function of lattice constant.

In order to find the most favourable structural configuration for the double layer graphene the relaxed 64 and 256 atom double layered graphene are optimized in order to obtain some notable equilibrium properties of the material. In so doing the lattice constant, the minimum energy, bulk modulus and its derivative were calculated using figure 5 (energy as a function of volume) and figure 6 (energy as a function of lattice constant), least squares fitted to the Murnaghan's equation of state. Again, $E(a)$ is found found to be [13]:

$$E(a) = a_0 + \frac{9V_0B_0V_0}{16}\left[\left(\frac{a_0}{a}\right)^2 - 1\right]^2 + A\left[\left(\frac{a_0}{a}\right)^3 - 1\right]^3 + B\left[\left(\frac{a_0}{a}\right)^2 - 1\right]^4 + 0\left[\left(\frac{a_0}{a}\right)^2 - 1\right]^5 \quad (8)$$

Where B_0 is the bulk modulus, V_0 the primitive volume and A and B are fit parameters. Where B_0 is the bulk modulus, V_0 the primitive volume and A and B are fit parameters.

Table 1. Calculated and measured lattice constant a, bulk modulus (B_0), its derivative (B'), minimum energy (E_0), and minimum volume (V_0).

	Graphene64 this work	Graphene256 this work	Graphene[10,13]	Graphite[13,14]
a(Å)	2.551	2.571	2.461	2.603
E_0(eV/atom)	-7.279	-7.300		
B_0(GPa)	130.000	130.000	700.000	33.800
B'	35.000	35.000	1.000	8.900
V_0(Å^3/atom)	19.987	20.088	6.076	35.120

The lattice constants are in good agreement with the measured [14] and calculated values [10, 13]. Although the bulk modulus is totally disagreeing with other calculations and experiments, it should also be noted that the model used here is a double layered structure (i.e graphene64 and graphene256), whereas calculations used a single sheet graphene. The vacuum distance of 15 Å used to minimized interactions between the models with their periodic images could also play a crucial role. Graphene64 and graphene256 equilibrium properties results are the similar.

4.2. Thermodynamics properties of a bilayer of graphene

Up to this point, ordinary temperature (300 K) properties of double layered models have been considered. Quantum mechanics effects are very important in understanding the thermodynamics

properties below the Debye temperature. Since the molecular dynamics method treats the motion of the atoms classically, we only consider the thermodynamics properties above the Debye temperature, where the quantum effect can be neglected [16]. The graphite Debye temperature of 2500 K along the a-axis has been considered [17].

4.3. Specific heat capacity and coefficient thermal expansion of bilayer of graphene 256 and 64 atoms

The specific heat capacity of a material represents the change in energy density E when the temperature changes by 1 K,

$$C_v = \frac{d\,U}{dT} \tag{9}$$

The specific heat and heat capacity are sometimes used interchangeably, with units of joules per kelvin mass, per unit volume, or per mole. The specific heat does not determine the thermal energy stored within a body only but also how quickly the body cools off or heats up [18].

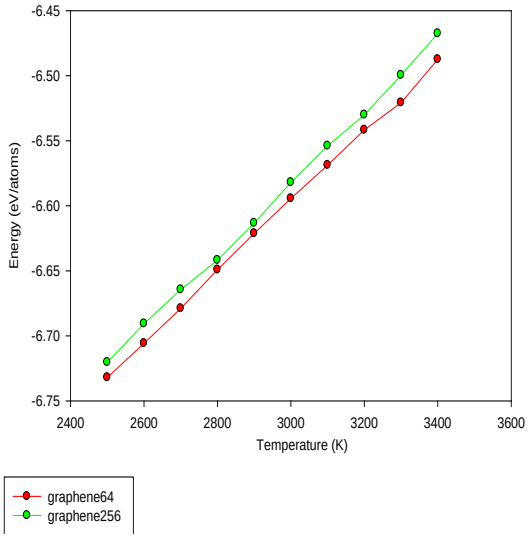

Figure 7. Energy as a function of temperature.

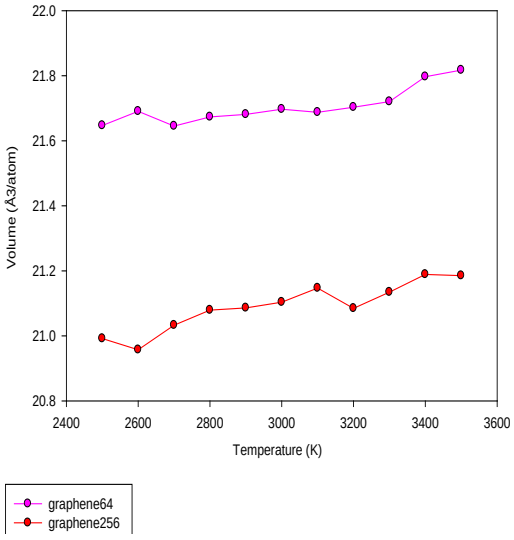

Figure 8. Volume as a function of temperature.

Figure 7 was used to calculate the specific heat capacitor of graphene 64 and graphene256. The specific heat capacity calculated for both systems is 3.42 k_B. This differs by 12% from the Dulong – Petit's law (3 k_B) of solids at high temperatures, although no experimental data on this has been considered. Zakharchenko et al [19] found out that the specific heat capacity of a single layer of graphene (SLG) and a bilayer of graphene (BLG) are similar and he also proves that the specific heat capacity at a high and low temperature are not the same. The specific heat of graphene has not been measured directly [20].

The coefficient of thermal expansion is one of the most important nonlinear thermal properties. It is obtained from the temperature derivative of lattice constant or temperature derivative of volume. This is given by:

$$\alpha = \frac{1}{V}\left(\frac{\partial V}{\partial T}\right)_P \tag{10}$$

The volumetric thermal expansion coefficient of graphene 64 and graphene 256 were calculated using fig 8. At a low temperature, the thermal expansion coefficient of graphene is expected to be negative and positive at high temperature [20, 19]. Most of the people who calculated thermal expansion coefficient at a low temperature used experimental method and those who calculated thermal expansion coefficient at a high temperature used the modelling method. Since our calculation was made at high temperature, we expect our thermal expansion to be positive. The thermal expansion

coefficient of graphene 64 atoms is 5.02×10^{-6} K^{-1} and for graphene 256 atoms is 9.76×10^{-6} K^{-1}. Both models have different thermal expansion coefficient but positive.

This is because the size effect thermodynamic properties [19,21]. Bao et al [21] calculated the coefficient of thermal expansion of graphene at a low temperature between 200 K -400 K using experimental method and found -7×10^{-6} K^{-1}. Jiang et al [21] calculated the coefficient of thermal expansion of graphene at a low temperature using nonequilibrium Green's function method; he got -6×10^{-6} K^{-1}. Zakharchenko et al [19] calculated the negative thermal expansion coefficient of single layer graphene and found the negative-to positive transition to occur at ~900 K.

5. Conclusion

Some of the structural properties are in agreement with the theoretical calculations and experimental data. This agreement shows the ability of Tersoff potential in combination with the molecular dynamics method, to predict the physical properties of various forms graphene. The bulk modulus is totally disagreeing with other calculations and experiments, it should also be noted that the model used here is a double layered structure whereas calculations used a single sheet graphene. The specific heat capacity of graphene64 and graphene256 is the same. The coefficient thermal expansion of both model are positive at a high temperature. Graphene256 is more stable than graphene64 because the minimum energy of Graphene256 is less than the one for graphene64.

References

[1] Meyer JC 2007 Nature Material 446 60
[2] Sarma SD 2011 Reviews of modern physics 83(2), 407
[3] Geim A K. and Novoselov KS 2007 Nature Materials 6 183
[4] Wang X, Zhi LX and Mullen K 2008 Nano Lett. 8 323
[5] Wang XR, Ouyang YJ, Li XL, Wang HL, Guo J and Dai HJ 2008 Phys. Rev. Lett. 100 206803
[6] Zhao JJ, Buldum A, Han J and Lu JP 2002 Nanotechnology 13, 195
[7] Schedin F 2007 Nature Material 6 652
[8] Liao L and Duan X 2010 Materials Science and Engineering R 70 354
[9] Neumann PL 2012 Nuclear Instruments and Methods in Physics Research B 282 130
[10] Reich S, Maultzsch J and Thomsen C 2002 Physical Review B 66 035412
[11] Tersoff J 1988 Physical Review B 27 6991
[12] Smith W, Forester TR and Todorov IT 2009, the DL_POLY 2 User Manual, STFC Daresbury Laboratory, Darebury, Warrington WA4 4AD Cheshire, UK
[13] Reich S, Thomsen C and Ordejón P 2002 Physical Review B 65 153407
[14] Hanfland M, Beister H and Syassen K 1989 Phys. Rev. B 39
[15] Mounet N and Marzari N 2005 Physical Review B 71 205214
[16] Moon WH, Son MS and Hwang HJ 2003, Physica 33 329
[17] Krumhansl J and Brooks H 1953, Journal of Physical Chemistry 21, 1663
[18] Pop E, Varshney V and Roy AK 2012, MRS Bulletin, Volume 37.1273
[19] Zakharchenko KV, Los JH, Katsnelson MI, Fasolino A 2010, Physical Review 81 235436
[20] Bao W, Miao F, Chen Z, Zhang H, Jang W, Dames C, and Lau CN 2009, Nat 4, 562
[21] Jiang J, Wang J, and Li B 2009, Physical Review B 80, 205429

First-principles calculations of the structural, electronic and optical properties of PdN and PdN_2

Mohammed S H Suleiman[1,2] **and Daniel P Joubert**[1]

School of Physics, University of the Witwatersrand, Johannesburg, South Africa
Department of Physics, Sudan University of Science and Technology, Khartoum, Sudan

E-mail: suleiman@aims.ac.za (M Suleiman)

Abstract. The atomic and electronic structures of PdN and PdN_2 were investigated using ab initio density-functional theory (DFT). We studied cohesive energy vs. volume data for a set of reported and hypothetical structures. Obtained data was fitted to a third-order Birch-Murnaghan equation of state (EOS) so as to identify the energetically most stable phases and to determine their equilibrium structural parameters. Electronic properties were investigated by calculating the band structure and the total and partial density of states (DOS). Some possible pressure-induced phase transitions were tested. To derive the frequency-dependent optical spectra (i.e. absorption coefficient, reflectivity, refractive index, and energy-loss), we performed GW_0 calculations within the random-phase approximation (RPA) to the dielectric tensor. Obtained results were compared with previous studies.

1. Introduction

In 2007, Crowhurst *et al.* [1] reported the synthesis of the new palladium nitride compound and argued for its PdN_2 stoichiometry and pyrite (C2) structure. However, many transition-metal nitrides are known to form more than one nitride [2], and first-principles methods are commonly employed to search for possible stable phases.

In this work, we consider PdN and PdN_2 stoichiometries in possible crystal structures. PdN is investigated in the following nine structures: NaCl (B1) structure, CsCl (B2) structure, the hexagonal structures of BN (B_k) and WC (B_h), wurtzite structure (B4), cooperite structure (B17), and the face-centered orthorhombic structure of TlF (B24); while PdN_2 is investigated in the following four structures: fluorite structure (C1), pyrite structure (C2), marcasite structure (C18), and the simple monoclinc structure of $CoSb_2$.

2. Electronic optimization details

Our electronic structure calculations were based on spin density functional theory (SDFT) [3, 4] within the projector augmented wave (PAW) method [5, 6] in which scalar kinematic relativistic effects are incorporated via mass-velocity and Darwin corrections in the construction of the pseudo-potentials, as implemented in VASP package [7, 8]. In solving Kohn-Sham (KS) equations [9]

$$\left\{ -\frac{\hbar^2}{2m_e}\nabla^2 + \int d\mathbf{r}' \frac{n(\mathbf{r}')}{|\mathbf{r}-\mathbf{r}'|} + V_{ext}(\mathbf{r}) + V_{XC}^{\sigma,\mathbf{k}}[n(\mathbf{r})] \right\} \psi_i^{\sigma,\mathbf{k}}(\mathbf{r}) = \epsilon_i^{\sigma,\mathbf{k}} \psi_i^{\sigma,\mathbf{k}}(\mathbf{r}), \quad (1)$$

the pseudo part of the KS one-electron spin orbitals $\psi_i^{\sigma,\mathbf{k}}(\mathbf{r})$ are expanded on a basis set of plane-waves (PWs) with energy cut-off $E_{cut} = 600$ eV. $\mathbf{\Gamma}$-centered Monkhorst-Pack meshes [10] were used to sample the first Brillouin zone (BZ), and the Perdew-Burke-Ernzerhof (PBE) parametrization [11] of the generalized gradient approximation (GGA) [12] was used for the exchange-correlation (XC) potentials. For static calculations of the total electronic energy and the density of states (DOS), partial occupancies were set using the tetrahedron method with Blöchl corrections, while in the geometry relaxation, the smearing method of Methfessel-Paxton (MP) was followed.

3. Equation of states and structural properties

To study the energy-volume $E(V)$ equation of state (EOS), and to determine the equilibrium parameters of each structure, we make isotropic variations of the cell volume while ions with free internal parameters were allowed to search for local minima on the Born-Oppenheimer potential hyper-surface [13], following the implemented conjugate-gradient (CG) algorithm, untill all Hellmann-Feynman force components [14] on each ion were smaller than $1 \times 10^{-2} eV/\mathring{A}$. The obtained cohesive energies E_{coh}, as a function of volume V per atom, were fitted to a Birch-Murnaghan 3rd-order EOS [15], and the equilibrium volume V_0, the equilibrium cohesive energy E_0, the equilibrium bulk modulus B_0 and its pressure derivative B_0' were determined by a least-squares method.

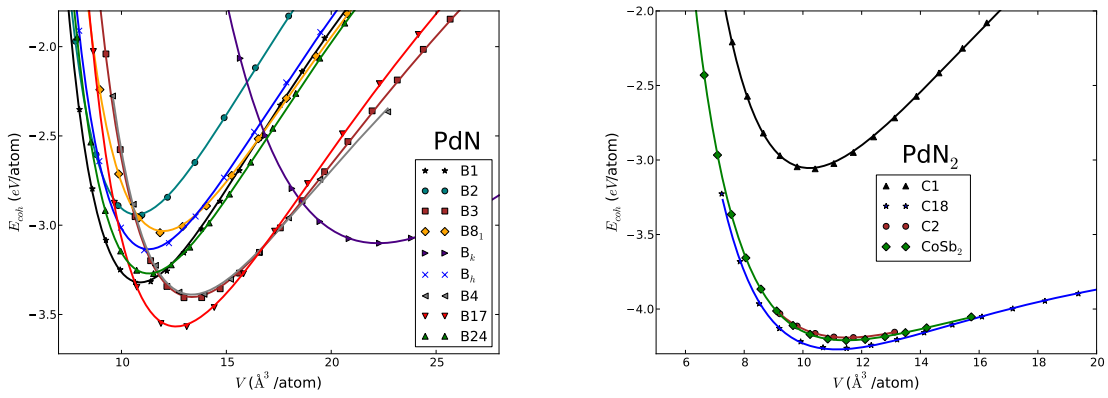

(a) (b)

Figure 1: (Color online.) Cohesive energy $E_{\rm coh}(eV/\text{atom})$ versus atomic volume V (Å^3/atom) for (a) PdN in nine different structural phases, and (b) for PdN_2 in four different structural phases.

In Fig. 1 we display the energy-volume EOS of all the studied structures, while in tabel 1, we present some of the obtained equilibrium structural parameters and compare them with some earlier theoretical calculations.

It is clear that the simple tetragonal structure of cooperite (B17) would be the energetically most stable phase of PdN (Fig. 1(a)). To the best of our knowledge, this structure has not been considered for PdN in any earlier work, though it was theoretically predicted to be the ground-state structure of platinum nitride[1] [20] in its experimentally reported stoichiometry PtN [21]. In Ref. [17] the $E(V)$ EOS for PdN in the B1, B2, B3 and B4 structures was studied. Within

[1] We also found it to be the most stable structure of CuN as well (to be reported elsewhere).

Table 1. Calculated equilibrium structural properties of some of the studied phases of PdN and PdN_2**:** Lattice constants ($a(\AA)$, $b(\AA)$, $c(\AA)$ and $\beta(^\circ)$), atomic volume $V_0(\AA^3/\text{atom})$, cohesive energy $E_{\text{coh}}(eV/\text{atom})$, bulk modulus B_0 (GPa) and its pressure derivative B_0'. The cited data are of previous DFT calculations.

Phase	a(Å)	b(Å)	c(Å)	$\beta(^\circ)$	V_0 (Å^3/atom)	$E_{\text{coh}}(eV/\text{atom})$	B_0 (GPa)	B_0'
PdN(B1)	4.444	–	–	–	10.97	3.325	207.7	4.98
	4.145 [16]	–	–	–	–	4.027 ± 0.15 [16]	–	–
	4.67 [17]	–	–	–	–	11.9 [17]	297.67 [17]	4.15 [17]
PdN(B4)	3.360	–	5.503	–	13.45	3.395	164.2	4.98
	3.37 [17]	–	5.26 [17]	–	–	11.43 [17]	171.34 [17]	4.63 [17]
PdN(B17)	3.061	–	5.389	–	12.62	3.579	190.4	4.99
PdN_2(C2)	5.169	–	–	–	11.51	4.192	69.3	5.4
	4.975 [18]	–	–	–	10.27 [18]	–	135 [18]	–
	4.843 [19]	–	–	–	18.887 [19]	–	156 [19]	9.48 [19]
PdN_2(C18)	3.173	4.164	5.082	–	11.19	4.264	76.6	6.1
	3.911 [18]	4.975 [18]	3.133 [18]	–	10.33 [18]	–	100 [18]	–
$PdN_2(CoSb_2)$	5.608	5.304	9.630	151.2	11.49	4.211	71.8	6.5
	5.071 [18]	5.005 [18]	5.071 [18]	–	10.43 [18]	–	93 [18]	–

this parameter sub-space, the relative stabilities arrived at in that work agree very well with ours. However, their obtained E_{coh} are more than twice the values we obtained, and the bulk moduli differ considerably!

In the studied parameter sub-space of PdN_2, the marcasite structure (C18) is the most energetically stable. The relative stability of C2 and $CoSb_2$ phases may be compared with Crowhurst *et al.* [1] who found PdN_2 in the baddeleyite structure (which is very close to $CoSb_2$ structure [22]) to be more stable than PdN_2(C2).

From a combined theoretical and experimental investigation, Åberg *et al.* [23] showed that for PdN_2(C2) both the electronic and the structural degrees of freedom have a strong pressure dependence. They claimed that the EOS cannot be accurately described within the GGA. Earlier calculations showed that PdN_2(C2) is very soft (see Ref. 22 in [1]). These two facts may explain the difficulty we found in relaxing this structure as well as they may explain the considerable differences found with and among the earlier reported structural properties.

4. Electronic properties

The DFT(GGA) calculated electronic band structures for PdN(B17) and PdN_2(C18) and their correponding total and partial DOS are displayed in Fig. 2 and Fig. 3, respectively. Both phases show clear metallic feature, though PdN_2(C18) has a very low TDOS around Fermi level E_F coming mainly from the d states of the Pd atoms.

5. Pressure-induced phase transitions

Enthalpy-pressure relations for PdN in some of the considered structures are displayed in Fig. 4. A point at which enthalpies $H = E_{coh}(V) + PV$ of two structures are equal defines the transition pressure P_t, where transition from the phase with higher enthalpy to the phase with lower enthalpy may occur.

Some possible transitions and the corresponding P_t's are depicted in Fig. 4. From both Fig. 1(a) and Fig. 4, it is clear that, in this parameter sub-space, B17 structure is prefered at pressures below ~ 25 GPa, while B1 structure, the most popular structure for transition-metal mono-nitrides, is favoured at higher pressures.

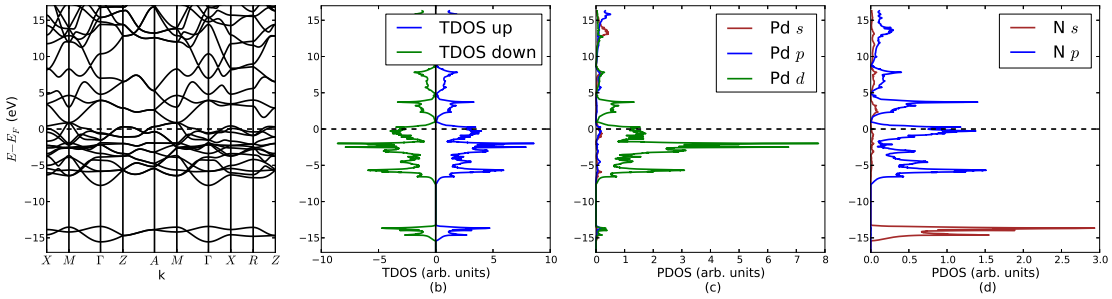

Figure 2: (Color online.) DFT calculated electronic structure for PdN in the B17 structure: **(a)** electronic band structure along the high-symmetry **k**-points, **(b)** spin-projected total density of states (TDOS); **(c)** partial density of states (PDOS) of Pd(s, p, d) orbitals in PdN; and **(d)** PDOS of N(s, p) orbitals in PdN.

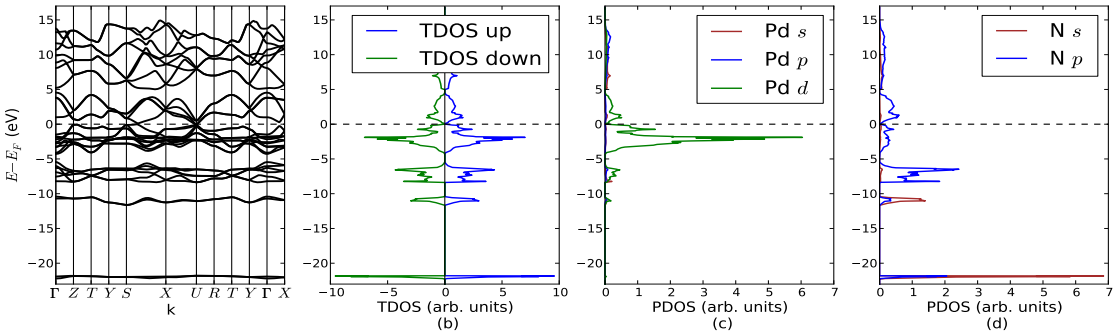

Figure 3: (Color online.) DFT calculated electronic structure for PdN_2 in the C18 structure: **(a)** electronic band structure along the high-symmetry **k**-points, **(b)** spin-projected total density of states (TDOS); **(c)** partial density of states (PDOS) of Pd(s, p, d) orbitals in PdN_2; and **(d)** PDOS of N(s, p) orbitals in PdN_2.

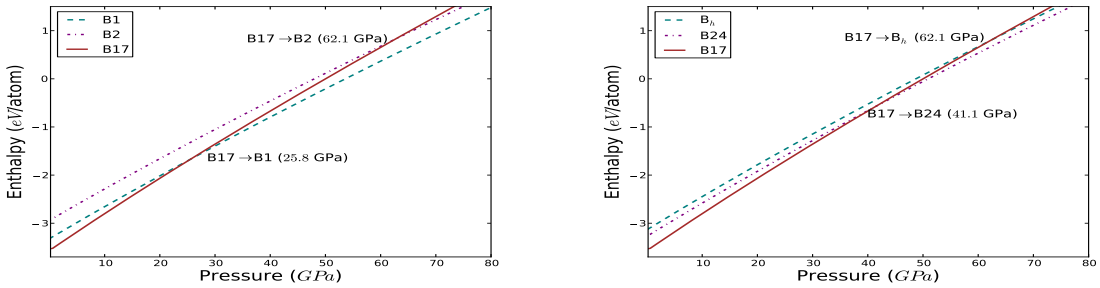

Figure 4: (Color online.) Enthalpy-pressure relations for some PdN phases in the phase transition pressure regions for the (a) B17→B1, B17→B2, (b) B17→B_h and B17→B24 phase transitions.

6. *GW* Calculations and Optical properties

In order to quantitatively improve the calculated electronic structure, and to investigate the optical spectra, we followed an alternative approach to DFT provided by many-body perturbation theory (MBPT), which leads to a system of quasi-particle (QP) equations [24]

$$\left\{ -\frac{\hbar^2}{2m}\nabla^2 + \int d\mathbf{r}' \frac{n(\mathbf{r}')}{|\mathbf{r}-\mathbf{r}'|} + V_{ext}(\mathbf{r}) \right\} \psi^{QP}_{i,\mathbf{k}}(\mathbf{r}) + \int d\mathbf{r}' \Sigma(\mathbf{r},\mathbf{r}';\epsilon^{QP}_{i,\mathbf{k}}) \psi^{QP}_{i,\mathbf{k}}(\mathbf{r}') = \epsilon^{QP}_{i,\mathbf{k}} \psi^{QP}_{i,\mathbf{k}}(\mathbf{r}). \quad (2)$$

To calculate the self-energy Σ, we followed the GW_0 self-consistent routine on the one particle's Green's function G within the random-phase approximation (RPA)[2] to the frequency-dependent dielectric tensor $\varepsilon(\omega)$. The obtained real $\varepsilon_{re}(\omega)$ and imaginary $\varepsilon_{im}(\omega)$ parts of $\varepsilon_{\mathrm{RPA}}(\omega)$ were used to derive the frequency-dependent absorption coefficient $\alpha(\omega)$, reflectivity $R(\omega)$, refractive index $n(\omega)$, and energy-loss spectrum $L(\omega)$:

$$\alpha(\omega) = \sqrt{2}\omega \left(\left[\varepsilon^2_{re}(\omega) + j\varepsilon^2_{im}(\omega) \right]^{\frac{1}{2}} - \varepsilon_{re}(\omega) \right)^{\frac{1}{2}} \quad (3)$$

$$R(\omega) = \left| \frac{\left[\varepsilon_{re}(\omega) + j\varepsilon_{im}(\omega) \right]^{\frac{1}{2}} - 1}{\left[\varepsilon_{re}(\omega) + j\varepsilon_{im}(\omega) \right]^{\frac{1}{2}} + 1} \right|^2 \quad (4)$$

$$n(\omega) = \frac{1}{\sqrt{2}} \left(\left[\varepsilon^2_{re}(\omega) + \varepsilon^2_{im}(\omega) \right]^{\frac{1}{2}} + \varepsilon_{re}(\omega) \right)^{\frac{1}{2}} \quad (5)$$

$$L(\omega) = \frac{\varepsilon_{im}(\omega)}{\varepsilon^2_{re}(\omega) + \varepsilon^2_{im}(\omega)} \quad (6)$$

Fig. 5 displays the real and the imaginary parts of $\varepsilon_{\mathrm{RPA}}(\omega)$ for PdN(B24) and the corresponding derived optical constants within the optical region. It is clear from the absorption coefficient $\alpha(\omega)$ spectrum (Fig. 5, low right) that GW_0 calculations show that B24 is a metallic phase of PdN.

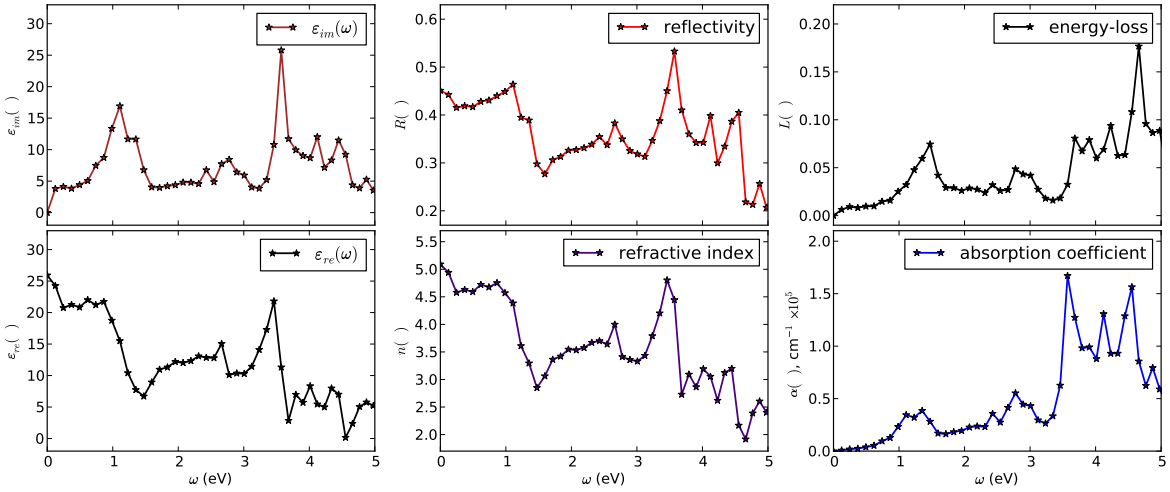

Figure 5: (Color online.) The real and the imaginary parts of the frequency-dependent dielectric function and the corresponding optical constants of PdN(B24).

[2] *c.f.* Ref.[25] and references there in

7. Conclusion

We have applied first-principles methods to investigate the structural, electronic and optical properties of some possible stoichiometries and crystal structures of palladium nitride. The considerable differences found with and among the earlier reported structural properties may invoke the need for deeper and more expensive investigation schemes such as in Ref. [23].

Acknowledgments

Suleiman would like to thank Dr. Mahlaga P. Molepo for carefully reading the manuscript and for giving valuable comments.

References

[1] Crowhurst J C, Goncharov A F, Sadigh B, Zaug J, Aberga D, Meng Y and Prakapenka V B 2008 *Journal of Materials Research* **23** 1 – 5 URL http://journals.cambridge.org/action/displayAbstract?fromPage=online&aid=7953263
[2] Wells A F 1984 *Structural Inorganic Chemistry* 5th ed (Oxford University Press)
[3] von Barth U and Hedin L 1972 *Journal of Physics C: Solid State Physics* **5** 1629–1642 URL http://iopscience.iop.org/0022-3719/5/13/012/
[4] Pant M and Rajagopal A 1972 *Solid State Communications* **10** 1157 – 1160 ISSN 0038-1098 URL http://www.sciencedirect.com/science/article/pii/0038109872909349
[5] Blöchl P E 1994 *Physical Review B* **50**(24) 17953–17979 URL http://link.aps.org/doi/10.1103/PhysRevB.50.17953
[6] Kresse G and Joubert D P 1999 *Physical Review B* **59**(3) 1758–1775 URL http://link.aps.org/doi/10.1103/PhysRevB.59.1758
[7] Kresse G and Hafner J 1993 *Physical Review B* **47**(1) 558–561 URL http://link.aps.org/doi/10.1103/PhysRevB.47.558
[8] Kresse G and Hafner J 1994 *Physical Review B* **49**(20) 14251–14269 URL http://link.aps.org/doi/10.1103/PhysRevB.49.14251
[9] Kohn W and Sham L J 1965 *Physical Review* **140**(4A) A1133–A1138 URL http://link.aps.org/doi/10.1103/PhysRev.140.A1133
[10] Monkhorst H J and Pack J D 1976 *Physical Review B* **13**(12) 5188–5192 URL http://link.aps.org/doi/10.1103/PhysRevB.13.5188
[11] Perdew J P, Burke K and Ernzerhof M 1996 *Physical Review Letters* **77**(18) 3865–3868 URL http://link.aps.org/doi/10.1103/PhysRevLett.77.3865
[12] Becke A D 1988 *Physical Review A* **38**(6) 3098–3100 URL http://link.aps.org/doi/10.1103/PhysRevA.38.3098
[13] Born M and Oppenheimer J R 1927 *Annalen der Physik* **84** 457–484
[14] Feynman R P 1939 *Physical Review* **56**(4) 340–343 URL http://link.aps.org/doi/10.1103/PhysRev.56.340
[15] Birch F 1947 *Physical Review* **71**(11) 809–824 URL http://link.aps.org/doi/10.1103/PhysRev.71.809
[16] Fernández Guillermet A, Häglund J and Grimvall G 1992 *Phys. Rev. B* **45**(20) 11557–11567 URL http://link.aps.org/doi/10.1103/PhysRevB.45.11557
[17] Deligoz E, Colakoglu K and Ciftci Y O 2010 *physica status solidi (b)* **247** 2155–2160 ISSN 1521-3951 URL http://dx.doi.org/10.1002/pssb.200945578
[18] Chen W, Tse J S and Jiang J Z 2010 *Journal of Physics: Condensed Matter* **22** 015404 URL http://stacks.iop.org/0953-8984/22/i=1/a=015404
[19] Wen-Jie Z and Yuan-Xu W 2009 *Chinese Physics B* **18** 3934 URL http://stacks.iop.org/1674-1056/18/i=9/a=053
[20] von Appen J, Lumey M W and Dronskowski R 2006 *Angewandte Chemie International Edition* **45** 4365–4368 ISSN 1521-3773 URL http://dx.doi.org/10.1002/anie.200600431
[21] Gregoryanz E, Sanloup C, Somayazulu M, Badro J, Fiquet G, kwang Mao H and Hemley R J 2004 *Nature Materials* **3** 294 – 297 URL http://www.nature.com/nmat/journal/v3/n5/full/nmat1115.html
[22] Friedrich A, Winkler B, Juarez-Arellano E A and Bayarjargal L 2011 *Materials* **4** 1648–1692 ISSN 1996-1944 URL http://www.mdpi.com/1996-1944/4/10/1648
[23] Åberg D, Erhart P, Crowhurst J, Zaug J M, Goncharov A F and Sadigh B 2010 *Phys. Rev. B* **82**(10) 104116 URL http://link.aps.org/doi/10.1103/PhysRevB.82.104116
[24] Kohanoff J 2006 *Electronic Structure Calculations for Solids and Molecules : Theory and Computational Methods* (Cambridge University Press; Cambridge)
[25] Aryasetiawan F and Gunnarsson O 1998 *Reports on Progress in Physics* **61** 237 URL http://stacks.iop.org/0034-4885/61/i=3/a=002

Efficiency of Open Quantum Walk implementation of the Dissipative Quantum Computing

Ilya Sinayskiy and Francesco Petruccione

National Institute for Theoretical Physics and Quantum Research Group, School of Chemistry and Physics, University of KwaZulu-Natal, Durban, South Africa

E-mail: sinayskiy@ukzn.ac.za

Abstract. A new type of quantum walk, exclusively based on dissipative dynamics is presented. An application of this open quantum walk for dissipative quantum computing is suggested. The approach is illustrated with the example of the phase estimation algorithm. It is explicitly demonstrated that open quantum walk based algorithms are more efficient than the traditional dissipative quantum computing approach. In particular, the open quantum walks can be designed to converge faster to the desired steady state and to increase the probability of detection of the outcome of the computation.

In the description of experimentally realizable quantum systems one should always include the unavoidable effect of the interaction with a dissipative and decoherent environment [**?**]. For most applications, the influence of decoherence and dissipation on the reduced systems needs to be eliminated or at least minimized. However, it was shown recently that the interaction with the environment not only can create complex entangled states [**?**, **?**, **?**, **?**, **?**, **?**], but also allows for universal quantum computation [**?**]. Recently, a framework for discrete time open quantum walks (OQW) on graphs was proposed [**?**, **?**], which is based upon exclusively dissipative dynamics. This framework is formulated as discrete time implementation of the special Kraus representation of completely positive maps. It was already demonstrated with the example of the Toffoli gate and the Quantum Fourier Transform with 3 and 4 qubits that the open quantum walk implementation of the corresponding algorithms outperforms the dissipative quantum computing model (DQC) [**?**]. In this work we will revise the open quantum walk implementation of a dissipative quantum computing model and with the example of the phase estimation algorithm we will demonstrate the outperformance of the corresponding OQW implementation of the DQC.

The open quantum random walks are formulated as walks on the set of nodes $\mathcal{V}$. The number of nodes is considered to be finite or countable infinite. The Hilbert space of the positions of the walker on the graph is denoted by $\mathcal{K}$ and the set of linearly independent orthonormal vectors $|i\rangle \in \mathcal{K}$ denotes basis. The internal degrees of freedom of the quantum walker, e.g. the spin or n-energy levels, will be described by a separable Hilbert space $\mathcal{H}$ attached to each node of the graph. So that any state of the walker is described by the density operator from the Hilbert space which is a direct product of the Hilbert spaces $\mathcal{H} \otimes \mathcal{K}$.

The transition in the internal degree of freedom of the walker due to the shift from node j

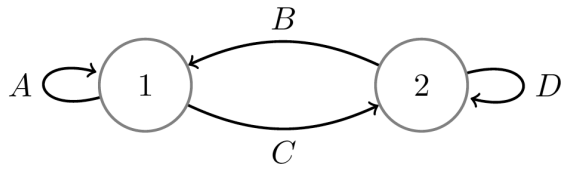

Figure 1. Schematic illustration of a walk on a two-node network, as the simplest non-trivial example of the OQW on the finite graph.

to node i is described by the bounded operator $B_j^i \in \mathcal{H}$. By imposing for each j that,

$$\sum_i B_j^{i\dagger} B_j^i = I, \tag{1}$$

we make sure, that for each node of the graph $j \in \mathcal{V}$ there is a corresponding completely positive map on the positive operators of $\mathcal{H}$: $\mathcal{M}_j(\tau) = \sum_i B_j^i \tau B_j^{i\dagger}$. However, the operators B_j^i act only on $\mathcal{H}$ wherefore we can introduce an operator $M_j^i \in \mathcal{H} \otimes \mathcal{K}$, as $M_j^i = B_j^i \otimes |i\rangle\langle j|$. It is shown that, if the condition expressed in Eq. (**??**) is satisfied, then $\sum_{i,j} M_j^{i\dagger} M_j^i = 1$. This latter condition defines a CP-map for density matrices on $\mathcal{H} \otimes \mathcal{K}$, i.e.,

$$\mathcal{M}(\rho) = \sum_i \sum_j M_j^i \, \rho \, M_j^{i\dagger}. \tag{2}$$

The above map defines the discrete time *open quantum walk* (OQW). It is shown [**?**] that for an arbitrary initial state, the density matrix $\sum_{i,j} \rho_{i,j} \otimes |i\rangle\langle j|$ will take a diagonal form after just one step of the open quantum walk. Hence, we will assume that the initial state of the system has the form $\rho = \sum_i \rho_i \otimes |i\rangle\langle i|$, with $\sum_i \mathrm{Tr}[\rho_i] = 1$. One can easy get an explicit formula for the iteration of the OQW from step n to step $n+1$: $\rho^{[n+1]} = \mathcal{M}(\rho^{[n]}) = \sum_i \rho_i^{[n+1]} \otimes |i\rangle\langle i|$, where $\rho_i^{[n+1]} = \sum_j B_j^i \rho_j^{[n]} B_j^{i\dagger}$. Generic properties of OQWs have been discussed in [**?**, **?**].

As an illustration of the application of the formalism of OQWs, we consider the walk on a 2-node graph (see Fig. 1). In this case for each node we have:

$$A^\dagger A + C^\dagger C = I, \quad B^\dagger B + D^\dagger D = I. \tag{3}$$

The iteration formula in this case reads,

$$\rho^{[n]} = \rho_1^{[n]} \otimes |1\rangle\langle 1| + \rho_2^{[n]} \otimes |2\rangle\langle 2|, \tag{4}$$

where the particular form of the $\rho_i^{[n]}$ $(i = 1, 2)$ is given by,

$$\begin{aligned} \rho_1^{[n]} &= A\rho_1^{[n-1]} A^\dagger + B\rho_2^{[n-1]} B^\dagger, \\ \rho_2^{[n]} &= D\rho_1^{[n-1]} D^\dagger + C\rho_2^{[n-1]} C^\dagger. \end{aligned} \tag{5}$$

Recently, Verstraete *et al.* [**?**] proposed a new model of quantum computation, based on dissipation, capable of performing universal quantum computation. The dissipative quantum

computing setup consists of a linear chain of time registers. Initially, the system is in a time register labeled by 0. The result of the computation is measured in the last time register labeled by T. Neighboring time registers are coupled to local baths. The result of the computation can be read out from the time-register T. In particular, for a quantum circuit given by the set of unitary operators $\{U_t\}_{t=1}^{T}$ the final state of the system is given by $|\psi_T\rangle = U_T U_{T-1} \dots U_2 U_1 |\psi_0\rangle$. It is shown that the unique steady state of the system in this case will be

$$\rho = \frac{1}{T+1} \sum_t |\psi_t\rangle\langle\psi_t| \otimes |t\rangle\langle t|. \tag{6}$$

Recently, it was shown that, using the formalism of OQWs one can perform dissipative quantum computations with higher efficiency. The explicit open quantum walk implementation of the Toffoli gate and the Quantum Fourier Transform has been reported [**?**]. If one needs to implement a circuit with the set of unitaries so that initial and final states are connected as $|\psi_T\rangle = U_T U_{T-1} \dots U_2 U_1 |\psi_0\rangle$, then the corresponding OQW implementation will be given by a linear chain of $T+1$ nodes with corresponding iteration formula:

$$\rho_j^{[n]} = \omega U_j \rho_{j-1}^{[n-1]} U_j^\dagger + \lambda U_{j+1}^\dagger \rho_{j+1}^{[n-1]} U_{j+1}, \quad j = 1 \dots (T-1), \tag{7}$$

$$\rho_0^{[n]} = \lambda \rho_0^{[n-1]} + \lambda U_1^\dagger \rho_1^{[n-1]} U_1, \tag{8}$$

$$\rho_T^{[n]} = \omega \rho_T^{[n-1]} + \omega U_{T-1} \rho_{T-1}^{[n-1]} U_{T-1}^\dagger, \tag{9}$$

where constants ω and λ are positive constants such that $\omega + \lambda = 1$.

In this case the unique steady state of the OQW will have the following form,

$$\rho_{SS} = \sum_{i=0}^{T} p_i |\psi_i\rangle\langle\psi_i|, \tag{10}$$

where p_i denote the steady state probabilities of detecting the walker at the node i. In the case of $\omega = \lambda$ all probabilities of detection will be the same, namely $p_i = 1/(T+1)$. In the case $\omega > \lambda$, the probability of detection of the walker at site T will be bounded between $1/(T+1) < p_T < 1$.

As an illustration of the OQW implementation of the quantum computing model, let us consider the quantum phase estimation algorithm with an unknown unitary operator on a one qubit Hilbert space, and 3 qubits as detection registers [**?**]. The algorithm consists of three steps: first a Hadamard operation on the measuring qubits (one unitary operation); second the application of conditional shifts with unknown unitary operator (3 unitary operators), and the last step is the inverse Quantum Fourier Transform on the three measuring qubits (9 unitary operations). In total we need to implement 13 unitary operations, this means that the OQW implementation will consist of 14 nodes $(0 \dots 13)$ with readout in the last node 13. The simulation of the OQW implementation of this algorithm is shown in Fig. 2. As in the case of the OQW implementation of the Toffoli gate and the Quantum Fourier Transform [**?**] the probability of successful readout grows together with the parameter ω.

We have briefly reviewed the formalism of open quantum walks on graphs and of dissipative quantum computing. With the help of the quantum phase estimation algorithm we have shown that the open quantum walk approach outperforms the original dissipative quantum computing model. By increasing the probability of forward propagation in the "time registers" in the transition operators of the open quantum walk we can increase the probability of the successful computation result detection and decrease the number of steps of the walk which is required to reach the steady state.

This work is based upon research supported by the South African Research Chair Initiative of the Department of Science and Technology and National Research Foundation.

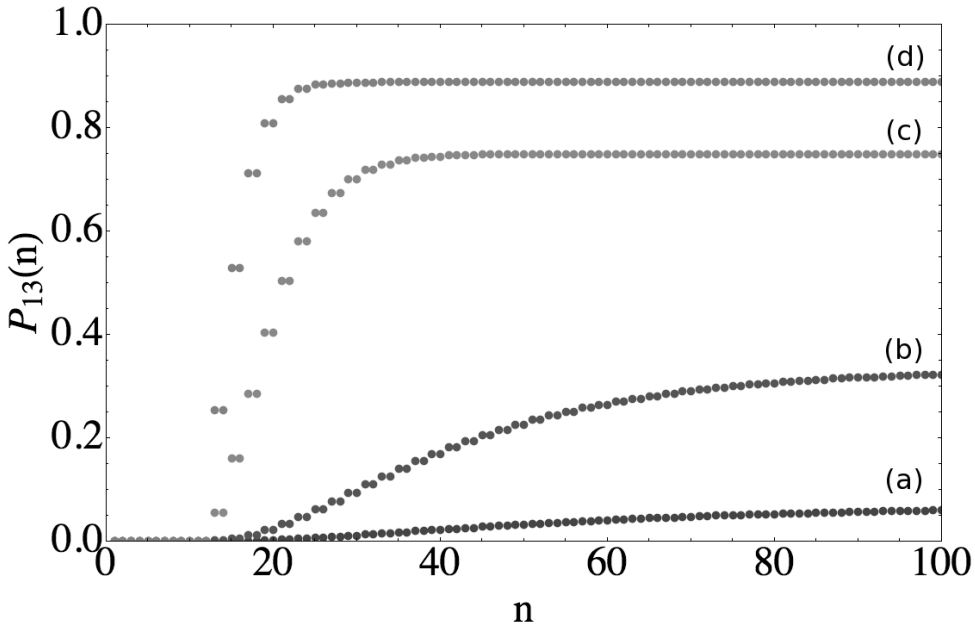

Figure 2. The dynamics of the detection probability in the final node 13 as function of the number of steps of the OQW in the implementation of the quantum phase estimation algorithm. Curves (a) to (d) correspond to different values of the parameter $\omega = 0.5, 0.6, 0.8, 0.9$, respectively.

References

[1] Breuer H-P and Petruccione F 2002 *The Theory of Open Quantum Systems* (Oxford: Oxford University Press)
[2] Diehl S, Micheli A, Kantian A, Kraus B, Büchler HP and Zoller P 2008 *Nature Phys* **4** 878
[3] Vacanti G and Beige A 2009 *New J Phys* **11** 083008
[4] Kraus B, Büchler HP, Diehl S, Kantian A, Micheli A and Zoller P 2008 *Phys Rev A***78** 042307
[5] Kastoryano MJ, Reiter F, and Sørensen AS 2011 *Phys Rev Lett* **106** 090502
[6] Sinaysky I, Petruccione F and Burgarth D 2008 *Phys Rev A***78** 062301
[7] Pumulo N, Sinayskiy I and Petruccione F 2011 *Phys Lett A* V**375** Issue 36 3157
[8] Verstraete F, Wolf MM and Cirac JI 2009 *Nature Phys* **5** 633
[9] Attal S, Petruccione F, Sabot C and Sinayskiy I, 2012 *J Stat Phys* Vol **147** 4 832
[10] Attal S, Petruccione F and Sinasykiy I, 2012 *Phys Lett A* V**376** 18 1545
[11] Sinayskiy I and Petruccione F 2012 *Quantum Inf Proc* V**11** Issue 5 1301
[12] Nielsen MA and Chuang IL 2000 *Quantum Computation and Quantum Information* (Cambridge: Cambridge University Press)